JOURNAL
OF THE
PHYSICAL SOCIETY
OF JAPAN

Being a continuation of
"Proceeding of the Physico-Mathematical Society of Japan"

Volume 6 – 7
1951 -52

Published by the
PHYSICAL SOCIETY OF JAPAN

Numerical Tables for the Phase and Intensity Measurements of Metalic Film (I)

By Kōzō Ishiguro

Department of Physics, University of Tokyo.

(Received March 23, 1950)

§ 1. Introduction.

In the optical investigations of metalic films, it is aimed to determine the refractive index and the thickness of the films from the measurements of transmission, reflection and rate of phase shift,(3) and it requires very troublesome calculations. Calculation in the reverse direction, namely the determination of the transmission etc. when the refractive index and the thickness are given, can be done more easily.(1)(4) In the present paper, it is intended to present tables and graphs of transmission, reflection and the rate of phase shift for the normal incidence and also for the oblique incident angle 70° in the index region which would be convieniently used for the measurements with silver films.

§ 2. Calculation.

According to the usual treatment, it is assumed that a uniform plane parallel metalic film is formed on a glass surface and a plane wave light falls from the air side. The fundamental equations for transmission and reflection are solved under such assumption by Murman,(1) Wolter,(2) etc.(4) It is convenient to start with the equations used by Wolter. But not using approximate formulas as Wolter, the exact numerical calculation will be made not only for the transmission and reflection but also for the rate of phase shift.

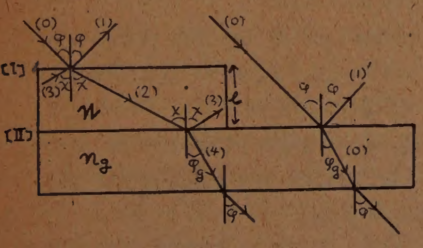

Fig. 1.

Following usual expression, the light wave is written in the form

$$E = E_0 \exp i(\omega t - \delta)$$

Generally at the boundary of two mediums (*a*) and (*b*), there exist

$$H_{//}^{(a)} = H_{//}^{(b)}$$
$$E_{//}^{(a)} = E_{//}^{(b)} \quad \ldots\ldots\ldots\ldots\ldots\ldots (1)$$

and
$$H = nE$$

These conditions are applied for the boundary [I] and [II] in Fig. 1. To indicate the palarization, the direction of magnetic vector will be adopted.

Thus, when the magnetic vector *H* oscillates perpendiculary (senkrecht) and parallel to the plane of incidence, it is denoted by the suffiix *s* and *p* respectively.

Now appling (1) for the perpendicularly and parallel polarized light for thin film as in Fig. 1, the following solutions are obtained.

$$\left.\begin{aligned} (H_p^{(4)} e^{-y}) / H_p^{(0)} &= 4 n_g / P \\ (H_s^{(4)} e^{-y}) / H_s^{(0)} &= 4 n_g / S \end{aligned}\right\} \quad \ldots\ldots\ldots\ldots (2)$$

where

$$\begin{aligned} P &= (1 + f n_g)(e^x + e^{-x}) - (X + iL / \cos\varphi) \\ &\qquad [(e^x - e^{-x}) / (\mathfrak{n} \cos\chi)] \\ S &= (f + n_g)(e^x + e^{-x}) - (Y + iLZ) \\ &\qquad [(e^x - e^{-x}) / (\mathfrak{n} \cos\chi)] \end{aligned} \quad \ldots\ldots\ldots\ldots (3)$$

and

$$\left\{\begin{aligned} x &= i(\omega l / c)\, \mathfrak{n} \cos\chi \\ y &= i(\omega l / c) \cos\varphi \\ \omega l / c &= 2\pi l / \lambda \\ \mathfrak{n} &= n - ik \\ &= \text{the complex refractive index of film} \end{aligned}\right. \quad \ldots\ldots\ldots\ldots\ldots\ldots (4)$$

$$\left\{\begin{array}{l} f = \cos\varphi_g / \cos\varphi \\ X = A/\cos\varphi - (1+fn_g)\cos\varphi \\ Y = Af\cos\phi - Bn_g\sin^2\varphi/\cos\varphi - (f+n_g)\cos\varphi \\ Z = f\cos\varphi + \{(B-1)/(A-1)\}n_g\sin^2\varphi/\cos\varphi \\ L = 2nk \end{array}\right. \quad \cdots\cdots\cdots\cdots(5)$$

$$\left\{\begin{array}{l} A-1 = k^2-n^2 \\ (B-1)/(A-1) = 1/(k^2+n^2)^2 = 1/\{(A-1)^2+L^2\} \end{array}\right. \quad \cdots\cdots(6)$$

In the case of $|x| \leqslant 1$, the following equations will be the fairly good approximations

$$e^x+e^{-x} \approx 2+(\omega l/c)^2(A-1)+i(\omega l/c)^2 L$$

$$(e^x-e^{-x})/(n\cos\chi) \approx i2(\omega l/c)$$

The values of f become for $n_g = 1.517$

φ	$\cos\varphi$	f
0	1.000	1.000
70	0.342	2.295

When P or S are written in the form $R+iI$, knowing the numerical values of n, k, $\omega l/c$, we get from (2)

$$H^{(4)}/H^{(0)} = |H^{(4)}/H^{(0)}|\exp(i\delta)$$

$$\delta = (2\pi/\lambda)\tau = (\omega l/c)\cos\varphi - i\,\mathrm{tg}^{-1}(I/R)$$

Putting $\tau/\lambda = \Delta$, $2\pi\Delta$ is the advanced phase in the metal film relative to the air layer of the equal thickness.

From (2), transmission for $\varphi = 0$ is given by

$$T_0 = (1/n_g)\left|H^{(4)}/H^{(0)}\right|^2_{\varphi=0} = (16n_g)/(P_0P_0^*)$$

where P_0 means the P value for $\varphi = 0$.

The more convenient quantity for the observations, the relative transmission is defined by

$$T_r = \left|H^{(4)}/H^{(0)\prime}\right|^2_{\varphi=0}$$

By the analogous calculations the (absolute) reflection for $\varphi = 0$ is given by

$$R_0 = \left|H^{(1)}/H^{(0)}\right|^2_{\varphi=0}$$

$$= \left|-1+(2Q_0P_0^*)/(P_0P_0^*)\right|^2$$

where

$$Q_0 = \left\{(e^x+e^{-x}) + n_g[(e^x-e^{-x})/(n\cos\chi)]\right\}_{\varphi=0}$$

§ 3. The notations in the graphs and tables.

The notations are the same as in § 2 and will be briefly explained for the sake of convenience.

Δ_0, Δ_{70P}, Δ_{70S}

Δ is the relative decrease of the optical path length in the film compared to the equal thickness of air layer and represented in the tables in permillage to the decrease of one wave length and Δ_0 means the value for the normal incidence and Δ_{70P}, Δ_{70S} means the value for the oblique incidence of angle 70° where suffixes P, S indicate that the magnetic vector of the incident light oscillates respectively in the incident plane and perpendicularly (senkrecht) to it.

The advancing of the phase in radian is given by

$$\delta = 2\pi\Delta = (2\pi/\lambda)\tau$$

For examples, when $\delta = +\pi/2$ or $\tau = +\lambda/4$ namely in the case of the advancement of the phase of $\lambda/4$, it is shown that

$$\Delta = +(1/4)\times 10^3 = +250$$

and in the case $\delta = -(\lambda/50)$ or $\tau = -(\lambda/100)$ it becomes $\quad \Delta = -10$

T_r: the relative transmission for the incident angle $\varphi = 0$ namely the percentage intensity ratio of the light transmitted through the glass plate with film to the light transmitted through the bare glass plate

T_0: the (absolute) transmission for $\varphi = 0$ — the intensity ratio in percentage of the transmitted light to the incidented light. The relation between T_0 and T_r is given by

$$T_0 = T_r\{4n_g/(1+n_g)^2\} \approx T_r/1.042$$

R_0: the (absolute) reflection — the intensity ratio percentage of the reflected light to the incidented light

The energy loss by the film is given by

$$A_0 = 100-(R_0+T_0) = 100-(R_0+[4n_g/(1+n_g)^2]T_r)$$

l = film thickness

λ = wave length of incidented light

$n-ik$ = refractive index of the film

$\omega l/c = (2\pi/\lambda)l$

	l (Å)				
$\omega l/c$ \ $\lambda(m\mu)$	0.1	0.2	0.3	0.4	0.5
700	111	222	334	446	556
590	94	188	282	376	469
500	79	159	238	318	398

Finally in the tables, the refractive index n_g of glass is assumed to be $n_g = 1.517$. But the change of 0.1 in n_g will affect for the value of Δ, T_r only about in the order of ± 1 even in the most unfavorable cases, as is pointed out by Murman.(1)

§ 4. The method of application.

To get the value of l, n, k from the observed values of Δ_0, Δ_{70P}, Δ_{70S}, T_r, R_0 we first seek in the tables the values of $\omega l/c$, n, k for which these quantities lie the nearest to the observed ones as a whole. We get then the following interpolating equations

$$\begin{aligned}
&\Delta_0+\left(\frac{\partial \Delta_0}{\partial h}\right)\delta h+\left(\frac{\partial \Delta_0}{\partial n}\right)\delta n+\left(\frac{\partial \Delta_0}{\partial k}\right)\delta k=\Delta_0 \text{ (obs.)}\\
&\Delta_P+\left(\frac{\partial \Delta_P}{\partial h}\right)\delta h+\left(\frac{\partial \Delta_P}{\partial n}\right)\delta n+\left(\frac{\partial \Delta_P}{\partial k}\right)\delta k=\Delta_P \text{ (,,)}\\
&\Delta_S+\left(\frac{\partial \Delta_S}{\partial h}\right)\delta h+\left(\frac{\partial \Delta_S}{\partial n}\right)\delta n+\left(\frac{\partial \Delta_S}{\partial k}\right)\delta k=\Delta_S \text{ (,,)}\\
&T_r+\left(\frac{\partial T_r}{\partial h}\right)\delta h+\left(\frac{\partial T_r}{\partial n}\right)\delta n+\left(\frac{\partial T_r}{\partial k}\right)\delta k=T_r \text{ (,,)}\\
&R_0+\left(\frac{\partial R_0}{\partial h}\right)\delta h+\left(\frac{\partial R_0}{\partial n}\right)\delta n+\left(\frac{\partial R_0}{\partial k}\right)\delta k=R_0 \text{ (,,)}
\end{aligned}
\qquad \ldots\ldots\ldots\ldots\ldots(7)$$

where Δ_0, Δ_P, Δ_S, T_r, R_0 on the left-hand side are those given by the tables, and the coefficients $\frac{\partial \Delta_0}{\partial h}$ etc. are also obtained from the tables, h being $h = 10\,(\omega l/c)$

From these equations δh, δn, δk are calculated in the same way as by the ordinary method of least squares. The required values are then

$$\omega l/c + 0.1\,\delta h,\quad n+\delta n,\quad k+\delta k$$

Of course it is very questionable to apply the method of least squares to the equations (7). It is assumed that the errors in Δ_0, Δ_{70P}, Δ_{70S}, T_r, R_0 are of equal weights, if they are expressed in the units used in the tables (percentage for intensity, permillage for phase shift), so that the simple sum of the squared errors is required to be minimum.

The example of such treatment will be seen in the following paper.(5)

References.

(1) H. Murman: Z. Phys. **80** (1933) 161.
(2) H. Wolter: Z. Phys. **105** (1937) 269.
(3) K. Ishiguro: J. Phys. Soc. Jap. **5** (1950) 187.
(4) Dennison-Hadley: J. O. S. A. **38** (1948) 483.
(5) J. Phys. Soc. Jap: **6** (1951) No. 2 (Now in press)

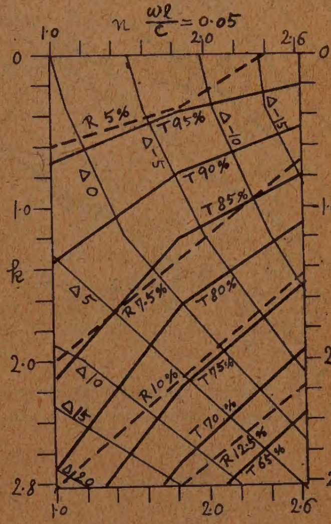

Fig. 2.

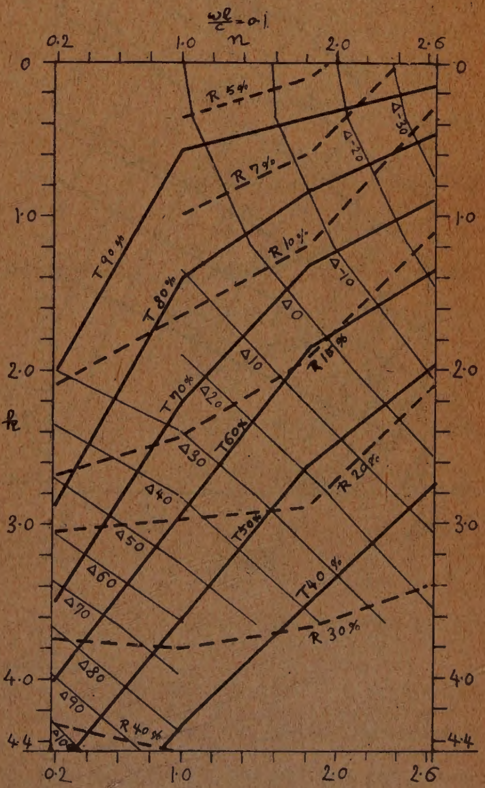

Fig. 3.

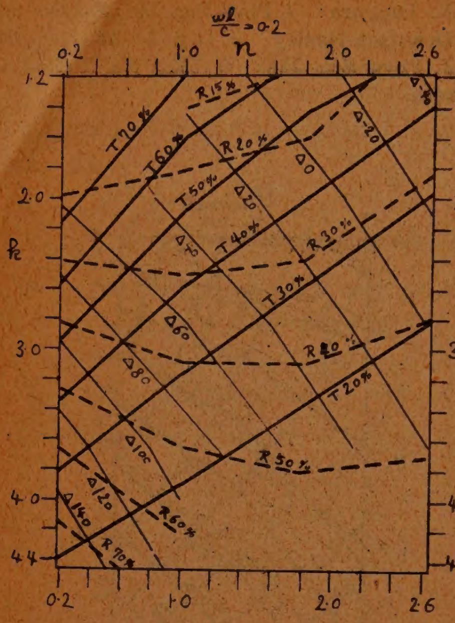

Fig. 4.

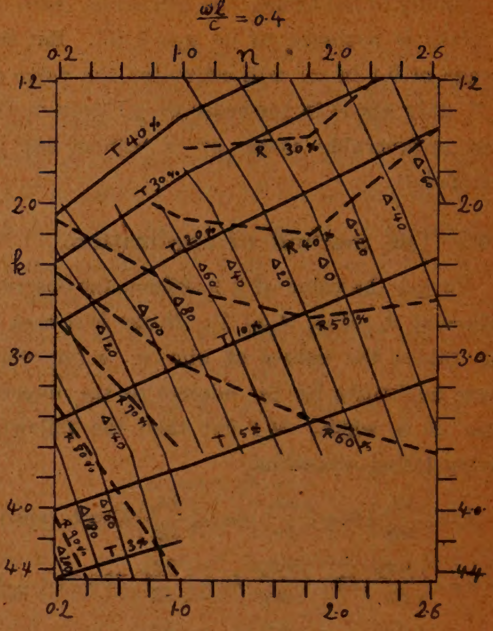

Fig. 6.

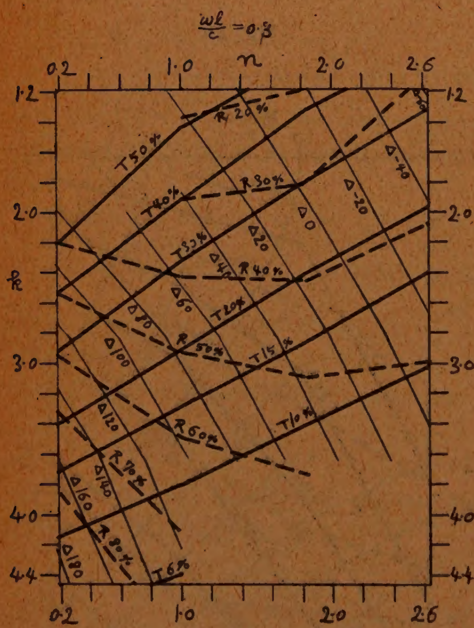

Fig. 5.

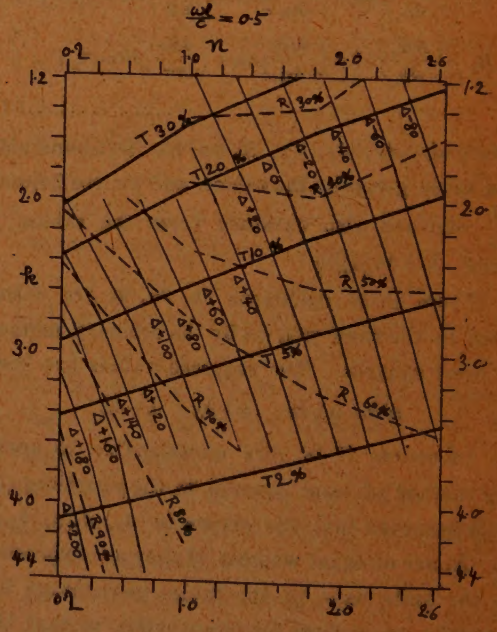

Fig. 7.

Numerical Tables for the Phase and Intensity Measurements of Metalic Film (II)

By Kōzō Ishiguro.

Department of Physics, University of Tokyo.

(Received March 23, 1950)

$$\frac{\omega l}{c} = 0.05$$

$k \diagdown n$		0.18	0.59	1.00	1.41	1.82	2.23	2.64	3.05	3.46
0	Δ_0			0	−4	−8	−14	−19	−27	−34
	Δ_{70P}			0	−6	−12	−21	−31	−43	−55
	Δ_{70S}			0	−5	−10	−14	−17	−22	−26
	T_r			100	100	100	99.5	98.9	97.6	96.2
	R_0			4.2	4.2	4.2	4.8	5.3	6.7	8.0
0.36	Δ_0			1	−4	−7	−13	−18	−26	−33
	Δ_{70P}			1	−5	−11	−19	−29	−39	−49
	Δ_{70S}			−2	−6	−10	−14	−17	−21	−25
	T_r			96.9	95.9	94.8	93.2	91.6	89.6	87.6
	R_0			4.6	4.9	5.0	5.8	6.4	7.9	9.3
0.77	Δ_0			3	−2	−5	−10	−16	−23	−30
	Δ_{70P}			4	−2	−8	−16	−25	−35	−44
	Δ_{70S}			−5	−7	−10	−13	−16	−20	−24
	T_r			93.5	91.8	90.0	87.3	84.5	82.0	79.4
	R_0			5.4	5.7	5.9	6.9	7.8	9.2	10.5
1.18	Δ_0			4	1	−3	−8	−13	−20	−26
	Δ_{70P}			6	1	−5	−13	−20	−30	−39
	Δ_{70S}			−7	−8	−9	−12	−15	−19	−23
	T_r			90.7	87.7	84.6	81.6	78.5	75.4	72.3
	R_0			6.1	6.6	7.1	8.1	9.1	10.5	11.9
1.59	Δ_0			8	4	1	−5	−10	−16	−22
	Δ_{70P}			11	6	0	−7	−15	−24	−33
	Δ_{70S}			−5	−7	−9	−12	−14	−18	−21
	T_r			88.6	83.9	79.1	76.2	73.3	69.7	66.1
	R_0			6.7	7.6	8.4	9.4	10.4	11.9	13.4
2.00	Δ_0			11	8	4	−1	−6	−12	−18
	Δ_{70P}			16	10	5	−2	−9	−18	−26
	Δ_{70S}			−4	−6	−7	−10	−12	−16	−19
	T_r			85.4	80.9	76.3	72.5	68.6	64.7	60.7
	R_0			7.8	9.0	10.1	11.0	11.8	13.4	15.0
2.41	Δ_0			17	14	10	5	−1	−7	−13
	Δ_{70P}			25	19	13	6	−2	−11	−19
	Δ_{70S}			−1	−3	−4	−7	−9	−13	−17
	T_r			82.9	76.7	70.4	67.2	64.0	60.0	55.9
	R_0			8.7	10.0	11.2	12.3	13.3	15.0	16.7
2.82	Δ_0			22	19	15	10	4	−2	−7
	Δ_{70P}			34	28	21	14	6	−3	−11
	Δ_{70S}			3	1	−1	−4	−6	−10	−14
	T_r			79.1	73.7	68.2	63.8	59.3	55.5	51.7
	R_0			10.2	11.4	12.5	13.7	14.9	16.7	18.4
3.23	Δ_0			29						
	Δ_{70P}			44						
	Δ_{70S}			7						
	T_r			75.6						
	R_0			12.1						
3.64	Δ_0	43	40	39						
	Δ_{70P}	66	60	53						
	Δ_{70S}	14	13	11						
	T_r	87.8	80.0	72.1						
	R_0	12.2	13.3	14.4						

$$\frac{\omega l}{c} = 0.1$$

$k \diagdown n$		0.18	0.59	1.00	1.41	1.82	2.23	2.64	3.05	3.46
0	Δ_0			0	−8	−15	−27	−38	−53	−67
	Δ_{70P}			0	−12	−24	−42	−60	−81	−102
	Δ_{70S}			0	−10	−19	−26	−34	−43	−52
	T_r			100	99.8	99.5	97.5	95.5	90.4	85.2
	R_0			4.2	4.4	4.6	6.5	8.4	13.2	18.0
0.36	Δ_0			1	−7	−14	−25	−35	−48	−61
	Δ_{70P}			2	−10	−22	−38	−54	−72	−90
	Δ_{70P}			−4	−12	−19	−27	−34	−42	−50
	T_r			94.1	92.1	90.0	86.5	83.0	77.8	72.6
	R_0			5.0	5.6	6.1	8.2	10.2	14.4	18.6
0.77	Δ_0			5	−3	−10	−20	−30	−42	−54
	Δ_{70P}			7	−4	−16	−31	−45	−62	−78
	Δ_{70S}			−9	−14	−19	−26	−33	−40	−48
	T_r			88.5	85.2	81.8	77.0	72.1	66.9	61.7
	R_0			6.3	6.9	7.5	10.5	13.4	16.7	19.9
1.18	Δ_0			8	1	−6	−15	−24	−35	−46
	Δ_{70P}			12	2	−9	−23	−36	−51	−65
	Δ_{70S}			−13	−16	−19	−25	−31	−38	−45
	T_r			83.0	78.1	73.2	68.2	63.1	58.0	52.9
	R_0			7.8	8.9	10.0	12.8	15.6	18.6	21.5
1.59	Δ_0			15	8	1	−9	−18	−28	−38
	Δ_{70P}			22	11	0	−14	−26	−39	−52
	Δ_{70S}			−10	−14	−17	−23	−28	−35	−42
	T_r			77.7	70.9	64.0	59.9	55.8	50.9	45.9
	R_0			9.5	11.7	13.9	15.5	17.0	20.2	23.4
2.00	Δ_0	30	26	22	15	7	−2	−11	−21	−30
	Δ_{70P}	47	39	31	20	9	−4	−16	−27	−38
	Δ_{70S}	−4	−6	−7	−11	−14	−20	−25	−32	−38
	T_r	89.7	81.0	72.3	64.9	57.4	53.5	49.5	44.9	40.2
	R_0	9.3	10.6	11.9	13.9	15.9	17.6	19.2	22.4	25.5

2.41	Δ_0	42	37	31	24	15	6	− 3	−13	−22
	Δ_{70P}	63	53	43	32	21	8	− 6	−17	−28
	Δ_{70S}	3	1	− 2	− 6	−10	−17	−24	−29	−33
	T_r	86.1	76.5	66.9	59.3	51.7	47.9	44.1	39.8	35.5
	R_0	12.5	13.7	14.9	16.5	18.1	19.9	21.7	24.8	27.9
2.82	Δ_0	53	47	40	32	23	14	5	− 4	−13
	Δ_{70P}	79	67	55	44	33	19	5	− 7	−18
	Δ_{70S}	10	7	4	− 1	− 5	−14	−22	−25	−28
	T_r	81.1	71.2	61.3	54.8	48.3	43.7	39.1	35.3	31.4
	R_0	17.0	17.9	18.7	18.9	19.0	22.2	25.3	28.0	30.6
3.23	Δ_0	66	59	51	42	33	23	14		
	Δ_{70P}	96	82	68	56	43	30	16		
	Δ_{70S}	18	15	11	6	1	− 7	−14		
	T_r	75.0	65.4	55.7	49.9	44.0	39.4	34.7		
	R_0	22.6	22.9	23.2	22.9	22.6	25.7	28.7		
3.64	Δ_0	79	70	61	52	42	32	22		
	Δ_{70P}	112	97	81	67	53	40	27		
	Δ_{70S}	26	22	17	12	7	1	− 5		
	T_r	67.9	58.9	49.9	44.2	38.5	34.6	30.7		
	R_0	29.1	28.8	28.4	28.8	29.2	30.7	32.1		
4.05	Δ_0	93	83	72						
	Δ_{70P}	126	110	94						
	Δ_{70S}	36	31	25						
	T_r	60.1	52.1	44.1						
	R_0	36.4	35.2	34.0						
4.46	Δ_0	106	95	83						
	Δ_{70P}	140	123	106						
	Δ_{70S}	45	39	33						
	T_r	51.9	45.1	38.3						
	R_0	44.3	42.1	39.8						

$$\frac{\omega l}{c} = 0.15$$

$k \backslash n$		0.18	0.59	1.00	1.41	1.82	2.23	2.64
1.18	Δ_0			11	1	− 9	−22	−34
	Δ_{70P}			16	1	−14	−32	−49
	Δ_{70S}			−20	−25	−29	−38	−46
	T_r			76.0	69.9	63.7	58.3	52.9
	R_0			10.1	11.7	13.3	16.5	19.6
1.59	Δ_0			20	11	1	−12	22.5
	Δ_{70P}			28	14	− 1	−19	−25
	Δ_{70S}			−16	−21	−25	−34	−37 −43
	T_r			75.0	65.5	55.9	50.3	
	R_0			12.7	14.4	16.0	19.3	44.7
2.00	Δ_0	44	37	29	20	10	− 3	−16
	Δ_{70P}	67	54	40	26	12	− 6	−24
	Δ_{70S}	− 6	− 9	−12	−17	−21	−30	−39
	T_r	82.7	75.5	68.2	58.4	48.5	43.3	38.0
	R_0	14.1	15.4	16.6	18.1	19.5	22.7	25.8
2.41	Δ_0	60	51	41	31	20	7	− 7
	Δ_{70P}	86	70	54	39	24	6	−12
	Δ_{70S}	4	− 1	− 5	−11	−16	−25	−34
	T_0	75.5	66.0	56.4	49.1	41.7	37.1	32.5
	R_r	20.4	21.0	21.6	22.7	23.7	26.6	29.4
2.82	Δ_0	75	64	52	41	29	16	3
	Δ_{70P}	104	86	68	52	35	18	1
	Δ_{70S}	14	9	3	− 4	−11	−20	−29
	T_r	67.0	57.2	47.4	41.5	35.6	31.7	27.8
	R_0	28.4	28.0	27.5	28.1	28.6	31.0	33.4
3.23	Δ_0	92	79	65	53	40	27	13
	Δ_{70P}	121	102	82	65	47	30	13
	Δ_{70S}	26	19	12	4	− 4	−14	−23
	T_r	57.8	48.3	38.7	34.5	30.3	27.1	23.8
	R_0	37.4	35.7	33.9	34.0	34.0	35.8	37.6
3.64	Δ_0	108	93	78	64	50	37	23
	Δ_{70P}	138	117	96	77	58	42	25
	Δ_{70S}	37	29	20	12	3	− 7	−16
	T_r	48.6	41.6	34.6	30.3	26.0	23.1	20.1
	R_0	46.7	43.7	40.7	40.3	39.8	41.0	42.1
4.05	Δ_0	123	107	90				
	Δ_{70P}	151	130	108				
	Δ_{70S}	49	40	30				
	T_r	39.9	34.6	29.3				
	R_0	55.6	51.6	47.6				
4.46	Δ_0	137	120	102				
	Δ_{70P}	163	142	120				
	Δ_{70S}	61	51	40				
	T_r	32.2	28.0	23.8				
	R_0	63.3	58.8	54.3				

$$\frac{\omega l}{c} = 0.20$$

$k \backslash n$		0.18	0.59	1.00	1.41	1.82	2.23	2.64
1.18	Δ_0			13	1	−12	−28	−43
	Δ_{70P}			18	− 1	−19	−40	−60
	Δ_{70S}			−26	−33	−39	−50	−61
	T_0			69.5	62.7	55.8	50.2	44.6
	R_r			12.3	14.2	16.0	19.9	23.7
1.59	Δ_0			24	12	− 1	−16	−33
	Δ_{70P}			32	14	− 4	−25	−46
	Δ_{70S}			−22	−29	−35	−47	−58
	T_r			60.5	54.0	47.5	41.9	36.3
	R_0			16.4	17.8	19.1	23.3	27.4
2.00	Δ_0	57	46	35	23	10	− 6	−22
	Δ_{70P}	83	65	46	29	11	−11	−32
	Δ_{70S}	− 8	−13	−17	−24	−30	−42	−54
	T_r	74.9	63.4	51.9	46.0	40.1	34.9	29.6
	R_0	21.0	21.4	21.8	22.9	23.9	27.6	31.3
2.41	Δ_0	76	63	49	35	21	5	−12
	Δ_{70P}	103	83	62	43	23	2	−19
	Δ_{70S}	5	− 2	− 8	−17	−25	−37	−48
	T_r	64.9	54.4	43.8	38.3	32.8	28.6	24.3
	R_0	29.6	28.9	28.2	29.0	29.7	32.6	35.4
2.82	Δ_0	94	78	62	47	31	15	− 1
	Δ_{70P}	123	100	77	56	35	15	− 5
	Δ_{70S}	17	9	1	− 9	−19	−30	−41
	T_r	54.4	45.4	36.4	31.4	26.3	23.2	20.0
	R_0	39.6	37.5	35.3	35.7	36.0	37.9	39.8

3.23	Δ_0	112	94	76	60	43	27	10
	Δ_{70P}	140	116	91	69	47	27	7
	Δ_{70S}	31	22	11	0	−11	−23	−35
	T_r	43.9	36.8	29.7	25.4	21.1	18.8	16.4
	R_0	50.1	46.5	42.8	42.6	42.3	43.4	44.4
3.64	Δ_0	130	110	90	72	54	37	20
	Δ_{70P}	156	131	105	82	59	39	19
	Δ_{70S}	45	33	21	9	− 3	−16	−28
	T_0	34.2	29.0	23.7	20.6	17.4	15.3	13.2
	R_r	60.3	55.3	50.3	49.1	47.9	48.6	49.3
4.05	Δ_0	145	124	103				
	Δ_{70P}	167	142	116				
	Δ_{70S}	59	46	32				
	T_r	25.8	22.2	18.6				
	R_0	69.3	63.5	57.6				
4.46	Δ_0	159	137	115				
	Δ_{70P}	178	153	127				
	Δ_{70S}	72	58	43				
	T_0	19.4	16.9	14.4				
	R_r	76.1	70.2	64.3				

$$\frac{\omega l}{c} = 0.25$$

k \ n		0.18	0.59	1.00	1.41	1.82	2.23	2.64
1.18	Δ_0			15	0	−15	−34	−52
	Δ_{70P}			25	− 2	−24	−48	−71
	Δ_{70S}			−32	−41	−49	−63	−77
	T_r			63.2	56.3	49.3	43.7	38.0
	R_0			14.5	16.4	18.2	23.0	27.7
1.59	Δ_0			28	12	− 4	−23	−41
	Δ_{70P}			35	13	−10	−33	−56
	Δ_{70S}			− 5	−26	−46	−60	−74
	T_r			53.2	46.6	39.9	35.0	30.1
	R_0			20.6	22.1	23.5	27.6	31.6
2.00	Δ_0	70	56	41	24	7	−12	−30
	Δ_{70P}	97	74	50	28	5	−18	−41
	Δ_{70S}	−11	−17	−23	−33	−42	−56	−70
	T_r	66.5	55.2	43.9	38.0	32.0	28.0	23.9
	R_0	27.7	27.6	27.4	28.3	29.2	32.5	35.8
2.41	Δ_0	91	73	55	37	19	0	−19
	Δ_{70P}	118	92	66	43	19	− 4	− 27
	Δ_{70S}	5	− 3	−10	−23	−35	−50	−64
	T_r	54.6	45.0	35.3	30.4	25.4	22.2	19.0
	R_0	39.1	36.9	34.7	35.0	35.3	37.8	40.2
2.82	Δ_0	111	90	69	50	31	12	− 7
	Δ_{70P}	138	110	82	58	33	10	−13
	Δ_{70S}	20	9	− 3	−16	−28	−43	−57
	T_r	43.2	35.6	27.9	24.0	20.0	17.6	15.2
	R_0	50.4	46.4	42.3	41.9	41.5	43.1	44.7
3.23	Δ_0	129	107	84	64	43	24	4
	Δ_{70P}	153	124	95	70	45	22	− 2
	Δ_{70S}	36	22	8	− 6	−20	−35	− 50
	T_r	32.8	27.2	21.6	18.6	15.6	13.9	12.1
	R_0	61.1	55.5	49.9	48.9	47.8	48.6	49.4
3.64	Δ_0	147	123	98	76	54	34	14
	Δ_{70P}	168	138	108	82	56	33	10
	Δ_{70S}	52	36	19	4	−11	−27	−42
	T_r	23.9	20.3	16.6	14.4	12.1	10.7	9.3
	R_0	70.6	64.0	57.4	55.7	54.0	54.1	54.2
4.05	Δ_0	161	136	110				
	Δ_{70P}	177	148	118				
	Δ_{70S}	66	49	31				
	T_r	16.9	14.7	12.4				
	R_0	78.3	71.3	64.3				
4.46	Δ_0	174	148	122				
	Δ_{70P}	186	157	128				
	Δ_{70S}	80	62	43				
	T_r	12.2	10.7	9.25				
	R_0	83.7	77.1	70.5				

$$\frac{\omega l}{c} = 0.30$$

k \ n		0.18	0.59	1.00	1.41	1.82	2.23	2.64
1.18	Δ_0			17	− 1	−19	−40	−61
	Δ_{70P}			21	− 4	−29	−56	−82
	Δ_{70S}			−38	−49	−60	−77	−94
	T_r			57.5	50.7	43.8	38.4	32.9
	R_0			16.6	18.5	20.4	25.7	31.0
1.59	Δ_0			31	12	− 8	−29	− 50
	Δ_{70P}			37	11	−15	−41	−67
	Δ_{70S}			−33	−45	−57	−74	−90
	T_r			46.8	40.2	34.1	29.8	25.4
	R_0			23.8	25.1	26.3	30.7	35.0
2.00	Δ_0	82	64	45	25	4	−17	−38
	Δ_{70P}	108	81	53	27	0	−26	−51
	Δ_{70S}	−12	−20	−28	−41	−53	−70	−86
	T_r	58.4	47.8	37.1	31.7	26.3	22.9	19.5
	R_0	34.5	33.1	31.6	32.1	32.6	35.9	39.2
2.41	Δ_0	104	82	60	39	17	− 5	−27
	Δ_{70P}	128	99	69	42	14	−12	−38
	Δ_{70S}	6	− 6	−18	−32	−46	−63	−80
	T_r	45.3	36.9	28.4	24.3	20.1	17.6	15.0
	R_0	47.5	43.6	39.7	39.5	39.2	41.4	43.6
2.82	Δ_0	126	93	75	52	29	7	−15
	Δ_{70P}	148	117	85	57	28	2	−24
	Δ_{70S}	23	8	− 7	−23	− 38	−56	−73
	T_r	33.8	27.6	21.4	18.3	15.2	13.3	11.45
	R_0	59.3	53.6	47.9	46.9	45.8	47.0	48.2
3.23	Δ_0	136	113	90	66	41	18	− 5
	Δ_{70P}	162	130	98	69	40	14	−13
	Δ_{70S}	40	23	5	−13	−29	− 48	−66
	T_r	24.1	19.9	15.7	13.6	11.4	10.1	8.74
	R_0	69.5	62.7	55.8	54.1	52.3	52.6	52.8
3.64	Δ_0	161	133	104	79	53	30	6
	Δ_{70P}	176	143	110	81	51	25	− 2
	Δ_{70S}	57	37	17	− 2	−20	−39	− 58
	T_r	16.4	14.0	11.5	10.0	8.4	7.5	6.49
	R_0	78.0	70.6	63.2	60.8	58.3	57.9	57.4

4.05	Δ_0	174	145	116				
	Δ_{70P}	184	152	119				
	Δ_{70S}	72	51	29				
	T_r	10.78	9.49	8.20				
	R_0	84.4	77.1	69.7				
4.46	Δ_0	187	157	127				
	Δ_{70P}	192	160	128				
	Δ_{70S}	86	64	41				
	T_r	7.47	6.68	5.78				
	R_0	88.6	81.8	74.9				

$$\frac{\omega l}{c} = 0.35$$

$k \backslash n$		0.18	0.59	1.00	1.41	1.82	2.23	2.64
1.18	Δ_0			19	−2	−23	−47	−70
	Δ_{70P}			22	−7	−35	−64	−93
	Δ_{70S}			−44	−58	−71	−91	−111
	T_r			52.3	45.8	39.2	34.1	29.0
	R_0			18.6	20.5	22.3	28.0	33.7
1.59	Δ_0			34	12	−11	−35	−59
	Δ_{70P}			38	9	−21	−50	−78
	Δ_{70S}			−39	−54	−68	−88	−107
	T_r			40.5	34.9	29.3	25.6	21.8
	R_0			26.7	27.8	28.8	33.2	37.6
2.00	Δ_0	93	71	48	25	2	−23	−47
	Δ_{70P}	117	86	54	19	−7	−35	−62
	Δ_{70S}	−13	−24	−34	−50	−65	−84	−103
	T_r	50.5	40.6	30.7	26.2	21.7	19.0	16.3
	R_0	41.2	38.3	35.3	35.4	35.5	38.6	41.7
2.41	Δ_0	116	90	64	39	14	−11	−36
	Δ_{70P}	137	104	70	39	8	−21	−50
	Δ_{70S}	6	−9	−23	−40	−57	−77	−97
	T_r	36.9	29.9	22.8	19.4	16.0	14.1	12.2
	R_0	55.3	49.7	44.0	43.2	42.3	44.2	46.1
2.82	Δ_0	139	109	79	53	26	1	−24
	Δ_{70P}	156	71	85	54	22	−8	−37
	Δ_{70S}	25	7	−12	−31	−49	−70	−91
	T_r	25.9	21.2	16.5	14.2	11.8	10.4	9.07
	R_0	66.9	59.7	52.5	50.8	49.0	49.8	50.5
3.23	Δ_0	156	125	94	66	38	12	−14
	Δ_{70P}	169	133	97	65	33	3	−27
	Δ_{70S}	43	22	1	−4	−9	−46	−83
	T_r	17.5	14.6	11.7	10.2	8.66	7.72	6.77
	R_0	76.2	68.4	60.5	58.0	55.4	55.2	55.0
3.64	Δ_0	173	141	108	79	50	23	−4
	Δ_{70P}	181	145	109	77	44	14	−16
	Δ_{70S}	61	38	14	23	31	−22	−75
	T_r	11.3	9.77	8.24	7.19	6.13	5.52	4.90
	R_0	83.2	75.4	67.5	64.4	61.2	60.3	59.3
4.05	Δ_0	185	152	119				
	Δ_{70P}	188	153	118				
	Δ_{70S}	76	51	26				
	T_r	7.27	6.51	5.75				
	R_0	88.2	80.8	73.3				
4.46	Δ_0	197	164	130				
	Δ_{70P}	195	161	126				
	Δ_{70S}	90	64	37				
	T_r	5.12	4.59	4.05				
	R_0	91.2	84.4	77.6				

$$\frac{\omega l}{c} = 0.40$$

$k \backslash n$		0.18	0.59	1.00	1.41	1.82	2.23	2.64
1.18	Δ_0			20	−4	−28	−54	−79
	Δ_{70P}			22	−10	−42	−74	−105
	Δ_{70S}			−50	−66	−81	−105	−128
	T_r			47.6	41.4	35.1	30.6	26.1
	R_0			20.4	22.4	24.3	29.8	35.3
1.59	Δ_0			35	11	−14	−41	−68
	Δ_{70P}			38	6	−27	−59	−90
	Δ_{70S}			−45	−62	−78	−101	−124
	T_r			35.9	31.2	26.5	22.7	18.8
	R_0			28.6	29.2	29.7	34.5	39.2
2.00	Δ_0	103	77	50	25	0	−29	−57
	Δ_{70P}	124	89	54	21	−12	−44	−75
	Δ_{70S}	−13	−26	−39	−57	−75	−98	−120
	T_r	43.5	34.9	26.3	22.8	19.3	16.4	13.4
	R_0	47.4	42.5	37.6	37.1	36.5	39.9	43.3
2.41	Δ_0	126	97	67	39	11	−18	−46
	Δ_{70P}	143	106	69	36	2	−31	−63
	Δ_{70S}	7	−11	−28	−48	−68	−91	−114
	T_r	29.9	24.3	18.6	16.1	13.5	11.5	9.52
	R_0	61.3	54.1	46.9	45.5	44.0	45.8	47.5
2.82	Δ_0	149	116	83	53	22	−7	−35
	Δ_{70P}	161	123	84	49	14	−19	−51
	Δ_{70S}	27	6	−16	−38	−60	−84	−108
	T_r	19.8	16.3	12.8	10.9	8.97	7.88	6.79
	R_0	72.3	63.6	55.8	53.7	51.5	51.7	51.8
3.23	Δ_0	166	132	97	66	34	4	−26
	Δ_{70P}	173	135	96	61	25	−8	−41
	Δ_{70S}	46	22	−3	−27	−51	−76	−101
	T_r	12.6	10.6	8.5	7.2	5.88	5.36	4.83
	R_0	80.7	72.4	64.0	61.1	58.1	57.1	56.1
3.64	Δ_0	183	147	111	79	46	15	−16
	Δ_{70P}	185	146	107	72	36	3	−31
	Δ_{70S}	64	37	10	−16	−42	−68	−93
	T_r	7.74	6.67	5.59	4.88	4.17	3.72	3.27
	R_0	86.8	78.9	71.0	67.0	63.0	61.7	60.4
4.05	Δ_0	195	159	122				
	Δ_{70P}	192	154	116				
	Δ_{70S}	79	51	22				
	T_r	4.71	4.17	3.62				
	R_0	90.8	82.7	76.4				
4.46	Δ_0	206	170	133				
	Δ_{70P}	199	162	124				
	Δ_{70S}	93	63	33				
	T_r	2.96	2.66	2.36				
	R_0	93.2	86.5	79.8				

$$\frac{\omega l}{c} = 0.45$$

k \ n		0.18	0.59	1.00	1.41	1.82	2.23	2.64
1.18	Δ_0			21	−6	−33	−61	−89
	Δ_{70P}			22	−14	−49	−83	−117
	Δ_{70S}			−56	−74	−92	−119	−145
	T_r			43.3	37.5	31.6	27.7	23.7
	R_0			22.1	23.9	25.7	31.0	36.3
1.59	Δ_0			37	9	−19	−49	−79
	Δ_{70P}			38	2	−34	−69	−103
	Δ_{70S}			−51	−70	−89	−116	−142
	T_r			31.4	27.4	23.3	19.9	16.5
	R_0			30.8	31.1	31.3	35.7	40.1
2.00	Δ_0	112	82	52	24	−5	−37	−68
	Δ_{70P}	131	92	53	17	−19	−54	−89
	Δ_{70S}	−13	−29	−45	−66	−86	−112	−138
	T_r	36.9	29.5	22.1	19.3	16.4	13.9	11.3
	R_0	53.2	46.7	40.2	39.3	38.3	41.2	44.1
2.41	Δ_0	136	103	69	38	7	−26	−58
	Δ_{70P}	149	109	68	31	−7	−43	−78
	Δ_{70S}	8	−13	−33	−56	−79	−106	−132
	T_r	24.0	19.5	15.0	13.0	11.0	9.36	7.71
	R_0	66.7	58.2	49.7	47.8	45.9	47.1	48.3
2.82	Δ_0	159	122	85	52	18	−15	−47
	Δ_{70P}	166	124	82	44	5	−31	−66
	Δ_{70S}	29	4	−21	−47	−72	−99	−126
	T_r	15.0	12.4	9.88	8.42	6.96	6.13	5.30
	R_0	76.9	67.8	58.6	55.9	53.2	53.9	52.5
3.23	Δ_0	176	138	99	65	30	+4	−38
	Δ_{70P}	177	135	92	54	16	−20	−56
	Δ_{70S}	48	20	−8	−36	−63	−91	−119
	T_r	9.0	7.66	6.32	5.33	4.34	4.00	3.65
	R_0	84.3	75.4	66.5	63.1	59.6	58.2	56.7
3.64	Δ_0	192	153	113	77	41	7	−28
	Δ_{70P}	188	145	101	64	27	−10	−46
	Δ_{70S}	67	36	5	−25	−54	−83	−111
	T_r	5.39	4.69	3.98	3.52	3.05	2.71	2.36
	R_0	89.4	81.3	73.1	68.7	64.2	62.6	60.9
4.05	Δ_0	203	164	124				
	Δ_{70P}	195	153	111				
	Δ_{70S}	81	49	17				
	T_r	3.32	2.93	2.53				
	R_0	92.5	85.3	78.1				
4.46	Δ_0	213	174	134				
	Δ_{70P}	201	161	120				
	Δ_{70S}	95	62	28				
	T_r	2.03	1.82	1.61				
	R_0	94.1	87.6	81.0				

$$\frac{\omega l}{c} = 0.50$$

k \ n		0.18	0.59	1.00	1.41	1.82	2.23	2.64
1.18	Δ_0			21	−8	−37	−69	−101
	Δ_{70P}			20	−19	−57	−94	−130
	Δ_{70S}			−61	−82	−103	−133	−162
	T_r			39.4	34.0	28.6	25.0	21.4
	R_0			23.8	25.2	26.6	31.6	36.6
1.59	Δ_0			38	7	−25	−58	−90
	Δ_{70P}			36	−4	−43	−80	−117
	Δ_{70S}			−56	−79	−101	−130	−159
	T_r			27.5	23.4	19.3	16.8	14.3
	R_0			33.2	33.4	33.6	36.9	40.1
2.00	Δ_0	121	88	54	21	−13	−46	−79
	Δ_{70P}	137	94	51	12	−28	−66	−104
	Δ_{70S}	−14	−33	−51	−75	−98	−127	−156
	T_r	31.4	25.0	18.5	15.6	12.7	11.1	9.43
	R_0	58.2	50.6	42.9	41.9	40.8	42.5	44.1
2.41	Δ_0	145	108	71	36	0	−35	−69
	Δ_{70P}	154	110	65	25	−16	−55	−93
	Δ_{70S}	9	−15	−39	−65	−91	−121	−150
	T_r	19.5	15.8	12.0	10.1	8.21	7.18	6.14
	R_0	71.1	61.9	52.6	50.2	47.8	48.1	48.4
2.82	Δ_0	168	122	87	50	13	−23	−59
	Δ_{70P}	170	125	79	38	−4	−43	−82
	Δ_{70S}	31	3	−26	−55	−83	−114	−144
	T_r	11.5	10.5	7.45	6.36	5.27	4.66	4.04
	R_0	80.6	65.9	61.0	57.7	54.4	53.6	52.8
3.23	Δ_0	184	143	101	63	24	−13	−50
	Δ_{70P}	180	133	85	46	7	−32	−71
	Δ_{70S}	50	19	−13	−44	−74	−106	−137
	T_r	6.51	5.52	4.52	3.98	3.43	3.06	2.69
	R_0	87.3	77.7	68.1	64.2	60.3	58.7	57.1
3.64	Δ_0	200	157	114	75	35	−3	−40
	Δ_{70P}	190	141	91	54	17	−22	−60
	Δ_{70S}	69	35	0	−33	−65	−98	−130
	T_r	3.72	3.23	2.74	2.42	2.10	1.86	1.62
	R_0	91.6	82.8	73.9	69.6	65.2	63.2	61.2
4.05	Δ_0	210	168	125				
	Δ_{70P}	196	150	104				
	Δ_{70S}	83	48	12				
	T_r	2.24	1.97	1.70				
	R_0	94.0	86.3	78.5				
4.46	Δ_0	220	178	135				
	Δ_{70P}	202	159	116				
	Δ_{70S}	97	61	24				
	T_r	1.22	1.10	0.98				
	R_0	94.8	88.3	81.8				

Statistical Mechanics of Adsorption from Multicomponent Systems I.

By Syû Ono.

Faculty of Engineering, Kyushu University, Fukuoka.

(Received April 30, 1950).

§ 1. Introduction.

The statistical derivation of the adsorption isotherm from a knowledge of the interatomic forces has been the subject of a number of investigations. Although most of these investigations are based on the idea of lattices, it seems to be doubtful that the lattice theories of adsorption lead to really satisfactory results. To make further progress we must start from the general development of the Gibbs phase integral for a system consisting of adsorbate molecules and an adsorbent. This may be achieved by adoption of the method of Ursell(1) and Mayer(2) for treating imperfect gases. Such a theory is developed in the author's recent paper(3). And purpose of the present paper is to attempt to discuss the adsorption from multicomponent system by using the theory of McMillan and Mayer(4), which is generalization of Ursell and Mayer for multicomponent systems.

In treating a problem involving the coordinates of an extremely large number of molecules it will be convenient to adopt a system of symbols of Mayer(5). Let us consider an infinite system containing σ types of molecular species, and use the subscript s(or t) to refer to a special species of type s(or t). The symbols without subscripts refer to a set of quantities:

$$\rho = \rho_1, \rho_2, \ldots, \rho_s \ldots, \rho_\sigma, \tag{1}$$

$$z = z_1, z_2, \ldots, z_s, \ldots, z_\sigma. \tag{2}$$

The symbol ρ_s indicates the density of molecules of species s, in molecules per unit volume, and z_s is the fugacity, normalized in density unit.

The letters k, m, n, etc., when written without subscripts, will be used to indicate sets of integers:

$$k = k_1, k_2, \ldots, k_s, \ldots, k_\sigma \tag{3}$$

of k_s molecules of type s. The shorthand notation:

$$k! = k_1!\, k_2! \ldots k_s! \ldots k_\sigma! \tag{4}$$

$$\rho^k = \rho_1^{k_1} \rho_2^{k_2} \ldots \rho_s^{k_s} \ldots \rho_\sigma^{k_\sigma} \tag{5}$$

$$z^k = z_1^{k_1} z_2^{k_2} \ldots z_s^{k_s} \ldots z_\sigma^{k_\sigma} \tag{6}$$

will be adopted.

The symbol

$$(i_s) = x_{is}, y_{is}, z_{is}, q_{1is}, q_{2is}, \ldots \tag{7}$$

indicates the configurational coordinates of the ith molecule of species s, and, in general, include internal coordinates, q_{1is}, $q_{2is}, \ldots$ as well as the Cartesian coordinates, x_{is}, y_{is}, z_{is}, of the center of mass. The coordinates of n_s molecules of a particular species s will be represented by

$$\{n_s\} = (1_s), (2_s), \ldots, (i_s), \ldots, (n_s). \tag{8}$$

And we will denote the coordinates of all the molecules of such a set n by

$$\{n\} = \{n_1\}, \{n_2\}, \ldots, \{n_s\}, \ldots, \{n_\sigma\}. \tag{9}$$

The volume elements are similarly expressed by $d(i_s)$, $d\{n_s\}$, and $d\{n\}$.

The thermodynamic state of the system will be fully determined by given temperature T and the fugacity set z.

§ 2. The Distribution Functions.

The distribution function $F_n(z, \{n\}, 0)$, a function of the coordinates of a set n of molecules, is defined by the statement that in an infinite system of fugactity set z, the probability that an appropriate set n of molecules will be found at the coordinates $\{n\}$ in the configuration element $d\{n\}$ is proportional to $\rho^n F_n(z, \{n\}, 0)$. It is to be noted that with this definition the functions F_n are so normalized that

$$\lim_{V\to\infty}\left[\frac{1}{V^n}\iint_V\cdots\int F_n(z, \{n\}, 0)d\{n\}\right] = 1. \qquad (10)$$

For the case where an adsorbent exists, we define the similar distribution function $F_n(z, \{n\}, 1)$, which is also a function of the coordinates of a set n of molecules. In the presence of an adsorbent, the single-molecule distribution function $F_s(z, (i_s), 1)$ is not a constant, while $F_s(z, (i_s), 0)$ is equal to unity for fluid or glassy systems as shown by Mayer and Montroll⑹. Here we assume that the potential energy between the ith molecule and the adsorbent as well as the potential energy of the pair of morecules approaches zero more rapidly than r_i^{-3}, r_i being the distance a part of the ith molecule and the surface of the adsorbent, so that the integrals which we will be concerned remain finite. Then $F(z, (i_s), 1)$ will be equal to unity for the molecule sufficiently distant from the adsorbent, and, in general, $F_n(z, \{n\}, 1)$ approaches $F_n(z, \{n\}, 0)$ if all distances of any molecules of the set n to the adsorbent become sufficiently large. Hence the probability that in an infinite system of fugacity set z, there be a set n of molecules at the point of the set $\{n\}$ within the volume element $d\{n\}$, one molecule at each point, irrespective of the positions of other molecules in the system, is $\rho^n F_n(z, \{n\}, 1)$. While the force exerted by the adsorbent decreases more rapidly than r_i^{-3}, the adsorption has no influence upon ρ, though the density near the adsorbent will be markedly different from ρ, and the normalization constant can be determined as

$$\lim_{V\to\infty}\left[\frac{1}{V^n}\iint_V\cdots\int F_n(z, \{n\}, 1)d\{n\}\right] = 1. \qquad (11)$$

According to the general theory of classical statistical mechanics, one may write

$$F_n(0, \{n\}, \varepsilon) = \exp -\frac{U(\{n\}, \varepsilon)}{kT}, \qquad (12)$$

in which k is Boltzmann's constant, T, is the absolute temperature, and ε assumes either 1 or 0. And here $U(\{n\}, 1)$ is the total potential energy of the system consisting of a set n of molecules and the adsorbent, and $U(\{n\}, 0)$ is the one of the system consisting of a set n of molecules alone. Then the grand partition function $\Xi(z, T, \varepsilon)$ at a fugacity set z is given by

$$\Xi(z, T, \varepsilon) = \sum\frac{z^n}{n!}\iint_V\cdots\int F_n(0, \{n\}, \varepsilon)d\{n\}, \qquad (13)$$

where ε assumes 1 or 0 according as the adsorbent is contained in the system or not. And let us denote the probabily that there be the set n of molecules in the volume and that the molecules of this set occupy (respectively) the corrdinates of the configuration $\{n\}$ within the volume element $d\{n\}$ by $P_n(V, z, \{n\}, 1)d\{n\}$ or $P_n(V, z, \{n\}, 0)d\{n\}$ according as the volume contains the adsorbent or not. Then we obtain, according to the definition of the grand partition function,

$$P_n(V, z, \{n\}, \varepsilon) = \frac{z^n F(0, n, \varepsilon)}{\Xi(z, T, \varepsilon)}. \qquad (14)$$

§ 3. Expansion of the Distribution Functions.

In the last section, it was shown that the distribution function at the fugactity set 0 can be computed from the potential energy of the system by using (12). One of our problems in this section is to investigate the method for calculating $F_n(z, \{n\}, \varepsilon)$ by expanding it in a power series in the set of fugacities. The probability that there be one molecule at each point of the set $\{n\}$ within the volume element $d\{n\}$, and exactly the set m of the other molecules somewhere in V will be the integral of $P_{n+m}(V, z, \{n+m\}, \varepsilon)d\{m\}$ over all positions $\{m\}$ within V devided by $m!$ the factor arising from the permutation of molecules among the positions. And the sum of these probabilities over all values of m is equal to the probability that there be one molecule at each point of the set $\{n\}$ within the volume element $d\{n\}$, irrespective of the other molecules in the system, being equal to $[\rho(z)]^n F_n(z, \{n\}, \varepsilon)d\{n\}$; therefore we obtain

$$[\rho(z)]^n F_n(z, \{n\}, \varepsilon)$$
$$= \sum_{m\geq 0}\frac{1}{m!}\iint_V\cdots\int P_{n+m}(V, z, \{n+m\}, \varepsilon)d\{m\},$$

$\rho_s(z)$ being a function of the fugacity set z. Using the expression (14) for $P_n(V, z, \{n\}, \varepsilon)$, we then have

$$\Xi(z, T, \varepsilon)\left[\frac{\rho(z)}{z}\right]^{-n} F_n(z, \{n\}, \varepsilon)$$
$$= \sum_{m\geq 0} \frac{z^m}{m!} \iint_V \cdots \int F_{n+m}(0, \{n+m\}, \varepsilon) d\{m\}. \quad (15)$$

Since $F_0(0, \{0\}, \varepsilon)$ is equal to unity, we obtain, from (13) and (15),

$$F_0(z, \{0\}, \varepsilon) = 1. \quad (16)$$

We shall now introduce

$$I_n\{n\} = \sum_{m\geq 0} \frac{(-z)^m}{m!} \Xi(z, T, \varepsilon)$$
$$\times \iint_V \cdots \int \left[\frac{\rho(z)}{z}\right]^{n+m} F_{n+m}(z, \{n+m\}, \varepsilon) d\{m\}. \quad (17)$$

Inserting (15) into (17), we obtain

$$I_n\{n\} = \sum_{m\geq 0} \sum_{k\geq 0} \frac{z^{m+k}(-)^m}{m!\,k!}$$
$$\times \iint_V \cdots \int F_{n+m+k}(0, \{n+m+k\}, \varepsilon) d\{n+k\}. \quad (18)$$

It is seen that for given value of m_s+k_s the sum of the coefficients is $(1-1)^{m_s+k_s}$, so that only the term $m=0$, $k=0$ remains. It follows that

$$I_n\{n\} = F_n(0, \{n\}, \varepsilon). \quad (19)$$

From (17) and (19), we have

$$F_n(0, \{n\}, \varepsilon) = \sum_{k\geq 0} \frac{(-z)^k}{k!} \Xi(z, T, \varepsilon)$$
$$\times \iint_V \cdots \int \left[\frac{\rho(z)}{z}\right]^{n+k} F_{n+k}(z, \{n+k\}, \varepsilon) d\{k\}, \quad (20)$$

in which the symbol k is used instead of m. Inserting $y+z$ instead of z in (15), and substituting (20) into the left-hand side of (15), we obtain the explicit expression for the functions at the fugacity set $y+z$ in terms of a double summation over numbers m and k of integrals of the functions at the fugacity set z. Regrouping terms according to the sum $m+k=M$, and using the multinomial expansion theorem, we find

$$\Xi(y+z, T, \varepsilon)\left[\frac{\rho(y+z)}{y+z}\right]^{n} F_n(y+z, \{n\}, \varepsilon)$$
$$= \Xi(z, T, \varepsilon) \sum_{M\geq 0} \frac{y^M}{M!} \iint_V \cdots \int \left[\frac{\rho(z)}{z}\right]^{n+M}$$
$$\times F_{n+M}(z, \{n+M\}, \varepsilon) d\{M\}. \quad (21)$$

The special case $n=0$ leads to the equation

$$\Xi(y+z, T, \varepsilon) = \Xi(z, T, \varepsilon) \sum_{M\geq 0} \frac{y^M}{M!}$$
$$\times \iint_V \cdots \int \left[\frac{\rho(z)}{z}\right]^{M} F_M(z, \{M\}, \varepsilon) d\{M\}, \quad (22)$$

which gives the grand partition function at the fugacity set $y+z$.

§ 4. Auxiliary Functions and Cluster Integrals.

In the present section we shall attempt to express $F_n(z, \{n\}, \varepsilon)$ as sum of products of the functions which are separable in the coordinates of the subsets of melecules n. For this purpose, it will be convenient to use the following symbols introduced by Mayer and Montroll. The symbol $\{m\}_n$ is used for set of m molecules, all of which are members of the set n. And the symbol $\{k\{m_i\}_n\}_u$ is for a complete set of k unconnected subsets $\{m_i\}(1 \leq i \leq k)$ of the set $\{n\}$. By unconected we mean that each member of the set $\{n\}$ occurs in one and only one subset $\{m_i\}_n$ of the set of subsets.

As shown by McMillan and Mayer, we may write the expansion of the distribution function $F_M(z, \{M\}, 0)$ in the form

$$E_M(z, \{M\}, 0) = \sum \{k\{m_i\}_M\}_u \prod_{i=1}^{k} g_m(z, \{m_i\}_M), \quad (23)$$

in which the summation goes over unconnected sets of subsets, and the product over all k subsets. An explicit definition of $g_m(z, \{m\})$ is given by

$$g_m(z, \{m\})$$
$$= \sum\{l\{M_j\}_m\}_u (-)^{l-1}(l-1)! \prod_{j=1}^{l} F_M(z, \{M_j\}_m, 0). \quad (24)$$

Since it is necessary to integrate the function $F_{N+M}(z, \{N+M\}, 0)$ in (21) over the coordinates $\{M\}$, we require an expansion of this function similar to (23). The complete expansion shown by McMillan and Mayer is

$$F_{N+M}(z, \{N+M\}, 0) = F_N(z, \{N\}, 0)$$
$$\cdot \sum \{k\{m_i\}_M\}_u \prod_{i=1}^{k} [g_m(z, \{m_i\}_M)$$
$$+ \sum \{n\}_N g_{nm}(z, \{n\}_N, \{m_i\}_M)], \quad (25)$$

in which $\sum\{n\}_N$ is used to indicate summation over all possible subsets $\{n\}_N$, including $\{n\}_N = \{N\}$. Then we obtain as the inverse of (25)

$$g_m(z, \{N\}) + \sum \{n\}_N g_{nm}(z, \{n\}_N, \{m\})$$
$$= \sum \{l\{M_j\}_m\}_u (-)^{l-1}(l-1)!$$
$$\times \prod_{j=1}^{l} \frac{F_{N+M}(z, \{N\}+\{M_j\}_m, 0)}{F_N(z, \{N\}, 0)},$$

of which the proof is similar to that of (24). Using an exactly analogous method to that used in the derivation of the inverse of the expansion of the potential of average forces made by McMillan and Mayer we have

$$g_{nm}(z, \{m\}, \{n\})$$
$$= \sum\{N\}_n \sum\{l\{M_j\}_n\}_u (-)^{n+l-N-1}(l-1)\,!$$
$$\cdot\left[\prod_{j=1}^{l}\frac{F_{N+M}(z, \{N\}_n+\{N_j\}_m, 0)}{F_N(z, \{N\}_N, 0)}-\prod_{j=1}^{l}F_M(z, \{M_j\}_m, 0)\right]. \tag{26}$$

Now we take up the expansion of $F_{N+M}(z, \{N\}+\{M\}, 1)$. It will be noted that the expansion of the distribution function of the system containing the adsorbent can be easily obtained if one regards the adsorbent as a molecule of the $\sigma+1$ st type. Thus we have

$$F_{N+M}(z, \{N+M\}, 1)$$
$$= F_N(z, \{N\}, 1)\sum\{k\{m_i\}_M\}_u \prod_{i=1}^{k}\Big[g(z, \{m_i\}_M)$$
$$+h_m(z, \{m_i\}_M)+\sum\{n\}_N$$
$$\cdot\{g_{nm}(z, \{n\}_N, \{m_i\}_M)+h(z, \{n\}, \{m_i\}_M)\}\Big], \tag{27}$$

where $h_m(z, \{m\})$ and $h_{nm}(z, \{n\}, \{m\})$ are respectively defined by

$$h_m(z, \{m\}) = \sum\{l\{M_j\}_m\}_u(-)^{l-1}$$
$$\times(l-1)\,![\prod_{j=1}^{l}F_M(z, \{M_j\}, 1)-\prod_{j=1}^{l}F(z, \{M_j\}, 0)], \tag{28}$$

and

$$h_{nm}(z, \{m\}, \{n\})$$
$$= \sum_l\{l\{M_j\}_m\}_u(-)^{n+l-1}(l-1)\,![\prod_{j=1}^{l}F_M(z, \{M_j\}_m, 1)$$
$$-\prod_{j-1}^{l}F_M(z, \{M_j\}_m, 0)]$$
$$+\sum\{N\}_n\sum\{l\{M_j\}_m\}_u(-)^{n+l-N-1}(l-1)\,!$$
$$\cdot\Big[\prod_{j=1}^{l}\frac{F_{N+M}(z, \{N\}_n+\{M_j\}_m, 1)}{F_N[z, \{N\}_n, 1)}$$
$$-\prod_{j=1}^{l}\frac{F_{N+M}(z, \{N\}_n+\{M_j\}_m, 0)}{F_N(z, \{N\}_n, 0)}\Big]. \tag{29}$$

We define the cluster integrals as

$$b_m(z) = \frac{1}{Vm\,!}\iint_V\cdots\int g_m(z, \{m\}_M)d\, m\}_M, \tag{30}$$

$$b_{nm}(z, \{n\}_N) = \frac{1}{m\,!}\iint_V\cdots\int g_{mm}(z, \{n\}_N, \{m\}_M)d\{m\}_M, \tag{31}$$

$$\gamma_m(z) = \frac{1}{am\,!}\iint_V\cdots\int h_m(z, \{m\}_M)d\{m\}_M, \tag{32}$$

$$\gamma_{nm}(z, \{n\}_N) = \frac{1}{m\,!}\iint_V\cdots\int h_{nm}(z, \{n\}_N, \{m\}_M)d\{m\}_M, \tag{33}$$

where α is the area of the surface of the adsorbent. If the surface is homogeneous from macroscopic standpoint, the cluster integrals (30)–(33) depend neither on the volume V nor on the area α. As to the calculation of the cluster integrals there remains the complicated problem how to choose the geometrical boundary to which the integration is carried out. One would determine this boundary so that the total amount of a reference component suitably chosen may be inaltered by insertion of the adsorbent.

Using the cluster integrals defined by (30) to (33) in the integration in the left-hand side of (21), we find

$$\iint_V\cdots\int F_{N+M}(z, \{N+M\}, \varepsilon)d\{M\} = F_N(z, N, \varepsilon)$$
$$\cdot M!\sum_{\mu_m}\prod_m\frac{[Vb_m(z)+\varepsilon a\gamma_m(z)+\sum\{n\}_N\{b_{nm}(z, \{n\}_N)+\varepsilon\gamma_{nm}(z, \{n\}_N)\}]^{\mu_m}}{\mu_m\,!} \tag{34}$$

in which the sum over μ_m is subject to the restiction $\sum m_s\mu_m = M_s$, since a subdivision of the $\{M\}$ coordinates into μ_m subsets of size m may be obtained in $M!/\Pi(m\,!)^{\mu_m}$ different ways. Then (18) becomes

$$\Xi(y+z, T, \varepsilon)\left[\frac{\rho(y+z)}{y+z}\right]^N F(y+z, \{N\}, \varepsilon) = \Xi(y+z, T, \varepsilon)\left[\frac{\rho(z)}{z}\right]^N F_n(z, \{N\}, \varepsilon)$$
$$\cdot\sum_{M\geqq 0}\left[\frac{y\rho(z)}{z}\right]^M\sum_{\mu_m}\prod_m\frac{[Vb_m(z)+\varepsilon a\gamma_m(z)+\sum\{n\}_N\{b_{nm}(z, \{n\}_N)+\varepsilon\gamma_{nm}(z, \{n\}_N)]^{\mu_m}}{\mu_m\,!}.$$

This can be rewritten in the form

$$\Xi(y+z, T, \varepsilon)\left[\frac{\rho(y+z)}{y+z}\right]^N F_N(y+z, \{N\}, \varepsilon) = \Xi(z, T, \varepsilon)\times\left[\frac{\rho(z)}{z}\right]^N F_N(z, \{n\}, \varepsilon)\exp\sum_{m\geqq 0}\Big[\Big\{Vb_m(z)+\varepsilon a\gamma_m(z)$$
$$+\sum\{n\}_N(b_{nm}(z, \{n\}_N)+\varepsilon\gamma_{nm}(z, \{n\}_N))\Big\}\Big\{\frac{y\rho(z)}{z}\Big\}^m\Big]. \tag{35}$$

For the case $N=0$, we have

$$\begin{aligned}&\Xi(y+z,T,\varepsilon)\\&\quad=\Xi(z,T,\varepsilon)\exp\sum_{m\geq 0}\left[\{Vb_m(z)+\varepsilon a\gamma_m(z)\}\left\{\frac{y\rho(z)}{z}\right\}^m\right].\end{aligned}\tag{36}$$

§ 5. Molecular Distribution near the Surface of Adsorbent.

The potential of average force $W_N(z,\{N\},\varepsilon)$ at the fugacity set z is defined by

$$W_N(z,\{N\},\varepsilon)=-kT\ln F_N(z,\{N\},\varepsilon).\tag{37}$$

In the limit of zero fugacity, we obtain from (12)

$$W_N(0,\{N\},\varepsilon)=U(\{N\},\varepsilon).\tag{38}$$

As shown by McMillan and Mayer, the component potentials of average force in the absence of the adsorbent is defined by either of two reciprocal sets of equations

$$W_N(z,\{N\},0)=\sum\{n\}_N w_n(z,\{n\}_N),\tag{39}$$

or

$$w_n(z,\{n\})=\sum\{N\}_n(-)^{n-N}W_N(z,\{N\}_n,0).\tag{40}$$

Similarly the potential of averrge force in the presence of the adsorbent can be written in the form

$$W_N(z,\{N\},1)=\sum\{n\}_N\{w_n(z,\{n\}_N)+\omega_n(z,\{n\}_N)\},\tag{41}$$

where $\omega_n(z,\{n\})$'s are defined by

$$\begin{aligned}&\omega_n(z,\{n\})=\sum\{N\}_n\\&\quad\cdot(-)^{n-N}\{W_N(z,\{N\}_n,1)-W_N(z,\{N\}_n,0)\}.\end{aligned}\tag{42}$$

Now we shall investigate the equations which may be utilized to calculate the distribution function near the surface of the adsorbent. Substitution of (36) into (35) leads to

$$\begin{aligned}&[\rho(y+z)]^N F_N(y+z,\{N\},\varepsilon)=(y+z)^N\\&\quad\cdot\left[\frac{\rho(z)}{z}\right]^N F_N(z,\{N\},\varepsilon)\exp\sum_{m\geq 0}\sum\{n\}_N\\&\quad\cdot\left[\{b_{nm}(z,\{n\}_N)+\varepsilon\gamma_{nm}(z,\{n\}_N)\}\left\{\frac{y\rho(z)}{z}\right\}^m\right].\end{aligned}\tag{43}$$

Substituting (37), (39) and (41) into (43), we have

$$\begin{aligned}&[\rho(y+z)]^N F_N(y+z,\{N\},\varepsilon)=(y+z)^N\left[\frac{\rho(z)}{z}\right]^N\\&\quad\cdot\exp\sum\{n\}_N\left[\left\{\sum_{m\geq 0}b_{nm}(z,\{n\}_N)\left(\frac{y\rho(z)}{z}\right)^m-\frac{w_n(z,\{n\})}{kT}\right\}\right.\\&\quad\left.+\varepsilon\left\{\sum_{m\geq 0}\gamma_{nm}(z,\{n\}_N)\left(\frac{y\rho(z)}{z}\right)^m-\frac{\omega_n(z,\{n\}_N)}{kT}\right\}\right].\end{aligned}\tag{44}$$

§ 6. Adsorption Isotherm.

According to the general properties of the grand partition function the average number of the molecules of species s is given by

$$n_s=\left[\frac{\partial(kT\ln\Xi)}{\partial\mu_s}\right]_{T,\ldots,\mu_r}\tag{45}$$

It will be proved in the subsequent paper that (48) holds for the system which contains an adsorbent.

We may write

$$z_s=\phi_s(T)\exp\frac{\mu_s}{kT},\tag{46}$$

where $\phi_s(T)$ is a function of the temperature alone. Then using the fugacity set as the independent variables, we rewrite (45) in the from

$$n_s=z_s\left[\frac{\partial\ln\Xi}{\partial z_s}\right]_{T,V,z_r}\tag{47}$$

It follows at once from (36) and (47) that the average number of the molecules of species r belonging to the system is given by

$$\begin{aligned}n_r(y+z,\varepsilon)=\frac{y_r+z_r}{y_r}\Bigg[&V\sum_{m\geq 0}m_r b_m(z)\\&\times\left\{\frac{y\rho(z)}{z}\right\}^m+\varepsilon a\sum m_r\gamma_m(z)\left\{\frac{y\rho(z)}{z}\right\}^m\Bigg],\end{aligned}\tag{48}$$

where ε assumes 1 or 0 according as the system contains an adserbent or not.

If one inserts an adsorbent in the system and admits of transfer of matters to or from the reservoir, the number of the molecules of any species contained in the system proper will increase or decrease. And it is seen that from (48) the increase of the number due to insertion of the adsorbent is given as

$$\begin{aligned}&n_r(y+z,1)\\&\quad-n_r(y+z,0)=a\frac{y_r+z_r}{y_r}\sum_{m\geq 0}m_r\gamma_m(z)\left\{\frac{y\rho(z)}{z}\right\}^m.\end{aligned}\tag{49}$$

Hence the number of adsorbed molecules of species r on the unit area of the adsorbent or the excess number of the molecules per unit area is expressed by

$$\theta_r=\sum_{m\geq 0}m_r\gamma_m(z)\left\{\frac{y\rho(z)}{z}\right\}^m,\tag{50}$$

which gives the equilibrium number of adsorbed molecules as a function of the fugacity set.

Sometimes θ_r may be negative, corresponding to the negative adsorption.

Since ρ_r is the number of molecules of species r per unit volume in the limit of infinite volume, one may write

$$\rho_r = \left(\frac{\partial n_r}{\partial V}\right)_{T, z_s}. \tag{51}$$

Using (48), we have

$$\rho_r(y+z) = \frac{y_r+z_r}{y_r}\sum_{m\geq 1} m_r b_m(z)\left\{\frac{y\rho(z)}{z}\right\}^m. \tag{52}$$

From (50) and (52), we can, in principle, express the adsorbed amount of molecules of any species as a function of the densities or the concentrations of σ types of molecules. Thus we obtain a set of adsorption isotherms.

References.

(1) H. D. Ursell, Proc. Camb. Phil. Soc. **23** (1927), 685.

(2) J. E. Mayer, J. Chem. Phys. **5** (1937), 67.

(3) S. Ono, Memoirs of Faculty of Engineering, Kyushu Univ. **12** (1950), 9.

(4) W. G. McMillan and J. E. Mayer, J. Chem. Phys. **13** (1945), 276.

(5) J. E. Mayer, J. Chem. Phys. **15** (1947), 187.

(6) J. E. Mayer and E. Montroll, J. Chem. Phys. **9** (1941), 2.

(7) R. H. Fowler, Statistical Mechanics (Cambridge, 1936), p. 253.

On the Activation of the Oxide Coated Cathode.

By Tetsuya ARIZUMI and Shin-ichiro NARITA.

Kobe Kogyo Corp.

(Received May 22, 1950)

§ 1. Introduction.

It is a special property of the oxide coated cathode that its emission depends largely upon the conditions of activation. Although this dependency is of great significance in the practical production of vacuum tubes, we have only poor knowledge(1) on the activation of the cathode because of a complicated process. Thus the first attack on this problem was begun by studing the recovery of emission from the cathode having been poisoned temporarily.

§ 2. Experimental Tube.

The construction of the experimental tube is almost similar as described in the previous paper(2). The tube 1 in Fig. 1 is a test diode in which both the thermionic emission and the conductivity of the cathode were simalteneousely determined. For the measurement of conductivity a probe was immersed in the oxide layer. The tube 2, 3 and 5 are an ionization gauge, a gas chamber containing an oxygen source(3) and a batalum getter, and a flash getter. A small amount of active carbon in the tube 4 is available for the sudden change of gas pressure, by means of immersing the chamber in liquid air or taking out from it.

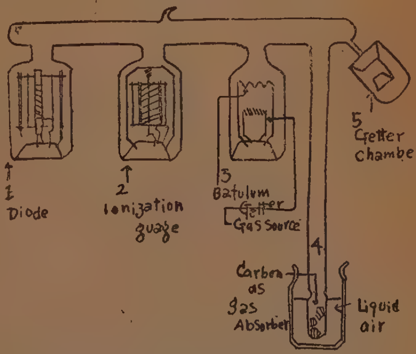

Fig. 1. The construction of the experimental tube

For two purposes to avoid the effect of the interface(4) and the reducing action of the base metal,(4) the electrolytic nickel was mainly used as a cathode sleeve, on which 6 milligramm of $BaCO_3$ and $SrCO_3$ mixture was sprayed. A fine nickel wire of 20 microns dia. was wound around this coated cathode and the same amount of carbonates were sprayed again. The experimental tube was thoroughly evacuated, the getter in the tube 5 was flashed and then the tube was tipped off. The activation of the cathode followed to the usual procedure.

§ 3. Diffusion of Barium Atoms.

The present investigation has two main purposes; The first object is to know the exact value of the diffusion energy of excess barium atoms and the second one is to know the dissociation energy of barium oxide.

The first purpose was fulfilled by the following procedure: The cathode having been kept at 600°K was exposed momentarily to a small amount of oxygen, produced by the chemical reaction $4CuO = 2Cu_2O + O_2$ and on the other hand the produced oxygen was immediately absorbed by the getter mirror in the tube 5. As soon as the thermionic emission decreases sufficiently, the cathode was cooled to the room temperature. For a while oxygen was thoroughly absorbed by the getter. Then, when the cathode was lighted at a constant temperature, the emission recovers gradually, but it does not recover to its original value. This final emisson lowers down as the times of repeating as shown in Fig. 1. In these procedure only the surface of the cathode is poisoned, but the reduced barium atoms in the interior are not destroyed. Moreover, no borium atoms can be supplied because of the low cathode temperature. Thus the recovery of emission is considered to be caused dy the diffusion of interior barium atoms to the surface. The results in Fig. 2 shows the decrease of concentration of free barium atoms, giving a direct evidence to the above consideration.

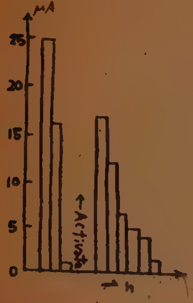

Fig. 2. Decrease of final emission:

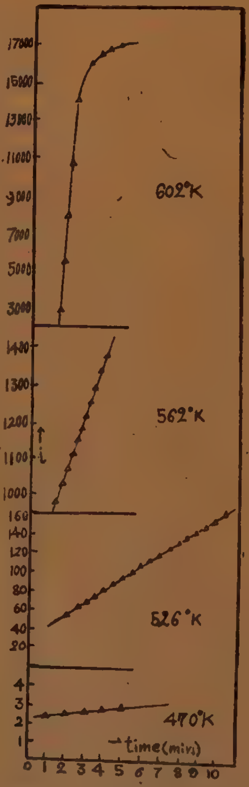

Fig. 3. Recovery of emission.

The recovery of emission obtained in such procedure is shown in Fig. 3. The increase of emission is linearly proportionol to time at every cathode temperature.

Appling the Wilson's(5) theory on the semiconductor to the oxide coated cathode, its emission is represented by

$$i \doteq D_1 A_1 n_0^{\frac{1}{2}} T^{\frac{5}{4}} \exp\left\{-\frac{e}{kT}\left(\frac{E}{2}+\phi\right)\right\} \qquad (1)$$

The formula holds for the well activated cathode at sufficiently high temperatures. On the other hand, the formula deduced by appling the Njiboer's(4) "frozen-in-hole" theory,

$$i = D_2 A_2 n_0 T^2 \exp\left\{-\frac{e}{kT}(E+\phi)\right\} \qquad (2)$$

holds for the insufficiently activated cathode at low temperatures. Both expressions, however, can be deduced from following two equations:

$$\frac{n(n+N)}{n_0-n} = \left(\frac{2\pi mkT}{h^2}\right)^{\frac{3}{2}} \exp\left(-\frac{eE}{kT}\right) \qquad (3)$$

and

$$i = neD\left(\frac{kT}{2\pi m}\right)^{\frac{1}{2}} \exp\left(-\frac{e\phi}{kT}\right) \qquad (4)$$

In the four formulae all notations are the same as used in the previous paper.(2) (1) is an approximation when n_0 is much larger than N in (3), while (2) corresponds to the approximation at the contrary case.

The present experiment is the procedure to vary n_0 under the constant temperature. At the beginning of the experiment, the concentration of free barium atoms is supposed to be like

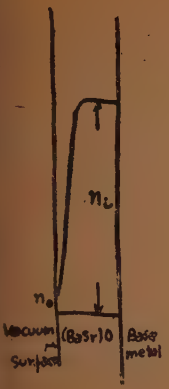

Fig. 4. Schematical diagramm of concentration distribution of free barium atoms at the beginning of the experiment.

schematically shown in Fig. 4. Thus the increment of surface concentration of n_0 is written by

$$\frac{dn_0}{dt} = \kappa(n_i - n_0) \tag{5}$$

As n_0 is neglisibly small at the beginning, the solution of (5) becomes

$$n_0 = \kappa n_i t \tag{6}$$

in which the diffusion coefficient κ is expressed by

$$\kappa = \kappa_0 \exp\left(-\frac{E_4}{kT}\right) \tag{7}$$

As the surface is in a deactivated state in the experiments, (6) may well be put into (2). Thus we obtain

$$i = D_2 A_2 T^2 \kappa n_i t \exp\left\{-\frac{e}{kT}(E+\phi)\right\} \tag{8}$$

representing that the increase of emission is linearly proportional to time.

Plotting the increments of emission with regards to $1/T$, the linear relations are found as shown by two curves 1 and 2 in Fig. 5. Appling Kawamura's⑺ result, $E=$ 1.7 e.v., E_4 is evaluated to be 0.75 e.v. and κ about 4×10^3 cm²/sec. The obtained diffusion energy is almost equal to Blewett's⑻ value having been determined by the time change of the emission.

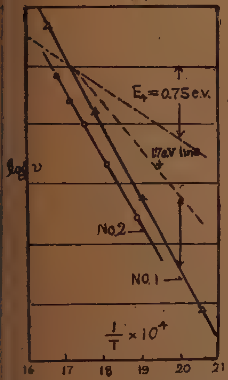

Fig. 5. The determination of diffusion energy.

§ 4. Activation Energy for Exciting a Barium Atom to a Impurity Centre.

4. Activation Energy for Exciting a Barium Atom to a Impurity Centre.

For the second purpose the following procedure was available: In this case the getter chamber 5 was tipped off from the experimental tube. The cathode at the high temperature was exposed to oxygen atomosphere of about 10^{-4} mm. Hg for a while and then the tube 4 was suddenly immersed in liquid air. Then the pressure decreases to 4×10^{-7} mm. Hg in several secs., but both the emission and conductivity recovers only slowly to the original value. In these processes not only the surface of the cathode but also its interior should be poisoned. Thus the dissociation of barium oxide is required for the recovery of emission.

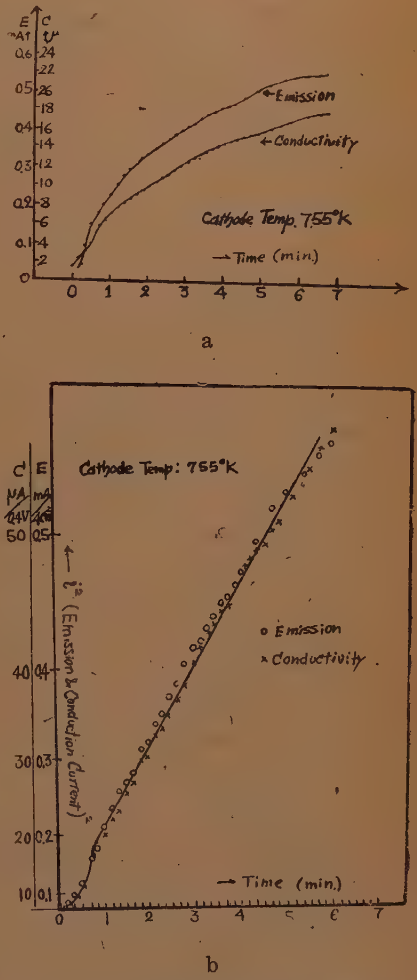

Fig. 6. The recovering of emission and conductivity.

Fig. 6a shows the recoveries of both emission and conductivity at 755°K. The cathode temperature is so high that the emission is represented by (1) and the conductivity by the expression⑼

$$\sigma = evA'n_0^{\frac{1}{2}}T^{\frac{3}{4}}\exp\left\{-\frac{eE}{2kT}\right\} \tag{9}$$

Thus the square value of both emission and conductivity becomes proportional to n_s. The curves i^2 and σ^2 *versus* t are shown in Fig. 6b, in which both curves coincide each other, suggesting that the increase of n_s is linearly proportional to time. The result that no time lag can be observed between two curves of conductivity and emission is well explained by the easiness of diffusion of free barium atoms at high cathode temperature. Fig. 7 is another example of the recovery of emission, in which a is i *versus* t curves while b is i^2 *versus* t curves. The increase of i is found to be in linear proportion to t so long as the cathode temperature is low and its activity is still insufficient, while in the contrary cases, i^2 proportional to t. From these results it is evident that the Njiboer's "frozen-in-hole" theory is correctly applied to the oxide coated cathode.

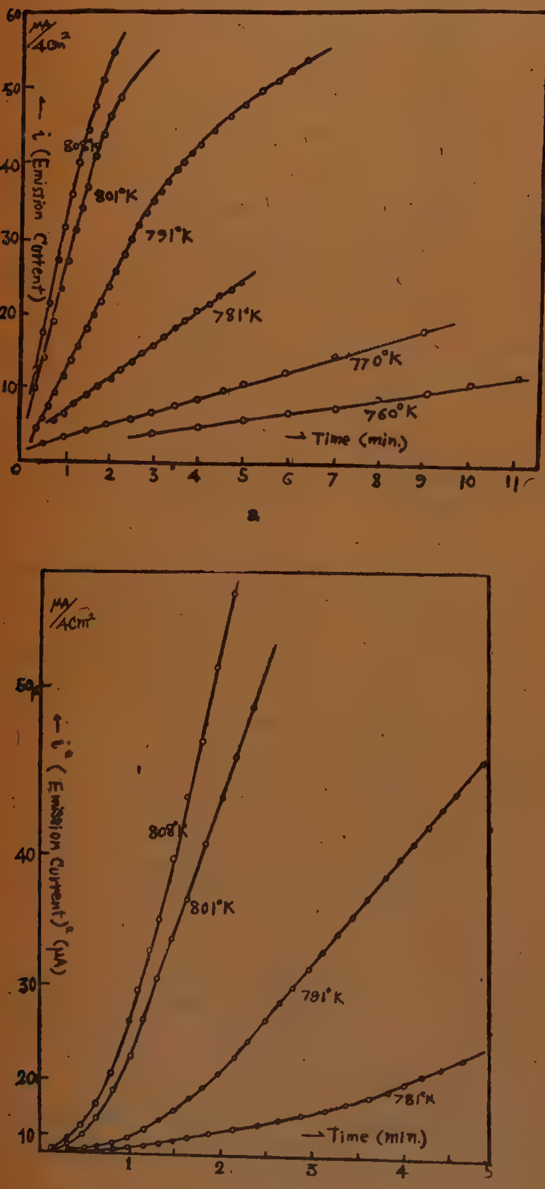

a

b

Fig. 7. The recovery of emission.

In these experiments, almost all free barium atoms are destroyed and thus the increase of emission should be begun by the dissociation of barium oxide, $2BaO = 2Ba + O_2$ at the cathode surface. The dissociation proceeds to the interior gradually. The increment of free barium atoms can be waitten by

$$\frac{dn_s}{dt} = Kn^2_{Bao} - K'n_s n_{O_2} \qquad (10)$$

The first term is equal to the amount of dissociated free barium and the second term is that of recombined barium atoms.

As the produced oxygen is soon absorbed by the active carbon, the second term in (10) can be neglected. Thus the solution of (10) becomes

$$n_s = Kn_{Bao}{}^2 t = K''t \qquad (11)$$

This shows the linear increase of the concentration of free barium atoms in good agreement with the experimental results.

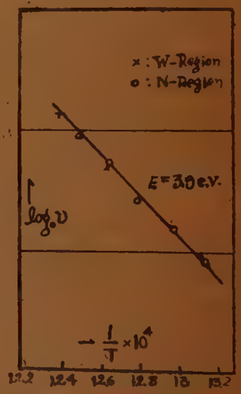

Fig. 8. The activation energy for exciting a barium atom from a normal lattice site to a impurity centre.

The inclination of i in Fig. 7a and i^2 in Fig. 7b are plotted in Fig. 8. It is found that there holds the linear relation in both cases. By means of the similar procedure as described in determining the diffusion energy, the activation energy E_s for transferring a barium atom from a normal lattice site to a impurity centre can be evaluated to be 3.9 e.V. This value agrees with Kawamura's estimation(1).

5. Dissociation Energy.

The Richardson lines at the oxygen pressure f 10^{-4} mm Hg were plotted by means of two ifferent procedures. At first the emission from he cathode, having been kept at a constant emperature was measured by lowering the temperature to a measuring point suddenly. The procedure means that only T is varied with n_0 being kept constant. The obtained Richardson line is shown by the curve b in Fig. 9. The work function at high temperature is 1.0 e.v., while it is 1.4 ev. at low temperatures.

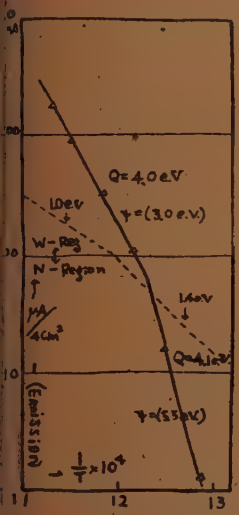

Fig. 9. The Richardson lines of the cathode being kept in equilibrium with oxygen.

Secondly, the emission of the cathode, having been kept at the measuring temperature for 30 mins., was plotted in the Richardson diagramm. In this procedure the equilibrium state between free barium and oxygen has already established at each emperature. Thus in this case both n_0 and T are two variables. The calculated work functions are much larger than these coresponding values in the first procedure (at high and low emperatures they are 3.0 e.v. aud 5.5 e.v. respectively) showing that n_0 decreases very much by the combination with oxygen.

If E_2 be the heat of activation, n_0 is derived rom the statistical mechanics, as follows;

$$n_0 = N\left(\frac{2\pi mkT}{h^2}\right)^{-\frac{3}{2}} \exp\left(-\frac{E_2}{kT}\right) \qquad (12)$$

ubstituting (12) in (1) and (2), we obtain

$$i = RT^{\frac{1}{2}} \exp\left\{-\frac{e}{kT}\left(\phi+\frac{E}{2}+\frac{E_2}{2e}\right)\right\} \qquad (13)$$

nd

$$i = R'T^2 \exp\left\{-\frac{e}{kT}\left(\phi+\frac{E}{2}+\frac{E_2}{e}\right)\right\} \qquad (14)$$

espectively. Thus the inclination of the Richrdson line obtained by the second procedure is the apparent work function, involving the dissociation energy E_2.

Subtracting the true work function, obtained by the first method, from the apparent ones in the second procedure, the dissociation energy E_2 can be estimated as 4.0–4.1 e.v.s. at all temperature range. The difference $E_2-E_3=0.2$ e.v. perhaps means the energy for combining two oxygen atoms to a molecule at the cathode surface.

§ 6. Summary.

1. Poisoning only the cathode surface, by the momentary exposure to oxygen, the recovery of emission was measured. From these results the diffusion energy of free barium atoms was estimated 0.75 e.v. in good agreement with Blewett's result.

2. The emission from the cathode having been destroyed in the oxygen atomsphere for a long time, recovers in linear proportion to time in the insufficiently activated state or at low temperatures, but at contrary cases the square values of the emission become proportional to time. The recovery of conductivity is quite parallel to that of emission. From these experiments it was concluded that the activation energy for tranferring a barium atom from a normal lattice site to a impurity centre is 3.9 e.v.

3. The emission of the cathode, exposed to the oxygen atomosphere for 30 mins., were plotted in the Richardson diagramm. The apparent work function is much larger than that obtained by the normal procedure. The dissociation energy was estimated from the experiments to be 4.1 e.v.

4. The emission formulae, derived by appling the Njiboer's "frozen-in-hole" theory to the oxide coated cathode, can explain all phenomena, described above giving the most powerful evidence for the validity of the theory.

References.

(1) H. Kawamura, A. Shinohara & K. Takahashi. J. Phys. Soc. Japan 3 (1948) 301.
(2) T. Arizumi & S. Narita, J. Phys. Soc. Japan 3 (1948) 356.

(3) A. Fineman & A. Eisenstein, J. App. Phys. **17** (1946) 663.

(4) H. Kawamura, Susaku-Butsuri Gakukai-Shi, **17** (1943) 503, in Japanese.

(5) A. H. Wilson, Proc. Roy. Soc. London (A) **133** (1931) 458.

(6) B. R. A. Njiboer, Proc. Phys. Soc. **51** (1937) 575.

(7) E. Nishibori & H. Kawamura, Proc. Phys-Math. Soc. Japan **27** (1939) 378.

(8) J. Blewett, Phys. Rev. **55** (1939) 713.

(9) F. Seitz, Modern Theory of Solids, (1940).

Effects of Mechanical Pressures on the Dielectric Properties of Polycrystalline Barium-Strontium Titanate.

By Gen SHIRANE and Katsuo SATO.

Tokyo Institute of Technology, Oh-okayama, Tokyo.

(Received June 9, 1950)

Abstract.

The effects of the following three kinds of mechanical pressures upon the dielectric properties of barium-strontium titanate ceramics have been investigated: (1) hydrostatic pressure, (2) compression parallel to the electrode surface and (3) compression normal to the electrode surface (as shown in Fig. 1). Especially the influences of these pressures on the Curie point and on the permittivity in the cubic region have been investigated.

With increasing hydrostatic pressure, Curie point of (Ba 75-Sr 25) TiO_3 is reduced with a slope of 6.0 ($\pm$0.5) $\times 10^{-3}$ degree·cm²/kg, and its permittivity vs. temperature curve is shifted to lower temperatures; these results are in good agreement with those of $BaTiO_3$ single crystals, recently published by Merz.(1) The Curie point of this sample is raised by the two kinds of compressions. On the other hand, permittivity is lowered in all temperature range by normal compression, but by parallel compression permittivity vs. temperature curve is shifted to higher temperatures. The effect of normal compression is in good agreement with the one investigated by Takagi, Sawaguchi and Akioka(2) about $BaTiO_3$ ceramics.

In the cubic region, the variation of the permittivity by these pressures can be interpreted by the phenomenological theory presented by Devonshire,(3) and the coefficients g_{11} and g_{12}, which were introduced in his theory, can be calculated using the results of our experiments. In addition, using cathode ray oscillograms measurements have been made on the effects of pressures on the polarization, and the results are consistent with the data of the permittivity measurements.

§ 1. Introduction.

About the effect of hydrostatic pressure, Vul(4) (in 1945) reported that the variation of the capacity of $BaTiO_3$ condenser is, at room temperature, $\Delta C/C = 0.12 \times 10^{-4}$ cm²/kg. in the range 300～2000 atmospheric pressures. And recently in the course of our experiments the effect of hydrostatic pressure on the Curie point of barium titanate single crystals was studied by Merz,(1) and a linear shift of the Curie point towards lower temperature is observed with a slope of -5.8×10^{-3} degree/atmos.

Effect of mechanical stress normal to the electrode surface (Fig. 1(3)) was studied by Takagi, Sawaguchi and Akioka(2) and it was found that the permittivity was reduced by the pressure. Among these results it must be emphasized that the effect of pressure is very conspicuous up to the temperatures above the Curie point. From this fact, it is evident that the dielectric properties of barium titanate are sensitive to the pressure regardless of the existence or not of "domain structure". And it seems that the detailed investigation of these effects, and especially of those in the cubic region, is very important to explain the essential nature of this material.

We investigate the effects of the three kinds of mechanical pressures as shown schematically in Fig. 1: (1) hydrostatic pressure, (2) compression parallel to the electrode and (3) compression normal to the electrode. Of course, the effects may be very different between single crystals and polycrystalline ceramics. But above the Curie point, i.e. in the region of cubic form, single crystals become isotropic and domain boundaries disappear, and in this region, the properties of ceramics may not be so different from that of single crystals. So, we have investigated these effects mainly above the Curie point.

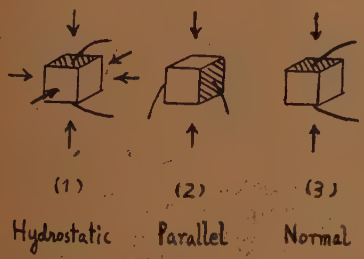

Fig. 1.
(1) hydrostatic pressure,
(2) compression parallel to the electrode,
(3) compression normal to the electrode.

Recently, in the course of our experiments, Devonshire proposed a phenomenological theory of the transition in barium titanate, and he estimated the value of coefficients g_{11} and g_{12} which give the variation of permittivity with strains. Later on, we shall compare our results with his theory.

§ 2. Expermental.

Samples used in our experiments are barium titanate and solid solution of barium-strontium titanate. Following the usual method, they are sintered in an electric furnace at 1400 °C after the calcination at 1200 °C. Specimens of the following compositions were prepared in this way:

A: $BaTiO_3$, Curie point 115 °C,
B: (Ba 75-Sr 25) TiO_3, Curie point 37 °C,
C: (Ba 60-Sr 40) TiO_3, Curie point -10 °C.

We mainly used the specimen *B*: (Ba 75-Sr 25) TiO_3, because the Curie point is reduced to 37 °C and the various measurements are easier. It has been known that the dielectric properties of the solid solution of Ba-Sr titanate are essentially similar to that of pure barium titanate.

The simple hydrostatic apparatus is shown in Fig. 2. This apparatus consists of vessel *A* and piston *B*. One electrode of a specimen *S*, immersed in the oil *O*, is connected to the piston (earth side), and another electrode is connected to a measuring circuit by lead wire *D*, which is insulated by a silica tube in a narrow hole *E*. This hole is filled with sealing wax, and oil-leak between piston and vessel is stopped by rubber packing *C*. This apparatus is compressed by an Amsler testing machine. Owing to the leakage of oil, pressure is limited by 500 kg/cm². The temperature of the oil can be adjusted by a heater *H*.

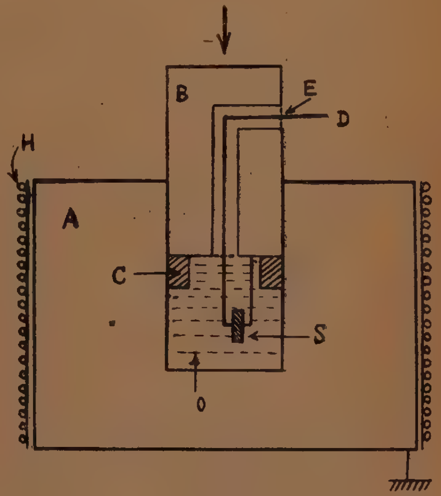

Fig. 2. Hydrostatic pressure apparatus.
A: vessel, *B*: piston,
C: rubber packing, *S*: specimen,
O: oil, *H*: heater.

For applying the compression normal or parallel to the electrode, specimens having the form shown schematicaly in Fig. 1, are compressed by the Amsler testing machine. On account of the fracture of the sample, maximum compression is limited by about 500~1000 kg/cm².

Permittivity is measured by a heterodyne method; its frequency is 1,000 kc/sec and its out-put about 2 V. By this method, the variation of capacity of 0.2 pF. can be detected, and since the capacities of our samples are more than 200 pF., this method allow us to detect the change of capacity with an accuracy of $\Delta C/C = 10^{-3}$.

When we apply mechanical pressure on a specimen, its shape changes and this dimensional correction to the capacity must be made. But this correction is of the order of magnitude as P/E, where E denotes Young's modulus, and in fact this is negligible in the following experiments.

§ 3. Results.

(1) Hydrostatic pressure.

At first, we have measured the permittivity as a function of hydrostatic pressure at room temperature (about 10 °C) and the results are shown in Fig. 3. In this temperature, the sample A: $BaTiO_3$ and B: (Ba 75-Sr 25) TiO_3 are under the Curie point and the sample C: (Ba 60-Sr 40) TiO_3 is above it. As the temperature of oil is raised by compression, we measure the value of the permittivity after the temperature recovers to its initial value. We use the specimen of thin plate (0.3 mm by 10 mm²) and of rather thick one (3 mm by 50 mm²): and obtain essentially the same results.

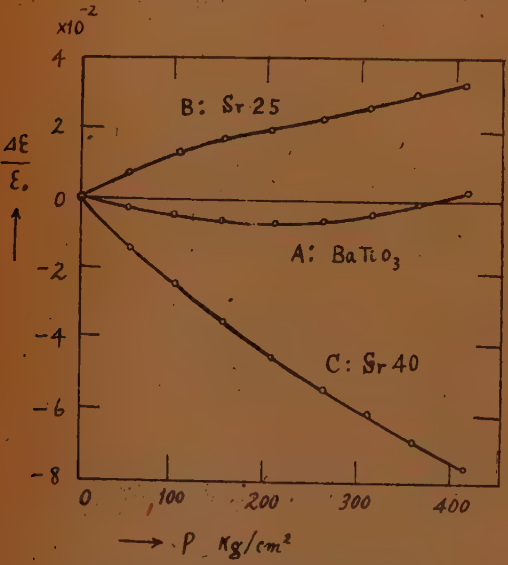

Fig. 3. ε vs. pressure curve.
A: $BaTiO_3$,
B: (Ba 75-Sr 25) TiO_3,
C: (Ba 60-Sr 40) TiO_3.

As shown in this figure, below the Curie point (sample B) the permittivity increases with increasing pressure, but above the Curie point (sample C) the situation is reversed. With respect to sample C (above the Curie point), $1/\varepsilon$ vs. pressure relation is almost linear, as plotted in Fig. 4, but this linearlity does not hold good for sample A and B. According to the measurement made by Vul,(4) $\Delta C/C$ of $BaTiO_3$ is 0.12×10^{-4} cm²/kg in the range 300~2000 atmos. In our experiments, permittivity decreases at first then increases. The slope is nearly equal to that obtained by Vul.

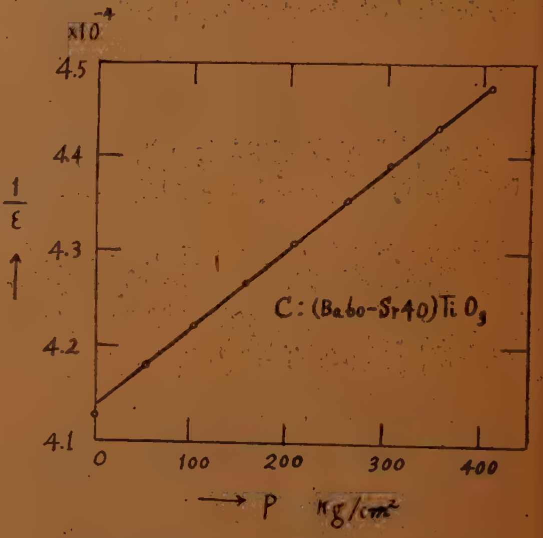

Fig. 4. $1/\varepsilon$ vs. pressure of sample C (Ba 60-Sr 40) TiO_3.

Then we measure the permittivity vs. temperature curves of sample B: (Ba 75-Sr 25) TiO_3 (Curie point 38 °C) under the various hydrostatic pressures (0~500 kg/cm²) and show one of the results in Fig. 5 (stress free and $P = 420$ kg/cm²). The temperature is measured by a copper-constantan thermo-couple inserted in the oil through the narrow hole E. As shown in the figure, the permittivity vs. temperature curve retains its shape and only shifts to lower tempetatures as the pressure is increased, and ferroelectric Curie point (where permittivity becomes maximum) falls linearly with a slope of

$dT_f/dP = -6.0(\pm 0.5) \times 10^{-8}$ degree·cm²/kg$(= -6.2 \times 10^{-9}$ degree·cm²/dyne). This result with respect to (Ba 75-Sr 25) TiO_3 is in good agreement with the data of Merz, though his data is obtained on $BaTiO_3$ single crystals $(-5.74 \times 10^{-9}$ degree·cm²/dyne).

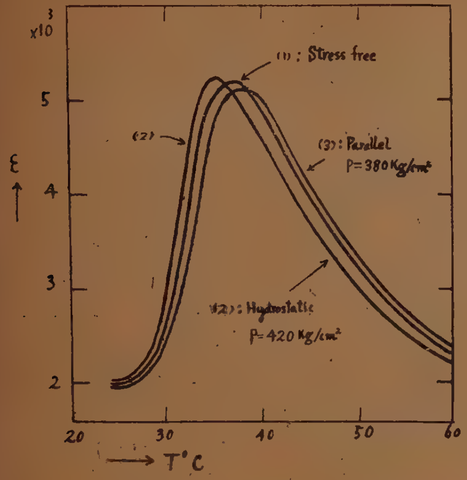

Fig. 5. ε vs. temperature curve of (Ba 75-Sr 25) TiO_3.
(1) stress free,
(2) hydrostatic pressure $P = 420$ kg/cm,
(3) parallel compression $P = 380$ kg/cm.

$1/\varepsilon$ calculated from the curve of Fig. 5 above the Curie point are plotted against temperature in Fig. 6, they are almost linear and nearly parallel to each other; i.e. Curie constant is not changed appreciably by pressure. Hence it becomes evident that $d/dP \cdot (1/\varepsilon)$ is nearly constant above the Curie point, though $d\varepsilon/dP$ is not so. From Fig. 4 and Fig. 6, $d/dP \cdot (1/\varepsilon)$ can be obtained, and in these cases of different compositions they are both $0.73(\pm 0.05) \times 10^{-7}$ cm²/kg when averaged over several specimens.

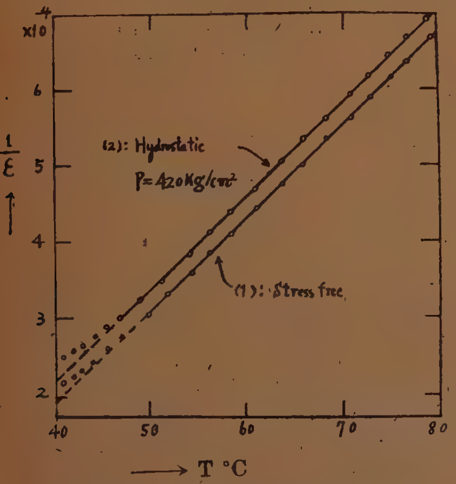

Fig. 6. $1/\varepsilon$ vs. temperature curves.
(1) stress free, (2) $P = 420$ kg/cm.

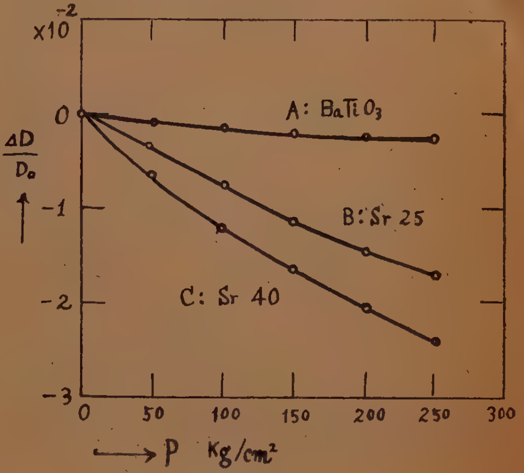

Fig. 7. $\Delta D/D$ vs. pressure curve.
A: $BaTiO_3$,
B: (Ba 75-Sr 25) TiO_3,
C: (Ba 60-Sr 40) TiO_3.

In addition we have measured the change of dielectric polarization. In order to observe the change of hysteresis loops on cathode ray oscillograms (50 cycle and 20 kv/cm) we have used a comparator. As shown in Fig. 7, the electric displacement D decreases in all samples and this result may be explained by the fact that the Curie point is lowered with increasing pressure. From another point of view, lattice constant decreases with increasing pressure and consequently polarization should be decreased.

(2) Compression parallel to the electrode surface.

For measuring this effect, we have prepared a cubic form specimen (edge-length is about 1 cm), and compress it on an Amsler testing machine (as shown in Fig. 1). Contact surface are insulated with baklite plates. Results with respect to sample A, B and C, at room temperature (about 10 °C) are shown in Fig. 8. Just on the contrary to the case of hydrostatic pressure, permittivity decreases below the Curie point (samples A and B) and above it the situation is reversed. In this experiment, to secure homogeneous compression; it is convenient to use a thin plate specimen at the expence of the accuracy of the permittivity measurement, because it has a narrow electrode surface. While in a cubic sample, which is convenient for permittivity measurement, it is rather difficult to apply homogeneous compression, because contact surface can not be made so exactly parallel that inevitably there should be some component of normal compression. And since effect of normal compression is much larger than parallel one, this error is not at all negligible. The accuracy of this experiment is lowest among the three experiments. $1/\varepsilon$ *vs.* pressure relation of sample *C* is not so linear as in the case of hydrostatic pressure, and this, to some extent, may be due to the above reasons. By the fracture of the specimen the pressure is limited by about 600 kg/cm².

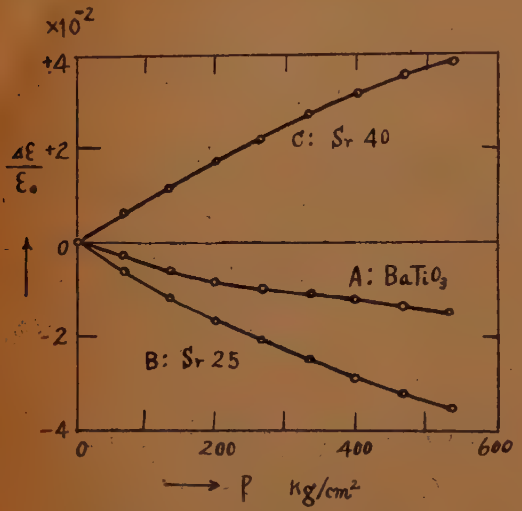

Fig. 8. ε *vs.* pressure curve.
A: $BaTiO_3$,
B: (Ba 75-Sr 25) TiO_3,
C: (Ba 60-Sr 40) TiO_3.

We have measured the ε *vs.* temperature curve under the pressure (stress free and $P=380$ kg/cm²), heating the sample in electric furnace and obtain the results depicted in Fig. 5. Ferroelectric Curie point is raised with the rate $dT_f/dP = 4.0\times10^{-3}$ degree·cm²/kg. This result may be reasonable, because the compression does act as if it compel the tetragonality normal to the compression. Just as in the case of hydrostatic pressure, $1/\varepsilon$ *vs.* temperature curves are almost linear and nearly parallel to each other. From this result and from Fig. 8 (sample *C*, Sr 40), $d/dP\cdot(1/\varepsilon)$ above the Curie point is calculated as $-0.30\ (\pm0.05)\times10^{-7}$ cm²/kg.

At last, we measured $\Delta D/D$ of sample *B* and *C*. In contrast with the case of hydrostatic pressure, polarization increase in both samples.

(3) Compression normal to the electrode surface.

As stated before, this effect was measured by Takagi, Sawaguchi, and Akioka⁽²⁾ on $BaTiO_3$ ceramics. We have again repeated the measure-

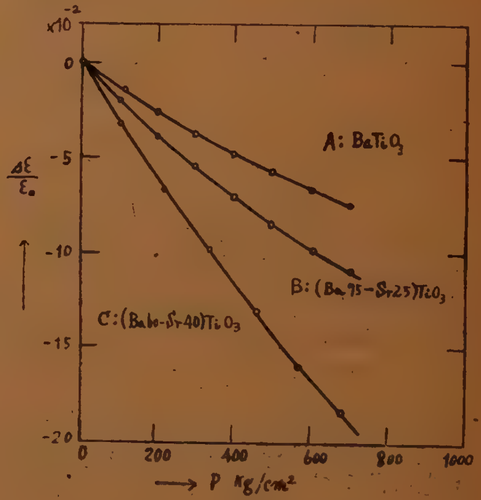

Fig. 9. ε *vs.* pressure curve under normal compression.
A: $BaTiO_3$,
B: (Ba 75-Sr 25) TiO_3,
C: (Ba 60-Sr 40) TiO_3.

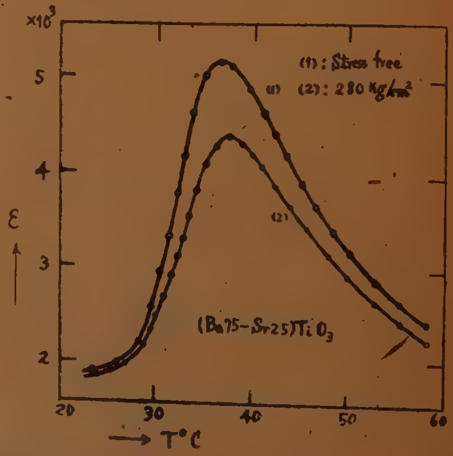

Fig. 10. ε *vs.* temperature curve.
(1) stress free (2) $P=280$ kg/cm².

ment to compare directly the effects of the three kinds of pressures with respect to the same samples used in the above two experiments. The results are in good agreement with theirs, and shown in Fig. 9 and Fig. 10. As in the case of hydrostatic pressure, $1/\varepsilon$ *vs.* pressure curve of sample *C* is almost linear, and ferroelectric Curie point T_f is raised with a nearly equal rate as in the case of parallel compression. We can estimate $d/dP \cdot (1/\varepsilon) = 1.30\ (\pm 0.20) \times 10^{-7}\ \mathrm{cm}^2/\mathrm{kg}$ above the Curie temperature with respect to sample *B* and *C*.

(4) Relaxation effect.

When the pressure is applied or removed, marked relaxation effect of permittivity is observed. One of them in the case of normal compression is shown in Fig. 11: *A* (below the Curie point) and *C* (above it). The tendency of the relaxation is different in the region above and below the Curie point. There may be some fear that the temperature of the sample is raised by the compression, but in fact the temperature change, measured by the thermo-couple soldered directly to the electrode surface, is always found to be less than 0.1 °C. And moreover, tendency of relaxation is in opposite sign to the temperature effect.

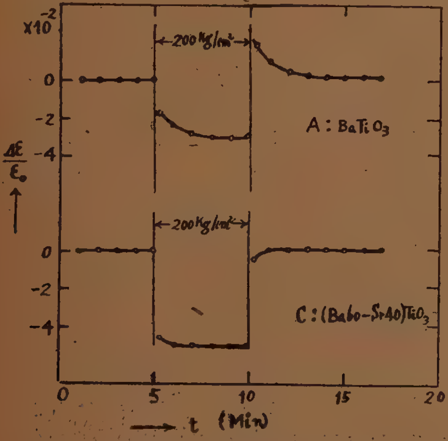

Fig. 11. Relaxation effect in the case of normal compression.
A: BaTiO$_3$; *C*: (Ba 60-Sr 40) TiO$_3$.

This relaxation is quite similar to the phenomena, which are observed when the electric field is applied or removed and which are investigated precisely by Partington, Planer and Boswell.⁽⁶⁾ This coincidence is rather interesting, for compression and electric field are very different in their nature.

There is also a certain relaxation effect in the case of parallel compression and the tendency seems to be similar. But in this case the change of permittivity is much less and so also the relaxation. In the case of hydrostatic pressure relaxation effect is covered by the temperature change of oil, so the existence of this effect is not so clear. When we measure the change of the polarization, a similar type of relaxation is observed.

§ 4. Discussion.

As stated before, we have obtained almost the same result as that of Merz concerning a linear shift of Curie point by the hydrostatic pressure. He assumed that the transition in BaTiO$_3$ at 120 °C is of the second order, and used the Ehrenfest's relation for the calculation of the change of the specific heat ΔC_p at the Curie point, and obtained the value $\Delta C_p = 4.9 \times 10^{-3}$ cal/g · degree which is of the same order of magnitude as the experimental values. Refering to optical and X-ray data of Kay and Vousden,⁽⁷⁾ however, we are declined to believe that this transition may be of the first order. Then we must use the Clausius-Clapeyron equation, which give the value of latent heat.

If l represents this latent heat, and ΔV the change of the volume at the Curie point, we have $dT_f/dP = T_f \cdot \Delta V/l$. For (Ba 75-Sr 25) TiO$_3$, dT_f/dP is -6.2×10^{-9} degree · cm²/dyne and T_f is 308 °K. If in the first approximation for Ba-Sr titanate, we use for ΔV the value of BaTiO$_3$, i.e. 0.02Å³ per unit cell, given by Kay and Vousden, we obtain $l \fallingdotseq 15$ cal/mol for this sample which is of the same order of magnitude as the experimental value of BaTiO$_3$ and the one of (Ba 90-Sr 10) TiO$_3$ measured by Sawada and Nomura.⁽⁸⁾

From our experiment it becomes evident that $d/dP \cdot (1/\varepsilon) = -1/\varepsilon^2 \cdot d\varepsilon/dP$ is nearly constant above the Curie point and may have the important physical meaning for this material than $d\varepsilon/dP$, the value of which is not constant even in the cubic region. The value of $d/dP \cdot (1/\epsilon)$ is not so exactly the same for all samples when the firing conditions are different. But the average value used above should be reasonable, in relative measure at least, from the following reason. If we apply to a specimen normal pressure once and parallel pressure twice, then the result must be equivalent to hydrostatic pressure. In fact the value obtained by the former process $(1.30-0.30\times 2 = 0.70)\times 10^{-7}$ is in the neighbourhood of the value of hydrostatic experiment (0.73×10^{-7}).

By the theory of Devonshire, $d/dP \cdot (1/\epsilon)$ is given by the following equation, if we assume that the coefficient of internal field does not vary by the strain.

$$\frac{d}{dp}\left(\frac{1}{\epsilon_x}\right)=\frac{\partial}{\partial x_x}\left(\frac{1}{\epsilon_x}\right)\frac{dx_x}{dp}+\frac{\partial}{\partial y_y}\left(\frac{1}{\epsilon_x}\right)\frac{dy_y}{dp}+\frac{\partial}{\partial z_z}\left(\frac{1}{\epsilon_x}\right)\frac{dz_z}{dp}$$
$$=\frac{1}{2\pi}\left\{g_{11}\frac{dx_x}{dp}+g_{12}\left(\frac{dy_y}{dp}+\frac{dz_z}{dp}\right)\right\}$$

where

$$2g_{11}=4\pi\frac{\partial}{\partial x_x}\left(\frac{1}{\epsilon_x}\right),$$
$$2g_{12}=4\pi\frac{\partial}{\partial y_y}\left(\frac{1}{\epsilon_x}\right)=4\pi\frac{\partial}{\partial z_z}\left(\frac{1}{\epsilon_x}\right).$$

ϵ_x is permittivity along the X-axis, and in our case (above the Curie point) it is the measured permittivity. x_x, y_y and z_z are the strain components along the three axes. This equation can be written for the three pressures in the following form:

(1) hydrostatic

$$\frac{d}{dp}\left(\frac{1}{\epsilon}\right)=\frac{1}{2\pi}\cdot\frac{1}{E}\left\{-g_{11}\cdot(1-2\sigma)-g_{12}\cdot 2(1-2\sigma)\right\}$$

(2) parallel

$$\frac{d}{dp}\left(\frac{1}{\epsilon}\right)=\frac{1}{2\pi}\cdot\frac{1}{E}\left\{g_{11}\cdot\sigma \qquad -g_{12}\cdot(1-\sigma)\right\}$$

(3) normal

$$\frac{d}{dp}\left(\frac{1}{\epsilon}\right)=\frac{1}{2\pi}\cdot\frac{1}{E}\left\{-g_{11} \qquad +g_{12}\cdot 2\sigma\right\}.$$

In these equations $d/dP \cdot (1/\epsilon)$ are given by our experiments and shown in the first column in Table 1. Mason⁽⁷⁾ found a Young's modulus $E = 1.13\times 10^{12}$ dynes/cm² and a Poisson's ratio $\sigma = 0.27$ for barium titanate ceramics at room temperature. Now we use these values in the first approximation for our barium-strontium titanate. If we choose $g_{11} = -1.00$, $g_{12} = -0.05$, we get the values shown in the second column of Table 1. It can be seen that the three equations are satisfied fairly well by two parameters g_{11} and g_{12}.

Table 1.

$d/dP \cdot (1/\epsilon)\times 10^7$ cm²/kg	observed	calculated
(1) hydrostatic	+0.73	+0.71
(2) parallel	−0.30	−0.32
(3) normal	+1.30	+1.34

The magnitudes of g_{11} and g_{12} are rather small compared with the values $g_{11} = -11.2$, $g_{12} = 0.8$ that were estimated by Devonshire for BaTiO$_3$ single crystals, but this difference should not be so serious. As the Young's modulus of single crystals was estimated by him as 4.0×10^{12} dyne/cm², so if we use this value, g_{11} and g_{12} become at once about 4 times larger. In agreement with his estimation, g_{11} is much larger than g_{12} so the factor x_x is predominant in these effects. g_{12} has an opposite sign to Devonshire's value, but this coefficient is very small and the discrepancy is not important. Thus the above agreement may be seen as an evidence that our experiments support the theory of Devonshire.

In conclusion, we wish to express our sincere thanks to Prof. Y. Takagi and Mr. E. Sawaguchi for their valuable discussion in the course of our experiments, and also to Prof. M. Masuda and Mr. Y. Tozawa for the facilities generously endowed by them. Expense of this research was defrayed from the Scientific Research Expenditure of the Educational Ministry.

References.

(1) W. J. Merz: Phys. Rev. **78** (1950) 52.
(2) Y. Takagi, E. Sawaguchi and T. Akioka: J. Phys. Soc. Japan **3** (1948) 270.
(3) A. F. Devonshire: Phil. Mag. **40** (1949) 1040.
(4) B. M. Vul and L. F. Vereshchagin: Compt. rend. U. S. S. R. **48** (1945) 634.
(5) H. F. Kay and P. Vousden: Phil. Mag. **40** (1949) 1019.
(6) J. R. Partington, G. V. Planer and I. I. Boswell: Phil. Mag. **40** (1949) 157.
(7) W. P. Mason: Phys. Rev. **74** (1949) 1134.
(8) S. Sawada and S. Nomura: J. Phys. Soc. Japan, **5** (1950) 231.

Statistics of the Three-Dimensional Ferromagnet (II).

By Takehiko OGUCHI.

Tokyo Institute of Technology, Oh-okayama, Tokyo.

(Received June 9, 1950).

§ 1. Introduction.

In Part I[1], the three-dimensional Ising problem was formulated to an eigenvalue problem, and its partition function was obtained by the perturbation method. The reasons why the author took the above method were as follows: first, because the eigenvalue problem would be the starting point to obtain the rigorous solution, and secondly the propagation of order would be obtain by the eigenvectors. In this paper, however, the latter object, i. e., the propagation of order is chiefly pursued by another method, in the form of the power series valid at low temperatures, which is easier than the eigenvalue method. The solution valid at high temperatures will be discussed in Part III. As the both series diverge near the Curie point, the property of the transition, which we are mainly interested in, cannot be clarified with this method.

§ 2. The Partition Function for Low Temperatures.

Let us take the Ising model of simple cubic lattice. On i-th lattice point, there is a spin which is characterized by μ_i. Let each of the spins be capable of two orientations which we characterize by $\mu_i = +1$ and $\mu_i = -1$. The forces on each spin depend only on the orientation of its immediate neighbours in addition to an external magnetic field H. Let the magnetic moment of each spin be m, and the spin interactions which are parallel or antiparallel to each other be $-(1/2)J$ or $+(1/2)J$ respectively. In some spin configuration "c", the total energy E_c is

$$E_c = -\frac{1}{2}J\sum_{<ik>}\mu_i\mu_k - mH\sum_i \mu_i\,, \tag{2.1}$$

where $\sum_{<ik>}$ is the sum over all pairs (i, k) which are nearest neighbours, and $\sum$ the sum over all spins (the total number is N). Thus the partition function f has the form,

$$f = \sum_c g_c e^{-E_c/kT}, \tag{2.2}$$

where $\sum_c$ means that the sum is carried out over all spin configurations which have all sorts of energy values. g_c is the number of the configurations which have the same energy value of E_c. As it is difficult to obtain the relations between all E_c and g_c, we will secure the finite terms which are dominant for low temperatures. For this purpose, we may develop it to a power series of the energy[2].

In the very lowest state all spins are oriented parallel to each other. The energy value is

Table I*.

State	reversed spins	excitation energy	g_c
0		0	1
1	O	$6J+2mH$	N
2	O—O	$10J+4mH$	3N
3	O···O	$12J+4mH$	$\frac{1}{2}N(N-7)$
4_1	O—O—O	$14J+6mH$	3N
4_2	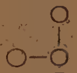	$14J+6mH$	12N
5_1	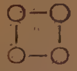	$16J+8mH$	3N
5_2	O—O···O	$16J+6mH$	3N(N−12)
6_1	O···O···O	$18J+6mH$	$\frac{1}{6}N^3-\frac{7}{2}N^2+\frac{64}{3}N$
6_2	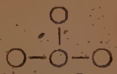	$18J+8mH$	20N
6_3	O—O—O—O	$18J+8mH$	3N
6_4	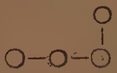	$18J+8mH$	60N

* In the second column, circles represent the reversed spins and full lines or dotted lines connect with the adjacent spins or remote spins respectively.

$3/2 \cdot NJ - NmH$. The first higher state is given by the reversal of a single spin and requires an excitation energy $6J+2mH$. As it does not matter which spin is reversed, the number of configurations is N. The second higher state corresponds to the reversal of two neighbouring spin (excitation energy is $10J+4mH$) and g_4 of it is $3N$. The third higher state corresponds to the reversal of two separated spins (excitation energy is $12J+4mH$) and g_4 of it is $\frac{1}{2}N(N-7)$, and so forth. Thus we obtain Table I. (The same calculations were also performed by Tanaka(5) independently from the author to terms of order β^{16}).

For convenience, we introduce the new variables β and θ;

$$e^{-J/kT} = \beta, \quad e^{-mH/kT} = \theta. \tag{2.3}$$

According to Table I, (2.2) becomes

$$f = \beta^{-\frac{3}{2}N}\theta^{-N}\Big[1+N\theta^2\beta^6+3N\theta^4\beta^{10}+\frac{1}{2}N(N-7)\theta^4\beta^{12}$$
$$+15N\theta^6\beta^{14}+\{3N\theta^8+3N(N-12)\theta^6\}\beta^{16}$$
$$+\Big\{\frac{N}{6}(N^2-21N+128)\theta^6+83N\theta^8\Big\}\beta^{18}\dots\Big]. \tag{2.4}$$

If there is no external magnetic field, θ is equal to unity, so

$$f=\beta^{-\frac{3}{2}N}\Big[1+N\beta^6+3N\beta^{10}+\Big(\frac{N^2}{2}-\frac{7}{2}N\Big)\beta^{12}+15N\beta^{14}$$
$$+(3N^2-33N)\beta^{16}+\Big(\frac{1}{6}N^3-\frac{7}{2}N^2+\frac{313}{3}N\Big)\beta^{18}\dots\Big]. \tag{2.5}$$

We are in need of the partition function per individual spin. This may be obtained if we raise f to the power $1/N$ in accordance with the statistical mechanics. Let us examine how is this operation related to the eigenvalues in Part I. In Part I, the partition function is connected with 2^k eigenvalues $\lambda_i (i = 1, 2, \dots, 2^k)$ as follows:

$$f = \sum_{i=1}^{2^k} \lambda_i^N \tag{2.6}$$

where k is the number of spins in one layer. As N is sufficiently large, all eigenvalues except the largest one $\lambda_{\max}$ may be neglected,

$$f = \lambda_{\max}^N. \tag{2.7}$$

Thus the partition function per individual spin $f^{1/N}$ corresponds to the largest eigenvalue $\lambda_{\max}$,

$$f^{\frac{1}{N}} = \beta^{-\frac{3}{2}}(1+\beta^6+3\beta^{10}-3\beta^{12}+15\beta^{14}-30\beta^{16}+101\beta^{18}..). \tag{2.8}$$

The spontaneous magnetization I is obtained by the thermodynamical relation;

$$\frac{I}{Nm} = \lim_{\theta\to 1}\frac{\partial \log f^{1/N}}{\partial \log 1/\theta}$$
$$= 1-2\beta^6-12\beta^{10}+14\beta^{12}-90\beta^{14}+192\beta^{16}-792\beta^{18}\dots \tag{2.9}$$

(2.9) is in agreement with (2.17) in Part I. Fig. 1 shows the relation between I/Nm and kT/J according to (2. 9). The part of the dotted line is of less accuracy on account of approaching to the limit of convergence of (2.9).

In the case of the one-dimensional ferromagnet, we are able to obtain the rigorous solution by means of the present method. For vanishing field, the number of configurations which have $2n$ of antiparallel spin pairs is $2\binom{N}{2n}$, factor 2 is because of exchanging + with −. As the excitation energy corresponding to it is $2nJ$, the partition function is

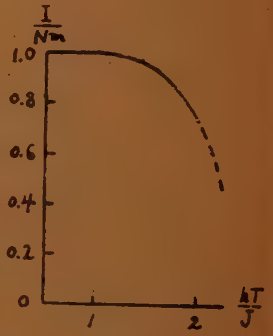

Fig. 1.

$$f = \sum_{n=1}^{N/2} 2\binom{N}{2n} e^{\frac{NJ}{2kT}-\frac{2nJ}{kT}}$$
$$= (e^{\frac{J}{2kT}}+e^{-\frac{J}{2kT}})^N+(e^{\frac{J}{2kT}}-e^{-\frac{J}{2kT}})^N. \tag{2.10}$$

This is in agreement with what is obtained by eigenvalue method.

§ 3. The Propagation of Order at Low Temperatures.

In order to interpret the diffuse scattering of X-rays by an alloy which is partially disordered, it is necessary to know how the presence of one atom at a certain lattice point affects the probability of finding the various kinds of atoms at any other lattice point. It may happen in future that the same knowledge will be demanded about the scattering of neutron by a ferromagnet. For convenience, we take the Ising model of ferromagnet in place of an alloy which contains two kinds of atoms. It is easy to change this into the case of the binary alloys.

Suppose that a certain site, let it be denoted by 0, is definitely known to be occupied by a +(or −) spin. We will investigate how this knowledge affects the probability for +(or −) spins at any other site, namely e. g. a site at a distance of one site away, two sites away,..., and n sites away. The partition function of those shall be denoted by $f_{01}, f_{02}, \ldots, f_{0n}$.

First, we consider f_{01}. In this case, we must calculate the partition function under the restriction of that 0th spin and 1st spin are parallel to each other. Thus we obtain Table II for f_{01} provided that there is no external magnetic field.

Table II.

State	excitation energy	g_c
0	0	1
1	6J	N−2
2	10J	3N−10
3	12J	$\frac{1}{2}N^2-\frac{11}{2}N+14$
4_1	14J	3N−14
4_2	14J	12N−56
5_1	16J	3N−16
5_2	16J	$3N^2-52N+192$
6_1	18J	$\frac{1}{6}N^3-\frac{9}{2}N^2+\frac{127}{3}N-128$
6_2	18J	20N−120
6_3	18J	3N−18
6_4	18J	60N−360

Using Table II,

$$f_{01}=1+(N-2)\beta^6+(3N-10)\beta^{10}+\left(\frac{1}{2}N^2-\frac{11}{2}N+14\right)\beta^{12}$$
$$+(15N-70)\beta^{14}+(3N^2-49N+176)\beta^{16}$$
$$+\left(\frac{1}{6}N^3-\frac{9}{2}N^2+\frac{376}{3}N-626\right)\beta^{18}\ldots \qquad (3.1)$$

Dividing f_{01} by f, we obtain the probability $C(0,1)$ for the case when both 0th and 1st spins are parallel to each other. Let us call it the correlation probability. And it corresponds to the molecular distribution function for liquid or imperfect gas.

$$C(0,1)=\frac{f_{01}}{f}$$
$$=1-2\beta^6-10\beta^{10}+14\beta^{12}-70\beta^{14}+176\beta^{16}-626\beta^{18}\ldots \qquad (3.2)$$

This results agrees with the one obtained by van der Waerden which is quoted in the paper of Ashkin and Lamb(4). The author has no opportunity to read his original paper.

By the same way, the following results are obtained:

$$C(0,1)=1-2\beta^6-10\beta^{10}+14\beta^{12}-70\beta^{14}+176\beta^{16}-626\beta^{18}\ldots$$
$$C(0,2)=1-2\beta^6-12\beta^{10}+16\beta^{12}-88\beta^{14}+212\beta^{16}-790\beta^{18}\ldots$$
$$C(0,3)=1-2\beta^6-12\beta^{10}+16\beta^{12}-90\beta^{14}+216\beta^{16}-818\beta^{18}\ldots$$
$$C(0,4)=1-2\beta^6-12\beta^{10}+16\beta^{12}-90\beta^{14}+216\beta^{16}-820\beta^{18}\ldots$$
$C(0,n)\ n\geqq 5$, equal $C(0,4)$ to terms of order β^{18},
(3.3)

It was Zernike(5) who first discussed the propagation of order. His results, however, were not good because he used rather rough approximation. According to Ashkin and Lamb(4), his results are rigorous in one-dimensional case, and become poorer as the dimension is increased. In simple cubic lattice,

$$\text{Zernike}\quad C(0,1)=1-2\beta^6+6\beta^8\ldots \qquad (3.4)$$

Comparison with (3.2) and (3.4) shows that Zernike's approximation for low temperatures is valid up to terms of the order β^6. As Bethe-Takagi's theory(6) does not treat with the propagation of order, we cannot get the correlation probabilities by that theory, but only $C(0,1)$ is obtained from short range order;

Bethe-Takagi

$$C(0,1)=1-2\beta^6-10\beta^{10}+14\beta^{12}-70\beta^{14}+192\beta^{16}-698\beta^{18}\ldots \qquad (3.5)$$

Comparison (3.2) and (3.5) shows that the discrepancy arises at the term of the order β^{16}. This approximation proves to be better in simple cubic lattice than in two-dimensional case, but perhaps this may be accidental.

Recently, Shimazu(7) improved on the Zernike's treatment combining it with the Bethe's theory. His results are following:

Shimazu

$$C(0,1)=1-2\beta^6-10\beta^{10}+14\beta^{12}-70\beta^{14}+192\beta^{16}\ldots$$
$$C(0,2)=1-2\beta^6-12\beta^{10}+16\beta^{12}-88\beta^{14}+2\beta^{15}+236\beta^{16}\ldots$$
$$C(0,3)=1-2\beta^6-12\beta^{10}+16\beta^{12}-89\beta^{14}+238\beta^{16}\ldots$$
$$C(0,4)=1-2\beta^6-12\beta^{10}+16\beta^{12}-90\beta^{14}+\beta^{15}+240\beta^{16}\ldots$$
$$C(0,5)=1-2\beta^6-12\beta^{10}+16\beta^{12}-90\beta^{14}+240\beta^{16}\ldots$$
$C(0,n)\ n\geqq 6$ equal $C(0,5)$ to terms of order β^{16}.
(3.6)

Comparing (3.6) with (3.3) and (3.4), it is clear that the Shimazu's method makes the Zernike's one better.

§ 4. The Correlation Probabilities of More Complicated Configurations.

As Ashkin and Lamb(4) have obtained the correlation probabilities of more complicated configurations in two-dimensional lattice by using eigenvectors, the author also obtains them in simple cubic lattice. As shown in Fig. 2, the correlation probabilities between 0 th spin and 1′th, 2′th,... spins on the next line shall be denoted by $C(0, 1')$, $C(0, 2')$,... These are

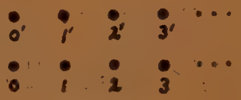

Fig. 2.

$$C(0,1')=1-2\beta^6-12\beta^{10}+16\beta^{12}-86\beta^{14}+209\beta^{16}-768\beta^{18}..$$
$$C(0,2')=1-2\beta^6-12\beta^{10}+16\beta^{12}-90\beta^{14}+216\beta^{16}-814\beta^{18}..$$
$$C(0,3')=1-2\beta^5-12\beta^{10}+16\beta^{12}-90\beta^{14}+216\beta^{16}-820\beta^{18}..$$
$C(0,n')n\geq 4$, equal $C(0, 3')$ to terms of order β^{16}. (4.1)

Next, the correlation probabilities between 0 th spin and 1″th, 2″th,... spins on the body diagonal direction are

$$C(0,1'')=1-2\beta^5-12\beta^{10}+16\beta^{12}-90\beta^{14}+216\beta^{16}-808\beta^{18}...$$
$$C(0,2'')=1-2\beta^5-12\beta^{10}+16\beta^{12}-90\beta^{14}+216\beta^{16}-820\beta^{18}...$$
$C(0,n'')n\geq 3$, equal $C(0, 2'')$ to terms of other β^{18}. (4.2)

Comparison with (3.3), (4.1) and (4.2) shows that in general

$$C(0, n)>C(0, n')>C(0, n''). \qquad (4.3)$$

(4.3) are easily understood by Fig. 3, since the distance from 0 th spin to 1 st, 1′th, 1″th spins becomes larger in order, the ordering effect becomes smaller in proportion to it. But whatever the direction is the correlation probability between 0 th spin and a spin very far away from it coincides with the following $C(0, \infty)$,

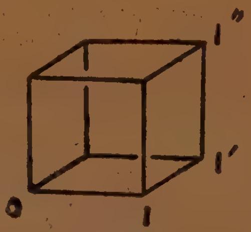

Fig. 3.

$$C(0, \infty)=1-2\beta^6-12\beta^{10}+16\beta^{12}-90\beta^{14}+216\beta^{16}-820\beta^{18}.. \qquad (4.4)$$

$C(0, \infty)$ are connected with the spontaneous magnetization I/Nm (in binary alloys, the long range order) as follows,

$$C(0, \infty)=\frac{1}{2}\{1+(I/Nm)^2\}. \qquad (4.5)$$

If one calculates I/Nm from (4.4) and (4.5), it agree completely with (2.9).

Next, when the initial arrangement to consider is an ordered pair of adjacent spins, that is, we know that 0 th spin and 1 st spin are parallel to each other, the correlation probabilities between them and 2 nd, 3 rd... spins shall be denoted by $C(01, 2)$, $C(01, 3)$,... These are as follows;

$$C(01, 2)=1-\beta^6-6\beta^{10}+6\beta^{12}-44\beta^{14}+84\beta^{16}-369\beta^{18}...$$
$$C(01, 3)=1-\beta^6-7\beta^{10}+7\beta^{12}-54\beta^{14}+102\beta^{16}-463\beta^{18}...$$
$$C(01, 4)=1-\beta^6-7\beta^{10}+7\beta^{12}-55\beta^{14}+104\beta^{16}-478\beta^{18}...$$
$$C(01, 5)=1-\beta^6-7\beta^{10}+7\beta^{12}-55\beta^{14}+104\beta^{16}-479\beta^{18}...$$
$C(01, n)n\geq 6$, equal $C(01, 5)$ to terms of order β^{18}. (4.6)

The same calculations are performed when the initial arrangement of ordered pair 0 th and 1 st is replaced with ordered pair of 1 st and 1′th spins;

$$C(11', 2)=1-\beta^5-6\beta^{10}+6\beta^{12}-43\beta^{14}+83\beta^{16}-358\beta^{18}...$$
$$C(11', 3)=1-\beta^5-7\beta^{10}+7\beta^{12}-54\beta^{14}+102\beta^{16}-459\beta^{18}...$$
$$C(11', 4)=1-\beta^5-7\beta^{10}+7\beta^{12}-55\beta^{14}+104\beta^{16}-478\beta^{18}...$$
$$C(11', 5)=1-\beta^5-7\beta^{10}-7\beta^{12}-55\beta^{14}+104\beta^{16}-479\beta^{18}...$$
$C(11', n)n\geq 6$, equal $C(11', 5)$ to terms of order β^{18}. (4.7)

Comparing between (4.6) and (4.7),

$$C(11', n)>C(0.1, n). \qquad (4.8)$$

The reason for (4.8) can be easily understood. In the diagram of Fig. 2 the ordering effect from 1′th is larger than that from 0 th, because the distance is shorter.

Whatever configurations of initial arrangement be taken, the calculations can be performed with the same principle. In these calculations this method is superior to that by eigenvectors. For example, when 0 th, 0′th, 1 st and 1′th spins are parallel to one another, the correlation probabilies between this cluster and 2 nd, 3 rd,...

spins shall be denoted by $C(00'11', 2)$, $C(00'11', 3)\ldots$ These are

$$C(00'11', 2)=1-\beta^{8}-5\beta^{10}+6\beta^{12}-31\beta^{14}+75\beta^{16}-291\beta^{18}\ldots$$
$$C(00'11', 3)=1-\beta^{8}-6\beta^{10}+7\beta^{12}-41\beta^{14}+94\beta^{16}-379\beta^{18}\ldots$$
$$C(00'11', 4)=1-\beta^{8}-6\beta^{10}+7\beta^{12}-42\beta^{14}+96\beta^{16}-395\beta^{18}\ldots$$
$$C(00'11', 5)=1-\beta^{6}-6\beta^{10}+7\beta^{12}-42\beta^{14}+96\beta^{16}-396\beta^{18}\ldots$$

$C(00'11', n)n \geq 6$, equal $C(00'11', 5)$ to terms of order β^{18}. (4.9)

As expected, the bigger the initial arrangement, the larger the correlation probabilities.

Lastly, when the initial arrangement is disordered pair, i. e., 0th spin is $+$(or $-$) while 1st spin is $-$(or $+$), the correlation probabilities for the case in which 2nd, 3rd, ... spins are $+$(or $-$), are denoted by $C'(01, 2)$, $C'(01, 3), \ldots$ respectively. These are

$$C'(01, 2)=\frac{1}{2}(1-\beta^{4}+\beta^{6}-4\beta^{8}+6\beta^{10}-20\beta^{12}\ldots)$$
$$C'(01, 3)=\frac{1}{2}(\qquad -\beta^{8}+2\beta^{10}-9\beta^{12}\ldots)$$
$$C'(01, 4)=\frac{1}{2}(\qquad -\beta^{12}\ldots) \quad (4.10)$$
$$C'(01, 5)=\frac{1}{2}(\qquad \ldots)$$

$C'(01, n)n \geq 6$, equal 1/2 to terms of order β^{12}

These series shows that at large distances the correlation probabilities arrising from the disordered pair approach the value 1/2. The disordered pair therefore has no ordering influence at all at large distances, since the probability of finding a $+$ or a $-$ spin at a given lattice point when the disordered pair is not present is also equal to 1/2. The spins of the disordered pair thus have the tendency to annul each other's ordering effect, the cancellation being completely at infinite distance.

The author thanks to Professors Y. Takagi and R. Kubo for valuable discussions and also to Professor H. Takahashi for useful suggestion which give him a motive of this calculations.

This work is due to the Subsidy for Scientific Researches of Department of Education.

References.

(1) T. Oguchi, J. Phys. Soc. Japan, **5** (1950) 75.
(2) F. Bloch, Zeits. f. Phys. **61** (1930) 206.
(3) T. Tanaka, Busseiron-Kenkyu, **20** (1949) 102, (in Japanese).
(4) J. Ashin and W. E. Lamb Jr, Phys. Rev. **64** (1943) 159.
(5) F. Zernike, Physica, **7** (1940) 565.
(6) H. A. Bethe, Proc. Roy. Soc. **150A** (1935) 552.
Y. Takagi, Proc. Phys.-Math. Soc. Japan, **23**, (1941), 44, 553.
(7) H. Shimazu, Prog. Theor. Phys. **4** (1949) 201.

Statistics of the Three-Dimensional Ferromagnet (III).

By Takehiko OGUCHI.

Tokyo Institute of Technology, Oh-okayama, Tokyo.

(Received June 9, 1950)

§ 1. Introduction.

In Part II⁽¹⁾, we discussed the propagation of order at low temperatures. Above the Curie point where there is no long range order, ordering effect still exists by means of short range order. As far as the author knows, however, there is no treatment of this problem for the three-dimensional ferromagnet. In this case the method of eigenvalue problem becomes too complex to draw out any concrete result. So in this paper, we will discuss it by a new method which resembles the virial expansion for imperfect gases.

§ 2. The Partition Function for High Temperatures.

In this paper we continue to consider simple cubic Ising ferromagnet. The partition function which has the same contents as (2.2) in Part II, is expressed in another form for vanishing fields as follows,

$$f=\sum_{\mu_i=\pm 1}\exp\Big(K\sum_{<ik>}\mu_i\mu_k\Big), \qquad (2.1)$$

where $K=J/2kT$. (2.2)

Since the notation are just the same as those in Part II, so we do not explain them any more except first summation $\sum\limits_{\mu_i=\pm 1}$, which is to be understood to extend over all possible states of the system, i.e., it would have to be written explicitly as

$$\sum_{\mu_i=\pm 1}=\sum_{\mu_1=\pm 1}\sum_{\mu_2=\pm 1}\cdots\sum_{\mu_N=\pm 1} \qquad (2.3)$$

As it is difficult to carry out the summation of (2.1) directly, one might try to expand in the power series of K⁽²⁾. But it is much easier to carry out the calculations transforming it into the form

$$f=(\cosh K)^{3N}\sum_{\mu_i=\pm 1}\prod_{<ik>}(1+\mu_i\mu_k\tanh K), \qquad (2.4)$$

and then expanding it in a power series of tanh K. Where $\prod\limits_{<ik>}$ means that the product is carried out over all connecting lines between the direct neighbours, namely "pairs". In developing the product, we get a sum of various products. But after it is summed over all values of the μ's, the greater parts of the terms will vanish. Non-vanishing terms are only those which consist of the pairs forming closed polygons in the same way as dual transformation by Wannier⁽³⁾. Of course, as they are in the three-dimensional lattice, these polygons are not always on one plane. These non-vanishing terms are independent of μ_i, so they are simply multiplied by 2^N when the summation $\sum\limits_{\mu_i=\pm 1}$ is carried through. Thus the partition function is expressed in the following form,

$$f=2^N(\cosh K)^{3N}\Big[1+\sum_n\Omega_n\kappa^n\Big], \qquad (2.5)$$

where $\kappa=\tanh K$. (2.6)

Ω_n is the coefficient which is to be calculated. It is so difficult to obtain analytically all Ω_n that we here have calculated the terms up to $n=8$ which are dominant for high temperatures. Non-vanishing terms are the following;

$$\Omega_4=\omega_4=3N$$

$$\Omega_6=\omega_6=22N$$

$$\Omega_8=\omega_8+\omega_4\times\omega_4=\frac{9}{2}N^2+\frac{375}{2}N.$$

where ω_n is the number of closed polygons each of which consists of n pairs, and $\omega_n\times\omega_n$ does not mean the ordinary multiplication but means the number of all configurations in which two polygons containing respectively n pairs exist not so as to hold any pair in common. Using (2.7),

$$f=2^N(\cosh K)^{3N}\Big[1+3N\kappa^4+22N\kappa^6+\Big(\frac{9}{2}N^2+\frac{375}{2}N\Big)\kappa^8\ldots\Big] \qquad (2.8)$$

Hence the partition function per individual spin valid for high temperatures is

$$f^{1/N}=2(\cosh K)^3[1+3\kappa^4+22\kappa^6+192\kappa^8\ldots] \qquad (2.9)^*$$

If we expand (2.9) in power series of K, we will obtain the same result that Ter Haar⁽⁴⁾ has obtained by the method of Opechowsky⁽³⁾ up to the terms of order K^6.

In the two-dimensional ferromagnet, Montroll⁽⁵⁾ has determined Curie point by searching a point at which two partition functions corresponding to ours, i.e. the formula (2.8) in Part II and the formula (2.9) in the present paper, have the same value. We have tried the same operation in the three-dimensional case. But unfortunately, due to poor convergence of (2.8) in Part II, a definite point, such as that in the two-dimensional case, cannot be determined, but the range of existence of the Curie point K_c may be concluded as follows⁽⁶⁾,

$$0.21<K_c<0.24. \qquad (2.10)$$

In the three-dimensional ferromagnet, the reason why above calculation is less accurate, may be attributed to the following two possibilities:—one is that the analytical property of the Curie point of the three-dimensional ferromagnet may differ from that of the two-dimensional one, and the other is that since the Curie point of the three-dimensional ferromagnet is higher that of the two-dimensional one, the series valid for low temperatures becomes less convergent near the Curie point.

---

* In reference (6), the coefficient of κ^8 is incorrect.

Recently Kikuchi⁽⁷⁾ obtained the Curie point of the three-dimensional ferromagnet by his approximation corresponding to the variational method of Kramers and Wannier⁽⁸⁾. His result exsists within the limits of (2.10). This shows that his approximation is good. It may be said in this connection it must be noticed that by the first approximation of Bethe, K_c is equal to 0.20.

§ 3. The Propagation of Order at High Temperatures.

Now, let us obtain the propagation of order in simple cubic lattice at high temperatures. The course of calculation is similar to that in Part II. We need the quotient of the partition function of the state in which some spin polarities are fixed and the ordinary partition function not restricted.

At first, let us consider f_{01}. In this case, we must calculate the partition function (2.4) in the restriction of that 0-th spin and 1-st spin are parallel to each other.

Thus non-vanishing terms are, in addition to closed polygons, those lines consisting of successive pairs (of course, they are not always on one plane) which start from 0-th spin and terminate at 1-st spin. Because the summations of 0-th and 1-st spins which make these terms vanish in § 2 are, from the first, taken off in the calculation of f_{01}. Thus,

$$f_{01} = 2^{N-1} (\cosh K)^{3N}[1+\sum \Omega_n^{(1)}\kappa^n], \qquad (3.1)$$

where

$$\begin{aligned}
\Omega_1^{(1)} &= \omega_{11} = 1 \\
\Omega_3^{(1)} &= \omega_{13} = 4 \\
\Omega_4^{(1)} &= \omega_4 = 3N \\
\Omega_5^{(1)} &= \omega_{15} + \omega_{11}\times\omega_4 = 3N+40 \qquad (3.2)\\
\Omega_6^{(1)} &= \omega_6 = 22N \\
\Omega_7^{(1)} &= \omega_{17}+\omega_{11}\times\omega_6\times\omega_{13}+\omega_4 = 34N+456 \\
\Omega_8^{(1)} &= \omega_8+\omega_4\times\omega_4 = \frac{9}{2}N^2+\frac{375}{2}N
\end{aligned}$$

ω_{nm} is the number of all configurations in which starting from 0-th spin and passing m pairs, it terminates at n-th spin which is a distance of n sites away from the 0-th spin without passing through the same spin more than once, (see, Fig. 1). $\omega_{nm}\times\omega_l$, like (2.7), does not mean the ordinary multiplication but means the number of all configurations in which ω_{nm} and ω_l exist not so as to hold any pair in common. Using (2.8) and (3.1) the correlation probability $C(0,1)$ is given,

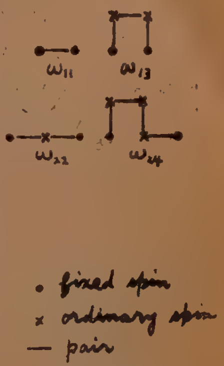

Fig. 1.

$$C(0,1) = \frac{f_{01}}{f} = \frac{1}{2}[1+\kappa+4\kappa^3+40\kappa^5+456\kappa^7\ldots) \qquad (3.3)$$

By the same way, the following results are obtained,

$$\begin{aligned}
C(0,1) &= \frac{1}{2}[1+\kappa+4\kappa^3+40\kappa^5+456\kappa^7\ldots] \\
C(0,2) &= \frac{1}{2}[1+\kappa^2+12\kappa^4+176\kappa^6+2348\kappa^8\ldots] \\
C(0,3) &= \frac{1}{2}[1+\kappa^3+24\kappa^5+504\kappa^7\ldots] \\
C(0,4) &= \frac{1}{2}[1+\kappa^4+40\kappa^6+1156\kappa^8\ldots] \qquad (3.4)\\
C(0,5) &= \frac{1}{2}[1+\kappa^5+60\kappa^7\ldots] \\
C(0,6) &= \frac{1}{2}[1+\kappa^6+84\kappa^8\ldots] \\
C(0,7) &= \frac{1}{2}[1+\kappa^7\ldots] \\
C(0,8) &= \frac{1}{2}[1+\kappa^8\ldots]
\end{aligned}$$

As may be seen,

$$C(0,n) = \frac{1}{2}[1+0(\kappa^n)] \qquad (3.5)$$

(3.5) shows that at large distances the correlation probabilities approach the value 1/2, and there is no ordering effect as was in the last section of Part II, which means there is no spontaneous magnetization or long range order. Figs. 2 and 3 show (3.3) in Part II and (3.4) in this paper.

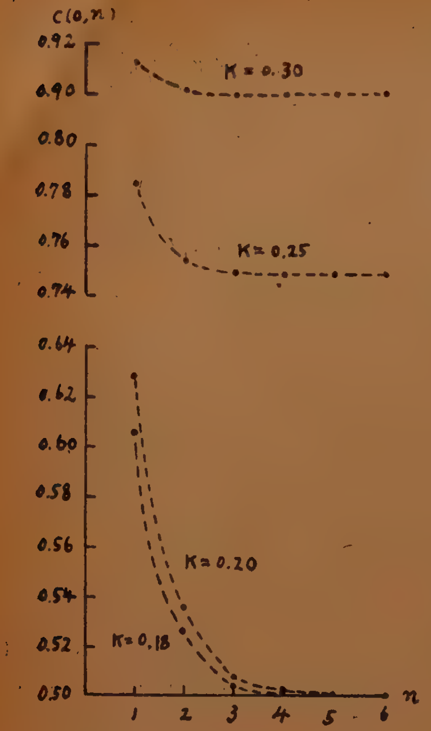

Fig. 2. The curves of $K=0.30$ and 0.25 are calculated according to (3.3) in Part II and those of $K=0.20$ and 0.18 according to (3.4) in this paper.

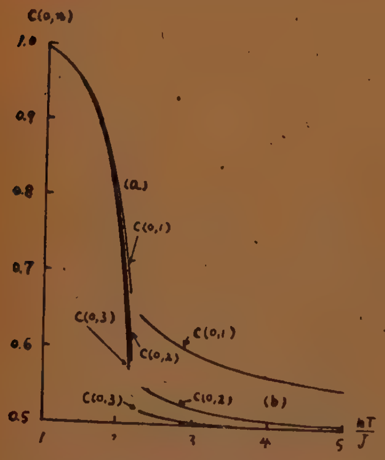

Fig. 3. The curves of (a) are calculated according to (3.3) in Part II and those of (b) acbording to (3.4) in this paper.

§ 4. The Paramagnetic Susceptibility.

In order to calculate the paramagnetic susceptibility, we must add the energy due to the external field H to the partition function (2.1). Thus.

$$f=\sum_{\mu_i=\pm 1}\exp\Big(K\sum_{<ik>}\mu_i\mu_k+C\sum_i \mu_i\Big)$$
$$=(\cosh K)^{3N}(\cosh C)^N\sum_{\mu_i=\pm 1}\prod_{<ik>}(1+\mu_i\mu_k\kappa)\prod_i \times(1+\mu_i\tanh C)\qquad(4.1)$$

where $C=mH/kT.\qquad(4.2)$

Since the susceptibility is the coefficient of $(\tanh C)^2$ in $\log f$, the terms in (4.1) required for our calculation are,

$$f=2^N(\cosh K)^{3N}(\cosh C)^N\Big[1+\sum_n \boldsymbol{\theta}_n\kappa^n\times(\tanh C)^2+\Omega_4\kappa^4\ldots\Big]\qquad(4.3)$$

$$\begin{aligned}\boldsymbol{\theta}_1&=\theta_1=3N\\ \boldsymbol{\theta}_2&=\theta_2=15N\\ \boldsymbol{\theta}_3&=\theta_3=75N\\ \boldsymbol{\theta}_4&=\theta_4=363N\\ \boldsymbol{\theta}_5&=\theta_5+\omega_4\times\theta_1=9N^2+1755N\\ \boldsymbol{\theta}_6&=\theta_6+\omega_4\times\theta_2=45N^2+8355N.\end{aligned}\qquad(4.4)$$

$\boldsymbol{\theta}_n$ is the total number of the following arrangements; starting from any spin, moving a lattice distance along a pair, we change the course at will and move a lattice distance along another pair, and repeat this operation n times. This is one of the so-called problems of random flights. Compared with the ordinary problem of random flights, the distinct points are that the paths are always on pair lines and that it is not allowed to pass through the same spin more than once. Owing to latter restriction, the alalitical evaluation of $\boldsymbol{\theta}_n$ is very difficult.

Thus according to the relation of thermodynamics, we can give the paramagnetic susceptibility as follows,

$$\chi=\lim_{c\to 0}\frac{N\mu^2}{kT}\frac{\partial^2}{\partial c^2}(\log f)$$
$$=\frac{N\mu^2}{kT}[1+6\kappa+30\kappa^2+150\kappa^3+726\kappa^4+3510\kappa^5+16710\kappa^6\cdots],\qquad(4.5)$$

or,

$$\frac{2N\mu^2}{J}\frac{1}{\chi}=\frac{1}{K}[1-6\kappa+6\kappa^2-6\kappa^3+30\kappa^4-54\kappa^5+318\kappa^6\cdots].\qquad(4.6)$$

§ 5. Other Lattice Types.

In the one-dimensional ferromagnet, the rigorous solution is obtained by above method. In this case, since there is no closed polygons, all terms containing μ's vanish, hence

$$f=(\cosh K)^N \sum_{\mu_i=\pm 1} \prod_{<ik>} (1+\mu_i\mu_k\kappa) = 2^N (\cosh K)^N, \tag{5.1}$$

$$f^{1/N} = 2(\cosh K), \tag{5.2}$$

This result is obtained by various method as mentioned before, but (5.1) is the simplest method among them. The correlation probabilities are also obtained exactly in the one-dimensional case. The results are following,

$$C(0,\,n)=\frac{1}{2}[1+\kappa^n]. \tag{5.3}$$

which is valid for all temperatures. Hence there can be no spontaneous magnetization or long range order in the one-dimensional case, because $C(0,\,n)$ tends to the value 1/2 when n increases (5.3) corresponds to the molecular distribution function in "Statistical mechanics of one-dimensional substance," by Nagamiya.(9)

Next, for body centered cubic (abbreviated) by b.c.c.) and face centered cubic (f.c.c.), the same calculations as that for simple cubic (s.c.) are also performed. Only the results shall be given,

$$\text{b.c.c.}\quad f^{1/N}=2(\cosh K)^4[1+12\kappa^4+148\kappa^6\cdots]. \tag{5.4}$$

$$\text{f.c.c.}\quad f^{1/N}=2(\cosh K)^6[1+8\kappa^3+33\kappa^4\cdots]. \tag{5.5}$$

The method to obtain the Curie point from partition function for low temperatures and that for high temperatures does not give a definite value on account of poor convergence.

The partition function for the paramagnetic region is easily obtained by Bethe-Takagi's approximation, in which the partition function per individual spin $f_z^{1/N}$ is given by,

$$f_z^{1/N}=2(\cosh K)^{\frac{z}{2}} \tag{5.6}$$

where z is the number of the nearest neighbours. It is interesting to compare (5.6) with (2.9), (5.4) and (5.5). Bethe-Takagi's approximation has one parameter more on the low temperature side, than on the high temperature side in short, their treatment is asymmetrical on both sides of Curie point. Thus the terms corresponding to the closed polygons which are to be an origin of dual transformation are missed.

The reciprocal of paramagnetic susceptibility χ is given by,

$$\text{b.c.c.}\quad \frac{2N\mu^2}{J}\frac{1}{\chi}=\frac{1}{K}[1-8\kappa+8\kappa^2-8\kappa^3+104\kappa^4\cdots], \tag{5.7}$$

$$\text{f.c.c.}\quad \frac{2N\mu^2}{J}\frac{1}{\chi}=\frac{1}{K}[1-12\kappa+12\kappa^2+36\kappa^3+180\kappa^4\cdots]. \tag{5.8}$$

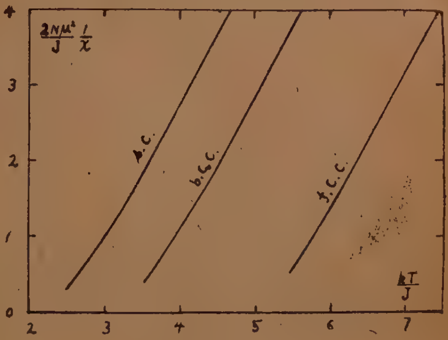

Fig. 4.

Fig. 4 shows $\frac{2N\mu^2}{J}\frac{1}{\chi}$ *vs.* kT/J from (4.6), (5.7) and (5.8). As shown in the figure, the Curie-Weiss' relation holds fairly well. But in the vicinities of the Curie points they deviate from straight lines. The theoretical paramagnetic Curie points K_p are obtained from the asymptotes of (4.6), (5.7) and (5.8) as follows,

$$\begin{aligned} &\text{s.c.} && K_p=0.17,\\ &\text{b.c.c.} && K_p=0.13,\\ &\text{f.c.c.} && K_p=0.08. \end{aligned} \tag{5.9}$$

In conclusion, the author wishes to express his sincere thanks to Professor Y. Takagi and Professor R. Kubo for their kind guidances and valuable discussions during the course of this work.

The expense of this research has been defrayed from the Scientific Research Expenditure of Department of Education.

References.

(1) T. Oguchi, J. Phys. Soc. Japan, **6**, (1951), 27.
(2) W. Opechowsky, Physics, **4**, 181, (1937).
(3) G. H. Wannier, Rev. Mod. Phys. **17**. 50, (1945).
(4) D. Ter Haar, Phys. Rev. **76**, 176 (1949).
(5) E. W. Montroll, J. Chem. Phys. **10**, 61, (1942).
(6) T. Oguchi, Busseiron-Kenkyu, **22**, 26, (1950) (in Japanese).
(7) R. Kikuchi, Busseiron-Kenkyu, **24**, 65, (1950) (in Japanese).
(8) H. A. Kramers and G. H. wannier, Phys. Rev. **60**, 263, (1941).
(9) T. Nagamiya, Proc. Phys.-Math. Soc. Japan, **22**, 705, (1940).

Dielectric and Thermal Properties of Barium·Lead Titanates.

By Shoichiro NOMURA and Shozo SAWADA.

Institue of Science and Technology, University of Tokyo.

(Received June 15, 1950)

§ 1. Introduction.

As in the case of barium·strontium titanates, barium·lead titanates ceramics have been reported to form solid solution(1) and to have higher Curie temperature than that of pure barium titanate in contrast to the case of barium·strontium titanates, but their detailed physical properties, i.e. permittivity, specific heat, thermal expansion, etc., have not yet been measured so far.*

Hitherto lead titanate has drawn less attention on account of being regarded only as a supplementary substance for barium titanate. The interesting features of lead·strontium titanates, however, seems to stimulate us to get the detailed knowlede of the lead titanate itself.(2)

As a preliminary work to clarify the physical properties of the lead titanate itself, we, therefore, have measured the permittivity, the specific heat and the thermal expansion of solid solutions of barium·lead titanates in the temperature range of room temperature to 400°C and found that a rather discontinous phase change occurred at the Curie point of the mentioned solution.

According to our preliminary measurement (unpublished), the permittivity of lead titanate of about 100 at room temperature increases with temperature, but we cannot make sure experimentally the existence of Curie point owing to its large loss factor at higher temperatures. Our results, however, seem to indicate qualitatively that lead titanate has a dielectric anomaly at a certain temperature higher than 500°C.

§ 2. Preparation of samples.

Barium· and lead·titanates ceramics were prepared separately by our usual method,(3) firing temperature being about 1250°C and 1200°C respectively. On firing lead titanate, an attention must be payed to prevent it from its reduction. Being pulverized, mixed in a needed molar concentration and pressed into a disk, the mixture was refired at 1300°C~1400°C for a few hours, and then was made into samples.

We used, as electrodes, fired-on silver paste, to which leading wires were connected by silver solder. For particular purpose, we repeated the above operation over again.

As the content of lead titanate increases, the apparent colour of the materials in bulk varies from yellow to slightly brown.

§ 3. Permittivity of samples with various molar percentages.

Fig. I shows one series of permittivity of barium·lead titanates with different concentration of the materials observed at 1043KC. As the content of lead titanate increases, the absolute value of permittivity becomes lower. In the case of 40%$BaTiO_3$+60%$PbTiO_3$, the permittivity at room temperature is about 100 and becomes ten times large at the transition temperature of about 380°C.

The relation between Curie temperature and molar ratio is illustrated in Fig. 2, which shows a linear relation between them. Assuming that this linear relation holds good in the total range of molar ratios, we find, by means of the extrapolation, that pure lead titanate has Curie point at about 560°C, which cannot be practically

---

* At the Meeting of Physical Society of Japan held on April, 1, 1950, K. Suzuki & S. Miyake pointed out that a large amount of discontinuity of lattice constants at the Curie point occurs for barium·lead titanate.

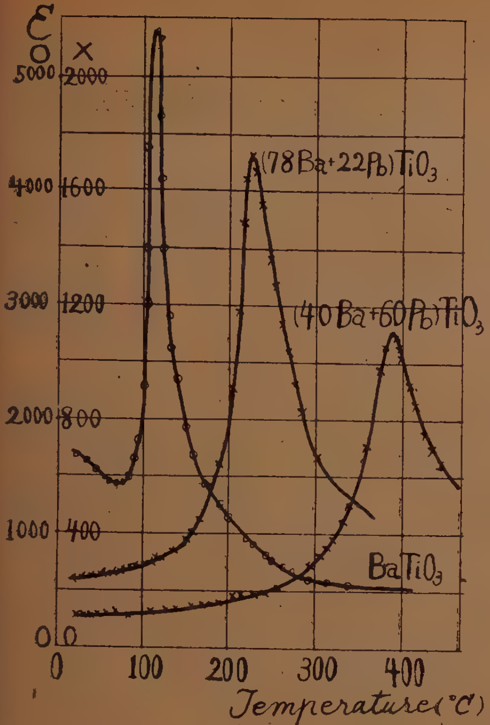

Fig. 1.

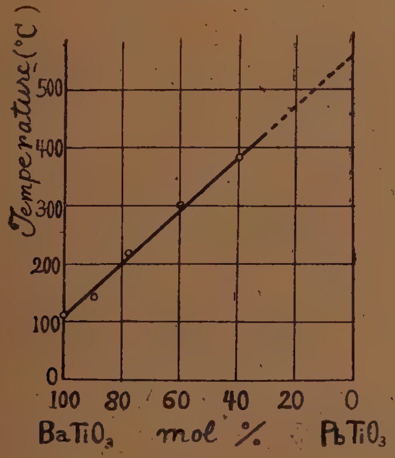

Fig. 2.

measured because of its large loss factor at such high temperatures.

Curie-Weiss' formula holds above the Curie temperature, that is

$$\varepsilon = \frac{C}{T-T_c}, \tag{1}$$

where C and T_c are constants to be determined empirically for each molar percentage.(4), (5), (6)

Fig. 3 shows C for several molar ratios. In

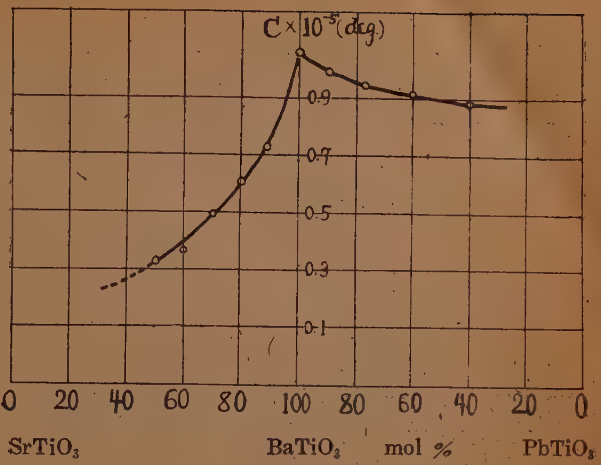

Fig. 3.

contrast to our results of barium-strontium titanates, in which C decreases rather rapidly with increasing percentage of strontium titanate, C is seen, in Fig. 3, to be nearly constant in the case of barium-lead titanate. In view of the ionic radius of Pb^{++} being nearer that of Ba^{++} than Sr^{++}, this fact may be expected to be realized according to the idea due to Santen-Jonker(4) & Roberts(6) regarding dielectric constant of simple crystal lattices, which says that C is most sensible to the thermal expansion.

§ 4. Thermal expansion.

The method of measurement and the aparatus (one type of dilatometer) are the same as used

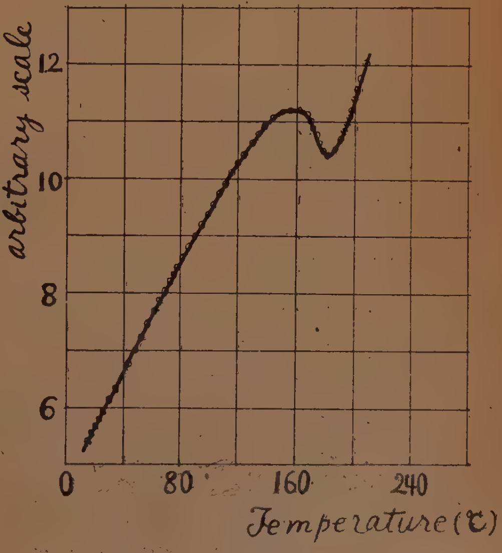

Fig. 4.

in the case of barium-titanate and barium-strontium titanate. The ordinate in Fig. 4 shows directly the scale reading for the sample of 80% $BaTiO_3+20\% PbTiO_3$, which scale is proportional to length at each temperature, where

$$l+l'=6.7 \text{ cm}, \quad D=281.0 \text{ cm}, \quad a=11.0 \text{ cm}, \quad r=0.189 \text{ cm} \qquad (2)$$

in the original notation.(3)

Up to about 155°C, the sample is observed to expand in a monotonous way and to contract at temperatures between 155°C and 180°C, after which it expands again. 180°C corresponds to the Curie point, as seen rather less distinctly, due to the abrupt increase of loss factor, in Fig. 5. These states of affairs have been found also in the cases of barium-titanate and barium-strontium titanate.

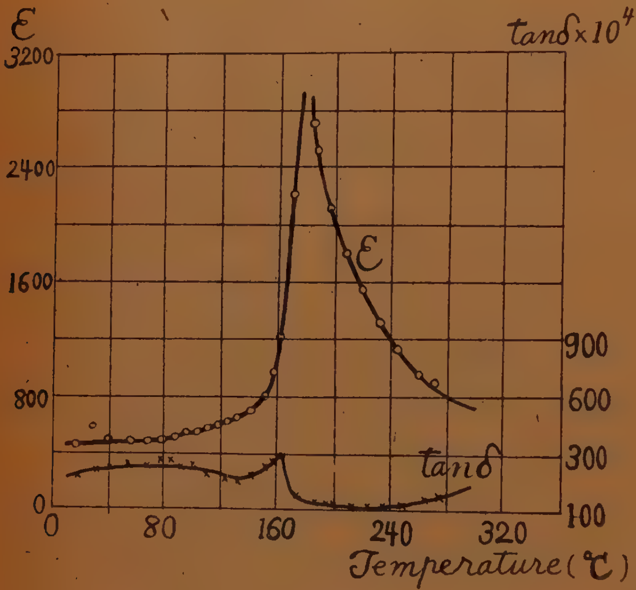

Fig. 5.

Using the data in Fig. 4, the thermal expansion coefficient β is obtained, as is plotted in Fig. 6. It is seen on the figure that β decreases gradually from room temperature, and is negative in the temperature range of about 20°C just below the transition point. The negative peak value of β is observed at 174°C in our case. The integrated relative contraction involved in the anomalous region becomes of 0.007%, which value is remarkably larger than that of barium titanate.

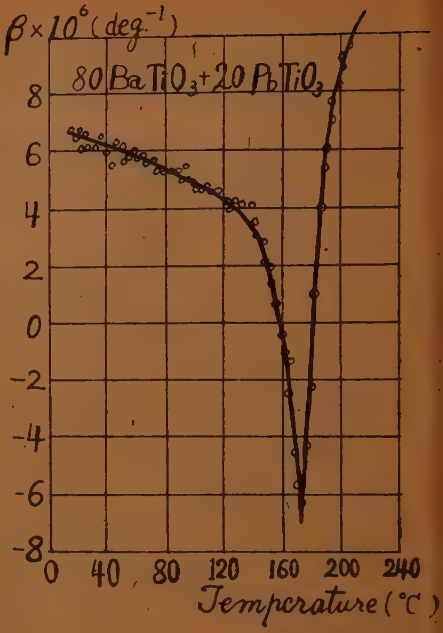

Fig. 6.

§ 5. Specific heat.

The specific heat was measured by the same method as used in the case of barium titanate(3) and a rather

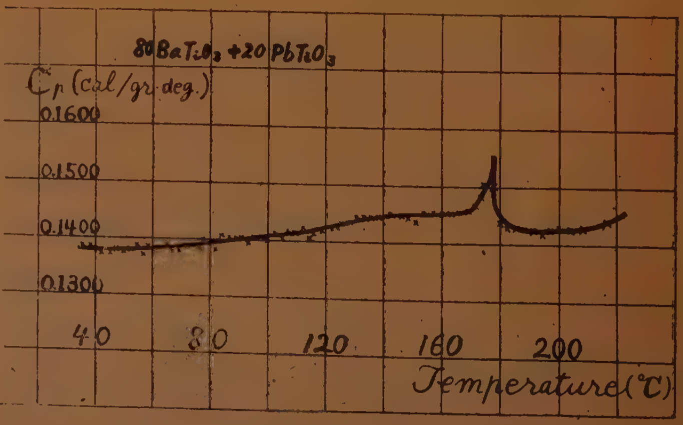

Fig. 7.

sharp anomaly was observed at the Curie temperature, which is illustrated in Fig. 7. The magnitude of the anomaly at the Curie point is not estimated by our measurement because of the feature being discontinous. As pointed out already, this method of measurement is not favourable for such samples that have poor thermal conductivity, and so, the results may probably give rather a average value of the samples.

§ 6. Discussion.

The changes at the transition point of the various physical quantities occurs rather discontinously and the amount of anomaly of thermal expansion is large as pointed out by Suzuki & Miyake. Regarding the crystal structure of lead titanate, the detailed investigation has not been carried out, but it has been estimated to have an orthorhombic symmetry. As the sample becomes richer in lead titanate, the asymmetry of crystal, for instance, the difference of a and c in the tetragonal region will probably be predominated. In consequence, it might be said that the jump at transition temperature of the various physical quantities becomes larger as was observed. In the case of barium-strontium titanate, the influence of adding of strontium-titanate is effected in the opposite side.

In the sequence of ionic radii of Ba^{++} (1.43Å), Pb^{++} (1.32Å), and Sr^{++} (1.27Å), Ba^{++} and Sr^{++} have the inert gas configuration, while Pb^{++} has not. The atomic polarizabilities associated with its electron configuration of the component atoms mentioned above may probably be considered to make important roles in the ferroelectric behaviours and the related phenomena of the materials.

Due to Roberts,(6) the relation between Curie-Weiss' constant C and thermal expansion coefficient β is given by

$$\frac{1}{C}=\beta-\frac{1}{3\alpha}\frac{d\alpha}{dT} \tag{3}$$

where α is the atomic polarizability. In our case, $1/C$ and β have the nearly same value of 9×10^{-6}, so that the change of permittivity with temperature is considered to be mainly due to the thermal expansion.

Futher detailed investigation of the lattice structure by X-rays is much desirable, in order to clarify the mechanism of the ferroelectricity of the material under consideration. Now works regarding lead titanate itself are in progress in our laboratory.

The authors wish to express their hearty thanks to Prof. T. Muto for his very kind advices and instructions.

References.

(1) A. von Hippel and co-workers; Ind. & Eng. Chem., **38** (1946), 1097.

(2) S. Nomura and S. Sawada; J. Phys. Soc. Japan., **5** (1950), 279.

(3) S. Sawada and G. Shirane; J. Phys. Soc. Japan., **4** (1949), 52.

(4) J. H. van Santen & G. H. Jonker; Nature, **159** (1947), 333.

(5) S. Roberts; Phys. Rev., **71** (1947), 890.

(6) S. Roberts; Phys. Rev., **76** (1949), 1215.

Theory of High Polymer Solutions.
I. Second Virial Coefficient for Rigid Ovaloids Model.

By Akira ISIHARA and Tsuyoshi HAYASHIDA.

Department of Physics, Faculty of Science, University of Tokyo.

(Read April 2, 1950; Received July 16, 1950)

§ 1. Introduction.

In the theories of high polymers we often use models either of a single compact body or of a pearl necklace type. But when their inter- or intramolecular interactions are taken into consideration, we sometimes come upon mathematical difficulties which are of similar nature in both cases. This is partly because we are required more or less to take account of the molecular shape or size even if we neglect the attractive potential. However, if these difficulties are overcome, an advance in our knowledge with respect to the behavior of macromolecules in solutions will assuredly be brought about. This paper is a trial for this purpose, and calculates the second virial coefficients which appear when the osmotic pressure π of high polymer solutions is expanded in the power series of concentration c;

$$\frac{\pi}{RTc}=\frac{1}{M_2}+A_2c+A_3c^2+\cdots\cdots, \tag{1}$$

where M_2 is the molecular weight of the solute, R the gas constant and T the absolute temperature. According to the theory of Zimm⁽¹⁾, the second and the third coefficients A_2 and A_3 are given by the expressions:

$$A_2=-\frac{N_0}{2VM_2^2}\int g_2\{2\}d\{2\}, \tag{2}$$

$$A_3=-\frac{N_0^2}{3VM_2^3}\int g_3\{3\}d\{3\}+4M_2A_2^2. \tag{3}$$

Here N_0 is Avogadro's number, V is the volume of the system, $\{n\}$ represents the coordinates of a set of n molecules, and the g-functions are connected with the F-functions as:

$$g_2(i,j)=F_2(i,j)-F_1(i)F_1(j), \tag{4}$$

$$g_3(i,j,k)=F_3(i,j,k)-F_2(i,j)F_1(k)-F_2(j,k)F_1(i)$$
$$-F_2(k,i)F_1(j)+2F_1(i)F_1(j)F_1(k). \tag{5}$$

(i) represents all the coordinates of i-th particle, and for a system containing n molecules

$$\frac{1}{V^n}F_n\{n\}d\{n\}$$

is the probability that the n specified molecules have the configurations specified by $\{n\}$ in the infinitesimal range of the coordinates correspond to $d\{n\}$.

To calculate A_2 we assume here a rigid body model. Then F must be zero when two particles interpenetrate one another; otherwise it assumes unity. Hence, A_2 will be given by,

$$A_2=\frac{4N_0v}{M_2^2}f, \tag{6}$$

$$f=-\frac{1}{8Vv}\int g_2\{2\}d\{2\}=\frac{1}{8v}\int_{A\cdot B\neq 0} dv_B, \tag{7}$$

where v represents the volume of one of the molecules, and the integration of Eq. (7) extends over all the configurations of one molecule where the common volume of two particles A and B does not vanish. The numerical factor f is unity in the case of spherical particles⁽¹⁾ and has been calculated approximately in the case of cylindrical and spheroidal particles⁽¹⁾⁽²⁾.

In the following sections we shall give, with more elaborate form than the article given by one of us⁽²⁾, the most general expression for f in the case of rigid ovaloid (see Eq. (35)) including various special cases (see Eqs. (5), (13), (18) and (24) of Part II of this series) as well as some new formulas of differential geometry. The method of the calculation is general and we hope that it will find many applications in other problems.

§ 2. The Principle of Calculation.

For the convenience of mathmatical treatment we consider, for a while, the particles as rigid smooth-ovaloids. The relative positions of two ovaloids A and B are determined by six parameters which compose a space G in the group of motions. This means that the relative positions are determined by the motions of B from a standard position, considering A to be fixed. Then its motions, corresponding to the relative positions in which A and B interset each other, constitute a subset I in the group G. The evaluation of the integral of Eq. (7) is reduced to search after the volume of I.

In order that the result does not depend on the choice of the standard position of B, we are required to seek for the Haar's measure $m(I)$ of I in G. It is obtained by integrating its characteristic function $f(x)$, $x \in G$, over whole G. In the group of motions G, translation group g is the normal subgroup and G/g is isomorphic to the rotation group. Let us perform the integration at first over each coset of g, and after that over G/g. (Fig. 1):

$$m(I) = \int_{G/g} d\bar{x} \int_g f(x\xi)\, d\xi, \qquad (8)$$

$$\xi \in g; \quad \bar{x} \in G/g.$$

The reason is that $\int_g f(x\xi)\, d\xi$, which means the integral of $f(x)$ over xg, is a function of subgroup $\bar{x}$ of x owing to $d\xi$ is the left invariant measure of g:

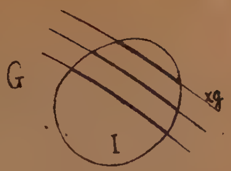

Fig. 1.

$$\int_g f(x\xi)\, d\xi = \int_g f(xa\eta)\, da\eta$$

$$= \int_g f(xa\eta)\, d\eta = \bar{f}(\bar{x}); \quad (a \in g).$$

Thus, if we remember $d\bar{x}$ is the left invariant measure of G/g,

$$\int_{G/g} f(\bar{b}\bar{x})\, d\bar{x} = \int_{G/g} \bar{f}(\bar{b}\bar{x})\, d(\bar{b}\bar{x}) = \int_{G/g} \bar{f}(\bar{y})\, dy\,.$$

Hence,

$$m(bI) = \int_{G/g} d\bar{x} \int_g f(bx\xi)\, d\xi = \int_{G/g} d\bar{x}\, \bar{f}(\bar{b}\bar{x}) = \int \bar{f}(\bar{x})\, d\bar{x},$$

$$\therefore \; m(bI) = m(I)\,.$$

This means $m(I)$ given by Eq. (1) does not depend on the standard position of B. In these equations we have already used the property that the Haar's measure of G can be factorized as $d\bar{x}d\xi$ using the Haar's measures of its normal subgroup g and the factor group G/g.

The infinitesimal volume element of Haar's measure of translation group g is the ordinary volume element of three dimensional Euclidean space and that of the rotation group G/g is given by⁽⁴⁾,

$$\frac{1}{8\pi^2} \sin\theta\, d\theta\, d\varphi\, d\tau = \frac{1}{8\pi^2} d\omega\, d\tau\,,$$

if we express its elements by

$$\begin{bmatrix} \sin\varphi\sin\tau + \cos\theta\cos\varphi\cos\tau, & -\cos\varphi\sin\tau + \cos\theta\sin\varphi\cos\tau, & -\cos\tau\sin\theta \\ -\sin\varphi\cos\tau + \cos\theta\cos\varphi\sin\tau, & \cos\varphi\cos\tau + \cos\theta\sin\varphi\sin\tau, & -\sin\theta\sin\tau \\ \sin\theta\cos\varphi, & \sin\theta\sin\varphi, & \cos\theta \end{bmatrix}. \qquad (9)$$

Now we think about the function $\bar{f}(\bar{x})$. This is obtained by the motion of B which keeps its orientation in space. The point o′ fixed in B describes a surface C when B moves around A always in touch with A (Fig. 2). A and B intersect each other when and only when o′ is a point of C: $\bar{f}(\bar{x})$ is the volnme of C. It can easily be demonstrated that C is another ovaloid.

§ 3. Ovaloid and Its Supporting Function.

We fix a coordinate system to ovaloid A and name its origin O and think a linear function $\alpha x + \beta y + \gamma z$ of x, y and z with constant coefficients α, β and γ which do not vanish simultaneously. It assumes a maximum value at a point $P(x, y, z)$

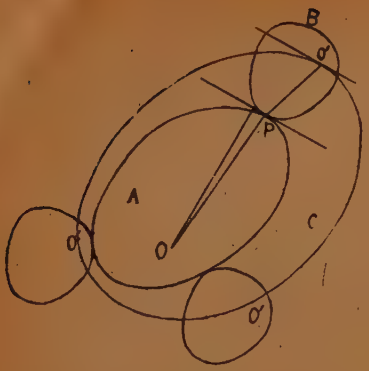

Fig. 2.

on the surface of A when (x, y, z) moves over the surface. The maximum value determined uniquely by α, β and γ is the so-called supporting function of the ovaloid with respect to the coordinate system, and it is denoted by

$$H(\alpha, \beta, \gamma) = \alpha x + \beta y + \gamma z\,. \tag{10}$$

As one can see easily, H is linear homogeneous function of its arguments α, β and γ:

$$H(\alpha, \beta, \gamma) = \alpha\frac{\partial H}{\partial \alpha} + \beta\frac{\partial H}{\partial \beta} + \gamma\frac{\partial H}{\partial \gamma}\,. \tag{11}$$

Hence,

$$\left.\begin{aligned} \alpha H_{\alpha\alpha} + \beta H_{\alpha\beta} + \gamma H_{\alpha\gamma} &= 0\,,\\ \alpha H_{\beta\alpha} + \beta H_{\beta\beta} + \gamma H_{\beta\gamma} &= 0\,,\\ \alpha H_{\gamma\alpha} + \beta H_{\gamma\beta} + \gamma H_{\gamma\gamma} &= 0\,,\\ \det(H_{\alpha\beta}) &= 0\,. \end{aligned}\right\} \tag{12}$$

At the point $P(x, y, z)$ where H is maximum (Fig. 2),

$$\alpha dx + \beta dy + \gamma dz = 0\,.$$

On the other hand from Eq. (8)

$$dH = x d\alpha + y d\beta + z d\gamma\,.$$

Accordingly,

$$x = \frac{\partial H}{\partial \alpha}, \quad y = \frac{\partial H}{\partial \beta}, \quad z = \frac{\partial H}{\partial \gamma}\,. \tag{13}$$

Then, if dx, dy and dz are the differentials along the principal lines of curvature and R the principal radius of curvature, it holds the Rodrigues' formula:

$$dx = R d\alpha, \quad dy = R d\beta, \quad dz = R d\gamma,$$
$$(\alpha^2 + \beta^2 + \gamma^2 = 1)$$

and we can see the eigenvalues of matrix $(H_{\alpha\beta})$ to be 0, R_1 and R_2 if R_1 and R_2 are the principal radii of curvature of the ovaloid. Now we can express the volume v, surface s and integral of mean radius of curvature ρ of an ovaloid by using H and R_1, R_2 as follows⁽⁵⁾⁽⁶⁾:

$$\left.\begin{aligned} v &= \frac{1}{3}\int H R_1 R_2 d\omega,\\ s &= \int R_1 R_2 d\omega = \frac{1}{2}\int H(R_1 + R_2) d\omega,\\ \rho &= \int H d\omega = \frac{1}{2}\int (R_1 + R_2) d\omega,\\ &(\alpha^2 + \beta^2 + \gamma^2) = 1 \end{aligned}\right\} \tag{14}$$

where $d\omega$ is the surface element on unit sphere in the direction of the arguments θ and φ of H, H being considered on the surface of unit sphere. The relation between this function $K(\theta, \varphi) = H(\sin\theta\cos\varphi, \sin\theta\sin\varphi, \cos\theta)$ and the supporting function $H(\alpha, \beta, \gamma)$ is:

$$\begin{aligned} K(\theta, \varphi) &= H(\sin\theta\cos\varphi, \sin\theta\sin\varphi, \cos\theta)\\ &= H(\alpha, \beta, \gamma)/\sqrt{\alpha^2 + \beta^2 + \gamma^2}\,, \end{aligned} \tag{15}$$

$$\begin{aligned} H(\alpha, \beta, \gamma) &= \sqrt{\alpha^2 + \beta^2 + \gamma^2}\\ &\times K\left(\cos^{-1}\frac{\gamma}{\sqrt{\alpha^2 + \beta^2 + \gamma^2}}, \frac{\pi}{2}\left(1 - \frac{\beta}{|\beta|}\right) + \tan^{-1}\beta/\alpha\right). \end{aligned} \tag{15}$$

Thus, the expression for the point $P(x, y, z)$ of Fig. 2 becomes:

$$\left.\begin{aligned} x = H_\alpha &= K\sin\theta\cos\varphi\\ &\quad + \frac{\partial K}{\partial \theta}\cos\theta\cos\varphi - \frac{\partial K}{\partial \varphi}\frac{\sin\varphi}{\sin\theta}\\ y = H_\beta &= K\sin\theta\sin\varphi\\ &\quad + \frac{\partial K}{\partial \theta}\cos\theta\sin\varphi + \frac{\partial K}{\partial \varphi}\frac{\cos\varphi}{\sin\theta},\\ z = H_\gamma &= K\cos\theta - \frac{\partial K}{\partial \theta}\sin\theta\,, \end{aligned}\right\} \tag{17}$$

and the matrix $H = (H_{\alpha\beta})$ becomes (App. 1)

$$\begin{aligned} H = {} & \cos^2\theta\left(\frac{\partial^2 K}{\partial \theta^2} + K\right)\begin{bmatrix} \cos^2\varphi, & \sin\varphi\cos\varphi, & -\cos\varphi\tan\theta\\ \sin\varphi\cos\varphi, & \sin^2\varphi, & -\sin\varphi\tan\theta\\ -\cos\varphi\tan\theta, & -\sin\varphi\tan\theta, & \tan^2\theta \end{bmatrix}\\ & + \cos\theta\frac{\partial}{\partial \theta}\left(\frac{1}{\sin\theta}\frac{\partial K}{\partial \theta}\right)\begin{bmatrix} -\sin 2\varphi, & \cos 2\varphi, & \sin\varphi\tan\\ \cos 2\varphi, & \sin 2\varphi, & -\cos\varphi\tan\theta\\ \sin\varphi, & -\cos\varphi\tan\theta, & \end{bmatrix}\\ & + \left(\frac{1}{\sin^2\theta}\frac{\partial^2 K}{\partial \varphi^2} + \frac{\cos\theta}{\sin\theta}\frac{\partial K}{\partial \theta} + K\right)\begin{bmatrix} \sin^2\varphi, & -\sin\varphi\cos\varphi, & 0\\ -\sin\varphi\cos\varphi, & \cos^2\varphi, & 0\\ 0, & 0, & 0 \end{bmatrix}. \end{aligned} \tag{18}$$

Therefore, the principal radii of curvature R_1 and R_2 are the eigenvalues of the matrix:

$$\begin{bmatrix} \dfrac{\partial^2 K}{\partial\theta^2}+K, & \dfrac{\partial}{\partial\theta}\left(\dfrac{1}{\sin\theta}\dfrac{\partial K}{\partial\varphi}\right) \\ \dfrac{\partial}{\partial\theta}\left(\dfrac{1}{\sin\theta}\dfrac{\partial K}{\partial\varphi}\right), & \dfrac{1}{\sin^2\theta}\dfrac{\partial^2 K}{\partial\varphi^2}+\dfrac{\cos\theta}{\sin\theta}\dfrac{\partial K}{\partial\theta}+K \end{bmatrix}. \tag{19}$$

§ 4. Calculation of the Integral.

To calculate the desired integral of Eq. (8) we use the formula of Eq. (14), and accordingly it is necessary to find the supporting function of the ovaloid C. In Fig. 2, $\overrightarrow{OO'}=\overrightarrow{OP}-\overrightarrow{O'P}$, and the differentials of $\overrightarrow{OP}$ and $\overrightarrow{O'P}$ are both orthogonal to the direction (α, β, γ), therefore that of $\overrightarrow{OP'}$ is also orthogonal to it. That is, the tangential plane of the ovaloid C at O′ is parallel to the common contact plane of the ovaloids A and B at P. Hence, it is understood that the supporting function of C is given by

$$H(\alpha, \beta, \gamma)+K(\bar{x};\ \alpha, \beta, \gamma),$$

when we denote the supporting function of A by $H(\alpha, \beta, \gamma)$ and that of B with respect to O′ and corresponding to the rotation $\bar{x}$ by $K(\bar{x};\, \alpha, \beta, \gamma)$. This shows the general fact that the sum of the supporting functions H and K of two ovaloids is also a supporting function of another ovaloid.

For the calculation of the integral of Eq. (8) we define the following linear differential expression of $H(\theta, \varphi)$ and $K(\theta, \varphi)$ which are both one valued functions on the surface of unit sphere:

$$\begin{aligned}(H, K) = &\left(\frac{\partial H}{\partial\theta^2}+H\right)\left(\frac{1}{\sin^2\theta}\frac{\partial^2 K}{\partial\varphi^2}+\frac{\cos\theta}{\sin\theta}\frac{\partial K}{\partial\theta}+K\right)\\ &-2\frac{\partial}{\partial\theta}\left(\frac{1}{\sin\theta}\frac{\partial H}{\partial\varphi}\right)\frac{\partial}{\partial\theta}\left(\frac{1}{\sin\theta}\frac{\partial K}{\partial\varphi}\right)\\ &+\left(\frac{1}{\sin^2\theta}\frac{\partial^2 H}{\partial\varphi^2}+\frac{\cos\theta}{\sin\theta}\frac{\partial H}{\partial\theta}+H\right)\left(\frac{\partial^2 K}{\partial\theta^2}+K\right).\end{aligned} \tag{20}$$

The origin of the conception of this expression is somewhat analogous to that when we generalize norm to inner-product. Then from Eqs. (19) and (20), we obtain:

$$(H, H) = 2R_1R_2, \tag{21}$$

and thus, from Eq. (14) the volume of the ovaloid having the supporting function $H(\alpha^2+\beta^2+\gamma^2=1)$ s given by

$$v=\frac{1}{6}\int H(H, H)\,d\omega. \tag{22}$$

The integral $\bar{f}(\bar{x})$ on the translation group of Section 2 is the volume of ovaloid C and thus is expressed as:

$$\bar{f}(\bar{x})=\frac{1}{6}\int (H+K(\bar{x}))(H+K(\bar{x}),\ H+K(\bar{x}))\,d\omega. \tag{23}$$

Therefore, if we denote the volume element dx of rotation group G/g which corresponds to the rotation of B by $1/8\pi^2\cdot d\omega_1\, d\tau_1$, the desired integral becomes:

$$m(I)=\frac{1}{8\pi^2}\int \bar{f}(\bar{x})\,d\omega_1\, d\tau_1. \tag{24}$$

To calculate this we show the above expression Eq. (20) is self-adjoint on the whole surface of unit sphere when we consider K operates on H. That is, if $L(\theta, \varphi)$ is another one-valued function on the surface as is $H(\theta, \varphi)$ or $K(\theta, \varphi)$, we shall demonstrate the following equality:

$$\int L(H, K)\,d\omega-\int H(L, K)\,d\omega=0. \tag{25}$$

For convenience we put:

$$L\frac{\partial H}{\partial\theta}-H\frac{\partial L}{\partial\theta}=P,$$

$$\frac{1}{\sin\theta}\frac{\partial H}{\partial\varphi}L-\frac{1}{\sin\theta}\frac{\partial L}{\partial\varphi}H=Q.$$

Then:

$$\begin{aligned}&\{L(H, K)-H(L, K)\}\sin\theta\\ &=\frac{\partial P}{\partial\theta}\left(\frac{1}{\sin\theta}\frac{\partial^2 K}{\partial\varphi^2}+\cos\theta\frac{\partial K}{\partial\theta}+\sin\theta\cdot K\right)\\ &\quad+\left(\cos\theta\cdot Q-\frac{\partial P}{\partial\varphi}-\sin\theta\frac{\partial Q}{\partial\theta}\right)\frac{\partial}{\partial\theta}\left(\frac{1}{\sin\theta}\frac{\partial K}{\partial\varphi}\right)\\ &\quad+\left(\frac{\partial Q}{\partial\varphi}+\cos\theta\cdot P\right)\left(\frac{\partial^2 K}{\partial\theta^2}+K\right)\\ &=\frac{\partial}{\partial\theta}\left[\sin\theta\left\{P\left(\frac{1}{\sin^2\theta}\frac{\partial^2 K}{\partial\varphi^2}+\frac{\cos\theta}{\sin\theta}\frac{\partial K}{\partial\theta}+K\right)\right.\right.\\ &\quad\left.\left.-Q\frac{\partial}{\partial\theta}\left(\frac{1}{\sin\theta}\frac{\partial K}{\partial\varphi}\right)\right\}\right]\\ &\quad-\frac{\partial}{\partial\varphi}\left\{P\frac{\partial}{\partial\theta}\left(\frac{1}{\sin\theta}\frac{\partial K}{\partial\varphi}\right)-Q\left(\frac{\partial^2 K}{\partial\theta^2}+K\right)\right\}.\end{aligned}$$

Hence, the left hand side of Eq. (25) becomes:

$$\begin{aligned}&\int_0^{2\pi}\int_0^{\pi}\{L(H, K)-H(L, H)\}\sin\theta d\theta d\varphi\\ &=\int_0^{2\pi}\left[\sin\theta\left\{P\left(\frac{1}{\sin^2\theta}\frac{\partial^2 K}{\partial\varphi^2}+\frac{\cos\theta}{\sin\theta}\frac{\partial K}{\partial\theta}+K\right)\right.\right.\\ &\quad\left.\left.-Q\frac{\partial}{\partial\theta}\left(\frac{1}{\sin\theta}\frac{\partial K}{\partial\varphi}\right)\right\}\right]_{\theta=0}^{\pi}d\varphi\\ &\quad-\int_0^{\pi}\left[P\frac{\partial}{\partial\theta}\left(\frac{1}{\sin\theta}\frac{\partial K}{\partial\varphi}\right)-Q\left(\frac{\partial^2 K}{\partial\theta^2}+K\right)\right]_{\varphi=0}^{2\pi}d\theta,\end{aligned}$$

and each integral vanishes. Thus Eq. (25) was established.

Now remembering Eq. (20) is linear with respect to H or K and using Eqs. (23) and (25), we obtain:

$$\bar{f}(\bar{x})=\frac{1}{6}\int H(H,H)d\omega+\frac{1}{6}\int K(\bar{x})(K(\bar{x}),K(\bar{x})d\omega$$
$$+\frac{1}{2}\int H(K(\bar{x}),K(\bar{x})d\omega+\frac{1}{2}K(\bar{x})(H,H)d\omega$$
$$=v_A+v_B+\int H(K(\bar{x}),K(\bar{x})d\omega+\frac{1}{2}\int K(\bar{x})(H,H)d\omega, \tag{26}$$

where v_A or v_B represents the volume of A or B respectively. Introducing Eq. (26) into Eq. (24),

$$m(I)=v_A+v_B+\frac{1}{16\pi^2}\int H(K(\bar{x}),K(\bar{x}))d\omega\,d\omega_1\,d\tau_1$$
$$+\frac{1}{16\pi^2}\int K(\bar{x})(H,H)d\omega\,d\omega_1\,d\tau_1. \tag{27}$$

In this equation the order of integration is to be noted. For example, if we write the last integral courteously, it is expressed

$$\frac{1}{16\pi^2}\int K(\theta_1,\varphi_1,\tau_1;\theta,\varphi)(H(\theta,\varphi),H(\theta,\varphi))$$
$$\times\sin\theta\,d\theta\,d\varphi\,\sin\theta_1\,d\theta_1\,d\varphi_1\,d\tau_1. \tag{28}$$

Here θ_1, φ_1 and τ_1 are the parameters of rotation in the case when we represent the rotation of B around O′ by the orthogonal transformation given by Eq. (9), and $K(\theta_1,\varphi_1,\tau_1;\theta,\varphi)$ represents the value of K of B in the direction θ, φ when it rotates by the angles θ_1, φ_1 and τ_1 from its standard position. We integrate Eq. (28) at first with respect to θ_1, φ_1 and τ_1. Then, the integral

$$\int K(\theta_1,\varphi_1,\tau_1;\theta,\varphi)d\omega_1\,d\tau_1 \tag{29}$$

does not depend on θ,φ. Because this is just equal to

$$\int K(\bar{x})d\bar{x}=\int K(\mathfrak{b}\bar{x})d\mathfrak{b}\bar{x}=\int K(\bar{\mathfrak{b}}\bar{x})d\bar{x};\ (\bar{\mathfrak{b}}\in G/g), \tag{30}$$

and if $\bar{\mathfrak{b}}$ is the constant rotation of B from (θ,φ) to (0, 0) which does not include θ_1, φ_1 and τ_1, then Eq. (29) becomes

$$\int K(\theta_1,\varphi_1,\tau_1;0,0)d\omega_1\,d\tau_1. \tag{31}$$

Thus, the above integral (29) was wholly separated with respect to $d\omega$ and $d\omega_1$. The first integral of Eq. (27) is separated in the same way with respect to its variables.

Now if B rotates from its standard positio by θ_1, φ_1 and τ_1 corresponding to $\bar{x}$ and th direction (θ,φ) fixed to B in the standard positio rotates to the direction (0, 0, 1), we can obtai the following relation from Eq. (9):

$$\begin{bmatrix}0\\0\\1\end{bmatrix}=\begin{bmatrix}&&\\&\cdot&\\\sin\theta_1\cos\varphi_1,&\sin\theta_1\sin\varphi_1,&\cos\theta_1\end{bmatrix}\begin{bmatrix}\sin\theta\cos\varphi\\\sin\theta\sin\varphi\\\cos\theta\end{bmatrix} \tag{32}$$

From this, we arrive at:

$$\theta=\theta_1,\quad\varphi=\varphi_1. \tag{33}$$

Hence,

$$K(\theta_1,\varphi_1,\tau_1;0,0)=K(\theta_1,\varphi_1),$$

and the integral of Eq. (31) was separated also with respect to ω_1 and τ_1. Accordingly, Eq. (29) becomes:

$$\int K(\theta_1,\varphi_1)d\omega_1\,d\tau_1=2\pi\rho_B, \tag{34}$$

where ρ_B is the integral of mean radius of curvature of B over its whole surface (Note that the corresponding integral in Eq. (14) must be done over the surface of unit sphere). The first integral of Eq. (27) is also separated with respect to ω_1 and τ_1, and therefore, we arrive at the final result:

$$m(I)=v_A+v_B+\frac{1}{8\pi}\int Hd\omega\int(K,K)d\omega_1$$
$$+\frac{1}{8\pi}\int Kd\omega_1\int(H,H)d\omega$$
$$=v_A+v_B+\frac{1}{4\pi}(\rho_A s_B+\rho_B s_A), \tag{35}$$

where s_A and s_B represent the surface areas of A and B, ρ_A is the analogous one to ρ_B.

§ 5. General Remarks.

Introducing Eq. (36) into Eq. (7) we finally obtain the explicit formula for f:

$$f=\frac{\rho s}{16\pi v}+\frac{1}{4}, \tag{36}$$

which corresponds to the case of homogeneous polymers. Kotani⁽²⁾ has shown that f is larger than 1 when the shape of polymer deviates slightly from sphere. This fact gives a method to determine the molecular shape and can be shown quite generally from Eq. (36), because this can be rewritten:

$$f=1+\left(\frac{\rho s}{16\pi v}-\frac{3}{4}\right), \qquad (36')$$

and the quantity in the bracket is not negative owing to the inequalities,

$$\rho^2 \geq 4\pi s \quad \text{and} \quad s^3 \geq 36\pi v^2. \qquad (37)$$

Here the equality holds only in the case of sphere.

So far we have treated the homogeneous case, but the case of heterogeneous polymers can easily be obtained owing to the form of Eq. (35). In this case the osmotic pressure is given by

$$\frac{\pi}{RT}=\sum c_i/M_i+\sum A_{ij}c_ic_j+\cdots\cdots, \qquad (38)$$

where c_i is the concentration of the i-th species of solute, M_i is its molecular weight and A_{ij} is defined as follows;

$$A_{ij}=-\frac{N_0}{2M_iM_jV}\int g_2(i,j)\,d(i)\,d(j). \qquad (39)$$

Since A_{ij} is given by Eq. (35) we can rewrite this equation as Eq. (6) simply by replacing its members by their number averages:

$$\left.\begin{aligned}\overline{M}_g &= \sum N_iM_i/\sum N_i,\\ \bar{v} &= \sum N_iv_i/\sum N_i,\\ \bar{\rho} &= \sum N_i\rho_i/\sum N_i,\\ \bar{s} &= \sum N_is_i/\sum N_i,\\ N_i &= c_i/M_i.\end{aligned}\right\} \qquad (40)$$

Again, from physical point of view, we can extend the result to the case of angular ovaloids. At least, the general principle of calculation explained in Section 2 can be applied to such cases or even to the cases other than ovaloids. We shall discuss these in later articles.

References.

(1) B. H. Zimm, J. Chem. Phys. **14** (1946), 164.

(2) M. Kotani, Read May, 1947.

(3) A. Isihara, J. Chem. Phys, **18** (1950).

(4) This can be shown by a calculation following, for example: H. Toyama, Proc. Acad. Sci. **24** (1949), 13.

(5) W. Blashke, Kreis u. Kugel. Jber. Deutsch. Math. Vereingung **24**, 1915.

(6) T. Bonnesen u. W. Fenchel, Theorie der konvexen Koerper. Ergebnisse der Math. u. ihrer Grenzgebiete.

Appendix 1.

For the sake of brevity, let

$$\left\{\begin{aligned}A &= \cos\theta\cos\varphi\frac{\partial}{\partial\theta}-\frac{\sin\varphi}{\sin\theta}\frac{\partial}{\partial\varphi},\\ B &= \cos\theta\sin\varphi\frac{\partial}{\partial\theta}+\frac{\cos\varphi}{\sin\theta}\frac{\partial}{\partial\varphi},\\ C &= -\sin\theta\frac{\partial}{\partial\theta},\end{aligned}\right. \qquad (A1)$$

then Eq. (17) becomes:

$$\left\{\begin{aligned}x &= (A+\sin\theta\cos\varphi)K,\\ y &= (B+\sin\theta\sin\varphi)K,\\ z &= (C+\cos\theta)K,\end{aligned}\right. \qquad (A2)$$

$$x^2+y^2+z^2=K^2+\left(\frac{\partial K}{\partial\theta}\right)^2+\left(\frac{1}{\sin\theta}\frac{\partial K}{\partial\varphi}\right)^2. \qquad (A3)$$

Also the matrix H can be written as follows:

$$H=\begin{bmatrix}A(A+\sin\theta\cos\varphi)K, & B(A+\sin\theta\cos\varphi)K, & C(A+\sin\theta\cos\varphi)K\\ A(B+\sin\theta\sin\varphi)K, & B(B+\sin\theta\sin\varphi)K, & C(B+\sin\theta\sin\varphi)K\\ A(C+\cos\theta)K, & B(C+\cos\theta)K, & C(C+\cos\theta)K\end{bmatrix} \qquad (A4)$$

where the following symmetrical relations succeed:

$$\left\{\begin{aligned}A(B+\sin\theta\sin\varphi) &= B(A+\sin\theta\cos\varphi),\\ B(C+\cos\theta) &= C(B+\sin\theta\sin\varphi),\\ C(A+\text{sih}\,\theta\cos\varphi) &= A(C+\cos\theta),\end{aligned}\right. \qquad (A5)$$

We, thus arrive at Eq. (18) and obtain the following expressions for the principal radii of curvature.

$$\begin{aligned}R_1+R_2 &= \left(\frac{\partial^2}{\partial\theta^2}+\frac{1}{\sin^2\theta}\frac{\partial^2}{\partial\varphi^2}+\frac{\cos\theta}{\sin\theta}\frac{\partial}{\partial\theta}+2\right)K(\theta,\varphi),\\ R_1R_2 &= \left(\frac{\partial^2K}{\partial\theta^2}+K\right)\left(\frac{1}{\sin^2\theta}\frac{\partial^2K}{\partial\varphi^2}+\frac{\cos\theta}{\sin\theta}\frac{\partial K}{\partial\theta}+K\right)\\ &\quad-\left(\frac{1}{\sin\theta}\frac{\partial^2K}{\partial\theta\,\partial\varphi}-\frac{\cos\theta}{\sin^2\theta}\frac{\partial K}{\partial\varphi}\right)^2.\end{aligned} \qquad (A6)$$

Theory of High Polymer Solutions.
II. Special Forms of Second Osmotic Coefficient.

By Akira ISIHARA and Tsuyoshi HAYASHIDA.

Department of Physics, Faculty of Science, University of Tokyo.

(Received July 16, 1950).

§ 1. Introduction.

It has been known that the theoies of high polymer solutions based on the lattice-model do not fit the experiments especially in the range of dilute solutions. The origin of this departure comes from the fact that in this range the solute molecules are dispersed in rather a compact form in the solvent, so that the places occupied by them can be distinguished comparatively well from the remaining part. Thus it is preferable to construct its theory on the line developed by McMillan-Mayer and Zimm(1) by using the probability $F\{n\}d\{n\}/V^n$ of finding polymers in the volume element $d\{n\}$ of configuration $\{n\}$, rather than to take up the average probability available to a numbered molecule, which is calculated by the lattice-model. Thus, in the preceding articles(2) we have calculated the general expression for A_2 of the expansion :

$$\frac{\pi}{RTc}=\frac{1}{M_2}+A_2c+\cdots, \qquad (1)$$

in the case of rigid ovaloid following the theory of Zimm. The calculation is somewhat mathematical but the rigorous result obtained is rather simple and is expressed by six molecular constants of two solute molecules: the volume v, mean of the mean radius of curvature $\rho/4\pi$ and the surface area s; which, in all, correspond to the dimension of the group of motions G. When all the molecules have the same shape, the result is expressed by

$$A_2=\frac{4N_0v}{M_2^2}f, \qquad (2)$$

$$f=1+\left(\frac{\rho s}{16\pi v}-\frac{3}{4}\right), \qquad (3)$$

where N_0 is Avogadro's number. In the heterogeneous case, we merely think of the three molecular quantities ρ, s and v as the number average quantities. They are calculated by the following formulas of differential geometry :

$$\left.\begin{aligned} v&=\frac{1}{3}\int HR_1R_2d\omega,\\ s&=\int R_1R_2d\omega=\frac{1}{2}\int H(R_1+R_2)\,d\omega,\\ \rho&=\int Hd\omega=\frac{1}{2}\int(R_1+R_2)d\omega, \end{aligned}\right\} \qquad (4)$$

where R_1 and R_2 are the principal radii of curvature of the ovaloid, $H(\theta,\varphi)$ is the supporting function considered on the surface of unit sphere and $d\omega$ is the surface element on the unit sphere belonging to the direction of (θ,φ). Although the formula (3) was deduced in the case of smooth ovaloid, the result may be considered to be also adaptable to the angular cases from the physical point of view. At any rate v and s can be easily calculated wheather we use Eq. (4) or not. Again, to calculate ρ in the case of angular ovaloids we must use the first expression of Eq. (4), because H can be fixed in this case. In the following sections we want to give explicit expressions for v, s, ρ and the numerical factor f in several cases.

§ 2. Angular ovaloids.

In this case the calculation of ρ is not so much harder than the opposite case, because if we put the contact plane to the ovaloids on a corner we can easily calculate the length of perpendicular to the contact plane that is H as a function of the direction (θ,φ). To illustrate this we begin with the case of circular cylinder.

(1) Cylindrical model. —length $2b$, radius a.

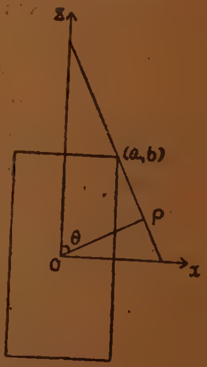

Fig. 1.

From Fig. 1, we see that the perpendicular O that is $H(\theta, \varphi)$ is given by

$$H(\theta, \varphi) = a \sin \theta + b \cos \theta.$$

hus, ρ is calculated as:

$$\rho = 4\pi \int_0^{\pi/2} (a \sin \theta + b \cos \theta) \sin \theta d\theta,$$
$$= 2\pi(b + a\pi/2).$$

n the other hand, the surface s and the volume v re

$$s = 2\pi a(a+2b)\,;\ v = 2\pi a^2 b.$$

herefore, f is given by

$$f = \frac{1}{4}\left\{1 + \frac{b}{a}\left(1 + \frac{a}{2b}\right)\left(1 + \frac{a\pi}{2b}\right)\right\}, \tag{5}$$

nd the second virial coefficient A_2 is

$$A_2 = \frac{N_0 v}{M_2^2}\left\{1 + \frac{b}{a}\left(1 + \frac{a}{2b}\right)\left(1 + \frac{a\pi}{2b}\right)\right\}. \tag{6}$$

Vhen $b \gg a$, this becomes to:

$$A_2 = \frac{4\pi N_0 a b^2}{M_2^2}, \quad (b \gg a) \tag{7}$$

vhich is just the same result calculated by Zimm y somewhat complicated integration. Fig. 2 represents Eq. (5) as a function of b/a. The cylindrical model corresponds to, for example, cellulose or tobaco mosaic virus.

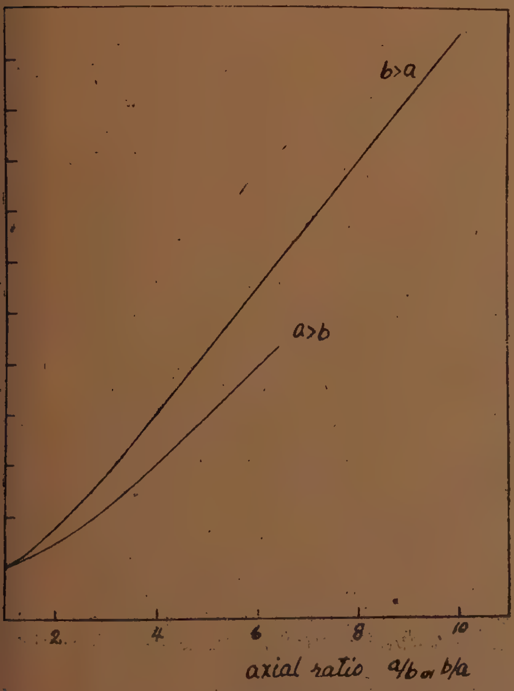

Fig. 2. f for cylindrical case as a funcion of axial ratio.

(2) Regular Tetrahedron. Though this shape has never been considered in the theories of high polymer solutions, we wish to calculate the correspoding coefficient A_2, because this corresponds to the second virial coefficient of imperfect gases when the precise molecular force is neglected. Let the length of the sides of regular tetrahedron be $2\sqrt{2}$, and consider the corners of tetrahedron are put on the circles of Fig. 3. The coordinate axes are parallel to BA, CA and DA and the origin O is put on the center of tetrahedron so that the coordinate of point A becomes (1, 1, 1). In this configuration, when a contact plane to the tetradron passes through the point A, it's equation is

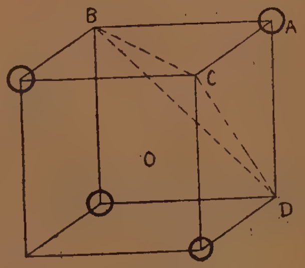

Fig. 3.

$$\alpha(x-1) + \beta(y-1) + \gamma(z-1) = 0, \tag{8}$$

where α, β and γ are the direction cosines, and the supporting function becomes

$$H(\alpha, \beta, \gamma) = \alpha + \beta + \gamma. \tag{9}$$

It can readily be understood that the perpendicular line from 0 to the contact plane (8) moves over the triangle ΔBCD when the plane rotates around A. Therefore, we can reduce the integral for ρ, which must be integrated over the surface of unit sphere to the surface integral on the triangles such as ΔBCD. (Fig. 4). The transformation of surface element is given by,

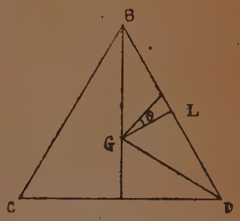

Fig. 4.

$$d\omega \doteq \frac{dS}{x^2+y^2+z^2}, \qquad x, y, z \in \Delta BCD. \tag{10}$$

Thus, we can calculate ρ in the following manner:

$$\begin{aligned} \rho &= 4\int_{\Delta BCD} \frac{x+y+z}{\sqrt{x^2+y^2+z^2}} \frac{dS}{x^2+y^2+z^2} \\ &= 24\int_{\Delta BGL} \frac{rdrd\theta}{\left(\frac{1}{3}+r^2\right)^{3/2}} = 4\sqrt{3}\pi. \end{aligned} \tag{11}$$

Because of ρ is linear with respect to the length of side, we obtain the following value for ρ corresponding to the tetrahedron of side-length 1:

$$\rho = \frac{\sqrt{3}}{2\sqrt{2}}. \tag{12}$$

On the other hand the corresponding values of volume and surface are:

$$v = 1/6\sqrt{2}, \quad s = \sqrt{3}.$$

Thus, we obtain for f:

$$f = 5/2. \tag{13}$$

In the more general case of arbitray side-length l, we are only required to multiply l on the left hand side of Eq. (12), whereas Eq. (13) remains invariant.

(3) **Regular Octahedron.** Let the side-length be $\sqrt{2}$, and the contact plane considered as above is put on A (0, 0, 1) of Fig. 5, and thus be expressed as

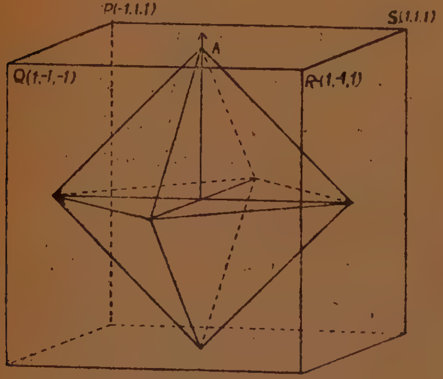

Fig. 5.

$$\alpha x + \beta y + \gamma (z-1) = 0.$$

In this case the integral for ρ can be reduced to the one over the square $PQRS$ and the analogous integrals which correspond to the cases when the contact plane is put on the other corners of the octahedron. Since H is given by

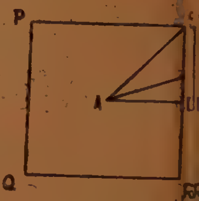

Fig. 6.

$$H(\alpha, \beta, \gamma) = \gamma, \tag{14}$$

we can evalute the integral just the same manner as the above case (see Fig. 6):

$$\begin{aligned} \rho &= 6\int_{PQRS} \frac{\gamma}{\sqrt{\alpha^2+\beta^2+\gamma^2}} \frac{dS}{\alpha^2+\beta^2+\gamma^2} \\ &= 48\int_{\Delta ALS} \frac{rdrd\theta}{(r^2+1)^{3/2}} = 4\pi. \end{aligned} \tag{15}$$

Therefore, if the side-length is 1, ρ is given by

$$\rho = \frac{4\pi}{\sqrt{2}} = 2\sqrt{2}\pi. \tag{16}$$

The volume and the surface area are given by

$$v = \sqrt{2}/3, \quad s = 2\sqrt{3}. \tag{17}$$

so that f becomes:

$$f = \frac{1+3\sqrt{3}}{4} \doteq 1.549. \tag{18}$$

f is also independent of the dimension but is characteristic of the shape.

We shall now stop these angular cases and tabulate the results of the above and the other cases; the calculation of the latter may be left to the reader.

$\rho/4\pi$ is a mean of mean radius of curvature and may be called a "mean radius". The corresponding figures in Tab. 1 show how the original shapes differ from the sphere. Precisely speaking, we must compare with each other by making, say, respective volume to be equal to each other. "Mean radii" thus calculated are also listed in Tab. 1. As one can see the order of magnitudes of mean radii is interesting and is very plausible.

§ 3. Ellipsoid of revolution.

Next we consider the ellipsoid of revolution:

$$\left.\begin{aligned} x &= a \sin\theta \cos\varphi, \\ y &= a \sin\theta \sin\varphi, \\ z &= b \cos\theta. \end{aligned}\right\} \tag{19}$$

Tab. 1.

Shape	Sphere	Cube	Regular Tetrahedron	Regular Octahedron	Cylinder	Circular disk	line segmct
Size	radius 1	side 1	side 1	side 1	length l radius a	radius 1	length 1
v	$4\pi/3$,	1,	$1/6\sqrt{2}$,	$\sqrt{2}/3$,	$\pi a^2 l$,	0,	0,
s	4,	6,	$\sqrt{3}$,	$2\sqrt{3}$,	$2\pi a(a+l)$,	2π,	0,
$\rho/4\pi$	1,	3/4,	0.61,	0.71,	$(l+a\pi/2)/4$,	$\pi/4$,	1/4,
mean radius	1,	1.21,	2.01,	1.46,	$1.23(l=4,\ a\doteq 1/\sqrt{3})$,	—	—
f	1,	11/8,	5/2,	$(1+3\sqrt{3})/4$,	$\dfrac{\pi a^2+(\pi+3)al+l^2}{8al}$,	—	—

Then H is given by

$$H=\sqrt{a^2\sin^2\theta+b^2\cos^2\theta}, \tag{20}$$

independent of φ. Thus, if we introduce the eccentricity ε:

$$\begin{aligned}\varepsilon^2&=\frac{a^2-b^2}{a^2}, \quad (a\geqq b:\ \text{oblate})\\ &=\frac{b^2-a^2}{b^2}, \quad (a\leqq b:\ \text{prolate})\end{aligned} \tag{21}$$

then the respective mean radius $\rho/4\pi$ is calculated as follows:

$$\begin{aligned}\rho&=2\pi a\left\{\sqrt{1-\varepsilon^2}+\frac{\mathrm{Sin}^{-1}\varepsilon}{\varepsilon}\right\}, \quad (\text{oblate})\\ &=2\pi b\left\{1+\frac{1-\varepsilon^2}{2\varepsilon}\log\frac{1+\varepsilon}{1-\varepsilon}\right\}, \quad (\text{prolate})\end{aligned} \tag{22}$$

and the surface is given by

$$\begin{aligned}s&=2\pi a^2\left\{1+\frac{1-\varepsilon^2}{2\varepsilon}\log\frac{1+\varepsilon}{1-\varepsilon}\right\}, \quad (\text{oblate})\\ &=2\pi ab\left\{\sqrt{1-\varepsilon^2}+\frac{\mathrm{Sin}^{-1}\varepsilon}{\varepsilon}\right\}. \quad (\text{prolate})\end{aligned} \tag{23}$$

Thus, we arrive at the same expression for f regardless of both types of spheroid:

$$f=\frac{1}{4}+\frac{\rho s}{16\pi v}=\frac{1}{4}+\frac{3}{16}\times\left(1+\frac{1}{\sqrt{1-\varepsilon^2}}\frac{\mathrm{Sin}^{-1}\varepsilon}{\varepsilon}\right)\left(1+\frac{1-\varepsilon^2}{2\varepsilon}\log\frac{1+\varepsilon}{1-\varepsilon}\right). \tag{24}$$

When $\varepsilon\ll 1$, we obtain f as a power series of ε in the following way⁽³⁾:

$$f=1+\frac{1}{15}\varepsilon^4+\frac{37}{60}\varepsilon^6+\dots \tag{25}$$

Fig. 7 shows the variation of f with axial ratio a/b. Comparing the above result with the experimental values of A_2, we can determine the axial ratio of solute molecules as ellipsoids of revolution. Actually f for Hemoglobin⁽⁴⁾ is 1.27 and for Serum Albumin⁽⁵⁾ 1.6. Accordingly, we obtain $a/b=2.5$ in the former case and 4 in the latter case. Assuming elongated shape, the viscosity-values become 4.6 for Hemoglobin and 5.6, for Serum Albumin whereas the diffusion-values are 3.7 and 5.0 respectively⁽⁶⁾. Comparing these values, the present result seems to be somewhat lower than the latter. In part this must be originated in the neglection of heat term in this treatment. But an attention must be paid to the fact that the viscosity and ultracentrifuge methods show sometimes the discrepancy of almost the same order of magnitude as the above results.

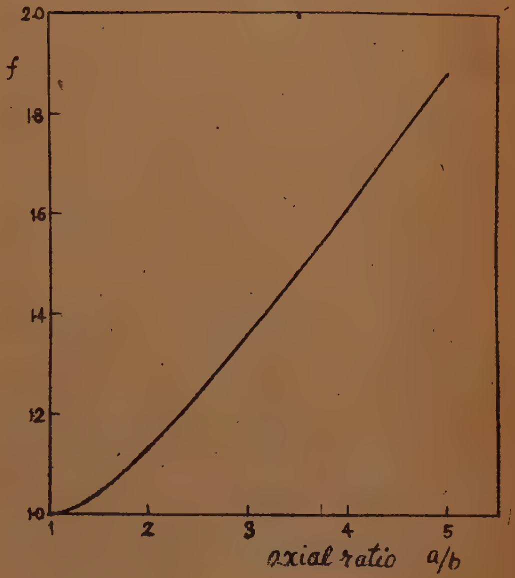

Fig. 7. f for spheroidal molecule.

This may be originated from the different average values of these different measurements.

§ 4. Concluding remarks.

In Fig. 8 we expressed the present result as the relation between A_2 and the intrinsic viscosity $[\eta]$. Although the intrinsic viscosity is merely related to one solute and A_2 to two solute molecules, the former is determined as A_2 by the shape of solute molecules. $[\eta]$ in Fig. 8 corresponds to the case of total Brownian motion⁽⁷⁾. By the parallel measurements of osmotic pressure and viscosity, and by comparing the results with the theoretical curve of Fig. 8, we can thus easily read the axial ratio of solute molecules as ellipsoids of revolution.

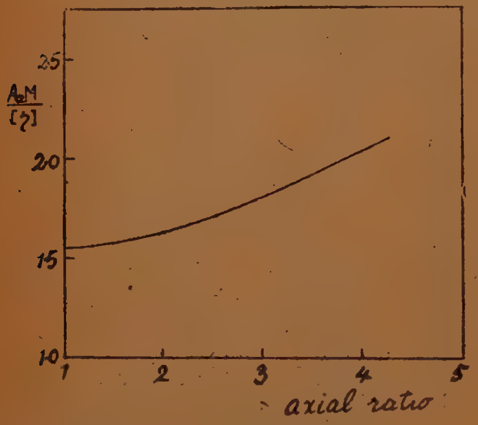

Fig. 8. Relation between intrinsic viscosity and A_2 for ellipsoidal molecules.

At the same time we have explicity expressed the parallelism between the osmotic pressure and the viscosity, which have often been recognized experimentally⁽⁸⁾. But it must receive an attention that the curve should be raised at least in accordance with the ratio between weight average molecular weight and number average molecular weight when we treat the heterogeneous polymers.

Another attention must be paid to the fact that the present results are confined to the case of rigid ovaloids where the attractive part of molecular potential is wholly neglected. Owing t this attractive potential the theoretical values o A_2 will be diminished from the above result Actually, in the case where the molecular interaction is strong enough A_2 assumes even negativ values.

At any rate, it is interesting that the coefficients illustrated in Figs. 2 and 7 are both increasing linearly with the respective major axi This will be also true for the second virial coefficient A_2, because the factor v/M_2^2 in Eq. (2 may not sincerely depend on the molecular length This tendency seems to be more reliable tha the values of A_2 themselves calculated in thi paper, and will be confirmed easily by paralle measurements of osmotic pressure and light scattering of high polymer solutions.

Note added in proof.

Fortunately, the conclusion in the last sectio of this paper is confirmed by the following ver comprehensive experiment:

P. Outer, C. J. Carr and B. H. Zimm, J. Chem. Phys. 18 (1950), 830.

References.

(1) B. H. Zimm, J. Chem. Phys. **14** (1946), 164.

(2) A. Isihara J. Chem. Phys **18** (1950), A. Isihara and T. Hayashida, J. Phys. Soc. Jap. **6** (1950).

(3) This result was alreads obtained by M. Kotan and was reported in the meeting of the Physical Society of Japan held 1946, but ha not been published. He has calculated this result by expanding the radius vector of nearly spherical particles in Legendre Polynomials.

(4) G. S. Adair, Proc, Roy. Soc. London **120A** (1923), 573.

(5) N. F. Burk, J. Biol. Chem. **98** (1932), 353.

(6) R. Simha., J. App. Phys. **13** (1942), 147.

(7) J. M. Burgers, Second Report on Viscosity and Plasticity. pp153 Amsterdam 1938.

(8) Dobry, Koll. Zeit. **81** (1937), 190. Alfrey, Bartvics and Mark, J. Amer. Chem. Soc, **65** (1943), 2819.

The Electric Susceptibility of Water Drop due to Ionic Polarization.*

By Osamu TUKIZI.

Electrical Communications Laboratory.

(Received June 21, 1950)

1. Introduction.

In several aspects of radio meteorology and n the analysis of tropospheric propagation roblems, it is necessary to know the electric usceptibility of a single water drop as a funcion of drop-size, temperature of the atmosphere, nd frequency of the waves. The susceptibility ormula which owes to Mie(1) and Stratton(2) has videly been employed to explain satisfactorily, o a certain extent, some of the phenomena conerning the microwave propagation through mist, ain, etc. Nevertheless there remains still a iscrepancy that the theory predicts minor magitude compared to that deduced from meteoroogical observations.

In liquid water a small fraction of molecules issociates at ordinsry temperatures into positive nd negative ions of equal numbers, which are orced in an electric field to move in opposite irections according to the sign of each ion. onic polarization rosults when they are confined within a sphere of drop and the polarization gives rise to an electric dipole which may be egarded as characterizing the water particle.

Liquid-theoretically, the polarization arises rom two different sorts of ionic transportation. In water each oxygen atom is surrounded on the average by four hydrogen atoms disposed in an approximately tetrahedral manner as shown in fig. 1. Ionization results when one of the two more distant hydrogen atoms approaches to an oxygen atom to form together a hydrogen ion. The hydrogen ion in water is accordingly to be represented by H_3O^+ instead of H^+.

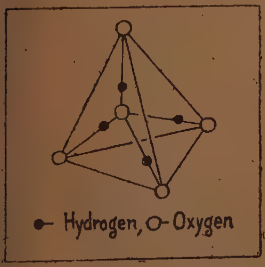

Fig. 1. Liquid water structure.

Transfer of the hydrogen atom, or more correctly a proton, from one molecule to another leaves the oxygen atom of the former molecule with one close and three distant hydrogen atoms and the oxygen atom with the closer hydrogen atom constitutes the OH^- ion.

When an electric field is applied, the H_3O^+ ion travels through neutral water molecules to some extent in the ordinary diffusion manner. On account of the anomalously high conductivity of water, however, the ion is regarded to be transfered also by the so-called prototropic process(3) in which a proton of the H_3O^+ ion is transfered to a neighbouring water molecule to transform it into a new ion. Thus the ionic transportation is seen to occur in two ways.

§ 2. Transfer Equation.

Consider first the diffusion of H_3O^+ ion. In order to displace in water from one point to another, an ion needs a suitable site in the direction of motion(4) and the production of such a site requires the expenditure of energy. Suppose a potential barrier as shown in fig. 2, and assume that the ion possessing energy larger than that of activation can pass over the barrier from an equilibrium position to an adjacent one at a distance λ, under the influence of an electric field E directed along the positve z-axis of a rectangular coordinate system. The energy in the initial state may be regarded as being increased by an amount αw, where w is the work done in moving the ion from one equilibrium state to the next and α is the fraction operative between

---

* Part of the paper presented 25 October 1949 at the th meeting of the Society of Terrestrial Electricity and Magnetism of Japan.

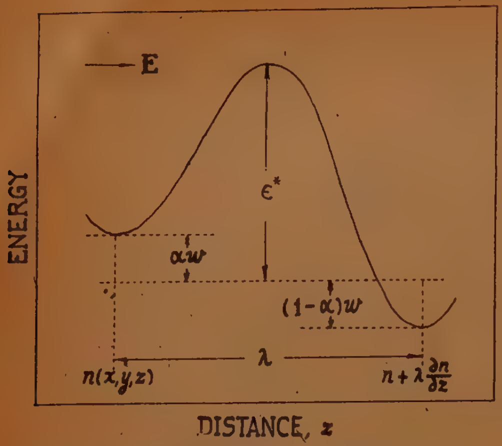

Fig. 2. Potential-energy barrier for ionic diffusion.

the initial and activated states; similarly, the energy of the final state is diminished by $(1-\alpha)w$; fig. 2.

If $f(T)$ and $f^*(T)$ are the partition functions of the ion in the equilibrium and activated states respectively and ϵ^* is the activation energy per ion at 0°K, then, according to the theory of absolute reaction rate⁽⁴⁾, the specific rate $\tilde{\omega}$, or the probability that an ion passes over the barrier in unit time is given by

$$\tilde{\omega} = (kT/h)\{f^*(T)/f(T)\}\exp(-\epsilon^*/kT), \qquad (1)$$

it being assumed that the transmission coefficient is unity and the tunnelling factor being neglected. The partition function $f(T)$ for the initial state is expressed as

$$f(T) = (2\pi mkT/h^2)^{\frac{3}{2}}\, v_f\cdot b_i \exp(-\epsilon_0/kT), \qquad (2)$$

where the first factor in the right-hand side is the translational contribution of a single ion of mass m moving in its free volume v_f, and k, T, h involved in these formulae have their usual significance; b_i is the combined rotational and translational partition function and ϵ_0 is the difference in energy per molecule at the liquid and gas states at 0°K.

The partition function $f^*(T)$ for the activated state, not including the contribution of the degree of translational freedom normal to the barrier, is written

$$f^*(T) = (2\pi mkT/h^2)^{\frac{2}{2}}\, v_f^{\frac{2}{3}}\cdot b_i^* \exp(-\epsilon_0/kT), \qquad (3)$$

and, on assuming that $b_i = b_i^*$, equation (1) yields

$$\tilde{\omega} = (kT/2\pi m)^{\frac{1}{2}} v_f^{\frac{1}{3}} \exp(-\epsilon^*/kT). \qquad (4$$

If $n(x, y, z)$ is the ionic density at the initia position, it will be seen that the net number ions c_z crossing unit area in unit time in th direction of field is given by

$$c_z = \lambda\left(\frac{kT}{2\pi m}\right)^{\frac{1}{2}} v_f^{-\frac{1}{3}}\Big[n e^{\alpha w/kT} - \left(n+\lambda\frac{\partial n}{\partial z}\right) e^{-(1-\alpha)w/kT}\Big] e^{-\epsilon^*/kT}, \qquad (5$$

or, since the work done w by the field $E=|E|$ moving an ion of charge e through a distance λ $eE\lambda$, by

$$c_z = \lambda^2\left(\frac{kT}{2\pi m}\right)^{\frac{1}{2}} v_f^{-\frac{1}{3}}\left[\frac{eE}{kT}n - \frac{\partial n}{\partial z}\right] e^{-\epsilon^*/kT}, \qquad (6$$

upon making the assumption that λ is so smal that $w \ll kT$.

Consider next the ionic transportation due t the prototropic process. To make the argumen general, it is supposed that the O-H linkage, th length of which is to be increased as the resul of the proton transfer, is inclined to the field a an angle ϕ. Then the magnitude of the effectiv field contributing to the proton transfer may b given by $\beta E \cos\phi$, where β is the factor arisin from the effect due to neighbouring molecules.

Accented notations will be used in the follow ing for the quantities which concern the proto corresponding to those used above in discussin the diffusion process. The specific rate $\tilde{\omega}'$ o proton transfer will be given, as an analogue o (4), by

$$\tilde{\omega}' = (kT/2\pi m')^{\frac{1}{2}} v_f'^{-\frac{1}{3}} \exp(-\epsilon^{*\prime}/kT). \qquad (7$$

This yields, for the probability that an ion passe in unit time over the energy barrier in the direction at the angle ϕ to the field,

$$\tilde{\omega}' \exp(-w'/kT) = (kT/2\pi m')^{\frac{1}{2}} v_f'^{-\frac{1}{3}} \exp\left[-\left(\epsilon^{*\prime} - \frac{w'}{2}\right)/kT\right], \qquad (8$$

where $w' = \lambda' e\beta E\cos\phi$ is the work done by th effective field in moving the proton of charge through the distance λ'. It has been assume for simplicity that the energy at the initial stat is increased by the amount $\alpha' w' = w'/2$.

Now, since the rotation of the molecules pro bably occurs rapidly, in comparison with the rocess under consideration, a proton in crossing he potential barrier has virtually travelled the istance from one oxygen atom to a position on he further side of an adjacent oxygen atom; this istance greater than λ' may be taken as λ, or he average dimension of a water molecule in ny direction, so that $\lambda \cos \phi$ gives the component irected along the field.

On putting $w'/kT = \delta \cos \phi$ weere $\delta = \lambda' e \beta E/2kT$, quation (8) yields for the velocity of proton rossing the barrier

$$\bar{v}_\phi = \lambda (kT/2\pi m')^{\frac{1}{2}} v_f'^{-\frac{1}{3}} \cos \phi \cdot \exp [(-\epsilon^{*\prime}/kT) + \delta \cos \phi]. \tag{9}$$

The proton transfer may occur in any direction nd it is equally likely of three protons belonging o an H_3O^+ ion that any one of them is transfered n the direction of external field. Hence (9) gives, or the mean velocity of proton, after averaged ver all directions and multiplied by three,

$$\bar{v} = 3\bar{v}_\phi = \delta\lambda (kT/2\pi m')^{\frac{1}{2}} v_f'^{-\frac{1}{3}} \exp(-\epsilon^{*\prime}/kT). \tag{10}$$

The transter of proton is equivalent to the novement of H_3O^+ ion in water, so that the umber of ions c_z' transported by the prototropic rocess along tbe positive z-axis is given by

$$c_z' = \bar{v}n = \frac{\beta}{2} \lambda\lambda' n \frac{eE}{kT} \left(\frac{kT}{2\pi m'}\right)^{\frac{1}{2}} v_f'^{-\frac{1}{3}} e^{-\epsilon^{*\prime}/kT}. \tag{11}$$

If in general the field depends on time, the onic density n, a function of time also, has to atisfy the equation of continuity

$$\frac{\partial n}{\partial t} + \nabla \cdot (\mathbf{c} + \mathbf{c}') = 0, \tag{12}$$

here $\mathbf{c}$ and $\mathbf{c}'$ designate respectively the vectors f ionic currents caused by the diffusion and rototropic processes. By use of (6) and (11), this quation reduces to

$$\frac{\partial n}{\partial t} = \zeta \nabla \cdot \left[\nabla n - \frac{eE}{kT} u(T) n\right], \tag{13}$$

ith

$$\zeta = \lambda^2 (kT/2\pi m)^{\frac{1}{2}} v_f^{-\frac{1}{3}} \exp(-\epsilon^*/kT)$$

$$u(T) = 1 + \frac{\beta}{2} \frac{\lambda'}{\lambda} \left(\frac{m}{m'}\right)^{\frac{1}{2}} \left(\frac{v_f}{v_f'}\right)^{\frac{1}{3}} \exp[(\epsilon^* - \epsilon^{*\prime})/kT]. \tag{14}$$

§ 3. Distribution Function.

A spherical water drop of radius a is supposed to be in an alternating field $\mathbf{E} = \mathbf{E}_0 e^{-i\omega t}$ whose vector is parallel to the z-axis. Since the field is symmetric about the axis, the two polar coordinates r and θ may be used instead of rectangular x, y, z, provided that the center of the sphere is at the origin and that θ is the angle made by r with the z-axis. Equation (13) then becomes

$$\frac{1}{\zeta}\frac{\partial n}{\partial t} = \frac{1}{r^2}\frac{\partial}{\partial r}\left(r^2 \frac{\partial n}{\partial r}\right) + \frac{1}{r^2 \sin\theta}\frac{\partial}{\partial \theta}\left(\sin\theta \frac{\partial n}{\partial \theta}\right) - \nu \left(\cos\theta \frac{\partial n}{\partial r} - \frac{\sin\theta}{r}\frac{\partial n}{\partial \theta}\right) \tag{15}$$

with

$$\nu = \nu_0 e^{-i\omega t}, \qquad \nu_0 = (e/kT) u(T) \, |\mathbf{E}_0| . \tag{16}$$

It may be of interest to note that equation (15) reduces to the one given by Debye(5) in the limiting case that r tends to λ, the average dimension of a water molecule.

If the applied field is static $\mathbf{E} = \mathbf{E}_0$, that is, $\omega = 0$ or $\nu = \nu_0$ by virtue of (16), the ionic current attains finally to an equilibrium so that (13) reduces in scalar representation to

$$\begin{cases} \dfrac{\partial n}{\partial r} - \nu_0 \cos\theta \cdot n = 0 \\ \dfrac{1}{r}\dfrac{\partial n}{\partial \theta} + \nu_0 \sin\theta \cdot n = 0, \end{cases} \tag{17}$$

with the appropriate solution

$$n = n_0 \exp(\nu_0 r \cos\theta) \qquad (n_0 = \text{const}). \tag{18}$$

Thus the ionic distribution is seen to be Maxwellian in a uniform static field.

Now, consider the case of the periodic field as of radio waves incident upon the sphere. By the transformation

$$n = \Psi(r, \theta, t) \exp\left(\frac{\nu}{2} r \cos\theta\right) \tag{19}$$

equation (15) reduces to

$$\frac{1}{\zeta}\frac{\partial \Psi}{\partial t} = \Delta\Psi + \left[i \frac{\omega}{\zeta}\frac{\nu}{2} r \cos\theta - \left(\frac{\nu}{2}\right)^2\right] \tag{20}$$

where Δ is the Laplacian operator for two coordinates r and θ. The function Ψ is expanded in powers of ν and all terms beyond the first order will be neglected since ν is, as a rule, very small for the field of radio waves. Thus

$$\Psi = \phi_0 + \nu\phi_1 + 0(\nu^2), \qquad (21)$$

and the functions ϕ_o and ϕ_1 depend on the position coordinates alone. Upon inserting the expression in (20) and on equating the coefficients of ν, it is seen that

$$\begin{cases} \varDelta\phi_0 = 0 \\ \varDelta\phi_1 + i\dfrac{\omega}{\varsigma}[\phi_1 + \dfrac{1}{2} r \cos\theta \cdot n_0] = 0. \end{cases} \qquad (22)$$

The integral ϕ_o of the first equation is apparently equal, by (21), to the Ψ without the field operating and it may be taken as a constant n_o, say, by virtue of (19). On putting again

$$\psi = \phi_1 + \frac{1}{2} r \cos\theta \cdot n_0, \qquad (23)$$

the second equation of (22) transforms to

$$\varDelta\psi + \kappa^2\Psi = 0, \qquad \kappa = (\omega/\zeta)^{\frac{1}{2}} e^{i\pi/4} \qquad (24)$$

The appropriate solution may be constructed from zonal harmonics $P_l(\cos\theta)$ and spherical Bessel functions $j_l(\kappa r)$ since ψ is to be finite at the origin;

$$\psi = \sum_{l=0}^{\infty} c_l j_l(\kappa r) P_l(\cos\theta) \qquad (25)$$

where c_l designate the coeffieients of expansion.

By analogy with (18), the boundary condition for n is assumed such that

$$(n)_{r=a} = n_0 \exp(\nu a \cos\theta) \simeq n_0(1 + \nu a \cos\theta) \qquad (26)$$

that is, for ψ, in virtue of (19), (21) and (23),

$$(\psi)_{r=a} = a \cos\theta \cdot n_0. \qquad (27)$$

Upon use of this condition, the coefficients c_l are determined in virtue of the orthogonality property of the Legendre function and the solution becomes finally

$$n \doteq n_0[1 + \nu a \{j_1(\kappa r)/j_1(\kappa a)\} \cos\theta]. \qquad (28)$$

In arriving at this result, an approximation has been made such that the exponential factor in (19) is expanded in powers of νr with terms beyond the first neglected provided that $\nu a \ll 1$ for $a \geq r$.

§ 4. Electric Susceptibility of A Singl Water Drop.

The distribution function derived in the prec ding section for the density of positive ions ma be regarded to a first approximation as valid als for that of negative ions, the constants involve in the function remaining unaltered, inasmuc as the OH⁻ ion possesses the mass and accor ingly the specific rate of transfer nearly equa to those of the H_3O^+ ion. It is then suppose that the ionic distribtion is symmetric with re spect to the xy-plane as the positive and negativ ions are of equal numbers in the sphere.

If N_o designates the number of water molecule in the drop, η the fraction of dissociation, and the averaged component of ionic coordinates along the direction of external field, the dipole momen $\boldsymbol{p}$ of the spherical drop is in magnitude given by

$$|\boldsymbol{p}| = 2\eta N_0 e\bar{z}. \qquad (29)$$

where, by use of (20),

$$\begin{cases} \bar{z} = A\displaystyle\int_0^a \int_0^\pi n(r, \theta, t)\, r^3 \cos\theta \sin\theta\, dr\, d\theta, \\ 1/A = \displaystyle\int_0^a \int_0^\pi n(r, \theta, t)\, r^2 \sin\theta\, dr\, d\theta. \end{cases} \qquad (30)$$

The integration is readily performed and leads to

$$\bar{z} = \nu\kappa^{-1} a j_2(\kappa a)/j_1(\kappa a). \qquad (31)$$

The dipole moment per unit field-strength define the electric susceptibility and, consequently, combination of (16), (29) and (31), divided by E, gives, for the complex susceptibility of a single drop χ,

$$\chi = \frac{|\boldsymbol{p}|}{|E|} = 2\eta N_0 u(\mathrm{T}) \frac{e^2 a}{kT} \frac{1}{\kappa} \frac{j_2(\kappa a)}{j_1(\kappa a)} \qquad (32)$$

where, by (24),

$$\kappa = (\omega/\zeta)^{\frac{1}{2}} \exp(i\pi/4). \qquad (33)$$

In the case of static field, evidently

$$\lim_{\kappa \to 0} \frac{1}{\kappa a} \frac{j_2(\kappa a)}{j_1(\kappa a)} = \tfrac{1}{5}; \qquad (34)$$

this gives for χ, as it would be, the same result as obtainable directly from (18).

On inserting numerical values in (32), it may readily be verified that the susceptibility of a water drop presents a greater magnitude than that given by the Mie-Stratton formula, if acount is taken of the ionic polarization induced within the drop. Numerical estimation has revealed that the ionic polarization of atmospheric water particles might provide a satisfactory account for the tropospheric reflection of radio waves, which will be discussed in a later issue of this journal.

The author wishes to express his sincere gratitude to Prof. A. Harashima of the Tokyo Institute of Technology for reading manuscript and for helpful comments.

References.

(1) G. Mie; Ann. d. Physik **25**, 377, 4. Folge (1908).

(2) J. A. Stratton; Proc. I. R. E. **18**, 1064 (1930).

(3) S. Glasstone, K. J. Laidler and H. Eyring; "The Theory of Rate Processes", New York (1941).

(4) H. Eyring; J. Chem. Phys. **4**, 283 (1936).

(5) P. Debye; "Polare Molekeln", Leipzig (1929).

On the Breakdown of Alumina at Higher Temperature.

By Hisao MIYAZAWA and Jun-ichi OKADA.

Matsuda Research Laboratory, Tokyo-Shibaura Electric Co., Kawasaki.

(Received June 21, 1950)

§ 1. Introduction.

On the dielectric breakdown of alkali halides a number of fine experimental and theoretical works have been done up to the present day because the phenomena offer some interesting problems that deal with electronic structure of solids.

It is important, however, from the practical standpoint such as vacuum tube technique, that the insulation performance must hold at very high temperatures and vacuums. Though there are numerous materials which may be called "insulators" at or below room temperatures, only few metal-oxides whose melting point is very high are applicable above 1000 °C for the purpose of the electrical insulation.

In the present paper we will take up alumina which is the most common one among them and investigate its behavior of breakdown at higher temperatures.

§ 2. The Temperature Dependency of the Breakdown Voltage.

We investigated first the temperature dependency of the breakdown strength because of its physical interest and practical importance.

The sample used was a heater with a spiral type electrode inserted into alumina layer as shown in Fig. 1. The heater was a tungsten wire, 25/100 mm diameter and 40 mm length, on which a layer of alumina was coated about 7/100 mm thick by means of electrophoresis and sintered at 1700 °C in a hydrogen furnace. After a fine tungsten wire 4/100 mm diameter had been closely wound about 100 turns at the middle part of the heater, alumina was sprayed on it until the wound wire was nearly buried, and sintered again by the above method.

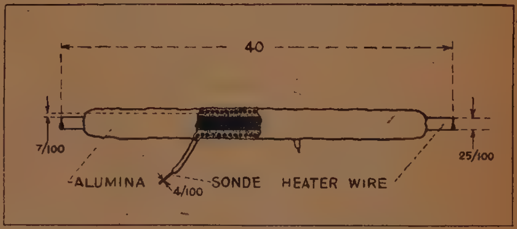

Fig. 1.

Measurement was done by a simple circuit shown in Fig. 2. Breakdown voltage V_m is the maximum A. C. voltage, which can be applied between the heating wire and the outer electrode, provided the voltage is slowly increased. The temperature was controlled by currents through the heating wire and was calibrated by the optical pyrometer. In Fig. 2, *T* is a transformer

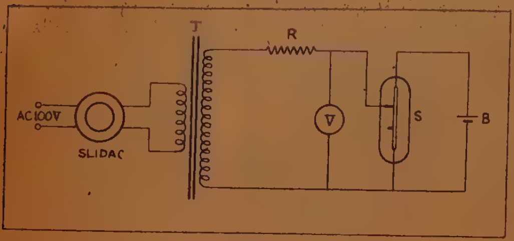

Fig. 2.

of which maximum secondary output is 2000 volts and of which output voltage is controlled by a slidac in the primary side, *V* is a voltmeter measuring the breakdown voltage, *S* is a sample which can be heated by a storage battery *B*, and *R* is protecting rheostat, 10 kiloohms maximum resistivity, which is adjusted properly in accordance with the breakdown strength.

To begin with, after evacuating to about 10^{-4} mm Hg, the sample was flashed for about 10 seconds at 1580 °K in order to exhaust the occluded gas without aging effect. In the next place, the temperature was decreased down to a definite value, then the voltage applied between electrodes was increased slowly from zero volts until the breakdown would occur. When the breakdown takes place, the voltmeter falls down to zero volts and the currents of several hundred milliamperes run through the alumina layer, leaving black spots in it.

The results obtained at various temperatures are shown in Fig. 3. In spite of the fluctuation of the observed values, their average points are placed on the full line shown in the figure. Though there are no experimental data between 1100 °K and room temperature, it is obvious that the curve below about 1200 °K is practically horizontal, while the temperature dependency above 1200 °K is remarkable. Hence the curve is divided into two sections. As for the latter section, log V_m *vs.* $1/T$ curve linearly and rapidly goes down in accordance with the temperature increasing. The same phenomena had been observed on the other ceramics,(1) (2) (3) and had been interpreted as follows; The section i dependent of the temperature is due to t "electron avalanches" in solids and is call "electronic" (or "disruptive") breakdown, whi the section dependent upon the temperature due to the Joule heat which is produced b currents and is called "thermal" breakdown.(4

By the way, as the operating temperature of the practical heaters of vacuum tubes is relativel high, let us consider the phenomenon of therma

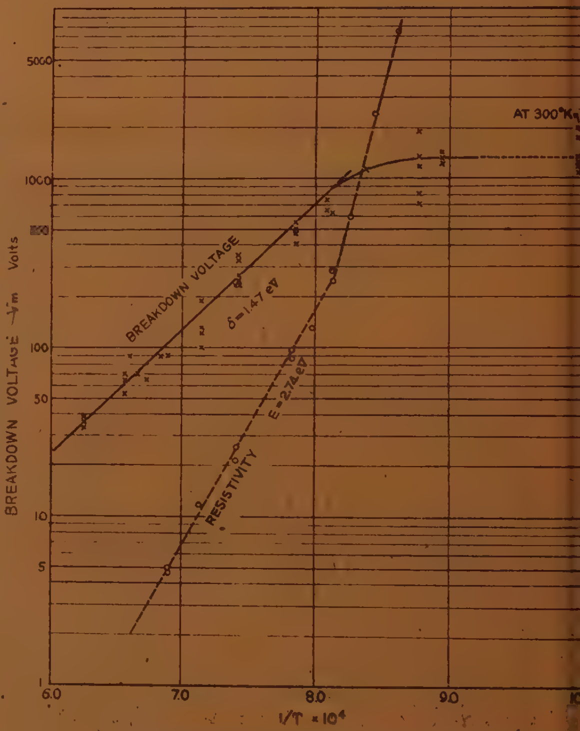

Fig. 3. Temperature effect on V_m & *R* of alumina

breakdown only. Since it is due to the Joule heat as stated above, it seems natural to investigate how the breakdown voltage depends on the resistivity of alumina layer. The experimental values of resistivity are shown in Fig. 3 by the broken line, and their temperature dependency can be expressed by the formula

$$R = R_0 \exp(E/kT)$$

which is characteristic of semi-conductor. From these data, activation energy *E* has come out 5 eV or 2.7 eV when $T < 1270$ °K or $T > 1270$ °K respectively. Though the reason why such a kink appears at about 1270 °K may be given in general by the Nijiboer's theory,[6] the adequacy of this theory is not obvious, because there is a possibility that the impurity alkaline atoms contained in the form of β-alumina may play current carriers as ions.[6] It may be interesting, however, that the kink nearly coincides with that of breakdown characteristics. The same phenomena have been observed recently on other ceramics.[8]

In the meantime, the temperature dependency of the breakdown voltage of alumina under consideration can be shown by the empirical formula

$$V_m = V_0 \exp(\delta/kT),$$

where experimental values of δ is about 1.47 eV. It is then pointed out that the value of δ is about one half that of the activation energy E measured above, that is to say,

$$\delta = E/2.$$

Hence we may expect that between the breakdown voltage V_m and the resistivity R there exists the relation

$$V_m \propto \sqrt{R}.$$

Such a relation has been observed as well on glass, porcelain and rock salt,[9] and its theoretical interpretation has been tried. However, below will be given a theoretical investigation for our experimental results.

§ 3. The Theory of Thermal Breakdown.

Since the Joule heat is essential in the case of thermal breakdown as mentioned above, the problem may be dealt with thermally. Let us start from the classical equation of the heat conduction and radiation for the simplified model.

When no electric field is applied between electrodes, the rate of temperature increasing in the alumina layer is given by the equation

$$vcd\frac{\partial T}{\partial t} = \kappa S_1 (T_f - T) - \varepsilon \sigma S_0 T^4, \qquad (1)$$

where v....volume of alumina layer between electrodes,
c.....specific heat of alumina,
d ....density of alumina,
κ.....thermal conductivity of alumina,
S_1....effective area of thermal conduction on the side of the heater,
T_f....temperature of heating wire,
ε.....emissivity of alumina,
σ.....Stefan-Boltzmann's constant,
S_0.....effective area of heat radiation.

Hence the equilibrium temperature T_0 in alumina layer is given by the equation

$$\kappa S_1 (T_f - T_0) = \varepsilon \sigma S_0 T_0. \qquad (2)$$

When the field is applied, the equation

$$vcd\frac{\partial T}{\partial t} = \frac{V^2}{R(T)} - \kappa S_1 (T - T_f) - \kappa S_2 (T - T_0) - \varepsilon \sigma S_0 T_0 \qquad (3)$$

determines the temperature increasing, where
$R(T)$ .resistivity of alumina layer at T°K,
S_2 ....effective area of heat conduction to the surrounding alumina.

Moreover, $R(T)$ has the form

$$R(T) = R_0 \exp(\beta/T), \qquad (4)$$

where β is 3.5×10^4 °K from the experimental result.

Now assuming $T \simeq T_0$, we obtain from (2) and (3)

$$vcd\frac{\partial T}{\partial t} = \frac{V^2}{R(T)} - (\kappa S + 4\varepsilon\sigma S_0 T_0^3)(T - T_0), \qquad (5)$$

where $S = S_1 + S_2$.

The condition in which an equilibrium temperature can exist is

$$\frac{\partial T}{\partial t} = 0, \qquad \frac{\partial}{\partial T}\left(\frac{\partial T}{\partial t}\right) < 0,$$

whereby the equilibrium temperature is given by

$$\frac{V^2}{R(T)} = (\kappa S + 4\varepsilon\sigma S_0 T_0^3)(T - T_0). \qquad (6)$$

On the other hand, when

$$\frac{\partial T}{\partial t} > 0, \qquad \frac{\partial}{\partial T}\left(\frac{\partial T}{\partial t}\right) > 0,$$

there exists no equilibrium temperature, and the temperature of alumina layer will increase until the breakdown takes place. Hence the critical condition of breakdown may be

$$\frac{\partial T}{\partial t} = 0, \qquad \frac{\partial}{\partial T}\left(\frac{\partial T}{\partial t}\right) = 0.$$

Then

$$\frac{\beta}{T^2}\frac{V^2}{R(T)}=\kappa S+4\epsilon\sigma S_0 T_0^3\,, \tag{7}$$

and from (6) and (7)

$$T^2-\beta T+\beta T_0=0\,.$$

Solving this equation, we find

$$T\doteqdot\beta \quad\text{or}\quad T_0+\frac{T_0^2}{\beta-2T_0}\quad(\beta\gg T_0)\,. \tag{8}$$

Since β is far higher than the melting point of alumina (2050 °C), the former solution of (8) is out of question. Hence, substituting the latter into (7), the relation between V_m and R may be obtained. But in order to simplify the result we will boldly put $T\doteqdot T_0$, since $T_0^2/(\beta-2T_0)\ll T_0$. Then the breakdown voltage V_m is given by

$$V_m^2\doteqdot\left\{\frac{T_0^2}{\beta}(\kappa S+4\epsilon\sigma S_0 T_0^3)\right\}R(T_0)$$

or

$$V_m\doteqdot\alpha\sqrt{R(T_0)}\,,\qquad \alpha\equiv\frac{T_0^2}{\beta}(\kappa S+4\epsilon\sigma S_0 T_0^3)\,. \tag{9}$$

This is the same relation as the empirical formula.

Since the proportional constant α in (9) can be determined numerically, we will now calculate the breakdown voltage V_m at $T=1350$ °K. Since

$R(1350\ ^\circ\text{K})=2.5\times10^{-5}\ \Omega$ (observed value),
$\kappa=1.67\times10^{-2}$ joule/sec. deg. cm.,
$\epsilon=0.4$,*
$\sigma=5.75\times10^{-12}$ joule/sec. deg.^{4} cm.^{3},
and $S=7.85\times10^{-2}$ cm.^{2}
$S_0=1.23\times10^{-1}$ cm.^{2}

are obtained from Fig. 4 which shows the dimensions of the sample, we find in the result

$$\alpha=0.46\ \text{volts}/\Omega^{1/2}$$

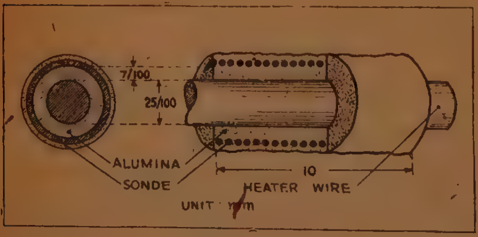

Fig. 4.

and then

$$V_{\text{calc.}}=238\ \text{volts}.$$

While the observed value is

$$V_{\text{obs.}}=250\ \text{volts}.$$

Hence their agreement seems to be sufficient.

§ 4. The Variation of the Resistivity and the Breakdown Voltage at Definite Temperature.

The empirical law between the breakdown voltage and the resistivity obtained in § 2,

$$V_m\propto\sqrt{R}\,,$$

could be verified by the simple theory investigated in § 3.

According to this law, the breakdown strength must increase to the higher value with the square root of resistivity increasing. Meanwhile, it is found that the resistivity of alumina, in addition to the initial variety owing to each sample, can be gradually increased by the aging process which is carried out at very high temperature by running heavy currents through the heater wire of the sample and evaporating the impurity (alkaline atoms or ions) in β-alumina. Hence the sample, after aging at various temperatures and time intervals as mentioned above, may have various values of the resistivity. With these samples we observed the resistivity dependency of the breakdown strength at a definite temperature and confirmed whether the relation between the breakdown voltage and the resistivity is subjected or not to the above law.

Fig. 5 shows the result at 1465 °K, which fairly proves the law of $V_m\propto\sqrt{R}$.

§ 5. Conclusion.

The temperature dependency of the breakdown strength of alumina at higher temperatures was investigated. Passing through the region independent to the temperature at comparatively low temperatures, the breakdown voltage of alumina decreases exponentially with the increasing temperature. Its temperature coefficient has a certain relation to the temperature coefficient of the electrical resistivity of alumina, which is expressed by the form

$$V_m\propto\sqrt{R}\,.$$

---

* We have to thank Dr. T. Azuma for the measurement of emissivity value of our sample.

This relation can be derived by the theory of thermal breakdown.

Up to the comparatively high temperature the brekdown strength of our samples does not depend on temperature. In this case the field strength is of the order of about 10^5 volts/cm., whereby the electronic breakdown probably occurs. But on such ceramics, the experiment cannot be carried out so precisely as in the case of alkali halides single crystal in which the discussion of solid theory is quantitatively applicable. Further, the theory itself may not cover such region at present.

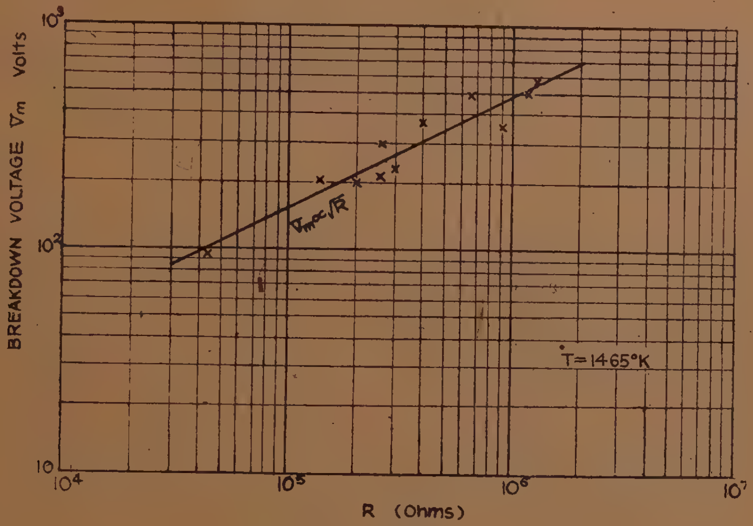

Fig. 5. Aging effect.

References.

(1) Whitehead: *Dielectric Phenomena* (London, 1932), pp. 170, 214.
(2) E. W. Lindsay, L. Berberich: E. E., **57**, 440 (1948).
(3) Moon, Norcross: J. Frank. Inst., **208**, 705 (1929).
(4) Inge, Walther: Zeits. f. Phys., **37**, 292 (1925).
(5) A. von Hippel: Zeits. f. Phys., **75**, 145 (1932).
(6) B. R. A. Nijboer: Proc. Phys. Soc., **51**, 575 (1939).
(7) Miyazawa, Okada: to be published.
(8) Lindsay, Berberich: *ibid.*
(9) Whitehead: *ibid.*

On the Magnetic After Effect due to the Irreversible Displacement of Domain Boundary (II)* **

The dependency on temperature and tension.

By Seijiro MAEDA.

The Research Institute for Iron, Steel and Other Metals, Tohoku University

(Read in November 1949, Received July 1, 1950)

§ 1. Introduction.

Recently, the author reported[1] on his experimental results concerning the magnetic after effect of a Cr-permalloy and it was then concluded that all the properties of observed after effect are explained well, if we assume that the displacement of the domain boundary proceeds very slowly at special regions in the ferromagnetic substances where the difference between final field H_f and a peak value of the critical field H_{om} is very small. Thus the irreversible displacement of the domain boundaries which follow subsequently such a slow displacement of the domain boundaries are strongly stemmed out, consequently the changes of magnetization are retarded from the change of external magnetizing field. From the same point of view, comparatively small changes of after effect due to the change of temperature are expected instead of the Richter's results[2] who observed a magnetic after effect of a carbonyl-iron. Also the decrease in amount of the after effect due to the tension applied is expected for the ferromagnetic substances with a negative magnetostriction constant (Ni type). In the present paper the experimental results on the dependency of after effect upon temperature and external tension are described and a discussion is given on the mechanism of the after effect from the same point of view as mentioned in the previous paper.

§ 2. Experimental Arrangements and Procedures.

Main part of the measuring method for the after effect is the same as described in the previous paper; the total changes of magnetic induction $B_n(t)$ during the period from t second after the instant of the breaking of the magnetizing circuit to the time at which the after effect practically finishes are measured by a ballistic galvanometer. In order to measure the dependency of after effect upon temperature an electric furnace for higher temperatures and a Dewar's Vessel for lower temperatures are set inside the magnetizing coil of the arrangements previously described and to apply tensions the weights of various values are used.

The similar considerations as mentioned in the previous paper also hold in these cases on the two apparent magnetic retardation due to an eddy current in the specimen and an inductance in the circuit of magnetizing coil and it is possible to conclude that these effects are negligible in our measurement of the after effect. The specimen used is a wire of Cr-permalloy with a diameter of 1.2 *mm*, 60 *cm* in length and is measured after sufficient annealling in a dry hydrogen atmosphere at 950°*C* for 6 *hrs*.

§ 3. Dependency on the Tensions Applied.

In order to study the behavior of the magnetic after effect under the action of external tension, the amounts of induction change which is caused by the change of initial magnetic field $H_i = 6.0$ *Oe* to various values of the final field H_f are measured. As an example of the results obtained,

---

* Report of the Research Institute for Iron, Steel and Other Metals, Tohoku University.

** This investigation was financed in part by the Grant-in-Aid of Fundamental Scientific Researches of the Ministry of Education for 1949. Item #D 892, "On the Magnetic After Effect of the Iron Alloys".

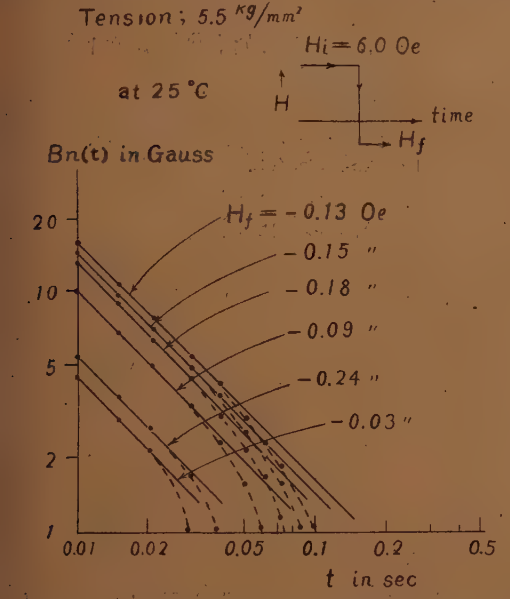

Fig. 1; Decaying characteristic curves for various values of H_f under tension of 5.5 *kg/mm* .

the values of $B_n(t)$ against t, for various values of H_f, in the case of a tension 5.5 kg/mm^2, at 25°C are plotted in Fig. 1. As can be seen from the figure a main part of the decaying characteristic curves is well expressed by a straight line with a common inclination of minus unity in a diagram of *log* $B_n(t)$ versus *log* t, that is

$$\log B_n(t) = \text{Const.} - \log t \qquad (1)$$

However, as pointed out in the previous paper, for comparatively large values of t the formula does not hold exactly. It is worth noticing that the inclination does not depend on the values of H_f. Those properties are already observed for the case of no tension. It is ascertained also that those relations hold true for various values of tensions applied ranging from 0 to 8.3 kj/mm^2. To obtain the relation of the amount of after effect and the final field H_f, the values of B_{no} against H_f for various values of the tensions applied are plotted in Fig. 2, where B_{no} is an amount of the induction change after $t = t_o = 1/100$ *sec.* and hereafter B_{no} is chosen as a parameter representing the amount of after effect. As can be seen from the figure also in these cases a maximum of the after effect appears and a final field strength H_f at which the effect shows a maximum value diminishes with increasing tension; for example, under the tension of 5.5 kg/mm^2 the maximum after effect occurs at $H_f = -0.13$ *Oe.* while that with no tension occurs at -0.09 *Oe.*. The amount of after effect also decreases with an increasing tension; for example, the amount of maximum value of after effect under the tension of 5.5 kg/mm^2 is only *ca.* 1/5.3 times of that with no tension.

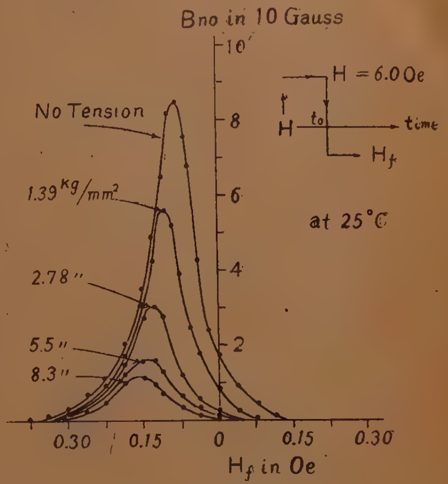

Fig. 2; B_{no} vs. H_f curves for various values of applied tensions.

§ 4. Dependency on the Temperature.

As the dependency of the effect upon the temperature is an important factor in discussing the mechanism of the after effect; the effects of the temperature on B_{no} and the decaying character of the after effect at the temperatures ranged -50°C to 200°C are measured and it was confirmed that the decaying character is not affected by the change of temperature and does not depend on the final field H_f as described in the last paper; for example. Fig. 3 shows the decaying character of the after effect for the cases of constant initial field H_i corresponding to magnetic saturation and of various values of final field H_f, at 170°C. As can be seen from it, a leading part of the decaying characteristic curve is also expressed well by a similar formula:

$$\log B_n(t) = \text{Const.} - \log t$$

except for comparatively large values of t just befor the after effect finishes as pointed out in

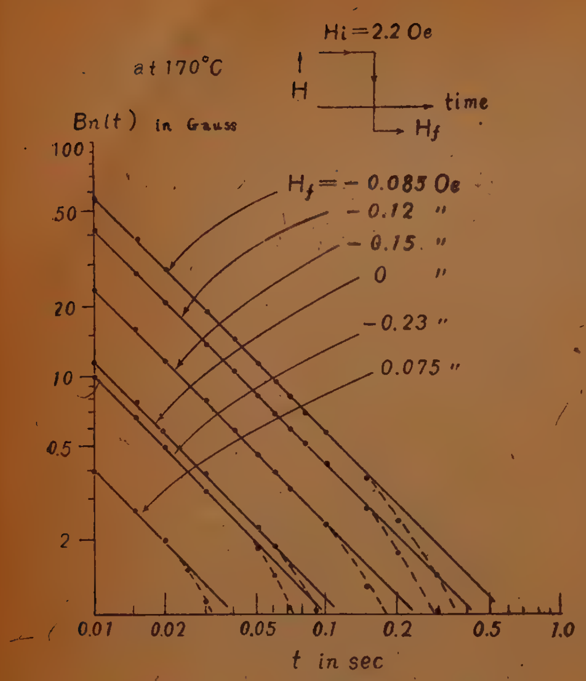

Fig. 3; Decaying characteristic curves for various values of H_f at 170°C.

the last section. This conclusion of the temperature independency of the decaying character holds not only in the cases in which saturatio field is chosen as the initial field but also for al the values of H_i. Fig. 4 shows a relation between the amounts of the after effect, B_{no} and the final fields H_f along the descending branch of the hysteresis loop for the various temperatures. As can be seen from it, the position of maximum after effect displaces to weak field side; it takes a value 0.10 Oe at -50°C, -0.09 Oe at 3°C and -0.085 Oe at 170°C, and these displacements coincide quantitatively well with that of maximum of $|\Delta B/\Delta H|$ obtained from the measured hysteresis loop. And the values of B_{no} increase with descending temperatures; for example, the maximum amounts of after effect for various temperatures are 123 gauss at -50°C, 93 gauss at 3°C and 55 gauss at 170°C and the ratio of them is 100 : 95 : 45. From the fact that the effect of the temperature on the decaying character observed here diverges widely from Richter's result, who observed a much stronger dependency of it on the temperature; it is concluded that the mechanism of the after effect observed here is essentially different from Richter's.

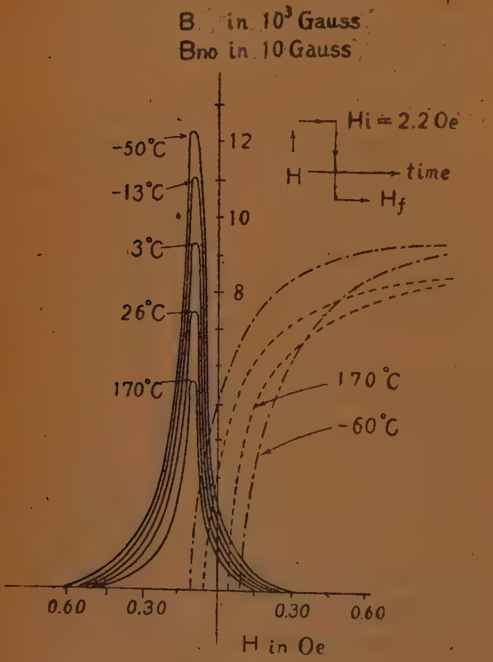

Fig. 4; ————; B_{no} vs. H_f cuoves for different temperatures, — · — · — ; B—H curves at -90°C and 170°C respectively.

§ 5. Discussion.

As described above the law of the change of magnetic induction $B_n(t)$ after the change of external magnetic field is not affected by the change of temperatures and action of external tenions. Thus, the decaying characteristics of the after effect for various temperatures and tensions applied is expressed by a simple relation

$$\log B_n(t) = \text{Const.} - \log t$$

Consequently, the model of the ferromagnetic substance previously proposed, which is responsible for the after effect, is considered also to hold true for the different temperatures and tensions applied.

Now, we will discuss the dependency of the amount of after effect B_{no} upon temperature. As described in the previous paper, B_{no} is expressed by the formula.

$$B_{no} = \beta(H_f)\,\Delta H_f \qquad (2)$$

where, $\beta(H_f)$ is rate change ΔB of the magnetic induction by the irreversible displacements of he total domain boundaries due to the change of xternal field ΔH_f, $\overline{\Delta H_f}$ is a definite value of a ange of external magnetic field, the value of hich is given by

$$\overline{\Delta H_f} = D/(a t_o) \qquad (3)$$

here, a is a velocity constant of displacement f the domain boundary as previously described, amely

$$V = a(H_f - H_o) \qquad (4)$$

and D is the distance on which the domain boundary displaces with slow velocity. At the steepest part of the hysteresis loop, the change of magnetic induction is mainly caused by the irreversible displacements of domain boundaries, hence it will not introduce any serious errors even if one assumes

$$\beta(H_f) = |\Delta B/\Delta H|$$

where $|\Delta B/\Delta H|$ is a rate change ΔB of magnetic induction due to the change ΔH of the external magnetic field along the descending branch of the hysteresis loop. Then the equation (2) is expressed by

$$B_{no} = |\Delta B/\Delta H|\,\overline{\Delta H_f} \qquad (5)$$

According to the formula (5), the dependency of B_{no} upon temperature is determined by that of $\overline{\Delta H_f}$ and $|\Delta B/\Delta H|$. Hence change of the field strength $H_f(\max)$ for a maximum value of B_{no} due to the tensions applied should coincides to that of magnetic field strength for maximum $|\Delta B/\Delta H|$ of the hysteresis loop. As an example, the hysteressis loop under an external tension of 5.5 kg/mm^2 and $B_{no}-H_f$ curve are shown in Fig. 5. As can be seen from the figure, field strength for the maximum value of $|\Delta B/\Delta H|$ changes from −0.09 *Oe* (no tension) to −0.13 *Oe* (5.5 kg/mm^2), and this change of the field coincides well with that $H_f(max)$. The similar consideration also hold on the effect of temperature; the hysteresis loops and $B_{no}-H_f$ curves at various temperatures are showm in Fig. 4. As it shows, the coercive force and the residual magnetism decrease with ascending temperatures and the displacement of $H_f(max)$ is well explained by considering that of field strength of the maximum $|\Delta B/\Delta H|$.

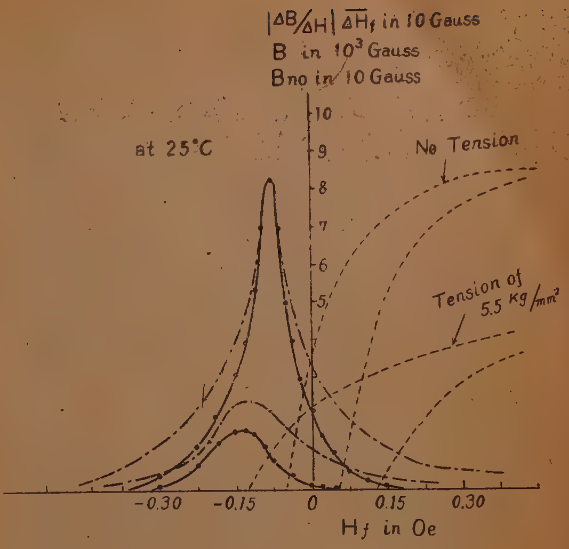

Fig. 5; ——————; $B_{no}-H_f$ curves
– – – – – –; $B-H$ curves
–·–·–·–·–; $|\Delta B/\Delta H|-H_f$ curves

Next, let us describe the change in amount of B_{no}. As can be seen from Fig. 4; the value of $|\Delta B/\Delta H|$ does not decrease more than 10% by change of temperature from −60°C to 170°C, so it does not introduce the observed change of B_{no}; Hence the main part of the change of B_{no} should be attributed to a change of $\overline{\Delta H_f}$ due to temperatures. Now, in equation (3) t_o is a constant value throughout the present measurement, and D is determined by the local distribution of the critical field $H_o(r)$. It is assumed that $H_o(r)$ takes no appreciable change in such a range of temperature. Moreover its amount and distribution may be determined by the elasticity, magnetostriction constant and the behavior of the domain structure, and the changes of these factors are not so conspicuous, so that D may be not so strongly change with the rise of temperature. Another factor a, the velocity constant, may increase with the rise of temperature; according to Huzimura's and Sixtu's experimental results on the large Barkhausen effect, a is almost invariant in the range of temperatures from that of liquid nitrogen to about 200°C when the difference H_f-H_o takes a value larger than 1 *Oe*. However, in the case when H_f-H_o takes a smaller value less than 10^{-1} *Oe*. the value of a increases widely with ascending temperatures.

Consequently we may assume that this character of a also holds in the general cases of the displacement of the domain boundary and in our case a may increases more strongly due to the rise of temperatures than the results obtained by their experiments, because the values of the difference $H_f - H_o$ are less than 10^{-3} *Oe*. Although quantitative comparison is not possible in this case, the temperature dependency of B_{no} may be qualitatively explained by considering mainly the change of velocity constant a due to temperatures.

Next, we consider the dependency of B_{no} upon the tension applied. As can be seen from Fig. 2, B_{no} strongly decreases with increasing tension. Now in the formula (5) for B_{no} the factor $\overline{\Delta H_f}$ is determined by equation (3). Although we have now no precise data on the dependency of a and D upon the tensions, it may be assumed that the changes of those quantities are not appreciable in such a small range of the tension. Therefore $\overline{\Delta H_f}$ is also considered as almost constant in value, hence the change of B_{no} must be due to the facter $|\Delta B/\Delta H|$ in equation (5). As can be seen from Fig. 5. a ratio of $|\Delta B/\Delta H|$ with a tension of 5.5 kg/mm^2 to that without tension is 1:3.6 while that of the observed value of B_{no} is 1:5.1. Thus, the calculated ratio of B_{no} is a little less than the observed one. Alternatively speaking the calculated values of B_{no} based on the apparent value of $|\Delta B/\Delta H|$ are larger than the observed one. A cause of this discrepancy may be considered as follows; with increasing tensions the reversible rotation of the spontaneous magnetization increases and a ratio of contribution of the irreversible displacement of the domain boundary to the actual change of magnetic induction may be decreased; therefore the slop of the observed hystersis loop diverges from the true value of $\beta(H_f)$ with the increase of applied tensions, hence with increasing of the tension the calculated B_{no} based on such $|\Delta B/\Delta H|$ diverges from observed B_{no}.

It is to be concluded that the behavior of the magnetic after effect of Cr-permalloy as well as its dependency on tension applied and temperature are well explained by considering the relaxation of irreversible displacement of magnetic domain boundaries. It is also here to be emphasized that relaxation of magnetization due to thermal diffusion of impurity atoms or plastic relaxation do not play the main roll concerning the present experiment.

The author wishes to acknowledge his thanks to prof. T. Hirone who supervised the present work.

References.

(1) S. Maeda; "On the Magnetic After Effect due to the Irreversible Displacement of Domain Boundary (I)," J. Phys. Soc. Japan, vol. 5, (1950) No. 5, p. 358.

(2) G. Richter; *Probleme der Technischen Magnetisierungskurve*, J, Springer, Berlin, 1938, 93.

(3) T. Huzimura; "On the Displacement Velocity of a Magnetic Domain Boundary by a Large Barkhausen Jump in a Ferromagnetic Substance" J. Phys. Soc. Japan, vol. 5 (1950) No. 2, p. 56.

(4) K.J. Sixtus; *Probleme der Technischen Magnetisierungskurve*, J. Springer. Berlin, 1938, 93.

(5) J.L. Snoek; Physica. Haag, vol. 8. 1939, 663.

(6) G. Richter, loc. cit.

Short Notes.

The Behaviours of Fe-Al, Fe-Si and Fe-Al-Si Alloys considered from the Standpoint of Ferromagnetic Superlattice.

By Hiroshi SATO and Hisao YAMAMOTO.

Research Institute for Iron, Steel and Other Metals, Tohoku University. Sendai, Japan.

(Read Nov. 16 (1948), received September, 16 (1950))

Formerly one of the authors attempted to explain the complicated behaviours of the superlattice in α phase Fe–Al alloys(1) using the statistical theory of ferromagnetic superlattice(2), and the explanations of these anomalous behaviours, such as the phase diagram, the dependency of the specific heat upon temperature and composition etc., of these alloys were successfully unified by the general concept of the interrelation betweed the origination of spontaneous magnetization and the formation of superlattice. Following the above consideration, these alloys belong to the case of ferromagnetic superlattice in which the magnetic Curie point falls with the development of order. This explanation is, however, only qualitative, and therefore, there is a room to bring out other explanations, especially about the origin of the appearance of many flat maxima in the specific heat-temperature curve. To make this point clear, the author studied the behaviours of the ternary alloys in which Al is replaced by Si along the composition line connecting Fe_3Al with Fe_3Si in the ternary diagram Fe–Al-Si; Fe_3Si has the same lattice type and belongs to the same type of ferromagnetic superlattice as Fe_3Al. In this composition range, high permeability alloy known as "Sendust" are included and therefore such an investigation also has possibilities to offer interesting materials for the study of high permeability problem. The results obtained are briefly given below:

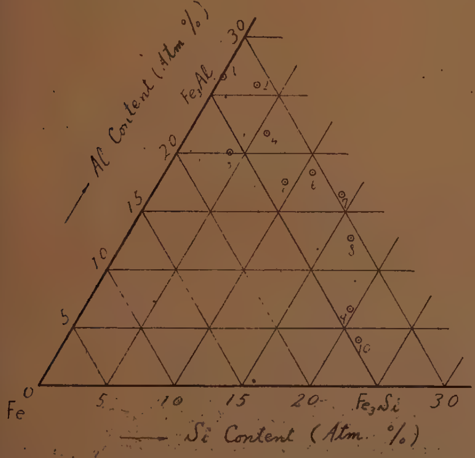

Fig. 1. Composition of samples chemically analysed.

The transition point of the binary type superlattice* $Fe_3(Al_{1-x}Si_x)$ $(0 \leq x \leq 1)$ (the peak C in the curves of Fig. 2), which is formed in this composition range, rises much more abruptly than the line which connects the transition point of Fe_3Al with that of Fe_3Si as shown in Fig. 3. This fact means that Al and Si atoms repulse each other in the nearest neighbouring sites.

The two flat maxima A, B in the specific heat-temperature curve in the case of Fe_3Al approaches each other by the addition of Si. Then they coincide together and become a sharp knick which is typical at the ordinary Curie point. These two maxima were explained in the previous paper as those of ferromagnetic transition and the separation into two as due to the interrelation between the origination of spontaneous magnetization and the formation of superlattice owing to the neighbourhood of the two transition points. As the content of Si increases, the transition point of order rises abruptly and the magnetic Curie point, on the other hand, remains nearly constant as shown in the Fig. 3, the transition points separate each other and hence the interrelation of these two phenomena can be considered to become weaker. The above results, therefore, not only give the experimental justification of the fundamental idea of the statistical theory of ferromagnetic superlattice, but also confirm the correctness of the explanation about Fe–Al alloys previously given.

The total energy change due to the decomposition of superlattice is remarkably small as compared to the ordinary one. This fact corresponds to that $Fe_3(Al_{1-x}Si_x)$ is the second order superlattice*.

The anomalous behaviours of the magnetic permeability of these alloys at high temperature are also explainable from the above circumstances.

The details of this work will be published in the Science Report of the Research Inst. Tohoku Univ. (Sci. Rep. RITU) in the near future.

---

* The explanation of these nomenclatures will be given in the full paper.

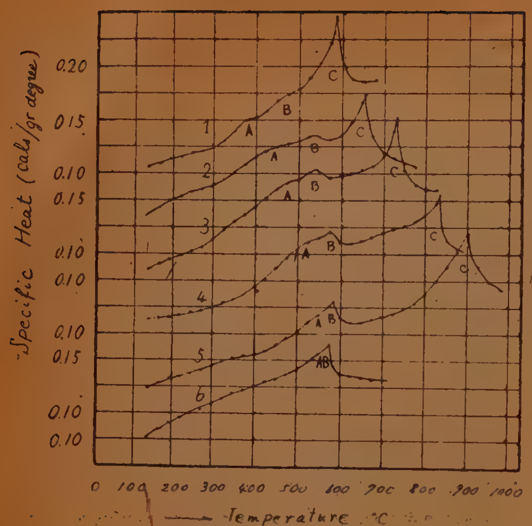

Fig. 2. Specific heat-temperature curves of Fe–Al–Si alloys. The figures on each curve indicate the composition of the alloys shown in Fig. 1.

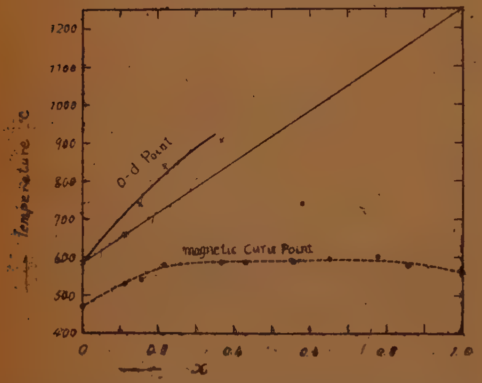

Fig. 3. Collected data on transformations of alloys $Fe_3(Al_{1-x}Si)$, in which each composition is reduced to this composition line keeping the Si content constant.

References.

Sci. Rep. RITU A, 1 78 (1949).
(1) H. Sato; J. Japan Inst. Metals, 13 No. 4-3 (1949)
(2) H. Sato; J. phys. Soc. Japan, 3 90 (1948). Proc. Phys. Soc. Japan, 3 1, 8, 16 (1948)

The Photo-disintegration of Be by the High Energy γ-rays.

By Bunsaku Arakatsu, Masateru Sonoda, Yoshiaki Uemura, Shinjiro Yasumi and Yoshio Saji.

Department of Physics, Faculty of Science, University of Kyoto.

(Received September 17, 1950)

The photo-disintegration of Be was observed for the γ-rays of 17.6 and 6.13 Mev. These γ-rays were produced by bombarding thick target of Li metal and CaF_2 with protons of energy of 500 Kev and 350 Kev, respectively, amounting to the intensity of the unseparated ion beam of 30∼60 μA. The proportional counters of methane flow type, were placed near the γ-ray source, one of which was coated with thick layer of BeO, and the other remained uncoated. The Be-coated counter was 6 cm in diameter and 20 cm in effective length. The pulses due to the α-particles ejected from the wall of the counters were counted usually by two scale-of-4 scalers, after being amplified by the respective 4-stage linear amplifier. Moreover, special cares were taken in order to discriminate a spurious count due to an accidental electromagnetic induction from the accelerating tube and other electric devices. Namely the pulses from each of the counters were fed respectively into the vertical and horizontal deflectors of a Braun-tube oscilloscope, so that the spurious pulse which took place simultaneously in both counters appeared as an oblique pulse on the oscilloscope screen. It was found that in general the spurious pulses were seldom in winter when the conditions of the high tension appearatus and the accelerating tube system were good. The linearity of the counter and amplifier system was ascertained by observing the integrated Bragg curve in the methane gas, for the various distance of a sample of the Th deposit from the counter window. The counts from the Be-coated counter were also recorded on a printing paper by an electromagnetic oscillograph. The γ-ray was measured with a G-M counter of lead wall of 6.5 mm in thickness, the counting efficiency of which was calculated theoretically by one of the authors. When the proportional counters were irradiated by the γ-rays, many pulses were observed in the Be-coated counter, but a few in the uncoated one. Moreover, the number of observed kicks from the Be-coated counter was found to be exactly proportional to that of the γ-ray counts. These facts show that the observed pulses from the Be-coated counter are definitely to be attributed to the α-particles ejected by Be irradiated by the γ-rays, but not to the particles emitted by $(n-\alpha)$

process induced by the neutrons, which might be produced by the (*D-D*) and (*Li-D*) reactions at the target. The oscillograph records were analysed and the following disintegration schema were concluded. Namely,

(1) $Be^9+17.6\,\text{Mev}\,\gamma\rightarrow \overset{*}{Be}{}^8+n$ ($\overset{*}{Be}{}^8$ in 7 Mev excited state)

$\overset{*}{Be}{}^8\rightarrow 2\alpha$

(2) $Be^9+17.6\,\text{Mev}\,\gamma\rightarrow Be^8+n$ (Be^8 in normal state)

$Be^8\rightarrow 2\alpha$

(3) $Be^9+6{,}13\,\text{Mev}\,\gamma\rightarrow Be^8+n$ (Be^8 in normal state)

$Be^8\rightarrow 2\alpha$

There remains some unexplained part in the range distribution curve, the interpretation of which is net yet obvious to us*. The cross-sections for these processes were found to be (1) $2.15\times10^{-27}\,cm^2$; (2) $5.1\times10^{-28}\,cm^2$, and (3) $1.62\times10^{-27}\,cm^2$ respectively. The value of (2) is, however, quite different from the theory of Guth and Mullin⁽¹⁾. More precise experiments are now in progress in our laboratory. It is, however, noticeable that the excited states of $\overset{*}{Be}{}^8$ of 4.8 Mev and probably also 3 Mev which were observed in the reactions by high speed ions seems to have no contribution in the photo-disintegration process. The details of the paper will be soon published in Memo. Coll, Sci. Kyoto Univ.

Reference.

(1) E. Guth and C. J. Mullin: Phys. Rev. **76** (1949) 234, 682.

(2) C. H. Muller and A.G.W. Cameron; Phys. Rev. **78** (1950) 78.

---

* It may be attributed to the 3 Mev excited state of Be^8, which was found to appear in the photodisintegration of C^{12} by the X-rays from a 24 Mev betatron⁽²⁾. The decisive conclusion can, however, not be derived because of the lack of the number of observed cases.

On Sensitive Color.

By Hiroshi KUBOTA.

Department of Applied Physics, Second Faculty of Engineering, Tokyo Univ.

(Received September 20, 1950)

When a white light passes through a thin plate of crystal placed between Nicol prisms, there appear beautiful colors, whose chromaticity is dependent on the retardation (γd), γ being the difference of refractive indices of the crystal for the light polarized perpendicularly each other, and d the thickness of the crystal. The color sensitivity, that is, the rate of change of chromaticity ΔC with the variation of retardation $\Delta(\gamma d)$, was calculated in the previous paper⁽¹⁾, and the retardation which gives the sensitive color (we shall denote it $(\gamma d)_0$), was given as the retardation at which $\Delta C/\Delta(\gamma d)$ is maximum. According to the result of the former paper⁽²⁾, $(\gamma d)_0$ is 262 mμ or its odd multiples in case of the symmetry Nicols (case (b) of the former paper), and in case of crossed Nicols, its even multiples, and the chromaticity of the sensitive color is nearly purpule in all cases.

Accordingly, the first order sensitive color in case of the crossed Nicols is $2\times(\gamma d)_0=524$ mμ. Whereas the older literatures concerning the sensitive color⁽³⁾ give a little larger values, e.g., 575 mμ, and the chromoticity is red, not purple.

To make clear the cause of this difference, the author has calculated for different light sources a new. In the former paper, the black-body of temperature 7000°K was used as the light source, as it has the energy distribution nearly equal to the mean day-light or I.C.I. illuminant C, but now the black-body of various temperature are used as the light source.

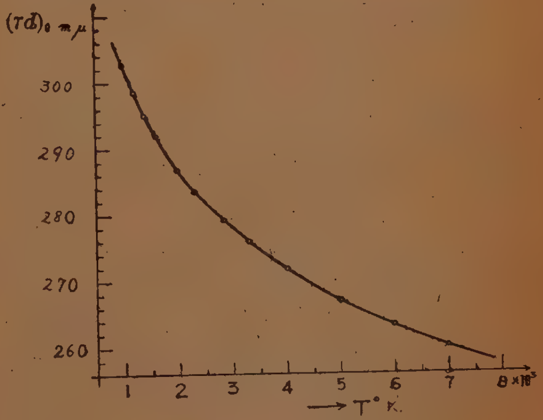

Fig. 1. Retardation of "Sensitive Color".

The result shows as given in Fig. 1, that $(\gamma d)_0$ decreases as the temperature T increases, and so far as the range of this calculation is concerened, they can be expressed by the equation

$$(\gamma d)_0=a+b/T^c$$

where a, b and c are the constants (the final values of them will be given in the later paper). The chromaticity of the sensitive color is also given in Fig, 2. From those figures, we know that the color temperature corresponding to the retardation 575 mμ is about 1900°K and the chromaticity of the sensitive color is nearly red. So the values of the older authors must be the results of the experiments by using the light source whose energy distribution is nearly equal to the black-body of temperature 1900°K. If we suppose that the electric lamp was used, then, as the color temperature of carbon lamp lies thereabout, the older values must be the one determined by using the carbon lamp as the light source.

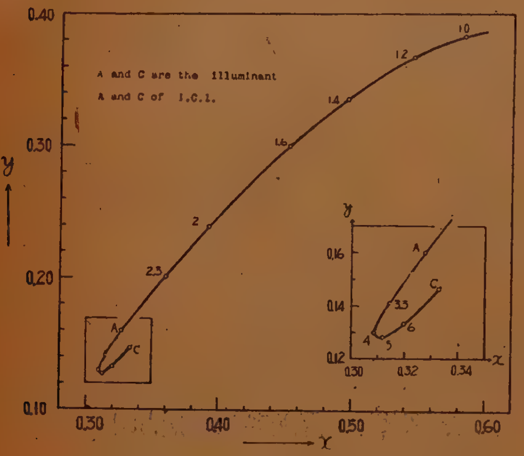

Fig. 2. Chromaticity of "Sensitive Color". (Numbers in the figure are the temperature of the light source in 10^3 K.)

As is clear from those results, in giving the chromaticity and the value of retardation of sensitive color, we must distinctly designate the energy distribution of the light source.

Reference.

(1) H. Kubota, J.O.S.A., **40** (1950), 146.
(2) H. Kubota, J.O.S.A., **40** (1950), 621.
(3) E. A. Wülfing, Sitz. Ber. der Heiderberger Akad. Wiss., **24** (1910), 1:
M. E. Mascart, Traité D'optique, (Paris, 1891) II, p. 74, etc.

On the Spiral Orbit Spectrometer with Two Converging Circles.

By Goro Miyamoto.

Faculty of Science, University of Tokyo.

(Received September 21, 1950)

A device to use the S-O-S principle for the mass spectrometer was already adopted in 1943 by Sagane, Miyamoto, Machida, Ota and Takagi, and was later reported at the Annual Meeting of this Society in 1946. By using hydrogen, potassium or bromine ions of energy 100～3000 eV, it was shown that the solid angle utilized was more than 60 percent of the whole solid angle 4π, when the resolving power was $M/\Delta M\approx50$ (at the hal width of the spectral line).

By further developing the idea, a mor convenient type of spectrometer has been constructed, which has two converging circles, thu enabling two kinds of particles with differen momenta to be measured simultaneously. Th new spectrometer is provided with two pairs o magnetic pole pieces, so that the vector potentia A of the magnetic field has two maxima at th radii ρ_1 and ρ_2, which correspond to converging circles. It is to be noted that the radii ρ_1 and ρ

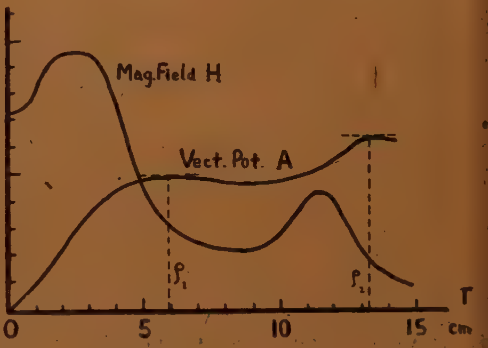

Fig. 1. Distribution of magnetic field strength on median plane and its vector potential. r: Distance from center.

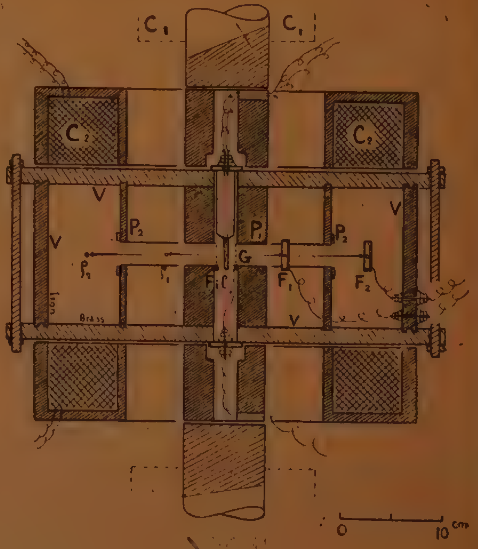

Fig. 2.

V: Vacuum case,
C_1: Coil to excite pole piece P_1,
C_2: Coil to excite annular pole piece P_2,
Fil: Filament,
G: Grid,
F_1, F_2: Faraday Boxes or counters.

remain practically constant when the magnetic field strength H is varied so as to have any desired values of $H\rho$ at the converging circles. The spectrometer is shown in Fig. 2 schematically, and the test by accelerated thermal electrons is also shown in Fig. 3 as an example.

More detailed reports on the practical application of the spectrometer as a beta-ray spectrometer and mass spectrometer will be shortly published in this Journal.

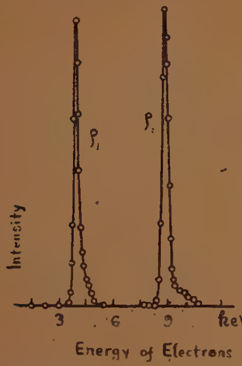

Fig. 3. Electron Intensities measured by F_1 and F_2.

Reference.

Miyamoto: Proc. Phys.-Math. Soc. Soc. Jap. **24** (1942) 676 (L) Nihon Sugaku-Buturigakukai Kaisi, **17** 557 (1943)

Iwata et all: Nihon Buturigakukai Kaisi, **2** (1947) 1.

Determination of the Optical Constants of Ag Films From the Measurements of Intensity and Phase Change [I].

By Kôzô ISHIGURO and Gorô KUWAHARA

Physics Department, University of Tokyo.

(Received March 23, 1950)

§ 1. Introduction.

In a previous paper(1), one of the authors proposed the application of double slit interferometer to the measurement of phase change undergone by the light transmitted through thin metallic or non-metallic films. In the present paper, combining such measurements of the phase change with the intensity measurements by means of photo-cell, the optical properties of silver film for mainly $\lambda = 590 m\mu$ were studied more closely.

Such measurements might give results essentially the same as the polarimetric study of Drude or Försterling(3). But the present method may be more simple and convenient for the general survey over the optical properties of thin films.

Some investigators prefer the method of ntensity measurements(4)(5) than the polarimetric method, but for the very thin films of Ag (thinner than 100Å) the determination of the refractive ndex only from the measurements of the intensity of reflected and transmitted light in the normal ncidence is essentially disadvantageous, even when the thickness is known. For; in *n, k* diagrams given in the previous paper(2), the curves of reflection and transmission become almost parallel each other and the cross point of the curves of the given transmission and reflection which gives the refractive index of the measured film is somewhat inaccurate. On the contrary the phase change curves cross perpendicularly to the transmission curves*. Accordingly the addition of the phase change measurements will increase the accuracy of the result.

§ 2. Experimental Technique.

The measuring instruments (the double slit interferometer and the photo-cell photometer) were the same as in the previous experiment(1). The silver to be studied was made by burning silver nitrate ($AgNO_3$) and the purity is considered to be very high. The silver films were deposited by evaporation in vacuum on the polished glass (BK7) plate. The distance between the Ag source and the glass plate was always adjusted to be 10 cm. The vacuum was the order of 10^{-4} mmHg. To avoid the evaporation of tungsten by over heating, the speed of evaporation was made rather slow, formation of siver film of 50 Å thickness taking about 2 minutes.

In some cases, the electron diffraction patterns were photographed. For the thinner samples, the reflection method was very difficult, being affected by charging up of films due to the reduced conductivity. However, in all cases, the electron diffraction patterns showed the typical patterns of pure silver crystals at least larger than 30 Å in size and with no special orientations to the base plate.

The measurements are divided into two classes with the small differences in the experimental treatments.

In the 1st series, after the glass was dipped in the washing solution ($H_2SO_4 + K_2Cr_2O_7$) for several hours and washed by running water and distilled water, it was dried in vacuum (not wiped by dried cloth). The silver was evaporated from a conic coil of tungsten wire as in Fig. 1 a. The silver was deposited only on the lower half between the two parallel streaks on the glass plate.

---

* The orthogonality of intensity constant- and phase shift constant- curves in the (n,k) plane of quite a general nature and is always satisfied by the transmitted as well as by the reflected light for any incident angle. The author owes this remark to the matheamtical considerations of Dr. Toshio Kato of the institute.

In the 2nd series, after the glass was washed as in the 1st series, it was wiped with the cleanly washed gauze and before the evaporation, cleaning by glow discharge with Al electrode was done for about 10 minutes. But to avoid the spattering, the strong current was not used. The silver film was deposited not only on the lower half between the streaks, but also on the upper half of the outer parts of the streaks as in Fig. 1 b.

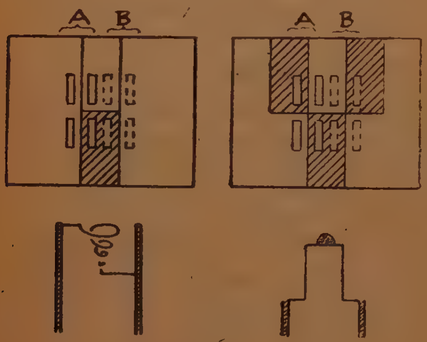

a b

Fig. 1.

By using such samples the sensitivity of the phase measurements was doubled and also the correction factors of the glass defects were reduced to one half of the former case.

§ 3. Measurements.

For the phase measurements⁽¹⁾, even when there is no film deposited Δ may be not zero, owing to defects of the glass plate. The correction ε for the 1st series is determined as the mean of several observations to the values

$\varepsilon = +0.006 \pm 0.002$ for $\varphi = 0°$

$\varepsilon = +0.007 \pm 0.002$ sor $\varphi = +70°$

$\varepsilon = +0.016 \pm 0.002$ for $\varphi = -70°$

where, φ (angle of incidence) $= +70°$ means the rotation of the glass plate by 70° in the anti-clock wise direction and $\varphi = -70°$ the rotation of the glass by 70° in the clock wise direction.

The difference of ε for the parallel and perpendicularly polarized light was not found with the accuracy of our instrument.

Clearly, for the 2nd series, the correction is $\varepsilon/2$.

In practice, α_0 the rotation angle of the compensator for the shift of one interference fring is adjusted to be about 160′ for $\lambda = 590 m\mu$ an its dispersion is given in Fig. 3.

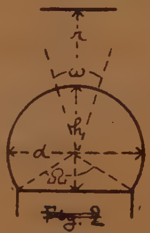

Fig. 2.

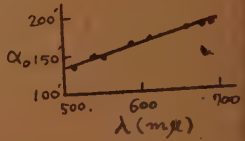

Fig. 3. Dispersion of the compensator

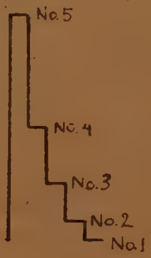

Fig. 4.

Though the relative transmission T_r was measured fo $\varphi = 0°$, the reflection R_0 wa not measured for $\varphi = 0°$ bu for about $\varphi = 10°$. Therefore the determination of optica constants of films, namely th thickness l and the refractiv index n-ik was made only fron the value of Δ_0, Δ_{70p}, Δ_{70s}, T_r and the value o the reflection R_0 was used to check the valu calculated from the determined optical constants

The determination of the film thickness, apar from the above method can also be made by th weighing of the evaporated quantity of silve according to the following formula.

In Fig. 2, the shape of silver is assumed t be spherical except the part which contacts wit the heating strip. From such source, W_g o silver evaporates and deposits uniformely on small plane upward the source to make the fil of the thickness l cm. The density of silver i assumed to be $\rho(=10.5)$. Then in the case o $d/h \leq 2$, it becomes

$$l = (d/h)\, W/(4\pi r^2 \rho)$$

When the silver droplet forms an ideal sphere d/h will be 1 and in the 1st series $d/h = 1$ wa assumed.

On the contrary in the 2nd series, it wa assumed that d/h was 2, namely the silver droplet formed an ideal semi-sphere.

Generally, for the determination of the fil thickness from the weight of the evaporate silver, the assumption of d/h or the form o ilver droplet seems to be troublesome origin of rrors and on this point, the heating strip as in he 2nd series is much better than the coil as n the 1st series.

In the following, $l=(d/h)W/(4\pi r^2\rho)$, with the olid density ρ, will be called weight thickness.

4. Results.

The observations were mainly done for $\lambda=$ 90$m\mu$ (1) 2nd series. The phase shift Δ_0, Δ_{70P} Δ_{70S} n permillage ans T_r, R_0, $A_0=100-(T_0+R_0)$ in ercentage are plotted against the weight thickess in Fig. 5, 6.

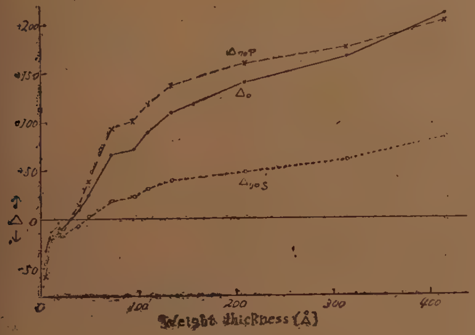

Fig. 5.

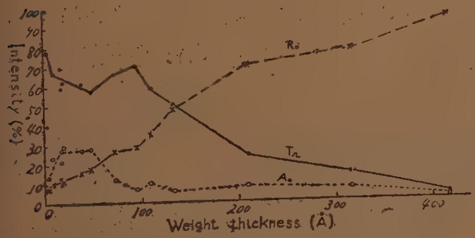

Fig. 6.

It is interesting that for the thicker films han 100 Å, the phase shifts have plus sign. amely the phase velocity of the light wave in he silver is faster than in the air.

Such is already recognized by Quincke and s believed to be the evidence that the refractive ndex of silver is less than unity, but as it has een seen in the previous paper(2), even when n s larger than unity, the phase shifts can have lus sign in some cases. The plus sign of phase hift is not the sufficient evidence of the refracive index being less than unity,

The determined n and k are shown in Fig. 7, eing plotted against the weight thickness. In the thicker region than 100 Å, k seems to decrease very slowly and n increase also very slowly with the decrease of the thickness.

Assuming $n=\xi/l+\eta$

and $k=\xi'/l+\eta'$

by the method of least squares, the constants become

$$\xi=15.3\pm6{,}2\ (\text{Å}),\quad \eta=0.11\pm0.04$$

and $$\xi'=-15.9\pm7.6\ (\text{Å}),\quad \eta'=3.84\pm0.05$$

In general, the values of η and η' show fairly good coincidence with the values of n and k of solid silver of following table

	Minor	Drude	Oppitz
n	0.18	0.18	0.20
k	3.64	3.67	3.44

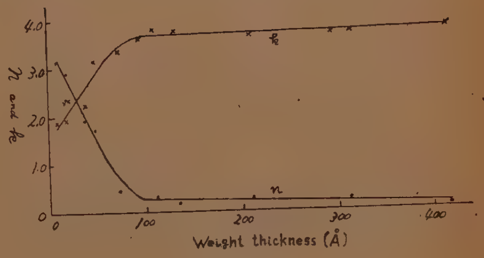

Fig. 7.

Under 100 Å, the change of n and k becomes very rapid and n begins to increase to the larger value than unity and k decreases to the smaller values. Such tendencies coincide with the results of many investigators(3)(4).

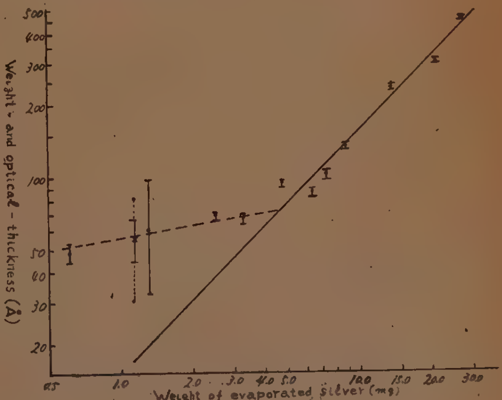

Fig. 8.

In Fig. 8, the measured optical thickness is plotted against the evaporated quantity of silver.

The straight line is $2W/(4\pi r^2\rho)$ which is the weight thickness in the case of an ideal semi-sphere.

The optical thickness, in the thicker region than 100 Å, shows fairy good coincidence with the weight thickness. Therefore it will be said that the silver films in such region have the same density with the solid metal and the thickness can be determined by weighing. But under 100 Å, there appear the definite discrepancies between the optical and weight thickness. Namely, the optical thickness decreases very slowly and seems to have a constant thickness of about 50 Å even in the case that the weight thickness is thinner than 10 Å (a few atomic layer thickness). Such result coincides with the observation of the electron diffraction study.

As it is noticed by several investigators(5)(17), in the transmission curve (Fig. 6), there appears a minimum near $l=50$ Å and at the same time the extinction (absorption+scattering)$=100-(R_0+T_0)$ has maximum value. But it must be noticed that even in this region, k (absorption or extinction coefficient) does not take a specially larger value than for the thicker films, while n begins to increasse rather rapidly. Therefore, the origin of the maximum extinction will not consist in the increase of the coefficient of absorption or extinction (for the scattering, assumes only the uniform body scattering), but the effect caused by the change of n and k at the same time will play important role.

For the physical meaning of the change of n and k in the thinner region with the discrepancy between the optical and weight thickness, it will require the closer considerations on the aggregated structure theory(8),

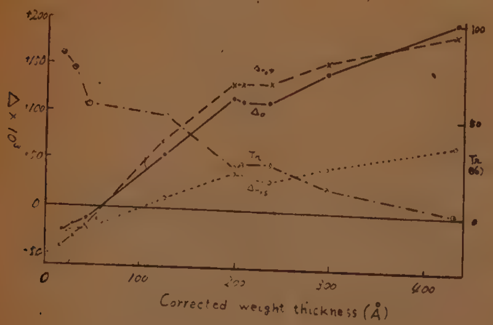

Fig. 9.

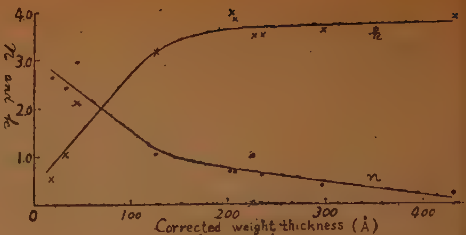

Fig. 10.

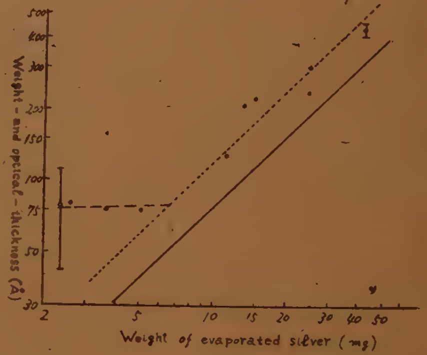

Fig. 11.

(2) lst series

The lst series were measured previousely t the 2nd series with less refinement of th technique. The results are shown in Fig. 9, 10.

The general tendency is the same as in the 2n series in spite of the differences in the cleanin treament. The remarkable difference is the fairl rapidincrease of n in the region thicker than 10 Å. In Fig. 11, the full line is the weight thicknes in case of an ideal sphere. The optical thicknesses are fairy larger than the weight thicknesses. It seems as if d/h were larger tha unity. The droplet in the tungsten coil ma have tendency to emit much more silver quantit in the upward direction than in other directions. The dotted line shows the mean corrected weigh thickness for $d/h=1.6$. The fairly large fluctuations mean that the heating coil is less adequat for the accurate measurements.

Below 100 Å there also appear the discrepanc between the weight and optical thicknesses. The latter seems to converge to a finite thicknes of about 75 Å.

(3) the other observations

The example of the dispersion of Δ_0 is show in Fig. 12. Δ_0 seems to decrease with the de-

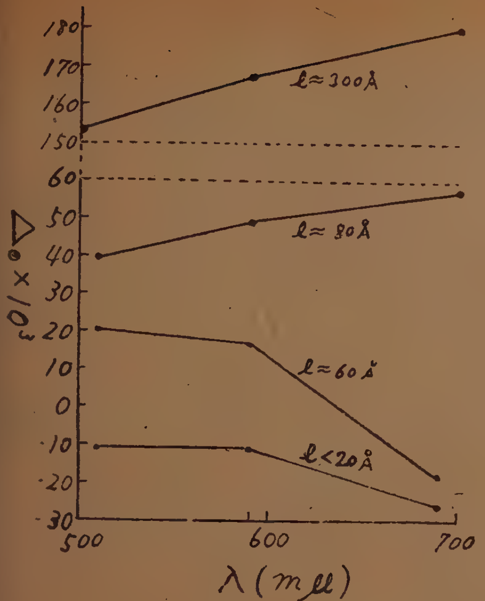

Fig. 12.

crease of the wave length of the incident light for the thicker films than about 80 Å but increase for the thinner films.

To reassure the minimum transmission below 100 Å, the five specimens of the different thicknesses were made at the same time using a stepped suspender as in Fig. 4 for reception of evaporated silver. In Fig. 13, 14, No. 1, the thickest film (about 90 Å weight thickness) is almost transparent, No. 3, the middle thickness is the deep blue (about 70 Å) and has the minimum transmission. No. 5, the thinnest (<30 Å) is reddish. From the comparison of the transmission, it might be mis-understood that the film thickness is decreasing in the order of No. 3, 4, 2, 5, 1, while the real order is No. 1, 2, 3, 4. 5. The transmission minimum seems to shift to the shorter wave length with the decrease of the film thickness. Such tendency coincides with the observations of Soezima⁽⁶⁾.

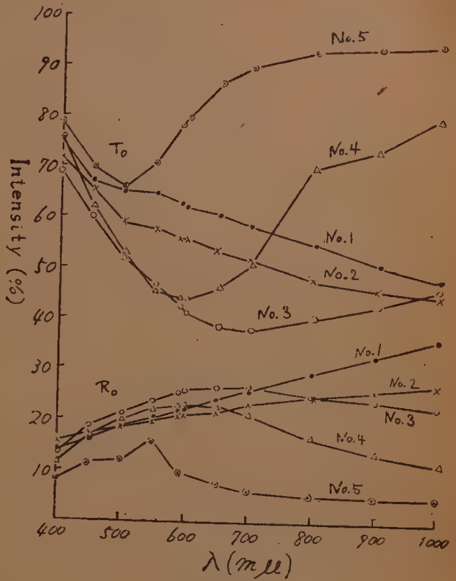

Fig. 13.

No.	1	2	3	4	5
Weight thickness (Å)	90	80	70	<50	<30
Δ_0 ($\lambda = 590$ mμ)	0·053	0·031	0·026	−0·010	−0·012

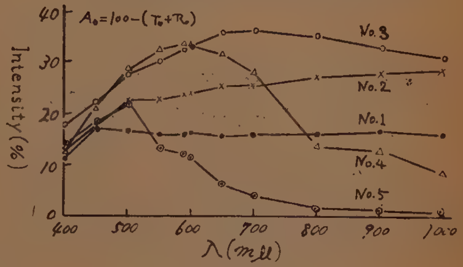

Fig. 14.

The observed phase shifts Δ_0 are shown in Fig. 14 which decrease with the order of the real thickness.

Determination of the Optical Constants of Ag Films From the Measurements of Intensity and Phase Change [II]

By Kôzô ISHIGURO and Gorô KUWAHARA,

Physics Department, University of Tokyo.

(Received March 23, 1950)

§ 5. The Example of the Procedure.

(1) The example of thick film

The evaporated quantity $W = 13.8$ mg

The weight thickness $l = 210$ Å

$\omega l/c = 0.224$

The measured value of the relative transmission and the reflection

$$T_r = 25.1\%, \quad R_0 = 70.6\%$$

The corrected value for the back reflection of the glass plate

$$T_r = 24.4\% \quad R_0 = 70.3\%$$

The detailed data for the intensity measurements are omitted.

The data of the phase measurements are as follows

$\alpha_0 = 164'$ $\lambda = 590$ mμ (with about 5 mμ breadth)

polarization	φ	position of slit	compensator reading in minutes						mean value	$\alpha = (A-B)/4$	$\varDelta = \alpha/\alpha_0$ +corr.
S	0°	A	2°	14.0 19.0	15.5 19.0	17.0 20.0	15.0 17.0	18.0 16.0	2°17.1	22.3	+0.136 +0.003 +0.139
		B	0°	42.0 48.0	50.0 52.0	50.0 51.0	45.0 45.0	47.0 48.5	0°47.9		
	+70°	A	1°	49.5 51.0	49.5 49.0	46.0 49.0	52.5 52.0	51.0 47.5	1°49.7	7.0	+0.043 +0.004 +0.047
		B	1°	15.0 23.0	19.5 20.5	26.0 21.0	21.5 23.0	24.5 24.5	1°21.9		
	−70°	A	1°	59.0 47.0	54.0 58.0	53.0 50.0	51.5 56.5	51.0 55.0	1°53.5	6.8	+0.041 +0.008 +0.049
		B	1°	24.0 25.0	21.0 25.0	29.0 26.0	29.0 28.5	32.0 25.0	1°26.5		
P	0°	A	2°	21.0 20.0	22.5 23.0	27.0 24.0	22.0 25.0	26.0 24.0	2°23.5	22.7	+0.138 +0.003 +0.141
		B	0°	49.0 52.0	56.0 56.5	46.0 52.0	53.5 54.5	53.0 55.0	0°52.8		
	+70°	A	2°	28.0 33.5	28.0 35.0	29.0 35.0	26.0 28.0	33.0 32.0	2°30.8	25.4	+0.155 +0.004 +0.159
		B	0°	46.0 45.0	48.0 51.0	45.0 48.0	57.0 52.0	48.0 52.5	0°49.3		
	−70°	A	2°	34.0 34.0	36.0 37.0	31.0 34.0	39.0 35.0	35.0 33.0	2°34.8	24.8	+0.152 +0.008 +0.160
		B	0°	55.0 58.0	59.0 54.0	57.0 55.0	56.0 52.0	55.0 54.0	0°55.5		

rom the above values, we get for the mean alues

$$\varphi = 0°, \quad \Delta_0 = (0.141+0.139)/2 \doteq +0.140$$
$$\varphi = 70°, \quad \Delta_p \doteq (0.159+0.160)/2 = +0.160$$
$$\Delta_s = (0.047+0.049)/2 \doteq +0.048$$

hen, for these values we search the nearest alues in the tables of the previous paper(2), and tart with the values of

$$\omega l/c = 0.25, \quad n = 0.18, \quad k = 3.64$$

nd the following equations were made according o (7) of the previous paper(2).

$$\begin{aligned} \Delta_0 &: \ 147+34(\delta h)-60(\delta n)+39(\delta k) \doteq 140 \\ \Delta_p &: \ 168+24(\delta h)-73(\delta n)+29(\delta k) \doteq 160 \\ \Delta_s &: \ 52+14(\delta h)-40(\delta n)+37(\delta k) \doteq 48 \\ T_r &: \ 24-21(\delta h)-9(\delta n)-19(\delta k) \doteq 24 \\ R_0 &: \ 71+21(\delta h)-16(\delta n)+21(\delta k) \doteq 70 \end{aligned} \tag{1}$$

Reserving the value of R_0 for the check of the calculation, from (1) by the least squares, we get

$$\delta h = -0.087$$
$$\text{or} \quad \delta(\omega l/c) = -0.0087$$
$$\delta n = +0.083$$
$$\delta k = +0.016$$

Thus for the present specimen, the optical thickness and the refractive index was determined to be

$$\omega l/c = 0.25-0.009 = 0.241 \pm 0.006$$
$$l \doteq 226 \pm 5 \text{Å}$$
$$n = 0.18+0.08 = 0.26 \pm 0.02$$
$$k = 3.64+0.02 = 3.66 \pm 0.06$$

The check of the above results becomes from (1)

	Δ_0	Δ_p	Δ_s	T_r	R_0
observation	140	160	48	24.4	70.3
calculation	140	160	48	24.7	67.8

(2) The example of thin film

$$W \doteq 0.6 \text{ mg} \quad \therefore \quad l = 9\text{Å}, \quad \omega l/c = 0.010$$
$$T_r \doteq 67.3\% \ (\text{corrected} = 67.0\%)$$
$$R_0 \doteq 12.4\% \ (\text{corrected} = 10.7\%)$$

The measured values of phase shift

$$\varphi = 0° \quad \Delta_0 \doteq (-0.014-0.014)/2 = -0.014$$
$$\varphi = 70° \quad \Delta_p \doteq (-0.017-0.022)/2 = -0.020$$
$$\Delta_s = (-0.014-0.017)/2 \doteq -0.016$$

Then, we start with the values of

$$\omega l/c = 0.05, \quad n = 3.05, \quad k = 2.00$$

in the tables(2) and get the following values

$$\delta h \doteq -0.045 \quad \text{or} \quad \delta(\omega l/c) = -0.0045$$
$$\delta n \doteq +0.12$$
$$\delta k = -0.061$$

Accordingly, the constants are determined to be

$$\omega l/c = 0.050-0.0045 = 0.0455 \pm 0.006$$
$$\text{or} \quad l \doteq 43 \pm 5\text{Å}$$
$$n = 3.05+0.12 = 3.17 \pm 0.18$$
$$k = 2.00-0.06 \doteq 1.94 \pm 0.13$$

The check of the results is as follows

	Δ_0	Δ_p	Δ_s	T_r	R_0
overvation	−14	−20	−16	67.0	10.7
calculation	−14	−20	−16	66.7	12.8

If we start with the values of $\omega l/c \doteq 0.05$, $n = 2.64$, $k = 1.59$ it will be found out to be

$$\delta(\omega l/c) = 0.001, \quad \delta n \doteq 0.48, \quad \delta k = 0.28$$
$$\text{or} \quad l = 48\text{Å}, \quad n = 3.12, \quad k = 1.87$$

and with $\omega l/c = 0.05$, $n = 2.64$, $k = 2.00$, they become to be

$$\delta(\omega l/c) = 0.000, \quad \delta n = 0.52, \quad \delta k = -0.14$$
$$\text{or} \quad l \doteq 47\text{Å}, \quad n = 3.16, \quad k = 1.86$$

§ 6. The Validity of the Uniformity of Film.

The above treatment of the film assumes that the film forms a uniform plane parallel layer. But in the region below about 100Å, the optical thickness is much thicker than the weight thickness and it seems to indicate that under a certain thickness, the film does not have the same density with the bulk silver metal or the film does not form a uniform layer and becomes to an assembly of small particles(8).

But as far as the dimension of the particles are much smaller than the wave-length ($2\pi r/\lambda < 0.1$, r = radius of the particle) and they are distributed in relative distances smaller than the wavelength, they may be treated as forming a uniform layer. And the observed specimens are believed to satisfy these conditions.

The next question is that when there are scattering by the particles, does it affect k in the refractive index? Of course if there are large particles and the uniformity of the incidented light is disturbed, it will be strongly harmful for our treatment, but the uniform scattering (in the dimension comparable with the wave length) in the layer will be included in k.

Because, the uniform scattering loss in the intensity will be represented as the damping of the amplitude and such a damped oscillation can also be the solution of the fundamental Maxwell's equations. The difference from the case of the pure metal layer lies in the fact that k must be divided into two parts k_1+k_2 and k_1 can be treated by the metal theoretical point of view but k_2 is not allowed to be included in it.

Thus the treatment of the uniform layer in the present paper will be allowed any how and the results will be considered to have correct meanings.

The pure silver was afforded by Mr. M. Inou of Hitachi Works and the study of the electron diffraction owed to Dr. S. Takagi of our institute.

In conclusion the authors wish to express their thanks for the kind guidance of Prof. M. Kiuchi.

References.

(1) K. Ishiguro: J. Phys, Soc. Jap. **5** (1950) 187
(2) K. Ishiguro: J. Phys. Soc. Jap. **6** (1951) 1
(3) For example, G. Essers-Rheindorf: Ann. d. Phys. **28** (1937) 297.
(4) H. Murmann: Z. Phys. **80** (1933) 161.
(5) F. Goos: Z. Phys. **100** (1936) 95.
(6) Y. Soezima: J. Sci. Res. Inst. **43** (1949) 252.
(7) S. Hirai: Matuda Kenkyu Jiho **19** (1941) 379 (in Japanese)
(8) G. Garnett: Trans. Roy. Soc. **203A** (1904) 385.
H. Falkenhangen: Gehrcke Hand. d. Phys. Opt. **I** (1927) 795.

Delayed Fracture in Creep of Copper.

By Takeo YOKOBORI.

Institute of Science and Technology, University of Tokyo.

(Received April 8, 1950)

Abstract.

The fluctuation phenomena on the creep fracture in copper were investigated experimentally. The observed fluctuations of time required for the occurrence of fracture after the application of load were analysed statistically, and it was shown that these creep fractures may be understood as a kind of rate process.

§ 1. Delayed Fracture in Creep of Copper.

The material used was commercial copper wire of 0.2 mm diameter. After the application of a constant load, the time t elapsed till the occurrence of fracture was measured by a stop-watch. Four series of tests were carried in which the weight of 878.5 gr, 862.5 gr, 840.5 gr and 808.5 gr was applied respectively. In each of these four cases about 100 specimens of 80 mm length were tested, while the steady strain rate was in the range of $10^{-2}\sim10^{-5}$ sec^{-1}. So, strictly speaking, it may be more reasonable to assume these fractures as plastic fractures rather than as creep fractures, but here the author used the name of the latter after an usual practice.

The frequency distribution curves of t mentioned above show some marked characteristics(1, 2) me in general trend, in all four cases. An ample is shown in Fig. 1, where the applied ad is 808.6 gr. In this case, the strain was easured accurately by cathetometer, and ch specimen followed quite the same strain-ne curve as shown in Fig. 2. This fact may taken as an indirect prove that the homo-neity of each specimen was quite satisfactory.

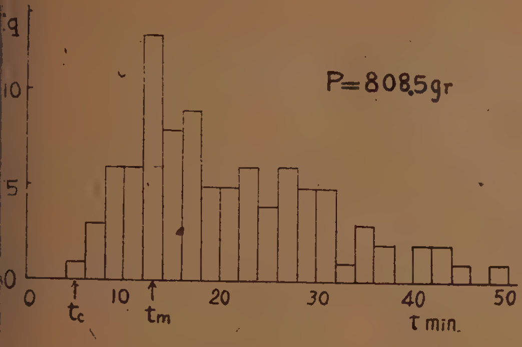

Fig. 1.

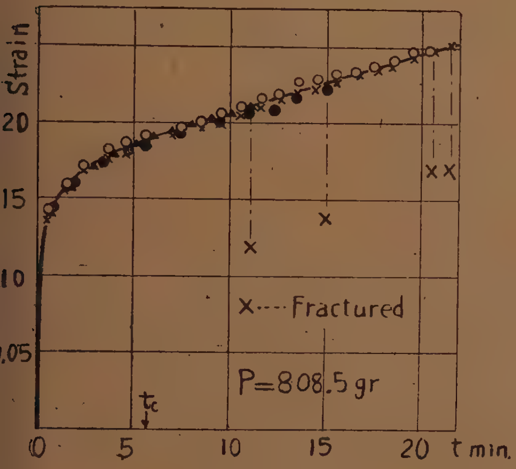

Fig. 2.

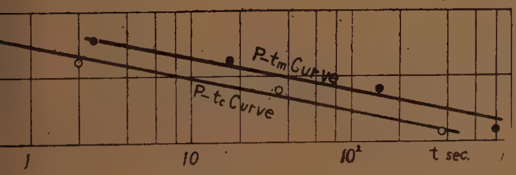

Fig. 3.

is interesting to notice that the critical time at which the distribution curve in Fig. 1 begins attain some finite value is very near the time which the transient creep strain rate begins to vanish as shown in Fig. 2. The relations between the applied load P and t_c as well as t_m corresponding to the maximum frequency in four cases are shown in Fig. 3. It may be worth of notice that these curves are the same in characters as the N-S curves of fatigue.

§ 2. Probability of Fracture.

The origin of the considerable fluctuations of t in the present experiment could not be sought for in the inhomogeneity of specimens as is already shown in Fig. 2.

The author intended, therefore, to treat the problem statistically according to the analogy with other related phenomena, as is already cited in the preceding report[1), 3)].

Now define the following quantity;

$\mu(t)$, The probability of occurrence of fracture in unit time after the lapse of time t.;

$q(t)dt$, the probability of occurrence of fracture between t and $t+dt$;

$p(t)=\int_t^{\infty} q(t)dt$, the probability of occurrence of fracture after t.

Then,
$$\mu(t)=-d(\log p)/dt \tag{1}$$

The abscissa of the frequency distribution curve in Fig. 1 corresponds to Zq, where Z is the total number of specimens. Then $Zp(t)$ can be calculated from these data, and the logarithms of them versus t are plotted as in Fig. 4. By differenciating this curves by t, it can be noticed that at the time t_c, μ begins to have a small finite value and then increases rapidly, approaching to a constant value μ_k.

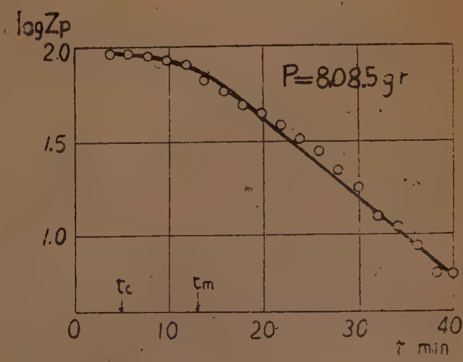

Fig. 4.

§ 3. Consideration as a Rate Process[4].

The satisfactory explanation of the physical meaning of $P-t$ curve such as in Fig. 3 has not yet been given. Possibly, this relation may be explained as a rate process as in the case of fracture of glass[1], although some modifications may be necessary for its detailed mechanism. The probability of the occurrence of macroscopic fracture is given by the chance of structure rearrangement[5]. Then, the probability of occurrence of fracture per unit time is represented by the following expression,

$$u = \frac{Z_0}{\tau} \exp[-(Q_0 - f(S_0))/KT), \qquad (2)$$

where, Q_0, the activation energy in the absence of an externally applied stress; S_0, the applied tensile stress; $f(S_0)$, the energy by applied stress; Z_0, the number of volume associated with rate reaction per unit volume; τ, the time required to form crack when the activation energy is available; K, Boltzmann constant; T, absolute temperature.

In the present case, the applied tensile stress S_0 may be assumed as uniform through the cross-sectional area in which the fracture may occur. The equation (2) may be written as

$$\mu = C \exp[-f(S_0)/KT], \qquad (3)$$

where C is a constant. As the change of volume by plastic deformation may be negligible, S_0 at t measured from the time t_c is represented by

$$S_0 = S(1 + \varepsilon_c + \alpha t), \qquad (4)$$

where, S, applied load divided by original cross-sectional area; ε_c, strain at t_c; α, a constant.

In ordinary creep test, the term αt is very small compared with $1+\varepsilon_c$, so it can be neglected without serious error. Actually in the present cases, $\alpha t < 0.07$ (Fig. 2). Thus, the equations (4) may be written approximately as follows,

$$S_0 = S(1 + \varepsilon_c). \qquad (5)$$

Therefore, the activation factor in (2) or (3) has some constant value only determined by the externally applied load.

It may be reasonable to assume that Z_0 in equation (2) does not attain a finite constant value from zero discontinuously at t_c, but i creases gradually approaching to the final valu after a certain time probably at t_m. Thus, fro (2) and (5) it is derived that the probability takes the constant value μ_k after t_m, and this in quite well accord with the experiments men tioned above.

Now, the values of μ_k were determined fo various values of stress S in the four series c experiments, and plotted against S in Fig. 5

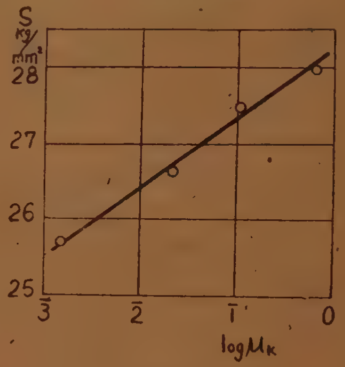

Fig. 5.

From this curve, the following relation between μ_k and S is obtained as in the case of glass[1],

$$\mu_k = A \exp[mS]. \qquad (6)$$

where A and m are some constant respectively independent of stress. On the other hand, in ordinary creep test, the term $\varepsilon_c + \alpha t$ in (4) is small compared with unity, and can be neglected without serious error. In all these four cases $\varepsilon_c + \alpha t < 0.20$, and if it is neglected in (4) S_0 becames to equal to S. From equation (3) $\mu = C \exp[f(S)/KT]$. If this equation is compared with (6), the following relation is obtained,

$$f(S) = BS, \qquad (7)$$

where B is a constant, independent of stress. The the expression for μ_k is represented approximately from the equation (2)

$$\mu_k = \frac{Z_0}{\tau} \exp[-(Q_0 - BS)/KT], \qquad (8)$$

which is apparently similiar to the strain rate equation as a rate process[6]. Thus the phenomena of delayed fractures in creep of copper may be explained as a rate process at least qualitatively.

Nearly the same considerations may hold also creep fractures of other metals. More ailed experiments such as on temperature endence or on size effect are hoped to develop ng this line of consideration.

In conclusion, the author wishes to thank fessor M. Hirata, physics department of this versity for his valuable suggestions and couragement. The author also wishes to press his thanks to Professor F. Nakanishi for discussions.

References.

) M. Hirata: Tokei-Suri-Kenkyu (in Japanese) (Bulletin of Mathematical Statistics) **3** (1949) 57.
) H. Kubota: J. Appl. Phys. Japan **17** (1948) 286.
(3) M. v. Laue: Ann. d. Phys. **76** (1925) 261.
(4) Grasstone, Laidler & Eyring: *Theory of Rate Processes* (1941).
(5) K. Omori: J. Eng. Kyushu. Univ. **16** (1941) 239.
(6) W. Kauzmann: Trans. A.I.M.E. **143** (1941) 57.
S. Dushmann, L. W. Dunbar, H. Hunthsteiner: J. App. Phys., **15** (1944) 108.
C. Zener, J. H. Hollomon: J. App. Phys. **17** (1946) 69.

Notes added in proof. After the presentation of this paper, he awared the report of the experimental study on the length dependency of the breaking strength of wire from the view point of probability had just been published by S. Kumagai and H. Kimura in Kikai-no-Kenkyu (Science of Machine) **2** (1950) 171.

Fatigue Fracture of Steel.

By Takeo Yokobori.

The Institute of Science and Technology, University of Tokyo.

(Received April 8, 1950).

Abstract.

Fatigue fracture of steel has been investigated, and the consideration developed here will in general hold for other metals. This line of thought may be applied to many other cases such as static fracture of brittle metals and yielding of polycrystalline metals.

1. Introduction.

It is often experienced that the number of les N, which material can withstand before cture, scatters widely, however equally the er conditions are kept in fatigue test. This ans that the S—N curve (S is the range of ess) becomes a band. If each specimen is nogeneous and has the same surface finish, the erved points has been supposed to fall quite sely on a fairly smooth curve and there would be le scatter. The author investigated the fatigue cture of steel and found that there exists ne law about the fluctuation of fatigue fracture and this fluction has some relation with the process of fatigue phenomena and that fatigue fracture may be explained as a kind of rate process.

§ 2. Delayed Fracture in Fatigue of Steel.

The author investigated this fluctuation on two kinds of steel.

Test A. The specimens prepared were steel of 0.41% carbon, annealed for 30 minutes at 870°C, and were finished by coarse emery. They had the yielding strength of 44.5 kg/mm², and were tested by Ono's Rotary Uniform Bending Tester under 2,000 r.p.m. Three series of experiment were carried out under the stress range of 38.6, 37.1, and 35.6 kg/mm^2 respectively (pure reversed stress, mean stress zero). Each series consists of tests with seventy specimens, Distribution curves of N are shown in Fig. 1a, Fig. 2a, and Fig. 3a, all of them exhibiting marked characteristics1)2)3).

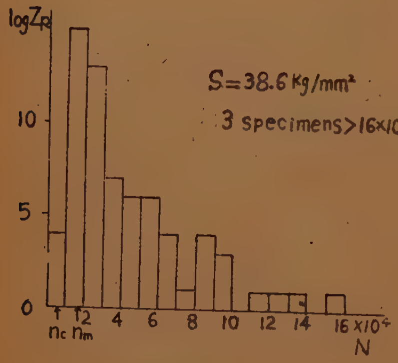

Fig. 1a.

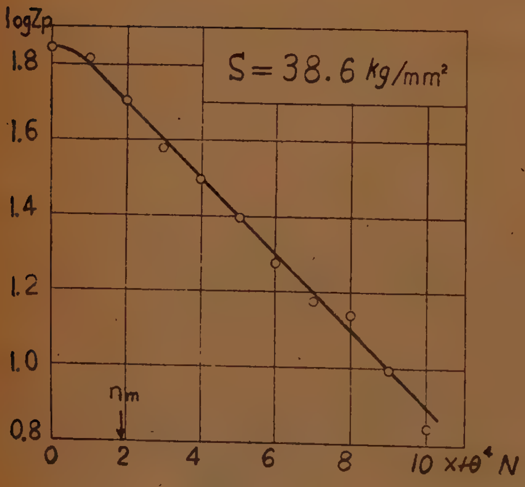

Fig. 1b.

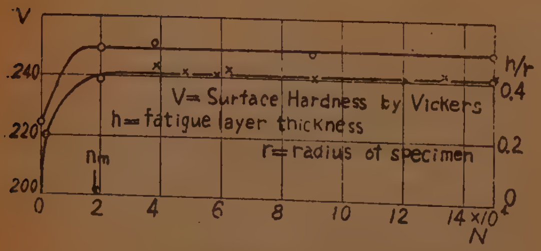

Fig. 1c.

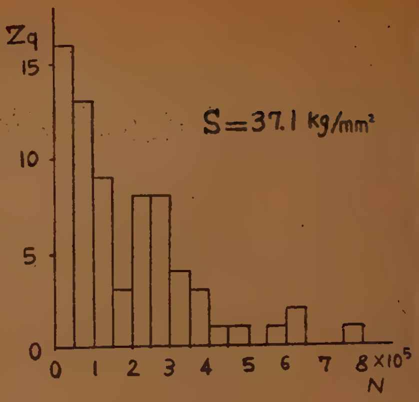

Fig. 2a.

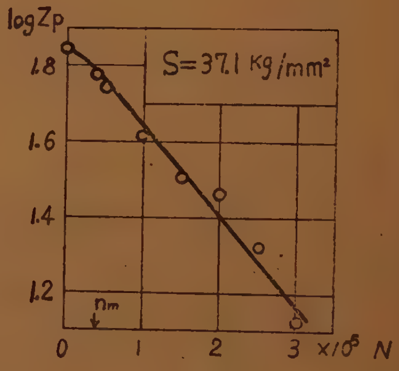

Fig. 2b.

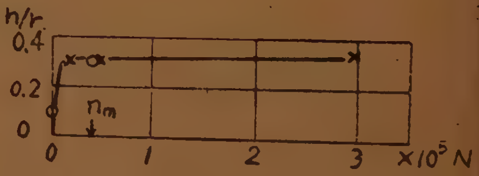

Fig. 2c.

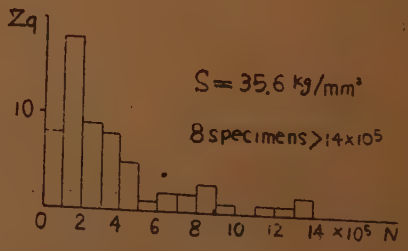

Fig. 3a.

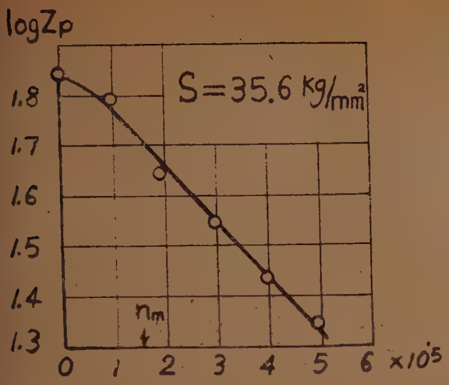

Fig. 3b.

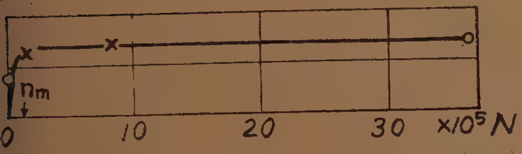

Fig. 3c.

Test B. The material prepared was a steel 0.12% carbon, annealed in the same way as in st A., and was highly polished by lapping finish. ese specimens have the yielding strength of .5 kg/mm² and were tested under the same contions as in test A. In this test, however, the ress range applied was 30.6 kg/mm². The results e shown in Fig. 4. As the specimen was cut om a single rod, the number of specimens was fortunately only 24 pieces, yet the charactertics of distribution curve are supposed to be the me as in test A, except that there is difierence the width of the band of scattering. From its lation to the fatigue-layer thickness discussed ter, it is supposed that the position n_m of the aximum distribution in Fig. 4 might shift toard the left if more specimens were tested.

3. Probability of Crack Occurrence.

In this section the probability of crack occurrence in test A and B will be discussed.[2)4)]

enoting, $\mu(n)$, the probability of crack occurrence in unit cycle at repeated cycle n, where n is measured from n_c at which the number of fractured specimens begins to have some finite value,

$q(n)dn$, the probability of crack occurrence between n and $n+dn$ after n cycles, and

$p(n)=\int_n^\infty q(n)dn$, the probability that the delay of fracture cycle will have a larger value than n,

then,

$$\mu(n) = -d(\log p)/dn. \qquad (1)$$

Abscissa of the distribution curve in Fig. 1a, Fig. 2a, Fig. 3a and Fig. 4 represents Zq, where

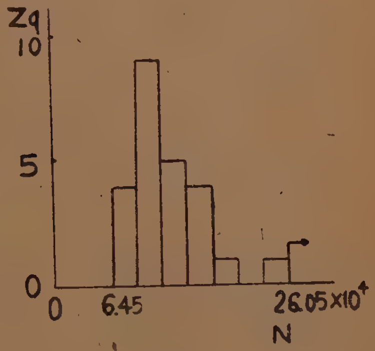

Fig. 4.

Z is the total number of tested specimens, $Zp(n)$ values are calculated from this and their logarithms are plotted for n as in Fig. 1b, Fig. 2b, Fig. 3b and Fig. 5. It can be noticed that after some repeated cycle n_c, μ begins to have a finite value and then increases and approaches a constant value μ_k. In test A, μ seems to have a constant value already at $n=0$, but this is because a larger value of dn is chosen. Actually μ becomes zero below cycle n_c. The meaning of this probability will be discussed in the following section.

§ 4. Relation Between Repeated Cycles and Fatigue Layer.

It has been proved by many experiments that structure of materials changes during fatigue process. In the present experiment, amount of fatigue is detected by etching[5)] and the thickness of fatigue layer (the part of cross-sectional area measured by ethching) is determined as the repeated cycle N is increased. The results are shown in Fig. 1c, Fig. 2c, Fig. 3c, Fig. 5. Detection of fatigue layer has also been possible by hardness test of cross-sectional are of the specimens as well as by etching (Fig. 1c and Fig. 6). Here, two remarkable facts have been observed. The one is that the range of n at which the probability of fracture approaches a definite value μ_k is approximately equal to the range of n at

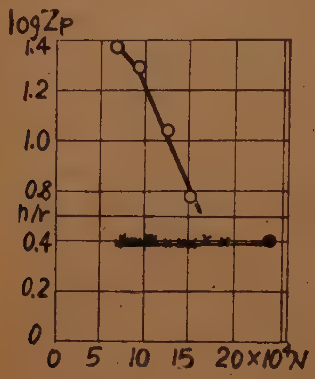

Fig. 5.

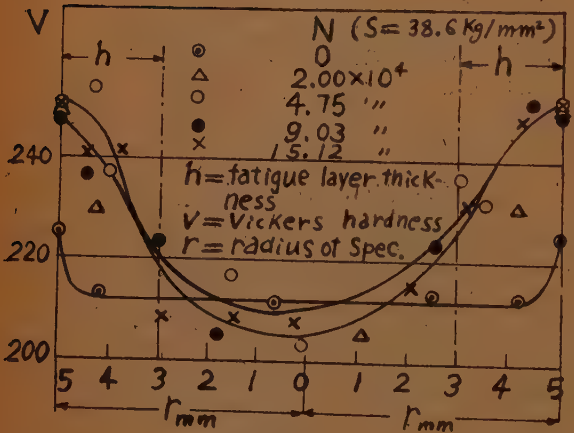

Fig. 6.

which the fatigue-layer thickness approac saturation (Fig. 7). The other fact is that n which the probability of fracture occurren begins to have a finite value is slightly larg than and yet close to n_0 at which fatigue lay appears (Fig. 7). These two facts suggest t there may be some relation between the p bability of fracture and fatigue-layer thickne Before this relation is discussed, fatigue-lay thickness as a function of repeated cycle N shou be founded theoretically. Week spots as sourc of micro-crack are assumed to take place stress concentration when stress is repeated a shear stress at the edge of the silp-band in t plastic inhomogeneity reaches a critical stress In case stress distribution is non-uniform as bending or in torsion, stress at the surface the rod will at first reach τ_f after some cyc n^*. Assuming that stress distribution is line radially across the cross-sectional area, the rel tion between stress range S and n^*, and betwee S and n, measured from n^*, that is $n=N-n$ at which shearing stress reaches τ_f at the dept of h from the surface of specimen are given b the following equations by using Orowan's idea

$$n^*=\frac{1}{\mathrm{A}}\log\frac{kS-\tau_y}{kS-\tau_f}. \quad (2$$

$$\frac{h}{r}=1-\frac{\tau_f}{kS-(kS-\tau_f)\exp[-An]}, \quad \text{for}\frac{kS}{\tau_y}>\frac{r}{r-h} \quad (3)$$

where r is a radius of the rod, τ_y is yieldin strength of microscopical region of plastic in

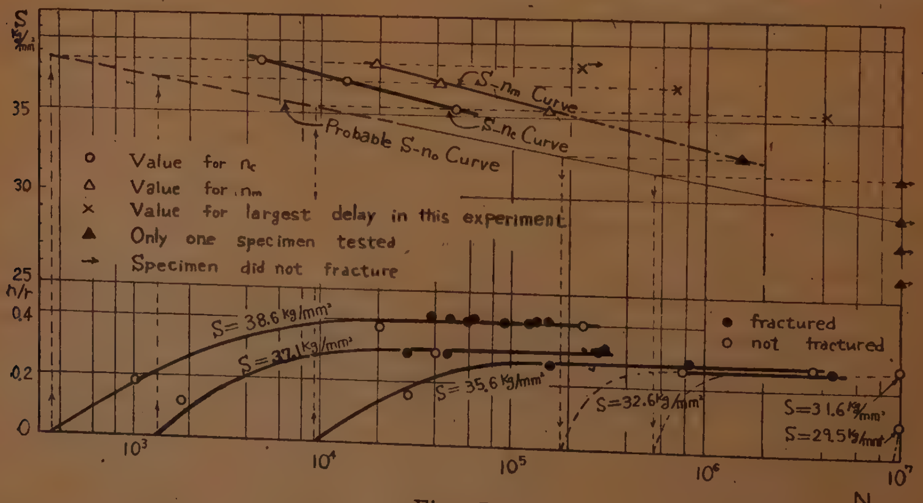

Fig. 7.

mogeneity. A and k are constants introduced Orowan. Macroscopic fatigue-layer may be sumed as the part, where stress has reached (i.e. $n^* \fallingdotseq n_0$). Then equation (2) stands for the lation between S and n_0 at which fatigue layer ppears, and eq. (3) for the relation between tigue-layer thickness for stress range S and n easured from n_0. As shown in Fig. 7 and Fig. 8 xperimental results are, at least qualitatively, ell in accord with this consideration.

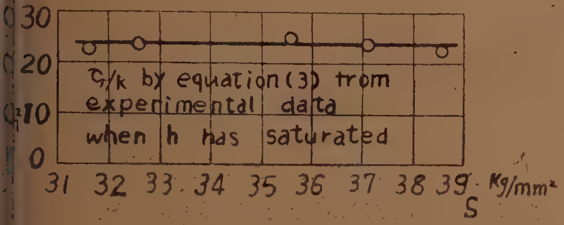

Fig. 8.

5. Fatigue Fracture as Rate Process.

. Mechanism of macroscopic fracture will here e treated as a rate process. By this consider-tion, the probability of macroscipic fracture is xpressed as the chance of rearrangement7). Then e probability of fracture per unit time is

$$\mu = \frac{Z_0}{\tau} \exp\left[-(Q_0 - f(S_0))/KT\right]. \qquad (4)$$

here Q_0 is an activation energy in the absence f an externally applied stress, S_0 is the applied nsile stress, $f(S_0)$ is an energy by applied stress, is the time riquired to form crack when activa-on energy is available, K is Boltzmann constant, nd T is absolute temperature, and Z_0 is the umber of volume associated with rate reaction er unit volume.

In case stress distribution is non-uniform long the cross section, (4) is generally expressed y

$$\mu = C\int \exp\left[f(S_0)/KT\right] dF. \qquad (5)$$

here C is const., and F is an area of the part here week spots exist in the cross section which ill undergo fracture by tensile stress. In fatigue henomena, fatigue layer may be taken as F (con-ribution of a part without fatigue to macro-racture is assumed to be little) and μ is the probability of fracture per unit cycle. If shearing stress within plastically inhomogeneous region is supposed to increase by further strain hardening after τ_f is reached, tensile stress S_0 at the part of stress concentration in the slip band is given by using Orowan's idea under the same condition as in equation (3):

$$S_0 = [kS - (kS - \tau_f)\exp(-An)]k_0(r-h)/r. \qquad (6)$$

where k_0 is a constant.

In case of rotary bending fatigue, equation (5) will have the following form:

$$\mu = C_0 r^2 \int_{1-\frac{h}{r}}^{1} \exp\left[f(S_0)/KT\right]\sqrt{y}\,dy. \qquad (7)$$

where C_0 is constant.

From (3), (6), and (7), it can be noticed that when repeated cycle increased and exceeds n_0, the probability of fracture begins to assume a finite value and thereafter increases with n and approaches a constant value μ_k.

The above experiments are well exlained by these considerations. Fracture which has been discussed above means macroscopic fracture developed in the fatigue layer. Once this macro-fracture starts, macro-crack rapidly extends, by the increased stress concentration caused by the crack itself, toward the axis of the rod, when the rest of the cross sectional area cannot withstand the applied load. Finally the rupture of the whole specimen takes place. In the distribution curve, n_c at which the number of fractured specimens begins to have finite value seems to be larger than n_0 at which the fatigue layer begins to appear. These two values would approach closer if more spemens were tested. The difference of n_c and n_0 may be due to the finite time of crack propagation from macroscopic fracture within the fatigue layer to the rupture of the whole specimen, as is discussed above, and the fact that fracture will take place at some finite value of μ_0.

It will be noted from (7) that there will be a stress range for which

$$\mu \leqq \mu_0 \qquad (8)$$

That is to say, no fracture will take place within this stress range regardless of the number of cycles repeated. This range is considered to correspond to endurance limit. According to equation (5) there might be some relation among endurance limit of bending, of torsion and of tension-compression, and in case of the same cross-sectional area, rotary bending may have at least higher limit than tension-compression test. And size-effect on endurance limit is expected according to eq. (5), that is, the larger the cross-sectional area becomes, the limit is lowered. All these facts are qualitatively well in accord with the experiments, but quantitative relation will be obtained by developing this line of consideration still further. The relation between μ_k and S is shown in Fig 9, and the relation is similar to the case of creep fracture[7] and of glass[2].

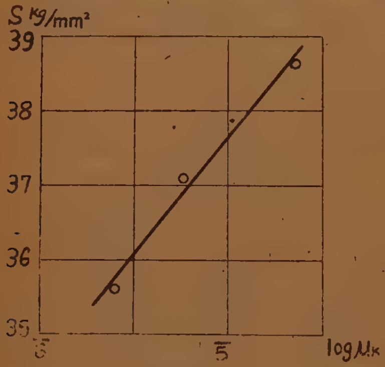

Fig. 9.

The author wishes to thank Professor M. Hirata, department of physics of this university, for his valuable suggestion and encouragement. The anthor also wishes to express his cordial thanks to professor F. Nakanishi for his discussions and to Professor N. Soda and S. Hukui, M. Kawamura for kindness for this research in this Institute.

Note added in Proof. When the author was carrying out this work, he did not know the experiment of H. Muller-Stock (refernce (1)) who obtained distribution curve for other purposes. It seems to be quite well in accord with the author's Test A and B.

References.

(1) H. Muller-Stock: Mitt. Kchle-u-Eisenforschung. **2** (1938) 83.
(2) M. Hirata: Tokei-Suri-Kenkyu (in Japanese) Bulletin of Mathematical Statistics) **3** (1949) 57.
(3) T. Yokobori: this volume.
(4) M. v. Laue: Ann. d. Phys. **76** (1925) 261.
(5) Nishihara & M. Kawamoto: Trans. Japan. Soc. Mech. Eng. **5** (1939) 43.
(6) E. Orowan: Proc. Roy. Soc. London. **171** (1939) 79.
(7) K. Omori: Journ. Eng. Kyushu. Univ. **16** (1941) 239.

The Foundation of the Quantisation of Turbulence

By Ken-ichi KUSUKAWA.

Physical Institute, Faculty of Science, Tôkyô Metropolitan University.

(Received June 16, 1950)

§ 1. Introduction.

I discussed the turbulence by the quantum-theoretical method in my former paper [4]. In this paper I explain the physical meaning of the quantisation of turbulence, and develop the former theory more strictly.

§ 2. Summary of the Theory Described in my Former Paper.

Taking the cartesian coördinates which are fixed with respect to the uniform general flow, the fundamental equation is expressed in the following form, when the Reynolds number $R_L =$

$|V|L/\nu$ is very small, and the inertia term can be neglected.

$$\rho\frac{\partial^2\boldsymbol{\omega}}{\partial t^2}=\rho\nu^2\triangle\triangle\boldsymbol{\omega}, \tag{2,1}$$

where $$V+\operatorname{grad} S=\frac{\partial\boldsymbol{\omega}}{\partial t},$$

$$\frac{\partial S}{\partial t}=\frac{p}{\rho}.$$

Then we can search the Lagrangian

$$L=(\rho/2)(\dot{\boldsymbol{\omega}},\dot{\boldsymbol{\omega}})-(iA^*/2)\operatorname{grad}(\boldsymbol{\omega},\boldsymbol{\omega})\\+(\rho\nu^2/2)(\triangle\boldsymbol{\omega},\triangle\boldsymbol{\omega})+\text{const}, \tag{2,2}$$

where A^* is a real constant vector.

Introducing the canonical variables $\boldsymbol{Q}\equiv\boldsymbol{\omega}$, and $\boldsymbol{P}$ from (2,2), we quantise the turbulence by the following commutation relations.

$$\left.\begin{aligned}{}[P_i(\boldsymbol{r}),Q_j(\boldsymbol{r}')]&=-ik\delta_{ij}\delta(\boldsymbol{r},\boldsymbol{r}'),\\ [P_i(\boldsymbol{r}),P_j(\boldsymbol{r}')]&=0,\\ [Q_i(\boldsymbol{r}),Q_j(\boldsymbol{r}')]&=0,\end{aligned}\right\} \tag{2,3}$$

Developing these variables in Fourier series, and considering the term of the viscosity as that of the perturbation, we estimate the transition probability.

Namely, the Hamiltoian is

$$\begin{aligned}\bar{H}&=\bar{H}_0+\bar{H}^1,\\ \bar{H}_0&=-(k^2/2\rho)\sum_N(\partial^2/\partial q^2_{1N}+\partial^2/\partial q^2_{2N}+\partial^2/\partial q^2_{3N})\\ &\qquad-\sum_N N^{\frac{1}{2}}3k(\pi\sigma/\rho l)^{\frac{1}{2}}\\ &\qquad+\sum_N(2\pi\sigma/l)N(q^2_{1N}+q^2_{2N}+q^2_{3N}),\\ \bar{H}^1&=-(8\pi^4\rho\nu^2/l^4)\sum_N N^4(q^2_{1N}+q^2_{2N}+q^2_{3N}),\end{aligned} \tag{2,4}$$

where l is the largest spacial period, N/l is the wave number vecter, and σ is $|A^*|\cos(A^*,N)$. When σ is positive, there can be stationary states, and characteristic values are

$$e_{jN}=(m-1)2k(\pi\sigma/\rho l)^{\frac{1}{2}}N^{\frac{1}{2}}=(m-1)h^*N^{\frac{1}{2}}. \tag{2,5}$$

The transition probability is

$$\begin{aligned}P\{m\to(m-2)\}&=\text{const}\times m(m-1),\\ P\{m\to(m+2)\}&=\text{const}\times(m+1)(m+2).\end{aligned} \tag{2,6}$$

Assuming the thermal equilibrium between the turbulence and the thermal motion, we have

$$\exp[-Eb/\kappa T]m(m-1)=\exp[-Ea/\kappa T](m+1)(m+2). \tag{2,7}$$

From (2,5) and (2,7) the distribution of energy with respect to "N" is obtained in the following form.

$$F_E(N)=A\sum_{j=1}^{3}\varepsilon_{jN}\cong Ah^*N^{\frac{1}{2}}[\exp\{N^{\frac{1}{2}}2h^*/\kappa T\}-1]^{-1}, \tag{2,8}$$

where A is a unversal constant.

§ 3. The Physical Meaning of the Constant "k".

The velocity of the fluid being the average velocity of the molecular motion, there exists the following uncertainty between the component of the velocity and the position

$$\triangle u\geqq cV^1/\pi nD^2\triangle x, \tag{3,1}$$

where V^1 is the average velocity of the molecular motion, D is the diameter of the molecule, n is the number of the molecules in unit volume, and C is a universal constant, which is considered to be of the order of 1.

The uncertainty-relation derived from (2,3) is

$$\rho\triangle x\triangle u\geqq k/4. \tag{3,2}$$

According to the gas theory, the coefficient of viscosity being proportional to $\rho V^1/n\pi D^2$, we have

$$k=\gamma\eta, \tag{3,3}$$

where η is the coefficient of viscosity, and γ is a universal constant. If the upper limit of $\triangle u$ is determined by $\triangle u_M$ (which is defined by the sensitivity of the measurement), the lower limit of $\triangle x$ (or the smallest volume element of the fluid $\triangle V=(\triangle x_m)^3$) must be determined from (3,2) in the following forms.

$$\triangle x_m=k/4\rho\triangle u_M,\quad \triangle V=(\triangle x_m)^3. \tag{3,4}$$

In this measurement, $\triangle V$ being the smallest drop of the fluid, its translational velocity can be measured only with the experimental error, but its spin can have no physical meaning.

§ 4. The Spin of the Smallest Volume Element.

We shall consider the kinetic energy of some part of the fluid which is rotating with an angular velocity "ω" like a rigid body. The kinetic energy is generally

$$E=\iiint(\rho v^2/2)dV. \qquad (4,1)$$

The same energy can be considered as the sum of the energy of every smallest volume element; that is

$$E=\sum_i(\rho\triangle V/2)v_i^2+\sum_i J\omega^2/2, \qquad (4,2)$$

where $\triangle V$ is the volume of the smallest element, J is its moment of inertia, and v_i is its translational velocity.

As it is known from the discussion of §3 that the second term of (4,2) cannot be measured by the hydrodynamical method, the hydrodynamical energy is defined by the following formula.

$$E_H=\sum_i(\rho\triangle V/2)v_i^2=\iiint(\rho v^2/2)dV-\sum_i J\omega^2/2. \qquad (4,3)$$

Thus the hydrodynamical energy can be obtained by subtracting the spin energy of the smallest drop from the usual kinetic energy of the fluid, which is considered to be able to be divided into the infinitesimal volume.

According to my former paper the first term of $\bar{H}_0$ is

$$\iiint(P.P)/2\rho dV=\iiint(\rho v^2/2+p)dV \qquad (4,4)$$

or the usual energy in the irrotational case. Then the second term of $\bar{H}_0$ means the term which must be subtracted as the spin energy of the smallest drop.

If this second term of $\bar{H}_0$; $\sum_{|N|<N_M}(2/3)h^*N^{\frac{1}{2}}$ $(l/N_M=\triangle x_m)$ is neglected, (2,5) being $\varepsilon_{j.N}=mh^*N^{\frac{1}{2}}$ the distribuion of energy with respect to "N" is

$$F_E(N)=A\sum_i\varepsilon_{iN}. \qquad (4,5)$$

When "$|N|$" increases, $F_E(N)$ of (4,5) becomes very large, and this formula is in conflict with the experiment.

§ 5. On the Last Term of $\bar{H}_0$.

The last term of $\bar{H}_0$ is equal to $\iiint(iA^*/2)$ grad$||Q||dV$, which represents some spacial periodicity. Experimentally the periodicity exists in the direction normal to the plane of the grid, therefore A^* can be assumed to be normal to the plane of the grid, or parallel to x-axis. Then this term represents the rotational energy of fluid which is not included in the first term of $\bar{H}_0$.

It is physically reasonable that there is no stationary state where σ is negative, or this rotational energy is negative.

$|A^*|$ represents the strength of the rotation, and may be defined by the geometrical character of the grid and the viscosity.

§ 6. On the Viscous Term: $\bar{H}^1$.

The viscous term $\bar{H}^1$ is considered as the term of the perturbation. Therefore we consider the turbulence to be destroyed or born only by the effect of the viscosity, although Heisenberg [2,3] and Weizäcker [5] have considered the larger turbulence to be destroyed by the smaller turbulence as well as by the viscosity.

§ 7. The Dissipation of the Energy.

In the theory by which the formula (2,7) was derived, it was neglected that the energy of the turbulence is dissipated by the thermal motion. We shall consider the effect of this dissipation. The rate of dissipation of energy$=-(dE_{turbulent}/dt)$

$$=(dE_{\text{thermal}}/dt)\infty 2h^*N^{\frac{1}{2}}D \qquad (7,1)$$

and $D=\exp\{-E_b/\kappa T\}m(m-1)-\exp\{-Ea/\kappa T\}$

$$(m+1)(m+2) \qquad (7,2)$$

where $E_a-E_b=2h^*N^{\frac{1}{2}}$, and D is the probability of the dissipation.

Now in the physical view point, D must be proportional to the probability of existence of the turbulence-quanta: (m-1).

D must be proportional also to $\exp\{-E_a/\kappa T\}$, if the thermal motion consists of the canonical ensemble also after the dissipation; that is

$$D=S(N)(m-1)\exp\{-E_a/\kappa T\}, \qquad (7,3)$$

where $S(N)$ is a function only of N. (According to Batchelor [1] S is proportional to N^2)

From (7,2) and (7,3) we have

$$m=\frac{[1+(3+S)\exp\{-N^{\frac{1}{2}}2h^*/\kappa T\}]+[1+(14-2S)\exp\{-N^{\frac{1}{2}}2h^*/\kappa T\}+(1+10S+S^2)\exp\{-N^{\frac{1}{2}}4h^*/\kappa T\}]^{\frac{1}{2}}}{2[1-\exp\{-N^{\frac{1}{2}}2h^*/\kappa T\}]} \qquad (7,4)$$

When N is very large,

$$m-1 \doteqdot 6[\exp\{N^{\frac{1}{2}}2h^*/\kappa T\}-1]^{-1}$$

and when N is very small

$$m-1 = 4[\exp\{N^{\frac{1}{2}}2h^*/\kappa T\}-1]^{-1},$$

Therefore from (2,5), the distribution function of energy with respect to "N" is practically represented in the all range of "N" in the following form

$$F_E(N) \doteqdot Aa^* N^{\frac{1}{2}} [\exp\{N^{\frac{1}{2}}2h^*/\kappa T\}-1]^{-1}, \quad (7,5)$$

where $O \leqq N \leqq N_M \quad N_M = l/\triangle x_m$.

This is the same formula with (2,8) which is introduced by more rough theory.

§ 8. The Spectrum of Turbulence.

We shall calculate the spectrum of energy with respect to the x-component of N: n_x. When the turbulence is perfectly isotropic,

$$f_E(n_x) = \sum_{n_X=const} F_E(N)$$
$$= Ah^* n_x^{\frac{1}{2}}[\exp\{n_x^{\frac{1}{2}}2h^*/\kappa T\}-1]^{-1}\int_{n_x}^{N_M} 2\pi N dN \quad (8.1)$$

As N_M is very large, (8,1) is practically expressed by the following formula

$$f_E(n_x) = A'h^* n_x^{\frac{1}{2}}[\exp\{n_x^{\frac{1}{2}}2h^*/\kappa T\}-1]^{-1}, \quad (8,2)$$

where A^1 can be determined by the condition

$$\int f_E(n_x)dn_x = 1 \text{ and } h^* = 2k(\pi|A^*|/\rho l)^{\frac{1}{2}}$$

When the turbulence is completely polarised, or N is parallel to A^*, $f_E(n_x)$ is of the same form as (8,2).

It was explained in my former paper that the theoretical formula (8,2) agrees with Taylor's experiment very well.

While, the spectrum of energy with respect to N is

$$f_E(N) = \sum_{N=const} F_E(N)$$
$$= \int_0^{\frac{\pi}{2}} \frac{A'h^* N^{\frac{1}{2}}\cos^{\frac{1}{2}}\theta}{\exp\{N^{\frac{1}{2}}\cos^{\frac{1}{2}}\theta 2h^*/\kappa T\}-1} N^2 \sin\theta d\theta, \quad (8,3)$$

where A^1 is a universal constant, and $h^* = 2k(\pi|A^*|/\rho l)^{\frac{1}{2}}$.

It is reasonable from the physical viewpoint that both $\lim\limits_{N\to\infty} f_E(N)$ and $\lim\limits_{N\to 0} f_E(N)$ vanish.

§ 9. Measurement.

When the permissible error of x and u is rather large, and we can have the following relation, $\rho\triangle x\triangle u \gg k$ we have not necessity for the quantisation. Therefore the discussion of the laminar flow can be expressed by the usual hydrodynamical method.

In the discussion of the turbulent flow, however, the velocity of the fluid is small, and $\triangle u$ must be very small. Then $\rho\triangle u\triangle x$ being comparable to "k", we must consider the quantisation. In this case, $\triangle x_m$ being rather large, the moment of inertia of the smallest drop and its spin energy cannot be neglected. For instance, in the case of air $\triangle x_m \triangle u_M \doteqdot k/4\rho = \gamma\eta/4\rho \doteqdot \gamma \times 173 \times 10^{-6}/4 \times 1293 \times 10^{-6} \doteqdot 1/10$ at 0°C, 760 mmHg, because γ is of the same order as 4. Now we cannot prove that no other Hamiltonian can satisfy the fundamental equation and then the flow pattern considered in my former paper can be only permissible one. But, as its spectrum agrees with experiments, this flow pattern is considered not to be so different from the actual flow.

I thank heartily Dr. I. Imai and Mr. R. Hama for their useful suggestions.

References.

(1) G. K. Batchelor: Proc. Roy. Soc. A. **195** (1949) 513–532.

(2) W. Heisenberg: Proc. Roy. Soc. A. **195** (1948) 402–406.

(3) W. Heisenberg: Z. f. Phys. **124** (1948) 628–657.

(4) K. Kusukawa: Journ. Phys. Soc. Japan **5** (1950) 412–416.

(5) C. F. von Weizsäcker: Z. f. Phys. **124** (1948) 608–627.

On the Recovery Process of Cold Worked Metals.

By Hirosi KANZAKI.

Second Faculty of Engineering, University of Tokyo.

(Received July 7, 1950)

§ 1. Introduction.

The energy stored during plastic deformation of metals is usually measured by the anomalous specific heat due to recovery of work-hardened metals. Taylor and Quinney(1) first measured the specific heat of cold worked metals and determined the value of stored energy. Recently, Suzuki(2) observed that the specific heat anomaly of cold worked copper due to recovery is composed of two stages.

The present author also measured the specific heat of cold worked copper, silver and aluminum when heated at constant heating velocity. The specimens used were polycrystalline copper (99.8% purity), silver (99.9% purity) and aluminum (99.9% purity). They were all annealed thoroughly before experiments and compressed by the testing machine at room temperature. The specific heat of these cold worked specimens was measured while they were heated at constant heating velocity (1°C per minute in every case). The details of experimental procedures have already been published(3), and concerning the experimental results thus obtained, some theoretical considerations will be given here.

§ 2. Anomalous Specific Heat due to Recovery.

Figs. 1, 2 and 3 show the specific heat—temperature curve for cold worked metals when heated at constant velocity. In these figures the "second heating curves" (black circles) are the specific heat—temperature curves for thoroughly annealed specimens. Therefore, the difference between "first" and "second" heating curves corresponds to the anomalous specific heat due to recovery.

In every case it is noticeable that the anomalous specific heat is composed of two stages; every curve has two "valleys". It was also observed that accompanying these specific heat anomaly, the physical properties of cold worked metals—the electrical resistance and mechanical hardness—gradually return to those of annealed metals. These results, I think, agree with those of Suzuki(2) at least qualitatively.

§ 3. Qualitative Discussion.

From the results derived in § 2, it is conceivable that the recovery of cold worked metals is composed of two sorts of processes each having different activation energy*. In this section I shall discuss them qualitatively.

According to Wood(4), the cold worked state of metals is described by two sorts of affairs, that is,

(1) the lattice distortion, and
(2) the grain fragmentation.

When the cold worked metal recovers, the recovery from lattice distortion always go ahead the recovery from the second.

Recently, the change in the magnetic properties of copper and aluminum was measured by Reekie and Hutchison(5). Their results support the conclusion by Wood.

In view of these facts, it is natural to think that the two processes observed in my experiments correspond to the recovery from lattice distortion and that from grain fragmentation, and that the activation energy of the first process is lower than that of the second process.

Here we shall return to Figs. 1, 2 and 3. In these figures it is remarkable that the curves for copper and silver resemble well each other, but those for aluminum do not. From the stand-

---

* The results obtained by T. S. Kê(6) on the internal friction of cold worked aluminum seem to coincide with my results in this respect. (see Fig. 2 of reference (6).).

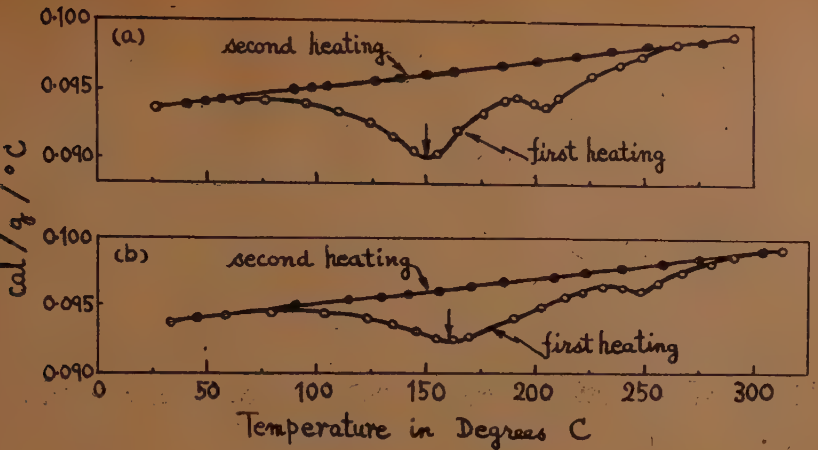

Fig. 1. Specific heat—temperature for cold worked copper.
(a) 65.0% compressed. (b) 53.5% compressed.

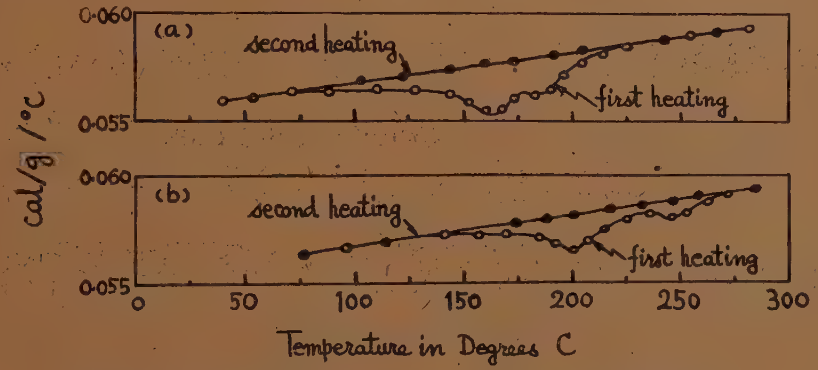

Fig. 2. Specific heat—temperature for cold worked silver.
(a) 54.7% compressed. (b) 40.5% compressed.

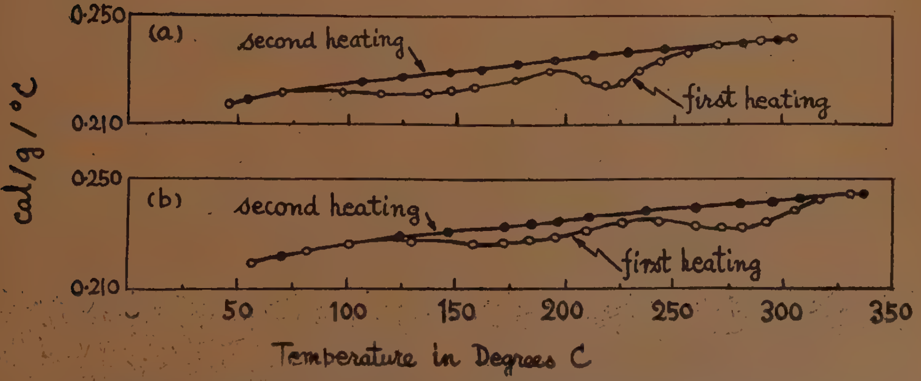

Fig. 3. Specific heat—temperature for cold worked aluminum.
(a) 70.0% compressed. (b) 60.0% compressed.

point described above, this fact shows that in aluminum deformed at room temperature the lattice distortion is much less than the case of copper and silver. This also coincides with the results by Wood and others(4)(5).

Before entering into quantitative discussion, I wish to note the bearing of the above consideration on the dislocation theory developed by Taylor(7), Seitz(8) and Koehler(8).

The strain energy due to lattice distortion (the strain energy released in the "first" stage of recovery process) ought to be thought to agree with the strain energy introduced by the dislocation centers (including their interaction energy). This energy is to be compared with the energy of the "dislocation lattice" calculated by Koehler(9). In other words, the first process of recovery may be considered as the recombination and the diffusing-out of dislocations.

Then, what is the energy released in the "second stage" in the experiments? This energy, accompanied by grain fragmentation, may be the strain energy connected with the "asterism" observed in the Laue x-ray pattern in deformed single crystals of metals. This type of strain was first suggested by Burgers(10) in the manner shown in Fig. 4, but has not yet been investigated quantitatively. Further experimental and theoretical investigations are necessary to understand this point.

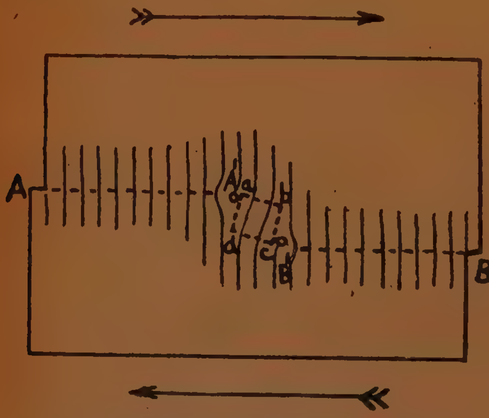

Fig. 4. Origin of asterism on basis of Burgers' picture.

In the next section I shall present the formula to give the reaction rate of recovery process, and show that the formula is consistent with my experiments and Koehler's results.

§ 4. Reaction Rate of Recovery Process.

According to the reaction rate theory developed by Eyring and others(11), I formally express the recovery process as follows. In the recovery process, the atoms in the cold worked or "dislocated" state is supposed to arrive at the annealed state through some intermediate state. We shall specify the "dislocated" state as "initial" state, the annealed state as "final" state and the intermediate state as "activated" state.

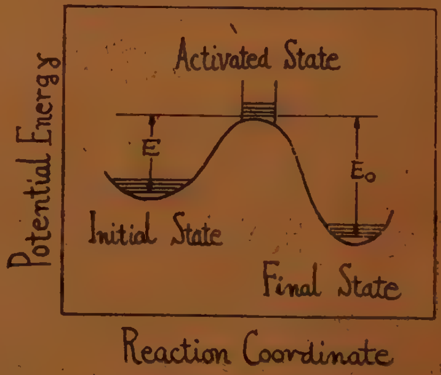

Fig. 5. Potential energy curve for the reaction.

In Fig. 5 the rate of reaction from left to right is given by

$$\kappa_+ = (kT/h) \exp (\Delta S^*/R) \exp (-E/RT), \qquad (1)$$

where ΔS^* and E are the entropy and energy difference between initial and activated states, R the gas contant, k the Boltzmann constant, T the absolute temperature and h is the Planck constant.

For the reaction from right to left, the rate is given by

$$\kappa_- = (kT/h) \exp (\Delta S^*_0/R) \exp (-E_0/RT), \qquad (2)$$

where ΔS^*_0 and E_0 are the entropy and energy difference between final and activated states.

Then, the net rate of recovery process κ is given by

$$\kappa = \kappa_+ - \kappa_- = (kT/h) \exp (\Delta S^*_0/R) \exp (-E_0/RT) \\ \{\exp (-\delta S/R) \exp (\delta E/RT) - 1\}, \qquad (3)$$

where

$$\delta S = \Delta S_0^* - \Delta S^*, \qquad \delta E = E_0 - E. \qquad (4)$$

Investigating this formula, we know that only the quantities δS and δE vary with the progress of plastic deformation. In equation (3), the entropy change δS due to cold work may be small compared with ΔS^*_0.

The value δE represents the energy increase due to cold work. This value may be calculated from the energy W released during recovery process. As the energy stored during cold work is not distributed uniformly through entire lattice but localized in dislocated regions in the lattice, δE may be expressed as

$$\delta E = nW. \qquad (5)$$

Here, the quantity n may be conveniently designated as the "energy concentration factor".

§ 5. Quantitative Discussion.

1. Totel energy released during recovery.

The total energy released during the recovery process is obtained by integrating anomalous specific heat along the temperature axis. Table 1 shows this energy and the external work done during plastic deformation. These values show reasonable agreement with those of Taylor⑴ and Suzuki⑵.

Table 1. ε, degree of cold working measured by the reduction of height of the specimen; W_m work done during plastic deformation; W_t, total energy released during recovery process; r, ratio of released total energy to work done $(= W_t/W_m)$.

Metal	ε (%)	W_m (cal/g)	W_t (cal/g)	r
copper	65.0	9.2	0.47	0.051
	53.5	6.2	0.34	0.054
silver	54.7	4.2	0.09	0.023
	40.5	2.1	0.06	0.033
aluminum	70.0	10.5	0.95	0.091
	60.0	7.2	0.84	0.110

2. Rate of recovery and dislocations in cold worked polycrystalline copper.

Using equation (3) we shall derive the value n for cold worked copper from my experimental results. To make the problem clear, we shall confine ourselves to the first stage of recovery process, because only the strain released in this stage may be handled with comparative ease.

First, we must determine the value E_0 in equation (3). In this paper, we shall assume it to be equal to the latent heat of fusion of copper 3,110 cal/mol.

Next, as we are concerned only with the first stage of recovery process, we must separate the energy released in this stage from that of the second stage. To do so, for the sake of simplicity we assumed the usual "relaxation equation"*

$$dW/dt = -AW, \quad A = A_0 \exp(-B/kT). \qquad (6)$$

As our experiments were carried out at constant heating velocity, we can fit the solution of (6) to the anomalous specific heat—temperature curve, taking into account of the dependence of temperature T upon time t. Thus we can obtain the value of energy released during the first stage of recovery, that is, the energy W in equation (5). The value is as follows;

for the 65.0% compressed copper (we shall call this sample as "a")

$$W_a = 0.30 \text{ cal/g} = 19.1 \text{ cal/mol}, \text{ and} \qquad (7.1)$$

for the 53.5% compressed copper (which shall be called "b")

$$W_b = 0.26 \text{ cal/g} = 16.5 \text{ cal/mol}. \qquad (7.2)$$

For these two samples the rate of recovery κ_a and κ_b must be equal at the temperature at which the first "valley" of specific heat is observed.

In Figs. 1(a) and 1(b), this temperature is found to be

for sample "a" $\quad T_a = 420°\text{K}, \qquad (8.1)$

for sample "b" $\quad T_b = 435°\text{K}. \qquad (8.2)$

---

* This equation may be the approximate formula corresponding to (3).

Then, what value of n is to be assumed to explain this variation of reaction rate due to term δE in equation (3)? Equation (3) can be simplified in our case, and for samples "a" and "b" we obtain,

$$T_a \exp(-E_0/RT_a) \exp(\delta E_a/RT_a) = T_b \exp(-E_0/RT_b) \exp(\delta E_b/RT_b). \qquad (9)$$

Inserting the numerical values given by (7) and (8) into (9) we obtain,

$$n = 41.5. \qquad (10)$$

We shall compare this value of n with the results by Koehler(9). He has calculated the energy of dislocation lattice shown in Fig. 6 by elasticity theory, and determined the separation distance of dislocations so as to obtain the experimental value of Taylor and Quinney(1). In the two dimensional expression, Koehler proposed a circular region of radius r_0 as a model of the dislocation center. Using this model we shall express the energy of cold worked metal as concentrated in these circular regions.

Koehler's results indicate us in the case of severely cold worked copper,

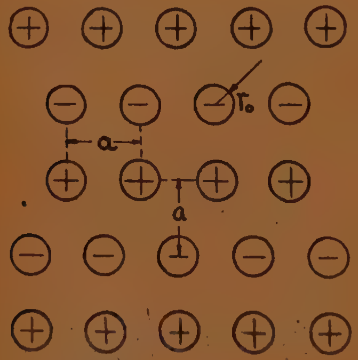

Fig. 6. Dislocations in retangular latties (after Koehler).

$$a = 74.5Å, \quad r_0 = 6.15Å, \qquad (11)$$

whete a is the separation distance of dislocations (Fig. 6).

Now the "energy concentration factor" n introduced by the author can be evidently given by $n = a^2/\pi r_0^2$. Using Koehler's results (11) we have

$$n = a^2/\pi_0{}^2 = 46.7, \qquad (12)$$

which is in satisfactory agreement with the above value $n = 41.5$ obtained in quite a different manner.

In conclusion the author expresses his sincere thanks to Dr. Y. Tani for his valuable suggestions and to Mr. S. Nagasaki for his helpful advices in the course of this work. He is also indebted to Dr. I. Imai for his kind guidance in preparing this article. This study was helped by the research grant given from the Ministry of Education.

References.

(1) G.I. Taylor and Quinney; Proc. Roy. Soc. **A163** (1937) 157.
(2) T. Suzuki: Sci. Rep. Tohoku Univ., in press.
(3) H. Kanezaki: J. App. Phys. Japan, (in Japanese).
(4) W.A. Wood: Proc. Roy. Soc. **A172** (1939) 231.
W.A. Wood: Proc. Phys. Soc. **52** (1940) 110.
(5) J. Reekie and T.S. Hutchison: Phys. Rev. **74** (1948).
(6) T.S. Kê: J. of Metals, **188** (1950) 575.
(7) G.I. Taylor: Proc. Roy. Soc. **A145** (1934) 362.
(8) F. Seitz and T.A. Read: J. App. Phys. vol. **12** (1941).
(9) J.S. Koehler: Phys. Rev. **60** (1941) 397.
(10) J.M. Burgers: Proc. Phys. Soc. **52** (1940) 23.
(11) S. Glasstone, K.J. Laidler and H. Eyring: The Theory of Rate Processes, (1941). p. 153.

On the Analysis of Quenching Circuit for Slow Counters.

By Goro FUJIOKA, Isao KITA and Osamu MINAKAWA

Meteorological Research Institute.

(Read April 28, 1949; Received July 31, 1950).

§ 1. Introduction.

The so-called fast counter has many excellent characters and is indispensable for the experiments of nuclear and cosmic-ray physics. The discharge of the fast counter is quenched by the dissociation of organic vapor besides the shielding effect of the space charge,(1) so that the amount of the vapor is necessarily reduced, and decomposed simpler gases such as CO_2, H_2, O_2 etc. are produced. Owing to these gases, the character of the counter becomes worse and is damaged at last. In addition to the dissociation of organic molecules, the delicate variation of the surface of the counter wall often makes the counter character decisively poor, the reason of which is not yet perfectly explained. Accordingly, in the experiment of long period as the routine observation of cosmic-ray intensities, it is very difficult to keep the counter characters constant all the while and to get the data in the same condition for long time of observations.

On the other hand, the slow counter is somewhat inferior to the fast counter in its characters, but its gas molecules are never dissociated by the discharge. Therefore the slow counter can be operated very stably for very long time by proper setting of external circuit, and in some experiments it is rather excellent.

The counter used in the experiment consists of a brass cylinder 4.5cm in diameter, with a fine tungsten wire for the central electrode. These are sealed in glass tube containing hydrogen at 80mm Hg pressure. The inner gas may contain a little amount of water vapor as impurity.

§ 2. Analysis of Johnson's Quenching Circuit.

When the central electrode of a slow counter is grounded and the negative potential on the cylindrical wall is raised gradually, the counter begins to operate from a definite potential V_A. Here V_A is the threshold potential. And when the potential is raised further, the counter ceases to operate suddenly and the continuous corona discharge begins at a definite potential V_m. Generally this counting region $V_m - V_A$ is within several volts, while V_A is about 1,000 volts, so that slow counter cannot practically be operated without external quenching circuit. It is, however, remarkable that this continuous discharge current never begins with zero but a definite value i_m(2), and all the external quenching circuits make use of this property.

The most primitive circuit for quenching the discharge is consisted of only a high resistance as 10^9 Ω, and other quenching circuits using vacuum tubes were also devised.(3) These and other modified circuits were tested for the improvement of counter characters but the results were almost the same. Then we used Johnson's circuit mainly because the treatment and the analysis are simplest of all as explained later. The circuit diagram and the notations are shown in Fig. 1.

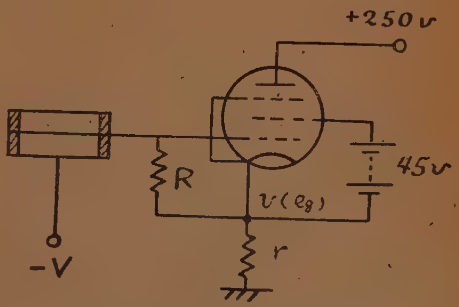

Fig. 1. Johnson's circuit.

In the present circuit, the potential difference across the counter electrodes is the sum of the applied negative potential V and the cathode potential $v(e_g)$, where e_g is bias voltage of the tube and equals to the product of discharge current i and R. When V is raised, the counter begins to operate at potential V_1 and ceases at potential V_2. Relations between (V_1, V_2) and (V_A, V_m) are as follows:

$$V_A = V_1 + v(0) \quad ,$$
$$V_m = V_2 + v(i_m R).$$

Therefore the length of the counting region is

$$V_2 - V_1 = V_m - V_A + v(0) - v(i_m R)$$
$$\approx v(0) - v(i_m R). \qquad (1)$$

In the case of a pentode, $v(e_g)-e_g$ curve is given typically in Fig. 2. From Eq. (1), when leak resistance is R and $i_m R = \mathrm{OA}$, then the counting region is BC. If $i_m R$ is lower than e_0 in the figure, we have no counting region and if $i_m R$ is higher than the cut-off voltage e_o, the counting region is equal to $v(o)$ in length. Therefore the minimum leak resistance to give the maximum counting region $v(o)$ is given by

$$i_m R = e_o \qquad (2)$$

In this way the relation between leak resistance R and the length of counting region becomes quite evident.

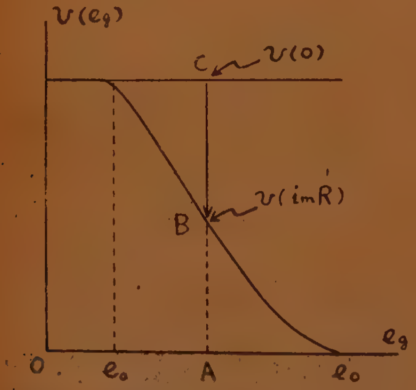

Fig. 2. Relation between the circuit character and the length of counting region.

After Werner(2), i_m being independent of R, differentiation of Eq. (1) with R gives

$$\frac{\partial V_2}{\partial R} = -\frac{\partial v(e_g)}{\partial e_g} i_m = -\mu i_m \qquad (3)$$

as V_1 is evidently independent of R. Therefore the dependency of the length of counting region (V_2-R curve) is expected to be similar to the vacuum tube character ($v(e_g)$-e_g curve). Experimental data of the above mentioned counter is shown in Fig. 3. The solid curve in the figure represents $v(e_g)-e_g$ relation and the dashed one is V_2-R relation. Similarity between both curves is satisfactory and the above discussion is verified experimentally.

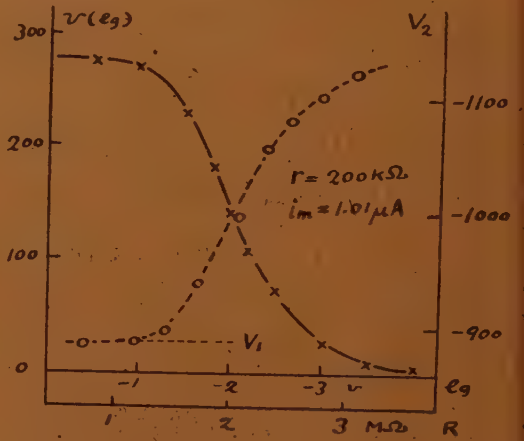

Fig. 3. Observed result of the circuit character and corresponding counting region V_2 as a function of R.

Comparision of both curves gives the experimental value of i_m. And in our case it is 1.01 μA, but the experimental error is considerably large.

§ 3. Equivalent Circuit.

In Johnson's circuit, the variation of output potential is approximately equal to that of cathode potential $v(e_g)$. Therefore, when the leak current through R is varied by Δi, the variation of output potential amounts to

$$\Delta V = v(i + \Delta i.R) - v(iR) = \frac{\partial v(e_g)}{\partial e_g} R \Delta i = \mu R \Delta i.$$

The equation shows that the circuit is equivalent to a resistance μR, so far as amplification factor μ is regarded as constant. Moreover, after a discharge is ceased, the recovering time constant of the output potential is easily shown to be μCR as is expected.

In the following experiments, therefore, we can regard Johnson's circuit as a high resistance μR. Of course this approximation is limited to the linear part of $v(e_g)-\epsilon_g$ relation and the voltage variation cannot exceed $v(o)$.

This discussion was verified experimentally from the shape of counter pulses.

§ 4. Experimental Data of the Circuit.

As related before, the counting region of a slow counter is mainly decided by leak resistance R so far as i_m is not varied, and if R is large enough it equals to $v(o)$

When a pentode UZ6C6 is used, the length of counting region depends on plate resistance r besides R. Relations between the length of counting region and leak resistance in the case of different plate resistances were measured. Fig. 4 is the results of the measurements when the screen voltage was kept at 45 V. With other screen voltages those curves are somewhat varied but there exist no essential differences among them.

In Fig. 5 are given the vacuum tube characters which correspond to curves in Fig. 4. Similarity between both of them is satisfactory as is the case in Fig. 3.

The values of i_m determined from different values of plate resistance are in agreement with each other within the experimental errors. In our measurement we got 1.01 ± 0.10 μA. The leak resistance to give the same length of counting region varies with different i_m, and is proportional to reciprocal i_m, because the product i_mR is essential for the action of the circuit. Thus we know how to use Johnson's circuit for the operation of any slow counter.

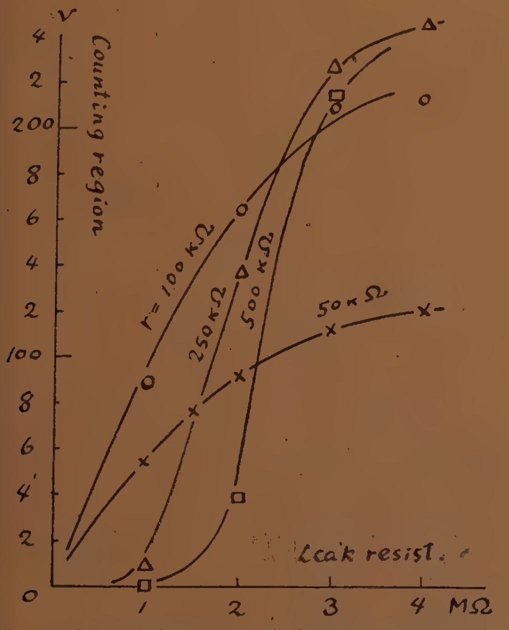

Fig. 4. Dependence of counting region on R by different plate resistances r's.

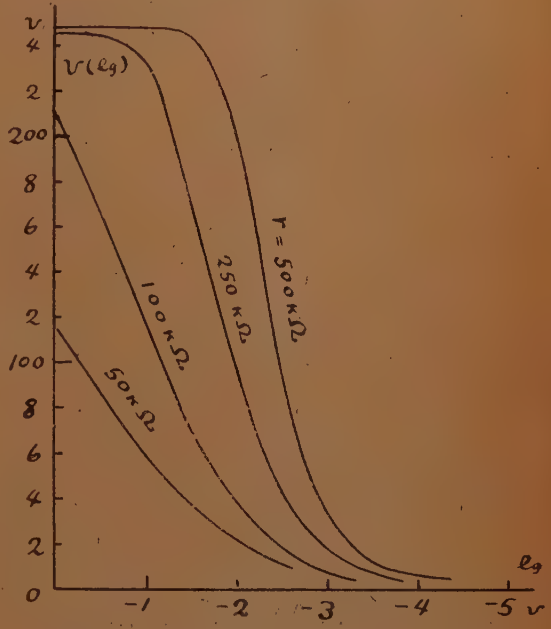

Fig. 5. Circuit characters corresponding to curves in Fig. 4.

§ 5. Counting Characters.

The length of counting region was given in the previous section, but it is shown experimentally that unless leak resistance is large enough, flat portion of the counting region does not appear in its full length. If leak resistance is large enough, counting character becomes flat over all the length. Counting characters of a slow counter by different leak resistances are given in Fig. 6, where plate resistance is 200 kΩ. To the contrary of fast counter, the counting characters of slow counter falls down towards the end of counting region as shown.

From Eq. (2) the minimum leak resistance to give the full counting region is about 3.5MΩ, but as shown in Fig. 6 we must use the higher resistance than this value to get flat character. The reason why the character curves fall down is that, with rather low leak resistance the pulse length of slow counter is much prolonged, when counter voltage is raised. This problem will be discussed in detail in the following paper.

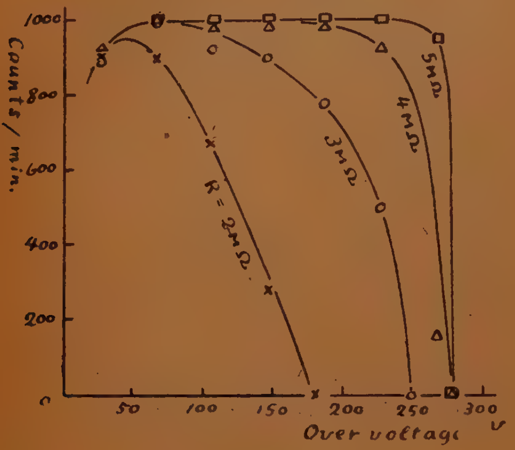

Fig. 6. Counting characters of a slow counter by different leak resistances.

Counting character in Fig. 7 is that of a fast counter. Dashed curve represents that of the same counter using an usual amplifier. The character is considerably improved by using Johnson's circuit and this is because the counter potential is lowered down below the starting potential and "Nachentladungen" are covered by the pulse of the circuit. The character is quite different from that of slow counter in Fig. 6, which means that the discharge mechanism of slow counter is essentially different from that of fast counter.

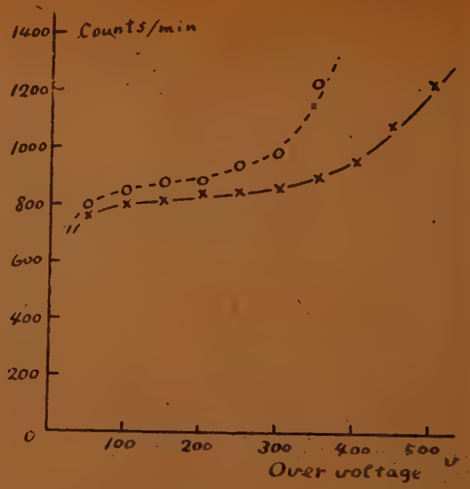

Fig. 7. Counting character of a fast counter measured by Johnson's circuit and ordinary amplifier. It is quite different from that of slow counter.

This work is partly indebted to the Ministry of Education for research grant.

References.

(1) Korff and Present; Phys. Rev. **65** (1944) 274.
Minakawa; Proc. Imp. Acad. Tokyo **19** (1943) 19.
(2) Werner; ZS. f. Phys. **90** 389 (1934); **92** (1934) 705.
(3) Neher and Harper; Phys. Rev. **49** (1936) 940.
Neher and Pickering; Phys. Rev, **53** (1938) 316.
Johnson; Rev. Scient. Instr. **9** (1938) 218.
Getting; Phys. Rev. **53** (1938) 103.

On the Discharge Mechanism of Slow Counter.

By Isao KITA.

Meteorological Research Institute.

(Read October 30, 1949; Received July 31, 1950).

§ 1. Introduction.

Pulse shapes of Slow Counter.

In the preceeding paper(1), it was pointed out that Johnson's circuit for quenching the G. M. counter dischage was equivalent to a high resistance μR, where μ is amplification factor of the circuit and R leak resistance. Therefore in the following discussions, we regard the quenching circuit of slow counter as a high resistance μR, although the slow counter used was operated by Johnson's circuit in practice.

The pulse shapes of slow counters can be observed on a screen of an oscilloscope without disturbing the genuine shape, if the cathode of the circuit is directly applied on the oscilloscope. The observed pulse shapes at various counter voltages are sketched in Fig. 1. In the experiment vacuum tube used is UZ6C6, leak resistance 5MΩ, plate resistance 200k Ω and the capacity of the counter system is 24 μμF. The pulse shapes are somewhat different with different circuit constants and counter properties, but they are essentially of the same type in all cases.

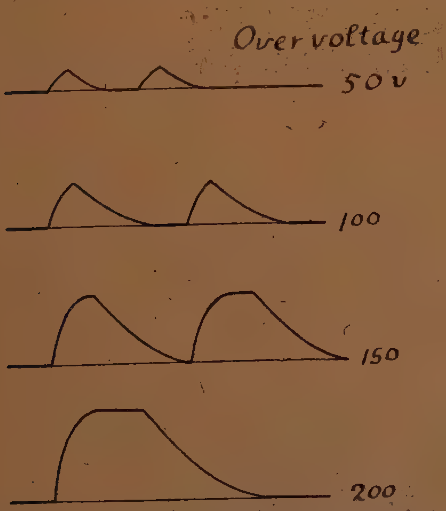

Fig. 1. Observed pulse shapes of a slow counter at various overvoltages.

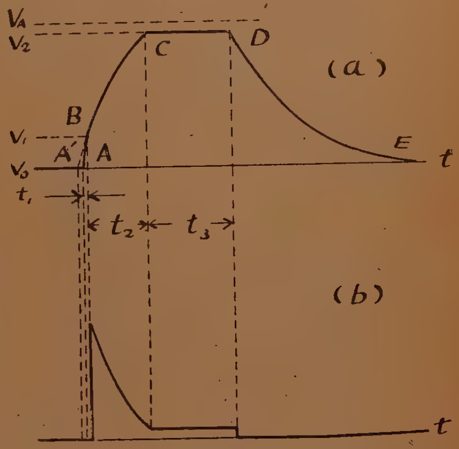

Fig. 2. Typical pulse shape of slow counter and the corresponding discharge current.

In Fig. 2(a) is shown a typical pulse shape in detail. As seen in the figure, the pulse consists of rising part ABC, horizontal part CD and decaying part DE. Rising part has a bend at B as shown. Roof CD does not appear at the beginning of counting region, but towards the end of the region its length grows longer and this part of pulses becomes continued at last. At D the pulse begins to decay exponentially. In the following these aspects of pulse shape will be discussed in connection with the discharge mechanism.

The so-called "Overshooting" reported by Montgomery and Montgomery(2) was not observed in our experiments. This may be due to the rather large capacity of the counter system.

§ 2. Discharge Mechanism of Slow Counter.

In the case of fast counter, the discharge, when triggered, is quenched at once and positive ions produced in the discharge expand in a form of thin sheath. So in the operation of fast counter, a low leak resistance can be used and accordingly the pulse shape is very sharp.

On the contrary, the discharge of slow counter is quite different from that of fast counter, as is known, and discussed here in detail.

(i) Rising part AB.—When an ionizing particle enters into counter volume, it ionizes gas molecules and produces electrons in the counter. These electrons move towards the central wire and grow to an avalanche in which are produced electrons, positive ions and gamma rays. In slow counter these ions and gamma rays can pull out another electrons and succesive discharges are developed, according to photoelectric effect and poor shielding effect of space charge. Thus, during the counter voltage is above V_m①③, the discharge connot be quenched but continues without interruption. Therefore the produced ions expand "in ion cloud" instead of ion sheath as is the case of fast counter.

At first we assume that the bend B in Fig. 2(a) corresponds to the time when the head of ion cloud reaches to the counter wall. Then the arrival time t_1 can be estimated approximately. For simplicity we regard ion cloud as a conductor and assume that counter voltage is not varied during the arrival time, then the field at the head of ion cloud (r from the center) is given by

$$X=\frac{V_0}{r\log b/r}, \qquad (1)$$

as is well known, where V_0 is counter voltage and b radius of counter wall. Arrival time t_1 is as follows,

$$t_1=\int_a^b dt=\int_a^b \frac{dr}{\kappa X}=\frac{1}{\kappa V_0}\int_a^b r\log\frac{b}{r}dr$$
$$=\frac{1}{2\kappa V_0}\left(\frac{b^2-a^2}{2}-a^2\log\frac{b}{a}\right)\approx\frac{b^2}{4\kappa V_0}, \qquad (2)$$

κ being ion mobility and a the radius of the central wire. Substituting $b=2.25$cm, $V_0=1040$ volts and $\kappa=140\ \frac{\text{cm/sec}}{\text{volt/cm}}$ (80mm Hg of hydrogen), t_1 is estimated as 8.7×10^{-6} sec.

However the experimental value of t_1 is 1.5×10^{-5} sec. and is about twice the calculated one. This may be rather satisfactory, considering that ion cloud is not of course a perfect conductor and the actual field strength at the head is weaker than that calculated from Eq. (1). Therefore the bend B is considered to be the time when the head of ion cloud reaches to the wall, as assumed.

To calculate V_0-V_1 (pulse height at B) is not easy but from observations it is only about a third or a fouth of final pulse height V_0-V_2.

(ii) Rising part BC.—After the head of ion cloud reaches to the counter wall, gas molecules and the wall supply new electrons and new avalanche are produced successively. Such many elementary discharges are repeated in far shorter time interval than that of BC, so that the discharge continues and the discharge current is decided uniquely as a one-valued function of counter voltage V. Its functional form is parabolic and represented as

$$i=\frac{2\kappa l}{b^2\log\frac{b}{a}}V(V-V_A), \qquad (3)$$

where l is effective length of slow counter and V_A threshold voltage. Substituting the numerical data in Eq. (3), we obtain

$$i=2{\cdot}6\times10^{-4}\,V(V-1{,}040), \qquad (3')$$

in our case i is represented in μA and V in volts.

On the other hand the observed relation between discharge current and counter voltage is shown in Fig. 3 and is represented by

$$i=2{\cdot}3\times10^{-4}\,V(V-1{,}040). \qquad (4)$$

Agreement between the calculated and the observed values is satisfactory.

Here we can replace Eq. (3) by

$$i=\frac{1}{\rho}(V-V_A);\ \rho=\frac{b^2\log\frac{b}{a}}{2\kappa lV}, \qquad (5)$$

where ρ is the internal resistance and regarded as constant because in practical use $V\gg V-V_A$. From Eq. (4), ρ is 4.3 $M\Omega$.

In fact Eq. (5) is valid only in steady state, but as related before transit time of positive ions through a counter can be neglected compared with the time interval BC (about 8×10^{-4} sec.). It is, therefore, regarded as a one-valued function of counter voltage throughout the time interval BC.

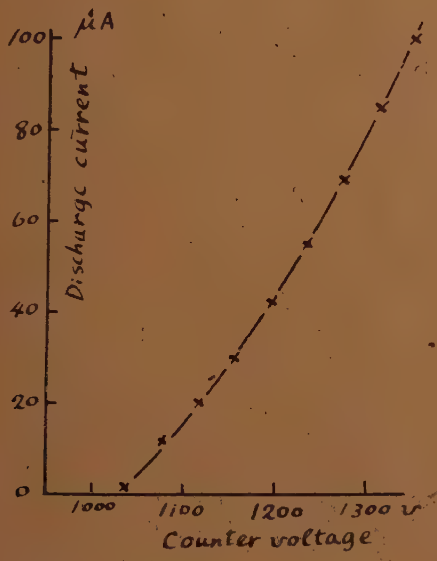

Fig. 3. Continuous discharge current of slow counter.

Now let i' be the current through leak resistance μR, then

$$i' = \frac{1}{\mu R}(V_0 - V), \tag{6}$$

where V_0 means the applied voltage and V the net potential across the counter. And let C the capacity of the counter system, then we have

$$-C\frac{dV}{dt} = i - i'.$$

Substituting Eq. (5) and (6) in the above equation,

$$-C\frac{dV}{dt} = \frac{1}{\rho}(V - V_A) - \frac{1}{\mu R}(V_0 - V).$$

This differential equation can be easily solved, giving

$$V - V_A = \frac{\rho}{\rho+\mu R}(V_0 - V_A) + \text{const.}$$
$$\times \exp\left\{-\frac{1}{C}\left(\frac{1}{\rho}+\frac{1}{\mu R}\right)t\right\}.$$

Potential V_1 at B give the integral constant, but $V_0 - V_1$ is small compared with the final pulse height $V_0 - V_2$. Consequently extrapolating the curve CB to A′ in Fig. 2(a), we get

$$V - V_A = \frac{\rho}{\rho+\mu R}(V_0 - V_A)\left[1 + \frac{\mu R}{\rho}\exp\right.$$
$$\left.\left\{-\frac{1}{C}\left(\frac{1}{\rho}+\frac{1}{\mu R}\right)t\right\}\right], \tag{7}$$

where time origin is at A′.

Thus the counter voltage V approaches to the final value $V_2 - V_0$ exponentially after Eq. (7) and V_2 is given by

$$V_2 - V_A = \frac{\rho}{\rho+\mu R}(V_0 - V_A). \tag{7'}$$

Reciprocal time constant of rising part is $\frac{1}{C}\left(\frac{1}{\rho}+\frac{1}{\mu R}\right)$ from Eq. (7), and it turns out $\frac{1}{C\rho}$, neglecting $\frac{1}{\mu CR}$ as ($\mu R \sim 1{,}000\mathrm{M}\Omega, \rho \sim 4\ M\Omega$). Therefore the time constant of rising part BC is independent of leak resistance and counter voltage, and is proportional to the capacity of the counter system.

Corresponding discharge current is

$$i = \frac{V - V_A}{\rho} = \frac{V_0 - V}{\rho+\mu R}\left[1 + \frac{\mu R}{\rho}\exp\left(-\frac{t}{C\rho}\right)\right], \tag{8}$$

and is shown in Fig. 2(b).

(iii) Horizontal part CD.—Towards the end of counting region, counter pulse begins to have its horizontal roof part as seen in Fig. 1. Its height corresponds to the final value of Eq. (7), extinguishing the exponential term and is given by Eq. (7′). The corresponding steady current is given from Eq. (8) as follows,

$$i = \frac{V_0 - V_A}{\rho+\mu R}. \tag{8'}$$

Generally this steady current is cut off after a short time t_3 and the pulse begins to decay exponentially thereafter. Undoubtedly t_3 increases with increasing counter voltage, but it is quite random in length in the same condition and is the quantity only statistically determined as an average value. According to Werner③ it is an exponential function of over voltage $V_2 - V_A$, i.e. that of final steady current.

In our experiment, moreover, it was distinctly observed that the life time t_3 was increased with increasing capacity of the counter system. In fact, if a large capacity such as 0.01 μF is added, continuous discharge current flows from the beginning and there exist no counting region. In practical use, therefore, the capacity of counter system must be kept as small as possible.

The problem of cutting off of the steady discharge current is an essential subject in discharge phenomena and not yet solved.

(iv) Decaying part DE.—After the steady discharge current is cut off, the counter voltage begins to recover exponentially and its time constant is μCR. This is easily verified experimentally. In this part we have of course no discharge current through counter as shown in Fig. 2(b).

From this dischage mechanism, the observed pulse shapes of slow counter can be explained satisfactorily.

§ 3. Pulse Height.

Pulse height of slow counter can be measured directly on a screen of an oscilloscope. From Eq. (7′)

$$V_0-V_2=\frac{\mu R}{\rho+\mu R}(V_0-V_A)\approx V_0-V_A$$

because $\mu R \gg \rho$. Therefore it is approximately equal to overvoltage V_0-V_A and does not depend on leak resistance μR.

Experimental results are shown in Fig. 4, in which pulse heights are equal to overvoltages within experimental errors, and they are not varied with different leak resistances. At the end of counting region, the operation of counters is broken down and pulses cease to appear as are shown by arrows in the figure.

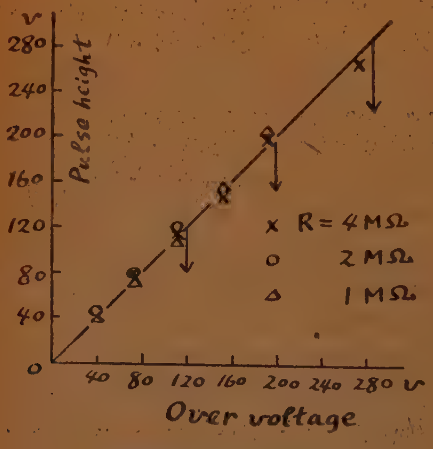

Fig. 4. Pulse heights of slow counter.

§ 4. Rise Time.

As related in § 2, after triggering of a discharge, counter voltage approaches exponentially to its final value that is given by Eq. (7′). Its time constant is $C\rho$, while exponential function $\exp(-x)$ seems almost to vanish with $x=4$. Therefore it is expected that the observed rise time t_2 including AB and BC is about four times the time constant.

$$t_2 = 4\,C\rho$$

Accordingly it is independent of both operating voltage and leak resistance and is proportional to the capacity of the counter system.

In Figs. 5(a), (b) and (c) are shown experimental results. In the experiment $\rho = 4.3$ MΩ, $C = 45$ $\mu\mu$F and other small mica condensers were added. It is difficult to determine precisely the end of rise time and experimental ambigui-

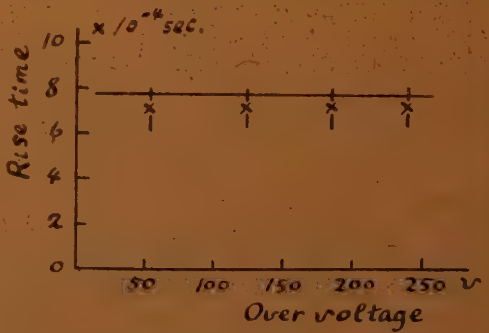

Fig. 5(a) Rise times of slow counter pulses when the overvoltage was varied.

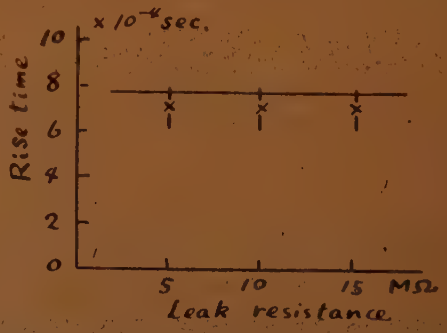

Fig. 5(b) Rise times of slow counter pulses when the leak resistance was varied.

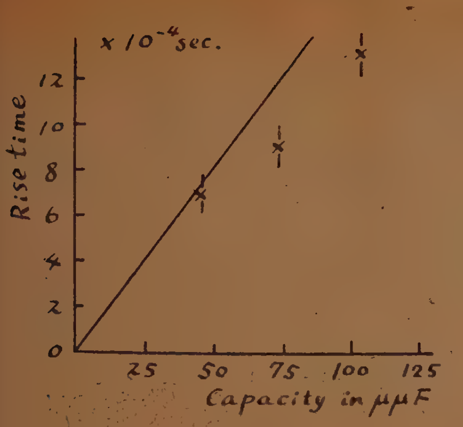

Fig. 5(c) Rise times of slow counter pulses when the capacity of counter system was varied.

ties shown in the figures are unavoidable. Within these experimental errors the observed values agree with the calculated data which are shown by solid lines in the figures. This agreement is rather good, considering the rough measurement of the rise time intervals.

As seen in the figure, rise time t_2 does not depend on leak resistance R. The higher the leak resistance, the smaller the steady discharge current i, and therefore the shorter the life time t_3 of pulse. Consequently high leak resistance is not injurious but makes dead time of counter discharge shorter. This is to the contrary of fast counter and is rather an unexpected result.

On the contrary large capacity of counter system is injurious for the operation of counters, because the rise time is proportional to the capacity and the dead time becomes longer in consequence. Therefore in practical use the stray capacity of the counter system must be kept as small as possible.

The author wishes to express his gratitude to Dr. O. Minakawa for his kind guidance and to Mr. G. Fujioka for his valuable discussions. This work is partly indebted to the Ministry of Education for research grant.

References.

(1) Fujioka, Kita and Minakawa: Jour. Phys. Soc. Japan: This issue.
(2) Montgomery and Montgomery: Phys. Rev. **57** (1940) 1030.
(3) Werner: Zs. f. Phys. **90** (1934) 384, **92** (1934) 705.

On the Temperature Effect of Geiger-Müller Counters.

By Goro Fujioka, Isao Kita, and Osamu Minakawa.

Meteorological Research Institute.

(Read Oct. 31, 1949; Received July 31, 1950)

§1. Introduction.

The variation of the character of G–M counters with temperature were treated briefly by Trost in his pioneer work⑴. Recently cosmic ray experiments using G-M counters at high altitudes are made frequently and in these cases the temperature should vary in appreciably wide range. Thus it seems necessary to investigate the effect of temperature upon counter characteristics.

Moreover, the change of the discharge with temperature might be a clue to the investigation of the discharge mechanism.

The variation investigated by Trost was mainly due to the liberation of gases from glass and can not be considered as the proper character of discharge. We investigated the effect of temperature upon threshold voltage and characteristic curve of counters.

The counter cylinder used is made of copper 45 mm in diameter, and the central wire of 0.1 mm tungsten. The counter is sealed in hard glass and evacuated at about 400°C. Then the copper cylinder is heated to 800°C by the induction furnace. The filling gas is a mixture of 90 mm Hg argon and 10 mm Hg ethyl alcohol vapour.

§ 2. Threshold Voltage.

The threshould voltage was determined on oscilloscope screen. An Example of the results is shown in Table I. There seems no systematic variation and we can conclude that the threshold voltage is not influenced by temperature, as expected from the theory of gas discharge.

Table I.

Temperature (°C)	21	34	37	41	49	57
Threshold voltage (V)	1034	1042	1038	1040	1042	1042
Temperature (°C)	65	72	78	84	93	99
Threshold voltage (V)	1038	1038	1036	1038	1036	1038

§ 3. Counting Characteristics.

The variation of characteristic curves with temperature in the case of rather good counter is shown in Fig. 1. It may be seen from the figure that the counting character is improved when the temperature is raised.

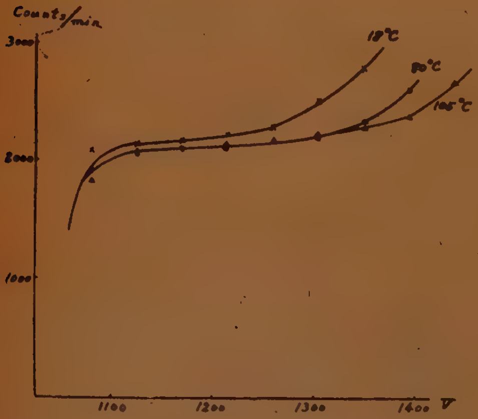

Fig. 1. Characteristic curves of good counter at various temperature.

Then counters with bad characteristics were tested. The results are shown in Fig. 2 and 3. The higher the temperature, the better the characteristics. But the characteristic is suddenly destroyed, when the temperature is raised over a certain value (different values in different counters). As long as the temperature is lower than this critical value, the characteristics are reproducible. But if the temperature is once raised too high, the characteristics are not soon recovered when the temperature is lowered, and it requires relatively long time (about some days) for the recovery.

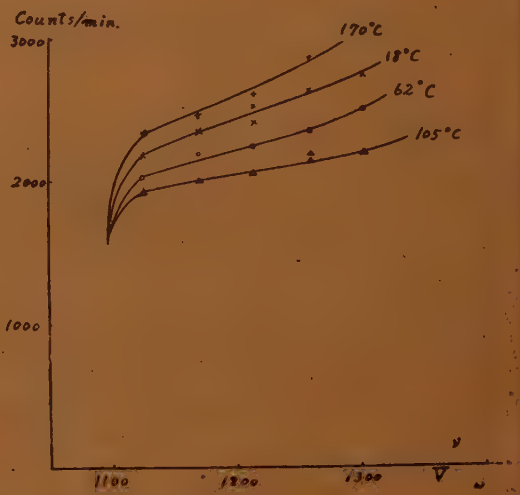

Fig. 2. Characteristic curves at temperature higher than the room temperature.

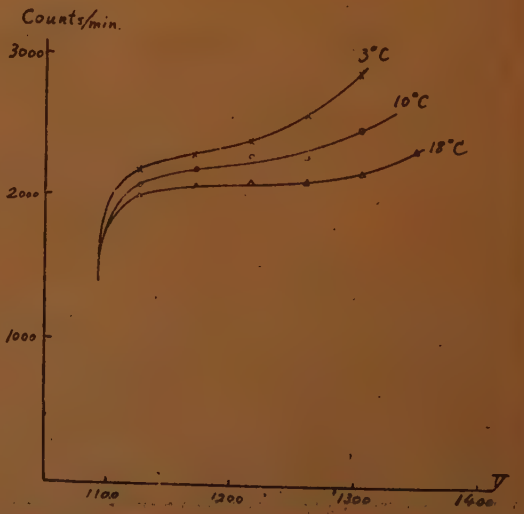

Fig. 3. Characteristic curves at temperature lower than the room temperature.

§ 4. "Nachentladung" and "Spontanentladung".*

As is well known, the rise of the characteristic curves is due to the occurence of spurious discharges, which are classified into two types, i.e. N.E. and S.E.. It seems to be of some interest for the discharge mechanism, to know which of these two types of discharges is responsible to the temperature effect. Then we measured the counts of a counter with and without N.E. simultaneously. The difference of these two values gives the number of N.E.. The rise of counting curve without N.E. is the measure of S.E.. Thus we can measure N.E. and S.E. and S.E. separately,

To eliminate N.E., the thyratron gate circuit, which does not transfer pulses in a certain interval after one pulse is transfered, was used. When the thyratron is once discharged, it does not respond to the subsequent pulses until its plate voltage recovers to a certain value. As N.E. distribute in about 12×10^{-4} sec. in the case of our counter dimensions and gas constitution(3), the insensitive time of the gate circuit was chosen as 15×10^{-4} sec.. Thus N.E. were entirely eliminated in the counts through the gate circuit. To make negligible the loss of true counts occured successively in this time interval, counters were operated without radioactive source. The natural counts were about 300/min..

To simplify the situation, counter with almost N.E. only and ones with almost S.E. only were used. An example of the results obtained with a counter with N.E. are shown in Fig. 4a and 4b. The solid curve of Fig. 4a represents the total counts and the dashed one is the counts filtered by the gate circuit. Circles and triangles are the data obtained soon after the original character was destroyed by the too high temperature with and without N.E., respectively. Fig. 4b gives the percentage of N.E. and circles correspond to the data of triangles and circles in Fig. 4a. We see that N.E. decreased when temperature was high, but if the temperature was raised too high S.E. appeared suddenly and N.E. increased at the same time. When the temperature was lowered again, S.E. did not vanish and the occurence of N.E. was not reduced to the original value. After one day this counter was almost recovered to its original character.

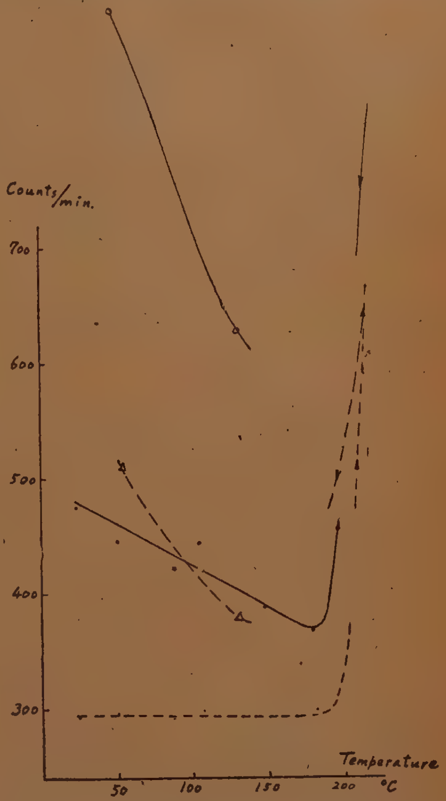

Fig. 4a. Counts with and without N.E. at various temperature. The overvoltage is 280 V.

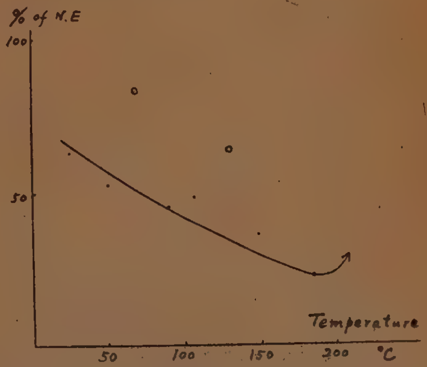

Fig. 4b. The probability of N.E. at various temperature derived from Fig. 5a.

But even at this destroyed state, the higher the temperature, the less N.E. and S.E., as long as the temperature is lower than the critical temperature.

---

* Hereafter abbreviated as N.E. and S.E., respectively.

The results obtained with the counter with S.E. are shown in Fig. 5. Curves are the ordinary characteristic curves. The figures represent the order by which the measurements were performed. The conditions are shown under the figure. In this case the temperature effect is similar to the case of N.E.. At any temperature, N.E. were not observed. On account of the steep rise of counts by counters with S.E., the overvoltage could not be raised so high, that N.E. might not appear in these voltage range.

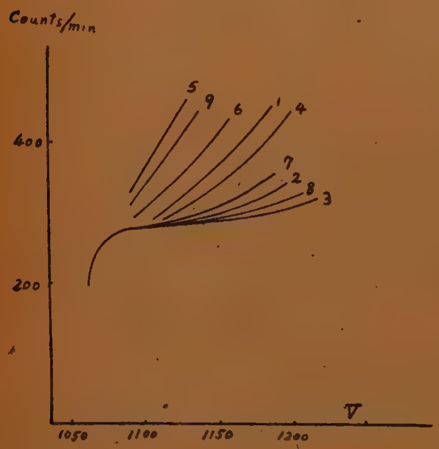

Fig. 5. Characteristic curves of a counter with S.E. at various temperatures.

1: 17.5°C 2: 45°C 3: 79°C
4: 108°C 5: 44°C, 2.5$^{\text{hr.}}$ after 4
6: 16°C, 18$^{\text{hr.}}$ after 4 7: 50°C, 40$^{\text{hr.}}$ after 4
8: 65°C, 42$^{\text{hr.}}$ after 4 9: 18°C, 65$^{\text{hr.}}$ after 4

When the counter with N.E., which had been operated several months, was used, N.E. increased appreciably as the temperature was raised to 69°C. But when the temperature was lowered it did not recover its old character. In this case the critical temperature mentioned above might be lowerd owing to the numerous discharge (of the order of 6×10^7 counts).

Generally speaking, N.E. as well as S.E. decrease when the temperature is raised, but when the temperature is raised over a certain value, they increase suddenly, and this after-effect does not vanish in about some days.

§ 5. Discussions.

Characteristics of newly constructed counters improve at high temperature as stated in § 3, therefore it seems desirable to operate counters at warmer conditions than the room temperature, if it is not too high. But, operated appreciably long, the situation is not so simple as seen in § 4, and some care is necessary when the temperature may become high.

The irreversible change at the high temperature may be due to the liberation of gases from glass or metals. By old counters the situation might be as follows; the small molecules of decomposed gases from alcohol might be almost adsorbed at the room temperature and the counter characteristics do not deteriorate so soon, but at higher temperature such injurious gases might be liberated easily and therefore characteristics become worse than at room temperature.

To operate counters at low temperature is undersirable even apart from the condensation of alcohol.

N.E. and S.E. behave similarly at least qualitatively when temperature is raised, though they are considered as quite different phenomena, because counters with almost N.E. only and those with almost S.E. only are present and because S.E. increase, though N.E. do not so increase, when the fraction of alcohol is raised(3).

On the origin of N.E. and S.E., one of us presented a phenomenological concept several years ago(4). N.E. might be caused by the secondary emission by small positive ions and S.E. might be due to the double layer, e.g. formed by large positive ion attached on the cathode wall.

When the temperature is raised, the collision frequency of imigrating positive ions and the probability of charge transfer would increase. (The imigration time depends mainly on the field intensity and not to the thermal velocity and also the gas temperature would not so influence the ion temperature.) Thus the number of small ions reaching the cathode will decrease at higher temperature, and so the decrease of N.E. may be qualitatively explained.

Korff and Present(5) gave a detailed treatment on the cause of "spurious discharge", but the problem is not so simple because the spurious discharge is not of one kind.

The decrease of S.E. might be due to the depression of the field strength of the double layer according to the increase of the distance between ion and the metal surface at high temperature, but to proceed to such extent seems to be too tentative at the present stage. It is sure that the condition of the cathode surface is essential to the occurence of N.E. and S.E., but it is so delicate and rich of variety that to investigate this point is very difficult and tedious.

This work was partly supported by the Scientific Research Expenditure of the Ministry of Education.

References.

(1) A. Trost: Zeits. f. Phys., **105** (1937), 399.
(2) O. Minakawa: Proc. Imp. Acad. Tokyo, **20** (1944), 288.
(3) O. Minakawa: ibid., **18** (1942), 644.
(4) O. Minakawa: ibid., **19** (1943), 19; also see (3).
(5) S.A. Korff and R. D. Rresent: Phys. Rev, **65** (1944), 274.

Studies on The K Absorption Band in the Colored Rock Salt Crystal.

By Yōichi UCHIDA, Masayasu UETA and Yoshio NAKAI.

(Received July 14, 1951)

§ 1. Introduction.

Extensive experimental works have been carried out on the colored centers of alkali-halides since the pioneer investigations of Pohl(1) and his school. At the present time it is known that the colored alkali-halides show F, F′ and U absorption, while potassium chloride has new absorptions called R, V, and M(2). The theoretical discussions concerning to the nature of these absorption centers particularly the F-center were given on experimental materials by Boer(3), Hughes(4), Mott(5), Tibbs(6), Seitz(7), Muto(8) etc. These paved the way to a better understanding of some of the most interesting properties of solids.

In the present paper a report is given of a new absorption band in a colored rock-salt crystal called K absorption which was already found by the present writers(9). The K absorption may be induced by several ways in NaCl, its maximum being situated at 295mμ. When irradiated with the light of its absorption the crystal exhibits luminescence accompanied by photoconduction. By this process, K-centers decay and transform into F-centers. The nature of this K-center may be explained by these properties.

§ 2. Formation of K-center and its Absorption.

NaCl crystal having K-absorption can be prepared by an apparatus shown schematically in Fig. 1. A rock-salt R with a dimension of 10 × 10 × 20 mm³. was placed between a flat anode A made of carbon or platinum and a pointed

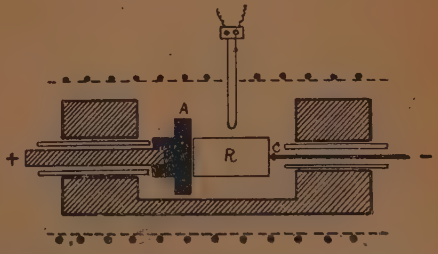

Fig. 1. Method for producing K-center in NaCl crystal.

cathode C of iron or platinum. An electric field of about 300∼400 volt/cm was applied between the electrodes. As is well known, when the crystal is held at a temperature above 500°C, brown-red F-discoloration results with its maximum absorption at 465mμ. But it was found when the temperature was maintained at about 400°C the crystal was, instead of F-coloration, discolored showing the appearance of pale-yellow. The absorption spectrum of this pale-yellow crystal was examined over the whole region of visible and ultraviolet. The apparatus used was shown in Fig. 2. The monochromator was of Littrow type with a parabolic mirror M (10cm diameter and 100cm focal length, aluminum plated) and a 30° quartz prism P. Light from mercury arc was sent through the first slit S_1 and monochromatic light from the second slit S_2 was passed through clear crystal and colored crystal placed alternately in the path of light. The transmitted light were measured photoelectrically by a Cs photocell C made of quartz and a Doležaleck quadrant electrometer Q (sensitivity: $750d/V$) connected as shown in the figure. Xylene was used for the high resistance R($\sim 10^{10}\Omega$). For visible region a 6V. 30 watt electric lamp was used for light source.

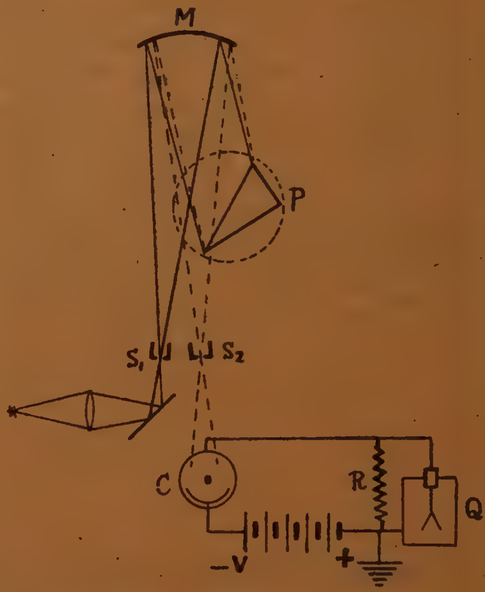

Fig. 2. Arrangement for measuring absorption.

The absorption curve is shown in Fig. 3, A. It consists of a principal peak K at 290∼295mμ,

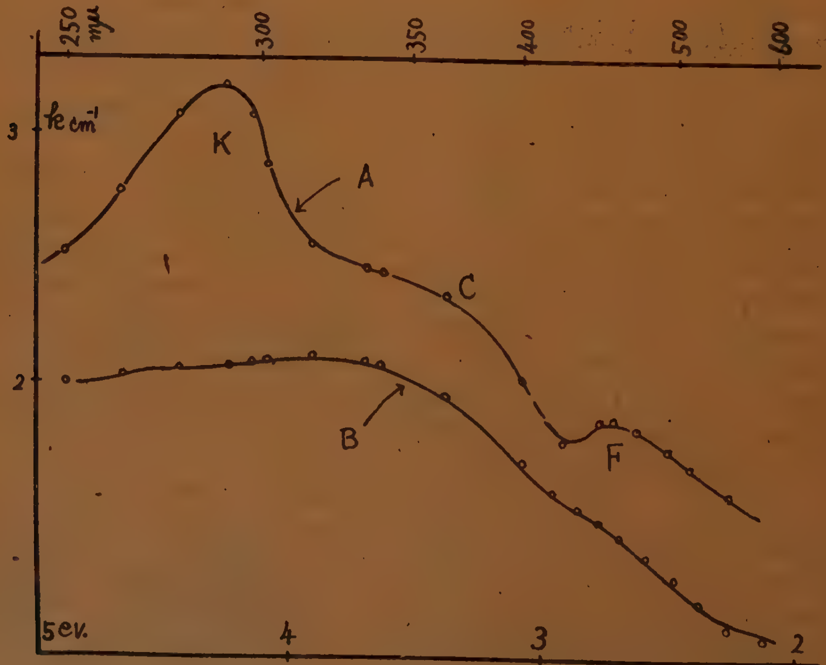

Fig. 3. Absorption coefficient
A: of crystal containing K-center
B: ditto after bleaching.

followed by a somewhat smooth region C and a subsidiary peak of the F band. Now it is well established that F-centers can be annihilated within the colored crystal, either by reversing the electrodes or by the thermal diffusion. But by these processes the crystal is never bleached completely and some very faint yellow color remains which is considered due to some colloids. The spectrum of the crystal containing this colloids is shown in Fig. 3, B. Now the region C of our spectrum may probably be identified with that of colloids.

So, excluding the portion C the new band K has a bell-shape ranging between 250~330mμ with its max. at 295 mμ.

§ 3. Properties of Crystal Containing K Centers.

Crystals containing K-centers possess a number of notable properties. Those which have been investigated are as follows:—

a) Transformation of F into K-centers.

K-centers may also be produced through F-centers in a following way: F-centers are produced in a rock-salt at 570°C, which is quenched quickly below to 400°C to prevent thermal diffusion of F and production of blue colloids. If at this temperature an electric field is applied from flat electrodes, it will be seen that the color of F gradually disappers as a whole, while K-centers appear as revealed from its absorption-spectra. This process may be interpreted in the following way: the electrons partially dissociated from F centers are attracted to some kind of center by the electric field, being trapped there to form a K-center. The fact that the K-coloration occurs always at the temperature of about 400°C or below, suggests that the density of these receptors is comparatively larger at these temperatures.

b) Transformation of K into F-centers.

Thermal: K and F-centers and colloids are induced simultaneously by the method of pushing electrons in from a pointed cathode, though the concentration of the colloids is very small. If we interchange the sign of electrode, the cloud of F coloring migrates back into the new anode. Thus the sample containing only K-centers (and colloids) may be obtained. If this sample is placed into an electric field from flat electrodes at temperature below 500°C, it will be seen that K-coloration changes into F-coloration. Thus under electric field K→F transformation occurs according to the appropriate temperatures. It will be noted that, in contrast to the fact that, F centers diffuse very fast even at 450°C K-centers are comparatively stable at that temperature and diffusion occur appreciably only at above 550°C.

Optical: When irradiated by the light lying in the new absorption, it was found that the sample containing K-centers emits blue and red luminescence bands, the former having its maximum intensity near F band. By continued irradiation, however, the blue band fades out. The red band is situated in the region coinciding with F′ band. But its intensity is so faint that its origin has not conclusively been determined.

The absorption spectrum of a crystal which thus lost the luminescence was examined (Fig. 4). The absorption coefficient decreases at the wavelength of K and increases at F-band, showing K-centers have been transformed optically into F-centers. This phototransformation accompanies the photoelectric conduction as will be described below.

c) The luminescence of K-center.

A crystal with K-centers was illuminated by the light of a quartz mercury vapor lamp through a blue filter transmitting down to 250mμ. The luminescence spectrum was photographed by a large aperture spectrograph provided with both collimator and camera lenses having 60cm focal length, and 12.5cm diameter; a glass prism of 10cm height with the other side of 15cm. An exposure of 15 min. was given to record the visible band on an "Agfa Isopan" plate. But for the infra-red band, 3.5h. exposure was required to secure a good impression on a "Fuji aero infrared" plate. The spectrum is reproduced in Fig. 5 in which two bands may be seen, one between 390~500mμ with maximum at 445mμ: the another between 600~800mμ with maximum at 700mμ respectively.

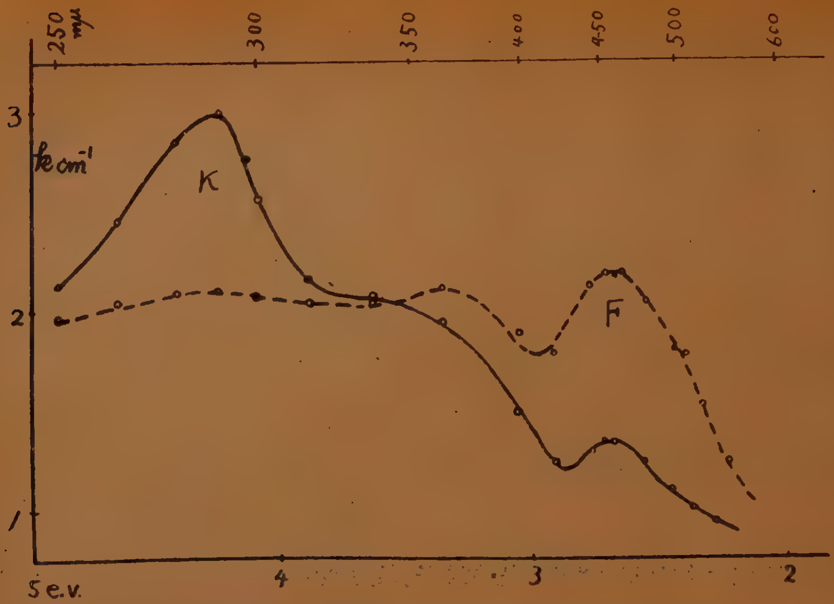

Fig. 4. Absorption coefficient before (full line) and after (dotted line) illumination.

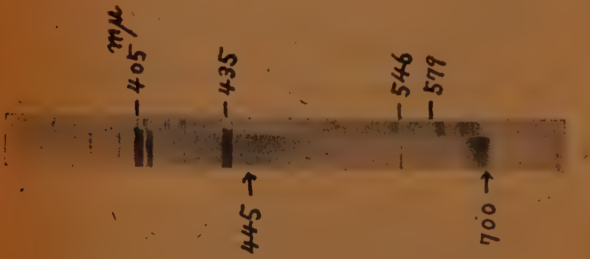

Fig. 5. Luminescence spectra (with comparison) showing two maxima at 445mμ and 700mμ.

There are reasons to attribute the blue band to the emission of F-center. By the K-absorption an electron may be considered to be raised to the conduction band as verified later by its photoconduction. If these conduction electrons recombine with a negative ion-vacancy an emission of F band will result. The discrepancy 0.12 e.v. between emission and absorption of F band may be explained by assuming the transition between the lowest edge of conduction band and the ground F state (Fig. 6). As is already mentioned, with continued illumination the power of emitting luminescence decays and the crystal shows reddish brown coloration. This fact indicates that the illumination reduces absorption at K and enhances at F as is seen in Fig. 4.

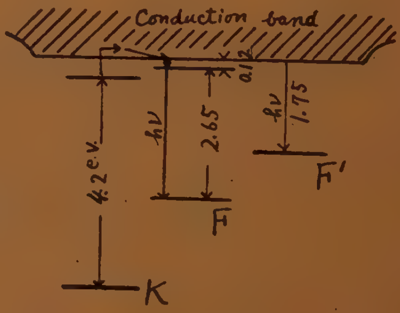

Fig. 6. Energy levels.

So the phototransformation of K into F-center was established.

The exciting region for the luminescence was investigated after the method of Hüniger and Rudolf⁽¹⁰⁾. Powdered NaCl with K-centers were spread over the glass side of a photographic plate P in Fig. 7, the gelatin film of which was stained with potassium chromate in order to cut below 3500A. This was held on the focal plane of a quartz spectrograph, through which a light from an under water spark S was sent. The light having the wave length effective to excite the powder crystal was impressed on the photographic film in contact with powders for a 30 min. exposure.

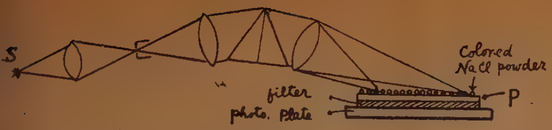

Fig. 7. Arrangement for studying exciting spectrum for luminescence.

Thus it was found that exciting wave-lengths lie within the range between 270～310mμ with maximum at 290～295mμ coinciding exactly with the K-absorption.

d) Photoconduction by K-centers.

As is already stated, the luminescence by K-absorption is accompanied with photoconduction, which has a very important meaning in the mechanism of phototransformation of K into F center. Photoconductivity was investigated by an arrangement sketched in Fig. 8. A piece of sample C with 3mm. thickness was held between

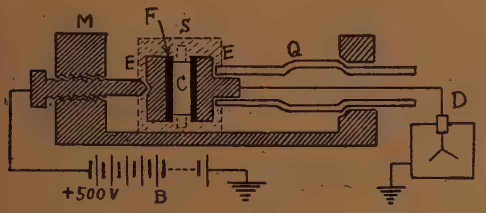

Fig. 8. Arrangement for studying photo-conduction.

the electrodes E and E′ supported on a metal block M and a quartz tube Q respectively. Crystal surfaces facing electrodes were painted by "Aquadag" and pressed on sheets of Pb-foil F to secure contact. The leading wire to an electrometer D was insulated by a quartz tubing Q from the support M. A potential difference of 500 V. was applied from the battery B. Whole system was enclosed in a metal case and was kept at the temperature 38°C in order to keep the crystal surface dry. The crystal was illuminated through a slit S transversally to the field. For the light source, a hydrogen discharge tube running at 2500 V. and 2～3 amp. was used. Its energy-distribution measured by a Moll-thermopile is shown in Fig. 9. The sample was slided along the focal plane of a quartz-spectrograph of $f/4.5$ aperture to illuminate with each monochromatic light.

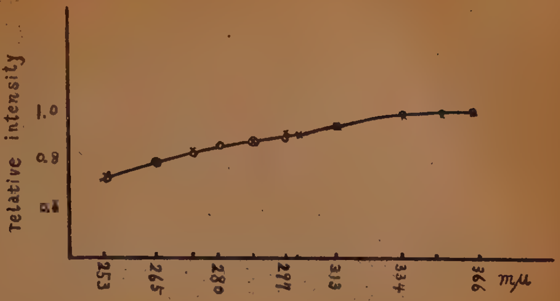

Fig. 9. Energy distribution of hydrogen continuum.

When a field was applied without illumination an electrolytic current i_0 flowed during the time interval t_0 and the potential of the electrometer was raised from V_0 to V_1. With illumination, an additional photo-current i flowed to the electrometer and charged it to the same potential difference V_1-V_0 in the time interval t. Calling C the capacity of the electrometer, following relation may be deduced,

$$C\times(V_1-V_0)=i_0t_0$$

$$C\times(V_1-V_0)=(i_0+i)t$$

hence the photocurrent is obtained by

$$i=i_0(t_0-t)/t$$

By this formula i (in arbitrary unit) is calculated for every wavelength as shown in second column of Table 1. Values corrected for equal energy distribution of light source are shown in the fourth column.

Table 1.

Wave-length (mμ)	Measured photo-current in arbitrary unit.	Energy of light source (relative value)	Corrected value of photo-current
350	5.2	1.0	5.2
330	4.5	0.98	4.5
310	5.5	0.94	5.8
302	5.7	0.89	6.4
297	5.5	0.89	6.2
289	6.0	0.85	7.1
280	6.1	0.85	7.2
274	5.1	0.82	6.2
265	4.2	0.78	5.4
253	3.9	0.72	5.4
245	3.8	0.65	5.8

The spectral photoconductivity curve is shown in Fig. 10 which shows its maximum coinciding with that of K-absorption.

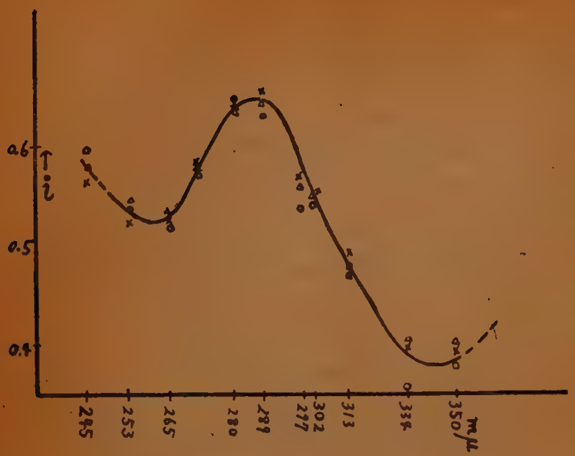

Fig. 10. Spectral sensitivity curve for photoconduction.

It is safely concluded that in consequence of K-absorption an electron is ionized into the conduction band, and luminesecence occurs by transition into F ground-level.

§ 4. Nature of K-centers.

We are now in a position to consider the nature of K-centers in NaCl. We have the following evidence showing similarity between the F and K centers:

1) K is a sort of trapping center of electrons which can be liberated thermally as well as optically. 2) K can be transformed into F. 3) F can be transformed into K. All these facts suggest that the K-center is some composite, one constituent of which is attributed to F center. Then the most straightforward model to be assumed for K-center may be the two negative ion-vacancies bonded by a single electron at the present stage of investigation, though such model has been already considered by F. Seitz(11) for Molnar's R-centers. The reasoning is as follows:

The positive and negative ion vacancies ($V+$ and $V-$ resp.) in the crystal lattice will attract to each other to form a pair of adjacent lattice vacancies ($V+V-$). It was shown from a simple calculation, the defect in alkali-halide is almost of this type. As the activation energy for migration of the pair was calculated by Dienes(12) as 0.375ev. in KCl, we may expect the high possibility of migration of these pairs even at room temperatures. It is very plausible that two pairs will attract to each other and to form a quartet. We may rather expect that abundant quartets are present especially in crystals long preserved at room temperatures. Among possible reactions occuring between quartet and electron, one may be

$$(V_+V_-)_2+e\rightarrow(V_-V_+V_-e)+V_+$$

and at sufficient high temperature

$$(V_-V_+V_{-\epsilon})\rightarrow(V_-V_{-\epsilon})+V_+$$

thus a (V_-V_-e) center will be formed.

Since in this model an electron revolves about in an axial field, its electronic orbits will correspond to those of two-center-system of same nuclear charges, the deepest being $1s\sigma$ or σ_g (1s). The whole potential curves of the (V_-V_-e)-center in the various electronic states as function of vacancy-separation could be obtained, if the potential energy due to the all ions around the center be added to its pure electronic energy. Although the latter may be correlated to pure electronic energies of $H_2{}^+$ molecule based on quantum mechanical calculation of Burrau and Hylleraas(13) and Teller(14), the former is not simple and consisted of various components, but it is easily seen that the overlapping energy become predominant already at large separation (about 5A for NaCl). As the consequence, the resultant curves may have the appearance as shown in Fig. 11. The ground $1s\sigma\,{}^2\Sigma_g^+$ and $2p\sigma{}^2\Sigma_u^+$ states do not separate so much, that transition between them correspond only to infra-red or thermal energy. Then transition to next excited states will correspond to K-absorption, if we identify the model of K-center with (V_-V_-e). Then by the absorption of K band the $1s\sigma_g$ electron jumps to higher levels, from which it will be thermally detached into conduction band. By this act one photoelectron and two negative ion-vacancies are formed, which migrate within crystal separately. The recombination of the electron with the vacancy thus produced will radiate luminescence. (phototransformation).

The authors are indebted to National Research Council of Education Ministry for financial aid.

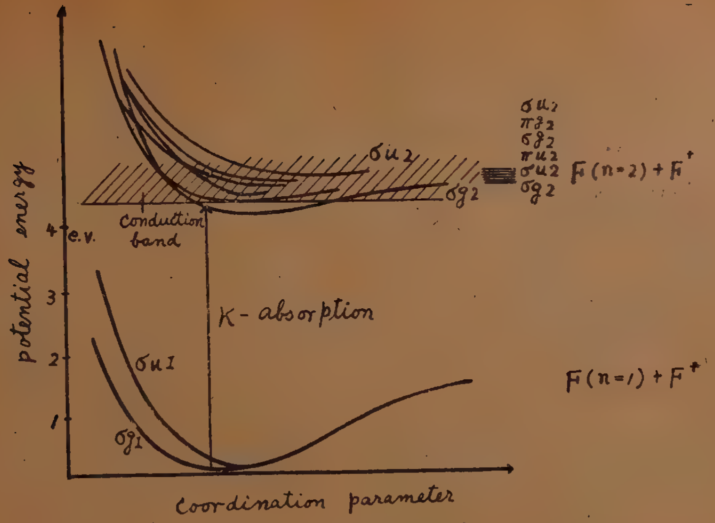

Fig. 11. Curves for potential energy *vs.* two negative ion separation (schematic)

References.

(1) R. W. Pohl: Proc. Phys. Soc. London (Sup.) **49** (1937) 3. Phys. Zeits. **39** (1937) 36.

(2) F. Seitz: Rev. Mod. Phys. **18** (1946) 384.

(3) J. H, de Boer: Rec. Trav, Chim. Pays-Bas. **56** (1937) 301.

(4) A. L. Hughes: Rev. Mod. Phys. **8** (1936) 299.

(5) N. F. Mott & R. W. Gurney: *Electronic Processes in Ionic Crystals.*

(6) S. R. Tibbs: Trans. Farad. Soc. **35** (1939) 1471.

(7) F. Seitz: *loc. cit.*

(8) T. Muto: Prog. Theo. Phys. **4** (1949) No. 2 181.

(9) Y. Uchida M. Ueta & Y. Nakai: J. Phys. Soc. Japan **4** (1949) No. 1, 57.

(10) M. Hüniger & J. Rudolf: Zeits. f. Phys. **117** (1940) 81.

(11) F. Seitz: *loc. cit.*

(12) G. J. Dienes: J. Chem. Phys. **16** (1948) 620.

(13) E. A. Hylleraas: Zeits. f. Phys. **71** (1931) 739.

(14) E. Teller: Zeits. f. Phys, **61** (1930) 458.

On the Secondary Electron Emission from the Thoria Coated Cathode and the Thin Film Deposited by Evaporation from the Cathode.

By Tetsuya ARIZUMI and Leona ESAKI.

Kobe Kogyo Corp. Kobe.

(Received July 7, 1950).

§ 1. Introduction.

The secondary electron emission from some kind of semi-conductor has been investigated by many authors⁽¹⁾. Above all the secondary emission from the oxide coated cathode⁽²⁾ has been studied in details for scientific and practical purposes.

In this paper the secondary emission from the thoria coated cathode and the thin film of thoria deposited by evaporation shall be described.

§ 2. Apparatus.

The experimental tube and circuit are schematically shown in Fig. 1. An electron gun system K, C, P_1, and P_2 was similar to that of the cathode ray tube except the cathode *K* having been coated with thoria. Both the electron gun system and the collector *C* were made of nickel. *M* and *A* were a mica shield and the aquadag film respectively to prevent stray electrons from entering into the collector. The target *T* was a tantalum ribbon of 0.05 mm. thickness, the front of which was coated by an uniform thoria layer of several microns and it could be heated directly. The tube of this construction was used only for studing the secondary emission from thoria.

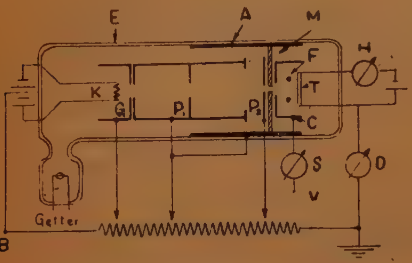

Fig. 1. The experimental tube for measuring the secondary emission from thoria.

In the tube used for measuring the secondary emission from thin film of evaporated substances, the target was a pure tantalum without any coating and two auxiliary thoria coated filaments, served as the sources of evaporation, were mounted between the collector and the target as in Fig. 2.

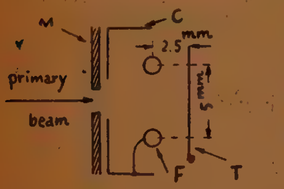

Fig. 2. The experimetal tube for measuring the secondary emission from thin film deposited by evaporation.

Every tube as evacuated on the three stage oil diffusion pump and sealed off after sufficient degassing of glass and all metal parts, activating the cathode and flashing barium in the getter chamber.

The temperature of the target was determined by a micro-optical pyrometer. As for the spectral emissivity for tantalum, Worthing's(3) data were available.

§ 3. Preliminary Experiments.

The blue fluorescence of considerable intensity, radiated from thoria excited by electron impact, gives a convenient means for focussing of the electron beam. By suitable adjustment of voltages on *G*, P_1, and P_2, the electron beam of about 1 mm^2 area was obtained over the primary electron energy from 500 to 2,500 *V* without changing the relative ratio of voltages on these electrodes. The dependency of the secondary current i_s and the difference $i_s - i_0$ (i_0 : primary current) upon the collector voltage were studied at first. For measuring the secondary current in the tube 2, *F* was connected to *G*. The results are shown in Fig. 3. The variation of i_s with respect to the collector voltage for the thoria coated cathode is almost similar to that of pure tantalum, indicating that the charging-up of the thoria surface(4) may well be neglected.

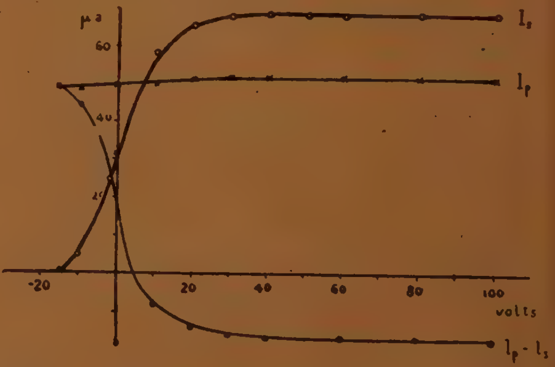

Fig. 3. The dependency of i_s upon the collector voltage.

Next the secondary yield δ is reproduced in Fig. 4 with abscissa being the primary current. All tubes have almost similar characteristics. The lower value of δ at primary current less

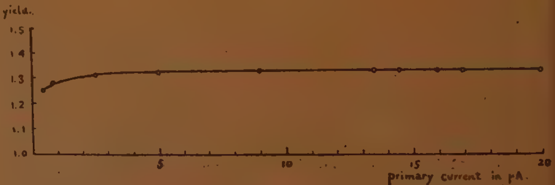

Fig. 4. The secondary yield versus the primary current.

than 1 μA is perhaps due to the construction of the tube. Thus the whole measurements were carried out at the primary current larger than 40 μA. The obtained δ differs from tube to tube only by 2 % at most.

§ 4. Secondary Electron Emission from the Thoria Coated Cathode.

The dependency of the secondary yield from the thoria coated cathode of two different activities upon the primary voltage are plotted in Fig. 7 (2) and (3). In the case of (2) the work function of the cathode was more than 3.0 e.v., while in (3) it was 2.7 e.v. In every cases δ has a broad maximum at about 1,000 V and $\delta_{\max}$ is 1.20 for the former cathode while it is 1.35 for the latter, showing that δ depends slightly upon the activity of the cathode. During the electron impact of the current 50 μA., for about 30 mins., δ increased by several percent, probably because the bombardment causes the dissociation of thoria at the cathode surface, which is identical to the activation of the cathode.

The secondary yield from the hot thoria were shown in Fig. 5. In this case both the thermionic and secondary currents were measured, and before and after such measurements, only the thermionic currents were detected. The difference of the collector currents in both procedures gives the secondary current. The secondary yield thus calculated seems to increase only very slightly at the higher temperature. Above 1,800°K, however, the thermionic current became so predominant that the secondary current might not be observed exactly. The sum of the thermionic and secondary currents also increased gradually during the measurement and at the same time the thermionic current observed soon after having cut off the primary current was always larger than that observed before the bombardment. Moreover both quantities became larger at the larger primary current. The increase of the total currents during the electron impact is almost equal to the difference of the thermionic currents, measured before and soon after the electron impact, suggesting that the increase in the total current is mainly due to the enhancement of the thermionic emission. These phenomena are not caused by the temperature rise of the target due to the electron impact or the charging-up of the surface, but the dissociation of thoria.

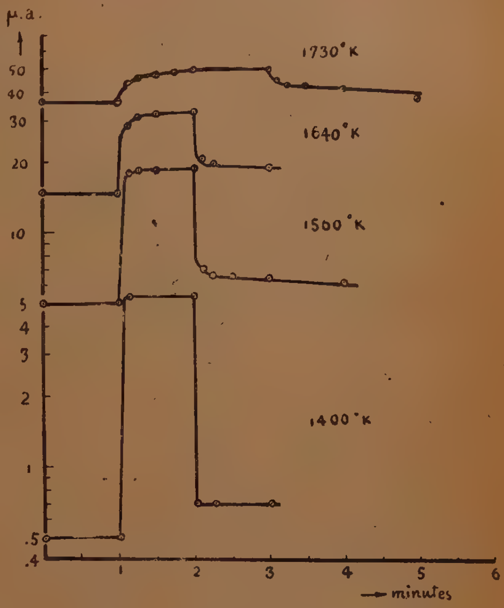

Fig. 5. The thermionic and secondary currents from hot thoria.

When the primary current is cut off, however, newly formed thorium atoms shall be lost by the recombination with residual oxygen. Thus the following differential equation will be derived,

$$\frac{dn}{dt} = C_1 - nC_2 \tag{1}$$

The first term is number of thorium atoms soon after the bombardment and the second term the amount of thorium lost by the combination with oxygen. The solution of (1) is

$$\log\left(\frac{N_\infty - N_0}{N_\infty - N}\right) = C_2 t \tag{2}$$

in which N_0 and N_∞ are values of n at $t = 0$ and $t = \infty$ respectively, and C_2 is expressed by

$$C_2 = kp\exp\left(-\frac{Q}{RT}\right) \tag{3}$$

p is the oxygen pressure and Q is the activation energy of recombination. For the cathode of insufficient activity, the following emission formula holds

$$i = DAT^2 n_0 \exp\left\{-\frac{e}{kT}(E+V)\right\} \qquad (4)$$

as described in the previous paper (5). Thus n in (2) may well be substituted by the emission current i. and (2) becomes

$$\log\left(\frac{i_\infty - i_0}{i_\infty - i}\right) = C_2 p \exp\left(-\frac{Q}{RT}\right) t \qquad (5)$$

in comparatively good agreement with the experimental results. The evaluated value of Q is 1.4 e.v., almost the same order as estimated in the previous paper(5).

The thermionic emission currents obtained soon after cutting off the primary current are plotted in Fig. 6. The work function of the cathode exposed to the electron beam decreased from 2.7 e.v. to about 2.0 e.v. From the previous results(5) the pressure of the present tube is estimated 3×10^{-7} mm. Hg.

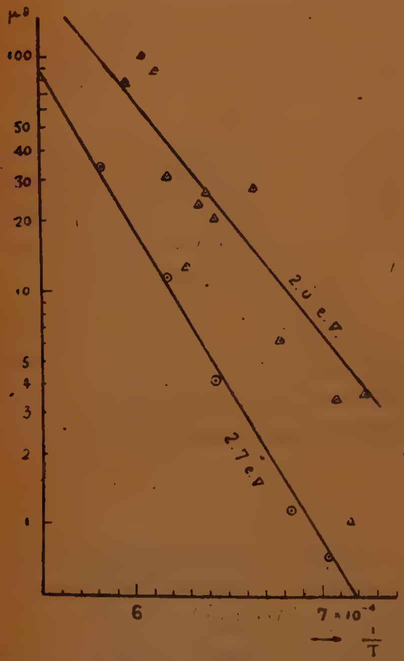

Fig. 6. The work function of thoria before and after the electron impact.

§ 5. Secondary Electron Emission from Thin Film Deposited by Evaporation.

The curve A in Fig. 7 and 8 are secondary yield for pure tantalum. When the auxiliary thoria coated filaments are heated at 1,960°K in the pressure of $10^{-1}\sim10^{-2}$ mm. Hg the curve 1 was obtained. Heating the filaments in high vacuum for several mins. successively, the secondary curve changed from A to H gradually. Differing from the thoria coated cathode the secondary emission from the deposited thin layer has a maximum at a much smaller primary voltage. E.A. Coomes(6) has carried out similar experiments on the thoriated tungsten. In his works the thoriated tungsten was used as the auxiliary filament instead of thoria coated one in our tube and tugsten as the target instead of tantalum. He has measured the covering factor θ of the target by the thermionic experiments. His three curves reprinted in Fig. 7 correspond to the target of $\theta = 0.68$, 0.94 and more than 1 respectively. Our curve H almost coincides with Coomes' curves,

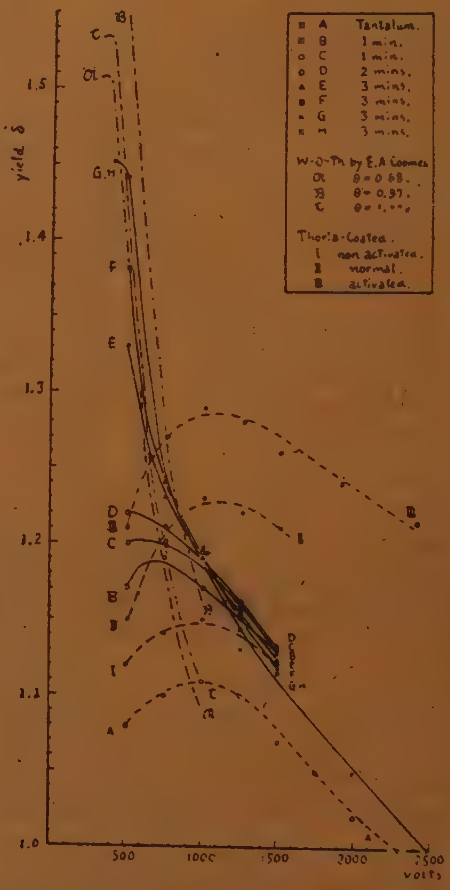

Fig. 7. The secondary emission from thoria and thin evaporated thin film of thoria.

but exactly the yield at higher primary voltages is always larger, while that at 400 V is slightly smaller than Commes' data. This seems to suggest that substances evaporated from the thoria coated cathode at 1960°K are not only thorium but also thoria itself. These two kinds of evaporated substances are supposed to form the patchy structure on tantalum. Assuming that the contaminated tantalum has a quite same secondary yield as the contaminated tungsten over whole primary voltages, the covering fraction of thoria can be calculated from the difference of yields in our experiments and Coomes' results. The covering fraction of thoria thus evaluated is 0.3, indicating that about 30% of total evaporated substances is thoria.

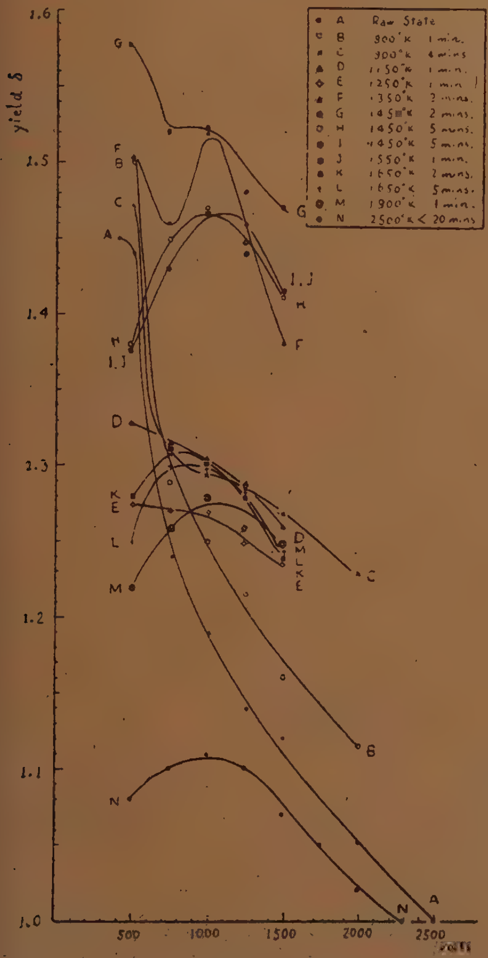

Fig. 8. The secondary emission from the contaminated tantalum.

Heating the contaminated tantalum of the state H at higher temperature for several mins, successively, the secondary yield curve changed from A to M in Fig. 8. The yield was measured at the cold state in all cases. The curve H in Fig. 7, is the curve A in Fig. 8. Heating the target at 900°K for 1 min., the secondary yield increased slightly over whole primary voltages but after further heating for 4 mins. the yield at primary voltage 500 V decreased, while the yield at larger than 1,000 V increased apparently. At 1,150° and 1,250°K the yield at the higher voltages did not increase, but that at 500 V decreased. Heating at 1,350° and 1,450°K for 2 mins., strange yield curves of two maxima obtained such as F and G. At 1,450° and 1,550°K the yield at the higher voltages did not change so much, but that at 500 V decreased. The heating at higher temperatures lowered down the whole curve without the change in its shape. When the target was heated at 2,500°K for 20 mins finally, the curve reached to N, quite identical to that of pure tantalum.

When the target is heated at high temperature, contaminated thorium converts into thoria by the recombination with the residual oxygen, resulting in the increase of the covering fraction of thoria, which makes the yield at the primary voltages larger than 1,000 V, increase. In every cases the yield curves are the sum of the yield of thorium and that of thoria. Thus the increase of the yield at 500 V shown in two curves F and G are supposed to be caused by the increase of the yield in thoria. As whole thorium convert into thoria the yield at 500 V begins to decrease again as H, J and K. By heating at further higher temperatures some part of thoria evaporates and other part coagulates into tiny crystals, resulting in the decrease of the secondary yield seen in curves K, L and M.

§ 6. Summary.

The results are summarized as followed:

(1) The secondary yield of the thoria coated cathode is comparatively small and it does not increase almost at higher temperatures. At the primary electron voltage of about 1,000 V δ be-

comes maximum and $\delta_{\max}$ depends slightly upon the activity of the cathode. No charging up of the surface is observed.

(2) The thermionic emission of the thoria increases by the electron impact due to the dissociation. The phenomenon is more predominant at the higher temperature.

(3) The evaporated substances from the thoria coated cathode are not only thorium but also thoria itself. The estimated percentage of thoria is about 30% at the cathode temperature of 1,960°K.

(4) The secondary yield from thorium on tantalum has maximum at the primary voltage of less than 500 V, while that from thoria has a maximum at about 1,000 V. Heating the target contaminated by the evaporated substances from the thoria coated cathode, the yield at 500 V decreases while the yield at 1,000 V increases gradually, suggesting that the contaminated thorium converts into thoria gradually. In conclusion, the authors wish to acknowledge all member in our laboratery for their sincere discussions. Especially we wish to express our particular thanks for Dr. Owaki and his assistants for their cooperation in preparing the experimental tubes.

References.

(1) H. Bruining, Physica, **5** (1938) 913.
H. Bruining & J. H. DeBoer, Physica, **6** (1939) 823 & 834.
(2) M. A. Pomerantz, Phys. Rev., **70** (1946) 33.
J. B. Johnson, Phys. Rev., **73** (1948) 1058.
S. Yoshida, I. Takeda & H. Arata, Monthly J. of Elec. Comm. Lab., (in Japanese) **2** (1949) 97.
(3) Worthing, Phys. Rev., **28** (1926) 190.
(4) L. Malter, Phys. Rev., **50** (1936) 48.
H. Kawamura & K. Hirano, Proc. Phys.-Math. Soc. Japan, **24** (1942) 211.
(5) T. Arizumi & L. Esaki, J. Phys. Soc. Japan **5** (1950) 163 and 174.
(6) E. A. Coomes, Phys. Rev., **55** (1939) 519.

On the Schottky Effect of the Oxide Coated Cathode

By Tetsuya ARIZUMI and Shin-ichiro NARITA.

Kobe Kogyo Corporation, Kobe.

(Received July 7, 1950)

§ 1. Introduction.

One of the authors(1) has pointed out that the abnormally small Richardson constant of the oxide coated cathode is mainly attributed to the coexistence of many different work functions, that is to say, the patchy structure of the cathode. Mahlmann's(2) recent paper seems to support our theory but there remains some doubt in some respects such that the work function of his cathode is larger than that of well activated one. In the present paper the Schottky effect of the oxide coated cathode will be studied for obtaining the experimental foundation of our theory.

§ 2. Theory.

The thermionic current from the oxide coated cathode is given by the following two relations:

$$\frac{n(N+n)}{n_0-n}=\left(\frac{2\pi mkT}{h^2}\right)^{\frac{3}{2}}\exp\left(-\frac{eE}{kT}\right) \tag{1}$$

and

$$i=n\frac{eD}{2\pi m}(2\pi mkT)^{\frac{1}{2}}\exp\left(-\frac{e\phi}{kT}\right) \tag{2}$$

In these formulae all notations are same as used in the previous paper(3). According to whether n_0 is much larger or much smaller than N, the following well known emission formula can be deduced respectively.

$$i = ADn_0^{\frac{1}{2}}T^{\frac{5}{4}}\exp\left\{-\frac{e}{kT}\left(\frac{E}{2}+\phi\right)\right\} \tag{3}$$

$$i = A'D'n_0T^2\exp\left\{-\frac{e}{kT}(E+\phi)\right\} \tag{4}$$

(3) is applicable to a well activated cathode at higher temperature, while (4) to an insufficiently activated one at lower temperature. Experimentally the thermionic work function of the cathode was found to decrease gradually from 1.7 e.v. to 1.0 e.v. as the cathode becomes activated⁽³⁾. Rigorously speaking, however, these formulae hold only for a single crystal.

As the practical cathode is of course composed of numerous fine crystals probably containing different quantity of excess barium, its emission current should be represented by the sum of emission of individual crystals. At high temperature, the difference in work function of individual crystals may well be neglected, because conduction electrons become so large that the emission of all crystals may be expressed by the relation (3). At low temperature, however, some crystals of comparatively small quantity of excess barium have larger work function than others. In other words, the cathode becomes to have the patchy structure and thus the deviation from the theoretical Schottky curve is considered to become remarkable at low temperature.

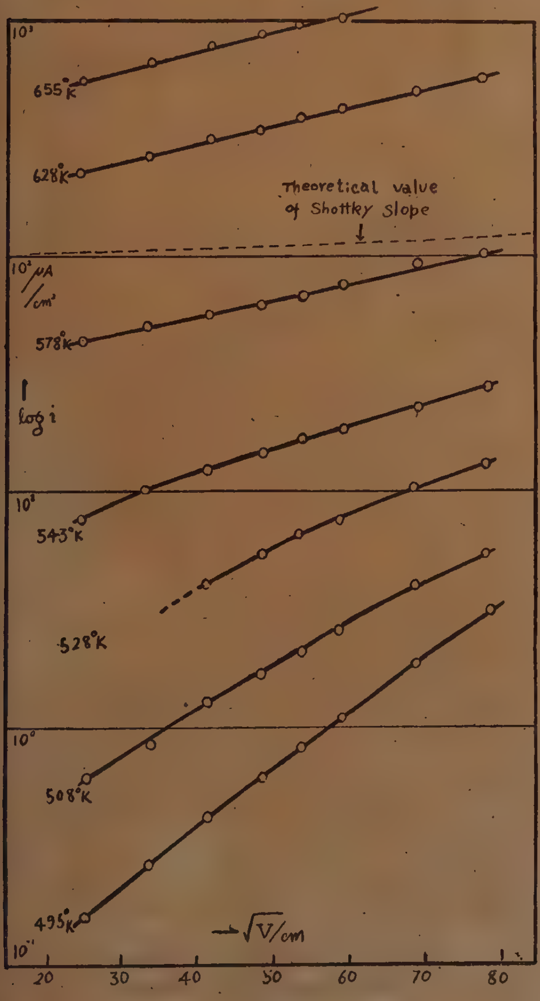

(a)

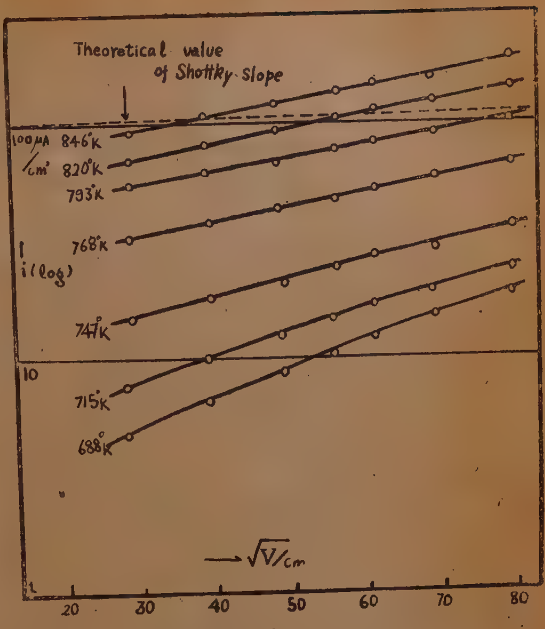

(b)

Fig. 1. Schottky curves of the oxide coated cathode: (a), activated cathode and (b), less activated cathode.

§ 3. Exerimental Results and Discussion.

The experimental tube was a diode of three separated anodes, customarily used for the thermionic experiments. The diameters of the cathode and anode were 1.3 mm. and 5 mm. respectively. The conductivity of the cathode was measured by an imbedded probe as described in the previous paper⁽⁴⁾.

The variation of the emission current with respect to the applied field strength are shown in Fig. 1 (a) and (b), in which (a) is curves for the activated cathode, while (b) for the less activated one. The inclinations of Schottky curves are almost linear and parallel each other so long as the cathode temperature is sufficiently high, but they are several times larger than expected from the thoretical calculation. This is caused by the surface roughness of the cathode as already pointed out by one of the authors⁽⁵⁾. At low temperature, however, the curves are not linear and their inclination becomes from five to fifteen times larger than the theoretical value, supporting the above mentioned prediction.

Re-plotting the obtained data in the Richardson diagramm, Fig. 2 (a) and (b) are obtained. At high temperature the work function is found to be 1.0 e.v., independently of the applied voltage, but at low temperature the work function ranges from 1.1 e.v. to 1.4 e.v. depending upon the applied voltage.

These results are considered to be originated from the patchy structure of the cathode. The theoretical calculation of the patch effect followed to A. Rose's⁽⁶⁾ procedure. Assuming the mosaic surface of two different work functions, as shown in Fig. 3, the relation between the patch field and the dimension of a patch is given as followed:

$$E_z = \frac{8\Delta V}{\pi S} \sum_{\substack{m,n \\ \text{odd}}} \left[\frac{(m^2+n^2)^{\frac{1}{2}}}{mn} \exp\left\{ \frac{\pi}{S}(m^2+n^2)^{\frac{1}{2}} z \right\} \sin\frac{m\pi}{S} X \cdot \sin\frac{n\pi}{S} Y \right] \tag{5}$$

All notations in (5) are same as defined in Rose's paper. The critical distance Z is represented by

$$\frac{d\phi}{dF} = Z \tag{6}$$

in which ϕ and F are the work function and the field strength respectively. The critical distance Z can be evaluated from Figs. 2 and 3. Both s ane ΔV are determined by choosing the experimental relation between F and Z to make the best agreement with the theoretical relation between E_z and Z. The estimated values of s and ΔV are about 3.10^{-4} cm. and 0.2 e.v., in the activated cathode, while they are $1 \cdot 10^{-3} \sim 3 \cdot 10^{-3}$ cm and 0.3∼0.4 e.v. in the cathode of low activity, suggesting that both the crystal size and the difference of the work functions become smaller as the cathode is activated.

The energy difference between the bottom of the conduction band and the Fermal level is written by

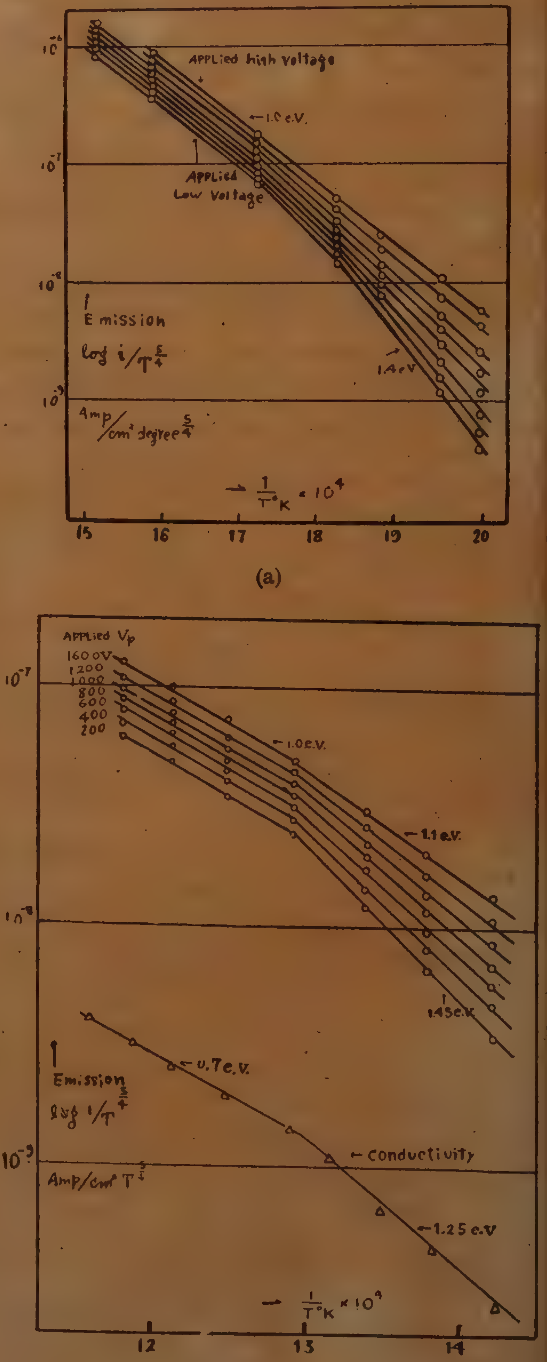

(a)

(b)

Fig. 2. The Richardson diagramm:
(a) activated cathode and
(b) less activated one.

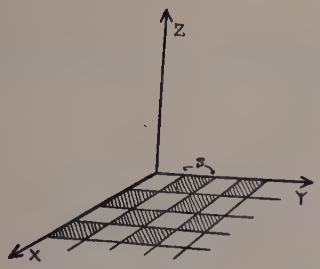

Fig. 3. The model of the patchy structure.

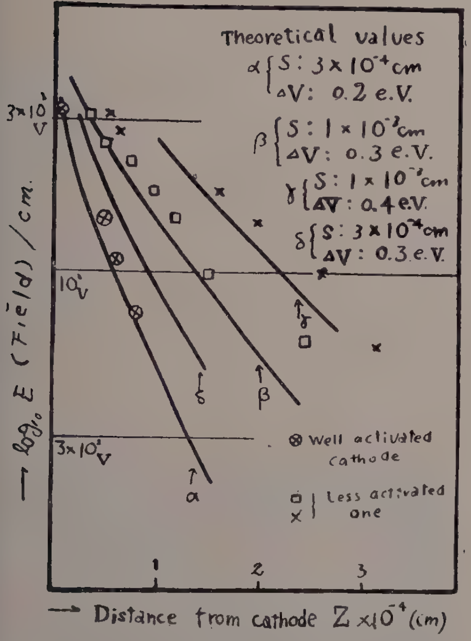

Fig. 4. The relation between the field strength and the critical distance.

$$W \doteqdot E\frac{N+n}{N+2n} \tag{7}$$

if n_0 is much larger than n and the term (3/2) (kT/e) is neglected. Thus the ratio of conduction electrons and that of free barium atoms in a well activated crystal to those in a less activated one can be evaluated, as presented in Table 1. The results show that the difference in the content of free barium atoms becomes smaller as the difference in the work functions becomes smaller.

It is added also that the discontinuous point in the Richardson line shifts to a higher temperature gradually as the activation of the cathode. An example is seen in Fig. 2, in which the discontinuity in the electrical conductivity is found to appear almost at the same temperature.

Table 1.

ΔV	when $n \approx N$ n/n'	n_0/n_0'	at high temperature n/n'
0.2 e.v.	4	6	2.4
0.3 e.v.	10	36	6
0.4 e.v.	25	30	7

§ 4. Summary.

The inclination of the Schottky curves are larger in the less activation cathode. At sufficiently high temperature they are parallel each other, but at low temperature they become steeper. The Richardson lines are also parallel at high temperature independently of the applied voltage, but they do not so at low temperature. These results can be understood from the patchy structure of the cathode. Applying Rose's theory, the average difference of work functions and the dimension of a crystal were estimated 0.2∼0.4 e.v. and $10^{-3}\sim10^{-4}$ cm. respectively. Both quantities become smaller as the cathode becomes activated. Such patchy structure is caused by the difference in the content of free barium atoms in individual single crystals.

We wish to acknowledge Mr. L. Esaki and all other members in our laboratory for their instructive discussions.

References.

(1) T. Arizumi: J. Phys. Soc. Japan **3** (1948) 191.

(2) G.W. Mahlmann: J. App. Phys. **20** (1949) 197.

(3) T. Arizumi & S. Narita: J. Phys. Soc. Japan **3** (1948) 356.

(4) T. Arizumi & S. Narita: J. Phys. Soc. Japan (now in press).

(5) T. Arizumi; Nippon Butsuri Gakkai-Shi (in Japanese) **1** (1947) 22.

(6) A. Rose: Phys. Rev. **49** (1936) 838.

Short Notes.

Effect of Stress on Domain Structure of Tungsten Trioxide WO_3.

By Ryuzo UEDA and Takeo ICHINOKAWA.

Department of Applied Physics,
Waseda University, Tokyo.

(Received October 20, 1950)

It has been recently found that the tungsten trioxide Wo_3 behaves like a ferroelectric and its monocrystal obtained from the melt is composed of multiple domains which are similar to that of $BaTiO_3$.(1),(2) Optilcal and X-ray observation performed by us showed that the crystal has a pseudo-orthorhombic symmetry; $a=7.278A$, $b=7.460A$, $c=3.838A$ and $\beta\sim90^0$. The c-axis is perpendicular to the flat plate of the monocrystal and the *a*- (or *b*-) axis within one domain component nearly perpendicular to the *a*- (or *b*-) axis in neighbouring components. The twinning occurs about {110} planes.(4)

We next studied the effect of temperature, electric field and the stress upon the domain structure of this substance. For $BaTiO_3$, these external factors have the large effect on the domain pattern below 120^0 at which temperature the multiple domains disappear. For WO_3, however, no distinct effect of temperature and the electric field was observed, although the pressure externally applied shows a remarkable effect upon domain pattern. The process under the stress seemed to be irreversible as shown in the accompanying photographs.

Fig. 1 shows the domain structure of WO_3, which is composed of many parallel stripes making an angle 45° to the plate edges and some wedge shaped domains as seen at the left hand corner of the photographs. The black arrow indicates the direction of the unidirectional pressure externally applied. A part bounded by a square in Fig. 1 is shown in the following enlarged photographs.

When a unidirectional pressure is applied, the domain components somewhat contract and twin boundary disappear gradually until the faint traces of the domain pattern can not be discriminated under the microscope (Fig. 3). When the stress is removed, however, the faint stripes recover their pattern very slowly, but their complete restoration to the original state could not be observed even 15 hours after the stress was removed (Fig. 4). If the pressure was furthermore increased after the twin boundary has vanished, the crystal became broken along the line parallel to one of the crystal edges. Under the external stress, tops of the wedge shaped domains recede from original positions to some extent and then stop there.

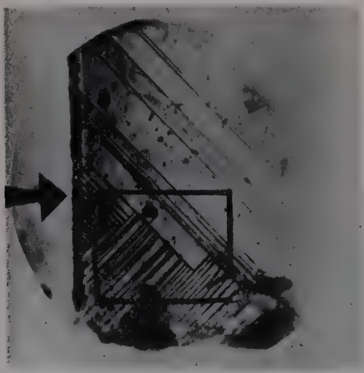

Fig. 1. A monocrystal of tungsten trioxide. The black arrow shows the direction of unidirectional pressure externally applied.

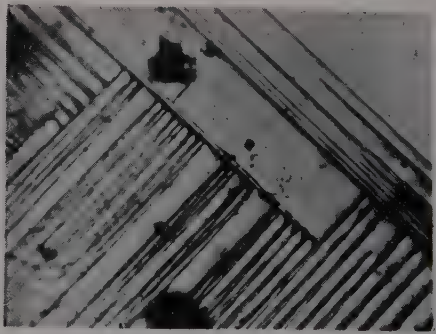

Fig. 2. A detail of the bounded square part of Fig. 1. The original state.

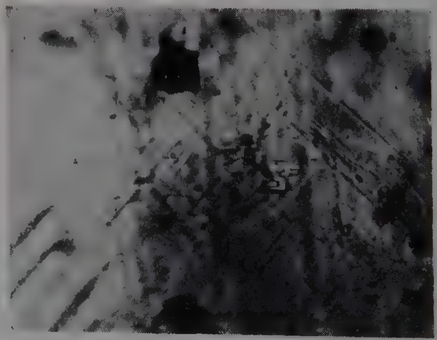

Fig. 3. The state under unidirectional pressure. The domain boundary has nearly vanished.

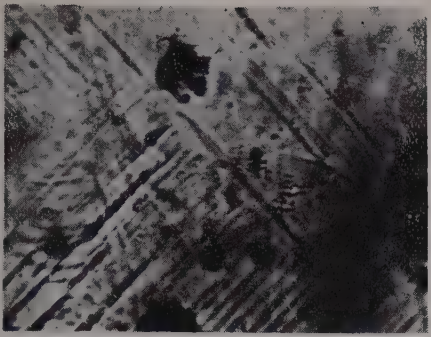

Fig. 4. The state 15 hours after the pressure was removed.

X-ray analysis of this substance performed by us showed that there is no distinct phase change from a low symmetry type to a high symmetry one between room temperature and about 500°C. The dielectric behavior of WO_3 is supposed to be different from that of $BaTiO_3$ in its nature.

The detail of the investigation will be reported in near future.

References.

(1) B.T. Matthias: Phys. Rev. **76** 430 (1949).

(2) K. Hirakawa: Busseiron-Kenkyu (in Japanese), **No. 26** (1950).
R. Ueda, T. Ichinokawa and Z. Kobayashi: ibid., **No. 29** (1950).

(3) R. Ueda and T. Ichinokawa: Phys. Rev. (in press).

Statistical Features in Static Friction.

By Hideo NAGASU.

(*Government Mechanical Laboratory*).

(Received Nov. 14, 1950).

The fluctuations of the coefficient of static friction between two steel blocks were measured under the following procedure.

Two test pieces of steel ($25 \times 25 \times 10$ mm^3) are piled up, each of the contacting surfaces having the same roughness, 10S,* finished by grinding. They are washed in ether after rinsed in benzol and dried up thoroughly. The upper block is pulled horizontally, *i.e.* in the direction parallel to the contact surface by the force f, where f is increased uniformly with time t, or $f = \alpha t$. When the upper block begins to slide at time t, the origin of which being taken that the force f begins to be applied, the coefficient of static friction μ is obtained by $\mu = \alpha t/L$, where L is the dead load normal to the contact surface. In this experiment L is always kept constant, $559g$, while α is varied in three ways, $0.9g/sec$, $1.8g/sec$, $4.8g/sec$, and the measurements were repeated more than 100 times for each value of α. Although the experimental conditions were maintained constant in all efforts, these observed values of μ showed noticeable fluctuations in wide range. By plotting each observed value of μ in the order of measurement, it is recognized that the mode of these fluctuations are the same from the begining till the end of experiment, namely, the whole observed values in one series of experiment may be looked upon as belonging to the same assemblage of some random events. Fig. 1 shows the frequency distribution of μ.

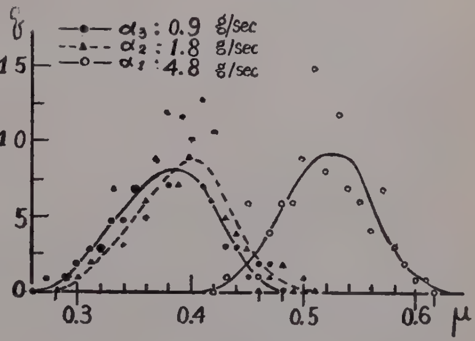

Fig. 1

Similar fluctuations have already been observed in sparking voltage[1] as well as in breaking strength of glass,[2] and successfully analysed by the statistical method. In the present case of friction, it seems natural to find the origin of the observed fluctuations, not in unavoidable lack of uniformity of experimental conditions, but in the stochastic nature of static friction itself.

In the course of experiment described above, if $W(t)$ is the probability that sliding does not happen till time t but happens in the next unit time interval, and $p(t)$ is the one that sliding happens later than t, we get

$$W(t)\,dt = -d\,[log\ p(t)].$$

$p(t)$ and $W(t)$, thus derived from the experimental data, are shown in Fig. 2 and Fig. 3 respectively. $W(t)$ increases rapidly with t, nearly satisfying the relation, $W(t) = A \cdot \exp(a\alpha t)$, where A and α being constant determined by the nature of contacting substances and temperature. This relation shows close resemblance, at least formal, to the case of breaking of glass by uniformly increasing stress. Starting from this relation we can calculate the probability that the coefficient of static friction lies between μ and $\mu+d\mu$,

---

* 10S means, after JES, the maximum height in the profil of surface is 4 μ–10 μ.

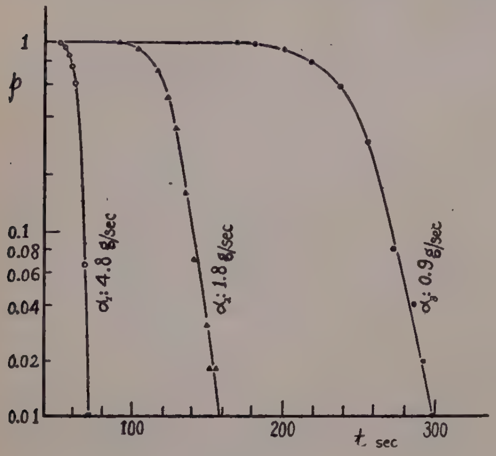

Fig. 2

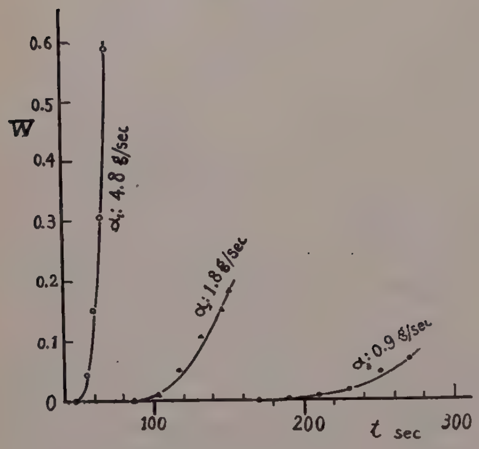

Fig. 3

$$q(\mu)\,d\mu = AL/\alpha\cdot\exp(aL\mu)$$
$$\times\exp[A/a\alpha\cdot\{1-\exp(aL\mu)\}]\,d\mu$$

which can explain pretty well the experimental result of Fig. 1.

We should, therefore, not expect a definite value for coefficient of static friction at any given condition, but refer to some statistical quantity. For example, let the coefficient of static friction with maximum frequency, μ_m, be such quantity,

$$\mu_m = 1/aL\cdot\log(a/A\cdot\alpha)\,,$$

showing clearly the effect of pulling rate of force α.

Details of experiment on the effect of surface roughness, oil film and material of test piece will be reported in near future.

The author expresses his hearty thanks to Prof. M. Hirata for his kind advice and encouragement.

Reference.

(1) L.B. Loeb, Rev. Mod. Phys. **20** (1948), 157.
(2) M. Hirata, Bull. Math. Statistics **3** (1949), 57.

Thermo-electromotive Force of BaO and (Ba-Sr)O

By Kin-ichi Noga.

Matsuda Research Laboratory,
Tokyo Shibaura Electric Co., Kawasaki.

(Received November 18, 1950)

The measurement of a thermo-electromotive force (T.E.M.F.) is one of the fundamental procedure in experimental study on the semiconductors, however, just a little have been reported on the T.E.M.F. in the oxide coated cathodes. So the author has carried out following experiments on this subject.

The construction of experimental vacuum tubes is shown in Fig. 1. In this figure, S_1 and S_2 are nickel sleeves, between which a layer of (Ba-Sr) CO_3 about 0.2mm in thickness is held. S_2 is pressed to S_1 with the tungsten spring P, to prevent S_1, (Ba-Sr)O and S_2 from the loose contact due to shrinkage in volume when (Ba-Sr) CO_3 is converted to (Ba-Sr)O. (J_1, J_2) and (J'_1, J'_2) are Pt-PtRh thermo-junctions of diameter of 0.03mm welded on the nickel sleeves. (L_1, L_2) and (L'_1,L'_2) are leads of diameter of 0.5mm made of the same materials as those used for the Pt-PtRh thermo-junctions. Thus there is no origin of misleading T.E.M.F. caused by the contact of different metals in the junction circuits. G is barium getter.

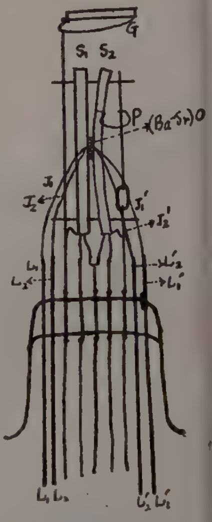

Fig. 1

Keeping S_1 at a constant temperature and varying the temperature of S_2, the T.E.M.F. $\Delta\theta$ for any temperature difference ΔT is obtained. $\Delta\theta$ is measured by means of zero method and ΔT is measured with two thermo-junctions (J_1, J_2) and (J'_1, J'_2). The relation between ΔT and $\Delta\theta$ is linear over the wide range from 0° to 50° C. From the gradients of these straight lines, $d\theta/dT$ can be obtained. The temperature dependency of $d\theta/dT$ is shown in Fig. 2. These curves correspond to several different activated stages

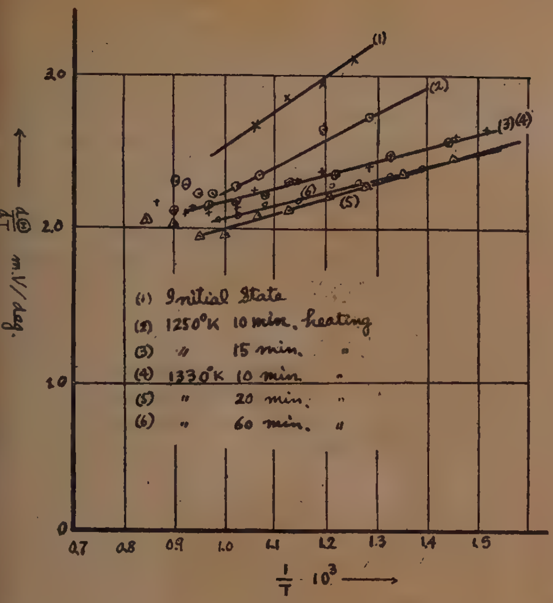

Fig. 2

designated in this figure. In three experimental tubes with (Ba-Sr)0 and two tubes with BaO, T.E.M.F's have large values from 1.8 to 2.8 $^{\mathrm{mV}}/_{\mathrm{deg}}$ in the temperature range from 750° to 1200°K. The chemical potential ζ's, evaluated from the following equation

$$\frac{d\Theta}{dT}=-\frac{\zeta}{eT},$$

have also unexpectedly large values of 1.8—2.6 e.v for our experimental values of $d\Theta/dT$. Using the next relation

$$\zeta=-\frac{\Delta E}{2}+\frac{kT}{2}\log\frac{nh^3}{2(2mkT\pi)^{3/2}},$$

the atomic concentrations n's of impurity centers are estimated from our experimental data at various temperature. These values were always lower than 10^{11} per cm³. The activation energies of thier conductivities $\frac{\Delta E}{2}$'s measured at the same time were about 0.4—0.6 e.v in the same temperature range. The above-mentioned values of concentrations of impurity centers are too small to be explained by the usual Wilson model with single impurity level proposed by Nishibori and Kawamura.(1)(2) The relation between the magnitude of T.E.M.F and the activity is remained unresolved.

Generally, the sign of T.E.M.F showed the N type semi-conductor for (Ba-Sr)O. But P type appeared for the very poor activated state. Unfortunately, the quantitative results could not be obtained since it's conductivity was very low.

Further, the additive term in T.E.M.F. proposed by J. Yamashita(3) has the value of 0.25 $^{\mathrm{mV}}/_{\mathrm{deg}}$ in these temperature rage, provided that the Debye temperature is 320°K. Debye temperature of BaO is estimated from the zero-point energy described in the work of Mayer and McMaltbie.(4) This additive term does not affect the general tendency in our case.

It is also impossible to explain the above-mentioned results and another model would therefore be required. But the data of T.E.M.F. are usually insufficient to offer us the exact information for the electronic state of the crystal. Hence, the author is intending to undertake the experiments on the Hall effect and optical properties in this crystal.

References.

(1) E. Nishibori and H. Kawamura: Proc. Phys.-Math. Soc. Jap. **22** (1940) 378.
(2) E. Nishibori, H. Kawamura and K. Hirano: Proc. Phys.-Math. Soc. Jap. **23** (1941) 37.
(3) J. Yamashita: Jour. Phys. Soc. Jap. **4** (1949) 310.
(4) J. M. Mayer and M. McMaltbie: Z. S. f. Phys. **75** (1932) 749.

Notes on the Thermoelectric Properties of Bismuth.

By Takao SATO.

Institute of Applied Science, Faculty of Engineering, University of Kyushu.

(Received July 1, 1950).

The value of the thermoelectric power is obtained from the thermoelectromotive force measured on a sample which is given a small temperature difference between its two ends. The thermoelectric power is calculated by dividing the thermoelectromotive force with the temperature difference. In this case the thermoelectromotive force is assumed to be proportional to the temperature difference between the two ends. This assumption may of course be correct for simple metals and alloys, but it seems worth while to test its validity for substances such as bismuth, having a semi-metallic property and a very complex electronic structure.

We measured the thermoelectromotive force of pure bismuth (Kahlbaum) and a bismuth alloy containing 0.2 atomic percent tin for varied temperature difference. The specimens are of a cylindrical form of about 5 mm in diameter and about 50 mm in length. The two ends of the sample are coupled with pure platinum wire, and the thermoelectromotive force is measured by a potentiometer. The temperature difference is measured by the deflection of a galvanometer connected with a Pt-PtRh differential thermocouple which is calibrated beforehand by a mercury thermometer carefully.

In order to know the electronic structure of the specimens, we measured first the temperature dependency of their electrical resistances. The results are shown in Fig. 1. The temperature coefficient of the pure bismuth is positive, but that of the bismuth alloy becomes negative⁽¹⁾ as general semi-conductors. The thermoelectromotive force of these specimens was measured for various temperature differences by keeping the one end of the sample rod at constant temperatures 16°C (room temperature), 110°C and 217°C, and from these data we calculated thermoelectric power for various temperature differences. We show it in Figs. 2 and 3 for the pure bismuth and the bismuth alloy, respectively. In the case of the pure bismuth, for 16°C and 110°C, the thermoelectric power has a sharp maximum at a temperature difference of about 0.5–0.8°C and is nearly constant beyond abont 3°C. For 217°C, the thermoelectric power first increases with the temperature difference and becomes nearly constant beyond about 2°C. In the case of the bismuth alloy, the variation of the thermoelectric power is similar for 16°C, 110° and 217°C, that is, the thermoelectric power increases rapidly with the temperature difference and then becomes constant beyond about 2°C.

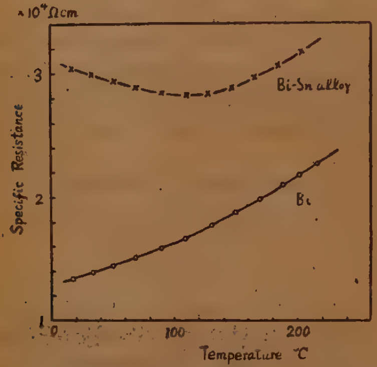

Fig. 1. The specific resistance *vs.* temperature curve of the pure bismuth and the Bi–Sn alloy.

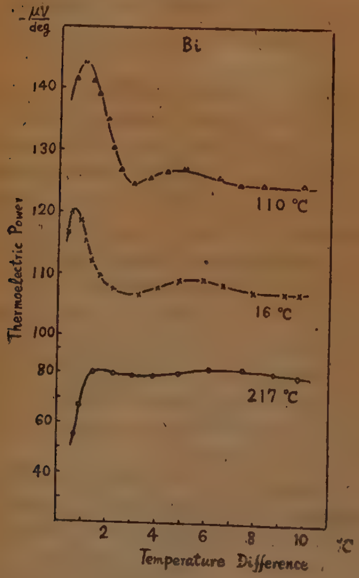

Fig. 2. The thermoelectric power *vs.* temperature difference curve of pure bismuth at the constant temperatures 16°C (room temperature), 110°C and 217°C.

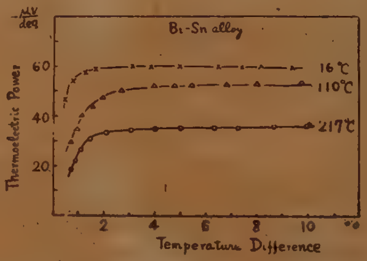

Fig. 3. The thermoelectric power *vs.* temperature difference curve of the Ai–Sn alloy at the constant temperature 16°C (room temperature), 110°C and 217°C.

Fig. 4 shows the temperature dependency of the thermoelectric power measured for a suitable temperature difference, namely, about 3–5°C for the pure bismuth and about 2–4°C for the bismuth alloy, wherein the thermoelectric power does not change abruptly with the temperature difference. In the case of bismuth alloy, anomalous behavior of the thermoeleotric power is not found though

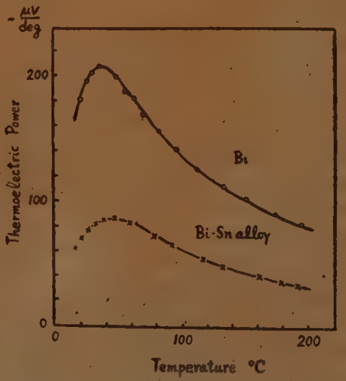

Fig. 4. The tgermoelectric power *vs.* temperature curve of the pure bismuth and the Bi–Sn alloy.

here is a temperature region of the negative emperature coefficient of the electrical resistance. For pure bismuth, the temperature dependency f the thermoelectric power differs from the result btained by Borelius and Lindth(2) which is showing no maximum in the low temperature region as bserved in our case.

From the above results, we found that the hermoelectric power of bismuth depends on the emperature difference, though the reason for it s not clear at present. Further studies are ecessary in order to reach a definite conclusion.

The writer is indebted to Prof. A. Okazaki for his valuable discussions and to Prof. K. Omori for his kind encouragement and continued interest.

References.

1) N. Thompson: Proc. Roy. Soc. **A 155** (1936) 111.

A. B. Focke and J. R. Hill: Phys. Rev. (2) **50** (1936) 179.

2) G. Borelius and A. E. Lindth: Ann. d. Phys. **51** (1916) 607.

A New Apparatus for Electric Arc Weldings.

By Tasaburô Yamaguti and Minoru Nishino.

Department of Physics, Faculty of Literature and Science, Ibaraki University.

(Received December 16, 1950)

Electric arc weldings of thin plates by lternating currents are known to be difficult, lthough some apparatuses, working with superposition of high frequency electric oscillations which stabilize the electric arcs, are invented. With use of our new apparatus to be described below, however, iron plates thicker than about .5 mm can be easily welded even by a nonprofessional in welding works. Moreover, warpngs of the plates welded are slighter and the peed of the welding is quicker than by the gas welding.

Fig. 1 shows the electric circuit of the pparatus. A_1 is the mother plates to be welded nd A_2 is the welding rod. T is a neon-transormer, and the terminals of the secondary of it re connected with a spark gap S and high tension ondensers, C_1 and C_2, both of which have capaities of about 1000 p.F. The primary of the eon-transformer is connected with the source E f alternating current power of 100 volts, 50 cycles vith insertion of a switch B.

The switch B being on, the currents of high requency oscillations flow through a closed circuit $C_1SA_1A_2C_2C_1$ (circuit 1), and at the same time due to the low voltage electric power, electric arcs start between the plates and the rod, both separated from each other. Maximum distances for the start of the arcs are about 4 mm to 7 mm for 6 kv to 15 kv of the secondary voltages of the neon-transformer to be used.(1) The inductance L of about 30 μH is inserted in a circuit 2, as shown in the figure 1, to prevent the high frequency current flowing through this circuit, and the resistance R to regulate the arc currents. C_3 is a condenser of 2 μF and 300 volts proof.

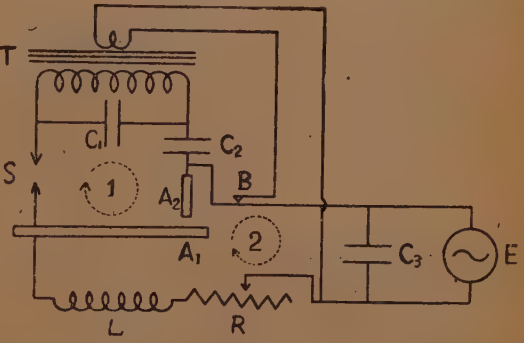

Fig. 1.

By using this apparatus, most suitable values of arc currents and diameters of the rods which weld iron plates of some thickness finely are determined experimentally. Results are shown in Fig. 2 taking the welding currents to the abscissa and the diameters of the rods of titanian type to the ordinate, and representing the values for fine weldings with coordinate points of white marks and others with black ones. The marks of different forms correspond to different thickness of the plates. We can see that the dotted lines,

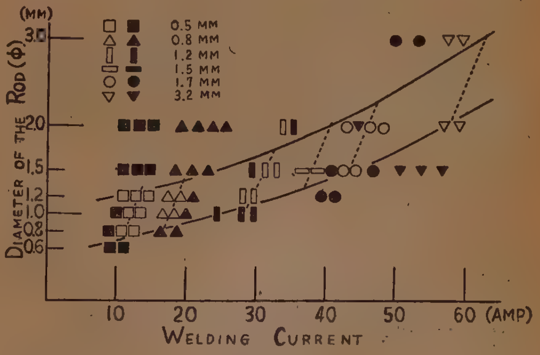

Fig. 2.

---

(1) Relations among the maximum distances and constants of elements of the high frequency oscillations are experimentally determined, and will be reported in Jour. App. Phys. Japan, 1951.

which express the most suitable current-diameter curve for each thickness, are nearly parallel, and can also see that the white marks are distributed between two curves represented by full lines. Thus, we can choose from this figure both an arc current and a rod which are most suitable for welding the plates of a given thickness.

To diminish the disturbances for the radio, all parts of the apparatus except the plate, the rod and a part of the circuits connected with them, are shielded electrically. With such shieldings the high frequency oscillations scarcely affect a radio placed in a distance more than about 50 meters from the apparatus, if the power for the radio and for the apparatus are not taken from the same transformer.

At the end, authors' thanks are due to Dr. H. Ogawa of the Hitachi Laboratory, who kindly manufactured the welding rods for their disposal.

Volume Change at Three Transitions in $BaTiO_3$ Ceramics.

Gen Shirane and Akitsu Takeda.

Tokyo Institute of Technology, Oh-okayama, Meguroku, Tokyo.

(Received December 20, 1950)

Linear thermal expansion of $BaTiO_3$ ceramics has been measured at temperatures from −170° to 200°C. The specimen was prepared from pure TiO_2 (99.2%) and $BaCO_3$ (99.6%) by a process of sintering at about 1400°C after the first calcination. Dielectric constant of this specimen shows three peaks at −77°, 16° and 125°C, corresponding to the well known three transitions in this substance(1) (Fig. 1).

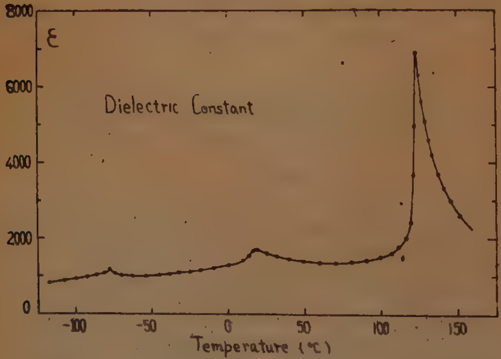

Fig. 1. Dielectric constant of $BaTiO_3$ at rising temperature (1 MC/sec).

The dilatometric test sample has a cylindrical form, 3 cm in length and 4 mm in diameter. Differential dilatation of this specimen relative to a silica rod was magnified about 1000 times as large by means of an optical lever. Measuring limit of this apparatus is $\Delta l/l = 3\times10^{-6}$. Fig. 2 shows the heating curve of $l-l_0/l_0$ where l_0 represents the length at 0°C. Linear thermal expansion coefficient β is plotted in the same figure. Cooling curve shows the same characteristic except a small hysteresis at the transitions.

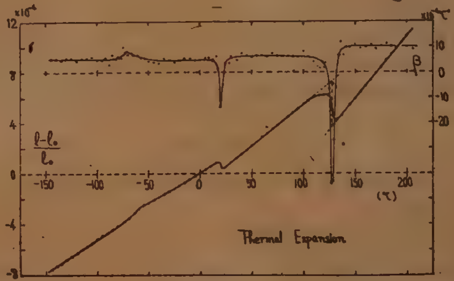

Fig. 2. Thermal expansion of $BaTiO_3$ ceramics; β is linear thermal expansion coefficient.

The changes of unit cell volume at the three transitions are estimated by extrapolation from the linear part of each phase:

$+0.008\text{Å}^3$ at −77°C,
-0.015Å^3 at 16°C,
-0.070Å^3 at 125°C.

In addition, linear thermal expansion coefficient of this specimen is estimated for each phase as follows:

5.2×10^{-6}/°C: below −77°C (Trigonal phase),
4.6×10^{-6}/°C: −77°∼16°C (Orthorhombic phase),
6.5×10^{-6}/°C: 16°∼125°C (Tetragonal phase),
9.8×10^{-6}/°C: above 125°C (Cubic phase).

This result shows qualitative agreement with the former dilatometric measurements(2)(3). But there are some differences between our data and the results of X-ray analysis of single crystal by Kay and Vousden(4) and by Rhodes(5). Some of the discrepancies may be due to the differences between the lattice change of a single crystal and the macroscopic change of ceramics.

Thermal expansion of (Ba 75-Sr 25) TiO_3 shows the same tendency, the volume changes being $+0.006\text{Å}^3$ (at −86°C), -0.011Å^3 (at −36°C) and -0.027Å^3 (at 34°C). On the other hand, the situation is slightly different for (Ba 95-Pb 5) TiO_3, the volume changes being $+0.006\text{Å}^3$ (at −96°C), $+0.007\text{Å}^3$ (at −14°C), and -0.040Å^3 (at 143°C).

We wish to express our sincere thanks to Professor Y. Takagi for his kind guidance and also to Mr. C. Kanzaki for giving us pure ingredients.

References.

(1) See, for instance, A. von Hippel: Rev. Mod. Phys. **22** (1950) 221.

(2) A. von Hippel, R. G. Breckenridge, F. G. Chesley and L. Tisza: Ind. Eng. Chem. **38** (1946) 1097.

(3) S. Sawada and G. Shirane: J. Phys. Soc. Japan **4** (1949) 52.

(4) H. F. Kay and P. Vousden: Phil. Mag. (7) **40** (1949) 1019.

(5) R. G. Rhodes: Acta Cryst. **2** (1949) 417.

Existence of the Superlattice $CuAu_3$.

By Makoto HIRABAYASHI.

Tokyo Institute of Technology,
Oh-okayama, Tokyo.

(Read November 5, 1950. Received December 27, 1950)

One of the best known order-disorder transformations in binary alloys is that of the Au–Cu system. The alloys of this system form an isomorphous series of solid solutions and crystallize upon a face-centered (cubic) lattice. According to theories there should be three superlattices at Cu_3Au, CuAu and $CuAu_3$. The results obtained at the first two compositions well conform to theoretical prediction, as has been shown by the X-ray investigations(1) and the measurements of specific heat(2). But at the third composition, only inconclusive evidence of a superstructure $CuAu_3$ has been obtained, though Johansson and Linde(3) noticed the presence of very weak superlattice lines in their X-ray diffraction photographs. Now in order to ascertain the existence of this superstructure $CuAu_3$, we measured at elevated temperatures the specific heat of an alloy containing 74 atomic % Au and performed at the same time the intensity measurements of X-ray diffraction patterns.

Fig. 1 gives the specific heat-temperature curves measured at a heating rate of about 2°C/min. The method used is a modification of the Sykes' one as already reported by NAGASAKI and TAKAGI(4). Curve A is obtained with the alloy quenched from 600°C into water. It shows at first a little heat evolution and then a little heat absorption. Curve B which refers to the specimen previously annealed at 200°C for 20 days and then slowly cooled to room temperature in 7 days, shows clearly an anomaly of λ-type peak at 243°C. The amount of energy $\varDelta E$ absorbed between 130°C and 270°C is calculated from this curve to be about 270 cal/mol. By further investigations it was found that the amount of transition energy is kept nearly constant for various periods of annealing provided it is longer than 30 days. The experimental value of $RT_c/\varDelta E$ is 2.6, where R is the gas constant and T_c the critical temperature. Generally speaking this value is very reasonable for the order-disorder transformation. The specimen treated in the above mentioned manner may thus be regarded as being almost in thermal equilibrium, or well ordered state.

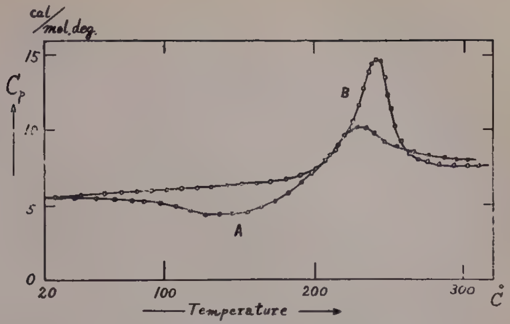

Fig. 1. Specific heat-temperature curves for a Cu–Au alloy of 74 atomic % Au.

We took several X-ray back reflection photographs of a polycrystalline specimen after annealing at 200°C for 1 month, using Cu-K_α radiation. An example of microphotometer traces of patterns reproduced in Fig. 2 shows the existence of superstructure lines such as (210), (211), (300) and so on. In order to get an evidence as to whether or not the order is perfect, we compared the relative intensities of normal and superstructure lines observed with those calculated for the perfect order. Both values agree within experimental errors. It may be concluded, therefore, that the alloy after the above mentioned treatment is almost perfectly ordered.

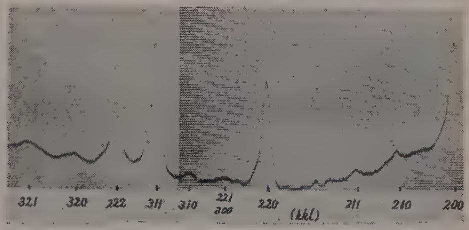

Fig. 2. Microphotometer trace of pattern for the well ordered alloy.

We measured the electrical resistivity of the well ordered alloy on reheating, and found that the transformation from an ordered state to a disordered state is accompanied by a decrease of resistivity. This rather queer behaviour was also reported by earlier investigators(5). Indeed this decrease seems to be inconsistent with the usual concept of order-disorder transformation, but the present author believes that it would probably be explained by the lattice distortions which can at times be accumuleted in highly ordered state⁽⁵⁾ owing to the inequality of the atomic radii between Au and Cu. The more detailed results will shortly be published in the Journal of the Japan Institute of Metals.

In conclusion, the author wishes to express his sincere thanks to Professor Y. TAKAGI and Mr. S. NAGASAKI for their valuable suggestions and continued interest in the course of this work.

References.

(1) E.C. Bain: Chem. and Met. Eng. **28** (1923), 65.

C.H. Johansson and J.O. Linde: Ann. d. Phys. **78** (1925), 439.

(2) C. Sykes and F.W. Jones: Proc. Roy. Soc. **A157** (1936), 213.

M. HIRABAYASHI, S. NAGASAKI and H. MANIWA: J. Jap. Inst. Met. **B 14** (1950), No. 3, 1.

(3) C.H. Johansson and J.O. Linde: Ann. d. Phys. **28** (1936), 1.

(4) S. NAGASAKI and Y. TAKAGI: J. App. Phy. Jap. **17** (1948), No. 5, 104.

(5) Y. TAKAGI: "On the Deviation of the Atomic Sites in Binary Alloys." Presented at the Annual Meeting Phys. Soc. Jap., University of Osaka, November 1∼5, 1950.

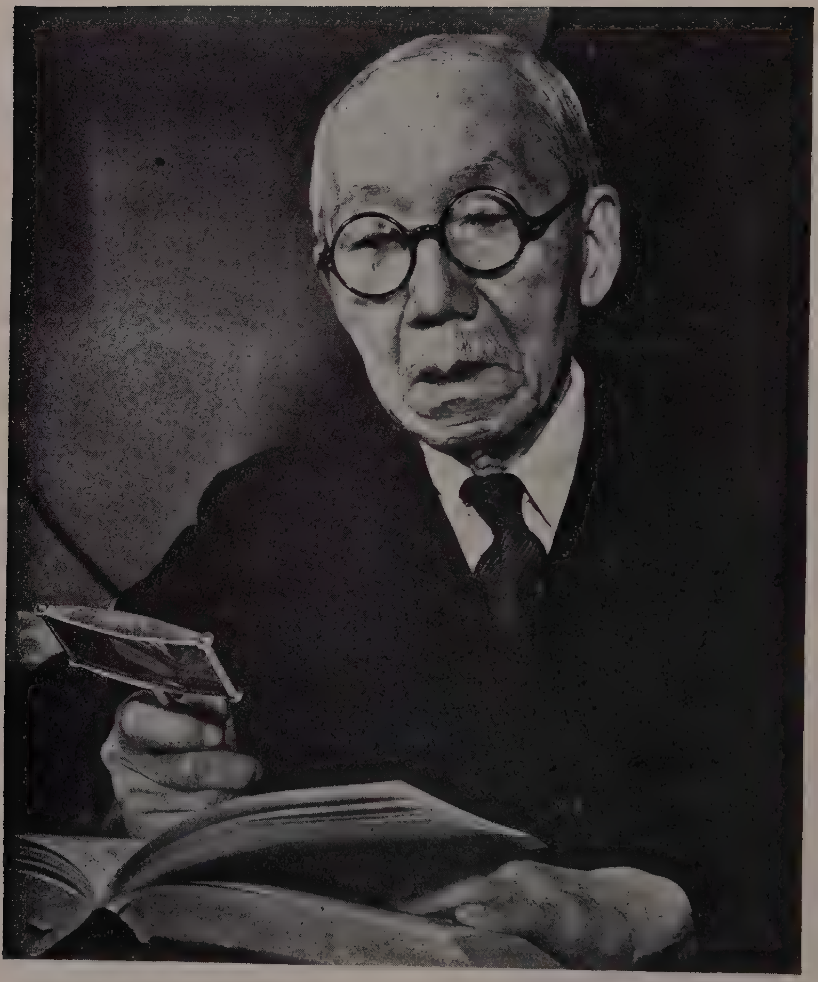

Photograph by Shigeru Tamura

Hantaro NAGAOKA
(1865–1950)

Obituary Notice of Professor Hantaro NAGAOKA

It is with profound grief that we record here the passing of one of the honorary members of the Society, Professor Hantaro Nagaoka, on Dec. 10th, 1950 at the age of 85.

Born on Aug. 18th, 1865, Professor Nagaoka graduated the course of physics in the College of Science of the Tokyo Imperial University in 1887. Getting his Doctor's degree in 1893, he went to Germany for three years' study. On returning home in 1896, he was appointed to professor of physics in the same university, which position he held until 1926, up to the time of his retirement. He was elected a member of Imperial Academy in 1905.

For a period extending over twenty years, namely from 1926 to 1945, he continued his research work at the Institute of Physical & Chemical Research in Tokyo (now Scientific Research Institute). It is to be mentioned that Prof. Nagaoka has been occupying a most important place in this Institute from the very beginning of its establishment in 1917.

Even after he left the Institute in 1945, he carried on his research work dealing with geophysical problems at home for five years up to 1950, indeed until just one hour before the end of his life.

The scope of his research works was extremely wide and extensive. In its earlier stage, a great deal of work was done on geophysics with Prof. A. Tanakadate, followed by those on magnetism and magnetostriction with Prof. K. Honda, both with considerable achievement. In its middle stage, his interest was turned to spectroscopy. His extensive contributions in this domain are notable, especially those on hyperfine structure and the Zeeman effect on various spectrum lines. Those and many other spectroscopic studies constituted in fact the main part of his work from 1900 to 1945.

Outstanding among his numerous works, amounting over 300, is his memorable paper concerning the atomic model which was read in 1903. The importance of this work immediately aroused the world-wide interest and recognition. Whereas it is true that many alterations were necessitated by later findings, the fact that an idea of this uniqueness had been introduced by Prof. Nagaoka prior to the celebrated work by Bohr in 1913, is no doubt of considerable significance and worthy of mention.

It is to be remembered that Prof. Nagaoka has always been taking great pains in instructing and giving guidance to the younger physicists who came in touch with him. When we consider that the enormous number of his pupils and followers, distributed all over Japan, are actually constituting the backbone of physics in this country, we cannot fail to be deeply impressed by the inestimable contribution he thus left behind him.

Honors were flooding in to meet his unparalled attainments, thus in 1912, he was nominated as one of the few Honorary Fellows of the Physical Society of London, among whom are Mme. Curie, Lorentz, Michelson and others. In 1925, he received the honorary degree of Doctor of Philosophy (honoris causa) from Cambridge University in England. In Japan, he was among the first recipients of "Bunkwa Kunsho", a medal of great distinction, in 1937.

As regards the prominent positions he held, we note that he was the first president of the Osaka University when it was newly established in Osaka in 1931. Further, he has been the president of the Imperial Academy during the years of 1939 & 1948. He was elected as an honorary member of our Society in 1950.

It would be superfluous to mention that very few men have ever had a career as brilliant as that of Prof. Nagaoka, and his name will long be remembered as one of the founders of physics in Japan.

Looking over his unprecedented career one cannot fail to recognize that at the base of his years of tireless endeavor lies the child-like simplicity for the love of Nature. We are reminded of the words Prof. Nagaoka has often been quoting himself: "In order to study Nature, one must be like a child."

T. T.

On the Superlattice Formation in Binary Alloys of Body Centred Cubic Type.

By Shoichi MATSUDA.

Faculty of Engineering, Ibaraki University.

(Received March 6, 1950).

§1. Introduction.

It is found experimentally that the superlattices of the type AB and A_3B are formed in several binary alloys of body centred cubic type, and that the behavior of their formations are manifold for different kinds of alloys. For example, the superlattices of both AB and A_3B types arise in Fe-Al system, but in Fe-Co system only the superlattice of type AB is found. The former theories* concerning the formation of superlattice are not sufficient to answer this problem. In those theories, the formation of superlattice is discussed by taking into account the interaction between atoms on nearest neighboring lattice points and the interactions between second neighboring atoms are considered as an only factor giving a small correction to the result. But it can be seen from the geometrical configuration of the A_3B type atomic arrangement that the latter interaction plays an important role in the formation of the superlattice of A_3B type. Then, taking both interactions into account and introducing proper parameters defining the degree of atomic arrangements of both types, the manifoldness of the superlattice formation in different binary alloys of body centred cubic type are discussed in this paper. The results reproduce the behavior of the superlattice formation in iron-aluminium system satisfactorily.

§2. Quantities Defining an Atomic Arrangement.

A body centred cubic lattice is considered to be made up of four interpenetrating face centred cubic lattices which have twice lattice constant of the original one (confer Fig. 1).

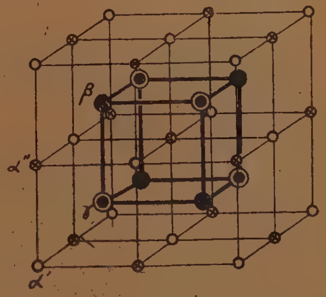

Fig. 1.

Those four kinds of lattice points are denoted by α'—, α''—, β and γ— sites respectively. However, if only AB and A_3B type superlattices are in consideration, distinction between α' and α'' sites is not necessary, so that both α' and α'' sites are denoted by α site for the following discussion. Let the number of lattice points (whole number of atoms) be N, then the numbers of A and B atoms are expressed by xN and $(1-x)N$ respectively. Let the numbers of α, β and γ sites be $\theta_\alpha N$, $\theta_\beta N$ and $\theta_\gamma N$. In the case considering now, $\theta_\gamma = 1/2$ and $\theta_\beta = \theta_\gamma = 1/4$. If the numbers of A and B atoms on i-site ($i = \alpha$, β, γ) are denoted by $A_i\theta_iN$ and $B_i\theta_iN$, then

$$A_\alpha + B_\alpha = A_\beta + B_\beta = A_\gamma + B_\gamma = 1\,. \qquad (1)$$

As the sum of A atoms on α, β and γ sites is equal to the total number of A atoms, so the following relation is obtained.

$$A_\alpha\theta_\alpha N + A_\beta\theta_\beta N + A_\gamma\theta_\gamma N = xN\,. \qquad (2)$$

As shown in (1) and (2) four relations exist among six atomic fractions A_α etc., so that, two of them, for example A_α and A_β are independent and are sufficient to specify the number of atoms on each site. Now we define new parameters P_1 and P_2 instead of A_α and B_α by the following expressions.

---

* Full bibliographic surveys are found in the following articles; C.F. Nix. W. Shockley: Rev. Mod. Phys., 10 (1938), 49. H. Sato: RITU, 1 (1949), 71.

$$\left.\begin{aligned} P_1 &= A_\alpha - B_\alpha = 2A_\alpha - 1\,, \\ P_2 &= A_\beta - B_\beta = 2A_\beta - 1\,, \end{aligned}\right\} \tag{3}$$

Then atomic fractions are expressed by

$$\left.\begin{aligned} &A_\alpha = \frac{1}{2}(1+P_1)\,, && B_\alpha = \frac{1}{2}(1-P_1)\,, \\ &A_\beta = \frac{1}{2}(1+P_2)\,, && B_\beta = \frac{1}{2}(1-P_2)\,, \\ &A_\gamma = 4x - \frac{3}{2} - P_1 - \frac{1}{2}P_2\,, && B_\gamma = \frac{5}{2} - 4x + P_1 + \frac{1}{2}P_2\,. \end{aligned}\right\} \tag{4}$$

Consequently, P_1 and P_2 can be seen as the quantities defining the order of atomic arrangement.

§3. Thermodynamic Functions Relating to Atomic Arrangement and Equilibrium Condition.

Let V_{AA}, V_{AB}, V_{BB} and W_{AA}, W_{AB}, W_{BB} be interaction potentials between atoms in the nearest and second neighboring lattice points denoted by suffix letters, and it is assumed that they are constant throughout the temperature change and also independent of the concentration of atoms. As the interatomic distance between the second neighboring atoms is only 1.15 times that of nearest neighboring atoms, so the magnitudes of both potentials are comparable each other in general. Then denoting the numbers of atomic pairs consisting of nearest and second neighboring atoms by $[A-A]_{\rm I}$, $[A-A]_{\rm II}$, etc. respectively, the configurational energy is given by

$$\begin{aligned} E = {} & W_{AA}[A-A]_{\rm I} + V_{AB}[A-B]_{\rm I} + V_{BB}[B-B]_{\rm I} \\ & + W_{AA}[A-A]_{\rm II} + W_{AB}[A-B]_{\rm II} + W_{BB}[B-B]_{\rm II}. \end{aligned}$$

Expressing with P_1 and P_2, it takes the following from**

$$\begin{aligned} E(P_1,\, P_2) = C + 2VN\Big\{ & (2x-1)(P_1 + \lambda P_2) \\ & - \frac{1}{2}P_1^2 + \frac{\lambda}{4}(P_1^2 - 2P_1P_2 - P_2^2)\Big\}, \end{aligned} \tag{5}$$

where

$$\left.\begin{aligned} & V = V_{AA} + V_{BB} - 2V_{AB}\,, \\ & W = W_{AA} + W_{BB} - 2W_{AB}\,, \\ & \lambda = 3W/4V, \\ & c = \left(4V_{BB} + V + 3W_{BB} - \frac{3}{4}W\right) \\ & \qquad + \{4(V_{AA} - V_{BB}) + 3(W_{AA} - W_{BB})\}x. \end{aligned}\right\} \tag{5}$$

On the other hand, configurational entropy of the alloy is expressed by

$$\begin{aligned} \Phi(P_1,\, P_2) &= k \log \prod_i \binom{\theta_i N}{A_i \theta_i N} \\ &= -\frac{kN}{4}(2A_\alpha \log A_\alpha + 2B_\alpha \log B_\alpha \\ &\qquad + A_\beta \log A_\beta + B_\beta \log B_\beta + A_\gamma \log A_\gamma + B_\gamma \log B_\gamma). \end{aligned} \tag{7}$$

Then, the free energy of the alloy relating to atomic arrangement can be given by

$$F(P_1,\, P_2;\, T) = E(P_1,\, P_2) - T\Phi(P_1,\, P_2).$$

Consequently, the following equilibrium conditions are obtained

$$\left.\begin{aligned} & \frac{\partial E}{\partial P_1} - T\frac{\partial \Phi}{\partial P_1} = \left\{2x - 1 - (1-2\lambda)P_1 - \frac{x}{2}P_2\right\} \\ & \qquad\qquad + X \log \frac{A_\alpha B_\gamma}{B_\alpha A_\gamma} = 0\,, \\ & \frac{\partial E}{\partial P_2} - T\frac{\partial \Phi}{\partial P_2} = 2\lambda\left\{2x - 1 - \frac{1}{2}(P_1 + P_2)\right\} \\ & \qquad\qquad + X \log \frac{A_\beta B_\gamma}{B_\beta A_\gamma} = 0\,, \end{aligned}\right\} \tag{8}$$

where $X = kT/8V$.

The order of atomic arrangement of the alloy in the equilibrium state is given by solving the above equations.

Now, we can distinguish the characteristics of atomic arrangement given by solutions of (8) as following three types. It is easily found that the equations (8) have a solution of a type

$$P_1 = P_2 = 2x - 1 \tag{9}$$

and it gives the random arrangement of atoms on the lattice points, for it becomes $A_\alpha = A_\beta = A_\gamma = x$ and $B_\alpha = B_\beta + B_\gamma = 1 - x$. Such an arrangement of atoms is designated by type III. Next, if there is such a relation as

$$P_1 + P_2 = 2(2x - 1) \tag{10}$$

between P_1 and P_2, the second equation of (8) is automatically satisfied. It is easily found that the relation (10) gives $A_\beta = A_\gamma$ and $B_\beta = B_\gamma$. These relations mean that the atomic arrangement for

---

** The calculation of the numbers of atomic pairs is carried out by using the method of zeroth approximation given by R. H. Fowler & E. A. Guggenheim "Statistical Thermodynamics", Cambridge (1939). 1314.

the solution of this case can be seen as an AB type superlattice, because of disappearance of distinction between β and γ sites. Such a atomic arrangement is denoted by type II. Lastly the atomic arrangement for the other solutions of (8) is denoted by type I. A_3B type superlattice is included in type I. If such three types of atomic arrangement can exist in equilibrium at the same temperature, the most stable state corresponds to the atomic arrangement having the least free energy.

§4. Atomic Arrangement in Equilibrium.

The formation of superlattice in consideration is greatly influenced by the ratio of the relative interaction potential V and W or the value of λ. We now discuss this problem for various cases under such assumption that the nearest neighboring atoms of different kinds is more stable than that of the same kind, that is, the case $V>0$. It was found by Bragg-Williams' theory that the ordering of atomic arrangement always occurs in this case if $W=0$.

(i) $W<0$ or $\lambda<0$: The atomic arrangement of type I forms when it holds (a)

$$A_\beta\theta_\beta N > A_\gamma\theta_\gamma N, \quad B_\gamma\theta_\gamma N > B_\beta\theta_\beta N$$

or (b) $$A_\beta\theta_\beta N < A_\gamma\theta_\gamma N, \quad B_\gamma\theta_\gamma N < B_\beta\theta_\beta N.$$

For each case, the following relations are obtained

$$\frac{\partial\Phi}{\partial P_2} = -\frac{kN}{8}\log\frac{A_\beta B_\gamma}{B_\beta A_\gamma}\begin{cases}<0 \text{ for (a)}, \\ >0 \text{ for (b)}.\end{cases} \tag{11}$$

Accordingly, in order that (8) has solutions, the following relations must hold

$$\frac{\partial E}{\partial P_2} = 2\lambda\left[2x-1-\frac{1}{2}(P_1+P_2)\right]\begin{cases}<0 \text{ for (a)}, \\ >0 \text{ for (b)}.\end{cases}$$

or, for $\lambda<0$

$$2x-1-\frac{1}{2}(P_1+P_2)\begin{cases}>0 \text{ for (a)}, \\ <0 \text{ for (b)}.\end{cases}$$

But the values of P_1 and P_2 in the above range do not satisfy (11) for both cases. If the solution of (8) exists in case of $\lambda<0$ excluding that of the type III, it must be $\partial\Phi/\partial P_2=0$ or $P_1+P_2=2(2x-1)$, which is the condition (10) for type II arrangement. Therefore the solution of type I does not exist. If eq. (8) has a solution, it must be that of type II.

(ii) $W=0$ or $\lambda=0$: This means no interaction between atoms on second neighboring lattice points. Putting $\lambda=0$ into second equation of (8), it follows $P_1+P_2=2(2x-1)$, that is, the relation (10) holds. And so the solution of type II exists alone excepting that of type III.

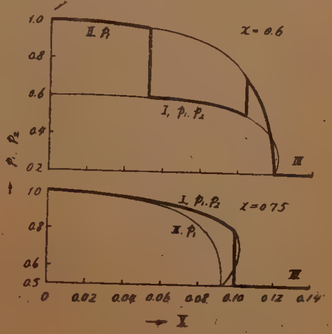

Fig. 2.

(iii) $W>0$ or $\lambda>0$: The atomic arrangement of type I arises in this case. Fig. 2 shows some examples of the stable solutions of equilibrium condition (8) for the case of $\lambda=0.5$ or $V:W=3:2$. The curve I etc. correspond to the solutions of type I (A_3B) etc. respectively. The thick full line indicates the most stable state which has the lowest free energy for given temperature (X) among the solutions of three types. In the case of $x=0.6$, for example, the atomic arrangement changes discontinuously at certain points as II→I→II→III successively with the rise of temperature, and in the case of $x=0.75$ as I→III.

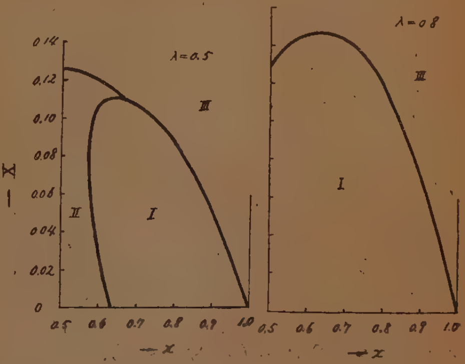

(a) (b)

Fir. 3.

From these results, the phase diagram of

Fig. 3a, showing the regions of stable existence of the atomic arrangements of three types, is obtained. The regions I, II and III are the existing ranges of tppe I (A_3B), II (AB) and III (random arrangement) respectively. The curve shows the transition temperature between different types of arrangements. The curve in the range $0 \leq x \leq 1/2$ has symmetric form about the atomic composition of $x = 0.5$. When λ becomes large, the range for type I (A_3B) predominates gradually. Fig. 3b. gives the phase diagram for the case of $\lambda = 0.8$ or $V:W = 3:3.2$. In this case, type II is unstable and only type I appears as the superlattice structure over the whole composition.

In general, for the cases of $\lambda = 0$an d $\lambda < 0$, the superlattice of type II (AB) arises alone. For the positive values of λ, the superlattice structure of type I (A_3B type) emerges in the range of type II and the area of its region in phase diagram becomes larger with increasing λ. With more increase of λ, the region I spreads over whole composition range, and the region of type II disappears as shown in Fig. 3b.

§5. Comparison with Experimental Results.

The superlattice formations in the case of body centred cubic lattice considered above are observed in Fe-Si, Cu-Zn, Fe-Co, Fe-Cr (metastable phase) Fe-Al alloy etc. Among these the superlattice in Fe-Al alloy in the phase of body centred cubic lattice is studied by Sykes-Evans⑴ Osawa-Murata⑵, Bradley-Jay⑶ etc. Although these experimental results do not coincide with each other, it can be concluded from the above cited investigations that the Fe_3Al type superlattice is formed near the composition of $Fe:Al = 3:1$ ($x = 0.75$), and Fe-Al type near the composition of $Fe:Al = 1:1$ ($x = 0.5$). Thus the phase diagram given by Osawa-Murata (*l.c*) is well reproduced by the above theoretical conclusion (Fig. 3a). Fig. 4 shows the relation between fractional number of aluminium atoms on γ sites and atomic composition by Bradley and Jay's experiment by X-ray analysis. In the composition range a-b, the fractional number of Al atoms varies along a straight line II for both rapidly cooled and annealed alloy; such arrangement of atoms corresponds to FeAl (AB) type superlattice. In the range b–c, the fractional number changes along curve I for annealed alloy and this arrangement is due to Fe_3Al (A_3B) type, while for quenched alloy, the fractional number changes along the straight line II corresponding FeAl (AB) structure. In the range c–d, perfect random state appears (straight line III). These results suggest that in equilibrium, the FeAl type superlattice is formed in a–b composition range. In b–c, Fe_3Al type exists at room temperature and FeAl type at higher temperature, and in c–d, there is no ordered arrangement of atoms. It can be considered that this result agrees qualitatively with theoretical one in the case of $\lambda = 0.5$. If one takes the temperature parameter X to be $X_1 = 0.11$ for quenching temperature and $X_2 = 0.09$ for room temperature, then the fractional number of B atoms (Al atoms) on γ sublattice can be calculated on the basis of the equilibrium condition (8) by putting $\lambda = 0.5$. The results thus obtained is shown in

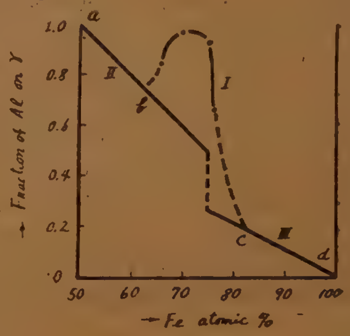

Fig. 4.

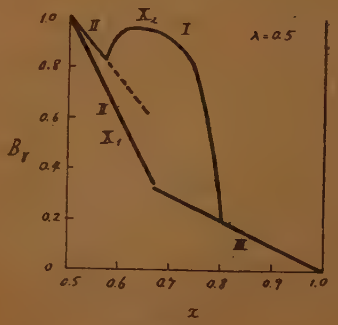

Fig. 5.

Fig. 5. The lines II and III indicate B_T for type II (AB) and type III (random distribution). The curve I is for type I (A_3B). If one compares Fig. 4 and Fig. 5, one will find the coincidence between the both theoretical and experimental results on atomic arrangement in Fe-Al system.

In cases of Fe-Co and Fe-Cr alloy, it is reported that AB type superlattice alone is found. These will be considered to be the cases of zero value of λ or negative value from the reason mentioned in the previous article.

In conclusion, the author expresses his thanks to Prof. T. Hirone for his kind advice throughout this work.

References.

(1) C. Sykes and H. Evans: Proc.Roy. Soc., **145A** (1934), 529.

(2) A. Osawa and T. Murata: Kinzoku-Gakkai Shi, **5** (1941), 259.

(3) A. J. Bradley and A. H, Jay: Proc. Roy. Soc., **136A** (1932), 210.
F. C. Nix and W. Shockley: Rev. Mod. Phys., **10** (1938), 49.

Structure of Thin Metallic Films Formed by Evaporation on Molybdenite.

By Yoshiro Kainuma.

Physical Institute, Nagoya University.

(Received Sept. 11, 1950).

§1. Introduction.

There are already many investigations by means of electron diffraction on the preferred orientation of metallic crystallites deposited on crystal surfaces by evaporation in a vacuum. Uyeda⁽¹⁾ studied the growth of submicroscopic silver crystallites on the cleavage surface of molybdenite and concluded that the preferred orientation is induced by the periodic field of surface force, denying the view that it is due to cracks and steps on the surface. A further investigation on this line was developed by Miyake and Kubo⁽²⁾ for many kinds of metals on zincblende and a few other crystals; and they discussed the formation of oriented crystallites with many experimental evidences.

In this paper the author reports on the results of a similar experiment with six face-centered cubic metals on the cleavage surface of molybdenite.

§2. Experimentals.

Metals used in this experiment were gold, copper, nickel, platinum and aluminium. They were evaporated in a vacuum with pressure less than 10^{-4} mm Hg and deposited on the cleavage surface of molybdenite placed in a small electric furnace. The temperature of the furnace was between room temperatures and 500°C. The evaporation was carried out after it had been kept constant for about 30 minutes. The thickness of the deposit was about 20∼100A estimated from the amount of evaporated metal. The specimen was cooled in the vacuum and remounted on the specimen-holder of an electron diffraction camera⁽³⁾. The diffraction pattern was obtained by the reflection method with the electrons of about 40 KV.

§3. Experimental Results.

(a) The type of orientation of silver crystallites on the cleavage surface of molybdenite studied by Uyeda⁽¹⁾ is shown schematically in Fig. 1; *viz.* (111) plane of silver is parallel to the cleavage surface and [110] axis of the former is parallel to [100] of the latter. There are two orientations, denoted by A and A′ in the figure, which are mirror reflections to each other across the (100) plane of the latter. In this case the diffraction pattern obtained when the primary beam is directed along [100] axis is symmetric across the central line, showing that both orientations appear with equal frequencies. This type of orientation, which we call the *symmetric* for convenience, was observed in many cases in the present experiments. In some cases, however, the *asymmetric* one was also observed, where one of the orientations predominated over the other (Photo. 1.).

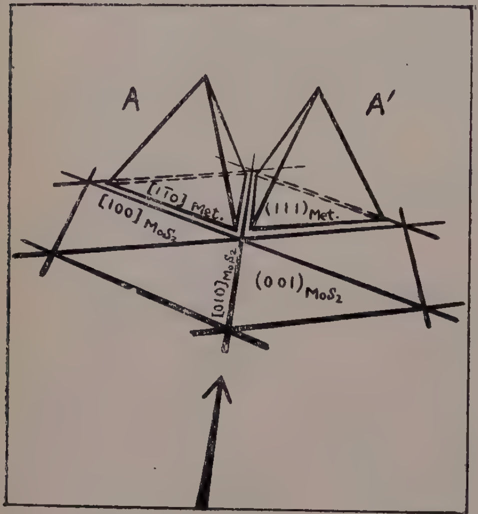

Fig. 1. Schematic picture of the symmetric type orientation.

All the experimental results are summarized in Fig. 2; the abscissa in this figure is the temperature of the base crystal at which the metal was deposited, and the cross means the symmetric type, the triangle the asymmetric one and the circle the random orientation.

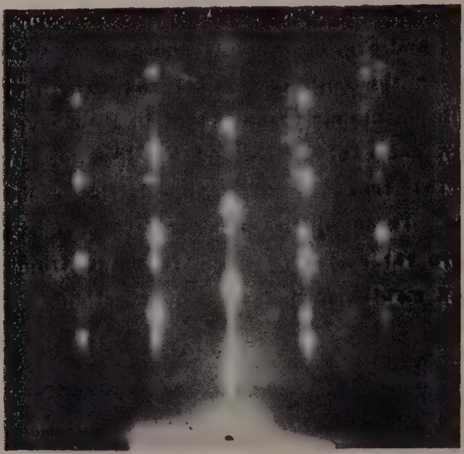

Photo. 1. The asymmetric type diffraction pattern produced by gold.

(b) If well cleft surfaces were used, the asymmetric pattern remained unchanged when different parts of the surface were irradiated by parallel displacements of the primary beam. Moreover, the pattern changed regularly to its mirror images across the central line when the crystal was turned by 60° around the axis normal to the surface. Some irregularities, however, were observed if the cleavage surfaces used were less perfect.

(c) It was verified by the following procedure that the prevailing orientation in the asymmetric type of gold is the same as that of nickel; *i.e.* both the A– or both the A′– orientation. Gold was evaporated on a half area of a specimen by covering the other half by a sheet of mica, and then nickel was evaporated on the other half. The asymmetric pattern of the same nature was

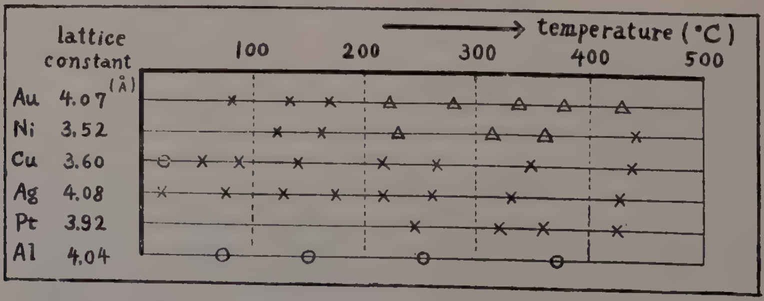

Fig. 2. Types of orientation observed.

× : the symmetric type △ : the asymmetric type
○ : the random orientation

obtained by irradiating each part of the specimen by displacing the incident beam in parallel.

(d) The transition temperature, where the symmetric type changed to the asymmetric one, was raised by about 90°C in the case of gold, if the evaporation was carried out without keeping the temperature constant for a long time.

§ 4. Discussions.

(a) Molybdenite belongs to the space group D_{6h}^{4}–C6/mmc of the hexagonal system and has a layered structure as shown in Fig. 3. Each layer which is a sandwich of S–Mo–S has only a trigonal axis perpendicular to the layer and the successive layer coincides with each other by a glide-reflection, *i.e.* the translation c/2 and the reflection across (100) plane. Therefore, the field of surface force should also be trigonal, and if there are no steps on the surface, the appearance of the asymmetric type of orientation is reasonable from the consideration of symmetry. The experimental results described in (b) of the previous section prove that a well cleft surface of molybdenite has *no steps* and a less perfect one has a few. This fact gives a strong support to the previous conclusion by Uyeda(4) that the preferred orientation is induced by the periodic field of surface force and not by steps and cracks.

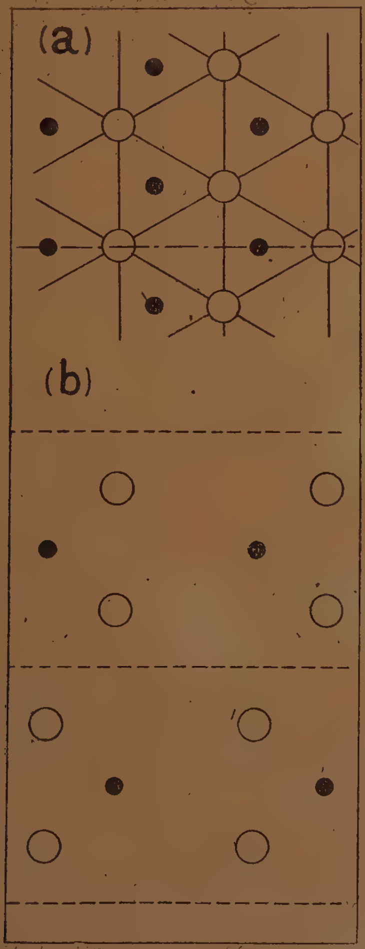

Fig. 3. Atomic arrangement in molybdenite crystal; the small circles are Mo and the large ones are S atoms.
(a) Basal projection of a sandwich layer.
(b) Vertical section through the chain line of (a).

(b) The field of surface force is trigonal as is described above, but the deviation from the hexagonal symmetry may be small because it is almost determined by the hexagonal array of sulphur atoms in the uppermost layer. The deviation may be due either directly to the molybdenum atoms in the second atomic layer or indirectly to the distortion of the sulphur atoms.

The atomic arrangement in the first layer of metallic crystallites which are in contact with the surface of molybdenite is the same for both A- and A′- orientation. They are discriminated by the arrangement (relative to the base crystal) in the second layer. The appearance of the asymmetric type means that the deviation from the hexagonal symmetry of the force is effective either directly in the position of the second layer or it is so indirectly through the distortion of the first layer.

(c) Aluminium showed only the random orientation. This may be caused by inevitable contaminations in our experiment. It may be reasonable to consider that contaminations may disturb the perfect orientation in general, and this effect is remarkably enhanced for aluminium, because this metal is exceedingly reactive than the other ones.

The reason why the asymmetric type occurs in some cases and the symmetric one in others cannot yet be made clear. The observed types of orientation given in Fig. 1. show correlations neither with the lattice constants nor with the degrees of chemical inertness to sulphur.

(d) Miyake(3) supposed that adsorbed oxygen molecules on the cleavage surface of zincblende might influence the orientations of copper and interpreted that the fall of transition temperature by baking was due to the desorption of adsorbed molecules. In the present case, however, the simple molecules such as nitrogen, oxygen, etc. might have been desorbed under the condition when the experiment was carried out, because the uppermost layer of molybdenite consists only of sulphur atoms. It is more reasonable to infer that the fall in the transition temperature is caused by the desorption of the long chain molecules such as reported by the author and Uyeda previously(4). They form oriented two-dimensional crystals on the cleavage surface of molybdenite. Their peripheries which may behave as if the steps of base crystals, may induce the symmetric type of orientation in a range of temperature where the asymmetric one should occur if the surface is clear enough.

In conclusion the author expresses his sincere thanks to Professor R. Uyeda for his kind guidance and encouragement and to Professor S. Miyake for his valuable discussions. The expense of this study was defrayed from the Grant in Aid for Foundamental Scientific Research of the Education Ministry.

References.

(1) R. Uyeda: Proc. Phys.-Math. Soc. Jap. **22** (1940) 1023; **24** (1942) 809.

(2) S. Miyake: Unpublished. S. Miyake: Busseiron Kenkyu **4** (1944) 17. Nippon Butsurigakkai-shi **1** (1946) 6. S. Miyake and M. Kubo: J. Phys. Soc. Jap. **2** (1947) 15; 20. M. Kubo and S. Miyake: J. Phys. Soc. Jap. **3** (1948) 114.

(3) R. Uyeda: X-sen **4** (1944) 28. G. Honjo: Busseiron Sosho **2** p. 214. (Asakura, Tokyo, 1949).

(4) Y. Kainuma and R. Uyeda: J. Phys. Soc. Jap. **5** (1950) 199.

Faraday Effect of Strong Electrolytes in Aqueous Solutions. IX. The Temperature Dependence of the Molecular Rotation Constants. 1.

By Atuyosi OKAZAKI.

Physical Institute, Faculty of Science, Kyusyu University.

(Received, June 1, 1950)

§1. Introduction.

In this paper we report the results of investigations of the magneto-optical rotations for *D*-lines of aqueous solutions of NaCl, KCl and KBr at 35°C. The apparatus and the method of procedure employed in the present measurements of the rotations are the same as shown in the previous paper(1).

The results are discussed in terms of the specific rotation constant which is defined by

$$[D]=\frac{n\omega\lambda^2}{s(n^2+2)^2}=\frac{n[\omega]\lambda^2}{(n^2+2)^2}, \qquad (1)$$

where n, ω and $[\omega]$ are, respectively, the refractive index, Verdet's constants (in min. per cm. gauss) and the specific rotation of a substance for the wave-length λ (in cm.), and s is its density.

The mixture rule for $[D]$ is expressed by the formula

$$[D]=\tau_1[D_1]+\tau_2[D_2], \qquad (2)$$

where $[D]$, $[D_1]$, $[D_2]$: the specific rotation constants of the solution, the solvent and the solute, respectively,

τ_1, τ_2: the grams of the solvent and the solute in 1 gram of the solution.

From the above formula we can find the dependence of the molecular rotation constant $\Phi \equiv M[D_2]$ of the electrolyte (M = its molecular weight) in aqueous solution upon the concentration.

§ 2. Experimental Results.

NaCl used was from Merck (guaranteed reagent), KCl Kahlbaum (kryst. zum Analyse) and KBr Merck (extra pure crystal). The concentration of a solution was determined by evaporation of a definite quantity of the solution, the salt thus obtained being dried at about 300°C in an electric drying oven until a constant weight of the salt was reached.

From a number of rotation measurements during the present experiment, we obtained the values 6.99° and 0.95° as the rotations due to the redistilled water at 35°C and due to the end plates of the polarimeter tube for D-lines when the magnetic field was reversed. By using the above value for water and the formula given by Rodger and Watson⁽²⁾ for Verdet's constant ω_t^D of water at t°C for D-lines, that is.

$$\omega_t^D = 0.01311\,(1-0.0000305t-0.00000305t^2), \qquad 3<t<98, \tag{3}$$

the change of magnetic potential on reversal of the field was found to be 32145 gauss cm.

The results obtained are tabulated in Table I, in which the densities s were determined by graphical interpolation from the data given by Hölemann and Kohner⁽³⁾, and Shibata and Hölemann⁽⁴⁾. The molecular rotations $M[\omega_2]$ of the electrolytes in solution, which can be calculated from Schönrock's mixture rule

$$[\omega] = \tau_1[\omega_1]+\tau_2[\omega_2], \tag{4}$$

are also given in the table so that they may be compared with the results at 25°C in the previous papers⁽⁵⁾. The values corresponding to $\tau_2 = 0$ were obtained by graphical extrapolation. It is shown from this table that the molecular rotations $M[\omega_2]$ of these electrolytes at 35°C are almost constant in the range of the concentration investigated, while at 25°C they tend to decrease with increasing concentration as shown in the previous paper.

In order to calculate the specific rotation constant $[D]$ of the solutions by means of the formula (1) using the $[\omega]$-values given in Table I, we need to use the values of the refractive indices measured at the same temperature as in the present measurement of ω. Thus the data concerning the refractive indices from Hölemann and Kohner⁽⁶⁾ for NaCl and KBr and Shibata and Hölemann⁽⁷⁾ for KCl were adopted. The values of the refractive indices n in the above data having been plotted against τ_2, the required value of n for a definite value of τ_2 was obtained by graphical interpolation. The calculated values of $[D]$ are shown in Table II. The $[D]$-values corresponding to $\tau_2 = 0$ is the specific rotation constant of pure water, viz. $[D_1]$. The molecular rotation constants $M[D_2]$ computed by means of the formula (2) are shown in the last column of the table.

Table I.

(The ω-value corresponding to $\tau_2 = 0$, i.e. Verdet's constant ω_1 of pure water, is obtained from the formula (3)).

$100\tau_2$	s	ω	$[\omega]$	$M[\omega_2]$
1. NaCl		M = 58.46		t = 35°C
0	0.99406	0.013047	0.013125	(1.18)
10.35	1.0673	0.01478	0.01385	1.175
13.87	1.0931	0.01538	0.01407	1.163
17.03	1.1171	0.01601	0.01433	1.181
21.39	1.1511	0.01685	0.01464	1.181
25.02	1.1807	0.01762	0.01492	1.187
2. KCl		M = 74.55		t = 35°C
0	0.99406	0.013047	0.013125	(1.24)
11.12	1.0652	0.01437	0.01349	1.22
14.11	1.0853	0.01480	0.01364	1.25
17.33	1.1072	0.01523	0.01376	1.25
21.33	1.1358	0.01577	0.01388	1.24
25.11	1.1637	0.01631	0.01402	1.24
3. KBr		M = 119.02		t = 35°C
0	0.99406	0.013047	0.013125	(2.23)
14.66	1.1070	0.01543	0.01394	2.23
17.78	1.1340	0.01594	0.01406	2.18
20.97	1.1622	0.01660	0.01428	2.21
25.59	1.2060	0.01757	0.01457	2.23
31.96	1.2718	0.01900	0.01494	2.24
36.90	1.3277	0.02014	0.01517	2.23

Table II.

$100\tau_2$	C	n_D	$[D]\times 10^{12}$ min. cm.^{2}	$M[D_2]\times 10^{10}$ min. cm.^{2}

1. NaCl $t = 35°C$

0	0	1.33142	4.263	(3.51)
10.35	1.975	1.3490	4.446	3.53
13.87	2.755	1.3552	4.499	3.49
17.03	3.511	1.3608	4.564	3.53
21.39	4.654	1.3687	4.639	3.52
25.02	5.708	1.3753	4.705	3.52

2. KCl $t = 35°C$

0	0	1.33142	4.263	(3.78)
11.12	1.678	1.3464	4.338	3.68
14.11	2.204	1.3504	4.375	3.77
17.33	2.812	1.3548	4.400	3.76
21.33	3.637	1.3604	4.422	3.73
25.11	4.498	1.3658	4.451	3.74

3. KBr $t = 35°C$

0	0	1.33142	4.263	(6.72)
14.66	1.443	1.3496	4.473	6.77
17.78	1.817	1.3538	4.499	6.65
20.97	2.229	1.3584	4.556	6.74
25.59	2.889	1.3652	4.627	6.76
31.96	3.947	1.3752	4.713	6.75
36.90	4.913	1.3838	4.756	6.67

In plotting $M[D_2]$-values against the concentration, the latter was expressed in equivalents per 1000 g H_2O which is represented by C as given in the 2nd column of Table II. We then obtained very nearly straight lines, for all the electrolytes under investigation, as shown in Fig. 1, so that an extrapolation to infinite dilution could be carried out. The resulting values for $C = 0$, i.e. the molecular rotation constant $M[D_2]$ in dissociated states, are given in the 1st line of the same table.

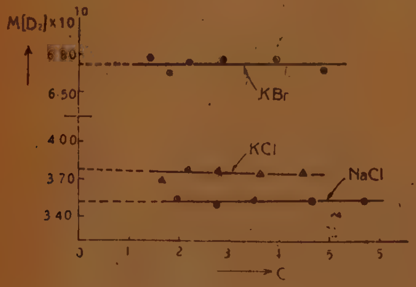

Fig. 1.

From Table II as well as Fig. 1 it is found that the $M[D_2]$-values of these electrolytes at 35°C are nearly independent of the concentration, while those at 25°C tend to decrease with increasing concentration as shown in the previous papers. This difference may be attributed to the increase of dissociation degree at higher temperatures. The molecular rotation constants at infinite dilution are smaller at 35°C than at 25°C, as shown in Table III.

Table III.

$M[D_2]$-values at infinite dilution.

Compounds	25°C	35°C
NaCl	3.77×10^{-10}	3.51×10^{-10}
KCl	4.05 〃	3.78 〃
KBr	6.94 〃	6.72 〃

It has been shown in the previous papers(8) that the molecular rotation constant of an electrolyte at infinite dilution is given by the sum of the component ionic rotation constants, i.e.

$$\Phi = \Phi_+ + \Phi_- .$$

According to this additive law, we have the differences between the two ionic rotation constants, i.e. the values for $K^+ - Na^+$ and $Br^- - Cl^-$, at 25°C and 35°C from Table III. It is found that these differences are nearly independent of the temperatures, as shown in Table IV.

Table IV.

	25°C	35°C
KCl—NaCl	0.28×10^{-10}	0.27×10^{-10}
KBr—KCl	2.89 〃	2.94 〃

In conclusion I wish to xpress my hearty thanks to Mr. H. Inomata for his assistance in this investigation. I am also indebted to the Japan Society for the Promotion of Scientific Research for financial aid.

References.

(1) A. Okazaki: Proc. Phys.-Math. Soc. Japan. **24** (1942), 40.
(2) J.W. Rodger and W. Watson: Phil. Trans. **A 186** (1895), 621.
(3) P. Hölemann and H. Kohner: Z. f. phys. Chem. **B 13** (1931), 338.
(4) Z. Shihata and P. Hölemann: ibid. **B 13** (1931), 347.
(5) A. Okazaki: Ryojun Coll. Eng., Mem. **9** (1936), 13; *ibid.* **9** (1936), 101; *ibid.* **12** (1939), 45.
(6), (7) *loc. cit.* These data refer to D_2-line (5876A).
(8) A. Okazaki: Ryojun Coll. Eng., Mem. **9** (1936), 101; *ibid.* **12** (1939), 45.

On the Temperature Effects of Spurious Counts in Geiger-Mueller Counters

By Motoharu KIMURA.

Department of Physics, Tohoku University, Sendai.

(Received July 6, 1950)

Abstract

The temperature effect on the rate of spurious discharges in G. M. counters (hard glass sealed-off type with out-gassed cathode of $2\,\mathrm{cm}\,\phi \times 5\,\mathrm{cm}$) was observed when they were heated and cooled at constant rates. As shown in Fig. 2∼9, on the heating stage, the rate of natural counts increased in various manners which depended on the filling gases and on the cathode material, and decreased rapidly on the cooling stage without exception. It was verified that these discharges were due to the so-called "Spontanentladung" of Trost and the occurrence of the double or triple discharges (Nachentladung) was very small. The plateau curves were taken with gamma ray source and also without any source before and after each experiment, and we could not find marked changes in them, though those with natural counts became generally better after cooled. The plateau lengths were generally between 100 to 500v, with the slopes of 0.6% to 10%/100v. The counts decreased exponentially with the square root of time when the counter was kept at constant temperature near 100°C after raised to that point. Tentative explanation can be made along the lines of so-called Malter effect of the thin oxide film of the cathode. But we can not neglect the effect of adsorption and evaporation of the quenching gas molecules and also the negative ions at the cathode surfaces.

§ 1. Introductions.

The temperature effects of the Geiger-Mueller counters were studied by Sonoda and Kimura⁽¹⁾, Minakawa⁽²⁾, Joyet and Simon⁽³⁾, Korff, Spatz and Hilbery⁽⁴⁾, Brown⁽⁵⁾, Parkash⁽⁶⁾ and by also Louw and Naudé⁽⁷⁾. Keuffel⁽⁸⁾ and Hereford⁽⁹⁾ have studied on the spurious discharges of the parallel plate counters, and Hereford have found some interesting results on the temperature effect of parallel plate counters. The researches of these authors are generally concerning the changes in the plateau characteristics by temperature, and it seems no definite conclusions are obtained till now, though the present author does not have a chance to know the results of Joyet et. al. and also of Korff et. al.

According to the investigation of A. Trost⁽¹⁰⁾, the spurious discharges in the G.M.C. can be devided into two sorts, that is the "Nachentladung" and the "Spontanentladung". The former is a discharge induced by a previous one occurring generally before about 10^{-4} sec. and the latter is a discharge which occurs spontaneously without any such agency. Present investigations are on the temperature effect of the spotaneous discharges of the self-quenching G.M.C. when it was heated and cooled rather rapidly.

§ 2. Experimental Arrangement.

The G.M. counters used in the present research are generally hard glass sealed-off type with cathodes of 2 cm in diameter and 5 cm in length made of various metals. In all cases the cathodes were out-gassed by heating in vacuum to red hot by high frequency induction furnace or baked in electric furnace for several hours at the temperature of about 360°C. The central wires were made of 0.09 mm or 0.1 mm W wire. The counter, after being sealed off with argon and adequate quenching vapor in it, was put in an electric furnace and heated at a constant rate. The amplifier was followed by two sorts of counting system, that is the scale of 16 hard valve scaling circuit and the scale of 2 with thyratrons. The latter, having a time constant of about 5×10^{-3} sec., can not resolve the "Nachentladung" from the previous discharge. The difference in the counts by the two scaling circuit, therefore, gives the rate of "Nachentladung". In the present experiments, the discharges which could be attributed to the "Nachentladung" were very rare in all cases as shown in Fig. 1, being generally 5∼3 counts per minute at most, and could fairly be neglected as compared to the spontaneous counts due to to the temperature effect. Neither radioactive source nor Pb shielding for cosmic rays were used in the course of observations. The counting rate by cosmic rays was generally of the order of 30 counts/minute which was very small as compared to the counting rate due to the heating effect.

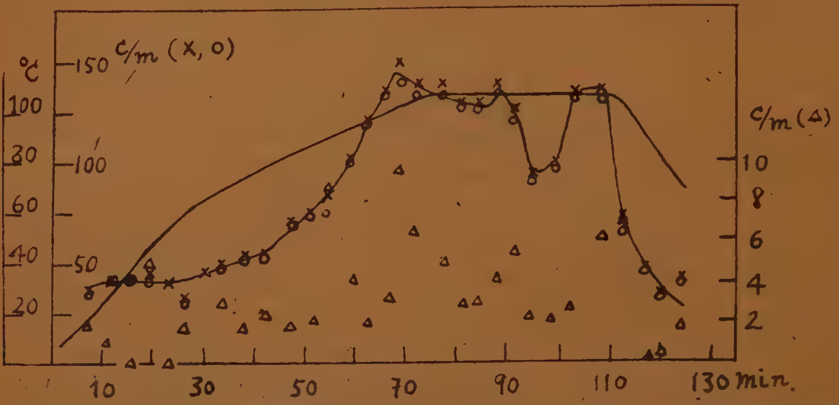

Fig. 1. Temperature effect in Fe-Argon-Alcohol G.M.C. (starting voltage: 780v., working voltage: 830v.)

× : counting rate by scale of 16
○: countihg rate by scale of 2
△: difference of × and ○ (mainly Nachentlandung)

§ 3. Experimental Results.

In almost all cases in the present experiments, the plateau curves were taken before and after the heating performance with a γ-ray source and also without any source near the counter. No marked change in the plateau curves was seen after the counter had cooled as compared to that before heating, though the plateau curves taken by natural counts showed sometimes better characteristics after the counter had nearly cooled off. During the course of heating experiment, the counter voltage was kept constant which was a little higher than the middle point of the plateau range, being generally 50 to 250 volts higher than the starting voltage.

(A) Temperature effect when the counter was heated and cooled at a constant rate.

The counter was heated at an almost constant rate (1°C/min. ∼3°C/min.) from room temperature to about 100°C∼160°C and then cooled.

As there are many factors which can be changed, that is, the rate of temperature change, the cathode material, filling gases, etc., it is almost impossible to cover all cases. Some of the results obtained are reproduced in Fig. 2∼9.

The experimental conditions are shown under respective figures. As seen in these figures, the rate of spontaneous counts increased enormously in many cases, and it decreased rapidly as soon as the counter began to cool without exception. The rate of spontaneous discharges on the cooling stage of the counter was very small even though the counter was still at a rather high temperature. Plateau curves taken before and after the heating experiments showed no marked difference, and the variation in the starting voltage could not be detected. It was difficult

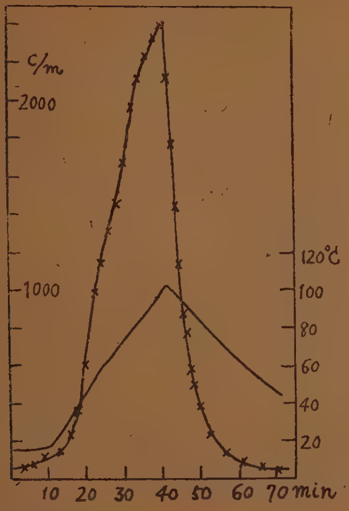

Fig. 2. Fe-Argon (95 mm)-Alcohol (10 mm) G.M.C.
st. v.: 880 v., wk. v.: 980 v.

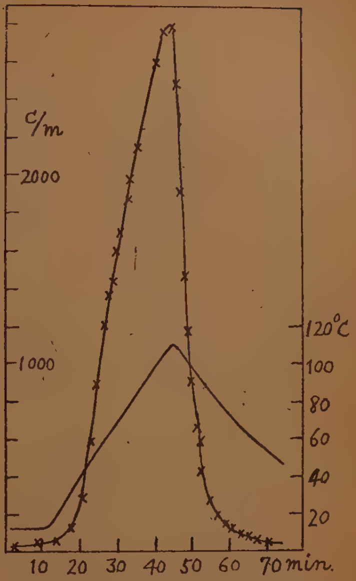

Fig. 3. Ni-Argon (66 mm)-Alcohol (10 mm) G.M.C.
st. v.: 830 v., wk. v.: 930 v.

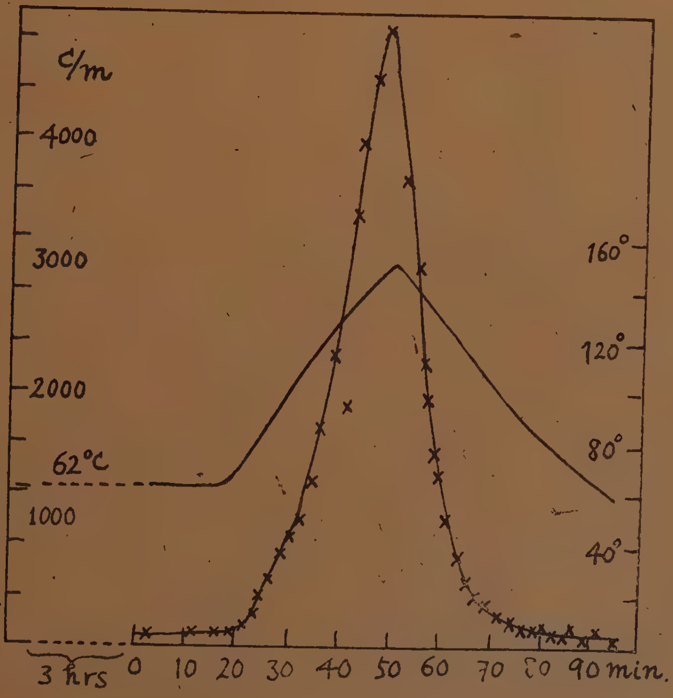

Fig. 4. Ni-Argon (66 mm)-Alcohol (10 mm) G.M.C. After maintained at 62°C for 3 hours.
st. v.: 830 v., wk. v.: 930 v.

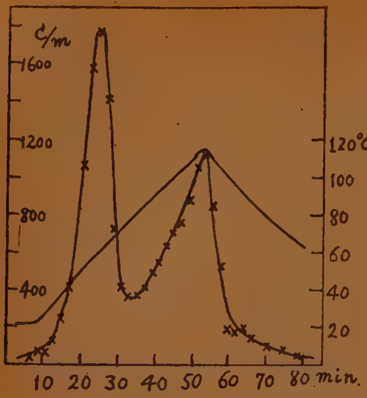

Fig. 5. Fe-Argon (98mm)-Ethylene (10mm) G.M.C.
st. v.: 890v., wk. v.: 1180v.

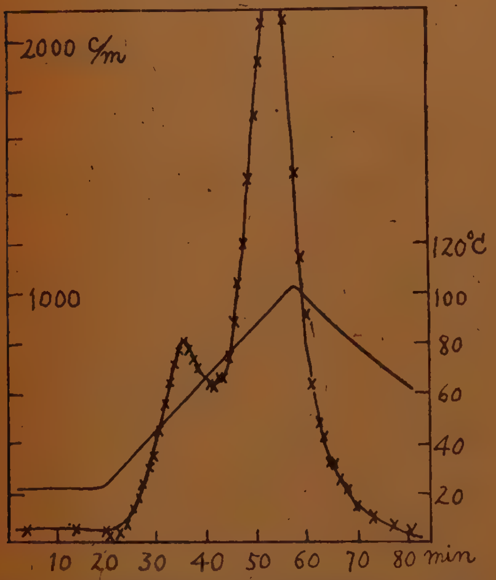

Fig. 6. Brass-Argon (90 mm)-Ethylene (10 mm) G.M.C.
st. v.: 920v., wk. v.: 1030v.

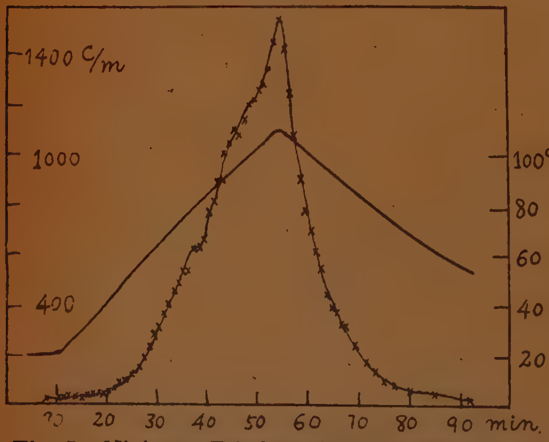

Fig. 7. Ni-Argon-Ethylene G.M.C. (Telex glass)
st. v.: 890v., wk. v.: 980v.

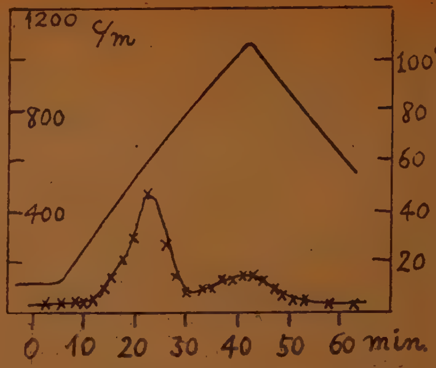

Fig. 8. Ni-Argon (67 mm)-Ethyl ether (9 mm)
st, v.: 800v., wk. v.: 860v.

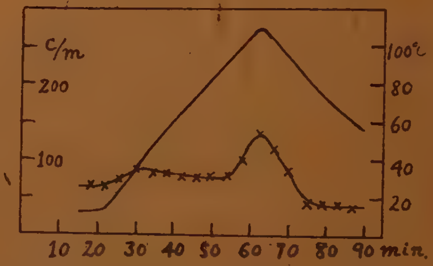

Fig. 9. Al-Argon (75 mm)-Ethyl ether (10 mm) G.M.C.
st. v.: 900v., wk. v.: 950v.

to get an accurate plateau curve when the counter was under temperature variation because the counting rate changed rapidly even at constant counter voltage. It was easily be known, however, that the characteristic curve showed steep rise with counter voltage whereas the starting voltage was the same as before and after heating. This shows that the increase in counting rate to be erroneous one due to the deterioration of insulation is extremely impossible. This point will be discussed in §4 again. The possibility of the change in the composition of the filling gas as a result of outgassing from the cathode and the counter wall by heating could also be excluded.

The increase in the spontaneous discharges was also seen when the counter voltage was raised to the working voltage from a value just below the starting voltage for short intervals from time to time (for 20 sec. one every 3 min.). This showed that the above increase in spontaneous discharges could not be attributed to the phenomena which are accelerated cumulatively by the previous counting discharges.

Our results of the experiments when the counter was heated and cooled by the constant rate will be summarized as follows, though the effects observed were not so perfectly reproducible.

(1) Argon-ethyl alcohol filling. The rate of the spontaneous discharges increased rapidly with the temperature rise, but not so rapidly when the temperature approached 100°C. The effect seemed to increase with the speed of temperature rise. When the rate was 1°C/min., no definite increase in spontaneous discharge was seen even at 70°C, and about 500 counts/min. were seen at 120°C. We may not be able to detect the change in natural counts by the variation of the room temperature which would occur usually. On the cooling stage, the counting rate decreased very rapidly and it returned to the initial value at about 50°C when the counter was cooled from 104°C by the rate of 1.6°C/min. In another example, the counting rate returned to the initial value at 105°C when the counter was cooled from 140°C by the rate of 2.5°C/min.

(2) Argon-ethylene filling. A rather sharp peak in the rate of spontaneous discharge was seen when the temperature rose to about 60°C in the case of charcoal steel and brass cathode. The relative height of this peak to that seen at the highest temperature was not reproducible, but the temperature corresponding to the peak was rather constant for all runs. The peak appeared equally both for Fe and brass counters although the plateau curve of brass counter was rather bad (plateau range: ~200 volts, slope: ~13%/100°V) as compared to the Fe one. In the case of Ni cathode, no marked peak was seen. It can safely be said, however, that the appearance of a peak at about 60°C has some relations to the properties of ethylene.

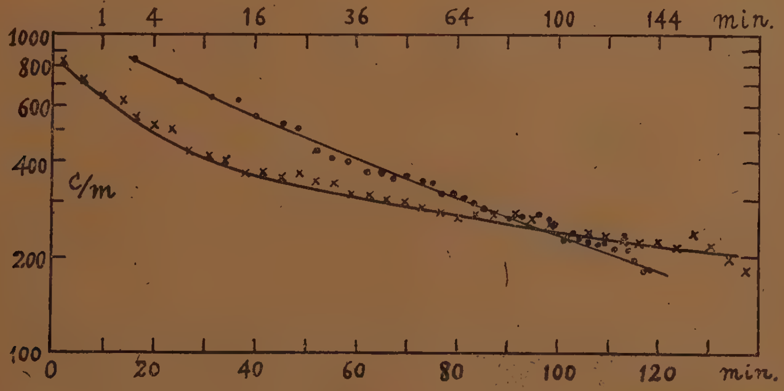

Fig. 10. Decay of spontaneous counts when the Fe-Argon-Alcohol counter was heated from room temperature and kept at 79°C±1°C.
• : upper abscissa (minutes after temperature rise stopped)$^{\frac{1}{2}}$
× : lower abscissa.

(3) Argon-ethyl ether filling. In the case of charcoal steel cathode, a rather broad maximum was seen on the warming stage as those in ethylene filling. No such maximum was seen for Al cathode.

(B) Temperature effect when the counter was kept at high constant temperature.

When the counter was heated to about 100°C with the same rate as those in the previous experiments, and then kept constant, the counting rate decreased gradually. The experiments of this kind were done only by Fe-argon-alcohol counters, an example of the results obtained being reproduced in Fig. 10. The counting rate seems to decrease exponentially with the square root of time elapsed after the moment when the temperature began to be kept constant.

(C) Photo-temperature effect.

The photo-sensitivity of G.M.C. generally shows very complicated character. The counting rate of our Fe-argon-alcohol counters showed an accelerative increase even under the irradiation by visible light of constant intensity, which is a phenomenon already pointed out by I. Nonaka⁽¹¹⁾.

The increasing tendency of the counting rate, however, was immediately stopped and began to decrease when the counter was heated as seen in Fig. 11. The counting rate increased again when the counter was warmed up to higher temperature which might safely be attributed to the same cause as in the cases of experiments (A). The counting rate decreased rapidly as in the previous cases when the counter began to cool. Thus the photo-sensitivity decreased enormously by the above heat treatment.

§ 4. Discussions.

Although we are not in the stage to draw any definite conclusion from the above experiments, following several mechanisms must be considered in relation to the observed phenomena.

(1) Thermoelectric emission from the cathode.

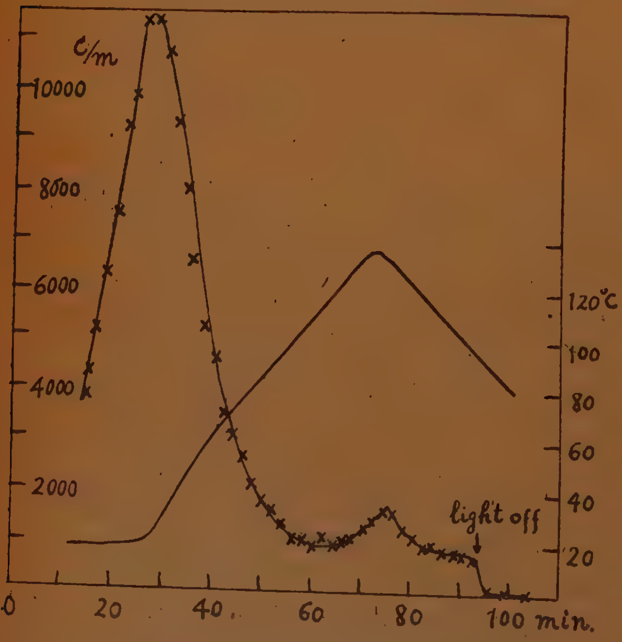

Fig. 11. Temperature effect of photo-counts due to yellowish red light from W filament.
Fe-Argon-Alcohol G.M.C.
st. v.: 780, wk. v.: 830v.

(2) Thin film field emission as a result of the electric double layer formed on the cathode surface. (Malter effect)

(3) Emission of electrons or negative ions accompanying the adsorption and evaporation of quenching vapor at the cathode.

(4) Electron emission from the fresh metal surface.

Beside these mechanisms, we must also consider the following possibilities.

(5) Emission of electrons from the cathode by the local strong electric field which is produced by a tiny charged dust which might be attached on the cathode.

(6) Induction of electric pulse on the central wire by the discontinuous change in the voltage distribution on the surface of counter glass.

Though the mechanism (6) can safely be excluded by the argument in §3, several tests were performed to ascertain this point. The increase in the spontaneous counts was also seen when the counter glass was made of Telex which is a glass of high insulation as Pyrex. Experiments by a counter with argon and alcohol at higher pressures showed the same temperature effect, and no spurious counts were observed when the counter voltage was below starting voltage, though it was much higher than the working voltage of other counters.

Mechanism (5) was assumed by Hereford to explain his observation by parallel plate counters. He assumed that tiny dusts of SiO_2 had adhered on the cathode plate when he baked the counter at 425°C. As SiO_2 has a specific resistivity of the order of 10^{14} ohm cm, with a negative temperature coefficient, it seems not impossible to explain his results along these lines. It seems impossible, however, to assume the same mechanism in our case, because we can observe the increase of spurious counts for the counters the cathode of which is out-gassed by high frequency electric furnace whereas the glass wall is not heated so high.

We can not neglect, however, the effect of thin film of oxide on the cathode surface. The phenomena of the thin film field emission had been observed by Malter(12), Hatoyama and Kimura(13), Tanaka(14), and also by Paetow(15). Minakawa(16) and others also observed the after effect of the same sort in G.M.C. It is not sufficient, however, to explain all the phenomena we observed, especially those concerning the effect of quenching gas by the so-called Malter effect alone. The adsorption of the quenching vapor molecules on the cathode surface may strongly affect the thin film field emission. Adsorption and evaporation of the quenching vapor on the cathode surface is a function of the temperature and its change, and they will influence strongly on the value k, that is the fraction of the field emission current contributing to the neutralization of the double layer. The rate of spontaneous discharge is proportional to $(1-k)$ which is considered to be of the order of $10^{-1}\sim10^{-10}$ as compared to 1. $(1-k)$ will be a complicated function of the properties of the adsorbed quenching vapor and also of the state of adsorption. In the case of ethylene some transition in the adsorbed state might have occurred at certain temperature.

We cannot, moreover, neglect the emission of negatively charged ions accompanying the evaporation of quenching vapor. The negative ions will loose electrons on the way to the wire, thus inducing the spontaneous discharges.

On the cooling stage of the cathode, it is very natural to assume the rapid decrease of $(1-k)$ as a result of the deposition of the quenching vapor.

The gradual decay of the rate of spontaneous discharges when the counter is kept at constant temperature can also be attributed to the same effect. In our case, however, the decay curve will not necessarily be of the same type as found by Hatoyama, Kimura(13) and Tanaka(14), that is the $1/\alpha t+1$ decay, on account of the variation in the adsorption state of the vapor on the cathode.

The photosensitivity in the G.M.C. is a rather complicated phenomenon. Newly prepared G.M. Counters (of brass and Fe cathode at least) are generally photo-nonsensitive and they become gradually sensitive even to visible light after the discharges of $10^5\sim10^6$ counts. This means that the work function of the cathode surface is lowered by the deposition of the cracked molecules of the quenching vapor which are produced by discharges. These deposit will be evaporated by heating and the reduction in the photosensitivity will result as seen in the present experiments.

Concerning the mechanism of (4), it is widely known since many years that the fresh metal surfaces emit electrons which can be detected by photographic plate. Kutzner(17), Lewis and Bureham(18), and recently, Wiedenbeck and Crane(19) and Kramer(20) have reported that they observed these electrons. According to Louw and Naudé(7), Kramer's experiment seems to be resembled to the present experiment, though the author is not able to know his experiment directly at present. According to Kramer, well polished metal surface gave rise to spurious counts in G.M.C. which decayed gradually with time and increased again when the counter was heated. Kramer concluded that electrons were emitted from the metal surface in the exothermal process. If this is true, our results may intimately related to his conclusion. We must notice, however, that the sense of variation of the rate of spurious discharge is opposite to Kramer's conclusion if we assume the adsorption of the quenching vapor to be an exothermal process.

Last of all, an explanation of the phenomena by the thermoelectron emission may be excluded by the fact that the discharge rate is not a function of the temperature itself but of the sense and rate of its change. Rough estimation of the constant A and ϕ in the Richardson formula, however, resulted in not so unreasonable values as follows:

$$\phi = 0.2\ \text{Volt},\quad A \doteqdot 10^{-7}\ \text{amp/cm}^2\,\text{deg}^2.$$

In conclusion it will be said that the researches of these effects using G.M.C. seems to offer another method of investigating the metal surfaces as pointed out by Kramer.

The author is much indebted to Prof. S. Nishikawa to his encouragement and discussion. The preparation of ethylene gas by Mr. S. Ikeda and the assistance of Mr. J. Akutsu in preparing the measuring instruments are much appreciated. The author is indebted to National Research Council for financial aid.

References.

(1) M. Sonoda and K. Kimura: Meeting of the Phys. Soc. Japan, Apr. 2 (1950).

(2) O. Minakawa et al: J. Phys. Soc. Jap. **6** (1951) 103.

(3) G. Joyet and M. Simon: Helv. Phys. Acta, **21** (1948) 184.

(4) S. A. Korff, W. Spatz and N. Hilbery; R.S.I., **13** (1941) 127.

(5) S. C. Brown: Nucleonics, **2–6**, 10; **3–2**, 50; **3–4** (1948) 46.

(6) O. Parkash: Phys. Rev., **76** (1949) 568.

(7) J. D. Louw and S. M. Naudá: Phys. Rev., **76** (1949) 571.

(8) J. W. Keuffel: R.S.I., **20** (1949) 202.

(9) F. L, Hereford: Phys, Rev., **77** (1950) 559.

(10) A. Trost. Z. f. Phys., **105** (1937) 399.

(11) I. Nonaka: Proc. Phys. Soc. Jap., **3** (1948) 322.

(12) L. Malter: Phys. Rev., **50** (1936) 48.

(13) M. Hatoyama and M. Kimura: Bul. Inst. Phys. Chem. Res., **15** (1936) 681.

(14) M. Tanaka: Proc. Phys. Math. Soc. Jap., **22** (1940) 899.

(15) H. Paetow: Z. f. Phys., **111** (1939) 770.

(16) O, Minakawa: Proc. Imp. Acad. Tokyo **19** (1943) 246. The author is indebted to Prof. I. Nonaka for his kind discussion on this point.

(17) W. Kutzner: Z. f. Phys., **23** (1924) 117.

(18) W. B. Lewis and W. E. Bureham: Proc. Camb. Phil. Soc., **32** (1936) 503.

(19) M. L. Wiedenbeck and H. R. Crane: Phys. Rev., **75** (1949) 1268.

(20) J. Kramer: Z. f. Phys., **125** (1949) 739.

Improved Counting Rate Meter for X-ray Measurement

By Gunji SHINODA and Teruichi TOMURA.

Osaka University.

(Received July 20, 1950)

Abstract.

A new type instrument for measurement of X-ray intensity with a G-M counter is described. The advantages of this counting rate meter are as follows; (1) statistical fractional standard deviations are constant throughout whole range of $1:10^4$, (2) probable errors are also made constant by means of logarithmic scale, (3) the time required for reading is shorter in higher counting rate, and (4) therefore it is benefitable to measure the counting rate from natural counting to saturate counting with probable error less than 3% using 0.8% accuracy meter and with only one scale.

§ Introduction.

As it is very convenient to use a counting rate meter when the counting rate is rather fast and high precision is not required, many circuits were devised, which have pre-amp., equalizer, integrator and indicator. The pulses from a G-M counter are at first amplified and equalized by a saturate amplifier or a one-shot vibrator. These pulses which have been made uniform in shapes are sent to *RC* tank circuit to obtain a voltage proportional to its counting rate. Such a tank circuit which consists of a capacitance shunted by a resistance is a simple and ordinary one, and the integration and averaging of the pulses are not possible except when the time-intervals between any successive pulses are amply short compared with the time constant of the tank circuit.

Statistical analysis of such a counting rate meter was done by Schiff and Evans⑴, and they showed that the voltage drop of the resistance is qxR and has the statistical expected fractional standard deviation of $(2xRC)^{-\frac{1}{2}}$. This is obtained under the assumption that the pulses have Poisson's distribution and mean counting rate of x; R and C being the values of resistance and capacitance forming that tank circuit respectively. Therefore the probable error occuring in reading is $0.675\,(2xRC)^{-\frac{1}{2}}$, and the equilibrium time i.e. the least time to attain the indication differing from the equilibrium average value by less than the unit of probable error occasioned by statistical fluctuations, is $RC(\frac{1}{2}\ln 2xRC+0.394)$. Moreover, the reading has a probable error m/f, where m is a constant determined from personal and instrumental condition and f is a fractional value of an indication to its full scale. These characteristics are shown in Fig. 1., and have the following disadvantages: (1) fractional standard deviations increase at lower counting rate, (2) errors of reading are more significant at lower counting rate than statistical deviations, (3) equilibrium time increases at higher counting rate, and (4) from these reasons the range of readings capable to obtain with single set of R and C is less than 1:10, therefore at least four sets of "RC"s are indispensable to measure the intensity of X-ray reflected by a crystal.

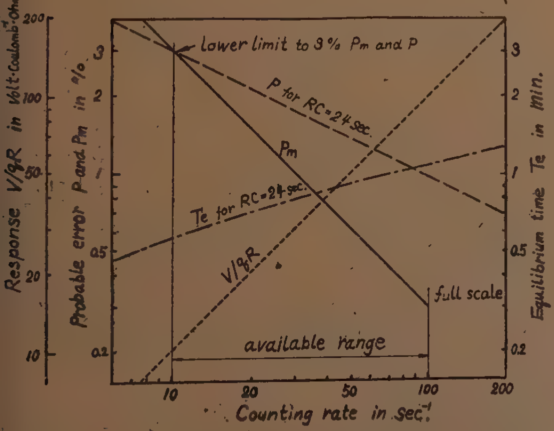

Fig. 1. Statistical Characteristics of the Ordinary Counting Rate Meter.

With a current meter having 0.3% accuracy and permiting maximum error of 3%, available range of counting rate is 1:10. The best time constant for counting rate 10～100 is 24 sec., and the time required to obtain one reading is in the range of about 0.5 to 1 min. Therefore to measure the all range of counting rate i.e. from natural to saturate counting, at least 5 sets of scale are necessary.

§ 2. Theoretical Considerations on the New Type Counting Rate Meter.

The above mentioned disadvantages will be eliminated by applying a variable time constant tank circuit which consists of a capacitance directly shunted by a Meagher and Bentley's logarithmic tube⑵. Fig. 2. shows such a tank circuit and its characteristics are as follows.

a) Response of the logarithmic tube.

The relation between V (response of the diode) and i (current through diode) is

$$\begin{aligned} V &= -(300\,kT/e)\ln i + \text{const.} \\ &= -(690\,kT/e)\log i + \text{const.} \qquad (1) \end{aligned}$$

where k is Boltzmann's constant, e is the electronic charge in e.s.u., and T is the temperature of the cathode. When a steady state is reached, the average current through the diode must be equal to that flowing into this tank circuit, or qx (q is electric quantity of one pulse and x is the average counting rate). Then this current produces an average potential drop of Eq. (1),

$$V = -(690\,kT/e)\log xq + \text{const.} \qquad (2)$$

therefore logarithm of x is obtained by the measurement of V.

b) Statistical fluctuation.

If the pulses obey Poisson's distribution, the expected fractional standard deviation caused by statistical fluctuation becomes

$$\sigma = (2xRC)^{-\frac{1}{2}} \qquad (3)$$

where σ is a fractional standard deviation in the case of RC tank circuit. In this relation, R and C have constant values, but in the case of logarithmic tube, the corresponding resistance i.e. dynamical resistance is

$$R = d(-V)/di = (390\,kT/ei) = (390\,kT/exq) \quad (4)$$

therefore Eq. (3) becomes

$$\sigma = (2x\,390\,kT/exq)^{-\frac{1}{2}}$$

or

$$= (600\,CkT/e)^{-\frac{1}{2}}\,q^{\frac{1}{2}} \qquad (5)$$

and the probable error p is

$$p = 0.675\,(600\,CkT/e)^{-\frac{1}{2}}\,q^{\frac{1}{2}} \qquad (6)$$

As this relation constains no varying quantities, probable error has a constant value independent of the counting rate.

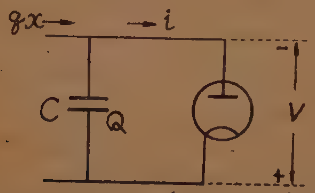

Fig. 2. Constant Fractional Standard Deviation Tank Circuit.

This tank circuit has the characteristics of variable time constant of constant fractional standard deviation.

c). Equiliprium time.

As shown in Fig. 2. charge in capacitance C is Q and

$$Q = CV,$$

The decrement of the electric charge Q during the time interval $(t, t+dt)$ is

$$dQ = C\,dV$$

and this is caused by the current flowing into C. This current is the difference of the current flowing into this tank circuit and that following away towards the logarithmic tube, then

$$-dQ = qx\,dt - i\,dt$$

and i becomes from Eq. (1)

$$i = \exp(e\,\text{const.}/300\,kT)\exp(-Ve/300\,kT) \qquad (7)$$

then

$$-dQ = qx\,dt - \exp(e\,\text{const.}/300\,kT)\exp(-Ve/300\,kT)\,dt = -C\,dV$$

therefore

$$-C\frac{dV}{dt} = qx - \exp(e\,\text{const.}/300\,kT)\exp(-Ve/300\,kT) \qquad (8)$$

and

$$-\int \frac{dV}{qx - A\exp(-V/B)} = \frac{t}{C} + \text{const.} \qquad (9)$$

where

$$A = \exp(e\,\text{const.}/300\,kT)$$
$$B = 300\,kT/e \qquad (10)$$

(I) In the case of $qx > A\exp(-V/B)$ i.e. when the counting rate is increasing.

$$\frac{B}{xq}\left[-\frac{V}{B} - \ln\{qx - A\exp(-V/B)\}\right] = \frac{t}{C} + \text{const.}, \quad x \neq 0 \qquad (11)$$

(II) In the case of $qx < A\exp(-V/B)$ i.e. when the counting rate is decreasing.

From Eq. (8),

$$-\frac{B}{qx}\left[-\frac{V}{B} - \ln\{-qx - A\exp(-V/B)\}\right] = \frac{t}{C} + \text{const.}, \quad x \neq 0 \qquad (12)$$

Moreover from Eq. (7) and (10)

$$-\frac{V}{B} = \ln(i/A) \qquad (13)$$

Combining Eq. (12) and (13),

$$\pm\frac{BC}{qx}\ln A\left(\pm\frac{qx}{i} \mp 1\right) = t + \text{const.}, \quad x \neq 0 \qquad (14)$$

Now at the time t_0, if an apparently equilibrium state is reached at the counting rate x_0, and then counting rate suddenly changes to x, i will be changed also and approaches gradually to the equilibrium value qx. At the equilibrium time T_e, i differs from its equilibrium value by less than probable error pqx.

i.e.

$$t = t_0 \qquad i = qx_0$$
$$t = T_e + t_0 \quad i = (1 \pm p)qx$$

therefore

$$T_e = \pm\frac{CB}{qx}\left\{\ln\left(\frac{p}{1 \mp p}\right) - \ln\left(\pm\frac{x}{x_0} \mp 1\right)\right\} \qquad (15)$$

or

$$T_e \doteqdot \pm 2.303\frac{CB}{qx}\left\{\log\left(\pm\frac{x}{x_0} \pm 1\right) - \log\left(\frac{p}{1 \mp p}\right)\right\} \qquad (16)$$

This relation is shown in Fig. 3. in which as a special case, if $C = 24\mu f$, $q = 10^{-8}$ coulomb, and

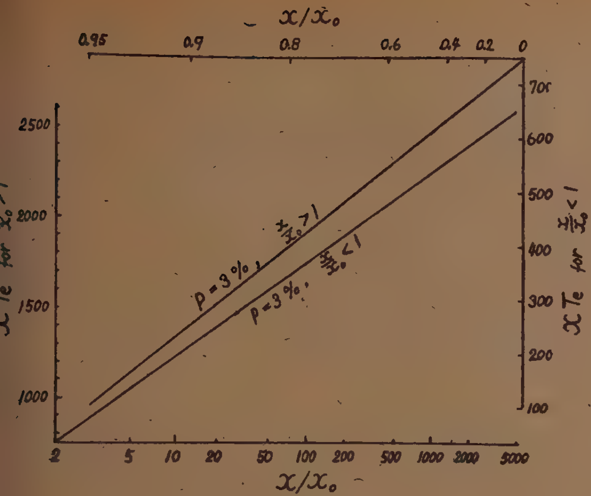

Fig. 3. Equilibrium time T_e.

For $C = 24\,\mu f$, $q = 10^{-8}$ coulomb, and $B \doteqdot 0.1$ volt, p becomes nearly 3%, T_e is the minimum time to obtain counting rate x after measuring counting rate x_0.

$B \doteqdot 0.1$ volt then $p \doteqdot 3\%$, and ones for $x=1\,\text{sec}^{-1}$. and $5000\,\text{sec}^{-1}$. are shown in Fig. 4.

d) Error of a reading

As the scale has a logarithmic one, fractional probable error of reading is constant throughout the whole range of the scale, and

$$p_m = nm$$

where

p_m: fractional probable error

n: ratio of full scale to zero scale

m: fractional probable error at the full reading by an ordinary division.

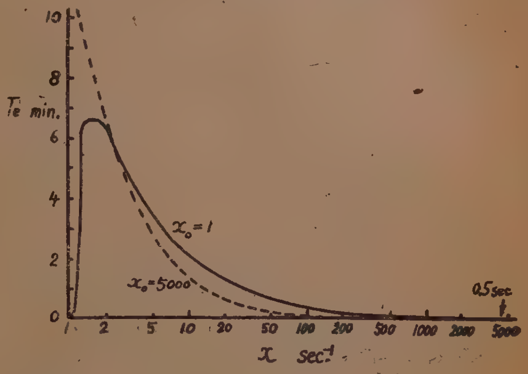

Fig. 4. Equilibrium Time for $x_0 = 1$ and $x_0 = 5000\,\text{sec}^{-1}$.

Other figures are the same as in Fig. 3. It is recongnized that the measurement of high counting requires very short time.

§ 3. Practical Circuit of the Counting Rate Meter.

From above analysis superiority of our circuit will be clear, but still there exist some problems which ought to be conquered. In the first place as the available upper limit of the logarithmic tube current is $30\,\mu$ A, then if we take $10^4:1$ as the range of intensity measurement, the minimum current will be $0.003\,\mu$ A or 3×10^{-9} Amp.

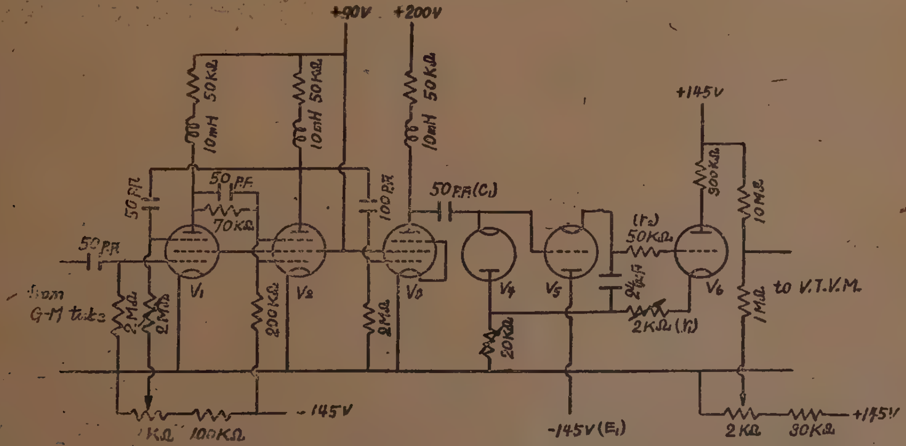

Fig. 5. Circuit of Constant Fractional Standard Deviation Type Counting Rate Meter.

$V_1 \sim V_3$: 6C6 as usual pentode, V_4: 6C6 as diode connection, V_5: 955, V_6: 6C6 as triode connection, E_1 and $2k\,\Omega$ vari-ohm are for compensation of dark current. $C_1 = 50$ pf-condenser is used for equalizing of electric quantity of a pulse. And r_2 is for half wave rectified X-ray.

Therefore the grid current of the tube to measure the logarithmic tube response must be less than 10^{-10} Amp. and this will not be realized if we use commerical tube obtainable in our country. To avoid this difficulty, it is preferable to use a triode whose grid and cathode are used as a logarithm diode, and to control the plate-current by the response of logarithm diode(3). In consequence of this modification, this tank circuit must be acted only by positive pulses.

In the second place, the electric charge of the pulses is controlled by a capacitance charge under constant voltage. In Fig. 5. tube V_3 is operated by over load, and tube V_4 and V_5 are the rectifier triodes. By supplying sufficient negative potential to their plates, the dark current can be reduced as low as 10^{-10} amp.

As the X-ray from our half wave rectified type apparatus has ripples of 60 c/s, the tank circuit must have a time constant longer than 1.2 sec. For this purpose it is benefitable to insert a 50 kΩ resistance to the tank circuit. The whole characteristics are shown in Fig. 6.

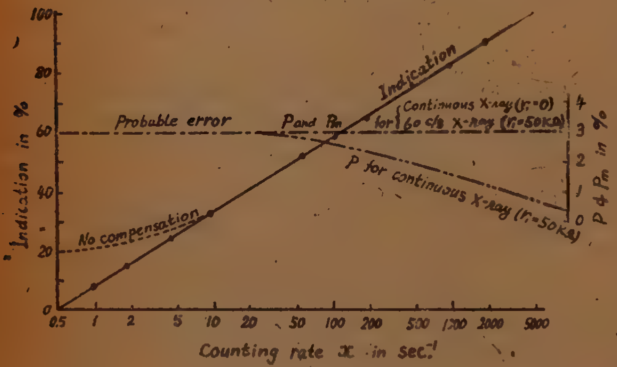

Fig. 6. Charcteristics of Constant Fractional Stantard Deviation Type Counting Rate Meter.

The characteristics obtained by us using a circuit shown in Fig. 5. By supplying negative potential to the plate of tube V_5 and a little positive potential to the cathode of V_6, perfect linearity is obtained over the range of counting rate from 0.5 to 5000 sec^{-1}. And the probable error caused by statistical fluctuation using 0.8% accuracy meter is 3% all over the range.

§ 4. Conclusion.

As shown above the error of this counting rate meter originated due to statistical fluctuation has a constant value and measurement will be done by only one scale throughout the whole measuring range i.e. from a natural counting up to the saturated counting with less than 3% probable error. The time required to obtain a satisfactory reading will become minimum when the counting rate is sufficiently high and the maximum accuracy will be obtained at this range.

In conclusion authors wish to express their sincere thanks to the financial aid of the Expenditure of Scientific Research of the Ministry of Education.

Reference.

(1) Schiff and Evans, Rev. of Sci. Inst. **7** (1936) 456/45.
(2) Meagher and Bentley, Rev. of Sci. Inst. **10** (1939) 336/339.
(3) W. J. Ives, Electronics **22** (1949) Aug. 102.

Angular Distribution of 3.1 Mev Neutrons Scattered by Proton.

By Yukiyasu Oda, Jyumpei Sanada and Shôtaro Yamabe.

Department of Physics, Osaka University.

(Received July 26, 1950).

§ 1. Introduction.

The angular distribution of fast neutrons scattered by proton has been usually measured by analysing the relative numbers of recoiling protons. Therefore the results relate to the neutrons which are scattered backward. The results hitherto obtained show the isotropic distribution at the energies of d—d neutrons. While, detecting the scattered neutrons directly, the forward angular distribution was studied by S. Kikuchi, H. Aoki and T. Wakatuki[1] They used ring scatterers and an ionization chamber filled with methane or hydrogen gas at high pressure. This method gives the absolute value of the differential scattering cross section. The differential scattering cross sections at several angles which they obtained were equal within realatively large experimental errors, but their absolute values were about a half of $\sigma_0/4\pi$, where σ_0 is the total scattering cross section for proton. Such small values for the forward scattering can not have a reasonable connection with the backward angular distribution[2]

We reexamined this point, as we got larger intensity of neutrons and better target geometry by some improvements of apparatus.

§ 2. Experimantal Arrangement and Procedure.

Experimental method was almost the same as that of the previous works. It is, however, convenient to describe it here together with the present conditions. The monoenergetic neutrons used were from the d—d reaction and were produced in heavy ice target by unanalysed beam of 100 μA and 300 kev deuterium ions accelerated by a Cockcroft-Walton set. The ion beam from the ion source of low voltage arc type, instead of Wien type as was used in the previous works, was considerably well focused, passing through a slit 6 mm in diameter placed at the distance of 25 cm from the target. The ion beam was so strong that the yield of neutrons was reduced by vapourisation of heavy ice. This difficulty was overcomed by allowing D_2O vapour to flow continuously on to a liquid-air-cooled target at the rate of about 0.2 cc of heavy water per hour.

The arrngement of the target, ring scatterer and detector is shown in Fig. 1. The neutrons from the d—d source was monitored by a cubic ionization chamber C_2 with sides 10 cm in length. It was filled with methane at 1 atm. and connected to a Shimizu type electrometer. The detector C_1 was a cylindrical ionization chamber connected to a quadrant electrometer. It was filled with methane at 50 atm. and its inner diameter was 3 cm and its effective length was 7.5 cm. Both ionization chambers were covered with lead plates and shielded to X-ray from the apparatus. θ is the scattering angle in laboratory system. The

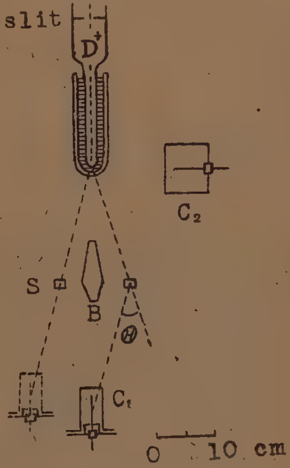

Fig. 1. The arrangement of the target, ring scatterer and detector.

distance between the target and the detector was 41.4 or 51.2 cm, and the ring scatterer S was placed midway. The size of ring scatterers is shown in Table I.

Table I. The size of ring scatterer and the scattering angle.

Materials	Inner diameter in cm	Outer diameter in cm	Scattering angle θ in deg.	Distance between target and detector in cm
Paraffin	6	10	22 ± 5	41.4
and	10	14	33 ± 5	41.4
Graphite	14	18	43 ± 5	41.4
Water	6	10	22 ± 5	41.4
Quartz and Silicon	6	14	22 ± 8	51.2

We measured the ratio $\Delta I/I_0$, where I_0 was the ionization current in C_1 produced by neutrons coming directly from the target, and ΔI was the increase of the ionization current in C_1 when the ring scatterer was placed in position. An absorber of paraffin cone, named B in Fig. 1, was inserted between the target and the detector to reduce the background ionization when we measured ΔI. Ring scatterers were of paraffin $C_{25}H_{52}$, graphite, water, quartz and silicon. We estimated the scattering by proton, subtracting the contribution of carbon or oxygen from the scattering of paraffin or water respectively. It was assumed that the ionization current produced by neutrons in the ionization chamber was proportional to the product of the energy of neutrons and the total scattering cross section for proton. Then the relation between $(\Delta I/I_0)$ for proton and the differential scattering cross section in laboratory system $\sigma(\theta)$ is written as follows:

$$\left(\frac{\Delta I}{I_0}\right)_{\text{proton}} = \frac{R^2 \cdot N \cdot \sigma(\theta)}{r^4} \cdot \frac{F(\theta/2)}{F(0)} \cdot \frac{\sigma_t(E_{\Theta}) \cdot E_{\Theta}}{\sigma_t(E_0) \cdot E_0} \cdot A$$

where $R =$ distance between the target and the detector C_1

$r =$ distance between the target and the ring scatterer and also between the ring scatterer and the detector C_1

$N =$ total number of atoms contained in the ring scatterer

$F(\theta/2)/F(0)$ represents the effect that the number and the energy of neutrons from target are different according to the angle $\theta/2$ between the deuterium ion beam and neutron produced, and that the scattered neutrons enter into the detector C_1 at an angle $\theta/2$ to its axis. We determined this factor experimentally as the ratio of the ionization current in C_1 when C_1 was placed at the angle $\theta/2$ shown by dotted line in Fig. 1 to when C_1 was placed at the angle 0 without the ring scatterer and the absorber in both cases.

$\sigma_t(E_{\Theta}) =$ total scattering cross section of neutrons scattered by proton by an angle θ. Therefore E_{Θ} respresents the energy of scattered neutrons. We used for the values of total scattering cross section the data obtained by C. L. Bailey et al[3].

$A =$ factor which was introduced as the correction for the absorption and the double scattering of neutrons in the scatterer.

We will give some description about the factor A in the following. In Fig. 2 we show one of

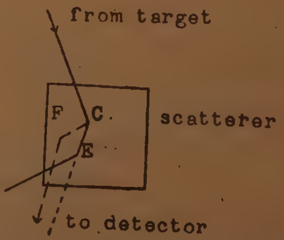

Fig. 2: One of sections of the ring scatterer and the path of neutrons.

the sections of the ring scatterer and the path of neutrons. The point C represents the position at which the collision of neutron with nucleus occurs. In the case of proton, the scattering is not isotropic in laboratory system and moreover neutrons lose their energy through collision. The value of $\sigma_t(E_\ominus)\cdot E_\ominus$ which is proportional to the ionization current in the detector C_1 decreases as $E_\ominus$ decreases. This relation is shown in Fig. 3. The decrease of the ionization current due to the neutrons which run in the direction to the detector after the first collision at the point C and are scattered out at a point E in Fig. 2 can not be compensated by the ionization current due to the neutrons which enter into the detector through double collisions at the point C and F in Fig. 2. After numerical calculation about the actual geometry, we determined the factor A. In the case of carbon or oxygen, however, we may assume for the purpose of correction that the scattering of neutrons is approximately isotropic and elastic. Hence, we may neglect the effect of the double scattering. As we take account of the absorption only, we put $A = \exp(-nt\sigma_t'/2\cos(\Theta/2))$ in the first approximation, where n is the number of atoms contained in unit volume of the scatterer and t is the thickness of the scatterer.

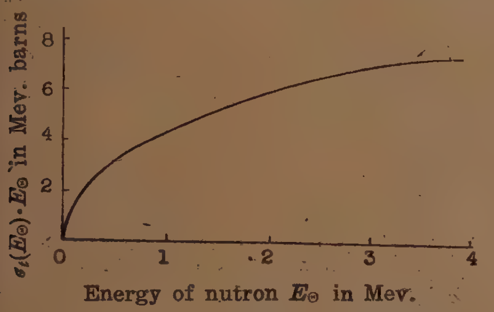

Fig. 3. The variation of $\sigma_t(E_\ominus)\cdot E_\ominus$ with the neutron energy.

§ 3. Result and Discussion.

The results are tabulated in Table II for proton and in Table III for carbon and oxygen.

The differential scattering cross section in the center of mass system $\sigma(\theta)$ shown in the sixth column of Table II was calculated by the formula $\sigma(\theta) = \sigma(\Theta)/4\cos\Theta$, where $\theta = 2\Theta$. The values in Table II and III were the mean of several ten measurement and the errors were the standard error plus errors from the correction factors.

In Fig. 4 $\sigma(\theta)$ is taken as ordinates and the scattering angle in the center of mass system θ as abscissae. The dotted line represents the value to be expected from isotropic scattering. The errors of the differential scattering cross section came mainly from the errors of the total scattering cross section which was used in the calculation of the sensitivity of the ionization chamber for the scattered neutrons.

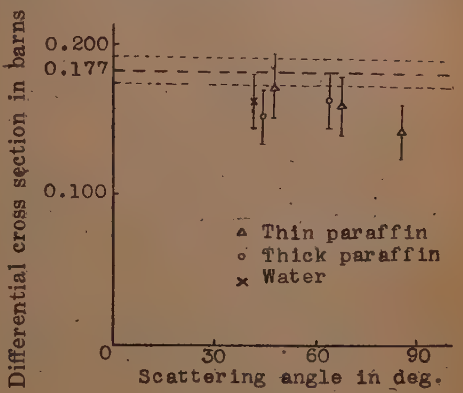

Fig. 4. The differential scattering cross section of 3.1 Mev neutrons scattered by proton in the center of mass system. Abscissae are the scattering angle in the center of mass system.

Graphite used as carbon sample was not completely pure and contained ash by several percent. Therefore the values of scattering cross section for carbon shown in Table III may be somewhat large. We could not find the suitable sample also for oxygen. We were obliged to use much quartz and silicon. The differential scattering cross section for oxygen was the value under the poor definition of the scattering angle. But the contribution of carbon or oxygen to the value $\Delta I/I_0$ of paraffin or water is small, about ten per cent, and the circumstances above described did not so greatly affect the values of the differential scattering cross section for proton.

From present results we may conclude that the forward scattering of 3.1 MeV neutrons by proton is not inconsistent with the isotropic scattering. Even the present results, however, have somewhat large errors. To obtain more precise

Table II. The differential scattering cross section of 3.1 Mev neutrons scattered by proton in the center of mass system.

Scattering angle θ in deg	Scatterer and its weight in gram	$(\Delta I/I_0)$ for proton in percent	$\frac{F(\theta/2)}{F(0)}$	A	Differential cross section in barns
44 ± 10	Paraffin 50.7	2.19 ± 0.07	0.85	0.84	0.166 ± 0.022
	Paraffin 94.9	3.10 ± 0.05	0.85	0.69	0.146 ± 0.017
	Water 94.1	2.32 ± 0.06	0.85	0.78	0.156 ± 0.019
66 ± 10	Paraffin 71.8	2.06 ± 0.06	0.81	0.84	0.153 ± 0.020
	Paraffin 141.4	3.38 ± 0.07	0.81	0.67	0.157 ± 0.019
86 ± 12	Paraffin 95.4	1.63 ± 0.06	0.77	0.83	0.136 ± 0.019
Total cross section $\sigma_t/4\pi = 0.177 \pm 0.009$ barns[3]					

Table III. The differential scattering cross section of 3.1 Mev neutrons scattered by carbon and oxygen.

Scattering angle θ in deg	Scatterer and its weight in gram	$(\Delta I/I_0)$ for proton in percent	$\frac{F(\theta/2)}{F(0)}$	A	Differential cross section in barns
22 ± 5	Graphite 153	1.87 ± 0.08	0.85	0.87	0.371 ± 0.026
	Oxygen 214 (SiO_2-Si)	0.53 ± 0.08	0.85	0.95	0.143 ± 0.026
33 ± 5	Graphite 157	1.43 ± 0.06	0.81	0.91	0.312 ± 0.026
43 ± 5	Graphite 187	1.10 ± 0.09	0.77	0.92	0.232 ± 0.023
Total cross section for carbon $\sigma_t' = 1.83 \pm 0.02$ barns					
Total cross section for oxygen $\sigma_t' = 1.48 \pm 0.08$ barns					

results it is desirable to replenish the auxiliary data, because of the indirect derivation of the scattering cross section. It is necessary also to reduce the statistical fluctuation, which was a few per cent in the present experiment.

§ 4. Acknowledgment.

We wish to express our thanks to Professors S. Kikuchi and T. Wakatuki for their constant encouragement and valuable advice. We are also very grateful to Dr. S. Sengoku who offered us graphite.

This work was supported by the grant for the promotion of science from the Ministry of Education.

References.

(1) S. Kikuchi, H. Aoki and T. Wakatuki, Proc. Phys. Math. Soc. Japan **21**, (1939) 410. T. Wakatuki, ibid. **22**, (1940) 430.

(2) J. H. Coon and H. H. Barschall, Phys. Rev. **70** (1946) 592.

(3) C. L. Bailey, W. E. Bennett, T. Bergstralh, R. G. Nuckolls, H. T. Richards, and J. H. Williams, Phys. Rev. **70** (1946) 583.

On the Scattering of Fast Neutrons from Li-D Reactions.

By Tetsuo WAKATSUKI and Kenzo SUGIMOTO.

Department of Physics, Faculty of Science, Osaka University.

(Received Septembr 17, 1950.)

Abstract.

Total scattering cross sections for 37 elements have been measured for heterogeneous fast neutrons of mean energy 6.5 Mev. Irregular variations of cross sections with atomic weights were observed at magic number nuclei but they were not all smaller than the neighbouring nuclei as is the case for inelastic scattering or capture processes. It is probable that elastic scattering cross sections become large at those nuclei. Other large irregular variation of cross section was found at Ti.

§ 1. Introduction.

The scattering of fast neutrons were studied by many authors. Dunning⁽¹⁾ measured scattering cross sections of Ra (α)—Be neutrons for 17 elements and concluded the cross sections to vary as $A^{2/3}$, where A is the atomic weight. Later Kikuchi and Aoki⁽²⁾ measured the scattering cross sections using monochromatic neutrons from D-D reactions (2.5 Mev) for 37 elements. They found that the scattering cross sections do not increase monotonously with atomic weights. Aoki⁽³⁾ showed that the scattering cross sections show resonances in the energy range between 2.1 and 2.8 Mev.

Recent measurements by Barshall and others⁽⁴⁾ showed many cases of resonance scattering especially for light elements in the energy range below 1 Mev.

Freier et al.⁽⁵⁾ showed broad resonance scattering for C, O, and Si between the energy range of 2.5 and 5.0 Mev.

Therefore departures from monotonic increase of cross sections with atomic weights as were found by Kikuchi and Aoki may partly be interpreted by resonance scattering of neutrons.

In fact, using more energetic neutrons, Amaldi et al.⁽⁶⁾ (14 Mev) and Sherr⁽⁷⁾ (25 Mev) obtained the results that the scattering cross sections increase monotonously with atomic weights.

We have reasons, however, to expect that densities of nuclear energy levels do not increase with atomic weights regularly as are expected from statistical nuclear models. From the stand point of orbit model of nucleus, nucleons fill successive closed shells, and the closing numbers appear to be 2, 8, 20, 50, 82, and 126⁽⁸⁾. These closing numbers (magic numbers) were deduced empirically and found many evidences in later works.

We thought the scattering cross sections for fast neutrons may also show some sort of irregular variations with atomic weights in the neighbourhood of these magic number nuclei.*

For the investigation of this point, the width of neutron energies should be greater than the spacing of resonance levels of compound nucleus to avoid the influence of individual resonance levels.

The spectrum of fast neutrons from Li-D reactions consists of several groups up to 14.5 Mev superposed on the continuous group on the low energy side.

It seemed very appropriate to use these Li-D neutrons since the mean energy measured by n-p scattering cross section in the present experiment was about 6.5 Mev, which leads to high excitation of compound nucleus where the spacing of energy levels is very close, and morever, effects of resonance levels would be averaged by the heterogeneity of neutron spectrum.

---

* S. Yamabe and J. Sanada, Lecture at the Phys. Soc. Meeting at Tokyo, April, 1950.

Kikuchi and Aoki(3) measured also the scattering of Li-D neutrons, but as the deuteron energy was only 350 kev, there is doubt whether there might be any contaminations of D-D neutrons.

By the performance of Osaka static generater we can now accelerate deuteron beams up to about 1 Mev, and it seemed worth while to carry out the experiment on the scattering of Li-D neutrons under better conditions.

§ 2. Experimental arrangements and procedures.

Neutron source and detector:

Neutrons were produced by bombarding a thick target of metallic lithium by 0.9 Mev unresolved deuteron beams accelerated by the Osaka static generater.

For the detection of neutrons a high pressure ionization chamber filled with hydrogen at 95 atmospheric pressures connected to vacuum tube electrometer was used. The chamber was 3.0 cm in inside diameter and 4.5 cm in effective length with iron wall 5 mm thick. Double reentrant electroks system was used and collecting field applied was 500 volts. This chamber was placed 40 cm apart from Li-target in the direction of deuteron beam. A similar ionization chamber but of larger size was placed beside the target as the monitor of the neutron intensity.

To avoid the effects of X-rays both chambers were shielded by lead sheets of 8 mm thickness.

Effects of X-rays and γ-rays:

Both chambers were proved to be insensitive to X-rays by the use of ion shutter in front of the target, but as γ-rays are emitted in Li-D reactions, the effects of γ-rays must be estimated. For this purpose we placed a Geiger-Müller counter inclosed in a lead box of 8 mm wall thickness at the position of the ionization chamber. The intensity of γ-rays detected by this counter was compared with γ-rays from the known quantity of radium source and intensity of ionization cuurent caused in the ionization chamber by this quantity of radium γ-rays was measured. It amounted to 1.6% of that cause by Li-D neutrons. In this estimation it is assumed that the ratio of the efficiencies of Geiger-Müller counter and the ionization chamber fo radium γ-rays and Li-D γ-rays is the same an that the counter responds only to γ-rays. Th effects of γ-rays of 1.6% is a reasonable valu as the number of quanta of γ-rays is estimate to be 3% of that of neutrons by Bonner et al.(9 The effects of γ-rays being very small and of the order of experimental errors, they were neglecte in calculating the neutron scattering cross sec-tions.

Derivation of the scattering cross section:

Total scattering cross sections were calculated from measurement of the decrease in neutron intensity when scatterers were placed midway between the neutron source and the ionization chamber. The size of scatterers were in most cases circular discs of 3 cm diameter and the thicknesses were adjusted to give about 60% transmission. Corrections due to neutrons which were scattered by scatterers into the ionization chamber were calculated by assuming the angular distribution of scattered neutrons to be given by the following formula.(10)

$$\sigma(\theta) = [\mathrm{RJ}_1\,(k\mathrm{R}\theta)/\theta]^3 \qquad (1)$$

$$R = (2.3+1.25\,A^{1/3})\ 10^{-12}\,\mathrm{cm} \qquad (2)$$

where $\sigma(\theta)$ is the differential scattering cross section for scattering angle θ, R the nuclear radius k the wave number, J_1 the Bessel function of the first kind, and A the atomic weight. The value of k was taken as 5.65×12^{12} which corresponds to neutron energy of 6.5 Mev in accord with the proton scattering cross section of 1.29 barn.

The intensity of neutrons scattered by the walls and floors was evaluated by introducing a thick paraffin cylinder of 3.5 cm diameter and 33.5 cm long between the source and the ionization chamber. It was measured from and subtracted as the background radiation.

§ 3. Results:

The results are tabulated in Table 1. and shown in Fig. 1.

Table I.

Element	Z	Molecule used	Thickness of scatterer in g/cm²	Size of scatterer in cm	Transmission in %		Atomic cross section in 10^{-24} cm²	Kikuchi Aoki corrected in 10^{-24} cm²
					Measured	Corrected		
H	1	$HC_{0.472}$	0.984	$D=5.1$	85.1	84.3±1.3	1.29±0.06	1.74±0.05
			1.96	$D=5.0$	72.3	70.7±1.4		
			2.94	$D=5.0$	58.0	55.6±1.0		
Li	3	$LiC_{1/2}O_{3/2}$	4.02	$D=3.6$	69.5	68.8±0.7	1.98±0.23	2.47±0.18
B	5	$BO_{3/2}$	4.90	$D=3.36$	69.5	68.5±0.5	1.57±0.19	2.02±0.13
C	6	C	4.64	5.0×5.0	69.9	68.1±0.8	1.64±0.05	1.22±0.04
O	8	$OSi_{1/2}$	7.46	$D=3.6$	64.2	63.2±1.0	1.91±0.11	1.32±0.06
F	9	$FCa_{1/2}$	9.43	$D=3.6$	56.4	55.2±0.9	2.10±0.14	1.25±0.11
Na	11	$NaC_{1/2}O_{3/2}$	5.3	$D=3.3$	69.5	68.6±0.8	2.52±0.26	2.27±0.09
Mg	12	Mg	3.09	3.57×3.54	84.9	64.2±1.2	2.24±0.19	1.80±0.07
Al	13	Al	7.08	$D=3.62$	70.4	69.4±1.4	2.29±0.13	2.08±0.05
Si	14	Si	8.72	$D=4.5$	67.7	65.8±0.3	2.25±0.03	1.94±0.05
S	16	S	7.46	$D=3.67$	70.4	69.3±1.1	2.60±0.12	2.18±0.09
Cl	17	$ClC_{1/4}$	6.77	$D=3.6$	70.0	69.0±1.5	3.07±0.22	2.44±0.07
K	19	KI	8.59	$D=3.6$	78.8	77.6±1.1	3.91±0.34	3.04±0.11
			14.65	$D=3.6$	62.8	61.2±1.0		
Ca	20	Ca	6.72	$D=3.6$	72.7	71.4±0.9	3.89±0.15	3.75±0.17
Ti	22	TiO_2	7.48	$D=3.6$	71.2	70.1±1.1	2.34±0.22	2.66±0.21
			10.77	$D=3.6$	62.3	60.8±0.8		
Cr	24	$CrO_{3/2}$	10.88	$D=3.6$	59.8	58.4±1.1	3.34±0.28	2.94±0.08
Mn	25	Mn	13.06	$D=3.6$	60.6	59.1±0.9	3.66±0.11	3.09±0.09
Fe	26	Fe	16.40	$D=3.60$	60.5	58.5±1.0	3.02±0.10	2.74±0.08
Ni	28	Ni	13.38	$D=3.60$	66.2	64.6±1.0	3.16±0.19	2.86±0.08
Cu	29	Cu	15.16	$D=3.64$	54.2	62.3±1.3	3.27±0.15	3.01±0.05
Zn	30	Zn	16.14	$D=3.64$	66.6	64.6±0.9	2.92±0.09	2.84±0.07
As	33	As	14.42	$D=3.6$	63.3	61.6±0.9	4.14±0.13	3.74±0.09
Br	35	BrK	6.92	$D=3.6$	77.4	76.2±1.3	4.22±0.38	3.29±0.23
			12.17	$D=3.6$	63.1	61.6±0.8		
Sr	38	$SrCO_3$	4.58	$D=3.6$	80.9	80.2±0.8	4.74±0.44	4.89±02.1
			10.47	$D=3.6$	59.8	58.5±1.3		
Zr	40	ZrO_2	4.27	$D=3.6$	62.7	82.0±1.1	5.61±0.68	
Ag	47	Ag	12.9	6.0×6.0	75.8	71.9±0.9	5.82±0.22	3.90±0.12
Cd	48	Cd	17.74	6.0×6.0	67.6	61.6±1.4	4.90±0.13	4.10±0.15
			16.19	$D=3.58$	68.1	65.7±0.8		
Sn	50	Sn	18.4	5.1×5.0	69.7	64.1±1.1	4.70±0.14	3.92±0.13
			15.02	$D=3.36$	71.7	69.9±1.0		
Sb	51	Sb	15.00	$D=3.63$	68.9	67.1±0.9	5.59±0.14	4.50±0.13
I	53	I	11.93	$D=3.6$	75.4	73.5±1.2	5.30±0.17	4.59±0.19
			17.95	$D=3.6$	65.9	63.7±1.0		
Ba	56	$BaCO_3$	4.49	$D=4.5$	84.3	83.1±0.9	5.47±0.46	6.11±0.22
			6.81	$D=3.6$	76.6	75.5±1.6		
			10.72	$D=3.6$	67.3	65.8±0.8		
Ce	58	CeO_2	7.62	$D=3.6$	73.4	72.2±1.4	8.29±0.76	
W	74	W	22.56	$D=3.6$	57.6	55.0±0.8	7.09±0.18	5.90±0.15
Hg	80	Hg	25.3	$D=3.6$	60.9	58.2±1.0	7.10±0.25	5.94±0.19
Pb	82	Pb	23.74	$D=3.63$	64.2	61.4±1.1	6.76±0.25	5.57±0.13
Bi	83	Bi	23.74	$D=3.57$	71.1	68.0±0.8	5.61±0.17	6.77±0.22
U	92	UO_3	12.7	$D=3.6$	66.7	65.1±1.0	10.20±0.67	

Z is atomic number.
D is diameter.

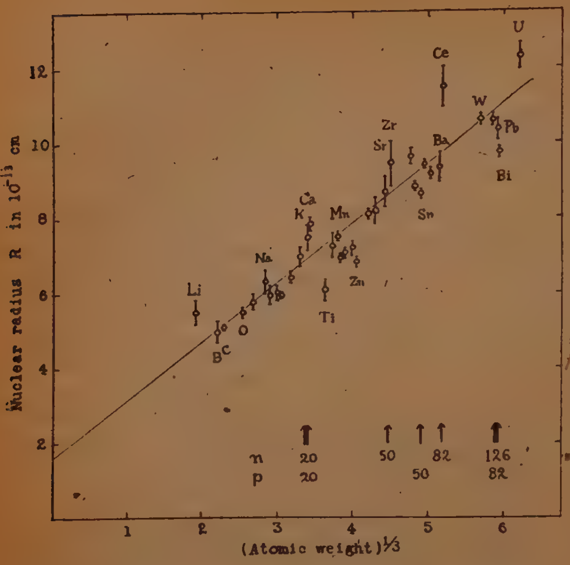

Fig. 1. Total cross sections for Li-D neutrons.

The values of cross sections obtained by using the different size or different thickness for the same element agreed with each other within experimental errors after the corrections were made by the procedure mentioned in section 2. The values shown in the eighth column of Table I. is the mean values thus obtained.

Tests for the exponential law was also made for paraffin and lead and was found that the exponential law holds untill 50% transmission. Therefore, we may consider the neutron cross sections not to vary so sensitively with energy that the cross sections obtained by transmission method become meaningless on account of the heterogeneity of the neutron energy.

If the ionization current by X-rays or γ-rays was considerable in our ionization chamber, absorption curve by lead would show steep drop at the beginning. As the absorption curve was proved to be exponential, we can regard it as another proof that the effects of X-rays or γ-rays can be neglected in our experiment.

In the last column of Table I, the values of Kikuchi and Aoki are shown. As their cross sections were calculated by assuming the angular distribution of scattered neutrons to be isotropic, we have recalculated them by the same procedure as in the present experiment. From the value of cross section for proton, the mean energy of neutrons in their experiment was taken as 4.3 Mev.

As seen from Fig. 1, the cross sections fall on a smooth curve which rises rapidly with atomic weight up to Ca. From the value of 3.89 barns for Ca, the cross section for Ti falls as low as 2,34 barns. Then the cross section curve again rises up to Zn. The next irregular point occurs at Sn, where the curve shows a dip. Similar dip observed at Bi is more pronounced and the value for U is as high as 10.20 barns in comparison with the value of 5.61 barns for Bi. The cross section for Ce is seen to be fairly large than the neighbouring nuclei although the probable error is relatively large on account of the small quantity of the specimen.

§ 4. Discussion.

We shall examine the anomalous behavior of the cross sections at closed shell nuclei. We may suppose, on the shell structure model of nuclei, that the density of energy levels at closed shell is so small that the capture cross section of neutrons becomes very small.

In fact it was pointed out by Mayer(8) that capture cross section of neutrons are very small at closed shell nuclei, and for fast neutrons of mean energy 1 Mev, Hughes and Shermann(11) observed the capture cross sections to be markedly small at closed shell nuclei by a factor of about 100 from the neighbouring nuclei.

Dips of cross sections at Sn and at Pb and Bi as seen from Fig. 1 may be explained in the above manner as they belong to magic number nuclei of proton number (p) 50 (Sn) and 82 (Pb) and neutron number (n) 126 (Bi). But when we look at the other magic number nuclei, i.e., K (for which 93% is n=20), Ca (n=20, p=20), Zr (48% is n=50), Sr (83% is n=50), and Ce (89% is n=82), we find the cross sections for K, Ca, Zr, and Ce to be larger, and also the value for Sr is not smaller than the neighbouring nuclei.

It is convenient for the purpose of finding out the anomalous behavior of cross sections (σ) to plot the nuclear radii (R) against atomic weight (A) by the relation

$$\sigma = 2\pi R^2 . \qquad (3)$$

As is seen from Fig. 2, Ti and Zn show smaller values which have no relation with magic number. Irregularities at magic nnmbers are also evident in Fig. 2.

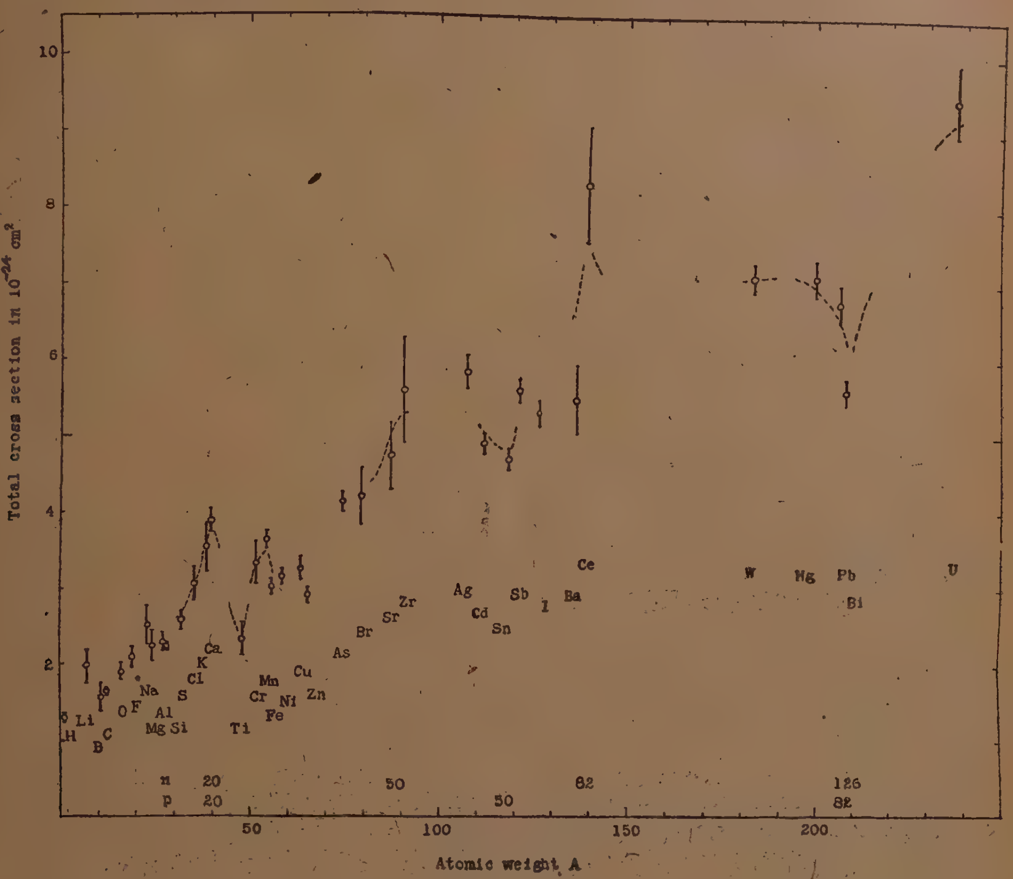

Fig. 2. Nuclear radius R calculated from the formula $\sigma = 2\pi R^2$, plotted against $A^{1/3}$, where σ is the total cross section and A, the atomic weight. The straight line represents the relation $R = 1.4 + 1.6\ A^{1/3}$.

We must, however, think of that the total cross section we have measured is the sum of elastic scattering, which has been interpreted as the diffraction of neutrons by nucleus, and the process leading to the formation of compound nucleus such as the inelastic scattering, disintegration, and capture.

The probability of the latter process is governed, without doubt, by the energy level density and is small at closed shell nuclei as is demonstrated by the experiment of Hughes and Shermann. The observation of γ-ray intensities produced by inelastic scattering of D-D neutrons (2.5 Mev) by Aoki(13) also shows small values at closed shell nuclei.

Therefore, the large values of total cross sections for magic number nuclei must be ascribed to elastic scattering.

As the ratio of elastic and inelastic scattering is not accurately known in the present experiment, we shall examine the case for D-D neutrons which were studied by Aoki and Nonaka.(13)

Aoki found no γ-rays due to inelastic scattering of D-D neutrons by Ca. If the cross section for inelastic scattering do not become anomalously large for our Li-D neutrons, we may expect the inelastic scattering cross section for Ca to be also very small than the neighbouring nuclei. Therefore, the large total cross section of Ca found in this experiment shows that elastic scattering cross section is very large for this magic number nucleus.

Nonaka measured the absolute cross section of inelastic scattering for Cu and, combining his result with that of Aoki, obtained separately the cross sections for elastic and inelastic scattering of D-D neutrons. His results show, besides other small irregularities, that elastic scattering cross sections are very large and inelastic scattering cross seceions are small for K, Ca, Sr, Ba, Pb, and Bi, which are all magic number nuclei. If the tendencies of inelastic scattering cross sections are not very different for Li-D neutrons as D-D neutrons,* we may also expect that elastic scattering cross sections are large for Sr, Ba, Ce, Pb, and Bi than the neighbouring nuclei, irrespective of the difference of neutron neutron energies.

The reason why the elastic scattering is large at magic number nuclei contrary to inelastic scattering may be explained qualitatively following the consideration of Bethe on the "continum theory of nucleus,"(15) In this theory, the nucleus is described by a sphere of radius R with an absorption coefficient with diffuse boundary. The formation probability of the compound nucleus depends on the diffuseness of the nuclear boundary rather than on the nuclear radius R. If the nucleus had a sharp boundary, the result would be a large reflectivity and a small sticking probability. Elastic scattering is the reflection from the nucleus and interpreted as shadow diffraction which goes mainly in the forward direction. The diffuseness of the nuclear boundary comes from the diffuseness of the region actually occupied by the particles in the nucleus and partly from the range of the nuclear forces.

It is quite plausible to think that at closed shell nucleus, the diffuseness of the nuclear boundary becomes small, leading to small inelastic scattering and large elastic scattering.

It seems plausible to think that at magic number nuclei the diffuseness of the nuclear boundary become small than the neighbouring nuclei, thus leading to small inelastic scattering and large elastic scattering.

There is another evidence in favour of this idea. Forward scattering of D-D neutrons were studied by us and the result shows that generally forward scattering becomes more prominent with increasing atomic number.(16) Inspite of this general rule, neutrons are more scattered in the forward direction by Fe $(Z=26)$ than scattered by Cu$(Z=29)$. From the above idea inelastic scattering should be larger at Cu than at Fe. Aoki observed for Fe about 80% more γ-rays than for Fe due to inelastic scattering of neutrons, which agrees with the above expectation.

It will be interesting to study whether the angular distribution of scattered neutrons is given by the formula (1) at closed shell nuclei.

Next, we shall compare the results with that of Kikuchi and Aoki. The differences should be ascribed to the influence of mean energy of neutrons.

Irregular variations of cross sections up to Ga observed by Kikuchi and Aoki became smooth in the present experiment and this may be interpreted by the little effect of the individual resonance levels as the excitation energy became large. But the large values for Ca and Sr, and small values for Ti, Sn and Pb are same in both cases. These characters are observed also in the scattering of D-D neutrons and show that they can not be interpreted by energetic resonance phenomena.

In conclusion, we wish to express our thanks to Prof. S. Kikuchi for his encouragement through the work, to Prof. K. Husimi and Messrs. J. Sanada and S. Yamabe for discussions, and to Mr. S. Ozaki for his valuable aids during the construction of the static generater. Our thanks are also due to Mr. O. Takayanagi for his technical assistances.

This work was supported by the grant for the promotion of science from the Ministry of Education.

References.

(1) J. R. Dunning, Phys. Rev. **45** (1934) 586; **48** (1935), 265.

---

* Kikuchi et al.(14) studied the inelastic scattering of Ra (α)—Be neutrons, with similar energy distribution as Li-D neutrons, and concluded that the general tendencies are almost the same as in the case of D-D neutrons. This fact may be regarded as the justification of the above assumptions. Of course, the study of inelastic scattering of Li-D neutrons are desirable to draw decisive conclusion and we are now going to investigate this problem in the next work.

(2) S. Kikuchi and H. Aoki, Proc. Phys. Math. Soc. Japan, **21** (1939), 75.
(3) H. Aoki, Proc. Phy. Math. Soc. Japan, **21** (1939), 232.
(4) L. W. Seagondollar and H. H. Barshall, Phy. Rev. **72** (1947) 439.
H. H. Barshall, C. K. Bockellmann, and L. W. Seagondollar, Phy, Rev. **75** (1948), 659.
R. K. Adair, H. H. Barshall, C. K. Bockellmann, and O. Sala, Phy. Rev. **75** (1949), 1124.
R. K. Adair, C. K. Bockellmann, and R. E. Peterson, Phy. Rev. **76** (1949), 308.
(5) G. Freier, M. Fulk, E. E. Lampi, and J. H. Williams, Phy. Rev. **78** (1950), 508.
(6) E. Amaldi, D. Bocciarelli, B. N. Cacciapuoti, and G. C. Trabacchi, Physical Society Cambridge Conference, p. 97, 1947.
(7) R. Sherr, Phy. Rev. **68** (1945), 240.
(8) M. G. Mayer, Phy. Rev. **74** (1948), 235; **78** (195), 19.
E. Feenberg, Phy. Rev. **77** (1950), 771.
(9) W. E. Bennet, T. V. Bonner, H. T. Richards, and B. E. Watt, Phys. Rev. **71** (1947), 9.
(10) G. Placzek and H. A. Bethe, Phy. Rev. **57** (1940), 1075.
(11) D. J. Hughes and D. Shermann, Phy. Rev. **78** (1950), 632.
(12) H. Aoki, Proc. Phys. Math. Soc. Japan, **18** (1936), 115.
(13) I. Nonaka, Proc. Phys. Math. Soc. Japan **25** (1943), 227; **26** (1944), 66.
(14) S. Kikuchi, H. Aoki, and K. Husimi, Proc. Phys. Math. Soc. Japan, **18** (1936), 297.
(15) H. A. Bethe, Phys. Rev. **57** (1940), 1125.
(16) S. Kikuchi, H. Aoki, and T. Wakatsuki, Proc. Phys. Math. Soc. Japan, **21** (1939), 410.
T. Wakatsuki and S. Kikuchi, Proc. Phys. Math. Soc. Japan, **21** (1939), 656.

On the Theory of Shock Waves Produced by a Rigid Wedge Moving through an Elastic Medium with Supersonic Velecities.

By Ken-ichi KUSUKAWA.

Physical Institute, Faculty of Science, Tôkyô Metropolitan University.

(Read April 6, 1947, Received July 17, 1950).

§ 1. Introduction.

It is well known that there exists a solution iscontinuous through a shock wave when an obstacle moves in a compressible fluid with supersonic velocities. In this paper we shall discuss he shock wave, which is grown when the two-imensional wedge moves through an elastic edium with supersonic velocities.

§ 2. Fundamental equations.

We shall take ξ-axis which divides the vertex ngle equally, and η-axis orthogonal to ξ-axis.

Assuming strains to be very small, and putting $V_\xi = V_0 + v_\xi$, $V_\eta = v_\eta$, we have

$$V_0^2 \partial^2 v_\xi / \partial \xi^2 = (\mu/\rho) \Delta v_\xi + \{(\lambda+\mu)/\rho\} \partial/\partial\xi (\operatorname{div} V), \quad (2,1)$$

nd

$$V_0^2 \partial^2 v_\eta / \partial \xi^2 = (\mu/\rho) \Delta v_\eta + \{(\lambda+\mu)/\rho\} \partial/\partial\eta (\operatorname{div} V), \quad (2,2)$$

here V_0 is the speed to uniform general flow, ρ is the density, λ and μ are the Lamé's constants, and $V = (v_\xi, v_\eta)$. Calculating $\partial/\partial\xi(2,1) + \partial/\partial\mu(2,2)$, we have,

$$(1-M^2)\partial^2 \operatorname{div} V/\partial\xi^2 + \partial^2 \operatorname{div} V/\partial\eta^2 = 0, \quad (2,3)$$

where $M = V_0(\lambda+2\mu)^{-1/2}\rho^{1/2} = V_0/c_\Theta > 1$,

and M is the Mach number.

While, calculating $\partial/\partial\xi(2,2) - \partial/\partial\eta(2,1)$, we have,

$$(1-M'^2)\partial^2 \operatorname{rot} V/\partial\xi^2 + \partial^2 \operatorname{rot} V/\partial\eta^2 = 0, \quad (2,4)$$

where $M' = V_0 \rho^{1/2} \mu^{-1/2} = V_0/Cr$

and M' is the Mach number in the equivoluminal case. (2,3) and (2,4) take the form of the wave equation.

§ 3. Irrotational case.

In this case $\operatorname{rot} V$ vanishes, and from (2,3) we have

$$\operatorname{div} V = f_1(\xi - \sqrt{M^2-1}\,\eta) + f_2(\xi + \sqrt{M^2-1}\,\eta). \quad (3,1)$$

From the form of the function (3,1), we can presume that there exist shock waves, which are the straight lines drawn through the origin (or the vertex of the wedge) with the inclination $\alpha = \pm \mathrm{Sin}^{-1} 1/M$, where α is the Mach angle.

Now taking the x-axis parallel, and the z-axis orthogonal, to this shock wave, we denote velocity components by U and W, normal and shearing stresses by σ and τ, and strains by ϵ and γ, respectively. And suffices "1", "2", represent the quantities in front of, or behind, the shock wave respectively. And the half vertex angle of the wedge is γ. From the continuity of mass, we have

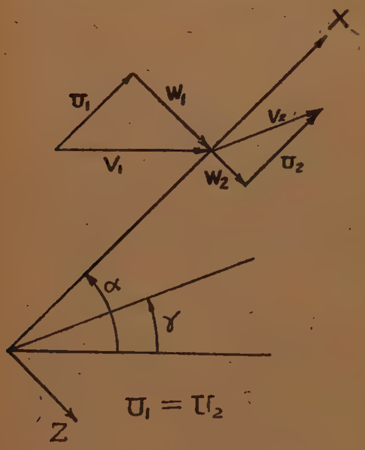

Fig. 1.

$$\rho_1 W_2 = \rho_1 W_2 = m. \qquad (3,2)$$

From the continuity of momentum, we have

$$\rho_1 W_1(W_2 - W_1) = \sigma z_2 - \sigma z_1 = (\lambda + 2\mu)(\epsilon z_2 - \epsilon z_1), \qquad (3,3)$$

and

$$\rho_1 W_1(U_2 - U_1) = \tau z x_2 - \tau z x_1 = \mu(\gamma z x_2 - \gamma z x_1) = 0, \qquad (3,4)$$

which represents the condition of non-rotation. From the continuity of energy, we have

$$\begin{aligned}&(1/2)m(W_2^2 - W_1^2) + (m/2\rho_1)[\lambda\{\varepsilon_{x_2} + \varepsilon_{y_2} + \varepsilon_{z_2}\}^2 \\ &\quad - \lambda\{\varepsilon_{x_1} + \varepsilon_{y_1} + \varepsilon_{z_1}\}^2 + 2\mu(\varepsilon^2{z_2} - \varepsilon^2{z_1})] = \sigma z_2 W_2 - \sigma z_1 W_1 \\ &\quad = \lambda(\varepsilon_{x_1} + \varepsilon_{y_1})(W_2 - W_1) + (\lambda + 2\mu)(\varepsilon_{z_2} W_2 - \varepsilon_{z_1} W_1). \qquad (3,5)\end{aligned}$$

Then, we assume the continuity of the shape and the area of the section of the tube of flow. That is

$$\varepsilon_{y_1} = \varepsilon_{y_2}, \quad \varepsilon_{x_1} = \varepsilon_{x_2}, \quad \gamma_{xy_1} = \gamma_{xy_2}. \qquad (3,6)$$

From these formulae, we get

$$\begin{aligned}&(W_2 - W_1)\left(\frac{W_1^2}{C_\theta^2} - 1\right) \\ &\quad \times \{W_1(W_2 - W_1) + (2\lambda/\rho_1)(\varepsilon_{x_1} + \varepsilon_{y_1}) + 2C_\theta^2 \varepsilon_{z_1}\} = 0. \qquad (3,7)\end{aligned}$$

Considering $\sin\alpha = 1/M = C_\theta/V_0 = W_1/V_0$, we have $W_1 = C_\theta$. Therefore the formula (3,7) contains no contradiction.

W_2 can be determined from the geometrical condition of the flow, or

$$\left.\begin{aligned}W_2 &= W_1 \times \tan(\alpha - \gamma)/\tan\alpha, \\ W_1 &= C_\theta = (\lambda + 2\mu)^{1/2} \cdot \rho^{-\frac{1}{2}},\end{aligned}\right\} \qquad (3,8)$$

The stresses are given in the following form.

$$\left.\begin{aligned}\sigma_{z_2} - \sigma_{z_1} &= (\lambda + 2\mu)\{\tan(\alpha - \gamma\ /\tan\alpha - 1\}, \\ \sigma_{x_2} - \sigma_{x_1} &= \lambda\{\tan(\alpha - \gamma)/\tan\alpha - 1\}, \\ \gamma_{zx_2} - \gamma_{zx_1} &= 0.\end{aligned}\right\} \qquad (3,9)$$

when γ is very small, $\sigma z_2 - \sigma z_1$ is reduced to $-\gamma\{\rho_1 V_0^2 (V_0^2/C_\theta^2 - 1)^{-1/2}\}$, which is corresponding to J. Ackeret's formula for the compressible fluid. Considering the case: $\sigma x_1 = \sigma z_1 = \gamma z x_1 = 0$, $\tau_{\xi\eta_2}$ and σ_{η_2} are given in the following formulae,

$$\tau_{\xi\eta_2} = \mu \sin 2(\alpha - \gamma)\{1 - \tan(\alpha - \gamma)/\tan\alpha\}, \qquad (3,10)$$

$$\sigma_{\eta_2} = -\{\lambda + 2\mu\cos^2(\alpha - \gamma)\}\{1 - \tan(\alpha - \gamma)/\tan\alpha\}. \qquad (3,11)$$

Therefore for the existence of the solution described above, the coefficient of friction of the wedge's surface must be

$$\eta_{fr} = \mu \sin 2(\alpha - \gamma)\{\lambda + \mu + \mu\cos 2(\alpha - \gamma)\}^{-1}. \qquad (3,12)$$

Because $0 < \eta_{fr} < \mu/(\lambda + \mu) < 1$, this solution can be realized practically.

At last from (3,2) (3,3) and (3,5), we obtain the relation in respect of ε and ρ,

$$\begin{aligned}&\{(\lambda + 2\mu)/2\}(\varepsilon z_2 - \varepsilon z_1)(1/\rho_2 + 1/\rho_1) + \{(\varepsilon z_2 - \varepsilon z_1)/2\rho_1\} \\ &\quad \times \{2\lambda\, \varepsilon_{x_1} + \varepsilon_{y_1}) + (\lambda + 2\mu)(\varepsilon_{z_2} + \varepsilon_{z_1})\} \\ &\quad = \lambda(\varepsilon_{x_1} + \varepsilon_{y_1})(1/\rho_2 - 1/\rho_1) + (\lambda + 2\mu)(\varepsilon z_2/\rho_2 - \varepsilon z_1/\rho_1), \qquad (3,13)\end{aligned}$$

which is corresponding to Rankine-Hugoniot's formula for the compressible fluid.

§ 4. Equi-voluminal case.

When $\operatorname{div} V = 0$, from (2,4) we have

$$\operatorname{rot} V = f_1(\xi - \sqrt{M'^2 - 1}\,\eta) + f_2(\xi + \sqrt{M'^2 - 1} \cdot \eta). \qquad (4,1)$$

From the form of the function (4,1) we can presume that there exist the shock waves whose wave fronts are the straight lines drawn through the origin (or the vertex of the wedge) with the inclination.

$$\beta = \mathrm{Sin}^{-1} Cr/V_0 \tag{4,2}$$

We shall take the coordinates and the notations which are same as those of the irrotational case.

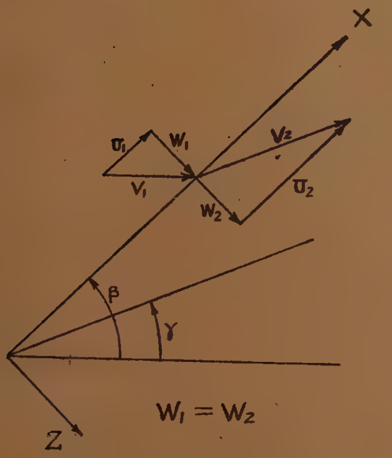

Fig. 2.

Considering the continuity of mass, momentum, energy, the form and the area of the section of the tube of flow, and the condition of equivoluminal flow, we have the following condition

$$U_2 = -\gamma zx_1 \cdot C_r. \tag{4,3}$$

While, from the geometrical condition, we have

$$C_r/U_1 = W_1/U_1 = \tan\beta,\ W_2/U_2 = W_1/U_2 = \tan(\beta-\gamma). \tag{4,4}$$

From (4,3) and (4,4) we obtain the following condition

$$\gamma zx_1 = -\cot(\beta-\gamma). \tag{4,5}$$

Therefore, the shearing strain in front of the shock wave must take the value given by the formula (4,5) for the existence of the solution described above. In this case, the shearing stress is given by the following formula.

$$\tau zx_2 - \tau zx_1 = \rho_1 Cr U_1\{\tan\beta/\tan(\beta-\gamma)-1\}. \tag{4,6}$$

Now we shall discuss the mechanical character of the surface in this case. The normal- and shearing stresses over the surface are

$$\tau_{\xi\eta_2} = -\tau xz_2 \cos 2(\beta-\gamma), \tag{4,7}$$

and

$$\sigma_{\eta_2} = -\tau xz_2 \sin 2(\beta-\gamma). \tag{4,8}$$

In order that the medium flows along the surface, the normal stress must be the pressure, ($\sigma_{\eta_2} < 0$), and for $\sigma_{\eta_2} < 0$, we have $\tau_{\xi\eta} > 0$, from the equations (4,7) and (4,8).

Then the positive shearing stress ($\tau_{\xi\eta} > 0$) means that the shearing force acts in the direction of the velocity of flow, therefore this case cannot be realized with usual method.

§ 5. Numerical calculations.

The values of $\varepsilon z_2 - \varepsilon z_1$ are calculated for several values of Mach number (for $\gamma = 5°$) in the following table. It is remarkable that $|\varepsilon z_2 - \varepsilon z_1|$ takes the minimum value for $M = 1.36$.

$\gamma = 5^\circ$							
M	1.06	1.15	1.31	1.36	1.56	2.00	2.92
$\varepsilon z_2 - \varepsilon z_1$,	−0.21945	−0.17546	−0.16090	−0.16038	−0.16551	−0.19238	−0.26388

I thank heartily Dr. I. Imai for his useful suggestion.

On the Theory of Shock Waves Produced by a Rigid Cone Moving through an Elastic Medium with Supersonic Velocities.

By Ken-ichi KUSUKAWA.

Physical Institute, Faculty of Science, Tôkyô Metropolitan University.

(Read April 6, 1947, Received July 17, 1950)

§ 1. Introduction.

I discussed the two-dimensional shock wave of the elastic medium in a former paper [1]. I shall discuss the three-dimensional flow along a circular cone with supersonic velocities in this parer.

§ 2. Fundamental Equations.

Setting the velocity components to be (v_x, v_y, V_0+v_z), and $\mathbf{V} = (v_x\, v_y\, v_z)$, the fundamental equation can be described in the following form

$$V_0^2\, \partial^2 v_x/\partial z^2 = (\mu/\rho)\Delta v_x + (\lambda+\mu)/\rho\, \partial\, \mathrm{div}\ \mathbf{V}/\partial x \text{ etc.} \quad (2,1)$$

where V_0 is the uniform flow at infinity and

$$|v_x|,\ |v_y| \text{ and } |v_z| \ll V_0 .$$

From (2, 1) we have

$$(1-M^2)\, \partial^2\ \mathrm{div}\ \mathbf{V}/\partial z^2 + (\partial^2/\partial x^2 + \partial^2/\partial y^2)\ \mathrm{div}\ \mathbf{V} = 0, \quad (2,2)$$

where $M = V_0/C_\theta = V_0 (\lambda+2\mu)^{-1/2} \rho^{1/2}$,
which is the Mach number.

§ 3. Solutions.

We shall take the z-axis along the axis of the cone, and introduce the cylindrical coördinates. Then (2, 2) beomes

$$\partial^2 \Phi/\partial r^2 + (1/r)\, \partial\Phi/\partial r + (1-M^2)\, \partial^2\Phi/\partial z^2 = 0 , \quad (3,1)$$

where $x = r\cos\theta$, $y = r \sin\theta$, $\mathbf{V} = \mathrm{grad}\,\Phi$.

The solution of (3, 2) about the cone are given in the following form,

$$\Phi = -az \cosh^{-1}(z/\alpha r) + a\{z^2-\alpha^2 r^2\}^{1/2}, \quad (3,2)$$

where $\alpha = \sqrt{M^2-1}$,
and $a = V_0 \tan\gamma\{(\cot^2\gamma - \cot^2\beta)^{1/2}$
$+\tan\gamma \cosh^{-1}(\cot\gamma/\cot\beta)\}, ^{-1}$
and γ is the half vertex angle,
Thus we have

$$\left.\begin{aligned} v_z &= \partial\Phi/\partial z = -a \cosh^{-1}(z/\alpha r) , \\ v_r &= \partial\Phi/\partial r = a\, \alpha\{(z/\alpha r)^2-1\}^{1/2} . \end{aligned}\right\} \quad (3,3)$$

The shock wave forms the cone whose half vertex angle is $\beta = \mathrm{Tan}^{-1}(1/\alpha)$.

§ 4. Strains.

The strains being considered to be very small, we have the following relations

$$\left.\begin{aligned} \partial u/\partial t + V_0\, \partial u/\partial z &= v_r , \\ \partial w/\partial t + V_0\, \partial w/\partial z &= V_0 + v_z , \end{aligned}\right\} \quad (4,1)$$

where u and w are the r-component and the z-component of the displacement, and v_r, and V_0+v_z are the r-component and the z-component of the velocity, respectively.
Integrating (4,1) we have,

$$u = f_1(z-V_0 t) + (1/V_0)\int^z v_r(r, z)\, dz ,$$

$$w = f_2(z-V_0 t) + z + (1/V_0)\int^z v_z(r, z)\, dz . \quad (4,2)$$

From (4,2) we can calculate the strains in the following form

$$\begin{aligned} e_{rr} &= \partial u/\partial r = (1/V_0)\partial/\partial r\int^z v_r(r, z)\, dz , \\ e_{\theta\theta} &= u/r = (1/r)\{f_1(z-V_0 t) + (1/V_0)\int^z v_r(r,z)\, dz\} , \\ e_{zz} &= \partial w/\partial z = f_2'(z-V_0 t) + 1 + (1/V_0)\, v_r(r, z) , \\ \gamma_{rz} &= \partial u/\partial z + \partial w/\partial r = f_1'(z-V_0 t) + (1/V_0)\, v_r(r, z) \\ &\quad + (1/V_0)\, \partial/\partial r\int^z v_z(r, z)\, dz . \end{aligned} \quad (4,3)$$

In order that the strains may be stationary, the functions f_1 and f_2 must take the following form

$$f_1 = 0 ,\ f_2 = -A(z-V_0 t) , \quad (4,4)$$

where A is a constant.
Assuming the strains in front of the shock wave to vanish, we can calculate the strains behind the shock wave form (4,3) and (4,4), thus

$$\varepsilon_{rr} = -(a\alpha^2/2V_0)[(z/\alpha r)\{(z/\alpha r)^2-1\}^{1/2} + \log\{(z/\alpha r)+((z/\alpha r)^2-1)^{1/2}\}],$$

$$\varepsilon_{\theta\theta} = (a\alpha^2/2V_0)[(z/\alpha r)\{(z/\alpha r)^2-1\}^{1/2} - \log\{(z/\alpha r) + ((z/\alpha r)^2-1)^{1/2}\}],$$

$$\varepsilon_{zz} = -(a/V_0)\log[(z/\alpha r)+\{(z/\alpha r)^2-1\}^{1/2}],$$

$$\Theta = \varepsilon_{rr}+\varepsilon_{\theta\theta}+\varepsilon_{zz} \tag{4,5}$$

$$= -(a/V_0)(1+\alpha^2)\log[(z/\alpha r)+\{(z/\alpha r)^2-1\}^{1/2}],$$

$$\gamma_{rz} = 2a\alpha/V_0\{(z/\alpha r)^2-1\}^{1/2},$$

$$\partial u/\partial z - \partial w/2r = 0.$$

As $\partial u/\partial z-\partial w/\partial r$ vanishes, the considered flow is non-rotational.

§ 5. Numerical Calculation.

Values of strains at the wall (or $r/z = \tan\gamma$) are calculated for several values of the Mach number for $\gamma = 5^0$ and are shown in the following Table.

Table I.

M	1.06	1.15	1.31	1.36	1.56	2.00	2.92
ε_{rr}	-0.4867	-0.4908	-0.4964	-0.4982	-0.5047	-0.5139	-0.5534
$\varepsilon_{\theta\theta}$	0.4826	0.4817	0.4790	0.4778	0.4732	0.4554	0.4302
ε_{zz}	-0.030732	-0.027431	-0.024703	-0.024094	-0.022209	-0.019505	-0.016320
Θ	-0.0348	-0.0365	-0.0421	-0.0445	-0.0537	-0.0780	-0.1395
γ_{rz}	0.170	0.170	0.171	0.171	0.171	0.171	0.172

Also we have calculated the strains at the cylindrical surface $r = 10$ for the case $\gamma = 5°$, $\beta = 40°$ The results of the calculation are shown in the following figure.

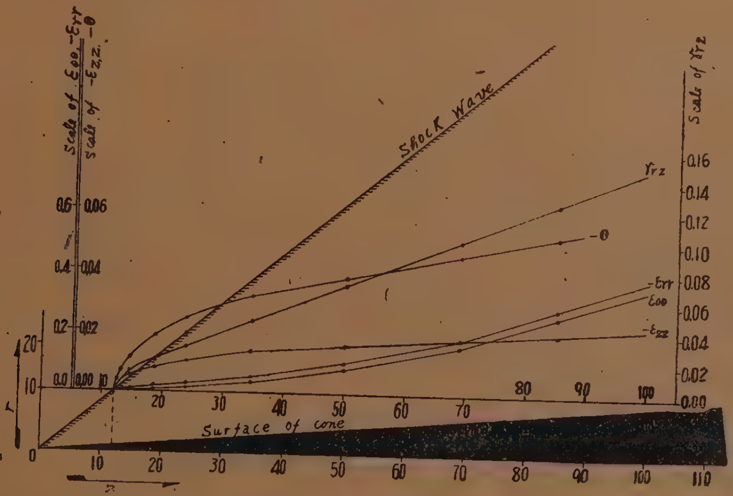

I thank heartily Dr. I. Imai for his useful suggestion.

References.

(1) Ken-ichi KUSUKAWA: Journ. Phys. Soc. Japan. **6** (1951).
(2) Th. v. KÁRMÁN and N. B. MOORE: Trans. Amer. Soc. Mech. Engr. **54** (1932) 303.

Application of the M^2-expansion Method to the Compressible Flow past an Elliptic Cylinder.

By Mitutosi KAWAGUCHI.

*Institute of Science and Technology, University of Tokyo.**

(Received July 29, 1950)

§ 1. Introduction and Summary.

As is well known, the two-dimensional irrotational flow of a compressible fluid can be dealt with by various methods, *e.g.*, the M^2-expansion method, the thin-wing-expansion method, and the hodograph method. The hodograph method can give successful results for several types of flow, but it is not suited for the discussion of the flow past an arbitrarily given obstacle. On the other hand, the thin-wing-expansion method can be only applicable to the flow past a thin obstacle, the region near the stagnation point being excluded.

Several years ago, Imai gave a formula which gives the velocity distribution on the surface of an obstacle of arbitrary shape, correctly to M^4, M being the Mach number [2]. In this paper, this formula will be applied to a uniform flow past an elliptic cylinder at zero angle of attack, in order to obtain the analytic expression, correct to M^4, for the velocity distribution over the elliptic cylinder. Numerical examples will be given for the cases $t=0.1$ and $t=0.5$, where t is the thickness ratio of the elliptic cylinder.

It should be mentioned here that the same problem has already been investigated by several writers employing various methods, thus by Kaplan [10], Tomotika and Tamada [11], Imai and Aihara [7], Imai [5], and Imai and Kawata [9] (the M^2-expansion method, correct to the order of M^2), by Imai [3], [6] and Hasimoto [1] (the thin-wing-expansion method), and by Tsien [12], and Imai and Hasimoto [8] (the hodograph method). Hence comparison of some of these investigations with the present one will also be made.

§ 2. Outline of Imai's Method.

For convenience a brief account will be given of the method of approximation given by Imai [2], [4].

As is well known, the region outside an arbitrary profile P in the z-plane can be conformally mapped on to a unit circle $Z=e^{i\theta}$ in the Z-plane by means of an analytic function of the form:

$$z=c_{-1}Z+c_0+c_1Z^{-1}+c_2Z^{-2}+\cdots,\ c_{-1}=\lambda e^{i\delta}, \tag{2.1}$$

the profile P itself being expressed as

$$x_P=x_P(\theta),\ y_P=y_P(\theta). \tag{2.2}$$

Let us assume that a uniform flow of velocity 1 and Mach nnmber M impinges on the profile P, in the direction making an angle α with the x-axis. Then the velocity distribution round the profile will be given by

$$q(\theta)=d\Phi/ds=(d\Phi/d\theta)(d\theta/ds), \tag{2.3}$$

where Φ is the velocity potential and ds is the line element along P, so that

$$dz_P/d\theta\equiv dx_P/d\theta+idy_P/d\theta=(ds/d\theta)\,e^{i\omega}, \tag{2.4}$$

and hence

$$ds/d\theta\equiv\sqrt{(dx_P/d\theta)^2+(dy_P/d\theta)^2}, \tag{2.5}$$

ω being the angle between ds and the x-axis.

Then we can write

$$\Phi(\theta)=\Phi_0(\theta)+M^2\Phi_1(\theta)+M^4\Phi_2(\theta)+\cdots, \tag{2.6}$$

with

$$\Phi_0(\theta)=2\lambda\cos(\theta-\alpha+\delta)-\kappa_0\theta, \tag{2.7}$$

$$\Phi_1(\theta)=P_1(\theta)-Q_1{}^*(\theta)-\kappa_1\theta, \tag{2.8}$$

$$\Phi_2(\theta)=P_2(\theta)-Q_2{}^*(\theta)-\kappa_2\theta, \tag{2.9}$$

where

$$P_1(\theta)+iQ_1(\theta)$$

$$=\frac{1}{4}\frac{d\Phi_0}{d\theta}\frac{d\theta}{ds}e^{-i(\omega-\alpha)}\int_{\theta_0}^{\theta}\left\{\left(\frac{d\Phi_0}{d\theta}\right)^2\frac{d\theta}{ds}e^{i(\omega-\alpha)}+2\kappa_0\right\}d\theta$$

$$-\frac{\lambda}{2}\cos(\theta-\alpha+\delta) \qquad (2.10)$$

$$P_2(\theta)+iQ_2(\theta)$$

$$=\frac{1}{16}\left\{\left(\frac{d\Phi_0}{d\theta}\right)^2\left(\frac{d\theta}{ds}\right)^2-1\right\}\frac{d\Phi_0}{d\theta}\frac{d\theta}{ds}e^{i(\omega-\alpha)}\int_{\theta_0}^{\theta}\left\{\left(\frac{d\Phi_0}{d\theta}\right)^2\frac{d\theta}{ds}e^{-i(\omega-\alpha)}+2\kappa_0\right\}d\theta$$

$$+\frac{1}{32}\frac{d}{d\theta}\left\{\frac{d\Phi_0}{d\theta}\frac{d\theta}{ds}e^{-i(\omega-\alpha)}\right\}\frac{d\theta}{ds}e^{-i(\omega-\alpha)}\left[\int_{\theta_0}^{\theta}\left\{\left(\frac{d\Phi_0}{d\theta}\right)^2\frac{d\theta}{ds}e^{i(\omega-\alpha)}+2\kappa_0\right\}d\theta\right]^2$$

$$+\frac{1}{16}\left\{\kappa_0\left(2\frac{d\Phi_0}{d\theta}\frac{d\theta}{ds}e^{-i(\omega-\alpha)}-1\right)-4\left(\frac{dQ_1^*}{d\theta}+i\frac{dQ_1}{d\theta}+\kappa_1\right)\right\}\frac{d\theta}{ds}e^{-i(\omega-\alpha)}\int_{\theta_0}^{\theta}\left\{\left(\frac{d\Phi_0}{d\theta}\right)^2\frac{d\theta}{ds}e^{i(\omega-\alpha)}+2\kappa_0\right\}d\theta$$

$$+\frac{1}{8}\frac{d\Phi_0}{d\theta}\frac{d\theta}{ds}e^{-i(\omega-\alpha)}\int_{\theta_0}^{\theta}\left[\left\{\kappa_0\left(\frac{d\Phi_0}{d\theta}\frac{d\theta}{ds}e^{i(\omega-\alpha)}-1\right)-4\left(\frac{dQ_1^*}{d\theta}-i\frac{dQ_1}{d\theta}+\kappa_1\right)\right\}\frac{d\Phi_0}{d\theta}\frac{d\theta}{ds}e^{i(\omega-\alpha)}+4\kappa_1\right]d\theta$$

$$+\frac{1}{4}[Q_1^*(\theta)-iQ_1(\theta)]-\frac{\gamma}{2}[P_1(\theta)+iQ_1(\theta)]-\frac{\gamma+1}{8}\lambda\cos(\theta-\alpha+\delta)$$

$$+\frac{\gamma+1}{16}\left(\frac{d\Phi_0}{d\theta}\right)^2\left(\frac{d\theta}{ds}\right)^2e^{-2i(\omega-\alpha)}\int_{\theta_0}^{\theta}\left\{\left(\frac{d\Phi_0}{d\theta}\right)^3\left(\frac{d\theta}{ds}\right)^2e^{2i(\omega-\alpha)}+3\kappa_0\right\}d\theta\,, \qquad (2.11)$$

where $\kappa_0, \kappa_1 \ldots$ are constants such that the circulation, Γ, round the profile is given by

$$\Gamma = 2\pi(\kappa_0+M^2\kappa_1+M^4\kappa_2+\cdots\cdots), \qquad (2.12)$$

and γ is the ratio of specific heats. $R^*(\theta)$ denotes the conjugate Fourier series corresponding to $R(\theta)$, so that, if

$$R(\theta) = a_0+\sum_{n=1}^{\infty}(a_n\cos n\theta+b_n\sin n\theta), \qquad (2.13)$$

hen

$$R^*(\theta) = \sum_{n=1}^{\infty}(a_n\sin n\theta-b_n\cos n\theta). \qquad (2.14)$$

Therefore, putting

$$P(\theta)+iQ(\theta) = \sum_{n=-\infty}^{\infty}C_n e^{ni\theta}, \qquad (2.15)$$

we have

$$P(\theta)-Q^*(\theta) = 2\Re\sum_{n=0}^{\infty}C_n e^{ni\theta}+\text{const.} \qquad (2.16)$$

Finally

$$\sum_{n=0}^{\infty}C_n e^{ni\theta} = \frac{1}{2\pi i}\int_C\frac{f(z)}{z-e^{i\theta}}dz\,, \qquad (2.17)$$

where $f(z)=\sum_{n=-\infty}^{\infty}C_n z^n$, and the path of integration C is a simple closed curve reconcilable with the unit circle and enclosing the point $z=e^{i\theta}$. The right-hand side of (2.17) may be most conveniently evaluated by the method of residues.

§ 3. Elliptic Cylinder.

We now consider a uniform flow, without circulation, past an elliptic cylinder at zero angle of attack, $\alpha=0$. For this purpose, we take, as the transformation function (2.1),

$$z = Z+\sigma^2/Z\,,\quad -1<\sigma^2<1\,. \qquad (3.1)$$

Putting $Z=e^{i\theta}$, we have

$$x_P = (1+\sigma^2)\cos\theta\,,\quad y_P = (1-\sigma^2)\sin\theta\,. \qquad (3.2)$$

Thus the profile in question is an ellipse whose thickness ratio is

$$t = (1-\sigma^2)/(1+\sigma^2)\,. \qquad (3.3)$$

Since, in this case, $c_{-1}=\lambda e^{i\delta}=1$, we have

$$\lambda=1\,,\qquad \delta=0\,. \qquad (3.4)$$

From (3.1)

$$dz = (1-\sigma^2/Z^2)\,dZ\,,$$

whence, putting $Z=e^{i\theta}$ and remembering (2.4), we get

$$\frac{d\theta}{ds}e^{-i\omega} = -i\frac{e^{-i\theta}}{1-\sigma^2e^{-2i\theta}}\,. \qquad (3.5)$$

Next, we have from (2.7) and (3.4)

$$\Phi_0(\theta) = 2\cos\theta\,. \qquad (3.6)$$

Combining (3.6), (2.8) and (2.10), Imai [5] has obtained

$$\Phi_1(\theta)=\Re\left[\frac{(1-\sigma^2)}{2\sigma^2}e^{i\theta}+\frac{(1-\sigma^2)^2(e^{2i\theta}-1)}{4\sigma^3(e^{2i\theta}-\sigma^2)}\log\frac{1+\sigma e^{i\theta}}{1-\sigma e^{i\theta}}\right.$$

$$\left.-\frac{(1-\sigma^2)^3e^{i\theta}}{4\sigma^4(e^{2i\theta}-\sigma^2)}\log\frac{1+\sigma^2}{1-\sigma^2}\right]+\text{const.}, \qquad (3.7)$$

and

$$P_1(\theta)+iQ_1(\theta)=\frac{1}{4}\frac{e^{2i\theta}-1}{e^{2i\theta}-\sigma^2}\left\{e^{-i\theta}+\frac{e^{i\theta}}{\sigma^2}\right.$$

$$\left.-\frac{(1-\sigma^2)^2}{2\sigma^3}\log\frac{1+\sigma e^{i\theta}}{1-\sigma e^{i\theta}}+C_1\right\}. \qquad (3.8)$$

We now proceed to the second approximation. For brevity, we shall only give the outline of the calculation and the final expression for $d\Phi_2/d\theta$.

Introducing (3.6), (3.7) and (3.8) into (2.11), and after integration, we have the explicit expression for $P_2(\theta)+iQ_2(\theta)$. Some parts in $P_2(\theta)+iQ_2(\theta)$ cannot be expressed in terms of elementary functions, remaining as indefinite integrals. From $P_2(\theta)+iQ_2(\theta)$ we have the expression for $f_2(z)$, by putting $e^{i\theta}=z$.

$f_2(z)$ is regular except at $z=0$, $\pm\sigma$, $\pm 1/\sigma$, and ∞. In view of (2.17), we have

$$\sum_{n=0}^{\infty} C_n e^{in\theta} = \frac{1}{2\pi i}\int_C \frac{f_2(z)}{z-e^{i\theta}}\,dz\,. \tag{3.9}$$

Since the poles of $f_2(z)/(z-e^{i\theta})$ included in C are evidently $e^{i\theta}$, 0, and $\pm\sigma$, we can write

$$\sum_{n=0}^{\infty} C_n e^{in\theta} = \mathrm{Res}\,(e^{i\theta})+\mathrm{Res}\,(0)+\mathrm{Res}\,(\sigma) + \mathrm{Res}\,(-\sigma)\,. \tag{3.10}$$

When we calculate some of these residues, we must alter the path of integration because of the logarithmic singularity of $f_2(z)$ at $\pm\sigma$, $\pm 1/\sigma$. Sometimes we must carry out straightforward integration along the path C and express these results by definite integrals involving σ as a parameter. In this way we can find an explicit expression for $\sum_{n=0} C_n e^{in\theta}$. Taking the real part of this function we have $\Phi_2(\theta)$; and differentiating $\Phi_2(\theta)$ we finally arrive at the expression for $d\Phi_2/d\theta$.

$$\begin{aligned}
d\Phi_2/d\theta = \; & A_1 \sin\theta + A_2 \sin 2\theta \log\frac{1+\sigma^2-2\sigma\cos\theta}{1+\sigma^2+2\sigma\cos\theta} + A_3 \,\mathrm{Tan}^{-1}\left(\frac{2\sigma\sin\theta}{1-\sigma^2}\right) + A_4 \sin\theta\left\{\log\frac{1+\sigma^2-2\sigma\cos\theta}{1+\sigma^2+2\sigma\cos\theta}\right\}^2 \\
& + A_5 \sin\theta\left\{\mathrm{Tan}^{-1}\left(\frac{2\sigma\sin\theta}{1-\sigma^2}\right)\right\}^2 + A_6\cos\theta\log\frac{1+\sigma^2-2\sigma\cos\theta}{1+\sigma^2+2\sigma\cos\theta}\,\mathrm{Tan}^{-1}\left(\frac{2\sigma\sin\theta}{1-\sigma^2}\right) \\
& + \left\{A_7\sin\theta + A_8 \sin 2\theta\log\left(\frac{1-\sigma^2}{\sigma^2}\right) + A_9\sin 2\theta\log\frac{1+\sigma^2-2\sigma\cos\theta}{1+\sigma^2+2\sigma\cos\theta} + A_{10}\,\mathrm{Tan}^{-1}\left(\frac{2\sigma\sin\theta}{1-\sigma^2}\right)\right\}\log\frac{1+\sigma^2}{1-\sigma^2} \\
& + A_{11}\sin\theta\left(\log\frac{1+\sigma^2}{1-\sigma^2}\right)^2 + (A_{12}\sin\theta + A_{13}\sin 2\theta)\,L_1(\sigma) + (A_{14}\sin\theta+A_{15}\sin 2\theta)\,L_2(\sigma) + A_{16}\sin\theta\, L_3(\sigma,\theta) \\
& + A_{17}\sin\theta\, L_4(\sigma,\theta) + A_{18}\sin 2\theta\, L_5(\sigma) + A_{19}\sin 2\theta\, L_6(\sigma) + A_{20}\sin 2\theta\, L_7(\sigma,\theta) + A_{21}\, L_8(\sigma,\theta) + A_{22}\sin\theta\, L_9(\sigma,\theta) \\
& + A_{23}\sin\theta\, L_{10}(\sigma,\theta) + \gamma\left[B_1\sin\theta + B_2\sin 2\theta\log\frac{1+\sigma^2-2\sigma\cos\theta}{1+\sigma^2+2\sigma\cos\theta} + B_3\,\mathrm{Tan}^{-1}\left(\frac{2\sigma\sin\theta}{1-\sigma^2}\right) + B_4\sin\theta\log\frac{1+\sigma^2}{1-\sigma^2}\right],
\end{aligned} \tag{3.11}$$

where

$$A_1 = -\frac{(1-\sigma^2)(2+\sigma^2)}{8\sigma^4} + \frac{(1-\sigma^2)^2(9+59\sigma^2+48\sigma^4+43\sigma^6+\sigma^8)}{32\sigma^6(1+\sigma^2)^2\Theta} - \frac{(1-\sigma^2)^4(6+31\sigma^2+6\sigma^4)}{16\sigma^6\Theta^2},$$

$$A_2 = \frac{(1-\sigma^2)^4(3+16\sigma^2+23\sigma^4+14\sigma^6+2\sigma^8)}{16\sigma^7(1+\sigma^2)^2\Theta^2} - \frac{(1-\sigma^2)^6(1+\sigma^2)^2(3+14\sigma^2+3\sigma^4)}{16\sigma^7\Theta^3},$$

$$A_3 = -\frac{(1-\sigma^2)^3(3+10\sigma^2-5\sigma^4+10\sigma^6+2\sigma^8)}{16\sigma^9\Theta} + \frac{(1-\sigma^2)^5(6+30\sigma^2+25\sigma^4+28\sigma^6+5\sigma^8)}{16\sigma^9\Theta^2} - \frac{(1-\sigma^2)^7(1+\sigma^2)^2(3+14\sigma^2+3\sigma^4)}{16\sigma^9\Theta^3},$$

$$A_4 = -\frac{3(1-\sigma^2)^6(1+3\sigma^2+\sigma^4)}{128\sigma^8\Theta^2} + \frac{(1-\sigma^2)^6(1+\sigma^2)^2(9+2\sigma^2+9\sigma^4)}{128\sigma^8\Theta^3} - \frac{3(1-\sigma^2)^8(1+\sigma^2)^4}{64\sigma^8\Theta^4};$$

$$A_5 = \frac{3(1-\sigma^2)^6(1-\sigma^2+\sigma^4)}{32\sigma^8\Theta^2} - \frac{(1-\sigma^2)^6(1+\sigma^2)^2(9-14\sigma^2+9\sigma^4)}{32\sigma^8\Theta^3} + \frac{3(1-\sigma^2)^8(1+\sigma^2)^4}{16\sigma^8\Theta^4};$$

$$A_6 = -\frac{3(1-\sigma^2)^5(1+\sigma^6)}{32\sigma^8\Theta^2} + \frac{3(1-\sigma^2)^7(1+\sigma^2)(3+2\sigma^2+3\sigma^4)}{32\sigma^8\Theta^3} - \frac{3(1-\sigma^2)^9(1+\sigma^2)^3}{16\sigma^8\Theta^4},$$

$$\begin{aligned}
A_7 = & -\frac{(1-\sigma^2)^4(9+46\sigma^2+5\sigma^4)}{64\sigma^8\Theta} + \frac{(1-\sigma^2)^4(9+41\sigma^2+22\sigma^4+37\sigma^6+7\sigma^8)}{16\sigma^8\Theta^2} - \frac{(1-\sigma^2)^6(1+\sigma^2)^2(3+14\sigma^2+3\sigma^4)}{8\sigma^8\Theta^3} \\
& + \left\{\frac{3(1-\sigma^2)^4}{8\sigma^4(1+\sigma^2)^2\Theta} - \frac{3(1-\sigma^2)^4}{4\sigma^4\Theta^2}\right\}\log 2\,, \qquad A_8 = \frac{(1-\sigma^2)^4}{4\sigma^3(1+\sigma^2)\Theta^2}
\end{aligned}$$

$$A_9 = -\frac{(1-\sigma^2)^6(3+2\sigma^2+3\sigma^4)}{64\sigma^7(1+\sigma^2)\Theta^2} + \frac{(1-\sigma^2)^6(1+\sigma^2)(3+2\sigma^2+3\sigma^4)}{16\sigma^7\Theta^3} - \frac{3(1-\sigma^2)^8(1+\sigma^2)^3}{16\sigma^7\Theta^4}$$

$$A_{10}=\frac{(1-\sigma^2)^3(3-14\sigma^2+14\sigma^4-14\sigma^6+3\sigma^8)}{64\sigma^9\Theta}-\frac{(1-\sigma^2)^5(15-16\sigma^2-14\sigma^4-16\sigma^6+15\sigma^8}{64\sigma^9\Theta^2}$$
$$+\frac{(1-\sigma^2)^7(1+\sigma^2)^2(3-\sigma^2+3\sigma^4)}{8\sigma^9\Theta^3}-\frac{3(1-\sigma^2)^9(1+\sigma^2)^4}{16\sigma^9\Theta^4},$$

$$A_{11}=\frac{3(1-\sigma^2)^4(1-4\sigma^2-2\sigma^4-4\sigma^6+\sigma^8)}{128\sigma^8(1+\sigma^2)^2\Theta}-\frac{3(1-\sigma^2)^4(3-6\sigma^2-2\sigma^4-6\sigma^6+3\sigma^8)}{64\sigma^8\Theta^2}$$
$$+\frac{3(1-\sigma^2)^6(1+\sigma^2)^2(3-2\sigma^2+3\sigma^4)}{32\sigma^8\Theta^3}-\frac{3(1-\sigma^2)^8(1+\sigma^2)^4}{16\sigma^8\Theta^4},$$

$$A_{12}=\frac{3(1-\sigma^2)^4}{8\sigma^4(1+\sigma^2)^2\Theta}-\frac{3(1-\sigma^2)^4}{4\sigma^4\Theta^2},\qquad A_{13}=\frac{(1-\sigma^2)^4}{2\sigma^3(1+\sigma^2)\Theta^2},$$

$$A_{14}=\frac{3(1-\sigma^2)^4}{8\sigma^2(1+\sigma^2)^2\Theta}-\frac{3(1-\sigma^2)^4(1+\sigma^4)}{8\sigma^4\Theta^2}+\frac{(1-\sigma^2)^6(1+\sigma^2)^2}{2\sigma^4\Theta^3},\qquad A_{15}=\frac{(1-\sigma^2)^4}{2\sigma(1+\sigma^2)\Theta^2},$$

$$A_{16}=-\frac{3(1-\sigma^2)^6}{8\sigma^6\Theta^2}+\frac{(1-\sigma^2)^6(1+\sigma^2)^2}{2\sigma^6\Theta^3},\qquad A_{17}=\frac{(1-\sigma^2)^5(1+\sigma^2)}{16\sigma^8\Theta}-\frac{(1-\sigma^2)^5(1+\sigma^2)(5-2\sigma^2+5\sigma^4)}{16\sigma^8\Theta^2}+\frac{(1-\sigma^2)^7(1+\sigma^2)^3}{4\sigma^8\Theta^3}$$

$$A_{18}=\frac{(1-\sigma^2)^4}{2\sigma(1+\sigma^2)\Theta^2},\qquad A_{19}=\frac{(1-\sigma^2)^4}{2\sigma^3(1+\sigma^2)\Theta^2},\qquad A_{20}=\frac{(1-\sigma^2)^5}{2\sigma^3\Theta^2},$$

$$A_{21}=-\frac{(1-\sigma^2)^4(1+\sigma^4)}{8\sigma^5(1+\sigma^2)\Theta}+\frac{(1-\sigma^2)^6(1+\sigma^2)}{8\sigma^5\Theta^2},\qquad A_{22}=\frac{(1-\sigma^2)^6}{8\sigma^8\Theta}-\frac{(1-\sigma^2)^6(1+\sigma^2)^2}{8\sigma^8\Theta^2},$$

$$A_{23}=\frac{(1-\sigma^2)^5(1+\sigma^2)}{8\sigma^{10}}-\frac{(1-\sigma^2)^5(1+\sigma^2)(1+\sigma^4)}{4\sigma^{10}\Theta}+\frac{(1-\sigma^2)^7(1+\sigma^2)^3}{8\sigma^{10}\Theta^2},$$

$$B_1=-\frac{(1-\sigma^2)^2}{8\sigma^4}+\frac{(1-\sigma^2)^2(9+26\sigma^2+10\sigma^4-6\sigma^6-7\sigma^8)}{32\sigma^6(1+\sigma^2)^2\Theta}-\frac{(1-\sigma^2)^4(3+7\sigma^2+3\sigma^4)}{8\sigma^6\Theta^2},$$

$$B_2=\frac{(1-\sigma^2)^4(1+\sigma^2)(3+3\sigma^2+\sigma^4)}{16\sigma^7\Theta^2}-\frac{3(1-\sigma^2)^6(1+\sigma^2)^3}{16\sigma^7\Theta^3},$$

$$B_3=-\frac{(1-\sigma^2)^3(3+3\sigma^2-2\sigma^4+3\sigma^6+\sigma^8)}{16\sigma^9\Theta}+\frac{(1-\sigma^2)^5(1+\sigma^2)^2(6+3\sigma^2+4\sigma^4)}{16\sigma^9\Theta^2}-\frac{3(1-\sigma^2)^7(1+\sigma^2)^4}{16\sigma^9\Theta^3},$$

$$B_4=-\frac{(1-\sigma^2)^4(9+18\sigma^2+\sigma^4)}{64\sigma^8\Theta}+\frac{(1-\sigma^2)^4(1+\sigma^2)^2(9+5\sigma^4)}{16\sigma^8\Theta^2}-\frac{3(1-\sigma^2)^6(1+\sigma^2)^4}{8\sigma^8\Theta^3},$$

and

$$L_1(\sigma)=\int_0^\sigma\frac{x}{x^2-\sigma^2}\log\frac{(1+\sigma x)(1-\sigma^2)}{(1-\sigma x)(1+\sigma^2)}dx,\qquad L_2(\sigma)=\int_0^\sigma\frac{x}{1-\sigma^2x^2}\log\frac{1+\sigma x}{1-\sigma x}dx,$$

$$L_3(\sigma,\theta)=\int_0^\sigma\frac{x(x^2-\cos 2\theta)}{1+x^4-2x^2\cos 2\theta}\log\frac{1+\sigma x}{1-\sigma x}dx,\qquad L_4(\sigma,\theta)=\int_0^\sigma\frac{x}{1+x^4-2x^2\cos 2\theta}\log\frac{1+\sigma x}{1-\sigma x}dx,$$

$$L_5(\sigma)=\int_\sigma^1\frac{x}{1-\sigma^2x^2}\log\frac{1+\sigma x}{1-\sigma x}dx,\qquad L_6(\sigma)=\int_0^\sigma\frac{x}{x^2-\sigma^2}\log\frac{(1+\sigma x)(1-\sigma^2)}{(1-\sigma x)(1+\sigma^2)}dx,$$

$$L_7(\sigma,\theta)=\int^\sigma\frac{-1}{1+\sigma^4-2\sigma^2\cos 2\vartheta}\,\mathrm{Tan}^{-1}\left(\frac{2\sigma\sin\vartheta}{1-\sigma^2}\right)d\vartheta$$

$$L_8(\sigma,\theta)=\int_0^\theta\frac{1}{1+\sigma^4-2\sigma^2\cos 2\vartheta}\log\frac{1+\sigma^2-2\sigma\cos\vartheta}{1+\sigma^2+2\sigma\cos\vartheta}d\vartheta$$

$$L_9(\sigma,\theta)=\int_0^\sigma\frac{x(1-x^4)}{(1+x^4-2x^2\cos 2\theta)^2}\log\frac{1+\sigma x}{1-\sigma x}dx,\qquad L_{10}(\sigma,\theta)=\int_0^\sigma\frac{x^3}{(1+x^4-2x^2\cos 2\theta)^2}\log\frac{1+\sigma x}{1-\sigma x}dx,$$

and

$$\Theta=1+\sigma^4-2\sigma^2\cos 2\theta. \tag{3.12}$$

From (3.5), we have

$$d\theta/ds=\pm\theta^{-1/2}. \qquad (3.13)$$

Introducing (3.6), (3.7), (311), (3.13) into (2.3), we have finally the velocity distribution on the surface of the elliptic cylinder, correct to the order of M^4.

To check the result, we consider the limiting case $\sigma\to 0$ $(t\to 1)$, Then we have for q_2

$$q_2=\left(\frac{1}{4}\sin 5\theta-\frac{23}{30}\sin 3\theta+\frac{11}{15}\sin\theta\right)+\gamma\left(\frac{1}{8}\sin 5\theta-\frac{11}{40}\sin 3\theta+\frac{23}{120}\sin\theta\right), \qquad (3.14)$$

which coincides with Imai's result for the circular cylinder [4]. On the other hand, if we make $\sigma\to 1$ $(t\to 0)$, then we have for q_2

$$q_2=-\frac{3}{8}t+\left(\frac{5}{8}+\frac{1}{8}\gamma\right)t^2\frac{\cos 2\theta}{\sin^2\theta}+\left\{\left(-\frac{39}{16}+\frac{57}{16}\frac{1}{\sin^2\theta}-\frac{5\pi}{8\sin^3\theta}\right.\right.+\gamma\left(-\frac{3}{4}+\frac{9}{8}\frac{1}{\sin^2\theta}-\frac{\pi}{4\sin^3\theta}\right)t^3, \qquad (3.15)$$

which coincides with the results of Imai [3] and Hasimoto [1] by the thin-wing-expansion method as far as t^3-terms.

§ 4. Numerical Discussion.

As numerical examples, we shall take elliptic cylinders of thickness ratio $t=0.1$ and 0.5.

To calculate $q_2(\theta)$, we must evaluate definite integrals L_1, L_2, ... L_{10}. These are calculated numerically and given in Table 1 for the cases $t=0.1$ and 0.5.

Table 1.

t	L_1	L_2	L_5	L_5
0.1	1.0292	1.0023	0.9695	0.3053
0.5	0.221900	0.081322	0.445587	0.334668

t	$\theta°$	L_3	L_4	L_7	L_8	L_9	L_{10}
0.1	9	−.7526	2.2668	−1.52566	−17.0886	6.358	8.558
	18	−.2977	1.2071	−2.42912	−20.4764	1.763	1.739
	27	−.0489	.7644	−2.84276	−21.4968	.744	.589
	36	.1021	.5437	−3.08037	−21.9351	.402	.269
	45	.2005	.4197	−3.23932	−22.1588	.255	.150
	54	.2668	.3451	−3.35744	−22.2861	.182	.097
	63	.3116	.2989	−3.45247	−22.3619	.142	.071
	72	.3404	.2707	−3.53398	−22.4063	.120	.057
	81	.3568	.2555	−3.60787	−22.4308	.109	.050
	90	.3617	.2507	−3.67831	−22.4384		
0.5	9	−.08680	.11832	−0.04575	−0.89958	.179916	.044521
	18	−.06383	.10715	−0.16057	−1.64409	.145702	.034769
	27	−.03571	.09405	−0.30315	−2.18543	.111248	.025265
	36	−.00872	.08211	−0.44566	−2.55558	.084594	.018224
	45	.01435	.07241	−0.57731	−2.80379	.066054	.013536
	54	.03274	.06503	−0.69648	−2.96936	.053684	.010533
	63	.04653	.05971	−0.80499	−3.07842	.045779	.008647
	72	.05605	.05615	−0.90559	−3.14718	.040652	.007508
	81	.06163	.05410	−1.00104	−3.18515	.037933	.006898
	90	.06347	.05344	−1.09398	−3.19730		

Using these values, we can give $q_2(\theta)$ immediately as in Table 2, where the values of $q_0(\theta)$ and $q_1(\theta)$ due to Imai and Kawata [9] are also given. We put $\gamma=1.4$ in these results.

Table 2.

	$t=0.5$			$t=0.1$		
$\theta°$	q_0	q_1	q_2	q_0	q_1	q_2
0	0	0	0	0	0	0
9	0.4530	−0.1396	−0.0516	0.9301	−0.0619	−0.0682
18	0.8173	−0.1484	−0.1629	1.0513	0.0120	−0.0131
27	1.0706	−0.0528	−0.1868	1.0794	0.0353	0.0172
36	1.2357	0.0708	−0.0854	1.0897	0.0449	0.0306
45	1.3416	0.1808	0.0745	1.0945	0.0496	0.0377
54	1.4099	0.2660	0.2346	1.0971	0.0522	0.0418
63	1.4536	0.3270	0.3667	1.0986	0.0537	0.0442
72	1.4806	0.3673	0.4617	1.0994	0.0546	0.0457
81	1.4953	0.3902	0.5183	1.0999	0.0551	0.0464
90	1.5	0.3976	0.5370	1.1	0.0552	0.0467

The velocity distributions over an elliptic cylinder of $t=0.1$, for the cases $M=0.7$ and $M=0.8$, are given in Fig. 1 and Fig. 2 respectively, where the results due to various methods are given for comparison. Discrepancy between the result by the thin-wing-expansion method and the present one is fairly large. This large discrepancy may be accounted for by the following fact. Near the point $\theta=\pi/2$, where the thin-wing-expansion method is considered very accurate, M^2-expansion method is less accurate because of large relative velocity. On the other hand, near the stagnation point where M^2-expansion method is considered very accurate, the thin-wing-expansion method fails because of large perturbation velocity. In the region where the discrepancy is largest, we cannot decide *a priori* which method will give more accurate result, but the writer thinks that M^2-expansion method will give better result, because it shows no divergent tendency all over the surface in contrast to the divergent behaviour of the thin-wing-expansion method near $\theta=9°$.

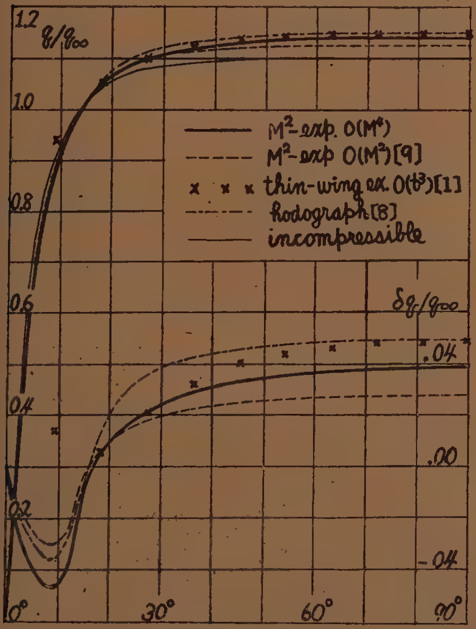

Fig. 1. The velocity distribution over an elliptic cylinder of $t=0.1$ at $M=0.7$.

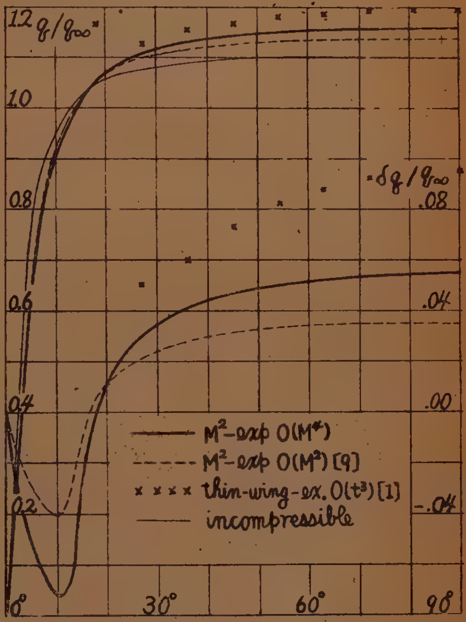

Fig. 2. The velocity distribution over an elliptic cylinder of $t=0.1$ at $M\doteqdot 0.8$.

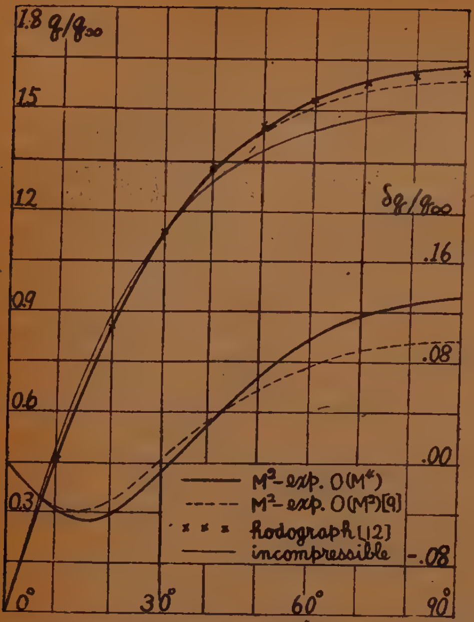

Fig. 3. The velocity distribution over an elliptic cylinder of $t=0.5$ at $M=0.5$.

The velocity distribution for the case of $t=0.5$, $M=0.5$ is given in Fig. 3 and compared with other results. In this case, M^2-expansion method shows fairly good convergence, and this result can be considered fairly accurate. Further, it is remarkable that the result of the hodograph method [12] ($\gamma=1.405$) is very close to our result.

Finally the critical Mach number M^* which are given by

$$\frac{q^2_{max}}{U^2}=\frac{c^2}{U^2}=\frac{1}{M^{*3}}-\frac{\gamma-1}{2}\left(\frac{q^2_{max}}{U^2}-1\right) \tag{4.1}$$

with usual notations are given in Table 3 for $t=0.1$, 0.5, and 1.0 (circular cylinder) and compared with the results of the zero and first approximations of the M^2-expansion method.

Table 3. Critical Mach number.

approx.	$t=0.1$	$t=0.5$	$t=1.0$
0	.8937	.6325	.4663
1	.8572	.5775	.4209
2	.8391	.5609	.4092

In conclusion the author wishes to express his heartiful gratitude to Prof. I. Imai for his guidance in the course of this work, and to Mr. H. Hasimoto who kindly showed his unpublished work to the author.

References.

(1) Hasimoto, H.; unpublished.

(2) Imai, I.; Rep. Aeron. Res. Inst., Tokyo Imp. Univ., No. 275 (1943).

(3) Imai, I.; Kagaku (Science), **14** (1944) 44.

(4) Imai, I.; Rep. Aeron. Res. Inst., Tokyo Imp. Univ., No. 290 (1944).

(5) Imai, I.; Proc. Phys.-Math. Soc., Japan, **26** (1944) 71.

(6) Imai, I.; unpublished.

(7) Imai, I., Aihara, T.; Rep. Aeron. Res. Inst., Tokyo Imp. Univ., No. 194 (1940).

(8) Imai, I., Hasimoto, H.; Journ. Math. Phys., **28** (1950) 205.

(9) Imai, I., Kawata, D.; Rep. Aeron. Res. Inst., Tokyo Imp. Univ., No. 325 (1945).

(10) Kaplan, C.; N. A. C. A. Tech Rep. No. 624 (1938).

(11) Tomotika, S., Tamada, K.; Rep. Aeron. Res. Inst., Tokyo Imp. Univ., No. 201 (1940).

(12) Tsien, H. S.; Journ. Aero. Sci., **6** (1939) 399.

On the Subsonic Flow of a Compressible Fluid past a Rankine Ovoid.

By Hidenori HASIMOTO.

Department of Physics, Faculty of Science, University of Tokyo.

(Received July 29, 1950).

1. Introduction.

While various methods of solving the nonlinear quations of steady subsonic flow past obstacles ave been successfully applied to the two-dimenional flow, their applications have been difficult n the case of three-dimensional flow, except for he flow around a sphere [1], [2], [3] and very lender obstacles.

Therefore, it may be much desirable to find ome typical flow patterns in the three-dimenional case. In the following we shall give the pproximate treatment of the flow past a thick ankine ovoid by the method of Janzen and Rayeigh.

2. Janzen-Rayleigh's Method and Stokes' Stream Function.

For the consideration of the boundary condiions Stokes's stream function is much more conenient than the velocity potential. Therefore he equations of motion will be expressed in erms of the stream function Ψ. Also, we shall se Janzen-Rayleygh's approximation, which may e considered to give satisfactory results for hick bodies.

The equation for axisymmetric irrotational low of a compressible fluid can be written in the orm:

$$\left\{1-\frac{1}{2}(\gamma-1)M^2(q^2-1)\right\}D^2\Psi$$

$$=-\frac{1}{2}M^2\left(\frac{\partial\Psi}{\partial r}\frac{\partial q^2}{\partial r}+\frac{1}{r^2}\frac{\partial\Psi}{\partial\theta}\frac{\partial q^2}{\partial\theta}\right), \tag{1}$$

vith

$$D^2=\frac{\partial^2}{\partial r^2}-\frac{\cot\theta}{r^2}\frac{\partial}{\partial\theta}+\frac{1}{r^2}\frac{\partial^2}{\partial\theta^2}, \tag{2}$$

$$q^2=u_r^2+u_\theta^2, \tag{3}$$

$$u_r=\frac{\rho_\infty}{\rho}\frac{1}{\sin\theta}\frac{\partial\Psi}{\partial\theta},\quad u_\theta=-\frac{\rho_\infty}{\rho}\frac{1}{r\sin\theta}\frac{\partial\Psi}{\partial r}, \tag{4}$$

$$\frac{\rho}{\rho_\infty}=\left\{1-\frac{\gamma-1}{2}M^2(q^2-1)\right\}^{\frac{1}{\gamma-1}}. \tag{5}$$

Here M is the Mach number of the undisturbed flow, which is taken as the unit of velocity, q the velocity, ρ the density, ρ_∞ the undisturbed density, and γ the adiabatic index.

Assuming that Ψ can be expanded in ascending powers of M^2 as

$$\Psi=\psi_0+M^2\psi_1+M^4\psi_2+M^6\psi_3+\cdots\cdots, \tag{6}$$

and substituting this in (3), (4), (5), we have

$$u_r=u_{r0}+M^2u_{r1}+\cdots\cdots, \tag{7a}$$

$$u_\theta=u_{\theta0}+M^2u_{\theta1}+\cdots\cdots, \tag{7b}$$

$$q^2=q_0^2+M^2q_1^2+\cdots\cdots, \tag{7c}$$

with

$$u_{r0}=\frac{1}{r^2\sin^2\theta}\frac{\partial\psi_0}{\partial\theta},\quad u_{\theta0}=-\frac{1}{r\sin\theta}\frac{\partial\psi}{\partial r},$$

$$u_{r1}=\frac{1}{r^2\sin^2\theta}\left(\frac{q_0^2-1}{2}\frac{\partial\psi_0}{\partial\theta}+\frac{\partial\psi_1}{\partial\theta}\right),$$

$$u_{\theta1}=-\frac{1}{r\sin\theta}\left(\frac{q_0^2-1}{2}\frac{\partial\psi_0}{\partial r}+\frac{\partial\psi_1}{\partial r}\right),$$

$$q_0^2=u^2_{r0}+u^2_{\theta0}. \tag{7d}$$

Substituting (6) and (7) in (1), we have finally

$$D^2\psi_0=0, \tag{8a}$$

$$D^2\psi_1=-\frac{1}{2}\left(\frac{\partial\phi_0}{\partial r}\frac{\partial q_0^2}{\partial r}+\frac{1}{r^2}\frac{\partial\phi_0}{\partial\theta}\frac{\partial q_0^2}{\partial\theta}\right). \tag{8b}$$

(8a) is evidently the equation for an incompressible fluid. Hence, starting from the known solution for an incompressible fluid, we can find the first order correction ψ_1 by the use of (8b).

§ 3. Application to Rankine Ovoid.

The velocity potential ϕ_0 and the stream function ψ_0 for the incompressible fluid flow past a Rankine ovoid can be expressed in the forms:

$$\phi_0=r\cos\theta-\frac{m}{4}\left(\frac{1}{r_1}-\frac{1}{r_2}\right), \tag{9}$$

$$\psi_0=\frac{1}{2}r^2\sin^2\theta-\frac{m}{4}\left(\frac{r\cos\theta+a}{r_1}-\frac{r\cos\theta-a}{r_2}\right), \qquad (10)$$

where r_1 and r_2 are the distances of an arbitary point P from a source A and a sink B respectively, each of strength m and situated at a distance a from the origin (Fig. 1).

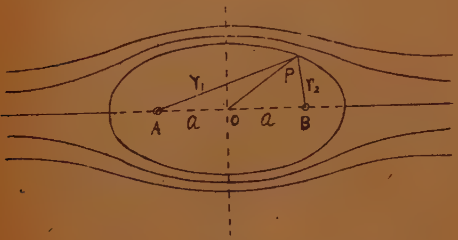

Fig. 1.

We now consider the case $a<1$, with $ma=1$, which corresponds to an ovoid not very different from a sphere of radius 1. In this case (10) can be approximately expressed in terms of the Legendre polynomials as

$$\psi_0=\left\{\frac{1}{2}(r^2-r^{-1})P_1'(\cos\theta)-\frac{a^2}{6}r^{-3}P_3'(\cos\theta)\right\}\sin^2\theta+O(a^4), \qquad (11)$$

where a dash stands for $d/d(\cos\theta)$.

Putting (11) in (8b) and making some reduction, we get

$$\begin{aligned}D^2\psi_1=\Big[&\left(\frac{9}{4}r^{-6}+\frac{9}{20}r^{-9}\right)P_1'(\cos\theta)\\&+\left(-r^{-3}+\frac{1}{2}r^{-6}+\frac{1}{20}r^{-9}\right)P_3'(\cos\theta)\\&-a^2\Big\{\left(\frac{18}{7}r^{-8}+\frac{9}{7}r^{-11}\right)P_1'(\cos\theta)\\&+\left(-\frac{23}{6}r^{-8}-\frac{2}{3}r^{-11}\right)P_3'(\cos\theta)\\&+\left(2r^{-5}-\frac{26}{21}r^{-8}-\frac{5}{42}r^{-11}\right)P_5'(\cos\theta)\Big\}\Big]\sin^2\theta\\&+O(a^4). \qquad (12)\end{aligned}$$

This can be solved by noting that

$$G=\frac{\sin^2\theta P_n'(\cos\theta)}{(k-1)(k-2)-n(n+1)}r^{-(k-2)}$$

is a particular solution of the equation:

$$D^2G=r^{-k}\sin^2\theta P_n'(\cos\theta).$$

Thus, taking into account the boundary conditions, we have finally

$$\begin{aligned}\psi_1=\Big[&\left(-\frac{2}{15}r^{-1}+\frac{1}{8}r^{-4}+\frac{1}{120}r^{-7}\right)P_1'(\cos\theta)\\&+\left(\frac{1}{10}r^{-1}-\frac{9}{55}r^{-3}+\frac{1}{16}r^{-4}+\frac{1}{880}r^{-7}\right)P_3'(\cos\theta)\\&+a^2\Big\{\left(-\frac{9}{140}r^{-6}-\frac{9}{616}r^{-9}\right)P_1'(\cos\theta)\\&+\left(\frac{23}{180}r^{-6}+\frac{1}{117}r^{-9}\right)P_3'(\cos\theta)\\&+\left(\frac{1}{9}r^{-3}+\frac{13}{126}r^{-6}+\frac{1}{504}r^{-9}\right)\Big\}\Big]\sin^2\theta\\&+a^2\sum_{n=0}^{\infty}A_{2n+1}r^{-(2n+1)}P'_{2n+1}(\cos\theta)\sin^2\theta, \qquad (1\end{aligned}$$

where A_{2n+1}'s are arbitary constants to be determined from the boundary conditions. No the form of the ovoid is given by $\Psi=0$, that i by $\psi_0+M^2\psi_1=0$. Hence it may be expected tha a fairly large variety of ovoid form would b obtained by assigning a suitable set of values t A_{2n+1}. For an incompressible flow $(M=0$ $\psi_0(r,\theta)=0$ gives a so-called Rankine ovoid. I we want to study the compressible flow past th same ovoid at some Mach number, we must determine A_{2n+1} in such a manner that $\psi_1(r,\theta)=$ is satisfied simultaneously with $\psi_0(r,\theta)=0$. Th exact satisfaction of this condition would requir in general an infinite number of A_{2n+1} to be determined. For an approximate treatment, however, it is sufficient to determine a few of A_{2n+} assuming all other A_{2n+1} to be zero, so that th condition $\psi_1(r,\theta)=0$ may be fulfilled at som suitably selected points. Some numerical examples will be given in the next section.

Finally it may be remarked that by puttin $a=0$ in (13) we can obtain the first order correction to the stream function for the compressib flow past a sphere. In fact, it can readily b seen that the relation $\psi_1(r,\theta)=0$ is exactly satisfied in this case.

§ 4. Numerical Examples.

A Rankine ovoid is defined by $\psi_0=0$, wher ψ_0 is given by (10). After a few trials it wa found that an ovoid of thickness ratio 0.9 can b obtained by taking $a^2=0.138$, $ma=1$. On th ovoid, $\theta=0$, $\pi/2$ correspond respectively to $r=$ 1.0864, 1.0297, 0.9778.

Next A_{2n+1} were determined so as to satisfy $\psi_1(r, \theta) = 0$ for $\theta = 0, \pi/4, \pi/2$. Thus we found

$$A_1 = 0.07058, \quad A_3 = -0.12787,$$
$$A_5 = -0.24145, \quad A_{2n+1} = 0 \ (n > 3).$$

In order to examine the forms of ovoids thus obtained, the equation $\psi_0 + M^2\psi_1 = 0$ was solved as follows:

$$r = 1 + \alpha^2\xi + \alpha^4\eta + O(\alpha^6),$$

where ξ and η are functions of M and θ. Thus

$$\begin{aligned}\Big\{\frac{3}{2}P_1' + M^2\Big(-\frac{17}{40}P_1' + \frac{117}{880}P_3'\Big)\Big\}\xi &= \frac{1}{6}P_3' + M^2\Big\{\Big(-A_1 + \frac{243}{3083}\Big)P_1' \\ &\quad - \Big(A_3 + \frac{319}{2340}\Big)P_3' - \Big(A_5 + \frac{109}{504}\Big)P_5'\Big\},\end{aligned}$$

$$\begin{aligned}\Big\{\frac{3}{2}P_1' + M^2\Big(-\frac{17}{40}P_1' + \frac{117}{880}P_3'\Big)\Big\}\eta &= \frac{1}{10}P_5' - \frac{1}{2}P_3'\xi + M^2\Big[\Big\{\Big(A_1 - \frac{1593}{3080}\Big)P_1' \\ &\quad + \Big(3A_3 + \frac{329}{390}\Big)P_3' + \Big(5A_5 + \frac{163}{168}P_5'\Big)\Big\}\xi \\ &\quad + \Big(-\frac{27}{20}P_1' + \frac{9}{40}P_3'\Big)\xi^2\Big].\end{aligned}$$

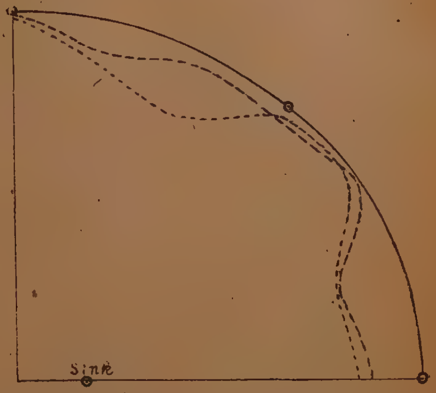

Fig. 2. The ovoids and their deviations from the original one $(r_0 + 100\delta r)$.
- - - - - $M = 0.5$, · · · · · $M = 0.6$,
——— Ovoid

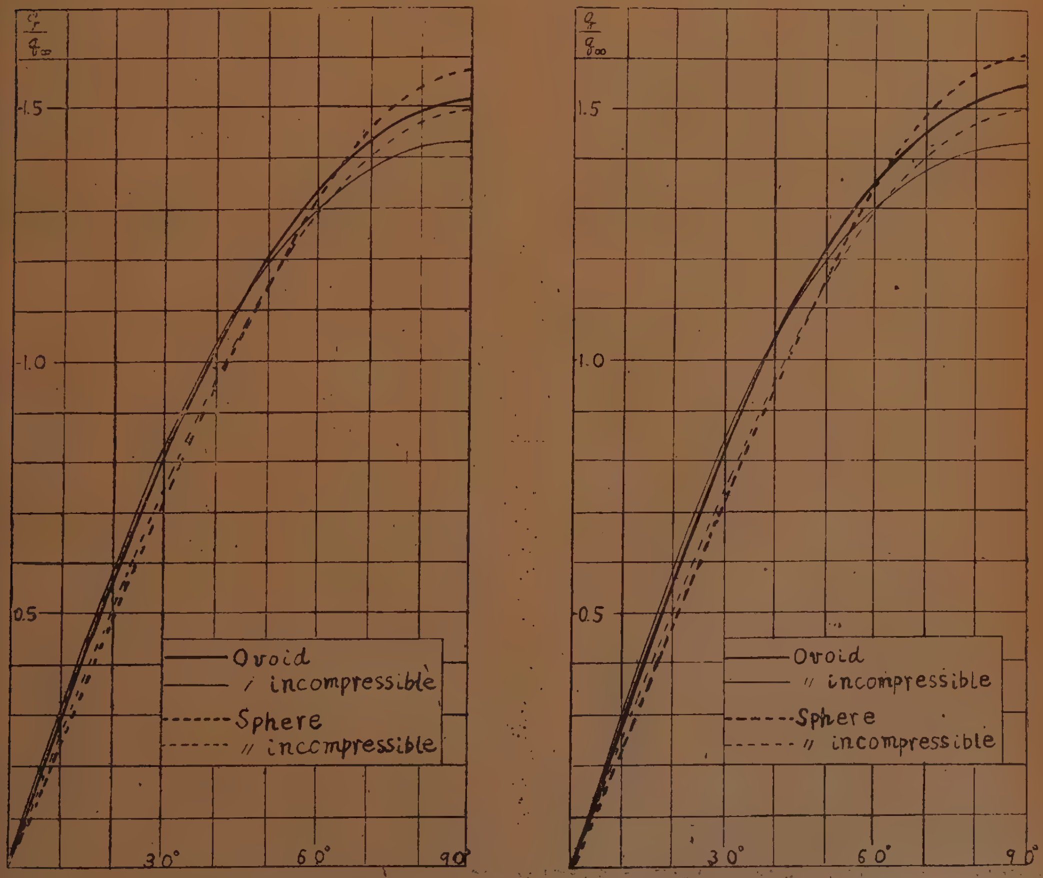

Fig. 3. (1) Velocity distribution over a Rankine ovoid of thickness ratio $t = 0.9$ at $M = 0.5$.
(2) Velocity distribution over a Rankine ovoid of thickness ratio $t = 0.9$ at $M = 0.6$.

The shapes thus obtained, for $M=0.5$, 0.6, as well as the original Rankine ovoid are shown in Fig. 2, where the deviations of the two ovoids from the original one are also shown in exergerated scale (one hundred times larger). They ar correct to the order of a^4. It will be seen tha the deviations are very small in spite of th fact that only three constants A_1, A_3, A_5 wer employed.

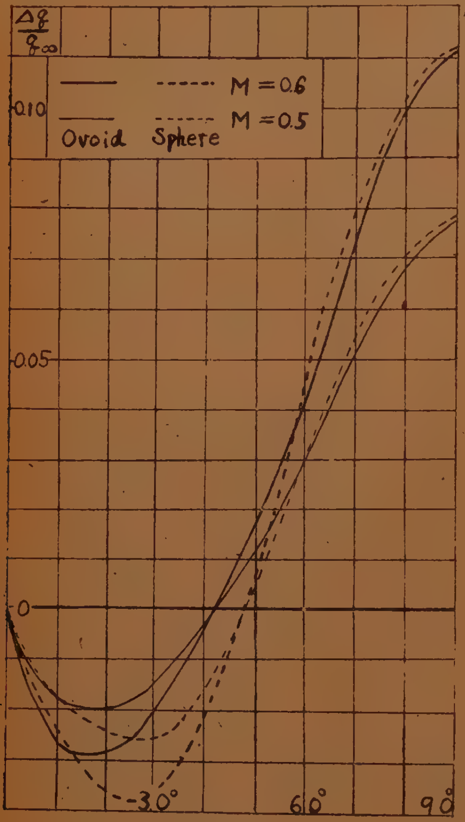

Fig. 4.

The velocity distribution on the surface o the ovoid was then calculated for three Mac numbers $M=0$, 0.5, 0.6. For this purpose, formula (3) was employed in conjunction with (7a) (7b), (7c), (7d). The results of calculation ar shown in Fig. 3, where the velocity distribution on a sphere for $M=0$, 0.5, 0.6 are also shown fo the sake of comparison. Finally, Fig. 4 gives the effect of compressibility on the velocity, $\Delta q=q-q_0$. It may be interesting to note that Δq is nearly equal for the ovoid of thickness ratio 0.9 and for a sphere, a fact which appears rather surprising.

In conclusion the author wishes to express his sincere thanks to Professor I. Imai for the guidance throughout the present work.

References.

(1) Kaplan, C.: N.A.C.A. Tech. Note. No. 762 (1940).
(2) Rayleigh, Lord: Phil. Mag. (6) **32** (1916), 1.
(3) Tamada, K.: Proc. Phys.-Math. Soc. Japan **21** (1939), 743.

Excitation of Atoms by Electron Collision I.

By Hisashi Horie.

Department of Physics, University of Tokyo.

(Received August 8, 1950)

§ 1.

The problem of excitation of atoms in complex configuration by electron collision has been treated by the group-theoretical method by Yamanouchi, who has carried out extensive formal and numerical caluculations for p^n-configurations with his collaborators.¹⁾ The interactions responsible for the excitation are however essentially the same as those of configuration interactions, so that the application of Racah's method, which proved to be very powerful for the theory of complex spectra,²⁾ also promises to simplify the calculations to great extent.

In this paper, we shall apply Racah's method to the excitation of atoms in l^n-, and $l^n l'$ -configurations by electron collision, and give the general formulae for its transition probability. Especially, for the d^n -configurations, more explicit formulae will be given.

§ 2.

We consider the probability that an atom in a state (αSL), which arises from given electron configuration, is excited by electron impact to a state ($\alpha' S' L'$) of the same configuration. It can be obtained as the transition probability between the initial state, in which the atom is (αSL) -state and an electron approaching with velocity $\boldsymbol{k}$, and the final state, in which the atom is found in ($\alpha' S' L'$) -state and the electron going away with velocity $\boldsymbol{k}'$. The atomic units will be used for all quantities, and the primed letter will express the quantities referring to the final state. α is the quantum number which, together with and L, specify each single atomic state and $\boldsymbol{k}$ and $\boldsymbol{k}'$ are, of course, velocities at sufficiently large distance from the atom. By the law of conservation of energy, we have the relation:

$$k'^2 = k^2 - 2\,(E_{\alpha' S' L'} - E_{\alpha SL})\,. \tag{1}$$

where $E_{\alpha SL}$ is the energy of the atom in (αSL) -state.

When we assume LS-coupling is approximately valid for the atom, the resultant spin S_1 of the atom and colliding electron must be conserved in this approximation. The direction of approach of the free electron (we shall call the colliding by the name of "free" electron, though the effect of the atomic field on the motion of electron is taken into account.) may be fixed arbitrarily owing to the spherical symmetry of the atomic field, and the incident plane wave may be decomposed into partial spherical waves, with the angular momenta l's. Thus we obtain the probability W that an atom in (αSL) -state makes transition to ($\alpha' S' L'$) -state in unit time by the collision of electron of unit density³⁾:

$$W = \frac{8\pi k'}{(2S+1)(2L+1)} \sum_{l,l'} V_l^{l'}\,, \tag{2}$$

where

$$V_l^{l'} = \sum_{S_1,L_1} (2S_1+1)(2L_1+1) \times (\alpha SL, lS_1L_1 |\, H \,| \alpha' S' L', l' S_1 L_1). \tag{3}$$

In (3), L_1 is the resultant orbital angular momentum of the initial atom and the incident partial l-wave which must be equal to the resultant orbital angular momentum of the final atom and the scattered l'-wave, and H is the interaction Hamiltonian between the initial and final systems.

Let the number of atomic electrons be n. Then the free electron will be indicated as $(n+1)$ th, and the distance of the free and atomic electron as $r_{i,n+1}$ $(i=1,2,\cdots,n)$. Assuming the orthogonality of the wave functions of the free and atomic electrons, it can easily be seen that only the term $\sum_{i=1}^{n}\frac{1}{r_{i,n+1}}$ gives rise to non-vanishing contribution in the interaction H.

§ 3.

In the case that the atomic electron configuration is $l_1{}^n$, we must, first of all, evaluate the matrix elements:

$$(l_1{}^n(\alpha SL)\,lS_1L_1|\sum_{i=1}^{n}\frac{1}{r_{i,n+1}}|l_1{}^n(\alpha'S'L')\,l'S_1L_1). \qquad (4)$$

These are just the same as the matrix elements which appear in the case of configuration interaction, and can readily be found following the method of tensor operator which has been developed by Racah, though the $(n+1)$th electron is not bound. Let $R_{nl_1}(r)$ be the normalized radial wave function of atomic electron, and $f_{kl}(r)$ that of free electron which has the velocity k, angular momentum l, and the asymptotic form $\sin(kr-l\pi/2+\delta_l)/kr$. Putting $rR_{n,l_1}(r)=P(r)$ and $krf_{kl}(r)=y_{kl}(r)$, we have the direct type integral $Q_\kappa(kl,k'l')$ and exchange type one $R_\kappa(kl,k'l')$.

$$\left.\begin{aligned}Q_\kappa(kl,k'l')&=\int_0^\infty\!\!\int P(r_1)y_{kl}(r_2)\frac{r_<{}^\kappa}{r_>{}^{\kappa+1}}P'(r_1)\\&\qquad\qquad y_{k'l'}(r_2)dr_1dr_2,\\R_\kappa(kl,k'l')&=\int_0^\infty\!\!\int P(r_1)y_{kl}(r_2)\frac{r_<{}^\kappa}{r_>{}^{\kappa+1}}P'(r_2)\\&\qquad\qquad y_{k'l'}(r_1)dr_1dr_2,\end{aligned}\right\}\qquad(5)$$

where the primed $P'(r)$ is used for taking into account the change of radial wave function due to the change of atomic state. As is well known, the matrix element (4) is expressible as the linear combination of integrals Q_κ's and R_κ's. We must first find the coefficients.

In the following, we shall use the notations of R.II. The coefficients of $Q_\kappa(kl,k'l')$ are found, by the straightforward application of the method of tensor operator, to be

$$(-1)^{L+l'-L_1}\,q_\kappa(l,l')\,W(Ll\,L'l';L_1\kappa)\,, \qquad (6)$$

where

$$\begin{aligned}q_\kappa(l,l')=&(l_1||C^{(\kappa)}||l_1)(l||C^{(\kappa)}||l')\\&\times(l_1{}^n\alpha SL||U^{(\kappa)}||l_1{}^n\alpha'S'L').\end{aligned}\qquad(7)$$

The calculation of coefficients of $R_\kappa(kl,k'l')$ is more complicated. It can be carried out by the analogous arguments as in § 5 of R.II. We find the coefficients of $R_\kappa(kl,k'l')$

$$(-1)^{L+l'-L_1}\sum_\rho r_{\rho\kappa}(l,l')\,W(Ll\,L'l';L_1\rho)\,, \qquad (8)$$

where

$$\begin{aligned}r_{\rho\kappa}(l,l')=&\bar{r}_{\rho\kappa}(l,l')\\&+(-1)^{S+\frac{1}{2}-S_1}\sqrt{6}\,W(S1/2S'1/2;S_11)\bar{\bar{r}}_{\rho\kappa}(l,l'),\end{aligned}\qquad(9)$$

and

$$\left.\begin{aligned}\bar{r}_{\rho\kappa}(l,l')=&(-1)^\rho\frac{2\rho+1}{2}(l_1||C^{(\kappa)}||l)(l_1||C^{(\kappa)}||l')\\&\times W(l_1l_1ll';\rho\kappa)(l_1{}^n\alpha SL||U^{(\rho)}||l_1{}^n\alpha'S'L'),\\\bar{\bar{r}}_{\rho\kappa}(l,l')=&(-1)^\rho(2\rho+1)(l_1||C^{(\kappa)}||l)(l_1||C^{(\kappa)}||l')\\&\times W(l_1l_1ll';\rho\kappa)(l_1{}^n\alpha SL||V^{(\rho)}||l_1{}^n\alpha'S'L').\end{aligned}\right\}\qquad(10)$$

In (9), the bars are used for distinguishing the properties for the spins of initial and final states, *i.e.*, the singly barred $\bar{r}_{\rho\kappa}$ is diagonal with respect to S like q_κ, but the doubly barred $\bar{\bar{r}}_{\rho\kappa}$ can have non-diagonal elements for $S'=S\pm1$.

Thus we have obtained from (5) and (7)

$$\begin{aligned}&(l_1{}^n(\alpha SL)lS_1L_1\left|\sum_{i=1}^{n}\frac{1}{r_{i,n+1}}\right|l_1{}^n(\alpha'S'L')l'S_1L_1)\\&\quad=(-1)^{L+l'-L_1}\sum_\kappa\{W(LlL'l';L_1\kappa)q_\kappa Q_\kappa\\&\qquad-\sum_\rho W(L'L'l';L_1\rho)\,r_{\rho\kappa}\,R_\kappa\},\end{aligned}$$

or, changing the indices of the second term in the right hand side,

$$\begin{aligned}&(l_1{}^n(\alpha SL)lS_1L_1\left|\sum_{i=1}^{n}\frac{1}{r_{i,n+1}}\right|l_1{}^n(\alpha'S'L')l'S_1L_1)\\&\quad=(-1)^{L+l'-L_1}\sum_\kappa W(LlL'l';L_1\kappa)\,(q_\kappa Q_\kappa\\&\qquad\qquad-\sum_\mu r_{\kappa\mu}R_\mu).\end{aligned}\qquad(11)$$

Inserting (11) in (3), we obtain

$$\begin{aligned}V_l{}^{l'}=&\sum_{S_1,L_1}(2S_1+1)(2L_1+1)\\&\times\{\sum_\kappa W(LlL'l';L_1\kappa)(q_\kappa Q_\kappa-\sum_\kappa r_{\kappa\mu}R_\mu)\}^2.\end{aligned}$$

Then, according to the orthogonality relation of $W(abcd;ef)$ [R. II. (42)]:

$$\begin{aligned}&\sum_e(2e+1)W(abcd;ef)W(abcd;eg)\\&\qquad\qquad=(-1)^{2f}\,\delta(f,g)/(2f+1)\,,\end{aligned}\qquad(12)$$

the summation over L_1 can be carried out at once, giving

$$V_l{}^{l'}=\sum_{S_1}(2S_1+1)\sum_\kappa\frac{1}{2\kappa+1}(q_\kappa Q_\kappa-\sum_\mu r_{\kappa\mu}R_\mu)^2$$

$$=\sum_{\kappa}\frac{1}{2\kappa+1}\sum_{S_1}(2S_1+1)\{(q_\kappa Q_\kappa-\sum_{\mu}\bar{r}_{\kappa\mu}R_\mu)$$
$$-(-1)^{S+\frac{1}{2}-S_1}\sqrt{6}\,W(S1/2S'1/2\,;S_11)\sum_{\mu}\bar{\bar{r}}_{\kappa\mu}R_\mu\}^2,$$

in which the relation (9) is used. Since $W(S1/2\,S'1/2\,;S_10)=(-1)^{S+\frac{1}{2}-S_1}\delta(S,S')/\sqrt{2(2S+1)}$, the summation over S_1 can also be carried out by making use of (12). Thus, finally, we obtain the following formula:

$$V_l^{l'}=\sum_{\kappa}\frac{2}{2\kappa+1}\{(2S+1)(q_\kappa Q_\kappa-\sum_{\mu}\bar{r}_{\kappa\mu}R_\mu)^2$$
$$+(\sum_{\mu}\bar{\bar{r}}_{\kappa\mu}R_\mu)^2\},\qquad(13)$$

where $q_\kappa(l,l')$, $\bar{r}_{\kappa\mu}(l,l')$ and $\bar{\bar{r}}_{\kappa\mu}(l,l')$ are given by (6) and (10), and integrals $Q_\kappa(kl,k'l')$ and $R_\mu(kl,k'l')$ by (4). Eqs. (2) and (13) give the general formula for the probability W that an atom whose electron configuration is l_1^n in (αSL)-state makes transition to ($\alpha'S'L'$)-state of the same configuration in unit time by the collision of electron whose space density is one per unit volume. According to the definitions of $q_\kappa(l,l')$, $\bar{r}_{\kappa\mu}(l,l')$ and $\bar{\bar{r}}_{\kappa\mu}(l,l')$, the first term in the parenthesis of (13) cannot give rise the spin change and only the second term contributes to the transition which the multiplicity changes.

The selection rules for the transition also can be deduced by (7) and (10), namely,

(i) $S'=S,\ S\pm1$,
(ii) $L'=L,\ L\pm1,\ \cdots,\ L\pm2l_1$,
(iii) $l'=l,\ l\pm2,\ \cdots,\ l\pm2l_1$.

In these selection rules, negative values of S', L' and l', of course, must be excluded. κ's in the summation of (13) which give the non-vanishing contributions satisfy the following two conditions; $\kappa=0,1,2,\ \cdots,\ 2l_1$ and $|l-l'|\leq\kappa\leq l+l'$ (in the terms of $Q_\kappa(kl,k'l')$, κ's are only even integers.), aud μ's satisfy the following two conconditions: $\mu=l+l_1, l+l_1-2,\ \cdots,\ |l-l_1|$ and $|l'-l_1|\leq\mu\leq l'+l_1$.

§ 4.

For the case that the atom has d^n-configuration, we shall give the formulae in more explicit form. As has been pointed out by R. III., the atomic state is completely determined by a set of quantum numbers (vSL) for d^n-configuration, where v is the seniority number. Selection rules are now

$$S'=S,\ S\pm1,\qquad L'=L,\ L\pm1,\ L\pm2,\ L\pm3,\ L\pm4,$$

and

$$l'=l,\ l\pm2,\ l\pm4.$$

The transition probability is given by (2) and (13)

$$W=\frac{8\pi k'}{(2S+1)(2L+1)}\sum_{l}\{V_l^l+V_l^{l+2}+V_l^{l-2}+V_l^{l+4}+V_l^{l-4}\},$$

where

$$V_l^{l'}=\sum_{\kappa}\frac{2}{2\kappa+1}\{(2S+1)(q_\kappa Q_\kappa-\sum_{\mu}\bar{r}_{\kappa\mu}R_\mu)^2+(\sum_{\mu}\bar{\bar{r}}_{\kappa\mu}R_\mu)^2\}.\qquad(l'=l,l\pm2,l\pm4)$$

We shall give non-vanishing $q_\kappa Q_\kappa-\sum_{\mu}\bar{r}_{\kappa\mu}R_\mu$ and $\sum_{\mu}\bar{\bar{r}}_{\kappa\mu}R_\mu$ in each case of $l'=l,\ l\pm2$ and $l\pm4$.

(a) $l'=l+4$.

$$q_4Q_4-\bar{r}_{4l+2}R_{l+2}\doteq\frac{45}{4}\left[\frac{(l+1)(l+2)(l+3)(l+4)}{(2l+3)(2l+5)(2l+7)}\right]^{\frac{1}{2}}\left(\frac{2}{9}Q_4-\frac{1}{2l+5}R_{l+2}\right)(d^nvSL||U^{(4)}||d^nv'S'L'),$$

$$\bar{\bar{r}}_{4l+2}R_{l+2}=-\frac{45}{2}\left[\frac{(l+1)(l+2)(l+3)(l+4)}{(2l+3)(2l+5)(2l+7)}\right]^{\frac{1}{2}}\frac{1}{2l+5}R_{l+2}(d^nvSL||V^{(14)}||d^nv'S'L').$$

(a′) $l'=l-4$.

The formulae will be obtained by replacing l by $l-4$ in the formulae of the case (a).

(b) $l'=l+2$.

$$q_2Q_2-(\bar{r}_{2l}R_l+\bar{r}_{2l+2}R_{l+2})=-\frac{5}{2}\left[\frac{15(l+1)(l+2)}{7(2l+3)}\right]^{\frac{1}{2}}\left\{\frac{2}{5}Q_2-\frac{1}{2l+3}\left(\frac{l}{2l+1}R_l+\frac{l+3}{2l+5}R_{l+2}\right)\right\}(d^nvSL||U^{(2)}||d^nv'SL'),$$

$$\bar{r}_{3l}R_l+\bar{r}_{3l+2}R_{l+2}=-\frac{35}{4}\left[\frac{3l(+1)(l+2)(l+3)}{7(2l+3)}\right]^{\frac{1}{2}}\frac{1}{2l+3}\left(\frac{1}{2l+1}R_l-\frac{1}{2l+5}R_{l+2}\right)(d^nvSL||U^{(3)}||d^nv'SL'),$$

$$\begin{aligned}&q_4Q_4-\\&(\bar{r}_{4l}R_l+\bar{r}_{4l+2}R_{l+2})=+\frac{45}{2}\left[\frac{l(l+1)(l+2)(l+3)}{7(2l-1)(2l+3)(2l+7)}\right]^{\frac{1}{2}}\left\{\frac{2}{9}Q_4-\frac{1}{2(2l+3)}\left(\frac{2l+7}{2l+1}R_l+\frac{2l-1}{2l+5}R_{l+2}\right)\right.(d^nvSL||U^{(4)}||d^nv'SL'),\end{aligned}$$

$$\bar{\bar{r}}_{2l}R_l+\bar{\bar{r}}_{2l+2}R_{l+2}=5\left[\frac{15(l+1)(l+2)}{7(2l+3)}\right]^{\frac{1}{2}}\frac{1}{2l+3}\left(\frac{l}{2l+1}R_l+\frac{l+3}{2l+5}R_{l+2}\right)(d^nvSL||V^{(12)}||d^nv'S'L'),$$

$$\bar{\bar{r}}_{3l}R_l+\bar{\bar{r}}_{3l+2}R_{l+2}=\frac{35}{2}\left[\frac{3l(l+1)(l+2)(l+3)}{7(2l+3)}\right]^{\frac{1}{2}}\frac{1}{2l+3}\left(\frac{1}{2l+1}R_l-\frac{1}{2l+5}R_{l+2}\right)(d^nvSL||V^{(13)}||d^nv'S'L'),$$

$$\bar{\bar{r}}_{4l}R_l+\bar{\bar{r}}_{4l+2}R_{l+2}=\frac{45}{2}\left[\frac{l(l+1)(l+2)(l+3)}{7(2l-1)(2l+3)2l+7)}\right]^{\frac{1}{2}}\frac{1}{2l+3}\left(\frac{2l+7}{2l+1}R_l+\frac{2l-1}{2l+5}R_{l+2}\right)(d^nvSL||V^{(14)}||d^nv'S'L').$$

(b′) $l'=l-2$.

The formulae will be obtained by replacing l by $l-2$ in the formulae of the case (b).

(c) $l'=l$.

$$\begin{aligned}&q_0Q_0-(\bar{r}_{0l}R_l+\bar{r}_{0l+2}R_{l+2}+\bar{r}_{0l-2}R_{l-2})\\&=\left[\frac{5(2l+1)}{2}\right]^{\frac{1}{2}}\left[2Q_0-\frac{1}{2(2l+1)}\left\{\frac{2l(l+1)}{(2l-1)(2l+3)}R_l+\frac{3(l+1)(l+2)}{(2l+3)(2l+5)}R_{l+2}+\frac{3(l-1)l}{(2l-3)(2l-1)}R_{l-2}\right\}\right](d^nvSL||U^{(0)}||d^nv'SL'),\end{aligned}$$

$$\begin{aligned}&\bar{r}_{1l}R_l+\bar{r}_{1l+2}R_{l+2}+\bar{r}_{1l-2}R_{l-2}\\&=\frac{3}{2}\left[\frac{15l(l+1)}{2(2l+1)}\right]^{\frac{1}{2}}\left\{\frac{1}{(2l-1)(2l+3)}R_l-\frac{l+2}{(2l+3)(2l+5)}R_{l+2}+\frac{l-1}{(2l-3)(2l-1)}R_{l-2}\right\}(d^nvSL||U^{(1)}||d^nv'SL'),\end{aligned}$$

$$\begin{aligned}&q_2Q_2-(\bar{r}_{2l}R_l+\bar{r}_{2l+2}R_{l+2}+\bar{r}_{2l-2}R_{l-2})\\&=5\left[\frac{5l(l+1)(2l+1)}{14(2l-1)(2l+3)}\right]^{\frac{1}{2}}\left\{\frac{2}{5}Q_2+\frac{1}{2(2l+1)}\left\{\frac{(2l-3)(2l+5)}{(2l-1)(2l+3)}R_l-\frac{3(l+2)(2l-1)}{(2l+3)(2l+5)}R_{l+2}-\frac{3(l-1)(2l+3)}{(2l-3)(2l-1)}R_{l-2}\right\}\right]\\&\qquad\times(d^nvSL||U^{(2)}||d^nv'SL'),\end{aligned}$$

$$\begin{aligned}&(\bar{r}_{3l}R_l+\bar{r}_{3l+2}R_{l+2}+\bar{r}_{3l-2}R_{l-2})\\&=-42\left[\frac{5(l-1)l(l+1)(l+2)}{14(2l-1)(2l+1)(2l+3)}\right]^{\frac{1}{2}}\left\{\frac{1}{(2l-1)(2l+3)}R_l-\frac{2l-1}{8(2l+3)(2l+5)}R_{l+2}-\frac{2l+3}{8(2l-3)(2l-1)}R_{l-2}\right\}\\&\qquad\times(d^nvSL||U^{(3)}||d^nv'SL'),\end{aligned}$$

$$\begin{aligned}&q_4Q_4-(\bar{r}_{4l}R_l+\bar{r}_{4l+2}R_{l+2}+\bar{r}_{4l-2}R_{l-2})\\&=\frac{27}{2}\left[\frac{5(l-1)l(l+1)(l+2)(2l+1)}{14(2l-3)(2l-1)(2l+3)(2l+5)}\right]^{\frac{1}{2}}\left[\frac{2}{9}Q_4-\frac{1}{2l+1}\left\{\frac{(2l-3)(2l+5)}{(2l-1)(2l+3)}R_l+\frac{(2l-3)(2l-1)}{2(2l+3)(2l+5)}R_{l+2}+\frac{(2l+3)(2l+5)}{2(2l-3)(2l-1)}R_{l-2}\right\}\right]\\&\qquad\times(d^nvSL||U^{(4)}||d^nv'SL'),\end{aligned}$$

$$\begin{aligned}&\bar{\bar{r}}_{0l}R_l+\bar{\bar{r}}_{0l+2}R_{l+2}+\bar{\bar{r}}_{0l-2}R_{l-2}\\&=\frac{1}{2}\left[\frac{5}{2l+1}\right]^{\frac{1}{2}}\left\{\frac{2l(l+1)}{(2l-1)(2l+3)}R_l+\frac{3(l+1)(l+2)}{(2l+3)(2l+5)}R_{l+2}+\frac{3(l-1)l}{(2l-3)(2l-1)}R_{l-2}\right\}(d^nvSL||V^{(10)}||d^nv'S'L'),\end{aligned}$$

$$\begin{aligned}&\bar{\bar{r}}_{1l}R_l+\bar{\bar{r}}_{1l+2}R_{l+2}+\bar{\bar{r}}_{1l-2}R_{l-2}\\&=3\left[\frac{15l(l+1)}{2(2l+1)}\right]^{\frac{1}{2}}\left\{\frac{1}{(2l-1)(2l+3)}R_l-\frac{l+2}{(2l+3)(2l+5)}R_{l+2}+\frac{l-1}{(2l-3)(2l-1)}R_{l-2}\right\}(d^nvSL||V^{(11)}||d^nv'S'L'),\end{aligned}$$

$$\begin{aligned}&\bar{\bar{r}}_{2l}R_l+\bar{\bar{r}}_{2l+2}R_{l+2}+\bar{\bar{r}}_{2l-2}R_{l-2}\\&=-5\left[\frac{5l(l+1)(l+2)}{14(2l-1)(2l+3)}\right]^{\frac{1}{2}}\frac{1}{2l+1}\left\{\frac{(2l-3)(2l+5)}{(2l-1)(2l+3)}R_l-\frac{3(l+2)(2l-1)}{(2l+3)(2l+5)}R_{l+2}-\frac{3(l-1)(2l+3)}{(2l-3)(2l-1)}R_{l-2}\right\}\\&\qquad\times(d^nvSL||V^{(12)}||d^nv'S'L'),\end{aligned}$$

$$\bar{\bar{r}}_{3l}R_l+\bar{\bar{r}}_{3l+2}R_{l+2}+\bar{\bar{r}}_{3l-2}R_{l-2}$$

$$=-84\left[\frac{5(l-1)l(l+1)(l+2)}{14(2l-1)(2l+1)(2l+3)}\right]^{\frac{1}{2}}\left\{\frac{1}{(2l-1)(2l+3)}R_l-\frac{2l-1}{8(2l+3)(2l+5)}R_{l+2}-\frac{2l+3}{8(2l-3)(2l-1)}R_{l-2}\right\}$$
$$\times(d^n vSL||V^{(13)}||d^n v'S'L'),$$

$$\bar{\bar{r}}_{4l}R_l+\bar{\bar{r}}_{4l+2}R_{l+2}+\bar{\bar{r}}_{4l-2}R_{l-2}$$

$$=27\left[\frac{5(l-1)l(l+1)(l+2)(2l+1)}{14(2l-3)(2l-1)(2l+3)(2l+5)}\right]^{\frac{1}{2}}\frac{1}{2l+1}\left\{\frac{(2l-3)(2l+5)}{(2l-1)(2l+3)}R_l+\frac{(2l-3)(2l-1)}{2(2l+3)(2l+5)}R_{l+2}+\frac{(2l+3)(2l+5)}{2(l-3)(2l-1)}R_{l-2}\right\}$$
$$\times(d^n vSL||V^{(14)}||d^n v'S'L'),$$

In the above formulae, $U^{(0)}$, $U^{(1)}$ and $V^{(10)}$ are diagonal matrices

$$(d^n vSL||U^{(0)}||d^n vSL)=n\left[\frac{2L+1}{5}\right]^{\frac{1}{2}},$$

$$(d^n vSL||U^{(1)}||d^n vSL)=\left[\frac{L(L+1)(2L+1)}{30}\right]^{\frac{1}{2}},$$

$$(d^n vSL||V^{(10)}||d^n vSL)=[S(S+1)(2S+1)]^{\frac{1}{2}}.$$

The tables of $U^{(2)}$, $V^{(11)}$ and $V^{(12)}$ are given in R. II and III, and $U^{(3)}$, $U^{(4)}$, $V^{(13)}$ and $V^{(14)}$ for d^2 and d^3 by Yanagawa[4].

§ 5.

We shall briefly add the result concerning the transition probability for excitation of an atom whose electron configuration is $l_1^n l_2$ by electron collision. Employing the parent term $l_1^n(\alpha SL)$ in order to refer to the atom of l_1^n -configuration in (αSL)-state in the preceding section, we shall specify the state of the atom in $l_1^n l_2$ -configuration by $l_1^n(\alpha SL)l_2S^*L^*$, where S^* and L^* are total spin and orbital angular momentum of the atom, respectively. In almost the same manner as the case of l_1^n -configuration, the propability that an atom of $l_1^n l_2$ -configuration in $(l_1^n(\alpha SL)l_2S^*L^*)$-state makes transition to $(l_1^n(\alpha'S'L')l_2S^*L^*)$-state in unit time by the collision of electron of unit density, is given by

$$W^*=\frac{8\pi k'}{(2S^*+1)(2L^*+1)}\sum_{l,l'}V_l^{l'*}, \tag{15}$$

where

$$V_l^{l'*}=\sum_\kappa\frac{l^2}{2\kappa+1}[(2S^*+1)\{\sum_{j=1,2}(q_\kappa^{(j)}Q_\kappa^{(j)}-\sum_\mu\bar{r}_{\kappa\mu}^{(j)}R_\mu^{(j)})\}^2+(\sum_{j=1,2}\bar{\bar{r}}_{\kappa\mu}^{(j)}R_\mu^{(j)})^2]. \tag{16}$$

The coefficients whose superscripts are (1), are intimately related to the coefficients for l_1^n -configuration as follows

$$\left.\begin{aligned}
q_\kappa^{(1)}&=(-1)^{l_2+\kappa-L'-L^*}\sqrt{(2L^*+1)(2L^{*\prime}+1)}\,W(LL^*L'L^{*\prime};l_2\kappa)\,q_\kappa,\\
\bar{r}_{\kappa\mu}^{(1)}&=(-1)^{l_2+\kappa-L'-L^*}\sqrt{(2L^*+1)(2L^{*\prime}+1)}\,W(LL^*L'L^{*\prime};l_2\kappa)\,\bar{r}_{\kappa\mu},\\
\bar{\bar{r}}_{\kappa\mu}^{(1)}&=(-1)^{l_2+\kappa-L'-L^*+3/2-S'-S^*}\sqrt{(2L^*+1)(2L^{*\prime}+1)(2S^*+1)(2S^{*\prime}+1)}\,W(LL^*L'L^{*\prime};l_2\kappa)\\
&\qquad W(SS^*S'S^{*\prime};\tfrac{1}{2}1)\bar{\bar{r}}_{\kappa\mu},
\end{aligned}\right\} \tag{17}$$

since we have chosen the parent terms just the same as the state of an atom of l_1^n-configuration. On the other hand, the coefficients for which the superscripts (2) are attached are non-vanishing only when the parent terms are not different from each other and will be given as follows

$$\left.\begin{aligned}
q_\kappa^{(2)} &= (-1)^{L+\kappa-l_2-L^{*\prime}}\sqrt{(2L^*+1)(2L^{*\prime}+1)}(l_2||C^{(\kappa)}||l_2)(l||C^{(\kappa)}||l')W(l_2L^*l_2L^{*\prime};L\kappa)\delta(\alpha,\alpha')\delta(S,S')\delta(L,L'),\\
\bar{r}_{\kappa\mu}^{(2)} &= (-1)^{L-l_2-L^*_1}\frac{2\kappa+1}{2}\sqrt{(2L^*+1)(2L^{*\prime}+1)}(l_2||C^{(\mu)}||l)(l_2||C^{(\mu)}||l')W(l_2l_2ll';\kappa\mu)\\
&\qquad\times W(l_2L^*l_2L^{*\prime};L\kappa)\delta(\alpha,\alpha')\delta(S,S')\delta(LL'),\\
\bar{\bar{r}}_{\kappa\mu}^{(2)} &= (-1)^{L-l_2-L^{*\prime}+S+\frac{1}{2}-S^{*\prime}}(2\kappa+1)\sqrt{(2L^*+1)(2L^{*\prime}+1)(2S^*+1)(2S^{*\prime}+1)}(\tfrac{1}{2}||S||\tfrac{1}{2})(l_2||C^{(\mu)}||l)(l_2||C^{(\mu)}||l').\\
&\qquad\times W(l_2l_2ll';\kappa\mu)W(l_2L^*l_2L^{*\prime};L\kappa)W(\tfrac{1}{2}S^*\tfrac{1}{2}S^{*\prime};\tfrac{1}{2}1)\delta(\alpha,\alpha')\delta(S,S')\delta(L,L').
\end{aligned}\right\}\quad(18)$$

The integrals $Q_\kappa^{(j)}$ and $R_\kappa^{(j)}$ $(j=1,2)$ are given by

$$\left.\begin{aligned}
Q_\kappa^{(1)}(kl,k'l') &= Q_\kappa(kl,k'l'),\\
R_\kappa^{(1)}(kl,k'l') &= R_\kappa(kl,k'l'),\\
Q_\kappa^{(2)}(kl,k'l') &= \iint_0^\infty P_{l_2}(r_1)y_{kl}(r_2)\frac{r_<^{\kappa}}{r_>^{\kappa+1}}P_{l_2}'(r_1)y_{k'l'}(r_2)dr_1dr_2,\\
R_\kappa^{(2)}(kl,k'l') &= \iint_0^\infty P_{l_2}(r_1)y_{kl}(r_2)\frac{r_<^{\kappa}}{r_>^{\kappa+1}}P_{l_2}'(r_2)y_{k'l'}(r_1)dr_1dr_2.
\end{aligned}\right\}\quad(19)$$

where $P_{l_2}(r)/r$ is the normalized wave function of the l_2-electron.

These results shows that the excitations of an atom of $l_1^n l_2$-configuration are divided into two classes: the first type is $l_1^n(\alpha SL)l_2S^*L^*\rightarrow l_1^n(\alpha'S'L')l_2S^{*\prime}L^{*\prime}$ which is similar to that of l_1^n-configuration and the second one is $l_1^n(\alpha SL)l_2S^*L^*\rightarrow l_1^n(\alpha SL)l_2S^{*\prime}L^{*\prime}$ which the parent terms are unchanged.

The author wishes to express his sincere thanks to Prof. T. Yamanouchi, under whose guidance this work was done, for his continual encouragement.

References.

(1) Yamanouchi and Kotani, Proc. Phys-Math. Soc. Japan **22** (1940), 14. Yamanouchi and Mashiko, Sūbutsu-kaishi **17** (1943), 581.

(2) G. Racah, Phys. Rev. **62** (1942), 438, and ibid **63** (1943), 367. These papers were cited as R. II and R. III, respectively.

(3) See the paper of Yamanouchi and Kotani, ref. (1) above.

(4) Yanagawa, unpublished.

Determination of Intermolecular Forces from the Equation of State of Gases. II.

By Taro KIHARA.

Department of Physics, Faculty of Science, University of Tokyo.

(Received August 31, 1950).

The equation of state of gases may be expressed in the form

$$pv = kT\left(1+\frac{B}{v}+\frac{C}{v^2}+\cdots\right)$$

(p= pressure, v= volume per molecule, k= Boltzmann constant, T= absolute temperature), where the coefficients B, C, ... are functions of the temperature, called second, third, ... virial coefficients.

For gases composed of spherically symmetric identical molecules, theoretical expressions for the virial coefficients were given by Born and Mayer⑴, on the assumption that classical statistics can be used, and that the potential energy of the whole system can be expressed as the total sum of terms, $U(r_{ij})$, each depending only on the distance r_{ij} between two molecules i and j. By means of the function

$$f(r) = \exp[-U(r)/kT]-1,$$

the expressions are

$$B = -\frac{1}{2}\int f(r_{12})d\tau_1 = -2\pi\int_0^\infty f(r)r^2dr,$$

$$C = -\frac{1}{3}\iint f(r_{12})f(r_{13})f(r_{23})d\tau_1 d\tau_2,$$

with

$$d\tau_i = dx_i dy_i dz_i.$$

The second virial coefficient $B(T)$ is positive for $T > T_B$, and negative for $T < T_B$, T_B being called Boyle temperature. Let us take the T_B as the unit of temperature, and the volume v_B, defined as

$$v_B = T_B\left(\frac{dB}{dT}\right)_{T=T_B}$$

as the unit of volume (cf. Table I). Let us further consider dimensionless "reduced virial coefficients"

$$B^*\left(\frac{T}{T_B}\right) = \frac{B(T)}{v_B}, \quad C^*\left(\frac{T}{T_B}\right) = \frac{C(T)}{v_B^2},$$

of which B^* satisfies the normalization-ralation:

$$B^*(1) = 0, \quad [dB^*(t)/dt]_{t=1} = 1.$$

As far as the law of corresponding state holds, these reduced virial coefficients are the same functions for all gases.

Table I.

	T_B	v_B
Ne	123°K	35.5Å^3
A	410	67.4
N_2	331	87.1
CH_4	510	94.4

For the "square- well" potential

$$U(r) = \begin{cases} \infty & r < \sigma \\ -\varepsilon & \sigma < r < g\sigma \\ 0 & g\sigma < r \end{cases}$$

it is possible to express the second and the third virial coefficients in a simple form of elementary functions⑵:

$$B = 4v_0\{1-(g^3-1)x\},$$

$$\begin{aligned} C(g<2) = 2v_0^2\{&5-(g^6-18g^4+32g^3-15)x \\ &+(-2g^6+36g^4-32g^3-18g^2+16)x^2 \\ &-(6g^6-18g^4+18g^2-6)x^3\}, \end{aligned}$$

$$\begin{aligned} C(g>2) = 2v_0^2\{&5-17x+(32g^3-18g^2-48)x^2 \\ &-(5g^6-32g^3+18g^2+26)x^3\}, \end{aligned}$$

where v_0 denotes the volume of the molecule:

$$v_0 = \pi\sigma^3/6,$$

and
$$x = \exp(\varepsilon/kT)-1.$$

In Fig. 1 these virial coefficients are shown in the reduced form, together with observed values for some typical gases. The square-well potential with $g \sim 2.0$ explains observed temperature variation of the second and the third virial coefficients very well.

From the Fig. 1 we may understand clearly the following facts: (i) The third virial coefficient C^* is sensitive to the shape of the intermolecular potential, whereas the second B^* is insensitive. (ii) If the hollow part of the potential curve of the assumed model is not sufficiently wide, the calculated C^* is too small.

For L-J potential

$$\begin{aligned} U(r) &= \frac{\lambda}{r^n}-\frac{\mu}{r^6} \\ &= U_0\left\{\frac{6}{n-6}\left(\frac{r_0}{r}\right)^n - \frac{n}{n-6}\left(\frac{r_0}{r}\right)^6\right\}, \quad n>6, \end{aligned}$$

the second and the third virial coefficients may be transformed into power series⑶⑷

$$B = 4v_0\sum_{t=0}^{\infty}\beta_t(n)x^t,$$

$$C = 10v_0^2\sum_{t=0}^{\infty}\gamma_t(n)x^t,$$

where

$$v_0 = \frac{\pi}{6}\left(\frac{\lambda}{kT}\right)^{\frac{3}{n}} = \frac{\pi}{6}r_0^3\left(\frac{6}{n-6}\frac{U_0}{kT}\right)^{\frac{3}{n}},$$

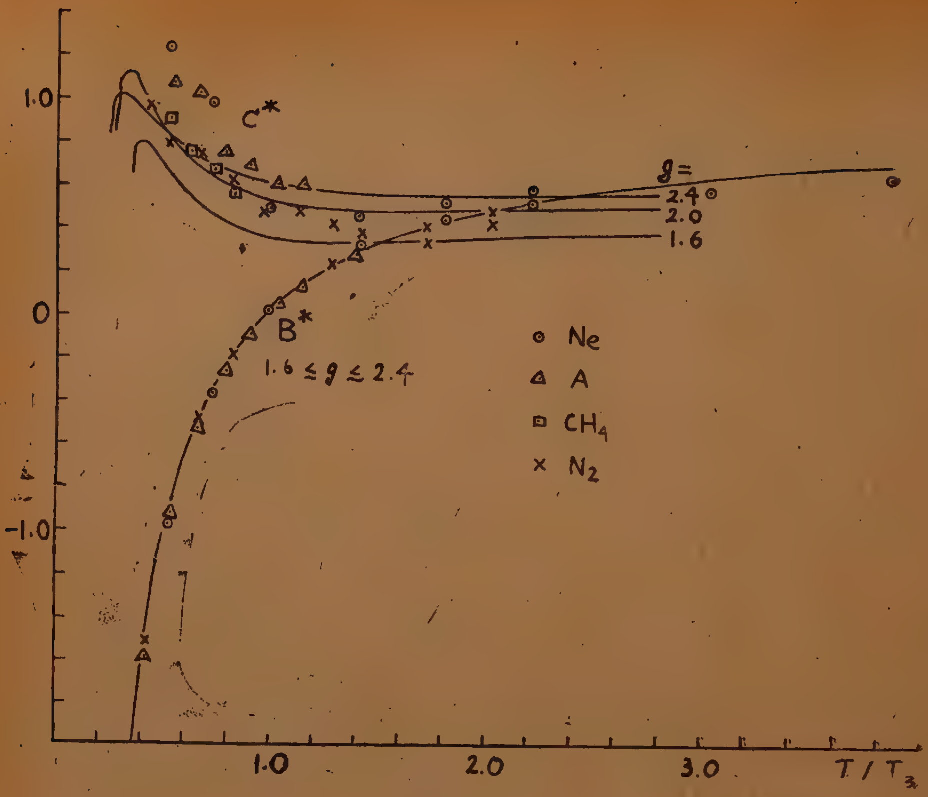
1.0
0
-1.0
C*
g =
2.4
2.0
1.6
B*
1.6 ≤ g ≤ 2.4
○ Ne
△ A
□ CH4
× N2
1.0
2.0
3.0
T / T_B

Fig. 1.

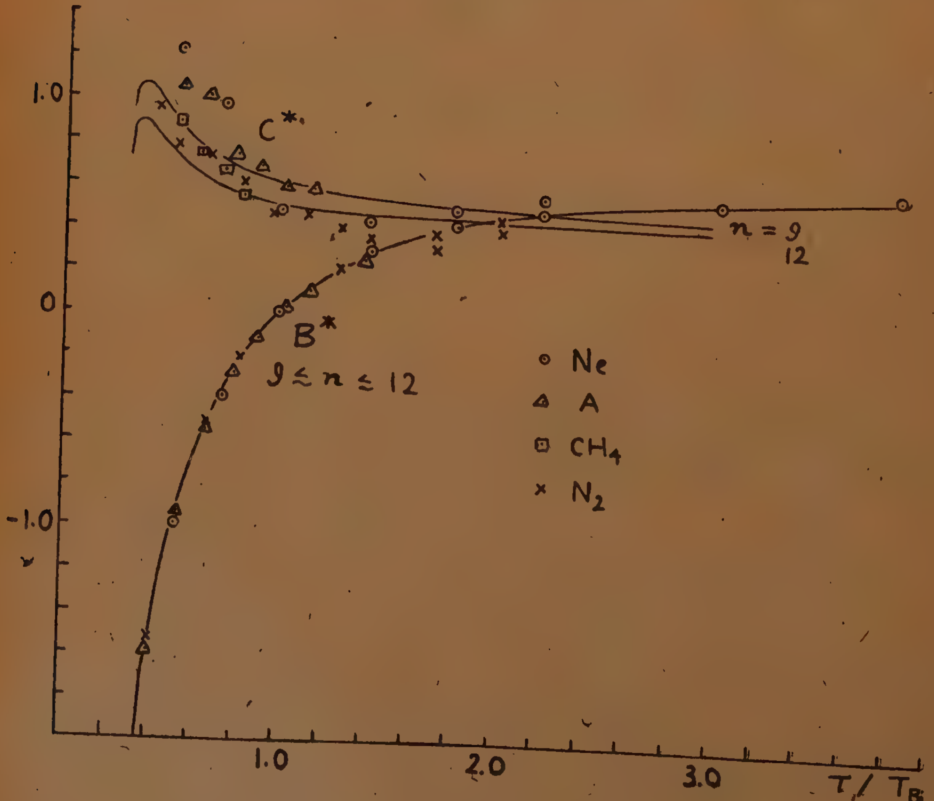
1.0
0
-1.0
C*
n = 9
12
B*
9 ≤ n ≤ 12
○ Ne
△ A
□ CH4
× N2
1.0
2.0
3.0
T / T_B

Fig. 2.

$$x = \frac{1}{2}\frac{\mu}{kT}\left(\frac{kT}{\lambda}\right)^{\frac{6}{n}} = \frac{n}{12}\left(\frac{6}{n-6}\frac{U_0}{kT}\right)^{\frac{n-6}{n}},$$

and

$$\beta_t(n) = -\frac{3}{n}\frac{1}{t\,!}\Gamma\left(\frac{6t-3}{n}\right), \quad t = 0, 1, \ldots$$

The $\gamma_t(n)$ are double integrals which are temperature-independent. β_t and γ_t are normalized as $\beta_0(\infty) = \gamma_0(\infty) = 1$.

Assuming $n=12$, the set $\gamma_t(12)$ was evaluated by the author⁽⁴⁾. (In the previous paper, notation $K_t(n)$, defined as $K_t(n) = (5/6)(n/12)^t\gamma_t(n)$ was used.) The calculated curve of C^* was definitely lower than the observed values, however, indicating that the hollow part of the assumed potential was too narrow.

Without making use of this series expansion, Bird and Spotz⁽⁵⁾ have recently evaluated the third virial coefficient of L-J model with $n = 12$, using punched-card method in order to obtain extreme accuracy. From comparison of the author's former calculation with their "exact" values, it is known that the numerical integration of $\gamma_t(12)$ may not have been sufficiently accurate, although no essential mistake was made in the conclusion.

$\gamma_t(12)$ has been recalculated, therefore, more accurately than before; the results are given in Table II. The recalculated C^* agrees well with Bird-Spotz's values.

Nevertheless, the calculated C^* is clearly smaller than the observed values, as shown in Fig. 2. We must adopt a molecular model with wider hollow part of the potential curve. L-J potential with repulsive index $n = 9$ may be such a model. (cf. Fig. 3. Two curves in the Fig. are mutually so "normalized" that they have the same T_B and the same v_B, using the relations

$$kT_B = 3.44\ U_0, \quad v_B = 1.20\ r_0^3 \quad \text{for } n = 12,$$
$$kT_B \doteqdot 4.57\ U_0, \quad v_B = 1.00\ r_0^3 \quad \text{for } n = 9.)$$

Accordingly the auther has evaluated the double integral $\gamma_t(9)$, and the values are given in Table II. In this case the calculated C^* agrees rather well with observed values, as it was anticipated, cf. Fig. 2.

Table II.

t	$\gamma_t(12)$	$\gamma_t(9)$
0	+1.383	+1.561
1	−2.562	−2.940
2	+1.215	+0.929
3	766	716
4	343	503
5	047	291
6	−0.112	105
7	168	−0.04
8	164	14
9	134	20
10	098	23
11	067	23
12	047	
13	028	
14	016	
15	009	
16	005	
17	003	

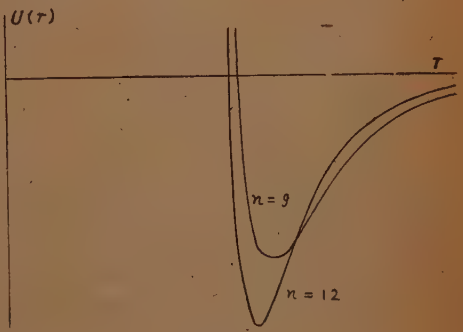

Fig. 3.

This agreement does not necessarily imply that the L-J model with $n = 9$ is better than the L-J model with $n = 12$. What we can know from the foregoing investigation is only that the width of the hollow part of the L-J potential with $n = 9$ is adequate. To explain transport phenomena in high temperature gases, the repulsive wall must be much harder than that of the L-J model with $n = 9$, as the author has pointed out⁽⁶⁾⁽⁷⁾. Even for monatomic molecules, such as neon and argon, L-J potential can not represent the true intermolecular potential so accurately. This model, however, may be used as a standard model of molecules in gases because of its mathematical simplicity.

The author wishes to thank Dr. R. B. Bird and Dr. E. L. Spotz and also Prof. J. O. Hirsch-

felder at the University of Wisconsin, who have sent him a private communication and have criticized his former works.

References.

(1) J. E. Mayer and M. G. Mayer: Statistical Mechanics (1940), Chap. 13.

(2) T. Kihara, Nippon Sûgaku-Buturigakkaisi **17** (1943) 11.

(3) Lennard-Jones, Proc. Roy. Soc. A **106** (1924) 463, Proc. Phys. Soc. **43** (1931) 461.

(4) T. Kihara, Jour. Phys. Soc. Japan **3** (1948) 265. This paper will be referred to as I.

(5) R. B. Bird and E. L. Spotz, private communication (Naval Research Report, University of Wisconsin, 1950).

(6) T. Kihara and M. Kotani, Proc. Phys.-Math. Soc. Japan **25** (1943) 602.

(7) T. Kihara: Imperfect Gases (1950), § 32.

Added in proof:

Contents of Ref. (5) were published in Bird, Spotz and Hirschfelder, J. Chem. Phys. **18** (1950) 1305.

Pressure Dependence of Sensitivity of Photoelectron Counters.

By Ryumyo Ito.

Optical Institute, Tokyo University of Education.

(Received October 4, 1950)

§ 1. Introduction.

A photoelectron counter can count each electron liberated by light, and is far more sensitive than any photocell. Rajewsky, the inventor of photoelectron counters[1], reported that 12 quanta/cm²·sec. of λ 2650 Å light was detectable by means of his counters[2]. Since then various photoelectron counters have been investigated. Visible light sensitive counters were constructed by Locher with the adoption of alkali metals for the cathode[3]. Duffendack and Morris studied how to make reliable photoelectron counters[4]. Photoelectron counters have often been employed for spectrophotometry with spectrographs[5]. Hydrogen is commonly used for the fillings, because it is inactive to metals and easily produces wide plateau regions for Geiger counters. The pressures of hydrogen generally used are about 50 mmHg or more, but the optimum conditions are not yet clear.

The author attempted to use a windowless photoelectron counter for the detector of extreme ultra violet light, and studied, experimentally, the dependence of the sensitivity of hydrogen-filled photoelectron counters on the pressures, and gave it some theoretical interpretations.

§ 2. Experiments.

The counters used are of the Geiger Müller type. They have copper cathodes 14 mm in inner diameter. The cylinder is 60 mm long, and has 3 holes of 3 mm in diameter, separated by 5 mm from each other in the side wall to receive the radiation. The anode is a piano wire 0.18 mm in diameter. The envelope is made of glass and has a quartz window 2 mm thick to pass the ultra violet light. The light source is a quartz low-pressure mercury lamp and is excited by A. C. furnished from a 10,000 volts transformer, whose primary voltage is automatically stabilized. Among the spectra of the mercury lamp, the dominant light which contributes to photoelectric emission is λ 2537 Å light. Hydrogen is used for the fillings. It is generated by electrolysis of KOH solution and stored in a vessel which contains P_2O_5 powder for dehydration. To quench the counter discharges, a high resistance (about 1×10^8 ohm) is employed. The coupling condenser to the amplifier is a $2\mu\mu F$ titanic condenser. The pulses from the counter are amplified, fed to a scale of eight counting circuit and then registered.

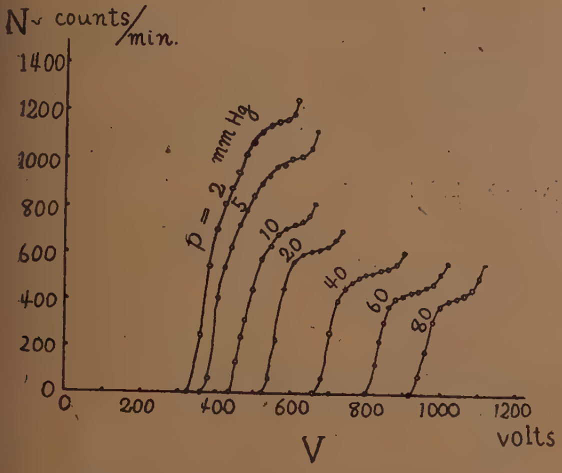

Fig. 1. Counting rate as a function of counter voltages for various pressures of fillings.

Fig. 1 shows the counting rates as a function of counter voltages for various pressures of fillings. We may presume that the counting rates at the centre of each plateau indicate the sensitivity, and Fig. 2 shows this counting rate plotted against the gas pressures. We find from Fig. 2 that the sensitivity of the photoelectron counters rises steeply with the decrease of gas pressures at less than 20 mmHg. As the plateau length is not different so much between the counters of the lowest pressure and the highest one, we prefer the lower pressure counters for the detector of faint light, on account of their high sensitivity, and we can also see that the photoelectron counters are useful for the extreme ultra violet light detection. Moreover, we may note from Fig. 2 that the lower pressure counters require much more overvoltages than the higher ones to reach the plateau.

§ 3. Theoretical Interpretation.

The sensitivity of photoelectron counters is decided by the photoelectric quantum efficiency of the counting probability of the photoelectrons. If the counting rate is not so great and the working condition of counters is in the plateau region, all photoelectrons that arrive at the vicinity of the central wire are counted, and the counting probability of the photoelectrons corresponds with the probability of reaching the anode. But some parts of the photoelectrons can not arrive at the anode,—for these electrons are repulsed by the gas molecules and return to the cathode.

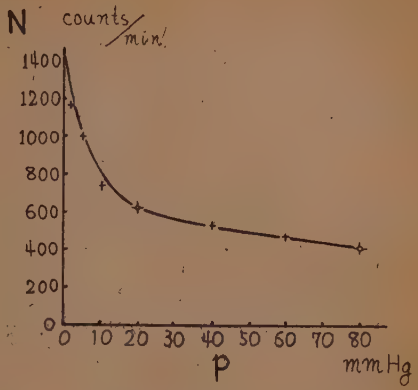

Fig. 2. Counting rate which shows sensitivity as a function of pressure of fillings. +: observed values, -○-: collated values for theory, —: theoretical result.

Thomson explained such back diffusion of photoelectrons in the case of parallel plate electrodes as follows[6, 7]. Let X be the strength of the electric field, n the density of photoelectrons in the vicinity of the cathode, k the mobility of electrons and C the root mean square velocity of electrons near the cathode, then the number of electrons flowing to the anode through a unit area is nkX, and the number of electrons which strike the cathode in a unit time is $nC/\sqrt{6\pi}$. The number of total photoelectrons n_0 is

$$n_0 = nC/\sqrt{6\pi} + nkX. \qquad (1)$$

The probability of photoelectrons reaching the anode ρ becomes, therefore,

$$\rho = nkX/n_0 = \frac{\sqrt{6\pi}\, kX}{C + \sqrt{6\pi}\, kX}. \qquad (2)$$

If the radius of the cathode of the Geiger Müller counters is far greater than the mean free path of electrons, we may apply Thomson's theory to the photoelectric phenomena in the counters. In the plateau region, as described above, the counting rate may be expressed by the product of the density of photoelectric emission and the reaching probability. When the pressure of the gas is above a few mmHg, the photoelectric efficiency can be conceived not to be affected by the pressure change, because at such pressure the adsorbed gas film is not affected by the pressure change. The counting rate is, therefore, proportional to the reaching probability shown by equation (2), and can be written as follows,

$$N = N_0 \frac{\sqrt{6\pi}\,kX}{C+\sqrt{6\pi}\,kX}, \qquad (3)$$

where the constant N_0 represents the number of electrons liberated from the cathode in a unit time. For Geiger Müller counters, the field strength is computed by the following equation,

$$X = \frac{V}{r_c \log (r_c/r_w)}, \qquad (4)$$

where V is the counter voltage and r_c, r_w are the radii of the cathode and anode respectively.

To apply this theory to the experiments the author substituted the observed values for X and k in equation (3), where the mobility was taken from Nielsen's data, corresponding to the values of X/p in our counters[8]. These values are shown in Table I. If we substitute the observed counting rates in the case of 20 mmHg and 80 mmHg of gas pressures for N, we obtain N_0 and C as follows,

$$N_0 = 1411 \text{ counts/min.}, \quad C = 2.15 \times 10^7 \text{ cm/sec}.$$

Equation (3) is, then, illustrated in Fig. 2 by the solid curve, and we find that the theoretical values agree almost exactly with the experimental results, and we can, therefore, conclude that the pressure dependence of the sensitivity of a Geiger counter is due to the back diffusion of photoelectrons.

Table I.

Pressure of Fillings (mmHg)							
p	2	5	10	20	40	60	80
Counter Voltage (volts)							
V	560	600	610	650	830	950	1050
Field Strength (volts/cm)							
X	183	197	200	213	272	312	344
X/p	92	39	20	10.7	6.8	5.2	4.3
Electron Velocity (105 cm/sec.)							
v	286*	127*	70	40	30	25	21
Observed Counting Rate (counts/min)							
$N_{obs.}$	1160	1000	730	630	530	470	420
Calculated Counting Rate (counts/min)							
$N_{cal.}$	1203	1015	826	630†	532	472	420†

*: Extraporated values.
†: Collated values.

From the definition of C, $1/2mC^2$ represents the mean kinetic energy of electrons whose velocities are distributed according to Maxwell-Boltzmann law, but the photoelectrons in the vicinity of the cathode must have the energy distribution represented by DuBridge's equation[9].* We take, therefore, the energy at the maximum of DuBridge distribution instead of $1/2\,mC^2$. When the temperature is 300° K and the mean kinetic energy of the photoelectrons is about 0.8 times the maximum energy, which is same as the difference between the quantum energy of light and the work function of the cathode. Let $h\nu$ be the quantum energy of light and ϕ the work function of the cathode, then the maximum energy E_m becomes

$$E_m = h\nu - e\phi = (1/2\,mC^2) \div 0.8 = 0.16 \text{ ev}.$$

Since the quantum energy of λ 2537 Å light is about 4.86 ev, we obtain

$$\phi = 4.70 \text{ volts}.$$

The previously reported values for the work function of copper range from 4.0 to 4.5 volts[10], and the work function obtained from above seems to tend towards a higher value, but we suppose the causes lie in the fact that the cathode is exposed to the discharge in hydrogen and the work function becomes apparently greater.

---

* By DuBridge's theory, the energy distribution function of photoelectrons is expressed as follows,

$$f(v)dV = A \frac{V\,dV}{e^{(V-V_m)e/kT}+1},$$

where A is a constant, V the kinetic energy of photoelectrons, V_m the maximum energy, k Boltzmann constant, e the electronic charge and T the absolute temperature.

In conclusion, the author wishes to express his sincere thanks to Professor Y. Fujioka for helpful suggestions and discussions.

References.

(1) B. Rajewsky: ZS. f. Phys., **63** (1930) 576.
(2) B. Rajewsky: Phys. Zeits., **32** (1931) 121.
(3) G.L. Locher: Phys, Rev., **42** (1932) 525.
(4) O.S. Duffendack and M.R. Morris: J.O.S.A., **32** (1942) 8.
(5) R. Hanau and R.A. Wolfe: J.O.S.A., **38** (1948) 377, etc.
(6) J.J. Thomson and G.P. Thomson: *Cond. Elec. through gases* (1928) p. 466.
(7) L.B. Leob: *Fund. Proc. of Elec. Discharge in Gases* (1939) p. 313.
(8) N.E. Bradbury and R.A. Nielsen: Phys. Rev., **49** (1936) 388.
(9) L.A. DuBridge: Phys. Rev., **43** (1933) 727.
(10) P.A. Anderson: Phys. Rev., **76** (1949) 388.

Short Notes.

The Ultraviolet Absorption Spectra of Glasses.

By Kikusaburo Osada.

Faculty of Engineering, Nagoya University.

(Received October 23, 1950).

It has been usually known that the ordinary glass was opaque at the wave-length shorter than λ3000A, but as far as the present author knows, the characteristic ultraviolet absorption spectra correlating with its structure have not yet been measured. Therefore, the absorption spectra of some kinds of the thin glass films with several microns thickness were measured to λ1800A by the quartz spectrograph (dispersion: 13.3A/mm. at λ2000A, 167A/mm. at λ3500A), and the results were obtained as shown in Fig. 1.

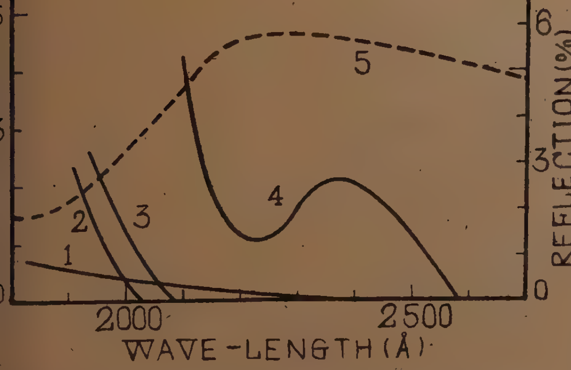

Fig. 1. (1) Sodium Glass. (2) Brownish Glass. (3) Greenish Glass. (4) Lead Glasss. (5) Reflectivity.

In the sodium glass, the absorption edge appears at λ2300A, and in the brownish and the greenish glass each at about λ2050A, but at the wave-length shorter than λ2000A, the absorption coefficient of the former is smaller than the others. In the lead glass, the absorption edge appears at λ2600A and an absorption band at λ2370A.

When illuminated with the ultraviolet radiation, the lead glass radiates a fluorescence of blue light, but others do not or very faint.

The characteristic absorption spectra are to correlate with the reflectivity, and when the spectrum of the sodium glass is compared with its reflectivity⁽¹⁾, we acknowledge that the coincidence between these is very good as shown in Fig. 1. As the refractive index of the lead glass is larger than that of the sodium glass, the absorption band of the former appears naturally of the longer wave-length.

To explain the mechanism of the band at λ2370A of the lead glass, the following experiments were carried out. As the components of these manufactured glasses are exceedingly complex, some kinds of glasses of the simple components are synthesized by use of the pure materials and the absorption spectra of these thin films are measured. In the lead glass ($3Na_2O.7SiO_2.PbO$), the same band appears, but not in others ($3Na_2O.7SiO_2.Fe_2O_3$, $3Na_2O.7SiO_2.TiO_2$, etc.). In the lead oxide film made on a quartz plate by the method of the evaporation of the metal in the air at the pressure of 5 ~ 10 mm Hg., the band also does not appear.

From these results and the well known network structure of glass⁽³⁾, the author considers that the origin of the appearance of this band is not the lead oxide, but the lead ion in the network of SiO_4, which is surrounded by (—O—Si), and the ion is also the centre of the fluorescence.

References.

(1) G. B. Sabine: Phys. Rev. **55** (1939) 1064.
P. G. Nutting: Phys. Rev. **16** (1903) 129.
(2) B. E. Warren: J. App. Phys. **8** (1937) 645.
E. Preston: J. Soc. Glass Tech. **26** (1942) 82.
J. I. Gerolouin: Comt. Rend. Acad. Sci. U.S.S.R. **38** (1943) 126.
S. Anderson: J. Amer. Ceram. Soc. **33** (1950) 45.

On the Ferroelectric Behaviors of Sodium Vanadate.

By Shozo SAWADA and Shoichiro NOMURA.

Institute of Science and Technology,
University of Tokyo.

(Received December 4, 1950).

Recently it has been pointed out that several kinds of crystals of XYO_3 type exhibit the ferroelectric properties similar to those of barium titanate. Especially the discovery of the ferroelectricities of $NaCbO_3$, $NaTaO_3$, etc.(1)(2) seems to be a rather remarkable one in the present-day research of the ferroelectric crystals since these substances do not contain any element of titanium group peculiar to $BaTiO_3$ and the related substances. Unfortunately the detailed information of the above mentioned substances has not been at hand yet. Now, in view of the above situation in the field of ferroelectrics-research, we have studied the physical properties of single crystals of $NaVO_3$ and found that this substance is perhaps a ferroelectric.

Plate-type single crystals of about 1 mm length are obtained by cooling the molten 1:1 mixture of V_2O_5 and Na_2CO_3. The external forms of crystals are of various kinds of types, i.e., square-, rectangular- and other ones, all of which are observed to glitter well and to be yellowish brown, transparent and hard. On putting them between the crossed nichols of a polarized light-microscope, the parallel bands are observed as in the case of barium titanate or tungsten oxide, and further, the brightnesses and darknesses of these bands are reversed with each other by rotating the crystals by 45°, although the detailed behavior of the mentioned reversion is different compared with barium titanate or tungsten oxide. These parallel bands may be considered to show ferroelectric domains for several reasons, the distribution of which is frequently irregular, together with the appearance of the crystals of a single domain. In heating process these domain patterns vanish at about 380°C, above which temperature, however, the birefringence exists still to a lesser amount. In cooling process the domain patterns appear at about 270°C, their distribution being not necessarily the same as the initial one. The effect of electric field and mechanical stress on the domain structure has not been observed through our preliminary observation at room temperature, which lies far below the above mentioned Curie point, as far as our field strength and amount of stress concern; which fact may be considered to be due to the large coercive field and the high hardness of this crystal.

Using a cathode ray oscillograph we are able to observe hysteresis loops as illustrated in the accompanying figures. When a crystal is heated at a constant impressed voltage, we have observed clearly the following characteristic phenomena, namely, (a) the loss is small at room temperature, (b) the hysteresis loop suddenly broadens and becomes angular at a certain temperature, (c) the loop-height increases slightly and the loop-breadth decreases gradually and (d) the loss vanishes at the about 380°C. On cooling the crystal, the corresponding characteristics are (e) the loss appears at about 260°C, (f) both the height and breadth of the loop change gradually and (g) the loop flattens near room temperature. The temperature at which the hysteresis loop suddenly broadens, decreases with the increase of the impressed voltage, and is also dependent on the career of the crystal. Though the hysteresis loop of a virgin crystal is unstable, it becomes stable gradually after some amount of heat treatments, which phenomena is well understood, though qualitatively, through the mechanism of the redistribution of domains.

The precise measurement of the permittivity of crystals can not be made for the sake of their small dimensions. Our preliminary measurements, however, reveal that the value of perimittivity at room temperature is small and only a slight hump is observed near 380°C, the appearance of such slight hump being quite different from the case of the ferroelectrics already known. Although the large value and the anomalous dependence on temperature of the permittivity have been hitherto considered to be necessary conditions for the ferroelectricity, such criterion seems to be inappropriate for the newly discovered characteristics of $NaVO_3$, which shows clearly the domain pattern and the hysteresis loop charac-

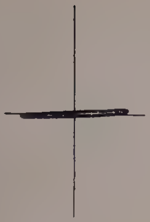

(a) 20°C

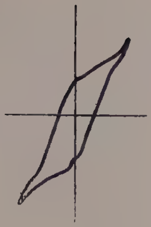

(b) 220°C

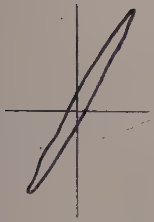

(c) 340°C

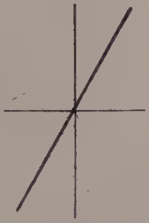

(d) 410°C

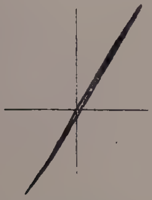

(e) 260°C

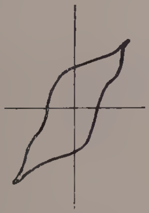

(f) 200°C

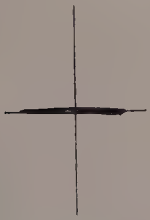

(g) 20°C

teristic of the ordinary ferroelectric substances.

The determination of the crystal structure of $NaVO_3$ by the X-ray analysis and the investigations of the substances such as $LiVO_3$ and KVO_3 are now in progress, the details of which will be published shortly.

The authors wish to express their hearty thanks to Prof. T. Muto for his very kind criticism.

References.

(1) Bull: Am. Phys. Soc., **24** ('49), No. 4, 28.
(2) B. T. Matthias: Phys. Rev., **75** ('49), 989.

The Height of the Water Column Produced by the Falling Ball.

By J. Nishiwaki.

Mizuho Metal Industry Co., Ltd., Tanashi, Tokyo.

(Received December 15, 1950)

The column of water produced by the ball falling under the action of gravity was photographed with the storobolight and high speed movie camera. The frequency of the storobolight was 1500 per min., and the speed of the camera was regulated to the 5000 pictures per min. on the 35 mm film.

The preliminary experiments were carried out with the two balls of about equal size:

(1) The ebonite ball, dia. = 19.7 mm, weight = 4.9g
(2) The glass ball, dia. = 20.5 mm, weight = 11.6g

and it was found that the heights of water columns produced by the ebonite ball, though it weighed less than the other, were higher than the ones by the glass ball for each falling height.

As this seemed to be the effects of the surface roughness of each ball, we carried on the experiments as followes:

The five glass balls of different diameters were painted with sand of different meshes. Their total diameters and weights were, thus respectively,

for	10,000 mesh,	17.5 mm,	9.0g,
for	2,500 mesh,	17.2 mm,	7.5g,
for	900 mesh,	18.0 mm,	7.5g,
for	256 mesh,	18.5 mm,	6.5g,
and for	64 mesh,	20 mm,	7.0g,

where meshes were measured per square inches.

For these balls, the heights of water columns were determined in the same way as above mentioned. The results are shown in Fig. 1. As seen from this figure, the water column has the smallest height for 10,000 mesh, becomes the larger, the greater the roughness is, and attains maximum height in the range of 900-256 meshes. And then it becomes smaller again.

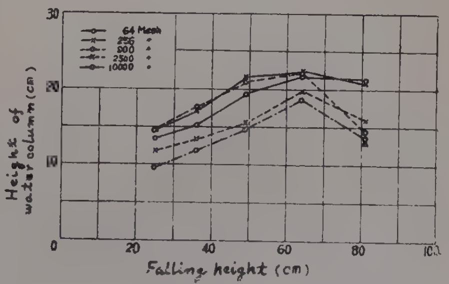

Fig. 1.

The point marked with triangle at the end of the curve for 10,000 mesh is the one datum obtained by using the other ball which had the about equal diameter (20.8 mm) to the ball for 64 mesh (See Fig. 2).

Hence this indicates that the difference shown above between the diameters of the balls did not have any effect on the heights of columns.

The ball used in the experiments are shown in Fig. 2.

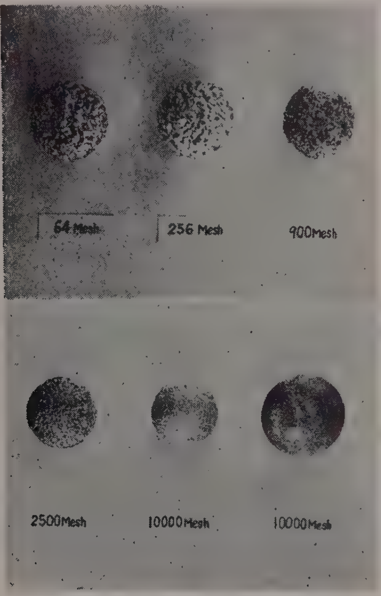

Fig. 2. The balls used in experiments.

Current Noise and Dielectric Breakdown in Alkali-halide Crystals.

By Chiyoe YAMANAKA and Tokuo SUITA.

Faculty of Engineering, Osaka University.

(Received Jan. 20, 1950).

It is generally believed that the dielectric breakdown in solids is produced by avalanches of electrons. We have observed the sizes of avalanches in some alkali-halides at high temperatures and their frequency distributions by a video-amplifier and filters.

Our specimens and measuring apparatus are shown in Fig. 1, where S_1 is a specimens which has 0.3-0.6 mm. thick, S_2 is 0.6 mm. in breadth between the electrodes, G is a galvanometer, R is a metallic resistance. Th is a thermocouple and an ammeter, B is a dry cell battery variable from 300 V to 1200 V, Br is a braun tube.

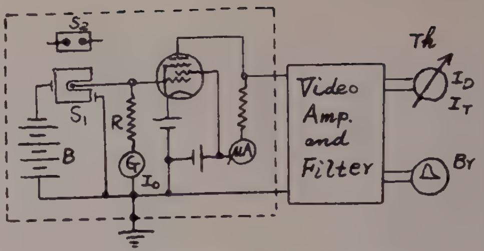

Fig. 1. Specimens and apparatus.

When I_0, the mean current throuth the specimen, flows, the mean square noise current $\bar{I}_D^2$ can be observed. According to Haworth and Bozorth, the average size of an avalanche is given by

$$\bar{N}^2/\bar{N} = \bar{I}_D^2/\bar{I}_T^2 2kT/eI_0R$$

where K is Boltzmann constant, T is absolute temperature, $\bar{I}_T^2$ is the thermal noise current produced in R.

One of our results for an avalanche size in KCl is given in Fig. 2 and Fig. 3.

In Fig. 2, The avalanche size increases with the applied voltage and its magnitude is about 10^3 at the 20% breakdown voltage at 200 C.

In Fig. 3, we estimated the avalanches-size at the voltage of 20% breakdown strength in each temperature. These results show that the sizes of avalanches are almost the same before the breakdown. The frequency distributions of noises in NaCl are shown in Fig. 4 and Fig. 5. We got these results by comparing the avalanche noises with thermal noise in a metallic input resistance. At lower temperatures than about 200°C. the avalanche noise was of radom character, that is uniform to a definite frequency (10^4–10^5 cycles)

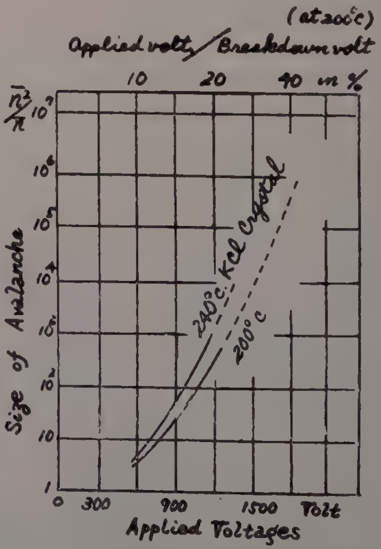

Fig. 2. Size of avalanches and applied voltages.

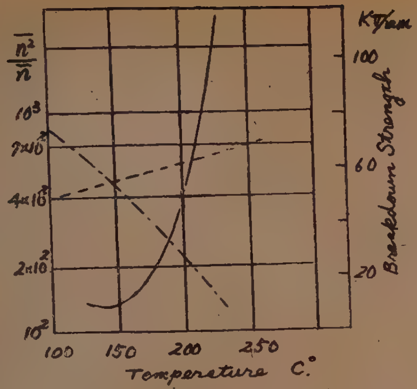

Fig 3. $\bar{n}^2/\bar{n}$ and T°C. KCl crystal.

In full line we show the size of avalanches at 1,200 V applied. In chain line --- the breakdown strength. In dotted line we show the size of avalanches at 20% voltage applied of the break-down strength (calculated).

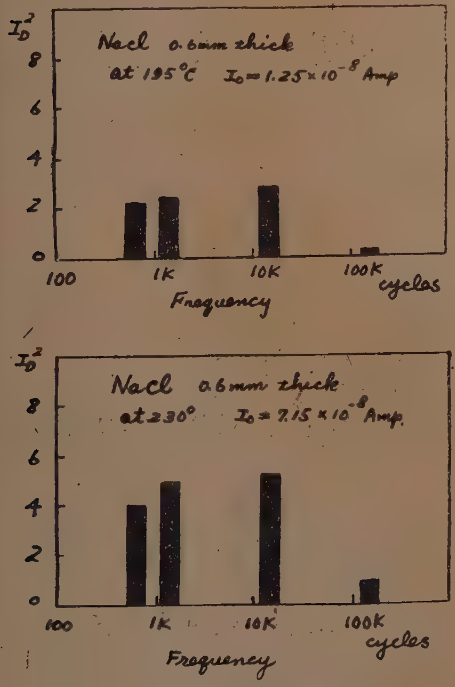

Fig. 5. Frequency distributions (1,200 volts applied).

over which its components tend to zero. But at temperatures higher than about 200°C. the results appear to show there are some interactions between avalanches. Noises in the surface currents were extremely small.

These results seem to show that the breakdown is produced by avalanches at such high temperature.

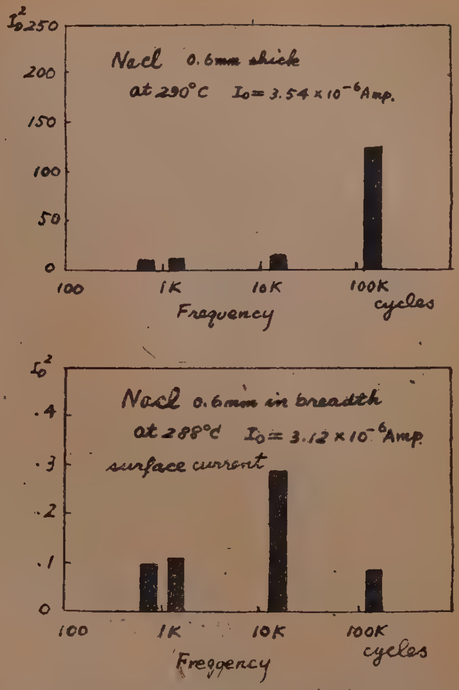

Fig. 5. Frequency distributions at high temperatures in body and surface current. (1,200 volts applied).

References.

(1) Haworth and Bozorth: Physics **5** (1934) 15.
(2) T. Suita: J.I.E.E. of Japan **69** (1949) 352.
(3) Seitz: Phys. Rev. **76** (1949) 1376.
(4) A. von Hippel: Phys. Rev. **76** (1949) 127.
(5) C. Yamanaka: Read before the annual Meeting of I.E.E. of Japan A **74** (1950).
(6) C. Yamanaka: ibid, the Kansai Meeting, Jan. **27** (1950).

On the Dielectric Loss in Polydisperse Polar Polymers.

By Syôten Oka and Osamu Nakada.

Kobayasi Institute of Physical Research,
Kokubunji, Tokyo.

(Received January 22, 1951).

Kirkwood and Fuoss(1) have developed a theory of dielectric dispersion and dielectric loss of polar polymers of the type $(CH_2CHX)_n$ at high dilution in a nonpolar plasticizer. Neglecting the mutual interaction between the linear polymer molecules and assuming free rotation about the $C-C$ bonds, they have succeeded to obtain a dielectric loss curve which has a much smaller value of maximum loss than that given by Debye's theory. The calculation was, however, made only for a monodisperse polymer and for a polydisperse polymer with an exponential distribution in chain length, and so it is not obvious from their results how the dielectric loss in a polydisperse system depends on the type of the distribution function.

In order to make this point clear, we have investigated the dielectric loss of a polydisperse polymer which is characterized by a rather general distribution function

$$\Phi_k(n) = \frac{k^k}{(k-1)!}\,\frac{1}{\bar{n}}\left(\frac{n}{\bar{n}}\right)^{k-1} e^{-k\left(\frac{n}{\bar{n}}\right)} \quad (k=1,2\ldots) \qquad (1)$$

Here $\bar{n}$ represents the average degree of polymerization. This formula was first derived theoretically by Schulz(2) under the assumption of homogeneous coupling of degree k in polymerization reaction, and it was found, indeed, that some polymers correspond to this formula. Differing from the original form, however, our $\Phi_k(n)$ satisfies the following normalization condition:

$$\int_0^\infty \Phi_k(n)\,dn = 1.$$

The exponential distribution function $\exp(-n/\bar{n})/\bar{n}$ used by Kirkwood and Fuoss is included in the formula (1) as a special case $k=1$. The values of $\bar{n}\Phi_k(n)$ are plotted in Fig. 1 for several values of k.

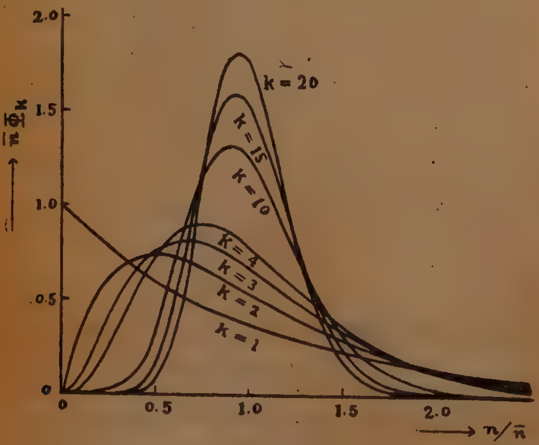

Fig. 1. Distribution in degree of polymerization for chain high polymer.

According to Kirkwood and Fuoss, the relaxation time distribution function $G(\tau,n)$ for a monodisperse polymer is given by

$$G(\tau,n) = \frac{\tau}{(\tau+\tau_\circ)^2}, \qquad \frac{4\tau_\circ}{n\pi^2} \leq \tau \leq \frac{n\tau_\circ}{6},$$
$$= \ 0\ , \qquad \tau > \frac{n\tau_\circ}{6} \text{ or } \tau < \frac{4\tau_\circ}{n\pi^2},$$
$$\tau_\circ = n\tau^*, \qquad (2)$$

where τ^* is a relaxation time of a magnitude appropriate to a single monomer unit. In the case of a polydisperse systems with the distribution function (1), we way write for the average relaxation time distribution function

$$G_k(\tau) = \int_0^\infty \frac{n}{\bar{n}}\,G(\tau,n)\Phi_k(n)dn, \qquad (3)$$

which after intergration gives

$$\bar{G}_1(\tau) = \frac{1}{\tau_0}\left[1+\frac{\tau}{\bar{\tau}_0}+\frac{\tau}{\bar{\tau}_0}\left(2+\frac{\tau}{\bar{\tau}_0}\right)\exp\left(\frac{\tau}{\bar{\tau}_0}\right)\mathrm{Ei}\left(-\frac{\tau}{\bar{\tau}_0}\right)\right]$$

$$\bar{G}_2(\tau) = \frac{1}{\bar{\tau}_0}\left[1-4\left(\frac{\tau}{\bar{\tau}_0}\right)-4\left(\frac{\tau}{\bar{\tau}_0}\right)^2\right.$$
$$\left.-4\left(\frac{\tau}{\bar{\tau}_0}\right)^2\left(3+2\frac{\tau}{\bar{\tau}_0}\right)\exp\left(2\frac{\tau}{\bar{\tau}_0}\right)\mathrm{Ei}\left(-2\frac{\tau}{\bar{\tau}_0}\right)\right]$$

$$\bar{G}_3(\tau) = \frac{1}{2\bar{\tau}_0}\left[2-6\left(\frac{\tau}{\bar{\tau}_0}\right)+27\left(\frac{\tau}{\bar{\tau}_0}\right)^2+27\left(\frac{\tau}{\bar{\tau}_0}\right)^3\right.$$
$$\left.+27\left(\frac{\tau}{\bar{\tau}_0}\right)^3\left(4+3\frac{\tau}{\bar{\tau}_0}\right)\exp\left(3\frac{\tau}{\bar{\tau}_0}\right)\mathrm{Ei}\left(-3\frac{\tau}{\bar{\tau}_0}\right)\right] \qquad (4)$$

for $k=1,2$, and 3 respectively. Here $\mathrm{Ei}(-\tau/\bar{\tau}_0)$ is the exponential integral and $\bar{\tau}_0 = \bar{n}\tau^*$. Numerical calculation shows that $\bar{G}_k(\tau)$ increases with increasing k for smaller values of τ and decreases for larger values of τ. In Fig. 2. are shown values of $\bar{G}_k(\tau)$ as functions of $\tau/\bar{\tau}_0$, and it may be seen that the curves approach, with increasing k, to the curve corresponding to a monodisperse polymer.

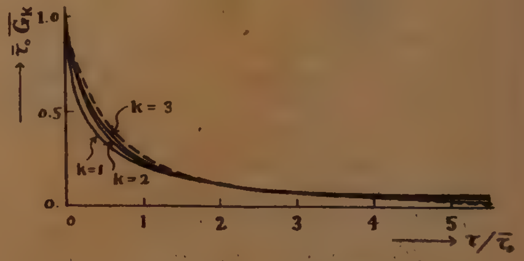

Fig. 2. Relaxation time distribution for polar chain high polymers with distribution function $\Phi_k(n)$. Broken line, for a monodisperse polymer.

Now the reduced loss factor corresponding to the relaxation time distribution $\bar{G}_k(\tau)$ is given by the formula

$$H_k(\omega) = \int_0^\infty \frac{\omega^2}{1+\omega^2\tau^2}\,\bar{G}_k(\tau)\,d\tau \qquad (5)$$

For the case $k=1$, the calculation was made by Kirkwood and Fuoss, and the maximum value of $H_1(\omega)$ was found to be 0.27 at $\omega\bar{\tau}_0 = 0.63$. When $k=2$, Eq. (6) becomes, after insertion of Eq. (4)

$$H_2(x) = \int_0^\infty \frac{xu}{4+x^2u^2}\left[1-2u-u^2-u^2(3+u)e^u\mathrm{Ei}(-u)\right]du \qquad (6)$$

with $x = \omega\bar{\tau}_0$. This function has been calculated by numerical integration, and it was shown to have a maximum at $x = 0.75$ of 0.272, which is slightly larger than the value 0.27 corresponding to the case $k = 1$, and is slightly smaller than the value 0.286 corresponding to a uniform degree of polymerization.

We have not calculated the loss maximum in the case $k = 3$, but it appears certain that the reduced loss maximum increases with increasing k, since the main contribution to the integral (5) near its maximum comes from smaller values of τ and $G_k(\tau)$ increases with k for smaller values of τ. This circumstance may correspond to the fact that the distribution curve $\Phi_k(n)$ becomes sharper and sharper with increasing k, thus tending more and more to a monodisperse curve.

References.

(1) J.G. Kirkwood, R.M. Fuoss: J. Chem. Phys. **9** (1941), 329.

(2) G.V. Schulz: Z. Phys. Chem. **B 43** (1939), 25.

A Proposal on the Measurement of the Recoil Spectrum using Gas Source.

By Tihiro OHKAWA.

Department of Physics, University of Tokyo.

(Recieved January 24, 1951).

Recently experiments on the measurement of recoiled nuclei in the beta-decays have been performed by several workers. Almost all of them, however, used solid sources, and it is very difficult to obtain reliable results.

It seems possible to obtain velocity spectra of recoiled nuclei using "gas sources" by the following method.

Under the electrostatic field, whose potential is given by $V = (k/2)(x^2+y^2-2z^2)$, a charged particle of the mass m and the charge e moves after the following equations.

$$x = x_0 \cos \alpha t + (v_{x0}/\alpha) \sin \alpha t$$
$$y = y_0 \cos \alpha t + (v_{y0}/\alpha) \sin \alpha t$$
$$z = z_0 \cosh \sqrt{2}\,\alpha t - (v_{z0}/\sqrt{2}\,\alpha) \sinh \sqrt{2}\,\alpha t$$

where x_0, y_0, z_0, and v_{x0}, v_{y0}, v_{z0} denote the initial positions and velocities of the particle respectively and α^2 is $(e/m)k$.

Hence we have at the instant $t = T (T = \pi/(2\alpha))$

$$\rho \equiv \sqrt{x^2+y^2} = \sqrt{v^2_{x0}-v^2_{y0}}/\alpha$$

that is, distances of particles from the origin don't depend on the initial positions x_0, y_0 of particles but on the magnitude of their initial velocities and the constant k. Namely, in the x-y plane, all particles which started at any points in any directions, reach, at the instant $t = \pi/(2\alpha)$, the common of radius $\rho = v_0/\alpha$ with center at the origin.

If an annular ion detector is set along the circumference of the circle and worked by the method of delayed coincidence between it and a beta-dector, which serves for determining the time origin, the velocity spectra can be taken as a function of the epoch T.

In case a particle outside (or inside) the detector starts initially in the inward (or outward) direction, it crosses once the detector before $t = T$. Therefore the particle does not contribute to the count.

Moreover, when z-components of the velocities of particles are taken into account, particles diverge for z-directions. It seems, however, easy to obtain the luminocity of several percents provided that the irresolution $\Delta v/v$ is limitted to be smaller than several percents.

The test using some suitable radioactive substances, A^{37} for example, are highly desirable for us.

Detailed discussions and notes on the trial experiments will be later reported in this jounal.

Effect of Turbulence on Flame Propagation in Gases.

By Seiichiro KUMAGAI and Ituro KIMURA.

Department of Mechanical Engineering, Faculty of Engineering, University of Tokyo.

(Received Jan. 29, 1951)

It is well known that flame propagation in gases is considerably accelerated by the agitation of gases. This is perhaps due to the increase in burning velocity caused by turbulence which is small in scale compared with the flame front. In our experiment on a cylindrical closed vessel (90 mm in diameter, 30 mm in length), we gave rise to turbulence by placing a hole plate or a grid in front of the spark igniter. Fig. 1 is one of the examples of the pressure records obtained by igniting 22 percent by volume town gas-air mixtures of normal pressure and room temperature.

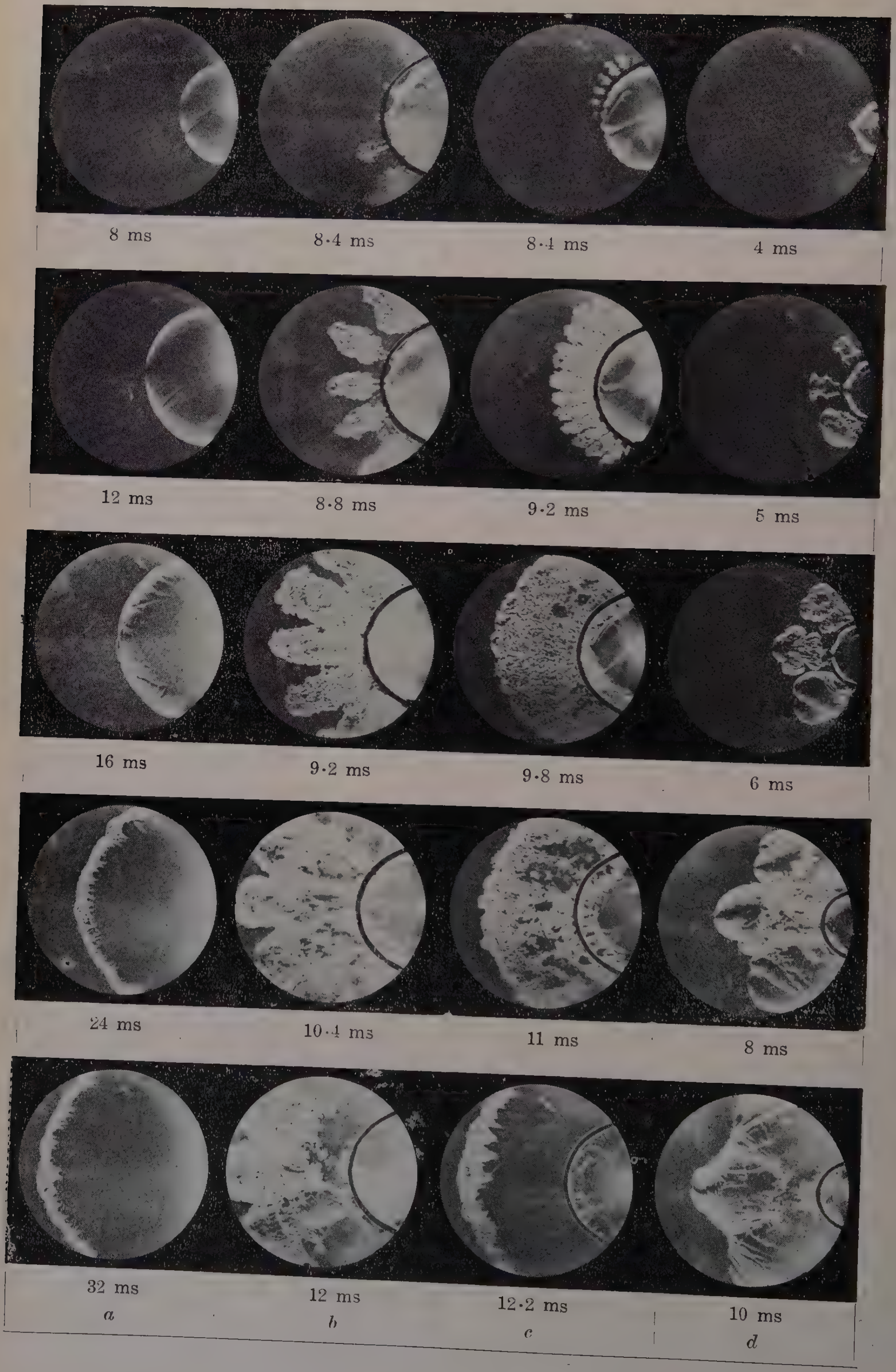
8 ms
8·4 ms
8·4 ms
4 ms
12 ms
8·8 ms
9·2 ms
5 ms
16 ms
9·2 ms
9·8 ms
6 ms
24 ms
10·4 ms
11 ms
8 ms
32 ms
a
12 ms
b
12·2 ms
c
10 ms
d

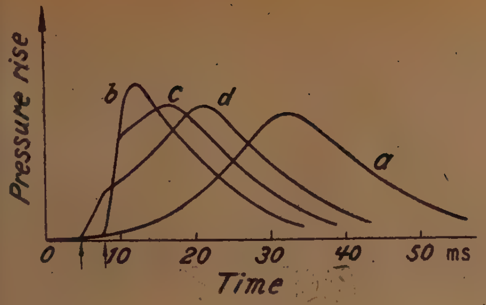

Fig. 1.

a: No obstacles are placed.

b: An arched plate with five holes 6 mm in diameter is placed.

c: A plate with seventy holes 2 mm in diameter, the size of which is same as that used in case of *b* is placed.

d: A plate with three holes 6 mm in diameter is placed nearer to the spark igniter than in case of *b*.

Figs. 2a—2d are the schlieren photographs, each of which corresponds to each of the pressure records in Fig. 1. When we compare both figures with each other, we can easily find out how turbulence accelerates the combustion of gases. The arrow mark in Fig. 1 corresponds to the position of the hole plate, and it is due to turbulence that burning velocity rapidly increases from here. When turbulence is not sufficiently intense, the increase in burning velocity is not so remarkable, and when turbulence is intense at the beginning and comes to disappear afterwards, burning velocity changes correspondingly.

Some photographe are given here, and full explanation will be made in another paper.

On the Transformation of Long Chain Acid Amides

By Tosio Sakurai.

Institute of Science and Technology, University of Tokyo.

(Received February 10, 1951).

The transformation of Palmitamide ($C_{15}H_{31}CONH_2$) and Stearamide ($C_{17}H_{35}CONH_2$) in solid phase, is newly found from their specific heat and electric conductivity measurments.

Commercial pure amides made by Kahlbaum are used for specific heat measurement without further purification, although Stearamide seems to contain a small amount of impurity. The method is the same as we used to measure the specific heat of normal alcohol previously(1). The results of the observation are shown in Fig. 1. Small anomalies are found at about 56°C for Palmitamide and 64°C for Stearamide. The heat of transformations are about 150 cal/mol and 155 cal/mol respectively.

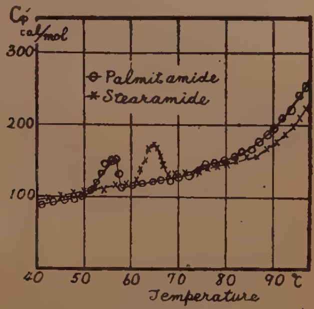

Fig. 1.
The specific heat of amides.

D.C. conductivity is measured under the dried air. Samples are recrystallized from benzol several times. The results are shown in Fig. 2. The electric conductivity of the Palmitamide increases remarkably after the transformation. Though the Stearamide shows no anomaly in the conductivity, it is not clear whether it is due to the effect of impurity or the property of the sample itself. The dielectric constant and loss of the Palmitamide are measured by H. Komatsu(2) under the frequency of 2 kilo cycles per second, and they both increase after the transformation, too.

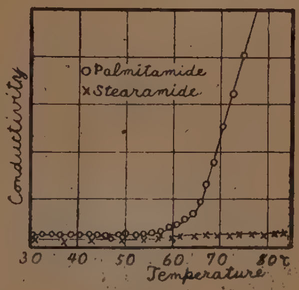

Fig. 2.
D.C. electric conductivity of amides.

The electric conductivity and dielectric constant of the long chain compound, which contains the hydrogen bond, are often attributed to the proton transfer(3)(4). As the amide seems to have hydrogen bonds, it is natural to regard this conductivity is due to the proton transfer, though the mechanism may be different from that of the alcohol(3).

The nature of the transformation is not clear yet, but it resembles to that of the alkali soaps found by P.A. Thiessen⁽⁵⁾, which occur near the melting points of the corresponding fatty acids, inspite of the great difference between the melting points of soaps and acids. Therefore these transformation may be due to the property of the fatty acid. From this stand point, these were called "*genotypical transformation*" by Thiessen. An analogous relation exists in the case of amides. This point was already discussed⁽⁶⁾, and the full note will be published later together with other experimental results.

References.

(1) Y. Kakiuchi, T. Sakurai and T. Suzuki: J. Phys. Soc. Jap. **5** (1950) 369.

(2) H. Komatu: not published.

(3) Y. Kakiuchi: Proc. Jap. Acad. **23** (1947) 65.
Y. Kakiuchi, H. Komatsu and S. Kyoya: J. Phys. Soc. Jap. **6** (1951) in press, J. Chem. Phys. **19** (1951) in press.

(4) J. D. Hoffman and C. P. Smyth: J. Am. Chem. Soc. **71** (1949) 431.
P.W. Crowe and C.P. Smyth: J. Am. Chem. Soc. **72** (1950) 4427.

(5) P.A. Thiessen and E. Ehrlich.: Z. f. Phys. Chem. **B19** (1932) 299.
P.A. Thiessen and E. Ehrlich.: ibid. **A165** (1933) 458.
P.A. Thissen and J.V. Klenck.: ibid, **A174** (1935) 335.

(6) T. Sakurai.: Rep. Inst. Sci. Tech. Univ. Tokyo. **4** (1950) 1.

Electric Conduction in Ionic Crystals (Part I)

Chisato Okazaki and Tokuo Suita.

Faculty of Engeneering, Osaka Uuiversity.

(Received February 19, 1951)

The electric conductivities of ionic crystals such as alkali halides show in general some discontinuites at about 200°C. This phenomenon is thought to be due to space charges in the crystal⁽¹⁾ and to be closely related to the dielectric breakdown strength of it⁽²⁾.

For the purpose of investigating the space charge effect, we measured the conductivities of KCl-(0.01 mole %) $SrCl_2$ mixed crystals and other ionic ones at various conditions of treatment, especially of the contacts between the crystal and the electrodes.

The specimens were the plates of single crystal cut along the cleavage surface (about 1 mm. in thickness and 2 cm. in width) which were grown by the Kyropoulos method.

The voltage required (about 1000 volt/cm.) was supplied by dry batteries, and the two electrodes of the specimen which were made of colloidal carbon were connnected to the earth in the absence of an applied voltage.

The current through the crystal was measured by a galvanometer at the temperature range from 150° to 300°C.

The conditions of the treatment are shown in Table I, where 1, 2 and 3 are the order of the treatment process. In the case of electrical treatment, the amounts of electric charges passing through the crystals were kept constant.

The results obtained are shown in Figs. 1, 2 and 3. There is a discontinuous point at about 200°C for the specimen (A) treated only by the thermal process, and the current through the crystal decreases with time to a steady value at temperatures lower than 200°C, but at higher temperatures it takes a constant value immediately after the field was applied. The specimen (B) treated by the 2nd electrical process at 275°C shows neither the discontinuity at about 200°C

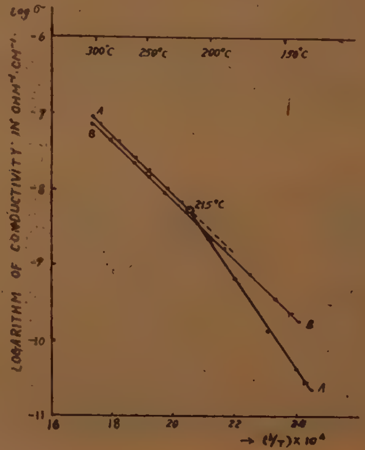

Fig. 1. Conductivities of $KCl \cdot SrCl_2$.

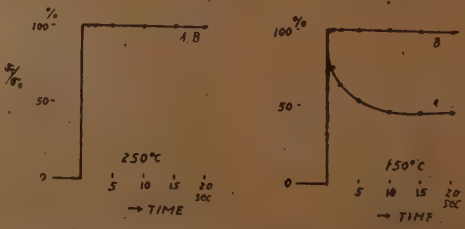

Fig. 2. Change of Current with time
σ_t: Current at t,
σ_0: Initial Current

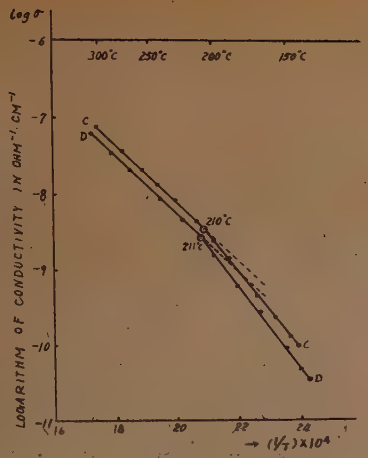

Fig. 3. Conductivities of KCl-SrCl$_2$.

nor the current decrease with time. But at the specimen (C) treated by the 2nd electrical process at 140°C the discontinuity does not disappear and the current decrease also exists. It is interesting to see that when we treat the specimen in wet air (about 70% in wetness) at room temperature during long hours after the electrical treatment has been done at higher temperatures (specimen D), the discontinuity appears again.

Table I.

No.	Treatments						
	1		2			3	
	°C	Hrs.	°C	Amp.	Min.	°C	Hrs.
A	140	10					
B			275	$4\cdot10^{-6}$	1/2	140	10
C	140	10	140	$9\cdot10^{-9}$	200		
D			280	$1.4\cdot10^{-6}$	2	room temp. then 140	10

The activation energies calculated from the inclination of the conductivities at higher temperatures are always 0.81 e.V., which accords with Lehfeld's results⁽³⁾ in a single crystal of KCl.

These results seem to show that:

(1) The discontinuity of the conductivity at about 200°C is due to the ionic space charges in the crystal,

(2) the space charges can be removed by the complete contact between the crystal and the electrodes with the help of the metallic dendrite,

(3) the intimate contact is destroyed by the water film adsorbed on the contact surface.

Reference:

(1) B. Hochberg and A. Walther: Z. Physik, **64** (1930) 392.
(2) T. Suita: J.I.E.E. (Japan), **69** (1949) 190.
(3) F. Seitz: Rev. Mod. Phys., **18** (1946) 384.

An Interpretation of the Dielectric Loss due to the Rotation of Dipoles.

By Nobuhiko Saitô.

Kobayasi Institute of Physical Research, Kokubunzi, Tokyo.

(Received Feb. 20, 1951).

§1. Introduction.

Recently the present author[1] has dealt with the effect of the Brownian motion upon the intrinsic viscosity of macromolecules and has given a general method for calculating the energy dissipation in the presence of the Brownian motion. This method must be applied to the problem of the dielectric loss due to the rotation of dipoles which was firstly treated by Debye. The usual method of calculating the electric loss is to calculate the electric energy loss. This energy loss is obviously due to the rotational friction of dipoles in a viscous medium. However the movement of the dipole is very complicated by the presence of the Brownian motion. In each processes the energy of a dipole is dissipated by the friction, but soon after a part of this dissipated energy is returned to the dipole by means of the Brownian motion. Therefore the energy dissipation is not caused by the total firictional forces.

§2. Outline of an Usual Method.[2]

Let the external electric field applied to the dielectrics be

$$E = E_0 e^{i\omega t} \tag{1}$$

The internal field which acts on a dipole is generally different from (1) both in absolute value and in phase, and is denoted as

$$F = F_0 e^{i(\omega t + \chi)} \tag{2}$$

Let θ be the angle between the direction of the field and the axis of the dipole. Then the distribution of the orientation of dipoles is determined

$$\frac{\partial\rho}{\partial t} = -\operatorname{div} j\rho = -\frac{1}{\sin\theta}\frac{\partial}{\partial\theta}(j_\theta\rho), \tag{3}$$

$$j_\theta = -\frac{F\mu}{f}\sin\theta - \frac{kT}{f\rho}\frac{\partial\rho}{\partial\theta} \tag{4}$$

where f and μ are respectively the friction constant and the dipole moment of the molecules. The well-known solution of Eq. (3) when $F\mu/kT \ll 1$ is given by

$$\rho = \frac{1}{4\pi}\left\{1 + \frac{1}{1+i\omega\tau}\frac{\mu F}{kT}\cos\theta\right\} \qquad (5)$$

$$\tau = f/2kT$$

and the average dipolement is given by

$$\bar{\mu} = \int \mu\cos\theta\rho d\Omega = \frac{\mu^2}{3kT}\frac{F_0}{\sqrt{1+\omega^2\tau^2}}e^{i(\omega t-\varphi+\chi)} \qquad (6)$$

from which is derived easily the complex dielectric constant $\varepsilon = \varepsilon_1 - i\varepsilon_2$. In particular

$$\varepsilon_2 = \frac{4\pi N_1\mu^2}{3kT}\frac{F_0}{E_0}\frac{\sin(\varphi-\chi)}{\sqrt{1+\omega^2\tau^2}} \qquad (7)$$

where N_1 is the total number of dipoles in unit volume. Therefore the energy dissipation during a period of the alternating field is calculated to be

$$\frac{1}{4\pi}\int_0^{2\pi/\omega} E\frac{\partial D}{\partial t}dt = \frac{E_0{}^2\varepsilon_2}{4}$$

$$= \frac{\pi N_1}{kT}\frac{E_0F_0\mu^2}{\sqrt{1+\omega^2\tau^2}}\sin(\varphi-\chi) \qquad (8)$$

§ 2. A New Method of Derivation.

As is mentioned in § 1, the energy dissipation is due to the friction of dipoles, but the effective frictional force is not the total frictional forces. The latter are minus the sum of the internal field, which is the sum of the external field and the field by the surrounding materials, and the random forces which drive the Brownian motion.

In our present case the instantaneous moment of force due to the external force is $E_0\mu\sin\theta\cos\omega t$. From Eq. (4) and (5), we have

$$j_\theta = \frac{F_0\mu\sin\theta}{f}\frac{\{-\omega^2\tau^2\cos(\omega t+\chi)+\omega\tau\sin(\omega t+\chi)\}}{1+\omega^2\tau^2}$$

+imaginary part.

Therefore the energy dissipation is calculated to be

$$-N_1\int\rho(\theta)\,d\Omega\int_0^{2\pi/\omega}E_0\mu\sin\theta\cos\omega t(j_\theta)_{\rm real}\ dt$$

$$= \frac{\pi N_1}{kT}\frac{E_0F_0\mu^2}{\sqrt{1+\omega^2\tau^2}}\sin(\varphi-\chi) \qquad (10)$$

This is identical with eq. (8).

References.

(1) N. Saito, J. Phys. Soc. Japan, in press.
(2) For example, H. Frölich, *Theory of dielectrics*, 1949. Oxford. P. Debye, *Polare Molekeln*, 1929. Leibzig.

A Study on the Solar Noise at 3300 m.c.

By Minoru ODA and Tatuo TAKAKURA.
Osaka City University.

(Received February 21, 1951)

Solar radio noise at 3300 m.c. was observed from April to Oct. 1950 for every two hours per day. Attention was paid to the average intensity and its fluctuation during two hours. Though the period of observation was too short to arrive at any decisive conclusions, some crude results will be mentioned and discussed here.

1) The intensity of solar noise at 3300 m.c. is approximately proportional to the whole disk sunspot number, reported from the Tokyo Astronomical Observatory, and shows no clear relation to the central zone sunspot number or whole disk sunspot group number.
2) Apparent period of fluctuation is about twenty minutes on the average and it is independent of the intensity.
3) The mean fluctuation of the intensity is approximately proportional to square root of the intensity.

If we assume the model that statistically independent sources grow and die at the period of ten minutes on the surface of the sun, the intensity and its fluctuation should be expressed by nP and $\sqrt{n}P$ respectively and the period of fluctuation should be about twenty minutes, where n is the number of sources and P is the average intensity of a source. Thus 2) and 3) are reasonably understood. Comparing with experimental results, we obtain $P\sim10^{-26}$ watts/cm/cycle/sec. seen at the surface of the earth and n is 1~2 times of the whole disk sunspot number.

Thus it is most probable that the solar noise comes from the sunspots, but it should be noted that the period of a source is rather short. Then it may be supposed that the magnetic field in the sunspot might have important rôle in the generation of radio wave.

The authors wish to express their hearty thanks to Prof. Y. Watase for his encouragement in the course of the observation.

Further observations are under preparation.

Dielectric Breakdown in Mixed Crystals of KCl and AgCl.

By Tokuo SUITA.
Faculty of Engineering, Osaka University.

(Received February 22, 1951)

Dielectric breakdown strengths of KCl and its mixed crystals KCl-AgCl (0.094 Mol %) were measured with D.C., A.C. (60～) and impulse (1.95×38.7) μs voltages over the temperature range from 15°C to 500°C.

The crystals were grown from the melt by the Kyropoulos method and cut along the cleavage surface [100]. The electrodes of the specimen prepared with cavity surface were made by painting colloidal carbon on the both sides.

Transformer oil was used as the ambiant medium at lower temperatures than about 210°C, and at higher temperatures the experiment was carried out in the atmosphere.

We took the time effect of the applied voltage into account, which is of great importance especially in the cases of D.C. and A.C..

The results obtained for D.C. are shown in Fig. 1, where (a), (b) and (c) curves represent qualitatively the time effect at that temperature region, E is the breakdown strength and t is the time of the applied voltage.

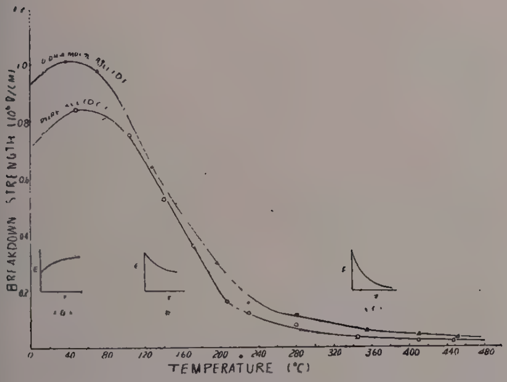

Fig. 1. Temperature dependence of the D.C. breakdwon strength of mixed KCl-AgCl crystals. Velocity of the applied voltage about 3 KV/S.

It will be seen that the breakdown strength of the mixed crystal at a given temperature is in general larger than that of pure KCl at the same temperature, and the difference between them appears to vanish at about 150°C.⁽¹⁾

It is emphasized that the former is larger than the latter even at higher temperatures, which is inconsistent with the results obtained by von Hippel and Lee in NaCl-AgCl mixed crystals.⁽²⁾

For A.C. we obtained the results which are shown in Fig. 2. The maximum value of the breakdown strength in A.C. is shifted to a higher temperature (150°C) than in D.C. (70°C) and the influence of AgCl molecules is also vanished at about 160°C.

For the impulse voltage, the effect of the foreign molecules is almost independent of the temperature except a smooth peak value at 80°C, and a vanishing point such as for A.C. and D.C. does not exist.

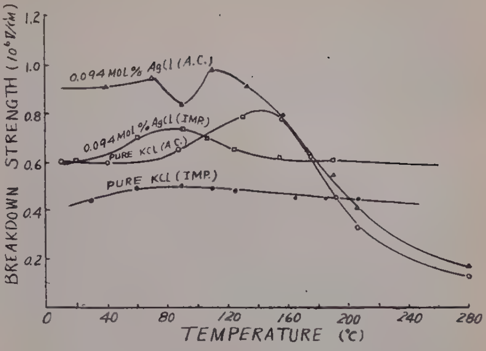

Fig. 2. The A.C. and impulse breakdown strengths of the mixed crystals.

It can be seen that at a given lower temperature than about 180°C the breakdown strengths increase in the order of impulse, A.C. and D.C., but at a higher temperature than this the order is reversed.

Our results seem to show that the occurence of the maximum value of the breakdown strengths is due to the space charges consisting of positive ions and electrons, and at higher temperatures than the vanishing point of the effect of AgCl molecules the electronic emission from the metallic dendrite which has been deposited on the cathode becomes a predominant factor in the breakdown phenomena⁽³⁾⁽¹⁾⁽⁴⁾.

Such mechanism of the breakdown as above described was proposed recently by us and by von Hippel and Alger⁽⁵⁾ independently, but in detail they were not consistent with.

Under impulse voltage the space charge effect decreases with the decrease of the time constant and the breakdown strength seems to be approximately determined by the mean free path of electron in the crystal which was calculated by Fröhlich⁽⁶⁾ who obtained the following relation

$$F_M^2(T) - F_P^2(T) = \text{constant}$$

where F_M and F_P are the breakdown strengths of mixed and pure crystals at a temperature T respectively.

References.

(1) T. Suita: J.I.E.E. (Japan) **69** (1949) 352. Electrotech. P. **1** (1949) 173.

(2) A. von Hippel & G.M. Lee: Phys. Rev., **59** (1941) 824.

(3) T. Suita: J.I.E.E. (Japan), **69** (1949) 190. Electrotech. P. **1** (1949) 15.

(4) T. Suita: J.I.E.E. (Japan), **71** (1951) 9.
(5) A. von Hippel & R.S. Alger: Phys. Rev. **76** (1949) 127.
(6) H. Fröhlich: Proc. Roy. Soy. A, **178** (1941) 493.

An Electron Microscope and Diffraction Study of Metallic Smoke.

By Riitsu Takagi.

Government Mechanical Laboratory, Sumiyoshicho, Suginamiku, Tokyo.

(Received February 27, 1951)

The white smoke produced when a molybdenum wire is heated in the atmosphere with electric current is found to be composed of plate-shaped particles of molybdenum trioxide $0.1\sim 1\,\mu$ in diameter (Fig. 1). Molybdenum trioxide is known to belong to the orthorhombic system and make a layer lattice with layers parallel to (010)[1]. In its electron diffraction transmission pattern (0k0) lines do not appear, indicating that the form of crystallites are thin plate parallel to (010). When a liquid drop is put on the surface of a collodion film, upon which the smoke has been caught beforehand, and let evaporate, then all of the thin, flat particles become to lie parallel to the surface of supporting film (Fig. 2). For electron beam normal to this film, all the diffraction rings except (h0k) disappear and, when the sample is rotated about an axis normal to the beam, a fiber pattern can be observed.

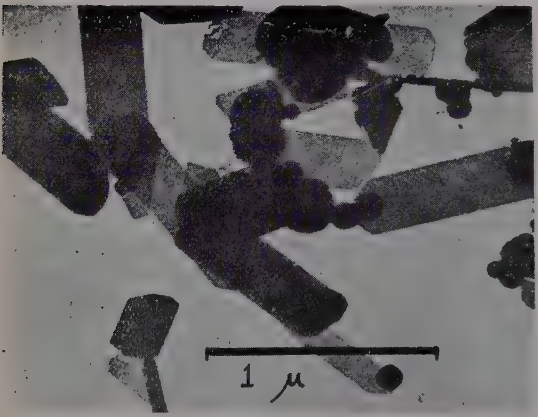

Fig. 1.

The green smoke obtained by direct current discharge between metallic chromium electrodes is also composed of plate-shaped particles of chromic oxide and the similar effect as found for molybdenum trioxide was observed.

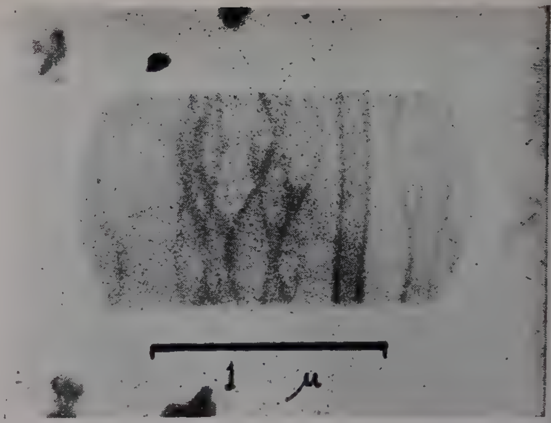

Fig. 2.

In the image of the particle in Fig. 2, many characteristic fringes can be seen. The appearance of them changes with the direction of the incident electron beam with respect to the crystallite. These fringes seem to be ones similar to those observed by R.D. Heidenreich in thin sections of aluminum[2], but here, as the thickness of the particle is supposed to be uniform, the strain, which is produced probably by the liquid, may be the only cause of the fringes. In fact, no fringe exists in the images of the particles in Fig. 1.

A detailed paper will be given later.

The author is grateful for valuable discussions of Prof. S. Miyake, Tokyo Institute of Technology.

References.

(1) e.g. R. Fricke and G.F. Hüttig: Hb. d. Allg. Chem. **IX**, (1937) 278.
(2) R.D. Heidenreich: J. App. Phys. **20** (1949) 993.

A High Pressure Cloud Chamber Observation of Cosmic Ray at 2740 m Elevation.

By Y. Watase, S. Miyake, K. Suga and O. Kusumoto.

Department of Physics, Osaka City University

(Read November 4, 1950; Received Feb. 28, 1951).

In recent several years, the cosmic ray has been studied with the high pressure cloud chamber of about 100 atm. by William(1), Shutt et al(2) and Valley et al(3). And valuable results have been obtained such as the meson decay and the nuclear interaction. A high pressure cloud chamber suitable for fiilling hydrogen, nitrogen, argon etc. at 100 atom. was constructed in our laboratory(4). In this summer, the experiment on the meson production in hydrogen is planned, and as a preliminary study various phenomena by the cosmic ray particles were observed in 75 atom. argon at Mt. Norikura (2740 m altitude) in last September.

The cloud chamber has the wall of gun metal 4 cm in thickness and its dia. and illuminated depth are 24 cm and 5 cm respectively. The stereoscopic photographs were taken with two cameras, each inclined by 5° to the axis of symmetry. By the random operation method, about 1250 pictures were taken without any shield material around the chamber. The sensitive time was about 1.5 sec and several cosmic ray tracks were shown in one expansion. Therefore, our experiment corresponds to the observation of cosmic ray phenomena generated in the free atmosphere of about 25 m in deepness during about 30 min.

Observed tracks are as follows.

(1) Single tracks

About 3000 tracks penetrating the cloud chamber without suffering so much multiple scattering were photographed. Their zenith angle dependence was $\cos^2\theta$.

(2) Shower

Many electron pairs generated in agron gas by cosmic ray-γ ray were observed. 153 showers having more than 3 tracks created in the upper chamber wall and 55 showers having more than 3 tracks created above the chamber and penetrating the gas in almost parallel were observed. They contain so-called extensive air showers and narrow showers. The inclination of these showers to the zenith distributed as $\cos^3\theta \sim \cos^4\theta$. 13 showers created in the lower wall and spread to the above were obtained.

(3) Heavily ionizing tracks

55 tracks, their main parts may be low energy protons.

(4) Decay of mesons

Two phenomena to be convinced μ meson-electron decay were observed. Energy of the electrons are about 10 MeV. and 5 MeV. respectively. (Fig. 1.)

(5) Stars

Stars having 2 or 3 prongs of 1-2 cm range were rather frequent. The low energy stars of 6 and 7 prongs and a high energy nuclear event of 5 branches were observed. (Fig. 2 and 3).

(6) Other event

A photograph as shown in Fig. 4 was observed. This seemed to be pair creation by an electron, or 3 particle decay of the cosmic ray particle, but the decisive conclusion is to be reserved.

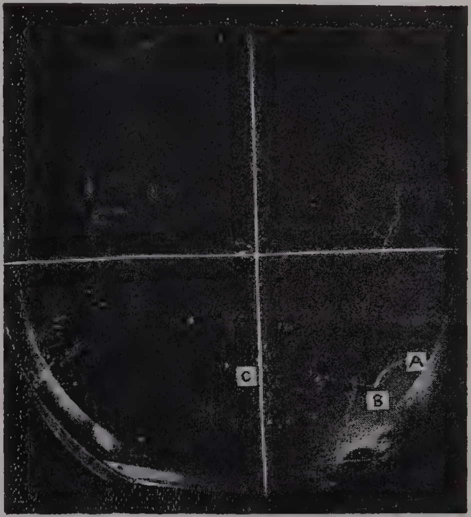

Fig. 1. μ meson-electron decay. At the point A, a meson entered into the chamber from the back. After flying to the center of depth increasing the ionization density, it stopped at the point B. The decay electron escaped the chamber toward the back, suffering the multiple scattering. Its energy is about 10 MeV.

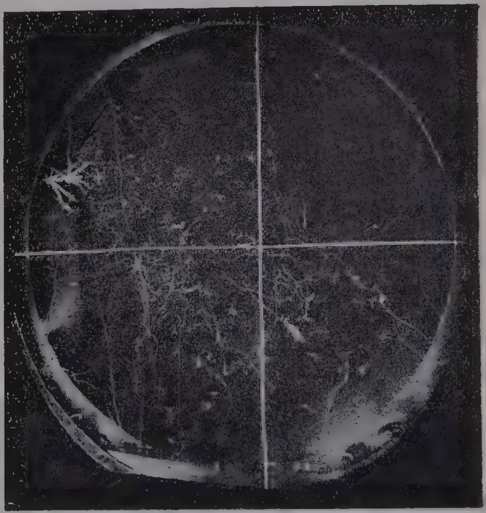

Fig. 2. 7-prongs low energy star. It was separated by sweeping field.

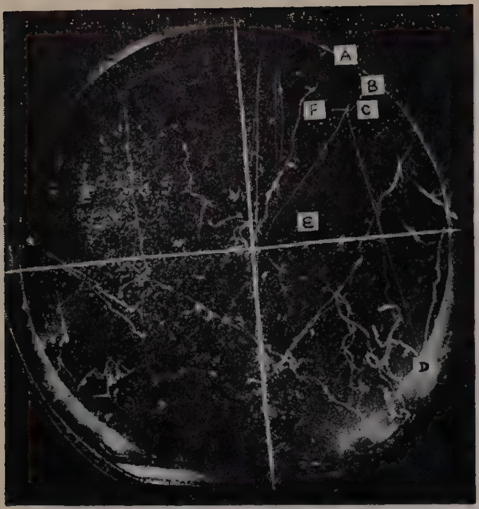

Fig. 3. High energy nuclear event. A: incident, from the chamber glass. B,C,D,E,F, are secondaries; B,D: towards the front glass; E: towards the back piston; C,F: stopped in the gas. The sharpness of the tracks is due to that it entered after expansion.

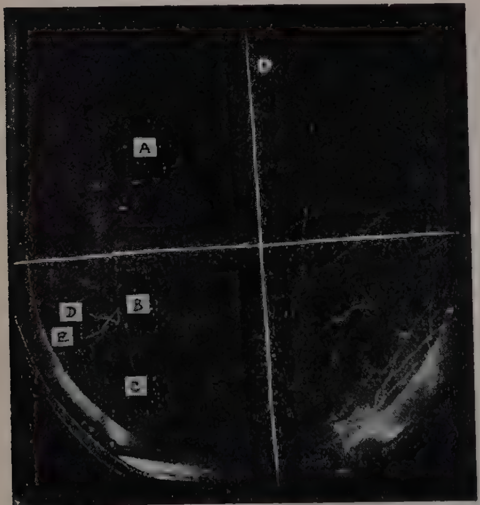

Fig. 4. A: incident particle. B: the point of act, 1.5 cm deep from the front glass. C,D,E: escaped to the front glass.

References.

(1) E. J. Williams and G. R. Evans: Nature **145** (1940), 818.

(2) R. P. Shutt, S. DeBendetti and T. H. Johnson: Phys. Rev. **62** (1942), 552.

(3) G. E. Valley, C. P. Leavitt and J. A. Vitale: Phys. Rev. **75** (1949) 201.

(4) Y. Watase, S. Miyake, K. Suga and O. Kusumoto: to be published.

Discussion of the Spectrum of Turbulence.

By Ken-ichi Kusukawa.

Physical Institute, Faculty of Science, Tōkyō Metropolitan University.

(Received March 5, 1951)

We shall have some discussion about my papers (1) and (2), where the spectrum of turbulence was deduced theoretically by the quantum-theoretical method.

§ 1. The Form of the Spectrum Function.

It is well known that the spectrum of turbulence must be proportional to $\exp(-a^2 k^2_x)$, (where k_x is the x-component of the wave number vector, and a is a characteristic constant,) according to the usual non-quantised theory, when the inertia term may be neglected. (cf. (3))

The spectrum of turbulence, however, takes the following form in the same condition by my theory. (cf. (1) and (2))

$$f(k_x) = 0.208\,\delta^3 k_x{}^{1/2}[\exp(\delta k_x{}^{1/2}) - 1]^{-1},$$

where k_x is the x-component of the wave number vector, and δ is a characteristic constant.

The reason of this discrepancy consists in the fact that the smallest volume element of fluid is considered to be finite, and the effect of its spin to be comparable to other effects. Indeed, such a situation may occur in the flow of the diffusion pump, where the pressure is very low and the density is very small.

§ 2. The Reversibility and the Irreversibility of the Process.

While the fundamental equation of motion of the viscous fluid has the irreversible character, for it is the first order differential equation with respect to time, the modified equation of motion

$$\rho\,\partial^2\mathbf{Q}/\partial t^2 = \rho\nu\triangle\mathbf{Q}$$

which is employed to quantise the system, has the reversible character for it is the second order differential equation with respect to time. It is reasonable that the phenomenon which may be quantised, is considered to be the reversible elementary process, and the irreversibility arises only in the discussion of its statistical character. In our case, the irreversibility of the equation of motion of the viscous fluid is represented in the following energy decay relation. (cf. 2))

The rate of dissipation of energy $\propto 2h^* N^{1/2}\mathrm{D}$ where

$$D=\exp(-E_b/\kappa T)m(m-1) \\ -\exp(-E_a/\kappa T)(m+1)(m+2)$$

§ 3. The Remaining Problems.

This quantisation of the flow may be applied to the phenomena which neither hydrodynamics nor the kinetic theory of molecular motion can discuss, such as the diffusion from a hole whose diameter is comparable to the length of the mean free path of the molecular motion.

The following facts remain to be studied theoretically.

(1) To introduce the general spin.

(2) The quantisation of the flow in the case of great Reynolds number.

References.

(1) K. Kusukawa: J. Phys. Soc. Japan **5** (1950) 412.

(2) K. Kusukawa: J. Phys. Soc. Japan **6** (1951) 86.

(3) G.K. Batchelor: Quart. Appl. Math. **6** (1948) 97.

The Noise of Decaying Electrets.

By Shoji Kojima and Kiyoe Kato.

Tokyo University of Education.

(Received March 9, 1951)

Recently Gutmann⁽¹⁾ mentioned in the review on the electret that the electric Barkhausen noise in the decay of the electret was observed by him. However, the full paper has not yet published. We have studied the relation between the noise and the charge of the electret precisely.

The electrets used were made of 50% rosin and 50% carnauba wax and formed by a field of 10,000 V/cm. Its shape was a circular disk with diameter of 5.5 cm and thickness of 0.5 cm. Every time two identical samples were produced simultaneously at the same condition. One of which was used to study on the noise and the other on the decay of the charge.

The charge of the electret was measured, without touching its surface, by a generating voltmeter shown in Fig. 1. An earthed vane V rotated with a constant speed between the surface of the electret E and the electrode A, from which an induced current was drawn out. The current was read with a galvanometer G after the rectification with a vacuum tube T. Since the rectified current did not indicate whether the induced charge of the electrode was positive or negative, we introduced the other electrode B which faced to the plate of a known potential. When the switch S was closed the algebraic sum of the charges could be measured, from which the sign of the charge was decided. The noise was observed with a low frequency amplifier and an oscilloscope. The pulses of the noise was counted with a thyratron counting device. The experiments have been carried out raising gradually the temperature of the electret to increase the rate of the decay, for the natural decay at the room temperature needs several years.

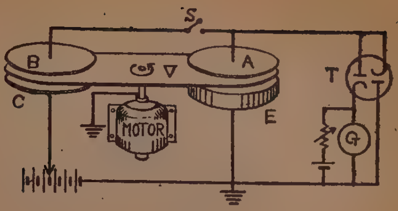

Fig. 1.

One of the results is shown in Fig. 2. The charge of the electret and the number of the pulses are plotted to the temperature which was raised at the rate of 1°C per minute. The result was not affected by reducing rate to 0.5°C per minute. The curves indicate that the noise starts at the time when the homocharge has built up.

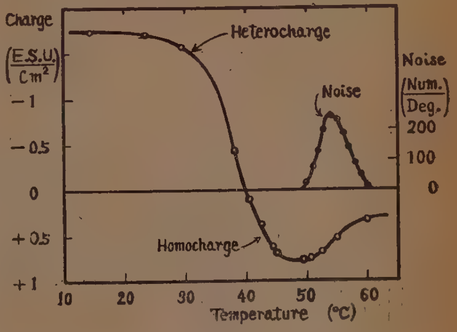

Fig. 2.

Gutmann observed the noise not only in the homocharge but also in the heterocharge. Our experiments show that the homocharge associates the Barkhausen noise, but the heterocharge does not.

We wish to express our sincere thanks to Dr. Y. Kakiuchi for suggesting this problem. Our thanks also due to the Ministry of Education for the research grant.

References.

(1) F. Gutmann, Rev. Mod. Phys. **20** (1948) 475.

Dielectric Properties of Lead Zirconate.

By Gen SHIRANE, Etsuro SAWAGUCHI and Yutaka TAKAGI.

Tokyo Institute of Technology, Oh-okayama, Tokyo.

(Received March 12, 1951)

Recent investigations on $PbZrO_3$⁽¹⁾ and solid solutions of the $Pb(Zr\text{-}Ti)O_3$ system⁽²⁾ suggest us that $PbZrO_3$ may be not a ferroelectric but an antiferroelectric notwithstanding a close resemblance between the permittivity curves of this substance and a well known ferroelectric, $BaTiO_3$. Now, further study has been made of the dielectric properties of *pure* lead zirconate.

The specimens were prepared from ZrO_2 of high purity and reagent-grade PbO. These ingredients were mixed in the equi-molar proportion and sintered at about 1200°C after a preliminary calcination. The sintered disks, 1mm in thickness, were coated on both sides with evaporated gold electrodes. Permittivity for these specimens was measured as a function of temperature by a heterodyne method at 1MC/sec and 10V/cm (Fig. 1). Above the Curie point at 233°C, the Curie-Weiss law $\varepsilon = C/(T-T_p)$ was found to be valid with $C = 1.2\times10^5\,^\circ\mathrm{C}$ and $T_p = 185^\circ\mathrm{C}$. These results are in good agreement with those obtained by Roberts.⁽³⁾

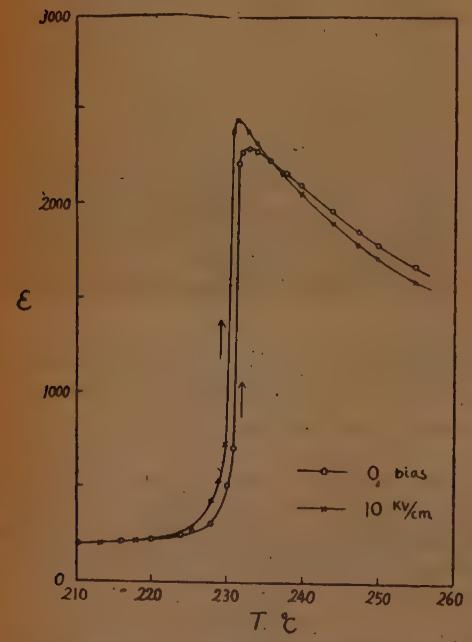

Fig. 1. Effect of D.C. biasing field of 10KV/cm on the permittivity of $PbZrO_3$ at rising temperature.

Effect of a D.C. biasing field of 10KV/cm on the Curie point of this substance was also studied with a result shown in Fig. 1. Dielectric measurements were carried out in a bath of liquid paraffin which was stirred vigorously and the temperature was measured with a copper-constantan thermo-couple directly attached to one of the electrodes. The Curie point was shifted towards lower temperature by 1.5°C under this biasing field and, at the same time, the peak value of permittivity slightly increased. These results are just in contrary to the case of barium titanate⁽⁴⁾ in which the rise of the Curie point by a biasing field was observed accompanying a considerable decrease of permittivity.

A circuit essentially similar to that of Sawyer and Tower⁽⁵⁾ was used to display the polarization-electric field curve at 50 cycle/sec on a cathode ray tube. In these pure specimens, typical hysteresis loops were not observed at any temperature and the curves were always almost linear except the one with a slight upward curvature (inverse *S* type) observed at just below the Curie point. Maximum polarization at 10KV/cm and 20KV/cm was estimated as a function of temperature (Fig. 2), and a sudden increase of polarization was observed at the Curie point in marked contrast with the case of barium titanate.⁽⁶⁾

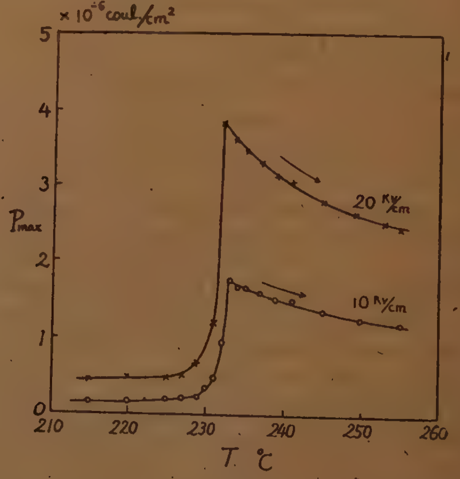

Fig. 2. Maximum polarization at 10KV/cm and 20KV/cm as a function of rising temperature.

Such a sudden increase of polarization at the Curie point is consistent with the lowering of the Curie point by D.C. biasing field from the thermodynamical point of view, as indicated by the Clapeyron-Clausius equation $dT_c/dE = -T_c\cdot\Delta P/L$, where L denotes the latent heat, ΔP the jump of polarization. Hence it seems reasonable to conclude that pure lead zirconate has no spontaneous polarization at below the Curie point and belongs to an antiferroelectric.

Detailed study is now in progress.

References.

(1) E. Sawaguchi, G. Shirane and Y. Takagi, J. Phys. Soc. Japan, to be published.

(2) G. Shirane and A. Takeda, J. Phys. Soc. Japan, to be published.

(3) S. Roberts, J. Ame. Cera. Soc. **33** (1950) 63.

(4) S. Roberts, Phys. Rev. **71** (1947) 890.

(5) C.B. Sawyer and C.H. Tower, Phys. Rev. **35** (1930) 269.

(6) J.K. Hulm, Nature, **160** (1947) 127.

X-ray Study on Phase Transition of Lead Zirconate, $PbZrO_3$.

By Ryuzo Ueda.

Department of Applied Physics,
Waseda University, Tokyo.

and Gen Shirane.

Tokyo Institute of Technology, Oh-okayama,
Meguro-ku, Tokyo.

(Read Nov. 1, 1950; Received March 19, 1951).

Recently some studies on the phase transition of lead zirconate, $PbZrO_3$, were reported.(1), (2) It was found that there exists a conspicuous peak of dielectric constants at about 220°C, accompanying a fairy large anomaly in dilatation and specific heat at the same temperature. The detailed study on the crystal structure of this substance is required for explaining the phase transition which is different in nature from that of $BaTiO_3$. Although X-ray powder analysis of this compound has been already reported by the several authors,(3) there are yet no detailed studies on the crystal structure and its temperature change.

A schematic representation of the powder photographs of $PbZrO_3$ at room temperature and 250°C is shown in Fig. 1. In Fig. 1-A, it is indicated that there are many faint additional lines due to the superlattice besides the strong lines of the basic tetragonal lattice, the lattice constants of the latter being:

$$a = 4.150 \text{ A}, \quad c = 4.099 \text{ A}, \quad c/a = 0.988.$$

Above the Curie point, the strong main lines which are marked by small circles in Fig. 1-A are retained, coalescing into the cubic lines of the perowskite type, whereas faint superlattice lines disappear (Fig. 1-B). The dimension of the superlattice is four times as large as that of the basic cell. The same conclusion has been recently obtained by Sawaguchi and others for monocrystals of this compound.

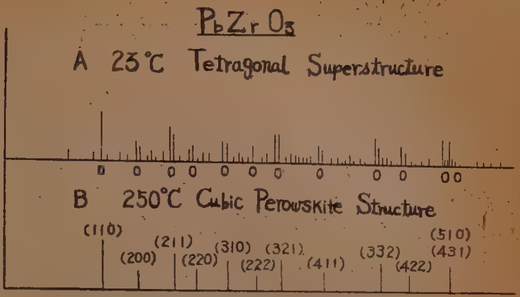

Fig. 1. Debye photogramms of $PbZrO_3(CuK_\alpha)$

The temperature dependence of lattice constants and lattice volume are plotted in Figs. 2 and 3. The lattice parameter a is nearly constant in the tetragonal region, but somewhat contracts near the transition temperature. The lattice constant c increases gradually with temperature until it coincides with a, but its change at the Curie point is rather steep. The Debye lines become diffuse between 180°C and 220°C, indicating the existence of strain due to crystal hybrids in this temperature range. The deviation of the axial ratio from unity is about 1% of the lattice dimension, which is in the same order of that for $BaTiO_3$ (Fig. 4).

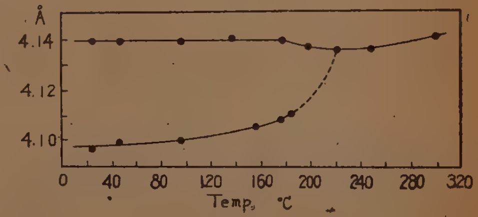

Fig. 2. Lattice constants *vs.* temperature curve of $PbZrO_3$.

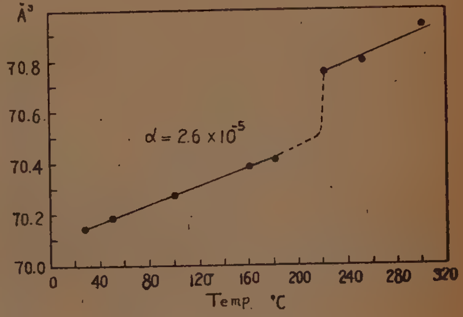

Fig. 3. Lattice volumes v.s. temperature curve of $PbZrO_3$

The thermal expansion α calculated from the lattice volume *vs.* temperature curve is 2.6×10^{-5}

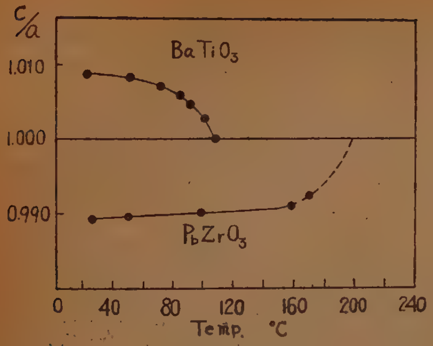

Fig. 4. Temperature dependence of axial ratios of BaTiO$_3$ and PbZrO$_3$.

in both phases below and above the Curie point. This value of α agrees satisfactorily with the result of the dilatometer measurements formerly reported by one of the present authors (G.S.).⁽²⁾

It is to be stressed that the superstructure of PbZrO$_3$ has a close relation to the dielectric response of this crystal.⁽⁴⁾ The more detailed studies on the crystal structure will be required for fuller account of its ferroelectricity.

The present authors wish to express their sincere thanks to Professors Miyake and Takagi, for their interests in this work, and also to Messrs. Waku and Hori for giving them some precious samples at authors' requests.

References.

(1) S. Roberts, J. Amer. Ceram. Soc., **33**, (1950). 63

(2) G. Shirane, E. Sawaguchi and A. Takeda, Phys. Rev. **80**, (1950) 485.

(3) A. Hoffman, Zeit. Phys. Chem. B, (1935) 28. H. D. Megaw, Proc. Phys. Soc. **58**, (1946) 133.

(4) G. Shirane, E. Sawaguchi and Y. Takagi, J. Phys. Soc. Japan, **6**, (1951) 208.

The Construction of a Small Linear Accelerator.

By Haruhiko MORINAGA.

Department of Physics, University of Tokyo.

(Received April 7, 1951)

A small linear accelerator for protons has been constructed in order to study the possibility of using such devices in bombarding experiments. A special type of cavity resonator suitable for the acceleration of relatively low energy particles, was developed for this purpose. In the preliminary tests for the cavity of the type shown in Fig. 1., it was found that the total sum of the voltages between five gaps was about 30,000 volts when the imput high frequency power is 60 watts. Actual cavity shown in Fig. 2. has nine gaps and a glass cylinder which may lower the shunt impedance of the cavity. It was found, however, that by giving sufficient clearances between the glass and the metal parts in vacuum, the loss in the glass could be minimized. High capacitance between electrodes also decreases the shunt impedance of the cavity, but it in turn increases the resonant wave-length. This fact is favorable for power generation and for injector requirements, because for such a small injector as we have, the use of too small wave-length would reduce the gap lengths and the size of the apertures of the electrodes too much. Resonant wave-length was found to be 4 meters for the cavity whose diameter and length are 1 meter and half a meter respectively. The first gap for 40 kilovolts injection energy was chosen to be 9 millimeters and the length of a gap and the length of the neighboring electrode are almost equal, both of which are made longer in accordance with the increase of the energy of the protons. Power is fed into the cavity by coupling the filament loop of a grounded anode oscillator with two TR594A transmitter tubes in push-pull connection, which is capable of giving h.f. power up to 4 kw. The order of the magnitude of the voltages between gaps was measured by a ring attached just in front of one of the electrodes by a spring, displacement of which was observed by a telescope through the window of the cavity. The chamber is evacuated up to 1×10^{-5} mmHg in the absence of the h.f. field, by a 6″ oil diffusion pump, the speed of which for air is 350 litre/sec., and its evacuation system was carefully designed not to reduce the speed too seriously. Ions to be accelerated are produced in a simple Philipps' gauge type ion source and pre-accelerated to about 70 kilovolts. About 20 micro-ampere unresolved beam was obtained from this source at the target 50 cm behind the cavity. For the detection of the accelerated protons, a little higher potential than that of injector was applied on a retarding electrode and those ions which jumped over it were deflected by a magnetic field and made to strike a phos-

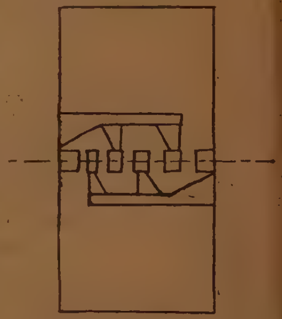

Fig. 1. Cavity for linear accelerator.

phorescent screen of an oscilloscope tube. With 45 kv injection energies and 3 kw plate imput of the oscillator, accelerated protons came to the screen, whose energies were estimated to be 150 kv. Energies of the protons will be increased by the rearrangement of electrodes and by feeding much more power into the cavity, especially by impulse operation.

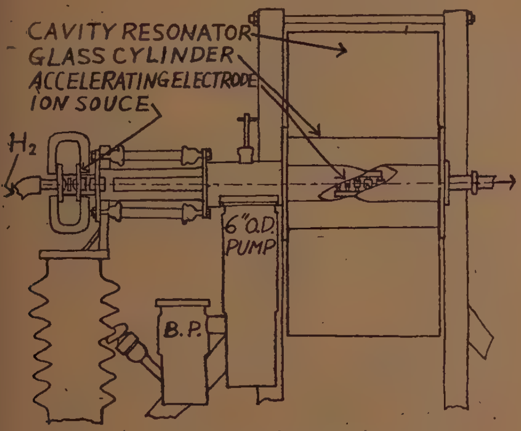

Fig. 2. Small linear accelerator.

The author wishes to thank Professor R. Sagane for supervising this work and for his constant encouragement. He also is very grateful to many persons who gave him many suggestions and conveniences. And he appreciates very highly the helpful assistance of Mr. E. Hasumi. This work was partly supported by the Scientific Research Expenditure of the Ministry of Education.

Current Amplification by Silicon *p-n* Junction.

By Yasuo Kanai.

The Electrical Communication Laboratory, Ministry of Telecommunications, Tokyo, Japan.

(Read Nov. 4, 1950, received Feb. 27, 1951)

It was suggested⑴ by W. Shockley that the transistor action,⑵ which is related to electrons and holes in semiconductor, could occur at *p-n* junction of semiconductor; namely, the *p-n* junction was available as emitter or collector in transistor sense. But the experiments of this sorts were not published yet. The author made the silicon *p-n* junction, and found the current amplification of this element was different in germanium transistor case.

Small amounts of phosphorus were doped in pure silicon and were molded to ingot. The upper part of this ingot was *p*-type and lower, *n*-type. This ingot was cut vertically and a sample of silicon, in which one part was *n*-type, the other, *p*-type, was made. The two ends of this sample were electroplated by Ni and soldered to leadwire. (See Fig. 1). Firstly the author found the anomalous phenomena, when a cat whisker was placed in vicinity of *p-n* junction and the circuit was connected as shown in Fig. 1. V was kept at constant voltage througout this experiment and the switch C was opened or closed, whereby the current I changed I_o or I_c respectively. Then the anomalous result

$$I_o > I_c \qquad (1)$$

was obtained. Secondly the author found the current amplification of this element when cat whisker was acted as collector and *p-n* junction as emitter, as shown in Fig. 2. The observed data were plotted in Fig. 3. In the range from

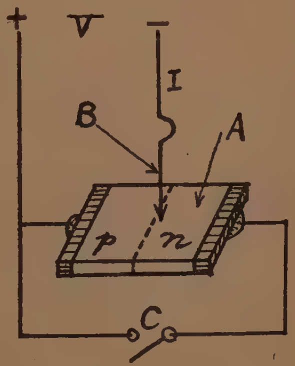

Fig. 1. A: Silicon sample.
B: Cat whisker
(0.2 mm ϕ W-wire)
C: Switch.

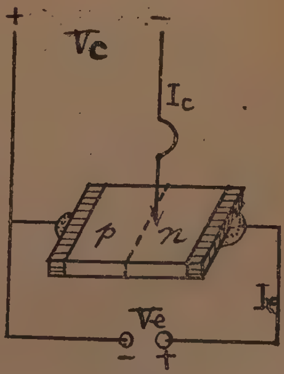

Fig. 2.

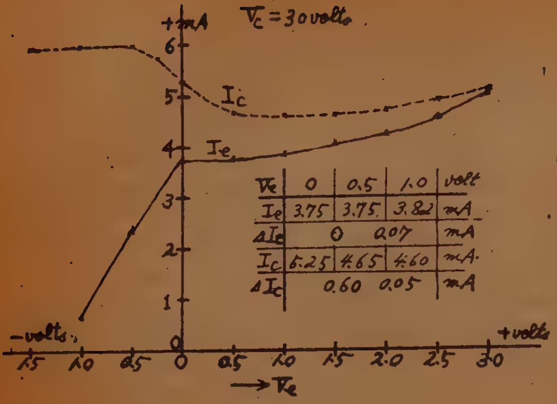

Fig. 3.

0 to 1 volt in emitter voltage, the change of collector current (ΔI_c) was larger than that of emitter current (ΔI_e). From Fig. 3 it was found that the current amplification factor $\alpha = \Delta I_c/\Delta I_e$ (at constant V_c) was very large in comparison with the value of α (about 2) in germanium transistor.(2) The different points of this characteristics of our case from germanium transistor were:

(a) emitter was reverse direction, hence the emitter resistance was the same order or larger than that of collector.

(b) current amplification was larger than germanium transistor.

(c) as emitter current was increased, collector current was decreased. This characteristic would be connected to the anomalous effect (1).

Above effect is found when cat whisker was placed on n-type portion near the p-n junction boundary and the same effect was also found when cat whisker was placed on p-type portion of p-n junction boundary and the connection and polarity of the circuit were changed correspondingly.

References.

(1) W. Shockley. Bell Sys. Tech. Jour. **28** (1949) 435.

(2) J. Bardeen and W.H. Brattain. Phys. Rev. **75** (1949) 1208.

The Temperature Dependency of Magnetization of Ferrites on the Basis of the Theory of Ferromagnetism.

By Hiroshi WATANABE.

Research Institute for Iron, Steel and Other Metals, Tohoku University.

(Received March 7, 1951)

Néel's theory of ferromagnetism[1] has succeeded in explaining the saturation magnetization and susceptibilities above the Curie point of magnetic ferrites and their solid solutions with zinc ferrite. Recent experiments on ferrites, in favor of this theory, are so numerous that we are led to the confirmation of the essential correctness of the underlying concept of this model.

The author calculated, basing on this model,

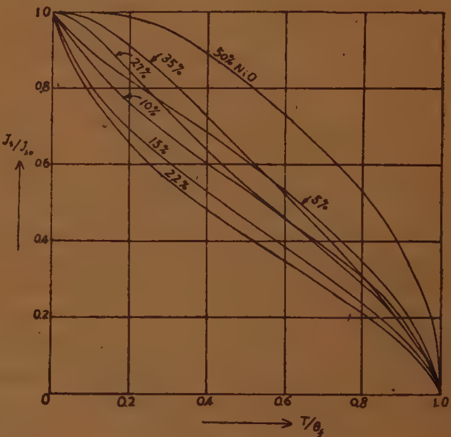

Fig. 1(a). Calculated temperature dependency of the saturation magnetization of Ni-Zn ferrites.

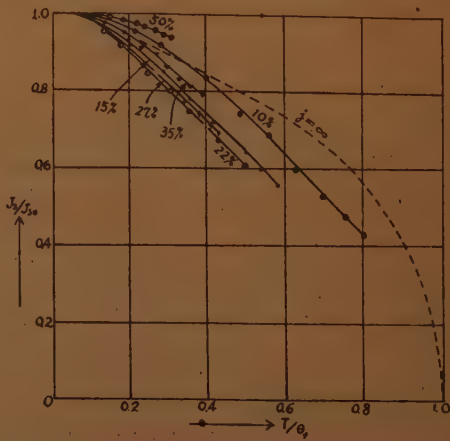

Fig. 1(b). Temperature dependency of saturation magnetization of Ni-Zn ferrites (Guillaud).

the temperature dependency of their saturation magnetization and Curie points for Ni-Zn ferrites. The results are shown and are compared with experiment²⁾ in Figs. 1∼2. The calculation corresponds to the approximation which neglects the fluctuation of the molecular field. As can be seen from the Figs., the theory gives stronger temperature dependency and higher Curie points than experiment, especially, for those ferrites whose compositions are near that corresponding to the transition point from Q-type of magnetization to R-type.³⁾ This disaccordance may be attributed to the approximation taken here; a better approximation is possible for the calculation of the saturation magnetization at absolute zero which takes into account that for ferrites containing considerable amounts of Zn-ferrite, the configuration of the neighbors of any given ion at 16c position has six possibilities of Fe^6, $Zn\ Fe^5$,⋯⋯. Each configuration might be regarded as being specified by different local Zn content. The result with this approximation is shown in Fig. 3, assuming $g=2$ and $\beta=-0.228$ all over the compositions. (β is the ratio of the 16c—16c interactions to 16c—8f interactions). The agreement with experiment is quite satisfactory.* The above value of β is somewhat higher than is predicted from the measurements of susceptibilites above the Curie points, which may be considered as an indication of the variation of interactions with temperatures. It is obvious that the results of Figs. 1 and 2 might be improved with this approximation, since the actual configurations of neighbors of an ion at 16c position are always different from the mean configuration, for which the temperature dependency of magnetization is the strongest, and the difference between ferromagnetic Curie point and paramagnetic Curie point which is considered to be caused by the fluctuation of the molecular field is the largest for the composition of R-Q boundary.

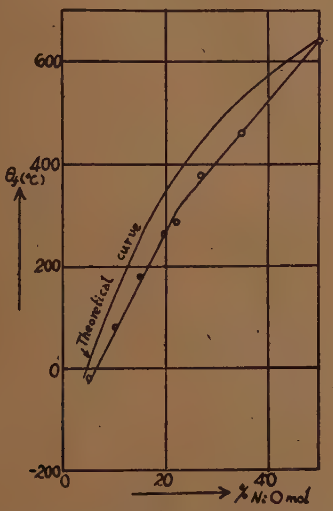

Fig. 2. Measured (Guillaud) and calculated Curie points of Ni-Zn ferrites.

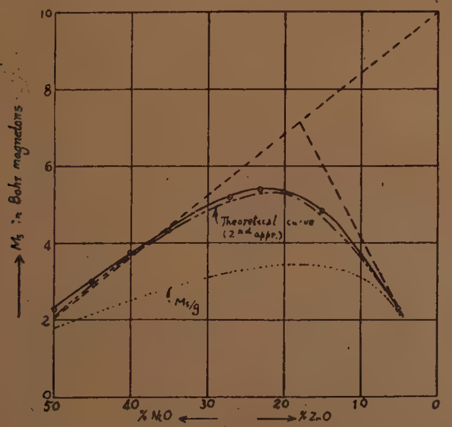

Fig. 3. Saturation magnetization per molecule given by Guillaud. ...M_s/g, g being taken from Okamura and Torizuka.

Recent measurements on g values for these ferrites at low temperatures⁴⁾ show that they are considerably higher than 2 near the composition of Q-R boundary. At present it is not clear whether this fact is caused by the inner magnetic field or by the ionic states of the divalent metal ions.

The author expresses his sincere thanks to Dr. K. Honda and to Prof. T. Hirone for their supervision, and to Prof. T. Okamura for kindly supplying the author his data prior to publication. A part of the fund for this investigation has been defrayed from the Scientific Research Funds of the Ministry of Education.

References.

(1) L. Néel: Ann. d. Phys. **(12) 3** (1948), 137; L. Néel; Ann. l'Inst. Fourier. **1** (1950) 163.
(2) C. Guillaud: C.R. **229** (1949), 1133.
(3) See reference 1.
(4) T. Okamura and Y. Torizuka: Read at the Meeting of the Physical Society of Japan, Sendai Section, on Dec. 16, 1950.

---

* Néel has given a similar argument but with somewhat different results from that given here; this may be due to a slight difference in minute assumptions made in the computation.

JOURNAL OF THE PHYSICAL SOCIETY OF JAPAN Vol. 6 No. 4 JULY—AUG., 1951

Excitation of Atoms by Electron Collision II.

By Hisashi HORIE.

Department of Physics, University of Tokyo.

(Received October 20, 1950)

§1. Introduction.

In a previous paper⑴, the problem of excitation of an atom by electron collision between the states of the *same* electron-configuration was investigated, and the formulae for the probabilities of excitation of this kind for the atoms in l_1^n- and $l_1^n\, l_2$-configurations were obtained. These processes which take place only in extremely rarified gases, are mainly of astrophysical interest. In laboratory experiments, on the other hand, the atoms usually change their electron configuration by excitation, which we shall deal with in this paper. Similar procedure as in the previous paper leads to the required formulae also in the present case. The ionization of atoms by electron collision, which may be regarded as the excitation of an atomic electron to continuous level, can be treated in the similar manner.

In this paper, the method of Racah is employed as in the previous paper. In §2, the probability of excitation of atoms in l_1^n-configuration by electron collision, and in §3, that of ionization by electron collision for such atomic configuration are obtained. The problems of excitation and ionization of atoms in some other typical electron configurations are treated with intimate correspondence to those for l_1^n-configuration in §4. More concrete formulae for the cases relating to p^n- and d^n-configurations are given in the last section.

§2. Probability of Excitation of Atoms in l_1^n-Configuration by Electron Collision.

The method for obtaining the probability that an atom in (γSL)-state makes transition to ($\gamma' S' L'$)-state by the impact of electron was given by Yamanouchi and Kotani⑵. Following this method, we obtained the probabilities for the excitation of atoms within the *same* electron configuration by electron collision using the method of tensor operator proposed by Racah⑶, in the previous paper I. Similar considerations can be applicable to the case that an atom makes transition to the state in some other electron configurations by electron impact, and we shall treat the probability that an atom in l_1^n-configuration from its (αSL)-state makes transition to ($S''L''$)-states in $l_1^{n-1}(\alpha' S' L')\, l_2$-configuration by electron collision, where ($\alpha' S' L'$) indicates the parent term.

The wave function of incident electron with velocity k is decomposed into partial spherical waves with angular momenta l as(*)

$$\psi_k(r) = \sqrt{4\pi}\sum_{l=0}^{\infty}\sqrt{2l+1}\, i^l \exp(i\delta_l)\, f_{k,l}(r)\, S_{l,0}(\theta,\phi), \tag{1}$$

where the direction of incidence of the electron is taken as the axis of quantization, and $S_{l,m}(\theta,\phi)$ is the normalized spherical harmonic. $y_{k,l}(r) = kr\, f_{k,l}(r)$ is the solution of the differential equation

$$\frac{d^2 y_{k,l}}{dr^2}+\left\{k^2-2U(r)-\frac{l(l+1)}{r^2}\right\}y_{k,l}=0\,, \tag{2}$$

where $U(r)$ is the mean field of the (αSL)-state of the atom in l_1^n-configuration(**). The phase shifts δ_l are determined by the asymptotic form of $y_{k,l}(r)$;

$$y_{k,l}(r) \sim \sin\left(kr-\frac{l\pi}{2}+\delta_l\right). \tag{3}$$

(*) Atomic units are used throughout this paper.

(**) For the sake of simplicity, we use the nomenclature "atom" irrespective of neutral atom or ion. The only formal difference appearing in this paper in the case of ion from that of atom arises in the asymptotic form of wave function which can be modified by adding the term $-\frac{1}{k}\log 2kr$ to the argument of sine function.

The wave function of the scattered electron with velocity k' is given by

$$\psi_{k'l'm'}(\mathbf{r}) = f_{k',l'}(r)\,S_{l',m'}(\theta,\phi)\,, \tag{1'}$$

where $y_{k',l'}(r) = k'r\,f_{k',l'}(r)$ satisfies

$$\frac{d^2y_{k',l'}}{dr^2} + \left\{k'^2 - 2U'(r) - \frac{l'(l'+1)}{r^2}\right\} y_{k',l'} = 0\,, \tag{2'}$$

where $U'(r)$ is the mean field of the $(S'L')$-state of the atom in $l_1^{n-1}\,l_2$-configuration, and $y_{k',l'}(r)$ has the asymptotic form

$$y_{k',l'}(r) \sim \sin\left(k'r - \frac{l'\pi}{2} + \delta_{l'}\right). \tag{3'}$$

The velocity k' of the scattered electron is determined by the conservation of energy as follows:

$$k'^2 = k^2 - 2(E_{S''L''} - E_{\alpha SL})\,, \tag{4}$$

where $E_{\alpha SL}$ and $E_{S''L''}$ are the energies of states $l_1^n\alpha SL$ and $l_1^{n-1}\,l_2\,S''L''$, respectively.

The probability that an atom in $l_1^n(\alpha SL)$-state makes transition to $l_1^{n-1}(\alpha'S'L')\,l_2S''L''$-state in unit time by the impact of electron of unit density whose velocity is k, is given by

$$W = 8\pi k' \sum_{l,l'} U_l^{l'}\,, \tag{5}$$

where

$$U_l^{l'} = \sum_{S_1,L_1} \frac{(2S_1+1)\,(2L_1+1)}{(2S+1)\,(2L+1)} \left|(l_1^n(\alpha SL)lS_1L_1|H| \times l_1^{n-1}l_2\,(S''L'')\,l'S_1L_1)\right|^2. \tag{6}$$

Here, S_1 and L_1 are the resultant spin and orbital angular momenta of the system of initial atom and incident l-partial wave which must be equal to those of the system of final atom and scattered l'-partial wave, respectively, since we neglect the spin-orbit interactions. The interaction Hamiltonian H, which gives rise to the transition, is equal to $\sum_{i=1}^{n} \frac{1}{r_{i,n+1}}$, assuming the orthogonality between the wave functions of atomic and colliding electrons. Here $r_{i,n+1}$ means the distance between the i-th electron and the colliding electron.

Therefore, our problem is reduced to the evaluation of $(l_1^n(\alpha SL)\,lS_1L_1\left|\sum_i \frac{1}{r_{i,n+1}}\right| l_1^{n-1}l_2(S''L'')\,l'S_1L_1)$ and the summation of the squares of these matrix elements multiplied by the statistical weights $(2S_1+1)\,(2L_1+1)$ with respect to S_1 and L_1. The first step can be accomplished by making use of Racah's method in the similar way as in I. Corresponding to I, (6) and (8)

$$(l_1^n(\alpha SL)lS_1L_1\left|\sum_i \frac{1}{r_{i,n+1}}\right| l_1^{n-1}l_2\,(S''L'')\,l'S_1L_1)$$
$$= (-1)^{L+l'-L_1} \sum_{\kappa} W(LlL'l'\,;L_1\kappa)\{q_\kappa(l,l')Q_\kappa(kl,k'l') + \sum_\mu r_{\kappa\mu}(l,l')R_\mu(kl,k'l)\}\,, \tag{7}$$

where $W(abcd\,;ef)$ is the W-function defined in R. II, (36′) and

$$\left.\begin{aligned} Q_\kappa(kl,k'l') &= \int_0^\infty\!\!\int P_1(r_1)\,y_{k,l}(r_2)\,\frac{r_<^\kappa}{r_>^{\kappa+1}}\,P_2(r_1)\,y_{k',l'}(r_2)\,dr_1dr_2\,, \\ R_\mu(kl,k'l') &= \int_0^\infty\!\!\int P_1(r_1)\,y_{k,l}(r_2)\,\frac{r_<^\mu}{r_>^{\mu+1}}\,y_{k',l'}(r_1)\,P_2(r_2)\,dr_1dr_2\,. \end{aligned}\right\} \tag{8}$$

Here, $P_1(r)/r$ is the normalized radial wave function of the l_1-electron in $l_1^n(\alpha SL)$-state, and $P_2(r)/r$ is that of the l_2-electron in $l_1^{n-1}\,l_2(S''L'')$-state. $q_\kappa(l,l')$ and $r_{\kappa\mu}(l,l')$ are obtained after straightforward calculation according to Racah's method as follows:

$$q_\kappa(l,l') = (-1)^{L'-l_1-L''}\sqrt{(2\kappa+1)\,(2L+1)\,(2L''+1)}\cdot\sqrt{n}(l_1^n\alpha SL\{|l_1^{n-1}(\alpha'S'L')\,l_1SL)$$
$$\cdot W(l_1Ll_2L''\,;L'\kappa)A_\kappa(kl,k'l')/Q_\kappa(kl,k'l')\,; \tag{9}$$

and

$$r_{\kappa\mu}(l,l') = \bar{r}_{\kappa\mu}(l,l') + (-1)^{S+1/2-S_1}\,2(1/2||s||1/2)\,W(S1/2\,S''1/2\,;S'1)\bar{\bar{r}}_{\kappa\mu}(l,l')\,,$$

with

$$\left.\begin{aligned} \bar{r}_{\kappa\mu}(l,l') &= (-1)^{L'-l_1-L''}\frac{2\kappa+1}{2}\sqrt{(2\mu+1)(2L+1)(2L''+1)}\cdot\sqrt{n}\,(l_1^n\alpha SL\{|l_1^{n-1}(\alpha'S'L')l_1SL) \\ &\quad\cdot W(l_1Ll_2L''\,;L'\kappa)\,W(l_1l_2l'l\,;\kappa\mu)B_\mu(kl,k'l')/R_\mu(kl,k'l')\,, \\ \bar{\bar{r}}_{\kappa\mu}(l,l') &= (-1)^{L'-l_1-L''+S'+1/2-S''}(2\kappa+1)\sqrt{(2\mu+1)(2L+1)(2L''+1)(2S+1)(2S''+1)}\cdot\sqrt{n} \\ &\quad\cdot(l_1^n\alpha SL\{|l_1^{n-1}(\alpha'S'L,l_1SL)(1/2||s||1/2)\,W(l_1Ll_2L''\,;L'\kappa)\,W(l_1l_2l'l\,;\kappa\mu) \\ &\quad\cdot W(1/2S1/2S''\,;S'1)B_\mu(kl,k'l')/R_\mu(kl,k'l')\,. \end{aligned}\right\} \tag{10}$$

where $(l_1^n \alpha S\{| l_1^{n-1}(\alpha' S' L')\, l_1 SL)$ is the coefficient of the fractional parentage which Racah introduced in R. III, and gave the tables of the coefficients for $l_1=1$ and 2. By R. II, (30), $\left(\frac{1}{2}\middle\| s \middle\| \frac{1}{2}\right)=\sqrt{3/2}$. And $A_\kappa(kl, k'l')$ and $B_\mu(kl, k'l')$ are defined as

$$\left.\begin{aligned} A_\kappa(kl, k'l') &= \frac{(-1)^\kappa}{\sqrt{2\kappa+1}}(l_1\|C^{(\kappa)}\|l_2)(l\|C^{(\kappa)}\|l')\,Q_\kappa(kl, k'l'), \\ B_\mu(kl, k'l') &= \frac{(-1)^\mu}{\sqrt{2\mu+1}}(l_1\|C^{(\mu)}\|l')(l\|C^{(\mu)}\|l_2)\,R_\mu(kl, k'l'), \end{aligned}\right\} \tag{11}$$

where $(l\|C^{(k)}\|l')$ is given by R. II, (51).

In order to obtain $U_l^{l'}$ in (6), we must carry out the summation over S_1 and L_1 inserting (7) into (6). But these summations were already done in I, (13), and we have only make use of the result. Thus, inserting (9) and (10) into I, (13), and dividing by the statistical weight ot the initial atomic state, we obtain

$$\begin{aligned} U_l^{l'} = 2(2L''+1)n(l_1^n\alpha SL\{| l_1^{n-1}(\alpha' S' L') l_1 SL)^2 \sum_\kappa W(l_1 L l_2 L''; L'\kappa)^2 \\ \times\Big[\Big\{A_\kappa(kl, k'l') - \frac{\sqrt{2\kappa+1}}{2}\sum_\mu \sqrt{2\mu+1}\; W(l_1 l_2 l' l : \kappa\mu) B_\mu(kl, k'l')\Big\}^2 \\ +3/2(2S''+1)W(1/2S1/2S''; S'1)^2(2\kappa+1)\Big\{\sum_\mu \sqrt{2\mu+1}\, W(l_1 l_2 l' l ; \kappa\mu) B_\mu(kl, k'l')\Big\}^2\Big]. \end{aligned} \tag{12}$$

Putting this expression into (5), we obtain the probability that an atom in (αSL)-state of l_1^n-configuration makes transition to $(S''L'')$-state of $l_1^{n-1} l_2$-configuration in nuit time by the collision of electron with velocity k whose space density is one per unit volume.

It is seen that the first term in the square bracket in the right hand side of (12) does not give rise to such transition that the multiplicity of the atomic state changes, but the second term contributes. By the property of $(l\|C^{(k)}\|l')$, R. II, (50′), and the definitions of A_κ and B_μ, (11), we obtain the conservation of parity at once, i.e.,

$$l_1+l_2+l+l' = \text{even}. \tag{13}$$

For given l_1, l_2 and l, κ-values such that $A_\kappa(kl, k'l')$ does not vanish, are restricted by the triangular condition $|l_1-l_2|\leq\kappa\leq l_1+l_2$ and $l_1+l_2+\kappa=\mathit{even}$, and l'-values by $|l-\kappa|\leq l'\leq l+\kappa$ and $l+l'+\kappa=\mathit{even}$. The conditions for $B_\mu(kl, k'l')$ are given by replacing κ, l_2 and l' by μ, l' and l_2 in those for $A_\kappa(kl, k'l')$. Selection rules for S'' and L'' are obtained by the property of W-function and above-obtained κ-values as follows:

$$\left.\begin{aligned} S'' &= S, S\pm 1, \\ L'' &= L, L\pm 1, \cdots, L\pm(l_1+l_2). \end{aligned}\right\} \tag{14}$$

Of course, negative values of angular momenta must be excluded.

§3. Probability of Ionization of Atoms in l_1^n-Configuration by Electron Collision.

The ionization of atoms in (αSL)-state of l_1^n-configuration by electron collision may be considered as, in the above-mentioned excitation $l_1^n(\alpha SL)\rightarrow l_1^{n-1}(\alpha' S' L')\, l_2 S'' L''$, the l_2-electron of the final atomic state makes transition to continuous level and final S'' and L'' are indefinite. Therefore, we can obtain the probability of ionization of atoms in l_1^n-configuration from the results concerning excitation in the preceding section.

For the incident electron, Eqs. (1), (2) and (3) hold in this case also. On the other hand, the wave functions of scattered electrons with velocities k' and k'' are represented by

$$\psi_{k'l'm'}(r) = f_{k'l'}(r) S_{l'm'}(\theta, \phi), \tag{1''}$$

and similar expression, where $y_{k',l'}(r) = k'r\, f_{k,'l'}(r)$ satisfies the differential equation

$$\frac{d^2 y_{k'l'}}{dr^2}+\left\{k'^2-2U'(r)-\frac{l'(l'+1)}{r^2}\right\} y_{k'l'} = 0, \tag{2''}$$

and $y_{k'',l''}(r) = k''rf_{k'',l''}(r)$ also similar differential equation. Here $U'(r)$ is the mean field of the atom in $(\alpha'S'L')$-state of l_1^{n-1}-configuration. $y_{k',l'}(r)$ has the asymptotic form

$$y_{k',l'}(r) \sim \sin\left(k'r - \frac{l'\pi}{2} + \delta_{l'}\right), \tag{3''}$$

and $y_{k'',l''}(r)$ has similar asymptotic form. The velocities of scattered electrons are conditioned by the conservation of energy as follows:

$$k'^2 + k''^2 = k^2 - 2\,(E_{\alpha'S'L'} - E_{\alpha SL}). \tag{15}$$

Now, the probability that an atom in $l_1^n(\alpha SL)$-state makes transition to the state $l_1^{n-1}(\alpha'S'L')$ after being singly ionized by the electron collision can be obtained by the above-mentioned procedure, from the course of obtaining the probability for excitation $l_1^n(\alpha SL) \rightarrow l_1^{n-1}(\alpha'S'L')\, l_2S''L''$. Following this idea, we first replace l_2 into l'' which are summed in later stage, and, for fixed l'', $U_l^{l'}$ in (12) are summed over all S'' and L''. This sum $\sum\limits_{S''L''} U_l^{l'}$, we shall denote by $U_l^{l'l''}$. On the other hand, in order to normalize the wave function of scattered electron with velocity k'', W in (5) must be multiplied by the factor $2k''/\pi$. Thus, the probability of ionization is given by

$$W = 16k'k'' \sum_l \sum_{l',l''} U_l^{l'l''}, \tag{16}$$

where $U_l^{l'l''} = \sum\limits_{S'',L''} U_l^{l'}$, or

$$U_l^{l'l''} = \sum_{S'',L''} \sum_{S_1,L_1} \frac{(2S_1+1)(2L_1+1)}{(2S+1)(2L+1)} \left|(l_1^n(\alpha SL), lSL \,|\, H \,|\, l_1^{n-1}(\alpha'S'L'), l''S''L'', l'S_1L_1)\right|^2 \tag{17}$$

Inserting (12) into (17), we can easily carry out the summation over S'' and L'' by the orthogonality relation of W-functions. Thus

$$\begin{aligned} U_l^{l'l''} = \frac{2}{2l_1+1} n(l_1^n\alpha SL \{| l_1^{n-1}(\alpha'S'L') l_1SL)^2 \Big[\sum_\kappa A_\kappa(l\,;l'l'')^2 \\ - \sum_{\kappa,\mu} \sqrt{(2\kappa+1)(2\mu+1)}\, W(l_1 l''l'l\,;\kappa\mu) A_\kappa(l\,;l'l'') B_\mu(l\,;l'l'') + \sum_\mu B_\mu(l\,;l'l'')^2\Big], \end{aligned} \tag{18}$$

where $A_\kappa(l\,;l'l'')$ and $B_\mu(l\,;l'l'')$ are obtained from $A_\kappa(kl, k'l')$ and $B_\mu(kl, k'l')$ by replacing l_2 and $P_2(r)$ by l'' and $y_{k'',l''}(r)$, respectively. In order to use similar notations as the paper by Watanabe⁽⁴⁾, we denote $\tilde{B}_\kappa(l\,;l'l'')$ and $R_\kappa(l\,;l'l'')$ instead of $A_\kappa(l\,;l'l'')$ and $Q_\kappa(l\,;l'l'')$; respectively. Making use of these notations, (18) may be written as

$$\begin{aligned} U_l^{l'l''} = \frac{2}{2l_1+1} n(l_1^n\alpha SL \{| l_1^{n-1}(\alpha'S'L') l_1SL)^2 \Big[\sum_\kappa B_\kappa(l\,;l'l'')^2 \\ - \sum_{\kappa,\mu} \sqrt{(2\kappa+1)(2\mu+1)}\, W(l_1 l'l''l\,;\kappa\mu) B_\kappa(l\,;l'l'') \tilde{B}_\mu(l\,;l'l'') + \sum_\mu \tilde{B}_\mu(l\,;l'l'')^2\Big], \end{aligned} \tag{18'}$$

where

$$B_\kappa(l\,;l'l'') = \frac{(-1)^\kappa}{\sqrt{2\kappa+1}} (l_1||C^{(\kappa)}||l')(l||C^{(\kappa)}||l'') R_\kappa(l\,;l'l'') \tag{19}$$

with

$$R_\kappa(l\,;l'l'') = \iint_0^\infty P_1(r_1) y_{k,l}(r_2) \frac{r_<^\kappa}{r_>^{\kappa+1}} y_{k',l'}(r_1)\, y_{k'',l''}(r_2)\, dr_1 dr_2, \tag{20}$$

and, $\tilde{B}_\mu(l\,;l'l'')$ and $\tilde{R}_\mu(l\,;l'l'')$ are obtained from $B_\mu(l\,;l'l'')$ and $R_\mu(l\,;l'l'')$ by interchanging l' and l'', respectively. Therefore, $U_l^{l''l'}$ is equal to $U_l^{l'l''}$, and $U_l^{l'l''}$ is symmetric with respect to R_κ and $\tilde{R}_\kappa$. Inserting (18′) into (16), we have the probability of ionization as

$$W=\frac{32k'k''}{2l_1+1}n(l_1^n\alpha SL\{|l_1^{n-1}(\alpha'S'L')l_1SL)^2\sum_l\sum_{l',l''}[\sum_\kappa B_\kappa(l;l'l'')^2$$
$$-\sum_{\kappa,\mu}\sqrt{(2\kappa+1)(2\mu+1)}\,W(l_1l'l''l;\kappa\mu)B_\kappa(l;l'l'')\tilde{B}_\mu(l;l'l'')+\sum_\mu\tilde{B}_\mu(l;l'l'')^2]. \tag{21}$$

It is seen from this formula that the probability of ionization depends on the initial and final atomic state only through the factor $n(l_1^n\,\alpha SL\{|l_1^{n-1}(\alpha'S'L')^2l_1SL)$ and $k'k''$, except the indirect dependence through the integrals R_κ and $\tilde{R}_\mu$. Therefore, if the summation in (21) are written down in terms of R_κ and $\tilde{R}_\mu$ for given l_1, it can be used for any ionization process in which the jumping electron is l_1-electron. For example, the values of $V_l^{l'l''}=(2S+1)(2L+1)\,U_l^{l'l''}$ for $p^5(^2P)+e\rightarrow p^4(^3P)+e'+e''$ in Table III of Watanabe's paper can be used in calculating the probability for any $p^n(SL)+e\rightarrow p^{n-1}(S'L')+e'+e''$, remembering that, according to (18′),

$$V_l^{l'l''}=2\cdot3\cdot5\cdot\frac{2}{3}\cdot\frac{3}{5}\Big[\sum_\kappa B_\kappa^2-\sum_{\kappa,\mu}\sqrt{(2\kappa+1)(2\mu+1)}\,W(l_1l'l''l;\kappa\mu)B_\kappa\tilde{B}_\mu+\sum_\mu\tilde{B}_\mu^2\Big]_{l_1=1}$$
$$=12[\sum_\kappa B_\kappa^2-\sum_{\kappa,\mu}\sqrt{(2\kappa+1)(2\mu+1)}\,W(l_1l'l''l;\kappa\mu)B_\kappa\tilde{B}_\kappa+\sum_\mu\tilde{B}_\mu^2]_{l_1=1}.$$

§ 4. Excitation and Ionization of Atoms in Some Other Configurations.

The probability of excitation of atoms by electron collision are given, in general, by decomposing the wave function of incident and scattered electron into their partial spherical waves, as follows

$$W=8\pi k'\sum_{l,l'}U_l^{l'}, \tag{22}$$

where k' is the velocity of scattered electron, and $U_l^{l'}$ represents the partial probability. For the excitation $l_1^n(\alpha SL)+e\rightarrow l_1^{n-1}(\alpha'S'L')\,l_2S''L''+e'$, $U_l^{l'}$ is given by (12). Now, we consider the case that an atom of any configuration is excited from its (γSL)-state by the impact of electron with velocity k through the jump of its l_1-electron to the state with angular momentum l_2. Then, the final atomic state is represented by $(\gamma'S'L'), l_2S''L''$, where $\gamma'S'L'$ denotes parent term. For such cases, the partial probability $U_l^{l'}$ can be

Table I.

Excitation $\gamma SL\rightarrow(\gamma'S'L')l_2S''L''$	Ionization $\gamma SL\rightarrow\gamma'S'L'$	$f(\gamma SL,\gamma'S'L')$
$l_3^n(\alpha'S'L')l_1SL\rightarrow l_3^n(\alpha'S'L')l_2S''L''$	$l_3^n(\alpha'S\,L')l_1SL\rightarrow l_3^n(\alpha'S'L')$	1.
$l_3^n(\alpha_1S_1L_1)\cdot l_1^2(S_2L_2)SL\rightarrow$ $l_3^n(\alpha_1S_1L_1)l_1(S'L')l_2S''L''$	$l_3^n(\alpha_1S_1L_1)\cdot l_1^2(S_2L_2)SL\rightarrow$ $l_3^n(\alpha_1S_1L_1)l_1S'L'$	$\sqrt{2}\,(l_3^n(\alpha_1S_1L_1)\cdot l_1^2(S_2L_2)SL\{|$ $l_3^n(\alpha_1S_1L_1)l_1(S'L')l_1SL)$
$l_1^n(\alpha_1S_1L_1)l_3SL\rightarrow$ $l_1^{n-1}(\alpha_1'S_1'L_1')l_3(S'L')l_2S''L''$	$l_1^n(\alpha_1S_1L_1)l_3SL\rightarrow$ $l_1^{n-1}(\alpha_1'S_1'L_1')l_3S'L'$	$\sqrt{n}\,(l_1^n(\alpha_1S_1L_1)l_3SL\{|$ $l_1^{n-1}(\alpha_1'S_1'L_1')l_3(S'L')l_1SL)$
$l_1^n(\alpha_1S_1L_1)\cdot l_3^p(S_2L_2SL)\rightarrow$ $l_1^{n-1}(\alpha_1'S_1'L_1')\cdot l_3^p(S_2L_2)(S'L')l_2S''L''$	$l_1^n(\alpha_1S_1L_1)\cdot l_3^p(S_2L_2)SL\rightarrow$ $l_1^{n-1}(\alpha_1'S_1'L_1')\cdot l_3^p(S_2L_2)S'L'$	$\sqrt{n}\,(l_1^n(\alpha_1S_1L_1)\cdot l_3^p(S_2L_2)SL\{|$ $l_1^{n-1}(\alpha_1'S_1'L_1')\cdot l_3^p(S_2L_2)(S'L')l_1SL)$

where

$$(l_3^n(\alpha_1S_1L_1)\cdot l_1^2(S_2L_2)SL\{|l_3^n(\alpha_1S_1L_1)l_1(S'L')l_1SL)=\sqrt{(2S'+1)(2L'+1)(2S_2+1)(2L_2+1)}\,W(S_1\tfrac{1}{2}S\tfrac{1}{2};S'S_2)$$
$$W(L_1l_1Ll;L'l_2),$$

$$(l_1^n(\alpha_1S_1L_1)l_3SL\{|l_1^{n-1}(\alpha_1'S_1'L_1')l_3(S'L')l_1SL)=\sqrt{(2S'+1)(2L'+1)(2S_1+1)(2L_1+1)}\,W(S_1\tfrac{1}{2}\tfrac{1}{2}S':SS_1')$$
$$W(L_1l_3l_1L';LL_1')(l_1^n\alpha_1S_1L_1\{|l_1^{n-1}(\alpha_1'S_1'L_1')l_1SL),^{(*)}$$

$$(l_1^n(\alpha_1S_1L_1)\cdot l_3^p(S_2L_2)SL\{|l_1^{n-1}(\alpha_1'S_1'L_1')\cdot l_3^p(S_2L_2)(S'L')l_1SL)=\sqrt{(2S'+1)(2L'+1)(2S_1+1)(2L_1+1)}$$
$$W(S_1S_2\tfrac{1}{2}S';SS_1')W(L_1L_2l_1L';LL_1')(l_1^n\alpha_1SL\{|l_1^{n-1}(\alpha_1'S_1'L_1')l_1SL).$$

(*) The values of these coefficients of fractional parentages for $l_1=2$, $l_3=0$ were given in Tables XIV—XVI of Rohrlich's paper: F. Rohrlich, Phys. Rev. **74**, (1948) 1381.

obtained by similar procedure as in §2, and thus, in general, $U_l^{l'}$ may be represented as

$$U_l^{l'} = 2(2L''+1)f(\gamma SL,\gamma' S' L')^2 \sum_{\kappa} W(l_1 L l_2 L'' ; L'\kappa)^2$$
$$\cdot\Big[\Big\{A_\kappa(kl, k'l') - \frac{\sqrt{2\kappa+1}}{2} \sum_{\mu} \sqrt{2\mu+1}\, W(l_1 l_2 l' l ; \kappa\mu) B_\mu(kl, k'l')\Big\}^2$$
$$+\frac{3}{2}(2S''+1)\, W\Big(\frac{1}{2} S \frac{1}{2} S'' ; S' 1\Big)^2 (2\kappa+1) \Big\{\sum_{\mu} \sqrt{2\mu+1}\, W(l_1 l_2 l' l ; \kappa\mu) B_\mu(kl, k'l')\Big\}^2\Big], \tag{23}$$

where $A_\kappa(kl, k'l')$ and $B_\mu(kl, k'l')$ are given by (11), but the wave functions in the integrals $Q_\kappa(kl, k'l')$ and $R_\mu(kl, k'l')$ must be taken in suitable way corresponding to the case concerned. $f(\gamma SL, \gamma' S' L')$ depends only its indicated arguments, and, for example, in excitation considered in §2

$$f(\gamma SL, \gamma' S' L') = \sqrt{n}\, (l_1^n \alpha SL \{| l_1^{n-1}(\alpha' S' L') l_1 SL) . \tag{24}$$

The probability of ionization of atoms by electron collision is given by

$$W = 16k'k'' \sum_{l} \sum_{l', l''} U_l^{l'l''} \tag{25}$$

where k' and k'' are velocities of scattered electrons, and $U_l^{l'l''}$ is the partial probability which corresponds to incident l-wave and scattered l'- and l''-waves. For the ionization $l_1^n(\alpha SL)+e \rightarrow l_1^{n-1}(\alpha' S' L')+e'+e''$, $U_l^{l'l''}$ is given by (18′). In other cases, $U_l^{l'l''}$ can easily be derived from $U_l^{l'}$ in the same way as stated in §3. Thus, we have the probability that an atom in (γSL)-state of any configuration is ionized by electron collision through ejecting its l_1-electron and the final atomic state is $(\gamma' S' L')$ as follows:

$$U_l^{l'l''} = \frac{2}{2l_1+1} f(\gamma SL, \gamma' S' L')^2 \cdot \Big[\sum_{\kappa} B_\kappa(l ; l'l'')^2$$
$$-\sum_{\kappa, \mu} \sqrt{(2\kappa+1)(2\mu+1)}\, W(l_1 l' l'' l : \kappa\mu) B_\kappa(l ; l'l'') \tilde{B}_\mu(l ; l'l'') + \sum_{\mu} B_\mu(l ; l'l'')^2\Big], \tag{26}$$

where $B_\kappa(l ; l'l'')$ is given by (19) and $\tilde{B}_\mu(l ; l'l'')$ is obtained by interchanging l' and l'' in $B_\mu(l ; l'l'')$, but, of course, R_κ and $\tilde{R}_\mu$ must be suitably chosen corresponding to the case considered.

In Table I, $f(\gamma SL, \gamma' S' L')$ which appear in treating the excitations and ionizations of some typical electron configurations are shown. By means of $f(\gamma SL, \gamma' S' L')$, if the formulae for the probabilities of excitation or ionization of atoms in certain configurations were written down, these can be applied to those of some other configurations. For example, Table III of Watanabe's paper for ionization $p^n \rightarrow p^{n-1}$ can be used for such ionization processes as $l^n p \rightarrow l^n$, $l^n p^2 \rightarrow l^n p$, $p^n l \rightarrow p^{n-1} l$ and $p^n l^m \rightarrow p^{n-1} l^m$, where l is arbitrary angular momentum.

§5. Excitation and Ionization of Atoms in p^n-and d^n-Configurations by Electron Collision.

As examples of foregoing procedure, we shall treat the problems of excitation and ionization of atoms in p^n- and d^n-configurations by electron collision. We shall, first, consider ionization. The partial probability is given by (18′) assigning $l_1 = 1$ and 2. $B_\kappa(l ; l'l'')$ given by (19′) are shown in Tables II$_p$ and II$_d$ for $l_1 = 1$ and 2, respectively, and $\tilde{B}_\mu(l ; l'l'')$ are derived from $B_\mu(l ; l'l'')$ by interchanging l' and l''. Tables III$_p$ and III$_d$ give the values of $W(l_1 l' l'' l ; \kappa\mu)$ for $l_1 = 1$ and 2. Table III of above-cited Watanabe's paper can be obtained by Tables II$_p$ and III$_p$ at once, remembering that $V_l^{l'} = (2S+1)(2L+1)\, U_l^{l'}$.

For the case of excitation, the partial probability is given by (12). $A_\kappa(kl, k'l')$ given by (11) can be obtained from $\tilde{B}_\kappa(l ; l'l'')$ by assigning l_2 for l'' and replacing $\tilde{R}_\kappa(l ; l'l'')$ by $Q_\kappa(kl, k'l')$, and $B_\mu(kl, k'l')$ from $B_\mu(l ; l'l'')$ by assigning l_2 for l'' and replacing $R_\mu(l ; l'l'')$ by $R_\mu(kl, k'l')$.

Table IIp.

κ	$(-1)^{g-l+l'+\kappa} B_\kappa(l;l'l'')$
$l'+1$	$\frac{1}{2l'+3}\sqrt{3(2l+1)(2l''+1)(l'+1)\frac{(l+l'-l''+1)!\,(l-l'+l''-1)!\,(l'+l''-l+1)!}{(l+l'+l''+2)!}}\;\frac{g!}{(g-l)!\,(g-l'-1)!\,(g-l'')!}R_{l'+1}(l;l'l'')$
$l'-1$	$\frac{1}{2l'-1}\sqrt{3(2l+1)(2l''+1)l'\frac{(l+l'-l''-1)!\,(l-l'+l''+1)!\,(l'+l''-l-1)!}{(l+l'+l'')!}}\;\frac{(g-1)!}{(g-l-1)!\,(g-l')!\,(g-l''-1)!}R_{l'-1}(l;l'l'')$

where

$$2g=l+l'+l''+1\,.$$

Table IId.

κ	$(-1)^{g+1-l+l'+\kappa}B_\kappa(l;l'l'')$
$l''+2$	$\frac{1}{2l'+5}\sqrt{\frac{15(2l+1)(2l''+1)(l'+1)(l'+2)}{2(2l'+3)}\frac{(l+l'-l''+2)!\,(l-l'+l''-2)!\,(l'+l''-l+2)!}{(l+l'+l''+3)!}}\;\frac{(g+1)!}{(g-l+1)!\,(g-l'+1)!\,(g-l''+1)!}R_{l'+2}(l;l'l'')\,.$
l''	$\sqrt{\frac{5(2l+1)(2l''+1)l'(l'+1)}{(2l'-1)(2l'+1)(2l+3)}\frac{(l+l'-l'')!\,(l-l'+l'')!\,(l'+l''-l)!}{(l+l'+l''+1)!}}\;\frac{g!}{(g-l)!\,(g-l')!\,(g-l'')!}R_{l'}(l;l'l'')$
$l''-2$	$\frac{1}{2l'-3}\sqrt{\frac{15(2l+1)(2l''+1)(l'-1)l'}{2(2l'-1)}\frac{(l+l'-l''-2)!\,(l-l'+l''+2)!\,(l'+l''-l-2)!}{(l+l'+l''-1)!}}\;\frac{(g-1)!}{(g-l-1)!\,(g-l'-1)!\,(g-l''-1)!}R_{l'-2}(l;l\,l'')$

where

$$2g=l+l'+l''\,.$$

Tsble IIIp. $W(1l'l''l;\kappa\mu)$.

$\kappa \backslash \mu$	$l''+1$	$l''-1$
$l'+1$	$\left[\frac{(2l')!\,(2l'')!\,(l+l'-l''+1)!\,(l-l'+l''+1)!}{(2l'+3)!\,(2l''+3)!\,(l+l'-l''-1)!\,(l-l'+l''-1)!}\right]^{\frac{1}{2}}$	$\left[\frac{(2l')!\,(2l''-2)!\,(l+l'+l''+2)!\,(l'+l''-l+1)!}{(2l'+3)!\,(2l''+1)!\,(l+l'+l'')!\,(l'+l''-l-1)!}\right]^{\frac{1}{2}}$
$l'-1$	$\left[\frac{(2l'-2)!\,(2l'')!\,(l+l'+l''+2)!\,(l'+l''-l+1)!}{(2l'+1)!\,(2l''+3)!\,(l+l'+l'')!\,(l'+l''-l-1)!}\right]^{\frac{1}{2}}$	$\left[\frac{(2l'-2)!\,(2l''-2)!\,(l+l'-l''+1)!\,(l-l'+l''+1)!}{(2l'+1)!\,(2l''+1)!\,(l+l'-l''-1)!\,(l-l'+l''-1)!}\right]^{\frac{1}{2}}$

Tnble III*d*. $W(2l'l''l;\kappa\mu)$.

$\kappa \backslash \mu$	$l''+2$	l''	$l''-2$
$l'+2$	$\left[\frac{(2l')!\,(2l'')!\,(l+l'-l''+2)!\,(l-l'+l''+2)!}{(2l'+5)!\,(2l''+5)!(l+l'-l''-2)!\,(l-l'+l''-2)!}\right]^{\frac{1}{2}}$	$\left[3!\,\frac{(2l')!\,(2l''-2)!\,(l+l'+l''+3)!\,(l+l'-l''+2)!\,(l-l'+l'')!(l'+l''-l+2)!}{(2l'+5)!\,(2l''+3)!\,(l+l'+l''+1)!\,(l+l'-l'')!(l-l'+l''-2)!\,(l'+l''-l)!}\right]^{\frac{1}{2}}$	$\left[\frac{(2l')!\,(2l''-4)!\,(l+l'+l''+3)!\,(l'+l''-l+2)!}{(2l'+5)!\,(2l''+1)!\,(l+l'+l''-1)!\,(l'+l''-l-2)!}\right]^{\frac{1}{2}}$
l'	$\left[3!\,\frac{(2l'-2)!\,(2l'')!\,(l+l'+l''+3)!\,(l+l'-l'')!\,(l-l'+l''+2)!\,(l'+l''-l+2)!}{(2l'+3)!\,(2l''+5)!\,(l+l'+l''+1)!\,(l+l'-l''-2)!\,(l-l'+l'')!\,(l'+l''-l)!}\right]^{\frac{1}{2}}$	$\left[\frac{(2l'-2)!(2l''-2)!}{(2l'+3)!(2l''+3)!}\right]^{\frac{1}{2}}\{(l+l'+l''+2)(l+l'+l''+3)(l'+l''-l-1)(l'+l''-l)$ $-4(l+l'+l''+2)(l'+l''-l)(l+l'-l'')(l-l'+l'')$ $+(l+l'-l''-1)(l+l'-l'')(l-l'+l''-1)(l-l'+l'')\}$	$\left[3!\,\frac{(2l'-2)!\,(2l''-4)!\,(l+l'+l''+1)!\,(l+l'-l''+2)!\,(l-l'+l'')!\,(l'+l''-l)!}{(2l'+3)!\,(2l''+1)!\,(l+l'+l''-1)!\,(l+l'-l'')!\,(l-l'+l''-2)!\,(l'+l''-2)!}\right]^{\frac{1}{2}}$
$l'-2$	$\left[\frac{(2l'-4)!\,(2l'')!\,(l+l'+l''+3)!\,(l'+l''-l+2)!}{(2l'+1)!\,(2l''+5)!\,(l+l'+l''-1)!\,(l'+l''-l-2)!}\right]^{\frac{1}{2}}$	$\left[3!\,\frac{(2l'-4)!\,(2l''-2)!\,(l+l'+l''+1)!\,(l+l'-l'')!\,(l-l'+l''+2)!\,(l'+l''-l)!}{(2l'+1)!\,(2l''+3)!\,(l+l'+l''-1)!\,(l+l'-l''-2)!\,(l-l'+l'')!\,(l'+l''-l-2)!}\right]^{\frac{1}{2}}$	$\left[\frac{(2l'-4)!\,(2l''-4)!\,(l+l'-l''+2)!\,(l-l'+l''+2)!}{(2l'+1)!\,(2l''+1)!\,(l+l'-l''-2)!\,(l-l'+l''-2)!}\right]^{\frac{1}{2}}$

In conclusion, the author wishes to express his sincere thanks to Prof. T. Yamanouchi, under whose guidance this work was done, for his continual encouragement.

References.

(1) H. Horiè: Journ. Phys. Soc. Japan, **6** (1951) 179, cited as *I*.

(2) T. Yamanouchi and M. Kotani: Proc. Phys.-Math. Soc. Japsn, **22**, (1940) 14.

(3) G. Racah: Phys. Rev. **62**, (1942) 438; **63**, (1943) 367, cited as R. II, and R. III, respectively.

(4) M. Watanabe: Journ. Phys. Soc. Japan, **4**, (1949) 203.

JOURNAL OF THE PHYSICAL SOCIETY OF JAPAN Vol. 6 No. 4 JULY.—AUG., 1951

Some Properties of the Ni-Mn Alloys of Intermediate Composition (I)

By Takao SATO

Physical Institute, Faculty of Science, Tokyo Metropolitan University.

(Received July 1, 1950)

§1. Introduction.

The properties of Ni-Mn alloys containing less than 40 percent manganese have been studied by Kaya and Kussmann(1) in connection with the existence of the superlattice alloy Ni$_3$Mn. But, the writer hopes to find interesting phenomena for Ni-Mn alloys containing more than 40 percent manganese, and especially about 50 atomic percent manganese, from the results of Valentiner and Becker.(2) So the writer has studied mainly the temperature dependency of the electrical resistance for the Ni-Mn alloys containing 50 and 47 atomic percent manganese and the temperature dependency of the thermoelectric power for that alloy containing 47 atomic percent manganese.

§2. Specimens.

The materials are Merk's manganese and electrolytic nickel. They are melted together in Tammann tube of magnesia and we have the alloys containing 47 and 50 atomic percent manganese. The specimen of 47 atomic percent manganese Ni-Mn alloy is so hard and brittle that it can not easily be sawed. And, as the specimen of 50 atomic percent manganese Ni-Mn alloy is extremely brittle, so it is necessary to handle it very carefully. We used the specimen in the cylindrical form of about 5 mm in diameter and about 10 mm in length for the measurement of the electrical resistance of 50 atomic percent manganese and one in the form of about 5 mm in diameter, about 50 mm in length for the measurements of the electrical resistance and the thermoelectric power of 47 atomic percent manganese.

§3. Results of Measurement.

1. The temperature dependency of the electrical resistance of the Ni-Mn alloy containing 47 atomic percent manganese.

We show the behavior of the temperature variation of the electrical resistance of the Ni-Mn alloy containing 47 percent manganese in Fig. 1. It resembles to that of the 40 atomic percent manganese Ni-Mn alloy observed Kaya and Kussmann.(1) Namely, the electrical resistance increases up to about 400°C and is nearly constant in the temperature region from 400°C to 500°C and decreases remarkably in the temperature region from 520°C to about 700°C and again becomes nearly constant in the region from 750°C to 900°C. The rate of heating and cooling is about 2-3°C/min.

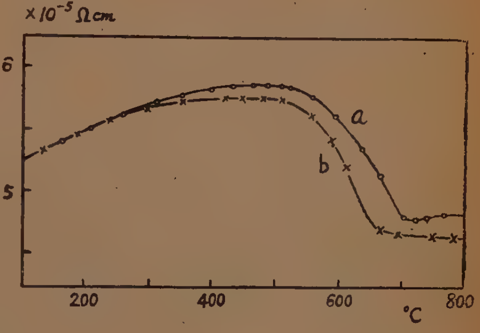

Fig. 1. The specific resistance *vs.* temperature curve for the 47 atomic prcent manganese Ni-Mn alloy. Curve *a* and *b* are the heating and the cooling curve, respectively, at the rate of about 2-3°C/min.

The heating curves after quenching from high temperature are shown in Fig. 2. At the room temperature, the specific resistance of the quenched specimen (5.2-5.4 × $10^{-5}\Omega$cm) is slightly larger than the annealed specimen (4.8 × $10^{-5}\Omega$cm). The temperature dependency of the specimens quenched from above 700°C has the similar tendency and the specific resistance has its maximum in the temperature region of 400-500°C. In the case of the specimen quenched from about 520°C, for example, the temperature *vs.* resistance curve has a small dip at about 200°C and has the flat part in a temperature region 400-500°C.

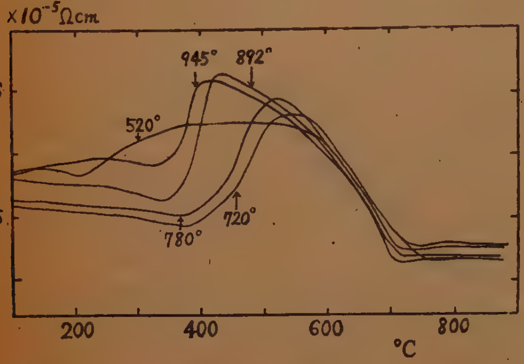

Fig. 2. The heating curves of the 47 atomic percent manganese Ni-Mn alloy quenched in water from the temperatures which are shown in figure. The heating rates are about 2-3°C/min.

In Fig. 3 the curve *a* is the heating curve of the annealed specimen and the curve *b* is that of the quenched specimen from 780°C. These are the results measured at the rate of 2-3°C/min. If the temperature of the quenched specimen is quickly raised to the temperature corresponding to the point *A* and *B* in Fig. 3, its specific resistance will have the values corresponding to the *A* and *B* points shown in the figure.

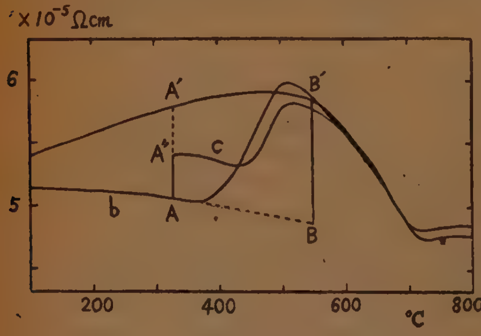

Fig. 3.

And then the specific resistance will increase to the values at *A'* and *B'* on the curve *a*, if we keep the temperature steady. After the specimen has been kept about 100 hours at 320°C (the temperature corresponding to the *A* point), the specific resistance reaches to the value at *A''* which lies between *A* and *A'*. Then the heating curve *c* in Fig. 3 is obtained at the rate of about 2-3°C/min. On the contrary, at 550°C (the temperature corresponding to the *B* point) the specific resistance increases so rapid that it takes only about 15 min. to reach to the *B'* point. Consequently, we may have different maximum point by heating the quenched specimen at different rate.

2. The temperature dependency of the electrical resistance of the Ni-Mn alloy containing 50 atomic percent manganese.

This alloy is extremely brittle and its handling is very difficult, but four nickel wires of 0.1 mm in diameter can be welded to the specimen along its length: the two end wires are used for the measurement of the main current and the others for the measurement of the potential drop between them. Hence the measurement of the temperature change of the resistance is easily done and the air quenching is easily possible.

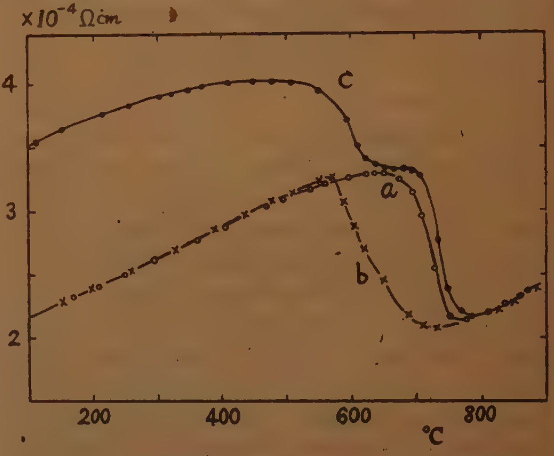

Fig. 4. The specific resistance *vs.* temperature curve of the 50 atomic percent manganese Ni-Mn alloy. The curve *a* and the curve *b* are the heating and the cooling curve, respectively, at the rate of about 2-3°C/min. The curve *c* is the heating curve of the specimen quenched in air from 890°C.

The results obtained are shown in Fig. 4, in which the form of the resistance *vs.* temperature curve *a* (heating rate of 2-3°C/min.) is resemble to the curve *a* in Fig. 1 for the 47 percent manganese alloy, but the temperatures corresponding to their maximum points are slightly different and the difference between the maximum points in the heating curve and the cooling one at the rate of about 2-3°C/min. is larger for the 50 atomic percent manganese alloy than for the 47 atomic percent one. At room temperature the specific resistance of the 50 atomic percent manganese alloy is about $1.9\times10^{-4}\Omega$cm which is about four times that of the 47 atomic percent one. If one quenches the former in air from 890°C, its specific resistance at room temperature becomes $3.4\times10^{-4}\Omega$cm which is about 1.8 times that of the annealed specimen.

The specific resistance of the quenched specimen on heating (curve *c*) has the positive temperature coefficient up to 500°C, decreases with increasing temperature and becomes nearly constant in the neighborhood of about 650°C. It coincides nearly with the curve *a* at about 700°C. If we quench the specimen from 650°C on the curve *c*, its specific resistance at room temperature becomes nearly equal to that of the annealed specimen. Hence, the quenching effect of the specimen quenched from 890°C will disappear in the temperature region above about 650°C. And further if we keep the specimen at 440°C on the curve *c*, about 1 hr., the resistance does not change any more.

3. The temperature dependency of the thermoelectric power of the Ni-Mn alloy containing 48 atomic percent manganese.

We see that the Ni-Mn alloy containing 47 percent manganese shows the anomalous behaviors of the electrical resistance at about 500-600°C, so we suppose the measurement of the thermoelectric power of this alloy may be interesting.

For the measurement of the thermoelectric power, we adopt the method used for the measurement of anomalous behaviors of the thermoelectric power of the Ni$_3$Mn(3) and Cu$_3$Au(4) superlattice alloys. The results, which were obtained when the specimen was coupled with platinum wire, are shown in Fig. 5. The rate of heating is about 1°C/min. In this figure, the curve *a* is the result of the annealed specimen, and the curve *b* is that of the specimen quenched from 880°C. The results, as may be expected, shows clearly the anomalous behaviors in the range of 500-600°C. The greatest value of the thermoelectric power for the annealed specimen is 30.5 μV/deg. and that for the quenched specimen is 53.5 μV/deg.

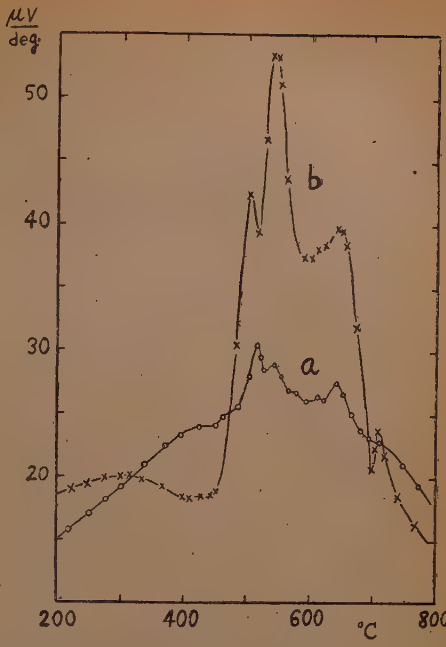

Fig. 5. The thermoelectric power *vs.* temperature curve of the Ni-Mn alloy containing 47 atomic percent manganese. The curve *a* is the heating curve of the annealed specimen and the curve *b* is that of the quenched one from 780°C. The heating rates are about 1°C/min.

§ 4. Discussion.

As mentioned above, the difference of the specific resistance at room temperature between the annealed and the quenched specimens is very small in the case of the Ni-Mn alloy containing 47 atomic percent manganese, but the specific resistance at room temperature of the quenched specimen of the 50 atomic percent manganse alloy is about 1.8 times that of the annealed specimen. Valentiner and Becker have suggested that the larger difference of the specific resistance between the annealed and the quenched specimens containing about 50 atomic percent manganese is due to the existence of a superlattice. However, the writer has not found any reasons that there is a superlattice. Namely, any characteristic features of order-disorder transformation are not found by an indirect method such as the measurement of the temperature dependency of the electrical resistance of the annealed and the quenched alloy containing 50 atomic percent manganese. Hence, the Ni-Mn alloy containing 50 atomic percent manganese may be the Ni-Mn compound as Dourdine(5) has suggested.

According to the X-ray analysis by Valentiner and Becker,(2) the Ni-Mn alloys containing 40-70 atomic percent manganese have the face-centered tetragonal lattice and their axial ratios *c*/*a* have only slight differences. Hence, the characteristic crystal structure does not appear in the 50 atomic percent maganese alloy corresponding to the Ni-Mn compound. The specific resistance of the 50 atomic percent manganese alloy is about 4 times that of the 47 atomic percent manganese alloy at room temperature. This fact is reasonable from the difference of brittleness between these two specimens and suggests that the alloy containing 50 atomic percent manganese has the almost filled Brillouin zone. Hence, the effective number of free electrons of that alloy may be smaller than that of the 47 atomic percent manganese alloy.

In the case of the 50 atomic percent manganese alloy, the increase of the specific resistance due to quenching may suggest that the state density of the 3d band at the surface of the Fermi distribution of the quenched specimen becomes larger than that of the annealed one.

On the other hand, in the case of the 47 atomic percent manganese alloy, the difference of the specific resistance at room temperature between the annealed and the quenched specimen is very small and the temperature dependency of the resistance of the quenched specimen of the 47 atomic percent manganese alloy (Fig. 2) is entirely different from that of the 50 atomic percent manganese alloy (Fig. 4 curve *c*). So we may suppose that the structure of the 3d band and the position of the Fermi surface may be changed by quenching, but their relative relation may be different from that of the 50 atomic percent manganese alloy.

The region of the negative temperature coefficient of the resistance comes to appear at the high temperature (500-700°C) in the case of the Ni-Mn alloys containing more than 30 percent manganese. In order to understand this fact, one needs to pay attention to the transformation of manganese.(6) The α Mn and the β Mn are a complex cubic structure with 58 and 20 atoms, respectively, in the unit cell. But the γ Mn is the face centered tetragonal structure. The α Mn transforms to the β Mn at about 700°C and the β Mn transforms to the γ Mn at about 1200°C. The measurement of the temperature dependency of the resistance of pure metallic manganese is very difficult, but has been done by Grube and Speidel(7) using the electrodeless method. Their result is shown in Fig. 6.

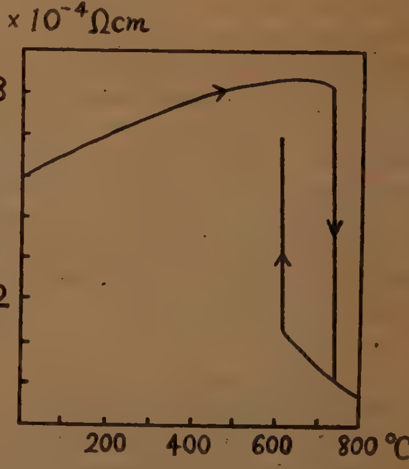

Fig. 6. The specific resistance *vs.* temperature curve in the transformation from the α Mn to the β Mn (after Grube and Speidel).

While, in the Ni-Mn alloys containing 40-70 percent manganese, the face-centered tetragonal structure is stable through all temperature regions, some factors relating to the transformation from the α Mn to the β Mn may not completely vanish by the nickel content in the Ni-Mn alloy. Consequently, the principal factor relating to the negative temperature coefficient of the alloys may be understood as in the Cu-Mn alloys.(8) Namely, there is some temperature region *kT* (*k*: Boltzmann's constant) where the state density near the surface of the Fermi distribution decreases very fast with increasing energy. In the case of the Cu-Mn alloys, the effect of the α Mn ⇄ β Mn transformation on the negative temperature coefficient of the resistance has not clearly been considered.

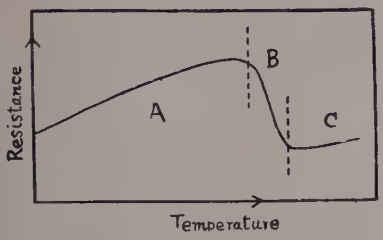

Fig. 7. The resistance *vs.* temperature curve of the Ni-Mn alloys of the intermediate composition, schematically.

The temperature dependency of the resistance of the Ni-Mn alloys of intermediate compositions may be considered in the three parts *A*, *B* and *C* as shown schematically in Fig. 7 and these parts should be due to the effects of the α Mn, $(\alpha+\beta)$ Mn and β Mn, respectively. This consideration for the electrical resistance of the Ni-Mn alloys is important to understand the mechanism of the transformation of manganese itself. As to this point, the writer will discuss in the other paper.

The writer is indebted to Prof. A. Okazaki for his valuable discussions and to Prof. K. Omori for his kind encouragement and continued interest.

References.

(1) S. Kaya and A. Kussmann: Zeit. f. Phys. **72** (1931) 292.
(2) S. Valentiner and G. Becker: Zeit. f. Phys. **93** (1935) 795.
(3) Takao Sato: Jour. Phys. Soc. Jap. **3** (1948) 198.
(4) Takao Sato: Jour. Phys. Soc. Jap. **5** (1950) 268.
(5) A. Dourdine: Rev. Mét. **29** (1932) 507, 565.
(6) A.J. Bradley and J. Thewlis: Proc. Roy. Soc. A. **115** (1927) 456.
G.D. Preston: Phil. Mag. **5** (1928) 1198, 1207.
(7) G. Grube and H. Speidel: Z. Elektrochem. **46** (1940) 233.
(8) Takao Sato: Jour. Phys. Soc. Jap. **5** (1950) 287.

JOURNAL OF THE PHYSICAL SOCIETY OF JAPAN Vol. **6** No. 4 JULY.—AUG., 1951

On Sub-boundary Structure of Aluminium.

By Harero IWAMURA and Nobuo SHIOTA
Faculty of Engineering, Ibaraki University.

(Received October 26, 1950)

§1. Introduction.

The idea of "block" and "sub-boundary" composing the crystallite grain of metals was accepted without much resistance long before their actual existence could be proved. More or less extended studies of the problem has began only in the last 15 years. The microscopic study on the sub-boundary structure of metals, recently carried out by Lacombe and his co-worker⁽¹⁾ seems to bring about a further development in this field. By using the same method, we performed some observations upon the effect of hydrogen gas on the structure of aluminium single crystal, and here we will report our preliminary experimental results and the related discussions from the view point of the theory of dislocation.

§2. Experimental Results.

Each specimen was electropolished in Jacquet's solution and then etched with a mixture of aqua regia and hydrofluoric acid (47% fuming HNO_3, 50% pure HCl and 3% HF). By the extention of 0.5 per cent, etch pits of pure aluminium single crystal are smaller than those of the single crystal prepared from the molten metal into which the water vapour was blown.⁽²⁾⁽³⁾ The lamellar lines are found in either case. (Photo. 1 (a) and (b)).

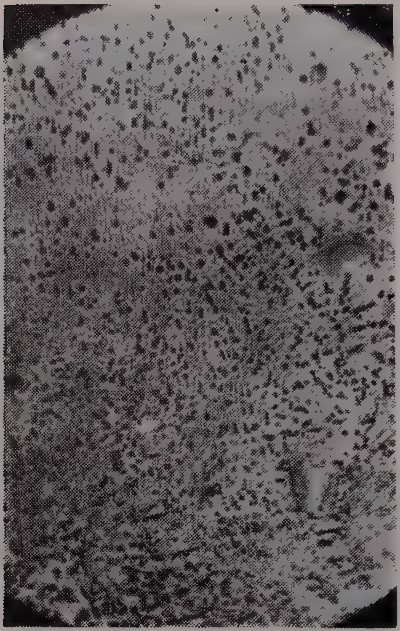

Photo. 1(a)×128

The etch pits of pure aluminium single crystal after the extention of 0.5 per cent.

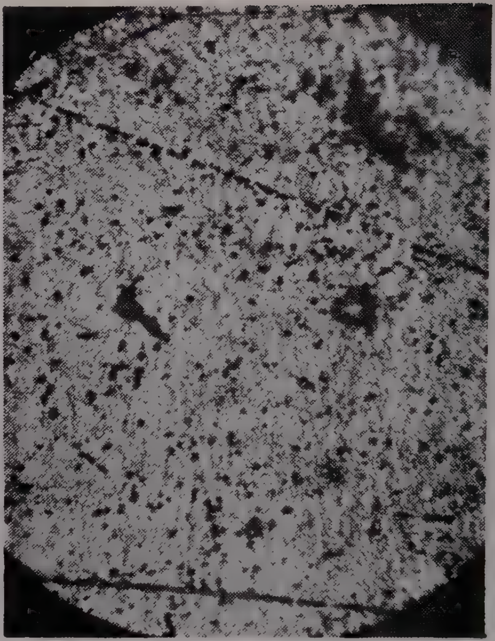

Photo. 2(a)×128

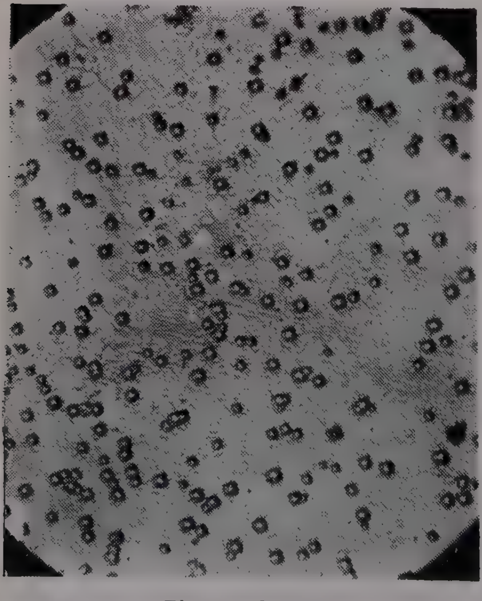

Photo. 1(b)×128

The etch pits of the single crystal prepared from the molten metal into which the water vapour was blown. After the extention of 0.5 per cent.

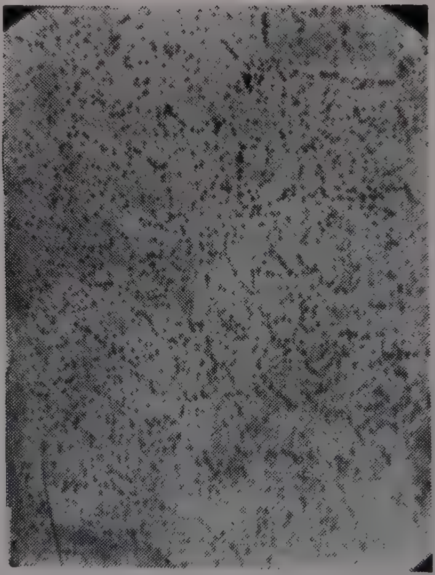

Photo. 2(b)×128

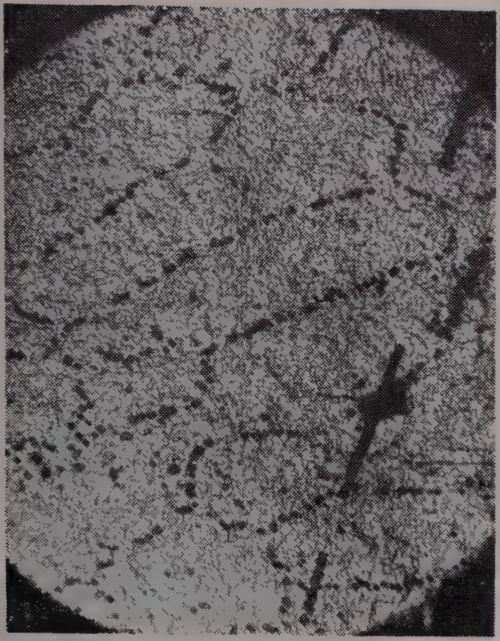

Photo. 2(c) × 128

(a) is the etch pits of pure aluminium, and (b), (c) are the structures of specimens including hydrogen gas after being reduced cold 60 per cent in section. (b) is the specimen blowed for 5 seconds and (c) is the specimen blowed for 15 seconds.

After being reduced cold 60 per cent in section, some etch pits are generated along straight lines and, on increasing the volume of included gas, the sub-boundaries are formed by these etch pits, the sizes of bounded area increasing at the same time. (Photo. 2 (a), (b) and (c)). And the sub-bourdaries have a tendency to disintegrate slightly in the annealing process for 44 hours at 620°C. (Photo. 1 (b)→Photo. 3 (a); Photo. 2 (b)→Photo. 3 (b)). The sizes of each pit become smaller and the spacing among them narrower on increasing the annealing time, namely the etch pits change into ones having a resemblance to pure aluminium crystal.

The etch figures of thin boards (1 mm in thickness and 10 mm in width) bent to 36.7 mm radius and annealed for 24 hours at 620°C are shown in Photo. 4 (a) and (b). After electro-polishing and etching, the specimens are bent more in order to develop the slip bands. (a) is the one of pure aluminium and (b) is the one of specimen including hydrogen gas. In the former, the straight boundaries are formed by etch pits perpendicularly to the slip bands and in the latter, the sub-boundaries are formed but the slip bands are hard to appear.

§ 3. Discussions.

As is decribed above we recognized that the sub-boundary structures are considerably changed by the content of hydrogen. Read and Schockley⁽⁴⁾ proposed that each

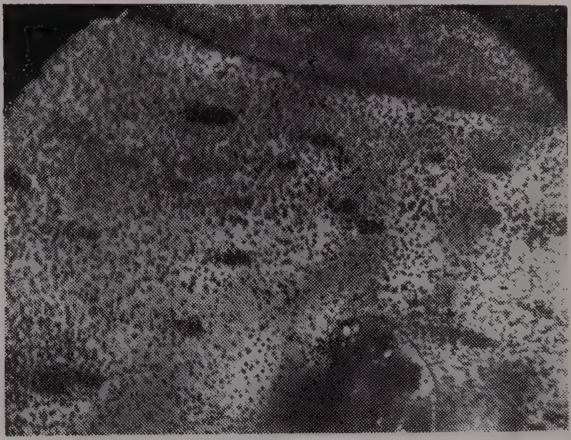

Photo. 3(a) × 128

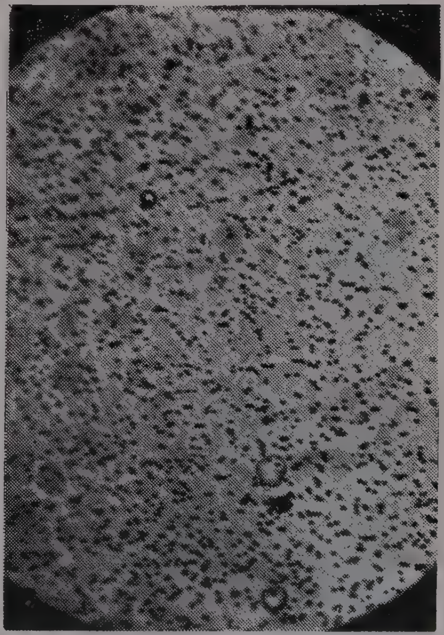

Photo. 3(b) × 128

Cold worked samples showing a tendency of sub-boundaries to disintegrate slightly in the annealing process for 44 hours at 620°C. Photo. 1 (b) → 3 (a): Photo. 2 (b) → 3 (b).

etch pit is originated at the edge-dislocation, where the free energy of the stressed material might be somewhat higher than elsewhere. The pit then grows to large size so that it becomes to be observed optically. Actually this proposal was confirmed by Nye's paper.(5)

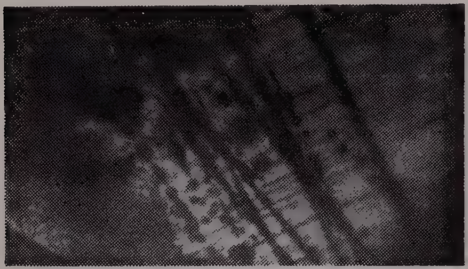

Photo. 4(a) × 400

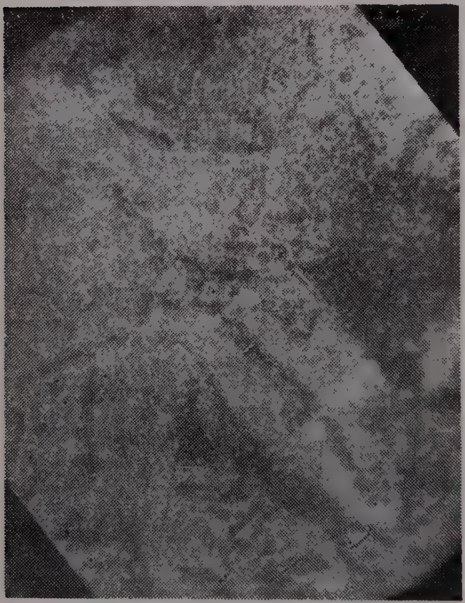

Photo. 4(b) × 400

The etch figures of thin boards bent to 36.7 mm radius and annealed for 24 hours at 620°C. (a) is the one of pure aluminium and (b) is the one of specimen including hydrogen gas.

In Read and Schockley's paper, if $\cos\varphi$ is equal to 1, namely when the each dislocation coincides with the direction of X axis, the disorientation angle θ is given as follows;

$$\theta=\frac{a}{D}\ \text{radian},$$

here, a is lattice onstant and D is the spacing between dislocations. The second column of Table 1 shows the value of θ calculated from the observed value of D measured from photo. 2 (b) and (c) by using above formula and by assuming an appropriate value of a. The general order of magnitude of θ and D is known to be 10^{-3} radians or less and 3×10^{-4} cm or less respectively(4), and the values in Table 1 are in a reasonable agreement with them.

Table 1.

Etch pits of the single crystal prepared from the molten metal into which the water vapour was blown for 5 seconds and for 15 seconds.

	Specimen blown for 5 seconds	Specimen blown for 15 seconds
Disorientation angle. (θ)	2.64×10^{-5} radian	1.12×10^{-5} radian
Spacing of etch pits. (D)	1.53×10^{-3} cm	3.65×10^{-3} cm
Linear size of sub-boundary structure. (L)	38 μ	84 μ

θ: calculated value. D & L: Observed values.

Here we have to pay attention that the values of D and sizes of bounded area become larger with increase of the volume of included hydrogen gas. Though we are generally apt to suppose that the resistance of the metal to the mechanical deformation becomes to decrease when the sizes of bounded area are large and the values of disorientation angle are small, the strength of crystal including hydrogen gas has a large value on the contrary. This fact can not be understood without taking account of some other factor. So we assume tentatively that the resistance of the metal to the mechanical deformation depends on the anchoring force for the edge-dislocation due to unsymmetrical distribution of hydrogen atmosphere rather than on the linear size or the disorientation of macro-mosaic and sub-grain, namely we assume that hydrogen atoms are drawn towards the dislocations as it is said with the impurity atoms in metals.(6)(7)

Fig. 1 is the schematic diagram showing the relation between potential energy and atomic coordinates. Potential barrier for the motion of dislocation may partly be higher on account of the effect of included hydrogen atom, and the inclination of potential barrier may becomes like as shown in the diagram, wherein C_1, C_2 and C_3 are the maximum inclination of shearing stress for the motion of dislocation. Namely, the anomalies of local field may be responsible to the difference of the sizes of etch pits for the specimen of pure aluminium and that including hydrogen gas, as actually observed in the above experiment on cold worked samples. This proposal is also supported by the fact that the single crystal of aluminium shows the discontinuous jump in the creep test only for the sample including hydrogen atoms.(8)

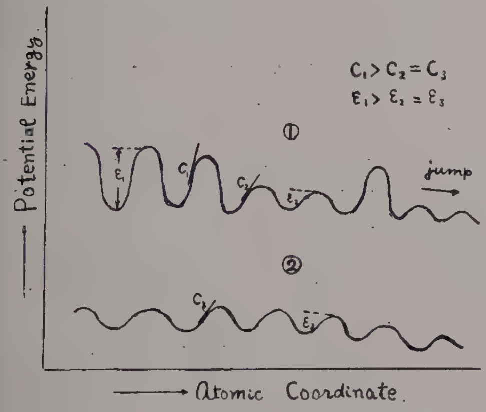

Fig. 1. Relation between Potential Energy and Atomic Coordinate
(1) Specimen Including Hydrogen Atoms.
(2) Pure Aluminium.

The writers wish to express their sincere thanks to Assis. Prof. Akiya Ookawa in Gakushuin University for his stimulating discussion throughout the course of this work.

References.

(1) P. Lacombe: Report. Conf. Strength. Solid. (1948) 91.
(2) H. Iwamura & N. Shiota: J. Appl. Phys. Japan. (in Japanese) **18** (1949) 251.
(3) H. Iwamura & N. Shiota: Japan. Inst. Metals. (in Japanese) **14** (1950) 65.
(4) W.T. Read & W. Schockley: Phys. Rev. **78** (1050) 275.
(5) J.F. Nye: Nature. **161** (1948) 367.
(6) A.H. Cottrell: R.C.S.S. (1948) 30.
(7) F.R.N. Nabarro: Ibid. (1948) 38.
(8) N. Shiota: Japan. Inst. Metals. (in Japanese) **14** (1950) A. 2.

JOURNAL OF THE PHYSICAL SOCIETY OF JAPAN Vol. **6** No. 4 JULY—AUG., 1951

Anomalous Hyperfine Structure in the Spectrum of Al II.

By Shigeki SUWA.
Institute of Science and Technology, Komaba-machi, Meguro-ku, Tokyo.

(Received June 10, 1950)

§1. Introduction.

The hyperfine structure (hfs.) of atomic spectra is studied usually for the purpose of obtaining important informations about atomic nuclei (the value of the spin, the magnetic moment or the quadrupole moment). But problems are still left to be investigated from the view point of spectral regularity itself. The anomalous hfs. which appears when the mutual distances of terms involved in the transition are so small that they are comparable with or smaller than the hyperfine splittings due to the nuclear spin, is one of the problems belonging to this category.(1) In order to clarify this problem, study of the hfs. of Al II, the most typical example, has been undertaken.

As was stated in a previous paper in Japanese(2), the above mentioned phenomena can be classified into two cases: (1) the case in which triplet separations are small, the singlet-triplet separation being not small, and (2) the case in which both separations are very small or vanish. The n^3D- and *nG*- series of Al II offer an example of the case (1) and (2), respectively.

In previous papers⑴,⑵ the result of experimental and theoretical investigation of the hfs. of 4^3P-4^3D was described in detail. In the present work the hfs. of 4^3P-5^3D, the next higher member of the 4^3P-n^3D series has been investigated more accurately than before, and compared with theory. The result, together with that of 4^3P-4^3D, seems to be sufficient to clarify the problem of the case (1).

The hfs. of the $4^{1,3}F-nG$ series of Al II, which is an example of the case (2), was studied and explained qualitatively by Paschen⑶ and by Goudsmit and Bacher⑷. But the resolving power attained by Paschen was not large enough for the details of the fine structure to be compared with theory. In the present work the hfs. of the above mentioned lines has been resolved so as to make interpretation of the observed structure by theory possible. A brief account of the result has been given at another place.⑸

§ 2. Experimental Arrangement.

The light source and the spectral apparatus used were almost the same as described previously: namely, the spectrum of Al II was excited in a water-cooled aluminium hollow cathode discharge tube filled with helium (instead of neon) of a few mm Hg pressure. The fine structure was examined by the use of a quartz Lummer plate (thickness = 4.43 mm), a glass Lummer plate (thickness = 4.67 mm) and a Fabry-Pérot etalon with the spacer in the

(a) 4^3P-5^3D

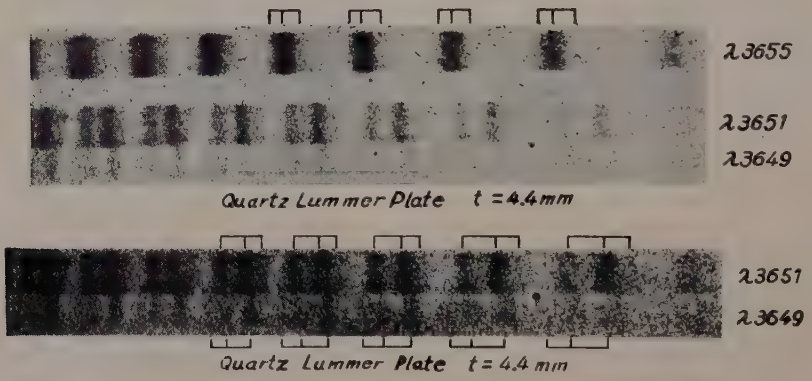
λ3655
λ3651
λ3649
Quartz Lummer Plate t = 4.4 mm
λ3651
λ3649
Quartz Lummer Plate t = 4.4 mm

(b) $4^{1,3}F-nG$

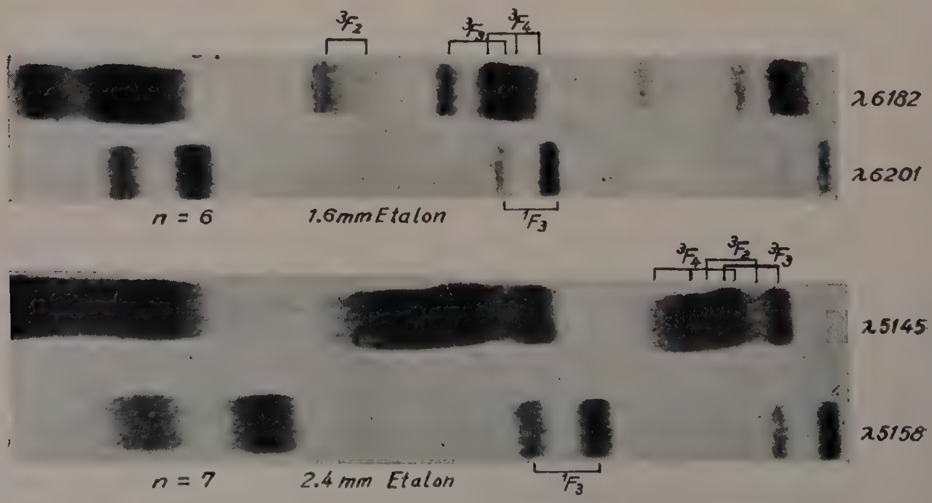

Fig. 1. Interference patterns of hfs. of Al II.

range 1.6 mm–3.2 mm.

§ 3. Hfs. of λλ3655,3651 and 3649 ($4^3P_{2,1,0}-5^3D$).

(a) Experimental result. In order to disperse the spectrum a glass prism spectrograph (dispersion about 8Å/mm in the region of 3600Å) was used so as to separate the above-mentioned three lines from each other sufficiently for examining their hfs. In this way preliminary data reported in the previous paper⁽²⁾ have been much improved. In Fig. 1(a) reproductions of the interference patterns of these lines taken with a quartz Lummer plate of thickness 4.43 mm is given. The result of measurement is shown in Fig. 2. λ3649 has now been found to consist of three components. The existence of the most refrangible component at $+0.189$ cm^{-1} of λ3655 has been confirmed and the component at -0.098 cm^{-1} has also been resolved.

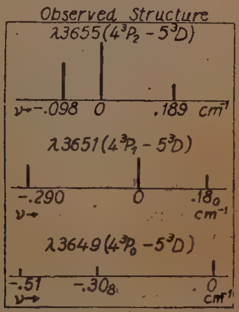

Fig. 2. Observed hfs. of 4^3P-5^3D.

(b) Comparison with theory. Though the result of the theoretical calculation for the hfs. of 4^3P-n^3D following the method of Güttinger and Pauli⁽⁶⁾ was reported previously in detail, the essential points will be described here once more.

The hfs. of the final levels 4^3P is known by the work of Heyden and Ritschl⁽⁷⁾. Taking into account that the triplet separations of n^3D are small and at most comparable with the splitting due to the nuclear spin, the hyperfine energy levels of n^3D are obtained by diagonalization of the matrix of the total Hamiltonian

$$H = H_0(J) + a(\mathbf{I}\cdot\mathbf{s}), \qquad (1)$$

where $H_0(J)$ is the energy of the atomic system when the effect of the nuclear spin is neglected. $\mathbf{I}$ and $\mathbf{s}$ are the spin operator of the nucleus and of the $3s$-electron, respectively, and a is the coupling constant between $\mathbf{I}$ and $\mathbf{s}$. This diagonalization was performed by calculating the matrix H in the $(L-S)$ coupling scheme, in which J^2 (and also $H_0(J)$) and S^2 are diagonal (S denotes the total electronic spin) and by solving the secular equations thus obtained for each possible value of F, the hyperfine quantum number. These secular equations involve three parameters $\alpha = H_0(^3D_3) - H_0(^3D_1)$, $\beta = H_0(^3D_2) - H_0(^3D_1)$ and a. α and β are the differences of the diagonal elements of $H_0(J)$ and represent the magnitude of the triplet separations of n^3D. Assuming that $a = 0.172$ cm^{-1} ⁽⁷⁾, the secular equations were solved numerically for various values of α and β. Thus the energy levels of n^3D were graphically represented by these solutions as functions of α and β. Then, the relative intensities of all the hfs. components of 4^3P-n^3D were also calculated numerically for each set of values of α and β, using the transformation matrix which makes the matrix H diagonal. As in the case of 4^3P-4^3D, best fit for α and β was sought in order to get agreement between the observed and the calculated structure of 4^3P-5^3D, finding that $|\alpha|$ and $|\beta|$ are very small, namely $0 \geq \alpha, \beta \geq -0.1$ cm^{-1}. The calculated structure for the two cases, $\alpha = \beta = 0$ and $\alpha = \beta = -0.1$ cm^{-1}, is given in Fig. 3. Taking into account that the components that lie mutually closer than about 0.08 cm^{-1} are not expected to be resolved due to the Doppler broadening, one sees that the calculated structure agrees with the observed one. So far we have assumed that $a = 0.172$ cm^{-1} which was given by Heyden and Ritschl⁽⁷⁾, but as will be described later, a more accurate value can be obtained, namely $a = 0.166$ cm^{-1}. After recalculating with the value of $a = 0{,}166$ cm^{-1}, it was found that this 3.5% correction of the value of a has little or no effect within the accuracy of the order of 0.01 cm^{-1} upon the result, though it appeared that for 4^3P-5^3D the numerical values were slightly improved. Owing to the fact that for any set of values of α and β falling in the region $0 \geq \alpha, \beta \geq -0.1$ cm^{-1}, the calculated values agree well with the observed ones (also for $a=0.166$ cm^{-1}) within the above-mentioned accuracy, the values of α and β could not be determined more precisely. At any rate, it has been found that the observed structure of 4^3P-5^3D can also be explained by the general theory, and that it represents a typical example of the above-mentioned case (1). For such small absolute values of α and β, a phenomenon analogous to the Paschen-Back effect occurs and 5^3D splits up first into three levels due to the coupling between the nuclear spin I and the total electronic spin S and then each of the three splits further, due to the spin-orbit interaction which gives rise to the triplet separation.

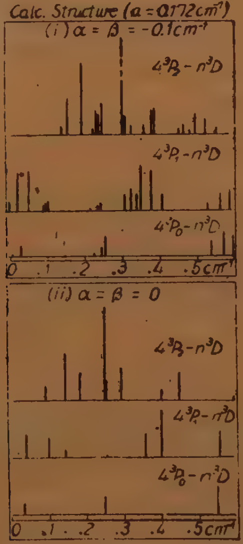

Fig. 3. Calculated hfs. of 4^3P-n^3D.

§4. Hfs. of the $4^{1,3}F-nG$ series.

(a) Experimental result. The hfs. of the $4^{1,3}F-nG$ series is difficult to study, since three lines 4^3F_4-nG, 4^3F_3-nG and 4^3F_2-nG lie close together and each of them has fine structure. By using interferometers of various order distance, it has been met with success to observe more detailed structure of these lines than ever reported. The interference patterns of these lines taken with a Fabry-Pérot etalon are reproduced in Fig. 1 (b).

4^1F_3-nG: The fine structure was measured for three members of the series, namely the lines λλ6201, 5158 and 4650 corresponding to $n=6$, 7 and 8, respectively. Each of these lines consists of two sharp components, in agreement with the result of Paschen. The structure is shown in the upper part of Fig. 5. Since these lines are sufficiently away from 4^3F-nG, the distance of the two components could be measured accurately, the result being given in Table I. It can be seen that the doublet separation is the same for $n=6$, 7 and 8 within experimental error. As is well known, the $(L-S)$ coupling is fully established in the spectrum of such a light element as Al, and no singlet term has hfs.. Therefore, we can assume the 4^1F_3 term to have no hfs., even if it is perturbed by other terms (which will be also singlets), and so obtain the information about the structure of nG directly from the structure of 4^1F_3-nG. Thus the nG term consists of only two levels, say nG^+ and nG^- (the higher one being denoted by nG^+), the mutual distance of which is independent of n. We may therefore assume that the multiplet separations of nG vanish entirely.

Table I. Doublet separation of 4^1F_3-nG.

n	λ(Å)	Δν(cm^{-1})
6	6201	0.500±0.001
7	5158	0.497±0.002
8	4650	0.498±0.005

4^3F-nG: Measurements were made for $n=6$ and 7, the result being given in Fig. 4. It was found that the structure is equal for $n=6$ and 7 within experimental error. 4^3F_4-nG, which was observed by Paschen to consist of two components or only one broad component, was newly found to have flag patterns on both sides of the central strongest component. 4^3F_3-nG consists of two components, the mutual distance being slightly smaller than that of 4^1F_3-nG. The distance could not be measured so accurately as in the case of 4^1F_3-nG, owing to experimental difficulties. 4^3F_2-nG, was reported by Paschen to consist of only two components. Each of them has now been found to have a further broadened structure, though not so well resolved. In Fig. 4 and 5, only the breadth of the component of short wave length side is shown. Since the breadth could not be measured accurately, any discrepancy between $n=6$ and 7 may be regarded to lie within experimental error.

(b) Interpretation of the structure of 4^3F-nG.

(i) *Structure of the nG term.* The total Hamiltonian H is given by (1), as in the case of n^3D. The matrix elements of H were evaluated in the $(J\text{-}J)$ coupling scheme in which $\boldsymbol{J}^2$ and j_g^2 are diagonal. Here j_g denotes the angular momentum of the ng-electron. As stated above, all the separations of the gross structure, namely the differences of the diagonal elements of $H_0(J)$ are assumed to vanish. Then the matrix of H was diagonalized by the transformation to the scheme in which $\boldsymbol{K}^2$ and j_g^2 are diagonal, where $\boldsymbol{K}$ is defined by

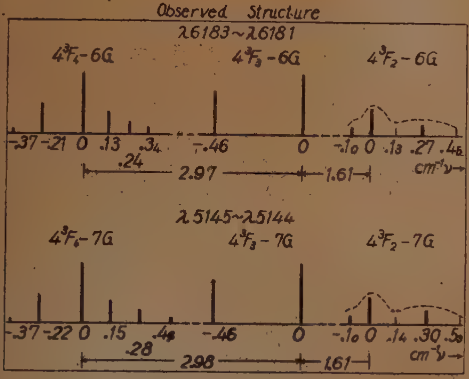

Fig. 4. Observed hfs. 4^3F nG.

$$\boldsymbol{K}=\boldsymbol{I}+\boldsymbol{s}. \tag{2}$$

(This scheme will be hereafter called the $(K\text{-}j_g)$ scheme for brevity.) Eigen values of H are given by $(5/4)a$ and $-(7/4)a$ for all values of F according as $K=3$ and 2 (namely $\boldsymbol{I}$ and $\boldsymbol{s}$ are parallel and antiparallel), respectively. The levels having these two energy values can be regarded as the above-mentioned nG^+ and nG^-, the mutual distance being given by $3a$. Then the numerical value of a, the coupling constant between $\boldsymbol{I}$ and $\boldsymbol{s}$, was obtained from the observed doublet separation of 4^1F_3-nG. Taking the mean of the values given in Table I, for $n=6$, 7 and 8, we obtain

$$3a=(0.499+0.001)\ \text{cm}^{-1}$$
$$a=(0.1663+0.0003)\ \text{cm}^{-1}.$$

(ii) *Structure of* 4^3F. The hfs. of 4^3F can be expressed approximately by the following splitting constants:

$$A(4^3F_3)=a/8,\ A(4^6F_3)=a/24,\ A(4^3F_2)=-a/6, \tag{3}$$

since the hfs. splitting will be only due to the 3s-electron. But in view of the circumstance that the $3s4f\,^3F$ is perturbed by other electron configurations (mainly by the $3p3d$-configuration)(8), the values given in (3) should be used only for the purpose of estimation and so the constants $A(4^3F_J)$ were empirically determined as described in the following discussion. (see (iv)). Further, the deviation from Landé's interval rule, which is caused by the repulsive perturbation between the levels of the same hfs. quantum number F arising from each of 4^3F_J, must be taken into consideration, since the triplet separations of 4^3F are not very large. The magnitude of this deviation, $\delta\nu$, was calculated for all pairs of levels, being found to be of the order of 0.01 cm⁻¹.

(iii) *Intensity.* In order to explain the observed structure theoretically, the intensities of the fine structure components must be calculated. The method of the calculation was similar to that adopted in the case of 4^3P-n^3D. Each of the two levels nG^+ and nG^-, described in (i) is two-fold degenerate and can be characterized for example by the two possible quantum number 9/2 and 7/2 of j_g. Thus the hyperfine energy states of nG can be represented by $\Psi^F(K,j_g)$ ($K=3$ or 2; $j_g=9/2$ or 7/2; $F=K+j_g,\ K+j_g-1,\ \ldots,\ |K-j_g|$) in the $(K\text{-}j_g)$ scheme. The wave function $\Psi^F(K,j_g)$ is given by a linear combination of the wave functions of the $(L\text{-}S)$ coupling scheme, $\Psi^F(J,S)$:

$$\Psi^F(K,j_g)=\Sigma_{J,S}\,M^F(K,j_g;J,S)\,\Psi^F(J,S)$$

The transformation matrix $M^F=((M^F(K,j_g;J,S)))$ was obtained as follows. First the matrix S_1^F which represents the transformation from the $(K\text{-}j_g)$ scheme to the $(J\text{-}J)$ scheme was calculated by diagonalizing H which was described in (i). Then, since the matrix S_2^F representing the transformation from the $(J\text{-}J)$ to the $(L\text{-}S)$ scheme is known by the general formulae(9), M^F was easily obtained by the matrix product $S_1^F\times S_2^F$. Transition probability from the upper state $\Psi^F(K,j_g)$ to the final state of $4^{1,3}F$ characterized by the quantum numbers J',

S' and F' (e.g. $S'=0$ for 4^1F, $S'=1$ for 4^3F) is given by the following expression (except a constant factor):

$$I(K,j_g,F;J',S',F')=(2F+1)\,\xi(F,F')\\ \times|\textstyle\sum_{J,S}M^F(K,j_g;J,S)A(J,S,F;J',S',F')|^2,$$

where $\xi(F,F+1)=(F+1)(2F+3)$, $\xi(F,F)=F(F+1)$ and $\xi(F,F-1)=F(2F-1)$. The matrix element $A(J,S,F;J',S',F')$, which corresponds to the transition $(J,S,F)\rightarrow(J',S',F')$, is, as in the case of 4^3P-n^3D, obtained by the well known formulae for multiplet intensity in the $(L\text{-}S)$ scheme⁽⁹⁾. Finally, the required relative intensity $I^{\pm}(J',S',F')$ of the component due to the transition from either of nG^+ or nG^- to the hyperfine level (J',S',F') of $4^{1,3}F$ is given by the sum of $I(K,j_g,F;J',S',F')$ over all the possible values of j_g and F:

$$I^{\pm}(J',S',F')=\textstyle\sum_{j_g,F}I(K,j_g,F;J',S',F')$$

All these quantities can be calculated numerically.

(iv) *Comparison with the calculation.* As was mentioned above, the hfs. of $4^{1,3}F-nG$ is independent of n. The mean of the observed structure for $n=6$ and 7 is given in Fig. 5.

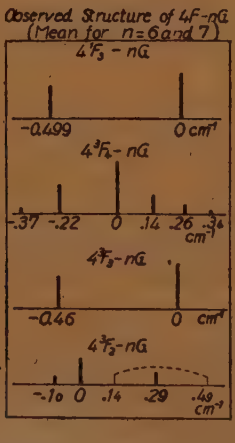

Fig. 5. Observed hfs. of $4^{1,3}F-nG$ of Al II.

4^3F_4-nG: In the calculation of the fine structure of this line, the value of $A(4^3F_4)$ was determined so as to get best agreement between theory and experiment, and it was found that $A(4^3F_4)\fallingdotseq0.021$ cm⁻¹. The structure calculated using this value of $A(4^3F_4)$ and applying the correction δ_μ that was mentioned in (ii) is shown in Fig. 6. The value of $A(4^3F_4)=0.021$ cm⁻¹ mentioned above agrees well either with that given by (3), namely $a/8=0.0208$ cm⁻¹, or with $(a/8)\times(35/36)=0.0202$ cm⁻¹ which is the value corrected taking into account the perturbation of $3p3d\,^3F$.

4^3F_3-nG: Owing to the smalless of $A(4^3F_3)$, the detailed fine structure of 4^3F_3 could not be resolved. According to our calculation, 4^3F_3-nG should be approximately a doublet, the separation being smaller than that of 4^1F_3-nG. The amount of this decrease of the doublet separation was found to be given approximately by $2A(4^3F_3)$. If the observed data only are considered, it seems that $A(4^3F_3)=0.02$ cm⁻¹. But it must be borne in mind that the error involved in measuring the doublet separation of 4^3F_3-nG has a large influence upon the value of $A(4^3F_3)$ determined in a purely empirical way. In fact, when $A(4^3F_3)=0.02$ cm⁻¹, the total separation of 4^3F_3 becomes 0.35 cm⁻¹, which does not coincide with the observed line breadth. Therefore, taking into account that both $A(4^3F_4)$ and $A(4^3F_2)$ determined experimentally agree with the values given by (3) or with those corrected by the consideration of the perturbation of the $3p3d$-configuration, we preferred the value $A(4^3F_3)=(a/24)\times(35/36)=0.0067$ cm⁻¹. In Fig. 6. is given the structure calculated for this value of $A(4^3F_3)$. In this case the distance between the centres of gravity of the group $4^3F_3-nG^+$ and $4^3F_3-nG^-$ becomes 0.486 cm⁻¹, which is slightly larger than the observed value. Thus, though $A(4^3F_3)$ could not be determined accurately, the observed structure has been at least qualitatively explained.

4^3F_2-nG: As in the case of $A(4^3F_4)$, the value of $A(4^3F_2)$ was found to be -0.029 cm⁻¹. In Fig. 6 the structure calculated for this value is given. The value -0.029 cm⁻¹ of $A(4^3F_2)$ agrees with that given by (3), namely $-a/6=-0.0277$ cm⁻¹, within experimental error.

§ 5. Conclusion.

As a concluding remark, one may say that the problem proposed in the introduction has been fully clarified by our investigation of the hfs. of the 4^3P-n^3D and $4^{1,3}F-nG$ series of Al II.

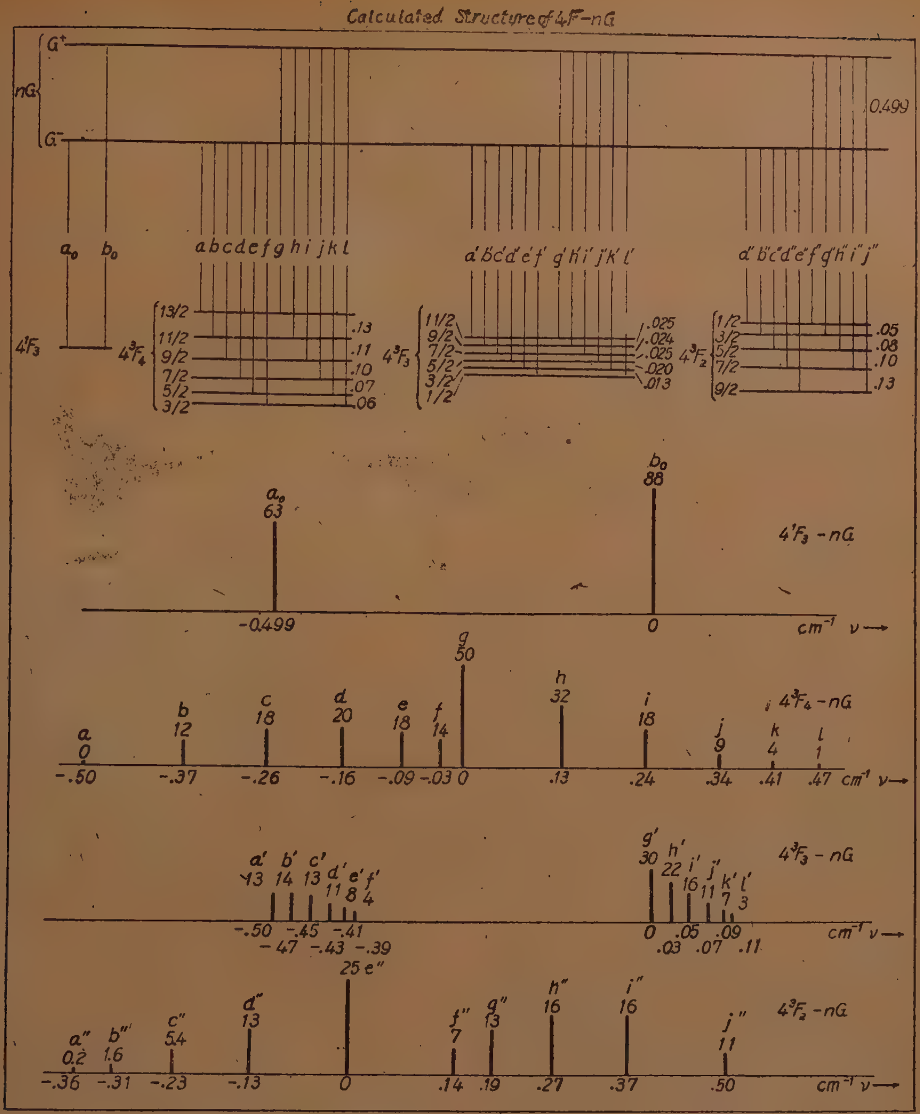
Calculated Structure of 4F–nG
G⁺
nG
G⁻
0.499
a₀ b₀
a b c d e f g h i j k l
a' b' c' d' e' f' g' h' i' j' k' l'
a" b" c" d" e" f" g" h" i" j"
4¹F₃
4³F₄ 13/2 11/2 9/2 7/2 5/2 3/2
.13 .11 .10 .07 .06
4³F₃ 11/2 9/2 7/2 5/2 3/2 1/2
.025 .024 .025 .020 .013
4³F₂ 1/2 3/2 5/2 7/2 9/2
.05 .08 .10 .13
a₀ 63
b₀ 88
4¹F₃ – nG
-0.499 0 cm⁻¹ ν→
4³F₄ – nG
a 0, b 12, c 18, d 20, e 18, f 14, g 50, h 32, i 18, j 9, k 4, l 1
-.50 -.37 -.26 -.16 -.09 -.03 0 .13 .24 .34 .41 .47 cm⁻¹ ν→
4³F₃ – nG
a' 13, b' 14, c' 13, d' 11, e' 8, f' 4, g' 30, h' 22, i' 16, j' 11, k' 7, l' 3
-.50 -.45 -.41 -.47 -.43 -.39 0 .05 .09 .03 .07 .11 cm⁻¹ ν→
4³F₂ – nG
a" 0.2, b" 1.6, c" 5.4, d" 13, e" 25, f" 7, g" 13, h" 16, i" 16, j" 11
-.36 -.31 -.23 -.13 0 .14 .19 .27 .37 .50 cm⁻¹ ν→

Fig. 6. Calculated hfs. of $4^{1,3}F-nG$ of Al II.

It might also be remarked that from the value of a obtained in § 4(i) the magnetic moment of Al^{27} could be calculated by the formula which is due to Goudsmit(10) and to Fermi-Segrè(11), and obtained $\mu = (3.62 \pm 0.01)$ n.m. This value agrees well with the value 3.6408±0.0004 n.m. which was determined by the magnetic resonance method(12).

In conclusion the writer wishes to express his sincere thanks to Professor K. Murakawa for his cordial and continued guidance throughout this work. Thanks are also due to Professor M. Kiuchi who took deep interest in this work.

References.

(1) S. Suwa: Phys. Rev. **76** (1949), 874.

(2) S. Suwa: Rep. of the Inst. of Sci. and Tech. **3** (1949), 268.

(3) R.A. Sawyer u. F. Paschen: Ann. d. Phys. [4] **84** (1927), 1.
F. Paschen u. R. Ritschl: Ann. d. Phys. [5] **18** (1933), 863.
F. Paschen: Sitz. Preuss. Akad. Wiss. **23** (1932), 502.

(4) S. Goudsmit and R.F. Bacher: Phys. Rev. **43** (1933), 894.

(5) S. Suwa: Phys. Rev. **78** (1950), 810.

(6) P. Güttinger u. W. Pauli: Zeits. f. Phys. **67** (1931), 749.

(7) M. Heyden u. R. Ritschl: Zeits. f. Phys. **108** (1938), 739.

(8) N.G. Whitelaw: Phys. Rev. **44** (1933), 544.
(9) e.g. E.U. Condon and G.H. Shortley: *The Theory of Atomic Spectra*, Cambridge, (1935).
(10) S. Goudsmit: Phys. Rev. **43** (1933), 637.
(11) E. Fermi u. E. Segrè: Zeits. f. Phys. **82** (1933), 729.
(12) J.E. Mack: Rev. of Mod. Phys. **22** (1950), 64.

JOURNAL OF THE PHYSICAL SOCIETY OF JAPAN, VOL. 6, NO. 4 JULY.-AUG., 1951.

Reactions of Barium Film with Oxygen. I.

By Akio KOBAYASHI and Saburo FURUYA.
Matsuda Research Laboratory, Tokyo-Shibaura Elec. Co., Kawasaki, Kanagawa-ken.

(Received September 17, 1950)

§1. Introduction.

It was found by Y. Ota,(1) that the reaction rate of a fresh film of barium with oxygen was independent on temperatures. He called this stage the early stage of the reaction. During the early stage the rate varied proportionally to pressure, then after that, slow and temperature dependent reaction, i.e. the final stage of the reaction, followed. He found also that the reaction rate of the final stage varied proportionally to the square root of pressure and had the activation energy of 17 to 20 Kcal/mol.

T. Arizumi and S. Kotani(2) found that preheating of getter films was very effective for the total adsorbed amount during the early stage. Thus there is the sintering phenomenon of a deposited granular film.

The authors studied the dependence of reaction rate on pressure, temperature and already reacted amount.(3)

§2. Experimental Methods.

Ota's methods of constant flow and constant volume were used. Fig. 1 shows the apparatus where G is a getter chamber of dia. 3 cm. Before flashing a getter greaseless stopcocks S$_4$, S$_5$ and S$_6$ were open for over-all evacuation, then the reaction chamber were heated above 300°C until pressure reached 3×10^{-8} mmHg.

A barium getter was mounted on the sphere of the bulb G. Two kinds of the getter were used, one of which was iron tubes containing barium metal, the other was barium berylliate mixed with zirconium powder. By heating the getter barium metal was deposited on the wall of the bulb.

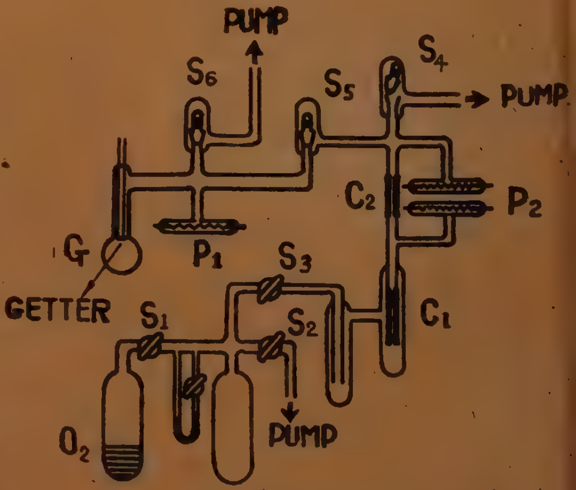

Fig. 1. Apparatus. G is the getter bulb, S$_4$, S$_5$ and S$_6$ greaseless stopcocks, C$_1$ the capillary tube, C$_2$ the flowmeter tube, P$_1$ the Pirani gauge.

For the case of the constant flow method, S$_4$ and S$_6$ were closed and S$_5$ opened. Potassium permanganate was served for the source of oxygen gas. When S$_3$ is opened, the gas flows into the reaction chamber through a liquid oxygen trap and through a capillary tube C$_1$ to maintain the flow constantly.

A capillary tube C$_2$, which is 0.6 mm in radius and 65 mm in length, serves for a flow-meter which consists of two tungsten wires as two arms of the bridge of a Pirani gauge. The pressure difference of both ends of the capillary is directly shown by a micro-ammeter in the bridge. Flowing speed is given as follows

$$\Delta p \frac{r^3}{l} 4.64\times 10^{-3}\ \text{mol/sec},$$

where r is the radius of the capillary tube, l its length in cm., Δp is pressure difference in mmHg.

Constant volume method is realized by closing S_5 at certain pressure. On this case pressure is measured by a Pirani gauge P_1 using a galvanometer of 10^{-8} amp. The volume closed by S_5 is 135 cc.

§ 3. Results obtained.

(A) The early stage of the reaction.

When the gas flows constantly in the reaction chamber after the deposition of barium by getter flashing, pressure is maintained constantly during certain time, and then it begins to rise steeply. Fig. 2 shows this behaviour of reaction at −75°C for Sample 2.

According to Ota, we separate the early stage from the final one at the point where the pressure begins to rise steeply. In the early stage, velocities of gas-flow q have equilibrium pressures p_{equil}, thus the reaction velocities s are equal to q.

Equilibrium pressures vary with flowing speed as shown in Fig. 3 and almost proportionally as shown in Fig. 4. Then we have the relation

$$s = k_1\, p_{equil} \quad \ldots\ldots\ldots\ldots\ldots\ldots\ldots\ldots(1)$$

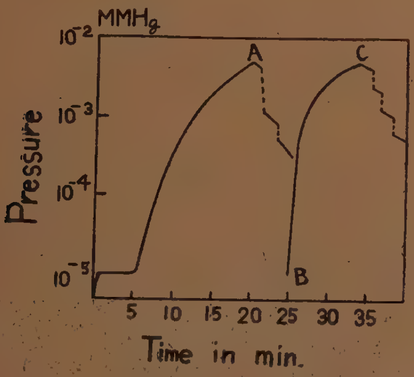

Fig. 2. Reaction at −75° C. O–A for constant flow, A–B and C– for constant volume method.

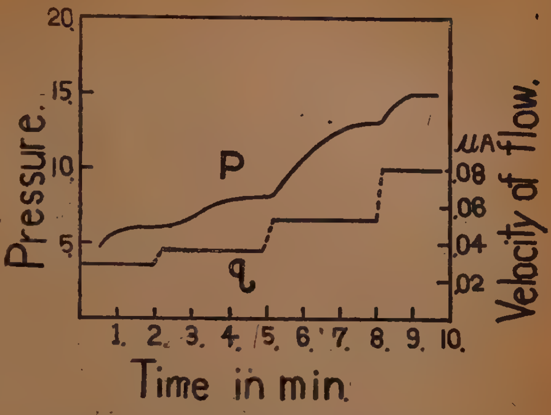

Fig. 3. Curve p is the equilibrium pressures and Curve q is the flowing speeds.

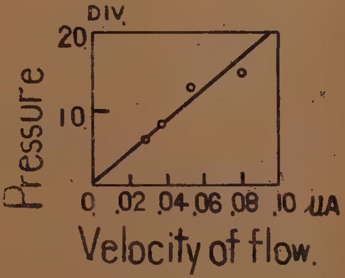

Fig. 4. Flowing speed versus equilibrium pressure in the early stage of the reaction.

The reaction velocities s in mol per sec. per sq. cm. are shown on Col. 7 in Tab. 1, p_{equil} on Col. 8 and the specific rate of the reaction as monomolecular reaction in cc. per sq. cm. per sec. on Col. 9. The total reacted quantities Q during the early stage shown on Col. 4 are mainly dependent on pressure at getter flashing and somewhat dependent on temperatures of the wall. Dividing Q by the geometrical area of barium film and by 5.38×10^{-10} mol which is the value per sq. cm. for the (100) net plane of barium oxide crystal, the apparent numbers of atomic layers of BaO crystal are obtained as shown on Col. 5.

Equilibrium pressures were almost constant when the getter bulb was cooled from 170° to −183° C. Therefore, the activation energy of the specific rates is almost null. It is plausible that chemical adsorption is the rate determining stage in the early stage, because the smallest number of layers

Table 1.

1	2	3	4	5	6	7	8	9	10
	Kind	Pressure at flashing mmHg.	Q in mol.	Apparent number of layers	Temperature at flashing	Flowing speed $10^{-11}\frac{\text{mol.}}{\text{sec. cm}^2}$	Equilibrium pressure mmHg.	Specific rate of reaction cc./sec.cm².	Area of bulbs cm².
1	tube	10^{-1}	3.90×10^{-6}	620	16° C	5.9	2.2×10^{-4}	4.9	107
2	tube	10^{-2}	1.08×10^{-7}	6.3	16° C	1.3	1×10^{-6}	26	28.3
3	tube	10^{-2}	2.05×10^{-7}	13	20° C	1.4	1.7×10^{-5}	14	28.3
4	tube	10^{-3}	2.90×10^{-8}	2.0	20° C	0.85	2.6×10^{-5}	6.0	28.3
5	berylliate	10^{-2}	1.30×10^{-7}	8.5	100° C	0.82	5.1×10^{-5}	3.0	28.3
6	berylliate	5×10^{-4}	1.75×10^{-8}	1.2	170° C	0.52	1.1×10^{-5}	8.4	28.3

observed is 1.2 and the values of the specific rate are near to the calculated one in Section 7.

When pressure at getter flashing is higher and hence the mean free path is small compared to the radius of the bulb, collisions of barium atoms result porous and granular structure of the metal film which causes the enhancement of adsorbed amount.

(B) The final stage of the reaction.

If the stopcock S_5 is closed, say, at the point A in Fig. 2, pressure begins to decrease under the method of constant volume. In order to maintain the thickness of the reacted material constantly, the greaseless stopcock S_6 is open stepwisely and reactions must be done only in the small time intervals.

Reaction rate from A to B in Fig. 2 can be expressed by the following equation

$$-\frac{v}{aRT}\frac{dp}{dt} = k_2 p^{\frac{4}{5}}, \quad \dots\dots\dots(2)$$

where a is the area of the getter film and v the volume of the reaction chamber. But increasing the amount reacted, there appears the equation of the reaction rate that

$$-\frac{v}{aRT}\frac{dp}{dt} = k_3 p. \quad \dots\dots\dots(3)$$

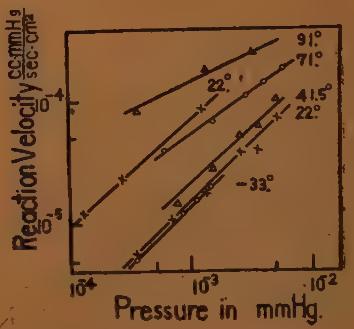

Fig. 5. The reaction velocity versus pressure for Sample 4. (1) −33° C, (2) 22° C, (3) 53° C, (4) 91° C, (5) 71° C, (6) 57° C, (7) 41.5° C, (8) 22° C.

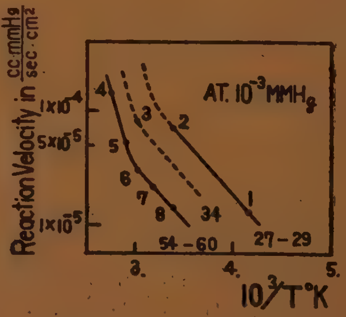

Fig. 6. Velocity versus $1/T°K$ at 10^{-3} mmHg.

Dependence of the reaction rate on temperature and pressure was next measured. Fig. 5 shows $vdp/dt + vs\ p$ plot for Sample 4. The pressure dependences of velocity are proportional to p for (1), (2), (6), (7) and (8), to $p^{\frac{5}{3}}$ for (3), (5) and to $p^{\frac{1}{2}}$ for (4). Fig. 6 shows velocity $vs. 1/T$ plot at the pressure 10^{-3} mmHg. Three curves correspond to 27~29, 34 and 54~60 atomic layers respectively. The curve (4) (5) (6) (7) (8) in Fig. 6 is represented by the following eq.

$$-\frac{v}{aRT}\frac{dp}{dt} = k_3 p + k_4 p^{\frac{1}{2}}, \quad \dots\dots(4)$$

where

$$k_3 = C_3 e^{-\frac{E_3}{RT}}, \qquad k_4 = C_4 e^{-\frac{E_4}{RT}}.$$

We obtained

$$E_3 = 4.6 \text{ Kg-cal} \quad \text{for Sample 4,}$$
$$= 8.0 \text{ Kg-cal} \quad \text{for Sample 6,}$$

and

$$E_4 = 23 \text{ Kg-cal} \quad \text{for Sample 4,}$$
$$= 32 \text{ Kg-cal} \quad \text{for Sample 6,}$$

and $C_4 \gg C_3$.

Reaction velocities below −50° C have generally very small value of activation energy of about 300 to 1800 cals.

§ 4. Relations between reacted amount and reaction rate.

Plotting the velocity versus the apparent number of the atomic layers of the oxide at 10^{-3} and 6×10^{-3} mmHg, we obtained the curves in Fig. 7 and thus the following equation hold that

$$-\frac{v}{aRT}\frac{dp}{dt} = \frac{K}{X^m}p\,, \quad \ldots\ldots\ldots\ldots(5)$$

where m is 1.07 for 10^{-3} mmHg and 1.3 for 6×10^{-3} mmHg. This is the reaction at −75° C, but at higher temperature, 170° C, velocities vary inversely proportionally to X^4.

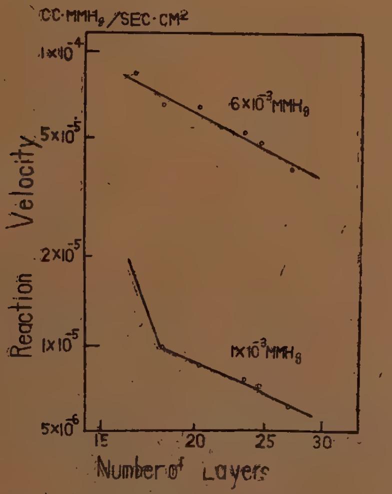

Fig. 7. Reaction velocity versus number of atomic layers.

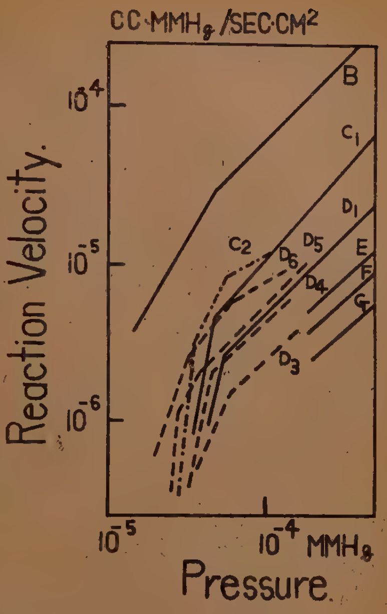

Fig. 8. Velocity versus pressure plot for Sample 6. Reacted amounts increase from C to G.

§ 5. Does the peroxide BaO_2 coexist with?

In order to verify the coexistence of peroxide, decomposition pressure of BaO_2⁽⁴⁾, which produced by heating the oxide at 1 mmHg of oxygen, was measured. The decomposition pressure is about 5×10^{-5} mmHg at room temperature and has activation energy of 18 Kg-cal. In the measured range of pressure and temperature, therefore, there exists the possibility of coexistence of BaO and BaO_2, but we may conclude that the peroxide, even if it coexists with, contributes scarcely for the reaction process, because no anomaly of the reaction velocity happens in passing over the pressure corresponding to the decomposition pressure.

§ 6. Critical pressure.

Curves in Fig. 8 show vdp/adt vs. p plots for Sample 6, where the reacted amounts increase from C to G. The curves have kinks where velocities decrease rapidly. Pressures at the kinks are critical pressures where the diffusion of gas molecules into the oxide becomes very slow and reaction system reaches nearly equilibrium state.

Critical pressures, therefore, increase with total reacted amount and decrease with temperature. Those have the activation energy of 5 Kg-cal per mol for the range 100° C to 170° C and 1 Kg-cal for the range −183 to 0° C.

§7. Discussions of the results.

The decomposition of oxygen molecules on the barium metal surface is rate determining in the early stage, for its temperature dependence is negligible and its specific rate is of the order of unity. If molecules are adsorbed on the lattice points on the surface of the metal, according to the following process that $O_2 \rightarrow 2O$ on the surface in an activated state → BaO in the final, the specific reaction rate k is given by the equation⁽⁵⁾

$$k = 2C_s \frac{\sigma}{\sigma_+} \frac{h^4}{8\pi^2 I (2\pi mkT)^{\frac{3}{2}}} e^{-\frac{E}{RT}}, \quad \dots(6)$$

where C_s is the number of lattice points 2.74×10^{14} per sq. cm. for the (100) face, I is the moment of inertia of O_2 19.27×10^{-40}, σ and σ_+ are the symmetry number. Now putting $E=0$, $\sigma=2$, $\sigma_+=1$ and $T=290°$ K in Eq. (6), we have

$$k = 0.28 \text{ cc. per sec. per sq. cm} \quad \dots(7)$$

This calculated value is 10~100 times smaller than the observed one. This may be due to somewhat rotational freedom at the activated state and partly the effect of superficial roughness. For the large contraction of volume resulted by oxidation, this reaction may proceed upto few atomic layer of BaO.

The final stage of reaction consists of several processes:

(a) In the transient region where the rate having small temperature dependence varies with $p^{\frac{2}{3}} \sim p^{\frac{4}{5}}$ as Eq. (2). It seems that this reaction consists of mixture of two processes, in one of which the adsorption is the rate determining stage, in the other the decomposition of gas molecules on the oxide is the rate determining. The former is proportional to pressure and the latter proportional to the square root of pressure.

(b) In the next stage the rate varies proportionally to pressure as Eq. (3) or (5) and has the activation energy of 0.3 to 1.8 Kg-cal below about −50° C and that of 4.0 to 8.0 Kg-cal above −30° C.

For the remarkable dependence of the reaction on the reacted amount and for its small activation energy, we may conclude that the diffusion of adsorbed molecules through grain boundaries of the oxide is the rate determining stage. Thus the diffusion velocity s is given by the equation

$$s = D_m \left(\frac{\partial n}{\partial x}\right)_X = -\frac{v}{aRT} \frac{dp}{dt}, \quad \dots(8)$$

where D_m is the diffusion coefficient of surface migration, n the concentration of adsorbed molecules. The distribution of concentration n is shown in Fig. 9, where the interface between the metal and the oxide is at the point O and that between the gas and the oxide is at X.

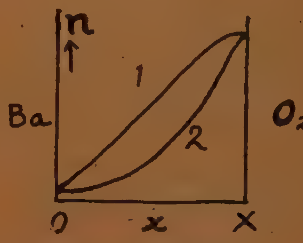

Fig. 9. Distribution of n in the oxide layer.

Introducing reduced units $n/n_X = c$, $x/X = Z$ in Eq. (8), it follows that

$$s = -\frac{v}{aRT} \frac{dp}{dt} = D_m \frac{n_X}{X} \left(\frac{\partial c}{\partial z}\right)_X, \quad (9)$$

where n_X is the value of n on the gas interface. n_X is nearly in equilibrium to the gas phase. Then, if the molecules cover the surface sparcely, it follows that

$$n_X = k_5 p. \quad \dots\dots\dots\dots\dots\dots(10)$$

Thus

$$s = -\frac{v}{aRT} \frac{dp}{dt} = D_m k_5 \frac{p}{X} \left(\frac{\partial c}{\partial z}\right)_X. \quad (11)$$

From the conditions of experiments c includes z, p, X and those initial values p_0, X_0. But, if X is not so different from X_0 in our conditions and c becomes nearly independent on p_0 after enough time to spend, Eq. (11) will have nearly the same from as Eqs. (3) or (5). This is the case in our conditions.

It is shown in Fig. 8 that the reaction rates include the initial conditions, so that curves C_1 and D_1, which are obtained by charging upto higher pressures, have smaller velocities respectively than curves C_2 and D_6 obtained by charging upto lower pressures. The distributions of n in the oxide on both cases are shown in Fig. 9, where Curve 1 corresponds to the former and Curve 2 to the latter. Hence it can be concluded by comparing those gradients at X that the rate of the latter is greater than the former. To avoid these complexity and ambiguity, one must take the method of constant pressure, one of which will be reported in the next paper.

(C) At higher temperatures, the rate varied with $p^{\frac{1}{2}}$ as the second term in Eq. (4) and had the large activation energy of 23~32 Kg-cal. It is plausible that the rate determining stage of this reaction is the diffusion of excess oxygen atoms through the barium oxide, because it occurs at higher temperatures and has sensitive dependence on the thickness of the oxide and its rate varies with the square root of pressure.

An oxygen molecule reacts on the surface of the oxide and makes two lattice defects of metal ions as follows

$$O_2 \rightarrow 2[B_a]_{\text{defect}} + 2[B_aO] .$$

From the mass action law it follows that

$$n_X = k_6\, p^{\frac{1}{2}} , \quad \ldots\ldots\ldots\ldots\ldots\ldots(12)$$

where n_X is the concentration of the defects on the gas interface. Then similarly to Eq. (9) the rate is given by the equation that

$$s = -\frac{v}{aRT}\frac{dp}{dt} = D_a k_5 \frac{p^{\frac{1}{2}}}{X}\left(\frac{\partial c}{\partial z}\right)_X , \quad (13)$$

where D_a is the diffusion coefficient of the defects and c, z are reduced units similar to those in Eq. (9).

References.

(1) Y. Ota: unpublished.

(2) T. Arizumi and S. Kotani: J. Phys. Soc. Japan, **5**, (1950) 70.

(3) O. Tsukagosi: Kaken Hōkoku, **20**, (1950) 73.

(4) H. le Chatelier: Comt. Rend., **140**, (1905) 1252.

(5) S. Glasstone, K. J. Laidler and H. Eyring: "*The theory of rate processes*" (1941), 349, 373.

JOURNAL OF THE PHYSICAL SOCIETY OF JAPAN Vol. 6 No. 4 JULY—AUG., 1951.

On the Surface Layer of Liquid Argon.

By Takechiyo INOUYE.

Medical College, Tokyo Jikei-kai.

(Received September 21, 1950)

§1. Introduction.

Many attempts have been made to solve the mechanism of surface tension. The quasi-lattice model is available for liquid at the temperatures not far from melting point. With this model Harashima⁽¹⁾ obtained good results for the surface energies of several liquids. He calculated also the surface tensions on the assumption that the free volume and the frequency of oscillation of surface molecule were different from those of inner molecule. The radial distribution function is more frequently used, because it is obtained experimentally by X-ray scattering and the temperature of liquid need not be near melting point. Among many theories the most reliable and powerful is perhaps the one due to Kirkwood⁽³⁾. Though the numerical calculation was made only for the liquid argon when the physical transition zone shrank to mathematical surface, his formulae for surface tension are sufficiently general and adequate for the calculation when the distribution of molecules in the surface layer differs from that in bulk. Following his theory the writer has calculated the surface tension and surface energy assuming that the liquid has the distinct transition layer.

§ 2. Theory.

Betweeen the liquid phase α and gaseous phase β there is a phase transition zone, in which the Gibbs dividing surface is taken and is assumed to be x-y plane, z axis being perpendicular to this directed from α to β. Define the densities $\rho_{\alpha\beta}$ by the relations, $\rho_{\alpha\beta}^{(1)} = \rho_\alpha^{(1)}$, $\rho_{\alpha\beta}^{(2)} = \rho_\alpha^{(2)} (z < 0)$, $\rho_{\alpha\beta}^{(1)} = \rho_\beta^{(1)}$, $\rho_{\alpha\beta}^{(2)} = \rho_\beta^{(2)} (z \geqq 0)$, $\rho_\alpha^{(1)}$ and $\rho_\beta^{(1)}$ being the densities of molecules in each homogeneous phase. The pair density $\rho^{(2)}$ is related to the radial distribution function $g^{(2)}$ by the equation, $\rho^{(2)} = \rho(z_1)^{(1)} \cdot \rho^{(1)}(z_1+z_{12}) g^{(2)}(z_1, \vec{R}_{12})$. With the superficial densities, $\rho_s^{(1)}(z) = \rho^{(1)}(z) - \rho_{\alpha\beta}^{(1)}$, $\rho_s^{(2)}(z, \vec{R}_{12}) = \rho^{(2)}(z, \vec{R}_{12}) - \rho_{\alpha\beta}^{(2)}$, the z_1- moments of $\rho_s^{(1)}$ and $\rho_s^{(2)}$ are defined:

$$[\Gamma_s^{(1)}]_\nu = \int_{-\infty}^{\infty} z_1^\nu \rho_s^{(1)}(Z_1) dZ_1,$$

$$[\Gamma_s^{(2)}]_\nu = \int_{-\infty}^{\infty} z_1^\nu (Z_1, \vec{R}_{12}) dZ_1, \quad (\nu = 0, 1, 2, \ldots). \tag{1}$$

Kirkwood's formulae for the surface tension γ and surface energy E^s are as follows:

$$\gamma = \int \frac{1}{R_{12}} \frac{dV}{dR_{12}} \left\{ z_{12} [\Gamma_s^{(2)}]_1 + \frac{1}{2} x_{12}^2 [\Gamma_s^{(2)}]_0 \right\} dv_{12}, \tag{2}$$

$$E^s = \frac{1}{2} \int V(R_{12}) \Gamma_s^{(2)}(\vec{R}_{12}) dv_{12}, \tag{3}$$

where $V(R_{12})$ is the potential between two molecules.

Now suppose that the liquid has the distinct surface zone of thikness ζ, the distribution function $g^{(2)}(\vec{R}_{12})$ in that zone is different from $g_\alpha^{(2)}$ and the density of molecules ρ is slightly lower than $\rho_\alpha^{(1)}$. Those are written by,

$$\begin{array}{lll} \rho^{(1)}(z) = 0, & g^{(2)}(z, \vec{R}_{12}) = 0 & (z > 0) \\ \phantom{\rho^{(1)}(z)} = \rho, & \phantom{g^{(2)}(z, \vec{R}_{12})} = g^{(2)}(\vec{R}_{12}) & (0 \geqq Z > -\zeta) \\ \phantom{\rho^{(1)}(z)} = \rho_\alpha^{(1)}, & \phantom{g^{(2)}(z, \vec{R}_{12})} = g_\alpha^{(2)}(R_{12}) & (-\zeta \geqq z), \end{array} \tag{4}$$

taking the boundary plane between gaseous phase and surface zone as $z = 0$, and assuming that the density $\rho_\beta^{(1)}$ is negligible.

From equation (4), the moments are now written as follows:

When $z_{12} \geqq 0$, $-z_{12} > -\zeta$,

$$\left.\begin{array}{l} [\Gamma_s^{(2)}]_\nu = (-1)^{\nu+1} \dfrac{z_{12}^{\nu+1}}{\nu+1} \rho_\alpha^{(1)2} g_\alpha^{(2)}(R_{12}) + (-1)^{\nu+1} \dfrac{z_{12}^{\nu+1} - \zeta^{\nu+1}}{\nu+1} \{\rho^{(2)} g^{(2)}(\vec{R}_{12}) - \rho_\alpha^{(1)2} g_\alpha^{(2)}(R_{12})\} \\ \qquad\qquad + (-1)^{\nu+1} \dfrac{\zeta^{\nu-1}(\zeta+z_{12})^{\nu+1}}{\nu+1} \rho_\alpha^{(1)} (\rho - \rho_\alpha^{(1)}) g_\alpha^{(2)}(R_{12}), \\ \text{when } z_{12} > 0,\ -z_{12} < -\zeta, \\ [\Gamma_s^{(2)}]_\nu = (-1)^{\nu+1} \dfrac{z_{12}^{\nu+1}}{\nu+1} \rho_\alpha^{(1)2} g_\alpha^{(2)}(R_{12}) + (-1)^{\nu+1} \dfrac{z_{12}^{\nu+1} - (\zeta+z_{12})^{\nu+1}}{\nu+1} \rho_\alpha^{(1)} (\rho - \rho_\alpha^{(1)}) g_\alpha^{(2)}(R_{12}), \\ \text{when } Z_{12} < 0, \\ [\Gamma_s^{(2)}]_\nu = (-1)^{\nu+1} \dfrac{(\zeta+z_{12})^{\nu+1} - \zeta^{\nu+1}}{\nu+1} \rho_\alpha^{(1)} \{\rho g^{(2)}(\vec{R}_{12}) - \rho_\alpha^{(1)} g_\alpha^{(2)}(R_{12})\} \\ \qquad\qquad - (-1)^{\nu+1} \dfrac{(\zeta+z_{12})^{\nu+1}}{\nu+1} \{\rho^2 g^{(2)}(\vec{R}_{12}) - \rho_\alpha^{(1)2} g_\alpha^{(2)}(R_{12})\}. \end{array}\right\} \tag{5}$$

Assume that ρ is constant throughout the surface zone, and put $\rho = (1+\varepsilon)\rho_\alpha^{(1)}$. Substitution (5) into (2) and (3) now yields

$$\begin{aligned} \frac{\gamma}{\pi \rho_\alpha^{(1)2}} = {} & \frac{1}{8} B_4 - \varepsilon\zeta \int_\zeta^\infty R^3 V' g dR - \frac{1}{4}(1+3\varepsilon)\zeta^2 \int_\zeta^\infty R^2 V' g dR + \frac{7}{24}(1+\varepsilon)\zeta^4 \int_\zeta^\infty V' g dR \\ & - \frac{1}{3}(1+2\varepsilon) \int_0^\zeta R^3 V' g dR - \frac{1}{8}(1+\varepsilon) \int_0^\zeta R^4 V' g dR + \frac{1}{2}\zeta^2 \int_0^\zeta R^2 V' g dR - \frac{1}{3}\zeta B_3 - \frac{1}{2}\zeta^2 B_2 \\ & + (1+\varepsilon)^2 H_1 - (1+\varepsilon)^2 \zeta^2 H_2 + (1+\varepsilon)^2 \zeta H_3 - (1+\varepsilon)^2 H_4 \\ & - \varepsilon(1+\varepsilon) K_1 - 2\varepsilon(1+\varepsilon)\zeta K_2 - (1+\varepsilon)^2 \zeta^2 K_3 + \varepsilon(1+\varepsilon) K_4 + (1+\varepsilon)^2 \zeta K_5, \end{aligned} \tag{6}$$

where

$$H_1 = \frac{1}{2\pi} \int_{(Z_{12}=\zeta\sim0)} R_{12}^{-1} V' z_{12}^2 g(\vec{R}_{12}) dv_{12}, \qquad H_2 = \frac{1}{2\pi} \int_{(Z_{12}=\zeta\sim0)} R_{12}^{-1} V' z_{12} g(\vec{R}_{12}) dv_{12},$$

$$H_3 = \frac{1}{2\pi} \int_{(Z_{12}=\zeta\sim0)} R_{12}^{-1} V' x_{12}^2 g(\vec{R}_{12}) dv_{12}, \qquad H_4 = \frac{1}{2\pi} \int_{(Z_{12}=\zeta\sim0)} R_{12}^{-1} V' x_{12}^2 z_{12} g(\vec{R}_{12}) dv_{12},$$

$$K_1 = \frac{1}{2\pi} \int_{(\theta=\pi/2\sim\pi)} R_{12}^{-1} V' z_{12}^3 g(\vec{R}_{12}) dv_{12}, \qquad K_2 = \frac{1}{2\pi} \int_{(\theta=\pi/2\sim\pi)} R_{12}^{-1} V' z_{12}^2 g(\vec{R}_{12}) dv_{12},$$

$$K_3 = \frac{1}{2\pi}\int_{(\theta=\pi/2\sim\pi)} R_{12}^{-1}V' z_{12}g(\vec{R}_{12})dv_{12}\,, \qquad K_4 = \frac{1}{2\pi}\int_{(\theta=\pi/2\sim\pi)} R_{12}^{-1}V' x_{12}^2 z_{12}g(\vec{R}_{12})dv_{12}\,,$$

$$K_5 = \frac{1}{2\pi}\int_{(\theta=\pi/2-\pi)} R_{12}^{-1}V' x_{12}^2 g(\vec{R}_{12})dv_{12}\,,$$

and
$$V' = dV/dR_{12}\,, \quad g \equiv g_\alpha^{(2)}(R_{12}), \quad g(\vec{R}_{12}) \equiv g^{(2)}(\vec{R}_{12}),$$

$$\frac{E^s}{\pi\rho_\alpha^{(1)2}} = -\frac{1}{2}D_3 - \zeta D_2 + \varepsilon\zeta\int_0^\infty R^2 VgdR - \frac{1}{2}(1+\varepsilon)\zeta^2\int_\zeta^\infty RVgdR + \frac{1}{2}(1+\varepsilon)\int_0^\zeta R^3 VgdR$$
$$-\zeta\int_0^\zeta R^2 VgdR + (1+\varepsilon)^2\zeta F_1 - (1+\varepsilon)^2 F_2 + (1+\varepsilon)^2\zeta G_1 + \varepsilon(1+\varepsilon)G_2\,, \tag{7}$$

where
$$F_1 = \frac{1}{2\pi}\int_{(z_{12}=\zeta\sim 0)} Vg(\vec{R}_{12})dv_{12}\,, \qquad F_2 = \frac{1}{2\pi}\int_{(z_{12}=\zeta\sim 0)} Vz_{12}g(\vec{R}_{12})dv_{12}\,,$$
$$G_1 = \frac{1}{2\pi}\int_{(\theta=\pi/2\sim\pi)} Vg(\vec{R}_{12})dv_{12}\,, \qquad G_2 = \frac{1}{2\pi}\int_{(\theta=\pi/2\sim\pi)} Vz_{12}g(\vec{R}_{12})dv_{12}\,,$$

and
$$B_\nu = \int_0^\infty R^\nu V' gdR, \qquad D_\nu = \int_0^\infty R^\nu VgdR.$$

§ 3. Functions used for calculation.

Eisenstein and Gingrich⁽³⁾ determined the radial distribution for liquid argon by their precise experiment. Kirkwood⁽⁴⁾ obtained theoretically the distribution function which was in good agreement with the experimental data. But in the calculation of surfaces tension he used the approximate function,

$$\begin{aligned} g(R) &= (a_1/R)^s \exp[(a_m/a_1)^t - (a_m/R)^t], && (0 \leqq R \leqq a_1) \\ &= 1 && (a_1 < R). \end{aligned} \tag{8}$$

This functions was first introduced in this theory of transport phenomena⁽⁵⁾, and is very useful especially when the first peak is a main part. These parameters are determined to fit the distribution from experiment and the equations,

$$p = \rho_\alpha^{(1)}kT - \frac{2\pi}{3}\rho_\alpha^{(1)2}B_3\,, \qquad \varDelta E_v = -2\pi N\rho_\alpha^{(1)}D_2\,, \tag{9}$$

where p is the pressure and $\varDelta E_v$ is the molar energy of vaporization. With a supplementary parameter b, the function,

$$\begin{aligned} g(R) &= b(a_1/R)^s \exp[a_m/a_1)^t - (a_m/R)^t], && (0 \leqq R \leqq a_1) \\ &= 1 && (a_1 < R) \end{aligned} \tag{10}$$

may be more convenient, though this is discontinuous at $R = a_1$ when $b \neq 1$.

Athough the consideration for the orientation of molecule is unnecessary for molecular liquids of argon type, the asymmetric distribution of surface molecules in the direction perpendicular to the boundary layer need be considered. Of course the molecules are not in static equilibrium in any way. When the gaseous and liquid phases, however, are in equilibrium, the nearest neighbours of a surface molecule may be found on the average on an ellipsoid of revolution compressed in z direction. An asymmetric distribution function,

$$\begin{aligned} g(\vec{R}_{12}) &= b\left(a_1/\sqrt{x_{12}^2 + y_{12}^2 + (1+\sigma)^2 z_{12}^2}\right)^s \exp\left[(a_m/a_1)^t - \left(a_m/\sqrt{x_{12}^2 + y_{12}^2 + (1+\sigma)^2 z_{12}^2}\right)^t\right], && (0 \leqq R_{12} \leqq a_1) \\ &= 1 &&, \ a_1 < R_{12}\,, \end{aligned} \tag{11}$$

will be used for the transition layer, where σ is a small correction parameter not exceeding a few percent. When the potential function is given by

$$V(R_{12}) = P/R_{12}^{12} - Q/R_{12}^6\,, \tag{12}$$

and the transformation of variables, $x_{12} = x$, $y_{12} = y$, $(1+\sigma)z_{12} = z$, $R_{12}^2 \doteqdot R^2 - 2\sigma z$, is made the equations (6) and (7) will be reduced to the following form, where σ- and ε-correction are separated in the first approximation.

σ-correction in γ:

$$\frac{\gamma}{\pi\rho_\alpha{}^{(1)^2}}=\frac{1}{8}B_1+\sigma\left(\begin{aligned}&-\frac{1}{10}\zeta^6\int_{(1+\sigma)\zeta}^{\infty}R^{-2}(14p+8q)g\,dR+\frac{1}{24}\zeta^4\int_{(1+\sigma)\zeta}^{\infty}(12p+6q)g\,dR\\&+\frac{1}{4}\zeta^2\int_{(1+\sigma)\zeta}^{\infty}R^2(10p+4q)g\,dR+\frac{1}{30}\zeta\int_{0}^{\infty}R^3(18p+6q)g\,dR\\&+\frac{1}{30}\zeta\int_{0}^{(1+\sigma)\zeta}R^3(18p+6q)g\,dR+\frac{1}{8}\int_{0}^{(1+\sigma)\zeta}R^4(8p+2q)g\,dR\\&-\frac{1}{4}\zeta^5V'(\zeta)g(\zeta)\end{aligned}\right) \tag{13}$$

where

$$p=-12P/R^{13},\qquad q=6Q/R^7.$$

σ-correction in E^s:

$$\frac{E^s}{\pi\rho_\alpha{}^{(1)^2}}=-\frac{1}{2}D_3+\sigma\left[\begin{aligned}&\zeta^4\int_{(1+\sigma)\zeta}^{\infty}R^{-1}\left(P/R^{12}-\frac{1}{2}Q/R^6\right)g\,dR+\zeta\int_{0}^{\infty}R^2(3P/R^{12}-Q/R^6)g\,dR\\&+\zeta\int_{0}^{(1+\sigma)\zeta}R^2(3P/R^{12}-Q/R^6)g\,dR-\int_{0}^{(1+\sigma)\zeta}R^3\left(2P/R^{12}-\frac{1}{2}Q/R^6\right)g\,dR\end{aligned}\right] \tag{14}$$

ε-correction γ:

$$\frac{\gamma}{\pi\rho_\alpha{}^{(1)^2}}=\frac{1}{8}B_1+\varepsilon\left[\begin{aligned}&\frac{1}{8}B_4-\zeta B_3+\frac{3}{4}\zeta^2B_2-\frac{7}{24}\zeta^4B_0+\frac{1}{4}\int_{0}^{\zeta}R^4V'g\,dR\\&+\frac{4}{3}\zeta\int_{0}^{\zeta}R^3V'g\,dR-\frac{3}{4}\zeta^2\int_{0}^{\zeta}R^2V'g\,dR+\frac{7}{24}\zeta^4\int_{0}^{\zeta}V'g\,dR\end{aligned}\right] \tag{15}$$

ε-correction in E^s:

$$\frac{E^s}{\pi\rho_\alpha{}^{(1)^2}}=-\frac{1}{2}D_3+\varepsilon\left[\begin{aligned}&-\frac{1}{2}D_3+3\zeta D_2+\frac{1}{2}\zeta^2D_1\\&-\frac{1}{2}\int_{0}^{\zeta}R^3Vg\,dR+\zeta\int_{0}^{\zeta}R^2Vg\,dR-\frac{1}{2}\zeta^2\int_{0}^{\zeta}RVg\,dR\end{aligned}\right] \tag{16}$$

§ 4. Parameters used for computation.

Kirkwood used the potential

$$V(R)=8.62\times10^{-8}/R^{11.4}-1.11\times10^{-10}/R^6 \tag{12a}$$

and found $a_1=4.50\,A$, $a_m=3.55\,A$, $s=7.0$, $t=14$ for liquid argon at 90°K. But the computed value of p in the equation of state (9) does not seem to be in good agreement with the experimental value. In the computation to follow, the potential of the type (12), with the experimental values $P=16.3\times10^{-8}$, $Q=1.07\times10^{-10}$ are used, which was obtained by Hirschfelder and others⁽⁶⁾, and it is found that the distribution function (11) with the parameter values,

$$a_1=5.02\,A,\quad a_m=3.54\,A,\quad s=5,\ t=12,\ b=0.9,$$

leads to the results more satisfactory. D_2 and B_3 are presented in Table I with the values expected from Eisenstein's experiment.

Table I.

	$D_2\times10^{12}$	$D_3\times10^{12}$	$B_3\times10^{12}$	$B_4\times10^{12}$
experiment	−0.828*		0.278	
cal. by Kirkwood	−0.737	−4.03	0.225	8.63
cal.	−0.844	−4.31	0.280	9.20

* molar energy of vapoarization ≃ 1590 cal./mol.

The radial distribution functions are shown in Fig. 1.

The radial distribution function (10) corresponding to the choice of parameters above mentioned has its first peak at $R_m = 3.81\,A$, and the first coordination number, when integrated to $R = 4.50$, is 9.8, both in good agreement with the experimental values.

5. Results and discussions.

Calculations of (13), (14), (15), (16), with these values of parameters lead to the results:

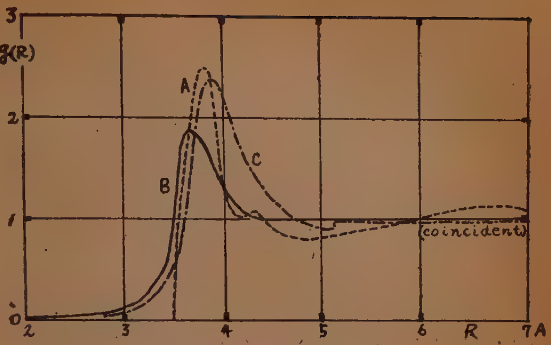

Fig. 1. Radial distribution functions for liquid argon at 90°K. Curve A from Eisenstein and Gingrich, curve B used by Kirwood for approx. cal., curve C used in this paper.

For $\zeta = 3.04\,A$,

$$\left.\begin{aligned} \frac{\gamma}{\pi \rho_\alpha{}^{(1)2}} &= 1.15\times 10^{-12}+\sigma(-36.3\times 10^{-12})+\varepsilon(-0.21\times 10^{-12}) \\ \frac{E^s}{\pi \rho_\alpha{}^{(1)2}} &= 2.16\times 10^{-12}+\sigma(3.42\times 10^{-12})+\varepsilon(-6.35\times 10^{-12}) \end{aligned}\right\} \qquad (17)$$

For $\zeta \doteqdot 5.0\,A$,

$$\left.\begin{aligned} \frac{\gamma}{\pi \rho_\alpha{}^{(1)2}} &= 1.15\times 10^{-12}+\sigma(-63\times 10^{-12})+\varepsilon(-6.6\times 10^{-12}) \\ \frac{E^s}{\pi \rho_\alpha{}^{(1)2}} &= 2.16\times 10^{-12}+\sigma(5.3\times 10^{-12})+\varepsilon(-12.6\times 10^{-12}) \end{aligned}\right\} \qquad (18)$$

The calculated values of γ and E_s for different σ and ε, when $\zeta = 3.04$ A, are presented in Table II, $\rho_\alpha{}^{(1)}$ being estimated as $2.13\times 10^{22}\,\mathrm{cm}^{-3}$ from Eisenstein's experiment.

Table II.

		γ (dyne/cm)	E^s (erg/cm²)
experiment		11.9	35
cal.	$\sigma=0.01,\ \varepsilon=-0.03$	11.2	34.0
	$\sigma=0.01,\ \varepsilon=-0.02$	11.2	33.1
	$\sigma=0,\ \varepsilon=0$	15.4	30.8

When $\zeta \doteqdot 5A$; $\gamma \doteqdot 8.6$, $E^s=35.1$ for $\sigma = 0.01$, $\varepsilon = -0.02$ and $\gamma = 9.6$, $E^s = 35.9$ for $\sigma = 0.01$, $\varepsilon = -0.03$.

For larger values of ζ, absolute value of coefficient of σ in γ, and that of ε in E^s increase, in which case the results are less adequate.

When the potential function (12a) is used instead of (12), the suitable choice of parameters in (10) leads to satisfactory values of D_2, D_3, B_3, B_4, differing only a few percent from those presented in the last row in Table I. The calculation of γ and E^s with these functions was not carried out to completion, but those made show that the results may not differ so much.

As the number of holes may be greater in the surface zone than in the fluid in bulk, it is justifiable that ε is negative, i.e. $\rho < \rho_\alpha{}^{(1)}$, but the absolute value of ε is not sure. Jura⁽⁷⁾ has suggested that the intermolecular distance of surface molecules should be about one percent larger than that of inner molecules for some solids. At any rate the assumption that $\varepsilon = -0.01 \sim -0.03$ is not so unreasonable. The supposition that liquids have distinct surface zones is not novel, and ζ-value obtained (3∼4A) agrees with the results of some writers⁽⁸⁾. Jura⁽⁷⁾ concluded from the calculation of surface energy of liquid argon and mercury that the surface zone should be about four molecule thick for the liquid, the intermolecular force of which was van der Waals type. In his case the distribution of molecules in surface zone was supposed to be the same as that of molecules in bulk, and it is expected the thickness may be more or less changed when the different distribution is used. There is no sufficient reason why the distribution in surface zone must be asymmetric as mentioned above and σ is nearly one percent, but the fact that the calculated values of γ and E^s for moderate ζ-, ε- and σ-values agree well with the experimental values, seems to support the assumption. As the potential function is not sufficiently precise and the distribution function is rough, there may be the objection that the calculation of correction terms on such a ground is not justifiable, but it may be mentioned that the calculation with another functions seems to lead to similar results, of which the numerical value may be different to some extent. It is desired to research for other liquids, and also is desired to compare the chemical potential of surface molecule with that of inner one as they are expected to be equal in an equilibrium state.

References.

(1) A. Harashima: Proc. Phys. Math. Soc. Japan, **22** 1940) 835; **23** (1941) 977:
(2) J. G. Kirwood and F. P. Buff: J. Chem. Phys., **17** (1949) 338.
(3) A. Eisenstein and N. H. Gingrich: Phys. Rev., **62** (1942) 261.
(4) J. G. Kirwood: J. Chem. Phys., **10** (1942) 394.
(5) J. G. Kirkwood: J. Chem. Phys., **17** (1949) 988.
(6) J. O. Hirschfelder, R. B. Bird and E. D. Spotz: J. Chem. Phys., **16** (1948) 968.
(7) G. Jura: J. Phys. and Colloid Chem., **52** (1948) 40.
(8) Raman and Ramdas: Phil. Mag., **3** (1927) 220.
J. Chem. Phys., **7** (1939) 818.

Recently J. C. Henniker (Rev. Mod. Phys., **21** (1949) 322) summarized many experimental data about the depth of the surface zone of liquid, but we think they are not applicable for our case as he mainly treated the orientation effected by solid surface using organic liquids.

JOURNAL OF THE PHYSICAL SOCIETY OF JAPAN Vol. **6** No. 4 JULY—AUG., 1951

On Some Exact Solutions of the Two-Dimensional Steady Flow of Compressible Fluid.

By Osamu SAITO.

Faculty of Engineering, Chuo University.

(Received September 21, 1950)

§1. Introduction.

In the previous paper we have proposed a new method for the solution of differential equations of two-dimensional steady flow of compressible fluid. In this paper we will discuss it minutely and show special cases.

§2. Fundamental equations.

Let ρ be the density, u and v two components of velocity along x and y axes respectively. For the irrotational flow, the velocity potential ϕ and the stream function ψ are given as follows:

$$\left.\begin{aligned} d\phi &= u dx + v dy, \\ d\psi &= -\rho v dx + \rho u dy. \end{aligned}\right\} \tag{1}$$

From these we obtain

$$\left.\begin{aligned} dx &= \frac{\cos\theta}{q} d\phi - \frac{\sin\theta}{\rho q} d\psi, \\ dy &= \frac{\sin\theta}{q} d\phi + \frac{\cos\theta}{\rho q} d\psi; \end{aligned}\right\} \tag{2}$$

where $q = \sqrt{u^2+v^2}$ and $\tan\theta = v/u$.

If we choose q and ψ as independent variables, equations (2) give

$$\left.\begin{aligned} \frac{\partial x}{\partial q} &= \frac{\cos\theta}{q}\frac{\partial\phi}{\partial q}, \\ \frac{\partial x}{\partial\psi} &= \frac{\cos\theta}{q}\frac{\partial\phi}{\partial\psi} - \frac{\sin\theta}{\rho q}, \end{aligned}\right\} \tag{3}$$

and

$$\left.\begin{aligned} \frac{\partial y}{\partial q} &= \frac{\sin\theta}{q}\frac{\partial\phi}{\partial q}, \\ \frac{\partial y}{\partial\psi} &= \frac{\sin\theta}{q}\frac{\partial\phi}{\partial\psi} + \frac{\cos\theta}{\rho q}. \end{aligned}\right\} \tag{4}$$

Since $\partial^2 x/\partial q\partial\psi = \partial^2 x/\partial\psi\partial q$ and $\partial^2 y/\partial q\partial\psi = \partial^2 y/\partial\psi\partial q$, we get following equations:

$$\left.\begin{aligned} \frac{\partial\phi}{\partial\psi} &= -\frac{q}{\rho}\frac{\partial\theta}{\partial q}, \\ \frac{\partial\phi}{\partial q}\frac{\partial\theta}{\partial\psi} - \frac{\partial\phi}{\partial\psi}\frac{\partial\theta}{\partial q} &= q\frac{d}{dq}\left(\frac{1}{\rho q}\right). \end{aligned}\right\} \tag{5}$$

These equations can be transformed as

$$\left.\begin{aligned} \frac{\partial\phi}{\partial\psi} &= -\frac{\partial\theta}{\partial w}, \\ \frac{\partial\phi}{\partial w}\frac{\partial\theta}{\partial\psi} - \frac{\partial\phi}{\partial\psi}\frac{\partial\theta}{\partial w} &= q\frac{d}{dw}\left(\frac{1}{\rho q}\right), \end{aligned}\right\} \tag{6}$$

where

$$w = \int\frac{\rho}{q}dq. \tag{7}$$

Consequently if we put

$$\phi = \frac{\partial F}{\partial w}, \quad \theta = -\frac{\partial F}{\partial\psi}, \tag{8}$$

the first equation of (6) will be satisfied automatically and the second may be transformed as follows:

$$\frac{\partial^2 F}{\partial w^2}\frac{\partial^2 F}{\partial\psi^2} - \left(\frac{\partial^2 F}{\partial w\partial\psi}\right)^2 = \frac{1}{\rho^2}\left(1+\frac{d\rho}{dw}\right) = f(w). \tag{9}$$

For adiabatic flow, we have

$$\rho = \left\{1-\frac{\gamma-1}{2}M^2(q^2-1)\right\}^{\frac{1}{\gamma-1}} \tag{10}$$

where γ is the ratio of specific heats, and M the Mach number of uniform flow at infinite distance, and the density and velocity at infinite distance are, for convenience, taken to be unity. Hence the right side member of (9) may be expressed as

$$f = \frac{1}{\rho^2}\left(1-\frac{q^2}{c^2}\right), \tag{11}$$

where c is the sound velocity and is expressed as follows:

$$c^2 = \frac{1}{M^2}\left\{1-\frac{\gamma-1}{1}M^2(q^2-1)\right\}. \tag{12}$$

§ 3. Critical condition.

From (2) we have, on a stream line $\psi = \text{const.}$,

$$dx = \frac{\cos\theta}{q}d\phi, \quad dy = \frac{\sin\theta}{q}d\phi. \tag{13}$$

Hence we know that the stream line has a cusp at the point where $d\phi$ changes its sign or velocity gradient diverges. But such a flow never occurs in reality because we can not neglect viscosity and heat conduction near this point. It is, therefore, a criterion of existence of potential flow that $d\phi$ does not vanish along any stream line. So the relation

$$\frac{\partial\phi}{\partial w} = 0 \text{ or } \frac{\partial^2 F}{\partial w^2} = 0 \tag{14}$$

holds along a stream line and on its cusp. On the other had $\partial^2 F/\partial\psi^2$ or $\partial\theta/\partial\psi$ does not diverge in general. Hence at the cusp the following relation holds:

$$\frac{\partial^2 F}{\partial w^2}\frac{\partial^2 F}{\partial\psi^2} = 0. \tag{15}$$

Then (9) gives

$$\frac{1}{\rho^2}\left(1-\frac{q^2}{c^2}\right) = -\left(\frac{\partial^2 F}{\partial w\partial\psi}\right)^2 \leqq 0 \tag{16}$$

or

$$q^2 \geqq c^2. \tag{17}$$

Hence it is only in a sonic or supersonic region that the velocity gradient diverges or a cusp occurs on a stream line. Furthermore, when the stream line is curved $\partial^2 F/\partial w\partial\psi = -\partial\theta/\partial w$ is not zero in general. Therefore in any curved flow velocity gradient diverges only in a supersonic region.

§ 4. The case when an intermediate integral exists.

If we solve the equation (9) under the condition that it has an intermediate integral, we obtain:

$$F = \pm\psi\int\frac{1}{\rho}\sqrt{\left(\frac{q}{c}\right)^2-1}\,dw + \alpha\psi + \chi(w), \tag{18}$$

where χ is an arbitrary function of w and α is an arbitary constant. F has a physical meaning only in the region:

$$q \geqq c. \tag{19}$$

Substituting (18) into (8), we obtain

$$\left.\begin{aligned} \phi &= \pm\frac{\psi}{\rho}\sqrt{\left(\frac{q}{c}\right)^2-1} + \chi', \\ \theta &= \mp\int\frac{1}{\rho}\sqrt{\left(\frac{q}{c}\right)^2-1}\,dw + \alpha, \end{aligned}\right\} \tag{20}$$

where $\chi' = \partial\chi/\partial w$. Inserting (20) in the first equations of (3) and (4) and integrating them, we obtain

$$\left.\begin{aligned} x &= x_0+(\psi/\rho q)[\pm\sqrt{(q/c)^2-1}\cdot\cos\theta-\sin\theta], \\ y &= y_0+(\psi/\rho q)[\pm\sqrt{(q/c)^2-1}\cdot\sin\theta+\cos\theta], \end{aligned}\right\} \tag{21}$$

where

$$\theta=-\alpha\mp[k\tan^{-1}\{k^{-1}\sqrt{(q/c)^2-1}\}-\tan^{-1}\sqrt{(q/c)^2-1}], \tag{22}$$

$$k^2 = (\gamma+1)/(\gamma-1), \tag{23}$$

and (x_0, y_0) is an arbitrary point on the stream line $\psi = 0$, x_0 and y_0 are given by the function $\chi(w)$ as follows:

$$x_0=\int\frac{\cos\theta}{q}\chi''\,dw,\quad y_0=\int\frac{\sin\theta}{q}\chi''\,dw. \tag{24}$$

It may be seen from (21) that the line on which w or q is constant is a straight line. The angle A between this line and the direction of velocity is given as follows. We make x-axis parallel to the direction of velocity at the point (x_0, y_0) considered. This is done by choosing such a value of α as θ vanishes. Then from (21) we obtain

$$\tan A=\pm1/\sqrt{(q/c)^2-1} \text{ or } \sin A=\pm c/q. \tag{25}$$

This relation shows that A is the Mach angle.

If we, for instance, take χ to be

$$\chi''=\mp(q/\rho)\sqrt{(q/c)^2-1}, \tag{26}$$

the stream line $\psi = 0$ is expressed as

$$x_0 = \sin\theta,\quad y_0 = -\cos\theta. \tag{27}$$

Therefore, this is a flow around a circular corner. (See Fig. 1 a, b) In these figures full lines are stream lines and dotted lines are Mach lines. In Fig. 1 b, certain stream lines have cusps and a thick line is the envelope of Mach lines.

In the general case when the stream line $\psi=0$ is given as $y_0=\Gamma(x_0)$, the relation between x_0 and θ takes the following form:

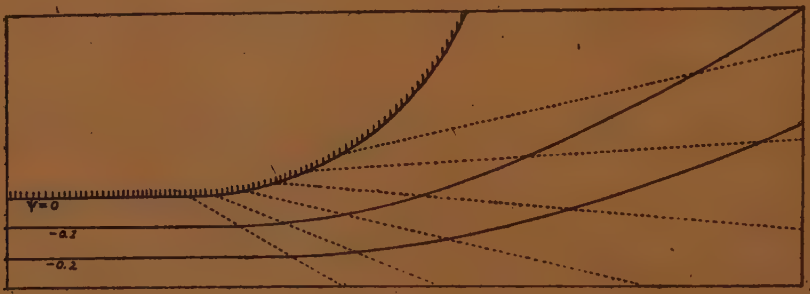

Fig. 1 a.

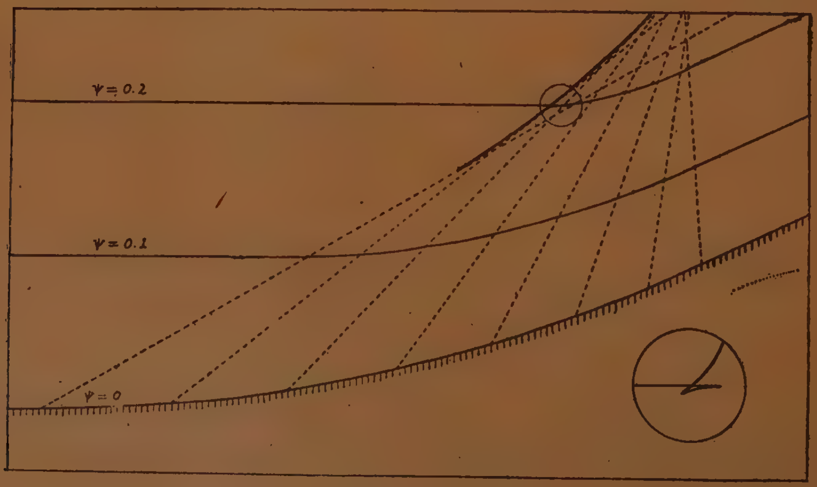

Fig. 1 b.

$$x_0 = g^{-1}\,(\tan\theta)\,, \tag{28}$$

where g^{-1} means the inverse function of $g(x_0) = dy_0/dx_0$. From (22) and (28) x_0 and also y_0 can be expressed as the functions of velocity q. Therefore we may obtain the stream lines by (21).

Consider, for example, the case when the stream line $\psi=0$ is given as $y_0 = e^{x_0}$. Then we get from (28)

$$x_0 = \log\tan\theta,\quad y_0 = \tan\theta\,. \tag{29}$$

Hence stream lines are given as follows:

$$\left.\begin{aligned} x &= \log\tan\theta+\frac{\psi}{\rho q}\left[\pm\sqrt{\left(\frac{q}{c}\right)^2-1}\cdot\cos\theta-\sin\theta\right],\\ y &= \tan\theta+\frac{\psi}{\rho q}\left[\pm\sqrt{\left(\frac{q}{c}\right)^2-1}\cdot\sin\theta+\cos\theta\right]. \end{aligned}\right\} \tag{30}$$

Fig. 2 represents these stream lines. No stream line can stretch infinitely to the right, but has an end point where the solution becomes imaginary, the local Mach number attaining unity. Certain stream lines have also cusps.

Consider again the flow where the stream line $\psi = 0$ is given as follows:

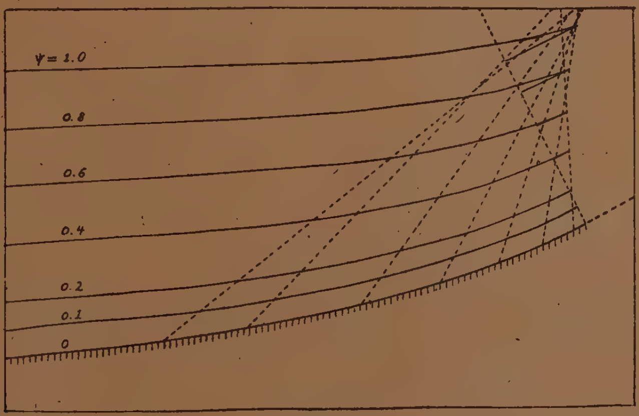

Fig. 2.

$$y_0 = \begin{cases} -1/x_0 & \text{for}\quad x_0 \leqq -3/2\,,\\ -4/27,\ x_0^2+1 & \text{for}\quad -3/2 \leqq x_0 \leqq 3/2\,,\\ 1/x_0 & \text{for}\quad 3/2 \leqq x_0 \end{cases} \tag{31}$$

Then we obtain from (28)

$$\left.\begin{aligned} &x_0=-\sqrt{\cot\theta},\ y_0=\sqrt{\tan\theta} && \text{for } x_0 \leqq -3/2\,,\\ &x_0=-(27/8)\tan\theta,\ y_0=-(27/16)\tan^2\theta+1 && \text{for } -3/2 \leqq x_0 \leqq 3/2\,,\\ &x_0=\sqrt{-\cot\theta}\,,\ y_0=\ -\tan\theta && \text{for } 3/2 \leqq x_0\,. \end{aligned}\right\} \tag{32}$$

These stream lines are given by (21) and shown in Fig. 3.

§ 5. Another solution.

Let us take a series $\sum\limits_{n=0}^{m} U_n\,\psi^n$ as F, then (9) is satisfied when $m = 1$, 2 or ∞. The solution which corresponds to $m = 1$ coincides with (18). The solution corresponding to $m = \infty$ will be discussed in the next paper. Here we will study the case when $m = 2$.

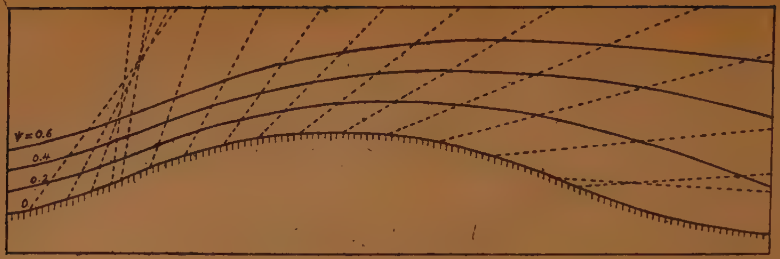

Fig. 3.

In this case the exact form of solution is shown as

$$F=\frac{(\psi+C)^2}{Aw+B}+\frac{1}{2}\int dw\int(Aw+B)fdw+D\psi+Ew+G, \tag{33}$$

where A, B, C, D, E and G are arbitrary constants. Inserting this in (8) we obtain

$$\left.\begin{aligned}\phi&=-\frac{A(\psi+C)^2}{(Aw+B)^2}+\frac{1}{2}\int(Aw+B)fdw+E,\\ \theta&=-\frac{2(\psi+C)}{Aw+B}-D,\end{aligned}\right\} \tag{34}$$

and then

$$\left.\begin{aligned}\frac{\partial x}{\partial q}&=\frac{\rho}{2q^2}\left\{\frac{4A^2(\psi+C)^2}{(Aw+B)^3}+(Aw+B)f\right\}\cos\left(\frac{2(\psi+C)}{Aw+B}+D\right),\\ \frac{\partial y}{\partial q}&=-\frac{\rho}{2q^2}\left\{\frac{4A^2(\psi+C)^2}{(Aw+B)^3}+(Aw+B)f\right\}\sin\left(\frac{2(\psi+C)}{Aw+B}+D\right).\end{aligned}\right\} \tag{35}$$

Here we may assume $B=C=D=0$ without any loss of generality. Hence

$$\left.\begin{aligned}\frac{\partial x}{\partial q}&=\frac{\rho}{2q^2}\left(\frac{4\psi^2}{Aw^2}+Awf\right)\cos\frac{2\psi}{Aw},\\ \frac{\partial y}{\partial q}&=-\frac{\rho}{2q^2}\left(\frac{4\psi^2}{Aw^3}+Awf\right)\sin\frac{2\psi}{Aw}.\end{aligned}\right\} \tag{36}$$

Integrating these equations, we get

$$\left.\begin{aligned}x&=\int_{q_0}^{q}\frac{\rho}{2q^2}\left(\frac{4\psi^2}{Aw^3}+Awf\right)\cos\frac{2\psi}{Aw}dq+P(\psi),\\ y&=-\int_{q_0}^{q}\frac{\rho}{2q^2}\left(\frac{4\psi^2}{Aw^3}+Awf\right)\sin\frac{2\psi}{Aw}dq+Q(\psi),\end{aligned}\right\} \tag{37}$$

were q_0 is an arbitrary constant, and P and Q are arbitrary functions of ψ, which are determined by the last equations of (3) and (4), namely

$$\left.\begin{aligned}P&=\left[-\frac{\psi}{qw}\sin\frac{2\psi}{Aw}-\frac{A(\rho+w)}{2\rho q}\cos\frac{2\psi}{Aw}\right]_{q=q}+a,\\ Q&=\left[-\frac{\psi}{qw}\cos\frac{2\psi}{Aw}+\frac{A(\rho+w)}{2\rho q}\sin\frac{2\psi}{Aw}\right]_{q=q_0}+b,\end{aligned}\right\} \tag{38}$$

where a and b are arbitrary constants.

The stream lines in the vicinity of $\psi=0$ are given by

$$\left.\begin{aligned}x&=\int_{q_0}^{q}\frac{\rho}{2q^2}wfdq+a,\\ y&=-\psi\int_{q_0}^{q}\frac{\rho f}{q^2}dq+\frac{\psi}{q_0}+b,\end{aligned}\right\} \tag{39}$$

where we choose $A = 1$. When $f = 1$, that is, the fluid is incompressible, (39) become

$$\left.\begin{aligned} x &= -\frac{1}{2}(1+w)e^{-w}, \\ y &= \psi e^{-w}, \end{aligned}\right\} \tag{40}$$

where arbitrary constants are assumed to be zero.

If we use a new variable z satisfying the relation

$$y = \psi z, \tag{41}$$

and eliminate w from (40), we obtain

$$x = -z(1-\log z)/2 \tag{42}$$

From (40) it is known that the velocity is zero at infinite distance. Fig. 4 represents these stream lines.

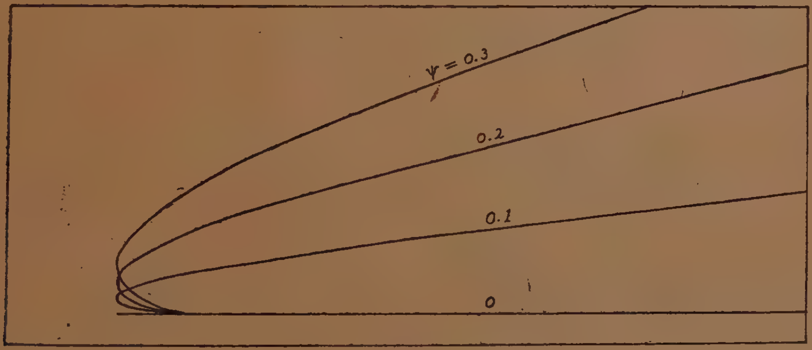

Fig. 4.

When f is not constant, that is, the fluid is compressible, f must be expressed as follows, corresponding to the zero velocity at infinite distance:

$$f = \left\{1 - \frac{\gamma+1}{2}q^2\right\}\left\{1 - \frac{\gamma-1}{2}q^2\right\}^{-\frac{\gamma+1}{\gamma-1}}. \tag{43}$$

This function changes its sign at the point where $q = \sqrt{2/(\gamma+1)}$. Therefore we know from (39) that the stream line has a cusp at that point. Fig. 5 shows these stream lines. The dotted line is the locus of cusps.

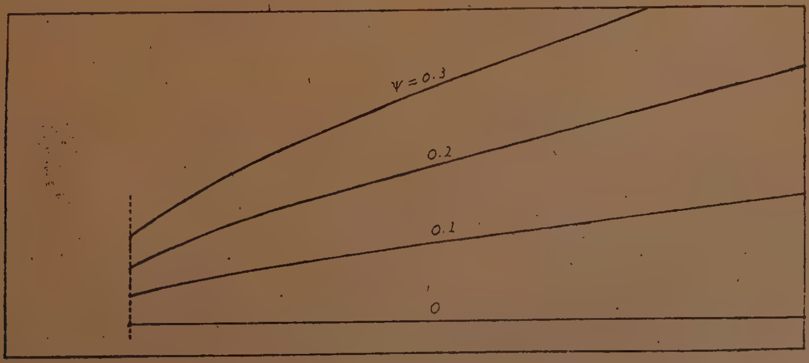

Fig. 5.

§ 6. Summary.

We obtain a new type of differential equations for the two-dimensional steady flow of compressible fluid, where we use velocity and stream function as independent variables. Two exact solutions are discussed, one of which represents supersonic flow and the other subsonic flow. We know that, in general, the infinity of velocity gradient or cusp of the stream line occurs only in the supersonic region so long as the stream line is curved.

The author wishes to thank Dr. A. Amemiya and Dr. I. Imai for their valuable advices.

Reference.

* O. Saito and A. Amemiya, Jour. Phys. Soc. Jap. 5 (1950), 201.

JOURNAL OF THE PHYSICAL SOCIETY OF JAPAN Vol. 6 No. 4 JULY—AUG., 1951

On the Relation between Creep and Vibrational Loss of Polymethylmetacrylate.

By Eiichi FUKADA.

Kobayashi Institute of Physical Research, Kokubunji, Tokyo.

(Received October 14, 1950)

Iwayanagi, Hideshima and Shibata¹⁾ have measured the torsional and flexural creep of polymethylmetacrylate and found the following relation between the shear strain y and the time t,

$$y = a + b\sigma \log(\theta + t) \tag{1}$$

where σ is the shearing stress, a and b are the numerical constants determined by the measurement and θ is an unknown constant, which has been introduced in order to avoid the dispersion of this formula at $t = 0$. Applying the Gross's method²⁾ to this formula they calculated the dispersion of Young's modulus with frequency.³⁾ The author calculated the vibrational loss by the same method and compared the theoretical and experimental results on both the Young's modulus and the vibrational loss.

From (1), it follows that

$$y(t) = y(0)[1 + C \log\{(\theta + t)/\theta\}] \tag{2}$$

where $y(0) = a + b\sigma \log\theta$ and $C = b\sigma/(a + b\sigma \log\theta)$. By the Gross's method the complex elastic modulus $E^* = E(1 + i \tan\delta)$ is derived from (2). Then the Young's modulus E and loss factor $\tan\delta$ are given by

$$E = E_\infty(1 + CA)/\{(1 + CA)^2 + (CB)^2\} \tag{3}$$

$$\tan\delta = CB/(1 + CA) \tag{4}$$

where E_∞ is the instantaneous Young's modulus and

$$A = \int_0^\infty \frac{\cos\omega t}{\theta + t} dt = -\cos\omega\theta \cdot \mathrm{Ci}(\omega\theta) - \sin\omega\theta \cdot \mathrm{si}(\omega\theta) \tag{5}$$

$$B = \int_0^\infty \frac{\sin\omega t}{\theta + t} dt = -\cos\omega\theta \cdot \mathrm{si}(\omega\theta) + \sin\omega\theta \cdot \mathrm{Ci}(\omega\theta). \tag{6}$$

Thus, when C and θ are given, E and $\tan\delta$ can be obtained by the numerical calculation at any frequency.

The value of C has been found to be 0.026 for torsion and 0.056 for bending from the experimental data by Iwayanagi and others.¹⁾ ³⁾ In the present case the numerical values $C = 0.08$ and $\theta = 0.8 \times 10^{-4}$ were found to be suitable to fit the theoretical curves to the measured values of loss factor and Young's modulus. The results are shown in Fig. 1. In the figure the solid line is the calculated curve and the ○ and × marks are the observed values. The instantaneous Young's modulus E_∞ is taken to be 5.5×10^{10}.[4)] The Young's modulus was obtained from the resonant frequency of the lateral vibration of the specimen and the loss factor was obtained by measuring the charge of the rectified damped current by the ballistic galvanometer.[5)] The dimension of the specimen was about 30 cm long, 2 cm wide and 0.6 cm thick for ○ mark, and about 15 cm long, 2 cm wide and 0.14 cm thick for × mark. The measuring temperature was both 22°C.

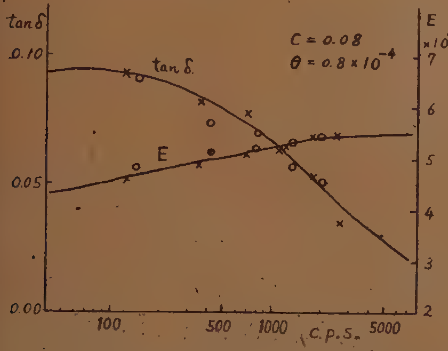

Fig. 1. Comparison between theoretical and experimental results on Young's modulus E and loss factor tan δ.

The agreement of theoretical and experimental results is good. The assumed value $C=0.08$ is of the same order of magnitude with the observed value $C=0.056$ by the flexural creep experiment. $\theta=0.8\times10^{-4}$ may be reasonable as it can not be observed in the creep experiment. Therefore, we can conclude that the vibrational loss of polymethylmetacrylate in the audiofrequency range is caused by the same mechanism as that of the static creep which shows the linear deformation with log t.

Now if the vibrational loss is related to the creep, we can expect the effect of the amplitude of the shear strain upon the vibrational loss. Fig. 2 shows the variation of loss factor due to the amplitude of strain at 357 c.p.s. and 19°C. We could follow the amplitude change of about 10^4 by measuring the half width of the resonance curve. The maximum shear strain at the loop of the lateral vibration corresponding to the amplitude 1 in the arbitrary unit of Fig. 2 is about 5.4×10^{-5}. The loss factor begins to decrease at about 5×10^{-8} of shear strain. This corresponds to 5×10^2 dyens/cm² of shear stress.

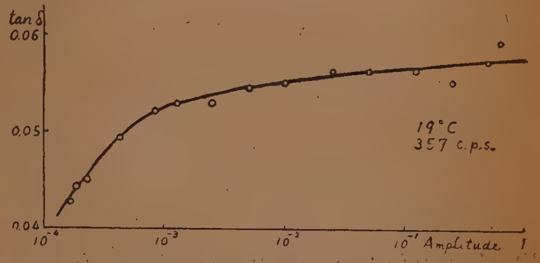

Fig. 2. Effect of the amplitude of strain on tan δ (in arbitrary unit).

The behaviour of a material exhibiting a viscoelasticity can be represented by the usual three element model. There a spring and a dashopt are connected in series and another spring is coupled with them in parallel. When the applied shearing stress is large we must take the Eyring's viscosity for the dashpot. Then the creep is linear with log t[6)] and the vibrational loss is relatively large and hardly depends on the amplitude of stress. When the applied shearing stress is sufficiently small we can take the Newtonian viscosity for the dashpot. Then the creep is represented by the form of $1-\exp(-\alpha t)$ and the vibrational loss is relatively small and does not depend on the amplitude of stress. In the medium magnitude of stress the Eyring's viscosity approaches to the Newtonian viscosity as the amplitude of stress decreases. Fig. 2 seems to show this gradual decrease of loss factor from the Eyring's viscosity to the Newtonian viscosity.

The author wishes to thank Dr. H. Kawai for his stimulating suggestions and discussions in this work.

Note added in proof. Lately the author has measured the flexural creep and stress relaxation on the same sample as used in vibration. The linearity with log t was observed in the shear strain of about 10^{-3}, which is of the same order as used by Iwayamagi and others, and C was found to be about 0.035 in both cases. This is inconsistent with the assumed $C=0.08$. As the shear strain in vibration test is less than 10^{-5}, it will be required to compare with the creep in such small strains.

References.

(1) K. Shibata, T. Hideshima and S. Iwayanagi: Rep. Sci. Res. Inst. **25**, (1949), 387. (in Japanese.)
(2) B. Gross: J. App. Phys. **18**, (1947), 212; **19**, (1948), 257.
(3) S. Iwayanagi, K. Shibata and T. Hideshima: Rep. Sci. Res. Inst. **26**, (1950), 44. (in Japanese.)
(4) W.C. Schneider and C.J. Burton: J. App. Phys. **20**, (1949), 48.
(5) E. Fukada: J. Phys. Soc. Japan. **5**, (1950), 321.
(6) A.V. Tobolsky and H. Eyring: J. Chem. Phys. **11**, (1943), 125.

JOURNAL OF THE PHYSICAL SOCIETY OF JAPAN, VOL. 6, NO. 4 JULY-AUG., 1951.

On the Magneto-Thermoelectric Power of Iron Crystal at High Temperature.

By Zenya FUNATOGAWA.
Yokohama National University, Japan.

(Received October 21, 1950)

§1. Introduction.

Although many investigations concerning the change in physical properties of ferromagnetic single crystals due to magnetization have been performed by many investigators, yet the investigations of the change in thermal e.m.f. due to magnetization have not been made. Those data will give, however, some important fundamental knowledge to make clear the mechanism of magnetization. The change in thermal electric power of the specimen due to magnetization or, as it is sometimes called, the magneto-thermoelectric power, is a difference between the thermoelectric powers of a demagnetized specimen and magnetized one against non-ferromagnetic metal, e.g., copper.

The magnitude of the magneto-thermoelectric power of a single magnetic domain or a single crystal with saturated magnetization is given from the symmetry properties of a cubic crystal as follows:

$$(E_m)_{\alpha\beta\gamma} = a_0 + a_1 \sum \alpha_i^2 \beta_i \gamma_i + a_2 \sum_{i \neq j} \alpha_i \beta_i \alpha_j \beta_j .$$

$$a_0 = -\frac{a_1}{3} .$$

In the above equations $(E_m)_{\alpha\beta\gamma}$ is the induced magneto-thermoelectric power along a direction with direction cosines β_1, β_2, β_3 against the principal axes of a cubic crystal, when the domain is magnetized in a direction α_1, α_2, α_3 and a temperature gradient is existing along a direction γ_1, γ_2, γ_3. a_1 and a_2 are constants at given temperature. In our case $\beta_i = \gamma_i$, so we get

$$(E_m)_{\alpha\beta} = a_0 + a_1 \sum \alpha_i^2 \beta_i^2 + a_2 \sum_{i \neq j} x_i x_j \beta_i \beta_j .$$

In order to determine the constants a_1 and a_2 by measurements of real crystal rods we must specify a standard distribution of magnetic domains because they are not distributed equally in the six directions of the easiest magnetization even when the rod as a whole is in the state of demagnetization as pointed out by S. Kaya and H. Takaki.⁽¹⁾ They also found that at the breaking point corresponding to the remanence, viz., the residual magnetization of a descending hysteresis curve, the domains are distributed in three directions of the easiest magnetization near the magnetic field in proportion to their direction cosines. Such a distribution of the elementary domains reduces as much as possible the component of magnetization $J_{\perp}$ normal to the axial direction of the crystal rod and minimize the magnetostatical energy by $2\pi J_{\perp}^2$ due to this component, 2π being the demagnetizing factor. It is, therefore, reasonable to adopt the breaking point as a standard state. The magnitude of the magneto-thermoelectric power between the saturation and the remanence of a crystal is given as

$$\begin{aligned}(E_m)_{\text{sat.-rem.}} &= a_0 + a_1 + 2(a_2 - a_1)(\beta_2^2\beta_3^2 + \beta_3^2\beta_1^2 + \beta_1^2\beta_2^2) \\ &\quad - \left[(a_0 + a_1\beta_1^2)\frac{\beta_1}{\beta_1+\beta_2+\beta_3} + (a_0 + a_1\beta_2^2)\frac{\beta_2}{\beta_1+\beta_2+\beta_3} + (a_0 + a_1\beta_3^2)\frac{\beta_3}{\beta_1+\beta_2+\beta_3}\right] \\ &= a_1\left[1 - \frac{\beta_1^3+\beta_2^3+\beta_3^3}{\beta_1+\beta_2+\beta_3}\right] + 2(a_2 - a_1)(\beta_2^2\beta_3^2 + \beta_3^2\beta_1^2 + \beta_1^2\beta_2^2)\,.\end{aligned}$$

From this equation the author⁽²⁾ determined the constants at the room temperature, namely,

$$(E_m)_{100} = \frac{2}{3}a_1 = 7.0 \times 10^{-7}\ \text{Volt/Deg,}$$

$$(E_m)_{111} = \frac{2}{3}a_2 = -1.3 \times 10^{-7}\ \text{Volt/Deg,}$$

where $(E_m)_{100}$ and $(E_m)_{111}$ are the magneto-thermoelectric power along [100] and [111] respectively.

The purpose of this experiment is to know the temperature dependency of the constants a_1 or $(E_m)_{100}$ and a_2 or $(E_m)_{111}$ in the same manner as above consideration at the room temperature.

§ 2. Experimental method and samples.

A Fe-Cu thermocouple was constructed by connecting each end of a specimen with copper wires. In all cases the hot junction was always about 20° C higher than the cold one that was measured by a copper-constantan differential thermocouple. The specimen was then placed in a vacuum quartz tube carrying two independent non-inductive windings of nichrome wire; the one was a long furnace for heating the specimen and the other a local one for controlling the temperature difference between the both ends of the specimen. The ordinary thermal e.m.f. arising from the Fe-Cu thermocouple was nearly balanced by connecting the copper leads as usual with a potentiometer. The magneto-thermoelectric force set up in consequence of magnetization of the specimen by a magnetizing coil surrounding the furnaces was determined by noting the deflection of a sensitive galvanometer.

Specimens used for this experiment were cylindrical rods made by Edwards' recrystalization method of electrolytic Swedish iron. The diameter, length, direction cosines of rod axis and the calculated and observed residual magnetization at room temperature are shown in Table I.

Table I.

Sample number	Diam. (mm.)	Length (mm.)	Direction cosines			$J_{r.\text{ calc.}}$	$J_{r.\text{ obs.}}$
			β_1	β_2	β_3		
1	1.930	140.0	0.749	0.571	0.167	1116	1115
10	2.842	189.6	0.996	0.065	0.054	1533	1535
105	1.955	230.4	0.659	0.542	0.522	992	995

Table II.

$(E_m)_{\text{sat.-rem.}} \times 10^8$ Volt/Deg.	20° C	120° C	220° C	320° C	420° C	520° C
$0.0993a_1 + 0.0142a_2$	10.5	8.0	6.2	4.2	2.0	0.3

Table III.

$(E_m)_{\text{sat.-rem.}} \times 10^8$ Volt/Deg.	20° C	120° C	220° C	320° C	420° C	520° C	620° C
$0.0072a_1 + 0.6518a_2$	−11.7	−11.4	−11.7	−11.1	−8.7	−6.4	−5.3

Table IV.

$(E_m)_{\text{sat.-rem.}} \times 10^8$ Volt/Deg.	20° C	120° C	220° C	320° C	420° C	520° C	620° C	720° C
$0.085a_1 + 0.464a_2$	−0.1	−1.3	−3.5	−4.0	−5.1	−3.7	−2.7	−1.3

Table V.

	20° C	120° C	220° C	320° C	420° C	520° C	620° C	720° C
$a_1 \times 10^8$ Volt/Deg.	106	83.6	63.5	41.0	19.0	6.0	0.8	0
$a_2 \times 10^8$ Volt/Deg.	−19.2	−18.2	−18.8	−15.5	−13.8	−9.6	−6.0	−2.8

The residual magnetization calculated by the Kaya's formula $J_{r.\,\text{calc.}} = J_\infty/(\beta_1+\beta_2+\beta_3)$, where J_∞ is the saturation value at given temperature, coincides satisfactorily with the observed value $J_{r.\,\text{obs.}}$ even at high temperature.

§ 3. Experimental results.

In all cases we measured the magneto-thermoelectric power at several points on the descending hysteresis curve at each temperature up to the Curie point.

In Fig. 1 the magneto-thermoelectric powers in the case of No. 10 specimen are shown as a function of magnetization. The values of $(E_m)_{\text{sat.-rem.}}$ at several temperatures are shown in Table II. As it shows the values of $(E_m)_{\text{sat.-rem.}}$ decreases almost linearly with temperature and become practically zero at about 600° C. The values of $(E_m)_{\text{sat.-rem.}}$ are given by a sum of the changes in magneto-thermoelectric power due to the discontinuous and rotational demagnetization. The 1st and 2nd terms in the 1st column in the table, namely $0.0993a_1$ and $0.0142a_2$, represent respectively the contributions of the former and the latter processes. If the bar axis coincides exactly with the tetragonal axis, both of the terms are reduced to zero and the remanence coincides with the saturation value.

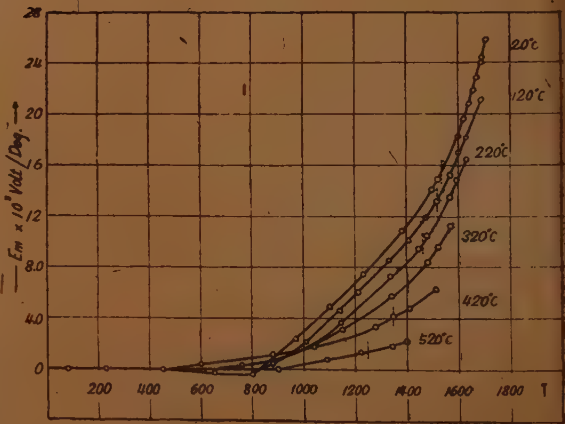

Fig. 1. The tetragonal crystal, No. 10. The remanent point is represented by a dotted line on the curve.

Fig. 2 shows the result of No. 105, a trigonal crystal. To avoid the confusion of the figure, the origin of the magnetization at 120° C is taken below by 100 from that at room temperature and so forth. The values of $(E_m)_{\text{sat.-rem.}}$ at several temperatures

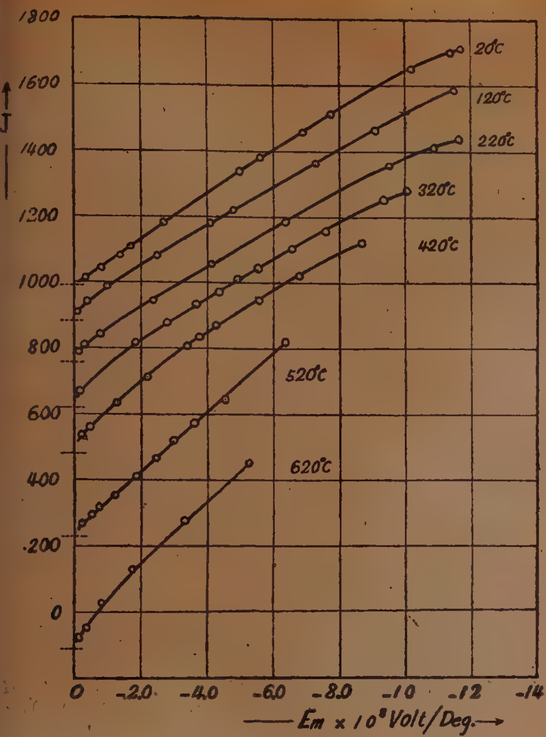

Fig. 2. The trigonal crystal, No. 105. The remanent point is represented by a dotted line on the curve.

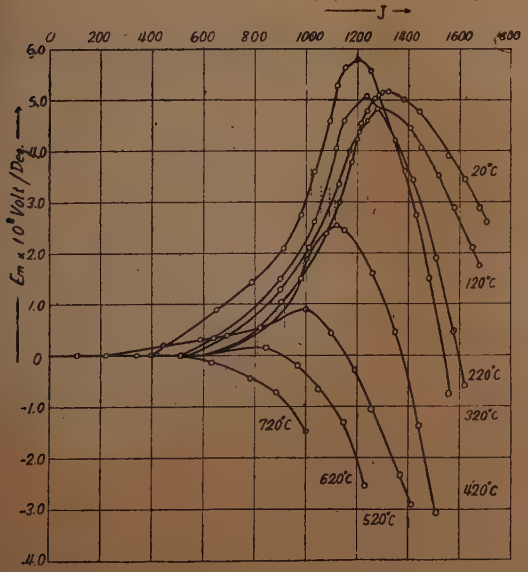

Fig. 3. The diagonal crystal, No. 1. The remanent point is represented by a dotted line on the curve.

are shown in the Table III. We know that the value of $|(E_m)_{\text{sat.-rem.}}|$ is almost constant until about 200° C and then decreases almost linearly with temperature and becomes practically zero at the Curie point.

The magneto-thermoelectric powers in other crystallographic directions can be calculated on the basis of the constants a_1 and a_2 which are determined from the results of Fig. 1 and 2. The results of No. 1 as shown in Fig. 3 and Table IV coincide with the expected values, that is $(E_m)_{\text{sat,-rem.}}$ decreases with temperature up to about 420° C and then increases to zero at the Curie point. It is also expected that the saturation value changes its sign at high temperature; notwithstanding the styles of the curves are not so much important because they are affected by the initial distribution of domains.

Fig. 4 shows the results of the polycrystal of iron. The saturation value changes its sign at high temperature.

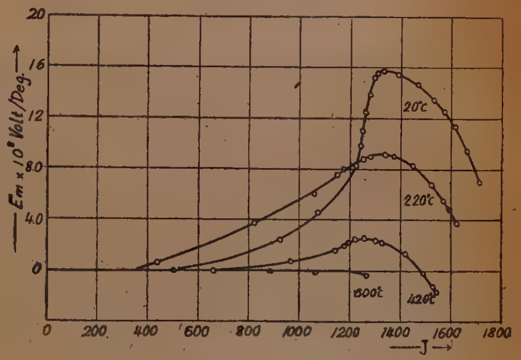

Fig. 4. The polycrystal.

§ 4. Discussion.

By the measurement of $(E_m)_{\text{sat.-rem.}}$ of the crystals at several temperatures we can calculate the constants a_1 and a_2 by solving the normal equation. We know that a_1 or $(E_m)_{100}$ decreases almost linearly with temperature to zero at about 600° C and $|a_2|$ or $|(E_m)_{111}|$ remains constant up to about 200° C and then decreases almost linearly with temperature to zero at the Curie point as shown in Fig. 5 and Table V. In the figure the magnetostrictive constants C (or λ_{100}) and λ (or λ_{111}) measured by H. Takaki(3) are shown.

An ordinary absolute thermoelectric power which shows an abrupt change just below the Curie point by appearence of spontaneous magnetization is independent of the direction of magnetization of domains and explained qualitatively by N. F. Mott(4) from the standpoint of modern metal theory.

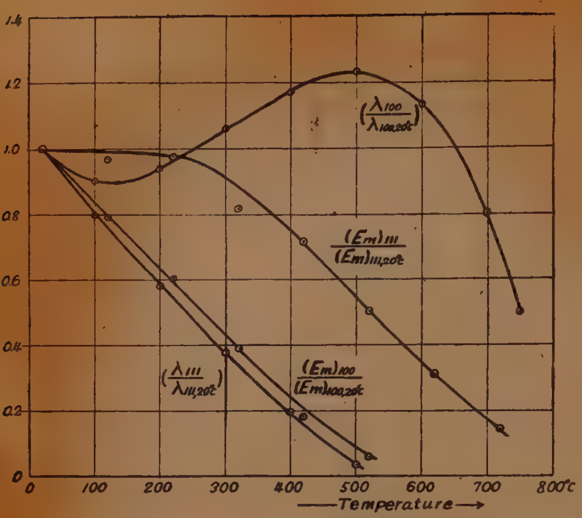

Fig. 5. Temperature dependency of the constants.

The magneto-thermoelectric power depends upon the direction of the magnetization. It is not sure at present whether these properties are directly related to ferromagnetism or only indirectly related — through the magnetostrictive lattice distortion, for instance, as was first pointed out by Ewing. As pointed out in the preceding paper⁽²⁾ that there is no intimate relation between the magnetostrictive lattice distorsion and the magneto-thermoelectric power, we may also accentuate this conclusion because, as shown in Fig. 5 the temperature dependency of the constants is in the contrary order and not in a close relation between them.

The magneto-thermoelectric power may depend upon the scattering processes in which an electron makes a transition from the *s*- to *d*-band as in the case of the magneto-resistance effect. We are now measuring the temperature dependency of the magneto-resistance effect in order to make clear the experimental relation between these effects.

The writer wishes to express his sincere thanks to Professor Dr. S. Kaya for his ready advice and for stimulating discussion throughout the course of the work. It is also a pleasure to thank Professor Dr. T. Muto for his kind advice and for generous discussion of the result.

References.

(1) S. Kaya and H. Takaki: Sci. Rep. Tohoku, Prof. Honda's Aniversary Vol. (1936), 314.
(2) Z. Funatogawa: J. Phys. Soc. Japan, 5 (1950), 311.
(3) H. Takaki: Zeits. f. Phys., 105 (1937), 92.
(4) N. F. Mott: Proc. Roy. Soc., 156 (1936), 368.

JOURNAL OF THE PHYSICAL SOCIETY OF JAPAN, VOL. 6, NO. 4 JULY-AUG., 1951.

Mechanical Barkhausen Effect

By Tohru KAMEI

Institute of Science and Technology, Komaba-machi, Meguro-ku, Tokyo

(Read April 29, 1949; Received November 13, 1950)

§1. Introduction.

When stress applied to a ferromagnetic substance is changed even slowly, directions of magnetization in some of the ferromagnetic domains change abruptly. This is known as mechanical Barkhausen effect, and is important to the study of the 90°-wall displacement of the domain. This paper describes the results of the experiment which was undertaken in order to study the above mentioned phenomenon in single crystals of iron. Shichijo⁽¹⁾ studied this phenomenon several years ago, using polycrystalline samples of silicon iron and of pure iron.

§2. Experimental Arrangement.

Iron single crystal rods of 2 mm diameter were examined. The length of the rods ranged from 60 mm to 100 mm. Prior to the examination, the single crystal samples were annealed at 790° C in the atomosphere of hydrogen and then cooled slowly to room temperature. The experimental arrangement is shown schematically in Fig. 1. Care was taken that the tension to be applied to the sample might be uniform. Both ends of the single crystal rod to be examined were soldered tightly to the inner walls of brass tubes denoted as T in Fig. 1. The weight W floated on water, and in order to increase or decrease the tension to be applied to the sample continuously, water was transferred to or from another vessel by means of siphon. The tension was changed within the elastic limit of the iron sample and the rate of change was 3.5 g/mm^2 per second. The search coil C consisted of a thin glass tube on which ♯50 enamelled copper wire was wound. The number of turns was 3000 and the length of the coil was 2 mm. Induced voltage in the coil was amplified by a 4-stage R-C coupled amplifier, the thermionic tubes UY 6301, two UZ 6C6,(2) and UY 76 being employed. The gain of the amplifier was about 120 db. The Barkhausen figure appearing on a Braun tube at various values of the applied tension was photographed by a camera that was equipped with a 4.5 F lens.

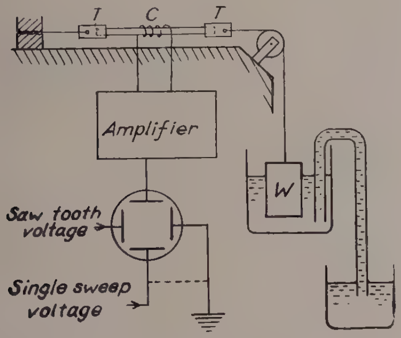

Fig. 1. Schematic diagram of the experimental arrangement

The deflecting plates were connected in two different ways according to the purpose of experiment. In order to examine the wave form of Barkhausen peaks, the plates were connected in an ordinary way: the amplified voltage was applied to the vertical deflecting plates, and saw tooth voltage was applied to the horizontal ones. Fig. 2 is a reproduction of the photograph taken by this method. Owing to repeated sweeps of the ground line, the figure of the ground line was so broadened that small peaks were lost in the back ground. In order to count the number of peaks and measure their heights even approximately, over-exposure of the ground line had to be avoided. For this purpose, therefore, single sweep voltage was applied to the deflecting plate that was otherwise earthed for an usual purpose. By applying at once single sweep and saw tooth voltage, singly swept records just like oscillographic records were obtained, examples being shown in Fig. 3. The wave form of the Barkhausen peaks obtained by this method were, however, deformed to some extent.

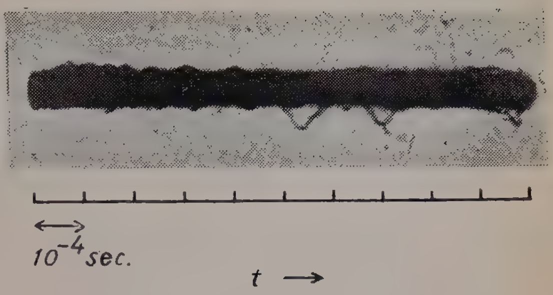

Fig. 2. Reproduction of the photograph when the deflecting plates were connected in an ordinary way.
Fe [100]. Decreasing Tension

§ 3. Experimental Results.

Only isolated Barkhausen peaks were observed at any value of tension, as shown by the examples in Fig. 2 and Fig. 3. Sometimes two (and scarcely three) peaks formed an isolated group. This is quite different from the case of magnetic Barkhausen effect in which complicated groups of peaks are observed and their wave form change along the hysteresis curve. Another different feature in the mechanical Barkhausen effect is that peaks appear on both sides of the ground line. This agrees with the fact that a ferromagnetic substance cannot be magnetized by a mere application of tension. Then it is expected that the sum of area of peaks appearing above the ground line is equal to the sum of area of peaks appearing below the ground line. Instead of measuring

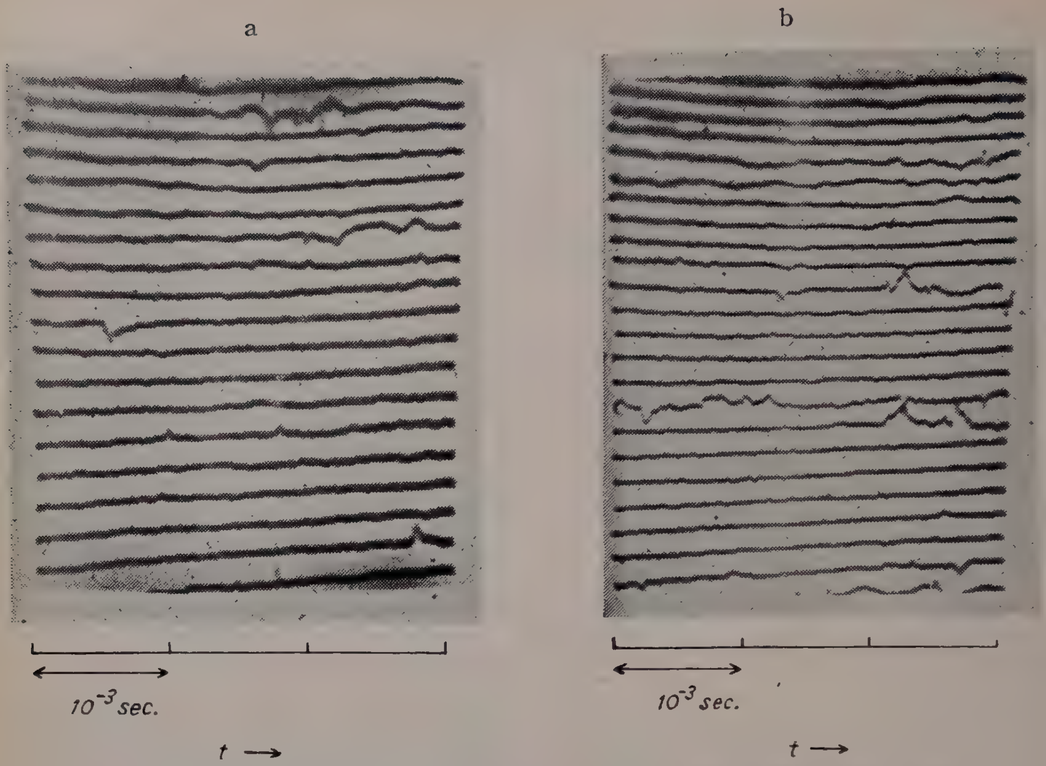

Fig. 3. Reproduction of the photographs when single sweep voltage was applied.
a. Fe [100]. Increasing Tension
b. Fe [100]. Increasing Tension

areas, heights of peaks were measured in this experiment. Amplification was so high that tube noises appeared on the photograph, although tubes with as low noises as possible were employed. Wave forms due to tube noise alone were examined and their maximum height was measured, and Barkhausen peaks that were higher than this height were considered as genuine peaks.

Plots of Barkhausen peaks *versus* time that were measured on photographs taken when single sweep voltage was applied is shown in Fig. 4. In these diagrams the time scale is chosen far smaller than the original photographs, so that the original detailed wave form of the peaks is not shown, the vertical deflection representing merely the height of the peak.

For each sample the heights of peaks appearing above and below the ground line were respectively summed up and the results are tabulated in Table 1. As expected, the sum of heights of peaks appearing above the ground line is generally equal to the sum of those appearing below the ground line.

Table 1.

Sample*	Direction of Peaks (above or below the ground line)	Sum of Heights (mm)	
		increasing tension	decreasing tension
[100]	above	252.7	31.4
	below	280.9	43.0
[100]	above	287.6	6.0
	below	315.7	30.0
[100]	above	176.4	20.5
	below	138.3	19.0
[100]	above	145.4	23.2
	below	151.6	28.9
[100]	above	241.8	7.0
	below	163.1	5.5
[100]	above	105.8	12.1
	below	118.7	3.9
[110]	above	240.5	14.9
	below	173.2	11.7

* [100] and [110] mean that the geometrical axis of the crystal rod coincided with the tetragonal and digonal direction respectively.

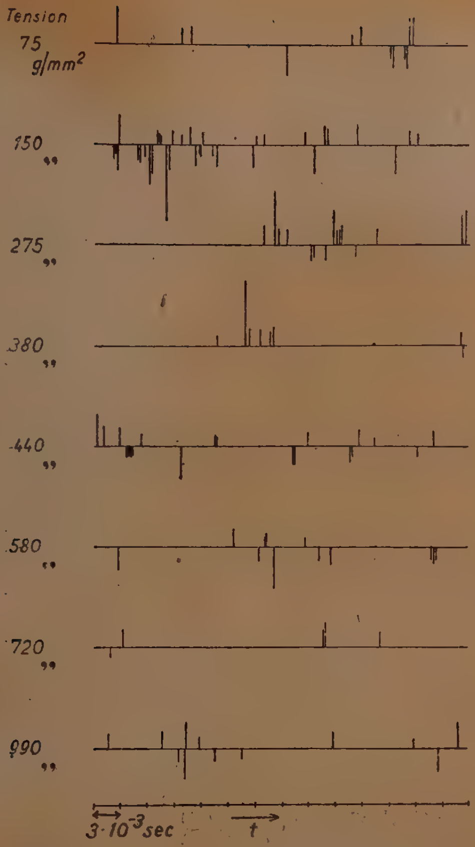

Fig. 4. Plots of Barkhausen peaks *versus* time when the tension was increasing.

Fig. 5 and Fig. 6 represent sum of heights of peaks *versus* the tension curve, in which sum of heights of peaks appearing for each interval of tension of 0.15 g/mm² is represented by each point. The curve for peaks above the ground line has the same tendency with that for peaks below the ground line. The curve for the case in which the applied tension was increasing has a form of Gaussian distribution and the maximum is situated at about 300 g/mm², but the curve has a tail towards larger tension. Even when the tension was larger than 1000 g/mm², peaks, although few in number, were still observed. When the tension was decreasing from a sufficiently large value, peaks were scarcely observed while the tension was larger than about 150 g/mm². Below this value of tension peaks began to appear, and the sum of heights increased rapidly as the tension approached zero. These tendencies were similar for various single crystal samples, being somewhat different in minute details.

§4. Discussion.

When external stress applied to an iron crystal overcomes the internal stress of the crystal, 90°-walls of the elementary domains are displaced irreversibly, giving rise to Barkhausen peaks. At the same time the iron crystal must undergo irreversible elongation characteristic of ferromagnetic substance, in addition to the ordinary reversible elastic one. The elongation *versus* tension curves in single crystals of iron were obtained by Murakawa,⁽³⁾ and Fig. 7 shows one of the curves obtained by him.

The curve consists of two parts: the one is of elastic nature and obeys Hooke's law as shown by a dotted line in Fig. 7, and the other of ferromagnetic origin. In the figure the resultant elongation is shown by a full line; therefore the ferromagnetic elongation corresponds to the difference between the dotted line and the full one. When the tension is increasing, the irreversible ferromagnetic elongation is mainly observed between *A* and *B*. In the case of mechanical Barkhausen effect, peaks are observed to be concentrated in this region. Above *B*, even when the tension was larger than 1000 g/mm², few peaks were observed. Strictly speaking, the elongation *versus* tension curve in this region is not parallel to the line representing the elastic elongation, due to the above mentioned few Barkhausen peaks and reversible rotation of the ferromagnetic domains. When the tension is decreasing in the region between *C* and *D*, the curve is almost parallel to the line representing the elastic elongation. In this region Barkhausen peaks were scarcely observed. When the tension is decreasing in the region between *D* and *R*, contraction of ferromagnetic origin is observed. Corresponding to this, Barkhausen peaks were observed in the region near *R*. When the applied tension is completely removed, a considerable amount of remanent elongation remains. This corresponds to the author's finding that sum of the heights of Barkhausen peaks observed when the tension was increasing from zero was larger than that of Barkhausen peaks observed when the tension was decreasing from a sufficiently large

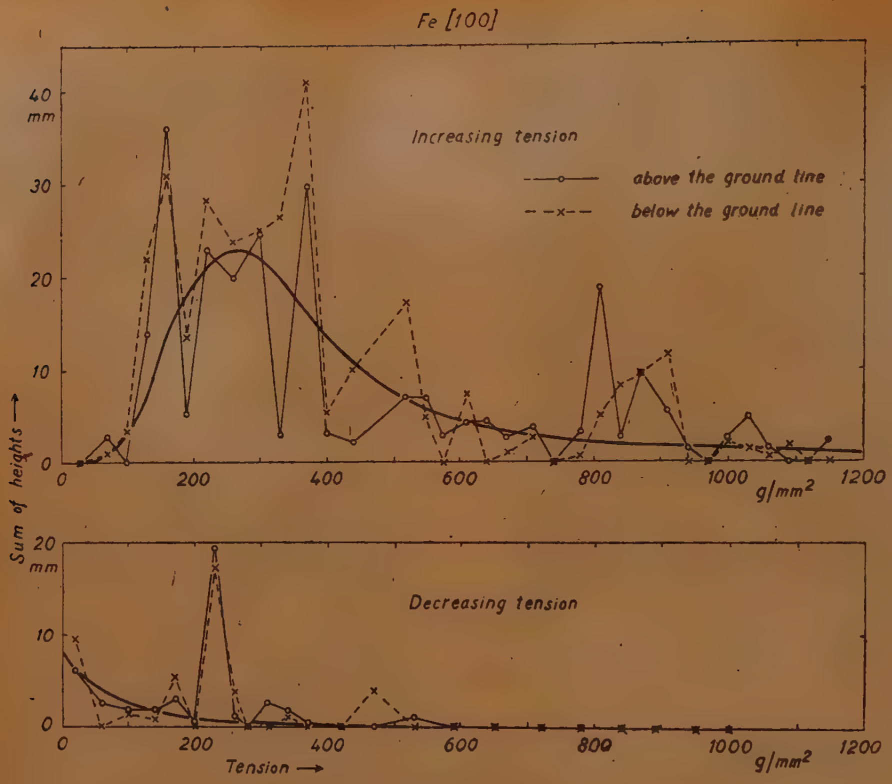
Fe [100]
Increasing tension
above the ground line
below the ground line
40 mm
30
20
10
0
Sum of heights →
0
200
400
600
800
1000
1200
g/mm²
20 mm
10
0
Decreasing tension
Tension →

Fig. 5.

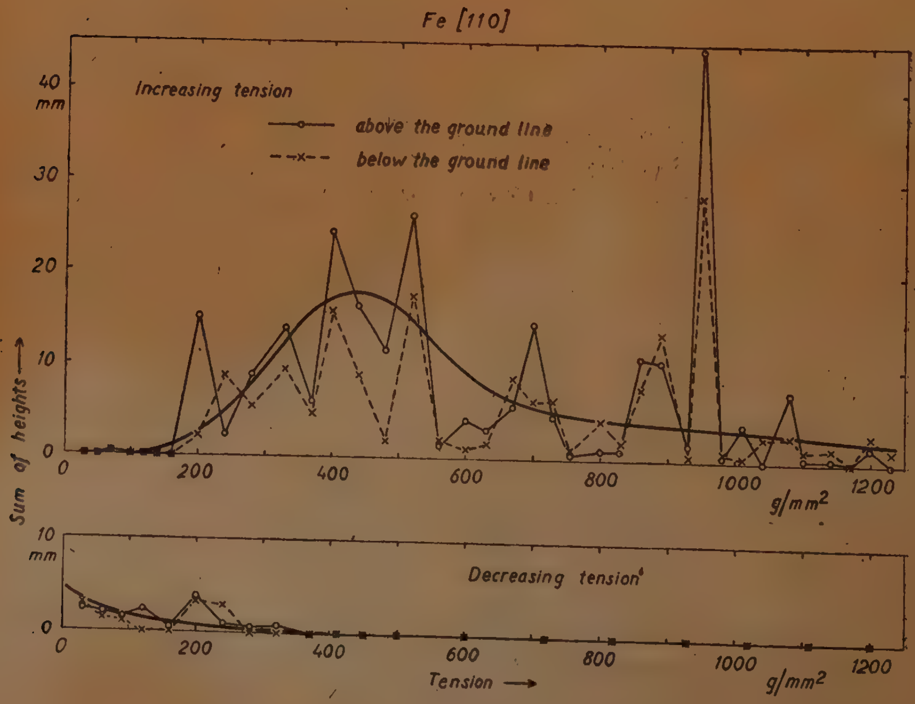
Fe [110]
Increasing tension
above the ground line
below the ground line
40 mm
30
20
10
0
Sum of heights →
0
200
400
600
800
1000
1200
g/mm²
10 mm
0
Decreasing tension
Tension →

Fig. 6.

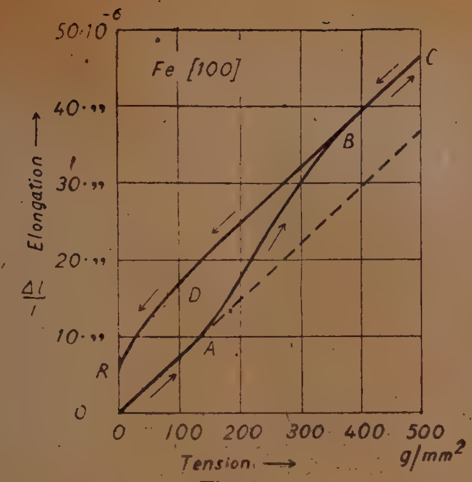

Fig. 7.

value. Thus the result of experiment on the mechanical Barkhausen effect is consistent with the elongation *versus* load curve.

The mechanical Barkhausen effect is thus suited for a microscopic examination of the mechanical property of ferromagnetic bodies, especially for the microscopic study of the distribution of internal stress existing in them.

The author wishes to express sincere thanks to Prof. Murakawa for his kind guidance and encouragement throughout this work.

References and Notes.

(1) Y. Shichijo: Nippon Buturigakkaisi, **1** (1946) 16.

(2) This tube is now obsolete for use in wireless technique, but still adequate for use in audio-amplification.

(3) K. Murakawa: Nippon Sûgaku-Butsurigakkaishi, **16** (1942) 88.

JOURNAL OF THE PHYSICAL SOCIETY OF JAPAN Vol. 6 No. 4 JUL.—AUG., 1951.

On the Phase Transition in Lead Titanate.

By Gen SHIRANE and Sadao HOSHINO.

Tokyo Institute of Technology, Oh-okayama, Tokyo.

(Received November 15, 1950)

§1. Introduction.

In the recent years, many experimental and theoretical investigations have been made on the peculiar properties of barium titanate, which shows a new type of ferroelectricity. It is known(1)(2)(3) that the solid solution of $BaTiO_3$ and $PbTiO_3$ shows ferroelectric properties of barium titanate type, having the Curie temperatures which rise with lead contents, attaining about 500°C for pure $PbTiO_3$. Although an evidence for the ferroelectricity of lead titanate was given by Roberts(4), no detailed investigations appear to have been made on the properties of this crystal.

According to Cole and Espenshied(5) the crystal structure of this substance seemed to belong to orthorhombic system but more recent investigations(6) show that it may possess a tetragonal structure with a rather large axial ratio. We have recently reported(7) that the solid solution of barium-lead titanate has a tetragonal structure, and the axial ratio increases with lead content. The tetragonality of $PbTiO_3$ is 1.063, being much larger than that of $BaTiO_3$, so that a more remarkable anomaly at the Curie point should be expected.

In order to obtain the detailed information on the phase transition in this crystal at about 490°C, we have performed an X-ray and a calorimetric study.

§2. Permittivity Measurement.

At first, we have measured the permittivity as a function of temperature. Ceramic specimens were prepared by sintering the mixture of PbO and TiO_2 at about 1100°C. It is difficult to obtain the hard sintered matures, and ceramics obtained are very porous and fragile, so that the precise values of permittivity and of the Curie constant can not be obtained.

Permittivity measurements have been made at temperatures from −170° to 550°C, with alternating field of 1 MC/sec. and about 2 volts/cm. As shown in Fig. 1, we have found only one transition at about 490°C, in contrast with the case of $BaTiO_3$ which shows three transitions in this temperature range. By extrapolating the Curie temperatures of $(Ba\text{-}Pb)TiO_3$ system, Jonker and van Santen(1) expected that the Curie point of $PbTiO_3$ may be in the range of 500~700°C. According to Waku and Hori(2) it is about 520°C. The Curie temperature observed by us is somewhat lower than these results.

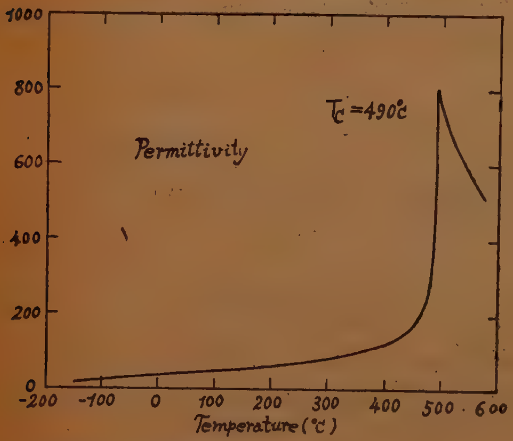

Fig. 1. Permittivity as a function of temperature.

As stated above, our ceramics are too porous for the exact estimation of the permittivity value. Nevertheless, the permittivity in the ferroelectric region is obviously much smaller than that of barium titanate. It is about 50 at room temperature. As in the other ferroelectrics, the Curie-Weiss law, $\varepsilon = C/(T-T_0)$ is also valid for this crystal, with $T_0 = 420°C$, $C = 1.1\times10^5°C$. This value of Curie constant is not so different from those of $BaTiO_3$ ($C=1.39\times10^5$ °C) and $PbZrO_3$ ($C = 1.36\times10^5$°C).(4)

§ 3. X-ray study.

The X-ray study of this crystal has been performed by the use of powdered specimen, and the Debye photographs were taken at various temperatures from 30° to 535°C, using the high temperature X-ray camera, of which the camera radius is about 55.5 mm.

The same ceramic specimen as used for the permittivity measurement was pulverized to fine powder, and it was sealed in very thin capillary tube made of hard glass (diameter = 0.5 mm), with a small content of pure silver powder for the calibration of the precise camera constant.

In the first place, the crystal structure at room temperature has been determined. The photograph, taken with Cu K_α radiation, shows tetragonal line as reported in the former publication.(7) That is, the crystal of lead titanate at 30°C belongs to tetragonal system with $a=3.894$ Å, $c=4.140$ Å and $c/a=1.063$*. We have then carried out a qualitative intensity measurement of this photograph and compared its result with that of $BaTiO_3$. From this comparison, we have ascertained that the atomic arrangement in this crystal is similar to that in $BaTiO_3$.(8)

Then we have investigated precisely the temperature changes in the lattice constants, the axial ratio and the volume of unit cell. At various temperatures, these values were calculated from (*143*), (*134*) and (*422*) lines taken by back reflection method. Obtained results are shown in Table I and Figs. 2, 3 and 4. As seen in these figures, the tetragonality of $PbTiO_3$ decreases with increasing temperature and the structure transforms to cubic lattice at the Curie point, 490°C, in accordance with our permittivity measurement. At 535°C, the lattice constant a is 3.960 Å.

The change of unit cell volume is shown in Fig. 5. It is remarkable that the volume of unit cell of this substance does not increase but slightly decreases with the temperature rise, and during the transitional region it decreases almost discontinuously by the amount of $\Delta v/v=4.4\times10^{-3}$, i.e. 0.27 Å^3 per unit cell. In the cubic region it increases normally. The volume expansion coefficient of this crystal is approximately given by

$$\beta = -16\times10^{-6} \text{ in the tetragonal region,}$$
$$\beta = 25\times10^{-6} \text{ in the cubic region.}$$

This peculiar results are supported by a dilatometric measurement described below.

---

* In the preceding note,(7) we have reported that $a=3.891$ Å, $c=4.141$ Å and $c/a=1.064$ which should be corrected as stated here.

Table I. Lattice Parameters.

Temp.(°C)	*c*-axis (Å)	*a*-axis (Å)	*c*/*a*	unit cell volume (Å^3)
30	4.140	3.894	1.063	62.77
110	4.125	3.899	1.058	62.72
200	4.104	3.907	1.050	62.65
300	4.081	3.918	1.041	62.65
325	4.073	3.921	1.039	62.61
350	4.066	3.923	1.037	62.58
400	4.046	3.930	1.029	62.49
410	4.041	3.933	1.028	62.50
425	4.036	3.934	1.026	62.45
440	4.030	3.936	1.024	62.43
450	4.028	3.937	1.023	62.44
460	4.021	8.938	1.021	62.37
470	4.016	3.942	1.019	62.31
480	4.011	3.942	1.018	62.31
490	—	3.958	1.000	62.03
510	—	3.959	—	62.05
525	—	3.960	—	62.09
535	—	3.960	—	62.10

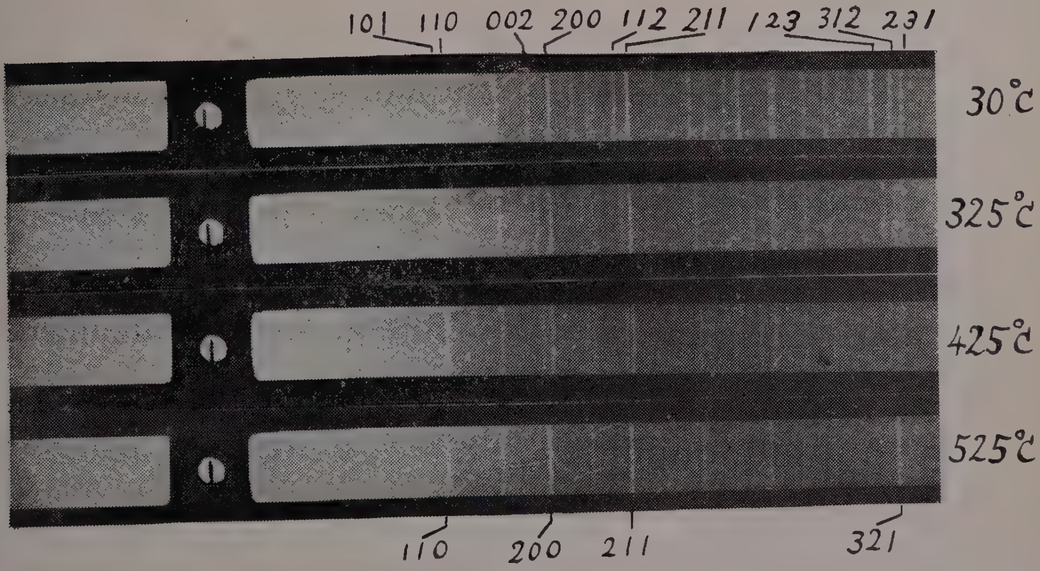

Fig. 2. Debye photographs at various temperatures.

It seems reasonable to suppose that the thermal expansion of $BaTiO_3$-type ferroelectrics is a result of superposition of normal expansion and abnormal contraction, the latter being caused by the temperature change of polarization. In this crystal, we consider, the latter one is large enouth to cover the former, so that the volume of $PbTiO_3$ as a whole contracts with temperature rise.

At present, we have no sufficient evidence to determine whether the change of structure at Curie point is discontinuous or not, though it is very steep. It seems difficult to determine this point experimentally. The single crystal study may be helpful for more detailed investigation.

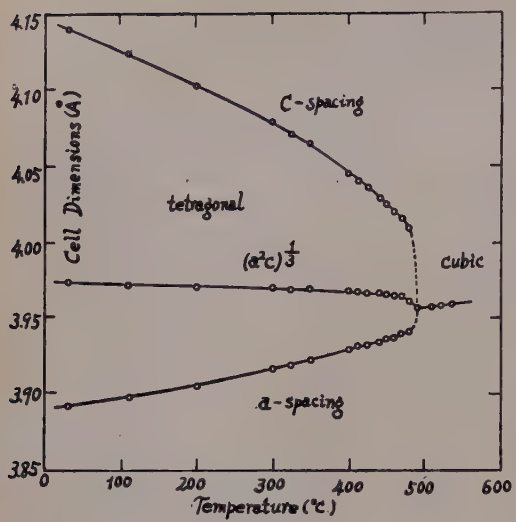

Fig. 3. Lattice spacing as a function of temperature.

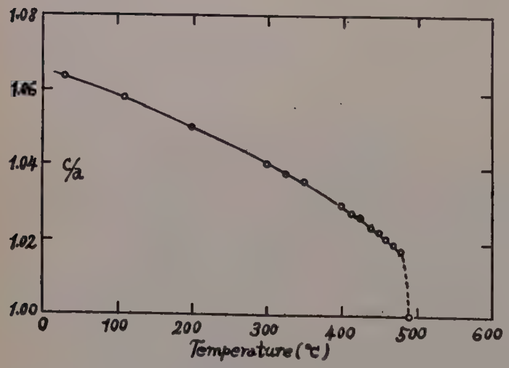

Fig. 4. Axial ratio as a function of temperature.

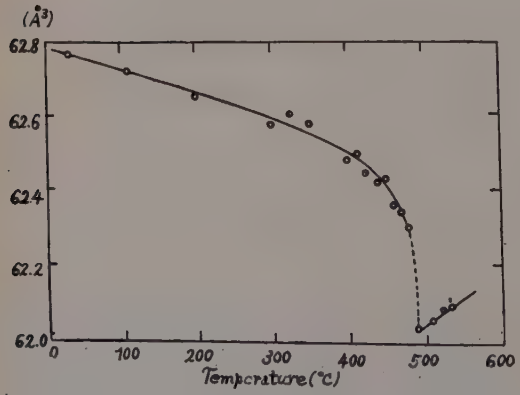

Fig. 5. Unit cell volume as a function of temperature.

§ 4. Dilatometric Measurement.

As stated above, the remarkable volume change of $PbTiO_3$ was found by X-ray analysis. To confirm this phenomenon, we have carried out a dilatometric measurement. We used a simple dilatometer constructed of silica rods and optical lever. Ceramic specimen was formed into a rod, 3 cm in length and 0.3 cm in diameter. Using this specimen, we can detect a dilatation as small as $\Delta l/l = 3\times10^{-6}$. In Fig. 6, we have shown $(l-l_0)/l_0$ as a function of temperature, where l_0 is the length at 30°C.

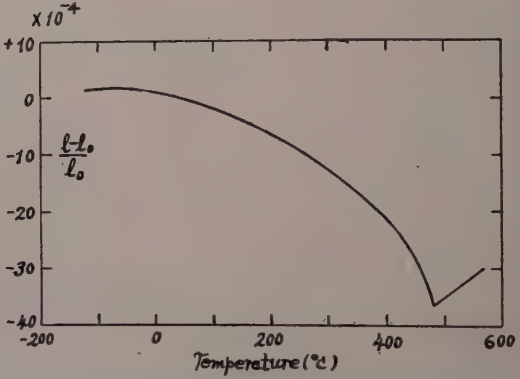

Fig. 6. Dilatometric curve of $PbTiO_3$ ceramics.

As shown in this figure, the length vs. temperature curve shows the same tendency as known by X-ray analysis, but we found that there is a complicated hysteresis in the cooling curve; this phenomenon is in common with $(Ba-Pb)TiO_3$ which contains $PbTiO_3$ more than 50%. Details will be mentioned in a later paper concerning this $(Ba-Pb)TiO_3$ solid solution.

In such substance, macroscopic length change of ceramics may not represent the real change of lattice spacing. But the heating curve is nearly reproducible; and in fact we obtain the average volume expansion coefficient from this curve.

$\beta = -18\times10^{-6}$ in the range 40°∼440°C,

$\beta = 25\times10^{-6}$ in the cubic region,

these values being in good agreement with the results of X-ray analysis.

§ 5. Specific Heat.

Using an adiabatic calorimeter of Naga-

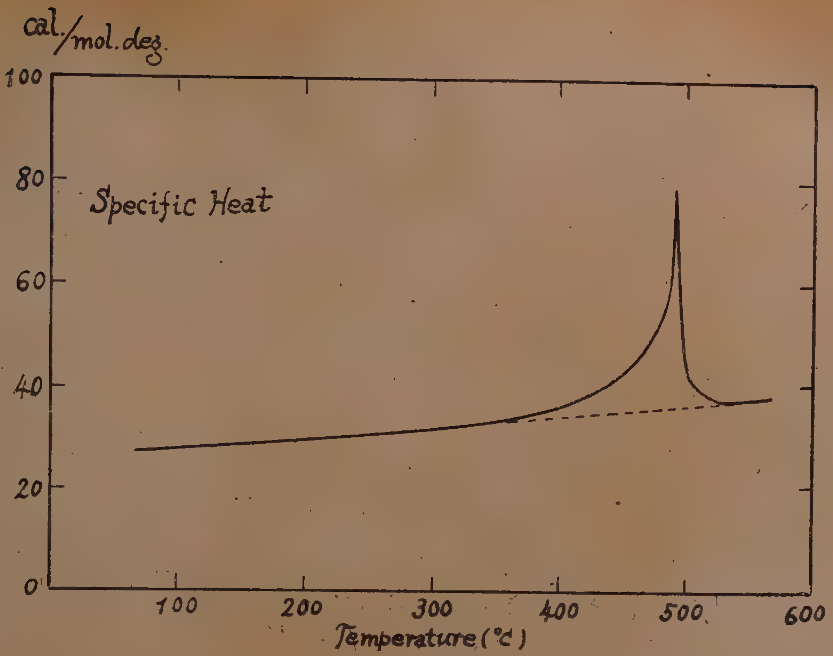

Fig. 7. Specific heat of lead titanate.

saki-Takagi type,(9) which is an improvement of Sykes' one,(10) we have measured the specific heat as a function of temperature.

We have used the same ceramic specimen as used for the above measurements. The powdered specimen of about 25 g in glass vessel of 2 g in weight was heated at a rate of about 2°C/min. Heat capacity of empty calorimeter was calibrated by the use of KCl as a standard substance. The specific heat vs. temperature curve is shown in Fig. 7.

As seen in this figure, there is a rather great anomaly of specific heat at the transitional region. The specific heat curve shows a sharp peak at 490°C. Attention must be paid to the fact that the specific heat shows an anomaly over a wide temperature range. Now we shall tentatively assume that the normal specific heat corresponds to the broken line shown in the figure. Then we can obtain the transition energy as 1150 cal/mol in the range 340°~540°C, the accompanying entropy change being about 0.80 *R*. This great anomaly is to be compared with the small transion energy in $BaTiO_3$(11) which is about 20~40 cal/mol.

According to the theory of barium titanate proposed by Devonshire(12), the anomalous internal energy due to the spontaneous polarization can be expanded as

$$E = A \cdot T_c \cdot P^2 + \cdots = B \cdot T_c (c/a - 1) + \cdots \qquad (1)$$

where T_c represents the Curie temperature and B depends on the piezoelectric and elastic constants. This relation between polarization and crystal strain was cofirmed experimentally by Merz(13) in the case of $BaTiO_3$. Though the value of spontaneous polarization of this crystal has not yet been estimated, we have found that c/a, which is 1.063 at 30°C, decreases considerably from a temperature far below the Curie point. Taking account of this fact, it seems reasonable to assume that the specific heat also has an anomaly in the same temperature range. So we have calculated the anomalous internal energy E as shown in Fig. 8, utilizing the normal specific heat shown in Fig. 7. This curve is quite similar to the temperature change of axial ratio c/a (Fig. 4). It is found that Eq. (1) holds approximately in this temperature range with $B \doteqdot 40$ cal/mol. On the other hand, we have estimated that B is about 15 cal/mol in the case of $BaTiO_3$

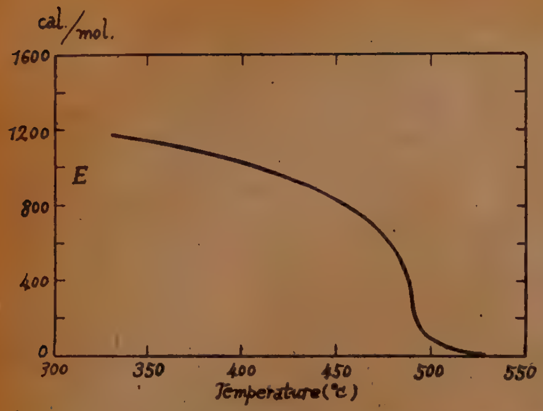

Fig. 8. Anomalous energy estimated from the specific heat curve.

At present, it is difficult to determine whether there is a latent heat at the transition point, 490°C.

§ 6. Summary.

(1) The nature of the phase transition in lead titanate at 490°C is essentially of the same type as the well known phase change in $BaTiO_3$ at 120°C. But the peculiar properties are exaggerated in the following several points.

(2) The tetragonality at room temperature is large ($c/a = 1.063$) and the change of lattice spacing at the transition is very drastic. Moreover, as the temperature is raised the unit cell volume does not increase but decreases gradually and at the transition point there is a great volume contraction.

(3) Corresponding to this large lattice change, a large transition energy was found. And the specific heat curve shows an anomaly from far below the Curie point, just corresponding to the change of tetragonality in the same temperature range.

(4) From these fact, it may be expected that the spontaneous polarization and coercive force are several times larger than that of $BaTiO_3$, although our ceramics is too porous to measure these values.

In conclusion, we wish to express our sincere thanks to Professor S. Miyake, Professor Y. Takagi and Dr. S. Sawada for their kind guidance in the course of this research, and also to Mr. E. Sawaguchi and Mr. K. Suzuki for their helpful advice on our work. This study was helped by the research grant from the Ministry of Education.

References.

(1) G. H. Jonker and J. H. van Santen: Chem. Weekblad, **43** (1947) 672.
(2) S. Waku and J. Hori: Reported at the Committee for the Piezoelectric Material, held at Tokyo, on 1st May 1950.
(3) S. Nomura and S. Sawada: J. Phys. Soc. Japan, **6** (1951) 36.
(4) S. Roberts: J. Am. Ceramic Society, **33** (1950) 63.
(5) S. S. Cole and H. Espenshied: J. Phys. Chem. **41** (1937) 445.
(6) I. Naray-Szabo: Naturw., **31** (1943) 202, 446.
H. D. Megaw: Proc. Phys. Soc. London, **58** (1946) 133.
(7) G. Shirane, S. Hoshino and K. Suzuki: J. Phys. Soc. Japan, **6** (1950) 453.
(8) H. D. Megaw: Proc. Roy. Soc., **A 189** (1947) 261.
S. Miyake and R. Ueda: J. Phys. Soc. Japan, **2** (1947) 93.
(9) S. Nagasaki and Y. Takagi: J. App. Phys. Japan, **17** (1948) 104.
(10) C. Sykes: Proc. Roy. Soc., **A143** (1935) 422.
(11) M. G. Harwood, P. Popper and D. F. Rushman: Nature, **160** (1947) 58.
H. Blattner, W. Känzig and W. Merz: Helv. Phys. Acta, **22** (1949) 35.
S. Sawada and G. Shirane: J. Phys. Soc. Japan, **4** (1949) 52.
(12) A. F. Devonshire: Phil. Mag., **11** (1949) 1040.
(13) W. Merz: Phys. Rev., **76** (1950) 1187.

JOURNAL OF THE PHYSICAL SOCIETY OF JAPAN Vol. 6 No. 4 JULY—AUG., 1951

On the Lambda Point of He^4—He^3 Mixtures.

By Akira HARASIMA.

Physical Institute, Tokyo Institute of Technology.

(Read November 4, 1950; Received November 25, 1950)

Summary

Properties of liquid helium has long since been investigated and many interesting phenomena are known to us. Recently it has become possible to obtain the isotope He^3 in pure form and a lot of interesting experiments have been done for various concentrations of He^3 in He^4. At first, ratio of the two components in the vapor and liquid phases was investigated and it was proposed by Taconis, Beenakker, Nier and Aldrich(1) that below the λ- point He^3 mixes only with the normal part of He^4. On the other hand, change of λ- point with the content of He^3 was investigated both experimentally and theoretically. Theories of the phenomena were proposed by Stout,(2) Rice,(3) De Boer(4) and Gorter(5). Their theories are based on the assumption that He^3 mixes only with the normal part of He^4 as proposed by Taconis and others. Experimental investigations were done by Abraham, Weinstock, and Osborne(6) for the range of concentrations of 0%—28% and by Daunt and Heer(7) for concentrations up to 89%.

Now theories thus far proposed are mainly thermodynamical, and it seems that molecular theories have not yet appeared. We shall here investigate the properties of the mixture of He^4 particles which obey Bose-Einstein statistics and He^3 particles which obey Fermi-Dirac statistics.

§ 1. The lambda point of He^4—He^3 mixture.

Attempts to interpret the properties of liquid helium by the theory of Bose-Einstein condensation of He^4 particles have been done since London's(8) theory on the problem. So it will be interesting to interpret on his line the phenomenon of lowering of λ- point with the content of He^3. Of course, only some general features of the present theory are expected to be compared with experimental data owing to the fact that there is many discrepancies between the properties of actual liquid helium and Bose-Einstein gas, where mutual interactions of particles are not taken into consideration.

Now let us make the following assumptions for a mixture of He^4 and He^3 particles whose numbers we denote by N_4 and N_3 respectively.

(A) The particles form a liquid phase by cohesional forces, but each particle moves in a constant average field. Though it needs work for a particle to get out of the liquid, it is perfectly free in the liquid.

(B) A constant volume is attached to each particle. The volume is assumed to be the same for He^4 and He^3, and in a first approximation does not change with temperature.

(C) In accordance with the idea of Taconis et al, we assume that He^3 particles can move only is the space of volume not occupied by the zero atoms (super-part), that is, in the volume

$$V\left(1-\frac{N_0}{N_3+N_4}\right),$$

N_0 being the number of the zero atoms of He^4*.

Let the number of states of energy ε_i of He^4 be G_i and that of states of energy ε_j of He^3 be G_j, and the numbers of He^4, He^3 particles in these states be N_i, N_j respectively. The number of complexions of the whole system is

$$W=\prod_{i=0}^{\infty}\frac{(N_i+G_i-1)!}{N_i!\,(G_i-1)!}\prod_{j=0}^{\infty}\frac{G_j!}{N_j!\,(G_j-N_j)!}, \tag{1}$$

and the energy is

$$U=\sum\varepsilon_i N_i+\sum\varepsilon_j N_j. \tag{2}$$

---

* The idea of entropy of mixing of He^3 and the normal part of He^4 is included in this assumption. The author thanks Dr. M. Toda for discussions on this point.

Now we can proceed in the usual manner to determine N_i and N_j so as to make the value of $\ln W$ maximum under the conditions that $U, \sum N_i, \sum N_j$ are constant. The problem becomes to make

$$
\begin{aligned}
A = U - kT \ln W = \varepsilon_0 N_0 + \sum_{i=1}^{\infty} \varepsilon_i N_i + \sum_{j=0}^{\infty} \varepsilon_j N_j \\
-kT[(N_0+G_0)\ln(N_0+G_0) - N_0 \ln N_0 \\
- G_0 \ln G_0 + \sum_{i=1}^{\infty}\{(N_i+G_i)\ln(N_i+G_i) \\
- N_i \ln N_i - G_i \ln G_i\} + \sum_{j=0}^{\infty}\{G_j \ln G_j \\
- N_j \ln N_j - (G_j - N_j)\ln(G_j - N_j)\}]
\end{aligned} \tag{3}
$$

minimum under the conditions

$$\sum N_i = \text{const.}, \quad \sum N_j = \text{const.}$$

We proceed in three steps. First, we make the number N_o of the zero atoms of He^4 and all the N_j's $(j=0, 1, 2, \ldots.)$ constant and vary N_i $(i=1, 2, 3, \ldots.)$. From the condition that A becomes minimum we can derive in the usual way the Bose-Einstein distribution

$$N_i = \frac{G_i}{e^{\alpha+\varepsilon_i/kT}-1}, \tag{4}$$

where α is determined by the condition

$$\sum_{i=1}^{\infty} \frac{G_i}{e^{\alpha+\varepsilon_i/kT}-1} = N_4 - N_0 = N^n, \ N^n: \text{number of normal particles of He}^4. \tag{5}$$

Secondly we vary N_j while N_o and N_i's are made to remain constant. From the condition $\delta A = 0$, we obtain Fermi-Dirac distribution

$$N_j = \frac{G_j}{e^{\alpha'+\varepsilon_j/kT}+1}, \tag{6}$$

where α' is determined by the condition

$$\sum_{j=0}^{\infty} \frac{G_j}{e^{\alpha'+\varepsilon_j/kT}+1} = N_3. \tag{7}$$

Substituting from (4), (6) into (3), we have

$$
\begin{aligned}
A = \varepsilon_0 N_0 - kT[(N_0+G_0)\ln(N_0+G_0) - N_0 \ln N_0 \\
- G_0 \ln G_0] - \alpha kT \sum_{i=1}^{\infty} N_i + kT \sum_{i=1}^{\infty} G_i \ln(1-e^{-\alpha-\varepsilon_i/kT}) \\
- \alpha' kT \sum_{j=0}^{\infty} N_j - kT \sum_{j=0}^{\infty} G_j \ln(1+e^{-\alpha'-\varepsilon_j/kT}).
\end{aligned} \tag{8}
$$

Lastly, we obtain the value of N_o which makes the value of A minimum. N_o is determined by

$$\frac{\varepsilon_0}{kT} + \alpha - \ln\frac{N_0+G_0}{N_0} - \sum_{j=0}^{\infty} \frac{\partial G_j}{\partial N_0} \ln(1+e^{-\alpha'-\varepsilon_j/kT}) = 0. \tag{9}$$

In this expression $\partial G_j/\partial N_o$ cannot be put equal to zero since the volume, in which He^3 particles move, varies by the assumption (C) when N_o varies.

If He^3 particles form ideal Fermi-Dirac gas, we have

$$G_j = \frac{4\pi g V}{h^3}\left(1 - \frac{N_0}{N_3+N_4}\right) p^2\, dp, \quad g: \text{spin weight},$$

and (9) becomes

$$
\begin{aligned}
\frac{\varepsilon_0}{kT} + \alpha - \ln\frac{N_0+G_0}{N_0} + \frac{4\pi g}{h^3}\frac{V}{N_3+N_4}\frac{1}{3m_3 kT} \\
\times \int_0^{\infty} \frac{p^4}{e^{\alpha'+p^2/2m_3kT}+1}\, dp = 0,
\end{aligned} \tag{10}
$$

where α' is determined by

$$\frac{4\pi g V}{h^3}\left(1 - \frac{N_0}{N_3+N_4}\right) \int_0^{\infty} \frac{p^2\, dp}{e^{\alpha'+p^2/2m_3kT}+1} = N_3. \tag{11}$$

At temperatures above the λ-point, the number of zero atoms is of the order of G_o, while at temperatures below the λ-point, N_o becomes of the order of N_4 and it becomes already large compared with G_o at temperatures very close to the λ-point. Hence, the λ-temperature T_λ is determined by the equations obtained from (10) and (11) by neglecting the third term of (10). We put $\alpha' = -\eta$, and obtain

$$\frac{\varepsilon_0}{kT_\lambda} + \alpha + \frac{4\pi g}{h^3}\frac{V}{N_3+N_4}\frac{1}{3}(2m_3 kT_\lambda)^{5/2} F_{3/2}(\eta) = 0, \tag{12}$$

$$\text{where } \frac{2\pi g V}{h^3}(2m_3 kT_\lambda)^{3/2} F_{1/2}(\eta) = N_3, \tag{13}$$

and

$$F_{3/2}(\eta) = \int_0^{\infty} \frac{x^{3/2}}{e^{x-\eta}+1}\, dx, \quad F_{1/2}(\eta) = \int_0^{\infty} \frac{x^{1/2}}{e^{x-\eta}+1}\, dx. \tag{14}$$

From (12) and (13), we have

$$\frac{\varepsilon_0}{kT_\lambda} + \alpha + \frac{2}{3} x \frac{F_{3/2}(\eta)}{F_{1/2}(\eta)} = 0, \tag{15}$$

where $x = N_3/(N_3+N_4)$. α is determined by (5) in which N_o is now taken to be equal to zero.

$$\sum_{i=1}^{\infty} \frac{G_i}{e^{\alpha+\varepsilon_i/kT_\lambda}-1} = N_4. \tag{16}$$

Now, we assume that there is an energy level which is $|\varepsilon_0|$ lower than the lowest level of the free motion of particles in the volume V. The gas, the particles of which have such energy values, is called by Goldstein$^{(9)}$ the modified ideal Bose-Einstein gas. (16) becomes

$$\frac{4\pi V}{h^3}\int_0^\infty \frac{p^2 dp}{e^{\alpha + p^2/2m_4 kT_\lambda} - 1} = N_4\,, \tag{17}$$

which can be rewritten as

$$\frac{V}{h^3}(2\pi m_4 kT_\lambda)^{3/2} F(\alpha) = N_4\,, \tag{18}$$

where

$$F(\alpha) = \sqrt{\frac{2}{\pi}}\int_0^\infty \frac{x^{1/2}}{e^{\alpha+x}-1}\,dx\,. \tag{19}$$

From (15) and (18), we have

$$\frac{V}{h^3}(2\pi m_4 kT_\lambda)^{3/2} F\left(-\frac{\varepsilon_0}{kT_\lambda} - \frac{2}{3}x\frac{F_{3/2}(\eta)}{F^{1/2}(\eta)}\right) = N_4. \tag{20}$$

Let the λ-point for $x = 0$, that is, for pure He^4, be T_{λ_0}.

$$\frac{V}{h^3}(2\pi m_4 kT_{\lambda_0})^{3/2} F\left(-\frac{\varepsilon_0}{kT_{\lambda_0}}\right) = N_4 + N_3\,. \tag{21}$$

From (20) and (21), we have

$$\left(\frac{T_\lambda}{T_{\lambda 0}}\right)^{3/2} \frac{F\left(\frac{|\varepsilon_0|}{kT_\lambda} - \frac{2}{3}x\frac{F_{3/2}(\eta)}{F_{1/2}(\eta)}\right)}{F\left(\frac{|\varepsilon_0|}{kT_{\lambda_0}}\right)} = 1 - x\,.$$

Let $T_\lambda / T_{\lambda_0} = \tau$ and $|\varepsilon_0| / kT_{\lambda_0} = \xi_0$. We have

$$\tau = \left[\frac{F(\xi_0)}{F\left(\frac{\xi_0}{\tau} - \frac{2}{3}x\frac{F_{3/2}(\eta)}{F_{1/2}(\eta)}\right)}\right]^{2/3} (1-x)^{2/3}\,, \tag{22}$$

where

$$\frac{2\pi g V}{h^3}(2m_3 k\tau T_{\lambda_0})^{3/2} F_{1/2}(\eta) = N_3\,. \tag{23}$$

Since the spin of He^3 is 1/2, we have $g=2$. (22) together with (23) is the final result. In (22) the factor $(1-x)^{2/3}$ expresses the effect of the dilution of He^4 by He^3.

§ 2. Lambda point of pure He^4.

For $x=0$, we have, putting N_4 in place of N_4+N_3,

$$F(\xi_0) = \frac{N_4 h^3}{V(2\pi m_4 kT_{\lambda_0})^{3/2}}\,. \tag{24}$$

Further for $\varepsilon_0 = 0$, that is, for ordinary ideal Bose-Einstein gas, we have

$$F(0) = \frac{N_4 h^3}{V(2\pi m_4 kT_{\lambda_0}{}^0)^{3/2}}\,. \tag{25}$$

Putting
$$\frac{|\varepsilon_0|}{kT_{\lambda_0}{}^0} = \xi_0{}^0\,, \tag{26}$$

we have
$$T_{\lambda_0}{}^0 / T_{\lambda_0} = \xi_0 / \xi_0{}^0\,. \tag{27}$$

From (24) and (25), we have

$$\frac{F(\xi_0)}{F(0)} = \left(\frac{T_{\lambda_0}{}^0}{T_{\lambda_0}}\right)^{3/2} = \left(\frac{\xi_0}{\xi_0{}^0}\right)^{3/2}. \tag{28}$$

Values of $\xi_0/\xi_0{}^0 = T^0{}_{\lambda_0}/T_{\lambda_0}$ and $\xi_0{}^0$ for various values of ξ_0 is listed in Table I.

§ 3. Results of calculation.

From (23), we have

$$\tau = \left[\frac{h^3}{4\pi V}\frac{N_3}{F_{1/2}(\eta)}\right]^{2/3} \frac{1}{2m_3 kT_{\lambda_0}{}^0}\left(\frac{T_{\lambda_0}{}^0}{T_{\lambda_0}}\right). \tag{29}$$

Since

$$T_{\lambda_0}{}^0 = \left(\frac{N}{2.612\,V}\right)^{2/3}\frac{h^2}{2\pi m_4 k}\,,$$

we have

$$\begin{aligned}\tau &= \left(\frac{2.612\pi^{1/2}}{4}\right)^{2/3}\frac{4}{3}\frac{x^{2/3}}{[F_{1/2}(\eta)]^{2/3}}\frac{T_{\lambda_0}{}^0}{T_{\lambda_0}} \\ &= 1.470\frac{x^{2/3}}{[F_{1/2}(\eta)]^{2/3}}\frac{T_{\lambda_0}{}^0}{T_{\lambda_0}}\,. \end{aligned} \tag{30}$$

Substituting this value into (22), we have

$$\begin{aligned}&\frac{F(\xi_0)}{(1.470)^{3/2}}\left(\frac{T_{\lambda_0}}{T_{\lambda_0}{}^0}\right)^{3/2} F_{1/2}(\eta)\frac{1-x}{x} \\ &= F\left(\frac{\xi_0}{1.470}\frac{T_{\lambda_0}}{T_{\lambda_0}{}^0}\frac{[F_{1/2}(\eta)]^{2/3}}{x^{2/3}} - \frac{2}{3}x\frac{F_{3/2}(\eta)}{F_{1/2}(\eta)}\right). \end{aligned} \tag{31}$$

Table I. Relation between ξ_0 and $T_{\lambda_0}/T_{\lambda_0}{}^0$, $\xi_0{}^0$.

ξ_0	$T_{\lambda_0}/T_{\lambda_0}{}^0$	$\xi_0{}^0$	ξ_0	$T_{\lambda_0}/T_{\lambda_0}{}^0$	$\xi_0{}^0$	ξ_0	$T_{\lambda_0}/T_{\lambda_0}{}^0$	$\xi_0{}^0$
0.20	1.6	0.32	0.28	1.7	0.48	0.36	1.9	0.67
0.22	1.6	0.36	0.30	1.7	0.52	0.38	1.9	0.73
0.24	1.7	0.40	0.32	1.8	0.57	0.40	2.0	0.80
0.26	1.7	0.44	0.34	1.8	0.62			

If we give ξ_0 we can find $F(\xi_0)$ and $T_{\lambda_0}/T_{\lambda_0}^0$ by Table I. By a graphical method we can find η from (31), and by (30) we have the value of τ. We take ξ_0 for an adjustable parameter and take $\xi_0=0.40$. The calculated value of τ as a function of x is shown by the thick line in Fig. 1. Experimental values of Abraham, Weinstock and Osborne and those of Daunt and Heer are also show in the figure. It may be said that the agreement is very satisfactory if we take $\xi_0=$ 0.40.

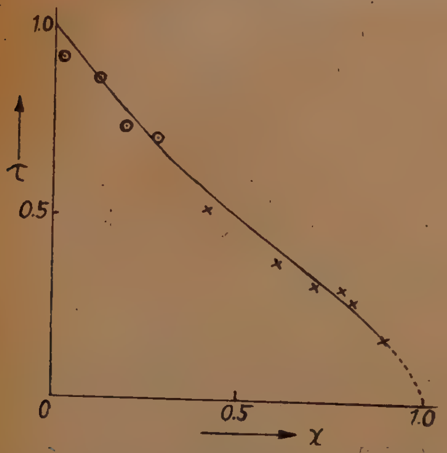

Fig. 1. Thick line: calculated values for $\xi_0=0.4$.
⊙ Experimental values of Abraham, Weinstock and Osborne.
× Experimental values of Daunt and Heer.

The author must acknowledge his indebtedness to his colleagues in the Toky Institute of Technology and to a group o friends in the Tokyo University for valuabl discussions and criticisms. The cost o this research has been defrayed from th Scientific Research Expenditure of the Department of Education.

References.

(1) K.W. Taconis, J.J.M. Beenakker, Alfred O. Nier, L.T. Aldrich: Phys. Rev. **75**, (1949), 1966.
(2) J.W. Stout: Phys. Rev. **74**, (1948), 605; **76**, (1949), 864.
(3) O.K. Rice: Phys. Rev. **76**, (1949), 1701; Olive G. Engel and O.K. Rice: Phys. Rev. **78**, (1950), 55.
(4) J. De Boer: Phys. Rev. **76**, (1949), 852.
(5) C.J. Gorter, J. De Boer: Phys. Rev. **77**, (1950), 569.
(6) B.M. Abraham, B. Weinstock, D.W. Osborne: Phys. Rev. **76**, (1949), 864.
(7) J.G. Daunt and C.V. Heer: Phys. Rew. **79** (1950), 46.
(8) F. London: Phys. Rev. **51**, (1938), 347.
(9) L. Goldstein: J. Chem. Phys. **14**, (1946), 276.

JOURNAL OF THE PHYSICAL SOCIETY OF JAPAN Vol. 6 No. 4 JULY.—AUG., 1951.

On the Phase Transition in Barium-Lead Titanate (1).

Gen SHIRANE and Kazuo SUZUKI.
Tokyo Institute of Technology, Oh-okayama, Tokyo.

(Received November 29, 1950)

§1. Introduction.

Investigations on titanate ceramics have shown that $BaTiO_3$ and solid solutions of $(Ba\text{-}Sr)TiO_3$ and $(Ba\text{-}Pb)TiO_3$ represent a new type of ferroelectrics. In the $(Ba\text{-}Sr)TiO_3$ system(1)(2), the Curie temperature decreases with the content of $SrTiO_3$. On the other hand, in the $(Ba\text{-}Pb)TiO_3$ system(3)(4)(5), the Curie temperature increases with lead content, tataining about 500°C for pure $PbTiO_3$.

An X-ray study of the phase change of $(Ba80\text{-}Pb20)TiO_3$ has been performed by Miyake and one of the authors(6), and a dilatometric measurement of the solid solution of the same content was made by Nomura and Sawada(6). Following their results, the volume contraction at the Curie point of this solid solution is much larger than that of $BaTiO_3$. In the preceding paper(7) it was reported that the phase transition in lead titanate is of the same type as that of $BaTiO_3$, but is more drastic in several points.

But it seems that no detailed investigations have been made on the whole range of this series, especially on the solid solutions near the $PbTiO_3$ side. We have carried out dielectric and X-ray study over various compositions of this series, comparing them with the extreme cases of pure $BaTiO_3$ and pure $PbTiO_3$. Dilatometric and calorimetric investigations will be reported in part (11).

§2. Permittivity Measurement.

Following the usual method, we have prepared the specimens of various contents. We have mixed $BaCO_3$, PbO and TiO_2 in the desired proportions and after the first calcination they were sintered at temperatures ranging from 1100° to 1400°C. The sintering temperature is lowered towards $PbTiO_3$ because of low melting point of PbO. It is difficult to obtain the well sintered matures when large percentages of lead are used.

The permittivity of this series were measured on heating as a function of temperature, and the several curves are shown in Fig. 1. Measuring frequency is 1MC/sec and the field strength is about 2 volt/cm. As seen in this figure, the Curie temperature increases with lead content from 120°C of $BaTiO_3$ continuously to 490°C of pure $PbTiO_3$. On the other hand, the other two transition temperatures of $BaTiO_3$, namely those at 5 C and −70 C, do not increase but decrease with lead content and soon go out of our measuring limit, −170°C.

The phase diagram thus obtained is shown in Fig. 2. It can be seen that the Curie temperature increases linearly at first up to 350°C for (Ba50-Pb50)TiO_3, then it begins to show a slight deviation from linearity.

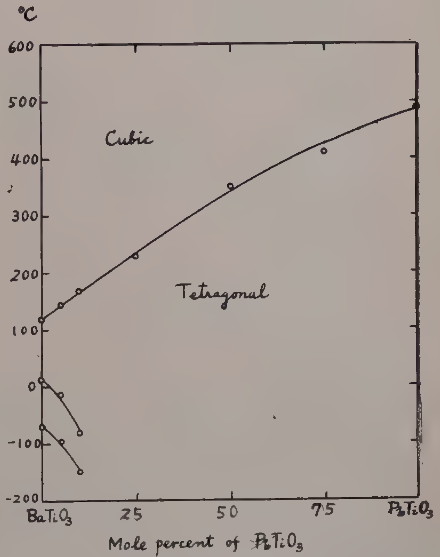

Fig. 2. Phase diagram of (Ba-Pb)TiO_3 series.

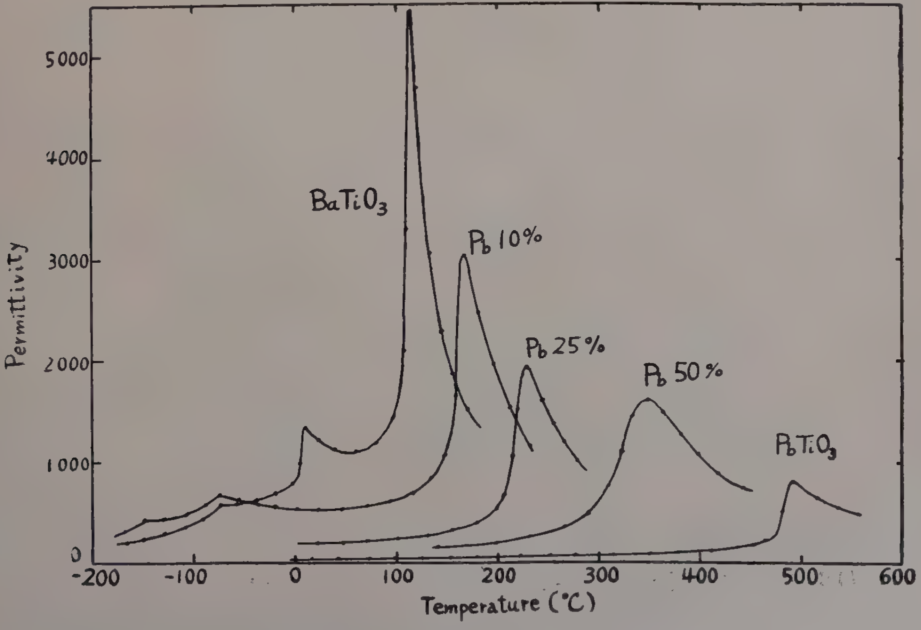

Fig. 1. Dielectric constants of (Ba-Pb)TiO_3 as a function of temperature.

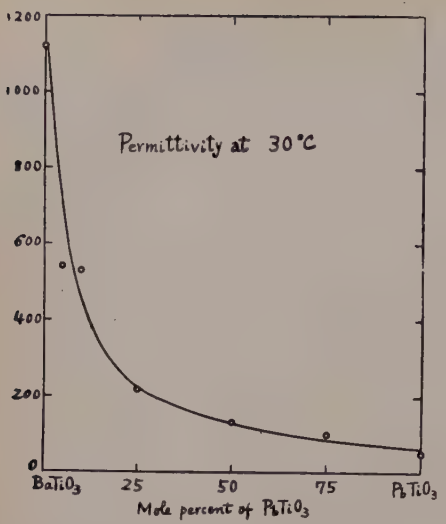

Fig. 3. Permittivity of (Ba-Pb)TiO_3 at 30°C.

The linear part of this curve is in agreement with former pulbications(3)(4)(5). The Curie temperature of $PbTiO_3$ is some what lower than the value 520°C obtained by Waku and Hori.(4)

As stated above, the solid solutions containing large percentages of $PbTiO_3$ are very porous and brittle, and the absolute values of the permittivity and the Curie constant cannot be determined unambiguously. But there is an evident tendency that the permittivity in the ferroelectric region decreases towards $PbTiO_3$ (Fig. 3).

In the cubic region, the Curie Weiss law, $\varepsilon = C/(T-T_0)$, is valid for all compositions. We have estimated the Curie constant C approximately and found that its value does not vary appreciably, being always in a narrow range between 1.0×10^5°C and 1.2×10^5°C. This result is in agreement with that of Nomura and Sawada(5).

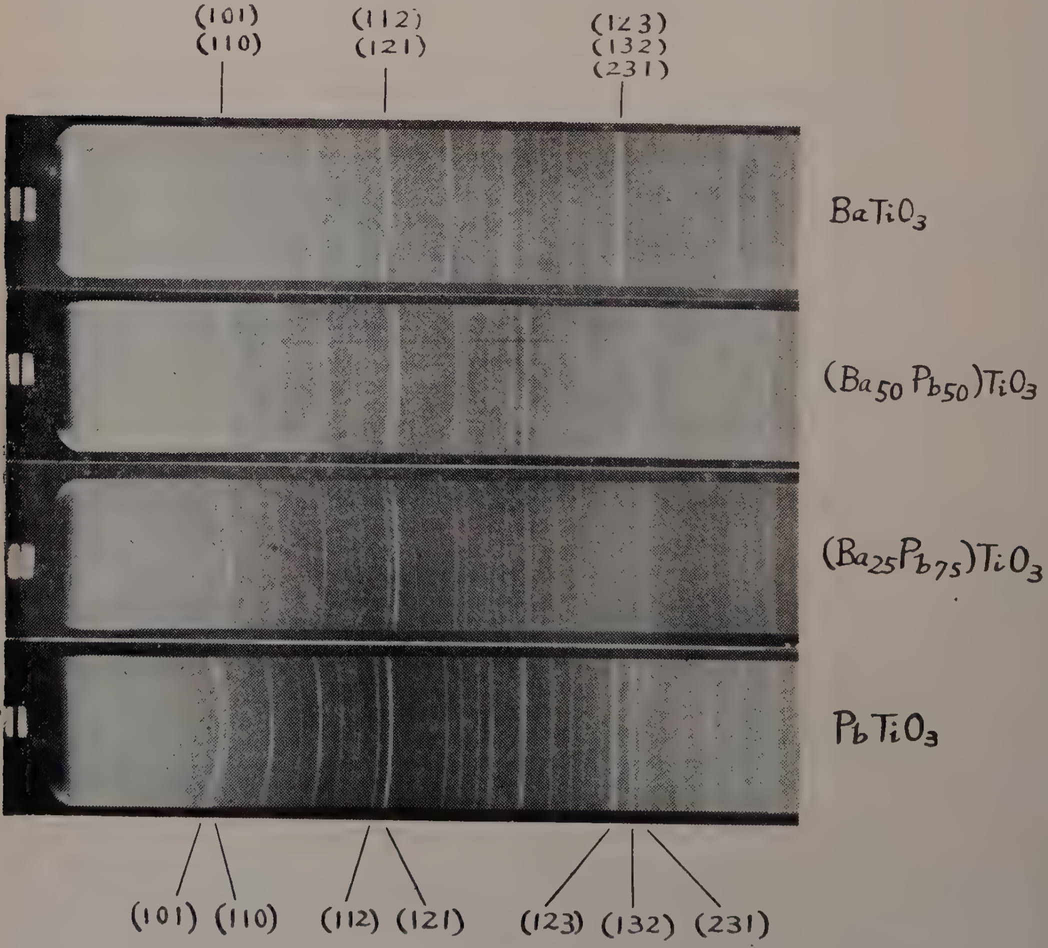

Fig. 4. Debye photographs of (Ba-Pb)TiO_3.

§ 3. X-ray Study.

An X-ray investigation of (Ba80-Pb20)-TiO_3 has been carried out by Miyake and one of the authors⁽⁶⁾ and it is found that at room temperature the axial ratio of this substance is larger than that of $BaTiO_3$. To obtain more detailed informations, we have performed an X-ray study of crystal structure of this series over the whole range of compositions.

The Debye photographs were taken with the powdered specimens, using Cu K_α radiation. The camera length is about 5 cm. We could explain well these photographs by assuming a tetragonal structure having the same atomic arrangement as that of $BaTiO_3$, i.e. perowskite structure. The precise lattice constants and the axial ratio at 30°C were calculated mainly from (*143*) and (*134*) lines, taken by back reflection method. The results are shown in Figs. 4, 5 and 6.

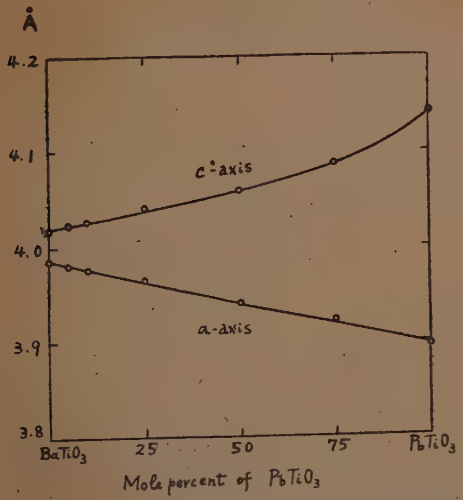

Fig. 5. Lattice constants of (Ba-Pb)TiO_3.

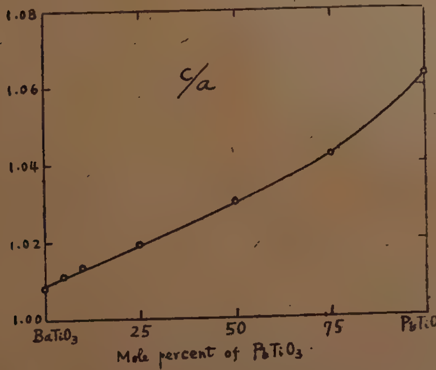

Fig. 6. Axial ratio vs. composition curve.

As the content of $PbTiO_3$ increases, the tetragonality c/a increases gradually and its change becomes rather steep towards the $PbTiO_3$ side. It is 1.063 for $PbTiO_3$.

We have shown the volume of unit cell $v = a^2c$ in Fig. 7. It decreases toward $PbTiO_3$, and this result can be explained if we take into account the ionic radii of Ba^{++} ion (1.35 Å) and Pb^{++} ion (1.10 Å). In the case of (Ba-Sr)TiO_3⁽¹⁾⁽⁸⁾, the Curie temperature decreases accompanied with the contraction of the unit cell volume. In this (Ba-Pb)TiO_3 series, the situation is different. This difference may presumably be due to the differences in the polarizabilities and in the electronic configurations between these ions. This phenomenon seems to suggest the inherent role of Ba ions in the ferroelectric character of barium titanate.

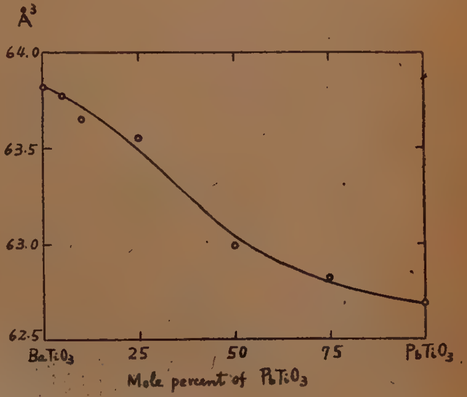

Fig. 7. Unit cell volume vs. composition curve.

All the numerical values of X-ray data are shown in Table I.

§ 4. Summary.

(1) Investigations by dielectric measurement and X-ray analysis have been made on the whole range of solid solutions of (Ba-Pb)TiO_3 series.

(2) The axial ratio c/a of this series increases with lead content accompanied with the rise of Curie temperature.

(3) The other two transition points in $BaTiO_3$ are depressed with lead content.

In conclusion we wish to express our sincere thanks to Mr. J. Hori for stimulating our interest in this problem and also to Professor S. Miyake and Professor Y. Takagi

Table I. Lattice parameters at 30°C.

% of $PbTiO_3$	c-axis (A)	a-axis (A)	c/a	unit cell volume (A^3)
$BaTiO_3$	4.019	3.985	1.008	63.82
5	4.024	3.981	1.011	63.77
10	4.026	3.976	1.013	63.65
25	4.041	3.966	1.019	63.56
50	4.058	3.940	1.030	62.99
75	4.086	3.921	1.042	62.82
$PbTiO_3$	4.140	3.894	1.063	62.69

for their kind guidance. We are also grateful to Mr. S. Hoshino for his helpful advice on our work.

This research was helped by the research grant of the Ministry of Education.

References.

(1) D. F. Rushman and M. A. Strivens: Trans. Faraday Soc. **42A** (1946) 231.
(2) A. von Hippel, R. G. Breckenridge, F. G. Chesley and L. Tisza: Ind. Eng. Chem. **38** (1946) 1097.
(3) G.H Jonker and J. H. von Santen: Chem. Weekblad. **43** (1947) 672.
(4) S. Waku and J. Hori: Reported at the Committee for the Piezoelectric Material held at Tokyo, on 1 st May 1950.
(5) S. Nomura and S. Sawada: J. Phys. Soc. Japan, **6** (1951) 36.
(6) K. Suzuki and S. Miyake: Reported at the meeting of the Phys. Soc. Japan, held at Tokyo, on 3rd April 1950.
(7) G. Shirane and S. Hoshino: J. Phys. Soc. Japan, **6** (1951) 265.
(8) G. Durst, M. Gotenhuis and A. G. Barkow: J. Am. Cer. Soc. **30**(4) (1950) 133.

J. PHYS. SOC. JAPAN **6** (1951) 278—279.

Short Notes.

On the Electret.

By Yoshinobu KAKIUCHI.

Institute of Science and Technology, University of Tokyo.

(Received, April 15 1951).

In recent years, studies on electret(1) became again active, and various interesting papers began to appear in current literatures. The present author have initiated the study of the problem some ten years ago, and although the results are still of preliminary one, it seems desirable to report some of them at the present stage. By saying electret, we mean Eguchi's electret, the mixture of carnauba wax and rosin solidified from their melts under a strong electrostatic field.

It is of paramount importance at first to answer the question to what component of the substance the effect is mainly due, because the materials used in common are by no means pure enough. For this purpose, carnauba wax was separated into (I) free wax alcohols and (II) esters (mainly melissyl cerotate) free from free acids and wax alcohols; and rosin into (III) abietic acid and (IV) more volatile resinous substances.

The above mentioned substances or their mixtures were solidified from their melts under the electric field as usual. After the surface charge was nullified by the irradiation with X-rays, the sample was mounted on the movable electrode E_1 (Fig. 1). The fixed electrode E_2 was connected to the electrometer. First, the electrode E_1, with the sample on it, was brought as near as possible to the electrode E_2, which was connected to the earth through the earthing rod R. It is essential to take care, lest the surface of the sample should touch the electrode E_2 in order to avoid the effect of the frictional charge due to surface contact. Then E_2 was

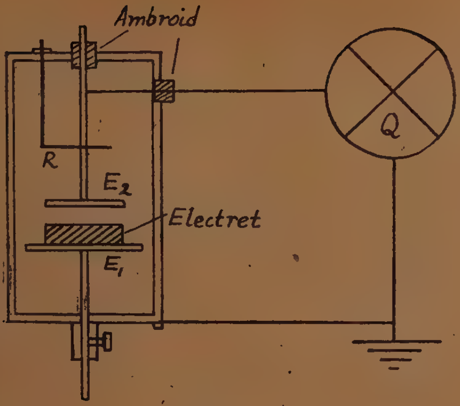

Fig. 1.

disconnected from the earth, and E_1 was lowered to the bottom of the shielding case. The charge induced on E_2, which is proportional to the charge of the electret was read by a quadrant electrometer Q.

Soon after the irradiation with X-rays, the charge did not appear, and its gradual recovery was observed. The result of the observation was summarized in Table I and Figs. 2 and 3. (I) showed the largest effect, the time of recovery, however, being extremely short. Mixture of (II) and (III) or (IV) also recovered the considerable amount of the charge, and its time of recovery was very long (Figs. 2 and 3, charge corresponding to homocharge).

Table I.

substance	effect
I	larger
II	no
III	no
IV	no
II+I	small
II+III	medium
II+IV	medium

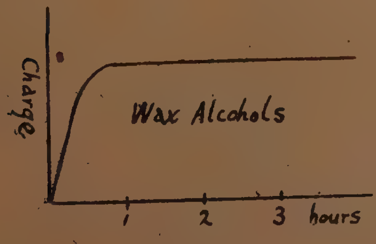

Fig. 2.

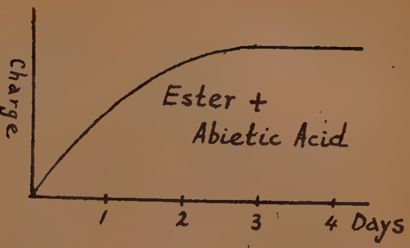

Fig. 3.

Because the essential features of the electret exist in wax ester- abietic acid mixture, it is highly desirable to study the mechanism of the electret first through the experiments on pure *melissyl-cerotate-and-abietic-acid-mixtur* , and the comprehensive program of preparing pure materials is now under progress in our laboratory and by a group in Scientific Research Institute.

It was concluded that it is essential for explaining the recovery and maintenance of the surface charge of the electret to assume the *continuous decay* of the polarization as suggested by Adams(2). The life time of the polarized wax ester and abietic acid mixtures was considered to be extemely long compared with that of alcohols, which fact explaining the permanency of the electret. The polarization was more easily destroyed by raising the temperature, and the depolarization current can be observed as was reported before(3)(4). Even the electret prepared ten years ago, gave up considerable amount of the charge by heating.

Recent experiment by Dr. S. Kojima(5) and his collaborator is of much interest in a sence that it suggests the discontinuity in the process of depolarization. Further discussions will be described in future together with the results of the experiments in detail.

The author expresses his gratitude to Profs. Emeritus S. Nishikawa and S. Kakiuchi for their interest and many valuable discussions.

References.

(1) For general references see:
Gutmann: Rev. Mod. Phys. **20** (1948) 475.
(2) Adams: J. Frank. Inst. **204** (1927) 469.
(3) Frei and Groetziner: Phys. Z. **37** (1936) 720.
(4) Kakiuchi: Sci. Pap. I. P. C. R. **40** (1940) 189.
(5) Kojima and Kato: J. Phys. Soc. Jap. **6** (1951) 207.

J. PHYS. SOC. JAPAN 6 (1951) 280–281.

On High Frequency Power Loss of Dielectrics.

By Ken'iti HIGASI and Yasumoto OZAWA.
Research Institute of Applied Electricity, Hokkaido University, Sapporo.

(Received April 26, 1951)

In text-books1) of dielectrics, loss factor, or sometimes loss tangent, has been taken as a measure of power loss, or of the rate of heat evolution in radio heating. In the present note we wish to point out that such a practice is apt to cause unnecessary confusion and lead eventually to misunderstandings of the true mechanism.

Since the Debye's theory of dipole rotation came to be regarded as a useful principle in interpretating dielectric phenomena, a fallacy of this theory has appeared:2) a polar substance generally absorbs selectively the electrical energy of a certain frequency. This misunderstanding of the theory appears to rest in the premises (1) that loss factor (or loss tangent) has an optimum value at a frequency; and (2) that power loss is proportional to these quantities.

The second premise is misleading: power loss P is related to the field intensity E, loss factor ε'', $\tan\delta$ and effective condnctivity σ by the following equations.

$$\left.\begin{aligned} P &= |\vec{E}|^2\,\sigma \\ &= |E|^2\,\frac{\varepsilon''\,\omega}{4\pi} \\ &= |E|^2\,\frac{\varepsilon\cdot f\cdot\tan\delta}{2} \end{aligned}\right\} \qquad \cdots\cdots\cdots(1)$$

And these dielectric quantities for an ideal Debye's dielectrics are plotted against angular frequency ω in Fig. 1. There is no peak in the conductivity-frequency curve, and also none in power loss, provided the field intensity is independent of frequency.3)4)5)

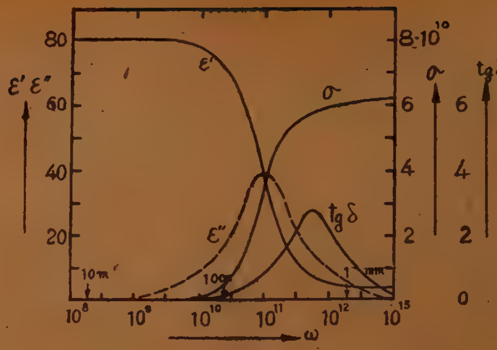

Fig. 1. Dielectric quantities ε', ε'', $\tan\delta$, and σ of a representative dipole liquid (water).

Again we may refer to the recent controversy concerning the electric behaviour of methyl palmitate. In 1948, Jackson and his co-worker6) found an anomaly in $\tan\delta$ of this substance and discussed the possible types of resonance absorption in dielectrics, although he showed a more cautious attitude toward this hypothesis in his second letter.7)8) In 1950, Cook and Buchnan9) referred to resonance again as the possible cause of the micro-wave absorption. However, this series of disputes might not have occurred if they had used conductivity instead of loss tangent in their discussions.

In the lower part of Fig. 2, the values7)8) of loss tangent of methyl palmitate were plotted against frequencies f, while its effective conductivities are shown in the upper part of the same graph. It is to be noted that in contrast to

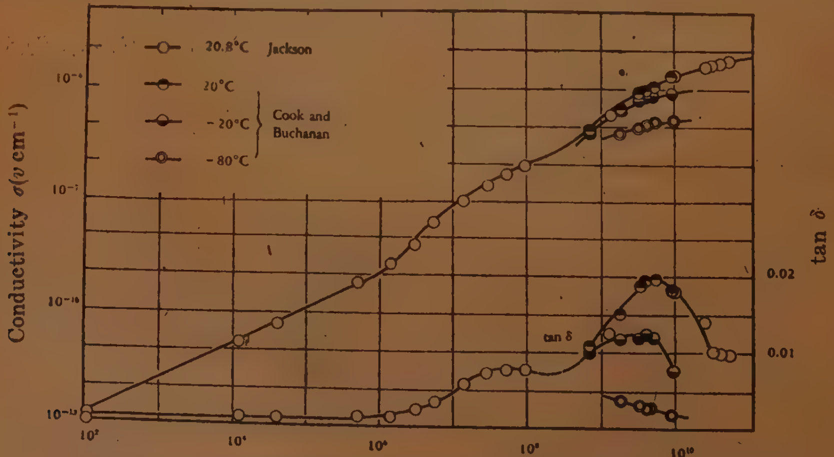

Fig. 2. Loss tangents and effective conductivities of methyl palmitate plotted against frequencies f.

tan δ there is no peak in the curves for σ in the whole range of frequencies.

We may take Fröhlich's[1] formula for resonance absorption.

$$\varepsilon-\varepsilon_{\infty}=\frac{1}{2}\Delta\varepsilon\left(\frac{1-i\omega_0\tau}{1-i(\omega_0+\omega)\tau}+\frac{1+i\omega_0\tau}{1+i(\omega_0-\omega)\tau}\right) \quad (2)$$

It can be proved from this that conductivity has a maximum near the resonance frequency, $\omega_0/2\pi$, provided that $\omega_0\tau>1/\sqrt{3}$, where τ is a relaxation time (see Fig. 2). At a glance at Figs. 2 and 3 it is evident that the observed phenomenon is related to the condition that $\omega_0\tau>1/\sqrt{3}$. And it follows from this that loss factor will have a maximum at $\omega\simeq 1/\tau$, i.e., approximately the condition for the Debye's type absorption holds.

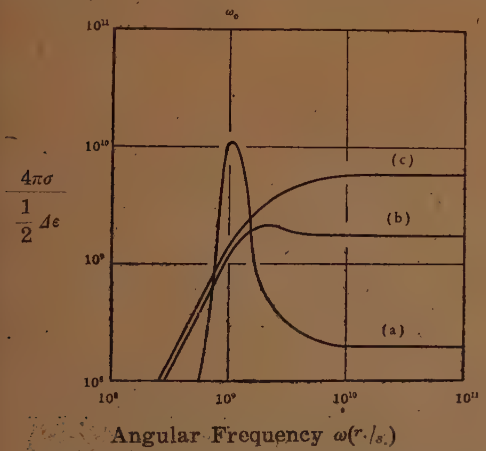

Fig. 3. The relation between effective conductivity and angular frequency

(a) $\omega_0\tau=10$, $\omega_0=10^9$
(b) $\omega_0\tau=1$, ,,
(c) $\omega_0\tau=1/\sqrt{3}$, ,,

$\Delta\varepsilon$ is a quantity independent of frequeney (see Fröhlich).

It is apparent therefore that one should not speak of resonance, even if he finds a maximum in the tan δ-f or ε''-f curves.

In conclusion, it is to be noted that high frequency conductivity is not only a useful measure of power loss in the high frequency region but also serves as a criterion for resonance absorption.

We wish to thank cordially Professor Asami for his help and encouragement. Our thanks are also due to Professor Jackson of London, Professor Fröhlich of Liverpool and Professor Kakiuchi for their interest in the work.

References.

1) Fröhlich: "Theory of Dielectrics" Oxford (1949).
2) Schupp: Siemens Werke, **25** (1938), 1.
3) Asami, Higasi and Ozawa: Nature, **165** (1950), 195.
4) Higasi: "The Theory and Application of High Frequency Phenomena" edited by Asami, Hokkaido University (1950), p. 7.
5) Ozawa: ibid., p. 33.
6) Dryden and Jackson: Nature, **162** (1948), 656.
7) Jackson: Natur, **164** (1949), 486.
8) Private communication of Prof. Jackson.
9) Cook and Buchnan: Nature, **165** (1950), 358.

J. PHYS. SOC. JAPAN **6** (1951) 281–282.

On the Shape of Radio-Frequency Spectrum.

By Seiichi SUEOKA.

Institute of Applied Mathematics, Second Faculty of Enginnering, University of Tokyo.

(Received December 5, 1950)

The absorption shape of the radio-frequency spectrum, due to diatomic molecules, in the nuclear magnetic resonance method has been discussed ingeneously by E. T. Feld and W. E. Lamb in the case of large rotational quantum number[1]. The essential points of their treatment consist in the following simplifications. In the first place, they regard J, the rotational quantum number, which is assumed large, as a classical quantity and thus treat m_J/J as a continuous variable, where m_J is the z-component of J. Secondly, they neglect the breadth of the absorption line at a definite m_J.

Therefore their result appears to be insufficient to apply to the case when the statistical means for J are to be taken or the half-widths of the peaks are to be considered accurately[2]. In order to study these points, we obtained more accurate results, by summing up the transition probabilities, belonging to a same nuclear transition but to different values of m_J. In the following, we use the same notations as in Lamb and Feld's paper.

In strong magnetic field, the Hamiltonian is given as follows:

$$H=\mu_0 g_I(\boldsymbol{H},\boldsymbol{I})+\mu_0 g_J(\boldsymbol{H},\boldsymbol{J})+H(Q),$$

and the quardrupole term $H(Q)$ is regarded as a perturbation. The first-order values of the above energy in m_I, m_J scheme are given by

$$E(m_I,m_J)=\mu_0 g_I m_I+\mu_0 g_J m_J$$
$$+\frac{e^2qQ}{4J(2J-1\ I(2I-1)}[3m_I^2-I(I+1)].[3m_J^2-J(J+1)].$$

Then the frequency $\nu_{m_J}(m_I)$ corresponding to the transition $\Delta m_J = 0$, $m_I \to m_I - 1$ is obtained as follows

$$\nu_{m_J}(m_I) = \nu_0 + \alpha m_J^2,$$

where $h\nu_0 = \mu_0 g_I |H| - \frac{\alpha}{3} J(J+1)$,

$$\alpha = qe^2qQ(2m_I - 1)/4J(2J-1)I(2I-1).$$

The probability for the above transition at a definite m_J has the following form which is already obtained[1].

$$P_{m_J}(m_I \to m_I - 1) = \frac{b^2}{b^2 + (\nu - \nu_{m_J})^2} \sin \pi t [b^2 + (\nu - \nu_{m_J})^2]^{1/2},$$

where b is the matrix element of the oscillating part of the Hamiltonian and is given by

$$b = \mu_0 g_I H_x' \sqrt{(I+m_I)(I-m_I+1)}\,/2.$$

The shape of the resonance spectrum may be represented by the following function $S_J(m_J)$ which corresponds to the shape-function of Lamb and Feld

$$S_J(m_I) = \sum_{m_J=-J}^{J} P_{m_J}(m_I \to m_I - 1).$$

Here we may neglect αm_J^2 in the argument of sine function, assuming the quadrupole moment as small; then we have

$$S_J(m_I) = \sin^2 \pi t [b^2 + (\nu - \nu_0)^2]^{1/2} \cdot \sigma_J,$$

$$\sigma_J = \sum_{m_J=-J}^{J} \frac{b^2}{b^2 + (\nu - \nu_0 - \alpha m_J^2)^2}.$$

Especially, the summation can be performed easily for the case of $J \to \infty$ as follows:

$$\sigma_\infty = \frac{ib}{2\alpha} \sum_{m_J=-\infty}^{\infty} \left[\frac{1}{m_J^2 + z^2} - \frac{1}{m_J^2 + \bar{z}^2} \right]$$

$$= \frac{ib\pi}{2\alpha} \left[\frac{1}{z} \cdot \frac{\sinh 2\pi z}{\cosh 2\pi z - 1} - \frac{1}{\bar{z}} \cdot \frac{\sinh 2\pi \bar{z}}{\cosh 2\pi \bar{z} - 1} \right],$$

where $\alpha z^2 = -(\nu - \nu_0) - ib$, $\bar{z}$ is conjugate complex to z.

Thus the final result is obtained as follows:

$$\sigma_\infty = \frac{b}{2\sqrt{b^2 + (\nu - \nu_0)^2}} A(\nu).$$

where

$$A(\nu) = \frac{B \sinh x - x^2 \sin(B/x)}{x(\cosh x - \cos(B/x))}$$

and

$$B = \frac{2\pi^2 b}{\alpha}, \quad x^2 = \frac{B}{b}\{\sqrt{b^2 + (\nu - \nu_0)^2} - (\nu - \nu_0)\}.$$

The function σ_∞ has the resonance at the point $\nu = \nu_0$ the first factor, which is the usual resonance function. On the other hand, $A(\nu)$ represents the amplitude which depends, however on $\nu - \nu_0$. One has therefore to take the effect of $A(\nu)$ into account to discuss the half-width of the peak accurately. $A(\nu)$ for the various values of B are obtained numerically and are represented in Fig. 1. The figure of σ_∞, taking into consideration of the first factor are represented in Fig. 2. From these, we can obtain the half-width of the resonance peak easily as follows:

$$2 \cdot 1b \text{ for } B = 1;\ 1{,}756 \text{ for } B = 0 \cdot 1.$$

Here we should notice that the resonance peak is displaced from the point $\nu = \nu_0$, when the value of B is taken 100 or 10. This may be due to the roughness of our approximation. This may be corrected by taking the summation over m_J in the range of finite J.

The total absorption shape is obtained by summing up the possible m_I's, that is $\sum_{m_I} S_J(m_I)$.

The author wishes to express his hearty thanks to Prof. T. Yamanouchi for his kind encouragement throughout this work.

Fig I

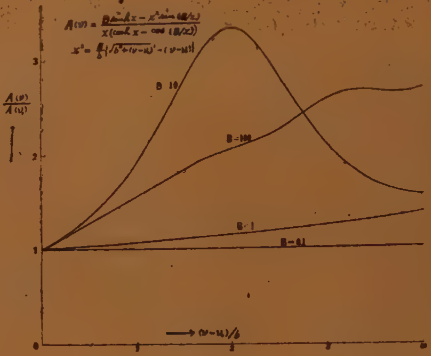

Fig. II.

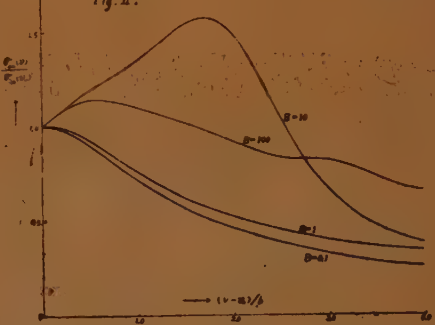

References.

(1) E. T. Feld and W. E. Lamb: Phys. Rev. **67** (1945), 15.
(2) P. Kusch: Phys. Rev. **75** (1949), 887.
(3) T. J. Bromwich: An Introduction to The Theory of Infinite Series, p. 314.

J. Phps. Soc. Japan 6 (1951) 283—284.

On the Noise of Pre-Breakdown Current.

By Hazimu Kawamura and Masami Onuki.
Department of Engineering, Osaka City University, Osaka.

(Received April 16, 1951)

The dielectric breakdown of solid was interpreted with electron avalanche for the first time by v. Hippel. According to the theory of Seitz,[2] even in the pre-breakdown region, there are electron avalanches which compose the pre-breakdown currents. Such an exceedingly noisy current in glass at the pre-breakdown region has been studied by Haworth and Bozorth[3] in 1934.

Our present specimens are transparent Indian micas about 10^{-3} cm in thickness and a few mm square in area, on whose surfaces aluminium films of about 1.5 mm diameter was deposited by evaporation in vacuum. The specimen was inserted between two hemi-spherical electrodes of about 3 mm diameter and the whole was coated with paraffin as shown in Fig. 1a.

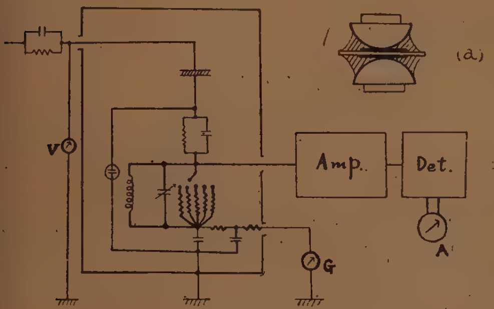

Fig. 1 a~b.

High voltages up to breakdown limit, which were around 3~5 kV, were supplied by an eliminator. Direct current through specimen i_0 was measured by a galvanometer *G*. The square of fluctuation current i was measured simultaneously by a micro-ammeter *A*, as the output of three stage resonant amplifier and quadratic rectifier as shown in Fig. 1b.

The maximum gain of the amplifier was about 110 db which could be decreased by an amount of 60 db by step of 10 db. The frequency of the amplifier was varied in four steps, 28 kc, 70 kc, 215 kc, and 600 kc, by changing the coils and condensers in the reson antcircuits.

If the avalanches are composed of n electrons in the average, the current flowing through the specimen is given by $i_0 = e\nu\bar{n}$, where ν is the number of avalanches per second. The average size of the avalanches can be given by

$$\frac{\bar{n^2}}{\bar{n}} = \frac{2kT}{ei_0R}\cdot\frac{\bar{i^2}-\bar{i_T^2}}{\bar{i_T^2}},$$

where R is the input resistance, and i_T is the thermal fluctuation noise of the resistance R. i_0 and $\bar{n^2}/\bar{n}$, measured at 600 kc for various specimens, are shown in Fig. 2, where the ordinate is the reduced voltage, whereby the breakdown voltage is taken as 100%.

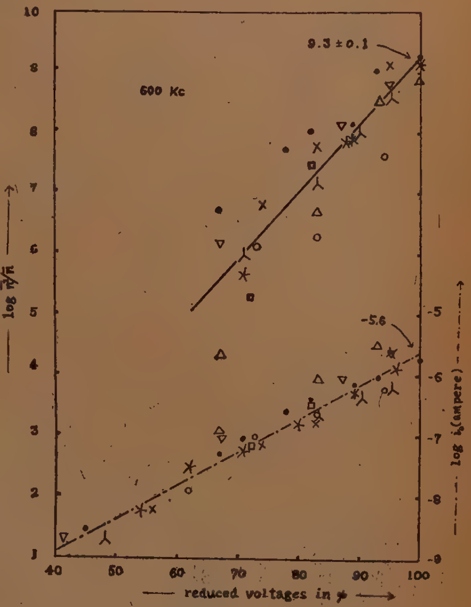

Fig. 2.

For lower frequencies such as 28 kc and 70 kc, the measured points are more scattered. $\bar{n^2}/\bar{n}$ at the breakdown field determined from these figures, are plotted in Fig. 3, which shows that the frequency character is almost flat, although it seems to increase slightly at frequencies lower than 100 kc.

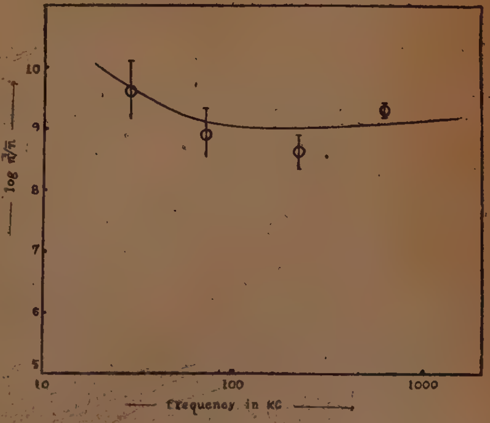

Fig. 3.

One of the points of ambiguities in this measurement is the occurrence of noisy current due to the surface leakage of the specimen. But these current can be removed by coating the specimen with paraffin wax, dipping in high temperature bath of paraffin of about 120° C. As Schoenfeld reported,[4] a large pulse is produced by the sudden discharge of local space charge between the electrode and the specimen, which occur in the case of rather bad contact and gives a noise decaying after the application of the voltage in a few second. We can avoid this effect by cleaning the surface of mica by exposing in glow discharge before the evaporation of the aluminium electrode. Nevertheless we cannot avoid the scattering of the measured points at frequencies lower than 70 kc, which probably is due to the noises owing to the above reason or discharge of inner localized space charge etc. The avalanche size, 10^9, which we have obtained is less than that estimated by Seitz which is 10^{12}. But, if his estimation is applied to the specimen 10^{-3} cm thick, we can obtain a number of 10^9 as the size of the avalanche at the breakdown, which coincides fairly well with our present measurement.

References.

1) A. von Hippel: Jour. Appl. Phys. **8** (1937) 815.

2) F. Seitz: Phys. Rev. **76** (1949) 1376.

3) F. E. Haworth, R. M. Bozorth: Physics **5** (1934) 15.

4) H. Schoenfeld: Ann. d. Phys. **9** (1934) 733.

Errata: On the Scattering of Fast Neutrons from Li-D Reactions.

By T. Wakatsuki and K. Sugimoto.

J. Phys. Soc. Jap. 6 (1951) 157.

P. 157	Abstract; line 1	37	should be read	36
P. 158	left column line 26	electroks	”	electrodes
	Formula (1)	$[RJ_1\ kR\theta)/\theta]^3$	”	$[RJ_1(kR\theta)/\theta]^2$
	Formula (2)	$(2.3+1.25A^{1/3})\,10^{-12}$	”	$(2.3+1.25A^{1/3})\,10^{-13}$
	right column line 33	5.65×12^{12}	”	5.65×10^{12}
	The last sentence in §2. Between words “form” and “and” the following words was dropped: “time to time during experiments and the value of about 6% was obtained”			
P. 159	Table 6th column line 10	64.2±1.2	should be read	84.2±1.2
	6th column line 24	54,2	”	64.2
	6th column line 31	62.7	”	82.7
	7th column line 19	3.16±0.19	”	3.16±0.10
	8th column line 24	4.89±02.1	”	4.89±0.21
P. 160	Fig. 1 and Fig. 2 must be interchanged, and the data corresponding to Zn must be removed from both figures.			
	right column line 8	Zn	should be read	Mn
P. 161	left column line 1	Ti and Zn	”	Ti
	left column line 1	show	”	shows
	left column line 2	values	”	value
	left column line 2	have	”	has
	Explanation of Fig. 2.	$1.4+1.6A^{1/3}$	”	$(1.4+1.6A^{1/3})\times10^{-13}$ cm
P. 162	left column The sentence from line 27 to 30 must be removed.			
	right column line 13	Fe	should be read	Cu
P. 163	left column line 8	75	”	73
	right column line 1	(195), 19	”	(1950), 16

JOURNAL OF THE PHYSICAL SOCIETY OF JAPAN, Vol. 6 No. 5 September—October, 1951

A Note on the Intensities of the Internal Conversion Lines of the Three Intense γ-rays of RaB.

By Seizaburo KAGEYAMA.

Physical Institute; Tokyo University of Literature and Science.

(Received December 12, 1950)

The relative intensities of internal conversion electrons of 240, 294 and 350 KeV γ-rays of RaB and ratios of those for K and L energy levels, α_K/α_L, have been investigated with a magnetic spectrometer of fair resolution and G-M counter technique.

Values of α_K obtained are in accord with the results of Ellis and Aston but those of α_L and α_M are slightly different from their values. The agreement between observed and theoretical values of α_K/α_L is satisfactory within the experimental error.

§1. Introduction.

In light elements, the ratios of the internal conversion coefficients of γ-rays for K and L shell, a_L/a_K, are sensitive for the multipole order and the nature of a radiation.⁽¹⁾ In heavy elements, however, these ratios are equal for electric dipole and quadrupole radiations, so far they are very hard. Hulme,⁽²⁾ for example, has found the $a_{L_1}:a_K=1:6.7$ always in extreme-relativistic case. His formula gives $a_{L_1}:a_K=1:7.0$ for dipole radiation of $h\nu=7.2\times10^5$ eV. According to Fisk,⁽³⁾ this ratio for quadrupole radiation remains practically constant down to $h\nu=2.5\times10^5$ eV.

Ellis and his coworkers⁽⁴⁾ performed, years ago, a precise measurement of the intensities of internal conversion lines of RaB, using a magnetic spectrometer of semi-circular focusing type. They determined it from the blackening of photographic plate. Their experimental values of the internal conversion coefficients, a_K, for three intense γ-rays of RaB seem to be definitely higher than the theoretical electric quadrupole curve, and nearer to that for magnetic dipole radiation.⁽⁵⁾

According to the theory, the *RATIOS* of the coefficients of K and L conversion a_{L_1}/a_K, however, are expected nearly equal for electric dipole, quadrupole, and magnetic dipole radiation. But the ratios obtained by Ellis and his coworkers deviate largely from the theoretical expectation.

In the previous paper,⁽⁶⁾ we have examined the relative intensities of the conversion electrons of RaC γ-rays, using a magnetic spectrometer of semi-circular focussing type and coincidence counting method with G-M counters. The ratios of the internal conversion coefficients of main γ-lines for different energy levels are tabulated in Table II in that paper. The ratios of a_{L_1}/a_K were practically constant and accord completely with the

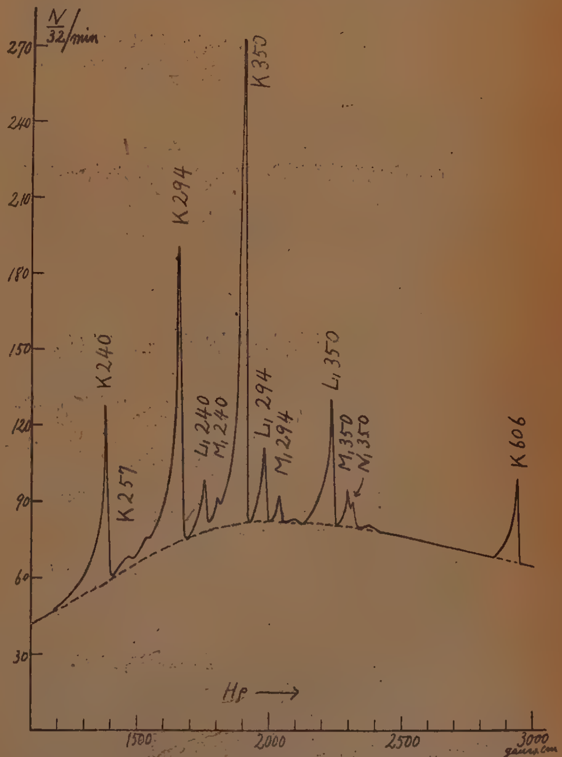

Fig. 1. Natural β-spectrum of RaB and a part of RaC (without recalculation for equal interval of Hρ).

theoretical value, except for the γ-rays of lowest energy, 606 KeV. In this line, the difference between the observed and theoretical values seemed to exceed the experimental error. But it could not be attributed to the effect of scattering by mica window.

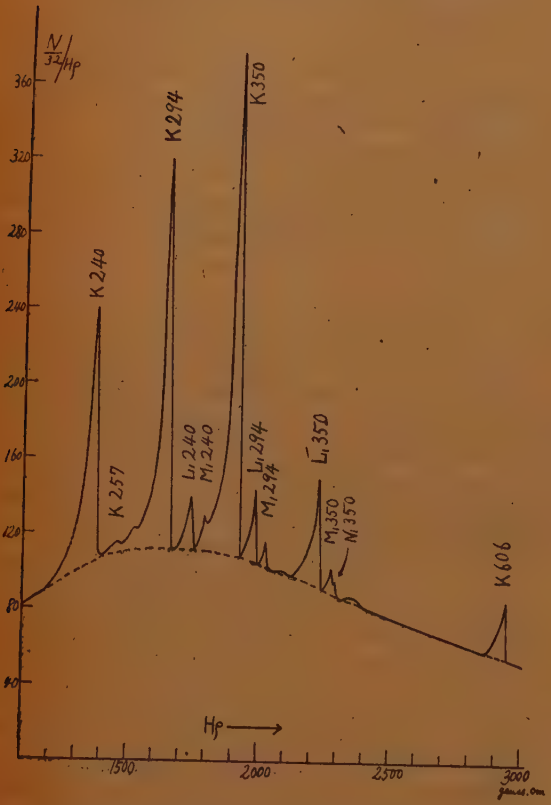

Fig. 2. Natural β-spectrum of RaB and a part of RaC (with recalculation for equal interval of Hρ).

Ellis says that in the case of RaB γ-rays, M_1 conversion line of 294 KeV γ-rays is weaker than that of 240 KeV γ-rays, but reverse is the case in K conversion lines of them.

We have re-examined the internal conversion lines of RaB γ-rays and studied carefully these points in question.

§2. Experimental Arrangement and Procedure.

We have used the same β-ray spectrometer and experimental procedure as described in the previous paper.(6) The strength of magnetic field was determined only relatively through exciting current and the deflection of a glavanometer coil which was suspended between the pole pieces of the magnet. The $H\rho$ values of the three intense K conversion lines were absolutely measured by Rogers(7) and Scott.(8) The difference of $H\rho$ value between K and L_1 conversion lines of 350 KeV γ-rays was precisely measured by Ellis and was found to be 361.4gauss.cm. On the basis of these values corrected for the retardation of electron in the glass wall of Rn tube, the $H\rho$ values of the conversion lines lying in this region were calculated from our relative measurement.

The sensitivity of the galvanometer system was about 5 gauss. cm. per scale division. Observation records were usually taken at an interval of one division in continuous region and 1/2 scale division around the conversion peak. $1\sim2\cdot10^4$ counts in continuous region and $4\sim5\cdot10^4$ counts around the conversion peaks were recorded.

To minimize the effect of the scattering by mica window, a single G-M counter having an entrance slit of $0.4\times10\text{mm}^2$ was used as detector and mica foil of about 0.5mg/cm^2 was served as the separator of counter and vacuum chamber in the main experiment. A thin window counter with 12 holes of 0.8mm in diameter and a mica separator $0.3\sim0.4\mu$ thick was also used for checking the absorption effect of the foil in lower energy region.

Rn up to 100mc. sealed in a glass ampule was used as the source of β-rays, the thickness of ampoule being about 2.7mg/cm^2. A 32-scaling circuit of vacuum triodes UY-56 served as the recorder.

§3. Experimental Results.

The experimental results are shown in Fig. 1-4 and also tabulated in Table I and II. Fig. 1 represents the experimental results on natural β-ray spectrum of RaB and a part of RaC spectrum in $H\rho$ scale without recalculation for equal interval of $H\rho$. The numbers near the conversion peaks denote the energies of the corresponding γ-rays in KeV and the letters K, L_1 and M_1 indicate the origin of the conversion line. Fig. 2 gives the β-particle distribution in $H\rho$ scale recalculated for equal interval of $H\rho$. In the latter figure, the area under the conversion peak, of course, is proportional to the number of conversion electrons of the γ-rays, i.e., to the intensity of the γ-rays (p) multiplied by the conversion coefficient (α). Fig. 3 and 4 depict $L_1 294 \sim L_1 350$ region and $L_1 \sim M_1$ 240 region enlarged respectively. The relative intensities of these conversion peaks are estimated from the distribution curve given in Fig. 2 and are shown in Table I, together with those obtained by English authors, the intensity of K606 line being assumed to be 40. The ratios of the internal conversion coefficients of different energy levels are also given in Table II.

Table I. Relative intensities of conversion electrons of the three intense RaB γ-rays.

Energy of γ-rays in KeV	Conversion level	Relative intensities: Ellis and Aston	Relative intensities: Present Writer
240	K	425	415±20
	L_1	63	60± 5
	M_1	13	17± 3
294	K	480	480±20
	L_1	64	75± 5
	M_1	11	20± 3
350	K	530	540±20
	L_1	85	95± 7
	M_1	42	30± 4
	N_1	8	5± 3
606	K	40	40

Table II. Ratios of the internal conversion coefficients of the three γ-lines of RaB for different energy levels.

Energy of γ-rays in KeV	α_{L_1}/α_K: Ellis and Aston	α_{L_1}/α_K: Present Writer	α_{M_1}/α_K: Ellis and Aston	α_{M_1}/α_K: Present Writer
240	0.12	0.15±0.015	0.03	0.05 ±0.01*
294	0.13	0.15±0.015	0.02	0.05 ±0.01*
350	0.16	0.17±0.015	0.08	0.055±0.01
606	0.22	0.18±0.015	0.04	0.07 ±0.01
Theoretical value	0.15			

* Weak N_1 conversion electrons will probably be included.

§4. Discussions.

The continuous β-ray spectrum obtained accord well with Gurney's experiment.⁽⁹⁾ Owing to the high resolving power of our spectrometer, however, the conversion peaks of L_1 and M_1 of three intense γ-rays were completely resolved from each other in our spectrum.

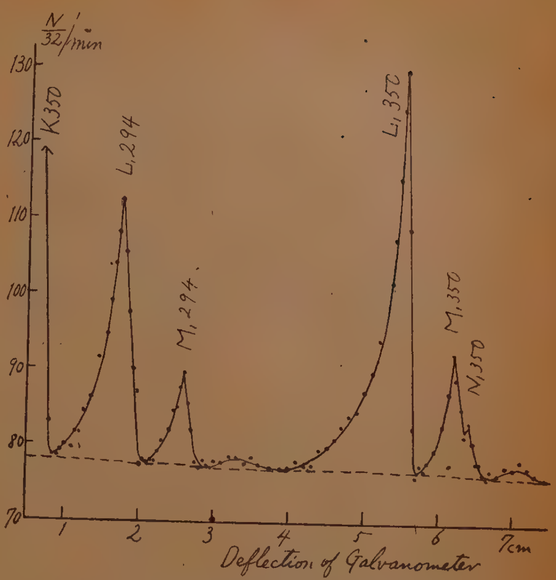

Fig. 3. Conversion peaks L_1 294, M_1 294, L_1 350, M_1 350 and N_1 350.

On the tails of the intensity distribution curve of K294 and K350, there are the superpositions of the conversion electrons of unknown γ-rays and the conversion electrons M_1 240 respectively. But the intensity of the conversion electrons of unknown γ-rays is very weak, and so the error in the estimation of the intensity of main line will not be large. The error in the estimation of the intensity of K350 due to the satellite M_1 240 also will not be large, because of the sharpness of the peak of the latter. The intensities of the three intense K-conversion lines accord completely with the results of English authors.

The intensity of L_1 240 also accord well with their result. Nevertheless the intensities of L_1 294 and L_1 350 conversion lines were found to be somewhat larger than theirs. The differences seem to exceed our experimental error. As for the origin of discrepancy, the following articles may be taken into consideration:

(1) the scattering by the mica window of counter,
(2) the straggling of β-particles of low velocity in the glass wall,
(3) the error in estimation of the area under conversion peak.

To suppress the effect of the scattering, we used a single counter for detector, as already described in §2. Moreover, we repeated the measurent with a thin window counter having a mica film of 0.3~0.4μ in thickness. The effect of absorption of electron by this thickness of mica may be entirely neglected in the energy region studied. But the relative intensities of L_1 294 and L_1 350 against K606 were found unchanged within the statistical error. The discrepancy, therefore, cannot be attributed to the scattering by mica window.

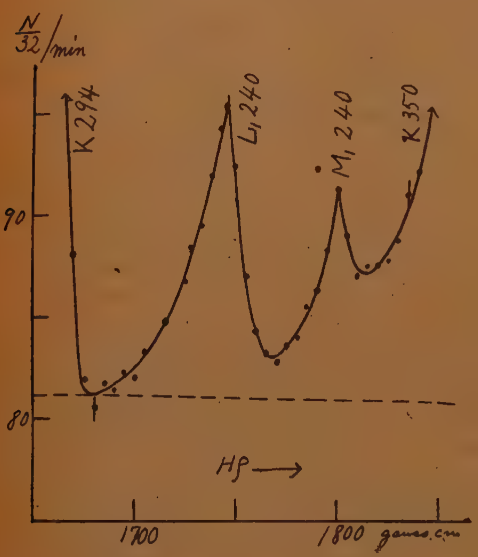

Fig. 4. Conversion peaks L_1 240 and M_1 240.

If the discrepancy had due to the straggling of the low energy β-particles in the glass wall of radon tube, the observed intensities would have changed with thickness of the glass wall. But no dinifite variation of relative intensities was recognized even with a glass ampoule of 3.85mg/cm^2, although the breadth of the conversion lines was somewhat broader than before. The error due to the third origin would be the largest in our experiment. But this error did not certainly exceed 4~5%. From the above, English authors may have underestimated the intensities of weaker lines. The estimation of the blackening of the plate by weak conversion line will not be easy under the strong background of continuous β-rays.

Conversion peak of L_1 257 seems to be completely masked by the tail of K350.

The $M_1$240 conversion peak is superposed by the tail of the intense peak K350. So the error in the estimation of its intensity will probably be a little larger than in the others. But, as seen from Fig. 4, its intensity is not so difficult to estimate. The intensity of M_1 294 conversion peak is twice as intense as compared with the result of English authors. This difference, however, can never be attributed to the superposition of $N_1$294 conversion electrons which we could not find out as well as English authors. If $N_1$294 conversion peak had so intense as would explain such large difference, as in the case of $N_1$350, the foot of $M_1$294 would have extended about 15 gauss. cm. further on the right side. We examined carefully this region, but the foot of $M_1$294 accord completely with the calculated value within the error of ±2 gauss. cm. and no trace of N_1 294 was found. So we concluded that even if there were superposition of $N_1$294, its contribution would be very small. The area of this peak, tabulated in Table I, therefore, gives practically the intensity of $M_1$294.

$M_1$350 conversion peak is not completely separated from $N_1$350 conversion peak. So the error in the estimation of its intensity will also be large as is in $M_1$240. But we believe that the intensity of $M_1$350 given by English authors is surely too large and the value given in Table I is more exact.

The intensity of $N_1$350 conversion peak may be estimated from its height, but its error will be large. No trace of $N_1$294 and $N_1$240 was detected in our experiment.

The region from $N_1$350 to K606 was studied only roughly, and so any conversion lines of weak RaB and RaC γ-rays would have missed.

From the considerations given above, we believe the ratios of the internal conversion coefficients, α_{L_1}/α_K, tabulated in Table II, are more exact than the results of English authors. The obtained ratios are in accord with the theoretical prediction within experimental error. Comparing these ratios with that of 606 KeV γ-rays of RaC, we also concluded that even if there were a superposition of the conversion electrons of unknown γ-rays on $L_1$606, it would be negligibly weak.

In conclusion, the author expresses his sincere gratitudes to Prof. Y. Fujioka for his encouragement and to Prof. M Miwa for his helpful suggestions and valuable discus-

sions. The author wishes to express his thanks to the Japanese Foundation for Cancer Research for the supply of radon through Dr. K. Tsukamoto with helpful interests, and also to Ministry of Education for financial aids.

References.

(1) Dancoff and Morison: Phys. Rev. **55** (1939) 122
Hebb and Nelson: Phys. Rev. **58** (1940) 486
Helmholz, Phys. Rev. **60** (1941) 415
(2) Hulme: Proc. Roy. Soc. **138** (1932) 643
(3) Fisk: Proc. Roy. Soc. **143** (1934) 674
(4) Ellis and Aston: Proc. Roy. Soc. **129** (1930) 180, Ellis and Skinner: ibid. **105** (1924) 165, Ellis, ibid. **143** (1934) 150
(5) Fisk and Taylor: Proc. Roy. Soc. **146** (1934) 178, Hulme, Mott, Oppenheimer and Taylor, ibid. **155** (1936) 315
(6) Miwa and Kageyama: Phys. Soc. of Japan **5** (1950) 416
(7) Rogers: Phys. Rev. **50** (1936) 515
(8) Scott: Phys. Rev. **46** (1934) 633
(9) Gurney: Proc. Roy. Soc. **109** (1925) 540

JOURNAL OF THE PHYSICAL SOCIETY OF JAPAN, Vol. 6 No. 5 September—October, 1951

The Second Virial Coefficient of Non-Spherical Molecules.

Taro KIHARA.

Department of Physics, Faculty of Science, University of Tokyo.

(Received April 14, 1951)

The Lennard-Jones model of molecules of spherical symmetry has been generalized to non-spherical models without sacrificing analytical integrability of the second virial coefficient. The essential generalization consists in the definition of the intermolecular distance, ρ, the intermolecular potential, U, being supposed to be a function of ρ only and

$$U(\rho)=U_0\left[\frac{m}{n-m}\left(\frac{\rho_0}{\rho}\right)^n-\frac{n}{n-m}\left(\frac{\rho_0}{\rho}\right)^m\right],\quad n>m>3.$$

As the simplest extension ρ is defined by the shortest distance between molecule cores, as which thin rods (disks) are adopted in case of prolonged (flat) molecules. Next, ρ is so defined that the model becomes an attracting spheroid. For these models the second virial coefficient has been integrated analytically and tabulated. The model constants have been determined for H_2, N_2, C_2H_4 and CO_2.

§1. Introduction.

Potentials between spherically symmetric molecules are approximated by the well-known Lennard-Jones model

$$U(r)=U_0\left[\frac{m}{n-m}\left(\frac{r_0}{r}\right)^n-\frac{n}{n-m}\left(\frac{r_0}{r}\right)^m\right],\quad n>m>3 \qquad (1)$$

where U_0 and r_0 indicate, respectively, the absolute value and the intermolecular distance of the potential minimum. Concerning the index of the attractive part of the potential the value $m=6$ is usually chosen since two sufficiently separating molecules attract each other with a potential proportional to r^{-6}. With this model, properties of gases—the second and the third virial coefficient,⁽¹⁾ coefficient of viscosity, etc.⁽²⁾—are quantitatively explained to a certain extent, and at the same time the model constants are determined for each gas molecule. (Ordinarily the value of n is previously chosen to 12 or 9.)

One of the merits of the L.-J. model is that the integration of the second virial coefficient concerning the model can be achieved analytically.

The model has been applied also to such molecules as H_2, N_2, CO_2 and C_2H_4 which are not spherically symmetric. This application, however, is unsatisfactory, especially when we want to treat liquid and solid states making use of the model constants determined from gaseous data.

On the other hand when high polymer solutions are treated theoretically, the polymers are often approximated by rigid bodies of long or flat shape, the attractive part of the intermolecular potential being wholly neglected. For the osmotic pressure, however, the attraction between polymers plays an important role.

For these reasons it is desirable to find more general models of molecules which contain the common L.-J. potential and rigid bodies of long or flat shape as their special cases. The aim of this paper is to introduce models of the above-mentioned characters and investigate their second virial coefficient.

Recently Corner(3) has treated this problem. He says in his paper, "I have tried to find an intermolecular potential which satisfies the three conditions of accuracy, generality and integrability." It may be true that his "four-center model" is more accurate, in some cases at least, than ours. However, since his formulation can not directly be applied to flat molecules and since the integration achieved by him is complicated and not analytic, his nodel of molecules is not so "general and integrable."

The usefulness of a model depends, to some extent, upon its capability of exact mathematical treatment. It is desirable, therefore, that the second virial coefficient concerning the adopted model can be integrated analytically.

In this paper we consider only interaction between indentical molecules,—i.e. in case of gases we take no notice of gas-mixture, and in case of polymer solutions we assume that all the polymers are of the same size.

SPHEROCYLINDRICAL MODEL.

§2. A Simple Model of Non-Spherical Molecules.

We first consider such molecules composed of two identical atoms as H_2 or N_2. Let us call the thin rod connecting two nuclei the "core" of the molecule and define the intermolecular distance, ρ, as the shortest distance between their cores. We assume that the intermolecular potential U, is a function of ρ only and assume furthermore

$$U(\rho)=U_0\left[\frac{m}{n-m}\left(\frac{\rho_0}{\rho}\right)^n-\frac{n}{n-m}\left(\frac{\rho_0}{\rho}\right)^m\right],\quad n>m>3. \qquad (2)$$

The model above introduced as regards diatomic molecules can be applied also to other molecules of prolonged shape, e.g. CO_2, C_2H_2, C_2H_4, C_2H_6. As the core of our model we may choose the thin rod connecting two oxygen nuclei for CO_2, two carbon nuclei for C_2H_2, C_2H_4 and C_2H_6.

For flat molecules, considering a thin circular disk as the core, we define the intermolecular distance ρ, as the shortest distance between their cores. Again we assume the potential (2). When we apply the model, for example, to benzene C_6H_6, we may choose to the core a disk which approxomates the hexagon composed of six carbon nuclei.

When we choose the index of the attractive part of the potential to $m=6$, our model is determined by the index of repulsive part n, absolute value of potential minimum U_0, intermolecular distance corresponding the minimum ρ_0, and the "core-length" (length of the rod-core or diameter of the disk-core) l. In the special case when $l=0$ our model is reduced to the common L.-J. model, and in the case when $n=\infty$ and $U_0=0$ our model becomes a simple rigid body of the shape as shown in Fig. 1. It may be adequate to call this shape "spherocylinder". We will call (a) and (b) prolate and oblate spherocylinder respectively. We will further call ρ_0 in Fig. 1 the minor axis and $l+\rho_0$ the major axis.

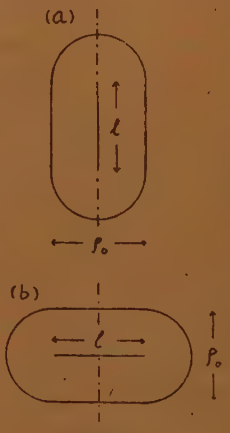

Fig. 1

For gas molecules choosing n to be 12 may be reasonable. For high polymers in solution it may be convenient to choose $n=\infty$ and idealize to attracting rigid spherocylinder, the attractive part of which depends, of course, also to the solvent.

§3. Integration of the Second Virial Coefficient.

The pressure of gases and osmotic pressure of polymers in solution can be expressed in the form

$$P=kT(v^{-1}+B(T)v^{-2}+C(T)v^{-3}+\ldots\ldots)$$

(v=volume per molecule, k=Boltzmann's constant, and T=absolute temperature), the coefficient $B(T)$ being called the second virial coefficient. For spherically symmetric molecules, e.g. for L.-J. potential (1), $B(T)$ is given, on the basis of classical statistics, by the formula

$$B(T)=\int_0^\infty[1-\exp(-U(r)/kT)]\,db_0(r)$$

where $b_0(r)$ denotes the second virial coefficient for rigid sphere with diameter r: $b_0(r)=2\pi r^3/3$. It is easy to understand that for our model (2) with core-length l holds the expression

$$B(T)=\int_0^\infty[1-\exp(-U(\rho)/kT)]\,db_l(\rho)\quad(3)$$

Here $b_l(\rho)$ denotes the second virial coefficient for rigid spherocylinder with the core-length l and the minor axis ρ (l being definite, ρ being variable).

According to Isihara(4) the second virial coefficient of any convex rigid molecule is given by

$$V+(4\pi)^{-1}MS$$

where S and V indicate the surface area and the volume of the molecule respectively, M is defined by the surface integral of the mean curvature:

$$M=\frac{1}{2}\int\left(\frac{1}{R_1}+\frac{1}{R_2}\right)dS,$$

R_1 and R_2 being the principal radii of curvature.

For prolate spherocylinder with core-length l and minor axis ρ, hold

$$V=\frac{\pi}{6}\rho^3+\frac{\pi}{4}\rho^2 l,\qquad S=\pi\rho^2+\pi\rho l,$$

$$M=2\pi\rho+\pi l$$

and we get

$$b_l(\rho)=V+\frac{1}{4\pi}MS$$

$$=\frac{2\pi}{3}\rho^3+\pi\rho^2 l+\frac{\pi}{4}\rho l^2.\quad(4)$$

For oblate one with core-diameter l and minor axis ρ hold

$$V=\frac{\pi}{6}\rho^3+\frac{\pi^2}{8}\rho^2 l+\frac{\pi}{4}\rho l^2,$$

$$S\doteq\pi\rho^2+\frac{\pi^2}{2}\rho l+\frac{\pi}{2}l^2,$$

$$M=2\pi\rho+\frac{\pi^2}{2}l$$

and we get

$$b_l(\rho)\doteq\frac{2\pi}{3}\rho^3+\frac{\pi^2}{2}\rho^2 l$$
$$+\frac{\pi}{4}\left(1+\frac{\pi^2}{4}\right)\rho l^2+\frac{\pi^2}{16}l^3.\quad(5)$$

Inserting (2) and (4) into (3), we obtain for prolate case

$$B(T)=\frac{2\pi}{3}\rho_0^3F_3(z)+\pi\rho_0^2 lF_2(z)$$
$$+\frac{\pi}{4}\rho_0 l^2F_1(z)\quad(6)$$

where

$$F_s(z)\doteq\int_0^\infty\left[1-\exp\left(-\frac{m}{n-m}\frac{z}{\xi^n}\right.\right.$$
$$\left.\left.+\frac{n}{n-m}\frac{z}{\xi^m}\right)\right]d(\xi^s).\quad(7)$$

$$z=U_0/kT.$$

$F_s(z)$ can be integrated with the same method adopted by Lennard-Jones(5), yielding

$$F_s(z)=-\frac{s}{n}\sum_{t=0}^\infty\frac{1}{t!}\Gamma\left(\frac{tm-s}{n}\right)$$
$$\left(\frac{n}{m}\right)^t\left(\frac{m}{n-m}z\right)^{\frac{n-m}{n}t+\frac{s}{n}}\quad(8)$$

Using (5) instead of (4) we have for oblate case

$$B(T)=\frac{2\pi}{3}\rho_0^3F_3(z)+\frac{\pi^2}{2}\rho_0^2 lF_2(z)$$
$$+\frac{\pi}{4}\left(1+\frac{\pi^2}{4}\right)\rho_0 l^2F_1(z)+\frac{\pi^2}{16}l^3.\quad(9)$$

In the case when $m=6$ and $n=12$, namely

$$U(\rho)=U_0\left[\left(\frac{\rho_0}{\rho}\right)^{12}-2\left(\frac{\rho_0}{\rho}\right)^6\right],\quad(10)$$

the values of F_3, F_2 and F_1 are given in the left half of Table I.

In the case when $n=\infty$, namely

$$U_0(\rho)=\begin{cases}\infty & \rho<\rho_0\\ -U_0(\rho_0/\rho)^m & \rho>\rho_0\end{cases}$$

we have

$$F_s(z)=\sum_{t=0}^\infty\frac{-s}{tm-s}\,\frac{z^t}{t!}.$$

Table I

$-\log_{10}z$	$F_3(z)$	$F_2(z)$	$F_1(z)$	$F_{-1}(z)$	$F_{-3}(z)$	$F_{-5}(z)$	$F_{-7}(z)$
−0.4	−9.859	−5.211	−1.784				
−0.3	−6.138	−3.008	−0.7761				
−0.2	−4.003	−1.776	−0.2221				
−0.1	−2.673	−1.027	0.1091				
0.0	−1.795	−0.5424	0.3198	1.591	2.683	3.82	5.12
0.1	−1.189	−0.2151	0.4600	1.478	2.392	3.38	4.55
0.2	−0.7587	0.0132	0.5562	1.403	2.204	3.11	4.24
0.3	−0.4465	0.1758	0.6234	1.351	2.084	2.96	4.07
0.4	−0.2170	0.2930	0.6710	1.319	2.009	2.87	4.02
0.5	−0.0469	0.3779	0.7045	1.297	1.968	2.85	4.06
0.6	0.0794	0.4392	0.7279	1.284	1.953	2,87	4.17
0.7	0.1729	0.4829	0.7436	1.276	1.957	2.92	4.35
0.8	0.2415	0.5134	0.7536	1.274	1.977	3.01	4.60
0.9	0.2911	0.5336	0.7591	1.277	2.012	3.14	4.91
1.0	0.3259	0.5459	0.7611	1.282	2.058	3.29	5.29
1.1	0.3493	0.5521	0.7603	1.291	2.116	3.47	5.74
1.2	0.3638	0.5534	0.7575	1.302	2.184	3.68	6.27
1.3	0.3715	0.5510	0.7528	1.315	2.262	3.92	6.91
1.4	0.3737	0.5457	0.7468	1.330	2.349	4.20	7.63
1.5	0.3718	0.5381	0.7396	1.346	2.446	4.51	8.46
1.6	0.3668	0.5287	0.7320	1.364	2.553	4.86	9.42
1.7	0.3594	0.5179	0.7228	1.383	2.669	5.25	10.53
1.8	0.3501	0.5062	0.7135	1.403	2.794	5.68	11.79
1.9	0.3396	0.4937	0.7038	1.424	2.930	6.16	13.24
1.0	0.3281	0.4806	0.6937	1.446	3.075	6.69	14.90

§4. Determination of Model Constants for Gas molecules.

The aim of this section is to determine the model constants as regards hydrogen H_2, nitrogen N_2, ethylene C_2H_4 and carbon dioxide CO_2 whose second virial coefficients are known in sufficiently wide temperature ranges.(6)

Let the core-length be equal to the distance between two nuclei as regards H_2 and N_2, the distance between carbon nuclei as regards C_2H_4 and the distance between oxygen nuclei as regards CO_2. These values are given in the second column of Table II. We take, furthermore, the exponents to $m=6$ and $n=12$, namely we assume (10).

Having thus fixed three constants l, m, n, we can draw calculated curves of B/l^3 vs. $\log_{10}(kT/U_0)$ for various values of ρ_0/l. By comparison between these curves and observed values of B/l^3 vs. $\log_{10}T$ we can determine ρ_0/l and U_0/k. The results are shown in Fig. 2 and Table II. ρ_0 and ρ_0+l may be compared to the minor and the major axis of the molecules respectively.

Table II

		Spherocylindrical Model				Spheroidal Model			
	l	ρ_0/l	U_0/k	ρ_0	ρ_0+l	ε_0	U_0/k	ρ_0	$\sqrt{l^2+\rho_0^2}$
H_2	0.74Å	3.80	39.4°K	2.81Å	3.55Å	0.223	32.4°K	3.24Å	3.32Å
N_2	1.10	3.15	124	3.47	4.57	0.260	101	4.09	4.23
C_2H_4	1.34	3.0	266	4.0	5.4	0.27	216	4.8	5.0
CO_2	2.2	1.7	279	3.7	5.9	0.43	224	4.6	5.1

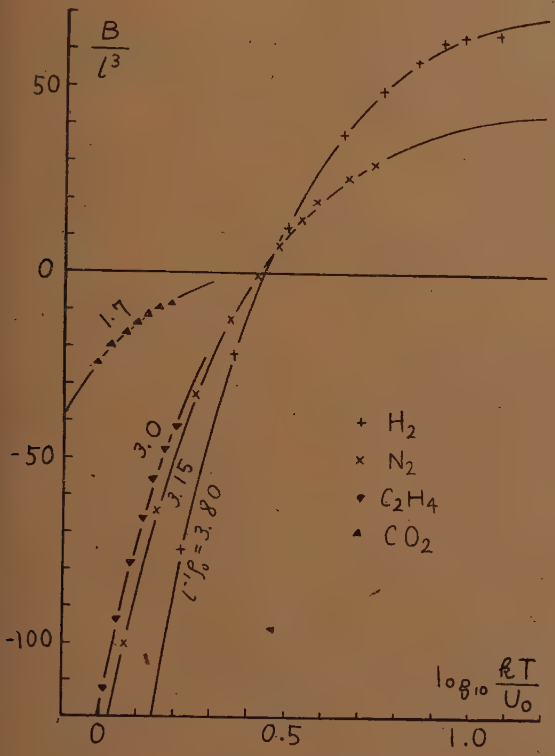

Fig. 2

SPHEROIDAL MODEL.

§5. Spheroidal Lennard-Jones Model.

Regarding solutions of high polymers, especially those of proteins, the polymers are often approximated by prolate or oblate spheroids. In gaseous state also spheroidal molecules are the most natural extensions of spherical molecules. It is desirable, therefore, to generalize the L.-J. model from spherical to spheroidal symmetry and derive a formula of the second virial coefficient for the generalized one.

Let us first treat prolate molecules. A thin rod being assumed as the core of the molecule, each molecule has a set of prolate spheroids confocal with the core. When two molecules are in a certain configuration with each other, two sets of spheroids can be constructed. Among these we can choose two, and only two, spheroids which are congruent and contacting with each other as shown in Fig. 3 (a). Let the length of the minor axis of these contacting ones be termed the distance between two molecules, ρ.

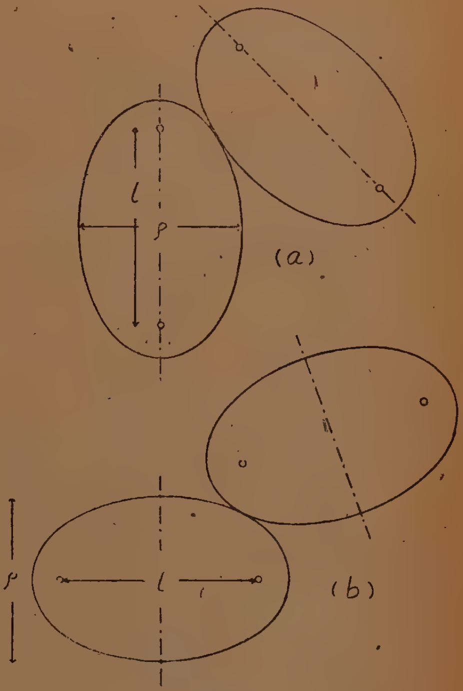

Fig. 3

Denoting by l the length between two focuses (i.e. the length of the core) and by ε the eccentricity of the contacting spheroid, we have the relation

$$\varepsilon^2 = l^2/(l^2+\rho^2). \qquad (11)$$

For vanishing focal length, for $l=0$, our intermolecular distance coincides with the common distance between the centers.

Now we assume that the intermolecular potential U is a function of ρ only and furthermore we assume the expression (2) of the L.-J. type.

For flat molecules we may proceed on the basis of oblate spheroids. We assume namely as the core of molecule a thin disk of diameter l and consider a set of oblate spheroids confocal with the disk. The distance between two molecules, ρ, is defined by the length of the minor axis of the contacting and congruent spheroids (cf. Fig. 3 (b)). We assume again the intermolecular potential (2).

For gas molecules choosing to 12 may be adequate. For high polymers in solution it may be convenient to choose $n=\infty$ and idealize to attracting rigid spheroid.

§6. Integration of the Second Virial Coefficient.

As regards the molecular model above introduced the second virial coefficient is given by the formula (3) where $b_l(\rho)$ denotes the second virial coefficeent for rigid spheroid with focal length l and minor axis ρ (l being definite, ρ being variable).

According to Isihara[(4)] $b_l(\rho)$ is given by

$$b_l(\rho)=4Vf(\varepsilon), \tag{12}$$

$$f(\varepsilon)=\frac{1}{4}+\frac{3}{16}\left(1+\frac{1}{\sqrt{1-\varepsilon^2}}\,\frac{\sin^{-1}\varepsilon}{\varepsilon}\right)\left(1+\frac{1-\varepsilon^2}{2\varepsilon}\log\frac{1+\varepsilon}{1-\varepsilon}\right) \tag{13}$$

where V is the volume of the spheroid

$$V=\begin{cases}(\pi/6)\,\rho^2\sqrt{l^2+\rho^2} & \text{prolate}\\ (\pi/6)\,\rho\,(l^2+\rho^2) & \text{oblate}\end{cases}$$

and ε indicates the eccentricity connected with l and ρ by eq. (11).

Considering that the quantity

$$E=(1-\varepsilon^2)^{-\frac{1}{2}}\sin^{-1}\varepsilon$$

satisfies the differential equation

$$(1-\varepsilon^2)\frac{dE}{d\varepsilon}-\varepsilon E=1$$

we get

$$\frac{1}{\sqrt{1-\varepsilon^2}}\sin^{-1}\varepsilon=\varepsilon+\frac{2}{3}\varepsilon^3+\frac{2\cdot4}{3\cdot5}\varepsilon^5+\frac{2\cdot4\cdot6}{3\cdot5\cdot7}\varepsilon^7+\cdots\cdots .$$

Making use of this formula and the well-known one:

$$\frac{1}{2}\log\frac{1+\varepsilon}{1-\varepsilon}=\varepsilon+\frac{1}{3}\varepsilon^3+\frac{1}{5}\varepsilon^5+\frac{1}{7}\varepsilon^7+\cdots\cdots$$

we obtain the power series expansion for the expression (13):

$$f(\varepsilon)=1+\frac{1}{15}\varepsilon^4+\frac{1}{15}\varepsilon^6+\frac{11}{175}\varepsilon^8+\frac{31}{525}\varepsilon^{10}+\cdots\cdots^{*}. \tag{14}$$

Inserting the relation (11) into (13), we obtain

$$f(\varepsilon)=\frac{1}{4}+\frac{3}{16}\left(1+\frac{1+\delta^2}{\delta}\tan^{-1}\delta\right)\left(1+\frac{\log(\delta+\sqrt{1+\delta^2})}{\delta\sqrt{1+\delta^2}}\right) \tag{15}$$

where

$$\delta=l/\rho.$$

The right-hand side of (15) is equal to $f(i\delta)$, the expression obtained formally from (13) with replacing ε by $i\delta\,(i=\sqrt{-1})$. Therefore, from (14), holds

$$f(\varepsilon)=1+\frac{1}{15}\left(\frac{l}{\rho}\right)^4-\frac{1}{15}\left(\frac{l}{\rho}\right)^6+\frac{11}{175}\left(\frac{l}{\rho}\right)^8-\frac{31}{525}\left(\frac{l}{\rho}\right)^{10}+\cdots\cdots$$

making use of which we can transform (12) into the power-series of ρ^{-1}:

---

[*] The corresponding expansion in Isihara's papers should be corrected.

$$b_l(\rho)=\frac{2\pi}{3}\rho^3\left[1+k_1\left(\frac{l}{\rho}\right)^2+k_2\left(\frac{l}{\rho}\right)^4+k_3\left(\frac{l}{\rho}\right)^6+\ldots\ldots\right]. \tag{16}$$

Here for prolate spheroid

$$k_1=\frac{1}{2},\quad k_2=-\frac{7}{120},\quad k_3=\frac{7}{240},\quad k_4=-\frac{1201}{67200},\quad k_5=\frac{1643}{134400},\ldots\ldots$$

for oblate spheroid

$$k_1=1,\quad k_2=\frac{1}{15},\quad k_3=0,\quad k_4=-\frac{2}{525},\quad k_5=\frac{2}{525},\ldots\ldots$$

Inserting (2) and (16) into (3), we obtain

$$B(T)=\frac{2\pi}{3}\rho_0^3\left[F_3(z)+k_1\left(\frac{l}{\rho_0}\right)^2F_1(z)+\ldots\ldots+k_\nu\left(\frac{l}{\rho_0}\right)^{2\nu}F_{3-2\nu}(z)+\ldots\ldots\right],$$

$$z=U_0/kT$$

where functions $F_s(z)$ are given by eqs. (7) and (8).

Table III

		Prolate Spheroid					
t	K_{t0}	t	K_{t1}	K_{t2}	K_{t3}	K_{t4}	K_{t5}
0	+1.0000	0	+0.5000	+0.4417	+0.4125	+0.3946	+0.3824
1	−1.0000	1	−0.1000	−0.1083	−0.1069	−0.1040	−0.1009
2	−0.3333	2	0455	0499	0486	0467	0449
3	2000	3	0294	0325	0314	0300	0288
4	1429	4	0217	0241	0232	0221	0212
5	1111	5	0172	0191	0184	0175	0168
6	0909	6	0143	0159	0152	0145	0139
7	0769	7	0122	0136	0130	0123	0118
8	0667	8	0106	0118	0113	0107	0103
9	0588	9	0094	0105	0100	0095	0091
10	0526	Oblate Spheroid					
11	0476						
12	0435	t	K_{t1}	K_{t2}	K_{t3}	K_{t4}	K_{t5}
13	0400	0	+1.0000	+1.0667	+1.1333	+1.1962	+1.2552
14	0370	1	−0.2000	−0.1905	−0.1810	−1.1732	−0.1668
		2	0909	0858	0807	0766	0735
		3	0588	0553	0518	0491	0470
		4	0435	0408	0381	0361	0346
		5	0345	0323	0302	0286	0273
		6	0286	0268	0250	0236	0226
		7	0244	0228	0213	0201	0193
		8	0213	0199	0186	0176	0168
		9	0189	0177	0164	0156	0149

Since this series does not converge for $l\gtrsim\rho_0$, it is convenient to rearrange the series into power-series concerning the eccentricity

$$\varepsilon_0=l\,(l^2+\rho_0^2)^{-\frac{1}{2}}$$

thus we have

$$B(T)=\frac{2\pi}{3}\rho_0^3\left[K_0(z)+\varepsilon_0^2K_1(z)+\varepsilon_0^4K_2(z)+\ldots\ldots\right] \tag{17}$$

with the coefficients

$$K_0=F_3,\quad K_1=k_1F_1,\quad K_2=k_1F_1+k_2F_{-1}\ldots\ldots$$

$$K_\nu=k_1F_1+\binom{\nu-1}{1}k_2F_{-1}+\binom{\nu-1}{2}k_3F_{-3}+\ldots\ldots+k_\nu F_{3-2\nu},\ \ldots\ldots$$

In the case when $m=6$ and $n=12$, $F_3(z)$ and $F_1(z)$ were already given in Table I. The calculated values of $F_{-1}(z)$, $F_{-3}(z)$, ... are added to the same table.

In the case when $m=6$ and $n=\infty$, (17) takes the following form of double power-series:

$$B(T)=\frac{2\pi}{3}\rho_0^3\sum_{\nu=0}^{\infty}\sum_{t=0}^{\infty}K_{t\nu}\frac{z^t}{t!}\varepsilon_0^{2\nu}$$

The coefficients $K_{t\nu}$ are given in Table III. Though $K_{t\nu}$ are rational numbers, they are tabulated in decimals.

§7. Determination of Model Constants for Gas Molecules.

Taking the exponents to be $m=6$, $n=12$, and choosing the focal length l as before, we can determine the remaining model constants as regards hydrogen, nitrogen, ethylene and carbon dioxide. The results are added to Table II. Fig. 4 shows the comparison between calculated curves and observed values.

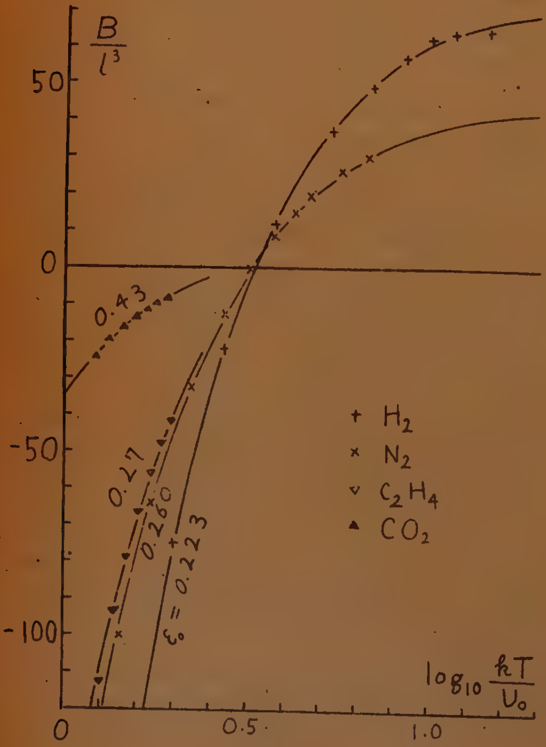

Fig. 4

The difference between the major and the minor axis of the spheroidal model, $(l^2+\rho_0^2)^{\frac{1}{2}}-\rho_0$, is much smaller than the corresponding quantity of the spherocylindrical one. From data of the second virial coefficient alone, it is impossible to assert generally which model represents real molecules more closely. However, as regards hydrogen molecule at least the spherocylindrical model seems to be better than the spheroidal one, because the length of the minor and major axes concerning the former are only a few percent smaller than the corresponding quantities of the potential curves calculated quantum-mechanically by Margenau and de Boer.(7)

The author wishes to thank Mr. A. Isihara and Prof. M. Kotani for their helpful discussions.

References.

(1) T. Kihara: J. Phys. Soc. Japan **3** (1948) 265, **6** (1951) 184.
R.B. Bird, E.L. Spotz: J.O. Hirschfelder, J. Chem. Phys. **18** (1950) 1395.
(2) T. Kihara, M. Kotani: Proc. Phys.-Math. Soc. Japan **25** (1943) 602.
J.O. Hirschfelder, R.B. Bird, E.L. Spotz: J. Chem. Phys. **16** (1948) 968, **17** (1949) 1343.
(3) J. Corner: Proc. Roy. Soc. **A192** (1948) 275.
(4) A. Isihara: J. Chem. Phys. **18** (1950) 1446; A. Isihara, T. Hayashida: J. Phys. Soc. Japan **6** (1951) 40, 46.
(5) Lennard-Jones: Proc. Roy. Soc. **A106** (1924) 463, Proc. Phys. Soc. **43** (1931) 461.
(6) The experimental data adopted by the present auther are mostly taken from D. M. Newitt: *High Pressure Plant and Fluid at High Pressures* (1940).
(7) H Margenau: Phys Rev. **63** (1943) 385, **64** (1943) 131. J. de Boer: Physica **9** (1942) 363.

JOURNAL OF THE PHYSICAL SOCIETY OF JAPAN, Vol. 6 No. 5 September—October, 1951

The Effect of the Brownian Motion on the Viscosity of Solutions of Macromolecules, I. Ellipsoid of Revolution.

By Nobuhiko SAITÔ.

Kobayasi Institute of Physical Research, Kokubunzi, Tokyo.

(Received February 20, 1951)

La viscosité intrinsèque depend sérieusement au rapport σ de gradient de vittesse à constante de diffusion rotatoire de particule. La théorie de Kuhn, Eisenschitz et autres et celle de Simha concernant l'effet de mouvement brownien à la viscosité sont critiquées et une théorie nouvelle est donnée. La principe fondamentale est que la dissipation d'énergie doit être calculée par le travail fait par la force extérieure contre le courant de densité de probabilité qui contient le courant de diffusion. Computations sont faites pour ellipsoïdes de révolution. Viscosités intrinsèques *décroissent monotoniquement* avec croissement de σ. Au cas où le mouvement brownien est suffisamment efficace, les résultats finals sont identiques à ceux de Simha.

§1. Introduction.

The intrinsic viscosity of the solution has an important bearing on the molecular structure and molecular weight of the solute molecules. Especially, if the particles suspended in a solution are large compared with the solvent molecules, it is possible, at least in principle, to relate the intrinsic viscosity of the solution to the shape and size of the suspended particles from macroscopic hydrodynamical consideration. Accordingly since the work of Einstein for spherical rigid particles numerous theories have been proposed for non-spherical particles. Let us consider a particle in a laminar flow. From purely hydrodynamical point of view, a non-spherical particle changes its position and orientation regularly by the flow. On the other hand the irregular Brownian motions, translational and rotatory, join thereto. In consequence the above mentioned regular movement of the particle is disturbed by these thermal motions, between which the rotatory Brownian motion has a serious effect on the flow property. The distribution of the orientation of the particle is not uniform and is determined by a generalized diffusion equation. This distribution function in a steady state is a function of $\sigma=g/D$, ratio of the velocity gradient to the rotatory diffusion constant. Accordingly there are proposed several theories¹⁾ about the effect of the Brownian motion on the viscosity of solutions, among which we cite the following two main opinions; the one is due to Kuhn,²⁾ Eisenscnitz,³⁾ Burgers,⁴⁾ and Peterlin⁵⁾ et al., and the other to Simha.⁶⁾ Following the former one calculates the increase in the energy dissipation per unit time by a suspended particle which is moving with the angular velocity determined solely from hydrodynamics at the moment when it takes a certain orientation, and then averages it over all the orientation with the distribution function ρ. In the latter theory which deals with the case of the complete Brownian motion, one first notices the fact of the disappearance of the orientation tendency of the particles in this case, and then one calculates the increase in the energy dissipation by a particle at rest oriented under some possible direction and averages it with the distribution function $\rho=1/4\pi$. This theory cannot afford any information about the dependency of the velocity gradient. Compared with the experiments, the results of Simha⁷⁾ give more reasonable values than the former and are widely used to determine the shapes and sizes of protein molecules. However we want to point out that both theories are incorrect and to propose a new theory in the following.

§2. Energy Dissipation by Particles with Brownian Motion.

Let us consider as a simple example a colloidal solution which is in sedimentation equilibrium in a field of gravitation.

Take one particle in this solution. This particle is exerted by the gravitational force and random forces which cause the Brownian motion. Therefore the equation of motion of the particle is written as follows, x-axis being taken downwards.

$$m\frac{du}{dt}=mg-fu+X(t), \tag{2.1}$$

where m, u, and f are respectively mass, velocity, and friction constant of the particle and $X(t)$ is the x-component of the random force, and g is the constant of the gravity. Solving this equation we have

$$u=\frac{g}{\beta}+\left(u_0-\frac{g}{\beta}\right)e^{-\beta t}+\frac{1}{m}e^{-\beta t}\int_0^t e^{\beta\xi}\cdot X(\xi)\,d\xi, \tag{2.2}$$

where u_0, is the initial velocity and $\beta=f/m$. The average velocity at time t, in the ensemble of particles which have the same initial velocity u_0 is given by

$$<u>=g/\beta+(u_0-g/\beta)e^{-\beta t} \tag{2.3}$$

because we have generally $<X(t)>=0$. This is nothing but the velocity which a particle will have in the case without Brownian motion. When $t\to\infty$ and after reaching to a steady state, we have

$$<u>_\infty=g/\beta, \tag{2.4}$$

which is different from zero. In consequence if we adopt the idea by Kuhn et al. that the energy dissipation is to be calculated by a movement determined without Brownian motion, it happens that an energy dissipation occurs in the case where a sedimentation equilibrium is established! This is obviously absurd. In this example the idea of Simha does not show any contradiction. In a laminar flow, however, we cannot regard the particle to be at rest. It is true that the orientation of the particle is uniform in the case of the complete Brownian motion, nevertheless, there is no necessary reason to assume the particle to be at rest, but the particle has only to rotate with uniform velocity in the average. In addition it seems strange to assume the particles to be at rest in the limiting case of spherical particles. Let us consider once more the colloidal solution in sedimentation equilibrium. The distribution or the density ρ of the particle is determined by

$$\frac{d}{dx}\left(\rho<u>_\infty-D\frac{d\rho}{dx}\right)=0, \tag{2.5}$$

where D is the diffusion constant

$$D=\frac{1}{2f^2}\int_{-\infty}^{+\infty}<X(t)\,X(t+\tau)>d\tau. \tag{2.6}$$

Putting

$$j=<u>_\infty-\frac{D}{\rho}\frac{d\rho}{dx} \tag{2.7}$$

and by the boundary condition that the vessel has a bottom, we have $j=0$ and the above equation is easily solved to be

$$\rho=\rho_0\exp(x<u>_\infty/D). \tag{2.8}$$

The essential principle of our theory[8] is that the energy dissipation is to be calculated from the work done by the external force against the current of the probability density defined by Eq. (2.7).

§ 3. Distribution Function of the Orientation of Particles in a Laminar Flow and the Current of the Probability Density.

The original flow pattern in assumed to be

$$\mathbf{V}^0=\mathrm{G}\mathbf{r}\quad \mathrm{G}=\begin{pmatrix}0&0&0\\ g&0&0\\ 0&0&0\end{pmatrix}\quad \mathbf{r}=\begin{pmatrix}x\\ y\\ z\end{pmatrix} \tag{3.1}$$

in (xyz)-system fixed in the space. The origin of the coordinate coincides with the center of the elliposoid, whose semi-axes are respectively a_1, $a_2=a_1$ and a_3. We take the principal axes of the ellipsoid to be the coordinate system ($\xi\eta\zeta$) fixed on it. The matrix of the transformation between the two systems is $\mathrm{A}=(a_{ik})$ (Fig. 1 and Table 1).

Table I. Components of $\mathrm{A}=(a_{ik})$

	ξ	η	ζ
x	$\cos\varphi\cos\theta\cos\psi-\sin\varphi\sin\psi$,	$-\cos\varphi\cos\theta\sin\psi-\sin\varphi\cos\psi$,	$\cos\varphi\sin\theta$.
y	$\sin\varphi\cos\theta\cos\psi+\cos\varphi\sin\psi$,	$-\sin\varphi\cos\theta\sin\psi+\cos\varphi\cos\psi$,	$\sin\varphi\sin\theta$.
z	$-\sin\theta\cos\psi$,	$\sin\theta\sin\psi$,	$\cos\theta$.

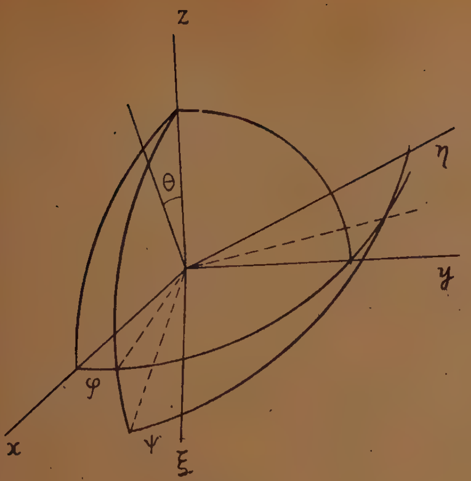

Fig. 1.

The distribution function ρ of the orientation of the particle is determined by the following generalized diffusion equation as a function of the Eulerian angles θ, φ, ψ, which determine the orientation of the particle,

$$\frac{\partial\rho}{\partial t}=-\operatorname{div} j\rho=0 \tag{3.2}$$

$$\mathbf{j}=\omega^0-(kT/\rho)\operatorname{grad}\rho, \tag{3.3}$$

where ω^0 is the angular velocity of the particle due to the velocity gradient of the flow in case without Brownian motion[9] and the operators div and grad must be interpreted as the ones in a Riemannian space.[10] Referring to $(\xi\eta\zeta)$-system, we have

$$\left.\begin{aligned} j_\xi&=\omega_\xi{}^0-\frac{D}{\rho}\left(\sin\psi\frac{\partial\rho}{\partial\theta}-\frac{\cos\psi}{\sin\theta}\,\frac{\partial\rho}{\partial\varphi}\right),\\ j_\eta&=\omega_\eta{}^0-\frac{D}{\rho}\left(\cos\psi\frac{\partial\rho}{\partial\theta}+\frac{\sin\psi}{\sin\theta}\,\frac{\partial\rho}{\partial\psi}\right),\\ j_\zeta&=\omega_\zeta{}^0, \end{aligned}\right\} \tag{3.4}$$

$$\left.\begin{aligned} \omega_\xi{}^0&=\dot\theta\sin\psi-\dot\varphi\cos\psi\sin\theta,\\ \omega_\eta{}^0&=\dot\theta\cos\psi+\dot\varphi\sin\psi\sin\theta,\\ \omega_\zeta{}^0&=\dot\psi+\dot\varphi\cos\theta, \end{aligned}\right\} \tag{3.5}$$

$$\left.\begin{aligned} \dot\theta&=(gp/4)\sin 2\theta\sin 2\varphi,\\ \dot\varphi&=(g/2)\,(1+p\cos 2\varphi),\\ \dot\psi&=-(gp/2)\cos\theta\cos 2\varphi,\\ p&=(a_3{}^2-a_1{}^2)/(a_3{}^2+a_1{}^2), \end{aligned}\right\} \tag{3.6}$$

where D is the rotatory diffusion constant. From Eqs. (3.2)-(3.6) ρ can be solved as a function of θ, φ, and ψ (§5). In case of the complete Brownian motion $\rho\to 0$, we have

$$\left.\begin{aligned} j_\xi&=(g/2)\,a_{31}=-(g/2)\cos\psi\sin\theta,\\ j_\eta&=(g/2)\,a_{32}=(g/2)\sin\psi\sin\theta,\\ j_\zeta&=(g/2)\,a_{33}=(g/2)\cos\theta. \end{aligned}\right\} \tag{3.7}$$

These equations mean that the particle can be regarded as rotating with the uniform velocity $g/2$ around the z-axis, contrary to Simha's assumption.

§4. Complete Brownian Motion.

The hydrodynamical problem of the rotating ellipsoid in a laminar flow was treated by Jeffery.[9] Following him and using his notations, the velocity of the fluid at (x, y, z) is given by

$$\left.\begin{aligned} u_\xi&=u_\xi{}^0-4\xi\frac{\Phi}{r^5}-\frac{4}{3}(H-H')\frac{\eta}{r^3}\\ &\qquad+\frac{4}{3}(G-G')\frac{\zeta}{r^3}\\ u_\eta&=u_\eta{}^0-4\eta\frac{\Phi}{r^5}-\frac{4}{3}(F-F')\frac{\zeta}{r^3}\\ &\qquad+\frac{4}{3}(H-H')\frac{\xi}{r^3}\\ u_\zeta&=u_\zeta{}^0-4\zeta\frac{\Phi}{r^5}-\frac{4}{3}(G-G')\frac{\xi}{r^3}\\ &\qquad+\frac{4}{3}(F-F')\frac{\eta}{r^3} \end{aligned}\right\} \tag{4.1}$$

where ξ, η, ζ are the coordinates of the point P in $(\xi\eta\zeta)$-system, and r is the distance from the origin and $\mathbf{u}^0$ $(u_\xi{}^0, u_\eta{}^0, u_\zeta{}^0)$ is the velocity of the original flow in $(\xi\eta\zeta)$-system,

$$\mathbf{u}^0\,(u_\xi{}^0, u_\eta{}^0, u_\zeta{}^0)=\mathrm{A}^{-1}\mathrm{GA}\,\mathbf{s} \tag{4.2}$$

$$\mathbf{s}=(\xi,\ \eta,\ \zeta).$$

Alternatively $\mathbf{u}^0$ is written as follows,

$$\left.\begin{aligned} u_\xi&=h_{11}\xi+h_{12}\eta+h_{13}\zeta+o_2\zeta-o_3\eta\\ u_\eta&=h_{21}\xi+h_{22}\eta+h_{23}\zeta+o_3\xi-o_1\zeta\\ u_\zeta&=h_{31}\xi+h_{32}\eta+h_{33}\zeta+o_1\eta-o_2\xi \end{aligned}\right\} \tag{4.3}$$

$$h_{12}=h_{21},\ h_{13}={}_{31},\ h_{23}=h_{32}.$$

These h's and o's can be expressed by a_{ik}'s. In particular

$$(o_1,\ o_2,\ o_3)=(g/2)\,(a_{31},\ a_{32},\ a_{33}). \tag{4.4}$$

It is assumed that the number of particles in unit volume is n and $n\rho$ particles among them have a same orientation (θ, φ, ψ), and the concentration is so dilute that the interaction between different particles is neglected.

Writing Eqs. (4.1) in (xyz)-system and calculating the average decreases of the velocities at the planes $x=h$ and $x=-h$, we can obtain for the effective velocity gradient g_{eff},[4]

$$\begin{aligned} g-g_{eff}=\frac{32\pi}{3g}\int n\rho\Big\{&Ah_{11}+Bh_{22}+Ch_{33}\\ &+(H+H')h_{12}+(G+G')h_{13}+(F+F')h_{23}\\ &-(H-H')\,o_3-(G-G')\,o_2-(F-F')\,o_1\Big\}\\ &\cdot d\Omega, \end{aligned} \tag{4.5}$$

where the integration is carried out over all the orientations of particles. Eq. (4.5) is rewritten by use of the relation due to Jeffery, as follows,

$$g-g_{eff}=\frac{16\pi}{3g}\int n\rho\Big\{\frac{\alpha_0''h_{11}^2+\beta_0''h_{22}^2+\gamma_0''h_{33}^2}{\beta_0''\gamma_0''+\gamma_0''\alpha_0''+\alpha_0''\beta_0''}+\frac{h_{12}^2}{a_1^2\gamma_0'}+\frac{(\alpha_0+\gamma_0)(h_{13}^2+h_{23}^2)}{\alpha_0'(a_1^2\alpha_0+a_3^2\gamma_0)}$$
$$+\frac{(a_3^2-a_1^2)\alpha_0'+(\alpha_0-\gamma_0)}{\alpha_0'(a_1^2\alpha_0+a_3^2\gamma_0)}(h_{13}o_2-h_{23}o_1)+\frac{(a_1^2+a_3^2)(o_1^2+o_2^2)}{a_1^2\alpha_0+a_3^2\gamma_0}+\frac{o_3^2}{\alpha_0}$$
$$+\frac{(a_3^2-a_1^2)h_{23}-(a_1^2+a_3^2)o_1}{a_1^2\alpha_0+a_3^2\gamma_0}\omega_\xi-\frac{(a_3^2-a_1^2)h_{13}+(a_1^2+a_3^2)o_2}{a_1^2\alpha_0+a_3^2\gamma_0}\omega_\eta-\frac{o_3}{\alpha_0}\omega_\zeta\Big\}d\Omega \tag{4.6}$$

where ω_ξ, ω_η, and ω_ζ are the components of the angular velocity given to the particle.

Along the line of thought of the author, j defined by Eq. (3.3) should be substituted for ω.

First we take up the case of the complete Brownian motion. Substituting Eqs. (3.7) into Eq. (4.6) for ω we have

$$g-g_{eff}=\frac{16\pi}{3g}\int n\rho\Big[\frac{\alpha_0''h_{11}^2+\beta_0''h_{22}^2+\gamma_0''h_{33}^2}{\beta_0''\gamma_0''+\gamma_0''\alpha_0''+\alpha_0''\beta_0''}+\frac{h_{12}^2}{a_1^2\gamma_0'}+\frac{2(h_{23}^2+h_{13}^2)}{\alpha_0'(a_1^2+a_3^2)}$$
$$+\frac{(a_3^2-a_1^2)^2(h_{13}^2+h_{23}^2)}{(a_1^2+a_3^2)(a_3^2\gamma_0+a_1^2\alpha_0)}-\frac{(\gamma_0-\alpha_0)}{\alpha_0'(a_3^2\gamma_0+a_1^2\alpha_0)}(h_{13}o_2-h_{23}o_1)\Big]d\Omega. \tag{4.7}$$

The specific viscosity η_{sp} is given by,[4)]*

$$\eta_{sp}=(g-g_{eff})/g_{eff}\cong(g-g_{eff})/g. \tag{4.8}$$

Defining ν by

$$\nu=\eta_{sp}/c_v \tag{4.9}$$

where c_v is the volume concentration $c_v=(4\pi/3)\,a_1^2a_3n$, we have after the integration with $\rho=1/4\pi$,

$$\nu=\frac{1}{a_1^2a_3}\Big\{\Big(\frac{\gamma_0''}{2a_1^2\alpha_0''\gamma_0'}+\frac{1}{2a_1^2\gamma_0'}-\frac{2}{\alpha_0'(a_1^2+a_3^2)}\Big)\frac{4}{15}+\frac{1}{3a_1^2\gamma_0'}$$
$$+\frac{4}{3\alpha_0'(a_1^2+a_3^2)}-\frac{2(a_3^2-a_1^2)^2}{5(a_1^2+a_3^2)\,(a_3^2\gamma_0+a_1^2\alpha_0)}\Big\}. \tag{4.10}$$

Eq. (4.10) is identical with the final result of Simha whose basic idea is quite different from ours. Presumably he has committed some errors in calculation. It has been shown[1) 7)] that using this Eq. (4.10) one can obtain the shapes of protein molecules which are in good agreement with the results by diffusion or sedimentation measurements. This fact turns out to be a powerful justification of our theory.

§5. Dependency on the Volocity Gradient, Non-Newtonian Viscosity.

Peterlin[5)] solved the Eq. (3.2) as a function of σ in power series of p with the result

$$\rho=\frac{1}{4\pi}\Big\{1+p\Big(-\frac{1}{2}\cos2\varphi+\frac{3}{\sigma}\sin2\varphi\Big)\frac{3\sigma^2\sin^2\theta}{\sigma^2+36}+p^2\Big[-\frac{3}{14}(3\cos^2\theta-1)+\frac{9}{560}(35\cos^4\theta-30\cos^2\theta+3)$$
$$+\Big\{\Big(1-\frac{60}{\sigma^2}\Big)\cos4\varphi-\frac{16}{\sigma}\sin4\varphi\Big\}\frac{15\sigma^2\sin^4\theta}{16(\sigma^2+100)}\Big]\frac{\sigma^2}{\sigma^2+36}+p^3[\ldots]+\ldots\Big\}. \tag{5.1}$$

When σ is different from zero, we must use Eqs. (3.4) for ω in Eq. (4.6) and Eq. (5.1) for ρ. Thus one obtains

$$\eta_{sp}=\frac{16\pi}{3g^2}\int n\rho Jd\Omega+\frac{16\pi D}{3g^2}\int n\rho\Big\{\frac{a_3^2-a_1^2}{a_1^2\alpha_0+a_3^2\gamma_0}\Big[\frac{\partial\rho}{\partial\theta}\,\frac{g}{4}\sin2\theta\sin2\varphi$$
$$+\frac{\partial\rho}{\partial\varphi}\,\frac{g}{2}\cos2\varphi\Big]+\frac{a_1^2+a_3^2}{a_1^2\alpha_0+a_3^2\gamma_0}\,\frac{g}{2}\,\frac{\partial\rho}{\partial\varphi}\Big\}d\Omega \tag{5.2}$$

$$\doteq\frac{16\pi}{3g^2}\Big[\int n\rho Jd\Omega+\frac{3g^2}{2}\,\frac{a_3^2-a_1^2}{a_1^2\alpha_0+a_3^2\gamma_0}\,\frac{D}{g}\int n\rho\sin^2\theta\sin2\varphi d\Omega\Big], \tag{5.3}$$

---

* To use this relation means that the energy dissipation is calculated by the work done by the flow. See also foot-note in Part II, §6, p. 302.

$$J=\frac{g^2}{4}\left(\frac{1}{2a_1^2\gamma_0'}+\frac{\gamma_0''}{2a_1^2a_0''\gamma_0'}-\frac{2}{a_0'(a_1^2+a_3^2)}\right)\sin^4\theta\sin^2 2\varphi$$
$$+\frac{g^2}{2}\frac{\sin^2\theta}{a_0'(a_1^2+a_3^2)}+\frac{g^2}{4}\frac{\cos^2\theta}{a_1^2\gamma_0'}, \tag{5.4}$$

where J is the term which comes from the terms ω^0 in Eqs. (3.4) and is the same as derived by Jeffery. Consequently ν defined by Eq. (4.9) is given by

$$\nu=\nu_p+\frac{6}{a_1^2a_3}\frac{a_3^2-a_1^2}{a_1^2a_0+a_3^2\gamma_0}\frac{D}{g}\int\rho\sin^2\theta\sin 2\varphi d\Omega \tag{5.4}$$

$$\nu_p=\frac{1}{a_1^2a_3}\left[\left(\frac{\gamma_0''}{2a_1^2a_0''\gamma_0'}+\frac{1}{2a_1^2\gamma_0'}\quad\frac{2}{a_0'(a_1^2+a_3^2)}\right)\int\rho\sin^4\theta\sin^2 2\varphi d\Omega\right.$$
$$\left.+\frac{2}{a_0'(a_1^2+a_3^2)}\int\rho\sin^2\theta d\Omega+\frac{1}{a_1^2\gamma_0'}\int\rho\cos^2\theta d\Omega\right] \tag{5.6}$$

where νp is Jeffery's term and was calculated by Peterlin using Eq. (5.1) for ρ. He gave the results of calculation for the case $f=a_3/a_1=8$ and$=1/8$. (Figs. 2 and 3). Therefore from the results of Perterlin and

$$\int\rho\sin^2\theta\sin 2\varphi d\Omega=\frac{12}{5}\frac{f\sigma}{(\sigma^2+36)}+\cdots \tag{5.7}$$

we can obtain ν as a function of σ, as is illustrated in Figs. 2 and 3.

The result of Peterlin shows that there exists in the case of the prolate ellipsoid of revolution a small maximum of ν near $\sigma=0$, which is inconsistent with the experiments, but our result eliminates this maximum and ν decreases monotonically with increasing σ. In addition we remark that the tangent of the curve is horizontal at $\sigma=0$.

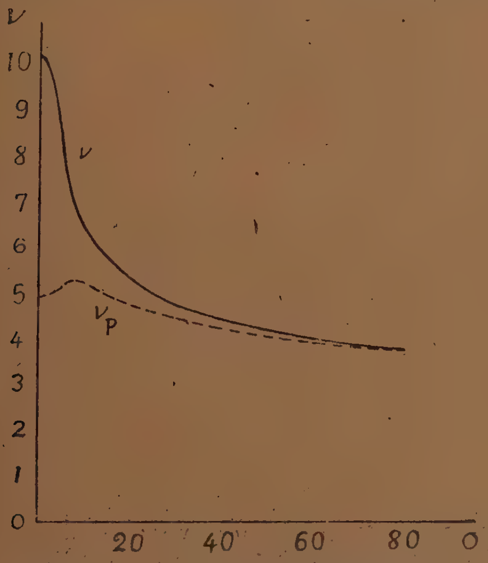

Fig. 2. ν *vs.* σ curve (prolate ellipsoid $f>1$).
Broken line is the result by Peterlin ν_p.

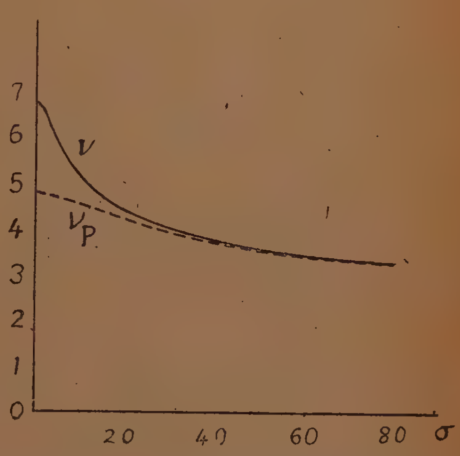

Fig. 3. ν *vs.* σ curve (oblate ellipsoid $f<1$)
Broken line is the result by Peterlin ν_p.

References.

1) See as a review, M.A. Lauffer: Chem. Rev. **31** (1942), 56.
2) W. Kuhn: Z. phys. Chem. **A161** (1932), 1; Koll. Zeits. **62** (1933), 269.
3) R. Eisenschitz: Z. phys. Chem. **A163** (1933), 133.
4) J.M. Burgers, *Second Report on Viscosity and Plasticity*, Amsterdam, 1938.
5) A. Peterlin: Zeits. f. Phys. **111** (1938), 232.
6) R. Simha: J. Phys. Chem. **44** (1940), 25.
7) J.W. Mehl, J.L. Oncley, R. Simha: Sicence **92** (1940), 132.
8) From this point of view can be derived the dielectric loss of the solutions of dipolar molecules, which is, of course, identical with the result derived by usual methods. See, N. Saitô: J. Phys. Soc. Japan **6** (1951), 201.
9) G.B. Jeffery: Proc. Roy. Soc. **A102** (1923), 161.
10) N. Saitô: J. Phys. Soc. Japan 4 (1949), 85.

JOURNAL OF THE PHYSICAL SOCIETY OF JAPAN, Vol. 6 No. 5 September—October, 1951

The Effect of the Brownian Motion on the Viscosity of Solutions of Macromolecules, II. Rigid Chain Molecules.*

By Nobuhiko SAITO.

Kobayasi Institute of Physical Research, Kokubunzi, Tokyo.

(Received February 20, 1951)

La théorie de l'article précédent est appliquée aux macromolécules en chaîne. Computations sont faites pour les pelotes rigides complètement perméables pour le solvent traitées auparavant par l'auteur, et les molécules filiformes rigides allongées d'après le modèle de Riseman et Kirkwood. Les résultats resemblent à ceux d'ellipsoïdes de révolution.

§6. Chain Molecules without Hydrodynamical Interaction among Segments.

For chain molecules we can not adopt the ellipsoidal model through which the flow can not penetrate. As an another extreme case we take a pearl-necklace model1)–4) which assumes free draining of the solvent. For a general pearl-necklace model we have published a calculation,4)** but there we adopted an erroneous method of Kuhn et al. for the effect of the Brownian motion. Therefore we want to recalculate here. Details and notations should be referred to the previous paper.

Let $\mathbf{R}_l$ the position of the l-th segment (spherical particle) and $\mathbf{F}_l$ the force acting upon the fluid by this segment. The perturbation of the velocity at the position $\mathbf{R}\,(x, y, z)$ is given by

$$\mathbf{V}'=\frac{1}{8\pi\eta_0}\sum_{l=-N}^{+N} X_l F_{ly}\left(\frac{xy}{R^5}\right)\mathbf{R} \qquad (6.1)$$

where X_l is the x-component of $\mathbf{R}_l$ and the segments are numbered from $-N$ to $+N$. From this relation the method of Burgers5) for calculating the specific viscosity leads for the intrinsic viscosity to

$$[\eta]=-\frac{N_A}{100M\eta_0 g}\int(\rho\sum X_l F_{ly})\,d\Omega \qquad (6.2)^{***}$$

where N_A and M are respectively the Avogadro's number and the molecular weight and ρ is the distribution function of the orientation of molecules which is determined by the differential equation of the same form as Eq. (3.2), and the integration is carried out over all the orientations. $\mathbf{F}_l$ is given by

$$\mathbf{F}_l=f\eta_0 a_l\{[\omega\times\mathbf{R}_l]-\mathrm{G}\mathbf{R}_l\} \qquad (6.3)$$

where ω is the augular velocity given to the particle, and it should be replaced by the current of the probability density given by Eqs. (3.4) with ω^0 substituted by Eqs. (9) of the previous paper.4) Thus in the same way as for the ellipsoid of revolution, one obtains finally

$$[\eta]=\frac{N_A f}{100M}\left[\frac{(P-R)^2}{4(P+R)}\int\rho\sin^4\theta\sin^2 2\varphi\, d\Omega + \frac{PR}{P+R}\int\rho\sin^2\theta\, d\Omega+\frac{P}{2}\int\rho\cos^2\theta\, d\Omega\right] + \frac{3N_A f}{200M}(R-P)\frac{D}{g}\int\rho\sin^2\theta\sin 2\varphi\, d\Omega. \qquad (6.4)$$

---

* This article is a continuation of the preceding one, Part I. Notations and equations therein are used and cited in the following.

** This paper contains some mistakes, we want to correct here.

2nd eq. in Eqs. (9) $\omega_\eta=g\,(a_{13}a_{21}R-a_{11}a_{23}P)/(R+P)$

1st eq. in Eqs. (10) $\omega_\xi=\dot{\theta}\sin\psi-\dot{\varphi}\cos\varphi\sin\theta$

1st eq. in Eqs. (11) $\dot{\theta}=-\frac{g}{4}\frac{(P-R)}{P+R}\sin 2\theta\sin 2\varphi$

3rd eq. in Eqs. (11) $\dot{\varphi}=-\frac{g}{2}\frac{P-R}{P+R}\cos\theta\cos 2\varphi$

3rd eq. in Eqs. (14) $dy^3=\sqrt{w_\zeta}\,(\cos\theta\, d\varphi+d\psi)$

2nd eq. in Eqs. (17) $w_\zeta\cos^2\theta$ should be removed.

Eq. (27) $F=\frac{7P^2+21PR+2R^2}{30(P+R)}+\left(\frac{g}{D}\right)^2\frac{P+4R}{6300}p^3+\dots$

*** Eq. (6.2) is derived from a simpler method which will serve as a further elucidation of our method. As is point out in foot-note in §4 the energy dissipation is the work done by the flow, which is given by

$$dW=-\sum_l(\mathbf{F}_l\mathbf{v}_l^0)=-g\sum_l X_l F_{ly}, \qquad (6.2')$$

where $\mathbf{v}_l^0$ is the velocity of the fluid at l-th segment. This equation leads immediately to the specific viscosity. This method should be compared with the one in refs. 1, 2 and 4, where dW is equated to be the work done by the frictional force which arises from the rotational motion ω. Both methods lead to the same results when there is no Brownian motion, but they must be distinguished in our case.

Only the first term of this equation in square bracket is the previous result. Eq. (6.4) is very analogous to Eq. (5.3) for the ellipsoid of revolution. Using Eq. (5.1) for ρ with $p=(R-P)/(R+P)$, $[\eta]$ is expressed as a power series of σ,

$$[\eta]=fN_A\frac{2P+R}{600M}-fN_A\sigma^2\frac{37P^2+27R^2+76PR}{1260000M}+\ldots\ldots \qquad (6.5)$$

§7. Rod-like Chain Molecules.

It has been shown that the free draining model is not adequate and several theories have been developed taking account of the hydrodynamical influence of partial immobilization of the solvent. However as it is difficult to treat the case of the most general pearl-necklace model as in the previous section, we take a rod-like linear chain as a simplest example in which concerns the rotatory Brownian motion. This model has been treated recently by Riseman and Kirkwood[9] (R-K), but they have adopted the idea of Simha for the effect of the Brownian motion. Therefore we will treat here again this problem. Details should be referred to R-K.

In the following it is assumed that the frictional constant of segments is same for all l and equals to f. The force acting upon the fluid by l-th segment is

$$\mathbf{F}_l=f\left([\omega\times\mathbf{R}_l]-\mathbf{u}_l^0-\frac{1}{8\pi\eta_0}\sum T_{lk}\mathbf{F}_k\right), \qquad (7.1)$$

$$T_{lk}=\frac{1}{|R_l-R_k|}+\frac{(\mathbf{R}_l-\mathbf{R}_k)(\mathbf{R}_l-\mathbf{R}_k)}{|R_l-R_k|^3}$$
$$=\frac{1}{b|l-k|}+\frac{1}{b|l-k|}\begin{pmatrix}0&0&0\\0&0&0\\0&0&1\end{pmatrix}, \qquad (7.2)$$

where $\mathbf{u}_l^0$ is the velocity of the original flow at l-th segment (Eq.3.1), b is the distance between consecutive segments, and ω should be substituted by Eqs. (3.4). Eq. (7.2) for T_{lk} is written in $(\xi\eta\zeta)$-system, rod-axis being taken as ζ-axis. It is easily shown that the angular velocity ω^0 which this rod-like chain would have in a laminar flow under the forces Eq. (7.1) without Brownian motion is the same as the one for a compact rod and is given by Eqs. (3.5) with $p=1$,

$$\omega_\xi^0=-ga_{23}a_{13},\ \omega_\eta^0=ga_{21}a_{13},\ \omega_\zeta^0=ga_{33}/2. \quad (7.3)$$

Hence Eq. (7.1) can be written separately in ξ, η and ξ-components, as follows,

$$F_{l\xi}=-f\frac{D}{\rho}\left(\cos\psi\frac{\partial\rho}{\partial\theta}+\frac{\sin\psi}{\sin\theta}\frac{\partial\rho}{\partial\varphi}\right)\zeta_l-\frac{f}{8\pi\eta_0}\sum_{\substack{k=-N\\ \neq l}}^{+N}\frac{1}{b|l-k|}F_{k\xi},$$

$$F_{l\eta}=f\frac{D}{\rho}\left(\sin\psi\frac{\partial\rho}{\partial\theta}-\frac{\cos\psi}{\sin\theta}\frac{d\rho}{d\varphi}\right)\zeta_l-\frac{f}{8\pi\eta_0}\sum_{\substack{k=-N\\ \neq l}}^{+N}\frac{1}{b|l-k|}F_{k\eta},$$

$$F_{l\zeta}=-fga_{23}a_{13}\zeta_l-\frac{f}{4\pi\eta_0}\sum_{\substack{k=-N\\ \neq l}}^{+N}\frac{1}{b|l-k|}F_{k\zeta}. \qquad (7.4)$$

$$\zeta_l=|\mathbf{R}_l|=bl.$$

For large N, these equations are approximated by the integral equations,

$$\phi_\mu(x)=f_\mu(x)-\lambda_\mu\int_{-1}^{1}K(x,t)\phi_\mu(t)dt,\ (\mu=\xi,\eta,\zeta) \qquad (7.5)$$

where

$$F_{l\mu}=\phi_\mu(x)N$$
$$f_\mu(x)=c_\mu x$$
$$c_\mu=\begin{cases}-\dfrac{fbD}{\rho}\left(\cos\psi\dfrac{\partial\rho}{\partial\theta}+\dfrac{\sin\psi}{\sin\theta}\dfrac{\partial\rho}{\partial\varphi}\right) & \text{for } \xi,\\ +\dfrac{fbD}{\rho}\left(\sin\psi\dfrac{\partial\rho}{\partial\theta}-\dfrac{\sin\psi}{\sin\theta}\dfrac{\partial\rho}{\partial\varphi}\right) & \text{for } \eta,\\ -fbga_{23}a_{13} & \text{for } \zeta.\end{cases} \qquad (7.6)$$

$$\lambda_\mu=\begin{cases}f/8\pi\eta_0 b=\lambda_1, & \text{for } \xi \text{ and } \eta\\ f/4\pi\eta_0 b=\lambda_2, & \text{for } \zeta.\end{cases}$$

$$K(x,t)=\begin{cases}1/(x-t) & -1\leqq t\leqq x-\delta,\\ 0 & x-\delta\leqq t\leqq x+\delta,\\ 1/(x+t) & x+\delta\leqq t\leqq 1,\end{cases}$$
$$\delta=1/N,\qquad x=l/N.$$

Because of

$$\frac{1}{2}\int_{-1}^{1}\phi(x)dx=0,$$

this integral equation is solved with the result,

$$\phi_\mu(x)=\sum_{\substack{k=-\infty\\ \neq 0}}^{+\infty}\frac{f_k\exp(i\pi kx)}{1-2\lambda_\mu\mathrm{Ci}\{|k|\pi\delta\}}, \qquad (7.7)$$

$$f_k=\frac{1}{2}\int_{-1}^{1}f(x)\exp(-i\pi kx)dx$$
$$=c_\mu(-)^k i/\pi k=-f_{-k},$$

$$\mathrm{Ci}(x)=\int_\infty^x\frac{\cos t}{t}dt,$$

i.e.,

$$\phi_\mu(x)=-2c_\mu\sum_{k=1}^{\infty}\frac{(-)^k\sin\pi kx}{\pi k\{1-2\lambda_\mu\mathrm{Ci}(k\pi\delta)\}}. \qquad (7.8)$$

Introducing these equations into Eq. (6.2) and using Eq. (5.1) with $p=1$, we have finally

$$[\eta]=\frac{N_A f N^2 b^2}{150 M_0 \eta_0}\Big[F(\lambda_2\delta)\int \rho \sin^4\theta \sin^2\varphi \cos^2\varphi \, d\Omega + \frac{D}{g} F(\lambda_1\delta)\int \rho \sin^2\theta \sin 2\varphi \, d\Omega\Big] \qquad (7.9)$$

where M_0 is the moleculer weight of monomer unit and

$$F(\lambda\delta)=\frac{6}{\pi^2}\sum \frac{1}{k^2(1-2\lambda \mathrm{Ci}(k\pi\delta))}$$

When λ_1, $\lambda_2 \to 0$ and hence $F(\lambda\delta)\to 1$, it is easily shown that Eq. (7.9) leads to Eq. (6.4) with $P=0$, $R=(2/3)ab^2N^3$ and

$$f(\text{in Eq. (6.4)})=f(\text{in Eq. (7.9)})/\eta_0 a.$$

In case of the complete Brownian motion $\sigma\to 0$ and $\rho=1/4\pi$, we have

$$[\eta]=\frac{N_A f}{18000\eta_0 M_0} N^2 b^2\Big[F(\lambda_2\delta)+\frac{3}{2}F(\lambda_1\delta)\Big] \qquad (7.10)$$

This is different from the equation derived by R-K.

§8. Translational and Rotatory Diffusion Constants.

In the problem of the diffusion constants does not occur the complexity of the rotatory Brownian motion. However as, the method of §7 that one solves the integral equations about F_i separately in their components in $(\xi\eta\zeta)$-axes, is slightly modified from that of R-K and has not need of an obscure approximation concerning an averaging procedure, we will give here the results without this approximation.

Translational diffusion constant,

$$D_1=\frac{kT}{fZ}2\lambda_1\Big\{\log Z-1+\frac{1}{2\lambda_1}\Big\},\quad Z=2N. \qquad (8.1)$$

perpendicular to the rod-axis,

$$D_3=\frac{kT}{fZ}2\lambda_2\Big\{\log Z-1+\frac{1}{2\lambda_2}\Big\} \qquad (8.2)$$

parallel to the rod-axis.

The observed diffusion constant is $D=(2D_1+D_3)/3$.

Rotatory diffusion constant

$$D_{rot}=\frac{3}{2}\,\frac{kT}{b^2N^3 f F(\lambda_1\delta)}. \qquad (8.3)$$

From Eqs. (7.10) and (8.3) it is seen that there does not exist such a precise connection between intrinsic viscosity $[\eta]$ and D_{rot}

$$D_{rot}=N_A kT/200 M \eta_0[\eta]$$

as pointed out by R-K without some approximation.

§9. Discussion.

It is well known that there exists such a phenomenon called structural viscosity that the specific viscosity decreases with increasing velocity gradient. The origins of this phenomenon are generally very complicated, especially in concentrated solutions. However, as for the intrinsic viscosity we can point out two causes of this effect, the one is the macro Brownian motion and the other the micro Brownian motion. The former causes the orientation of the molecules and the latter the deformation of the molecules. We have treated in the above sections the case of the macro Brownian motion. Analogously we can treat the latter case, but this problem will be deferred to later work.

The author would like to express his gratitude to Dr. S. Oka and other members of the Laboratory for their discussions and interests. He is also indebted to the Ministry of Education for research grant.

References.

1) M. L. Huggins: J. Phys. Chem. **43** (1939), 439.
2) P. Debye: J. Chem. Phys. **14** (1946), 636.
3) H. A. Kramers: J. Chem. Phys. **14** (1946), 415.
4) N. Saitô: J. Phys. Soc. Japan **4** (1949), 85.
5) J. M. Burgers: *Second Report on Viscosity and Plasticity*, Amsterdam, 1938.
6) J. G. Kirkwood, J. Riseman: J. Chem. Phys. **16** (1948), 565.
7) P. Debye, A. M. Bueche: J. Chem. Phys. **16** (1948), 573.
8) W. Kuhn, H. Kuhn: Helv. Chim. Acta **30** (1947), 1233.
9) J. Riseman, J. G. Kirkwood: J. Chem. Phys. **18** (1950), 512.

Note added in proof.

Recently Kirkwood (Rec. trav. chim. **68** (1949), 649) has developed a general theory of the micro Brownian motion of flexible macromolecules in a viscous fluid, and Kirkwood and Auer (J. Chem. Phys. **19** (1951), 281) has applied this theory to the visco-elastic properties of solutions of rod-like macromolecules as treated in §7 of this paper. Their result is same as our Eq. (7.10). They also give the rigidity for shear wave, but they do not derive the non-Newtonian viscosity. The author wishes to express his sincere thanks to Professor J. G. Kirkwood for reading the manuscript, agreeing with the conclusions and sending a reprint of the above-mentioned paper.

JOURNAL OF THE PHYSICAL SOCIETY OF JAPAN, Vol. 6 No. 5 September—October, 1951

The Light Scattering by Non-Spherical Particles in Solutions.

By Nobuhiko SAITO and Yuichi IKEDA.

Kobayasi Institute of Physical Research, Kokubunzi, Tokyo.

(Received February 2, 1951)

The angular distribution of the intensity of light scattered by macromolecules in solution has been calculated numerically, assuming these molecules as ellipsoids of revolution and cylinders whose dielectric constant is slightly different from that of the solvent. The results are given in graphs and they will be useful for the determination of the shapes of large protein molecules such as vaccinia virus.

§1. Introduction.

Recently, since Debye's proposal1), the scattering of light in solutions of macromolecules has been widely used as a powerful method for measuring the molecular weights, for determining the molecular shapes and for studying the behaviors of molecules in solution. And thereafter there have been accumulated numerous important informations about the properties of molecules in solution. In order to determine the shape and size of a macromolecule, it is usual to presume the shape of the molecule with variable parameters and then determine them so as to be in best accord with the measured angular distribution of the intensity of the scattered light. Consequently it is necessary to calculate the angular distributions of the intensities of the lights scattered by molecules of various possible shapes.

At present, however, the angular distributions of the scattered lights are calculated only for spherical particles, rods and random coil models of the flexible linear polymers. It will be useful to calculate the angular distributions for ellipsoids and cylinders in order to apply this method to some kinds of proteins or to polymers for which the random coil models are not suitable. The object of the present paper is to calculate the angular distributions of the scattered lights by ellipsoids and cylinders of various dimensions.

§2. The Assumptions and the Fundamental Equations.

The current formulas for the angular distributions of the intensities of the lights scattered by spheres, rods and random coils mentioned above are obtained from the following assumptions: 1) the solvent is assumed to be a continuous medium with dielectric constant ε. 2) the solute molecules are also isotropic particles with dielectric constant $\varepsilon+\varDelta\varepsilon$ slightly different from that of the solvent.

The first assumption is not serious if one substracts the scattered light by pure solvent from the total scattering by solutions. The second assumption also will be justified because one can choose as the solvents those satisfying this condition. It means that the light scattered in the direction perpendicular to the incident rays is completely polarized, nevertheless the depolarization is usually observed in the experiments. However, we also adopt this assumption for the sake of simplicity. In addition it is assumed that the solution is so dilute that the mutual interferences of the scattered lights by different particles are neglected.

Take a coordinate system (xyz) fixed in the space with the origin at the center of a particle. Let us consider a plane wave progressing in the direction of $-x$. The electric vector of this wave is assumed to be in the Z-direction. Then the components of the electric vector of the scattered light at the point P with the coordinates $\mathbf{r}\,(x, y, z)$ $(|\mathbf{r}|=r)$ are given under the above assumptions by Rayleigh2), as follows:

$$E_x=-\frac{k^2}{4\pi r}\frac{\varDelta\varepsilon}{\varepsilon}\frac{xz}{r^2}Q,$$

$$E_y=-\frac{k^2}{4\pi r}\frac{\varDelta\varepsilon}{\varepsilon}\frac{yz}{r^2}Q, \qquad (1)$$

$$E_z=\frac{k^2}{4\pi r}\frac{\Delta\varepsilon}{\varepsilon}\frac{x^2+y^2}{r^2}Q,$$

$$Q=\int\int\int E\exp(ikr')\,dx'dy'dz' \qquad (2)$$

where $k=2\pi/\lambda$, λ being the wave length in the solution, $\mathbf{r}'$ ($|\mathbf{r}'|=r'$) is the vector from a point P′ (x', y', z') in the molecule to the point P (x, y, z), and E is the electric vector at the point P′ which is expressed as $E=E_0\exp\{i\omega(t+kx')\}$, where ω is the circular frequency of the light. The integration in Eq. (2) is carried out over the volume of the particle. Denoting the unit vectors in the directions of $\mathbf{r}$ and the propagation of the incident rays as $\mathbf{e}$ and $\mathbf{e}_1$ and the vector representing the point P′ as $\mathbf{s}$, one obtains

$$r'=r-(\mathbf{s}\cdot\mathbf{e})$$

because r is very large. (Fig. 1).

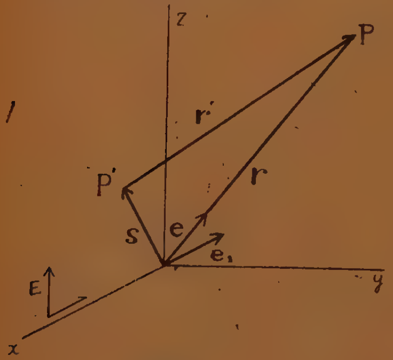

Fig 1

Accordingly we have

$$Q=E_0\,e^{i(\omega t-kr)}\,Q_0, \qquad (3)$$

$$Q_0=\int\int\int\exp\{ik\mathbf{s}\cdot(\mathbf{e}-\mathbf{e}_1\}dv. \qquad (4)$$

The intensity I of the scattered light at the point P is given by

$$\begin{aligned}I/I_0&=(|E_x|^2+|E_y|^2+|E_z|^2)/E_0^2\\&=\frac{\pi^2}{\lambda^4r^2}\left(\frac{\Delta\varepsilon}{\varepsilon}\right)^2Q_0^2(1-\cos^2\theta_1),\end{aligned} \qquad (5)$$

where I_0 is the intensity of the incident light and θ_1 is the angle between $\mathbf{e}$ and z-axis.

If the incident light is an unpolarized light, we have

$$\frac{I}{I_0}=\frac{\pi^2}{\lambda^4r^2}\left(\frac{\Delta\varepsilon}{\varepsilon}\right)^2Q_0^2(1+\cos^2\phi), \qquad (6)$$

where ϕ is the angle between $\mathbf{e}$ and $\mathbf{e}_1$. The observed intensity of the scattered light is given by averaging Eqs. (5) and (6) over all the orientations of the particle, i.e., we must calculate

$$J=\frac{1}{4\pi}\int Q_0^2\,d\Omega. \qquad (7)$$

For convenience of the integration of Q_0, we choose as the new x-axis the direction bisecting the angle between $\mathbf{e}$ and $\mathbf{e}_1$, and take a coordinate system $(\xi\eta\zeta)$ fixed in the particle. Letting (a_{ik}) represent the matrix of the transformation between the two coordinate systems (xyz) and $(\xi\eta\zeta)$, we have

$$\begin{pmatrix}x\\y\\z\end{pmatrix}=\begin{pmatrix}a_{11}&a_{12}&a_{13}\\a_{21}&a_{22}&a_{23}\\a_{31}&a_{32}&a_{33}\end{pmatrix}\begin{pmatrix}\xi\\\eta\\\zeta\end{pmatrix} \qquad (8)$$

Consequently we have

$$ik\mathbf{s}\cdot(\mathbf{e}-\mathbf{e}_1)=i2k(a_{11}\xi+a_{12}\eta+a_{13}\zeta)\sin(\phi/2). \quad (9)$$

Our task is to calculate the integrations of Eqs. (4) and (7) considering Eq. (9).

§3. Ellipsoids of Revolution.

Let the ellipsoid be

$$\frac{\xi^2}{a^2}+\frac{\eta^2}{b^2}+\frac{\zeta^2}{c^2}=1 \qquad (10)$$

in $(\xi\eta\zeta)$-sytem. Transforming to (XYZ)-system by

$$\xi=aX,\quad \eta=bY,\quad \zeta=cZ, \qquad (11)$$

we have

$$Q=abc\int\int\int_{X^2+Y^2+Z^2\leq1}\exp\{i(k_1X+k_2Y+k_3Z)\}dXdYdZ \qquad (12)$$

$$=4\pi abc(\sin K-K\cos K)/K^3, \qquad (13)$$

where

$$\left.\begin{aligned}k_1&=2aka_{11}\sin(\phi/2)\\k_2&=2bka_{12}\sin(\phi/2)\\k_3&=2cka_{13}\sin(\phi/2)\end{aligned}\right\} \qquad (14)$$

$$K^2=k_1^2+k_2^2+k_3^2. \qquad (15)$$

Assuming $b=c$, we have

$$\begin{aligned}K^2&=4k^2\{a^2a_{11}+b^2(1-a_{11}^2)\}\sin^2(\phi/2)\\&=4k^2\{b^2+(a^2-b^2)\cos^2\theta\}\sin^2(\phi/2)\end{aligned} \qquad (16)$$

where θ is the angle between x and ξ axes ($a_{11}=\cos\theta$). Now, we have to proceed to the computation of Eq. (7),

$$J=\frac{1}{4\pi}\int\frac{(\sin K-K\cos K)}{K^3}d\Omega,\ d\Omega=2\pi\sin\theta d\theta. \ (17)$$

Putting

$$2ak\sin(\phi/2)=\alpha,\quad 2bk\cos(\phi/2)=\beta, \tag{18}$$

$$\frac{a^2-b^2}{b^2}=\begin{cases}+p, & (a>b),\\ -p, & (a<b),\end{cases}\quad p>a. \tag{19}$$

$$\cos\theta=t,$$

we have

$$K^2=\beta^2(1\pm pt^2) \tag{16'}$$

and

$$J=\int_0^1\frac{(\sin K-K\cos K)^2}{K^6}dt=\frac{\pi}{2}\int_0^1\frac{(J_{3/2}(K))^2}{K^3}dt. \tag{20}$$

$$J_0=J(\alpha=0)=1/9. \tag{21}$$

In particular, when $a\gg b$,

$$\frac{J}{J_0}=-\frac{9}{10\alpha^6}-\frac{3}{2\alpha^4}+\frac{3}{5}\frac{\cos 2\alpha}{\alpha^2}\left(1-\frac{1}{2\alpha^2}+\frac{3}{2\alpha^4}\right)+\frac{3}{5}\frac{\sin 2\alpha}{\alpha^3}\left(\frac{1}{2}+\frac{3}{\alpha^2}\right)+\frac{6}{5\alpha}\int_0^{2\alpha}\frac{\sin x}{x}dx. \tag{22}$$

Eq. (20) is estimated by numerical integration. It is the ratio J/J_0 of the intensity of the scattered light in an arbitray direction to that in $\phi=0$, which is easily obtained by experiments.

In Fig. 2 J/J_0's are plotted as functions of α or β according to the prolate or oblate ellipsoids of revolution with parameters of axial ratios $f=a/b$. The more useful quantities are J_{45}/J_{135}'s, ratios of the scattered lights in directions of $\phi=45$ and 135, called dissymmetry coefficients. These are plotted in Fig. 3. The abscissa is $2a/\lambda$ ($2b/\lambda$) when the ellipsoids are prolate (oblate).

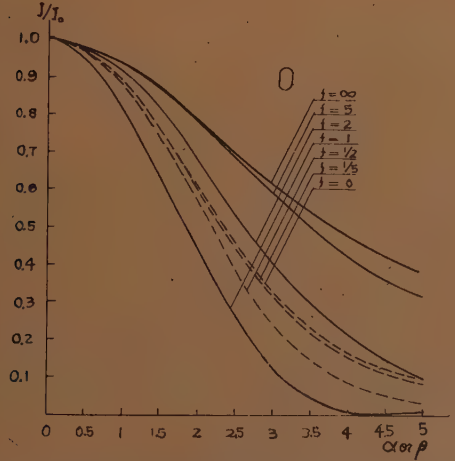

Fig. 2. Angular Distributions of the Scattered Lights by Ellipsoids of Revolution.
———— prolate ellipsoids, abscissa $\alpha=2ak\sin(\phi/2)$
.... oblate ellipsoids, abscissa $\beta=2bk\sin(\phi/2)$

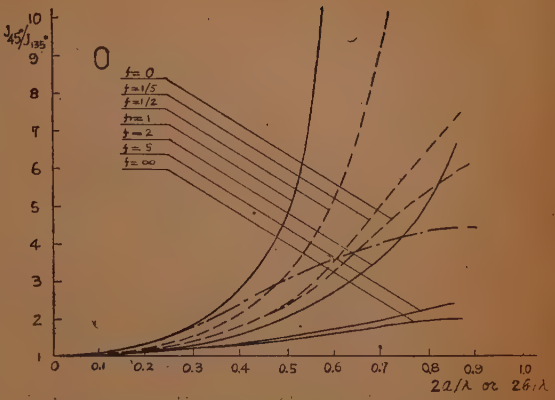

Fig. 3. Dissymmetry Coefficients of the Scattered Lights by Ellipsoids of Revolution.
———— prolate ellipsoids, abscissa $2a/\lambda$
.... oblate ellipsoids, abscissa $2b/\lambda$
-·—·-·— random coil models, abscissa $2R/\lambda$, where R is the mean square distance from the center of gravity.

§4. Circular Cylinders.

The analogous calculations are also performed in the case of the cylinder which is assumed to have a length $2a$ and a diameter $2b$.

Taking ξ-axis in the direction of the axis of the cylinder, we have in place of Eq. (12) in the case of the ellipsoid,

$$Q_0=ab^2\int_{-1}^{1}dX\iint_{Y^2+Z^2\leq 1}\exp\{i(k_1X+k_2Y+k_3Z)\}dYdZ, \tag{23}$$

where k_1, k_2, and k_3 are those defined by Eqs. (14) (with $b=c$), and using α and β defined by Eqs. (18), and putting

$$K^2=k_2^2+k_3^2=\beta^2(1-a_{11}^2)=\beta^2\sin^2\theta,$$

Q_0 is calculated to be

$$Q_0=4\pi ab^2\frac{\sin k_1}{k_1}\frac{J_1(K)}{K}=4\pi ab^2\frac{\sin(\alpha\cos\theta)}{\alpha\cos\theta}\frac{J_1(\beta\sin\theta)}{\beta\sin\theta}. \tag{24}$$

The results of the numerical calculations of Eq. (7) are shown in Fig. 4. In particular when $a\gg b$,

$$J/J_0=\frac{1}{\alpha}\int_0^{2\alpha}\frac{\sin x}{x}dx-\frac{\sin^2\alpha}{\alpha^2}, \tag{25}$$

which was already derived as the equation for rod-like particles. The dissymmetry coefficients are plotted in Fig. 5.

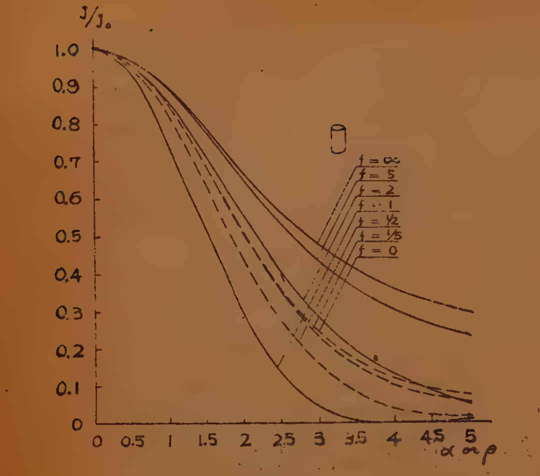

Fig. 4. Angular Distributions of the Scattered Lights by Cylinders.
———— prolate cylinders ($f=a/b>1$), abscissa $\alpha=2ak\sin(\phi/2)$,
············ oblate cylinders ($f<1$), abscissa $\beta=2bk\sin(\phi/2)$,

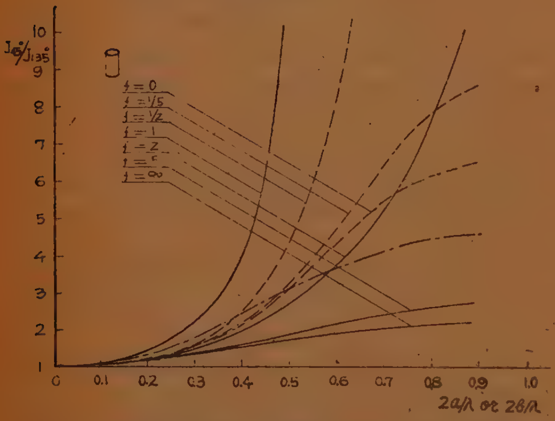

Fig. 5. Dissymmetry Coefficients of the Scattered Lights by Cylinders.
———— prolate cylinders, abscissa $2a/\lambda$,
············ oblate cylinders, abscissa $2b/\lambda$,
—·—·- random coil models, abscissa $2R/\lambda$.

§5. Discussions.

When we obtain the angular distribution by measuring the intensities of the scattered light and eliminating the goniometric factor $(1-\cos^2\theta_1)$ or $(1+\cos^2\phi)$, it is possible to determine the shape and size of the particle comparing with Fig. 2 or Fig. 3. However, if the dimensions of the particle are too small compared with the wave length in the solvent, J/J_0 is nearly equal to 1, and does scarcely change with ϕ. Therefore the molecules whose dimensions can be determined by the light scattering must have, at least, one dimension longer than about 1/10 of the wave length. From this reason, it is hopeless to apply this method to such proteins as the hemoglobin or the serum albumin. This method will be applied with success to large proteins such as tobacco mosaic virus or vaccinia virus.

On the other hand, it is usual to use the equations of viscosity, diffusion or sedimentation constant, derived from the hydrodynamical considerations, based on the models of the ellipsoid of revolution in order to determine the shapes and sizes of protein molecules. Indeed, it is a useful assumption to assume the non-spherical protein molecule to be an ellipsoid of revolution, however, there are some proteins which resemble cylinders rather than ellipsoids. It is almost impossible to answer hydrodynamically whether the ellipsoid of revolution or the cylinder is the better approximation for the model of a protein. By the method of the light scattering, one can answer this question, when the precision of the experiment is sufficiently high. We notice the fact that the angular distribution is very sensitive to the slight deviation from the case $f=1$, but does not vary anymore greatly when f or $1/f$ exceeds 10, as is seen in Fig. 3 or Fig. 5.

If the volume per molecule is known by another method, Fig. 3 or 5 serves to determine the size of the molecule.

In cellulose derivatives, it is known that they are rod-like and the Eq. (25) is applicable when the degrees of polymerization are not so large and that they are random coiled when the degrees of polymerization are sufficiently large. But when one wishes to deal with those of the moderate degrees of polymerization, then, the equations for ellipsoids or cylinders will serve as measures for the shapes of the molecules. In Figs. 3 and 5, the results by random-coil models are plotted for references.

The authors would like to express their gratitude to Dr. S. Oka for his interest and encouragement. They are also indebted to the Ministry of Education for researh grant.

References.

1) P. Debye: J. App. Phys. **15** (1944) 456.
J. Phys. Colloid Chem. **51** (1947) 18.
2) Lord Rayleigh: Phil. Mag. **12** (1881) 81.

JOURNAL OF THE PHYSICAL SOCIETY OF JAPAN, Vol. 6 No. 5 September—October, 1951

On the Theory of Surface Tension of Regular Solution.

By Terutosi MURAKAMI, Syû ONO, Mikio TAMURA* and Michio KURATA.**

Faculty of Engineering, Kyushu University, Faculty of Engineering, Kyoto University and Tokyo Institute of Technology.***

(Received May 1, 1951)

By using the quasi-crystalline model, the grand partition function of a binary solution, in which the molecular fractions are considered to be functions of the distance from the surface, is constructed. And the concentration is determined so as to make the system be in thermodynamical equilibrium. The surface tension and the surface excess amounts of components obtained in such a manner does not conflict with the Gibbs adsorption formula. Guggenheim's theory of the surface tension of regular solution, based on the monolayer model, is a special case of the present theory. The monolayer theory, however, is in contradiction with the Gibbs formula, since the system cannot reach equilibrium state if the difference of composition from the bulk phase is confined to such a thin region as mono-or two-molecular layer.

§1. Introduction.

Theories of the surface tension of binary solution, based on the quasi-crystalline model, have been elaborated by Shuchowizky,[1] Belton and Evans,[2] and Guggenheim.[3] The essential assumption in these papers is that the difference in composition of the surface from the bulk is confined to a mono-molecular layer. Recently Defay and Prigogine[4] have pointed out that the monolayer model leads to the result conflicting with the Gibbs adsorption formula except for the perfect solutions, and they took into account the possible presence of two monolayers in the surface phase.

On the other hand, one of the present authors has established the general theory of multimolecular[5] adsorption in regular solution, and has calculated the change in concentration near the surface. And this method is also applicable to the theory of the surface tension of regular solution. The main purpose of the present paper is to calculate the surface tension and the change in concentration at the free surface of regular solution from the mutilayer model previously used. And it will be later seen that this model leads to the result in complete agrement with Gibb's theory.

In our present theory, the presence of molecules in the vapor phase is neglected as in Guggenheim's and Defay and Prigogine's theories. It is, however, obvious that we must take into account the presence of the holes in liquid phases as well as the presence of molecules in the vapor phase to carry out more quantitative calculation of the surface tension of a binary solution as in the case of the surface of pure liquid.[6] Such calculation was carried out with a certain approximation by one of the authors.[7]

§2. Surface Tension and Multimolecular Layer Model for Surface.

Let us consider a binary solution, in which the two kinds of molecules are denoted by A and B respectively. It is first assumed that the quasi-crystalline lattice is the same in the surface layer as in the bulk phase. And we number the lattice planes parallel to the surface from 1 to l, and neglect the presence of molecules in the vapor phase. These planes are assumed to have the same area a. Then we may assume that the molecules are distributed uniformly in each of these layers.

Let the molecular fractions of A and B in the rth layer be x_r and y_r respectively, so that

$$x_r+y_r=1. \tag{1}$$

Since x_r and y_r approach to x_L and y_L respectively, the molecular fractions in the bulk phase, at great distance from surface, they must obey the following condition:

$$x_L=\lim_{r\to\infty} x_r, \qquad y_L=\lim_{r\to\infty} y_r. \tag{2}$$

The total numbers of A and B molecules are respectively given by

$$N_A = na\sum_{r=1}^{l} x_r, \qquad N_B = na\sum_{r=1}^{l} y_r, \tag{3}$$

where n is the number of lattice sites per unit area of each layer.

Let z be the number of nearest neighbors of a given molecule inside the solution. And consider now any molecule in a given layer. Let the number of its nearest neighbors in this layer be gz and the number of its nearest neighbors in the other layers be $2hz$. Then, by definition we have

$$g+2h=1. \tag{4}$$

Using the Bragg-Williams approximation, we assume complete randomness in each layer. Then the total number of AB contacts is given by

$$\frac{1}{2}zna\sum_{r=1}^{l} p_{ABr},$$

where

$$\left.\begin{aligned} p_{ABr} &= x_rY_r+y_rX_r,\\ X_r &= hx_{r-1}+gx_r+hx_{r+1},\\ Y_r &= hy_{r-1}+gy_r+hy_{r+1}. \end{aligned}\right\}\text{for } r\geqq 2, \tag{6a}$$

and

$$\left.\begin{aligned} p_{AB1} &= x_1Y_1+y_1X_1,\\ X_1 &= gx_1+hx_2,\\ Y_1 &= gy_1+hy_2. \end{aligned}\right\} \tag{6b}$$

Here, (6b) is due to the absence of molecules in the vapor.

Now we denote by ε_{AA}, ε_{BB} and ε_{AB} the energies of an AA, a BB and an AB contact respectively, and define $\Delta\varepsilon$ by

$$\Delta\varepsilon = 2\varepsilon_{AB}-\varepsilon_{AA}-\varepsilon_{BB}. \tag{7}$$

The grand partition function of the system is given by

$$\Xi = \left[\exp\left\{\frac{z\varepsilon_{BB}+2\mu_B}{2kT}\right\}\right]^{N_A+N_B}\Xi^*, \tag{8a}$$

where

$$\Xi^* = \sum_{x_ry_r}\exp\left\{-\frac{nazh(x_1\varepsilon_{AA}+y_1\varepsilon_{BB})}{2kT}\right\}$$
$$\times\prod_{r=1}^{l}\frac{(na)!}{(nax_r)!\,(nay_r)!}$$
$$\times\exp\left\{\frac{2nax_r(\mu_A-\mu_B)+na(\varepsilon_{AA}-\varepsilon_{BB})}{2kT}\right\}$$
$$\times\exp\left\{-\frac{nazp_{ABr}\Delta\varepsilon}{4kT}\right\}, \tag{8b}$$

where T is the absolute temperature and k is Boltzmann's constant and the summation extends over all sets of x_r and y_r subject to (1).

According to the general properties of the grand partition function* we have

$$\gamma a = -kT\ln\Xi + PV, \tag{9}$$

where γ is the surface tension, V is the volume of the total system excluding the portion corresponding to vapor phase, and P is the pressure. Substituting (8) into (9), and replacing Ξ by its maximum term as usual, we obtain,

$$\gamma a = na\sum_{r=1}^{l}(\psi_r - x_r\mu_A - y_r\mu_B) + PV, \tag{10}$$

where

$$\psi_1 = \frac{1}{2}z\Big[-x_1\varepsilon_{AA}-y_1\varepsilon_{BB}+\Big\{gx_1y_1$$
$$+\frac{1}{2}h(x_1y_2+y_1x_2)\Big\}\Delta\varepsilon + hx_1\varepsilon_{AA}+hy_1\varepsilon_{BB}\Big].$$
$$+kT(x_1\ln x_1+y_1\ln y_1), \tag{11}$$

$$\psi_r = \frac{1}{2}z\Big\{-x_r\varepsilon_{AA}-y_r\varepsilon_{BB}$$
$$+\frac{1}{2}(x_rY_r+y_rX_r)\Delta\varepsilon\Big\}+kT(x_r\ln x_r$$
$$+y_r\ln y_r) \qquad \text{for } r\geqq 2. \tag{12}$$

And the condition of the maximization is

$$\mu_A-\mu_B+\frac{1}{2}z(\varepsilon_{AA}-\varepsilon_{BB})$$
$$=\frac{1}{2}zh(\varepsilon_{AA}-\varepsilon_{BB})+\frac{1}{2}z\Big\{g(y_1-x_1)$$
$$+h(y_2-x_2)\Big\}\Delta\varepsilon+kT\ln\frac{x_1}{y_1}$$
$$=\frac{1}{2}z(Y_r-X_r)\Delta\varepsilon+kT\ln\frac{x_r}{y_r} \qquad (r\geqq 2)$$
$$=\frac{1}{2}z(Y_L-X_L)\Delta\varepsilon+kT\ln\frac{x_L}{y_L}. \tag{13}$$

(13) is the condition for equilibrium, and may be written in the form of the difference equation which is essentially equivalent to the one derived by one of the authors in the alternative way[5].

§3. Surface Tension and the Gibbs Adsorption Formula.

The grand partition function for the bulk phase which consists of l equivalent layers of the area a is given by

---

* Equation (9) can be proved in the manner as shown in Guggenheim's book[8].

$$\Xi_L=\left[\exp\left\{\frac{z\varepsilon_{BB}+2\mu_B}{2kT}\right\}\right]^{N_A+N_B}\Xi_L^*, \qquad (14a)$$

$$\Xi_L^*=\sum_{x_Ly_L}\frac{(nal)!}{(nalx_L)!(naly_L)!}\exp\left\{\frac{nalx_L(\mu_A-\mu_B)}{kT}\right\}$$
$$\times\exp\left\{\frac{znalx_L(\varepsilon_{AA}-\varepsilon_{BB})}{2kT}\right\}\exp\left\{-\frac{nalp_{ABL}\Delta\varepsilon}{4kT}\right\}, \qquad (14b)$$

where p_{ABL} is defined by $p_{ABL}=2x_Ly_L$ which is equal p_{ABr} given by (6), if all x_r's anb y_r's are equal to x_L and y_L respectively. And the pressure of this system is expressed by

$$PV_L=kT\ln\Xi_L. \qquad (15)$$

This can be written in the form

$$PV=-nal(\psi_L-x_L\mu_A-y_L\mu_B), \qquad (16)$$

where

$$\psi_L=\frac{1}{2}z\left\{-x_L\varepsilon_{AA}-y_L\varepsilon_{BB}+\frac{1}{2}p_{ABL}\Delta\varepsilon\right\}$$
$$+kT(x_L\ln x_L+y_L\ln y_L). \qquad (17)$$

Let Γ_A and Γ_B be the surface excesses per unit area of A and B respectively:

$$\Gamma_A=n\sum_{r=1}^{l}(x_r-x_L), \quad \Gamma_B=n\sum_{r=1}^{l}(y_r-y_L). \qquad (18)$$

Inserting (16) in (10) and using (18), we obtain

$$\gamma=n\sum_{r=1}^{l}(\psi_r-\psi_L)-\mu_A\Gamma_A-\mu_B\Gamma_B. \qquad (19)$$

By using (13) and the relation $\Gamma_A=-\Gamma_B$, we easily obtain from (19)

$$d\gamma=-\Gamma_Ld(\mu_A-\mu_B), \qquad (20)$$

which shows that the surface tension obeys the Gibbs adsorption formula. And from (13) we have

$$\frac{d(\mu_A-\mu_B)}{dx_L}=-z\Delta\varepsilon+\frac{kT}{x_Ly_L}. \qquad (21)$$

(20) and (21) give

$$\frac{d\gamma}{dx_L}=-\frac{\Gamma_A}{x_Ly_L}(kT-zx_Ly_L\Delta\varepsilon), \qquad (22)$$

which is Gibbs' adsorption formula for regular solution, first derived by Hildebrand.[9] Consequently the multi-layer model for surface is not in contradiction with Gibbs' theory.

And it is evident that the surface tension of pure liquids, consists of A or B alone are, respectively, given by

$$\left.\begin{aligned}\gamma_A&=\frac{1}{2}zh\varepsilon_{AA},\\ \gamma_B&=\frac{1}{2}zh\varepsilon_{BB}.\end{aligned}\right\} \qquad (23)$$

§4. Critique of the Monolayer Model for Surface.

In the present section, we shall criticize Guggenheim's monolayer theory and Defay and Prigogine's two-layer theory. If we set $x_r=x_L$ and $y_r=y_L$ for $r\geqq 2$ in the formulae of the previous sections, we shall obtain the results of monolayer theory. For example, using (23), we may rewrite (10) in the form

$$\gamma=x_1\gamma_A+y_1\gamma_B-n\left[\frac{z}{2}\{2h(x_1-x_L)^2+gx_1y_1\}\Delta\varepsilon\right.$$
$$\left.-kT\left(x_1\ln\frac{x_1}{x_L}+y_1\ln\frac{y_1}{y_L}\right)\right]. \qquad (24)$$

Bearing the condition given by (13) in mind, we can rewrite (24) in the form

$$\gamma=\gamma_A+n\left[\frac{z}{2}g(y_1^2-y_L^2)\Delta\varepsilon-\frac{z}{2}hy_L^2\Delta\varepsilon\right.$$
$$\left.+kT\ln\frac{x_1}{x_L}\right]$$
$$=\gamma_B+n\left[\frac{z}{2}g(x_1^2-x_L^2)\Delta\varepsilon-\frac{z}{2}hx_L^2\Delta\varepsilon\right.$$
$$\left.+kT\ln\frac{y_1}{y_L}\right] \qquad (25)$$

which is in complete agreement with the formula derived by Guggenheim. And the surface excesses given by (18) become

$$\Gamma_A=n(x_1-x_L), \quad \Gamma_B=n(y_1-y_L), \qquad (26)$$

x_1 being determined by (25). From (25) we obtain

$$\frac{d\gamma}{dx_L}=-\frac{\Gamma_A}{x_Ly_L}\{kT-z(1-h)x_Ly_L\}, \qquad (27)$$

which corresponds to (22) in the preceding section. Defay and Prigogine have pointed out that (27) is inconsistent with Hildebrand's formula (22) except when the solution is perfect, and showed that the two-layer model leads to the adsorption formula differing from the Gibbs formula only by the term of the second order in $(z\Delta\varepsilon/kT)$. They have, however, not explained the reason for discrepancy between the result of the monolayer theory and the Gibbs formula. But, according to the stand point of the multilayer adsorption theory described here, the origin of the above discrepancy may be understood as follows.

Let us assume that the surface layer consists only of the first N layer in which the molecular fractions are different from those in bulk phase and that $x_{N+1}=x_{N+2}=\dots=x_L$. Then we have, according to the condition of maximization (13), unless the solution is perfect,

$$\frac{1}{2}zh\{(y_N-y_L)-(x_N-x_L)\}=0, \qquad (28)$$

which immediately results in $x_N=x_L$, contradicting with the initial assumption of the N-layer model for the surface. The above result implies that such a set of the molecular fraction that $x_1 \neq x_2 \neq \dots \neq x_{N+1}=\dots=x_L$ cannot give the maximum term in the grand partition function. In other words, for the case of finite layer model, the quantities calculated from (10) and (16) cannot correspond to the thermodynamical quantities in true equilibrium state. And in such a case the equation which corresponds to (20) becomes

$$d\gamma=-\Gamma_A d(\mu_A-\mu_B) + \frac{1}{2}zh\Delta\varepsilon\{(y_N-y_L)-(x_N-x_L)\}dx_L. \qquad (29)$$

It is easily seen that the result obtained from (29) contradicts with Hildebrand's formula (22). Thus for Guggenheim's monolayer model the condition for equilibrium is violate unless $x_1=x_L$, which contradicts with th requirement of the model. And if $x_1 \neq x_L$ i demanded, $d\gamma$ must obey (29) which togethe with (21) gives (27). And for the case o Defay and Prigogine's two-layer model, th situation is not essentially different from th one in the case of monolayer model, thoug it may give more correct results than th monolayer model gives. In facts, it has bee demonstrated by one of the present authors[5] that the moelcular fractions in the secon layer are almost equal to those in the bul phase.

References.

1) Shuchowitzky; Acta Physicochimica U.R.S.S., **1** (1944), 176.
2) Belton and Evans: Trans. Faraday Soc., **41** (1945) 1.
3) E. A. Guggenheim: Trans. Faraday Soc., **46** (1950), 150.
4) R. Defay and I. Prigogine, Trans. Faraday Soc., **46** (1950), 199.
5) S. Ono, Memoirs of the Faculty of Engineering, Kyushu Univ., **12** (1950), 1.
6) S. Ono, Memoirs of the Faculty of Engineering, Kyushu Univ., **10** (1947), 195.
7) M. Kurata, Busseiron Kenkyu, No. 27 (1950), 37 (in Japanese).
8) R. H. Fowler and E. A. Guggenheim, *Statistical Thermodynamics*, (Cambridge 1939) p. 234.
9) J. H. Hildebrand, *Solubility* (Reinhold, 1939) p. 190.

JOURNAL OF THE PHYSICAL SOCIETY OF JAPAN Vol. 6 No. 5 September—October, 1951

A Statistical Theory of Molecular Rotation in Normal Solid Hydrocarbons and Alcohols.

By Yoshinobu KAKIUCHI.

Institute of Science and Technology, University of Tokyo. Meguroku, Tokyo.

(Received, December 7, 1950)

Molecules in certain normal long chain solid hydrocarbons or alcohols are well known to rotate around their long axis in high temperature phase. A simple statistical theory of rotational transformation similar to Bethe's theory of order-disorder transformation in alloys is attempted, assuming that molecules librate around their equilibrium position and sometimes change their orientation by thermal agitation. A sharp anomaly in observed specific heat is explained as the result of the cooperative transformation from ordered to disordered state in molecular orientation. The large value for the observed heat of transformation is attributed to the internal degrees of freedom of the molecule, perhaps mainly of twisting modes of vibration. The effect of lattice expansion accompanied by the transformation is not taken into account in the present treatment.

§1. Introduction.

During the last two decades, experimental evidences for molecular rotation in various molecular crystals such as solid hydrogen, chlorine or long chain hydrocarbons and alcohols have been gradually accumulated. Among them the last mentioned case, to which we shall concern in this present paper, seems to be the most suitable for theoretical treatment, on account of the fact that their molecules have only one degree of freedom, namely the rotation around their long axis.

Before proceeding to the details of the theoretical treatment of our problem, however, the experimental evidences for molecular rotation shall be summarised for later use. Müller(1) has observed that the crystal lattice of normal paraffins of carbon number 21~27 changes from orthorhombic to hexagonal form through a certain transition point, but the symmetry of molecules is so low that he has come to the conclusion that each molecule rotates around their long axis in hexagonal structure. Other experimental evidences for molecular rotation in hydrocarbons have been quite lacking till the appearence of Andrew's recent work,(2) which confirmed experimentally the abrupt narrowing of proton magnetic resonance line of normal octacosane n-$C_{28}H_{58}$ and dicetyl n-$C_{32}H_{64}$ at a certain temperature, which was reasonably attributed to the rotation of molecules suggested by Müller.

As for alcohols, Bernal(3) has concluded the existence of the molecular rotation in dodecyl alcohol from X-ray studies. Its dielectric(4)(5)(6) and thermal studies,(7) however, seem not to be sufficient for supporting the above conclusion. Dielectric measurements by Baker and Smyth,(4) Higasi and Kubo,(5) and Hoffman and Smyth(6) suggest the molecular rotation in several normal alcohols. Recent X-ray measurements by Ott,(8) and independently by the author and his collaborator(9) has confirmed the quite similar change in lattice type of hexadecyl alcohol (cetyl alcohol) as in paraffins which strongly supports the molecular rotation. The author and his collaborators(10) have also found a sharp anomaly in specific heat of alcohols at the transformation point which may well be interpreted as the result of the cooperative setting-in of molecular rotation (Fig. 1). This is perhaps the *first* reliable data on the specific heat of long chain compound which provides us the rather concrete experimental justification for the molecular rotation. These results, together with dielectric as well as proton magnetic resonance measurements above mentioned, will be sufficient to settle the problem of molecular rotation in paraffins and alcohols.

Finally it should be mentioned that Hoffman and Smyth(11) observed recently, the existence of similar rotation of molecules in long chain alkyl bromides.

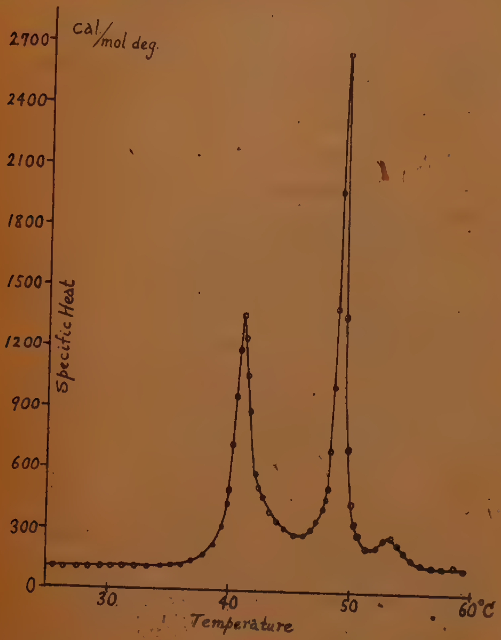

Fig. 1. Anomalous Specific Heat for Hexadecyl Alcohol (Right Peak Shows the Latent Heat of Fusion).

§2. Theory.

The possibility of molecular rotation in crystals was first established by Pauling(12) in a quantum mechanical way. The rotation of a molecule is, however, greatly affected by the state of rotation of its neighbors and which situation leads to the process which is essentially cooperative. Although Fowler(13) has attempted to propose the first, but rather formal theory, Kirkwood(14) has formulated a refined statistical theory of the phenomena in question, corresponding to the stage of approximation equivalent to that of the Bragg-Williams theory of the order-disorder transformation in alloys.(15) Further, Nagamiya(16) also has developed a similar treatment in discussing the problem of rotational transformation in NH_4Cl crystal.

The neglection of short range order in the present problem, however, *is not* a good approximation since the coupling with the nearest neighbors is rather strong compared with the one in case of alloys, although the objection to the neglection of the interaction between the more distant pairs than the nearest neighbors become less serious in the latter case.

We, therefore, shall here carry out the treatment corresponding to the Bethe approximation(17), based upon the idea which was discussed in author's previous paper.(10) The model is rather a simplified one, suitable for the mathematical manipulation, but the essential feature of the phenomena may be considered to be described correctly.

Since normal paraffins and alcohols are almost perfectly similar in their crystal structure, we shall concern only with paraffins in the following. Each molecules of paraffin crystal are straight in form and packed rather closely within the unit cell, which contains two molecules in it, as shown in Fig. 2. The circle in the figure represent the CH_2 group considered as a whole, and its radius is taken to be equal to the van der Waals' radius of the group. It will be clear that when the molecule begins to change its orientation, it necessarily influences the orientation of its neighbors, owing to the rather close packed arrangement, thus the problem being *essentially cooperative.*

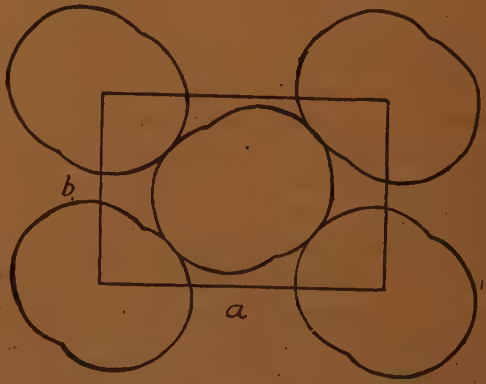

Fig 2.

If we consider the molecule of infinite chain length, the force acting between one CH_2 group of the molecule A, and the other CH_2 groups of the molecule B which lie on the same vertical line (CH_2 groups represented by white or black circles only) will be summed up into a force parallel to the plane which is perpendicular to the long axis (Fig. 3). Therefore, the sum of the forces acting between the white (or black) groups of molecule A, and the black (or white) groups of molecule B is also parallel to the plane considered above. Hence the force between two infinitely long chain molecules may be considered to be equivalent to that between two hypothetical diatomic molecules, the centers of the atoms of which are to be located at the projection of CH_2 groups on the plane as shown in Fig. 3. Thus the problem is completely reduced to the two dimensional one on the mentioned plane of projection. As the mutual interaction of the molecules is mainly due to both van der Waals' attraction and short range repulsion, the neglection of the interaction between more distant neighbors will be well justified.

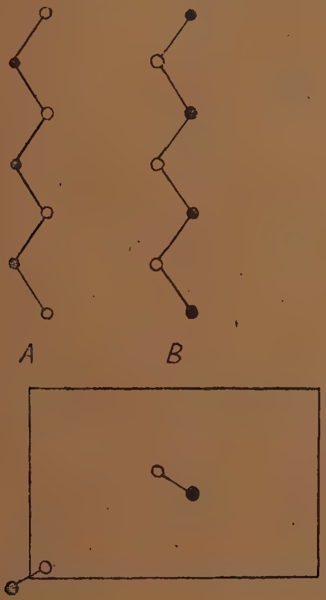

Fig. 3.

Each molecules will at first be librating around the original stable position. As the temperature rises, they will gradually take random orientations. Since the perfect free rotation seems to be hardly possible, in view of the size of the molecule, the *cog-wheel-like rotation* may be only permitted.(10) In order to simplify the problem, the lattice is assumed to be nearly hexagonal and *we shall take for the possible orientation to be the following two* separated by the potential barriers; the one is the original position and the other is its mirror image with respect to the plane passing through the center of the unit cell and perpendicular to a-axis. These positions are represented by suffices 1 and 2 respectively in the figure (Fig. 4). For the sake of convenience, the former is called the right position and the latter the wrong one as in order-disorder theory in alloys. There are five different types of interaction energy between molecules, their examples being namely (A_1,B_1), (A_1,B_2), (A_1,O_1), (A_1,O_2) and (A_2,O_1), where the notations specifying each of the orientations of molecules are shown in Fig. 4. Since the first four of them are small compared with the last, each of them may be *assumed to be equal* in its magnitude, and the last one to be larger than the former by the amount V.

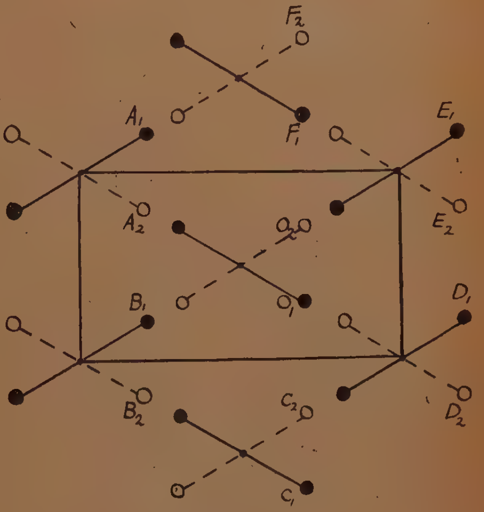

Fig. 4.

From Bethe's self consistency condition to be satisfied by the relative probabilities of the occupation of any lattice site, we may obtain the value of the statistical parameter ε which indicates the reduction of the probability of the surrounding molecules in any specified group occupying the wrong position due to the ordering influence of the molecules in the outside region of the group. Notations used in the following shall be listed below.

r_n : relative probabiltity that n neighbors out of six are in wrong positions, when the central molecule is right.
w_n: relative probability that n neighbors out of six are in wrong positions, when the central molecule is wrong.
x : $\exp(-V/kT)$

The relative probability for a pair with low interaction energy is taken to be 1, while that for high energy pair may be written as $\exp(-V/kT)$. Then it is obvious that $r_0=1$. As for r_1, among six possible configurations two are of high energy, hence the relative probability becomes $(4+2x)\varepsilon$, the factor ε being to be multiplied since one wrong molecule exists among six nearest neighbors. Similarly in case of r_2, out of fifteen configurations, eight of them contain one high energy pair and one of them contains two high energy configurations. Thus we obtain

$$\left.\begin{aligned} r_0 &= 1 \\ r_1 &= (4+2x)\,\varepsilon \\ r_2 &= (6+8x+x^2)\,\varepsilon^2 \\ r_3 &= (4+12x+4x^2)\,\varepsilon^3 \\ r_4 &= (1+8x+6x^2)\,\varepsilon^4 \\ r_5 &= (2x+4x^2)\,\varepsilon^5 \\ r_6 &= x^2\,\varepsilon^6 \end{aligned}\right\} \qquad (1)$$

Similarly,

$$\left.\begin{aligned} w_0 &= x^2 \\ w_1 &= (2x+4x^2)\,\varepsilon \\ w_2 &= (1+8x+6x^2)\,\varepsilon^2 \\ w_3 &= (4+12x+4x^2)\,\varepsilon^3 \\ w_4 &= (6+8x+x^2)\,\varepsilon^4 \\ w_5 &= (4+2x)\,\varepsilon^5 \\ w_6 &= \varepsilon^6 \end{aligned}\right\} \qquad (2)$$

Therefore,

$$\left.\begin{aligned} r &= \sum r_n = (1+x\varepsilon)^2\,(1+\varepsilon)^4 \\ w &= \sum w_n = (\varepsilon+x)^2\,(1+\varepsilon)^4 \end{aligned}\right\} \qquad (3)$$

$$\left.\begin{aligned} \varepsilon\frac{\partial r}{\partial\varepsilon} &= \frac{4r\varepsilon}{1+\varepsilon}+\frac{2x\varepsilon r}{1+x\varepsilon} \\ \varepsilon\frac{\partial w}{\partial\varepsilon} &= \frac{4w\varepsilon}{1+\varepsilon}+\frac{2\varepsilon w}{x+\varepsilon} \end{aligned}\right\} \qquad (4)$$

Hence the relative probability w' that one of the neighbors is wrong is

$$\begin{aligned} w' &= \frac{1}{6}\sum n(r_n+w_n) = \frac{1}{6}\,\varepsilon\left(\frac{\partial r}{\partial\varepsilon}+\frac{\partial w}{\partial\varepsilon}\right) \\ &= \frac{2(r+w)\varepsilon}{3(1+\varepsilon)}+\frac{x\varepsilon r}{2(1+x\varepsilon)}+\frac{\varepsilon w}{3(\varepsilon+x)} \end{aligned} \qquad (5)$$

The condition for self-consistency requires

$$w' = w \qquad (6)$$

and from (5) and (6),

$$\frac{w}{r} = \frac{2\varepsilon(1+x\varepsilon)+x\varepsilon(1+\varepsilon)}{2(\varepsilon+x)+x(1+\varepsilon)}\cdot\frac{x+\varepsilon}{1+x\varepsilon} \qquad (7)$$

which may be written as

$$\frac{(2+x)\varepsilon+2\varepsilon^2 x}{3x+(2+x)\varepsilon} = \frac{\varepsilon+x}{1+\varepsilon x} \qquad (8)$$

using (3). One root for ε is $\varepsilon=1$ and the remaining two roots are the soultion of the quadratic equation

$$3x^2\varepsilon^2+2(2x^2+2x-1)\varepsilon+3x^2 = 0 \qquad (9)$$

and as the solution must be real, x must satisfy the relation

$$(2x^2+2x-1)^2-9x^4 \geqq 0 \qquad (10)$$

which requires

$$0 \leqq x \leqq 0.290 \qquad (11)$$

or

$$0 \leqq \exp(-V/kT) \leqq 0.290 \qquad (12)$$

Roots of equation (9) is

$$\varepsilon = \frac{(1-2x-2x^2)\pm\sqrt{(1-2x-2x^2)^2-9x^4}}{3x^2} \qquad (13)$$

The excess energies due to configurations corresponding to r_n and w_n are, as is easily shown, $x\dfrac{\partial r_n}{\partial x}V$ and $x\dfrac{\partial w_n}{\partial x}V$ respectively. Therefore, the mean excess energy per molecule is equal to $\sum\limits_n x\dfrac{\partial}{\partial x}(r_n+w_n)\,V/(r+w)$. If E is the energy per mol, and N is the number of molecules per mol,

$$E = N\sum_n x\frac{\partial}{\partial x}(r_n+w_n)V/(r+w) \qquad (14)$$

From (3) and (13), together with the relation $x=\exp(-V/kT)$,

$$E = \frac{NV\{\varepsilon(1+x\varepsilon)+(\varepsilon+x)\}x}{(1+x\varepsilon)^2+(\varepsilon+x)^2} \equiv NV\varphi(x) \qquad (15)$$

and the specific heat per mol is given by

$$C = \frac{dE}{dT} = \frac{NV^2}{KT^2}\,x\,\frac{d\varphi}{dx} \qquad (16)$$

From (10) and (13) it will be clear that $\dfrac{d\varphi}{dx} = \infty$ at $x=0.290$. This value of x corresponds to the curie temperature

$$\Theta = \frac{V}{k\ln 0.290} = 0.807\,\frac{V}{k} \qquad (17)$$

The anomalous specific heat at the Curie point, however, remains finite because $\dfrac{d\varphi}{dx} = 2$ at the correspoding temperature, and its magnitude is, from (16) and (17)

$$C_{\Theta}=\frac{0.58NV^2}{kT}=0.89\,Nk \qquad (16')$$

Above the Curie temperature, we have only one root of $\varepsilon=1$ and the energy reduces to

$$E=NV\frac{x}{1+x} \qquad (18)$$

which leads to

$$C=\frac{Nx}{(1+x)^2}k\left(\frac{V}{kT}\right)^2=1.533\frac{Nkx}{(1+x)^2}\left(\frac{\Theta}{T}\right)^2 \qquad (19)$$

thus the anomalous specific heat *has a tail* as shown in Fig. 5.

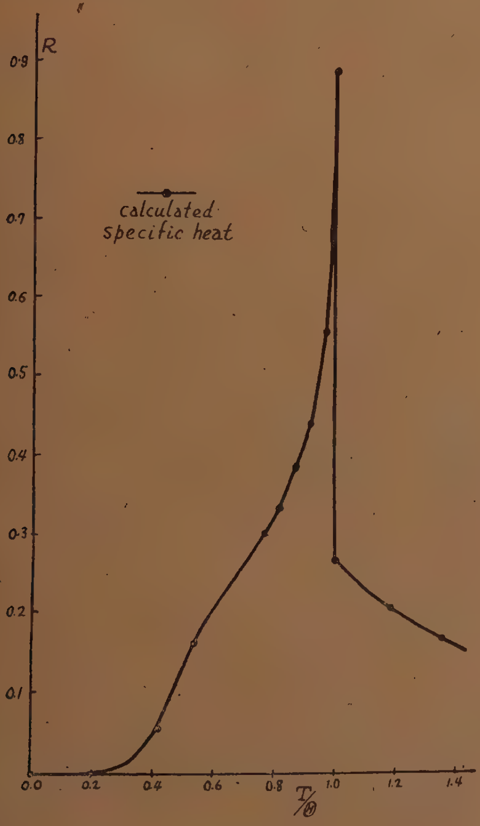

Fig. 5. Calculated Specific Heat Anomaly

Long range order S is defined by

$$S=\frac{r-w}{r+w}=\frac{(1+x\varepsilon)^2-(x+\varepsilon)^2}{(1+x\varepsilon)^2+(x+\varepsilon)^2} \qquad (20)$$

which actually vanishes at and above the Curie point, indicating that the molecules have random orientations, namely are in rotational states (Fig. 6).

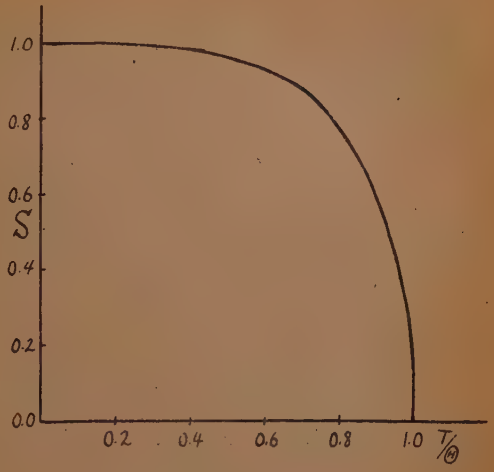

Fig. 6. Long Range Order

§3. Further refinement of the treatment.

The above results are in qualitative agreement with the results of specific heat measurement in normal hexadecyl alcohol. However, the above treatment has its drawback in several respects. Firstly, Garner, Bibber and King[18] have measured the heat of (rotational) transition of normal paraffins, although they have not mentioned the nature of the transition. According to their results, *the heat of transition is roughly proportional to the carbon number n.* (Fig. 7). This may be easily understood from (15) or (18) by assuming

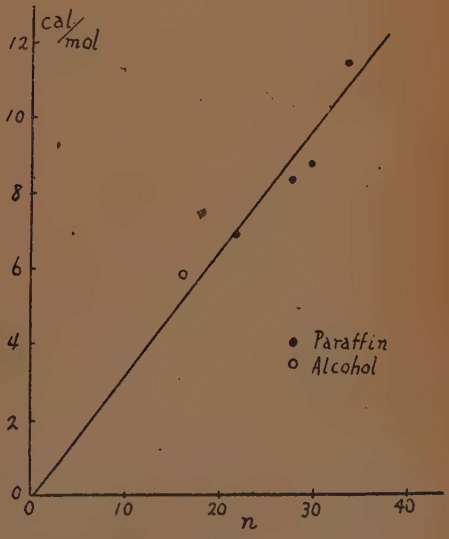

Fig. 7.

$$V = nV_0 \qquad (21)$$

where V_0 is the energy per CH_2 goup. However, this leads to the conclusion that the Curie point Θ is proportional to n, namely

$$\Theta = 0.807\frac{V}{k} = 0.807\,n\,\frac{V_0}{k} \qquad (22)$$

which *seriously contradicts with the experiment.* Müller's observation shows that Θ is less dependent upon the carbon number (Table I).

Furthermore, so long as we tacitly adhere to the original assumption that the molecule is perfectly rigid and can only rotate or librate as a whole, the entropy of transformation per mol. is of the order of $Nk \log 2 \approx 1.4$ cal./mol. deg., *irrespective of the carbon number n* contained in a molecule, since the number of possible orientations is limited into two. The entropy estimated from the specific heat data is much higher than this value, being roughly *proportional* to the carbon number n. *These considerations lead to the conclusion that the internal degrees of freedom of molecules must play an important role.*

The vibrations of paraffin molecules in crystal have been investigated by many authors,(19)(20)(21) according to which there exist two groups of Raman lines, the one of lower wave number (240cm^{-4}) corresponding to the stretching vibrations of C-C bonds, and the other of higher wave number ($900\ \text{cm}^{-1}$) which is attributed to the variation of 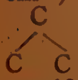 bond angles. The rough estimate of specific heats assuming Einstein functions shows that these modes of vibrations must be actually taken into account in order to explain the unusually large values of specific heat of solid paraffins even at the lower temperature phase in which the rotation of molecules does not occur. This is in accord with the fact that the specific heat per gram of paraffins tends to a certain limiting value as the carbon number increases.(23) The specific heat per mol is, therefore, proportional to the molecular weight, i.e. the carbon number (Fig. 8). This would not be understandable unless we consider the excitation of internal degrees of freedom of the molecule.

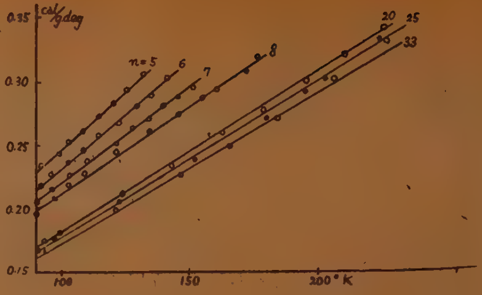

Fig. 8. Specific of Normal Paraffins
(*Parks, Huffman and Thomas*)

The third and the last possibility is to take into account the twisting vibration of the molecule, the details of which are not fully investigated yet.(19) According to Müller's works(23) on the dielectric behaviors of polar long chain compounds, however, the effect of twisting seems possibly large, and it seems also to be responsible for a part of the specific heat at the low temperature phase. The possibility of the twisting vibration may suggest that, while rotation takes place, every CH_2 groups of two neighboring molecules often *fit with each other in a complicated manner*, one group lies on one side of CH_2 group of the neighboring molecule, and the next CH_2 group of the same molecule lies for instance on the other side. Because the lattice is observed to expand slightly as the transformation proceeds, which results in the lowering of the potential barrier to be overcome by the molecule in changing their orientations, the fitting-in of the neighboring molecules may easily occur at the temperature near the Curie point.

Taking these situations into consideration, we may attempt in the following a tentative solution of the problem in a somewhat schematic way. The fitting in of the molecule is assumed to arise only in the configurations which we called high energy type (A_2 and O_1 for example). If we consider the spatial configurations of the CH_2 group in further detail, it may soon become obvious that there are *four* ways of fitting of a CH_2 group in the molecule A and the corresponding CH_2 group in molecule O, as shown in Fig. 9(a). Owing to the large twisting possibility of the chain, it may well be assumed that there is *little correlation* between the way of fitting of one CH_2

group and the next one of the same molecule, thus each CH_2 group being considered to have the possibility of taking one of those four configurations independently.

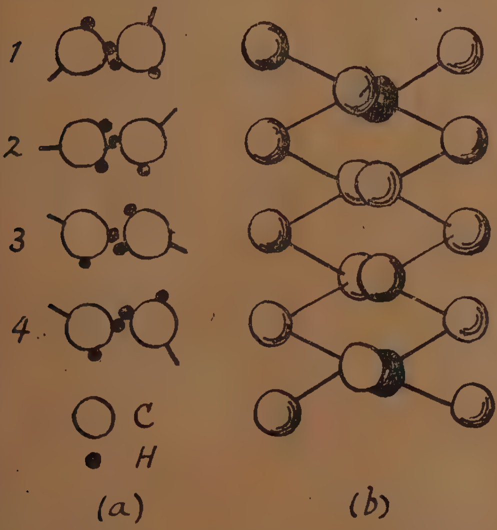

Fig. 9. Fitting-in of molecules

Because, out of n CH_2 groups within a molecule, approximately a half of them contribute to the fitting (see Fig. 9b) and there are four ways of fitting of each groups, the number of ways of fitting-in of a *pair of molecules* of high energy type becomes $(4)^{n/2}=2^n$. The relative probability x of high energy configuration of molecules containing n carbon atoms should, therefore, be multiplied by a factor of 2^n. Thus we have

$$x = 2^n e^{-V/kT} \tag{23}$$

The validity of all the formulas is unchanged except (11) or (12), which should be

$$0 \leqq x \doteq 2^n e^{-V/kT} \leqq 0.290 \tag{24}$$

Hence the transformation point Θ is obtained from the equation

$$n \ln 2 - \ln 0.290 = V/k\Theta$$

namely,

$$\Theta = \frac{V}{k(n \ln 2 - \ln 0.290)} \tag{25}$$

Putting $V=nV_0$, V_0 being the height of the potential barrier per CH_2 group, we obtain

$$\Theta = \frac{V_0}{k\{\ln 2 - (\ln 0.290)/n\}} \tag{26}$$

The slight increasing tendency of Θ with the number of carbon atoms is clearly seen from equation (26), and the calculated value of the Curie points assuming

$$\frac{V_0}{k} = 245 \text{ degree} \tag{27}$$

are compared with the observed value (Table I).

Table I
Calculated and Observed Curie Temperature

n	$\Theta cal.$	$\Theta obs.$ (Muller[1])
24	329°K	313°K
26	331	319
27	332	322
29	333	330
30	334	331
31	334	335
34	336	341
44	339	359
∞	353	—

The energy of transformation becomes from (18) and (21)

$$E = \frac{0.290}{1.290} NnV_0 = 0.225\, NnV_0 \tag{28}$$

being proportional to the carbon number n. The equation (28), together with (27), gives the correct order of magnitude for the heat of transition. In case of $C_{26}H_{54}$ for instance, its calculated value is 2.86 kcal/mol, whereas the observed value is 8.73 kcal/mol. A part of the discrepancy will be perhaps due to the neglection of lattice expansion during the transformation, and the remaining part to our oversimplified assumption regarding to interaction energy and possible orientation of molecules.

The anomalous specific heat at the Curie point is from (16) and (27)

$$C_\Theta = 0.89 n^2 R \tag{29}$$

being proportional to the square of the carbon number n. The only available data are the one for hexadecyl alcohol,[10] the anomaly amounting to 1400 cal/mol.deg at the transition point. The calculated value is smaller by a factor of 3, namely 460 cal/mol.deg.

4. Discussions

The effect of the lattice expansion and the lattice vibration upon the transformation following the molecular rotation is entirely *neglected* in our calculation. The fact that the lattice really expands at the transformation may be the cause of more abrupt rise of the anomalous specific heat than theoretically expected.

Throughout the whole treatment, the chain is *assumed to be infinite*, and the carbon number n comes into theory only in a sense that the interaction energy of the molecules is expressed as n times the energy per molecule calculated for the infinite chain. The dependency of transformation temperature upon the carbon number, however, is explained in a qualitative manner as described in the above treatment, and the effects of the finite length of the chain and of the substituted end group are to be taken into account only in the second approximation, which seems hardly of interest, judging from the simplicity of the model considered.

As we disregard the lattice distortion, the problem of the large hysteresis often existing in the transformation is entirely out of the scope of this treatment.

The essential point in the assumption necessary to deduce the correct n dependency of the transformation point and the heat of transformation (consequently the entropy of transition too) is the factor 2^n appearing in the relative probability for high energy configuration. It is perhaps of some interest to investigate the Raman lines for the crystal in rotational state in order to get some information about the twisting modes of vibration.

Another statistical treatment of the rotational transition of long chain molecules was attempted by Hoffman and Smyth(11) in case of alkyl halides. Their treatment is in the main analogous to Fowler's theory,(13) which contains some ambiguity as Kirkwood(14) has pointed out, and its general scheme seems to be not suitable for the interpretation of our problem.

The author wishes to express his sincere thanks to Profs. T. Muto and R. Kubo for their valuable discussions and criticisms.

References

1) Müller: Proc. Roy. Soc. **138** (1932) 514
2) Andrew: J. Chem. Phys. **18** (1950) 607
3) Bernal: Nature **129** (1934) 870
4) Baker and Smyth: J. Amer. Chem. Soc. **60** (1938) 1229
5) Higasi and Kubo: Sci. Pap. I.P.C.R., **36** (1939) 4286
6) Hoffman and Smyth: J. Amer. Chem. Soc. **71** (1949) 431
7) Phillips and Mumford: J. Chem. Soc. **1934** 663
8) Ott: Z. f. Phys. Chem. **193** (1944) 218
9) Sano and Kakiuchi: J. Phys. Soc. Jap. **4** (1949) 178
10) Kakiuchi, Sakurai and Suzuki: J. Phys. Soc. Jap. **5** (1950) 369
11) Hoffman and Smyth: J. Amer. Chem. Soc. **72** (1950) 171
12) Pauling: Phys. Rev. **36** (1930) 430
13) Fowler: Proc. Roy. Soc. **149** (1935) 1
14) Kirkwood: J. Chem. Phys. **8** (1940) 205
15) Bragg and Williams: Proc. Roy. Soc. **145** (1934) 699
16) Nagamiya: Proc. Phys. Math. Soc. Jap. **25** (1943) 540
17) Bethe: Proc. Roy. Soc. **150** (1935) 550
18) Garner, Bibber and King: J. Chem. Soc. **1931** 1533
19) Pitzer: J. Chem. Phys. **8** (1940) 711
20) Kirkwood: J. Chem. Phys. **7** (1939) 506
21) Mizushima and Simanouti: J. Amer. Chem. Soc. **71** (1949) 1320.
22) Parks, Huffman and Thomas: J. Amer. Chem. Soc. **52** (1930) 1032
23) Müller: Proc. Roy. Soc. **138** (1932) 514.

JOURNAL OF THE PHYSICAL SOCIETY OF JAPAN, Vol. 6 No. 5 September—October, 1951

Proton Conduction through Solid Alcohols due to Molecular Rotation.

By Yoshinobu KAKIUCHI, Hachiro KOMATSU and Susumu KYOYA.

Institute of Science and Technology, University of Tokyo
Meguroku, Tokyo.

(Received December 7, 1950)

The anomalous electric conductivity in higher normal alcohols is often attributed to the proton transfer accompanied by the rotation of molecules around their long axis. The direct experimental justification for the above idea is attempted, where results are described in the following. The gas produced as the result of the electric conduction is identified spectroscopically with hydrogen, and its amount is found to coincide with the expected value, assuming that the current is conducted solely by protons. The effect of the added long chain compounds is observed and the result seems to be well understood on the basis of the *proton-transfer-and-molecular-rotation* mechanism.

§1. Introduction.

It is well known that normal solid alcohols have anomalous dielectric constant(1) and electric conductivity(2) between the transformation temperature and the melting point. The rotation of molecules around their long axis in solid phase above the transformation point was concluded from dielectric data by Baker and Smyth,(3) as well as from X-ray measurements by Ott(4) and independently by one of the authors and his collaborator.(5) Specific heat measurements in our laboratory also confirmed the above conclusion.(6)

Anomalous dielectric constant and electric conductivity was already attributed to the large mobility of protons forming hydrogen bonds by one of the present authors(2), who has also pointed out that these anomaly must closely related to the rotation of molecules around their long axis.(8) Hoffman and Smyth(9) considered it to be due to the mechanism as exactly the same as in case of the water, which has been discussed by Hückel(10) and Eyring.(11) Namely, protons forming hydrogen bonds in alcohol crystal happen to displace a little, and as the result, ROH_2^+ ion which is similar to oxonium ion will be formed. As the molecule rotates around their long axis, it is possible for such an ion to have a chance of giving a proton to one of its adjacent molecules which in turn becomes an ROH_2^+ ion. When the electric field exists, the number of protons moving in the direction of the field is larger than that moving in the opposite direction, the electric conductivity being thus established.

In the above considerations, the charge is considered to be carried by protons mainly from two reasons. One is the fact that the conductivity decreases gradually after the application of the voltage to the electrodes, showing the existence of the polarisation due to ionic conduction. If the electrodes are short circuited, the current will flow in the opposite direction. The other is a rather chemical one, namely the fact that the hydrogen atoms in OH bond are more dissociable than other atoms in the molecule. The direct experimental evidence for the proton conduction, however, is hitherto entirely lacking, with which the present paper should mainly be concerned.

The present authors have succeeded to detect spectroscopically the hydrogen gas evolved at the negative electrode as the result of the electrolytic conduction, and the results of the experiments together with the conductivity measurements are discussed in connection with the mechanism of the proton conduction through solid alcohols.(12)

§2. Spectroscopic Evidence for Proton Conduction.

The sample of cetyl alcohol was placed in a cylindrical condensor, whose electrodes were insulated by a micalex spacer (Fig. 1).

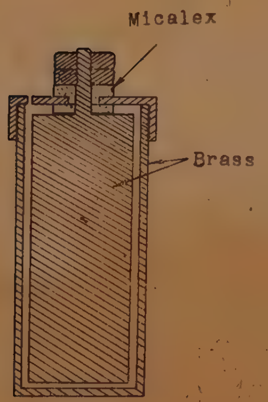

Fig. 1. Condensor

The surfaces of the electrodes were nickel plated in order to avoid the chemical reaction with the sample. The temperature of the sample was measured by a copper-constantan thermo-couple. The condensor was suspended in an evacuated glass cylinder through the leads connected to tungsten wires, sealed to the removable top, which is fitted to the cylinder with ground joint (Fig. 2).

After the vessel was wholly evacuated, the stop cocks S_2 and S_4 were closed, and the current of some 40 μA was made to flow through the sample whose temperature was always kept constant within the range 45°~48°C. After being left for two hours, S_5 was closed and then S_4 was opened and the gas produced was thus introduced to the discharge tube D. The liquid air trap was nescessary in order to prevent the vapor of cetyl alcohol from going into the discharge tube. Because the foreign gas adsorbed in the electrodes affected the discharge greatly, the electrodeless discharge through the gas to be examined was observed.

High frequency oscillation of wave length of about 2 meter was generated by an ordinary Hartley circuit using a triode T311, the plate voltage of which being about 1000 volts. A copper tube 6 mm in diameter and 43 cm in length is bent in U-form, the distance between parallel parts being 11.9 cm, and put into the plate circuit as shown in Fig. 3. The secondary coil with the same dimensions with the primary, is shunted by an adjustable parallel plate condensor. The voltage output was applied to the tin foil electrodes coiled at the outer surface of the discharge tube. The discharge through the gas was observed by a quartz spectrograph. When the voltage was not applied to the electrodes, the color of the discharge was somewhat bluish and its spectrum was very weak (Photo. 1a). On the contrary, when the voltage was applied to the sample

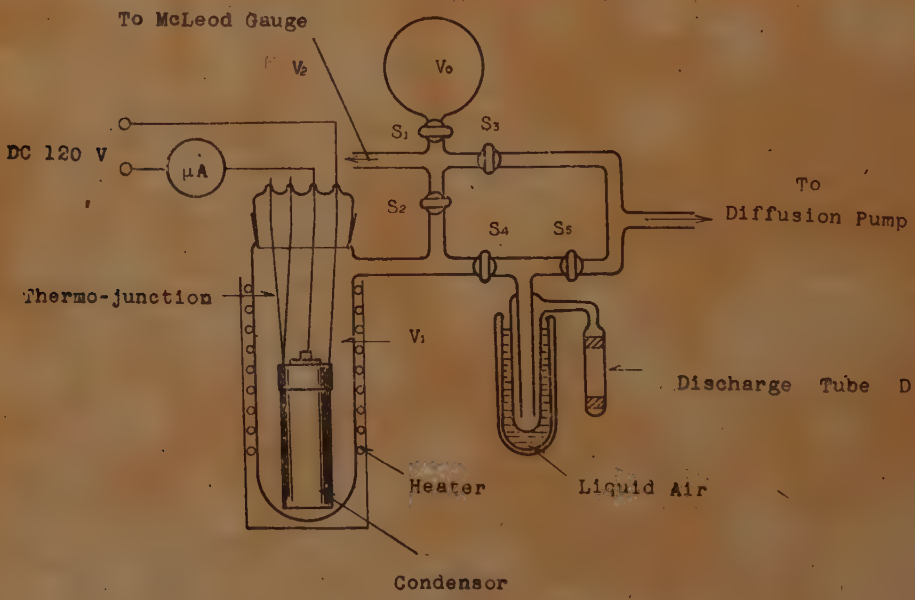

Fig. 2.

and the current flowed through it, the color of the discharge through the gas evolved was reddish white, its spectrum being attributed to the hydrogen (Photo. 1b). Balmer series due to atomic hydrogen and the band spectra due to hydrogen molecule were easily identified.(13) At the temperature below and above the hexagonal region, where the conductivity was much smaller, the intensity of hydrogen spectra was also negligible. Therefore, it may be clear that the *hydrogen is evolved* as the result of the electrolytic conduction of alcohol.

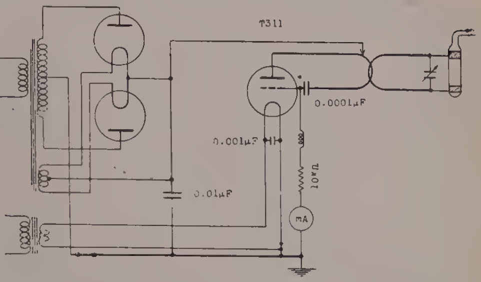

Fig. 3. Oscillator for discharge

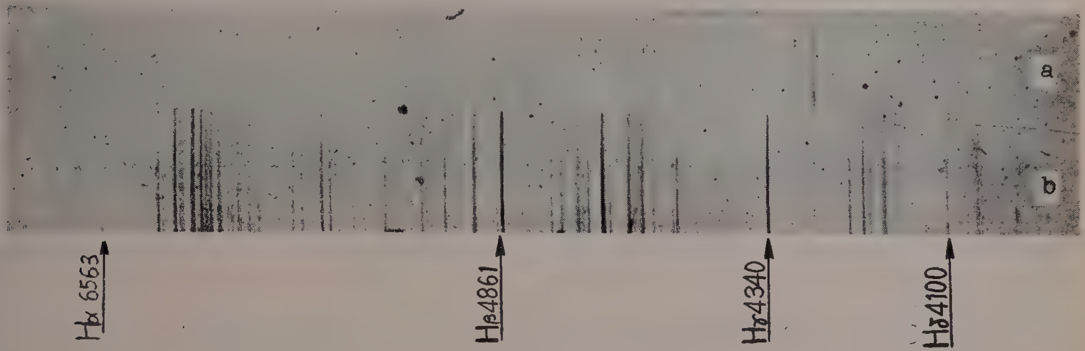

Photo. 1. Spectra of the gas.

§ 3. Faraday's Law.

If the above considerations be correct, the relation between the charge carried by the current and the amount of the gas evolved must obey the Faraday's law. In order to verify this relation, the current flowing through the sample and the pressure of the gas were recorded against the time elapsed, by means of a microammeter and a McLeod gauge.

The amount of the gas evolved may be calculated from its volume and the pressure. Because the temperature of the gas in the cylinder is higher than the room temperature, the volume V_1 of the cylinder and the volume V_2 of the remaining part including the guage, must be estimated separately. The general procedure for the determination of the volume run as follows, making use of a reservoir of volume V_0. Firstly, all cocks S_1, S_2, S_3, S_4 and S_5 were opened and the whole system was thoroughly evacuated. Then the cocks S_2 and S_4 were closed and the cylinder was filled with the gas evolved. In this case the cylinder was kept at the room temperature. Next, the cock S_3 was closed, and the measurement was done in the following manner.

(a) S_1 closed and S_2 opened, and the volume and the pressure are

V_1+V_2 and p_a respectively.

(b) S_2 closed and S_1 opened,

V_0+V_2 and p_b

(c) S_1 closed and S_2 opened,

V_1+V_2 and p_c

(d) S_1 opened, $V_0+V_1+V_2$ and p_d.

The effect of the residual gas, the amount of which is small and is mainly determined by the pumping speed, may be only to be taken into account for the reservoir, which is larger in volume compared with V_1 and V_2. Let the residual pressure be p_0, then the relations:

$$p_0V_0+p_aV_2+p_0V_1=p_b+V_2 \qquad (1)$$

$$p_aV_1+p_bV_2=p_c(V_1+V_2) \qquad (2)$$

$$p_bV_0+p_c(V_1+V_2)=p_d(V_0+V_1+V_2) \qquad (3)$$

will hold between V's and p's. As the result of the measurement, V_1 and V_2 were found to be 230 cc and 190 cc respectively. The total mol number n of the gas is given by

$$n=\frac{p}{R}\left(\frac{V_1}{T_1}+\frac{V_2}{T_2}\right), \tag{4}$$

where R is the gas constant and T_1 and T_2 are the temperature of the parts V_1 and V_2 respectively. The amount of the charge Q carried by the current during the time interval t is obtained by numerical integration from the data for the magnitude of the current flowed, and is plotted against the mol number of the gas evolved.

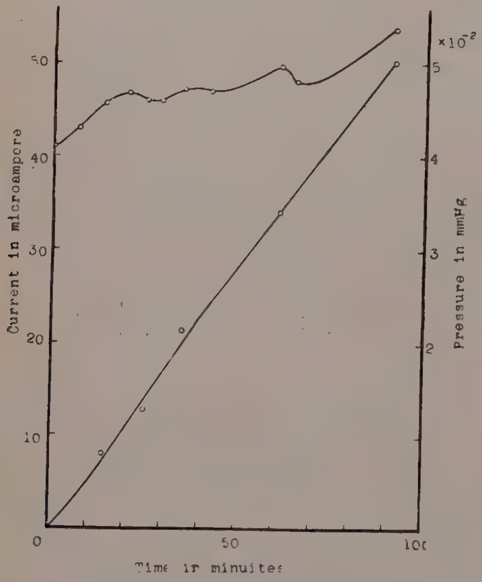

Fig. 4a. Current and Pressure data

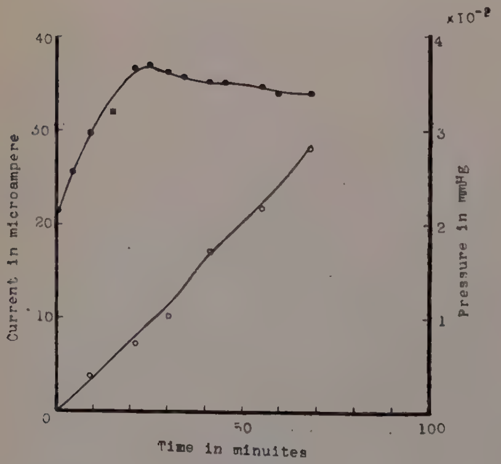

Fig. 4 b.

Typical examples of the measurements are shown in Fig. 4 and Tables I and II. It may be noticed, in spite of the apparent difference between the data in measurements I and II, that the relation between the charge carried by the current and the quantity of the gas evolved coincides perfectly in both cases as Fig. 5 shows. The mol number of the gas evolved when one coulomb of the charge is carried through alcohol is calculated from the above result and found to be 4.64×10^{-3} mol/coulomb. If all the charge is carried by protons which change perfectly into the gas, the corresponding figure should be 5.18×10^{-3} mol/coulomb, according to Faraday's law of electrolysis. Hence *the greater part* of the charge is considered to be conducted by protons.

Table I (measurement I)

Charge carried $Q\times10^3$ coulomb	Mol. number of hydrogen $n\times10^7$	$n/Q\times10^6$ mol/coul.
36.3	1.76	4.84
66.8	2.77	4.15
94.6	5.14	5.15
169.5	7.49	4.42
260.8	11.05	4.23
	Mean	4.61

Table II (measurement II)

Charge carried $Q\times10^3$ coulomb	Mol. number of hydrogen $n\times10^7$	$n/Q\times10^6$ mol/coul.
13.9	0.86	6.18
37.2	1.60	4.31
57.2	2.26	3.96
80.8	3.83	4.73
110.3	4.79	4.34
136.9	6.19	4.52
	Mean	4.67

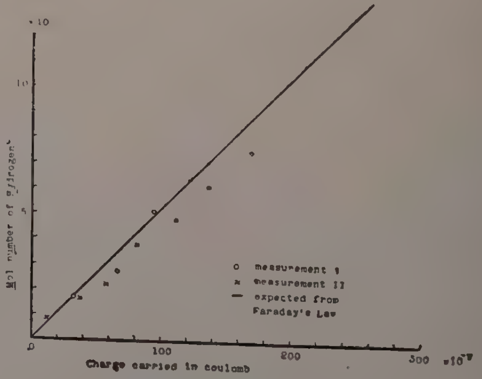

Fig. 5. Verification of Faraday's Law.

§4. The Experimental Procedure for the Conductivity Measurements.

As the direct proof of the mechanism of proton conduction would be very difficult, the following indirect method of investigation was adopted. Namely, the conductivity of cetyl alcohol and its mixtures with long chain normal paraffins, alcohols or acids of various carbon numbers was measured, and the effect was discussed in the light of the supposed mechanism of proton conduction.

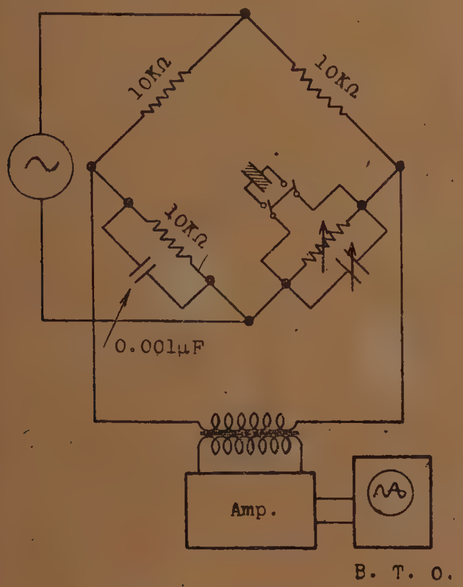

Fig. 6. Wien Bridge

In order to avoid as far as possible the effect of polarisation upon the conductivity, the measurement was conducted under the frequency of 560 cycles per second. Because the dielectric constant of the sample became also large, it was necessary to separate carefully the real and the imaginary parts of the dielectric constant. The Wien type bridge was used for this purpose, condensor put in parallel to the sample and its shunted resistance were both varied in order to balance the bridge (Fig. 6). The loss of the sample became so large at the temperature corresponding to the hexagonal phase (tan $\delta \approx 3.5$), tan δ of the fixed arm was also adjusted to a large value. The magnitude of the resistance put in parallel to the sample was properly adjusted according to the magnitude of the loss of the sample. The voltage output of the bridge was detected by a Braun tube oscilloscope through an amplifier. The sample was put into a condensor of variable electrode distance, equipped with a micrometer, micalex being used as an insulating material (Fig. 7). Only the result for the conductivity is interested here, and the data for the dielectric constant will be described in a separate paper to be published later.

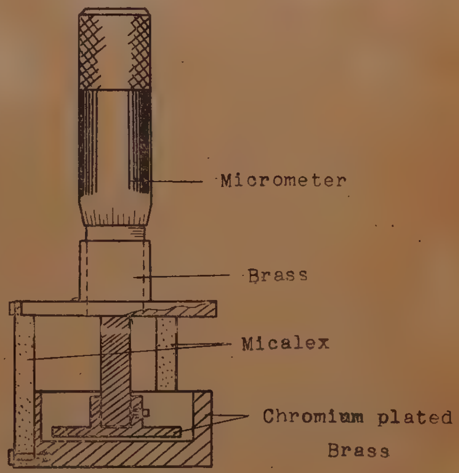

Fig. 7. Condenser for conductivity Measurement

§5. The Result of the Conductivity Measurement.

The conductivity of the pure cetyl alcohol is shown in Fig. 8, which shows a sharp peak at the solidifying point. The maximum value of the conductivity for the mixture of alcohol with paraffins, alcohols or acids in molar ratio of 2 : 1 are shown in Fig. 9. These results show that the normal long chain compounds whose carbon number is greater than that of the original alcohol, enormously decrease the conductivity.

As for the result for the substances, whose carbon number is equal to or less than that of cetyl alcohol, there was a marked difference between alcohols, paraffins and acids. The effect of the added alcohols was relatively small, and that of the paraffins next, that of the acids being most conspicuous. In no case, however, the conductivity increased by the addition of the substances above mentioned.

The above results seem to support the view that the conduction is carried about

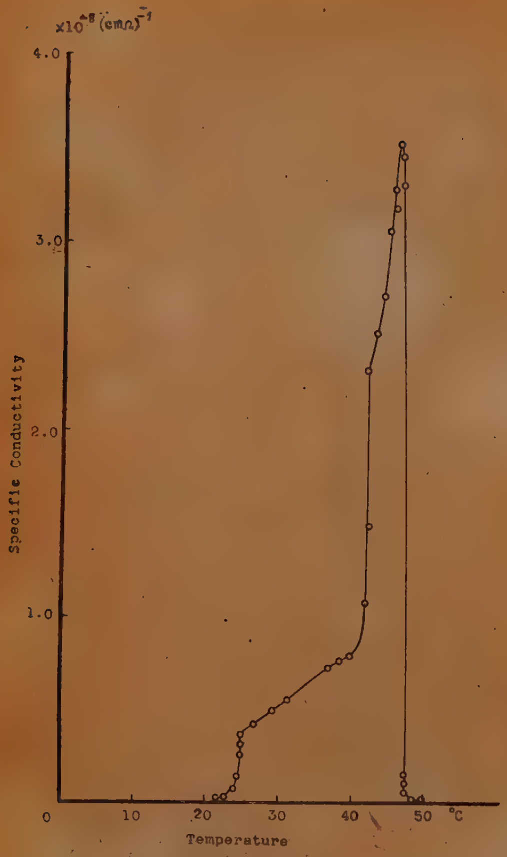

Fig. 8. Conductivity of cetyl alcohol

through the mechanism above postulated, namely the proton transfer from one molecule to the other, succeeded by the rotation of the molecule with an extra proton thus the proton being able to be transferred to the next molecule. Therefore, the conduction may be considered to be suppressed in two ways. Firstly, if the rotation of the molecule is suppressed in some way or other, the chain of the proton transfer process may be interrupted. Secondly, if certain alcohol molecules are replaced by the other kind of molecules, which can neither give nor accept protons, the chain would be again interrupted.

According to the experimental results obtained the compounds having longer chain length than cetyl alcohol are considered to suppress the rotation greatly, whereas those of equal or shorter chain length disturb the rotation in a lesser degree. This explains the fact that the conductivity is remarkably smaller in the sample mixed with the substances with longer carbon chains.

Next, we shall concern with the result for the mixtures added with molecules whose carbon number is equal to or less than cetyl alcohol molecule. In case of acids, the protruded oxygen atom attatched to the carbon

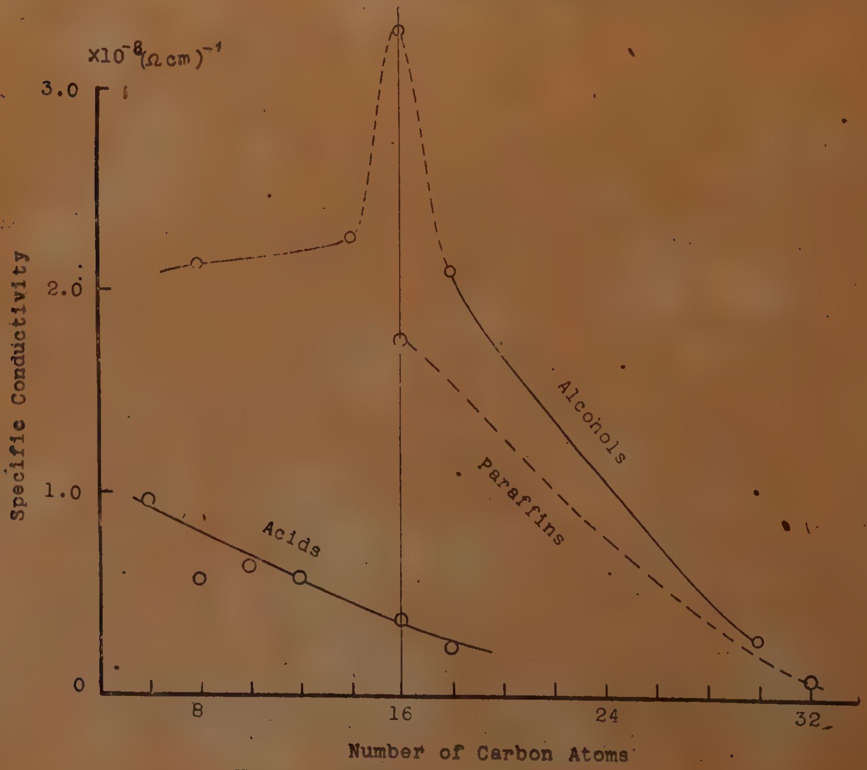

Fig. 9. Conductivity of the mixture.

atom through double bonds, and the tendency of forming a dimer whose long chains are not coaxial, may suppress the molecular rotation greatly. On the contrary, the paraffin suppresses the rotation little, and their molecules only do neither give nor take over protons to adjacent alcohol molecules. Therefore, the decrease of the conductivity is smaller compared with acids. In case of alcohol molecules, they almost supress neither the rotation nor proton transfer, the decrease of conductivity is far less conspicuous.

Above considerations may suggest that the *proton-transfer-and-molecular-rotation* mechanism is a plausible explanation for the observed anomalous conductivity.

§6. Hydrogen Bonds in Alcohol Crystals and the Mechanism of Proton Conduction.

No structure analysis has ever been attempted about the single crystal of alcohols. Wilson and Ott(14) have examined the long spacing of alcohols in some detail, and have concluded that c-spacing of the unit cell corresponds to the length of the two molecules, arrayed end to end, OH groups being closely situated. Because the short spacings of alcohols are nearly the same with that of the paraffins, the mode of packing of the chain in the crystal may also be considered to be similar to the case of paraffin crystal. Therefore, the projection of molecules on the c plane may be like that shown in Fig. 10, black circles showing the site to which each oxygen atom belong. As the infrared investigation by Davies(15) shows the definite existence of hydrogen bonding, the arrangement of the lower half of the unit cell relative to the upper, may be, for instance

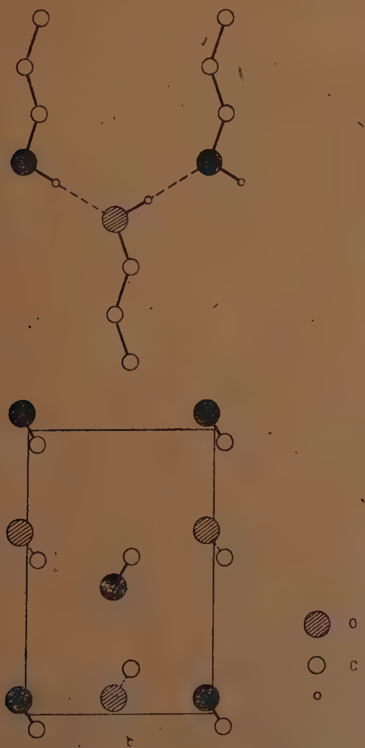

Fig. 10. Supposed Structure of Alcohols

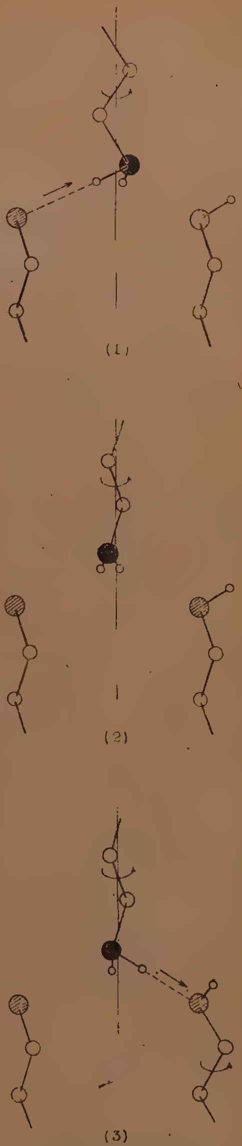

Fig. 11. Mechanism of Proton Transfer

something like that shown in Fig. 10, hydrogen bonds being expressed by the dotted lines in the figure. The formation of hydrogen bonds in the direction of the *a* axis seems to be difficult because of the larger distance between the oxygen atoms belonging to adjacent molecules. As the oxygen atom in alcohol molecule have a lone pair of *2p* electrons, it is considered to have the opportunity to form a positive ion of oxonium type, which has the similar bonding character to ammonia, namely three *p* bonds. The formation of oxonium type ion cannot be occurred, however, without the rotation of the molecule, because the OH bond to be newly formed as the result of the proton transfer must be nearly perpendicular to the plane containg C-O-H atoms of the alcohol molecule, whereas the direction of the existing hydrogen bond does not fulfill the condition (Fig. 11). Therefore, the rotation of molecules as a whole may be necessary to explain the transfer of protons through alcohol crystal. In the above discussions, however, the possibility for protons to travel through the crystal interstitially cannot be entirely ruled out, and further details concerning these points will be discussed in the following papers. Authors wish to express their sincere thanks to many of the members of the institute for their giving them samples and many valuable discussions. Their thanks are also due to the Ministry of Education for finantial aids.

References.

1) Baker and Smyth: J. Amer. Chem. Soc. **60** (1938) 1229
Higasi and Kubo: Sci. Pap. I.P.C.R. **36** (1939) 286
2) Bartoli: Beib. Ann. d. Phys **17** (1884) 712
Kakiuchi: Proc. Jap. Acad. **23** (1947) 65
3) Baker and Smyth: loc. cit.
4) Ott: Z. f. Phys. Chem. **193** (1944) 218
5) Sano and Kakiuchi: J. Phys. Soc. Jap. **4** (1949) 178
6) Kakiuchi, Sakurai and Suzuki: J. Phys. Soc. Jap. **5** (1950) 369
Kakiuchi: J. Phys. Soc. Jap. **6** (1951) 313
7) Kakiuchi: Proc. Jap. Acad. **23** (1947) 65
8) Sano and Kakiuchi: loc. cit.
9) Hoffman and Smyth: J. Amer. Chem. Soc. **71** (1949) 431
10) Hückel: Z. f. Elektrochem. **34** (1928) 546
11) Glasstone, Laidler and Eyring: *Theory of Rate Process* (1941) New York
12) Kakiuchi, Komatsu and Kyoya: J. Chem. Phys. **19** (1951) 132
13) Richardson and Tanaka: Proc. Roy. Soc. **106** (1924) 663
Kapuscinski and Eymers: Proc. Roy. Soc. **122** (1929) 58
14) Wilson and Ott: J. Chem. Phys. **2** (1934) 231
15) Davies: J. Chem. Phys. **8** (1940) 577

Note Added in Proof:—

The problem of the structure and the stability of the oxonium ion was one of the subjects of our continued interest in those years. Recently we have succeeded to prove its existence in hydrogen perchlorate monohydrate by the method of proton magnetic resonance absorption, whose results are to be published in August 1951 issue of *the Journal of Chemical Physics* and the comming issue of *the Journal of the Physical Sciety of Japan.* Once the problem is elucidated, the same will be true about ROH_2^+ ions above mentioned, the difference being apparent only in the second approximation.

JOURNAL OF THE PHYSICAL SOCIETY OF JAPAN, Vol. 6 No. 5, September—October, 1951

On the Phase Transition in Barium-Lead Titanate (II)

By Gen SHIRANE and Akitsu TAKEDA.

Tokyo Institute of Technology, Oh-okayama, Tokyo.

(Received November 29, 1950)

The dilatometric and specific heat measurements have been made on the whole range of solid solutions of (Pb-Ba) TiO_3 system. The linear thermal expansion coefficient in the tetragonal region decreases with increasing Pb content and it becomes even negative on the $PbTiO_3$ side, whereas the expansion coefficient in the cubic region is almost constant independent of the compositions. Anomaly of the specific heat also increases considerably towards $PbTiO_3$, just corresponding to the dilatometric data and to previously reported X-ray data.

§1. Thermal Expansion.

Measurement of linear thermal expansion has been made on the same ceramic specimen used previously for the dielectric and X-ray study. The relative dilatation between a specimen and a silica rod is magnified by an optical lever about 1000 times as large. We have used the specimen 3cm in length and 4mm in diameter, and have been able to detect a dilatation $\Delta l/l$ as small as 3×10^{-6}. Using this dilatometer, we have measured the dilatation of copper rod, at temperatures from 30° to 550°C, and obtained a satisfactory result in good agreement with the former measurements.

Some of the curves on heating are shown in Fig. 1. As expected, there are large anomalies at their transition points. For the convenience of comparison, we have shown $(l-l_0)/l_0$ as a function of temperature, where l_0 represents the length at 0°C.

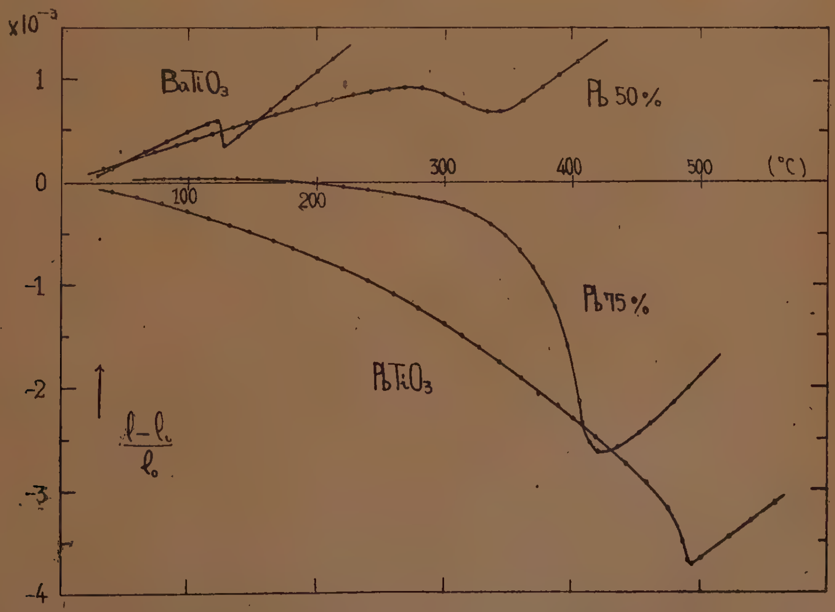

Fig. 1. Thermal expansion of (Ba-Pb) TiO_3.

With increasing content of $PbTiO_3$ the volume contraction at the Curie point becomes more and more increased. The linear thermal expansion coefficient β_t in the tetragonal region decreases with lead content. On the other hand, the coefficient β_c in the cubic region is almost constant independent of the composition, i.e. $8\sim10\times10^{-6}$/°C.

These values are shown in Fig. 2. Because of the non-linearity of the thermal expansion in the tetragonal region we were unable to estimate unambiguously the value of β_t of the specimens in the proximity of the $PbTiO_3$ end.

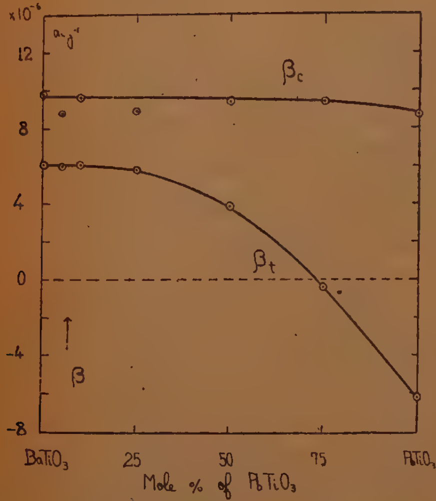

Fig. 2. Linear thermal expansion coefficients, β_t in the tetragonal region and β_c in the cubic region.

It must be emphasized that in the tetragonal region the volume of the solid solutions near the $PbTiO_3$ end does not increase but decreases from the first with increasing temperature. As already stated in the preceding paper,⁽²⁾ the thermal expansion of a ferroelectrics of $BaTiO_3$-type may be assumed as a result of superposition of a normal expansion and an abnormal contraction, the latter being caused by the decrease of spontaneous polarization. In these solid solutions, presumably the latter effect becomes more and more predominant with lead content, and at last it may happen that the latter masks entirely the effect of normal expansion, resulting in the rather curious volume contraction over a wide range of temperatures. This tendency is also in accordance with the large value of tetragonality of these substances.⁽¹⁾

In the specimens having large anomalous volume change in heating curve, there is a great hysteresis in cooling curve. For example, Fig. 3 shows one cycle of hysteresis curve for $PbTiO_3$ (a→b→c→d→e). In this case, heating and cooling rate is about 2°C/min. It seems curious that the length of the specimen increases after a cycle. This phenomenon may have an intimate relation with the following fact which we have frequently experienced during measurements. When these ceramics repeatedly pass through the transition temperature, they become more and more fragile and sometimes they are broken to pieces as if they effloresce. In these crystals, an extraordinary large change of lattice spacing at the transition point may cause such great strains in a ceramics as are intolerable. When the temperature is not raised through the Curie point, the hysteresis is very small. (e→f→e)

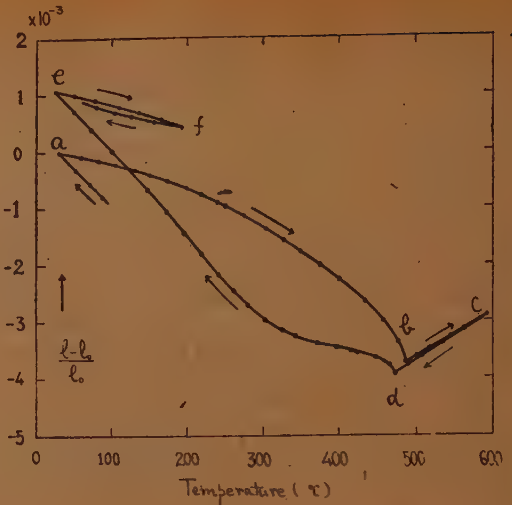

Fig. 3. Length of $PbTiO_3$ *vs.* temperature for both rising and falling temperatures.

In spite of the existence of great hysteresis, the heating curve is approximately

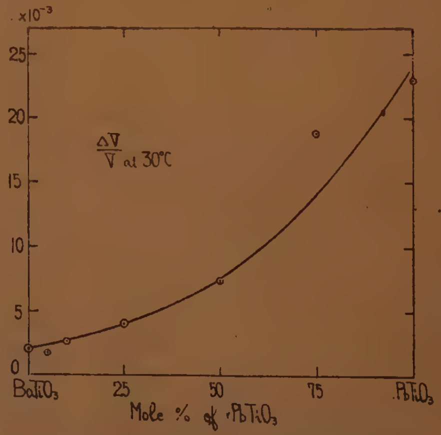

Fig. 4. Abnormal volume expansion at 30°C estimated by extrapolation from cubic region.

reproducible and may well represent the change of lattice volume, as shown experimentaly in the case of $PbTiO_3$.⁽²⁾

We have estimated the unstrained volume at 30°C by extrapolation from the cubic region and thus determined the abnormal volume expansion at 30°C (Fig. 4). As seen in this figure, the crystal strain due to the spontaneous polarization increases with lead content, just corresponding with the increase of tetragonality.

§2. Specific Heat.

Using an adiabatic calorimeter of Nagasaki-Takagi type⁽³⁾, the specific heat of these solid solutions has been measured. The powdered specimen of about 25g, contained in a glass vessel of 2.6g, was heated at a rate of 1°~2°C/min. The results are shown in Fig. 5.

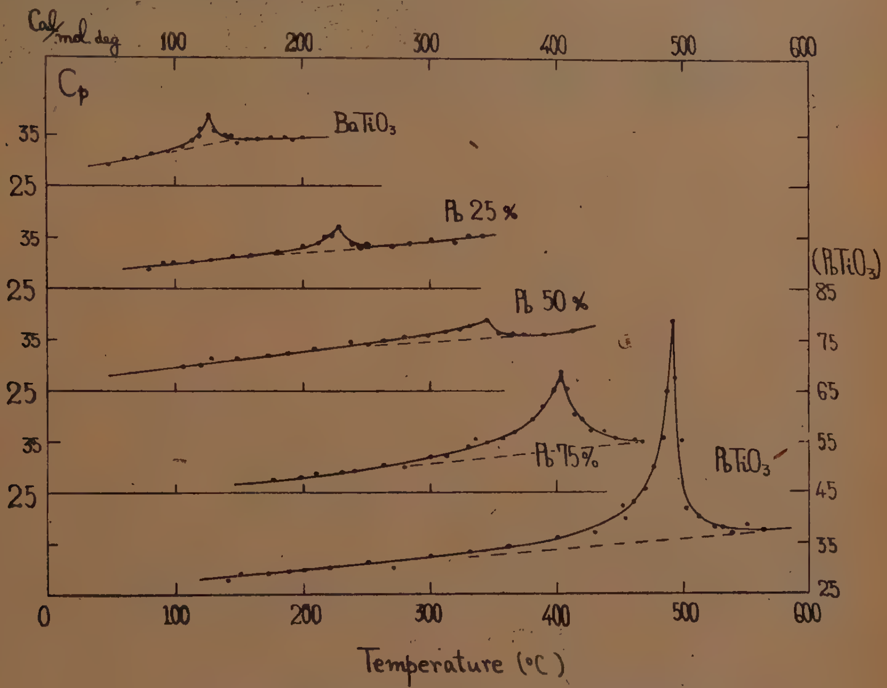

Fig. 5. Specific heat as a function of temperature.

As expected, the specific heat anomaly increases considerably with lead content, corresponding to the anomalies in the thermal expansion. Though it is difficult to estimate accurately the transition energy from these curves, we have tentatively assumed that the normal specific heat corresponds to the broken lines shown in the figure. Transition energies thus obtained are shown in Fig. 6. These values, of course, include some of the changes in polarilzation energy distributed over temperatures below the transition points. The result concerning $BaTiO_3$ is in agreement with the former publications⁽⁴⁾.

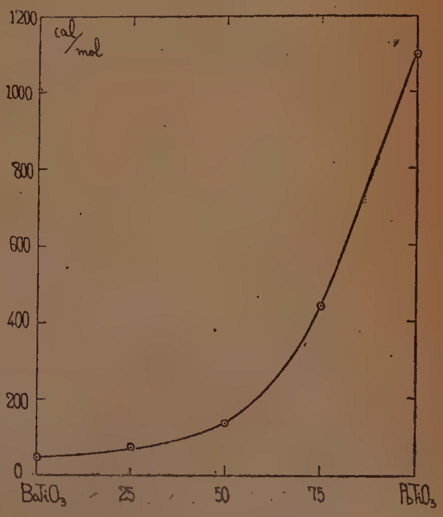

Fig. 6. Transition energy estimated from the specific heat curve.

§3. Spontaneous Polarization.

Using cathode-ray oscillogrammes we have obtained the hysteresis loops of $BaTiO_3$, (Ba95-Pb5) TiO_3 and (Ba90-Pb10) TiO_3 as shown in Eig. 7. These three specimens have the same shape, 1.5cm^2 in area and 0.5mm in thickness. Applied field is 50cycle/sec and the maximum field strength is 30kv/cm. As expected, the spontaneous polarization increases with lead content, but the increase of coercive field is more conspicuous.

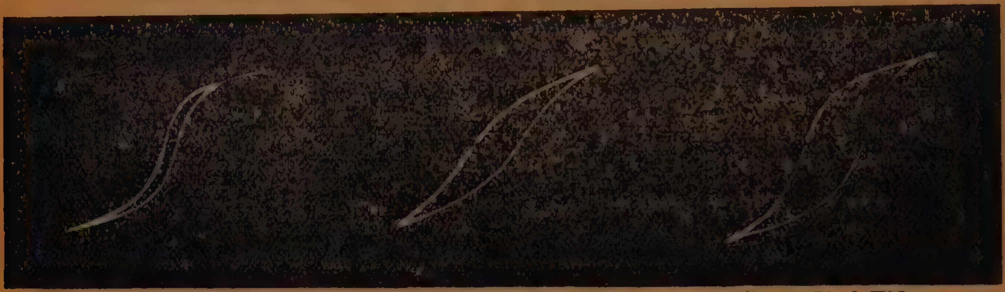

$BaTiO_3$ $(Ba_{95}—Pb_5)\ TiO_3$ $(Ba_{90}—Pb_{10})\ TiO_3$

Fig. 7. Hysteresis loops at 50cycle/sec and 30kv/cm (20°C).

It is difficult to estimate these quantities for all solid solutions since the greater is the lead content the more porous and poorly formable becomes the ceramics. Moreover, the estimation at room temperature may be very difficult even with well sintered ceramics because of a large coercive field.

Recently, it was reported by Nomura and Sawada⁽⁵⁾ that the spontaneous polarization of the single crystal of $PbTiO_3$ is very large, i.e. about 90~100 microcoulombs/cm^2. This result is in good accordance with our X-ray and thermal study.

In conclusion we wish to express our sincere thanks to Professor Y. Takagi for his kind guidance in the course of this research and also to Mr. M. Hirabayashi and Mr. E. Sawaguchi for their helpful advice on our work.

This research was helped by the research grant of the Ministry of Education.

References.

(1) G. Shirane and K. Suzuki: J. Phys. Soc. Japan **6** (1951) 274.

(2) G. Shirane and S. Hoshino: J. Phys. Soc. Japan **6** (1951) 265,

(3) S. Nagasaki and Y. Takagi: J. App. Phys. Japan **17** (1948) 104.

(4) M. G. Harwood, P. Popper and D. F. Rushman: Nature **160** (1947) 58.
H. Blattner, W. Känzig and W. Merz: Helv. Phys. Acta. **22** (1949) 35.
S. Sawada and G. Shirane: J. Phys. Soc. Japan **4** (1949) 52.

(5) S. Nomura and S. Sawada: Reported at the annual meeting of the Physical Society of Japan held at Osaka, on 1st November 1950.

JOURNAL OF THE PHYSICAL SOCIETY OF JAPAN, Vol. 6 No. 5 September—October, 1951

Phase Transition in Lead Zirconate.

By Etsuro SAWAGUCHI, Gen SHIRANE and Yutaka TAKAGI.

Tokyo Institute of Technology, Oh-okayama, Tokyo.

(Received February 28, 1951)

Detailed investigations on the dielectric and the thermal properties of $PbZrO_3$ have been made and compared with those of ferroelectric $BaTiO_3$. In contrast with barium titanate, volume change at the transition near 220°C has turned out to be expansion, being $\delta V/V = 2.7 \times 10^{-3}$, and a large amount of anomalous specific heat of *ca.* 400 cal./mole have been found. Spontaneous polarization estimated from the hysteresis loop, and the effects of D.C. bias upon the permittivity and especially the shift of the transition point all imply that a spontaneous polarization may not exist below the Curie point. Since the dielectric constant, nevertheless, becomes extraordinarily high at the Curie point, it must be reasonable to say that lead zirconate belongs to a new type of dielectrics, say, *antiferroelectrics.* When the sample contains some additional materials, *a narrow region of ferroelectric phase* has been observed between antiferroelectric and paraelectric ones. The temperature range of this phase is sensitively affected by the amount and the species of the additional materials.

§1. Introduction.

In summer 1949, Waku and Hori⁽¹⁾ found from permittivity measurement that the behaviour of lead zirconate with a transition at about 220°C is very similar to that of well known barium titanate. Recently, Roberts⁽²⁾ has also reported a close resemblance of dielectric properties of $PbZrO_3$ and some solid solutions of $PbZrO_3$ and $BaZrO_3$ to the properties of barium titanate, and has suggested that lead zirconate should be a ferroelectric below its Curie point 236°C.

Roughly speaking, the crystal structure of lead zirconate is also similar to that of barium titanate, namely it is cubic perovskite type at above the Curie temperature while it becomes slightly tetragonal below the transition point. However the tetragonality occurs, so to speak, in the opposite sense as compared with the case of barium titanate, that is $c/a = 0.988$ in lead zirconate⁽²⁾⁽³⁾ while $c/a = 1.010$ in barium titanate.⁽⁴⁾⁽⁵⁾ Besides, the existence of a certain type of superstructure with a period of three times as large as a has been reported by Hoffmann.⁽⁶⁾ Now our detailed investigations on the properties of this material add many contradistinctions and consequently lead us to a conclusion that, contrary to barium titanate, lead zirconate may belong to an anti-ferroelectric below its transition temperature.

§2. Preparation of Samples.

Our samples were synthesized to a ceramic form from PbO or refined $PbCO_3$ and ZrO_2. The equi-molar part of both ingredients were fully mingled and formed in the disks about 3 cm in diameter and of optional thickness, then were preliminarily calcined in an electric furnace at a temperature about 1200°C. To obtain fine ceramics a so called refiring process was adopted. The refiring temperature was selected at about 1300°C and the duration of the maximum temperature was about an hour.

The ceramics thus obtained are relatively hard, yellowish brown in colour. By spectroscopic analysis, a little amount of impurities such as Si and Fe were detected in ZrO_2 chemicals as well as ceramic $PbZrO_3$, but quantitative estimation have not been obtained yet.

§3. Results of Measurements.

1) Thermal Expansion.

The thermal expansion has been measured by a simple dilatometer consisting of several silica tubes and an optical lever. The sample of a ceramic pillaret 3cm in length was used. With this instrument the accuracy of our measurement attains to about 3×10^{-6}. Fig. 1 shows $(l-l_0)/l_0$ as a function of temperature, where l_0 represents the length at 0°C. The heating rate was about 1°C/min. As clearly shown in the figure there is an anomalous volume expansion at the transitional region.

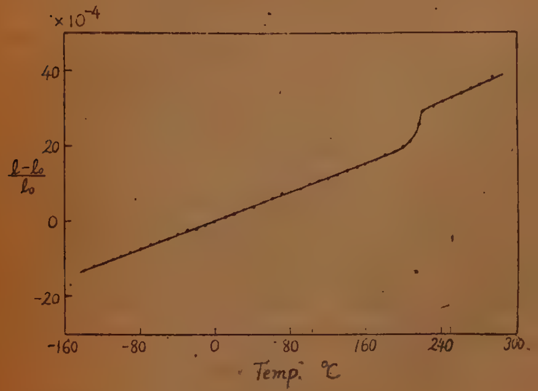

Fig. 1. Dilatation *vs.* temperature curve.

The volume change $\delta V/V$ during the transition is about 2.7×10^{-3}, namely 0.20Å^3 per unit cell, provided that the lattice constant $a=4.15$Å. In respect to not only the sign but also the magnitude, this large volume expansion at the transition is very contradistinct as compared with a small volume contraction observed with barium titanate⁽⁷⁾ at 120°C.

The linear thermal expansion coefficients are almost the same in both phases below and above the Curie point, they are 8.4×10^{-6}/°C.

2) Dielectric Constant.

Dielectric constant for 1 MC/sec and 2 volt/cm was measured at temperatures from -160° to 300°C with a heterodyne method or at times with a resonance method. The specimens for this measurement were cut out from ceramics into slabs of about 1cm^2 in area and 3 mm in thickness. The electrodes were made of gold foil evaporated on to their faces. To avoid an error due to humidity the specimens were kept in a vacuum flask and the temperature was measured by a copper-constantan thermocouple set beside the specimen. Fig. 2 shows the result for heating and cooling with a rate of about ±1°C/min.

On heating, we have found only one transition near 224°C in contrast to the three transitions known in barium titanate. Below this transition point the permittivity is scarcely dependent on temperature, being always nearly 80. A sudden change occurs at the transition with a steep increase of permittivity to more than 20 times as large as its value at room temperature, and then decreases monotonously on further heating.

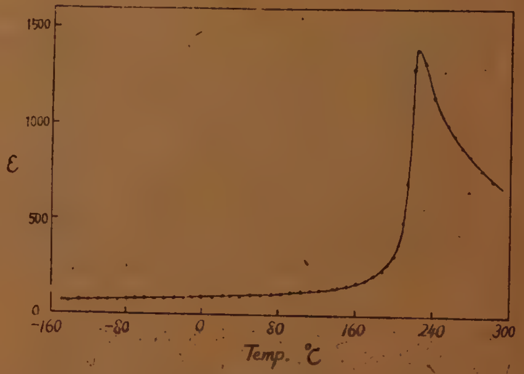

Fig. 2. Dielectric constant as function of temperature.

(a) rising temperature.

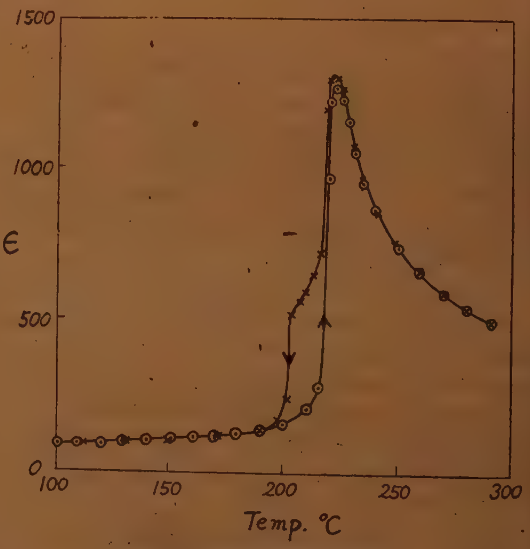

(b) falling temperature.

At above the Curie point we have confirmed that the permittivity can be well represented by a Curie-Weiss law $\varepsilon=C/(T-T_p)$, putting the Curie constant $C=1\times10^5$°C and the paraelectric Curie temperature $T_p=200$°C. Though this Curie constant shall be regarded as an outlooked value for we could not correct the value taking into account the porosity of the sample, yet it may be sure at least that the order of magnitude is nearly the same as that of barium titanate, namely 1.4×10^5°C.

On cooling, the maximum permittivity ppears at 223°C succeeded by an abrupt rop, but, nevertheless, it does not fall through he step to the initial low value but stays at certain intermediate value. On further ooling the second change takes place at 03°C accompanied by a sudden decrease of rmittivity and the plots now rejoin exactly the initial curve.

Hysteresis Loops and Dielectric Polarization.

To investigate the nature of new transi- on at 203°C, hysteresis loops have been bserved on a cathode ray tube with a method milar to Sawyer and Tower(8). A sample, bout 1cm^2 in area and 1 mm in thickness, nmersed in liquid paraffin, was heated by an ectric furnace. Lest the electric loss should ise the temperature of the specimen, the ectric field was applied each time only for short period, namely for about a half second. The curves thus obtained at various temperatures are shown in Fig. 3. The applied electric field was about 17 KV/cm (maximum amplitude), and 50 cycles per second.

Hysteresis character was scarcely perceived at temperatures below 200°C, but as the temperature approaches the Curie point, it begins to be clearly perceived. And above the Curie temperature it disappears again, though the loop does no more recover a simple straight line but takes a form of ellipse, presumably on account of increased conductivity at high temperatures. On cooling, on the other hand, legible hysteresis loop has been observed over a broad range from 223° to 203°C in contrast to the heating case. Just corresponding to the sudden change on permittivity at 203°C, the hysteresis character suddenly fades out and loop deforms to almost the horizontal line at this very point.

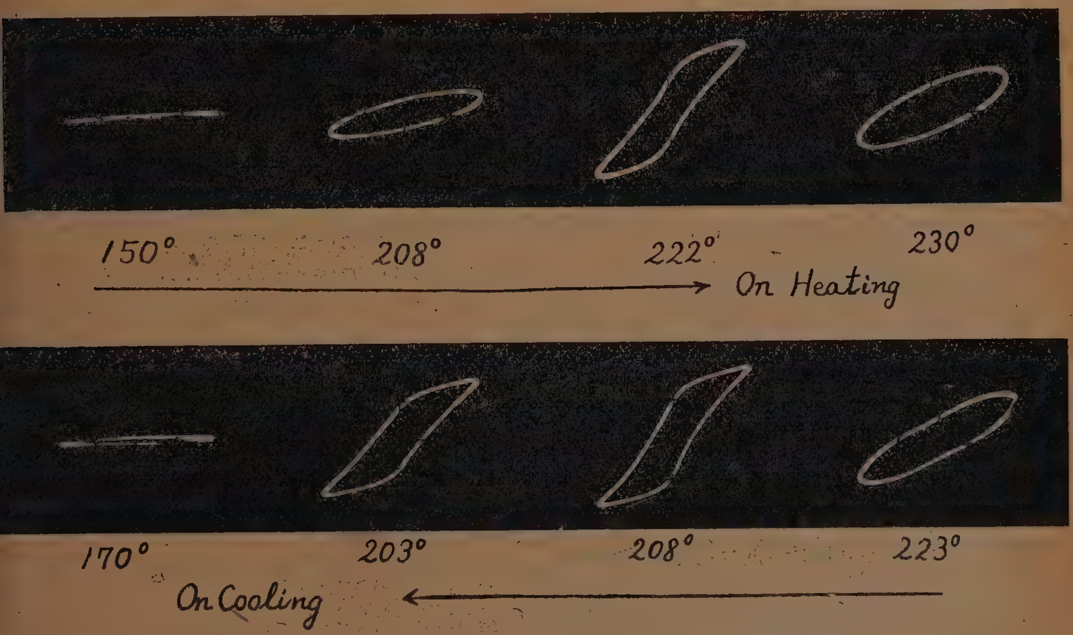

Fig. 3. Hysteresis loops at both rising and falling temperatures.

The estimation of the spontaneous polari- tion is very desirable. But, since the ramic lead zirconate was far from saturated nder our experimental conditions, we had plot the maximum polarization obtained the field strength of 17 KV/cm in Fig. 4. ver the temperature range below 200°C the larization hardly shows an appreciable lue, as the temperature rises it increases gradually until at last the maximum value is obtained just at the Curie point, thereafter it drops very rapidly. Gradual rise of polarization at far above the Curie point may be understood as an effect due to increase of conductivity, while in the case of cooling, the polarization maintains its large value over the broad temperature range from 223° till 203°C and then it drops suddenly to the initial value.

Considering from the hysteresis loops and the maximum polarizations, the state existing on cooling between 223° and 203°C is certainly a ferroelectric one, whereas below 203°C, it must be either that the state, though ferroelectric, becomes to be accompanied by an enormously large coercive force, or that it changes into another phase of small or no spontaneous polarization at all. But from above experiments alone, it is very hard to discriminate between these alternatives. So we have carried out the following experiments to answer this question.

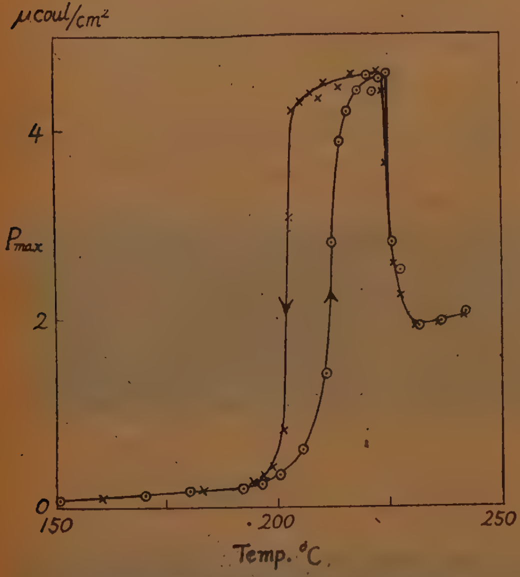

Fig. 4. Temperature dependence of maxmum polarization P_{max} for the field strength of 17 KV/cm. The P_{max} scale is rather approximate.

4) Specific Heat.

To clarify this newly found phenomena covering the range from 203° to 224°C the specific heat measurement may be one of the most powerful means. We have at first measured the specific heat on heating using the adiabatic calorimeter of Nagasaki-Takagi type.(9) Powdered lead zirconate of about 45g was heated in vacuum in a thin glass vessel at a rate of about 0.5°-1°C/min. One of the results is shown in Fig. 5. As might be expected, there is a prominent peak of anomalous heat around the Curie point. The transition energy is about 400cal./mole and the entropy change calculated from the heat absorbed is found to be about 0.40

This transition energy is very large compar with that of barium titanate, the latter bei about 40cal./mole.(7)(10) Perhaps the mo part of the transition energy may come fro the latent heat, for from the sudden chan observed in the permittivity etc. the transiti seems to be of the first order.

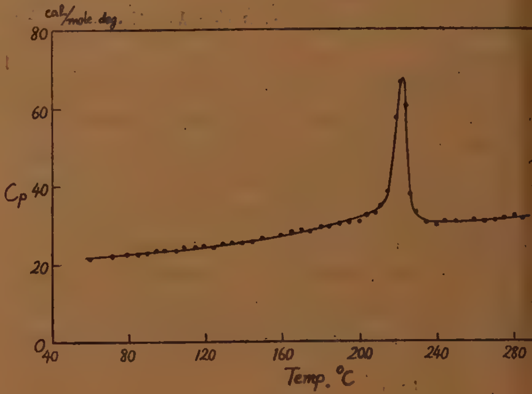

Fig. 5. Specific heat curve at rising temperature.

For the measurement on cooling we ha made use of the same apparatus, though t measuring process is now different in pri ciples and not at all adiabatic. Since it very difficult to take out with a given rate known amount of energy away from t specimen, we have adopted a method simil to conduction calorimetry.(11) At first t sample was heated in vacuum to above 280 and then it was left cooling owing to t energy loss due to heat radiation. Meanwhi by making use of an electric furnace s outside the calorimeter, we have adjusted t temperature of the outer concentric cylind

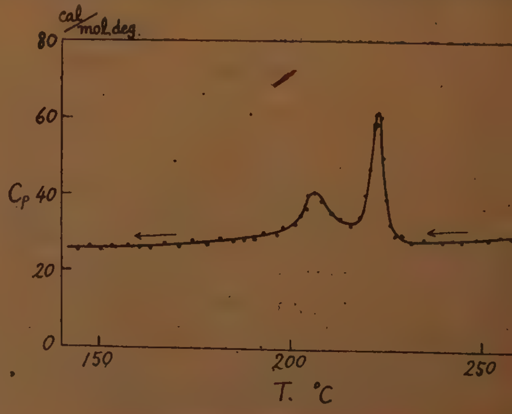

Fig. 6. Specific heat on cooling.

f copper, in which the glass vessel is ontained, in such a way as it is always kept wer than that of the specimen by 9°C as ccurately as possible. Thus obtaining a oling rate *vs.* temerature curve, and, comaring this with the data obtained on heating ig. 5), we can estimate the specific heat on oling (Fig. 6).

Just corresponding to the two changes on oling curves of the dielectric polarization ig. 4) and of permittivity (Fig. 2), there are fact two peaks of anomalous specific heat. he amounts of two transition energies turn ut to be nearly the same, each being 200 al./mole. Hence it seems that the transition t 203°C cannot in any way be interpreted as mere consequence of coercive field. It must e a true phase change accompanied by a net ecrease of intrinsic polarization itself.

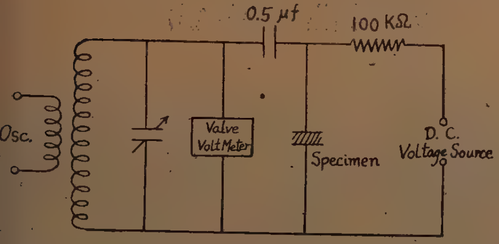

Fig. 7. The circuit for permittivity measurement under D.C. bias.

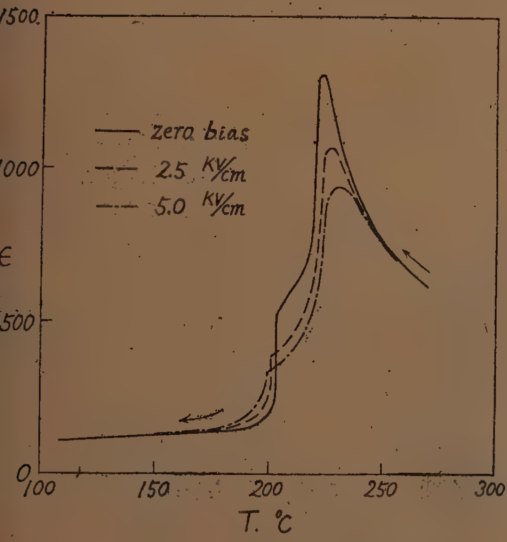

ig. 8. Dielectric constants measured on cooling at 1MC/sec, and under D.C. bias, the field strength being 2500volt/cm, 5000volt/cm and zero respectively.

5) The Influences of D. C. Bias upon the Permittivity and the Transition Point.

Another support for the transition at 203°C can also be provided by a study of the effect of D.C. bias upon the permittivity (Fig. 8). As clearly seen in the figure, at above 200°C the permittivity decreases considerably when the field was applied while at below 200°C the bias made the permittivity slightly increase, and this tendency was just contrary compared with the case of barium titanate. Moreover, it turns out to be true that the upper Curie point shifts to the higher temperature side with a rate of about 0.0009°C/bias-volt with increasing bias, while the lower transition point moves downward with a rate of about 0.0007°C/bias-volt. Hence the D.C. bias does surely stabilize the corresponding ferroelectric state between the two transitions.

Because of the abruptness of the transitions observed in all measurements, both change seem to be the first order transitions, and the Clausius-Clapeyron equation $-dTc/dE = Tc \cdot \delta P/L$ may be available at these points, where Tc denotes the transition temperature, E the strength of the biasing field, and L the latent heat. Upon inserting the observed values into the equation, we obtain $\delta P = 29$ microcoul/cm^2 and $\delta P = -35$ microcoul/cm^2 for the transitions at 203°C and 223°C respectively. Though these values are only approximate, for the precise values of L and dTc/dE are both very difficult to determine, yet it may be said at least that our conclusion that the spontaneous polarization in the temperature range below 203°C must either be very small or be entirely vanishing is powerfully supported by this reasoning.

§4. Discussion.

So far we have given several reasons for believing the following diagram:

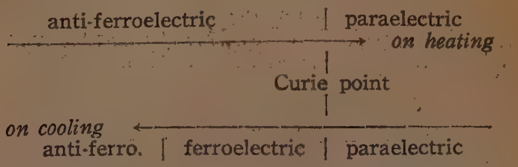

The appearance of three succesive states, i.e. para-, ferro- and anti-ferroelectric, shall be noted.

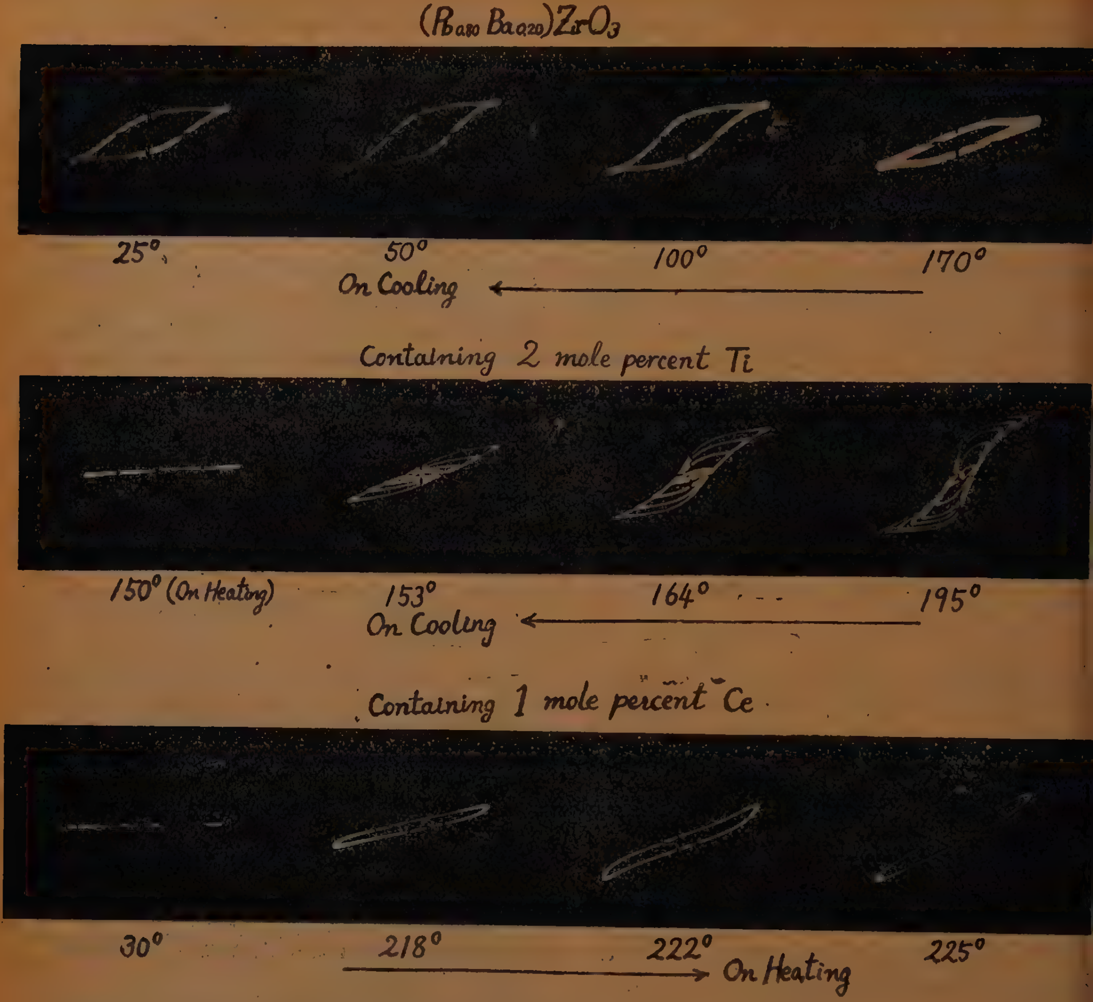

Fig. 9. Hysteresis loops at various temperatures,
a) $(Pb_{0.80}\ Ba_{0.20})\ ZrO_3$ (maximum amplitude 40 KV/cm)
b) lead zirconate containing 2 mole percent Ti instead of Zr (maximum amplitude 5~25 KV/cm)
c) lead zirconate containing 1 mole percent Ce instead of Zr (maximum amplitude 25 KV/cm).

During observation of hysteresis loops we have noticed that the ferroelectric region can sensitively be affected by a little adulterates. In Fig. 9, the hysteresis loops of lead zirconate containing a little Ba or Ti or Ce are reproduced. $(Pb_{0.80}\ Ba_{0.20})ZrO_3$ shows a clear hysteresis loop and the form is very similar to that of barium titanate. It is surely ferroelectric below the Curie point *ca.* 150°C, and is corresponding to the results of piezoelectric measurements by Roberts.(2) The lead zirconate which contains 2 mole percent of Ti instead of that part of Zr showshy steresis on heating over the temperature range from *ca.* 170° to 225°C, while on cooling from 225° to 150°C. On the lower transition point a remarkable temperature hysteresis was perceived. On the other hand, if Ce was contained in lead zirconate, even in concentration as little as 1 mole percent, the hysteresis characteristic was never discerned clearly at any temperature, and ferroelectric region was eliminated. But a characteristic form was perceived at the very vicinity of the transition point 224°C, only if a very intense field of *ca.* 25 KV/cm was applied. Thus we have seen how substantially the characteristic of dielectrics might be changed by a slight amount of impurities.

Using a pure lead zirconate, Roberts⁽²⁾ has measured the dielectric constant as function of rising and falling temperatures, and has found the Curie point at 236°C on heating and 232°C on cooling, but there has been no anomaly corresponding to our lower transition point at 203°C. We can guess therefore that the appearance of ferroelectric state in our lead zirconate may be caused chiefly because of some impurities in our sample. Perhaps in a pure lead zirconate even the narrowest region of ferroelectric state should never happen to occur. The circumstance thus surmised for pure specimens is

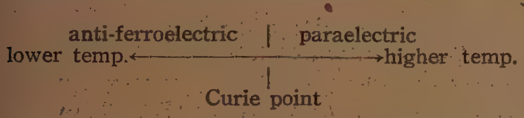

It seems to us very interesting that a ferroelectric as well as an antiferroelectric state be realized in one and the same material at different temperature range, and that the region of their respective stability be sensitively affected by the impurities. The possibility for such circumstances, though not strictly applicable but logically similar, has recently been discussed by one of us. Takagi⁽¹²⁾ has investigated the rotational phase transition in body centered cubic lattice with identical and rotatable point dipoles on every lattice corner site and highly polarizable but non-polar ions on every body center site, and has shown that the free energies for both phases, ferroelectric and antiferroelectric ones, are nearly the same at the same temperature. And if the polarizability of body center ions is to be increasing with temperature, such a phase transition from an antiferroelectric state to a ferroelectric one then finally to a paraelectric one is indeed theoretically possible.

For a rigorous discussion about the properties of lead zirconate, the other knowledge such as that about the detailed crystal structure should of course be taken into account. We are now in the course of investigation on X-ray patterns, on various dielectric properties of purified lead zirconate and on the properties of the solid solutions of $PbZrO_3$ and $PbTiO_3$.

The authors are indebted to Mr. J. Hori for stimulating their interest in this material, to Dr. S. Roberts for valuable exchange of informations and to Mr. A. Takeda for assistance with the permittivity measurements. We are also grateful to Mr. T. Hukazawa for favouring of the chemical analysis, and to Messrs. T. Kuroda and T. Yamamoto for the gift of ZrO_2 chemicals. We are indebted to the Ministry of Education for the research grant.

References.

(1) S. Waku and J. Hori, private communication (summer, 1949)
(2) S. Roberts, J. Am. Ceram. Soc. **33** (1950) 63.
(3) H. D. Megaw, Proc. Phys. Soc. London, **58** (1946) 133.
(4) S. Miyake and R. Ueda, J. Phys. Soc. Japan **2** (1947) 93.
(5) H. D. Megaw, Proc. Roy. Soc. London, **189** (1947) 261.
(6) A. Hoffmann, Z. Phys. Chem. B**28** (1935) 65.
(7) S. Sawada and G. Shirane, J. Phys. Soc. Japan, **4** (1949) 52.
(8) C. B. Sawyer and C. H. Tower, Phys. Rev. **35** (1930) 269.
(9) S. Nagasaki and Y. Takagi, J. App. Phys. Japan, **17** (1948) 104.
(10) M. G. Harwood, P. Popper and D. F. Rushman, Nature **160** (1947) 58.
(11) W. Bantle and P. Sherrer, Helv. Phys. Acta, **13** (1940) 214.
(12) Y. Takagi, Presented at the Meeting of the Phys. Soc. Japan held at Osaka Univ., on Nov. 4, 1950.

JOURNAL OF THE PHYSICAL SOCIETY OF JAPAN, Vol. 6 No. 5 September—October, 1951

On the Phase Transition in Barium-Lead Titanate.

By Kazuo SUZUKI.

Tokyo Institute of Technology, Oh-okayama, Tokyo.

(Received March 3, 1951)

The temperature change in lattice parameters of solid solutions of barium titanate containing 10, 12, 20 and 25 mole per cent of lead titanate have been studied mainly by the X-ray method for the range from −130°C to 300°C. It was found that the lattice parameter-temperature curves for the solid solutions of 12 and 20 per cent lead titanate have characteristic features as follows:

(1) a-parameter-temperature curves show a considerable linearity from lower temperatures up to the Curie point.

(2) A large amount of discontinuity of a– and c–parameters takes place at the Curie point.

(3) The superposition of cubic lines upon tetragonal lines is observed in a temperature range near the Curie point. The lattice volume calculated from tetragonal phase shows an abnormal contraction.

These results are not explained by the Devonshire's theory in its original form, but they can be explained fairly well by using higher order approximation.

§1. Introduction.

There have been performed very numerous studies on pure barium titanate concerning its physical properties as well as its crystal structure. Recently it has been found that lead titanate and barium-lead titanate also possess a ferroelectricity similar to barium titanate.⁽¹⁾ According to studies of Shirane and the present author,⁽²⁾ barium-lead titanate ceramics show a temperature change of lattice parameters which is similar to that of barium titnate in general but with larger values of the axial ratio c/a and a remarkable rise of the Curie temperature with increasing lead content.

It was, however, found that the lattice parameter-temperature curve for these solid solutions, especially near barium titanate side, have characteristic features which are alike neither to pure barium titanate nor pure lead titanate. The present author, therefore, intended to make an X-ray study specifically on barium-lead titanate containing relatively small lead content, and tried some theoretical considerations on the results experimentally obtained.

§2. Experimental procedure.

Specimens are ceramics forming solid solutions of barium and lead titanates containing 10, 12, 20 and 25 mole per cent of lead titanate which were prepared by sintering the mixtures of appropriate ratios of $BaCO_3$, PbO and TiO_2 at about 1200°C. For the purpose of X-ray measurements these were ground to plates with the thickness of about 0.4 mm and the area about 4×6 mm. The thinness of the plates was necessary in order to establish uniform temperature distribution and to obtain correct values of temperature of samples.

For high temperature X-ray camera an electric furnace was specially designed which is of so small heat capacity that the desired temperature can be reached in a very short time. As to the attainment of low temperatures, we have used a low temperature micro-thermostat of the type as described by Ubbelohde and Woodward.⁽³⁾ The sample is placed in a chamber which is drilled in a copper rod, the latter being attached at the bottom of a vessel filled with a cooling medium (dry ice, liquid oxygen, etc.). The lowest temperature attained by this apparatus was −130°C. The temperature control was performed mainly by heating current in a small coil wound around the chamber. Temperature was measured by copper-constantan thermocouple (0.25 mm in diameter), calibrated at several points, the junction being set on the back of the sample. The relative accuracy was within ±0.1°.

The Debye photographs were taken by

a back reflection camera using Cu Kα radiation. The distance from sample to film was determined by Au (511) line and was about 45 mm. The lattice constants of respective samples were determined from {510}, {431} lines. The Curie points of the samples were determined by dielectric measurements as well as by the Debye photographs taken by the temperature camera. For the purpose of comparison an X-ray measurement was made also on pure barium titanate.

§ 3. Experimental Results.

High temperature range. The X-ray photographs revealed the fact that all the solid solutions examined have tetragonal structures from room temperature up to the Curie point, and cubic structures of perovskite typea bove the Curie point. In Fig. 1 we show the temperature change in lattice parameters and in Fig. 2 the temperature change in axial ratio c/a. In the latter figure, abscissa is the temperature expressed in degrees absolute divided by the Curie point (Tc) of each specimen. The solid solution of 10% lead titanate shows a lattice parameter-temperature curve which is similar to that of pure barium titanate, but, when the lead content was increased to 12%, the following three new features begin to appear:

(1) A considerable linearity of a-parameter-temperature curve was noted from room temperature up to the Curie point, a characteristic which is in contrast with the curve for pure barium titanate.

(2) A large amount of discontinuiy of a-and c-parameters takes place at Curie point.

(3) The superposition of cubic lines upon tetragonal lines is observed in a temperature range near the Curie point, which shows the possibility of a coexistence of two phases. As the temperature is raised to about 10° below the Curie point the cubic lines begin to appear superposing on the tetragonal lines, and the nearer as approach to the Curie point, the stronger become the cubic lines, and the tetragonal lines become weak, reducing the tetragonality.

Those characteristics remain by the solid solution of 20% lead titanate. For sample added with the lead titanate more than 25% and also for pure lead titanate, however, the a-parameter-temperature curve is like that of pure barium titanate, i.e., the linearity in the range from room temperature up to the Curie point disappears.

Fig. 3 shows the lattice volume-temperature curves calculated from the curves of Fig. 1. The volume expansion coefficients of solid solutions are approximately equal to that of pure barium titanate, namely 2.0×10^{-5} deg.$^{-1}$ in the tetragonal region and 3.8×10^{-5} deg.$^{-1}$ above the Curie point. As was stated previously, there coexist two phases near the Curie point by 12 and 20% lead titanate. The lattice volumes calculated from tetrag-

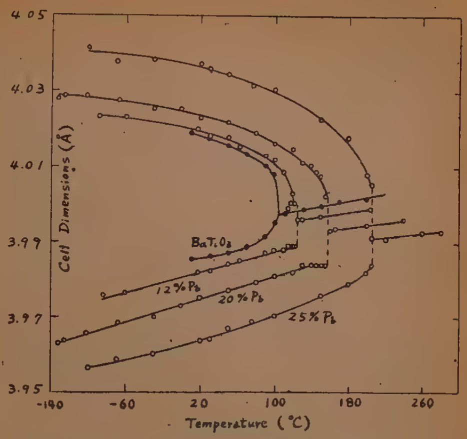

Fig. 1. Lattice parameters as a function of temperature.
The upper branch being c, the lower branch a, of tetragonal phase.

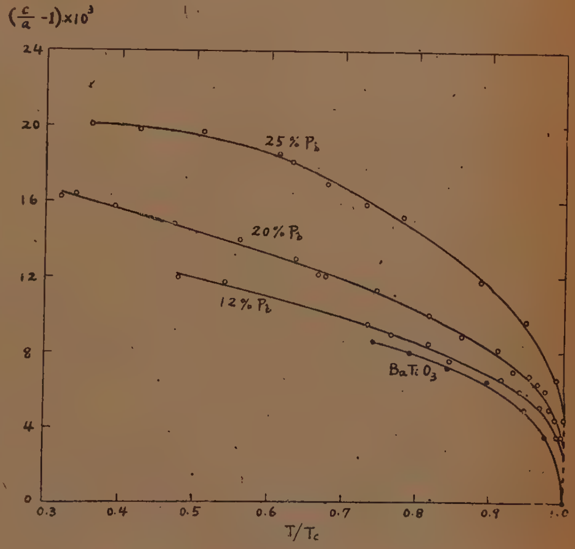

Fig. 2. Axial ratio as a function of temperature.

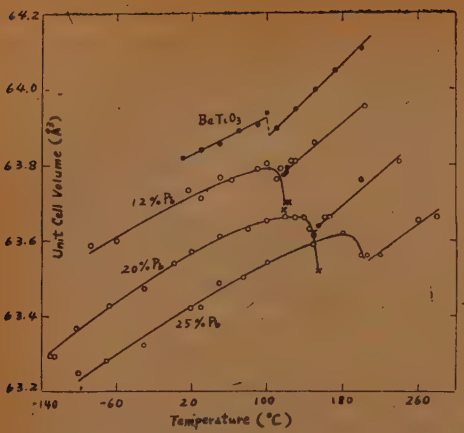

Fig. 3. Lattice volume as a function of temperature.

onal lines become smaller than the values extrapolated from the curve of cubic region, which are indicated by cross (×) in Fig. 3, while those calculated from cubic lines are on the line extrapolated from cubic region, which are indicated by solid circles (•). The total volume change should correspond to a sum of the values for cubic and tetragonal structures with appropriate weights at respective temperatures, and the resultant may not show such abnormal contraction as the case of the tetragonal lattice only, but only a normal contraction as already observed by Nomura and Sawada(4) by dilatometer measurement.

Low temperature range. As to the lower temperature range it was revealed from X-ray photographs taken by the low temperature camera that the transition point from tetragonal to orthorhombic phase at about 0°C for pure barium titanate was depressed rapidly when increased lead content, and by 20% lead titanate it becomes below -130°C, being out of our measured temperature range. This effect was also ascertained by the dielectric measurements made by Shirane *et al.*(5) The change of X-ray pattern for 12% lead titanate having Curie point at about -90°C takes place as follows: as the temperature is lowered the separation of {510} {431} lines become larger, indicating large tetragonality, wherein the linearity of the temperature change of *a*-parameter is maintained. But when the temperature attains below the lower transition point, these lines become severely diffused. This diffuseness have already been observed on pur barium titanate by many investigators(6) an have been attributed to the distribution c internal stresses owing to complex domain which develop when the crystal transform from tetragonal to orthorhombic structure This explanation will be applied in our cas of the solid solutions also.

§4. Discussion.

Devonshire(7) has developed a genera phenomenological theory and succeeded i obtaining general relation among dielectri and elastic properties as well as lattic change of barium titanate by assuming a expression of free energy containing up t the fourth power of polarization. But it wa found that the present result, described i above paragraphs, can not thoroughly b explained by his theory in its original form in many respects. For instance, the temperature change in lattice parameters of th solid solutions of 12 and 20% lead titanat have, as is stated above, characteristics no alike to that of pure barium titanate. Namely, the *a*-parameter changes with temperature almost linearly in the tetragonal range and moreover the volume of the tetragona lattice shows an abnormal contraction nea the tetragonal-cubic transition point, i.e., contracts even below the extrapolated volume of the cubic region, the facts being in contradiction to the theory.

In order to make these discrepancie more clearly the quantity $c-a_0/a-a_0$ (which is, in Devonshire's expression, equal to z_z/x_x was calculated from the curves shown in Fig 1, whereby a_0 is corresponding to the extra polation of the cubic lattice constant above Curie point. In Fig. 4 this quantity is plotte as the function of temperature. Abscissa i the absolute temperature divided by th Curie point (Tc) of each specimen.

From the form of the free energy use by Devonshire(7) it is concluded that $|z_z/x_x|$ i a constant independent of temperature, being determined by the material constants. It i however seen from the figure that this doe not hold strictly for all specimen. By pure barium titanate $|z_z/x_x|$ value decrease gradually at first as the temperature is raise from room temperature. At about 80°C i begins to increase, the rate of increase being

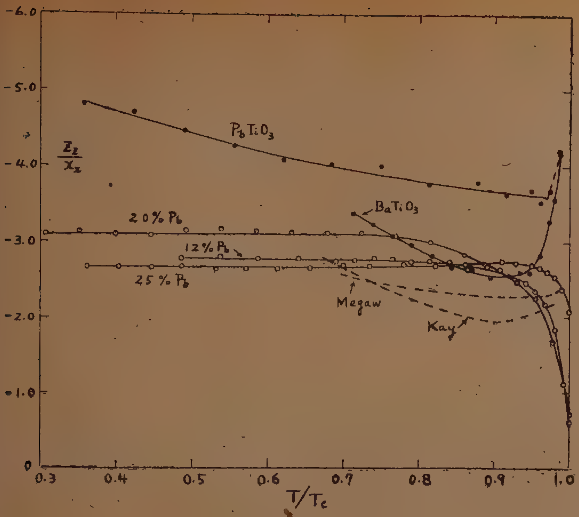

Fig. 4. z_z/x_x as a function of temperature.

very steep near the Curie point. In the figure we have shown also the values calculated from the data by Kay⁽⁶⁾ and by Megaw⁽⁸⁾ which are in accordance with our results in their general trend. By pure lead titanate the tendency of decreasing is maintained until very near the Curie point. On the other hand, by the solid solutions $|z_z/x_x|$ values are constant over large temperature range from lower transition point, and they decrease continuously near the upper transition point in contrast with the increase observed for pure barium titanate.

In order to explain these observed characteristics showing deviations from the theory in varied ways, it seems to be required to take account of higher terms in the free energy expression. We tried therefore an extension of Devonshire's theory by making it to include terms up to sixth power of polarization in the expression of the free energy A as follows:

$$\begin{aligned}A=&\frac{1}{2}c_{11}(x_x{}^2+y_y{}^2+z_z{}^2)+c_{12}(y_yz_z+z_zx_x+x_xy_y)\\&+\frac{1}{2}c_{44}(x_y{}^2+y_z{}^2+z_x{}^2)+\frac{1}{2}\chi''P_z{}^2\\&+\frac{1}{4}\xi_{11}''P_z{}^4+g_{11}z_zP_z{}^2+g_{12}(x_xP_z{}^2+y_yP_z{}^2)\\&+h_{11}z_zP_z{}^4+h_{12}(x_xP_z{}^4+y_yP_z{}^4)\\&+\frac{1}{2}k_{11}z_z{}^2P_z{}^2+\frac{1}{2}k_{12}(x_x{}^2P_z{}^2+y_y{}^2P_z{}^2)\end{aligned}$$

where the last four terms are of newly added ones.

The rate of change in unit cell volume with polarization is then expressed as

$$x_x+y_y+z_z=-\frac{a+bP_z{}^2}{c+dP_z{}^2}\cdot P_z{}^2,$$

where

$$\begin{aligned}a&=(c_{11}-c_{12})(g_{11}+2g_{12}),\\b&=(c_{11}-c_{12})(h_{11}+2h_{12})+g_{11}k_{12}+2g_{12}k_{11},\\c&=(c_{11}-c_{12})(c_{11}+2c_{12}),\\d&=(c_{11}+c_{12})k_{11}+c_{11}k_{12}.\end{aligned}$$

Similarly, z_z/x_x vs. polarization relation is obtained as

$$\frac{z_z}{x_x}=-\frac{\alpha+\beta P_z{}^2}{\gamma+\delta P_z{}^2},$$

where

$$\begin{aligned}\alpha&=(c_{11}+c_{12})g_{11}-2c_{12}g_{12},\\\beta&=(c_{11}+c_{12})h_{11}-2c_{12}h_{12}+g_{11}k_{12}.\\\gamma&=c_{12}g_{11}-c_{11}g_{12},\\\delta&=c_{12}h_{11}-c_{11}h_{12}-g_{12}k_{11}.\end{aligned}$$

Though the comparison of these formulas with experimental results can not be complete on account of many material constants included in the formulas which are unknown experimentally at present, we can show at least as below that the general trend of the experimental curve is qualitatively well explained by assuming reasonable relations among them as well as a monotonous change of value of polarization with the temperature.

Pure barium titanate. g_{11} and g_{12} were found to be negative from the Devonshire's

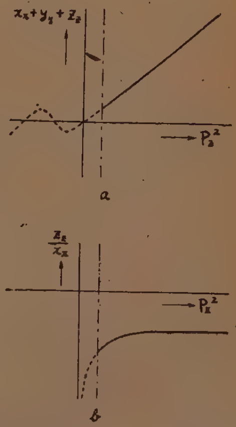

Fig. 5 a. $x_x+y_y+z_z$ as a function of square of polatization.
b. z_z/x_x as a function of square of polarization.

theory, which was also ascertained experimentally,(9) so that $a<o$. Since $x_x+y_y+z_z$ should increase with polarization, $b<o$. Of course $c>o$. So that, if we assume only $d>o$, then we obtain a relation of volume change and polarization as shown in Fig. 5a.

As to the temperature change in the value of z_z/x_x, we obtain the curve shown in Fig. 5b if assumed

$$\beta\gamma-\delta a<o, \quad \frac{a}{\gamma}>o, \quad \frac{\beta}{\delta}>o.$$

From these curves, by taking account of the monotonous change of polarization with temperature, we can explain qualitatively fairly well the experimental curves for pure barium titanate as shown in Figs. 3 and 4. The conditions given to respective constants as above are all consistent with each other.

Solid solutions. It is assumed $a>o$, $b>o$, $c>o$, $d<o$, then we obtain the curve of $x_x+y_y+z_z$ as a function of polarization which is shown in Fig. 6a. As is seen in the figure, $x_x+y_y+z_z$ should start from a negative value at the Curie point if we assume that a finite spontaneous polarization appears abruptly at this point. This fact just corresponds to the feature of temperature change experimentally observed in lattice volume near the Curie point as shown in Fig. 3.

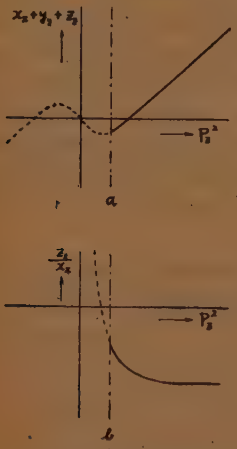

Fig. 6 a. $x_x+y_y+z_z$ as a function of square of polarization.
b. z_z/x_x as a function of square of polarization.

As to the temperature change in z_z/x_x, if we assume

$$\beta\gamma-\delta a>o, \quad \frac{a}{\gamma}<o, \quad \frac{\beta}{\delta}>o,$$

then we obtain the curve shown in Fig. 6b. This explains well the features seen in Fig. 4. It is again noted in this case that the above restrictions given to these constants are all consistent with each other.

From the above consideration we can see that the experimental results reported in the previous paragraphs are not contradictory to the general thermodynamical relations.

The author expresses his sincere thanks to Professor S. Miyake for his kind guidance in the course of his research.

References.

(1) G. H. Jonker and J. H. Van Santen: Chem. Weekblad, **43** (1947) 672.
(2) G. Shirane and K. Suzuki: J. Phys. Soc. Japan, **6** (1951) 274.
(3) A. R. Ubbelohde and I. Woodward: Proc. Roy. Soc., A **188** (1947) 358.
(4) S. Nomura and S. Sawada: J. Phys. Soc. Japan, **6** (1951) 36.
(5) G. Shirane and A. Takeda: J. Phys. Soc. Japan, **6** (1951) (to be published).
(6) H. F. Kay and P. Vousden: Phil. Mag., **40** (1949) 1019.
(7) A. F. Devonshire: Phil. Mag., **40** (1949) 1040.
(8) H.D. Megaw: Trans. Faraday Soc., **42** A (1946) 224
(9) G. Shirane and K. Sato: J. Phys. Soc. Japan, **6** (1951) 20.

JOURNAL OF THE PHYSICAL SOCIETY OF JAPAN, Vol. 6 No. 5 September—October, 1951

A Study on Corrosion-Process of Iron by Means of Electron Diffraction.*

By Ryuji ABE.

Physical Institute, Nagoya University, Nagoya Japan.

(Received February 24, 1951)

A systematic study was made on corrosion-products of iron by means of electron and X-ray diffraction, with the following results;

When metallic iron is immersed in salt solution, amorphous white precipitate, $Fe(OH)_2$, is formed as the primary corrosion-product.

(1) $Fe(OH)_2$ thus formed changes into lepidocrocite, γ-$Fe_2O_3.H_2O$, when pH of the solution so very low and oxidation takes place rapidly, while under usual conditions it is oxydized partly lepidocrocite, which combines with the remaining $Fe(OH)_2$ to form green rust, $2FeO.Fe_2O_3.H_2O$.

(2) The green rust is oxydized, under usual conditions, to lepidocrocite, while in case oxygen in the solution is less, it changes partly to lepidocrocite, which combines with the remaining green rust giving magnetite, Fe_3O_4. On the other hand, when oxidation is accelerated by H_2O_2, it changes to haematite, α-Fe_2O_3.

(3) Goethite, α-$Fe_2O_3.H_2O$, was never observed in corrosin-products of metallic iron, and it was concluded that it is formed only from ferric salts: for example from the unstable yellow substance, which is precipitated in aqueous $FeCl_3$ solution under certain conditions.

(4) This very substance was assumed as β-$Fe_2O_3.H_2O$ by Weiser and Milligan, but it is more reasonable to identify it with $Fe(OH)_3$ isomorphous to $Al(OH)_3$. Its unit cell was determined by X-ray data: monoclinic, a=8.99, b=5.12, c=9.92 and β=86°34′.

§1. Introduction.

Ordinarily when a piece of iron is immersed in salt solution, a yellowish brown rust, γ-$Fe_2O_3.H_2O$, is formed, but in some case a reddish brown rust, α-$Fe_2O_3.H_2O$, appears. Deiss and Schikorr(1) verified by their experiment that the former is formed from $Fe(OH)_2$ when oxidation took place slowly, while the latter when it is rapid. They assumed a corrosion-process of iron to be as follows:

(1) When iron is corroded, $Fe(OH)_2$ is formed at first.

(2) If the supply of oxygen is abundant, $Fe(OH)_2$ changes to amorphous ferric hydroxide, $Fe(OH)_3$, and crystallizes in the form of α-$Fe_1O_3.H_2O$.

(3) If the oxygen supply is less abundant, $Fe(OH)_2$ is oxidized partly to $Fe(OH)_3$ and the latter combines with the former to form green rust.

(4) The green rust in the process (3) is oxidized to γ-$Fe_2O_3.H_2O$, when excess oxygen is present.

(5) The green rust in (3) combines with $Fe(OH)_2$ to form magnetite, Fe_3O_4, when oxygen is insufficient.

They could learn little about the green rust, except that it is a basic ferrous ferrite, because it is a very unstable compound. Recently Yoshioka(2)(3) studied the corrosion process of iron by means of electron diffraction, and concluded that the chemical formula for the green rust is $2FeO.Fe_2O_3.H_2O$. He supported Deiss and Schikorr's process because his observations concerning the chemical reaction of the green rust agreed well with it. It was pointed out by the author, however, that it contradicts with their experimental result that they observed green color before the formation of α-$Fe_2O_3.H_2O$, because green rust should not be formed in the process (2).

The author extended Yoshioka's experiment to remove the contradiction and to obtain a more reasonable explanation of corrosion process. In this paper a short summary of his experiments and conclusions is

---

* The expence of this study was defrayed from the Grant in Aid for Fundamental Scientific Research of the Educational Ministry.

described.

§2. Formation of Green Rust.

When aqueous 0.1% NaCl solution, previously heated to remove oxygen, is electrolyzed with pure iron electrodes, a white precipitate appears around the anode. This rust is $Fe(OH)_2$, and immediately oxidized when exposed to air. The author tried to study how this substance changes when oxidized very slowly. A vey small amount of gelatin (about 0.1 gr/cc) was added to the solution to make thin films containing $Fe(OH)_2$ for a specimen of electron diffraction. This was also favourable to prevent $Fe(OH)_2$ from abrupt oxidation. After it was electrolyzed for a few minutes at about 30°C with a current density of about 100 mA/sq.cm, a white precipitate $Fe(OH)_2$ was sucked up quickly into a pipette and poured on a thin aluminum plate with small holes on which the film was to be formed. Then the plate was quickly mounted on the specimen chamber of a diffraction camera and the air was pumped out promptly before the drop dried up. A diffraction pattern (No. 1) was taken after pumping, then air was introduced into the camera and the specimen was exposed to it for 3 minutes (the first exposure). After the air was pumped out again, a diffraction pattern (No. 2) was taken, then air was introduced again and so on. The second, third and fourth exposures were for about 10, 50 minutes and 3 days respectively. The color of the specimen, at first, greenish white, gradually turned green after each exposure, but no other color was observed even after the last exposure. The experiment was repeated a few times and the results agreed with each other qualitatively. The diffraction pattern for each exposure is illustrated schematically in Fig. 1, where the intensity of Debye-Scherrer rings is given against the reciprocal of spacing. In this figure, the diagrams of the observed patterns are analysed and assigned to the four components, i.e. the green rust, γ-$Fe_2O_3.H_2O$, Fe_3O_4 (or γ-Fe_2O_3) and T.R.S.*, denoted respectively by G, γ, M and T. The pattern of $Fe(OH)_2$ seems to be present in none of the diagrams. This may be due to the amorphous nature of $Fe(OH)_2$. In the pattern No. 1, taken immediately after the preparation, the strong lines of γ-$Fe_2O_3.H_2O$ are present besides those of the green rust. The former lines gradually decreased in intensity after every exposure and only those of the latter remained in No. 4, after fifty minutes exposure. Though in No. 2 and No. 3 a few lines coincide with those of magnetite, the existence of the latter is uncertain because some of its strong lines are absent. In No. 5, after three days exposure, the green rust completely disappears while T.R.S. predominates instead.

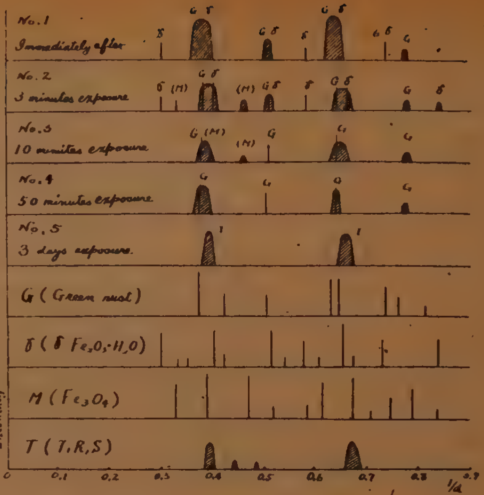

Fig. 1

From the above observations it is supposed that at first γ-$Fe_2O_3.H_2O$ is formed by the oxidation of $Fe(OH)_2$, and then it combines gradually with $Fe(OH)_2$ to form the green rust.

§3. Oxidation of Green Rust.

According to Deiss and Schikorr, the green rust changes in water to magnetite when the supply of oxygen is poor and to γ-$Fe_2O_3.H_2O$ when it is abundant. These facts were verified by Yoshioka[2] and again by the author. The latter observed, moreover, another reaction when the oxidation takes place very rapidly.

In the solution, prepared as before, a small amount of H_2O_2 was added to accelerate the oxidation. When the solution was subjected to electrolysis, the color of the rust formed around the anode was at first green, and instantaneously changed to reddish brown. The last product was subjected to diffraction test and was identified as α-Fe_2O_3. The observed color agreed with that of α-Fe_2O_3. It is thus verified that α-Fe_2O_3 is formed from the green rust when the latter is oxidized very rapidly.

---

* The name T.R.S. was given by Miyake(4) for a substance which shows only two strong rings. Yoshioka(2) proposed that it is an imperfect crystal of magnetite.

§4. Formation of α-$Fe_2O_3.H_2O$ and $Fe(OH)_3$.

The author could not obtain α-$Fe_2O_3.H_2O$ at any stage of experiment of electrolysis mentioned in the previous sections. To produce this rust and study the process of its formation, an experiment was carried out according to Weiser and Milligan's method.⁽⁵⁾ They reported in their paper that a yellow precipitate was formed at first when aqueous $FeCl_3$ solution was heated at about 90°C for a few days and that it changed gradually to reddish brown rust, α-$Fe_2O_3.H_2O$. They considered the yellow substance to be a kind of ferric hydroxide and named it β-$Fe_2O_3.H_2O$, because they verified that it is not identical with any compound of iron containing chlorine. Moreover, they concluded by their X-ray analysis that the substance might have an orthorhombic lattice whose unit translations are a=5.28A, b=10.24A and c=3.34A.

Table I

Yellow substance				β-Fe_2O_3 $.H_2O$		$Fe_2(OH)_3$	
X-rays		Electron		X-rays		calculated	
I	l/d	I	l/d	I	l/d	l/d	index
w	0.144		—		—	0.145	(101)
vw	0.155		—		—	0.154	(101)
mw	0.202		—	m	0.189	0.202	(002)
w	0.226		—		—	0.224	(110) (200)
vw	0.224		—		—	0.243	(111)
						0.249	(111)
mw	0.295		—		—	0.297	(112)
s	0.310	m	0.309	s	0.302	0.309	(202) (112)
m	0.390	w	0.386	m	0.382	0.390	(020) (310)
vs	0.403	vs	0.401	vs	0.391	0.404	(004)
s	0.448	s	0.446	w	0.435	0.448	(400) (220)
m	0.480	m	0.487		—	0.486	(222)
sm	0.523	m	0.520	sm	0.512	0.520	(321)
						0.528	(321)
sm	0.583	m	0.585	w	0.568	0.594	(224)
vs	0.620	vs	0.616	s	0.610	0.618	(404)
s	0.672	s	0.669			0.671	(600)
sm	0.707	s	0.700	w	0.692	0.710	(602)
m	0.738	sm	0.744				
m	0.774	m	0.772			0.780	(040)
	—	m	0.842				
		m	0.880				
		sm	0.950				

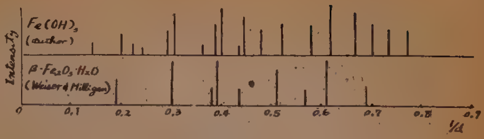

Fig. 2.

The author obtained the yellow precipitate by the same method. Electron diffraction and X-ray patterns of this substance agreed well with the X-ray pattern obtained by Weiser and Milligan. The results are given in Table I and illustrated in Fig. 2. This substance changed to α-Fe_2O_3 after heating in vacuum furnace at about 350°C for an hour. It may change gradually to α-Fe_2O_3 $.H_2O$ in solution, though its pattern was not obtained by electron diffraction, since good specimens could not be obtained in the present experiment.

Although a formula $Fe_2O_3.H_2O$ (β) was given to the yellow substance by Weiser and Milligan, this seems to be incorrect, because no crystal structure for $Fe_2O_3.H_2O$ is adequate to the unit cell given by them in view of the fact that the close packing of oxygen ions decides the crystal cell. The author prefers the formula $Fe(OH)_3$ for this substance by the following two reasons:

(1) It is known that the crystal structures of certain iron and aluminium oxides and hydroxides are isomorphous to each other. Assuming the yellow substance to be $Fe(OH)_3$ and to be structurally isomorphous to $Al(OH)_3$, hydrargillite, its lattice constants can be estimated (Table II). The Debye-Scherrer rings deduced from the estimated lattice constants agreed well with those of the yellow substance as shown in Table I.

Table II

Substance	Symmetry	a	b	c	β
$Al(OH)_3$	monoclinic	8.6236	5.0602	9.699	85°26'
$Fe(OH)_3$	monoclinic	8.99	5.12	9.92	86°34'

(2) The density of the yellow substance, 3.12±0.1 cited by Weiser and Milligan, is in better agreement with that calculated from the above lattice constants, 3.11, than that calculated from the Weiser and Milligan's values, 3.245.

It was difficult, however, to calculate the intensities of the Debye-Scherrer rings precisely on the basis of the assumed crystal structure, because the parameters of the crystal could not be determined accurately.

§ 5. Effect of Hydrogen Ion Concentration.

In the series of experiments described above, all the solutions used in electrolysis were neutral. Studies were made, moreover, on the effect of hydrogen ion concentration. A small amount of pure HCl or NaOH was added to 0.1% NaCl solution to change pH. The precipitate attached around the anode was subjected to diffraction study. The results are described and summarized in Table III.

Table III

pH	Final product	Corrosion process	
		in Fig. 3a by the author	in Fig. 3b by Deiss and Schikorr
< 2	γ-$Fe_2O_3.H_2O$	(4)	
4 ~ 5	α-Fe_2O_3	(4), (5), (6)	(I), (II)
7 ~ 8	γ-$Fe_2O_3.H_2O$	(4), (5), (7)	(I), (III), (IV)
>11	Fe_3O_4	(4), (5), (8)	(I), (III), (V

(1) pH<2. Although no precipitate was visible by naked eye, the anode, when tested by the reflection method, showed a very sharp pattern of γ-$Fe_2O_3.H_2O$. It is certain therefore that a very small amount of γ-$Fe_2O_3.H_2O$ is formed.

(2) pH: 4~5. The precipitate formed around the anode was green at first, and changed reddish brown in a few minutes. The final precipitate was identified to be α-Fe_2O_3 by the diffraction study.

(3) pH: 7~8. This is the case of neutral solution previously described. The final product is γ-$Fe_2O_3.H_2O$ or Fe_3O_4.

(4) pH: <11. The precipitate around the anode was at first green and changed black in a few minites. The green substance, of course, may be the green rust and the final product is Fe_3O_4 as revealed by its pattern and color inherent to Fe_3O_4.

When a great amount of NaOH was added to the solution, no precipitate was detectable by naked eye and the anode showed no diffraction pattern. This might be due to the surface state of the anode inadequate for electron diffraction.

§ 6. Discussion and Summery.

From the above experimental results, the corrosion process of iron proposed by Deiss and Schikorr was revised to a more reasonable one. The old and the revised schemes are illustrated schematically in Fig. 3a and 3b. In these figures solid lines indicate oxidation, dehydration or both and the dotted lines indicate association or dissociation. The main points of revision and the reason for it are as follows:

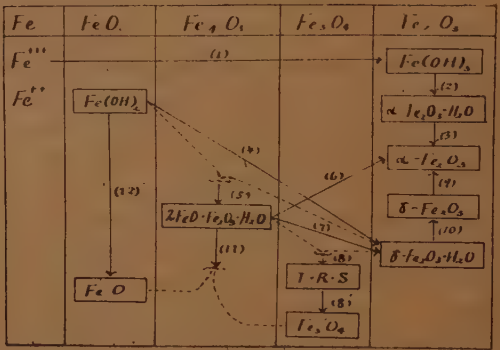

Fig. 3a. The revised scheme by the author. Explanation of the processes (1), (2) and (3) are given in §4; (4) and (5) in §2 and §3; (6), (7), (8) and (8') in §3. No description is given in this paper for processes (9), (10), (11) and (12). See reference (7) for the processes (9), (10); reference (2) for the process (11). The process (12) is given by a supposition which may occur when $Fe(OH)_2$ is heated in vacuum.

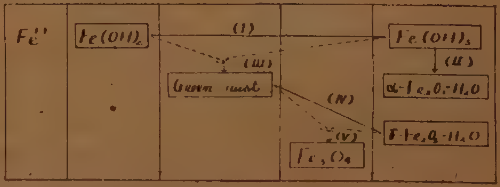

Fig. 3b. The old scheme by Deiss and Schikorr.

(1) $Fe(OH)_3$ in Deiss and Schikorr's scheme was substituted by γ-$Fe_2O_3.H_2O$ in the present one. The experimental result in §2 supports this revision, because γ-$Fe_2O_3.H_2O$ was observed before the green rust was formed from $Fe(OH)_2$. A proof for this conclusion was also obtained by the following experiment: When γ-$Fe_2O_2.H_2O$ and $Fe(OH)_2$, both prepared separately, are mixed under little oxygen supply, the color of the mixed solution changed blue gradually. The diffraction pattern of the blue precipitate was the same as that of the green rust i.e. $2FeO.Fe_2O_3.H_2O$. This proves the formation of $2FeO.Fe_2O_3.H_2O$ by the combination of γ-$Fe_2O_3.H_2O$ and $Fe(OH)_2$. It is suggested through this observation that the inherent color of $2FeO.Fe_2O_3$.

H_2O is blue.* The green color of the green rust may be due to the admixture of a small amount of the yellowish brown rust, γ–$Fe_2O_3.H_2O$.

(2) A new reaction was added that the green rust changes to α–Fe_2O_3 by abrupt oxidation as in §2. This may remove inconsistency in the old scheme described in the introduction, i.e. the green color was observed before α–$Fe_2O_3.H_2O$ is formed. The author infers that the final product in this case may not probably be α–$Fe_2O_3.H_2O$ as reported by Deiss and Schikorr, but its anhydride. This interpretation may be reasonable, since H_2O_2 is not so serious in the chemical analysis carried out by them. Thus the most important inconsistency of the old scheme is removed.

(3) In the present experiment, α–$Fe_2O_3.H_2O$ was never formed in the corrosion process of pure iron. The author infers that only γ–$Fe_2O_3.H_2O$ is formed directly from $Fe(OH)_2$ by oxidation. α–$Fe_2O_3.H_2O$ may be produced only from ferric salts, say $FeCl_3$, as described in §4. It became clear that ferric salts change to $Fe(OH)_3$ before the formation of α–$Fe_2O_3.H_2O$.

(4) The experimental result in §5 shows that the revised scheme of corrosion process need not to be altered even when pH of the solution is varied over a wide range. The effect of pH is only to change oxidation velocity: $Fe(OH)_2$ and $2FeO.Fe_2O_3.H_2O$ are oxidized the faster, the more acidic the solution is. Though the reason for this fact is not clear, it is likely that the basic substances $Fe(OH)_2$ and $2FeO.Fe_2O_3.H_2O$ tend to change to an acidic substance γ–$Fe_2O_3.H_2O$ in acidic solution.

(5) Finally some data on iron oxides and hydroxides are shown in Table IV for reference.

§7. Acknowledgement.

The author wishes to express his sincere thanks to Prof. R. Uyeda for his kind guidance through out this work, to Mr. H. Yoshioka for his discussion and to Prof. M. Kubo and Prof. K. Yamasaki for their helpful advices.

Table IV. Iron oxides and hydroxides

Valence	Chemical formula	Color	Space group	Symmetry	Lattice constants	Reference
Fe^{++}	FeO	Black	O_h^5	Cubic	a=4.332	Wyckoff(9)
	$Fe(OH)_2$	White	D_{3d}^3	Hexagonal	a=3.24 c=4.47	Wyckoff(8)
Fe^{++} $+Fe^{+++}$	$2FeO.Fe_2O_3.H_2O$	Blue		Orthorhombic	a=5.305 b=3.160 c=7.834	Yoshioka(3)
	Fe_3O_4 Magnetite	Black	O_h^7	Cubic	a=8.374	Wyckoff(9)
Fe^{+++}	α–Fe_2O_3 Hematite	Reddish brown	D_{3d}^6	Hexagonal	a=5.4135 α=55°17′	Wyckoff(9)
	γ–Fe_2O_3	Reddish brown		Cubic	a=8.30	Wyckoff(6)
	α–$Fe_2O_3.H_2O$ Goethite	Reddish brown	V_h^{16}	Orthorhombic	a=4.64 b=10.0 c=5.03	Wyckoff(9)
	γ–$Fe_2O_3.H_2O$ Lepidocrocite	Yellowish brown	V_h^{17}	Ortnorhombic	a=3.87 b=12.4 c=3.06	Wyckoff(9)
	$Fe(OH)_3$	Yellow	C_h^5	Monoclinic	a=8.99 b=5.12 c=9.92 β=86°34′	Author

---

* L. Pauling noticed(6) that the deep, intence color is often observed for a substance which contains an element in two different oxidation states. In case of iron oxides and hydroxides it was also observed that color of the compounds in such states is deep an intence: $2FeO.Fe_2O_3.H_2O$ is blue and Fe_3O_4 black. Color of iron oxides and hydroxides is shown in Table IV.

References.

(1) E. Deiss and G. Shikorr: Z. anorg. allgem. Chem. **172** (1928) 32.
(2) H. Yoshioka: J. Phys. Soc. Jap. **4** (1949) 270.
(3) H. Yoshioka: Kagaku **18** (1948) 413.
(4) S. Miyake: Sci. Pap. Inst. Phys. Chem. Research, Japan, **36** (1939) 363.
(5) H. B. Weiser and O. W. Milligan: J. Am. Chem. Soc. **57** (1935) 238.
(6) L. Pauling: General Chemistry (1949) 457.
(7) L. A. Welo and O. Baudish: Chem. Rev. **15** (1934) 45.
(8) Ralph W. G. Wyckoff: *The Structure of Crystals, Second Edition* (1934).
(9) Ralph W. G. Wyckoff: *The Structure of Crystals, Supplement to the Second Edition* (1935).

JOURNAL OF THE PHYSICAL SOCIETY OF JAPAN, Vol. 6 No. 5 September—October, 1951

Electron Microscope and Diffraction Studies of Chromic Oxides.

By Riitsu TAKAGI.

Government Mechanical Laboratory, Sumiyoshicho, Suginamiku, Tokyo.

(Received February 27)

The size, shape and crystallinity of chromic oxides prepared by various methods have been studied. The particles of chromic oxide obtained by the calcination of chromium trioxide at 400°~1300°C are of granular and irregular shape, while those obtained by the calcination of fluid mixture of chromium compound are plate-like, often exhibiting hexagonal shape, the flat surfaces of these crystals being parallel to (001). Higher calcination temperature up to 1600°C merely increases the size of the particles, so that the distinction between the two types in shape remains as before.

§1. Introduction.

Green powders of chromic oxides prepared by calcining compounds of chromium were investigated by an electron microscope and electron diffracton transmission method. It was found that the size and shape of the particles differred according to the method of preparation, and although their crystalline structure remained the same, rhombohedral system, their diffraction patterns varied with the shape of the particles. The change of the relative intensities of the x-ray diffraction lines of chromic oxides observed by S. S. Sidhu[1] seems to have some connection with these facts.

§2. Experimental Procedure.

Fine powders of chromic oxide prepared were put in a two per cent amyl acetate solution of collodion and well dispersed by ultrasonics of 400kc for about a minute. A drop of this solution was pipetted upon the surface of the water of about 60°C to form a thin film of collodion, within which particles of chromic oxide were imbedded. This film was picked up by a 200-mesh wire screen and examined in an electron microscope or electron diffraction apparatus. In this case flat particles lie parallel to the collodion film. When the diameter of the smallest particle exceeded about 0.1μ, no diffraction pattern was available.

§3. Samples Obtained by Heating Chromium Trioxide.

The shape of the particles of chromic oxide obtained by calcining chromium trioxide at a comparatively low temperature was of irregular form as seen in Fig. 1. The intensity distribution of electron diffraction rings of it (Fig. 2b) resembles that for x-ray diffraction given by Hanawalt (Fig. 2a). When the calcining temperature became higher, the particles grew granular at first and then larger in size, but did not show a well-defined crystalline shape (Fig. 3.).

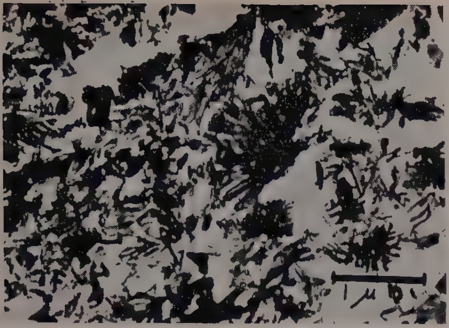

Fig. 1. Cr_2O_3 obtained by calcining CrO_3 at 600°C.

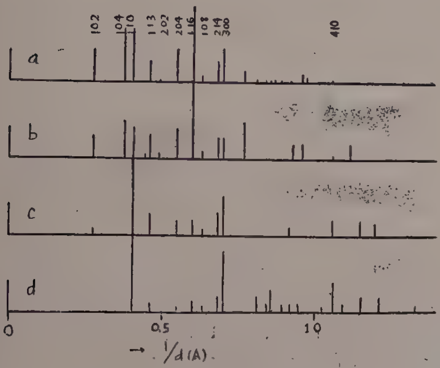

Fig. 2. a. An x-ray diffraction pattern of Cr_2O_3 by Hanawalt. b,c,d. Electron diffraction patterns of the samples shown in Fig. 1,4,5, respectively.

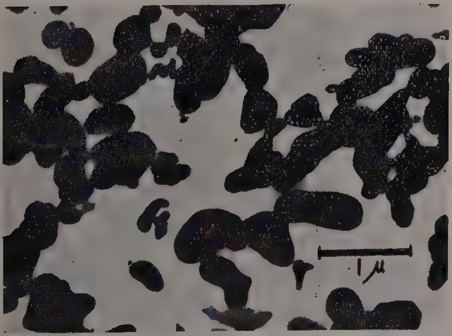

Fig. 3. Cr_2O_3 obtained by calcining CrO_3 at 1300°C.

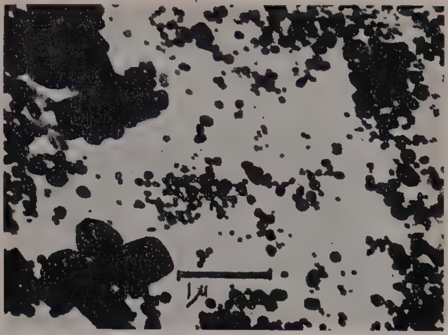

Fig. 4. Cr_2O_3 obtained by calcing a mixture of CrO_3 and C_2H_5OH at 1100°C.

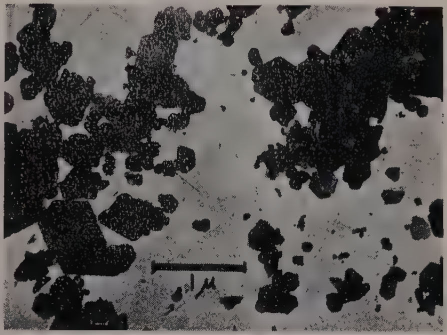

Fig. 5. Cr_2O_3 obtained by calcining a mixture of $Na_2Cr_2O_7{\cdot}2H_2O$ and S at 1100°C.

§4. Samples Prepared Otherwise.

Fig. 4 shows the sample obtained by calcining a mixture of chromium trioxide and alcohol at about 1100°C, and Fig. 5 shows the sample obtained by calcining a mixture of sodium dichromate and sulphur at about 1100°C. The shape of the particles is hexagonal and plate-like. Their electron diffraction patterns are given in Fig. 2c and d, respectively. The relative intensity of the reflections from (110), (300) and (410) in Fig. 2 c or d is exceedingly stronger than that in Fig. 2a in comparison with the reflection from (116). This gives a proof for that the c-axes of the crystals, which were perpendicular to the flat plate of the particles, were generally parallel to the electron beam in these two samples. In fact, hexagonal N-pattern was often observed. Similar results were obtained when potassium dichromate was used instead of sodium dichromate.

§5. Conclusion.

From the experiments described above, it became clear that the particles of chromic oxide obtained by calcining chromium trioxide in the atmosphere are of granular and irregular shape, whereas the particles of chromic oxide obtained in other methods by calcining a fluid mixture of chromium compound are hexagonal crystals having plate-like shape, with the surfaces parallel to (001).

The author wishes to express sincere thanks to Prof. S. Miyake of Tokyo Institute of Technology for valuable discussions, to Messrs. T. Kawada and S. Yoshida of this Laboratory for kind encouragements and to Mr. Shoichi Yoshida for preparation of specimens.

Reference.

1) S. S. Sidhu: Phys. Rev. **58** (1940), 206.

JOURNAL OF THE PHYSICAL SOCIETY OF JAPAN, Vol. 6 No. 5 September—October, 1951

Space Charge Effect in the Oxide Cathode Layer.

By Takuzo SHINDO.

Electrical Communication Laboratory, Tokyo, Japan.

(Received August 1, 1950)

It was concluded theoretically that space charge may be formed in the oxide cathode layer near the surface, when electric field at the cathode surface is sufficiently strong so that the diode may be regarded to operate in the Schottky region. The calculations are carried out for one-dimensional model and neglecting the interface layer, which exists usually between the base metal and the oxide coating.

As the result of this space charge, the slope of the Schottky plots are several times greater, than that predicted by the Schottky theory for metal surfaces.

This space charge may be responsible for the microsecond emission decay observed by Sproull and others.

§1. Introductions.

As is well known (BaSr)O cathode is an N-type Semiconductor having excess Barium atoms as the active centers and its thermionic emission is well understood by the Nijboer-Wilson model of the semiconductor. The oxide coated cathodes are usually prepared first by applying carbonates of the alkaline earth elements to a base metal and then converting the carbonates to oxides in vacuum. Thus an interface is formed between the base metal and the cathode layer.

In the steady state condition of the thermionic emission, the electrons are brought into the oxide layer from the base metal through the interface, flowing through the oxide layer and then those having a sufficient energy to surmount the surface potential barrier are emitted to the vacuum. When the anode potential is raised enough, the emitted electrons are readily collected to the anode without forming a space charge between the electrodes.

In this paper, the writer intends to point out theoretically that a space charge may be formed in the oxide layer and some of the experimental data can be explained as an effect of this space charge layer. This space charge may be responsible for the micro-second emission decay which was observed by Sproull and others.⁽¹⁾

§2. Fundamental Concept.

The electrone mission from an N-type semiconductor having electrons in its conduction band follows the well known formula

$$j=en^{-}D_0\sqrt{\frac{kT}{2\pi m}}\,e^{-\frac{\chi}{kT}}=en^{-}\Phi_0, \qquad (1.1)$$

where j is the saturation current density, k is the Boltzmann constant, T is the cathode temperature in °K, e and m are the charge and mass of the electron, χ is the height of the surface potential barrier and D_0 the mean transmission coefficient for electrons at the emitting surface.

In the presence of an electric field E at the cathode surface, χ is lowered proportional to $\sqrt{E}$ as a result of the Schottky effect. Disregarding this effect, however, the current j is entirely independent of the electric field E as seen from the equation (1.1). But, on the other hand, the continuity of the current j in the oxide layer requires a definite strength of an electric field to act across the oxide layer. This electric field will not in general be in accord with a field which may be produced by applying certain amount of potential differences between the electrodes. Thus, in general, a space charge will be formed up in the oxide layer so as to fit into the continuity equation.

For simplicity, we shall disregard the

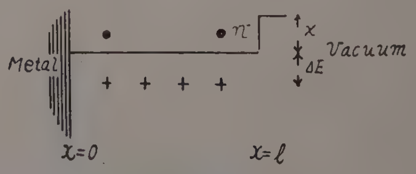

Fig. 1.

existence of an interface layer between the base metal and the oxide layer, but the inclusion of an interface layer will not cause any difficulty to our theory.

Considering a one-dimensional model of the oxide layer (as shown in Fig. 1), the current j is determined by an equation:⁽²⁾

$$j=en^-\mu E_r^{(i)}-eD\frac{dn^-}{dx}, \tag{1.2}$$

where

μ: the mobility of the conduction electrons,

$$E_r^{(i)}=E^-+E^+$$

E^-: an electric field produced by the conduction electrons,

E^+: a field produced by the vacant active centers whose mobilities are considered to be zero,

D: the diffusion coefficient of the electrons.

The j current in equation (1.2) is determited by the equation (1.1), so that the equation (1.2) can be regarded as an equation for the electron density n^-. The fields E^- and E^+ are in turn related to the charge densities by the Poisson equations:*

$$\left.\begin{aligned}\frac{dE^-}{dx}&=\frac{4\pi e}{\kappa}n^-=N_0(1+f(x))\\ \frac{dE^+}{dx}&=-N_0\quad\left(N_0=\frac{4\pi e}{\kappa}n_0^-=\text{constant}\right)\end{aligned}\right\}\tag{1.3}$$

where κ is the dielectric constant of the oxide.

Thus the resultant field $E_r^{(i)}$ is obtained by the equation

$$E_r^{(i)}=E^-+E^+=N_0\left[\int f(x)\,dx+E_0\right], \tag{1.4}$$

where E_0 is a constant of integration. Inserting Eqs. (1,3) and (1.4) in (1.2) and putting

$$I=\frac{4\pi}{\kappa}j, \tag{1.5}$$

we obtain an equation to determine the electron distribution in the oxider layer:

$$I=N_0^2(1+f)\,\mu\left(\int f dx+E_0\right)-DN_0\frac{df}{dx}, \tag{1.6}$$

where I, or j, is determined by Eq. (1.1), in which n^- is obtained from the value of $f(x)$ at the surface of the cathode.**

§ 3. Integration of Eq. (1.6)

In solving the Eq. (1.6), it is convenient to introduce a function defined by

$$1+f(x)=e^{-g(x)} \tag{2.1}$$

Then we obtain an equation for $g(x)$

$$\frac{I}{\mu N_0^2}e^g=\int(e^{-g}-1)\,dx+E_0+\frac{D}{\mu N_0}\,\frac{dg}{dx}. \tag{2.2}$$

Differentiating with respect to x and denoting the differential coefficients with the primes we obtain

$$\left.\begin{aligned}g''-qe^gg'-\frac{1}{l_0^2}(1-e^{-g})=0\\ q=I/DN_0=eI/\mu N_0kT\\ 1/l_0^2=\mu N_0/D=eN_0/kT.\end{aligned}\right\}\tag{2.3}^{***}$$

This is an exact differential equation for the electron distribution which can only be solved by a numerical method. But for the present purpose it will be sufficient to solve the equation (2.3) approximately under the assumption $|g|\ll 1$. Introducing a new variable

$$X=x/l_0 \text{ and } \dot{g}=dg/dx \text{ etc.,}$$

Eq. (2.3) is transformed into

$$\left.\begin{aligned}\ddot{g}-Qe^g\dot{g}-(1-e^{-g})=0\\ Q=q^{l_0}=\frac{I}{\mu}\sqrt{\frac{e}{N_0^3kT}}\end{aligned}\right\}\tag{2.4}$$

Expanding the function g in a series

$$g=g_0+g_1+g_2+\cdots\cdots,$$

where g_n is a small quantity of the nth order, g_0 being determined by

$$\ddot{g}_0-Q\dot{g}_0=0. \tag{2.5}$$

The linearized equation (2.5) can be easily integrated under appropriate boundary conditions and, as will be shown later, Eq. (2.5) has sufficient accuracy in our case.

---

* In deriving Eq. (1.3), the positive ions are considered to be uniformly distributed across the oxide layer and the conduction electrons has a density n_0^- in the absence of an external field.

** Strictly speaking, n^- in Eq. (1.1) should be determined from the total amount of the free electrons found in a layer below the emitting surface whose width is equal to the mean free path of the conduction electrons. If, however, function $n^-(x)$ and hence $f(x)$ varies slowly with x, as in our case, n^- may be determined from the value of $f(x)$ at the surface of the cathode.

*** The diffusion coefficient D is related to the mobility μ by the Einstein relation, $\mu/D=e/kT$.

As we have disregarded the interface layer, the electron density in the oxide layer must join smoothly to that in the base metal, whereby the function g_0 should satisfy following condition,

$$g_0=0 \quad \text{at} \quad X=0. \tag{2.6a}$$

At the emitting surface we must require another condition, such as:

$$g_0=g_l \quad \text{at} \quad X=L=l/l_0,$$

where l is the thickness of the oxide layer (see Fig. 1), and g_l is related to the current j with an Eq. (1.1). The solution of the Eq. (2.5) under these boundary conditions can be obtained at once

$$g_0=g_l e^{-a_1 L}\,(e^{a_1 X}-e^{-a_2 X}),$$

where a_1 and a_2 are given by

$$a_1=\frac{1}{2}\,(Q+\sqrt{Q^2+4}),$$

$$-a_2=\frac{1}{2}\,(Q-\sqrt{Q^2+4}).$$

Practically we can neglect the second term $e^{-a_2 X}$ and take

$$g_0=g_l e^{-a_1(L-X)} \tag{2.7}$$

as a solution of the Eq. (2.5)

Resultant field $E_r^{(i)}$ is obtained from the Eq. (1.4) which in the first approximation can be written

$$E_r^{(i)}(x)=N_0\left(-\int g_0 dx+E_0\right),\ E_r^{(e)}=\kappa E_r^{(i)}, \tag{2.8}$$

where g_0 should be inserted from the Eq. (2.7). To determine the constant E_0, insert the Eq. (2.8) into (2.2) and solve this equation with respect to E_0, taking into account the fact that a_1 is a solution of the equation

$$a_1^2-Qa_1-1=0.$$

Thus we obtain (retaining the first order terms only)

$$E_0=ql_0^2=1/\mu N_0^2. \tag{2.9}$$

The field strength at the cathode surface can then essily be calculated by the Eqs. (2.7), (2.8) and (2.9), giving

$$E_r^{(e)}=\kappa\,(e^{-gl}\Phi_0/\mu-N_0 l_0/a_1\cdot g_l). \tag{2.10}$$

The emission current I (or j) is related to a value g_l by the equation (1.1), whereby

$$I=N_0 e^{-gl}\Phi_0$$

or

$$j=\frac{\kappa}{4\pi}N_0 e^{-gl}\Phi_0. \tag{2.11}$$

Thus we can calculate a relationship between the emission current j and the field strength $E_r^{(e)}$ at the cathode surface by the above Eqs. (2.10) and (2.11).

§4. Consideration of the Schottky Effect.

In the presence of an electric field $E_r^{(e)}$ at the cathode surface, the surface potential barrier is lowered as the result of the Schottky effect. The Eq. (1.1) should then be replaced by(3)

$$\left.\begin{aligned} j&=en^{-}\Phi_0\exp\left(\frac{4.39}{T}\sqrt{E_r^{(e)}}\right)=en^{-}\Phi\\ \Phi&=\Phi_0\exp\left(\frac{4.39}{T}\sqrt{E_r^{(e)}}\right), \end{aligned}\right\} \tag{3.1}$$

where $E_r^{(e)}$ is to be measured in volts/cm. The Eq. (2.10) is also to be replaced by

$$E_r^{(e)}=\kappa\left(e^{-gl}\frac{\Phi}{\mu}-\frac{N_0 l_0}{a_1^*}g_l\right), \tag{3.2}$$

where a_1^* can be determined by the equations

$$\left.\begin{aligned} a_1^*&=\frac{1}{2}\,(Q^*+\sqrt{Q^{*2}+4})\\ Q^*&=\frac{e^{-gl}}{\mu}\Phi\sqrt{\frac{e}{N_0 kT}} \end{aligned}\right\} \tag{3.2'}$$

The Eq. (3.2) is a transcendental equation in $E_r^{(e)}$ which can be solved only by numerical method. Such calculations are not so difficult, since the Schottky effect has only a little effect in the small ranges of $E_r^{(e)}$ and, on the other hand, the Eq. (3.2) can easily be solved for a special case of $g_l=0$.

§5. Numerical calculations.

Positive potentials applied to the diode anode will provide an increasing anode current, first in accord with the Langmuir-Child space charge relationship and then, at higher voltages, following a Schottky type behavior. A plot of log j *vs.* $\sqrt{E}$ should yield a straight line which has a slope several times greater than that predicted by the Schottky theory for metal surfaces.

To compare our result with those behavior, the current j and the field $E_r^{(e)}$ should be calculated from the Eqs. (3.1) and (3.2) to plot log j vs. $\sqrt{E_r^{(e)}}$.

The numerical values which we have

employed in this calculations are as follows. As the density n_0^- of the conduction electrons in thermal equilibrium at 1000°K a value

$$n_0^- = 5 \times 10^{14}\ cm^{-3},$$

was chosen.⁽⁵⁾ From this value we can calculate the electron densities at various temperature by means of Nijboer formula taking the energy gap ΔE between the donor level and the bottom of the conduction band to be 0.7ev. and $\chi = 0.3$ev. The calculated densities are given in the second column of Table I.

Table I.

T (°K)	n_0^- cm^{-3}	Φ_0 $cm.\ sec^{-1}$	l_0 cm
800	5.56×10^{13}	0.568×10^5	8.28×10^{-5}
900	1.88×10^{14}	0.978×10^5	4.78×10^{-5}
1000	5.00×10^{14}	1.52×10^5	3.09×10^{-5}

The third column of this Table gives the values of Φ_0 which can be computed from Eq. (1.1) taking $D_0 = 1.0$ and $\chi = 0.3$ev. The field strength at the cathode surface can then be calculated from the Eq. (2.10) with a given value of g_l. The emission current j is then given by the Eq. (2.11) for this value of g_l. The relationship between j and $E_r^{(e)}$ is shown in Fig. 2 for two values of the cathode temperatures. In this calculations we took $\mu = 100$ cm²/volts. sec. and $\kappa = 10$ as the reasonable values of the mobility μ and dielectric constant κ. These values were regarded as constants independent of temperature.

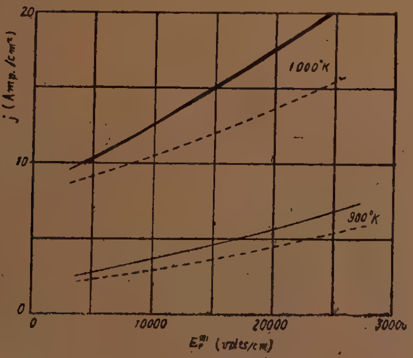

Fig. 2. The relations between the emission current j and the field strength at the cathode surface.
—— Including the Schottky effect.
- - - disregarding the Schottky effect.

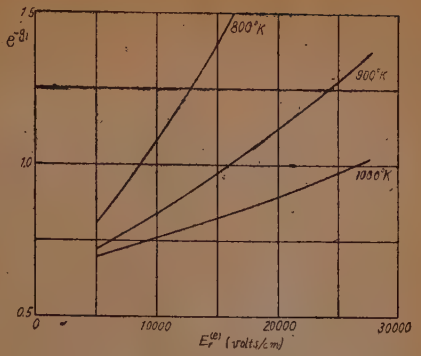

Fig. 3. The electron density at the cathode surface versus the field strength at the cathode surface. A region for $e^{-g_l}>1$ is the negative space charge and that for $e^{-g_l}<1$ is the positive space charge.

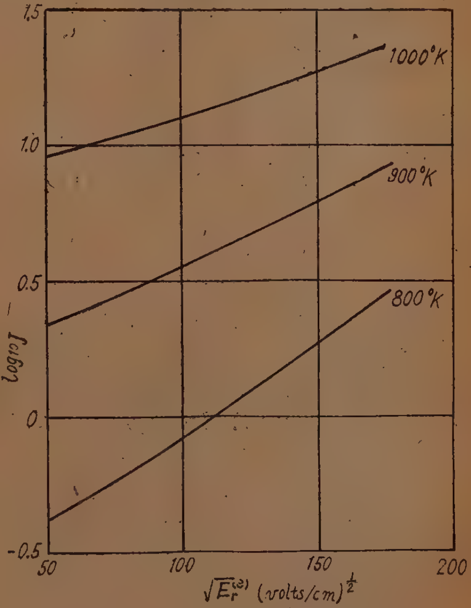

Fig. 4. Schottky plots of the saturation current densities, where j in Amp./cm². and $E_r^{(e)}$ in volts/cm.

The corrections due to Schottky effect are then taken into account in the following manner. We take as a zeroth approximation of the Eq. (3.2) the values obtained by the Eq. (2.10) and solve this equation by a step by step method. The calculations are not so tedious in the small ranges of $E_r^{(e)}$ and the first step calculations give fairly accurate values. For higher values of $E_r^{(e)}$ Eq. (3.2) can easily be solved exactly for a special value of $g_l = 0$. The values thus calculated are shown in Fig. 2. In Fig. 3 the electron densities at the cathode surface are shown as a function of $E_r^{(e)}$. The field strength $E_r^{(e)}$ in Fig. 3 takes into account the Schottky effect correctly.

A characteristic length l_0 (given by the Eq. (2.3), which gives a measure of the space charge layer, is shown in the fourth column of the Table I. Fig. 4 shows the Schottky plots i.e. log j vs. $\sqrt{E_r^{(e)}}$ for three values of the cathode temperatures. The curves in Fig. 4 show the correct temperature dependence of the emission current although small curvatures are observed from the curves.

§6. Second Approximation.

The solution of the Eq. (2.4) can be obtained more accurately by calculating the second approximation g_1. The calculations are simple but somewhat lengthy. We have obtained a solution neglecting the Schottky effect. The field strength $E_r^{(4)}$ obtained by the use of g_1 is

$$E_r^{(4)}(l)=e^{-gl}\frac{\Phi_0}{\pi}-\frac{N_0 l_0}{a_1}\left(gl-\frac{a}{2}g_l^2\right), \qquad (5.1)$$

where

$$a=\frac{a_1+\frac{1}{2}}{3a_1^2-Qa_1}.$$

The field strength $E_r^{(4)}$ calculated by Eq. (5.1) with the numerical constants quoted above are shown in Fig. 5 with the corresponding values of the current j. In Fig. 5 a full line shows the values obtained by the first approximation formula (2.10). The comparison of these data shows that it is sufficiently accurate to use the first approximation formula in the ranges of g_l considered above. Therefore we have carried out the calculations by the use of first approximation formula throughout this paper.

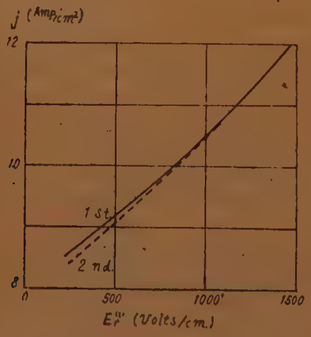

Fig. 5. Comparison between the first approximation and the second preoximation.

§7. Conclusions.

It was pointed out from the above data that the space charge may be formed in the oxide cathode near the surface, when a space charge predicted by Langmuir does not exist between the electrodes. In the Schottky region the space charge inside the oxide layer is necessary for explaining the slopes of the curves such as shown in Fig. 4 and the correct temperature dependencies. An existence of the interface layer will introduce no essential difficulties in our theory but some further complications. In above calculations the conduction electrons are not in thermal equilibrium with the donors and to calculate the electron density at thermal equilibrium, we must take into account the shift of the Fermi level in the space charge region correctly. The corrections due to this effect may be carried out according to the recent paper of J. C. Slater.⁽⁶⁾ It would be necessary to calculate this effect by the self-consistent method. The existence of the space charge layer inside the cathode layer is, however, not to be doubted.

The space charge predicted here would be responsible for the microsecond emission decay. Calculations on this line will be carried out in near future.

References.

1) Sproull R. L.: Phys. Rev. **67** (1945) 166.
2) Mott and Gurney: *Electronic Prccesses in Ionic Crystals Chap. V.*
3) Handb. d. Exp. Phys. Bd. XIII2 S. 258 G1. (124).
4) A. Eisenstein: *Advance in Electronics I.* p. 38.
5) Cited above (4) p. 39.
6) J. C. Slater: Phys. Rev. vol. **76** (1949) 1592.

JOURNAL OF THE PHYSICAL SOCIETY OF JAPAN, Vol. 6 No. 5 September—October, 1951

Creep Phenomena of Selenium Rectifiers.

By Masao TOMURA.*

Matsuda Research Laboratory of Tokyo Shibaura Electric Co., Ltd., Kawasaki.

(Received September 30, 1950)

Creep phenomena of selenium rectifiers, i.e. initial decaies of hard flows were observed, and polarization effects were found in the barrier layers at the same time. By observing discharge currents due to the above effect, characteristics of the polarization were studied. As the polarization voltage increases with the duration of application of the reverse voltage, the effective voltage through the barrier layer decreases, resulting the decay of the hard flow. The characteristics of the decaies were calculated on the stand points of the polarization effect and the non-uniform structure of the barrier layer. And the relaxation time of the decay was discussed by considering that the polarization effect was owing to ionic space charges in the barrier layer.

§1. Introduction.

At present metal rectifiers such as cuprous oxide and selenium rectifiers are used in various communication circuits, as for instance, a varistor etc.; whereby their characteristics are desired to be superior especially in life and initial dynamic natures.

From this stand point, the above initial relaxation effects which are called as creep phenomena of the rectifier will be studied and only hard flows are taken up as the first step of this survey in this paper. Here the creep is ment as the initial decay of the current in the duration of several minutes and must be distinguished from the aging phenomena of the rectifiers which last for several years. Untill now, the existence of creep has been reported(1), but no studies are found on its mechanism.

§2. Characteristics of Initial Decay.

The sample which is used in this experiment is just the same as the one used in the preceding survey(2). Its area is 2 cm². Observations are carried on at 14°C. The initial decay of the hard flow is observed by the usual method of characteristic measurement of the rectifier.

Hard flows at 3~30 volts of applied voltages decrease by about 30% of the initial values in 5 minutes and recover their initial values by setting free in about the same durations. Hence observations are able to be carried on successively in turn.

Decay of the current becomes almost constant practically in about 3 minutes as shown in Fig. 1, so the final current at the infinite time j_∞ may be obtained graphically through observations of about 3 minutes long,

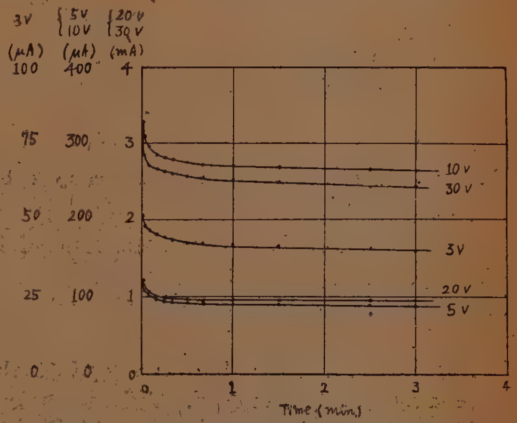

Fig. 1. Initial decaies of the hard flows at various voltages.

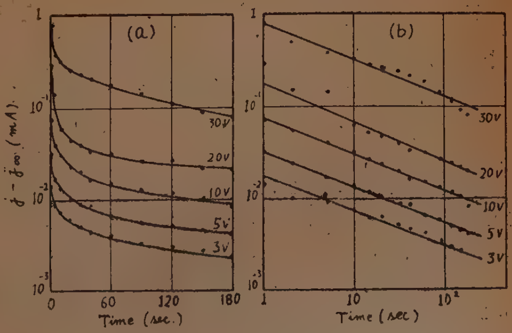

Fig. 2. Relations between $j-j_\infty$ and time.

---

* Now at the Institute of Polytechnics of Osaka City University.

Two kinds of plotting of $j-j_\infty$ *versus* t curves are shown in Fig. 2, where j is the magnitude of hard flow at time t. The initial value j_0 can be obtained in Fig. 2(a) by extrapolating to $t=0$, for $j-j_\infty$ must be finite at $t=0$ from the physical meaning and the straight part of the curve in the region of small t makes this extrapolation possible in the figure.

As for characteristics of the hard flows, their current *versus* voltage curves are shown in Fig. 3.

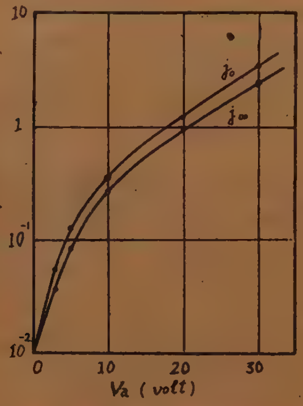

Fig. 3. The hard flow *vs.* applied voltage curves. The upper curve is for the initial current and the lower for the final current.

§3. Polarization in the Barrier Layer by Applied voltages.

The author finds a polarization effect in this experiment; that is, immediately after removing the applied voltage through the rectifier, we can observe discharge currents flowing in the reverse direction against the current by the applied field. This effect is a well known polarization effect which is observed in conductivity measurements of dielectrics.(3) Its mechanism has not been explained clearly, but the space charge of ions which diffuse through the crystal is found to be the cause of this effect, making the effective field through the crystal smaller and an antielectromotive force appear when the applied voltage is removed. In other words, this phenomenon is the charging and discharging processes of ions through dielectries.

The same phenomenon as the above is observed in our case. Immediately after removing the applied voltage, both electrodes of the rectifier are short-circuited through galvanometer of low resistance which i about one tenth of the resistance of th rectifier, and the discharge currents are observed with time.

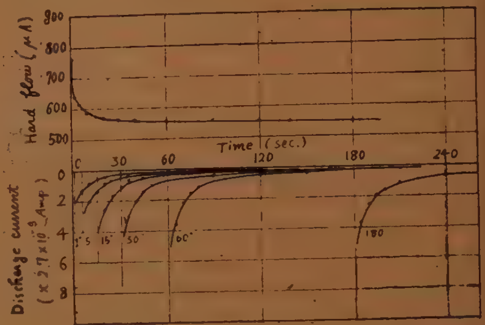

Fig. 4. Initial decay at 15 volts and discharge currents for various duration of the applying voltage.

Fig. 4 shows these currents. Applied voltages of 15 volts are impressed for 1, 5, 15, 30, 60 and 180 seconds and discharge currents are observed with time immediately after removing the outer fields. Each observation is carried on after 30 minutes o the preceding one, in which duration the polarization effect disappears almost completely, whereby allowing the hard flow to be reproducible again almost in the same manner, resulting in an unique curve of *versus* t as shown in the figure. The figure shows that the longer the duration of the applying voltage, the larger is the magnitude of the discharge current and the decrease of the hard flow with time.

Other features of the discharging currents are shown in Fig. 5 and Fig. 6. We must notice that some fractions of discharging current are short-circuited through the internal resistance of the barrier layer, but this fact does not alter the following discussions essentially.

Next, magnitude of the antielectromotive force will be estimated. From the standpoint that the initial decay of hard flow is owing to the decrease of the effective field across the rectifier by the above polarization effect, the decrease of the current corresponds to the antielectromotive force. As the applied voltage is dropped mainly only through the barrier layer, also the polarization occurs in that layer only. We may consider tha

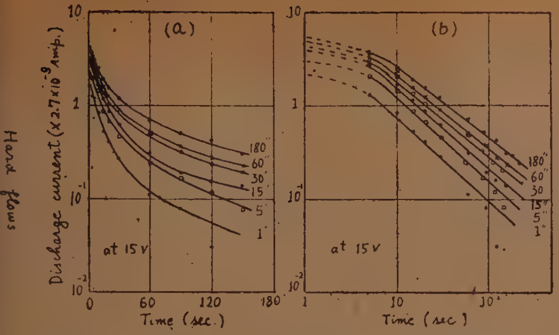

Fig. 5. Variations of polarization currents with time for various duration of an applying voltage. The dotted curves in (b) are obtained by extrapolation in (a).

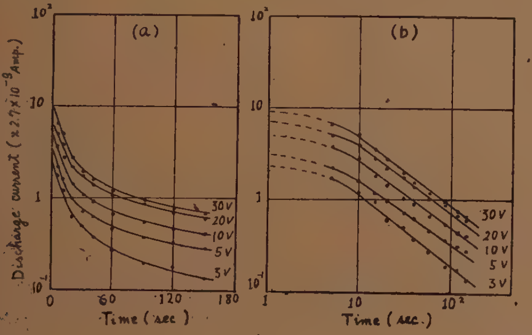

Fig. 6. Variations of polarization currents with time for various applying voltages. The dotted parts in (b) are obtained by extrapolation in (a).

the initial effective voltage in the barrier layer decreases by the amount $V_{p\infty}$, that is, the polarization voltage at infinite time, to make the initial current j_0 fall to j_∞. Thus $V_{p\infty}$ will be estimated as a voltage which is necessary to change j_0 to j_∞ on the curve of j_0 *versus* V_a in Fig. 3. This estimation is valid when the curve of j_0 *versus* V_a is approximately the same as that of j_∞ *versus* V_a. The result is shown in Fig. 7. This feature is just the same as that of the normal polarization of dielectrics.(4)

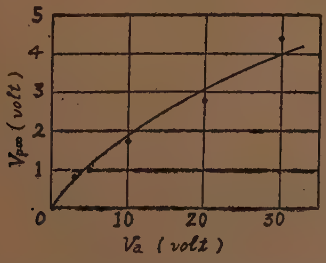

Fig. 7. Relation between the final polarization voltage $V_{p\infty}$ and applied voltages V_a.

§4. Initial Decay of the Hard Flow by the Polarization Effect.

As the polarization voltage V_p is developed across the polarization capacitor* charged up with ions, its relation with time is expressed by the next equation.

$$V_p = V_{p\infty}\left(1-e^{-\frac{t}{\tau}}\right) \tag{1}$$

Here τ is the time constant of relaxation which is determined by the physical constants of the capacitor. Then the effective voltage impressed through the barrier layer is

$$\begin{aligned} V &= V_\infty + (V_{p\infty} - V_p) \\ &= V_\infty + V_{p\infty} e^{-\frac{t}{\tau}}, \end{aligned} \tag{2}$$

where V_∞ is the final effective voltage across the barrier layer. (See Fig. 8.)

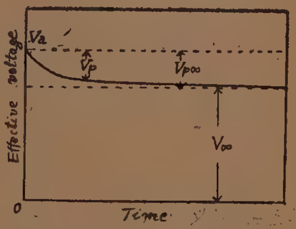

Fig. 8. Variation of the internal field with time in the barrier layer.

On the other hand, the current in the blocking direction is shown approximately as

$$j = ae^{\beta\sqrt{V}}, \quad j_\infty = ae^{\beta\sqrt{V_\infty}}. \tag{3}$$

Here j_∞ is the current at $t=\infty$; and a and β are constants. These equations hold when V or V_∞ are not small and are found to be valid in our measurements. (See Fig. 9.)

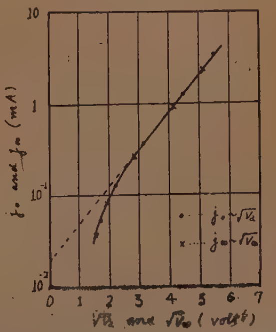

Fig. 9. Hard flow *versus* applied voltage curve.

---

* The word 'polarization capacitor' comes from Hochberg and Joffé.(4)

Thus we obtain from Eq. (2) and (3)

$$j-j_\infty=a\left(e^{\beta\sqrt{V_\infty+V_{p\infty}\exp(-t/\tau)}}-e^{\beta\sqrt{V_\infty}}\right) \quad (4)$$

Taking V_a as the applied voltage, we can easily show that $V_\infty \gg V_{p\infty}\exp(-t/\tau)$ at each voltage from Fig. 7, because $V_\infty=V_a-V_{p\infty}$. (See Table 1.) Then the next approximation may be used.

$$\left(V_\infty+V_{p\infty}e^{-\frac{t}{\tau}}\right)^{\frac{1}{2}}=\sqrt{V_\infty}+\frac{V_{p\infty}}{2\sqrt{V_\infty}}e^{-\frac{t}{\tau}}$$

Eq. (4) then reduces to

$$j-j_\infty=a\varepsilon^{\beta\sqrt{V_\infty}}\left\{\exp\left(\frac{\beta V_{p\infty}}{2\sqrt{V_\infty}}e^{-\frac{t}{\tau}}\right)-1\right\} \quad (5)$$

From Fig. 9 a is known as 18 μ A which is obtained by extending the linear part of the curve $\log j_\infty=\log a+\beta\sqrt{V_\infty}$ to $V=0$. Accordingly, $\exp(\beta\sqrt{V_\infty})$ in Eq. (3) is 128 at 30volts of ~~applied voltage,~~ making $\beta\sqrt{V_\infty}$ equal to 4.85. Thus, $\beta V_{p\infty}/2\sqrt{V_\infty}$ is 0.36 at that voltage and smaller than this value at other applied voltages in our experiment. (See Table 1.) Lastly, Eq. (5) becomes approximately to

$$j-j_\infty=a\varepsilon^{\beta\sqrt{V_\infty}}\cdot\frac{\beta V_{p\infty}}{2\sqrt{V_\infty}}e^{-\frac{t}{\tau}} \quad (6)$$

The above formula shows a linear relation between log $(j-j_\infty)$ and $-t/\tau$.

Table I

V_a (volts)	30.0	20.0	10.0	5.0	0.0
$V_{p\infty}$ (volts)	4.0	3.1	1.9	1.1	0.7
V_∞ (volts)	26.0	16.9	8.1	3.9	2.3
j_∞ (mA)	2.3	0.92	0.26	0.083	0.037
$\exp(\beta\sqrt{V_\infty})$	128	51	14	4.6	2.1
$\beta\sqrt{V_\infty}$	4.9	3.9	2.6	1.6	0.74
$\beta V_{p\infty}/2\sqrt{V_\infty}$	0.36	0.36	0.30	0.21	0.12

In the previous report(5) non-uniform structures of the barrier layer are found in our samples. From this fact, we may suppose the same structure of the polarization capacitor and the value of τ must be distributed, making the relation (6) modified to another form. Wagner(6) and Voglis(7) have reported on dielectric relaxation effect of insulators and have shown that the dependence of relaxation current on time transforms itself from an exponential form to a power form owing to the distribution of relaxation constants. In the same manner our relation (6) will be changed to the next.

$$j-j_\infty=A(t+\theta)^{-n} \quad (7)$$

Here A, n and θ are constants. In general, various kinds of relation will be derived according to the form of the distribution function of τ, but we may presume the existence of a linear relation between log $(j-j_\infty)$ and $-n\log t$ in a certain range of time. The effects of the above non-uniform nature of polarization capacitor are possiblly seen in figures (a) and (b) of Fig. 2, 5 and 6, where Eq. (7) seems likely to hold rather than Eq. (6).

§5. Discussion.

If we take q as the quantity of ions flowing into the polarization capacitor C, and V as the polarization voltage developed through it, a relation

$$C=q/V \quad (8)$$

is obtained. From Fig. 4 we can estimate the order of q as 5×10^{-7} Amp.sec.* for the case of applying voltage of 15 volts for 3 minutes** and from Fig. 7 V as 2.5 volts, so C becomes 0.1 $\mu f/cm^2$. Considering that the capacity of barrier layer is 0.01 $\mu f/cm^2$ in order, the polarization layer, that is, the space charge layer of diffused ions, which is the cause of polarization effect, is about one tenth of the barrier layer in thickness.

Next, the resistance for the movement of ions which flow into or out of the polarization capacitor will be obtained. At the same condition as mentioned above, that is, at 15 volts of applied voltage for 3 minutes, the initial discharge current from the capacitor is about 2×10^{-8} amp. (See Fig. 4) and the effective voltage across the barrier layer at that instant is about 13 volts, because the applied voltage is 15 volts and the antielectromotive force is 2.5 volts. Thus the resistance for the flow of ions is $1.2\times10^9\ \Omega/\text{cm}^2$. We must notice that this resistance is independent of the resistance of the barrier layer which is for the electronic carrier, being much smaller in order. Then the relaxation time constant which determines the charging and discharging process of the capacitor accompanying the appearing and disappearing of polarization voltage, is of the order of 10^2 seconds. This value is allowable for τ found in the present observations. (See Fig. 2 (a), 5 (a) and 6 (a).)

---

* Fig. 5(b) shows that n in Eq. (7) is smaller than unity, making q not to converge, but from the physical meaning of this phenomenon it must converge to a certain value. From this consideration the curve in the figure must bend down at higher values of t and this tendency appears at even $t=180$ sec. in the figure.

** The polarization voltage caused by applying voltage for 3 minutes is almost equal to $V_{p\infty}$ practically.

As for the voltage dependence of the present effect, from Eq. (6) we can derive approximately a linear relation between log $(j-j_\infty)$ and $\sqrt{V_\infty}$ for a given time. The experimental results are in Fig. 10 and they show the validity of the above relation.

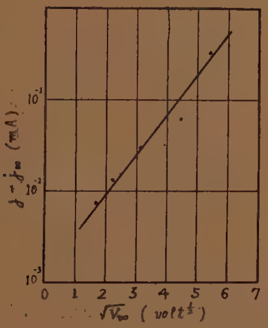

Fig. 10. The curve of $j-j_\infty$ *versus* $\sqrt{V_\infty}$. The inclination of the curve is just equal to that of Fig. 9, showing that in Eq, (3) and (6) coincide with each other.

§6. Conclusion.

In the present survey the relaxation phenomenon of the hard flow of the selenium rectifier is studied and it is found that the polarization effect occured in the barrier layer is the cause of this phenomenon. The Joule's heat occuring in the barrier layer by the passage of currents may influence the above considerations a little in the real case.

An antielectromotive force is observed also in the forward direction, but the creep phenomenon has another type than that in the blocking direction, perhaps owing to the intense Joule's heat occuring in the barrier layer.

The temperature dependence of the polarization effect is tried to detect but the relaxation time is so large to carry on measurements in short succession at low temperatures. For instance, no appreciable decay of polarization is observed in almost one hour at -180°C in case of our sample.

Hysterisis phenomena, often observed in measuring of characteristics of the selenium rectifier, may perhaps be attributed to the polarization effect, because the results will be influenced so much, if rectifier currents are measured while polarization still remains. It will be desired to avoid the relaxation effect of the selenium rectifier that surveies are carried on materials of the front electrode metal and impurities in selenium itself.

The auther wishes to express his sincere thanks to Dr. A. Kobayashi and his collaborators for their encouragements.

References.

(1) H. K. Henish: "*Metal Rectifiers*", Oxford, (1949).
(2) M. Tomura: J. Phys. Soc. Jap. **5** (1950), 349.
(3) M. F. Manning and M. E. Bell: Rev. Mod. Phys. **12** (1940), 215.
(4) E. Hochberg und V. Joffé: Z. f. Phys. **66** (1930), 172.
(5) M. Tomura: J. Phys. Soc. Jap. **5** (1950), 222.
(6) X. W. Wagner: Ann. d. Phys. **40** (1913), 817.
(7) G. M. Voglis: Z. f. Phys. **109** (1938), 52.

JOURNAL OF THE PHYSICAL SOCIETY OF JAPAN, Vol. 6, No. 5 September—October, 1951

On the Plastic Deformation of Zinc Bicrystal I.

By Tomoyosi KAWADA.

Government Mechanical Labaratory, Ministry of International Trade and Industry, Suginami-ku, Tokyo.

(Received November 18, 1950)

The stress-strain curves of zinc speciemens consisting of two crystals has been studied in order to discuss the effect of grain boundaries. In each crystal of the bicrystal specimens the inclination of base plane was fixed at 50° while the angle α between the plane of grain boundary and the plane containg both the specimen axis and the direction of maximum slope of the slip plane was varied as 0°, 45°, 90°,..... 315°. The specimen extended fairly well and the stress-strain curve varied systematically with the change of α in each crystal. The shape of the cross-section of the specimen changed sometimes into the elliptical form and sometimes into the heart-shaped or the wing-shaped form according to the angle α. Moreover the specimen twisted in some cases.

§1. Introduction.

Except for a few properties such as elastic moduli and electrical resistivity, many properties of polycrystals cannot be explained by simply taking appropriate average over single crystals, since they are influenced by grain boundaries. In order to discuss the effect of such grain boundaries, it is necessary to distinguish the actual properties of grain boundaries from the mutual interaction of the neighbouring grains on one another.

The only quantitative results concerning the mechanical properties of grain boundaries were obtained by T. S. Kê(1), who has clarified the viscous behaviour of grain boundaries in several metals. On the other hand, the mutual interaction of neighbouring crystals has been observed by a number of workers, and one of the most important investigations on such effects is that by B. Chalmers(2). He prepared cylindrical specimens of tin consisting of two crystals, separated by a longitudinal boundary. The crystals were orientated similarly with respect to the axis of the cylindrical specimen so that a rotation through a certain angle A about this axis of specimen would bring one into coincidence with the other. Using a specially designed extensometer he examined the yield stress, i.e., the minimum strees that causes a measurable extension, and plotted it against the angle A. Thus, he was led to a conclusion that the grain boundary consists of transitional lattice, but he did not take the stress-strain curves.

In the present experiment we have studied the stress-strain curve as well as the change of the shape of cross-section of zinc bicrystal specimens. The deformation of zinc is simple and easy to analyse as compared with that of tin, since the former belongs to hexagonal lattice while the latter to tetragonal lattice. Thus, we have been able to discuss qualitatively the mutual interaction of neighbouring crystals.

§2. Experimental procedure.

The bicrystal specimens were all made from the same ingot of "Kamioka" zinc (Zn: 99.994%, Pb: 0.003%, Cu: 0.001%, Fe: 0.002%, Cd, Bi, Ag: trace) by Chalmers' moving furnace method.

Now we use the following notations:

χ_1, χ_2: angle between the specimen-axis and the direction of maximum slope of the slip-plane, the suffixes 1 and 2 referring respectively to each crystal of the bicrystal.

α_2, α_2: angle between the plane of grain boundary and the plane containing both the specimen-axis and the direction of maximum slope of the slip-plane. They are measured in the counter-clockwise sense from the grain boundary.

For the sake of simplicity we used seed crystal whose direction of slip coincided with the direction of maximum slope of the slip-plane. Thus, the direction of slip of each crystal of bicrystal was almost equal to the direction of maximum slope of the slip-plane. We tried to prepare bicrystal whose χ_1 and χ_2 were both 50°, because, if χ_1 and χ_2 were small, twinning occurred during elongation so that the course of extension-test became very complicated. Bicrystal specimens whose χ_1 and χ_2 were small could be prepared easily, but those for which χ_1 and χ_2 were about 50° were seldom grown more than 2~3 cm in length. Thus, the gauge length of specimens used in our experiment was 15 mm. We tried to prepare specimens whose α_1 and α_2 vary at an interval of 45° as shown in Fig. 1. In this figure, the circle represents the cross-section of the specimen and the diameter in the middle represents the grain boundary, while the arrows in the two semi-circles represent respectively the directions of α_1 and α_2. As shown in the figure, α_1 is equal to 90°, 45° and 0° in series A, B and C respectively, while in each series α_2 varies from 0° to 360° at an interval of 45°. The other series for which α_1 is more than 135° are equivalent to some of the above series. Of these 24 types, 11 types are equal to each other, so that there remain only 13 independent types. Moreover, of these 13 types, Nos. 3, 10 and 17 are all single crystals if the angles α and χ assume exactly the values as shown in Fig. 1. Thus we aimed to prepare specimens such that (1 in series A, $\alpha_1=90°$ and $\alpha_2=270°\rightarrow0°\rightarrow90°$; (2) in series B, $\alpha_1=45°$ and $\alpha_2=0°\rightarrow360°$; (3 in series C, the type No. 21. But, in practice, we could not obtain such bicrystals that assumed exactly the desired values of α and χ, because it was very difficult to fix two thin flexible seed crystals in good orientation, notwithstanding that the continuation of the seed crystal and the crystal grown from the seed were fairly good.

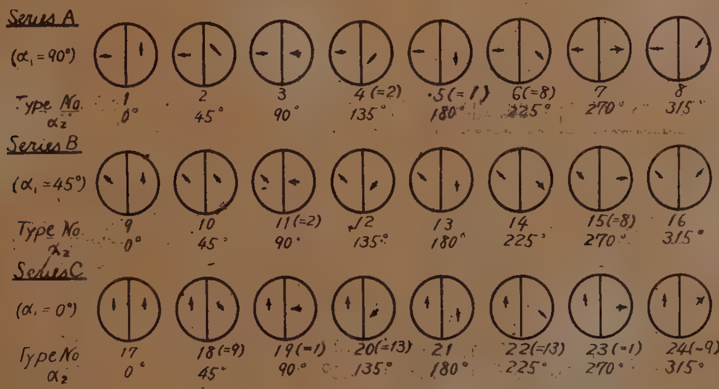

Fig. 1

The orientation of specimens was determined by X-ray for the single crystals and by optical reflection method for the bicrystals⁽³⁾. Polanyi type tensile testing mechine was used, by which we could measure load and elongation within the errors of ±10g and ±1μ respectively. The diameter of the specimen was about 2 mm, its gauge length 15 mm and the tensile speed 5μ/sec.

§3. Results of experiments.

We shall now describe the results of experiments concerning the stress-strain curv and the change of external appearance o the specimen during extension. As mentione before, we could not prepare specimens tha

Table 1.

Specimen No.	α_1	α_2	γ_1	γ_2	Tensile Strength kg/mm²	Elogation %
11	90°	268°	55°	55°	1.18	115
99	90°	275°	56°	46°	1.14	133
6	90°	280°	70°	63°	1.14	147

had exactly the orientations as shown in Fig. 1, and the orientation differed a little from specimen to specimen. Moreover, some fluctuations were found in the results of the tension test, one example of such fluctuations being shown in Table 1 and Fig. 2. (Here we aimed at the preparation specimens for which $\alpha_1=90°$, $\alpha_2=270°$ and $\chi_1=\chi_2=55.°$) It will be seen that the effect of large value of χ clearly appears in case of specimen of No. 6. In every type, a typical one was selected from the results of tension test for 3~5 specimens. They are shown in Table 2 and Fig. 3A, 3B and 3C.

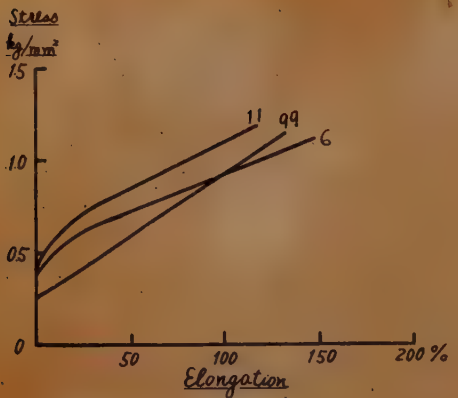

Fig. 2

Table 2.

Series A

Specimen No.	Type	α_1	α_2	χ_1	χ_2	Tensile strength km/mm²	Elongation %
5	single crystal			47°		1.36	170
99	7	90°	275°	56°	46°	1.14	133
94	7–8	83°	305°	54°	54°	1.60	175
130	8	81°	319°	52°	56°	1.70	153
71	8–1	98°	345°	57°	62°	1.92	135
107	1–2	103°	16°	60°	55°	1.68	100
41	2–3	80°	75°	56°	47°	1.30	100
134	3	90°	90°	58°	58°	1.20	107

Series B and C

Specimen No.	Type	α_1	α_2	χ_1	χ_2	Tensile strength km/mm²	Elongation %
22	7–16	77°	285°	50°	50°	1.78	172
124	16	63°	312°	53°	45°	1.90	120
101	16–17	44°	338°	62°	62°	2.12	100
19	14	56°	202°	72°	68°	1.29	115
154	10	40°	48°	45°	50°	1.65	140
68	12	25°	155°	67°	60°	2.18	75
106	21	17°	196°	41°	50°	1.38	100

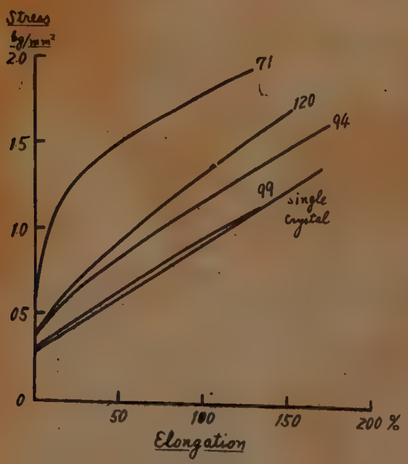

Fig. 3. A.

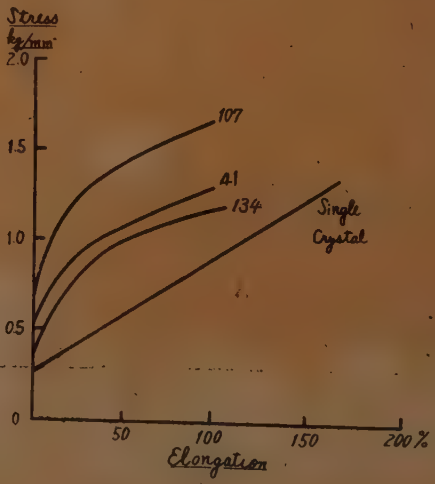

Fig. 3. B.

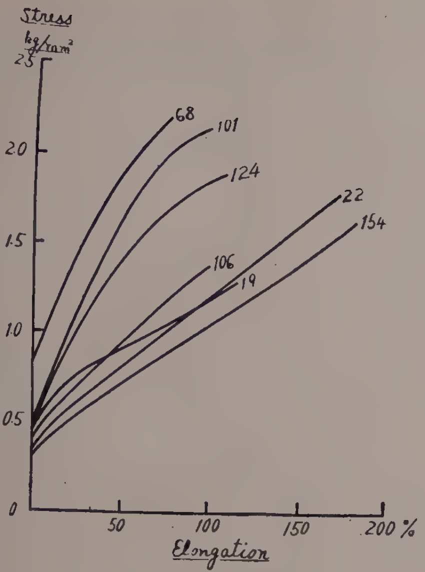

Fig. 3. C.

As mentioned before, we used cylindrical specimens with gauge length of 15 mm and diameter of about 2 mm, so that the specimens did not elongate sufficiently. Thus, for example, a single crystal specimen with gauge length of 15 mm fractured at the elongation of 150%, while a specimen with gauge length of about 30 mm elongated more than 300%. However, the stress-strain curves of both specimens were almost similar in form till the former specimen fractured. Thus in the above results the data of elongation have only a comparative meaning.

The stress-strain curve for the specimen of the type No. 7 was almost equal to that of a single crystal and the shape of cross-section of the specimen after elongation was an ellipse as shown in Fig. 4. The stress-strain curve of the specimens of type Nos. 8 and 1 rose as the value of α_2 increased from 270 to 360. The external appearance of the specimen was changed during elongation, a photograph of the cross-section of the specimen of the type No. 1 after extension being shown in Fig. 5. Moreover, the specimen of the type No. 8 twisted when it was elongated as shown in Fig. 6, i.e., the specimen twisted in one direction from one end to about the middle of the specimen and then twisted back. This twisting could be seen apparently when the specimen was elongated more than 100% and the direction seemed to be indefinite. The results of the tension test for the specimens of the types No. 2 and No. 3 resemble to those for the specimens of the types No. 8 and No. 7, i.e., the stress-strain curves descended as the value of α_2 increased from 0° to 90° and the shape α_2 of cross-section after tension test was quite similar to that of the specimens of the types No. 8 and No. 7. The only difference was that by some chance the specimen fractured at the cleavage surface. In this surface there appeared no step at the grain boundary, but the surface was not so flat as in the case of single crystal, notwithstanding that it seemed

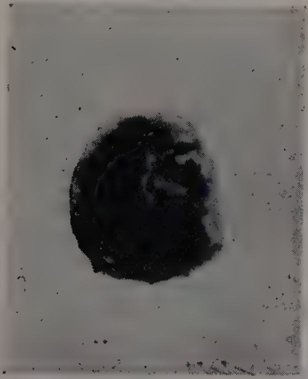

Fig. 4 ×12
$\alpha_1=90°$, $\alpha_2=275°$ $\varepsilon=25\%$

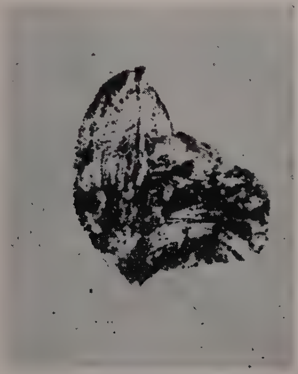

Fig. 5 ×15
$\alpha_1=100°$, $\alpha_2=350°$ $\varepsilon=66\%$

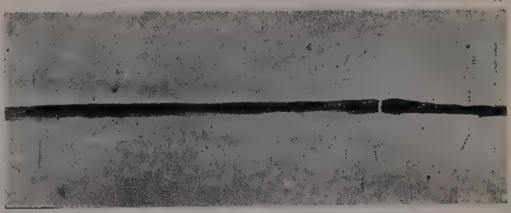

Fig. 6
$\alpha_1=84°$, $\alpha_2=350°$, $\varepsilon=100°\%$

bright and beautiful.

The specimen of the type No. 16 is thought to have smaller values of a_1 and $2\pi-a_2$ as compared to the specimen of the type No. 7. As the values of these angles became smaller, the stress-strain curve rose and the elongation decreased, while the shape of cross-section became heart-shaped as shown in Fig. 7.

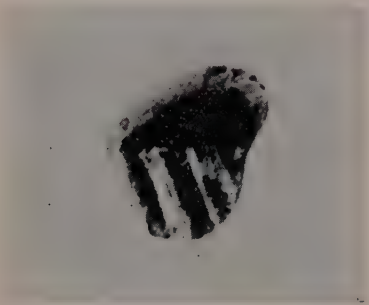

Fig. 7 ×15
$\alpha_1=30°$, $\alpha_2=315°$ $\varepsilon=50\%$

If, in the specimen of the type No. 7, the value of a_1 decreases and the value of 2π-a_2 increases, it becomes similar to the specimen of the type No. 14. The stress-strain curve rose only slightly as compared to that of the specimen of the type No. 7. The shape of cross-section became elliptic when the elongation was small, but when the specimen was elongated more than 100% it became as shown in Fig. 8.

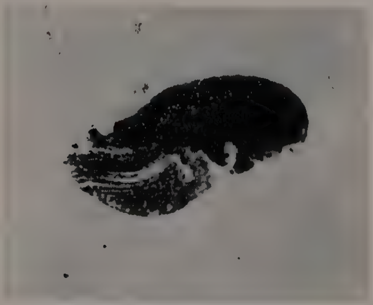

Fig. 8 ×15
$\alpha_1=128°$, $\alpha_2=282°$, $\varepsilon=100\%$

The specimen of the type No. 10 is merely a single crystal if we could prepare the specimen exactly as shown in Fig. 1, but in reality the values of a_1 and a_2 assume somewhat different values so that the stress-strain curve rose slightly as compared with that of the single crystal.

Some of the specimens used in our experiment such as the type No. 12 had rather small values of a_1 and $\pi-a_2$ as described in Table 2. Thus, it is not appropriate to compare their results with the result of other types, especially with that of the type No. 16. The stress-strain curves rose considerably high and the shape of cross-section became heart-shaped as in the case of the type No. 16. As an intermediate one between two types No. 14 and No. 16 comes the type No. 15, which is similar to type No. 8, while the intermediate type between two types No. 10 and No. 12 is the type No. 11, which is similar to the type No. 2. Each of their stress-strain curves lay about midway between those of their mother types.

The type No. 21 in series C is considered to be an extreme case of the type No. 14, and the directions of slip of both crystals are parallel to the grain boundary. The stress-strain curve rose slightly as compared to the type No. 14.

Specimens in series B sometimes twisted as in case of the type No. 8 when they were elongated fairly well, but the amount and the direction of twisting were rather indefinite.

As to the fracture of bicrystal, we found that except for a few cases as described before, the specimens of all types were drawn down to wedge-shaped and then fractured without showing any cleavage fracture.

References

1. T. S. Kê: Phys. Rev., **71** (1947) 533: **72** (1947), 41.
2. B. Chalmers: Proc. Roy. Soc., **162** (1937) 120.
2. B. Chalmers: Proc. Phys. Soc., **47** (1935) 733.

JOURNAL OF THE PHYSICAL SOCIETY OF JAPAN, Vol. 6 No. 5 September–October, 1951

Young's Modulus and Internal Friction of Polyvinylalcohol.

N. TOKITA and H. KAWAI.

Kobayasi Institute of Physical Research, Kokubunji, Tokyo.

(Received January 13, 1951)

The dynamical Young's moduli (E) and the internal friction $\frac{\Delta W}{2\pi W}$ (ΔW: energy dissipation per cycle) of amorphous films of *P.V.A.* were observed under the various conditions. (1) Effect of temperature; E is almost constant at the room temperature, but it decreases rapidly beyond the characteristic temperature, which may be considered as the 2nd-order transition temperature, and it tends to the constant value at higher temperature. $\frac{\Delta W}{2\pi W}$ increases gradually from the room temperatnre and saturates to the constant value at higher temperature. (2) Effect of humidity; E increases slightly up to R. H. 35% and beyond this point it decreases rapidly with increase of humidity, $\frac{\Delta W}{2\pi W}$ is almost constant up to 25% but it increases rapidly beyond this point and tends to the constant value at higher degree of humidity. Besides, effects of tention, degree of polymerization and frequency were reported shortly. The experimental formula which represents the temperature dependence of E was devised and this formula also was suitable to the experimental results of *P.V.C.* The attempt to explain this formula from the statistical treatment of crystallite part and amorphous part was tried.

§1. Introduction.

As the first step of the studies of the mechanical behavior of highpolymers, we chosed Polyvinylalcohol (*P.V.A.*) which had the suitable properties for our experiments; for example, it had a simple chemical structure and a convenient temperature at which some of the physical properties changed rapidly.

Using the dynamical method,⁽¹⁾ which was reported in the previous paper by the authors the Young's modulus and the internal friction of *P.V.A.* have been studied under the various conditions; *e.g.*, the temperature, the humidity, and the tension etc.

From these experimental results, we found an empirical formula for the temperature dependence of Young's modulus.

In this paper we will report the experimental results, the empirical formula, and the simple consideration of it.

§2. Preparation of Samples.

We made use of the thin films of *P.V.A.* as the samples, which are prepared as follows:

The powder of *P.V.A.* which has a known average degree of polymerization determined by the viscosity measurements was dissolved in the distilled water and the bubbles in this solution were taken out. A small amount of this solution was poured on the glass plate floating on the mercury to make a flat film and dried very slowly in a desiccator at 40°C. After about 48 hr, the thin film was prepared and it's thickness was about 4.0×10^{-2}*mm.* From this film, the small ribbons (about 5*mm.* width, 25*mm* length, and 4.0×10^{-2}*mm* thickness) were cut off and used for our measurements.

§3. Experimental Results.

Since the method used to measure was reported in the previous paper, we will not explain it in detail in this paper.

(1) The Effect of Temperature.

Fig. 1 shows the experimental results of temperature dependence of Young's modulus (E), internal friction $\left(\frac{\Delta W}{2\pi W}\right)$, and the dissipated energy per cycle (ΔW) under the following conditions: the degree of polymerization 900, the tension 160 g/mm^2, the vibrating frequency 260 c/s, and the relative humidity (*R.H.*) 0%. In abscissa, the temperature is denoted in centigrade and in ordinate, the

Young's modulus and the internal friction are denoted in logarithmic scale.

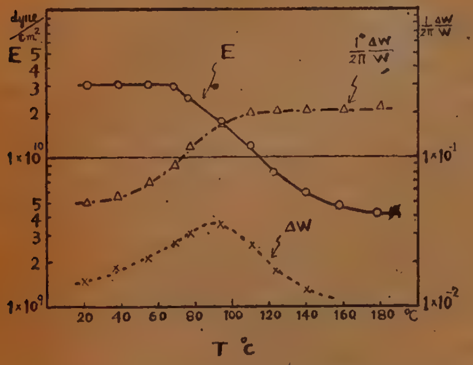

Fig. 1. The temperature dependence of E, $\frac{\Delta W}{2\pi W}$, and ΔW.

From room temperature to 68°C the Young's modulus is constant (3.0×10^{10} *dyne/cm*²). It, however, begins to decrease rapidly with a rise of temperature beyond 68°C and tends to the definite value (3.6×10^{9} *dyne/cm*²) gradually.

Because the temperature at which the value of Young's modulus changes rapidly is characteristic of *P.V.A.*, we will describe this temperature as T_0 hereafter.

The values of internal friction, $\frac{\Delta W}{2\pi W}$, where ΔW and W are the dissipated energy per cycle and the energy of vibration respectively, increase from room temperature and show the maximum gradient at about 70°C and tend the constant value (2.0×10^{-1}) at higher temperature.

In our experimental condition the product of Young's modulus and the internal friction shows the value which is proportional to ΔW at the constant strain. As shown in Fig. 1, the value of dissipated energy ΔW has a maximum value in the vicinity of 89°C.

We carried out the measurements elevating the temperature at various speeds (3 *min*, 15 *min*, and 1 *hr* per degree), but we could not find any difference between them.

(2) The Effect of Tension.

Fig. 2 shows the experimental results of the same sample under the various tensions, 160 *g/mm*², 220 *g/mm*² and 290 *g/mm*². The values of Young's modulus increase to 3.0×10^{10}, 3.4×10^{10}, and 3.7×10^{10} *dyne/cm*² respectively. The characteristic temperature, T_0, shows the tendency to decrease towards the lower one, 68°C, 50°C, and 46°C with increase of tensions. We do not find any remarkable difference in the internal friction.

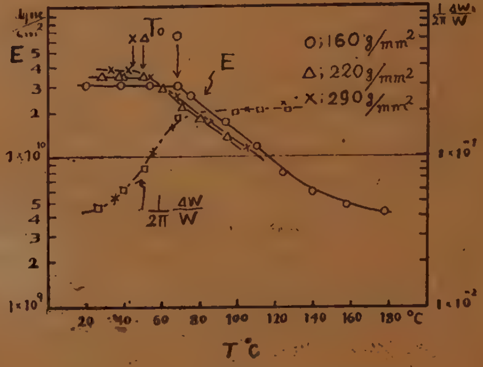

Fig. 2. The tension dependence of E, $\frac{\Delta W}{2\pi W}$, and T_0.

(3) The Effect of Relative Humidity.

Fig. 3 shows the experimental results of humidity dependence of Young's modulus and the internal friction at the tension 160 *g/mm*² and the temperature 30°C. It is shown that the Young's modulus increases a little with increase of humidity, but beyond *R.H.* 35% it decreases rapidly. It was impossible to observe the Young's modulus at higher humidity than 80% by our measuring method on account of the flow of *P.V.A.* films. The value of internal friction is almost constant from *R.H.* 0% to about 25%, but it increases rapidly beyond 25% and gradually tends to the definite value.

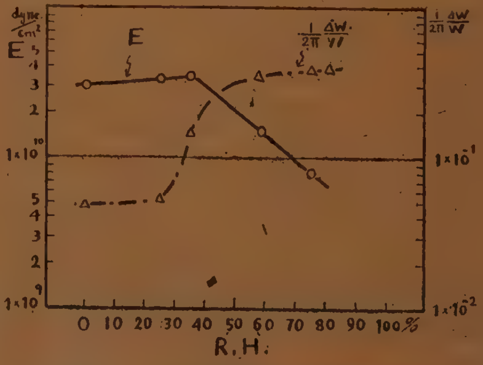

Fig. 3. The humidity dependence of E, $\frac{\Delta W}{2\pi W}$ at 30°C.

It is very interesting to us that there is a remarkable similarity between the temperature effect and the humidity one.

Fig. 4 shows the results of temperature dependence of Young's modulus and the internal friction at the various humidities (0%, 25% and 56% at 30°C). Though the results at 0% and 25% show no remarkable difference, the value at 56% is peculiar: namely, Young's modulus is so small and the internal friction is large even at low temperature.

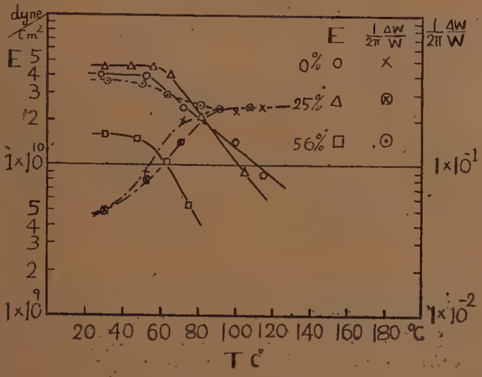

Fig. 4. The temperature dependence of E, $\frac{\Delta W}{2\pi W}$ at various humidities.

(4) The Effect of Degree of Polymerization.

We observed the temperature effect about the three kinds of *P.V.A.* films which had the different degrees of polymerization (900,1000, 1300). We could not find any difference in these Young's moduli, internal friction, and characteristic temperatures within our experimental errors. Therefore, the vibrational properties of *P.V.A.* are not affected at all due to such a difference of degree of polymerization.

(5) The Effect of Frequency.

The measurements of the vibrational properties over the wide frequency range have not yet been carried out. At least, however, it has been observed that the Young's modulus, the internal friction, and the characteristic temperature between 200 *c/s* and 1000 *c/s* are almost constant at the same conditions, but these values very much depend on the temperature and the humidity.

§4. An Empirical Formula for Temperature Dependence of Young's Modulus.

First we examined whether the viscoelastic behavior of *P.V.A.* can be explained by Kuhn's model, which consists of the various Maxwell models connected in parallel (see Fig. 5.). From this model the following relationship between the elastic constant and the temperature is derived:(2)(3)

$$\frac{\log G_L-\log G}{\log G_L-\log G_H}=e^{-\frac{E_m}{RT}}, \qquad (1)$$

where G_L and G_H are the elastic constants at low and high temperature respectively, and E_m is the average activation energy.

There must be the linear relation between the logarithm of the left hand of Eq. (1) and $1/T$ (°K). The dotted curve (in Fig. 6) calculated by Eq. (1) using the values of Fig. 1 is not straight, therefore it is impossible to explain the Young's modulus of *P.V.A.* by Kuhn's model.

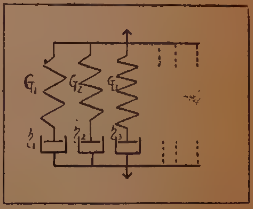

Fig. 5. Kuhn's model.

We derived, next, the following empirical formula,

$$\frac{\log E_L-\log E}{\log E-\log E_H}=A\cdot e^{-\frac{B}{T}}, \qquad (2)$$

where E_L, E_H are the Young's moduli at low and high temperature respectively, A and B are both constants.

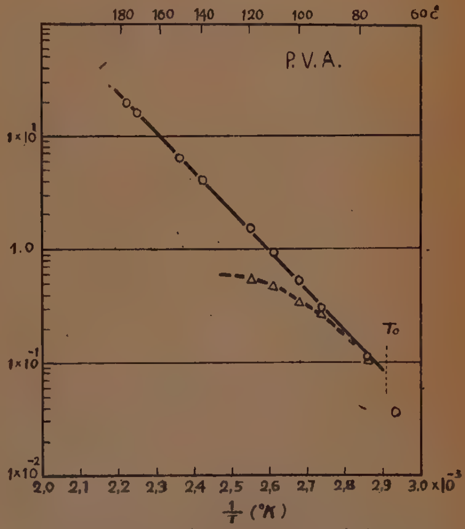

Fig. 6. The result by Eq. (2) (solid line) and result by Kuhn's model (dotted line) for *P.V.A.*

As shown in Fig. 6, the solid line calculated by Eq. (2) using the same values in

Fig. 1 is the straight one at higher temperature than T_0. Therefore Eq. (2) gives a good relationship between the Young's modulus and the temperature in the case of *P.V.A.* By applying this formula to the experimental results of Polyvinylchloride (*P.V.C.*),⁽⁴⁾ it was showed that Eq. (2) was also acceptable (see Fig 7).

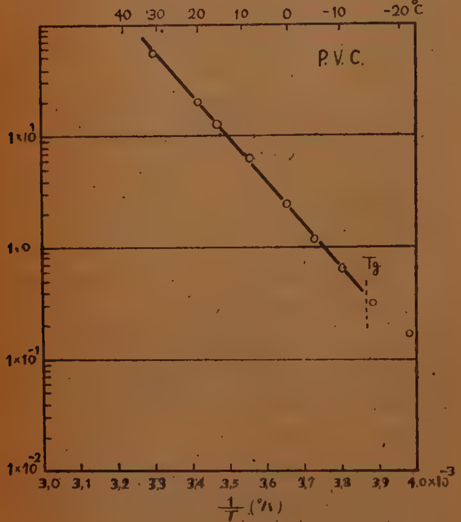

Fig. 7. The result by Eq. (2) for *P.V.C.*

§5. Discussion.

We know that *P.V.A.* and *P.V.C.* consist of the crystallite parts and the amorphous parts.⁽⁵⁾ Now we consider the potential diagram as Fig. 8, where the state denoted by 1 is that each molecule conbines with each other and makes a crystallite or a junction forming the network, the other state denoted by 2 is that each molecule rotates freely, namely, the amorphous state.

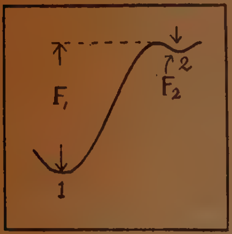

Fig. 8.
Potential diagram.

We denote the number of crystallites in N_L and N_H at low and high temperature respectively. N_1, and N_2 being the numbers of crystallites at 1 and 2 state respectively at any temperature, there is a following relation in thermal equilibrium,

$$\frac{N_2}{N_1}=e^{-\frac{\Delta F}{RT}}, \tag{3}$$

where $\Delta F=F_1-F_2$ is the difference between the free energies at 1 and 2 state (see Fig. 8).

From the following relations between N_L, N_H, N_1 and N_2,

$$N_2=N_L-(N_1+N_H) \tag{4}$$

and

$$N_1=(N_1+N_H)-N_H, \tag{4'}$$

Eq. (3) can be transfered as follows,

$$\frac{N_L-(N_1+N_H)}{(N_1+N_H)-N_H}=e^{\frac{\Delta S}{R}}\cdot e^{\frac{-\Delta E}{RT}}, \tag{5}$$

where ΔS and ΔE are the differences between these entropies and these energies respectively.

If we may assume the next relation between the Young's modulus, E, and the number of crystallites, N,

$$\log E=a\cdot N, \tag{6}$$

where a is constant, it will be possible to explain the emperical formula Eq. (2). By the experimental results of vulcanization of rubber,⁽⁶⁾ it may be shown that the relationship as Eq. (6) is plausible for rubber, therefore, we consider that Eq. (6) may be reasonable for *P.V.A.* and *P.V.C.* but the experiments to prove this relation for the highpolymer have not yet been carried out.

We calculated the values of ΔE and ΔS for *P.V.A.* and *P.V.C.* using Eq. (2), (5), and Eq. (6), namely,

for *P.V.A.* $\Delta E=15.0$ *Kcal/mol*,
$\Delta S=40.5$ *E. U.*,
for *P.V.C.* $\Delta E=17.8$ *Kcal/mol*,
$\Delta S=66.3$ *E. U.*

If we postulate that there is any functional relation between E and N, we may explain the effects of humidity and tension qualitatively. The water molecules, in the beginning, are adsorbed to the *O-H* radicals of amorphous parts, then the Young's modulus and the internal friction are almost constant. But as soon as the intermolecular hydrogen bonds of crystallites begin to be broken by the adsorbed water molecules, the Young's modulus will decrease very rapidly, for the number of crystallites at 1 state decreases.

Next, the temperature T_0, at which the crystallites begin to be excited to the 2 state, decreases to the lower one, as the values of ΔE decrease with increase of tension.

The consideration about the internal friction has not yet been established.

If we decide the temperature at which N_1 is equal to N_2 from the experimental results of ΔE and ΔS, we get the value 87°C. This value is almost equal to the temperature of maximum value of ΔW, 89°C. We are very interested in this result, for this may give some suggetions about the mechanism of internal friction.

References.

(1) H. Kawai and N. Tokita: J. Phys. Soc. Jap. **5** (1950), 17.
(2) J. Furukawa: Bull. Inst. Chem. Res. Kyoto Univ. **21** (1950) 20.
(3) R. Simha: J. App. Phys. **13** (1942), 201.
(4) T. Alfrey: *Mechanical Behavior of Highpolymers.* p. 437. (1948)
(5) T. Alfrey: J. Colloid. Sci. **4** (1949), 211.
(6) R. Houwink: *Elasticity, Plasticity and Structure of Matter.* p. 182, (1937).

JOURNAL OF THE PHYSICAL SOCIETY OF JAPAN, Vol. 6 No. 5 September—October, 1951

Effects of Firing Temperature on the Dielectric Properties of Barium-Titanate Ceramics.

By Akio KOBAYASHI and Hiroo HINO.

Research Laboratory, Tokyo Shibaura Electric Co.

(Received October 21, 1950)

The slopes of tan δ for voltage and the initial tan δ of barium-titanate ceramics, which were fired at three different temperatures has been measured in the temperature range from 150°C to −183°C. It was shown that below the Curie point the voltage region, where the values of initial tan δ did not change, were larger and the slopes of tan δ smaller, the higher the firing temperatures. Temperature dependence of the voltage region giving constant tan δ show three remarkable knicks corresponding to the phase changes of the crystals.

It has been well known that the dielectric characters of barium-titanate ceramics are greatly influenced by the firing conditions, that is firing temperature and firing time. Because it has been very difficult to sinter the pure barium carbonate and pure titanium oxide, so we introduced a few per cent of ZrO_2 and CaO for mineralizer. We measured three kinds of samples under the different firing conditions; in which (1) Sample BT-(1) was fired at the temperature 1420°C. for 7 hours, then kept in the prepared oven at 1000°C. and cooled naturally, (2) Sample BT-(2) was fired at 1430°C. for 7 hours more, after the same firing as Sample (1), and cooled naturally, and (3) at last Sample BT-(3) was fired at 1460°C. for 7 hours more, after the same firing and cooled naturally, and (3) at last Sample BT-(3) was fired at 1460°C. for 7 hours more, after the same firing as for Sample (2), and cooled naturally.

We have used a Wien-bridge at audio-frequencies to measure the dielectric constant and tan δ. The Curie points of those three samples were all coincident with the temperature 120°C. Thus we may expect that our mineralizers do not change the lattice consitant of $BaTiO_3$.

Moreover, besides the Curie point, the anomalous points of dielectric constant,(1) i.e. the polymorphic transition points, were found in the vicinity of 70°C. and 5°C., which have been shown by the single crystal.(1)

The results are shown in the following table. It is shown in the table that by the firing at the higher temperature, the dielectric constant becomes smaller. The same tendency is also shown in that is given by the slope of the curve plotting $1/\varepsilon$ vs T above the Curie point.

Now the dependency of ε and tan δ upon the small a.c. field is very interesting problem. For the rochelle salt it has been investigated by B. Kurtschatow & I. Kurtschatow(4) and by A. Zeleny & J. Valasek that the critical field strength E_0, from which the dielectric constant started up steeply, was named the jump field. On the rochelle salt, David⁽⁶⁾ has explained the above results by the analogy of ferromagnetism, but it has not yet been shown what are the sensitive factors for the value E_0.

At first, we measured the a.c. dependency of ε, but its variation was very slow, and hence the Jump field could not be accurately defined from those curves, whereas the dependency of tan δ upon the a.c. field strength had very clear kinks to define the jump field. The results are shown in Fig. 1.

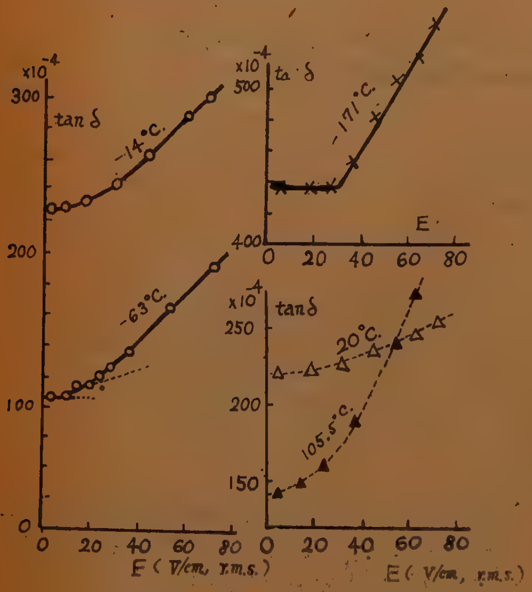

Fig. 1. The dependency of tan δ upon the small a.c. field strength E measured at the frequency 8 Kc. for Sample BT-(2)-C.

For instance, at -171°C. tan δ is constant up to the value of 30 V/cm, where the field is the r.m.s. value, and this value corresponds to the jump field of ε.

The field dependency of tan δ beyond E_0 is approximated by the following equation;

$$\tan\delta \times 10^4 = mE + a$$

where E is the a.c. field strength in V/cm
m and a are the temperature dependent constants

From those results it is shown that for $BaTiO_3$ Rayleigh's law is established alike to the rochelle salts. Fig. 2 shows the temperature dedency of E_0 and m of the above equation.

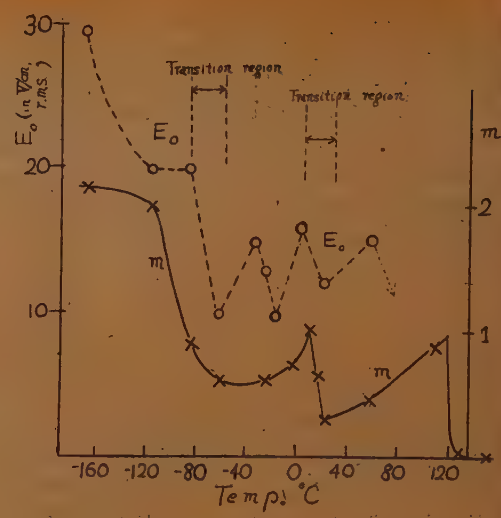

Fig. 2. The temperature dependency of E_0 and m for Sample BT-(2)-c.

At last the hysteresis curves were figured on a Braun tube. The coercive force E_c for Sample (2) is shown in Fig. 3. The coercive forces E_c have nearly the same value for different samples, and the temperature dependency of E_c is interesting in such the points that it shows the polymorphic transitions near 70°C. and 5°C.

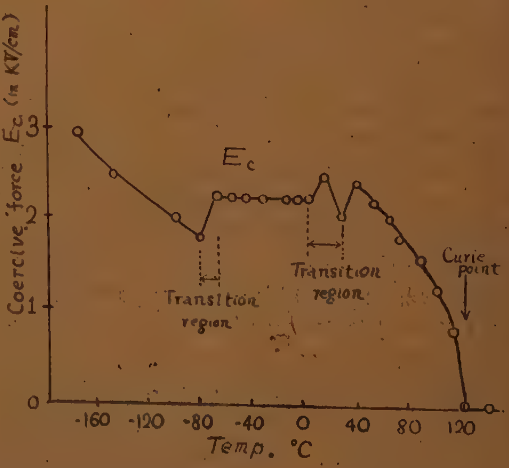

Fig. 3. The temperature dependency of Coercive force E_c from the hysteresis curve for Sample BT-(2)-b.

The following Table is summarized the observed results;

Table

Sample	BT (1)-b	BT (2)-c	BT-(3)-b
Firing-temp. & Firing-time	1420°C. 7 hrs.	1420°C.+1430°C 7 hrs. 7 hrs.	1420°C+1430°C+1460°C 7 hrs. 7 hrs. 7 hrs.
ε at 20°C. 1/C	1,590 0.76×10^{-5}	954 1.05×10^{-5}	255 $2.10 \quad 10^{-5}$
E_0 in V/cm. m } at −180°C.	20. 2.8	32. 2.3	40. 1.5

We can derive the results as follows; the higher the firing temperature and the longer the firing time, (1) the dielectric constant ε becomes the smaller, (2) the jump field E_0 becomes the larger, and (3) the slope m of tan δ becomes the smaller.

But the coercive force E_c is scarcely depenpent on firing temperatures. In order to explain the above results, we may assume that the higher the firing temperature, (a) both the numbers of crystallites and those of domains per unit volume become smaller, and (b) the solubility of the impurities (perhaps Zr ions in Ti ion lattice points) and the internal stresses (perhaps dislocations) caused by them become the larger. We can expain the (1) to (3) results by the above assumptions. (1) Up to the jump field E_0, the displacement of domain boundaries suffers the reversible change. As the induced charges are proportional to the field strength, so tan δ becomes constant for E, which is now shown from our experimental results. Now, if the assumption (a) is correct, according to the growth of crystallite by firing, the numbers of crystallites and domains contained in them become smaller, hence the dielectric constant ε becomes smaller. Moreover, by the assumption (b), as the internal stresses prevent the displacement of domain boundaries, so the induced charges becomes smaller, that is, ε becomes smaller.

(2) Next, beyond the value E_0 the irreversible displacements are occured. By the assumption (a), therefore, the domain size becomes larger and its displacement of boundaries needs for the large field strength, then it will be shown that the value E_0 becomes larger. Also by (b), it will be shown that this is correct, whereas it needs for the larger field to overcome the higher potential of internal stresses which is caused by the solved impurities. (3) The quantity m shows the hardness of the displacement of boundaries by the applied field beyond E_0. The higher the potential hump caused by the impurities is, the degrees of jump displacement of boundaries (the Barkhausen effect) becomes smaller, therefore, it may give a smaller value of m.

Accordingly, it is revealed that both assumptions are consistent with the experimental results.

The authors thank to Mr. Togashi and Mr. Nakamura for preparing the samples and to Dr. H. Takahashi for his stimulating dissussions. The experiment was achieved by the expenditures of scientific research of the Ministry of Education.

References

(1) A. von Hippel, R.G. Breckenridge, F.G. Chesley & Laezle Tisza: Ind. & Eng. Chem. **38**, (1946) 1097.
(2) W.J. Merz: Phys. Rev, **76**, (1949) 1221.
(3) J.H. van Santen & G.H. Jonker: Nature **159**, (1947) 333; Science **109**, (1949) 632.
J.C. Slater: Phys Rev. **78**, (1 50) 748.
(4) B. Kurtschatow & I. Kurtsahatow: Phys. Z. Sowj. **3**, (1933) 321.
(5) A. Zeleny & J. Valasek: Phys. Rev. **46**. (1934) 450.
(6) R. David: Helv. Phys. Acta. **8**, (1935) 431.

JOURNAL OF THE PHYSICAL SOCIETY OF JAPAN, Vol. 6 No. 5 September—October, 1951

Resistance to the Penetration of a Bullet through an Aluminium Plate.

Jien NISHIWAKI.

Mizuho Metal Industry Co., Ltd., Tanashi, Tokyo.

(Received December 15, 1950)

Neglecting the small values of the frictional force, the resistance dRv to the elementary surface area $d\sigma$ of a bullet was theoretically deduced as

$$dRv=\left(P_0+\frac{\rho}{g}v^2\sin^2\gamma\right)\sin\gamma\cdot d\sigma$$

where v is the velocity of the bullet, ρ the specific weight of the aluminium, g the acceleration of the gravity and γ the angle between the surface $d\sigma$ and the direction of its motion.

Finally, P_0 is the statical contact pressure acting on the surface $d\sigma$ and, from the results of the statical penetration test carried out with the cylindrical mandrel, the author gave it the constant value for each thickness ε of the aluminium plates.

Assuming that P_0 is independent of the angle γ, the velocity drops suffered by the conical bullets from passing through the aluminium plates were calculated from the above equation for three values $2\gamma=180°$, $90°$, $60°$ of the conical angle and four values $\varepsilon=3.2$, 4.9, 8.2, 1.21mm respectively. (Here considered only the case of the normal attack.)

These calculated values were found to be consistent with the experimental results which were obtained with respect to the same bullets shot at the same aluminium plates by a rifle.

§1. Introduction.

Several assumptions[1] have been suggested for the calculation of the frictional resistance opposed to projectiles in the bore of a gun. One of them will be used to calculate the resistance suffered by a bullet from passing through an aluminium plate.

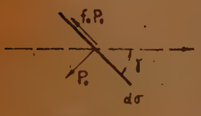

Fig. 1.

Suppose that the elementary surface $d\sigma$ moves slowly along a straight line through the aluminium making the angle of γ with the direction of motion (Fig. 1).

The resistance dR_0 to the motion will be

$$dR_0=P_0d\sigma(\sin\gamma+f_0\cos\gamma) \tag{1}$$

where P_0 is the contact pressure acting on the surface, and f_0 is the coefficient of statical friction between the aluminium plate and the contact surface.

If the volocity v of the bullet is sufficiently large, it is assumed that the particles of aluminium which come in contact with the contact surface are pushed back in the direction normal to it with a velocity equal to the component of v parallel to this direction, then the quantity of aluminium $\rho/g\cdot d\sigma\cdot {}^{dx}/_{dt}\cdot\sin\gamma$ which is displaced by the surface $d\sigma$ in a unit of time t, will give the momentum

$$\frac{\rho}{g}d\sigma\frac{dx}{dt}\sin\gamma\cdot v\sin\gamma=\frac{\rho}{g}d\sigma\, v^2\sin^2\gamma.$$

The dynamical pressure exerted on the surface must therefore be equal to $\rho/g\cdot v^2\sin^2\gamma$, where ρ and g are the specific weight of aluminium and the acceleration of gravity respectively.

Hence, in this case, Eq. (1) is replaced by

$$dR=\left(\sin\gamma+f_{v\cos\gamma}\cos\gamma\right)\left(P_0+\frac{\rho}{g}v^2\sin^2\gamma\right)d\sigma \tag{2}$$

where $v\cos\gamma$ is the relative velocity between aluminium plate and surface $d\sigma$, and $f_{v\cos\gamma}$ the coefficient of kinetic friction.

§2. Calculation for Conical Bullets.

The resistance to the conical bullets will be computed for three values $2\gamma=180°$, $90°$, and $60°$ of the conical angle (See Fig. 2), and only the case of normal attack is considered. For $2\gamma=180°$, the bullet becomes cylindrical.

Neglecting small values of $f_{v\cos\gamma}\cos\gamma$, Eq. (2) reduces to

$$dR_v=\left(P_0+\frac{\rho}{g}v^2\sin^2\gamma\right)\sin\gamma\cdot d\sigma$$

If the weight of the bullet is equal to p, the equation of motion is given by

$$\frac{p}{g}\frac{dv}{dt}=-\int\left(P_0+\frac{\rho}{g}v^2\sin^2\gamma\right)\sin\gamma\cdot d\sigma \quad (3)$$

Now it is assumed that the contact pressure P_0 has the constant value for each thickness of the aluminium plate because of the experimental results shown in the following article that it is independent of the angle γ if it is not too small as above mentioned.

Hence, Eq. (3) becomes

$$\frac{p}{g}\frac{dv}{dt}=-\left(P_0+\frac{\rho}{g}v^2\sin^2\gamma\right)\sin\gamma\int d\sigma \quad (4)$$

Denoting the depth of penetration by x which is measured from the front surface of the plate to the point of the bullet, the thickness of the plate by ε, and the height of the conical part of the bullet by h, we evaluate the integral of Eq. (4) in three steps:

1 $o\leqq x\leqq\varepsilon$

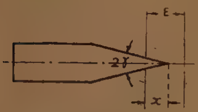

Fig. 2.

2 $\varepsilon\leqq x\leqq h$

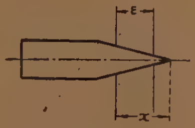

Fig. 3.

3 $h\leqq x\leqq h+\varepsilon$

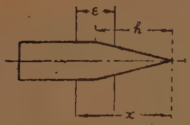

Fig. 4.

here, assumed $h\geqq\varepsilon$.

For the 1st step the area of the contact surface between the bullet and the plate is expressed by

$$\int d\sigma=\pi x\tan\gamma\cdot\frac{x}{\cos\gamma}$$

$$=\pi x^2\frac{\tan\gamma}{\cos\gamma}$$

while for the 2nd step, it is given by

$$\int d\sigma=\pi\left\{x^2-(x-\varepsilon)^2\right\}\frac{\tan\gamma}{\cos\gamma}$$

and finally for the 3rd step

$$\int d\sigma=\pi\left\{h^2-(x-\varepsilon)^2\right\}\frac{\tan\gamma}{\cos\gamma}$$

Introducing these expressions for $\int d\sigma$ into Eq. (4) respectively, we obtain the following integrals:

$$\left[\log\left(P_0+\frac{\rho}{g}v^2\sin^2\gamma\right)\right]_{V_0}^{V_1}$$

$$=-\frac{2\rho}{p}\pi\tan^2\gamma\sin^2\gamma\cdot\frac{\varepsilon^3}{3}$$

$$\left[\log\left(P_0+\frac{\rho}{g}v^2\sin^2\gamma\right)\right]_{V_1}^{V_2}$$

$$=-\frac{2\rho}{p}\pi\tan^2\gamma\sin^2\gamma\left\{\frac{h^3}{3}-\frac{(h-\varepsilon)^3}{3}-\frac{\varepsilon^3}{3}\right\}$$

$$\left[\log\left(P_0+\frac{\rho}{g}v^2\sin^2\gamma\right)\right]_{V_2}^{V'}$$

$$=-\frac{2\rho}{p}\pi\tan^2\gamma\sin^2\gamma\left\{h^2(h+\varepsilon)\right.$$

$$\left.-\frac{h^3}{3}-h^3+\frac{(h-\varepsilon)^3}{3}\right\}$$

where V_0 is the initial velocity at $x=0$, and V_1, V_2 and V' are the final velocities for each step at $x=\varepsilon$, h and $h+\varepsilon$ respectively.

Summing up these three equations, we obtain

$$\log\frac{P_0+\frac{\rho}{g}V'^2\sin^2\gamma}{P_0+\frac{\rho}{g}V_0^2\sin^2\gamma}=-\frac{2\rho}{p}\pi\tan^2\gamma\sin^2\gamma\cdot h^2\varepsilon \quad (5)$$

where $h\tan\gamma$ is equal to the radius of the bullet. Denoting this by a, and rearranging, the following final result is obtained:

$$V'^2=\exp\left(-\frac{2\rho}{p}\pi a^2\sin^2\gamma\cdot\varepsilon\right)\left\{V_0^2-\frac{gP_0}{\rho\sin^2\gamma}\right.$$

$$\left.\left[\exp\left(\frac{2\rho}{p}\pi a^2\sin^2\gamma\cdot\varepsilon\right)-1\right]\right\} \quad (6)$$

If start with the assumption $h<\varepsilon$, the same expression should be obtained.

§3. Determination of P_0.

Each of the aluminium plates which were 3.2, 4.9, 8.2 and 12.1mm thick were statically penetrated by a mandrel. The diameter of this head is equal to the bullet dia. 6.5mm, and Brinell hardness of these plates are 40-49. The tests were done with the simple cam mechanism (Fig. 5), except for the 12.1mm plate which was tested by the ordinally Amsler testing machine.

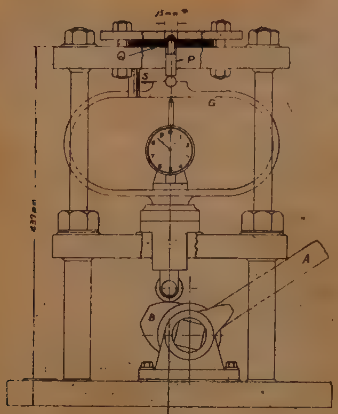

Fig. 5.

P: Mandrel, Q: Al plate, G: Pressure gauge,
A: Handle lever, B: Cam, S: Scale.

Thus the relations between the load P and the depth of penetration x were measured. The results are shown in Fig. 6—9.

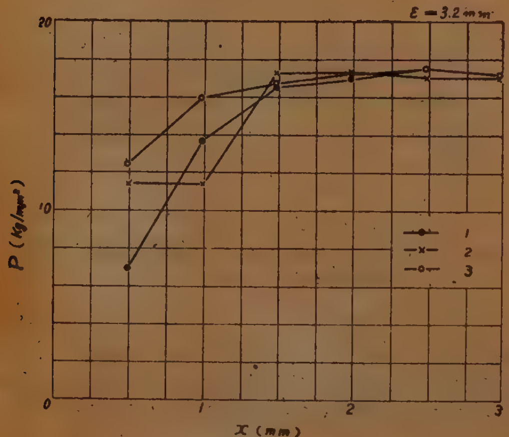

Fig. 6.

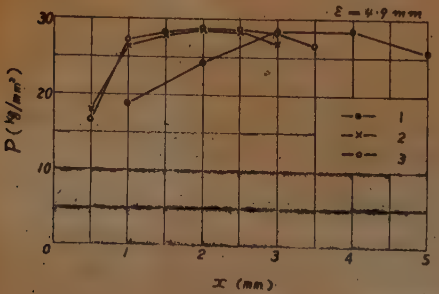

Fig. 7.

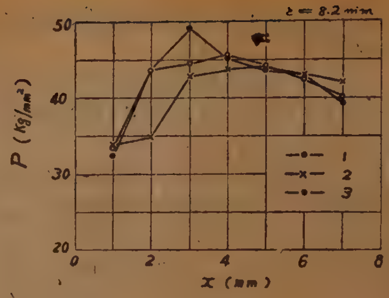

Fig. 8.

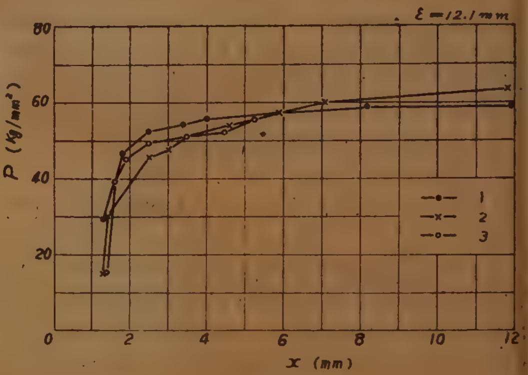

Fig. 9.

The time required for the complete penetration were about 1min. for 3.2mm, 1.5min. for 4.9mm, 3min. for 8.2mm and 4min. for 12.1mm plate, and the mandrel suffered no deformation.

Neglecting the small ranges of x for the ascending parts of these curves, we may regard P as independent of x and represent the contact pressure P_0 by the maximum of each curve.

Hence it follows:

$P_0 = 17\text{kg/mm}^2$ for $\varepsilon = 3.2\text{mm}$
$P_0 = 29\text{kg/mm}^2$ for $\varepsilon = 4.9\text{mm}$
$P_0 = 45\text{kg/mm}^2$ for $\varepsilon = 8.2\text{mm}$
$P_0 = 60\text{kg/mm}^2$ for $\varepsilon = 12.1\text{mm}$

The relation between P_0 and ε may be expressed by

$$P_0 = 5.4\ \varepsilon$$

where P_0 and are ε measured with kg/mm² and mm respectively.

§4. Relation between V_0 and V'.

Substituting the above determined values of P_0 and the following data:

$2a = 6.5\text{mm}$, $\rho = 2.7\text{g/cm}^3$
$p = 5.5\text{g}$ $g = 9.8\text{m/sec}^2$

into Eq. (6), we computed the values of V'

related to V_0 for each value of ε and h, and compared the with them experimental results.

The expriments were carried out in the usual manner; a number of steel bullets[2] were shot by a rifle aiming at the aluminium plate, and initial and final velocities which each bullet had in the front and rear of the plate were measured by the electro-magnetic oscillograph with the wire tergets.

Fig. 10 shows the results in the case of the cylindrical bullet for which $2\gamma=180°$.

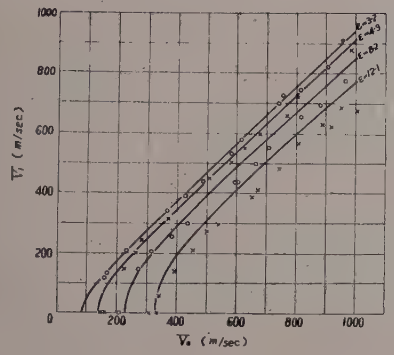

Fig. 10.

The curves represent the theoretically derived relations and the marking points the experimental data. For $\varepsilon=3.2$ and 4.9mm the experimental values lie nearly on the theoretical curves. But for $\varepsilon=8.2$ and 12.1 the experimental values lie considerably lower than the theoretical curves, except for the range of low velocities. This inconsistency may be attributed to the fact that the larger V_0 and ε are, the more the bullet is deformed, and thus the resistance suffered by it exceeds the theoretical value. In Fig. 11 and 12 are shown the deformation of the bullet for each initial velocity.

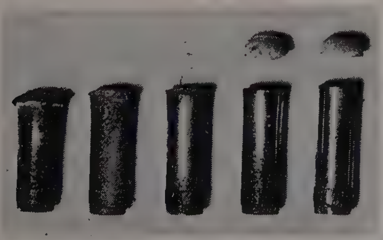

Fig. 11. Deformation of the bullets. From the left V_0=901, 691, 590, 369 and 229m/sec respectively for ε=3.2mm. On the upper, are shown the Al parts punched out.

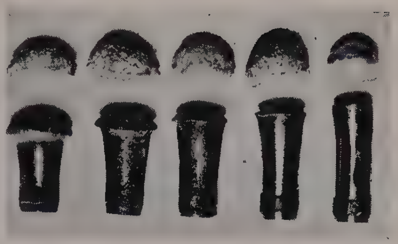

Fig. 12. Deformation of the bullets. From the left V_0=914, 806, 669, 592 and 335m/sec respectively for ε=12.1mm. On the upper, are shown the Al parts punched out.

Therefore, if the bullet were rigid enough and suffered no deformation, the experimental results should almost be consistent with the theoretical.

The results for the conical bullet are shown in Fig. 13—16.

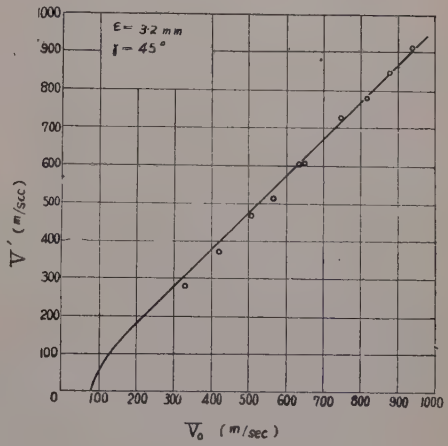

Fig. 13.

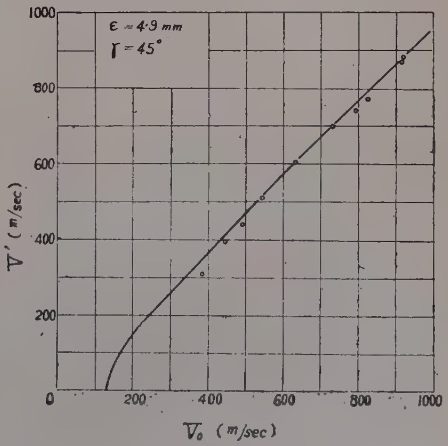

Fig. 14.

---

(2) Thebulletswere all made to weigh 5.5 g.

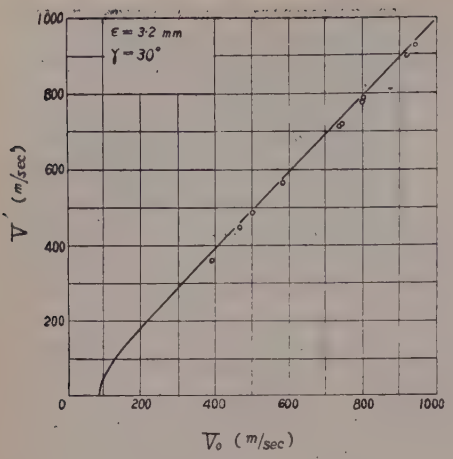

Fig. 15.

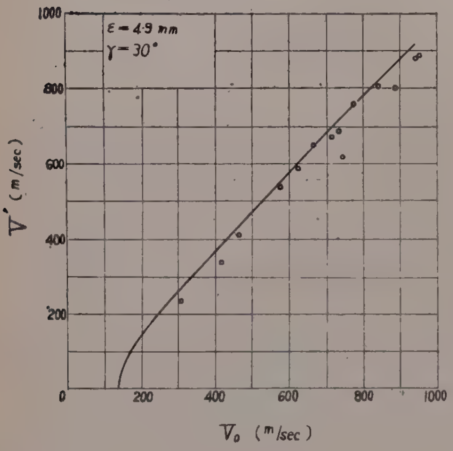

Fig. 16.

As shown from these figures, the experimental data for low velocities seem to deviate from the theoretical curves. This tendency may be due to the fact that the conical bullet with low initial velocities did not keep the straight line through the plates, and hence we could not obtain the correct data in the neighbourhood of the velocities just enough to penetrate the plates. By this reason, we did not research in the case of the other 8.2 and 12.1mm plates.

§5. Conclusion.

Using a statical test, a method has been developed to evaluate the velocity drop which a bullet suffers when it penetrates an aluminium plate with high speed. The theoretical values have been found to be consistent with the experimental ones when the deformation of the bullet was not too large.

The author believes that the same method may be applied with success to the penetration through other materials such as lead, clay, sand, etc.

Reference.

(1) R. Sutterlin, Mem. de l'Artill. franc., **96** (1939), 18.

JOURNAL OF THE PHYSICAL SOCIETY OF JAPAN, Vol. **6** No. 5 September—October, 1951

Mode Conversion Losses in a TE_{01} Type Cavity Resonator with Tilted End-plate

By Koichi SHIMODA.

Department of Physics, Faculty of Science, University of Tokyo.

(Received February 2, 1951)

A cylindrical cavity resonator of TE_{013} mode was constructed and its Q-value was measured at the frequency of 3075 Mc/sec. It was found that the ~~Q-value~~ is reduced, when the end-plate of the cavity is slightly tilted. The optimum Q-value ($Q_0=7.53\times10^4$) agrees well to that calculated from the d.c. conductivity of the wall material (copper). It may be considered that some other modes (TE_{11}, TE_{12} and TM_{11} modes) of waves are generated from the primary TE_{01} mode and they are lost as heat and radiation, when the end-plate is tilted. Thereby the resonance of TE_{01} mode is damped by mode conversion which is calculated assuming the deformation of the cavity wall is small. The calculated result agrees well to the observed Q-value of the cavity with tilted end-plate.

§1. Introduction.

A hollow cavity is widely used as a microwave resonator, which is made in various forms. There are many modes of oscillations for each cavity resonator. Among them the TE_{01n} mode of a cylindrical cavity is the only mode in which the normal component of the electric field is zero everywhere on the cavity wall. The field components of TE_{01n} mode are:

(neglecting time factor, exp $(j\omega t)$)

$$\begin{aligned} E_r &= o, \\ E_\varphi &= AJ_0'(k_0 r)\sin\beta z, \\ E_z &= o, \\ H_r &= -A\frac{\beta}{k}\sqrt{\frac{\varepsilon}{\mu}}J_0'(k_0 r)\cos\beta z, \\ H_\varphi &= o, \\ H_z &= -A\frac{k_0}{k}\sqrt{\frac{\varepsilon}{\mu}}J_0(k_0 r)\sin\beta z, \end{aligned} \tag{1}$$

and

$$\begin{aligned} \beta &= \frac{n\pi}{b}, \\ k_0 &= \frac{y_0}{a} = \frac{3.8317}{a} \\ k &= \frac{2\pi}{\lambda} = \frac{\omega}{c}, \end{aligned} \tag{2}$$

where a is the radius and b is the length of the cylindrical cavity, the wall of which is assumed to be made of perfect conductor. The resonant frequency, $\omega/2\pi$, or wavelength, λ, is determined by the following relation.

$$k^2 = k_0^2 + \beta^2. \tag{3}$$

When the conductivity of the cavity wall is not infinite but pretty high, the unloaded Q of the cavity is represented in good approximation by the following equation in which only the ohmic loss is considered.

$$\frac{1}{Q_0} = \frac{\delta}{a}\,\frac{k_0^2 + 2\beta^2 a/b}{k_0^2 + \beta^2}, \text{ and } \delta \doteq \frac{\mu}{\mu_0}\sqrt{\frac{2}{\pi\mu\sigma}} \tag{4}$$

Here μ and σ is the permeability and conductivity of the cavity wall in m.k.s. units.

Because the r-f current in the wall is always perpendicular to the cylinder axis, the current does not cross the edge of the cylinder and the contact loss of the piston has no effect. This is quite favorable for practical use to vary the resonant frequency by changing the cavity length. Moreover, Q of the TE_{01n} cavity is higher than other modes of resonance whose volume are nearly same as the TE_{01n} cavity.

Although the TE_{01n} mode has many merits, in practical construction it is found by some workers that its Q is usually lower than the calculated value of equation (4). Some part of the loss is considered to be caused by a rather broad resonance of TM_{11n} mode, the resonant frequency of which is the same as TE_{01n} mode in a perfectly cylindrical cavity, because

$$J_0'(x) = -J_1(x). \tag{5}$$

This type of loss, which may be called mode degeneracy loss, can be eliminated practically by inserting absorbing material or conductor which disturbs TM_{11n} mode but not TE_{01n} mode. It is found, however, that Q is still smaller than the calculated value in many cases, even if the above mentioned loss is excluded.

§2. Experiments on a Cylindrical TE_{01n} Cavity Resonator.

To clarify the cause of losses, a cylindrical TE_{013} cavity was constructed for 10 centimeters range. The cavity is made of commercial copper. The inner radius of the cylinder is 10.7 centimeters and it is tunable by a sliding piston. The TE_{013} mode of resonance occurs about 17.6 centimeters in length for waves of 3100 Mc/s. This cavity is excited and measured through a single waveguide coupled by a window cut in the middle of the cylindrical wall. In order to suppress TM_{113} mode, three short rods of 3 millimeters in diameter and 20 millimeters in length are inserted perpendicularly on an end-plate.

This cavity has 12 different modes of resonance for 3100 Mc/s in the range form 15 to 22.5 centimeters in cavity length. The number is doubled in the rough if the direction of polarization is considered. Among them TE_{013} mode must have the highest Q. It has been found that if the cylinder is slightly deformed from perfect circular cylinder, its Q decreases very much. For example, when one of the end-plates is tilted, measured Q of the TE_{013} mode suffers considerable decrease as shown in Fig. 1 (a). In this case

Q is appreciably lowered, when the end-plate is tilted by only a few minutes in angle. On the other hand, other modes are not effected so critical as shown in Fig. 2 (b) for an example. If many metallic wires are stretched radially across the cylinder, TE_{013} mode is not disturbed but other modes are considerably suppressed. In such cylindrical cavity tilting of an end-plate effects on Q rather little, which is shown in Fig. 1 (c).

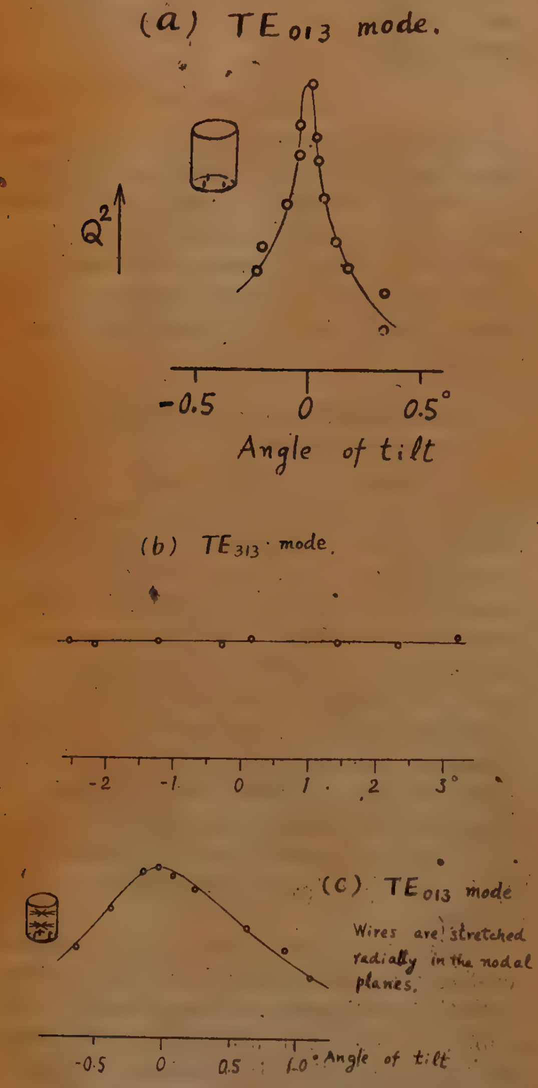

Fig. 1.

From the value of input standing wave ratio and the maximum loaded Q measured by adjusting end-plates the unloaded Q of the cavity can be obtained. The average result is

$$Q_0=(7.53\pm0.27)\times10^4.$$

This is in good agreement with the calculated value of $Q_0=7.72\times10^4$, assuming that microwave conductivity of copper is equal to the low frequency value of $\sigma=5.68\times10^7$ mhos per meter.

§3. Theory of Mode Conversion Losses Caused by Tilting End-Plate.

When the end-plate of a cylindrical cavity resonator is not perpendicular to the cylinder axis, the electromagnetic field of a certain mode in a perfect cylinder is distorted. The electric field in a slightly deformed cavity may be expressed as

$$\mathbf{E}=\mathbf{E}_0+\varepsilon\mathbf{E}_1, \qquad (7)$$

where $\mathbf{E}_0$ is the electric field of a certain normal mode in the undeformed cavity and $\varepsilon\mathbf{E}_1$ is a perturbation term, which may be expanded by orthogonal modes of fields in a cylindrical waveguide.

The cylindrical coordinates, r, φ, z, are so chosen that z-direction is the cylinder axis and $\varphi=0$ is the direction perpendicular to the normal of tilted end-plate as shown in Fig. 2. The boundary condition at the end-plate is then given by

$$\mathbf{n}\times\mathbf{E}=0, \text{ at } z=\varepsilon r\sin\varphi. \qquad (7)$$

Here $\mathbf{n}$ is the normal of the end-plate and ε is the tilting angle.

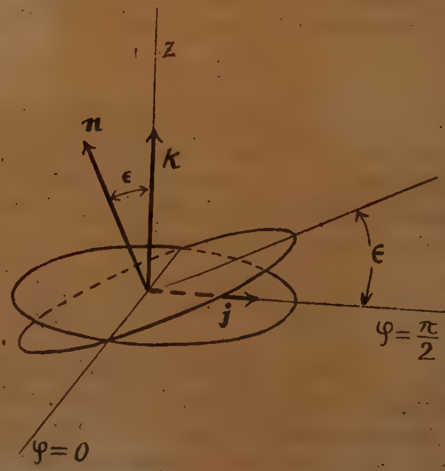

Fig. 2.

When we put $\mathbf{k}$ and $\mathbf{j}$ the unit vectors in the direction of z and $\varphi=\pi/2$ respectively, we have

$$\mathbf{n}=\mathbf{k}-\varepsilon\mathbf{j}. \tag{8}$$

On the other hand, the boundary condition for $\mathbf{E}_0$ is given by

$$\mathbf{k}\times\mathbf{E}_0=0, \text{ at } z=0. \tag{9}$$

The perturbation field, $\mathbf{E}_1$, can therefore be calculated from equations (6)—(9).

As the next step, we shall calculate the perturbation field in terms of normal modes in the waveguide. We let orthogonal functions of the cylindrical waveguide be $(\mathbf{E}_i, \mathbf{H}_i)$, which are normalised so that the energy flow of each mode of waves in the waveguide is unity. This requires

$$\frac{1}{4}\int_F(\bar{\mathbf{E}}_i\times\mathbf{H}_i+\mathbf{E}_i\times\bar{\mathbf{H}}_i)_z\,dF=1, \tag{10}$$

where integration is made in a cross-section of the waveguide. We may now expand the tangential component of perturbation field as follows.

$$\mathbf{E}_{1t}=\sum_i A_i\mathbf{E}_{it},$$

where

$$A_i=\frac{\int_F \mathbf{E}_{1t}\cdot\mathbf{E}_{it}\,dF}{\int_F |\mathbf{E}_{it}|^2\,dF}. \tag{11}$$

Therefore, we have A_i^2 for the energy flow of i-th mode of waves. Since the waves propagate along z-direction and are reflected by another end-plate of the cavity, the converted power flow to i-th mode is not equal to A_i^2 by the reaction of reflected waves upon the primary waves. In our experimental cases, however, the end-plates have bad contacts with cylinder walls and there are some long and narrow slots left, in order to slide and tilt the end-plates. We may presume that all resonant modes except TE_{01n} suffer considerable losses by radiation and contact resistance. Therefore, it would not be far from truth that the power flow of i-th mode of waves converted from TE_{01n} mode becomes nearly equal to A_i^2, and the total converted power is approximately given by

$$P=\sum_i A_i^2,$$

where the summation not be made for cut-off modes.

We know the field components of TE_{01n} mode in a cylindrical cavity as we see in equations (1). Thus we see that on the tilted end-plate, $z=\varepsilon r\sin\varphi$. the electric field, $\mathbf{E}_0$, has only φ-component of the form

$$E_{0\varphi}=A\varepsilon\beta r J_0'(k_0 r)\sin\varphi. \tag{12}$$

Using equations (6), (7), (8) and (12), the perturbation field which has only φ-component in the first order approximation is written

$$E_{1\varphi}=-A\varepsilon\beta r J_0'(k_0 r)\sin\varphi. \tag{13}$$

Using equations (11) and (13), mode conversion losses by tilting the end-plate can be calculated.

Since equation (13) contains $\sin\varphi$ term in it, the expansion coefficients of the i-th mode, A_i, become zeros for the modes whose φ-components have not $\sin\varphi$ term. In our case, therefore, only TM_{11}, TM_{12},......and TE_{11}, TE_{12},......modes need to be considered for calculation of conversion power.

(1). First we calculate the conversion of power to TM_{11} mode whose field components are:

$$\begin{aligned}
E_r&=-N_{10}J_1'(k_0 r)\cos\varphi\cdot\exp[j(\omega t-\beta z)]\\
E_\varphi&=N_{10}\frac{J_1(k_0 r)}{k_0 r}\sin\varphi.\ \exp.[j(\omega t-\beta z)]\\
E_z&=-N_{10}j\frac{k_0}{\beta}J_1(k_0 r)\cos\varphi.\exp[j(\omega t-\beta z)]
\end{aligned} \tag{14}$$

where

$$k_0=\frac{\nu_0}{a}=\frac{3.8317\ldots}{a},$$

and

$$\frac{H_\varphi}{E_r}=-\frac{H_r}{E_\varphi}=\frac{k}{\beta}\sqrt{\frac{\varepsilon}{\mu}}.$$

N_{10} is the normalisation factor which is given by

$$\frac{1}{N_{10}}=\frac{\pi a^2}{4}\ \frac{k}{\beta}\sqrt{\frac{\varepsilon}{\mu}}\,[J_1'(y_0)]^2. \tag{15}$$

Using equation (11), the expansion coefficient becomes

$$A_{10}=\frac{A\varepsilon\beta}{N_{10}k_0},$$

and the power flow is given by

$$A_{10}^2=A^2\varepsilon^2\frac{\pi^3 a^4}{y_0^2\lambda_g\lambda}\sqrt{\frac{\varepsilon}{\mu}}[J_1'(y_0)]^2. \tag{16}$$

On the other hand, the resonant energy of TE_{01n} mode is given by

$$W=\frac{\varepsilon}{2}\int|\mathbf{E}_0|^2dv=\frac{A^2}{4}\varepsilon\pi a^2b[J_0(y_0)]^2. \tag{17}$$

Then we find the Q of the conversion loss to TM_{11} mode alone being represented by

$$\frac{1}{Q_{10}}=\frac{A_{10}^2}{\omega W}=2\pi\varepsilon^2\frac{a^2}{y_0{}^2\lambda_g b}$$

$$\doteqdot 1.30\times10^{-4}\cdot\frac{a^2}{\lambda_g b}\theta^2, \tag{18}$$

where θ is the angle of tilt in degrees.

(2) Next we calculate the conversion of power to TE_{11} mode. The field components are:

$$E_r=N_{11}\frac{J_1(k_1z)}{k_1z}\cos\varphi.\ \exp[j(\omega t-\beta_1z)],$$

$$E_\varphi=N_{11}J_1'(k_1r)\sin\varphi.\ \exp[j(\omega t-\beta_1z)], \tag{19}$$

$$E_z=0,$$

$$\frac{H_\varphi}{E_r}=-\frac{H_r}{E_\varphi}=\frac{\beta_1}{k}\sqrt{\frac{\varepsilon}{\mu}},$$

where

$$k_1=\frac{y_1}{a}=\frac{1.841}{a},\ \text{and}\ k^2=k_1^2+\beta_1^2.$$

The normalisation factor, N_{11}, is given, using equation (10),

$$\frac{1}{N_{11}^2}=\frac{\pi a^2}{4}\frac{\beta_1}{k}\sqrt{\frac{\varepsilon}{\mu}}\left(1-\frac{1}{y_1^2}\right)[J_1(y_1)]^2. \tag{20}$$

And the expansion coefficient of TE_{11} wave, is given by

$$A_{11}=\frac{2A\varepsilon\beta}{N_{11}a^2}\cdot\frac{\int_0^a J_1(k_1r)J_1'(k_1r)r^2dr}{\left(1-\frac{1}{y_1^2}\right)[J(y_1)]^2}$$

Carrying out a little numerical calculation, we find approximately that

$$A_{11}^2=0.945\times10^{-2}\cdot A^2\varepsilon^2a^4\beta^2\frac{\beta_1}{k}\sqrt{\frac{\varepsilon}{\mu}}. \tag{21}$$

Using equations (17) and (21), we find that the mode conversion loss from TE_{01n} mode to TE_{11} wave is represented by

$$\frac{1}{Q_{11}}=\frac{A_{11}^2}{\omega W}\doteqdot 1.417\times10^{-4}\cdot\frac{\lambda^2}{\lambda_{g1}}\frac{a^2}{\lambda_g^2\,b}\theta^2 \tag{22}$$

where θ is also in degrees and λ_{g1} is the guide-wavelength of TE_{11} mode of waves. λ_g is that of TE_{10} wave and equal to $2b/n$ for the TE_{01n} cavity resonator.

(3) The mode conversion loss to TE_{12} mode can be calculated as the former case, when we put $k_2=y_2/a$ instead of k_1, where $y_2=5.332$ is the root of the second zero of $J_1'(x)=0$. Normalisation factor is given by

$$\frac{1}{N_{12}^2}=\frac{\pi a^2}{4}\frac{\beta_2}{k}\sqrt{\frac{\varepsilon}{\mu}}\left(1-\frac{1}{y_2^2}\right)[J_1(y_2)]^2. \tag{23}$$

Thus we find the mode conversion loss from TE_{01n} mode to TE_{12} wave in the form

$$\frac{1}{Q_{12}}=2\cdot72\times10^{-4}\cdot\frac{\lambda^2}{\lambda_{g2}}\frac{a^2}{\lambda_g^2\,b}\theta^2. \tag{24}$$

§4. Comparison with Experiment.

Since other modes having $\sin\varphi$ term in the φ-component are cut off in our experimental cavity, the total mode conversion loss of TE_{01n} mode of resonance is given by

$$\frac{1}{Q_c}=\frac{1}{Q_{10}}+\frac{1}{Q_{11}}+\frac{1}{Q_{12}}.$$

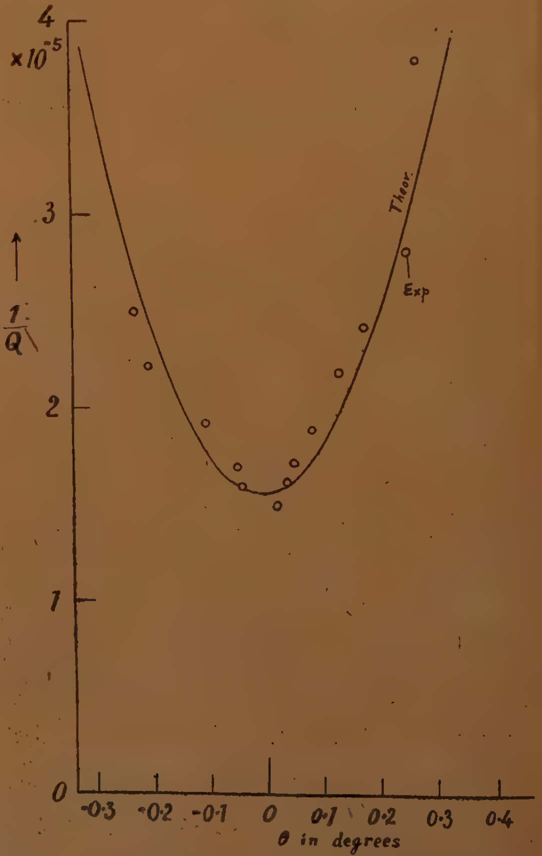

Fig. 3.

Experimental values are: $a=10.7$, $b=17.4$, $\lambda=9.7$, $\lambda_g=11.6$, $\lambda_{g1}=10{\cdot}1$, and $\lambda_{g2}=15.4$ centimeters. Substituting these values in equations (18), (22) and (24), we have

$$\frac{1}{Q_{10}}=7.52\times10^{-5}\cdot\theta^2,$$

$$\frac{1}{Q_{11}}=6.51\times10^{-5}\cdot\theta^2,$$

$$\frac{1}{Q_{12}}=8.24\times10^{-5}\cdot\theta^2.$$

and the sum is

$$\frac{1}{Q_c}=22.27\times10^{-5}\cdot\theta^2.$$

Using experimental value of unloaded Q,

$$\frac{1}{Q_0}=1.33\times10^{-5},$$

and measured Q value of waveguide coupling is written in the form

$$\frac{1}{Q_w}=0.21\times10^{-5},$$

The loaded Q of the cavity becomes therefore

$$\frac{1}{Q}=\frac{1}{Q_o}+\frac{1}{Q_w}+\frac{1}{Q_c}.$$

This is compared with experiment in Fig. 3. The calculated values agree well with experiment within experimental accuracy.

We may conclude therefore that the decrease of Q by tilting the end-plate is chiefly caused by mode conversion. In other words, if the cavity has a form of perfect circular cylinder, the resonant energy of TE_{01n} mode is absorbed only by ohmic loss of that mode. But if not, not a little energy is absorbed in other modes by mode conversion. Also, when the cylinder is slightly deformed such as the ellipsoidal form, the mode conversion will appear as likely as the case of tilting the end-plate.

In conclusion the author expresses his thanks to Assist. Prof. H. Takahashi for valuable discussions and encouragement throughout this work. He is also indebted to the Ministry of Education for financial supports.

JOURNAL OF THE PHYSICAL SOCIETY OF JAPAN, Vol. 6 No. 5 September—October, 1951

On the Asymptotic Behaviour of Three-dimensional Compressible Fluid Flow at a Great Distance from a Body, I.

(The Force and Moment on a Solid Body in a Stream of Compressible Fluid)

By Hidenori HASIMOTO.

Department of Physics, Faculty of Science, University of Tokyo.

(Received December 16, 1951)

The steady irrotational isentropic continuous subsonic flow of a perfect gas past an arbitary three-dimensional body with arbitary distribution of sources on its surface is considered. Based on the thing-wing-expansion method, the velocity potential Φ is expanded in the form $\Phi=U(x+A_1r^{-1}+A_2r^{-2}+\ldots\ldots)$, $A_1=a_0f^{-1}$, $A_2=f^{-3}[a_{10}\cos\theta+\sin\theta(a_{11}\cos\omega+a_{1-1}\sin\omega)]$, $f=(1-M^2\sin^2\theta)^{1/2}$, where U is the velocity of the undisturbed flow of Mach number M streaming in the positive direction of x-axis, and $x=r\cos\theta$, $y=r\sin\theta\cos\omega$, $Z=r\sin\theta\sin\omega$. Using this expression, the force (X, Y, Z) and moment (M_x, M_y, M_z) experienced by the body are found to be: $X=\rho_\infty Q_\infty U$, $Y=Z=0$, $M_x=0$, $M_{y,z}=\pm4\pi a_{1,\pm1}\rho_\infty U^2(1-M^2)^{-1}$, where $\rho_\infty Q_\infty$ is the total strength of sources, and ρ_∞ the density at infinity.

§1. Introduction and Summary.

If we know the asymptotic behaviour of fluid flow at a great distance from a body, we can find the formulae for the force and moment experienced by the body by considering the conservation of linear and angular momenta. Since Glauert⁽¹⁾ pointed out that the Kutta-Joukowski theorem is also applicable in the case of a compressible fluid, two-dimensional irrotational fluid flow past a cylindrical body has been discussed by several authors.$^{(2)}$ And the most complete form and proof have been obtained by Imai$^{(3)}$ making use of his M^2-expansion and thin-wing-expansion methods.

In view of the fact that the real fluid flow is three-dimensional, it is highly desirable to study the flow in the three-dimensional case.

In this paper we shall first show that the velocity potential Φ can be expressed as

$$\Phi = U[r\cos\theta + A_1 r^{-1} + A_2 r^{-2} + \dots\dots], \qquad (1.1)$$

where U is the velocity of the undisturbed flow, streaming in the positive direction of the x-axis, (r, θ, ω) are the polar coordinates having the x-axes as the polar axis, A_1 is a function of θ only (which is zero when the total outflow at infinity is zero), and A_s, $s>1$) are all functions of (θ, ω).

Table 1

	y	z	x
r	$\sin\theta\cos\omega$	$\sin\theta\sin\omega$	$\cos\theta$
θ	$\cos\theta\cos\omega$	$\cos\theta\sin\omega$	$-\sin\theta$
ω	$-\sin\omega$	$\cos\omega$	0

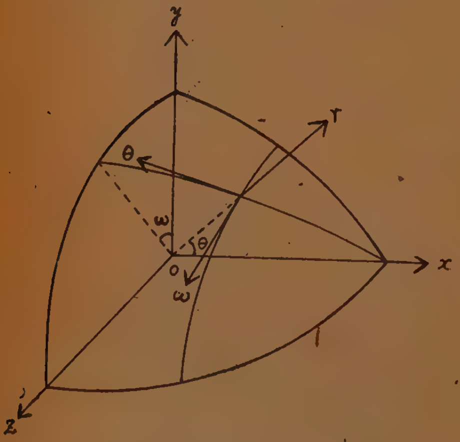

Fig. 1.

The analysis is based on the so-called thin-wing-expansion method. Then, making use of the asymptotic expressions of the velocity field, especially of the explicit functional forms of A_1, and A_2, the formulae for the force and moment will be obtained, the former of which is the thrust $\rho_\infty QU$ correspoding to the result obtained by Imai for a cylinder, where $\rho_\infty Q$ is the total outward flow at infinity. There is no lift. The thrust is also zero when Q is zero. The moment vanishes for an axisymmetric flow. These results are naturally to be expected. In addition it is found that the moment about the direction of fluid flow vanishes in our case.

§2. General expression for the velocity potential in the case of a uniform flow past an obstacle.

Recently Imai$^{(4)}$ has pointed out that the affin transformation employed in the Plandtl-Glauert and his thin-wing-expansion methods is very usefull in the two-dimensional case. His idea is as follows: at large distances from a body, deviations from the uniform flow will be so small, that the thin-wing-expansion method will be used successfully.

The three-dimensional case seems to be more adapted to this idea in view of the fact that the blocking effect due to the obstacle is less than that for the two-dimensional case.

The equation of motion of a compressible perfect fluid past a body can be expressed as follows:

$$2C_\infty^2\left\{1-\frac{\gamma-1}{2}M^2\left(\frac{q^2}{U^2}-1\right)\right\}\Delta\Phi =$$
$$=(\mathbf{grad}\,\Phi,\ \mathbf{grad}\,q^2) \qquad (2.1)$$

$$q^2=(\mathbf{grad}\,\Phi)^2, \qquad (2.2)$$

where U, C_∞, $M=U/C_\infty$ are respectively the fluid velocity, the sound velocity and the Mach number of the undisturbed flow. In the following analysis we shall take $U=1$ for simplicity. On the assumption that the disturbance at a great distance from the body is very small, Φ may be expressed as $\Phi=x+\phi$, where ϕ is small, say of the order of $r\varepsilon$. Moreover, we shall assume that we can write

$$\Phi=x+\phi_1+\phi_2+\dots\dots, \qquad (2.3)$$

where ϕ_1, ϕ_2, ..are respectively $O(r\varepsilon)$, $O(r\varepsilon^2)$...

We now write

$$x=\xi,\ y=\eta/\mu,\ z=\zeta/\mu\ \ \mu=\sqrt{1-M^2} \qquad (2.4)$$

Substituting (2.3), (2.4) in (2.1) and considering the order of magnitude of the various terms, we get

$$\Delta_\mu \phi_1 = 0, \tag{2.4}$$

$$\Delta_\mu \phi_2 = M^2(k\phi_{1\xi}{}^2 + \phi_{1\eta}{}^2 + \phi_1{}^2{}_\zeta)_\xi, \tag{2.5}$$

……………………………………………

$$\Delta_\mu \phi_n = \text{polynomial in } \phi_{m\xi_i}; \text{ and } \phi_{m\xi_i\xi_j} \quad (n>m;\ \xi_i, \xi_j = \xi,\ \eta,\ \zeta), \tag{2.6}$$

where

$$\Delta_\mu = \frac{\partial^2}{\partial\xi^2} + \frac{\partial^2}{\partial\eta^2} + \frac{\partial^2}{\partial\zeta^2}, \quad k = 1 + \frac{\gamma+1}{2\mu^2}M^2. \tag{2.7}$$

Now

i) $\partial\phi/\partial\xi_i$ are one-valued and continuous in the field of flow.

ii) $\partial\phi/\partial\xi_i \to 0$ as $r\to\infty$.

Taking into account these conditions, the solution of the equation (2.4) is

$$\phi_1 = \sum_{p=0}^{\infty}\sum_{m=0}^{p} R^{-(p+1)} P_p^m(\cos\Theta)(b_{pm}\cos m\Omega + b_{p-m}\sin m\Omega) \tag{2.8}$$

$$= b_0R^{-1} + R^{-2}[b_{10}\cos\Theta + \sin\Theta(b_{11}\cos\Omega + b_{1-1}\sin\Omega) + O(R^{-3}), \tag{2.8}$$

Where, $R^{-(p+1)} P_p^m(\cos\Theta)\begin{matrix}\cos\Omega\\ \sin\Omega\end{matrix}$ is a spherical harmonics of degree p, and b_{pm}'s are arbitrary constnts, and $(R,\ \Theta,\ \Omega)$ are the polar coordinates in the $(\xi,\ \eta,\ \zeta)$ space, which are connected with $(r,\ \theta,\ \omega)$ by the formulae:

$$R = rf,\ \Theta = \cos^{-1}(f^{-1}\cos\theta),\ \Omega = \omega, \quad f = (1-M^2\sin^2\theta)^{1/2} \tag{2.9}$$

From (2.8) we see:

i) if $b_0 \neq 0$, the relation $\phi_1 = O'(r\varepsilon) = O'(r^{-1})$ gives $\varepsilon = O'(r^{-2})$ so that $\phi_2 = O'(r^{-3})$, $\phi_3 = O'(r^{-5})$, $\phi_n = O'(r^{-(2n-1)})$ …… .

ii) if $b_0 = 0$ no outflow at infinity), the relation $\phi_1 = O'(r\varepsilon) = O'(r^{-2})$, gives $\varepsilon = O'(r^{-3})$, so that $\phi_2 = O'(r^{-5})$, $\phi_3 = O'(r^{-8})$ .., $\phi_n = O'(r^{-(3n-1)})$…, This is a very important result which should be compared with the two-dimensional case, where ε is respectively $O'(r^{-1})$ and $O'(r^{-2})$. In general, using the spherical harmonics, (2.6) can be reduced to the form

$$\Delta_\mu\phi_n = \sum C_{plm} R^{-p} P_l{}^m(\cos\Theta)\begin{matrix}\cos m\omega\\ \sin m\omega,\end{matrix}$$

a particular solution of which is

$$\phi_n = \sum\frac{C_{plm}R^{-(p-2)}P_l{}^m(\cos\Theta)}{(2-p)(3-p)-l(l+1)}\begin{matrix}\cos m\omega\\ \sin m\omega;\end{matrix}$$

provided $(2-p)(3-p) \neq l(l+1)$.

Therefore, substituting (2.8) into the right hand side of (2.5), ϕ_2 can be obtained. Repeating this process successively, ϕ can be found in the form:

$$\phi = \bar\phi_1 + \bar\phi_2 + \sum_{n=5}^{\infty} R^{-n}B(\Theta,\omega),$$

where $\bar\phi_1$ is given by (2.8), and

$$\bar\phi_2 = -2M^2(kG_1 + G_2),$$

with

$$G_1 = -\frac{2}{5}b_0{}^2R^{-3}(P_1-P_3) - b_0R^{-4}[b_{10}\Big(\frac{1}{15} + \frac{13}{21}P_2 - \frac{24}{35}P_4\Big) + \Big(\frac{5}{21}P_2{}^1 - \frac{6}{35}P_4{}^1\Big)(b_{11}\cos\omega + b_{1-1}\sin\omega)],$$

$$G_2 = -\frac{1}{5}b_0{}^2R^{-3}(3P_1 - 2P_3) + b_0R^{-4}[b_{10}\Big(-\frac{1}{5} - \frac{10}{7}P_2 - \frac{48}{35}P_4\Big) - \Big(\frac{6}{7}P_2{}^1 + \frac{12}{35}P_4{}^1\Big)(b_{11}\cos\omega + b_{1-1}\sin\omega)].$$

If we return to $(x,\ y,\ z)$ space by (2,9), the velocity potential can be written as

$$\Phi = U[r\cos\theta + A_1r^{-1} + A_2r^{-2} + \sum_{n=3}^{\infty}A_n(\theta,\omega)r^{-n}],$$

where

$$A_1 = a_0f^{-1},\ a_0 = b_0,$$

$$A_2 = f^{-3}[a_{10}\cos\theta + \sin\theta(a_{11}\cos\omega + a_{1-1}\sin\omega)],$$

$$a_{10} = b_{10},\quad a_{11} = \mu b_{11},\quad a_{1-1} = \mu b_{1-1}. \tag{1.1'}$$

Thus Φ takes the form (1.1).

3. Formulae for the force and moment,

We shall now proceed to find the formulae for the force and moment experienced by an obstacle in a uniform flow of a compressible fluid,

By considering the balance of the momentum and of the angular momentum of the fluid contained between the body and a sphere of radius r with centre at the origin, we obtain the following expression for the force $F(X, Y, Z)$ and moment $M(M_x, M_y, M_z)$ experienced by the body:

$$\mathbf{F} = -\int_0^{2\pi}\int_0^{\pi}\Big\{p\frac{\mathbf{r}}{r} + \rho\mathbf{V}\cdot q_r\Big\}r^2\sin\theta\, d\theta\, d\omega, \tag{3.1}$$

$$\mathbf{M} = -\int_0^{2\pi}\int_0^{\pi}[\mathbf{r}, \rho\mathbf{V}]q_r r^2\sin\theta\, d\theta\, d\omega, \tag{3.2}$$

where p is the pressure, ρ the density, q_r the radial velocity $\mathbf{r}$ the radial vector, $\mathbf{V}$ the velocity vector, and $[\mathbf{r}, \mathbf{V}]$ is the vector product of $\mathbf{r}$ and $\mathbf{V}$.

In order to calculate **F** and **M** we have only to know ρ, p, q_r, **V** correct to the order of r^{-2} and r^{-3} respectively, and make r sufficiently large.

Now, the velocity compoments in the r, θ, ω direction and ρ, q are respectively (see Fig. 1).

$$q_r=\partial\Phi/\partial r=U[\cos\theta-a_0f^{-1}r^{-2}-2f^{-3}r^{-3}g]$$
$$+O(r^{-4}),$$
$$q_\theta=\partial\Phi/r\partial\theta=U[-\sin\theta+a_0M^2f^{-3}r^{-2}\cos\theta\cdot$$
$$\sin\theta+3M^2f^{-5}gr^{-3}\cos\theta\sin\theta$$
$$+f^{-3}r^{-3}g_\theta]+O(r^{-4}),$$
$$q_\omega=\partial\Phi/r\sin\theta\partial\omega=Uf^{-3}r^{-3}(-a_{11}\sin\omega$$
$$+a_{1-1}\cos\omega)+O(r^{-4}),$$
$$\rho=\rho_\infty+(d\rho/dq^2)_\infty(q^2-U^2)+\ldots\ldots,$$
$$p=p_\infty+(dp/d\rho)_\infty(\rho-\rho_\infty)+\ldots\ldots,$$

where, in virtue of Bernoulli's theorem,

$$(dp/d\rho)_\infty=c_\infty^2,$$
$$(d\rho/dq^2)_\infty=(d\rho/dp)_\infty(dp/dq^2)_\infty=-\rho_\infty/2c_\infty^2.$$

Further

$$q^2-U^2=q_r^2+q_\theta^2+q_\omega^2-U^2$$
$$=U^2[-2a_0r^{-2}f^{-3}\cos\theta-2r^{-3}f^{-5}$$
$$\{f^2g_\theta\sin\theta+(2+M^2\sin^2\theta)g\cos\theta\}], \quad (3.3)$$

with

$$g=a_{10}\cos\theta+\sin\theta(a_{11}\cos\omega+a_{1-1}\sin\omega),$$
$$g_\theta=-a_{10}\sin\theta+\cos\theta(a_{11}\cos\omega+a_{1-1}\sin\omega).$$

Substituting (3.3) in (3.1) and making some reductions, we find that

$$X=-\int_0^{2\pi}\int_0^{\pi}\{p\cos\theta+\rho q_r(q_r\cos\theta-q_\theta\sin\theta)\}$$
$$r^2\sin\theta d\theta d\omega$$
$$=-\int_0^{2\pi}\int_0^{\pi}[(p_\infty+\rho_\infty a_0U^2r^{-2}f^{-3}\cos\theta)\cos\theta$$
$$+\rho_\infty U^2\{\cos\theta-a_0(1-M^2)r^{-2}f^{-3}\}$$
$$(1-a_0r^{-2}f^{-3}\cos\theta)]\times r^2\sin\theta d\theta d\omega+O(r^{-1})$$
$$=2\pi a_0\rho_\infty U^2\int_0^{\pi}(1-M^2)f^{-3}\sin\theta d\theta+O(r^{-1}).$$

Making $r\to\infty$ we get

$$X=4\pi a_0\rho_\infty U^2. \quad (3.4)$$

On the other hand the total outward flow at infinity $\rho_\infty Q_\infty$ is

$$\rho_\infty Q_\infty=\lim_{r\to\infty}\int_0^{2\pi}\int_0^{\pi}\rho q_r r^2\sin\theta d\theta d\omega$$
$$=\lim_{r\to\infty}\int_0^{2\pi}\int_0^{\pi}\rho_\infty U[\cos\theta-a_0(1-M^2)f^{-3}r^{-2}]$$
$$r^2\sin\theta d\theta d\omega$$
$$=-2\pi a_0\rho_\infty U\int_0^{2\pi}(1-M^2)f^{-3}\sin\theta d\theta$$
$$=-4\pi a_0\rho_\infty U. \quad (3.5)$$

Hence

$$a_0=-\rho_\infty Q_\infty/4\pi\rho_\infty U,$$

and

$$X=-\rho_\infty Q_\infty U. \quad (3.6)$$

This is a thrust opposing to the direction of the flow and an analogue of Imai's result in the two-dimensional flow. On the other hand, in the expressions:

$$Y=-\int_0^{2\pi}\int_0^{\pi}\{p\sin\theta\cos\omega+\rho q_r(q_r\sin\theta\cos\omega$$
$$+q_\theta\cos\theta\cos\omega-q_\omega\sin\omega)\}r^2\sin\theta d\theta d\omega,$$
$$Z=-\int_0^{2\pi}\int_0^{\pi}\{p\sin\theta\sin\omega+\rho q_r(q_r\sin\theta\sin\omega$$
$$+q_\theta\cos\theta\sin\omega+q_\omega\cos\omega)\}r^2\sin\theta d\theta d\omega,$$
$$(3.7)$$

there remain only terms of the order r^{-1}, on acconnt of linear factors $\cos\omega$, $\sin\omega$. This shows that the lift vanishes for a continuous simple-connected flow.

Next, we shall find the moment. In the Cartesian coordinates, components of the moment are, by (3.2), (see Table 1),

$$M_x=-\int_0^{2\pi}\int_0^{\pi}\rho q_r(rq_\omega\sin\theta)r^2\sin\theta d\theta d\omega;$$
$$M_y=\int_0^{2\pi}\int_0^{\pi}\rho q_r(rq_\theta\sin\omega+rq_\omega\cos\theta\cos\omega)$$
$$r^2\sin\theta d\theta d\omega,$$
$$M_z=\int_0^{2\pi}\int_0^{\pi}\rho q_r(-rq_\theta\cos\omega+rq_\omega\cos\theta\sin\omega)$$
$$r^2\sin\theta d\theta d\omega. \quad (3.8)$$

Now, q_ω is of the order of r^{-3} from (3.3) and is linear in $\cos\omega$ and $\sin\omega$ while the first terms in the expansions of ρ and q_r do not contain ω. Thus, we see that M_x must be zero when r is made infinitely large.

Calculation of M_z are straightforward; after some reductions we get:

$$M_z=a_{11}\rho_\infty U^2\int_0^{2\pi}\int_0^{\pi}[f^{-3}\{-\cos^2\theta\sin^2\omega$$
$$-2\sin^2\theta\cos^2\omega-M^2\cos^2\theta\sin^2\theta\cos^2\omega\}$$
$$-f^{-1}\cos^2\theta\cos^2\omega]\sin\theta d\theta d\omega+O(r^{-1})$$

$$=-2\pi a_{11}\rho_\infty U^2\int_0^\pi f^{-3}\sin\theta d\theta$$

$$=-4\pi a_{11}\rho_\infty U^2/(1-M^2). \qquad (3.9)$$

In the same manner

$$M_y=2\pi a_{1-1}\rho_\infty U^2\int_0^\pi f^{-3}\sin\theta d\theta$$

$$=4\pi a_{1-1}\rho_\infty U^2/(1-M^2). \qquad (3.9')$$

Or if we compare these with (1.1) and (1.1′) we find

$$M_y=2\rho_\infty U^2\int_0^{2\pi}\int_0^\pi A_2(\theta,\omega)\sin\omega d\theta d\omega, \qquad (3.10)$$

$$M_z=-2\rho_\infty U^2\int_0^{2\pi}\int_0^\pi A_2(\theta,\omega)\cos\omega d\theta d\omega. \qquad (3.10')$$

Where ω is measured from the y-axis. Thus, if only $A_2(\theta,\omega)$, the coefficient of r^{-2} in the asymptotic expressions for the velocity potentials is known, the moment of the body can be calculated immediately by (3.10) and (3.10′). In this case the moment about the direction of fluid is zero. These results seem to be rather surprising.

In conclusion, the author wishes to express his sincerest thanks to Professor I. Imai for his continual guidance and encouragement in this work.

References.

(1) Glauert, H: Proc. Roy. Soc.; A **118** (1928) 113.
(2) Bateman, H: Proc. Nat. Acad. Sci. U.S.A., **24** (1938) 246.
Demchenko, D: Publ. Sci. Tech. Min. Air., No. 144 (1939).
Gröbner, W: Lufo. **20** (1943) 184.
Batchelor, G. K.: Quart. Appl. Math., **2** (1945) 318.
(3) Imai, I: Proc. Phys.-Math. Soc. Japan., **24** (1942) 231.
Imai, I: Rep. Aeron. Res. Inst. Tokyo Imp. Univ., No. 294 (1944).
Imai, I: Nippon Sūgaku-Buturi Gakkaisi (Journ. Phys.-Math. Soc. Japan)., **17** (1943) 495.
(4) Imai, I: To be published.

JOURNAL OF THE PHYSICAL SOCIETY OF JAPAN, Vol. 6 No. 5 September—October, 1951

Experimental Study of the Spectrum of Isotropic Turbulence, I.

Hiroshi SATO.

Institute of Industrial Science, University of Tokyo.

(Received December 20, 1950)

Some measurements were made on the turbulence behind the grid. The wind-tunnel is of the single open-jet type and the range of test section covers from 20 to 70 times of mesh length.

In the first place, the decay of total energy is proved to be inversely proportional to the distance from grid. Energy spectrum which is observed at various positions on the center line, is nearly the same as those previously reported. The decay of spectral components was measured directly by moving the hot-wire anemometer along the axis of wind-tunnel. In the low wave number region, energy decay follows the inverse power law. But at high wave number, decay is severer at first and gradually becomes to the state of energy equilibrium. The last result seems to be influenced by the free jet mixing.

§1. Introduction.

Recent developments in the hot-wire technique have brought in the possibility of determining the statistical characteristics of turbulence in the wind-tunnel. Thus, energy decay and velosity correlation were determined by various authors,(1)(2)(6) and several interesting features were revealed. As for the energy spectrum, however, measurements are rather scanty, and many unknown facts remain. An attempt was therefore made to study experimentally the characteristics of turbulence by improving the method of measurements on energy spectrum.

§2. Equipment.

Wind-Tunnel.

The wind-tunnel used is of the single open-jet type having a rectangular cross-section of 60cm × 60cm (Fig. 1). The intensity of turbulence of the airstream is about 0.3%. It is rendered turbulent by a grid attached at the exit nozzle.

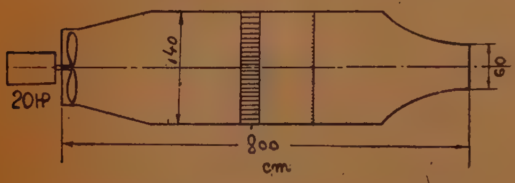

Fig. 1. Planform of Wind-Tunnel.

Hot-Wire.

The wire is the platinum Wollaston having 4—5 microns in diameter and 5mm in length. The central portion of 1mm length is etched. The working temperature is about 200 deg. C, electric current being 30—40 mA and resistance about 20 ohms. The time constant M is 0.0008—0.0012 sec.

Input Stage.

The block diagram of whole electric circuit is as Fig. 2. The input stage consists of a Wheatstone bridge and a switching network. The plate current of vacuum tube is used to heat the wire. The reason will be explained later.

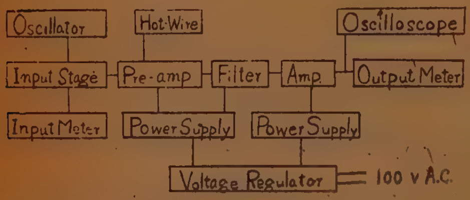

Fig. 2. Block Diagram of Circuit.

Amplifier.

The amplifier used is of the ordinary type (Fig. 3 a, b). It is constructed from a voltage amplifier, an impedance changer, a compensating network of the thermal lag of hot-wire, and a power amplifier. D. C. high tension is supplied from 100V alternating current. Without compensation the maximum over-all gain is about 0.2 A/mV, and frequency response is flat from 10 c/s to 10,000 c/s within the error of 0.3 db.

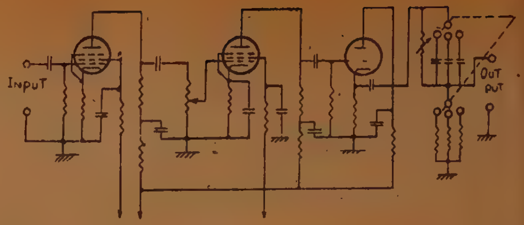

Fig. 3. a. Pre-Amplifier.

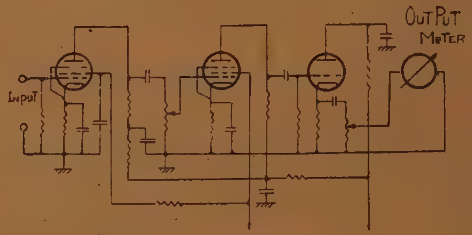

Fig. 3. b. Power Amplifier.

Compensating Network.

The sensitivity of the hot-wire anemometer falls down in the high frequency region. Methods of compensation have been proposed by many authors. Mock and Dryden once pointed out⁽³⁾ that C-R compensation was inferior to that of L-R. But we reconsidered the C-R compensation from a new point of view, and deciced to use it.

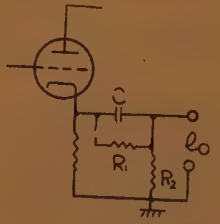

Fig. 4. a. Compensating Network.

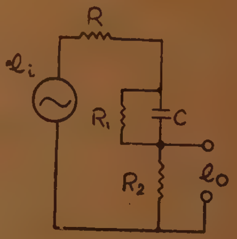

Fig. 4. b. Equivalent Circuit.

The network of Fig. 4 a. is equivalent to that of Fig. 4. b. where R is the output impedance. We get the equation

$$e_0/e_i=\{(m+1)(s^2+1)+l+jsl\}/\{(m+l+1)^2+s^2(m+1)^2\},$$

where $l=R_1/R_2$, $m=R/R_2$, $s=\omega CR_1$.

When $m<1$,

$$\left|\frac{e_0}{e_i}\right|=\frac{1-m/(1+l)}{1+l}\left\{1-\frac{ms^2l}{[(1+l)^2+s^2](1+l)}\right\}\left\{\frac{1+s^2}{1+s^2/(1+l)^2}\right\}^{\frac{1}{2}}$$

The ideal characteristics of compensation is given by Dryden(4) as,

$$|e_0/e_i|_D=(1+M^2\omega^2)^{\frac{1}{2}}.$$

With $CR_1=M$ the ratio of the two is

$$|e_0/e_i|_D/|e_0e_i|=K[\{1+s/(1+l)\}^{-\frac{1}{2}}-ms^2l\{(1+l)^2+s^2\}^{-\frac{3}{2}}],$$

where K is a constant independent of frequency.

Putting $CR_2=1\times10^{-5}$, $m \ll 1$, we can reduce the compensation error to 0.5 db at 5,000 c/s. An example of compensation characteristics is shown in Fig. 4. c.

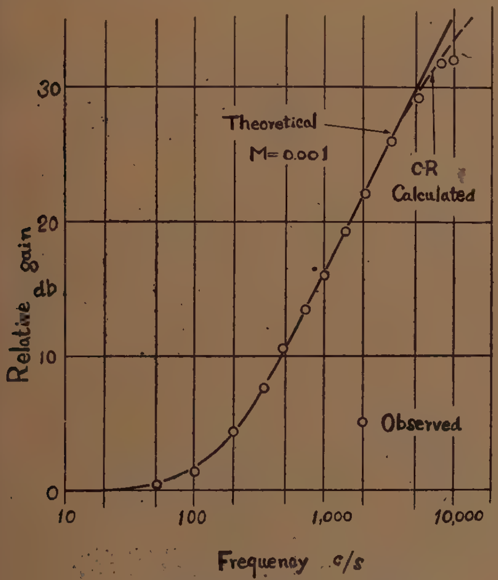

Fig. 4. c. Compensation Characteristics.

Filter.

A band-pass filter was newly constructed. It is of the phase-shift type (Fig. 5). The tuning frequency is changed by two selecting switches and there are 40 measuring spots between 2 and 5,000 c/s. The sharpness of resonance is adjustable and the maximum Q is about 50 over all ranges.

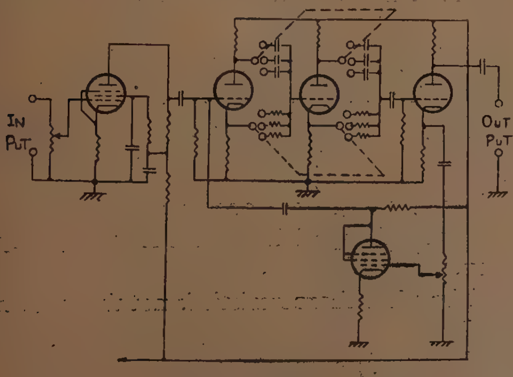

Fig. 5. Filter.

§3. Measurement of Frequency Response of Hot-Wire.

The thermal lag of hot-wire was measured by the method of Ziegler(5) and Dryden(3), that is, by superposing the alternating current on the D. C. heating current. The plate current of vacuum tube was used for D. C. heating and added A. C. was obtained by swinging its grid with an audio-oscillator.

By this connection we can avoid the trouble of shunting A. C. by a low-impedance battery. The results of measurements are shown in Fig. 6. From these data we can determine the time constant M, and adjust the compensation.

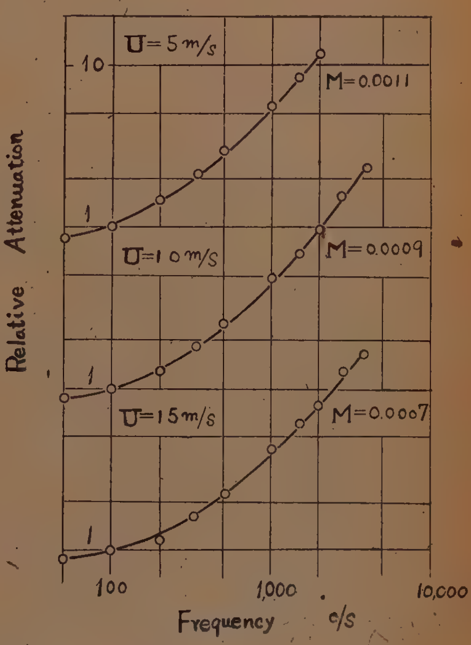

Fig. 6. Frequency Response of Hot-Wire.

§4. Decay of Total Energy.

The intensity of turbulence was measured. The decay curves under various conditions are shown in Fig. 7. The fact that the points are in a straight line when the data are arranged in the form of U^2/u^2 versus x, seems to prove the inverse decay law of Batchelor(1) and others.

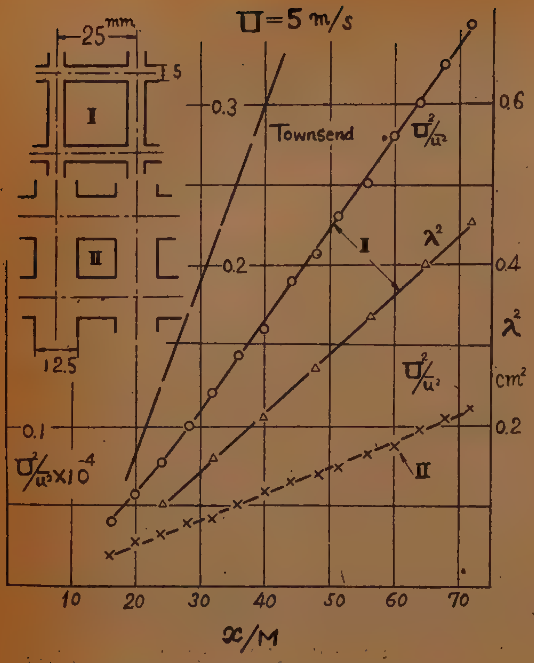

Fig. 7. a. Decay of Total Energy.

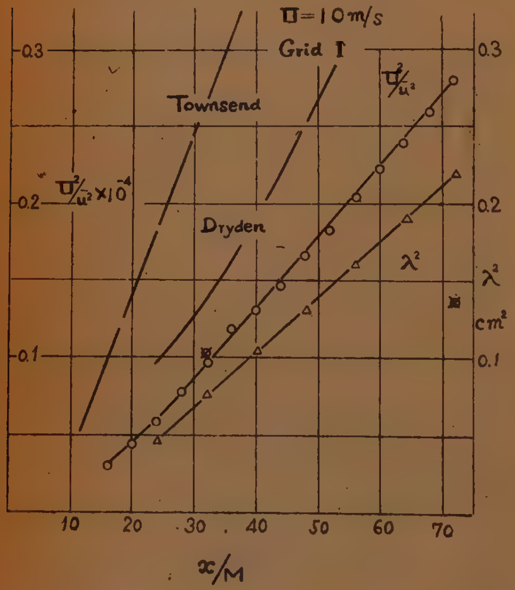

Fig. 7. b. Decay of Total Energy.

The disagreement with the results of Townsend⁽¹⁾ and Dryden⁽⁶⁾ seems to be due to the difference in grid shape. In fact there is a difference between the curves obtained by grid I and II of the same mesh length and different bar breadth. From these curves we can calculate the micro-scale of turbulence by the equation,

$$\frac{1}{\lambda_2}=\frac{U}{10\nu}\frac{\overline{u^2}}{U^2}\frac{d}{dx}\left(\frac{U^2}{\overline{u^2}}\right)$$

Curves for λ^2 are also shown in Fig. 7. The mark ⊠ is the value of λ^2 calculated from the spectrum.

§5. Energy Spectrum.

One dimensional energy spectrum of $\overline{u^2}$ was measured. The results in the case of grid I, U=10m/s are shown in Fig. 8. The measured frequency is 16 to 4,500c/s, the corresponding wave number being 0.016 to 4.5 /cm.

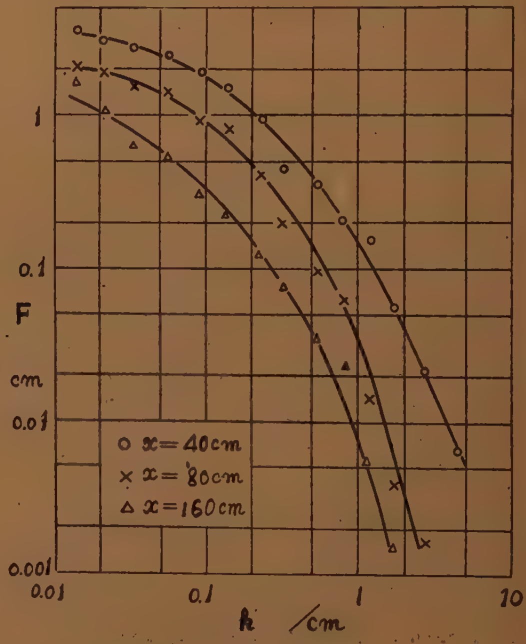

Fig. 8. Energy Spectrum.

Positions of hot-wire were changed from 40 to 160cm behind the grid. The curve for x=40cm is normalized, i.e. $\int_0^\infty Fdk=1$ where k is the wave number, for other positions total energy ratio is multiplied to the value of normalized $F(k)$. Measured points are not in a fair curve. The errors may be due to three facts.

(i) The spectral components fluctuate with a long period, especially for the low frequency region.

(ii) The filter characteristic is not the perfect cut-off.

(iii) The sharper the filter is, the smaller the input voltage, so the amplification becomes very difficult.

It is the author's opinion, however, that these difficulties are not unconquerable. More accurate results will be reported in the subsequent paper.

From the measured curves we can observe the following;

(i) There is no maximum in the spectrum. The maximum might occur in the low frequency region which is beyond the present measurements. But it is an essential question whether such a low frequency fluctuation would be called by the name of turbulence in the wind-tunnel.

(ii) There is a domain where -5/3 power law is valid, but it is not so wide.

(iii) From normalized spectrum curves we can calculate the value of λ from the equation,

$$1/\lambda^2=(2\pi)^2\int_0^\infty F(k)\,k^2dk.$$

The calculated values are shown in Fig. 7. The agreement with the result from the total energy decay is fairly good.

(iv) Accuracy is not sufficient to inform about the deformation law of spectrum in the decay process.

§6. Decay of Spectral Components.

Due to the energy transference between the components of different wave numbers, the spectrum curve changes its shape during the decay. This is an important problem in the study of the structure of turbulence. Since, however, the measurement of spectrum is not so easy for the reasons above described, and since the temporal changes of measuring system may make the result erroneous, sufficient accuracy cannot be expected in comparing the spectrum curves measured at various positions. Therefore, we adopted an alternative method with a view to improving the accuracy. The procedure is as follows:

(i) We select a spot of the filter, control the variable resistor to get the proper indication of the output meter.

(ii) Travel the hot-wire longitudinally and read the output meter.

(iii) By plotting this reading against the distance behind the grid, we get the decay law of spectral components.

This method is very simple and makes us free from the sensitivity and frequency response of hot-wire, the compensation of high frequency, and the temporal changes of measuring system.

Experiments were made in the two cases of $U=5$ m/s and 10 m/s using the grid I. The decay curve is shown in Fig. 9. a, b., where the spectral component at the position 40 cm behind the grid is taken as unity.

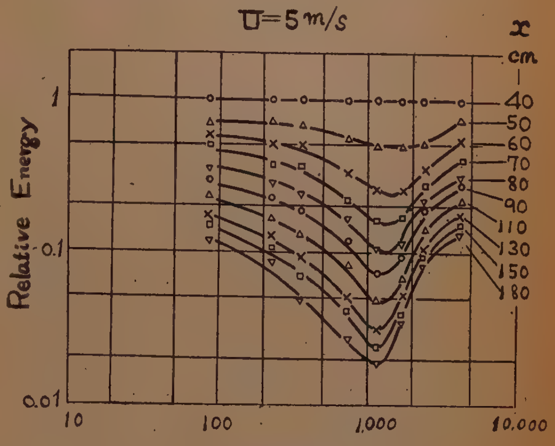

Fig. 9. a. Decay of Spectral Components.

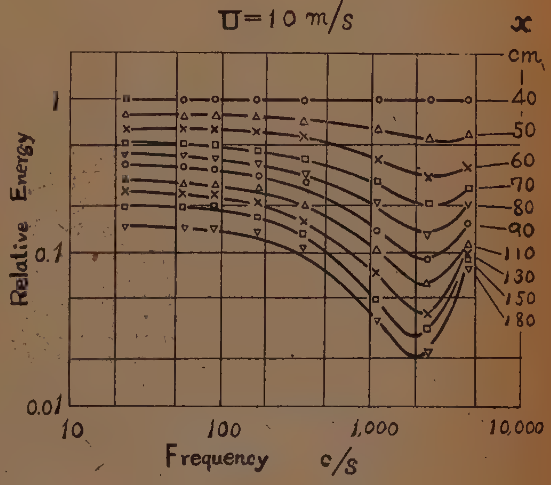

Fig. 9. b. Decay of Spectral Components.

Influences of noise and other disturbances were checked by making the heating current of hot-wire off and stopping the wind. In both cases the outputs were zero.

In Fig. 9 we observe the following:

(i) The decay law is different for components of different wave numbers.

(ii) The decay of total energy is represented by the part of comparatively small wave numbers.

(iii) There exists the wave number for which the decay is most severe; it moves to the lower wave number during the decay.

(iv) Both results of different wind speed coincide each other, when the relative energy components are plotted against the wave number. So the turbulence produced by grid is independent of the wind speed so far as the spectral component decay is concerned.

§7. Conclusion.

In the initial period⁽²⁾ of turbulence we obtained the following results:

(i) The decay of total energy is inversely proportional to the distance behind the grid.

(ii) Measured spectrum is nearly the same with those of previous authors; the range for which the inverse five thirds law is valid is not so wide.

(iii) For the decay of spectral components, the rate of decay is not uniform over all ranges of wave numbers, the severest decay occurring at a certain wave number. The wave number of the severest decay seems to move to the lower wave number during the decay.

The author wishes to express his hearty thanks to Prof. I. Tani and Prof. H. Kumagai for their encouragements and advices.

Acknowledgements are also due to Mr. H. Shono for his valuable advices in constructing equipments and to Mr. K. Seimiya for his assistance in measurements.

References.

(1) G. K. Batchelor, and A. A. Townsend: Proc. Roy. Soc. A. **190** (1947) 534-550.
(2) G. K. Batchelor, and A. A. Townsend: Proc. Roy. Soc. A. **193** (1948) 539-558.
(3) W. C. Mock, Jr., and H. L. Dryden: N.A.C.A. Tech. Rep. No. **448** (1932).
(4) H. L. Dryden, and A. M. Kuethe: N.A.C.A. Tech. Rep. No. **342** (1930).
(5) M. Ziegler: Versl. d. Kon. Akad. v. Wetensch. **33** (1930) 723.
(6) H. L. Dryden, G. B. Schubauer, W. C. Mock, Jr., and H. K. Skramstad: N.A.C.A. Tech. Rep. No. **581** (1937).

JOURNAL OF THE PHYSICAL SOCIETY OF JAPAN, Vol. 6 No. 5 September—October, 1951

Some Remarks on the Dynamical and Thermal Structure of a Heated Turbulent Fluid.

By Eiichi INOUE.

Geophysical Institute, Tokyo University.

(Received March 1, 1951)

Spectral functions for the velocity and temperature fluctuations in heated turbulent flow are obtained in the forms:

$$F(k)\sim\varepsilon^{2/3}k^{-5/3},\quad G(k)\sim(K/K_H)^2Q^2\varepsilon^{-2/3}k^{-7/3}$$

for the intermediate scale of turbulence element (turbulon) and

$$F(k)\sim(\varepsilon/\nu)k^{-3},\quad G(k)\sim Q^2\varkappa^2k^{-5}$$

for the smallest scale. Here k is the turbulon wave number, ε the rate of energy dissipation, Q that of heat transfer, ν the kinematic viscosity, $\varkappa$ the heat diffusivity, K the turbulent viscosity, and K_H the turbulent heat diffusivity. Then the concept of smallest turbulon is defined as the intersection of two forms of the spectral function. Thus it turns out that the scale of smallest dynamical turbulon coincides with that of smallest thermal turbulon provided the Prandtl number $\nu/\varkappa$ is equal to K/K_H.

§1. Introduction.

Recently the author⁽¹⁾ has dealt with the thermal properties of a heated turbulent fluid. After this time, however, the author has been acquainted with other author's papers on this problem. One is the theoretical treatment by A. M. Obuhov⁽²⁾ and A. M. Yaglom⁽³⁾ in quite different results from the present author's, and the other is the paper of S. Corrsin and M. S. Uberoi⁽⁴⁾ which contains experimental results.

On the other hand, the author⁽⁵⁾ has also dealt with the concept of the smallest turbulon in a turbulent fluid. Thus it seems somewhat worthwhile to discuss these problems again especially for the dynamical and thermal structure of a heated turbulent fluid.

In this paper the dynamical and thermal structure of a heated turbulent fluid is considered with special respect to the dynamical and thermal properties of the smallest turbulon. And some of results are compared herein with the recent experimental results of Corrsin and Uberoi.

§2. Dynamical and Thermal Structure of a Turbulent Fluid.

In general any turbuleht fluid is supposed to be composed of turbulons (or eddies) of many ranks. These turbulons are separated in three ranges, i.e. in ranges of the largest turbulon, the intermediate turbulon and the smallest turbulon. In each range, the scale Λ and the velocity V are closely connected with each other owing to the mutual interaction of turbulons. At present we must consider the mechanism of mutual interaction separately in three ranges.

In the range of the largest turbulon, the turbulent viscosity $K_0 \doteqdot \Lambda V$ is assumed to be kept constant irrespective of the rank of turbulon. From this assumption the relationship between Λ and V is obtained as

$$V = \frac{K_0}{\Lambda}. \tag{2.1}$$

Thus for this range the turbulon spectral function is obtained as

$$F(k) \sim K_0^2 \, k, \tag{2.2}$$

where k denotes the turbulon wave number given by

$$k \sim 1/\Lambda. \tag{2.3}$$

In the range of the intermediate turbulon, the turbulon state is assumed to be described by the dissipation rate ε of turbulon energy only. From this assumption we can get following relations:

$$V^3/\Lambda \sim K(V/\Lambda)^2 \sim \varepsilon, \tag{2.4}$$

$$K = \Lambda V \sim \varepsilon^{1/3} \Lambda^{4/3}, \tag{2.5}$$

$$F(k) \sim \varepsilon^{2/3} k^{-5/3}. \tag{2.6}$$

In the range of the smallest turbulon, the relationship between the scale and the velocity fluctuations can be also described as

$$V^2 \sim (\varepsilon/\nu) \, \Lambda^2, \tag{2.7}$$

$$F(k) \sim (\varepsilon/\nu) \, k^{-3}, \tag{2.8}$$

assuming the mechanism of the laminar dissipation⁽⁵⁾.

The concept of the largest turbulon is defined as the intersection of two spectral functions (2.2) and (2.6) as

$$k_0 \sim K_0^{-3/4} \varepsilon^{1/4}, \tag{2.9}$$

and accordingly

$$\Lambda_0 \sim K_0^{3/4} \varepsilon^{-1/4} \tag{2.10}$$

$$V_0 \sim K_0 \Lambda_0^{-} \sim K_0^{1/4} \varepsilon^{1/4}. \tag{2.11}$$

Thus we can regard the length Λ_0 as the representative of influence of the turbulent viscosity K_0.

Quite similarly we can define the concept of the smallest turbulon by the intersection of two spectral functions (2.6) and (2.8) as

$$k\infty \sim \nu^{-3/4} \varepsilon^{1/4}, \tag{2.12}$$

and accordingly

$$\Lambda\infty \sim \nu^{3-1/4} \varepsilon^{-1/4}, \tag{2.13}$$

$$V\infty \sim \nu \Lambda\infty^{-1} \sim \nu^{1/4} \varepsilon^{-1/4} \tag{2.14}$$

Hence, as was pointed out by G.K. Batchelor⁽⁶⁾, the length $\Lambda\infty$ can be conceived as the representative of influence of the laminar viscosity ν.

On the other hand, if a heated turbulent fluid is considered, a certain mechanisms of internal heat transfer owing to the mutual interaction of turbulons must be assumed.

These assumptions have already been dealt with by the present author⁽¹⁾ and in a quite different way by Obuhov⁽²⁾ and Yaglom.⁽³⁾.

In the author's treatments the transfer rate Q of heat energy per unit time and unit mass of turbulon has been assumed to be the essential quantity which is supposed to be corresponding to the dynamical quantity ε for the dynamical state of turbulons, that is to say,

$$Q \sim K_H (T/\Lambda^2). \qquad (2.15)$$

Hence, comparing it with the relation (2.4), the relationship between the turbulon kinetic energy and the turbulon temperature T is in general shown to be

$$V^2 \sim \frac{1}{\sigma} \frac{\varepsilon}{Q} T. \qquad (2.16)$$

In the above relation σ is shown to be the ratio K/K_H, where K_H means the turbulent heat diffusivity, and is eventually shown to be the Prandtl number ν/κ of a fluid material, where κ means the laminar heat diffusivity. And eventually the spectral functions for the temperature fluctuations are obtained as

$$G(k) \sim \sigma^2 Q^2 \varepsilon^{-2/3} k^{-7/3} \qquad (2.17)$$

and

$$G(k) \sim Q^2 \kappa^2 k^{-5} \qquad (2.18)$$

for the intermediate and the smallest turbulon range respectively.

To the contrary, in Obuhov's and Yaglom's treatments another special quantity N is assumed to be the essential quantity, that is

$$N \sim K_H (T/\Lambda)^2. \qquad (2.19)$$

Comparing the above relation with (2.4) we can get readily

$$\frac{K_H}{N} T^2 \sim \frac{K}{\varepsilon} V^2,$$

$$V^2 \sim \frac{1}{\sigma} \frac{\varepsilon}{N} T^2. \qquad (2.20)$$

Accordingly, in the intermediate range the negative five-thirds power law for the temperature fluctuation is obtained as

$$G'(k) \sim \sigma N \varepsilon^{-1/3} k^{-5/3}. \qquad (2.21)$$

The above result is noting but what has been obtained by Obuhov and Yaglom.

In order to decide the superiority between these two distinctly different assumptions, precise experiments are necessary.

Recently Corrsin and Uberoi⁽⁴⁾ have carried out some measurements of both $F(k)$ and $G(k)$ in a small-scale heated jet. Since the used jet is of small scale, it seems reasonable to deal with only the region of high wave number, say more than 2~3 cm⁻¹, in their experimental results. Figs. 1 and 2 which contain respectively $F(k)$ and $G(k)$ are reproduced from Fig. 14 of Corrsin's and Uberoi's paper for the highest wave number region. In Fig. 1 we may be able to find both ranges of $F(k)$ corresponding respectively to the −5/3 power and the −3 power law. And in Fig. 2 there seems to exist the anticipated region of $G(k)$ corresponding to the −7/3 power law.

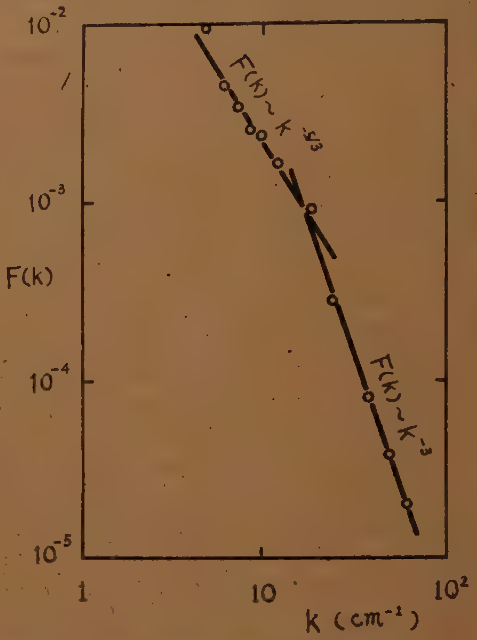

Fig. 1. Exprimental Results of $F(k)$ in a Jet. (Corrsin and Uberoi 1950)

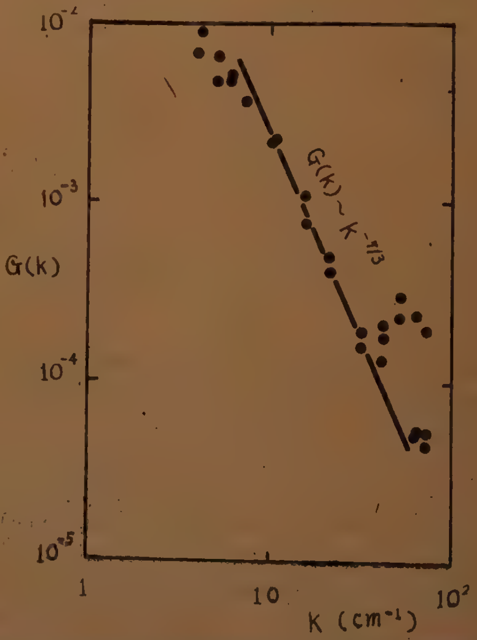

Fig. 2. Experimental Results of $G(k)$ in a Heated Jet. (Corrsin and Uberoi 1950)

§3. Relationship between the Dynamical Smallest Turbulon and the Thermal Smallest Turbulon.

The concept of the smallest turbulon is ordinarily the representative of domain of laminar state in a turbulent fluid. Thus it has seemed reasonable to the anthor to suppose that the domain of laminar energy dissipation and that of laminar heat transfer must be identical. And accordingly the proportionality coefficient σ in (2.16) has been deduced to be the Prandtl number⁽⁷⁾.

On the other hand, the dynamical smallest turbulon is defined in §2 as the intersection of two spectral functions for the intermediate and the smallest turbulon range as (2.12). Quite similarly we can also define the thermal smallest turbulon as the intersection of two temperature spectral functions (2.17) and (2.18). In fact, this point is shown to be

$$k_{\infty H} \sim \kappa^{-3/4}\sigma^{-3/4}\varepsilon^{1/4}, \qquad (3.1)$$

and under the condition that σ is corresponding to the Prandtl number, it becomes

$$k_{\infty H} \sim \nu^{-3/4}\varepsilon^{1/4} \qquad (3.2)$$

showing that the smallest turbulon is exactly equivalent to the dynamical smallest turbulon.

§4. Dynamical and Thermal Correlation in a Heated Turbulent Fluid.

It is well known that the correlation coefficients for the fluctuating quantities in a turbulent fluid can be deduced mathematically from the spectral functions for those quantities by means of the Fourier transform⁽⁸⁾.

In fact, the author⁽¹⁾ has discussed the correlation coefficients for the temperature fluctuations in a heated turbulent fluid for the intermediate turbulon range as follows:

Eulerian : $S(t)=1-(t/T_0)^{4/3}$, (4.1)
Taylor-Kármánian : $S(r)=1-(r/\Lambda_0)^{4/3}$. (4.2)

where T_0 and Λ_0 denote respectively the passage-time and the length of the effective largest turbulon in the fluid. On the other hand, those for the velocity fluctuations are also shown to be⁽⁹⁾

Eulerian : $R()=1-(t/T_0)^{2/3}$, (4.3)
Taylor-Kármánian : $R(r)=1-(r/\Lambda_0)^{2/3}$. (4.4)

Therefore, provided the effective largest turbulons for the temperature and the velocity fluctuations are identical, we can get readily the simple relations between S and R as

$$1-S(t)=\{1-R(t)\}^2, \qquad (4.5)$$
$$1-S(r)=\{1-R(r)\}^2. \qquad (4.6)$$

These relations are schematically shown in Fig. 3.

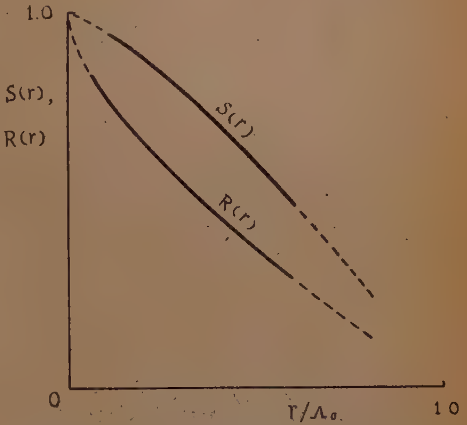

Fig. 3. The Schematical Diagram for $S(r)$ and $R(r)$

It seems worthwhile to point out that there exist very distinct differences between S and R, for which it would be comparatively easy to be detected experimentally.

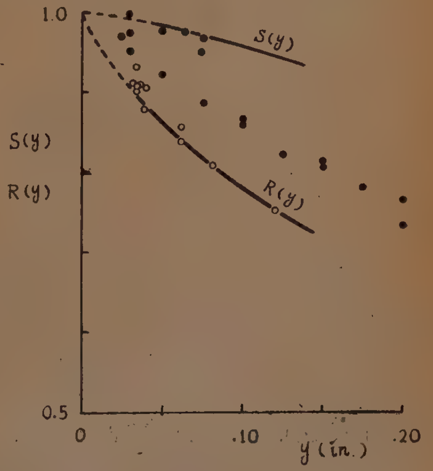

Fig. 4. Experimental Results of $S(y)$ and $R(y)$ in a Heated Jet. (Corrsin and Uberoi 1950)

Recently Corrsin and Uberoi⁽⁴⁾ have carried out such experimental measurements in a small-scale heated jet. Fig. 4 is reproduced from Fig. 32 in their paper. In this figure the theoretical curves for $S(r)$ and $R(r)$ are also drawn, being fitted at a relevent point on $R(r)$ i.e. $r=0.009$ in. and $R(r)=0.80$. Although the agreement for $R(r)$ curve in Fig. 4 is found to be sufficiently good, the agreement for $S(r)$ curve seems to be restricted only to a particular region. However, this discrepancy in $S(r)$ curve might be partly due to the fact that the effective largest turbulon for $S(r)$ is not identical with that for $R(r)$.

§5. Conclusion.

Recently there have been proposed two different assumptions to deal with the thermal structure of a heated turbulent fluid. From one of them the -7/3 power law of the temperature spectrum in the intermediate turbulon range is obtained, and from the other the -5/3 power law is obtained.

In this paper the author has intended to make clear the opposition of them. Of course, the final decision must be given by the precise experimental results. And making use of the recent results of Corrsin and Uberoi, some most opposite points are examined.

At the present stage of the experimental works, however, it seems difficult to decide the superiority betweten these two assumptions.

Acknowledgement——In conclusion I wish to express my sincere thank to Dr. F. R. Hama, The Johns Hopkins University, for his kindness having enabled me to have a chance to see Corrsin's and Uberoi's recent paper.

References.

(1) E. Inoue: Geophys. Note, Tokyo Univ., **3** (1950), No. 34.
(2) A. M. Obuhov: Izv. Akad. Nauk SSSR, ser. Geogr. Geofiz., **13** (1949), 58.
(3) A. M. Yaglom: Doklady Akad. Nauk SSSR, **69** (1949), 743.
(4) S. Corrsin and M. S. Uberoi: NACA Tech. Note, No. 2124 (1950).
(5) E. Inoue: Rept. Inst. Sci. Technol. Univ. Tokyo, **4** (1950), 194.
(6) G. K. Batchelor: Quart. Journ. Roy. Met. Soc., **76** (1950), 133.
(7) E. Inoue: Geophys. Note, Tokyo Univ., **3** (1950), No. 35.
(8) G. I. Taylor: Proc. Roy. Soc. A, **164** (1938), 476.
(9) E. Inoue: Journ. Met. Soc. Japan, **28** (1950), 367.

Short Notes.

J. PHYS. SOC. JAPAN Vol. 6 (1951) 397

On the Deviation from the Ohm's Law at the Anode Surface of the Cuprous Oxide Rectifiers.

By Mitsuo ONO.
Department of Applied Physics, Faculty of Engineering, Nagoya University.

(Received February 8, 1951)

The self-capacity of the selenium rectifiers at high frequencies decreases monotonously as the bias voltages varies from small positive to large negative voltages, and it does not fluctuate much when the bias voltage has small positive or negative values(1). But this is not the case for the cuprous oxide rectifiers with graphite. In this case, the curve of capacity v.s. bias voltage is not monotonous, and the capacity decreases sharply as the bias voltage approaches zero, as shown in Fig. 1.

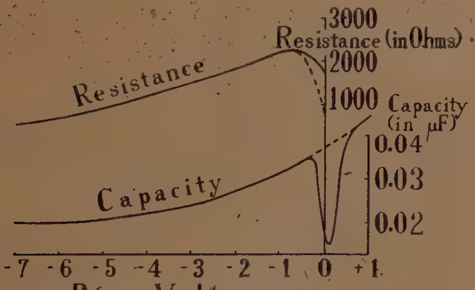

Fig. 1.

This fact may be explained on the assumption that there exists a non-Ohmic resistance in series to the rectifier, which has a resistance only for small electric field, as it is in the case of the "thyrite"(2). If we can know the non-Ohmic resistance R, which is zero for sufficiently high voltages, we shall be able to reduce the curves of Fig. 1. to the case where R is absent. On the other hand, assuming the capacity changes monotonously as shown in the dashed line in Fig. 1, we can, from the experimental curve, calculate R and the resistance as a function of bias voltage for the ideal case in which R is absent. These results are shown in Fig. 2. and in the dashed line in Fig. 1.

As the rectifiers are operated continually, the self-capacity for the zero bias voltage gradually decreases, and the resistance increases, but the effect is small for large negative voltages. It may be possible that the agings phenomena have partly their origin in the increase of the values of R above mentioned.

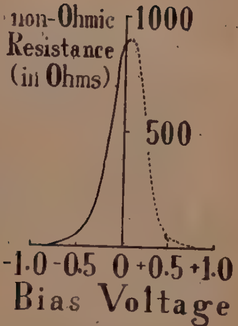

Fig. 2.

The non-Ohmic resistances R will be the contact resistance between the graphite anode and the cuprous oxide, because we can hardly recognize such an effect on the rectifiers with gold anode.

References.

(1) M. Ono: Memoirs of the Faculty of Engineering, Nagoya University, Vol. (1949), 136.
(2) K. B. Mac Eachron: G. E. Rev., (1930), 92.

J. PHYS. SOC. JAPAN Vol. 6 (1951) 397—398

On the Masses of Charged Particles of the Cosmic Radiation in Nuclear Emulsions.

By Seitaro YAMAGUCHI and Masaomi TAKAHATA.
Department of Physics, Faculty of Science, Osaka University.

(Read Nov. 4, 1950, Received April 4, 1951)

It has been impossible to determine the mass of charged particle by grain counting in nuclear emulsion when the fading of the latent images was to be considered, but by the following method both the values of masses and fadings of cosmic radiation are evaluated at the same time.

In the case that the charge and the velocity of two particles are equal, the following equations are satisfied,

$$\frac{N_1}{N_2}=\frac{R_1}{R_2}=\frac{M_1}{M_2} \qquad (1)$$

where N_1, R_1, M_1; N_2, R_2, M_2 represent their total grain numbers, residual ranges and masses respectively, see, (1),* (2).*

Then the relation

$$\log N = \log R + \log f(R/M) \qquad (2)$$

are obtained.

If the range-grain curves have bending portions in $\log N \sim \log R$ plot, these curves of two particles of different masses coincide each other by translating in direction 45° to the $\log R$ axis.

And when the grains decrease by "fading", we assume that the fading occurs as the relation $\alpha N = N'$ is staisfied at all points of R, where N' is the total grain number in observation and N is the one obtained if the plate is measured soon after the particle has passed through it.

Then the relation

$$\log N' - \log \alpha = \log R + \log f(R/M) \qquad (3)$$

are obtained.

For the particles of same masses, $\log N \sim \log R$ curve can be translated parallel to $\log N$ axis in accord with the change of fading coefficient α,

Thus, when the mass of any particle M_1 is known, it can be taken as the standard and unknown mass M_2 and fading coefficient α of the other particle can be determined, M_1/M_2 is given by the distance of translation in direction 45° to $\log R$ axis by using the relation

$$\sqrt{2}\,(\log R_1 - \log R_2) = \sqrt{2}\,\log (M_1/M_2) = \text{const} \quad (4)$$

And $\log \alpha$ is given by the distance of translation parallel to $\log N$ axis in the relation (3).

We observed four N.T.B. plates, 50 μ thick, which were exposed during 47 days on Mt. Norikura (2840 M) and were processed simultaneously in D-19 developer (3)*.

Each track was observed by using ×100 ×10 oil immersion lens, then the grains of those were counted only when the track stopped in emulsion, where the tracks of short range were omitted, and 29 tracks were observed.

The standard curve is taken by combining the longest curves of Proton, Deuteron and ω particle, and the mass of unknown one was determined by the method above mentioned.

The results thus ontained are shown in Table I.

Further investigations are now going on. We wish to express our sincere thanks to Professer Y. Watase for his encouragement in the course of our research and also to Professer K. Kimura and others of Kyoto University for their allowance for the use of their N.T.B. plates.

References.

(1)* E. Fermi, Nuclear Physics, 138-139 p.

(2)* A. I. Alikhanian et al. J. of Exp. and Theor. Phys. USSR 19 (1949) 664, 667.

(3)* K. Kimura, S. Tokunaga, R. Ishiwari & K. Yuasa: Memoirs of the College of Science, University of Kyoto, Ser. A, Vol. XXVI. Nos. 1 & 2. Article 17, 1950.

Table I

Track No *	Nature of Particle	Range in μ	Mass Me	Fading coefficient	Remarks
17	α	1970			Standard
13	?	430			prong of star
8	ω_1	3300	6500 7200	0.79	
18	ω_2	2220	6500–7600	0.85	
28	D_1	2900	3400-3800	1.00	
1	D_2	1600	3300–3600	0.75	
16	D_3	1440	3600-4000	0.90	prong of star
7	D_4	1070	3100 3600	0.89	
11	D_5	620	$>P$		$\neq P$
10	D_6	500	$>P$		$\neq P$
3	P_1	2650	1800	0.77	standard of mass
4	P_2	1640	1800–2000	0.86	prong of star
20	P_3	980	2000–2250	1.00	
5	P_4	880	2100 2250	1.03	
23	P_5	840	2000-2250	0.93	
26	P_6	840	2000-2250	1.10	
19	P_7	790	2000-2250	0,93	
25	P_8	650	1800–2100	1.00	
24	P_9	600	1800 2100	0.98	
14	P_{10}	560	1500-1900	0.83	
12	P_{11}	510	1300-1900	0.76	
21	P_{12}	410	$\geqq P$		Produced from meson No. 22
9	ζ	930	770– 810	0.79	
2	η	1020	630– 660	0.71	
6	ξ	700	410– 495	0.80	
22	?	350	$>\pi$		produce heavy particle No. 21
27	?	400	$>\pi$		
15	μ_1	400	185– 210	1.02	
29	μ_2	640	185– 170	0.95	

* Track no. 1–7, 8–16, 17–24, 25–29 belong no. 1, no. 2, no. 3, no. 4, plate respectively.

J. PHYS. SOC. JAPAN Vol. 6 (1951) 398—400.

An Application of Proportional Counters to Mass Determination (1)

By Masafumi INOKI.

Physics Institute, Yamanashi University, Kofu.

(Received May 21, 1951)

At sea level, we have measured the mass of slow cosmic ray particles, whose velocities are less than half light velocity, with an apparatus consists of two proportional counters and a cloud chamber. As is shown in Fig (I), the two proportional counters and four or five aluminium foils are placed in the cloud chamber. The specific ionization of the particles stopped in the cloud chamber is measured with the proportional counters and their range is determined with the number of foils through which the particle has passed. The thickness of aluminium foils is 1 mm in the first, 0.5 mm in the second and 0.1 mm in the third experiment. No absorbers are used over the cloud chamber except concrete roof corresponding to 5 cm lead.

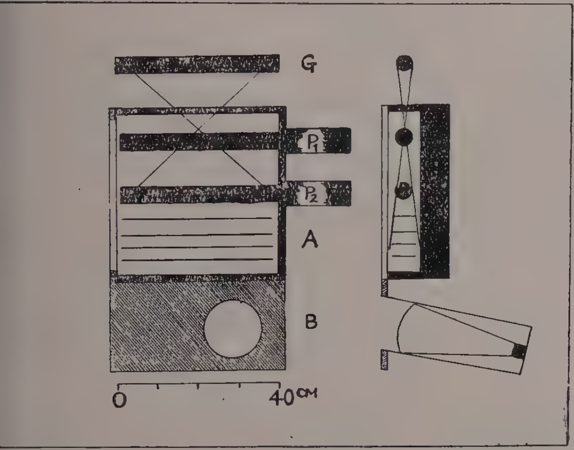

Fig. (1), The schematic diagram of the apparatus showing the cloud chamber, Geiger counter G, two proportional counters (P_1, P_2), the absorbers (A) and the Braun tube (B).

The cloud chamber is expanded when three fold coincidence occurs among one Geiger counter placed over it and two proportional counters in the cloud chamber. By a suitable selection of pulses from the proportional counters, we succeeded to take the cloud chamber photogaphs of slow cosmic ray particles only. Therefore we could save time and expenses of taking the photographs of the fast particles.

In the measurement of the specific ionization, when the size of pulses from the two proportional counters were different, we used the smaller one, to elimiate the large error of the estimation of the specific ionization due to the emergence of large blobs of ionization caused by the secondary electrons of the primary particle inside one proportional counter tube. The error of the specific ionization due to different path length of the particles inside the proportional counter tube was corrected by using the stereoscopic cloud chamber photographs. The probable error of the specific ionization was determined by the measurement of the specific ionization of fifty fast cosmic ray particles and found it to be $22\sqrt{D}\%$, where D is the specific ionization in unit of the minimun ionization. As the probable error of the range, we used a quarter of the thickness of the absorber.

We have obtained forty-six particles stopped in the absorbers, fifteen particles of them being surmised from their features as very slow protons Then we have determined the mass of the remaining thirty-one particles. The experimental values of specific ionization versus range of these particles are plotted in Fig. (2), in which also the theoretical curves for mesons, electron and proton are shown.

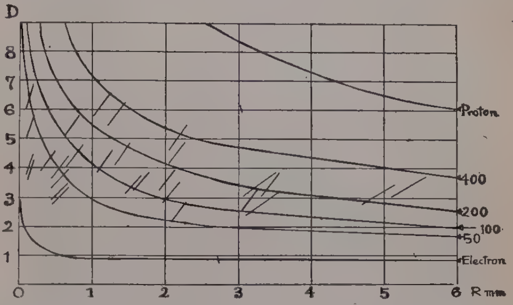

Fig. (2). The relation between range and specific ionization. The diagonal lines have their centers at the observed values of range and specific ionization. The length of the lines is such that the projection on R and D co-ordinates are the extent of twice of the probable errors, $2\varDelta R$, $2\varDelta D$.

Considering the various errors and estimating the accuracy of this experiment, it seems to be reasonable that the sixteen particles whose masses are distributed between 122 and 376 may be μ-mesons and the three particles having larger masses than 376 may be protons, while twelve particles having masses smaller than 122 are not certain whether they belong to μ-meson or a new meson, lighter than μ, because their experimental values are exceedingly apart from the values of μ-meson, even if taking errors into consideration. If they belong to μ-meson, the small estimation of the mass value may be due to some instrumental effect or some unknown abnormal absorption of slow μ-meson by the absorbers. We have calculated the weighted mean of the sixteen masses mentioned above and found it to be $M=190.0\pm11.6$. This value coincides with μ-meson mass which has been measured hitherto by the various authors.

The intensity of the slow μ-meson stopped in 1 mm aluminium plate was about 1/13,400 of the total cosmic ray particles and it coincides with the data by Chang.(1) The total time of the operation was about 350 hours and the total number of the photographs taken was 1420. According to this research, the forty-six slow particles mentioned above are to be contained in about 186,000 cosmic ray particles at sea level.

Finally, the author wishes to thank the late Dr.

Fig. (3), The typical cloud chamber photograph of the slow μ-meson, taken by the front camera.

Y. Nishina who gave the author a suggestion on this study. He is also indebted to Professor Robert. B. Brode of the University of California for his useful instruction given recently concering the method of mass determination.

Reference.

(1) W. Y. Chang; Rev. Mod. Phys. (1949) 166

J. PHYS SOC. JAPAN Vol. 6 (1951) 400—401.

Note on Rayleigh's Problem for a Bent Flat Plate

By Hidenori HASIMOTO
Department of Physics, Faculty of Science, University of Tokyo

(Received May 24, 1951)

With cylindrical coordinates O (r,θ,z) an infinitely thin infinite bent plate coincident with two half planes $\theta=0$, $\theta=\alpha\,(r\geqq 0)$ is initially at rest surrounded by viscous incompressible fluid at rest; starting at time $t=0$ the plate is made to move uniformly with velocity W parallel to z axis, and we are required to determine the subsequent motion of the fluid in the region $0<\theta<\alpha$, and the skin friction on the plate.

This problem is of particular interest, as it gives the qualitative picture of the boundary layer growth on a plate. Thus in 1911 Rayleigh(1) considered the case $\alpha=\pi$, and recently Howarth(2) treated the case $\alpha=2\pi$ with a view to discussing the edge effect on the boundary layer growth. In order to study the corner effect of a bent plate, we have treated the general case $0<\alpha<2\pi$. Thus, we have obtained, as in Howarth's treatment, a solution in terms of confluent hypergeometric functions, which can be simplified by means of the integral representation of these functions; in particular we have found a very simple expression for the skin friction of the plate. Also it was found that in the case of $\alpha=\pi/m$ (m=integer), even the velocity distribution can be expressed in a closed form in terms of error and exponential functions. Recently we became aware that the case $\alpha=\pi/m$, had already been studied by Sowerby,(3) giving the same solution as ours. However, his solution is confined only to the case $\alpha=\pi/m$, and the outer problem is left untouched.

In this note will be given a brief outline of our method and results obtained. The skin friction τ on the plate can be expressed as

$$\tau=\frac{2\beta\mu w}{\pi(\nu t)^{1/2}}e^{-\eta}\sum_{n=1}^{\infty}\frac{\Gamma(k/2+1)}{\Gamma(k+1)}\eta^{(k-1)/2}{}_1F^1(1+k/2,1+k,\eta), \tag{1}$$

where $k=(2n-1)\beta$, $\beta=\pi/\alpha$. $\eta=r^2/(4\nu t)$, μ is the viscosity, ν the kinematic viscosity, and ${}_1F^1$ the confluent hypergeometric functions. Using the formulae,

$${}_1F^1(k/2+1,k+1,\eta)=e^{\eta}\frac{\Gamma(k+1)}{\Gamma(k/2)\Gamma(k/2+1)}\int_0^1 e^{-q\eta}q^{k/2-1}(1-q)^{k/2}dq, \tag{2}$$

$$\frac{z^{k/2-1}}{\Gamma(k/2)}=\frac{1}{2\pi i}\int_{Br}\frac{e^{zp}}{p^{k/2}}dp \qquad z>0, \tag{3}$$

and

$$\sum_{n=1}^{\infty}\frac{1}{p^{(2n-1)\beta/2}}=\frac{p^{-\beta/2}}{1-p^{-\beta}}, \qquad Re(p)>1, \tag{4}$$

we get finally

$$\frac{(\pi\nu t)^{1/2}}{\mu W}\tau=\operatorname{erf}\eta^{1/2}+8\beta\pi^{-3/2}\sin\frac{\beta}{2}\pi\cdot e^{-\eta}\int_0^{\infty}\frac{\sin hu\cos h\beta u}{\cos k2\beta u-\cos\beta\pi}\gamma(\eta^{1/2}\sin hu)du+2\sum_{n=1}^{n<\pi/(2\alpha)}(-)^n\cos n\alpha\cdot\exp(-\eta\sin^2 n\alpha)\cdot\operatorname{erf}(\eta^{1/2}\cos n\alpha), \tag{5}$$

where $\gamma(x)$ is a tabulated function:(4)

$$\gamma(x)=e^{-x^2}\int_0^x e^{t^2}dt=\int_0^{\infty}e^{-t^2}\sin 2xt\,dt. \tag{6}$$

If $\beta=2m$, the second term on the right-hand side of (5) vanishes, so that (5) reduces to Sowerby's result. If $\beta=2m+1$ the integral in (5) can be evaluated by the contour integration of $(\cos h2\beta z-\cos\beta)^{-1}\sin kz\cos h\beta z\exp(2i\eta^{1/2}t\sin hz)$, thus reducing to Sowerby's result. It may also be noted that the last term of (5) vanishes when $2\geqq\beta\geqq1/2$ $(\pi/2\leqq\alpha\leqq2\pi)$. Subtracting from τ Rayleygh's value $\tau_R=\mu w(\pi\nu t)^{-1/2}$, integrating from $r=0$ to ∞, we get

$$\frac{E}{\mu W}=\int_0^\infty(\tau-\tau_R)dr=-\frac{2}{\pi}+\frac{8\beta K}{\pi^2}\sin\frac{\beta}{2}\pi+2\sum_{n=2}^{n<\pi/(2\alpha)}(-)^n$$

$$(1-\frac{2n}{\pi}\alpha)\cot n\alpha$$

$$=2\sum_{k=1}^{n}(-)^k\cot k\alpha,\quad \alpha=\pi/(2m+1), \tag{7}$$

where

$$K=\int_8^\infty\frac{u\,\mathrm{tgh}\,u\cdot\cos h\beta u}{\cos h2\beta u-\cos\beta\pi}du \tag{8}$$

represents the total excess of the skin friction over Rayleigh's value. The integrals of (5) and k are suited for the numerical integration. When $\beta=\pi/\alpha$ is a rational number, K can be caluculated analytically by the contour integration. For example, we get

α	β	K	$E/\mu W$	$E/\mu W$
90°	2	finite	$-2/\pi$	-0.6366
120°	3/2	$[\sqrt{6}/18-\sqrt{2}/8]\pi^2+\sqrt{2}\pi/6$	$-[3/2-2/\sqrt{3}]$	-0.3453
135°	4/3	$[\sqrt{3}/16-1/9]\pi^2+\sqrt{3}\pi/12$	$-[16\sqrt{3}/27+2/(3\pi)-1]$	-0.2386
180°	1	$\pi/4$	0	0
240°	3/4	$[\pi/3-(\sqrt{3}/9-\sqrt{2}/4+1/8)\pi^2]/S$	$3/\sqrt{2}-2/\sqrt{3}-3/4$	0.2166
270°	2/3	$\sqrt{3}\pi/6+\pi^2/9$	$-2/(3\pi)+8\sqrt{3}/27$	0.3010
300°	3/5	$[5\pi^2/\sqrt{3}+5\pi-6\pi^2 tg\pi/10]/T$	$2/\sqrt{3}-2.4\mathrm{tg}(\pi/10)$	0.3749
360	1/2	$\pi/\sqrt{2}+\sqrt{2}\pi^2/8$	1/2	0.5

Here $S=\sin(3\pi/8)$, $T=12\sin(3\pi/10)$.
E being known, we can make the same discussion for the plate of finite breadth as done by Howarth and Sowerby. In conclusion the author express his cordial thanks to Professor I. Imai for his continuous guidance and encouragement.

References.

(1) Rayleigh, Lord Phil. Mag. (6), **21** (1911) 697
(2) Howarth, L. Cambr. Phil. Soc. **46** (1950) 127
(3) Sowerby, L. Phil. Mag. **42** (1951) 176
(4) Terazawa, K. Sci. Rep. Tohoku Imp. Univ. Ser I. **6** (1917) 169

J. PHYS. SOC. JAPAN Vol. **6** (1951) 401—402.

On the Band-System of Neutral OD.

By Hirobumi OURA.
Institute of Low Temperature Science,
Hokkaido University.

(Received May 31, 1951)

The ultraviolet ray emitted by neutral OD molecules was obtained by geissler discharge in the vapour of heavy water, and the 2nd order spectrum by concave grating having radius 6.5 m was analysed. Spectral lines were classified in the (0,1) band 194 lines, in (1,1) 130, in (1,0) 145, in (1,2) 113, in (2,2) 78, in (2,1) 113, respectively. The anaylsis of the (0,0) band was reported in previous paper.(1)

The bands involving the same vibrational level of Σ state listed below were compared with each other, applying combination principle. (0,0) (0,1); (1,0), (1,1), (1,2); (2,0),(2) (2,1).

The bands involving the same vibrational level of $^2\Pi$ state listed below were compared with each other. (0,0), (1,0), (2,0); (0,1), (1,1) (2,1), (3,1)(2); (1,2), (2,2).

The values of A for $^2\Pi$ state' which is a coefficient of magnetic interaction between resultant electric orbital and spin angular momenta, were calculated. They show $^2\Pi$ levels are inverted and belong to intermediate state between Fund's case a and b. Increasing J from 1 to 20, A increases from -140 to -96, that is, the state approaches from case a to case b. We can hardly find systematic change in A, between $v''=0$, 1 and 2.

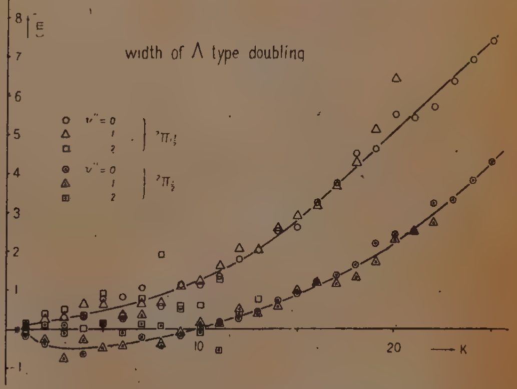

The width of the Atype doubling of the $^2\Pi$ state is shown in Fig. 1.

The rotational constants obtained from the observed values of B_0', B_1', B_2', B_3', B_0'', B_1'' and B_2'' by the least squares are shown below in cm^{-1} unit.

$B_0'=9.043$, $B_0''=9.862$,
$B_e'=9.208$. $B_e''=9.991$,
$\alpha'=0.331$, $\alpha''=0.258$.

The distances between O and D in their equilibrium positions are calculated from B_e.

$r_e'=1.012$Å, $r_e''=0.971$Å.

The band origins are shown in Table I.

The vibrational constants obtained from the values of Table I. by the least squares are shown below in cm^{-1} unit.

V' \ V''	0		1		2
0	32477.4	*2632.0*	29845.4		
	2213.9		*2215.4*		
1	34691.3	*2630.5*	32060.8	*2540.9*	29519.9
	2110.3		*2110.9*		*2106.8*
2	36801.6	*2629.9*	34171.7	*2545.0*	31626.7
			2106.9		
3			36178.6		

$\omega'=2313.50$, $x'\omega'=49.18$,
$\omega''=2716.13$, $x''\omega''=42.15$.

These vibrational and rotational constants show good coincidence with those calculated from the constant of OH⁽³⁾ taking isotope effect into consideration.

The dissociation energy is

$D_0'=22488\text{cm}^{-1}=2.789\text{e.V.}$,
$D_0''=34227\text{cm}^{-1}=4.244\text{e.V.}$,
$D_e'=23632\text{cm}^{-1}=2.930\text{e.V.}$,
$D_e''=35575\text{cm}^{-1}=4.411\text{e.V.}$

The relations between these constants found by Kratzer,⁽⁴⁾ Birge,⁽⁴⁾ Mecke,⁽⁵⁾ Allen and Longair,⁽⁶⁾ and Rydberg⁽⁷⁾ were examined.

The wave number of all lines classified, etc. are printed in "Low Temperatur Science" **6**. p. 41—70, (1951) in detail. (in Japanese.)

References.

(1) H. Oura and M. Ninomiya, Proc. Phys-Math. Soc. Japan. **25**, (1943) 335.
(2) About the bands (2,0) and (3,1), the values reported by M. Ishaq were used.
M. Ishaq, Proc. Roy. Soc. **195**. (1937) 110.
(3) T. Tanaka and Z. Koana, Proc. Phys-Math. Soc. Japan. **16**, (1934) 365.
(4) W. Jevons, "*Roport on Band Spectra of Diatomic Molecules*" University press, Cambrege. p. 29.
(5) R. Mecke, Zs. f. Phys. **32**, (1925) 823.
(6) H. S. Allen and A. K. Longair, Phil. Mag. **19**, (1935) 1032.
(7) R. Rydberg. ZS. f. Phys. **73**, (1931) 376.

J. PHYS. SOC. JAPAN Vol. **6** (1951) 402—403.

A Hodoscope Study on the Penetrating Shower.

By Yuzuru WATASE, Minoru ODA, Tadayoshi KUBOZOE and Shigeru HIGASHI
(*Osaka City University*)

(Received June 4, 1951)

Recently it is plausibly believed that the secondary particles of the penetrating showers are mostly composed of nucleons and pi-mesons, and their mean free path relative proportion and their are under investigation by many authors. Present authors would like to report some preliminary results of an experiment performed at sea level by a counter hodoscope.

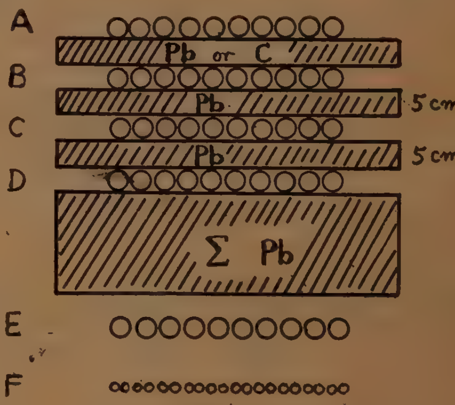

Fig. 1.

Experimental arrangement is sketched in fig. 1. *A,B,C,D*, and *E* trays are of ten counters of 4 cm dia. and 40 cm effecive length. and *F* tray is of twenty counters of 2 cm dia. and 40 cm effective length. The master pulse was generated by coincidence of two or more of *B* counters, three or more of *C* counters and any one of *D* counters. Thus, 15000 events were recorded during 1444 hours. In these events the case in which two or more *D* counters and one or two *A* counters discharged was regarded as local penetrating shower produced by the top layer of lead. This method, to select the penetrating showers dividing the absorber into two parts was superior to other usual method, because the correction needed was considerably small in this case. When two or more side counters discharged the record was omitted from statistics. Chance coincidences and knock on electrons from the lead were taken into account, but they were very small in amount. The thickness of lead absorber between *D* and *E* trays was changed from zero to twenty cm. Thus 1137 records of penetraing showers were obtained. When two neighboring *A* counters discharged, it interpreted as at least one particle was emitted backward and this was confirmed by other experiment. Thirty percents of penetrating showers emit backward particles.

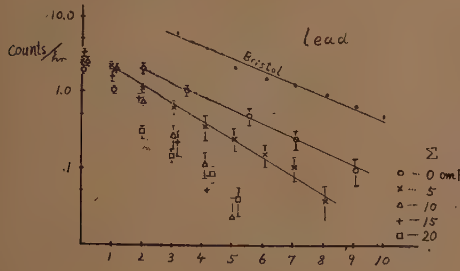

fig. 2

Experimental results obtained are shown in fig. 2 and 3. Fig. 2 represents the multiplicity spectrum of penetrating showers produced at the top layer of lead of 5 cm where abscissa and ordinate represent the multiplicity of secondaries measured by E and F trays and counting rate respectively. Chances of missing the secondary particles were taken into account. Multiplicity spectrum of thin tracks in emulsion obtained by Bristol group⁽¹⁾ is translated in this condition and plotted in the figure. The slope of the curve seems to agree with the spectrum under 10 cm lead, though absolute frequency does not so well agree. The mean free path of secondary particles which can penetrate at least 20 cm lead is estimated from the decrease of average multiplicity with increasing lead thickness and of the rate of penetrating showers having at least two secondaries under increasing lead absorber. Thus it is estimated as 300±100g/cm². It should be noted that the mean free path estimated by the latter method needs a correction concerning the shape of the multiplicity spectrum. as shown in fig. 2, the spectrum decrease with increasing the thickness of lean absorber up to 20 cm lead, but there is no remarkable variation beyond 20 cm lead.

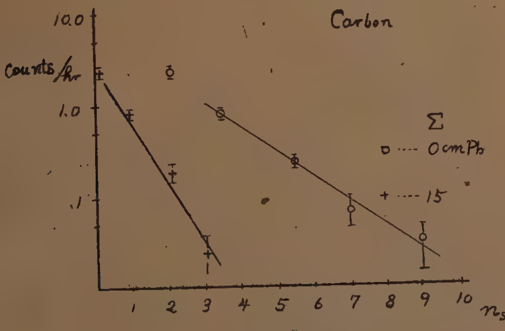

fig. 3

In fig. 3 multiplicity spectrum of penetrating showers which were produced at top layer of carbon 7 g/cm² is shown. In this case the multiplicity spectrum is considerably different from that of lead and this fact may be rationally comprehended.

This work was done as a preliminary part of study which will be performed by the present authors and S. Ozaki and T. Kitamura.

Reference.

(1) R. H. Braun, U. Camerini, P. H. Fowler, H. Heitler, D. T. King, and C. F. Powell, Phil Mag **40** (49) 862

J. PHYS. SOC. JAPAN Vol. 6 (1951) 403—404.

A Study on the Extensive Air Shower

By Y. WATASE, M. ODA, S. HIGASHI and
T. KUBOZOE

(Osaka City University)

(Received June 4, 1951)

In the course of the hodoscope study of the local penetrating shower, reported in this issue, we have frequently observed the cases in which more than three counters in A tray discharged. It was regarded as the air showers accompanied by penetrating particles which discharged B and C counters and opened the hodoscope master circuit. In order to see the density spectrum of this shower F tray was placed just above A tray. Density spectrum estimated by the number of discharged F counters is shown in fig. 1 by curve (a) where the hodoscope master is $B \geqq 2$ $C \geqq 3$ $D \geqq 1$ coincidence. These showers cannot be explained by the knock-on showers produced by the roof. The density spectrum of these air showers accompanied by at least one particle which discharge the E counter under 30cm Pb is shown in fig. 1 by curve (b). Comparing these two curves it may be concluded that the denser the air shower is, the larger the chance of accompanying hard particles become.

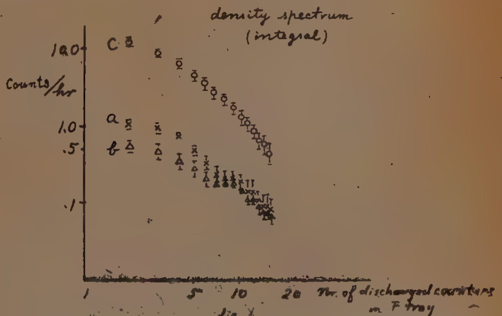

fig 1

In order to confirm this conclusion, F tray was divided into three groups and was set outdoors about 3 m apart from the main part of the arrangement.

In this case the master coincidence of the hodoscope was three-fold coincidence of F groups. The density of the shower was estimated by the number of discharged F counters and the existence of hard particles was checked by B,C,D and E trays. Density spectrum thus obtained is shown in fig. 1 by curve (c). Since the master pulse is generated only by the soft radiations in this case the frequency is considerable larger than that in the previous case. In fig. 2 the relation between the density estimated by F tray and the number of discharged $A,B,C\,D$ and E counters is shown.

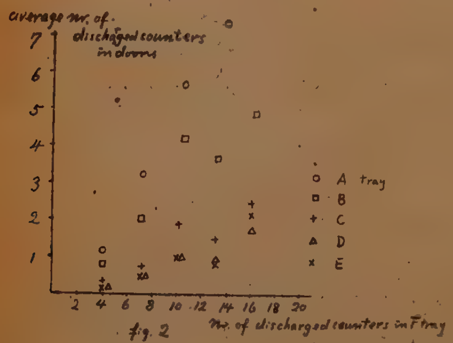

fig. 2

From this result it may be concluded that on the average about 2 percents of the shower particles can penetrate at least 30 cm Pb and this percentage becomes considerably large in the case of very dense air showers.

J. PHYS. SOC. JAPAN Vol. **6** (1951) 404—405.

On the Rate of the Nucleation in the Recrystallization

By Takeo YOKOBORI

(Institute of Science and Technology, University of Tokyo)

(Received June 5, 1951)

The formation of recrystallization nuclei was regarded as a Markoff process.[1][2] Hence, the probability distribution function $1-P$ is given by

$$dP/dt=-mP \qquad (1)$$

where m is the rate of nucleus formation. Thus, the probability density function q is represented by

$$qdt=m\exp\left(-\int_0^t mdt\right)dt\,. \qquad (2)$$

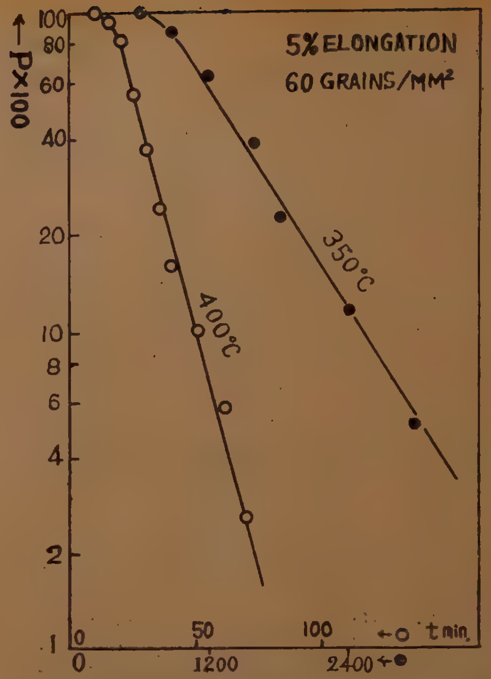

Fig. 1. Calculated from Anderson and Mehl's data.

where q corresponds to N, the rate of nucleus formation between t and $t+dt$ in Anderson and Mehls' experiments.[3] When the curve of log P versus t plotted from these data, m can be obtained from the slope of the curve as shown in Fig. 1. It is understood from Fig. 2 that m thus determined begins to have some finite value at some time (after incubation time), increases and thereafter have some constant value m_0 almost all over the time concerned. By the analysis used above, it can be known that m_0 increases with increase of temperature (Fig. 1), prior plastic deformation, and grain number per unit area of specimens. These effects are well understood from the nucleation theory,[4] which leads to

$$m=ZkT/h\,\exp[(-\Delta f^{*}+\Delta F^{*})/kT] \qquad (3)$$

Eq. (3) shows that the increase of temperature increases m, and prior plastic deformation decreases maximum free energy for nucleus formation ΔF^{*}. And nuclei will preferentially generate at the grain

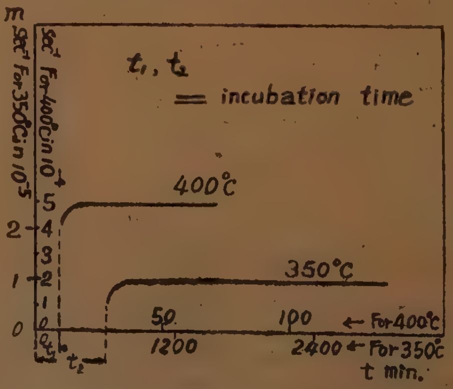

Fig. 2. Calculated from Anderson and Mehl's data.

boundaries which increase with grain number per unit area of specimens. Further investegation is desired to decide whether the appearnce of the part where m appearently increases in the time curve is due to an actual increasing of m or due to the distribution of different incubation times.

The author wishes to express his deep thanks to Prof. M. Hirata. for his very kind guidance and encouragement.

References.

(1) M. Hirata: Bull. Math. Statis. (in Japanese) **3** (1949) 57
(2) T. Yokobori: J. Phys. Soc. Japan. **6** (1951) 78 and 81
(3) W. A. Jonson and R. F. Mehl: Trans. Amer. Inst. Min. Met. Eng. **161** (1945) 140
(4) D. Turnbull and J. C. Fisher: J. Chem. Phys. **19** (1949) 71

J. PHYS. SOC. JAPAN Vol. 6 (1951) 405—406.

On the Color of Chromatic Polarization

By Hiroshi KUBOTA
Institute of Industrial Science, Tokyo University, Chiba-City.

(Received June 13, 1951)

Although the color of a crystal plate placed between two Nicol's prisms and illuminated by white light are well known, they are described with color names and lacked objectivity. To save this defect, the author has studied to describe these colors colorimetrically, some of which were shown in the former paper⁽¹⁾. In this note, we shall show a simple method of getting the interference color of a crystal plate.

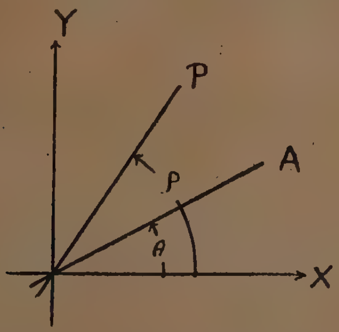

Fig. 1
X, Y: planes of polarization in crystal plate.
P: plane of polarization of polarizer.
A: plane of polarization of analyser.

If we take the planes of polarization of light in crystal as X and Y axes and taking the angle between X and the plane of polarization of the polarizer P and the analyser A as ρ and θ as shown in Fig. 1, then the amplitude of the light coming out from the analyser is as follows, taking the light from the polarizer as $\exp(i\omega t)$,

$$T=\cos\rho\cdot\cos\theta\cdot\exp(i\omega t)+\sin\rho\cdot\sin\theta\exp i(\omega t+\delta)$$

where $\delta=2\pi(\mu d)/\lambda$, in which λ is the wave length and μ the difference of refractive indices for mutually perpendicularly polarized light in the crystal and d the thickness of the crystal plate, so (μd) is the retardation of light during the passage of crystal.

This equation shows that the light coming out from the analyser can be considered as the sum of two beams with phase difference δ, while the interference color of two beams is already studied in the previous paper, so we can describe the color of crystal plate by utilizing the result of it.

According to it, the dominant wave length of the interference color is determined by the phase difference δ. The amplitudes of the two beams, taken as B and C in the former paper, determine the purity of the color through a factor $\varepsilon=(B-C)^2/4BC$. The smaller the $|\varepsilon|$ is, the larger is the purity of the color and the purity becomes maximum when $\varepsilon=0$ and -1, whereas the colors are complementary to each other in cases of $\varepsilon\geqq 0$ and $\varepsilon<0$ for the same δ.

Now, in the case of the crystal plate, as $B=\cos\rho\cdot\cos\theta$ and $C=\sin\rho\cdot\sin\theta$, accordingly,

$$\begin{aligned}\varepsilon&=(\cos\rho\cos\theta-\sin\rho\sin\theta)^2/4\cos\rho\cos\theta\sin\rho\sin\theta\\&=(1-\tan\rho\cdot\tan\theta)^2/4\tan\rho\cdot\tan\theta.\end{aligned}$$

So $\varepsilon=0$ when $\tan\rho\cdot\tan\theta=+1$, that is when $\rho+\theta=\pi/2$, and $\varepsilon=-1$ when $\tan\rho\cdot\tan\theta=-1$, that is when $\rho-\theta=\pi/2$. So, if we take ρ and θ as abscissa and ordinate, then the loci of the points of maximum purity become a set of straight lines. In Fig. 2, they are shown with full ($\varepsilon=0$) and dotted ($\varepsilon=-1$) lines respectively. Other loci of the points on which ε is constant (equi-ε curves) are also given in the figure for $\varepsilon=0.125$, 0.8, 3.0 and -1.13, -1.80, -4.09, although they are not straight lines. With this figure, we can, not only easily find ε-values when θ and ρ are given, but also able to get the general view of the mode of change of color by the rotation of the crystal plate or Nicol's prisms. That is, (a) if we fix the crystal and analyser (at $\theta=\theta_0$) and rotate the polarizer only, then ε changes as the function of ρ along the straight line passing through $\theta=\theta_0$ and parallel to the ρ-axis and (b) if we fix the crystal plate and polarizer (at $\rho=\rho_0$) and rotate the analyser only, then the corresponding locus is the straight line which passes through $\rho=\rho_0$ and parallel to the θ-axis. Finally, (c) if we fix the Nicol's prisms and rotate the crystal plate only, then as $\rho-\theta=\gamma=$const., the points which satisfy this condition are on the straight line running parallel to the bisector of X and Y axes. In the figure, the case when the angle γ is kept 50° is given by thick broken line for example.

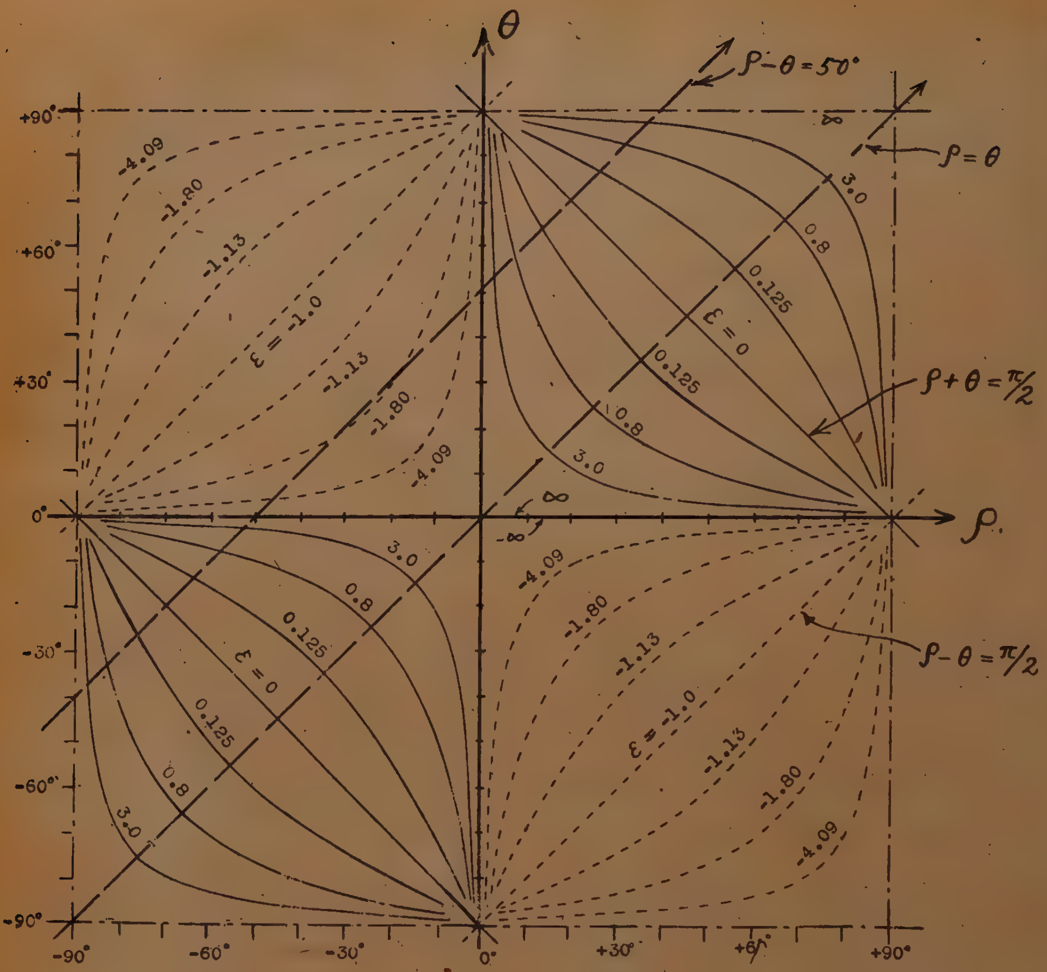

Fig. 2. Equi-ε curves.

In this case, purity increases or decreases as the crystal rotates. As seen in the figure, we are able to let ε take the value 0 certainly by the rotation of the crystal, but except in case of $\gamma=\pi/2$, ε never takes the value -1. The bisector of X and Y itself is the one on which $\rho=\theta$, that is the case of parallel Nicols, and the purity is maximum when it intersects with the locus of $\rho+\theta=\pi/2$, that is the case of $\rho=\theta=\pi/4$ (diagonal position).

As shown above, this graph will, together with the graph which gives the dominant wave length of the color, which was given in the previous paper⁽¹⁾, make the mode of change of color clear in a very simple way.

Reference.

(1) H. Kubota, Jour. Phys. Soc., Japan. 5, (1950) 10

J. PHYS. SOC. JAPAN Vol. 6 (1951) 406—408.

On the Anomalous Structures of Zinc Oxide.

By Kenzo TANAKA, *Physical Institute, Faculty of Science, Kyoto University, and* Hatsujiro HASHIMOTO, *Kyoto Technical University.*

It was reported by Finch in 1934 that he had found a pseudomorphic zinc oxide in the surface coating of zinc melt. To ascertain its existence, we used similar films from melt of electrolytic zinc. The substrate of the film was either nickel or copper. The specimen was set in the electron diffraction apparatus with heating device and was heated. The transmission pattern was observed continuously and some photographs were taken during the heating process.

The diffraction pattern taken at room temperature consisted of spots and rings, and one of them is shown in Fig. 1. Most of the spots were due to normal zinc crystals, but some spots were found to be at the positions which could not be identified with spots for normal zinc. The spacings for the anomalous spots are shown in Table 1. Two kinds of spots were also found at the positions corresponding to the prohibited (00*n*) where *n* is odd and (111) reflections of zinc, but by taking photographs at different settings of the specimen for the electron beam they were explained as arising from double reflections from other planes of zinc. All of the rings of the pattern were identified with the reflections of ZnO except for one with spacing of 1.75 Å which corresponds to the prohibited (003) reflection of ZnO.

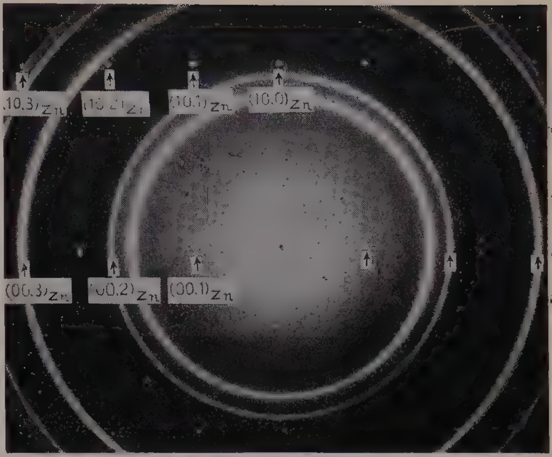

Fig. 1. Electron diffraction pattern at room temperature spots of Zn, rings of ZnO and extra spots.

By heating the specimen in the vacuum of the diffraction apparatus oxidation of the film took place gradually, and all the spots became faint and disappeared at 300∼350°C and there appeared a different pattern. This pattern consisted of rings due to normal ZnO of the dimensions of $a=3.25$ Å and $c=5.23$Å, and some extra rings. ZnO crystals in the film were in fibrous arrangement with fiber of [001] normal to the surface of the film. When the specimen was set so that the normal of the film made an angle of about 20° with the incident beam, the diffraction pattern changed to the type shown in Fig. 2.

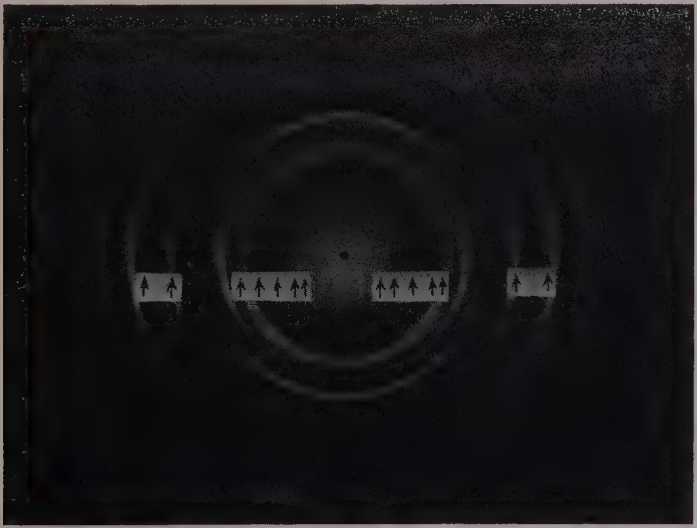

Fig. 2. Electron diffration pattern at 300°–350°C. Rings indicated with arrows (↑) are due to intermediate phase II.

These extra rings faded out at about 400°∼500°C and by further heating the whole pattern became that of normal ZnO. The extra rings can be explained as due to a hexagonal crystal (Phase II) of dimensions of $a=9.75$ Å and $c=10.46$ Å which agree with $3a$ and $2c$ of normal ZnO structure, and its unit cell contain 18 units of ZnO crystal. The anomalous

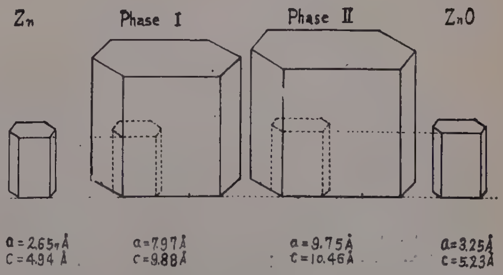

Fig. 3. Schematic representations of two phases as compared with Zn and ZnO cells.

spots obtained at room temperature can also be explained as due to a hexagonal crystal (Phase I) of dimensions $a=7.97$ Å and $c=9.88$ Å which also agree with $3a$ and $2c$ of normal Zn crystal. The spacings and the indices calculated for these structures are shown in Tables 1 and 2 and their dimensions are shown schemematically in Fig. 3.

Table 1. Phase I.

d(Å) obs.	d(Å) calc.	hkl
4.94	4.94	002
3.45	3.45	200
3.22	3.25	003 201
2.82	2.82	202

Table 2. Phase II.

d(Å) obs.	d(Å) calc.	hkl
8.44	8.44	100
6.56	6.56	101
4.85	4.87	110
3.89	3.90	201
3.56	3.58	112
3.26	3.28	202
2.02	2.00	223
1.73	1.74	006

Though the atomic arrangement in these structures are not yet determined, these two structures seems to be intermediate phases between Zn and ZnO, the one being zinc crystal with small excess of oxygen atoms and the other ZnO crystals with small lack of oxygen atoms. In these cases the pseudomorphism reported by Finch was not observed. These intermediate phases and pseudomorphism of Finch were however not observed in similar heating process of zinc films prepared by evaporation method.

Reference.

G.I. Finch, Proc. Phys. Soc., London, **46**, (1934) 148.

J. PHYS. SOC. JAPAN Vol. **6** (1951) 408—409.

A Method for Determining the Concentration Dependence of Diffusion Coefficient

By Hiroshi FUJITA and Akira KISHIMOTO

Department of Fisheries University of Kyoto.

(Received August 3, 1951)

1. Recently, with reference to the material diffusion in high polymeric substances an attention has been concentrated on the calculation of the dependence of diffusion coefficient on the concentration of diffusing material from experimental sorption data. Thus, Crank and his asscciates (2) have developed a certain kind of the method of successive approximations, and also Prager (4) has used a method of approximating the actual concentration dependence by a step function. These methods are rather involved in practical applications and, therefore, it might not be of no use to present herein a different and somewhat simpler procedure for dealing with this matter.

2. As has been shown in Prager's paper cited, for a film of area A normal to the direction of diffusion, the sorbed mass in the film, Q, may be expressed by the equation:

$$Q=2A\sqrt{t}\,K(C_f) \tag{2.1}$$

when the time t is small enough and if the resistance to material transfer at the film surface where the film is contracted with the solution of concentration C_f may be neglected. Here, $K(C_f)$ is to be determined if the form of the diffusion coefficient D(c) is actually given.

Some time ago, one of us (H.F.) (3) has given an approximate method of solving one-dimensional diffusion equation involving diffusion coefficient with an arbitrary concentration dependence basing on Yamada's new idea (5) for dealing approximately with the laminar boundary layer equation. According to this method the form $K(C_f)$ may be expressed approximately by:

$$K(C_f)=\sqrt{D(0)C_f}\left\{\frac{1}{8\sqrt{\beta}}+\frac{1}{12}\alpha\sqrt{\beta}\right\}, \tag{2.2}$$

where α denotes

$$\alpha=\frac{30}{D(0)C_f}\int_0^{C_f}D(c)dc, \tag{2.3}$$

and β is a larger posive root of the quadratic equation:

$$24\alpha\frac{D(C_f)}{D(0)}\beta^2+\left\{\alpha-108\frac{D(C_f)}{D(0)}\right\}\beta+\frac{3}{2}=0. \tag{2.4}$$

The accuracy of Eq. (2.2) is chiefly dependent on the form of $D(c)$. A detailed discussion on this point will, however, be made in our future work.

The actual form of $K(C_f)$ is obtainable experimentally, and our problem is to calculate $D(c)$ from this experimental information by making use of the formulae described in the above.

$$\sqrt{D(0)}=\lim_{C_f\to 0}\left\{\frac{K(C_f)}{C_f}\;\frac{1}{\left(\frac{1}{8\sqrt{\beta}}+\frac{1}{12}\alpha\sqrt{\beta}\right)}\right\}, \tag{2.5}$$

while from Eqs. (2.3) and (2.4) we see that $\alpha\to 30$, $\beta\to 1/12$ as $C_f\to 0$. Thus, the value of D(0) may be obtained from the relation:

$$D(10)=\left\{\frac{1}{1{\cdot}155}\lim\frac{K(C_f)}{C_f}\right\}^2. \tag{2.6}$$

Next, we assume for D(c) a polynomical representatational representational representation as:

$$D(c)=D(0)\,(1+k_1c+k_2c^2+\ldots\ldots\ldots\ldots). \tag{2.7}$$

Unknown coefficients, k_1, k_2, ..., may be detertfimined by ting the given plot of $K(C_f)$ with the above formulae (2.2), (2.3) and (2.4) at suitably selected points of C_f after substituting Eq. (2.7) into them. The number of points must be taken equal to that of unknown coefficients to be determined.

Practically, it is also of considerable significance to approximate the actual from of D(c) by an exponential representation as:

$$(2.8) \qquad D(c)=D(0)\exp(\lambda c),$$

with one parameter λ. This form of concentration dependence of the diffusion coefficient has recently been illustrated by Boyer (1) on the polystylene-chloroform system. Further evidence will also be found directly form Prager's result on the isobutane-polyisobutylene system.

3. To check our method described we shall then apply it to Prager's system by assuming the exponential concentration dependence on diffusion coefficient as indicated in Eq. (2.8).

First, the value of $D(0)$ is obtained as: $D(0)=1.50\cdot10^{-9}$ cm²/sec. Next, we determine the value of λ in such a way that $K(C_f)$ given by Eq. (2.2) coincides exactly with the corresponding experimental value at $C_f=0.0182$ gr/cc. We have then $\lambda=44.9$ cc/gr. On substituting these values of $D(0)$ and λ into Eq. (2.8) gives the result indicated in the second column in an accompanying table. In the third column in this table is shown the corresponding result computed by Prager. Agreement between these two is fairly good in general. Finally, using $D(0)$ and λ obtained above we recalculate the value of $K(C_f)$ from Eq. (2.2) and subsequent formulae and compare it with the corresponding experimental one obtained by Prager. This comparison is made in the fourth and fith columns in the above table. It will be seen that our calculation well reproduces the observed value on the isobutane-polyisobutylene system.

C_f(gr/cc)	$D\times10^{9*}$ (authors')	$D\times10^{9}$ (Prager's)	$K\times10^{6**}$ (calculated)	$E\times10^{6}$ (observed)
0.0000	1.50	1.8	0.00	0.00
0.0091	2.25	2.3	0.46	0.45
0.0182	3.40	3.4	1.05	1.05
0.0273	5.10	5.1	1.81	1.79
0.0364	7.65	7.4	2.74	2.73
0.0455	11.5	10.3	3.99	3.93

*unit: cm^2/sec. **unit: gr/cm^2 sec$^{\frac{1}{2}}$.

The similar analysis basing on the polynomical approximation to D(c) will be reported elsewhere in the future.

References.

1. Boyer, R. E., Jour. Polymer Sci., **5**, (1950) 139.
2. Crank, J. and his associates, Trans. Earaday Soc., **45**, (1949) 240, 636, 1119.
3. Fujita, H., Mem. Coll. Agr. Kyoto Univ., No. **59**, (1951) 31; Bull. Jap. Soc. Sci. Fish., in the press.
4. Prager, S., Jour. Chem. Phys., **19**, (1951) 537.
5. Yamada, H., Rep. Res. Inst. Fluid Eng., **3** (3), (1947) 29.

J. PHYS. SOC. JAPAN Vol. **6** (1951) 409—410.

On the Form of Pole Pieces used in New Spiral Orbit Spectrometer.

By Mitsuo SAKAI and Yozo NOGAMI.

Physics Department, Faculty of Science, Univ. of Tokyo.

(Received August 6, 1951)

An intermediate test of isotope separation was done recently in our laboratory using a spiral orbit spectrometer and the results show that this type of separator has promising future as an isotope separator. This fact leads one to hope for the construction of a large sized separator which is capable of separating isotopes in practical quantity. We report here a form of magnet pole pieces which have several advantages for a large separator.

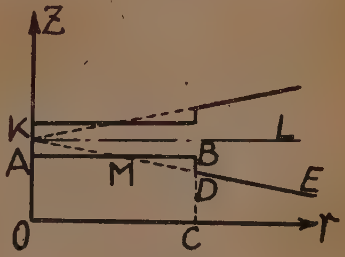

Fig. 1

The shape of the pole piece consists, as is shown in Fig. 1, of a cylindrical part ABC and a part of cone CDE, which has its apex at the center of the median plane K, and is so situated that the line KD passes M, the middle point if AB. The magnetic field created by this pole pieces will be ideally as shown in Fig. 2 and the θ-component of its vector potential (taking a cylindrical coordinate system) can be easily calculated as follows:

Taking oc$=r_0$ and oa$=H_0$,

$$0<r<r_0: \quad A=\frac{1}{r}\int_0^r H_0 r dr=\frac{H_0 r}{2}$$

$$r_0<r: \quad A=\frac{1}{r}\int_0^{r_0} H_0 r dr+\frac{1}{r}\int_{r_0}^{r}\left(\frac{H_0 r_0}{2r}\right) r dr$$

$$=\frac{1}{r}\frac{H_0 r_0^2}{2}+\frac{1}{r}\frac{H_0 r_0}{2}(r-r_0)=\frac{H_0 r_0}{2}$$

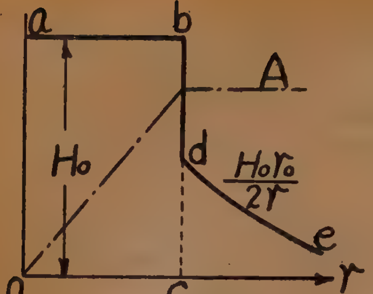

Fig. 2

Consequently, magnitude of the vector potential becomes constant for r larger than r_0 and this type of magnetic field is, as previously pointed out by one of the authors,(1) very advantageous for the spectrometer.

The actual model used in our test has two pole pieces of the form described above and they also serve as top and bottom cover of the spectrometer chamber, as is shown in Fig. 3. The form of magnetic field and vector potential are shown in Fig. 4. As the above calculation was for an ideal case, the most favorable field was obtained by trial and error, changing the gap between two poles. The best value of the gap was a little larger than that of the calculation.

Forms of spectrum of thermal electron were observed with an oscilloscope, superposing alternative voltage on accelerating potential. In this model of 1/20 scale, the gap was too narrow without proper care for focusing, the effect of scattering became very large, but this drawback will disappear in a large apparatus.

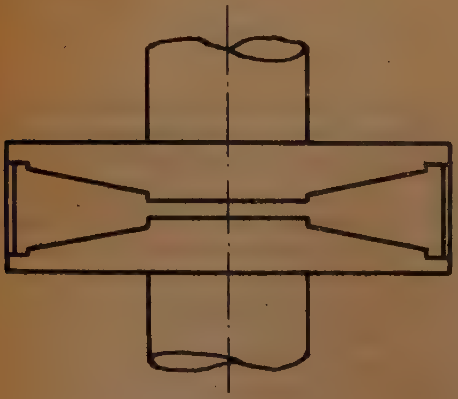

Fig. 3

The characteristic points of this type of spectrometer chamber can be summarized as follows:

1) Costly non-magnetic alloys are necessary only for the cylindrical part of chamber and as this part does not require large thickness, the cost for construction can be cut down considerably.
2) As the pair of pole pieces which have approximate form of an uniform stress disc, serve for end plates, we need not worry about the deformation of pole piece arrangement due to atmospheric pressure and magnetic force which becomes a problem in a large apparatus.
3) By using this type of pole pieces, we can get an excellent magnetic field very easily.

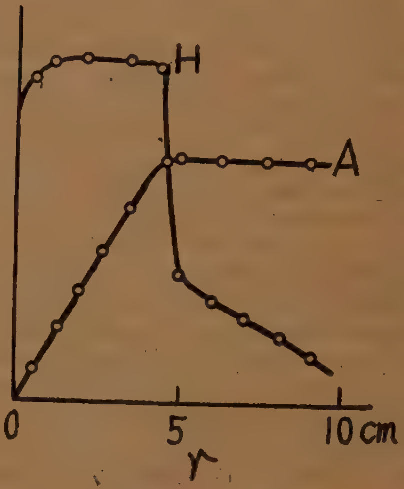

Fig. 4

Reference.

(1) M. Sakai: J. Phys. Soc. Japan 5 (1950) 184.

J. PHYS. SOC. JAPAN Vol. 6 (1951) 410—411.

A Note on the Hole Theory of Liquid.

By Tsugihiko SATO and Syû ONO.
Faculty of Engineering, Kyushu University, Fukuoka.

(Received August 13, 1951)

The authors' previous paper on the hole theory of liquid contains numerical error which has been pointed out by Rowlinson.(2) This error necessitates certain reversions of the results. The values of the ratio of the volume of the cell to the generalized free volume, τ/ω, in reference 1 should be multiplied by factor 5; the corrected values are given in Table I. They seem to agree with the values of Prigogine and Garikian.(3) If these values are used for the calculation of the critical temperatures, T_c, we have $kT_c/\phi_0=0.8$, ϕ_0 being the constant in the intermolecular potential given by $\phi(r)=\phi_0\{(r_0/r)^{12}-2(r_0/r)^6\}$.

Table I

kT/ϕ_0	0.750	0.800	0.934	1.066	1.200	1.267	1.333
τ/ω	131.0	119.0	102.5	87.48	77.97	73.77	70.01

Thus the calculated values of T_0 would be in rather poor agreement with expreiment, as far as we ignore the interaction between the molecules which are not nearest neighbors. It is, however, well known that such interaction increases the attractive terms by about 20%. To take into account the correction for the above-mentioned effect we shall assume that ε in Eq. (20) of reference 1 is given by $\varepsilon(a)=\phi_0\{1.011(r_0/a)-2.409(r_0/a)\}$, which gives $\varepsilon/\phi_0=1.216$ at $a/r_0=1.05$, while Eq. (12) of reference 1 gives $\varepsilon/\phi_0=0.925$. The numbers 1.011 and 2.409 were obtained from Lennard-Jones and Ingham.(4) This assumption may be approximately correct, because this model becomes identical with Lennard-Jones and Devonshire's model if there exist no holes. Then we obtain $KT_0/\phi_0=1.10$ from Eq. (20) of reference 1 and the result tabulated in Table I. If the values of ϕ_0/k determined by Hirschfelder, Bird and Spotz(5) are employed, the critical temperatures shown in Table II are obtained.

Table II

	ϕ^0/k	T_c (cal.), °K	T_c (exp.), °K
Ne	35.7	39	44
A	124	136	151
N_2	91.5	101	126

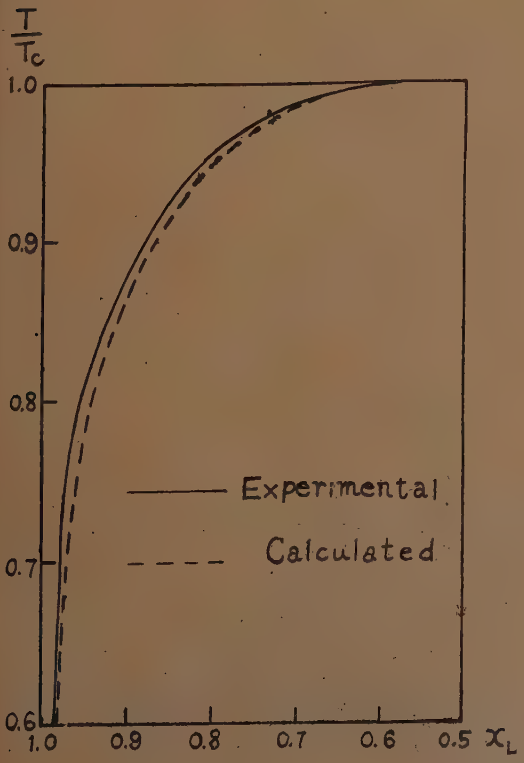

Fig. 1.

The variation of x_L, the concentration of holes in liquid phase, with temperature, which is calculated by using Eqs. (21) and (22) of reference 1, is shown in Fig. 1.

The authors should like to express their thanks to Dr. J. S. Rowlinson for his valuable remark on the authors' previous paper.

References.

(1) T. Sato and S. Ono: J. Phys. Soc. Japan, **4** (1946), 103.
(2) J. S. Rowlinson, private communication.
(3) I. Prigogine and G. Garikian: J. de Chim. Phys., **4** (1948), 274.
(4) J. E. Lennard-Jones and A. E. Ingham: Proc. Roy. Soc., **A107** (1925), 636.
(5) J. O. Hirschfelder, R. B. Bird and E. L. Spøtz: Chem. Rev., **44** (1949), 205.

J. PHYS. SOC. JAPAN Vol. **6** (1951) 411—413.

Isotope Separation by Radiofrequency Electric Field.

By Nobuhiko YAMAMURO.
Tokyo Institute of Technology.
Oh-okayama, Tokyo.

(Received August 14, 1951)

Several attempts have been reported on the mass separater or the mass spectrometer using radiofrequency electric field and some idea which belongs to this field was also proposed by E. Takeda at the annual meeting of Physical Society of Japan in 1946.

This note reports a trial following the new principle: Isotopic ions from the ion source are accelerated uniformly by the d.c. electric field and enter the narrow space where the radiofrequency field is applied. In this space various forces act on the ions corresponding to the phases of the radiofrequency field. Let the initial accelerating d.c. volutage and the peak value of the radiofrequency field be V_i and V_0 respectively, then the voltage applied to ions is

$$V_\theta=V_i+V_0\sin\theta.$$

Therefore the maximum value of this voltage, which corresponds to $\theta=\frac{\pi}{2}$, is $V=V_i+V_0$. The ions accelerated by this maximum voltoge can travel the next long equipotential space of the length S during the time t, which is given by

$$t=\frac{S}{v}=S\sqrt{\frac{M}{2eV}}$$

with v the velocity of the ions and M the mass of them. In order to most accelerate once more these ions at the end of the equipotential space by the same radiofrequency field, the period T of this field must satisfy the next condition:

$$t=\left(n+\frac{1}{2}\right)T, \qquad n=0,\ 1,\ 2, \ldots\ldots .$$

We have therefore the frequency

$$f=\frac{2n+1}{2S}\sqrt{\frac{2eV}{M}} \tag{1}$$

or

$$M=\frac{eV}{2S^2}\left(\frac{2n+1}{f}\right)^2 \tag{2}$$

The ions satisfying the condition (2) have the energy $e(V_i+2V_0)$, and can go through the space where the retarding potential $V_r=V_i+2kV_0\ (k\leqq 1)$ is applied. So these ions only can be collected on the collector. By ajusting the value of k, we can control the amount of the collected ions and the resolving power of the separation.

According to the equation (1), odd multiples of the fundamental frequency (corresponding to $n=0$) may equally well satisfy the condition of the maximum acceleration. Therefore the selection of the most effective value of n must be considered. Briefly we shall think the separation of the binary isotopic mixture of mass M_1 and M_2. The transit time for each ion to pass through the equipotential space is

$$t_1=S\sqrt{\frac{M_1}{2eV}}, \qquad t_2=S\sqrt{\frac{M_2}{2eV}}$$

respectively, and their difference being

$$\tau=S\sqrt{\frac{1}{2eV}}(\sqrt{M_1}-\sqrt{M_2}).$$

Thus if we select the frequency as satisfying the condition

$$\tau=\frac{1}{2f_b},$$

the energy difference between the isotopes would be maximum, since one of the ions receive the maximum energy at the end of the equipotential space, while the others lose it. The ratio of the best frequency f_b to the fundamental one f_0 is given by

$$\frac{f_b}{f_0}=2n+1=\frac{\sqrt{M}}{\sqrt{M_1}-\sqrt{M_2}}, \quad M=\frac{M_1+M_2}{2} \tag{3}$$

and this determines the desired value of n.

A schematic figure of the apparatus constructed is shown in Fig. 1. It has the dimension of 30cm in length and 5cm in outer diameter. F is the filament heating the Li_2O surface. The ions are accelerated by d.c. field between A_1 and A_2. B_1 and B_2 are connected to the earth and C is connected to the radiofrequency oscillator. D is the retarding electrode and E is the collector.

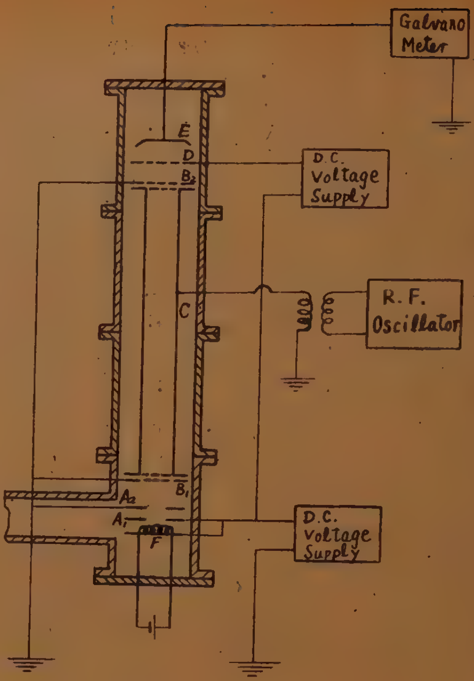

Fig. 1

The experiments have been done on the lithium isotopes. The value of n is decided by equation (3) as 6 and the frequency f_b is selected as 4Mc. for the total acceleration voltage V of about 500volts.

Fig. 2 shows the mass spectrum obtained under the following condition: $f=4.14$Mc, $V_0=200$volts, $V_r=390$volts ($k=0.975$), and $S=20$cm. The abscissa shows the initial acceleration voltage V_i and the ordinate shows the ion current (in ampere) collected. The peak of mass 6 corresponds to $n=5$ and that of mass 7 to $n=6$, other peaks falling out of the figure.

Fig. 3 gives the other example, which was obtained under the different condition $V_0=200$volts and $V_r=330$volts ($k=0.825$). In this case the ion current of mass 7 was increased to 2.7×10^{-8} amp.

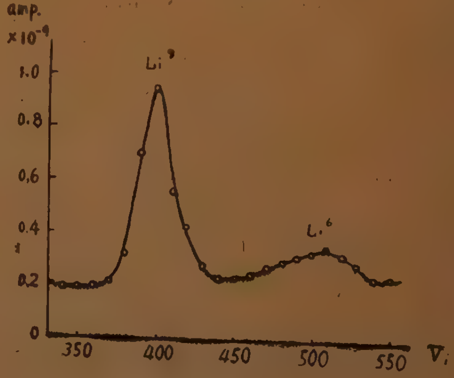

Fig. 2

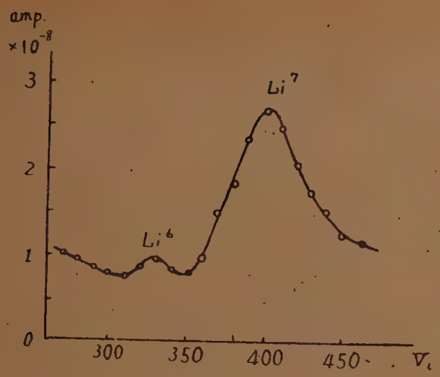

Fig. 3

The present method will be used for the separation of other light isotopes. The ion current obtained was only the order of 10^{-8} amperes, but if we consider the small size and the low cost of this apparatus, this will not be disappointment. There will be also some possibility to extend this principle for the simple mass spectrometer.

References.

(1) W. H. Bennett: J. App. Phys. **21** (1950) 143.
(2) A. F. Henson: J. App. Phys. **21** (1950) 1063.
(3) H. D. Smyth report (Isotron).

J. PHYS. SOC. JAPAN Vol. **6** (1951) 413—414.

A New Method of Trapping Oil Vapour.

By C. HAYASHI,
Department of Physics, Tokyo University, Tokyo.

(Received August 20, 1951)

A method of trapping oil vapour backdiffusing from an oil diffusion pump is proposed with some results of preliminary experiment. Instead of using customary cold surface, the surface wet with a low vapour oil is used. The backdiffusing oil first condenses on the surface, and then reevaporates from the surface corresponding to the vapour pressure which should obey Raoult's theorem, of the mixed liquid surface. The trap using this principle is simple and economical compared with that of cold surface, and will have some practical importance.

The results were published briefly at the meeting of the Physical Society of Japan held last autumn with the priority declaration of patent but the author wishes to abolish the declaration.

The apparatus used for simple preliminary experiment is shown in Fig. 1, and the results obtained are shown in Table I.

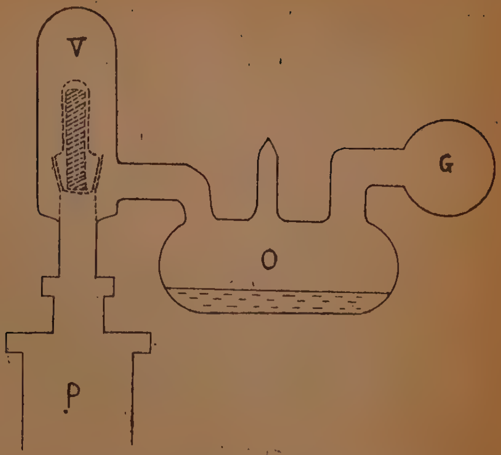

Fig. 1.
P: three stage vertical type metal fractiona ion pump.
V: magnetically operated greaseless valve.
G: hot cathode ionization gauge.
O: the vessel filled with trapping oil.

Table I.

Pump oil	Trapping oil	Ultimate vacuum with and without the trapping oil in O.	
		with	without
Alkyl Naphthalene	A*	8×10^{-7} mmHg	1.0×10^{-6}mmHg
Alkyl Naphthalene	A*	4×10^{-6} mmHg	4×10^{-5} mmHg

* Specially prepared by Mr. B. Miya, Kao Soap Co., Ltd.

In the similar test using two stage non-fractionation metal pump and Alkyl Naphthalene both in trap and pump, the value of the ultimate vacuum was observe to be reduced from 1.5×10^{-5}mmHg to 1.0×10^{-5}mmHg by the trap. This seems to be consistent with the view that the ultimate vacuum of a oil difiusion pump is limited by the volatile components in the pump oil, which exist inherently in the oil or produced by dissociation during operation of the pump.

For the practical purpose, of course, the trapping oil must repeat the circulation process of purifying and trapping. But the temperature necessary for the purifying process will perhaps be low, and the oil, whose vapour pressure is extremely low but not suitable for pump oil because of the fear of thermal dscomposition, will be allowed to be used.

The results obtained seem to deviate too much from Raoult's theorem. But the theorem is not yet proved to hold in such a high vacuum region.* And, after all, the phenomena includes many other unknown factors such as the condensation coefficient between two oils, the diffusion coefficient between two oils in liquid phase, and so on, and is hardly to be analyzed numerically without much more accumulation of experimental results.

---

* c.f. K. Hickman. Rev. Sci. Instrum. **22** (1951) 141.

J. PHYS. SOC. JAPAN Vol. 6 (1951) 414—415.

Use of Phosphorous Pentoxide as a Dehydrating Agent in High Vacuum Technique.

By C. HAYASHI.
Department of Physics, Tokyo University, Tokyo.

(Received August 26, 1951)

As is wellknown, it is almost water vapour that should be evacuated in the region of the vacuum of 10^{-3}mmHg to 10^{-5}mmHg, provided we do not deal with the system containing additional flow of gases or vapours, the use of proper method of taking up the water vapour will save the time necessary for evacuation.

One of the method of this kind is the use of liquid air trap. But the use of the trap is often too cumbersome to put in practice. Here, the use of phosphorous pentoxide is recommended according to the following results, which prove the usefulness of phosphorous pentoxide. Precautions must, of course, be paid for the chemical activities of phosphorous pentoxide and pump oil is likely to be not serious in the region of the vacuum down to 10^{-5}mmHg. The equilibrium pressure of phosphorous pentoxide in a high vacuum system was estimated to be 10^{-6}mmHg, according to the following three results obtained by useing the apparatus shown in figure 1.

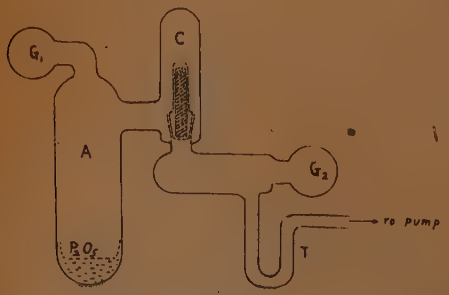

Fig 1

G_1 and G_2: hot cathode ionization gauge
C: magnetically operated greaseless valve

(1) The ultimate vacuum measured with and without phosphorous pentoxids in the vessel A were both 7×10^{-7}mmHg at 10°C.

(2) There observed no pressure rise in the vessel A containing phosphrous pentoxide after three hours of isolation from pumping. The isolation was accomplished by closing the valve C after the ultimate vacuum was reached.

(3) When the gauge G_1 showed the value of the pressure about 5×10^{-6}mmHg the valve C was closed and the gauge was switched off.

It was observed that the pressure in the vessel A decreased to about 1×10^{-6}mmHg after three hours of the isolation.

In the procedures of (2) and (3), the pressure rise in the vessel A was measured by the kick given to the gauge G_2 at the moment the valve C was opened. If the gauge G_1 was kept switched on during the isolation, its reading increased to 4×10^{-5} mmHg after eighty minutes without showing any saturation to be expected, probably due to degassing and decomposition of residual gases or vapours in the gauge. The conductance T was about 70cm³/sec, considerably smaller than the value (300cm³) of the vessel A, and any appreciable pressure change in A should have given some kick on the gauge G_2.

The equilibrium pressure increased to 2×10^{-5} mmHg at 53°C of the surrounding temperature of the vessel A.

Thse value of the equilibrium pressure are considerably lower than the values quoted in the literatures.

The velocity of absorbing water vapour was measured by using the apparatus shown in Figure 2.

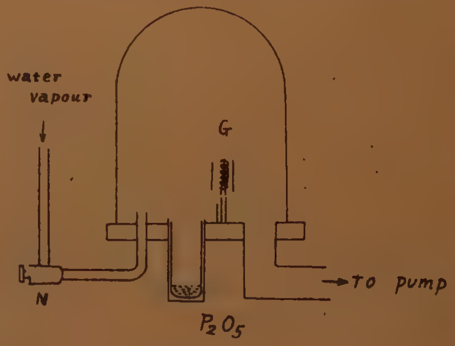

Fig 2

G: hot cathode ionization gauge
N: needle valve

From the values of the flow rate Q_1 and Q_2, which gave the same pressure P in the bell jar with and without the exposure of the known quantity of phosphorous pentoxide respectively, the sorption velocity per unit area at the pressure P was deduced from the following equation,

$$S=\frac{Q_1-Q_2}{PA},$$

where A denotes the surface area of the phosphorous pentoxide.

The results obtained are as follows.

Condition of the surface	S (per apparent unit area)
Covered with considerable thickness of liquid film	400cm^3, sec
Wet but not covered with any appreciable film	700cm^3/sec

The sorption velocity was observed to be nearly constant in the region, 5×10^{-4}mmHg to 2×10^{-5} mmHg.

The velocity at the pressure of 2×10^{-4}mmHg was independent to the surrounding temperature up to about 50°C.

These values of the sorption velocity correspond to six to three percent of the ideal sorption, and to about one to one third of the sorption velocity of a diffusion pump with its connecting pipes. The Ho coefficient of diffusion pump usually increases with increase in pump size, and the use of phosphorous pentoxide becomes less efficient with increase in pump size.

But it should be noted that the space required for the use of phosphorous pentoxide is rather facial opposed to the volumetric in the case of using the diffusion pump.

An evacuation chart with the exposure of phosphorous pentoxide is shown in Figure 3 compared with the curve (upper one) obtained without the use of phosphorous pentoxide.

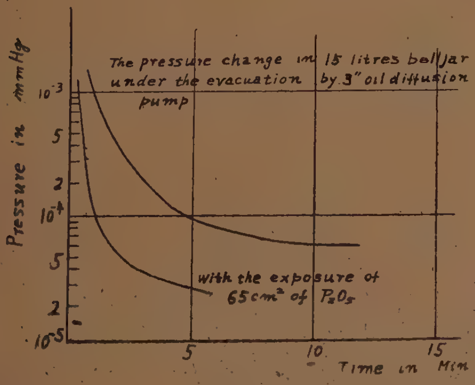

Fig 3

J. PHYS. SOC. JAPAN Vol. 6 (1951) 415—416.

The Ion Source of Electron Oscillation Type.

By Kineo TSUKADA.
Tokyo University of Education.

(Received September 14, 1951)

The ion source of electron oscillation type⁽¹⁾ seems to be suitable for the isotope separator which utilizes the ions from all directions between 2π radians, e.g. the spiral orbit spectrometer⁽²⁾. An ion source of this type has been constructed and found to have relatively high efficiency and high yield.

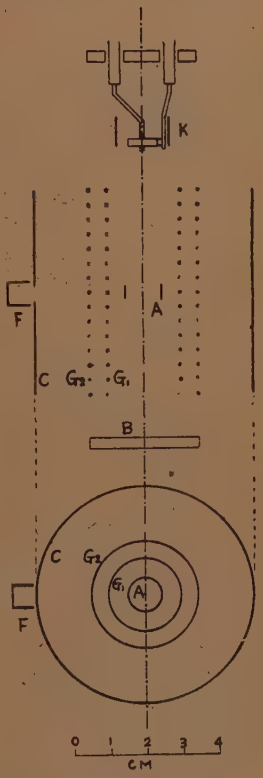

Fig. 1

Electrode		Working v.g.
K:	cathode	0 v
A:	anode	40∼60 v
B:	baffle	0 v
G_1:	1st grid	0 v
G_2:	2nd grid	0∼−800 v
C:	collector	0∼−800 v
F:	Faraday cage	100∼−800 v

The construction was axial-symmetrical as shown in Fig. 1. The 1st grid G_1, the 2nd grid G_2 and the collector C of cylinder type was set coaxially. On the symmetry axis, the ring anode A was mounted between the cathode K and the baffle B which were both at zero voltage. K was oxide coated one and its heating wattage was 10w. The nearly uniform magnetic field made by the solenoids was applied parallel to the symmetry axis of the apparatus.

The discharge mechanism was supposed to be similar with that of the Phillips ionization gauze. At the pressure of $10^{-4}\sim10^{-3}$mmHg and the relatively low anode voltage V_A such as 40~70v in the hydrogen gas, an intense discharge could be sustained. In this case the strength H of the magnetic field was more than about 200 gauss. When the 2nd grid voltage V_{G2} was lower than some negative value and the 1st grid voltage was zero, the plasma of the discharge seemed to be localized inside G_1. Then the ions were pulled out from the plasma by G_2 and reached to C with negative voltage. This experiment was made on the hydrogen gas.

Fig. 2 shows the typical curves for the collector current I_C and the 2nd grid current I_{G2} *vs.* V_{G2}. When the anode current I_A was less than 250mA, I_C was directly proportional to I_A. In the range of V_A between 40 and 80v, I_C had an week maximum at about 60v. When H increased from 300 to 600 gauss, I_C decreased about 10%. At the pressure of 1×10^{-3}mmHg I_C was several per cent larger than at 1×10^{-2}mmHg.

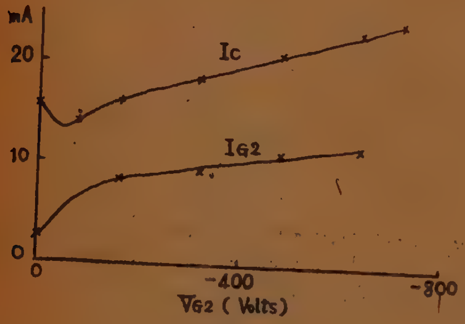

Fig. 2.

I_A=120 mA, V_A=55v,
H=360 gauss, V_G=400v,
pressure~2×10^{-3} mmHg

The results of the measurement by the Faraday cage F showed that the percentage of the ions contained in I_C, which were pulled out from the plasma by G_2, was about 50% and the ions had the energy spread of 30~60v. In the case of Fig. 2, where I_A was 120mA and I_C about 20mA, the ion current was about 10mA, and the energy spread is about 30v. However, this analysis was not accurate because of the magnetic field and the secondary electron emission from C.

Most of these results were little affected by the dimension of each parts.

When this ion source is set to work in the isotope separator, the problem of vacuum will be important. When the condensible vapour is used, this may be easily solved. Heavy atoms seem to be unfavourable by the reason of the energy spread. But, when their ionization potential is lower than that of the hydrogen atom, the anode voltage V_A becomes lower, then the energy spread of the ions becomes narrower.

I wish to express my sincere thanks to Prof. Sagane of Tokyo University and Prof. Kojima for their cordial and continued guidance.

References.

(1) Finkelstein: Rev. Sci. Inst. **11** (1940), 94.
(2) Miyamoto: Proc. Phys.-Math. Soc. Jap. **24** (1942), 676.

Errata.

On the Theory of Recrystallization of Cold-Worked Metals.

By Ryukiti HASIGUTI.

(J. Phys. Soc, Japan, **4** (1949), 358.)
(J. Phys. Soc. Japan, **5** (1950), 14.)

Vol.	P.	Col.	Line.	for	read
4	358	right	28	320Å. at 400°K.	3600Å at 400°C.
5	14	right	5	E_t	E_i
5	15	left	17	mus	must
5	15	left	20	k_f-k_f	k_f-k_b
5	15	right	24	$(E+E^1)$	$(E+E_1)$
5	16	right	1	proces	process
5	16	right	5	get	(delete)
5	16	right	36	10^4	10^5
5	16	right	37	least	(delete)
5	16	right	41	4Å at 283°K.	80Å. at 300°C.
5	16	right	41	320Å at 400°K.	3600Å at 400°C.

Numerical Tables for the Phase and Intensity Measurements of Metallic Film (II)

By K. ISHIGURO.

(Vol. 6. No. 1 Page 6)

$\frac{\omega l}{c}$	n	k	Symbol	Wrong	Correct
0.05	1.00	3.64	Δ_0	39	36
0.25	1.00	1.18	Δ_{70P}	25	20
0.35	1.41	1.18	Δ_{70S}	58	-58
0.35	1.00	1.59	Δ_{70S}	39	-39
0.35	1.41	3.23	Δ_{70S}	-4	-20
0.35	1.82	3.23	Δ_{70S}	-9	-40
0.35	2.23	3.23	Δ_{70S}	-46	-62
0.35	1.41	3.64	Δ_{70S}	23	-9
0.35	1.82	3.64	Δ_{70S}	31	-31
0.35	2.23	3.64	Δ_{70S}	-22	-53
0.45	2.23	1.18	Δ_0	61	-61
0.45	1.82	1.59	Δ_{70S}	89	-89
0.50	0.59	2.82	Δ_0	122	128
0.50	0.59	2.82	T_r	10.5	9.5
0.50	0.59	2.82	R_0	65.9	70.8

JOURNAL OF THE PHYSICAL SOCIETY OF JAPAN Vol. 6, No. 6 NOV.—DEC., 1951

The Vibrational Properties of Wood. II.

By Eiichi FUKADA.

Kobayashi Institute of Physical Research, Kokubunji, Tokyo.

(Received October 20, 1950)

When the moisture content is reduced from the air-dried state, the internal friction of wood increases and the peak in tan δ-frequency curve shifts to the lower frequency. The Young's modulus and tan δ decreases and peak of tan δ shifts to the higher frequency with the increase of temperature at the absolutely dried state. The experimental activation energy was found to be about 1000 cal/mol. It is larger for the broad-leaved tree than for the needle-leef tree. The frequency character of tan δ can be explained by superposing both Eyring's and Newton's viscosity.

§1. Introduction.

In the previous report[1] it has been shown that the frequency character of the logarithmic decrement of wood is specified to A type for the needle-leef trees, B and B′ type for the broad-leaved trees. The decrement of A type increases gradually with frequency but the decrement of B type shows the maximum in the audiofrequency range in the air-dried state. In this report there will be shown the change of this behaviour due to the decrease of moisture content by drying as well as the temperature effect in the dried state. As a measure of internal friction, henceforward, we shall take tan δ rather than the logarithmic decrement λ, where δ is the delayed phase angle between the stress and the strain, in view of the theoretical considerations. The relation between these two quantities are as follows,

$$\tan\delta = \lambda/\pi \qquad (1)$$

§2. Variation due to the Moisture Content.

Fig. 1 shows the measuring results of tan δ for Bishūhinoki, one of the needle-leaf trees which belong to A type, in the thoroughly dried state (mark △) compared with the air-dried state (mark ○). This specimen is the same with that used in Fig. 6 and Fig. 7 of the previous paper[1]. The figures of percentage show the moisture content in weight and the notation // or ⊥ means that the axis of fiber is parallel or perpendicular to the direction of the length of the specimen. In both cases tan δ increases with drying and the maximum peak appears like the B type. This behaviour is the same in many other needle-leaf trees. As stated in the remark of the previous paper the needle-leaf trees show also the peak in the frequency above 5000 c.p.s. in the air-dried state. Therefore the drying shifts the peak to the lower frequency and increases the absolute values of tan δ. The mark ⊗ in Fig. 1 shows the measuring results after being left in the atmosphere untill the moisture content becomes nearly the same with the original case. The measured value approaches to the original one but is not the same. The same moisture content and the same temperature of measurement do not necessarily reproduce the same measuring results. This may be due to the hysteresis of the absorption of moisture or some permanent change in the structure by drying. Generally the properties of wood are very sensitive to the moisture and temperature so that it was so difficult to reproduce the same results at will under the various conditions.

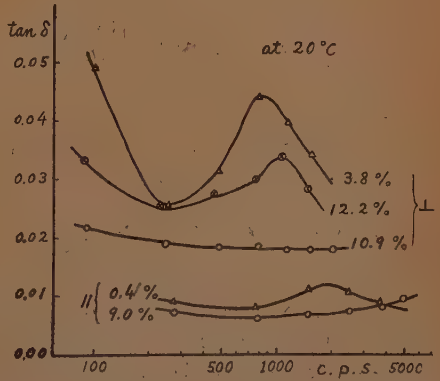

Fig. 1. Variation of tan δ for Bishūhinoki (needle-leaf tree) due to the moisture content. % shows the moisture content, // or ⊥ represents that the axis of fibers is parallel or perpendicular to the direction of the length of the specimen respectively.

Fig. 2 shows the variation of tan δ for Tabu, one of the broad-leaved trees. The peak shifts to the lower frequency by drying. Young's modulus E hardly changes with the moisture content if we make the correction for the expansion of volume by the absorption of moisture. E_s in Fig. 2 shows the static Young's modulus obtained by measuring the static deflection under the known load. These behaviours were also demonstrated for Kuroezomatsu (Spruce) in another report.[2] In short, when the moisture content increases from zero, the Young's modulus does not change, the peak frequency of tan δ increases and the absolute value of tan δ decreases. When the moisture content exceeds the so-called fiber saturation point tan δ increases again as reported by the other authors.[3]

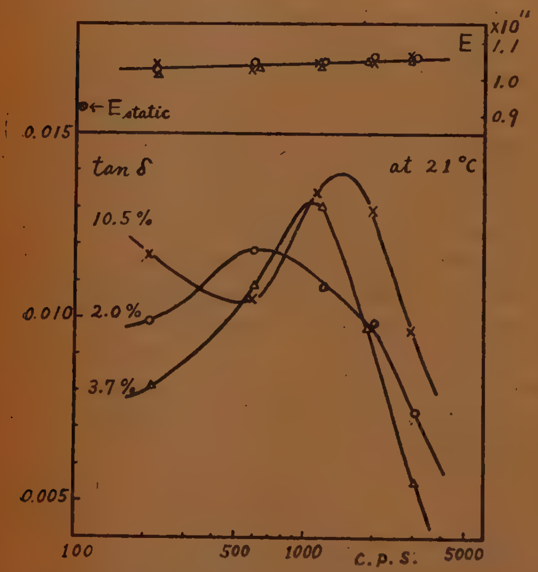

Fig. 2. Variation of tan δ for Tabu (broad-leaved tree) due to the moisture content. % shows the moisture content.

§ 3. Variation due to the Temperature.

Since the moisture in wood evaporates as heated above room temperature we could not measure the variation due to the temperature under the constant moisture content. So we have measured the temperature dependence of Young's modulus E and internal friction tan δ at the absolutely dried state, where the absolutely dried state means the state dried for long hours in the thermostat at about 100°C until the further decrease of weight of specimen can not be found. The results for Tabu are shown in Fig. 3. As the temperature rises the absolute value of tan δ decreases and the frequency at peak shifts to higher frequency. Young's modulus decreases with the temperature rise.

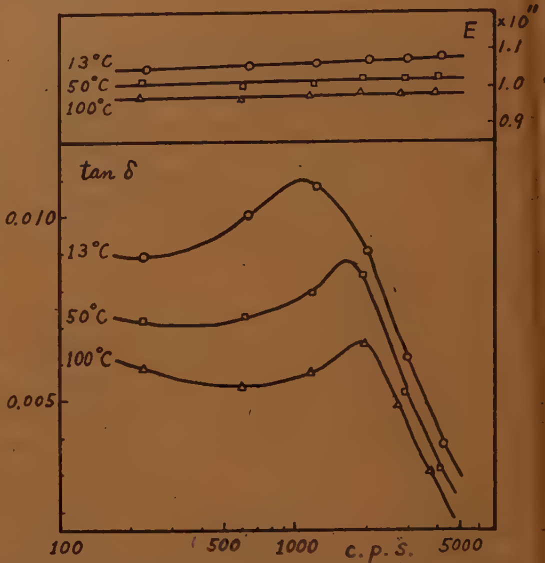

Fig. 3. Temperature dependence of E and tan δ for Tabu at absolutely dried state.

This behaviour was also reported[2] for Kuroezomatsu (Spruce), a needle-leaf tree. In figures in that report, Fig. 3 and Fig. 6 in this report part I, the measuring values of Young's modulus were observed to decrease at high frequencies. This apparent decrease was caused by neglecting the correction for the shearing force and the rotatory inertia[4] in the lateral vibration.* When this correction is taken the Young's modulus is nearly constant or slightly increases in the whole measurable frequencies as shown in Fig. 2 and Fig. 3.

Now tan δ of wood is divided into two part. One is decreasing with frequency and the other has a maximum peak. In order to investigate the temperature dependence of former part of tan δ we made the measurement for Tabu at dried state at about 230 c.p.s. between −30°C and 110°C. The results are shown in Fig. 4. and Fig. 5. Both Young's modulus and internal friction decreases as the temperature rises. Below 0°C there is no particular change, but the temperature coefficient of both E and tan δ

---

* The author thanks to Dr. O. Nomoto for his remark on this correction.

is a little different above and below 0 C. The mark ○ is the data at cooling and the mark ⊗ is at heating.

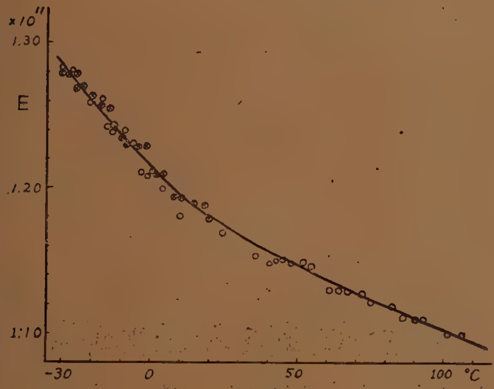

Fig. 4. Young's modulus vs. temperature for Tabu at about 230 c.p.s.

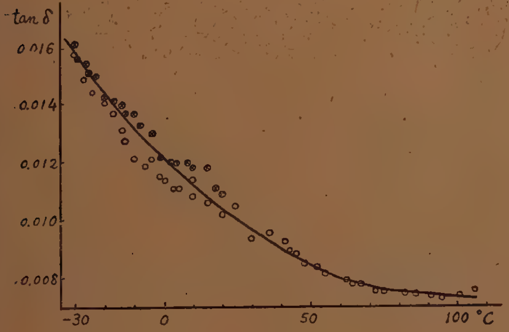

Fig. 5. Internal friction vs. temperature for Tabu at about 230 c.p.s.

§ 4. Activation Energy.

The peak frequency in tan δ vs. frequency curve shifts to high frequency as the moisture content or measuring temperature increases. It is supposed that this may be due to some relaxation phenomena in the structure of wood. If we plot the reciprocal of frequency at maximum against the reciprocal of the absolute temperature 1/T, we can obtain a straight line, so that the following relation is valid.

$$1/2\pi f = \tau = \tau_0 \exp(A/RT) \qquad (2)$$

where τ is the relaxation time, τ_0 a constant, R the gas constant and A the activation energy. It was found to be $A = 1200$ cal/mol for Tabu and $A = 890$ cal/mol for Kuroezomatsu.[2] The activation energy is larger for the broad-leaved tree than for the needle-leaf tree in accord with the experimental results that the peak frequency is lower for the former at the air dried state.

The activation energy of basic part of tan δ is obtained from the data in Fig. 5. When we define the complex Young's modulus $E^* = E + i\omega\eta$ as usual, the viscosity coefficient η is calculated from the following relation,

$$\eta = E \cdot \tan\delta / 2\pi f \qquad (3)$$

Fig. 6 shows $\log_{10}\eta$ plotted against $1/T$. From this linear relation we put

$$\eta = \eta_0 \exp(B/RT) \qquad (4)$$

where η_0 is a constant and B the activation energy. It was found to be $B = 1300$ cal/mol for Tabu and $B = 650$ cal/mol for Kuroezomatsu. The activation energy of basic part of tan δ is nearly the same with that of the peak part of tan δ. Therefore the both parts will be caused by the same kind of the dissipative mechanism.

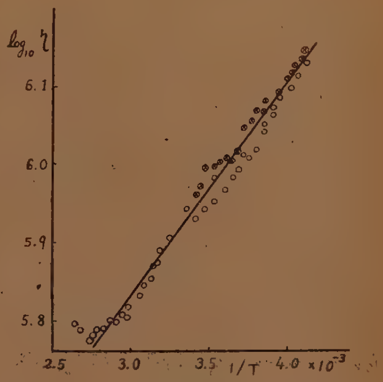

Fig. 6. $\log_{10}\eta$ vs. $1/T$ for Tabu at about 230 c.p.s.

Since the peak frequency of tan δ increases and the absolute value decreases as the moisture content increases at the same temperature, the activation energies A and B are considered to diminish with the increase of moisture content. The water seems to play the roll of plasticizer in the viscosity of wood. The experiment varying the moisture content is so difficult that the reliable relation between the activation energy and the moisture content has not yet been obtained.

§ 5. Frequency Dependence of the Internal Friction.

Previously the author has reported[5] that the frequency dependence of the internal friction of polymethylmetacrylate can be derived from the constants in the creep experiment. The tensile creep of woods by Minami[6] shows the following relation between strain ε and time t;

$$\varepsilon=\varepsilon_1+k\log_{10}t \tag{5}$$

where ε_1 is the strain at one second after applying the stress and k is a constant proportional to the magnitude of stress. Then we can derive the above mentioned basic part of the internal friction from the constant $C=0.434\,k/\varepsilon_1$ and the suitably assumed constant θ as the same manner as polymethyl metacrylate. In curve (1) of Fig. 7, C is estimated to be 0.006 from the Minami's data at small stress and θ is taken as $10^{-3}/2\pi$. The Young's modulus calculated from these values shows hardly any change with frequency, which is in accord with the experimental results.

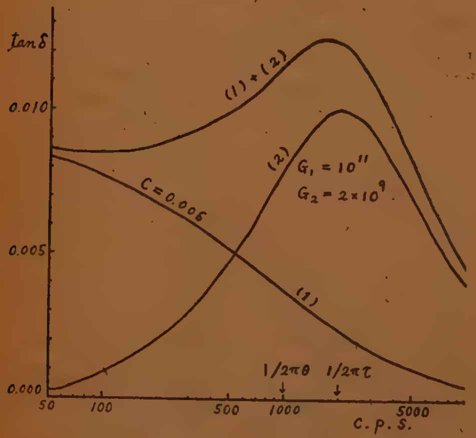

Fig. 7. Two parts of the internal friction.

The linear relation between ε and $\log t$ can be derived using the so-called three element model having the Eyring's viscosity in its dashpot. The rate of flow is described as $A_2\sinh B_2\sigma_2$, where σ_2 is applied stress, A_2 and B_2 are the constants.[7] At the very small stress the viscosity will be the usual Newton's type and the rate of flow is represented as σ_2/η, where η is the viscosity coefficient.

Now we suppose that the internal friction due to the Newton's viscosity is superposed over that due to the Eyring's viscosity. If a spring, whose Young's modulus is G_1, is connected parallel with a dashpot and another spring, whose Young's modulus is G_2, we can get the wellknown dispersion formula.[8] Then the total change of Young's modulus Δ_G is expressed by G_2/G_1 and the relaxation time $\tau=\eta/G_2$ and $(\tan\delta)_{\max}\sim\Delta_G/2$. Experimentally we find no appreciable value of Δ_G in these frequencies and $(\tan\delta)_{\max}$ is of the order of 0.01 or less. G_1 may be the actually measured one, about 10^{11}. If we assume G_2 to be in the order of 10^9, then Δ_G is less than a few percent, that is, within the experimental error and $(\tan\delta)_{\max}$ is fit to the measured value. For instance we take $G_2=2\times10^9$, then $\Delta_G=0.02$ and $(\tan\delta)_{\max}=0.01$. τ is determined from the frequency at maximum of $\tan\delta$ according to the relation $\tau=1/2\pi f$. If we take $f=2000$ c.p.s., $\tau=0.8\times10^{-4}$ is obtained.

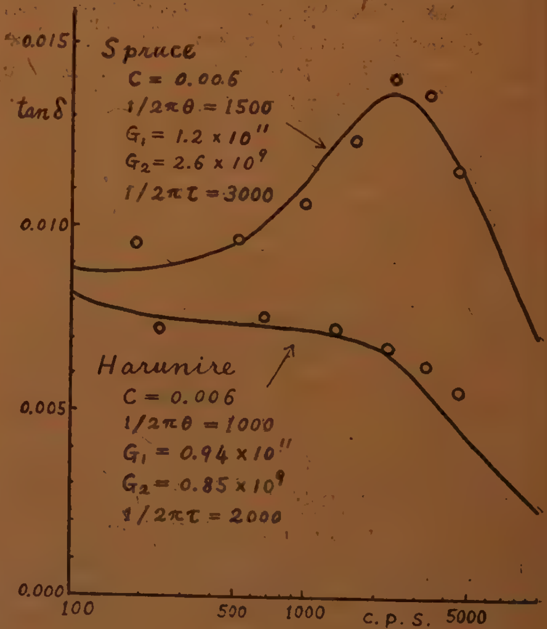

Fig. 8. Comparison between theoretical and experimental results.

Curve (2) in Fig. 7 is calculated by taking $G_1=10^{11}$, $G_2=2\times10^9$ and $1/2\pi\tau=2000$. The superposed curve (1)+(2) represents well the actual experimental results. The necessary quantities to calculate this curve are C and θ for (1) and G_1, G_2 and τ for (2). C is obtained from the creep experiment and θ is determined to fit the calculated curve to the measured values. G_1 and τ are obtained from the vibraion experiment and only G_2 is assumed in the order of 10^9 so that the calculated height of peak becomes consistent with the observed value. Various types of $\tan\delta$ vs. frequency curve A, B and B′ as reported in part I can be represented by choosing the suitable G_2. The examples are shown in Fig. 8 for Kuroezomatsu and Harunire. The solid line is the calculated curve using the constants written in the figure. The mark ○ is the experimental results.

§ 6. Coexistence of Eyring's and Newton's Viscosity.

We can explain the frequency dependence of internal friction by considering both Eyring's and Newton's viscosity. The former arises at large stress and the latter at small stress. Therefore the large and small stresses are acting at the same time in the specimen. Perhaps this may be due to the magnification and reduction of inner stress by the many cracks or air gaps in the structure of wood.⁹⁾ The distribution of stress in the specimen is also caused by the lateral vibration itself. The maximum magnitude of stress used in the ordinary measurement was estimated about 0.5 ~5 kg/cm² at the vicinity of the loop of lateral vibration. The magnification ratio of stress due to the presence of the narrow crack would be of the order of 10^2. Therefore the actual inner stress would reach to the experimental range of stress used in the tensile creep by Minami.

When we consider the peak of $\tan\delta$ is caused by the Eyring's viscosity at small stress, we can express the frequency at maximum of $\tan\delta$ as

$$f_m=\frac{kT}{2\pi h}e^{\Delta S/R}e^{-\Delta H/RT} \tag{6}$$

where ΔS is the entropy of activation and ΔH is the heat of activation. By plotting $\log f_m/T$ against $1/T$ we could obtain $\Delta H=490$ cal/mol, $\Delta S=-39$ cal/mol. deg. for Tabu and $\Delta H=220$ cal/mol, $\Delta S=-38$ cal/mol. deg. for Kuroezomatsu.

Our consideration explains well the frequency dependence of internal friction and the temperature dependence of the frequency at maximum of $\tan\delta$, but it fails to elucidate the decrease of the absolute value of $\tan\delta$ with the increase of temperature. Further, in the experiment of creep $B_2\sigma_2$ is nearly constant, so that we can not equate $\sinh B_2\sigma_2=B_2\sigma_2$ when we approach to the case of small stress. The constants A_2 and B_2 at large stress depend on the magnitude of stress and are different from the constants A_2 and B_2 at very small stress, which relate to the Newton's viscosity.

The author wishes to express his sincerest gratitude to Dr. Heiji Kawai for his helpful guidance and discussions throughout this work. This research is indebted to the grant in aid for the Ministry of Education.

References

1) E. Fukada: J. Phys. Soc. Japan. **5** (1950), 321.

2) E. Fukada: Nature. **166** (1950), 772.

3) Y. Tani: Ohyobutsuri. **9** (1940), 372. (in Japanese.)

4) S. Timoshenko: Vibration Problems in Engineering. (1937), 337.

5) E. Fukada: J. Phys. Soc. Japan. **6** (1951), 254.

6) Y. Minami: J. Aeron. Res. Inst. Tokyo Imp. Univ. No. 174, (1939), 23. (in Japanese)

7) A. V. Tobolsky and H. Eyring: J. Chem. Phys. **11** (1943), 125.

8) C. Zener: Elasticity and Anelasticity of Metals. (1948), 46.

9) A. A. Griffith: Phil. Trans. Roy. Soc. Lond. **A221** (1921), 163.

JOURNAL OF THE PHYSICAL SOCIETY OF JAPAN Vol. 6, No. 6, Nov.—Dec., 1951.

The Physical Properties of Cuprous Sulfides-Semiconductors.

By Eiji HIRAHARA.
Hiroshima Municipal Techinical College.

(Received December 23,1950)

Cuprous sulfide has been observed to have two transition points at about 110°C and 470°C respectively, of which the latter one has been found out experimentally by the writer. The exsistence of the phase transition at 470°C has been confirmed experimentally by the measurements of electronic and ionic conductivity, thermal linear expansion, heat capacity, specific heat and thermo-electromotive force. We, therefore, propose that cuprous sulfide has three polymorphic phases, namely α-phase (above 470°C), β-phase (470°C∼110°C) and γ-phase (below 110°C). In the γ-phase, it behaves as a P-type semiconductor (sulphur excess), and its electrical conductivity increases exponentially with temperature. In the β-phase, we have observed the rather remarkable ionic currents together with the sharp decrease of electronic currents. On proceeding to the α-phase, the ionic currents abruptly disappear and electronic currents increase to the larger amount than that in the γ-phase. The transition enery at 110°C has been observed to be more than ten times (about 4.8 cal/gr.) larger than that at 470°C.

In the β-phase, the anomalous thermo-electromomotive force has been sometimes observed, which may be considered to be caused by the heterogeneous distribution of the movable copper ions.

§ 1. Introduction.

Cuprous sulfides are produced naturally as "Chalchocite", which are known to be brilliant, steel-gray crystallized minerals. The mineralogical properties have already been studied by many workers. We have made experimentally the detailed investigations of the physical properties of cuprous sulfides, and found out its several characteristic properties unknown thus far. Namely, the cuprous sulfides have been found to have three polymorphisms, two transition points being situated at about 110°C, and 470°C respectively. A low temperature transition at 110°C has already reported by Posnjak[1] and the crystal structures above and below the transition point are investigated by Alsen,[2] Barth,[3] Rahlfs[4] and Buerger.[5]

The existence of a high temperature transition at 470°C, however, has been established to exist by our experimental observations of the various kinds of physical properties. We, therefore, shall propose for these three polymorphic phases to be named α-phase (above 470°C), β-phase (470°∼110°C) and γ-phase (below 110°C).

A remarkable ionic current has been observed in β-phase but not in α- and γ-phases. The specimens used were prepared from a pure copper block and sulphur by heating at 600°C in a vacuum Pyrex tube.

§ 2. Ionic Conductivity.

According to C. Tubandt and his co-workers[6], an ionic current in such crystal was observed at 220°C, its charge-carriers being copper ions only. We, however, have measured the detailed behaviours of temperature dependence of an ionic conduction in the wider temperature range

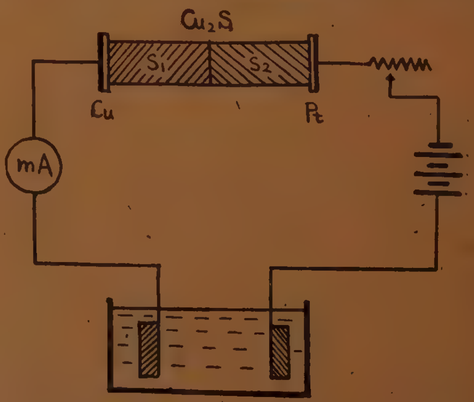

Fig. 1. Schematic diagram of measurements apparatus for Ionic Conductivity.

from room temperature to about 600°C by the similar method as C. Tubandt's.

The schematic diagram of the apparatus is shown in Fig. 1.

Two specimens with the same dimension are situated between a copper anode and a platinum cathode, the whole set of which is put into an electric furnacc in oder to keep the specimens at any desired temperatures. The total currents (of electronic and ionic origins) have been measured by means of a copper coulometer, and, further, the ionic currents have been estimated, as usual, by weighing the segregated copper and sulphur onto a platinum cathode and copper anode respectively.

Table 1. Results of measurements of Ionic Conductivity.

Temp.	150°C	200°C	300°C	400°C	500°C
$cm^{-1}.ohm^{-1}$ σ_i	0.0031	0.0144	0.089	0.1994	0.0147
$l_n\sigma_i$	−5.776	−4.240	−2.419	−1.612	−4.219
I_i/I_e	0.003%	0.11	0.61	1.27	0.07

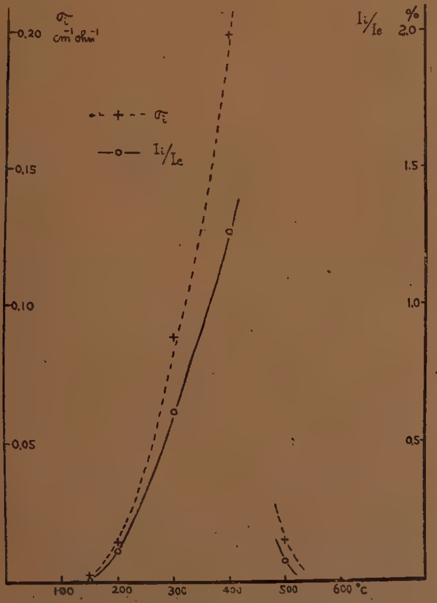

Fig. 2. Ionic Conductivity and the ratio of Ionic and Electronic Currents.

The results obtained are as follows; an ionic current does not appear in the temperature range below 100°C. At 150°C it begins to appear as far as our experimental accuracy does concern and increases with temperature, and at about 500°C it disappears rather abruptly. These results are summarized in Table 1 and Fig. 2, in which σ_i is ionic conductivity and I_i/I_e the ratio of ionic current to electronic current. As seen in Fig. 2, a following relation holds between the ionic conductivity σ_i and the absolute temperature T,

$$\sigma_i = \sigma_0 \cdot \exp(-E/kT),$$

where E is an activation energy in ionic conduction. From the linear relation between $\log \sigma_i$ and $1/T$ as shown in Fig. 3, the value of E has been estimated to be about 0.4 ev in these specimens. Even though the ionic conductivity is rather remarkable, the ratio of the ionic conductivity to the electronic conductivity is a few percents at most.

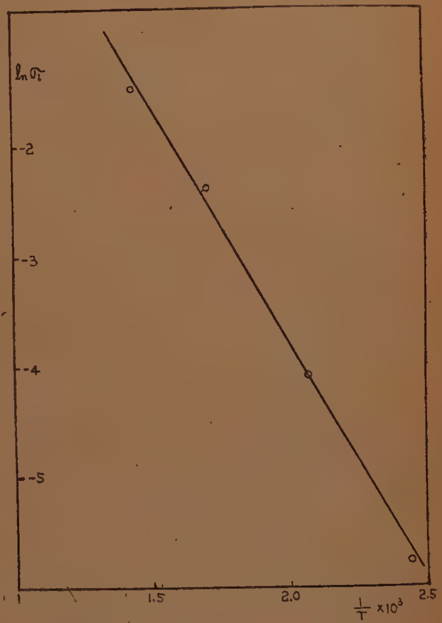

Fig. 3. Activation energy of Ionic Conduction

§ 3. Electronic Conductivity.

As mentioned in the preceding section, the cuprous sulfide has been found experimentally to have ionic conductivity in addition to an electronic one in the limited range of temperatures. But due to the small ratio of σ_i/σ_e its total electric conduction (electronic and ionic) will be approximately of electronic nature. The electric conductivity was measured, by the usual method using a potentiometer with sonde, in the range from room temperature to about 600°C. The results obtained are shown in Fig. 4 which may be taken to show an electronic conductivity for the above reason. The conductivity increases, according to the exponential law, with the temperature-increase from the room temperature, which behaviour is characteristic for semi-conductor. At about 110°C, however, the electronic conductivity drops suddenly to the lower value and then increases gradually with temperature. At about 470°C, it jumps up to a large value and then retains the exponential increase with temperature.

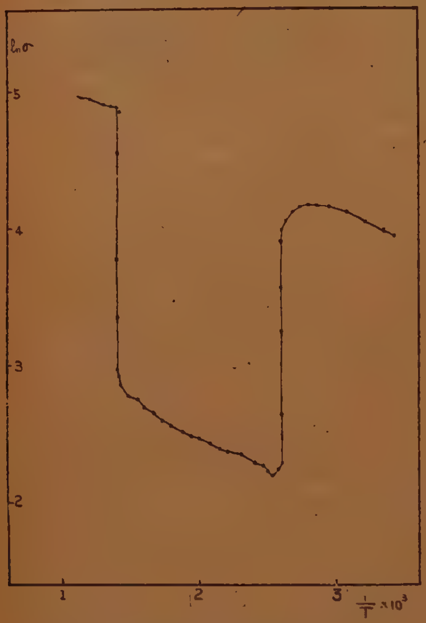

Fig. 4. Electric Conductivity of Cuprous sulfide

A small value of electronic conductivity in the range from 110°C to 470°C may be considered to be closely associated with the appearance of ionic current, as mentioned in the preceding section.

As the ionic motion begins to prevail, the periodic field of crystal lattice is greatly distorted, which situation leads to the shorter mean free path of conduction electrons and holes, and to the poor electronic conduction in the temperature between 110°C and 470°C. Thus it may be concluded that there exist clearly three phases in the cuprous sulfide, namely α-phase (above 470°C), β-phase (from 110°C to 470°C) and γ-phase (below 110°C). In the β-phase we have a rather remarkable ionic current together with the sharp decrease of electronic current.

§ 4. Thermal Linear Expansion.

In order to confirm further the existence of the two transition points at 110°C, and 470°C, the measurements of a thermal linear expansion have been performed. The schematic diagram of the apparatus for the measurement is shown in Fig. 5. Two quartz rods (G_1, G_2) are put into a vacuum electric heating furnace (A). A specimen (S) is fixed on an end of one rod. Relative displacements caused by thermal expansion of the specimen are detected by a rolling mirror (M) together with a lamp and telescope (L and T). The relations between a linear elongation (Δl) and temperatures (°C) are described in Fig. 6 in which we have

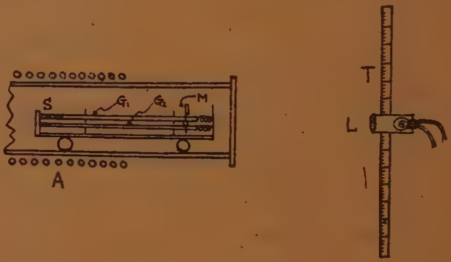

Fig. 5. Schematic diagram of apparatus for the measurements of thermal linear expansion.

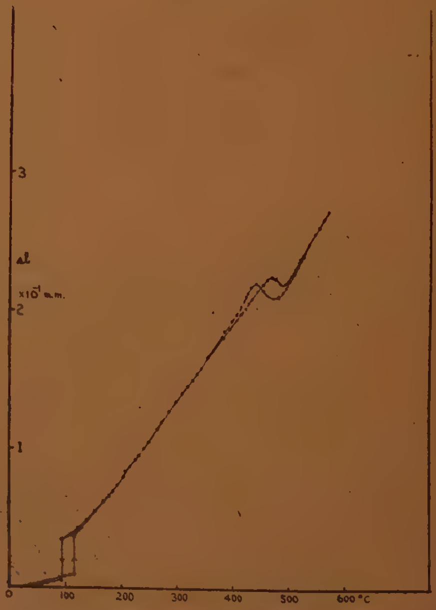

Fig. 6. Results of the thermal linear expansion.

actually observed two anomalies at 110°C and 470°C respectively as is expected. The discrepancy between the heating and cooling curves will perhaps be due to the relaxation phenomena. The one anomaly ($\gamma \leftarrow\rightarrow \beta$) in the lower temperature side is observed to take place in a narrow range of temperature, while the other one ($\beta \leftarrow\rightarrow \alpha$) in the higher temperature side to occur rather gradually in the somewhat wider range of temperature. The coefficients of linear expansion in α, β, and γ-phases are of about 2.76×10^{-5}, 2.42×10^{-5} and 6.10×10^{-6} respectively.

§ 5. Anomalous Heat Capacity.

From the results described in § 4, we may presume that there is an anomalous heat capacity at two transition points. Therefore, the relative heat capacities at various temperatures in the mentioned temperature range have been measured. The schematic diagram of an apparatus is shown in Fig. 7. A specimen (S_1) and a standard material (S_2) are put into a vacuum electric heating furnace as above. The standard material is a copper block with same dimension as the specimen. A thermo-couple Th_1 is used to measure the temperature of the standard material and the furnace, and another Th_2 is made use of as a differential thermo-couple between the specimen and the standard material in order to measure the temperature difference between them. The results obtained are shown in Fig. 8, in which a upper curve stands for a heating curve (endothermic) and a lower curve a cooling one (exothermic). The abscissa is the temperature in centigrade, the ordinate an arbitary scale of the deflection in Galvanometer connected with the ends of a differential thermo-couple Th_2. The amount of an anomaly at lower temperature transition is larger than that at higher temperature.

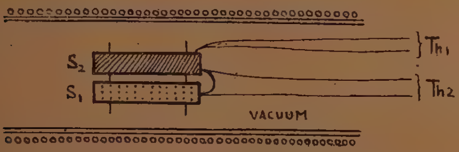

Fig. 7. Schematic diagram of apparatus for measurements of anomalous heat Capacity.

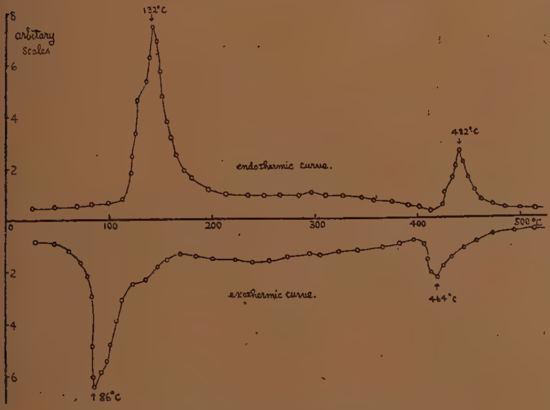

Fig. 8. Anomalous heat capacity of Cuprous sulfide.

§ 6. Specific Heat.

The measurements of specific heat have been performed with the well known Sykes' method,⁽⁷⁾ using an apparatus schematically shown in Fig. 9. In Fig. 9, A is a powder sample contained in alminium vessel, B a thick copper receiver, C a steel cylinder which is used for the interior of the box to be kept vacuum.

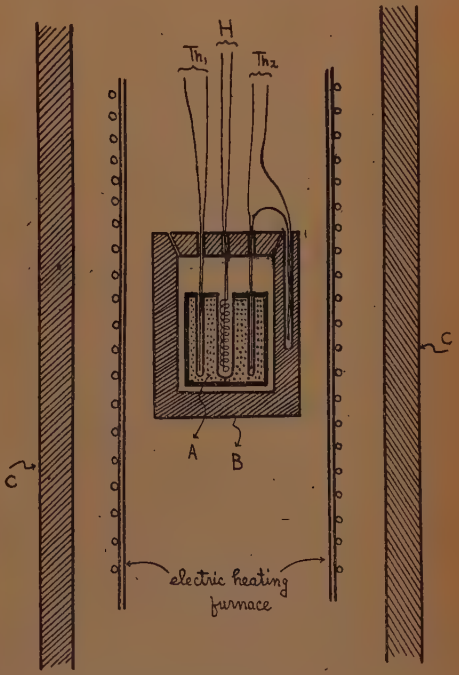

Fig. 9. Schematic diagram of apparatus for measurements of Specific heat.

H is a thermal energy supplied to the sample, Th_1 and Th_2 are two thermo-couples, the former of which is employed to measure the temperature of the sample, and the latter serves to measure the temperature difference between the sample and the outer copper receiver. The specific heat of sample will be estimated by observing both the time rates of supplied heat energy (ampere × voltage) and temperature risings, the results of which are represented in Fig. 10.

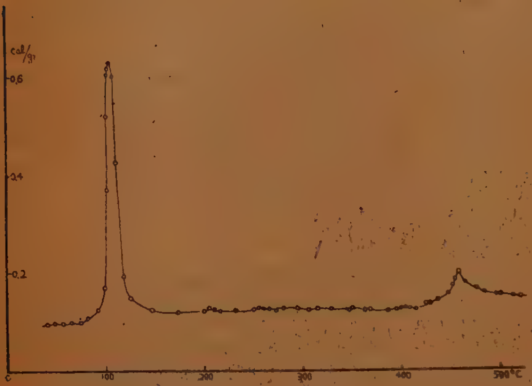

Fig. 10. Temperature dependence of Specific heat.

From the observed curve in Fig. 10, the transition energies may be estimated to become of 4.8 cal/gr at 110°C and 0.3 cal/gr at 470°C respectively. These results will suggest us that these transitions may probably be the characteristic processes similar to the order-disorder transitions to be realized in some alloys, which are known to require a rather small transition energy in contradistinction to the transition process associated with latent heat. As for the low temperature transition at 110°C, Buerger[5] has already reported that the orthorhombic lattice below 110°C has changed into the ortho-hexagonal one in passing through the temperature of 110°C, the former being a super cell containing 24 cells of the latter. The nature of the higher temperature transition, however, is yet unknown at present.

§ 7. Anomalous Thermo-electromotive Force and Thermal Diffusion of Copper Ions.

(a). A thermo-electromotive force is measured in the range from room temperature to 600°C; a specimen is shaped in the form of cylinder of 5 mm. in diameter and 25 mm. in length, which is inserted between two copper electrodes. To one of the electrodes is attached a small electric heater, which is heated by an direct current to maintain the stable temperature difference between the two electrodes. The specimen-supporter is put into a vacuum electric furnace as usual. The results in most specimens are quite similar to that described by a curve *A* in Fig. 11, in which there is no remarkable anomaly at 110°C and 470°C. A thermo-electromotive force is of about 1 mv/deg. and has the positive sign, that is, the potential at the junction of low temperature is higher than one at the junction of higher temperature in accordance with the property of *P*-type semi-conductor. Some of the specimens, however, show anomalous maxima in β-phase as shown in Fig. 12, in which curves *A* and *A′* denote heating and cooling curves respectively. When this specimen is set, in inverted direction, between electrodes, thus preparing the opposite temperature gradient to the former case, we have the results represented by curves *B* and *B′* in Fig. 12.

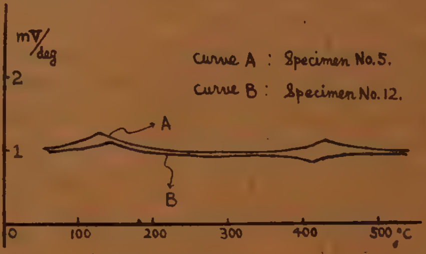

Fig. 11. Thermoelectromotive force of homogeneous specimens.

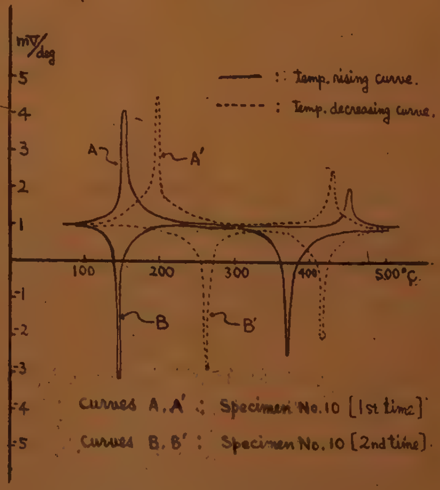

Fig. 12. Anomalous thermo-electromotive force

The curve *B* and *B′* correspond to those of heating and cooling processes respectively.

These anomalous phenomena may be due to the non-uniform distribution of copper ions caused by the thermal diffusion in specimen with temperature gradient. To produce the uniform distribution of copper ions, therefore, a specimen was carefully prepared in a specially deviced heating furnace, the observes thermo-electromotive forces of which are shown by a curve *B* in Fig. 11.

From the repeated measurements on this same specimen, however, we obtain the results shown in Fig. 13, which may be taken to show the anomaly due to the heterogeneous distribution of copper ions caused by the thermal diffusion. Especially, at the temperature of the anomaly being observed, it should be noted that, just after the measurement of the thermo-electromotive force, the potential difference of a considerable magnitude continues to be observed, for a few minutes, between both sides of the specimen inspite of removing the temperature gradient in it. This phenomenon may be considered to be closely related to the non-uniformity caused by the diffusion of copper ions.

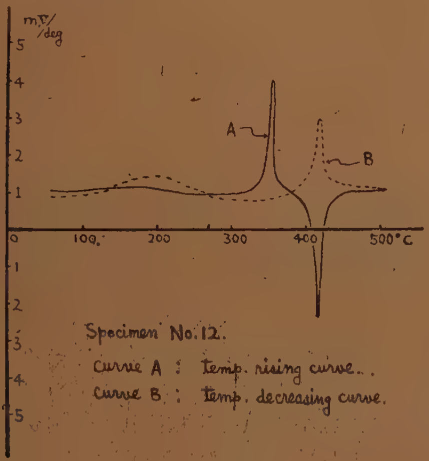

Fig. 13. Anomalous thermo-electromotive force.

(b). As mentioned above, the copper ions may be considered to easily migrate and diffuse in such a specimen with small temperature gradient. This fact was made clear by the following experimental measurements. Eight pieces of a small specimen (3 mm. × 3 mm. × 5 mm.) are arranged side by side between two platinum electrodes and this pile is put into a vacuum electric furnace. Both sides of this pile (namely electrodes) are maintained at 180°C and 380°C respectively, thus producing temperature difference of 200°C between two electrodes, for about 30~40 hours. Before and after the mentioned heat treatment, each of eight specimens was weighed precisely, and the results obtained are shown in Table 2 and 3. From these results the diffusion of copper ions is seen to take place so easily from the high temperature side to the low temperature one, and the mentioned anomalous thermo-electromotive force in the β-phase may be considered to be ascribed to the heterogeneous distribution of copper ions due to the temperature gradient.

Table 2. {Sp. No. 1 High temp. side (380°C)
Sp. No. 8 Low temp. side (180°C)

No	Before diffusion	After diffusion	difference
1	122.70 mg	121.08 mg	−1.62 mg
2	139.46	138.43	−1.03
3	149.10	148.29	−0.81
4	145.76	145.75	−0.01
5	131.47	131.69	+0.22
6	134.81	135.47	+0.66
7	122.17	123.11	+0.94
8	124.61	126.09	+1.48

Table 3. {Sp. No. 1. Low temp. side (180°C)
Sp. No. 8. High temp. side (380°C)

No	Before diffusion	After diffusion	difference
1	121.08 mg	122.49 mg	+1.41 mg
2	138.43	139.39	+0.96
3	148.29	148.86	+0.57
4	145.75	146.06	+0.31
5	131.69	131.46	−0.23
6	135.47	134.86	−0.61
7	123.11	122.13	−0.98
8	126.09	124.56	−1.53

In conclusion, the author wishes to express his thanks to Prof. T. Muto of University of Tokyo for his kind guidance and encouragement.

References.

1) E. A. Posnjak, and H. E. Merwin; Econ. Geol. **10** (1915) 491.
2) N. Alsen; Geol. Förehigs. Stockholm, Förhandlinger. **53** (1931) 111.
3) T. Barth; Central Mineral Geol. Polännt. **(A)** (1926) 284.
4) P. Rahlfs; Zeit. f. Phys. Chem. **(B) 31** (1936) 157.
5) N. W. Buerger; Econ. Geol. **36** (1941) 19.
N. W. Buerger; Amer. Mineral. **27** (1942) 712.
N. W. Buerger, and M. J. Buerger; Amer. Mineral **27** (1942) 216, **29** (1944) 56.
6) C. Tubandt, S. Eggert, and G. Schibbe; Zeits. anorg. allgem. Chem. **117** (1921) 1.
7) C. Sykes and F. W. Jones; Journ. Inst. Metals. **2** (1936) 257.

JOURNAL OF THE PHYSICAL SOCIETY OF JAPAN Vol. 6, No. 6 NOV.—DEC., 1951

The Electrical Conductivity and Isothermal Hall Effect in Cuprous Sulfide, Semi-Conductor.

By Eiji HIRAHARA.
Hiroshima Municipal Technical College.

(Received January 29, 1951)

The experimental measurements of the isothermal Hall effect on the γ-cuprous sulfide were performed with the following results.

In the stoichiometric specimens, the values of Hall constant $\boldsymbol{R}$ are about $3\sim4\times10^{9}\left[\frac{\text{Volt}\cdot\text{cm}}{\text{Gauss}\cdot\text{amp}}\right]$, mobility μ and mean free path l are about $12[\text{cm}^2/\text{Volt}\cdot\text{sec}]$, $9[\text{cm}]$, respectively. These values of $\boldsymbol{R}$, μ and l decrease in the β-phase.

As compared with the stoichiometric specimens, the values of μ and l in the sulphur excess specimens do not increase so much as the conductivities do. On the contrary, in the sulphur deficient specimens, the decrease of μ and l is not so remarkable in comparison with that of conductivities. These phenomena may be considered that the impurity scattering due to the free electrons and holes makes the values of μ and l reduce.

§1. Introduction.

The experimental studies on the physical properties of cuprous sulfides have been reported by the author several times[1)2)] with the conclusion that there is a new transition point at about 470°C.

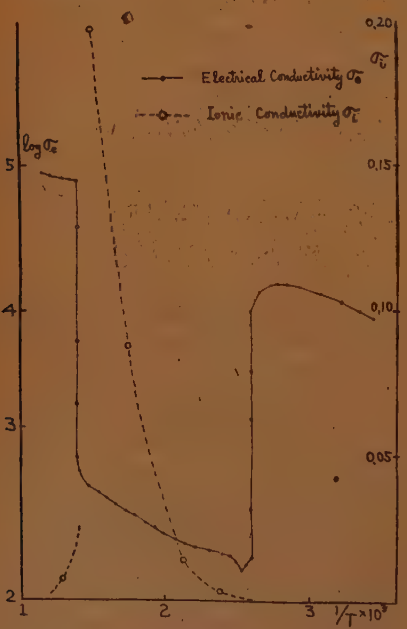

Fig. 1. Ionic and Electrical Conductivity.

The results obtained are as follows; the cuprous sulfides have three phases, namely α-phase (above 470°C), β-phase (470°∼110°C), and γ-phase (below 110°C). In the γ-phase they show the characteristic properties of P-type semi-conductors as like cuprous oxides, in the β-phase, they have a remarkable ionic current, and in the high temperature α-phase the ionic current scarcely appears.

While the low temperature transition between γ-and β-phase has been already reported by the several authors,[3)4)5)] the high temperature transition between β-and α-phase had not been observed before the author. The abbreviate results obtained by the author about electric and ionic conductivity are shown in Fig. 1. The γ-cuprous sulfides are P-type semi-conductors, and their conductivity is caused by the behaviour of electron holes in full bands, which have been shown by the measurements of electrical conductivity and thermo-electromotive force.

Now again, the characteristic behaviour of electron holes have been observed by the measurements of the Hall-effects for γ-phase cuprous sulfides, and we could have estimated the number of the impurity centers, the mobility and mean free path of electron holes. And also, indefinite as the results were, we would say that we had observed a noteworthy phenomenon that the electron holes were scattered by the impurity centers.

§2. Apparatus and Experimental Procedures.

The experimental studies of the Hall effect in Semi-conductors have been reported by many workers; about cuprous oxides previously W. Vogt,⁶⁾ E. Engelhard⁷⁾ and recently S. J. Angello,⁸⁾ W. Feldman⁹⁾ and T. Okada¹⁰⁾ have investigated, about Zinc oxides P. H. Miller¹¹⁾ has studied. But about cuprous sulfides it seems that no workers have studied on the stand points of modern idea.

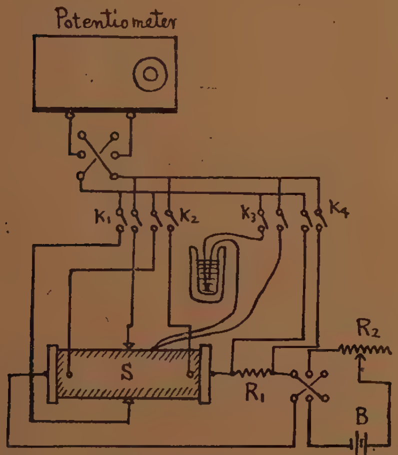

Fig. 2. Schematic diagram of apparatus for measurement.

The cuprous sulfides are prepared from pure copper block and pure sulphur powder in a vacuum Pyrex glass tube at about 600°C, and as specimens are formed about 1 mm × 3 mm × 15 mm. Fig. 2 shows a schematic circuit diagram of apparatus for measurement of Hall effect and conductivity.

The main currents through the specimen are supplied by a battery B (about 20 Volts), in this circuit a standard resistance R_1 (100 Ω) is set, in order to know the values of the main currents by measuring the potential difference between the ends of this resistance.

Fine wolfram wires (diameter 0.2 mm) are used as the measuring proves of Hall potential and resistance, which contact on the platinum spots sputtered on the surface of specimen. The wolfram wire has the advantage of being able to retain its spring at the higher temperatures. The potential differences raising from the Hall effect, resistance, electro-motive-force of thermo couples and the potential drops of main currents in standard resistance are measured by the K-type potentiometer through the swiches K_1, K_2, K_3 and K_4 respectively. To raise the temperatures of specimen, the specimen holder is inserted into a small electric furnace, which is 1.3 cm in diameter, 15 cm in length and its heating wires are made of wolfram because it is non ferromagnetic substance. The pyrex glass tube (dia. 16 mm) containing above mentioned furnace and specimen will be set between the electro-magnet poles, which yields about 9000 Gauss at the gap of 20 mm. between the poles.

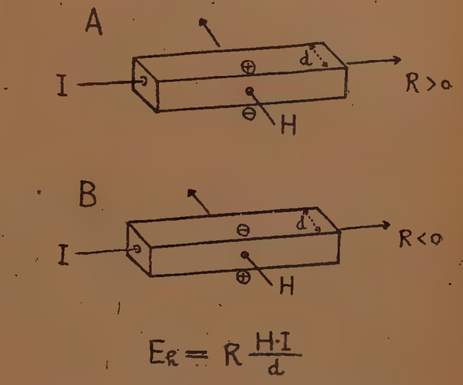

Fig. 3. The sign of Hall Constant.

When the currents I flow through the specimen and the magnetic field H are applied perpendicular to the currents, the following Hall potential E_h appears normal to both the currents and magnetic field

$$E_h = R\frac{HI}{d}$$

where d is the thickness of the specimen in the direction of the magnetic field, R is the Hall coefficient, its sign is positive for P-type conductors (Fig. 3 A), negative for N-type conductors (Fig. 3. B). In Fig. 3, the Hall potentials are positive on the upper side for the case A, on the lower side for the case B.

Expressing E_h in volt, H in Gauss, I in ampere and d in cm, the dimension of R is [Volt·cm/Gauss·amp], but when R is expressed in [cm³/amp·sec],

$$R[\mathrm{cm}^3/\mathrm{amp\cdot sec}] = 10^8 \times \frac{E_h \times d}{H \times I}.$$

In practice, to determine the true Hall voltage E_h, the following procedure was carried out: In the first time, the Hall effect was measured with the magnetic field in a certain direction.

This yielded V_1 in the equation

$$V_1 = E_h + V_g + V_c + V_T ,$$

where V_g is the potential difference arising from that the Hall-probes contact on the no equipotential lines on the specimen, V_c is the contact potential difference between the probe and specimen (rectification appears!), and V_T is the thermo electric potential between two Hall-probes in different temperatures. In the next time, the measuremeet was repeated with the magnetic field in the opposite direction. This gave V_2 changing the sign of E_h in the expression

$$V_2 = -E_h + V_g + V_c + V_T .$$

The true Hall-potential E_h was obtained using the relation

$$E_h = \frac{1}{2}(V_1 - V_2) .$$

With this apparatus, it was possible to measure the Hall-effect and conductivity in the temperature range from -20°C to 250°C with continuous variation. The low temperatures was obtained by cooling with a mixture of the anhydrous calcium chloride and ice blocks.

§3. Results of Measurements.

In the range of the low temperatures, the Hall-potentials were the order of 10^{-5} volts with the main currents about 40 mA through the specimen, and with the magnetic fields 9000 Gauss, but raising the temperature with increasing conductivity, the Hall-potentials decreased gradually to $10^{-6} \sim 10^{-7}$ volts about 100°C. In the range of β-phase above 110°C it was impossible to obtain the accurate results because the ionic currents appearing in the β-phase disturbed the main currents and so the Hall-potentials.

The conductivity and Hall constant have been measured on the many specimens in the manner above mentioned, the typical five spemens of which are as follows.

The typical specimens are a chemical stoichiometric one (Specimen No. 31), two specimens containing sulphur 0.1% in excess (Sp. No. 34), 0.2% in excess (Sp. No. 36) more than stoichiometric one, and two specimens containing sulphur 0.1% in defect (Sp. No. 41), 0.15% in defect (Sp. No. 44) less than stoichiometric one. The percentages of sulphur above mentioned are the ones of sulphur to the sulphur constituents of the cuprous sulfides.

The results obtained from these specimens are shown in Figs. 4~8, which are showing the Hall constant R, conductivity σ, mean free path l, and mobility μ, as a function of reciprocal absolute temperatures.

In all specimens, the temperature dependency of conductivity is as same as that the author reported previously,[1)2)] that is, the coductivity increased with temperature in γ-phase (below 110°C) and decreased rapidly in β-phase (above 110°C).

The signs of Hall constants were positive, which meant the cuprous sulfides were P-type semi-conductors, this was compatible with the results obtained from the many previous measurements on the other physical properties.

The values of Hall constants decreased from the order of 10^{-9}[Volt·cm/Gauss·amp] in the stoichiometric specimens (No. 31), to the order of 10^{-10} in the specimens containing sulphur in excess which had a conductivity increasing with sulphur contents. On the other hand, the Hall constants increased to the order of 10^{-8} on the sulphur deficient specimens which had poor conductivity. Now, the mobility and mean free path of electron holes calculated from the conductivity and Hall constant are shown in the above figures, of which calculations will be mentioned later.

In the β-phase, at some temperature the Hall potential showed often a large value (several tens times as ordinary values) which are not indicated now in the above figures to avoid to confusion. These anomaly will be considered to be analogaous to the phenomena which were observed in the measurements on the thermo-electric power,[4)] that is, in the β-phase the mobility of copper ions increased with ionic currents, and it contributed to the anomalous large values of Hall potentials. But the rigorous interpretation of these anomaly is not given yet because no detailed theoretical considerations of Hall-effects in which the mobility of electrons and copper ions are considered simultaneously have been performed.

§4. Analysis of results and considerations.

From the above results of the measurements on the conductivity and Hall effect, we may calculate the mobility μ, the mean free path l of the electron holes, the numbers n of free electron excited into impurity levels and the

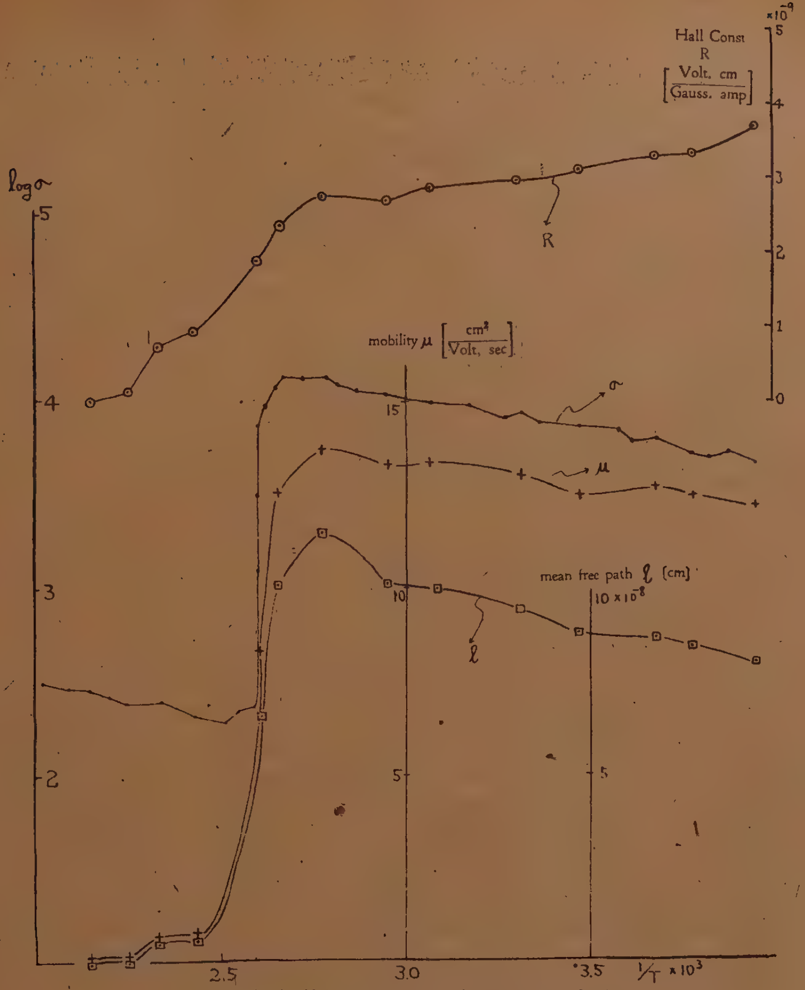

Fig. 4. Specimen No. 31 (Stoichiometric)

numbers n_b of impurity centers.

At first, we must investigate whether the electron holes are degenerate or not, because the cuprous sulfides are fair conducting substances. The expressions of the conductivity σ and Hall constant R change more or less whether the electron holes are degenerate and obey the Fermi-Dirac statistics, or are non-degenerate and obey the Boltzmann statistics. The limiting temperature T_0, between degenerate and non-degenerate states is given as follows,⁽¹²⁾

$$(1)\quad T_0=\frac{h^2}{2mk}n^{2/3}\approx 1.7\times10^{-10}\times n^{2/3}.$$

When the value of T_0 in (1) for the numbers n of the electron holes of the sample treated is much larger than the value of actual temperature T, that is, for $T_0 \gg T$, the electron holes of the treated sample are degenerate, and for $T_0 \ll T$, are non-degenerate.

For the samples treated in this paper, $n \approx 10^{18}$, so $T_0=160°\mathrm{K}$ for these values of n. For the temperature T in our case, $T_0 \ll T$, the electron holes may be treated as non-degenerate states.

The relations between the conductivity σ, the numbers n and the mobility μ of the free electron holes are⁽¹³⁾

$$(2)\quad \sigma=ne\mu\,,$$

$$(3)\quad \sigma=\frac{4}{3}\frac{nle^2}{(2\pi kmT)^{1/2}}\,.$$

The relation between the μ and the l is

$$(4)\quad \mu=\frac{4}{3}\frac{el}{(2\pi mkT)^{1/2}}\,.$$

Inserting the numerical values into (4), if m is the free electron mass, μ may be written in e.s.u. as follows,

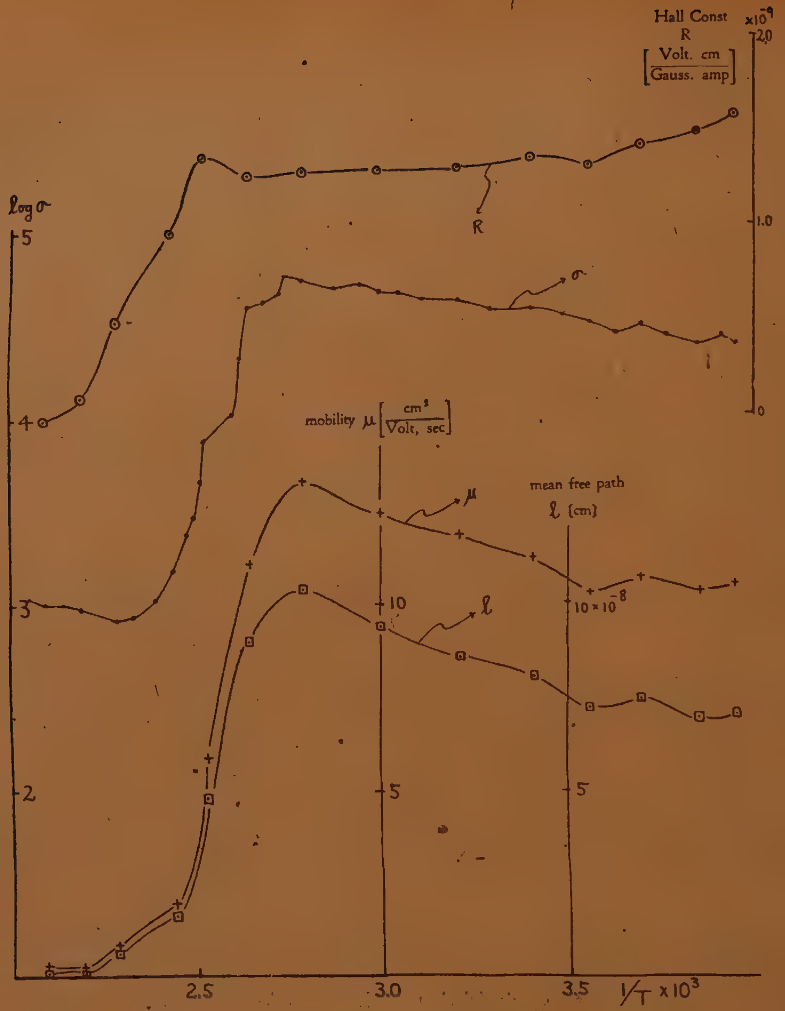

Fig. 5. Specimen No. 34 (0.1% S. excess)

(4′) $\mu=7.22\times10^{11}\times l\times T^{-\frac{1}{2}}$ (e.s.u)

and in the dimension [cm²/Volt·sec],

(4″) $\mu=2.43\times10^{9}\times l\times T^{-\frac{1}{2}}$ [cm²/Volt·sec].

Between R and n, there is the relation[14] (in the case of nondegenerate states,)

(5) $$R=\frac{3\pi}{8en}$$

expressing R in [cm³/amp·sec] and [Volt·cm/Gauss·amp]

(5′) $R=7.4\times10^{18}\times\frac{1}{n}$ [cm³/amp·sec]

(5″) $R=7.4\times10^{10}\times1/n$ [Volt·cm/Gauss·amp].

From (2) and (5′)

(6) $\mu=0.85\times\sigma\times R$

where R is expressed in [cm³/amp·sec], σ in [amp/volt·cm], and from (2) and (5″)

(6′) $\mu=0.85\times10^{8}\times\sigma\times R$

where R is expressed in [Volt·cm/Gauss·amp].

These expressions are all available when the effects of the definite fixed impurity atoms and the mobile ions are neglected, but treating these equations provisionally we estimate values of μ and l from the observed values of R and σ for trial. So obtained values of μ and l are shown in Fig. 4∼8 respectively. At the temperature ranges of γ-phase (below 110°C), μ is about 10[cm²/Volt·cm], l is oder of 10^{-8} cm. When the temperature rises into the range of β-phase (above 110°C) the conductivity σ decrease rapidly as well as μ and l. This anomaly may be due to the fact that in the β-phase the disordering of lattice increases with ionic currents. Therefore, the above expressions do not seem to be available to such a sample having an ionic currents in the β-phase, but on

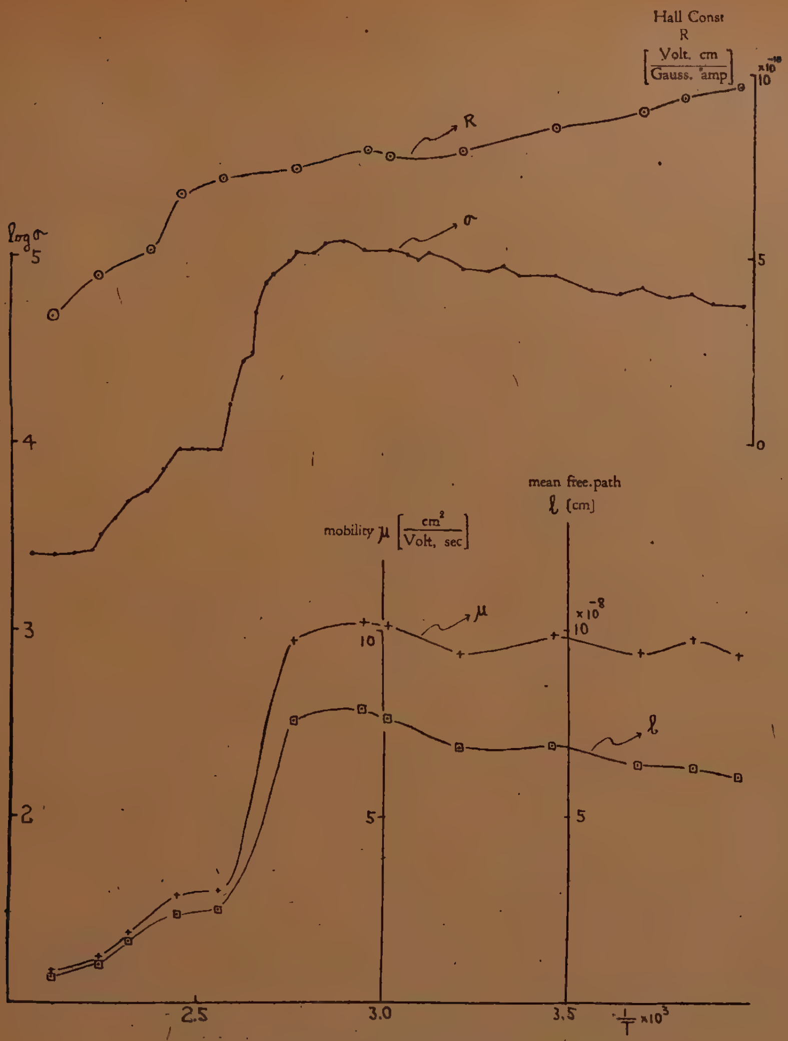

Fig. 6. Specimen No. 36 (0.2% S. excess)

the γ-phase (below 110°C) these expressions may be considered approximately to be applicable.

It is a noteworthy phenomenon that in spite of the conductivity of the specimens (No. 34, No. 36) containing impurity sulphur excess show larger values than the one of the stoichiometric sample (No. 31), the mean free path l and the mobility μ of the formers are smaller than the ones of the latter. This may be understood if we consider that the predominance of impurity scattering makes the values of μ and l reduce. And also in the samples (No. 42, 44) containing sulphur less than the stoichiometric sample (No. 31), the conductivity, reduces remarkably, but the l and μ reduce not so remarkably. This may mean the diminution of the scattering of impurity,

Let us now estimate the number of impurity centers in the samples.

The relation between the number n_b of impurity atoms in unit volume and the number n of free electrons (or electron holes) in unit volume is[15]

$$(7)\quad n = n_b^{1/2}\left[2\frac{(2\pi mkT)^{3/2}}{h^3}\right]^{1/2}\exp(-E/2kT),$$

where E is the energy separation between the top of filled band and the impurity level. Inserting n in (7) into (5), we have

$$R = \frac{3\pi}{8}\frac{1}{ne}$$

$$= \frac{3\pi}{8e}\cdot n_b^{-1/2}\left[2\frac{(2\pi mkT)^{3/2}}{h^3}\right]^{-1/2} e^{E/2kT}$$

$$= 1{,}06\times10^{12}\times n_b^{-1/2}\times T^{-3/4}\times e^{E/2kT}\ (\text{e.m.u.}).$$

where an effective mass m is approximately equal to the free electron mass. In Fig. 9 is

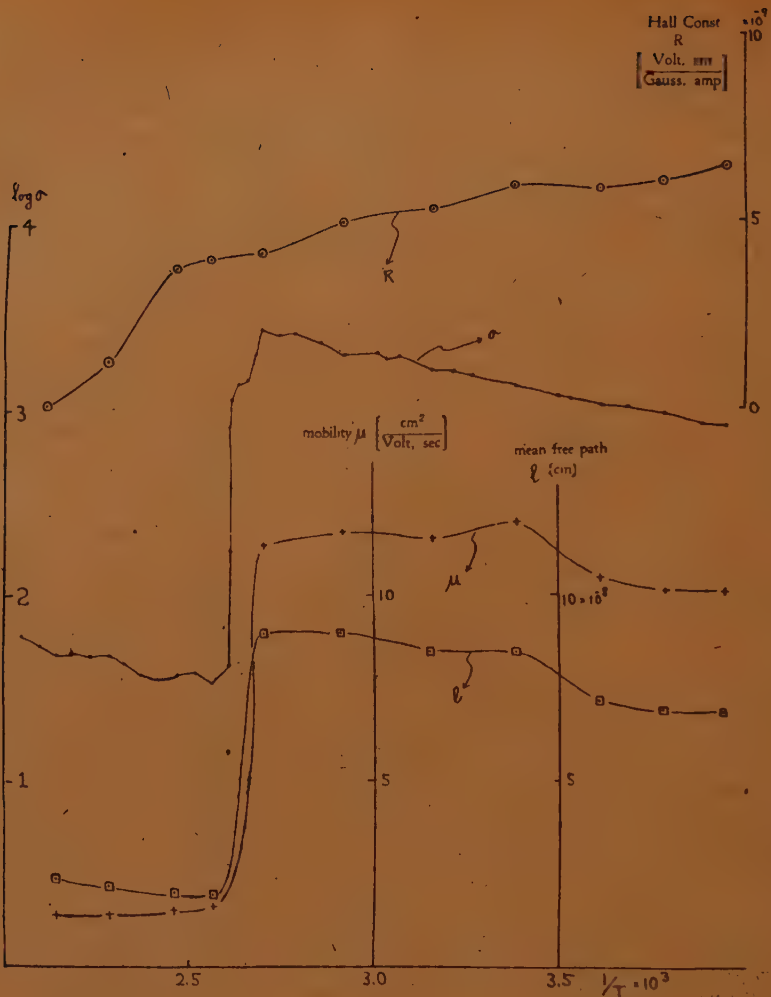

Fig. 7. Specimen No. 41 (0.1% S. deficit)

a plot of log R as a function of the inverse absolute temperatures. At the range of temperature below 110°C (γ-phase), there is a linear relation between log R and $1/T$. The gradient of this linearity gives an activation energy of each sample at γ-phase, and its values are same order as the values obtained from the linearity between log σ and $1/T$. The values of activation energy E obtained from the conductivity are given in Table I.

The values of n obtained from (5) are shown in Fig. 10. As sbown in Fig. 9 and 10, the fact that there are the linear relation between log R or log n and $1/T$, means that the number n_b of impurity centers don't depend so much on temperatures, then we may calculate the the values of n_b at a certain temperature in γ-phase (e.g. 17°C) and show this values in the Table I.

The crystal structure of a stoichiometric γ-cuprous sulfide is by Buerger[5], a rhombic structure; $a=11.90$A, $b=27.28$A, $c=13.41$A. Using these data and density 5.8[3], the number of molecules in cm^3 are 2.23×10^{22}/cm^3. And then it may say that the 0.1% and 0.2% sulphur excess samples (No. 34 and No. 36) have to contain 2×10^{19}/cm^3 and 4×10^{19}/cm^3 impurity sulphur atoms respectively. While, the values of n_b obtained from the measured R are large by the factor 10^2 as the above values, and further the sulphur deficient samples (No. 41 and No. 44) are measured to contain the impurity sulphur $10^{19}\sim10^{20}$. From these facts, it may be considered as follows; in the stoichiometric samples and even in the sulphur deficient samples there may be partially sulphur

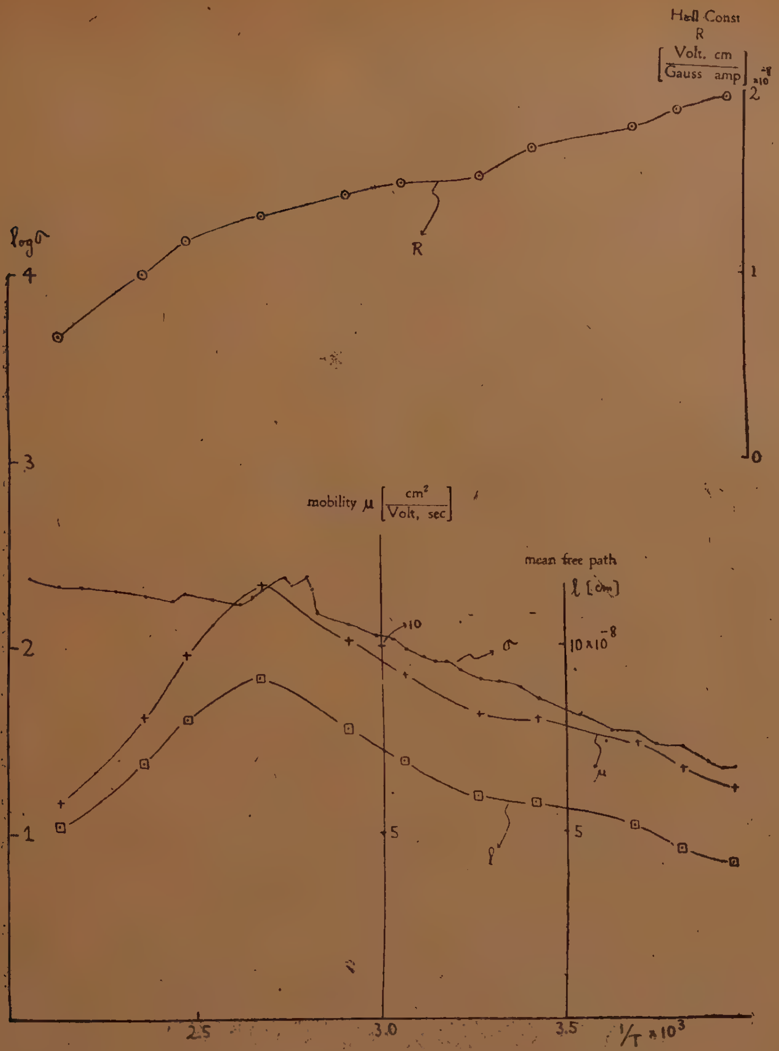

Fig. 8. Specimen No. 44. (0.15% S. deficit)

Table 1.

Specimen	Activation energy *E*	Free electron holes *n* (at 17°C)	Impurity Centers n_b (measured)	Impurity Sulphur n_b'
No. 36 0.2% S. excess	0.052 eV	8.6×10^{19}	2.57×10^{21}	4×10^{19}
No. 34 0.1% excess	0.056	5.2×10^{19}	1.03×10^{21}	2×10^{19}
No. 31 Stoichiometric	0.062	2.4×10^{19}	2.8×10^{20}	
No. 41 0.1% S. deficit	0.076	1.2×10^{19}	1.3×10^{20}	
No. 44 0.15% S. deficit	0.102	4.4×10^{18}	4.65×10^{19}	

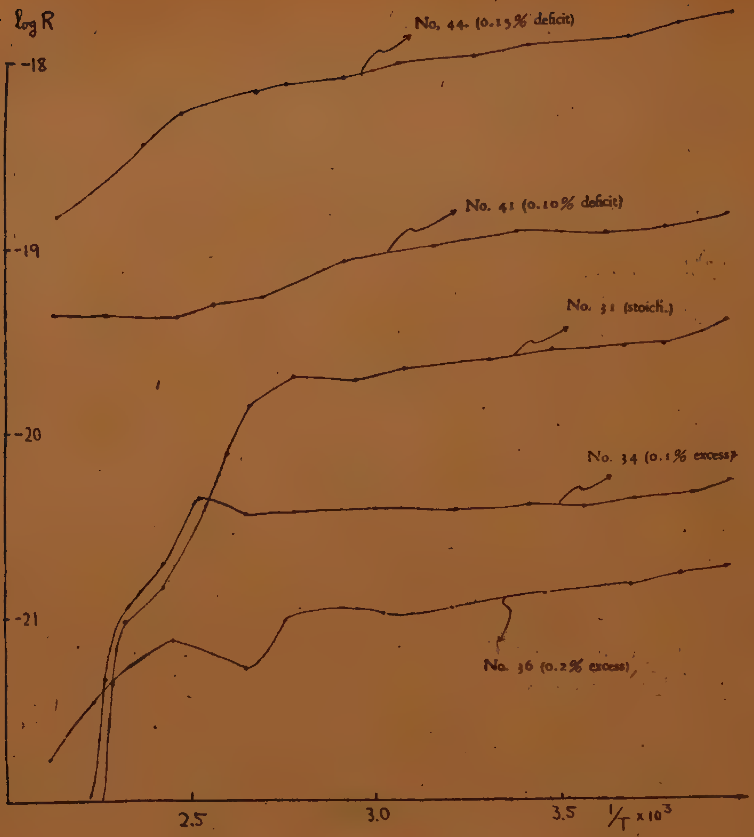

Fig. 9. $\log R \sim 1/T$.

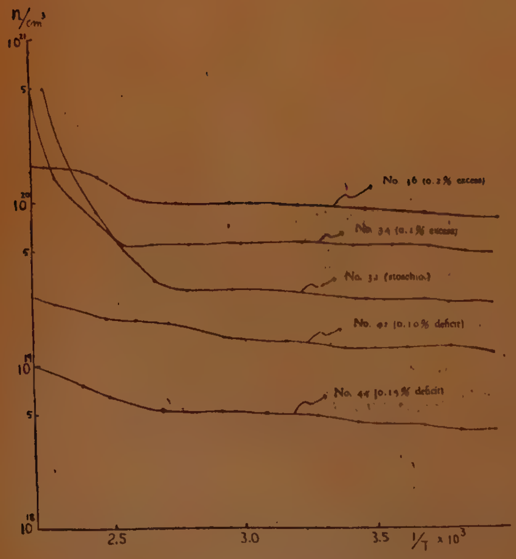

Fig. 10. $\log n \sim 1/T$

excess parts in a sample, and these sulphur excess parts behave as a sulphur excess sample (P-type). This consideration will be supported by Buerger's X-ray crystal analysis[16)5)] which explains cuprous sulfides are ready to make a solid solution with cupric sulfides CuS.

The energy separation E between the filled band and impurity level decrease with the increase of impurity sulphur atoms. The number n_b of impurity atoms and E are shown in Fig. 10.

Finally, keenly feeling the necessity of the experimental and theoretical studies on the mobility of electrons and ions in β-phase, we have intenting to study on these subjects.

In conclusion the author wishes to express his hearty thanks to Prof. Dr. T. Muto of University of Tokyo

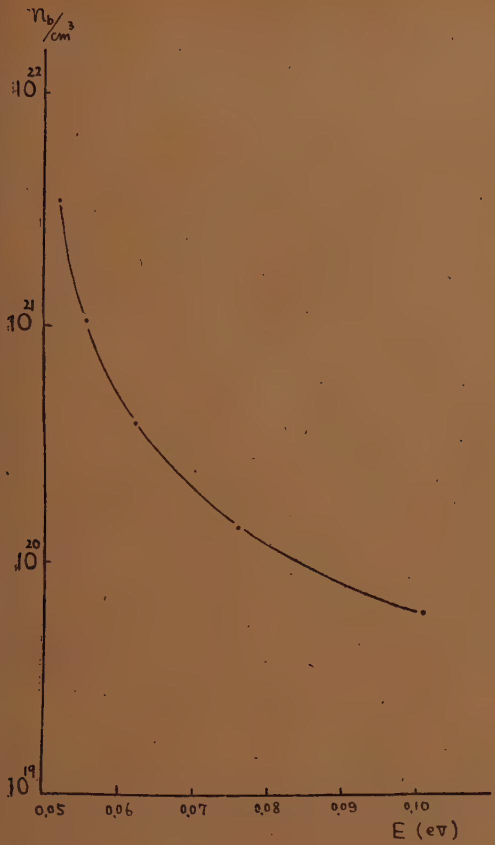

Fig. 11. *E* and impurity centers.

for his guidance in this work and to Assist. Prof. Dr. J. Yamashita of University of Tokyo for his kind discussions. This work was supported by the research grant of the Ministry of Education.

References

1) Eiji Hirahara: Busseiron Kenkyu **7** (1947) 19.

Eiji Hirahara: The Jour. Phys. Soc. Japan. **2** (1947) 211.

2) Eiji Hirahara: Proc. Phys. Soc. Japan. **4** (1949) 10.

Eiji Hirahara: ibid. **4** (1949) 12.

3) E. A. Posnjak and H. E. Merwin: Econ Geol. **10** (1015) 491.

4) P. Rahlfs: Zeits. f. Phys. Chem. (B). **31** (1936) 157.

5) M. J. Buerger and N. W. Buerger: Amer. Mineral. **27** (1942) 216, **29** (1944) 56.

6) W. Vogt. Ann. d. Phys. **7** (1930) 183.

7) E. Engelhard: Ann. d. Phys. **17** (1933) 501.

3) S. T. Angello: Phys. Rev. **62** (1942) 371.

9) W. Feldman: Phys. Rev. **64** (1943) 113.

10) T. Okada: Busseiron Kenkyū **19** (1949) 15.

11) P. H. Miller: Phys. Rev. **60** (1941) 890.

12) A. Sommerfeld und H. Bethe: Hand. d. Phys. Bd. 24/2 S. 345.

13) F. Seitz: The Modern Theory of Solids (1940) 190.

14) ibid. P. 192.

15) ibid. P. 188.

16) N. W. Buerger: Amer. Mineral. **27** (1942) 712, **29** (1944) 56.

JOURNAL OF THE PHYSICAL SOCIETY OF JAPAN Vol. 6, No. 6 NOV.~DEC., 1951

Theory of the Specific Heat of Graphite.

By Kozo KOMATSU and Takeo NAGAMIYA.

Department of Physics, Naniwa University, Sakai and Department of Physics, Faculty of Science, Osaka University.

(Read October 23, 1949: Received January 31, 1951)

The graphite crystal is considered as a system of thin elastic plates spaced at a constant distance. An elastic force is assumed to act between each neighboring plates in such a way that a local change of the spacing between them produces at that point a tension or a pressure normal to the plates whose magnitude is proportional to that change. The vibrations of this system are assumed to be separable into independent parts: the bending vibrations in which the displacements occur normal to the planes of the plates, and the extensional and shearing vibrations in which the displacements occur parallel to them. The frequency distributions of their normal modes are studied. The values of the elastic constants of the plates that determine the latter vibrations are derived from the force constants of benzene molecule, while the value of the bending modulus of the plate is determined by fitting the calculated specific heat curve with the observed one. The constants of the elastic force acting between neighboring plates are derived from the measured elastic constants of graphite (mainly the compressibility). Small contributions of the electronic specific heat and the C_p-C_v correction are added to obtain the total specific heat. The result is in good agreement with experiment.

§ 1. Introduction and the Scope of the Theory.

It is well known that the specific heat of graphite at low temperatures changes nearly proportional to T^2, rather than to T^3. It seems that Debye's theory[1] can not be applied to such a system as graphite that has a remarkable layer structure. Nernst[2] and Magnus[3] attempted to explain the experimental curve of the specific heat of graphite by use of two characteristic temperatures. The calculated values from Magnus' formula agreed with the experimental ones in the temperature range above 100°K, but discrepancies were considerable below this. The aim of the present work is to develope a comprehensive theory of the specific heat of graphite based on its peculiar crystalline structure.

The distance between the carbon atoms which lie in the neighboring atomic layers is 3.40Å, which is considerably larger than the distance between the atoms in the same layer, which is 1.42Å. Accordingly, the interaction between the neighboring atoms in the different layers is considerably less than that between the neighboring atoms in the same layer. It may thus be reasonable to consider that the lattice vibrations consist of two approximately independent parts, namely one the two dimensional vibrations of separate layers for which the displacements of the atoms occur parallel to their planes, and the other layers for which the displacements occur normal to them. For the former we may assume that each layer is vibrating independently of other layers, and may simplify the problem by treating each layer as a two dimensional elastic continuous medium, or a thin elastic plate. For the latter, the vibrating system may be replaced by a system of such thin elastic plates spaced at a constant distance, an elastic force acting between each neighboring two sheets. The elastic constants of the plate (extensional, shearing and bending moduli) should be connected with the valence forces between the carbon atoms in a single layer, while the elastic force constant between the neighboring layers is to be derived from the compressibility data. Since the direct experimental data of the valence forces are unavailable, we wish to determine two of the elastic constants of the plate (extensional and shearing moduli) from experiments of the vibrations of benzene molecule by making a slight modification, and the remaining one by fitting the calculated specific heat curve with experiment.

§ 2. 1. The Two Dimensional Vibrations of a Layer.

A hexagonal crystal had in general five independent elastic constants, $c_{11}, c_{12}, c_{13}, c_{33}, c_{44}$, ($c_{66}=2(c_{11}-c_{12})$). We can omit such constants that refer to the z-axis (the normal to the plane). For the vibrations of the layers in which the atomic displacements are confined to its plane, we have to deal with only two independent constants, c_{11} and c_{12}. A hexagonal layer can therefore be considered as isotropic. We shall treat it as a *continuous* isotropic medium. The velocities of the transverse and the longitudinal waves in it are[4]

$$v_t=\sqrt{\frac{E}{2\rho(1+\sigma)}},\quad v_l=\sqrt{\frac{E}{\rho(1-\sigma^2)}},\qquad (1)$$

respectively, where ρ, E and σ are the volume density, the Young's modulus and the Poisson's ratio, respectively. It is more convenient, however, to use those constants which refer to surface rather than to volume. Denoting the distance between the adjacent layers by c, we shall define ρ' and E' as follows:

$$\rho'=c\rho\,;\quad E'=cE.\qquad (2)$$

Then (1) can be written

$$v_t=\sqrt{\frac{E'}{2\rho'(1+\sigma)}},\quad v_l=\sqrt{\frac{E'}{\rho'(1-\sigma^2)}}.\qquad (3)$$

Treating the problem just as in Debye's theory of a three-dimensional continuum, we obtain the distribution function of the normal modes $f(\nu)$, the maximum frequency $\nu_{\max}$ and the characteristic temperature Θ as follows:

$$f(\nu)=\frac{2\pi V}{c}\left(\frac{1}{v_t^2}+\frac{1}{v_l^2}\right)\nu,\qquad (4)$$

$$\nu_{\max}=\left\{\frac{\pi V}{2cN}\left(\frac{1}{v_t^2}+\frac{1}{v_l^2}\right)\right\}^{-\frac{1}{2}},\qquad (5)$$

$$\Theta=\frac{h}{k}\left\{\frac{\pi V}{2cN}\left(\frac{1}{v_t^2}+\frac{1}{v_l^2}\right)\right\}^{-\frac{1}{2}},\qquad (6)$$

where V, N, h and k are the atomic volume, Avogadro's number, Planck's constant and Boltzmann's constant, respectively.

At high temperatures we can derive the following approximate formula of the specific heat C:

$$\frac{C}{C_\infty}=1-\frac{x^2}{24}+\frac{x^4}{720}-\frac{x^6}{24192}+\frac{x^8}{86400}-\cdots,\qquad (7)$$

and at low temperatures

$$\frac{C}{C_\infty}=\frac{14.42}{x^2}-\frac{2x}{e^x-1}-6x\sum_{n=1}^{\infty}e^{-nx}\left(\frac{1}{nx}+\frac{2}{n^2x^2}+\frac{2}{n^3x^3}\right).\qquad (8)$$

Here C_∞ is: $2R=3.97$ cal/deg. mole and $x=\Theta/T$.

§ 2. 2. The Determination of the Elastic Constants of the Layer and of the Characteristic Temperature.

The force constants between the carbon atoms in the hexagonal layer of graphite are not known. However, the force constants between the carbon atoms of a benzene molecule have been determined by the analysis of the infra-red absorption spectra and the Raman spectra. Through adequate modifications we can obtain from these constants a fairly accurate estimation of those of graphite layer.

Wilson[5] discussed the planar vibrations of a benzene molecule on the assumption that the potential energy φ is a quadratic function of the coordinates, as follows:

$$\begin{aligned}2\varphi=&p_b\{(\varDelta R_{12})^2+(\varDelta R_{23})^2+\cdots+(\varDelta R_{61})^2\}\\&+q_b a^2\{(\varDelta\gamma_1)^2+(\varDelta\gamma_2)^2+\cdots+(\varDelta\gamma_6)^2\}\\&+h_b(b-a)^2(\lambda_1^2+\lambda_2^2+\cdots+\lambda_6^2)+\cdots.\end{aligned}\qquad (6)$$

The constants a and b are shown in Fig. 1a, and the coordinates R_{ij} and γ_i in Fig. 1b. $\varDelta R_{ij}$ and $\varDelta\gamma_i$ are the deviations of R_{ij} and γ_i from their equilibrium values, and λ_i is the angle of deviation of the carbon-hydrogen bond from the bisector of the carbon-carbon bond angle. Using α_i and β_i in Fig. 1b, (9) can be transformed into

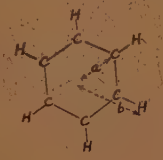

Fig. 1a. Benzene molecule.

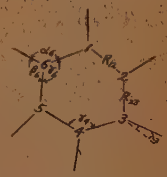

Fig. 1b. Distorted benzene molecule and the explanation of the coordinates used in the potential energy function.

$$\begin{aligned}2\varphi=&p_b\{(\varDelta R_{12})^2+(\varDelta R_{23})^2+\cdots+(\varDelta R_{61})^2\}\\&+q_b'a^2\{(\varDelta\gamma_1)^2+(\varDelta\gamma_2)^2+\cdots+(\varDelta\gamma_6)^2\}\\&+1/2\cdot h_b(b-a)^2\cdot\{(\varDelta\alpha_1)^2+(\varDelta\beta_1)^2\\&+(\varDelta\alpha_2)^2+(\varDelta\beta_2)^2+\cdots+(\varDelta\alpha_6)^2\\&+(\varDelta\beta_6)^2\}+\cdots\end{aligned}\qquad (10)$$

where $\varDelta\alpha_i+\varDelta\beta_i+\varDelta\gamma_i=0$ and

$$q_b'=q_b-\frac{h_b}{4}\frac{(b-a)^2}{a^2}.\qquad (11)$$

Using the expression (9) for the potential energy, Wilson derived the formula for the frequencies of the normal vibrations. Lord and

Andrews⁶⁾ made an identification of the observed spectral lines and obtained the following values of the force constants:

$$p_b=7{,}58\times10^5\ \text{dynes/cm}\,,$$
$$q_b=0.65\times10^5\ \text{dynes/cm}\,,$$
$$h_b=0.76\times10^5\ \text{dynes/cm}\,.$$

From these values and $a=1.39\,\text{Å}$, $b-a=1.08\,\text{Å}$, we obtain for the constant q_b' appearing in (10)

$$q_b'=0.54\times10^5\ \text{dynes/cm}\,.$$

We shall employ p_b and q_b' (instead of q_b) with a modification mentioned below. Both q_b' and q_b correspond to the change of the valence angle γ_t, but q_b' is preferable to q_b, since all three angles α, β, γ appear in a symmetric way in (10). α, β, γ are equivalent in the case of graphite, so that the coefficient $\frac{1}{2}h_b(b-a)^2$ in (10) should be replaced by $q_b'a^2$ for that case, and the resulting formula is perfectly symmetric in α, β, γ.

Now, it is a well known fact that the value of the force constant p connected with the variation of the length of C—C bond varies nearly in linear relation with the bond order. Using the values 4.96×10^5 dynes/cm for C_2H_6, 9.79×10^5 dynes/cm for C_2H_4 and 7.58×10^5 dynes/cm for benzene, we have by an interpolation

$$p_g=6.71\times10^5\ \text{dynes/cm}$$

for graphite. As for the constant q_g' of graphite, we have at present no reliable method of its estimation, so that we shall simply put

$$q_g'=q_b'\cdot p_g/p_b=0.48\times10^5\ \text{dynes/cm}\,.$$

To determine the elastic constants E' and σ defined in the previous section from these force constants, it is convenient to introduce at first the areal dilatation modulus k' and the surface rigidity n', according to the definitions analogous to those which correspond to the usual three-dimensional volume modulus k and the rigidity n. It is easily seen that they are connected with E' and σ by

$$E'=4k'n'/(k'+n'),\quad \sigma=(k'-n')/(k+n). \tag{12}$$

Evidently, k' is directly connected with p_g.

Considering a uniform expansion of the honeycomb network of carbon atoms, we can derive the following relation

$$k'=p_g/2\sqrt{3}=1.94\times10^5\ \text{dynes/cm}\,.$$

The derivation of the relation between n' and p_g, q_g' must be carried out more carefully. Since there are two atoms in a unit cell, we must determine for a given shearing strain the change of the relative positions of the two simple sublattices under the condition that the potential energy of the whole system takes its minimum value. We have

$$n'=2\sqrt{3}\,p_gq_g'/(p_g+6q_g')=1.16\times10^5\ \text{dynes/cm}.$$

From (12), (3) and (6) we have

$$E'=2.90\times10^5\ \text{dynes/cm}\,,$$
$$\sigma=0.25\,,$$
$$v_t=1.23\times10^6\ \text{cm/sec}\,,$$
$$v_l=2.01\times10^6\ \text{cm/sec}$$

and $\Theta=2440°$.*

§ 3. The Frequency Distribution Function for the Vibrations Perpendicular to the Layers, and the Contribution of these Vibrations to the Specific Heat.

Making the assumption mentioned in § 1, we have the equation of vibration of the system of plates in the form

$$\frac{\partial^2 w_n}{\partial t^2}=-\kappa^2\left(\frac{\partial^4 w_n}{\partial x^4}+2\frac{\partial^4 w_n}{\partial x^2\partial y^2}+\frac{\partial^4 w_n}{\partial y^4}\right)+\mu^2(w_{n+1}+w_{n-1}-2w_n). \tag{13}$$

This equation is the equation of the transverse vibration of a thin elastic plate⁸⁾ except for the second term on the right hand side which cares for the elastic interaction between each neighboring plates. Here w_n represents the displacement of the plate at a point (x, y) in the n-th layer, and κ^2 and μ^2, each multiplied by ρ', are the bending elastic constants and the

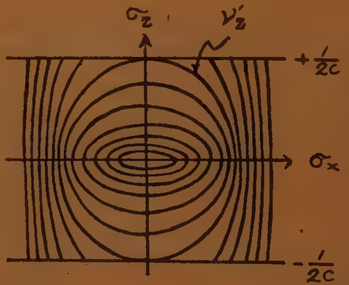

Fig. 2. The schema of the contour $\nu=$const. in the σ-space.

---

* Miller and Crawford⁷⁾ discussed more fully the planar vibration of benzene than Wilson, using more number of force constants. However, the constants were not obtained separately. Making some rough estimation, we obtained from their values almost the same value of the characteristic temperature as that given here.

Hooke's force constant between the neighboring plates, respectively.

Puttnng

$$w_n = w_n^0 e^{2\pi i(\sigma_x x+\sigma_y y+\sigma_z nc-\nu t)}, \tag{14}$$

we have

$$\nu^2 = 4\pi^2\kappa^2(\sigma_x^2+\sigma_y^2)^2+\mu^2/\pi^2\cdot\sin^2\pi c\sigma_z . \tag{15}$$

The contour $\nu=$const. is a surface of revolution about the σ_z-axis in the σ-space. The volume of the σ-space enclosed by this surface alone $(\nu\leqq\mu/\pi)$, or by this surface and the planes $\sigma_z=\pm1/2c(\nu\geqq\mu/\pi)$ is respectively

$$V(\nu)=\frac{1}{\kappa}\int_0^{1/\pi c\cdot\sin^{-1}\pi\nu/\mu}\sqrt{\nu^2-\mu^2/\pi^2\cdot\sin^2\pi c\sigma_z}\,d\sigma_z \qquad (\nu\leqq\mu/\pi)\,; \tag{16}$$

$$V(\nu)=\frac{1}{\kappa}\int_0^{1/2c}\sqrt{\nu^2-\mu^2/\pi^2\cdot\sin^2\pi c\sigma_z}\,d\sigma_z \qquad (\nu\geqq\mu/\pi)\,. \tag{17}$$

(a) The case $\nu\leqq\mu/\pi$.

From (16) we have for the distribution function of the frequencies per one gramme atom of graphite

$$f(\nu)=\frac{V}{\kappa}\int_0^{1/\pi c\cdot\sin^{-1}\pi\nu/\mu}\frac{d\sigma_z}{\sqrt{1-\mu^2/\pi^2\nu^2\cdot\sin^2\pi c\sigma_z}}$$

$$=\frac{V\nu}{\kappa\mu c}\int_0^{\pi/2}\frac{d\psi}{\sqrt{1-\pi^2\nu^2/\mu^2\cdot\sin^2\psi}}. \tag{18}$$

The definite integral is a complete elliptic integral and (18) can be written

$$f(\nu)=\frac{V\nu}{\kappa\mu c}\mathrm{K}\left(\frac{\pi\nu}{\mu}\right). \tag{19}$$

(b) The case $\nu\leqq\mu/\pi$.

From (17) we have

$$f(\nu)=\frac{V}{\kappa}\int_0^{1/2c}\frac{d\sigma_z}{\sqrt{1-\mu^2/\pi^2\nu^2\cdot\sin^2\pi c\sigma_z}}$$

$$=\frac{V}{\pi\kappa c}\int_0^{\pi/2}\frac{d\psi}{\sqrt{1-\mu^2/\pi^2\nu^2\cdot\sin^2\psi}}$$

$$=\frac{V}{\pi\kappa c}\mathrm{K}\left(\frac{\mu}{\pi\nu}\right). \tag{20}$$

Thus, putting $\nu_z'=\mu/\pi$, we have

$$f(\nu)=\frac{V}{\pi\kappa c}\cdot\frac{\nu}{\nu_z'}\mathrm{K}\left(\frac{\nu}{\nu_z'}\right) \qquad (\nu\leqq\nu_z'), \tag{21}$$

$$f(\nu)=\frac{V}{\pi\kappa c}\mathrm{K}\left(\frac{\nu}{\nu_z'}\right) \qquad (\nu\geqq\nu_z'). \tag{22}$$

The entire form of the function $f(\nu)$ is shown in Fig. 3. It will be seen that this curve is very much different from that of the three-dimensional continuum; $f(\nu)$ is proportional to ν for low frequencies, instead of to ν^2 as in Debye's theory. Since the distribution function (4) is also proportional to ν, the total specific heat is proportional to T^2 at low temperatures, in agreement with experiment.

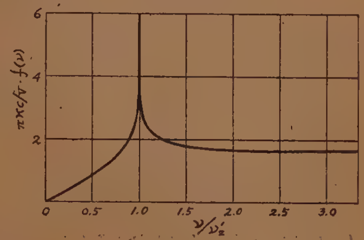

Fig. 3. The frequency distribution function for the vibrations perpendicular to the layers.

In order to calculate the Hooke's force constant $\rho'\mu^2$ from the measured value of the compressibility, we shall assume that the compression by a force parallel to the direction of the z-axis produces no extension or contraction in the direction x- or y-axis. Now, we can estimate the compressibility at the atmospheric pressure from experiments by Bridgman⁹⁾ as $K=2.96\times10^{-12}$ cm²/dyne. Denoting the Young's moduli in the direction perpendicular and parallel to the layer by $E_\perp$ and $E_\parallel$ respectively, the above assumption yields

$$K=\frac{1}{E_\perp}+\frac{2(1-\sigma)}{E_\parallel}. \tag{23}$$

Inserting in this the relations $E_\parallel=E'/c$ and $\rho'\mu^2=E_\perp/c$, and using the values of E' (from which we have $E_\parallel=8.53\times10^{12}$ dynes/cm²) and σ previously determined, we have

$$E_\perp=3.60\times10^{11}\text{ dynes/cm}^2,\quad \mu=1.17\times10^{13}/\text{sec}.$$

Then

$$\nu_z'=\mu/\pi=3.73\times10^{12}/\text{sec}\,,\quad \Theta_z=179°,$$

where Θ_z is defined by $k\Theta_z=h\nu_z'$.

Using the parameter x defined by $h\nu/kT=x\cdot\Theta_z/T$, the contribution of the vibrations under consideration to the specific heat is given at once by

$$C'=\frac{Vk\nu_z'}{\pi c\kappa}\left[\int_0^1\frac{\left(\frac{\Theta_z x}{T}\right)^2\exp\left(\frac{\Theta_z x}{T}\right)\mathrm{K}(x)x\,dx}{\left\{\exp\left(\frac{\Theta_z x}{T}\right)-1\right\}^2}+\int_0^{x'}\frac{\left(\frac{\Theta_z x}{T}\right)^2\exp\left(\frac{\Theta_z x}{T}\right)\mathrm{K}\left(\frac{1}{x}\right)dx}{\left\{\exp\left(\frac{\Theta_z x}{T}\right)-1\right\}^2}\right]. \tag{24}$$

Here x' is the maximum value of x which can be determined from the degree of freedom of the vibrating system. To that purpose we must know the value of κ appearing in (16) and (17). κ should have some relation with the bending force constants of benzene molecule, but we have at present no satisfactory means of estimating κ from the latter. We therefore determine it by fitting the calculated specific heat curve with the observed one. In this way we obtained

$$\kappa = 3.83\times10^{-3}\ \mathrm{cm^2/sec}\,,\quad x'=8.0\,.$$

Crawford and Miller[10)] discussed the bending vibrations of benzene molecule and obtained the bending force constant B in combination with other small constants b_0, b_m, b_p in the following form;

$$B-2b_0+2b_m-b_p=2.03\times10^{-4}\ \mathrm{dynes/cm}\,,$$
$$B-b_0-b_m+b_p=1.57\times10^{-4}\ \mathrm{dynes/cm}\,.$$

From the value of κ mentioned above we obtained the corresponding constant B_g for graphite, neglecting b's, as 0.97×10^{-4} dynes/cm.

§ 4. The Electronic Specific Heat.

The band structure of graphite was studied in detail by Wallace[11)]. According to him, the dependence of the energy eigenvalue of the $2p_z$ electrons on the wave vector k (k_x, k_y, k_z) is

$$E=E_0-\frac{1}{2}\gamma_1\Gamma-\left[\frac{1}{4}\gamma_1^2\Gamma^2+\gamma_0^2|S|^2\right]^{\frac{1}{2}}\,,\quad(25)$$

where the following abbreviations are used:

$$\Gamma=2\cos2\pi k_zc\,,\quad(26)$$

$$S=\exp(-2\pi ik_xa)+2\cos\sqrt{3}\,\pi k_ya\cdot\exp(\pi ik_xa)\,.\quad(27)$$

The density of the electronic energy states near the corner of the zone $(\varepsilon<2\gamma_1)$ is given by

$$N(E)=\frac{2V\gamma_1}{q\pi^2a^2c\gamma_0^2}\left\{2+\pi\frac{|\varepsilon|}{\gamma_1}+\frac{3}{4}\left(\frac{\varepsilon}{\gamma_1}\right)^2+\cdots\right\}.^{**}\quad(28)$$

In the above equations γ_0 and γ_1 are resonance integrals, ε the energy value measured from a corner of the first or the second zone which has the form of a regular hexagon.

We can estimate the breadth of the band as roughly equal to 9 ev. from the data of the fine structure of K_α emission line given by Broili, Glocker and Kiessig.[12)] Comparing this value with the formula (25) we have $\gamma_0=3$ev. On the other hand, Coulson's theoretical estimation is $\gamma_0=0.9$ ev., $\gamma_1=0.09$ ev. Here we arbitrarily adopted the former value $\gamma_0=3$ ev. and determined γ_1 by taking the same value of the ratio γ_1/γ_0 as Coulson's, so that $\gamma_1=0.3$ ev.

Using (28), the total energy of the $2p_z$ electrons per one gramme atom is

$$U=\frac{2N\gamma_1}{\sqrt{3}\,\pi^2\gamma_0^2}\int_0^\infty\frac{1}{e^{\varepsilon/kT}+1}\left[2\varepsilon+\frac{\pi}{\gamma_1}\varepsilon^2+\frac{3}{4\gamma_1^2}\varepsilon^3+\cdots\right]d\varepsilon\,,\quad(29)$$

where the energy at $T=0$ is taken as zero and the relation $N=4V/3\sqrt{3}\,a^2c$ was used. The expansion in the integrand of (29) is available only for the energy range $\varepsilon<2\gamma_1$, but we can safely use it in the whole of integration range up to about 1000°K,*** if our choice of a large value of γ_0 is allowed. Carrying out the integration we have

$$U=\frac{2N\gamma_1}{\sqrt{3}\,\pi^2\gamma_0^2}\left[1.64(kT)^2+1.80\frac{\pi}{\gamma_1}(kT)^3+5.68\cdot\frac{3}{4\gamma_1^2}(kT)^4+\cdots\right].\quad(30)$$

Differentiating (30) with respect to T and putting the numerical values into the constants, we have for the electronic specific heat

$$C_e=6.7\times10^{-7}T(3.29+0.49\times10^{-2}T+0.14\times10^{-5}T^2+\cdots)\ \mathrm{cal/deg.\,mole}.\quad(31)$$

§ 5. C_p-C_v Correction.

The well known formula

$$C_p-C_v=AC_p^2T\,,\quad A=\alpha^2V/C_p^2K\quad(32)$$

will be used for our calculation, though these relations are known to be valid only for the solids in which atoms are acting with each other by central forces.[13)] Putting the values $\alpha=2.2\times10^{-5}$/deg, $C_p=2.08$ cal/deg. mole at

---

** The constants a and c in our notation differ from those of his original paper by simple numerical factors $1/\sqrt{3}$ and 1/2, respectively. We also corrected for his error of the numerical factor before the curled bracket of (28) which has its origin in (5.3) in his original paper, by multiplying a factor $1/2\pi$.

*** If Coulson's values are adopted, the formula (30) will be available only for the temperature range up to room temperature. The resulting electronic specific heat will become 6 times as large as that given here at room temperature, although it amounts to only 0.3% of the total specific heat.

Table 1. Results of the numerical calculations of the specific heat of graphite.

T°K	C (7), (8)	C' (24)	C_e (31)	$\Delta C = C_p - C_v$ (32)	$C_p = C + C' + C_e + \Delta C$ calculated	C_p observed	C_p cal. by Debye formula
30	0.01	0.06			0.07	0.04	0.002
40	0.02	0.10			0.12	0.08	0.005
50	0.03	0.15			0.18	0.13	0.009
60	0.04	0.20			0.24	0.17	0.016
70	0.05	0.26			0.31	0.22	0.025
80	0.06	0.31			0.37	0.27	0.038
90	0.08	0.36			0.44	0.33	0.05
100	0.10	0.41			0.51	0.40	0.07
120	0.14	0.51			0.65	0.54	0.12
150	0.22	0.65			0.87	0.77	0.24
170	0.27	0.75			1.02	0.94	0.34
200	0.38	0.88			1.26	1.19	0.58
220	0.47	0.96			1.43	1.38	0.74
250	0.60	1.07			1.67	1.65	0.99
270	0.70	1.11			1.81	1.81	1.18
300	0.84	1.23		0.01	2.08	2.08	1.49
320	0.94	1.31		0.01	2.26	2.25	1.69
350	1.10	1.37		0.01	2.48	2.49	2.01
400	1.36	1.48		0.02	2.86	2.86	2.49
450	1.62	1.55		0.02	3.19	3.20	2.91
500	1.84	1.63		0.03	3.50	3.50	3.28
550	2.05	1.68		0.04	3.77	3.77	3.61
600	2.24	1.72		0.05	4.01	4.01	3.89
650	2.41	1.75		0.05	4.21	4.23	4.14
700	2.55	1.79		0.06	4.40	4.42	4.35
750	2.69	1.83		0.07	4.59	4.59	4.53
800	2.81	1.85		0.08	4.74	4.74	4.70
850	2.91	1.86		0.09	4.86	4.87	4.84
900	3.00	1.87	0.01	0.10	4.98	4.97	4.96
950	3.08	1.88	0.01	0.11	5.08	5.08	5.07
1000	3.15	1.88	0.01	0.12	5.16	5.16	5.16

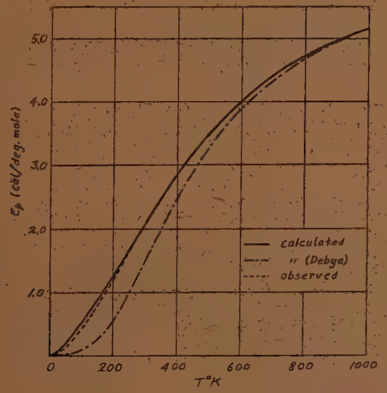

Fig. 4. Comparison of the calculated specific heat curves with that observed.

room temperature, we have for the $C_p - C_v$ correction the values given in Table 1.

§ 6. Comparison with Experiment.

The observed values given in Table 1 were taken from the following sources; Landolt-Börnstein⁽¹⁴⁾ (30°—90°K), Jacobs and Parks⁽¹⁵⁾ (90°—300°K), and Spencer⁽¹⁶⁾ (300°—1000°K). The agreement between the observed values and the calculated ones is almost complete above the temperature 250°K. Below this the calculated values are somewhat larger than those observed. By taking a larger value of κ than that given above, the agreement below the temperature 100°K can be improved, although the agreement in the high temperature range will then be spoiled to some extent.

For the sake of comparison, we have also given the calculated values from Debye's formula in Table 1 and in Fig. 4.

The present work was supported by the Grant in Aid for Fundamental Scientific Research from the Ministry of Education.

References.

1) P. Debye: Ann. d. Phys. **39** (1921), 789.
2) W. Nernst: Ann. d. Phys. **36** (1911) 395.
3) A. Magnus: Ann. d. Phys. **70** (1923), 303.
4) A. E. H. Love: The mathematical theory of elasticity (1934), 497.

5) E. B. Wilson, Jr.: Phys. Rev. **45** (1934), 706.

6) R. C. Lord, Jr. and D. H. Andrews: J. Phys. Chem. **41** (1937), 149.

7) F. A. Miller and B. L. Crawford, Jr.: J. Chem. Phys. **14** (1946), 282.

8) Lord Rayleigh: Theory of Sound I, (1937), 352.

9) P. W. Bridgman: Proc. Am. Acad. Arts. Sci. **76** (1945), 9.

10) B. L. Crawford, Jr. and F. A. Miller: J. Chem. Phys. **17** (1948), 249.

11) P. R. Wallace: Phys. Rev. **71** (1947), 622.

12) H. Broili, R. Glocker und H. Kiessig: Ergebnisse der technischen Röntgenkunde IV. (1934), 94.

13) E. Grüneisen: Handb. d. Phys. X. Kap. I.

14) Landolt-Börnstein: Phys.-Chem. Tabellen IIb (1931), 1232.

15) C. J. Jacobs and G. S. Parks: J. Am. Chem. Soc. **56** (1934), 1513.

16) H. M. Spencer: J. Ind. Eng. Chem. **40** (1948), 2152.

JOURNAL OF THE PHYSICAL SOCIETY OF JAPAN Vol. 6, No. 6 NOV.—DEC., 1951

On the Stark Effect of Helium in Strong Electric Field (II).

By Seiichi SUEOKA and Masachiyo SATO.

Institute of Applied Mathematics, Second Faculty of Engineering,
University of Tokyo.

(Read Nov. 5, 1950, Received February 7, 1951)

To explain the resonance phenomena of the Stark lines of He atom, a general method is found in the paper (I) to solve the secular equations, taking into account of the matrix elements between the states with different principal quantum numbers, n and n'.

Along the line of this general method, we performed the numerical computations for the ortho-helium in the case of $n=6$ and $n'=7$. Numerical tables and diagrams representing the relations of the Stark energies and field strengthes are obtained for the respective values of magnetic quantum numbers, $m=1, 2, 3$ and 4. From these results we find that the pair of levels approaching nearest and repelling each other is as follows:

repelling levels	m value	energy difference (cm^{-1})	field strength (kV/cm)
6^3H——7^3S	0	6·6	177
6^3H——7^3P	1	6·6	226
6^3H——7^3D	2	11·0	301

§1. Introduction.

The resonance phenomena of the Stark effect of helium atom in strong electric field have been attempted to be explained quantitatively by taking into account of the interaction between the states with different principal quantum numbers, and actual calculations of the energy displacements due to the field have been carried out for the case of $n=4$ and 5 in the paper (I) already published.[1] In this paper, we shall extend the calculation to the energy displacements for the states of $n=6$ and 7 by the same method as in (I).

§2. Calculations in the case of $n=6$, $n'=7$.

The states to be considered in the case of $n=6$ and 7 for each given value of m are as follows:

$m=0$: $6S$, $6P$, $6D$, $6F$, $6G$, $6H$; $7S$, $7P$, $7D$, $7F$, $7G$, $7H$, $7I$,
$m=1$: $6P$, $6D$, $6F$, $6G$, $6H$; $7P$, $7D$, $7F$, $7G$, $7H$, $7I$,
$m=2$: $6D$, $6F$, $6G$, $6H$; $7D$, $7F$, $7G$, $7H$, $7I$,
$m=3$: $6F$, $6G$, $6H$; $7F$, $7G$, $7H$, $7I$,
$m=4$: $6G$, $6H$; $7G$, $7H$, $7I$,

and so on.

Here, we neglect the $7I$ state in the following on the same ground as in § 4, (I). Then the hypermatrices (3) in (I), are written in the following forms for respective values of m.

$m=0$,

$$\begin{bmatrix} E_0, & A_{00}F, & 0, & 0, & 0, & 0 \\ \tilde{A}_{00}F, & E_1, & A_{10}F, & 0, & 0, & 0 \\ 0, & \tilde{A}_{10}F, & E_2, & A_{20}F, & 0, & 0 \\ 0, & 0, & \tilde{A}_{20}F, & E_3, & A_{30}F, & 0 \\ 0, & 0, & 0, & \tilde{A}_{30}F, & E_4, & A_{40}F \\ 0, & 0, & 0, & 0, & \tilde{A}_{40}F, & E_5 \end{bmatrix},$$

$m=1$,

$$\begin{bmatrix} E_1. & A_{11}F, & 0, & 0, & 0 \\ \tilde{A}_{11}F, & E_2, & A_{21}F, & 0, & 0 \\ 0, & \tilde{A}_{21}F, & E_3, & A_{31}F, & 0 \\ 0, & 0, & \tilde{A}_{31}F, & E_4, & A_{41}F \\ 0, & 0, & 0, & \tilde{A}_{41}F, & E_5 \end{bmatrix},$$

$m=2$,

$$\begin{bmatrix} E_2, & A_{22}F, & 0, & 0 \\ \tilde{A}_{22}F, & E_3, & A_{32}F, & 0 \\ 0, & \tilde{A}_{32}F, & E_4, & A_{42}F \\ 0, & 0, & \tilde{A}_{42}F, & E_5 \end{bmatrix},$$

$m=3$,

$$\begin{bmatrix} E_3, & A_{33}F, & 0 \\ \tilde{A}_{33}F, & E_4, & A_{43}F \\ 0, & \tilde{A}_{43}F, & E_5 \end{bmatrix},$$

$m=4$,

$$\begin{bmatrix} E_4, & A_{44}F \\ \tilde{A}_{44}F, & E_5 \end{bmatrix},$$

where 0 denotes a zero matrix of two dimensions and

$$A_{l,m}=\sqrt{\frac{(l+1)^2-m^2}{4(l+1)^2-1}}\begin{bmatrix} \int_0^\infty R_{6,l+1}(r)R_{6,l}(r)r^3dr, & \int_0^\infty R_{7,l+1}(r)R_{6,l}(r)r^3dr \\ \int_0^\infty R_{6,l+1}(r)R_{7,l}(r)r^3dr, & \int_0^\infty R_{7,l+1}(r)R_{7,l}(r)r^3dr \end{bmatrix}$$

As for the numerical values of the radial integrals appearing in the matrix elements of $A_{l,m}$, those of the diagonal parts are found from the formula

$$\int_0^\infty R_{n,l+1}\cdot R_{n,l}r^3dr=-3n\sqrt{n^2-(l+1)^2}/2\ ,$$

and while those of nondiagonal parts are evaluated numerically. Thus we find

$$A_{0,m}=\sqrt{\frac{1-m^2}{3}}\begin{bmatrix} -53.245, & 16.557 \\ 10.868, & -72.746 \end{bmatrix}$$

$$A_{1,m}=\sqrt{\frac{4-m^2}{15}}\begin{bmatrix} -50.912, & 19.943 \\ 8.4556, & -70.436 \end{bmatrix}$$

$$A_{2,m}=\sqrt{\frac{9-m^2}{35}}\begin{bmatrix} -46.765, & 23.772 \\ 6.2668, & -66.408 \end{bmatrix},$$

$$A_{3,m}=\sqrt{\frac{16-m^2}{63}}\begin{bmatrix} -40.249, & 28.118 \\ 4.2590, & -60.318 \end{bmatrix},$$

$$A_{4,m}=\sqrt{\frac{25-m^2}{99}}\begin{bmatrix} -29.850, & 33.063 \\ 2.3741, & -51.439 \end{bmatrix},$$

The eigenvalues of the above hypermatrices are obtained by the same procedure as (5), (6), (7) and (8) in (I). The secular determinants corresponding to (11) have the following forms.

$m=0$;

$$\begin{aligned} \| & \Lambda_5A_{40}^{-1}\Lambda_4A_{30}^{-1}\Lambda_3A_{20}^{-1}\Lambda_2A_{10}^{-1}\Lambda_1A_{00}^{-1}\Lambda_0-F^2(\Lambda_5A_{40}^{-1}\Lambda_4A_{30}^{-1}\Lambda_3A_{20}^{-1}\Lambda_2A_{10}^{-1}\tilde{A}_{00} \\ & +\Lambda_5A_{40}^{-1}\Lambda_4A_{30}^{-1}\Lambda_3A_{20}^{-1}\tilde{A}_{10}A_{00}^{-1}\Lambda_0+\Lambda_5A_{40}^{-1}\Lambda_4A_{30}^{-1}\tilde{A}_{20}A_{10}^{-1}\Lambda_1A_{00}^{-1}\Lambda_0 \\ & +\Lambda_5A_{40}^{-1}\tilde{A}_{30}A_{20}^{-1}\Lambda_2A_{10}^{-1}\Lambda_1A_{00}^{-1}\Lambda_0+\tilde{A}_{40}A_{30}^{-1}\Lambda_3A_{20}^{-1}\Lambda_2A_{10}^{-1}\Lambda_1A_{00}^{-1}\Lambda_0) \\ & +F^4(\tilde{A}_{40}A_{30}^{-1}\Lambda_3A_{20}^{-1}\Lambda_2A_{10}^{-1}\tilde{A}_{00}+\tilde{A}_{40}A_{30}^{-1}\Lambda_3A_{20}^{-1}\tilde{A}_{10}A_{00}^{-1}\Lambda_0+\tilde{A}_{40}A_{30}^{-1}\tilde{A}_{20}A_{10}^{-1}\Lambda_1A_{00}^{-1}\Lambda_0 \\ & +\Lambda_5A_{40}^{-1}\tilde{A}_{30}A_{20}^{-1}\Lambda_2A_{10}^{-1}\tilde{A}_{00}+\Lambda_5A_{40}^{-1}\tilde{A}_{30}A_{20}^{-1}\tilde{A}_{10}A_{00}^{-1}\Lambda_0+\Lambda_5A_{40}^{-1}\Lambda_4A_{30}^{-1}\tilde{A}_{20}A_{10}^{-1}\tilde{A}_{00}) \\ & -F^6\cdot\tilde{A}_{40}A_{30}^{-1}\tilde{A}_{20}A_{10}^{-1}\tilde{A}_{00}\|=0\ , \end{aligned} \tag{13}$$

$m=1$;

$$\|\Lambda_5A_{41}^{-1}\Lambda_4A_{31}^{-1}\Lambda_3A_{21}^{-1}\Lambda_2A_{11}^{-1}\Lambda_1-F^2(\Lambda_5A_{41}^{-1}\Lambda_4A_{31}^{-1}\Lambda_3A_{21}^{-1}\tilde{A}_{11}+\Lambda_5A_{41}^{-1}\Lambda_4A_{31}^{-1}\tilde{A}_{21}A_{11}^{-1}\Lambda_1$$

$$+\Lambda_5A_{41}^{-1}\tilde{A}_{31}A_{21}^{-1}\Lambda_2A_{11}^{-1}\Lambda_1+\tilde{A}_{41}A_{31}^{-1}\Lambda_3A_{21}^{-1}\Lambda_2A_{11}^{-1}\Lambda_1)+F^4(\Lambda_5A_{41}^{-1}\tilde{A}_{31}A_{21}^{-1}\tilde{A}_{11}$$

$$+\tilde{A}_{41}A_{31}^{-1}\Lambda_3A_{21}^{-1}\tilde{A}_{11}+\tilde{A}_{41}A_{31}^{-1}\tilde{A}_{21}A_{11}^{-1}\Lambda_1)\|=0\,, \tag{14}$$

$m=2$;

$$\|\Lambda_5A_{42}^{-1}\Lambda_4A_{32}^{-1}\Lambda_3A_{22}^{-1}\Lambda_2-F^2(\Lambda_5A_{42}^{-1}\Lambda_4A_{32}^{-1}\tilde{A}_{22}+\Lambda_5A_{42}^{-1}\tilde{A}_{32}A_{22}^{-1}\Lambda_2+\tilde{A}_{42}A_{32}^{-1}\Lambda_3A_{22}^{-1}\Lambda_2)$$

$$+F^4\cdot\tilde{A}_{42}A_{32}^{-1}\tilde{A}_{22}\|=0\,, \tag{15}$$

$m=3$;

$$\|\Lambda_5A_{43}^{-1}\Lambda_4A_{33}^{-1}\Lambda_2-F^2(\Lambda_5A_{43}^{-1}\tilde{A}_{33}+\tilde{A}_{43}A_{33}^{-1}\Lambda_3)\|=0\,, \tag{16}$$

$m=4$;

$$\|\Lambda_5A_{44}^{-1}\Lambda_4-F^2\cdot\tilde{A}_{44}\|=0\,, \tag{17}$$

where Λ_l represents

$$\Lambda_l=\begin{pmatrix}\lambda-\varepsilon_{6,l}\,, & 0\\ 0\,, & \lambda-\varepsilon_{7,l}\end{pmatrix},$$

$\varepsilon_{n,l}$ being measured from $\varepsilon_{63}=\varepsilon_{64}=\varepsilon_{65}$ ($6F$, $6G$, $6H$ levels). The numerical values of $\varepsilon_{n,l}$ for ortho-helium are, in atomic units, as follows:

$$\begin{aligned}&\varepsilon_{60}=-0.0^21479, && \varepsilon_{61}=-0.0^3322,\\ &\varepsilon_{62}=-0.0^413, && \varepsilon_{63}=\varepsilon_{64}=\varepsilon_{65}=0,\\ &\varepsilon_{70}=0.0^22764, && \varepsilon_{71}=0.0^23483,\\ &\varepsilon_{72}=0.0^23676, && \varepsilon_{73}=\varepsilon_{74}=\varepsilon_{75}=0.0^23685.\end{aligned}$$

Then, we obtain the following algebraic equations for $y=10^8F^2$, by expanding the determinants (13), (14), (15), (16) and (17).

(i) $m=0$, $$y^6+a(\lambda)y^5+b(\lambda)y^4+c(\lambda)y^3+d(\lambda)y^2+e(\lambda)y+f(\lambda)=0\,, \tag{18}$$

where

$$\begin{aligned}a(\lambda)=&-251.47\times10^4\lambda^2+59.733\times10^2\lambda-6.4896\,,\\ b(\lambda)=&\,15305._5\times10^8\lambda^4-7574.9\times10^6\lambda^3+1357.7\\ &\times10^4\lambda^2-75.536_5\times10^2\lambda+7.1226\\ c(\lambda)=&-30991\times10^{13}\lambda^6+24485._5\times10^{11}\lambda^5\\ &-72687._5\times10^8\lambda^4+10190\times10^6\lambda^3-725.23\\ &\times10^4\lambda^2-10.486\times10^2\lambda-1.9469._5\,,\\ d(\lambda)=&\,24845\times10^{18}\lambda^8-27451\times10^{16}\lambda^7+11824\\ &\times10^{14}\lambda^6-24966._5\times10^{11}\lambda^5+25302\\ &\times10^8\lambda^4-1013.3_5\times10^6\lambda^3+31.519._5\times10^4\lambda^2\\ &+11.155\times10^2\lambda+0.089894_5\,,\\ e(\lambda)=&-80465\times10^{22}\lambda^{10}+11905._5\times10^{21}\lambda^9\\ &-68893._5\times10^{18}\lambda^8+19388\times10^{16}\lambda^7\\ &-25522._5\times10^{13}\lambda^6+4978.5_5\times10^{10}\lambda^5\\ &+3010.6_5\times10^8\lambda^4-314.39_5\times10^6\lambda^3\\ &-8.6332\times10^4\lambda^2-0.58866_5\,,\\ f(\lambda)=&\,84324\times10^{26}(\lambda+0.0^21479)(\lambda+0.0^3322)\\ &\times(\lambda+0.0^413)\lambda^3(\lambda-0.0^22764)\\ &\times(\lambda-0.0^23483)\times(\lambda-0.0^23676)\\ &\times(\lambda-0.0^23685)^3\,.\end{aligned}$$

(ii) $m=1$, $$a(\lambda)y^4+b(\lambda)y^3+c(\lambda)y^2+d(\lambda)y+e(\lambda)=0, \tag{19}$$

where

$$\begin{aligned}a(\lambda)=&\,1686.6\lambda^2-4.6226\lambda+0.0^3\,76597,\\ b(\lambda)=&-10891\times10^5\lambda^4+62639\times10^2\lambda^3-12154._5\lambda^2\\ &+11.287\lambda+0.0^329922,\\ c(\lambda)=&\,19310\times10^{10}\lambda^6-17465\times10^8\lambda^5+60562._5\\ &\times10^5\lambda^4-99554\times10^2\lambda^3+7656.0\lambda^2\\ &-4.5733\lambda+0.0^345126,\\ d(\lambda)=&-11805\times10^{15}\lambda^8+15428\times10^{13}\lambda^7\\ &-78365\times10^{10}\lambda^6+19738._5\times10^8\lambda^5-25878\\ &\times10^5\lambda^4+13908\times10^2\lambda^3+465.89\lambda^2\\ &+0.0^432996,\\ e(\lambda)=&\,2028.2\times10^{20}(\lambda+0.0^3322)(\lambda+0.0^413)\\ &\times\lambda^3(\lambda-0.0^23483)(\lambda-0.0^23676)\\ &\times(\lambda-0.0^23685)^3.\end{aligned}$$

(iii) $m=2$, $$y^4+a(\lambda)y^3+b(\lambda)y^2+c(\lambda)y+d(\lambda)=0\,, \tag{20}$$

where

$$\begin{aligned}a(\lambda)=&-24698._5\times10^2\lambda^2+6595.9_5\lambda-7.0585_5,\\ b(\lambda)=&\,12929._5\times10^8\lambda^4-76843\times10^5\lambda^2+15987\\ &\times10^3\lambda^2-10559\lambda+6.3656_5,\\ c(\lambda)=&-18590._5\times10^{13}\lambda^6+18194\times10^{11}\lambda^5\\ &-64781\times10^8\lambda^4+10821._5\times10^6\lambda^3-86531\\ &\times10^2\lambda^2-69.883\lambda,\\ d(\lambda)=&\,58687._5\times10^{17}(\lambda+0.0^413)\lambda^3\\ &\times(\lambda-0.0^2367)(\lambda-0.0^23685)^3.\end{aligned}$$

(iv) $m=3$, $$a(\lambda)y^2+b(\lambda)y+c(\lambda)=0, \tag{21}$$

where

$$\begin{aligned}a(\lambda)=&\,40.448\lambda^2-1.2317\lambda+0.0^220309,\\ b(\lambda)=&-21.429\times10^4\lambda^4+12.975\times10^3\lambda^3-2.5336\\ &\times10^2\lambda+2.4403\lambda,\\ c(\lambda)=&\,150.55\times10^6\lambda^3(\lambda-0.0^23685)^3.\end{aligned}$$

(v) $m=4$, $$y^2+a(\lambda)y+b(\lambda)=0\,, \tag{22}$$

where

$$\begin{aligned}a(\lambda)=&-240.23\times10^2\lambda^2+549.65\lambda-6.2700,\\ b(\lambda)=&\,5700.3\times10^4\lambda^2(\lambda-0.0^23685)^2.\end{aligned}$$

The algebraic eqs. (18), (19), (20), (21) and (22) are solved numerically for the definite value of λ, which is varied from -0.0020 to 0.0050 with the interval of 0.0002. In certain cases, however, particulary in the neighbourhood of the resonance, it is necessary to adopt finer intervals. The results are shown in the Tables (II), (III), (IV) and (V). The feature of the variation of energy due to the increase of the field is shown in the Fig. I.

Table II. Relation between λ and F for $m=0$.

$10^2\lambda$	10^4F					
−0.20	4.6598	1.8672	1.4108	0.95054	0.57039	0.26844
−0.18	4.4204	1.7513	1.2865	0.91283	0.51115	0.20531
−0.16	4.1824	1.6266	1.1711	0.86951	0.45066	0.12257
−0.14	3.9456	1.5220	1.0338	0.82800	0.38997	——
−0.12	3.7098	1.4270	0.89012	0.78135	0.32896	——
−0.10	3.4749	1.3394	0.77904	0.69220	0.26791	——
−0.08	3.2404	1.2575	0.72744	0.53635	0.20669	——
−0.06	3.0061	1.1799	0.68664	0.36640	0.14446	——
−0.04	2.7690	1.1049	0.64801	0.20112	0.072240	——
−0.02	2.5282	1.0314	0.61023	0.071027	——	——
−0.004	2.3293	0.97318	0.58272	0.15526	0.045967	0.011299
0	2.2778	0.95683	0.57256	0.24026	0	0
0.014	2.0924	0.89852	0.54284	0.46688	0.096000	0.041853
0.02	2.0054	0.86681	——	——	0.12812	0.058709
0.024	1.9456	0.83713	0.63408	0.53443	0.14860	0.069863
0.04	1.6634	——	——	0.50226	0.22612	0.11323
0.05	1.3205	1.1026	0.91915	0.48310	0.27309	0.13989
0.06	——	——	0.82325	0.46542	0.31891	0.16627
0.078	——	——	0.74998	0.43102	0.40308	0.20804
0.08	——	——	0.74268	0.41531	0.41521	0.21849
0.084	——	——	0.72850	——	——	0.22906
0.088	——	——	0.71483	0.41873	0.44327	0.23922
0.10	——	——	0.67622	0.50357	0.39204	0.27108
0.12	——	——	0.61620	0.59401	0.35936	0.32151
0.124	——	——	——	——	0.35986	0.32665
0.126	——	——	0.62414	0.59677	0.34862	0.33688
0.132	——	——	0.65260	0.57942	0.35282	0.33740
0.14	——	——	0.69145	0.55608	0.37309	0.32339
0.16	——	——	0.79036	0.49919	0.42431	0.28763
0.168	——	——	0.83299	0.47449	0.44645	0.27324
0.18	——	——	0.89775	0.47227	0.44589	0.25149
0.20	——	——	1.0183	0.52537	0.38916	0.21460
0.22	1.2839	——	——	0.57677	0.33531	0.17628
0.24	1.9720	——	——	0.62812	0.28297	0.13500
0.26	2.3092	1.2080	0.80195	0.68025	0.23120	0.086148
0.264	2.3697	1.2408	——	——	0.22102	0.074133
0.274	2.5161	1.3116	0.71303	0.63704	0.19587	——
0.28	2.6003	1.3507	0.72925	0.57485	0.18073	——
0.30	2.8734	1.4757	0.78084	0.39380	0.13014	——
0.32	3.1368	1.5948	0.83275	0.24142	0.079895	——
0.34	3.3953	1.7152	0.88461	0.10033	0.042653	——
0.36	3.6509	1.8368	0.93643	0.017533	——	——
0.38	3.9048	1.9597	0.98765	0.19748	0.031700	0.029905
0.40	4.1578	2.0842	1.0394	0.32598	0.10154	0.062648
0.42	4.4105	2.2101	1.0913	0.44761	0.15942	0.095729
0.44	4.6629	2.3374	1.1432	0.56461	0.21249	0.12942
0.46	4.9153	2.4661	1.1952	0.67758	0.26390	0.16289
0.48	5.1680	2.5962	1.2473	0.78712	0.31453	0.19608
0.50	5.4210	2.7281	1.2993	0.89383	0.36472	0.22905

Table III.

Relation between λ and F for $m=1$.

$10^2\lambda$	10^4F			
−0.20	2.3583	1.2777	0.90431	0.49863
−0.18	2.2378	1.2215	0.82164	0.45076
−0.16	2.1163	1.1666	0.73678	0.40178
−0.14	1.9934	1.1126	0.64935	0.35204
−0.12	1.8684	1.0598	0.55922	0.30128
−0.10	1.7364	1.0078	0.46626	0.24916
−0.08	1.5960	0.95650	0.37016	0.19531
−0.06	1.4368	0.90549	0.27076	0.13811
−0.04	1.2339	0.85367	0.16750	0.068588
−0.02	0.90933	0.77151	0.070482	——
0	——	0.77246	0	0
0.02	4.7661	0.72170	0.14458	0.062173
0.04	1.8557	0.67461	0.27082	0.12171
0.06	1.4834	0.62936	0.40062	0.18133
0.08	1.2787	0.58273	0.54250	0.24073
0.082	1.2617	0.57796	0.55729	0.24687
0.084	1.2450	——	——	0.25287
0.086	1.2287	0.58237	0.57374	0.25890
0.088	1.2127	0.59955	0.56735	0.26490
0.10	1.1207	0.69610	0.54013	0.30115
0.110	1.0426	0.78725	0.51822	0.33151
0.114	1.0059	0.83158	0.50953	0.34371
0.118	0.94412	0.90211	0.50092	0.35589
0.12	——	——	0.49707	0.36165
0.14	——	——	0.45648	0.42090
0.142	——	——	0.45172	0.42764
0.144	——	——	——	——
0.146	——	——	——	——
0.148	——	——	0.45263	0.43265
0.15	1.0129	0.94969	0.45954	0.42796
0.16	1.1661	0.85214	0.48815	0.40938
0.18	1.4298	0.73965	0.55070	0.36832
0.20	1.7627	0.63890	0.61884	0.32734
0.208	1.9359	0.63244	0.61454	0.31094
0.21	1.9847	0.64147	0.60301	0.30683
0.22	2.2776	0.67502	0.55760	0.28623
0.24	3.4559	0.74109	0.47077	0.24585
0.26	——	0.80729	0.38769	0.20588
0.28	——	0.87347	0.30684	0.16654
0.30	——	0.94021	0.22699	0.12840
0.32	——	1.0075	0.15325	0.084868
0.34	——	1.0757	0.081062	0.031005
0.36	——	1.1449	0.010555	——
0.38	1.2159	0.76176	0.050396	0.021708
0.40	1.2941	1.0983	0.13158	0.059418
0.42	1.4116	4.3006	0.20600	0.097072
0.44	1.5925	1.3980	0.27534	0.13467
0.46	1.7722	1.4736	0.34129	0.17221
0.48	1.9408	1.5456	0.40553	0.20970
0.50	2.1005	1.6168	0.46974	0.24750

Table IV.

Relation between λ and F for $m=2$.

$10^2\lambda$	10^4F			
−0.20	4.8149	2.0497	1.5213	0.65695
−0.16	4.3300	1.7777	1.3180	0.53728
−0.12	3.8530	1.5400	1.0694	0.41224
−0.10	3.6172	1.4371	0.92372	0.34752
−0.08	3.3833	1.3440	0.76418	0.28126
−0.06	3.1506	1.2582	0.59172	0.21331
−0.04	2.9186	1.1789	0.40679	0.14368
−0.02	2.6856	1.1027	0.20872	0.072273
0	2.4489	1.0303	0	0
0.02	2.2033	0.95958	0.23915	0.075862
0.04	1.9290	0.88615	0.51221	0.15281
0.05	1.7804	0.83523	0.68821	0.19202
0.052	1.7463	0.81214	0.73989	0.19994
0.06	1.5886	——	——	0.23170
0.066	1.4179	0.94141	0.90536	0.25480
0.068	1.3067	1.1059	0.84576	0.26381
0.08	——	——	0.78671	0.31259
0.10	——	——	0.72002	0.39549
0.125	——	——	0.64359	0.50224
0.132	——	——	0.62266	0.53292
0.136	——	——	0.61061	0.55075
0.14	——	——	0.59777	0.56953
0.142	——	——	0.58865	0.58167
0.144	——	——	——	——
0.148	——	——	0.59937	0.58026
0.15	——	——	0.60961	0.57318
0.158	——	——	0.64661	0.54925
0.165	——	——	0.67855	0.52921
0.18	——	——	0.74800	0.48693
0.20	——	——	0.84251	0.43183
0.22	——	——	0.94105	0.37806
0.24	1.4747	1.4287	1.0656	0.32119
0.244	1.7195	1.1556	1.1304	0.31443
0.25	1.9086	——	——	0.29868
0.26	2.0956	1.0771	0.98897	0.27263
0.27	2.2715	1.1574	0.83351	0.24673
0.28	2.4315	1.2149	0.71850	0.22102
0.30	2.7290	1.3222	0.52485	0.17007
0.32	3.0100	1.4289	0.35573	0.11973
0.34	3.2829	1.5363	0.20094	0.070047
0.36	3.5513	1.6454	0.055283	0.021035
0.38	3.8167	1.7559	0.079104	0.028705
0.40	4.0808	1.8681	0.21069	0.076923
0.42	4.3436	1.9819	0.33673	0.12492
0.44	4.6052	2.0987	0.45802	0.17261
0.46	4.8614	2.2171	0.57613	0.21994
0.48	5.1300	2.3320	0.69074	0.26698
0.50	5.3920	2.4514	0.80237	0.31374

Table V.

Relations between λ and F for $m=3$ and 4.

$m=3$			$m=4$		
$10^2\lambda$	10^4F		$10^2\lambda$	10^4F	
−0.20	2.4174	0.94014	−0.20	4.8757	1.7607
−0.18	2.2962	0.85825	−0.18	4.6199	1.6135
−0.16	2.1753	0.77424	−0.16	4.3679	1.4617
−0.14	2.0542	0.68790	−0.14	4.1196	1.3047
−0.12	1.9322	0.59905	−0.12	3.8757	1.1420
−0.10	1.8080	0.50745	−0.10	3.6363	0.97260
−0.08	1.6788	0.41289	−0.08	3.4015	0.79640
−0.06	1.5390	0.31513	−0.06	3.1715	0.61206
−0.04	1.3738	0.21393	−0.04	2.9457	0.41879
−0.02	1.1301	0.10899	−0.02	2.7238	0.21538
−0.01	0.90358	0.055020	0	2.5040	0
0	0	0	0.02	2.2833	0.23046
0.017494	(∞)	0.098938	0.04	2.0549	0.48249
0.02	3.8268	0.11347	0.06	1.7980	0.77726
0.04	1.6821	0.23170	0.068	1.6703	0.92361
0.06	1.3910	0.35556	0.072	1.5911	1.0129
0.08	1.2236	0.48596	0.076	1.4830	1.1317
0.10	1.0934	0.62494	0.08	—	—
0.12	0.97399	0.77956	0.10	—	—
0.14	—	—	0.20	—	—
0.16	1.0736	0.81386	0.206	1.7438	1.4493
0.18	1.2718	0.71893	0.212	1.9323	1.2964
0.20	1.4978	0.63234	0.22	2.1052	1.1717
0.22	1.7786	0.54985	0.24	2.4524	0.94948
0.24	2.1726	0.47022	0.26	2.7611	0.77140
0.26	2.8747	0.39287	0.28	3.0560	0.61223
0.28	5.5258	0.31734	0.30	3.3446	0.46392
0.28701	(∞)	0.29133	0.32	3.6299	0.32284
0.30	—	0.24352	0.34	3.9137	0.18694
0.32	—	0.17099	0.36	4.1968	0.05505
0.34	—	0.099695	0.38	4.4795	0.07906
0.36	—	0.029484	0.40	4.7624	0.19979
0.38	0.76283	0.039793	0.42	5.0454	0.32369
0.39	1.0204	0.074109	0.44	5.3287	0.44575
0.40	1.2128	0.10823	0.46	5.6120	0.56622
0.42	1.5081	0.17589	0.48	5.8962	0.68533
0.44	1.7434	0.24288	0.50	6.1806	0.80320
0.46	1.9472	0.30924			
0.48	2.1319	0.37504			
0.50	2.3042	0.44033			

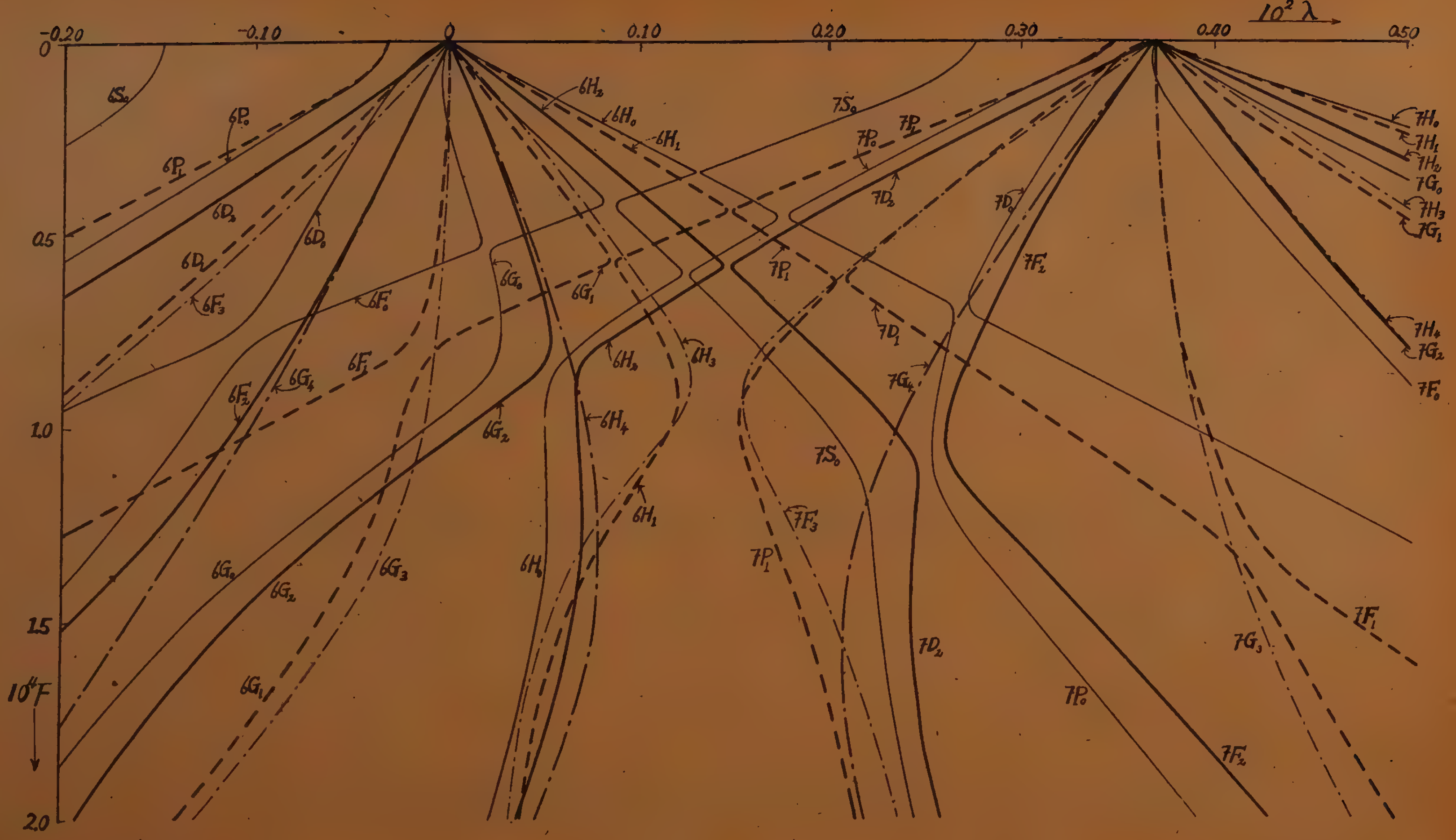

Fig. I. Energy and field strength diagram for ortho-helium in the case of $n=6$ and $n=7$. (Designation of terms is used in the sense of nL_m and different kinds of lines are used for different m values.)

§ 3. Conclusion.

As the results of our calculations in § 2, the energy differences and the field strengthes where the repelling pairs of levels approach nearest causing resonance, are obtained approximately from Fig. I as follows. (Here we adopt the practical units instead of atomic units.)

repelling pair of levels	resonance field strength. (kv/cm)	approximate min. energy difference (cm^{-1})
$6H_0—7S_0$	177	6.6
$6G_0—6H_0$	216	15.4
$7S_0—7P_0$	236	13.2
$6F_0—6G_0$	277	11.0
$6H_0—7S_0$	313	8.8
$7P_0—7D_0$	~ 360	11.0
—	—	—
$6H_1—7P_1$	226	6.6
$6G_1—6H_1$	295	6.6
$7P_1—7D_1$	321	8.8
$6F_1—6G_1$	~ 410	43.9
$6H_1—7P_1$	~ 490	68.1
—	—	—
$6H_2—7D_2$	301	11.0
$6G_2—6H_2$	~ 430	41.7
$7D_2—7F_2$	~ 565	41.7
—	—	—
$6H_3—6F_3$	462	59.3
—	—	—
$6H_4—7G_4$	~ 770	285.0

The numerous photographs showing resonance are obtained by Y. Ishida,[2] but there is few results which are analysed. As an example, we would take the case, $6^1P_0 \rightarrow 2^1P_0$ and $7^1D_0 \rightarrow 2^1P_0$. In this case, the resonance field strength is 165 kv/cm~171 kv/cm, and the min. energy difference is about 31.8 cm^{-1}. The difference between ortho- and parhelium is not so important for strong field, except for the small variations of the starting values (for zero field) and the converted level order of parhelium (P level). Therefore, it may be allowed to make the qualitative comparison between them. Taking the converted order of P state of parhelium into account, we should correspond the resonance $6^1P_0—7^1D_0$ to the resonance $7^3S_0—7^3P_0$, if we presume that the first resonance between $6^1P_0—7^1S_0$ arises in very approached point and thus is perhaps observed as if the lines cross each other. Thus the numerical values, 236 kv/cm and 13.2 cm^{-1} for the resonance $7^3S_0—7^3P_0$ are to be compared with the experimental values, 165~171 kv/cm and 31.8 cm^{-1} of the resonance $6^1P_0—7^1D_0$. We must be satisfied with such qualitative comparison.

In conclusion, the authors wish their hearty thanks to Prof. T. Yamanouchi for his kind encouragement and valuable advices and to Prof. H. Kubota for his kind advices. The authors are also indebted to Mr. J. Miida and Miss. I. Ota for their assistance in numerical computations.

References.

1) S. Sueoka: J. Phys. Soc. Jap. **5** (1950), 244. Hereafter this is denoted as (I).

2) Y. Ishida: Sc. Pap. I. P. C. R., **14** (1930), 49.

3) J. S. Foster: Proc. Roy. Soc. London, **117** (1928), 137.

JOURNAL OF THE PHYSICAL SOCIETY OF JAPAN Vol. 6, No. 6, NOV.—DEC., 1951

On the Transformation of Chaplygin's Equation Into Fuchs-Frobenius Normal Form.

By M. Z. V. KRZYWOBLOCKI.

University of Illinois, Urbana, Illinois.

(Received March 15,1951)

Introduction.

Various transformations of Chaplygin's hodograph equation into forms more suitable for the application of classical mathematical methods of solution are known. Chaplygin himself, followed by Demtchenko, Busemann, Kármán. Tsien, and others, applied an approximation solution by using the tangent at one point. Poritsky [4] applied a series of tangents. Bergman [1] proposed an extension of Kármán-Tsien method by taking into account a polynomial of third degree in ρ^{-1} and Mathur [2] reduced Chaplygin's equation to Kummer's first confluent hypergeometric equation by taking into account a limited number of terms of the pressure-volume expansion. There are known solutions of Chaplygin's equation in from of hypergeometric series. In the present note we shall show that the Chaplygin's equation may be easily reduced to the normal form of Fuchs and Frobenius.

§1. Basic Equations.

The usual isentropic flow conditions are assumed:

(1) $p=\text{const.}\,\rho^{\gamma}$, $a^2=dp/d\rho=\gamma p\rho^{-1}$,
$a_0^2=\gamma p_0\rho_0^{-1}$,

(2) $q^2=2(\gamma-1)^{-1}(a_0^2-a^2)$,

where the symbol a denotes the velocity of sound, q the velocity of compressible fluid flow, and the subscript 0 the conditions at rest. The velocity of flow into a vacuum is given by

(3) $q_m^2=2(\gamma-1)^{-1}a_0^2=2\beta u_0^2$, $\beta=(\gamma-1)^{-1}$,

and the generalized Bernoulli's equation is

$$\frac{1}{2}q^2+\int_{p_0}^{p}\rho^{-1}dp=0\,. \tag{4}$$

The following relations are known:

(5) $\rho_0^{-1}\rho=[1-\frac{1}{2}(\gamma-1)q^2a_0^{-2}]^{\beta}$,

(5a) $a_0^{-2}a^2=1-\frac{1}{2}(\gamma-1)q^2a_0^{-2}$.

Let $\tau=q^2q_m^{-2}$, then from (5) and (5a) one obtains:

(6) $\rho_0^{-1}\rho=(1-\tau)^{\beta}$,

(6a) $a_0^{-2}a^2=(1-\tau)$, $\tau=1-p\rho_0(p_0\rho)^{-1}$.

From (1), one has: $p=p_0\rho_0^{-\gamma}\rho^{\gamma}$, $dp=C\gamma\rho^{\gamma-1}d\rho$, $C=p_0\rho_0^{-\gamma}$, and from (6) $d\rho=-\rho_0\beta(1-\tau)^{\beta-1}d\tau$. Combining one obtains:

(7) $\rho^{-1}dp=-C\gamma\beta\rho_0^{1/\beta}d\tau$.

Inserting (7) into (4) results in the formula

$$q^2=2\gamma(\gamma-1)^{-1}p_0\rho_0^{-1}\int_0^{\tau}d\tau=2\gamma\beta p_0\rho_0^{-1}\tau\,. \tag{8}$$

Dividing both sides of (8) by a^2 from (6a) one easily obtains:

(9) $q^2a^{-2}=G(\tau)=2(\gamma-1)\tau(1-\tau)^{-1}$.

§2. Transformation of Chaplygin's Equation.

Chaplygin's equation

(10) $q^2\psi_{qq}+(1+q^2a^{-2})q\psi_q+(1-q^2a^{-2})\psi_{\theta\theta}=0$,

transforms by means of formulas

$$\partial/\partial q=2qq_m^{-2}\partial/\partial\tau\,,$$
$$\partial^2/\partial q^2=2q_m^{-2}\partial/\partial\tau+4q^2q_m^{-4}\partial^2/\partial\tau^2\,,$$

into the form:

(11) $4\tau^2\psi_{\tau\tau}+(4+2G)\tau\psi_{\tau}+(1-G)\psi_{\theta\theta}=0$.

Let:

$$\psi=A_0\theta+\textstyle\sum_{k=1}^{\infty}A_k\tau^{k/2}Y_k(\tau)\exp(ik\theta)\,,$$

then after all the transformations are performed, equation (11) can be expressed in the form:

(12) $\tau^2D^2Y_k+\tau P_1DY_k+P_2Y_k=0$, $k=1,2,\ldots$

(12a) $P_1=\dfrac{1}{2}(G+2k+2)$,

$P_2=\dfrac{1}{4}k(k+1)G$,

(12b) $D^2=d^2/d\tau^2$, $D=d/d\tau$.

For each value of k this is the normal form of Fuchs and Frobenius [3]. Of course, solutions of (12) must coincide with solutions in form of hypergeometric series obtained by previous authors.

§3. Solutioa of the Normal Form.

Solution of (12) follows the classical method [3, p. 62]. As is seen, $\tau=0$ is a typical singularity where Fuchs's conditions are satisfied, and $\{P_i(\tau)\}$, $i=1, 2$, are holomorphic at $\tau=0$. To obtain the formal solution in power series we introduce the operator $\delta=\tau D$, so that $\tau^2D^2=\delta(\delta-1)$ [3, p. 26] and (12) may be written in the form

$$F(\tau, \delta)Y=\delta^2Y_k+Q_1(\tau)\delta Y_k+Q_2Y_k=0, \quad k=1, 2, \ldots \tag{13}$$

where

$$Q_1=P_1-1, \quad Q_2=P_2. \tag{13a}$$

For illustrative purposes take the fixed value of k. Then the coefficients (P_i) and (Q_i) are mutually expressible as linear functions of one another with constant coefficients, so that both sets are holomorphic together. Expand the coefficients in Mac-Laurin series:

$$Q_i(\tau)=\textstyle\sum_{j=0}^{\infty}Q_{ij}\tau^j, \quad i=1, 2, \tag{14}$$

and write

$$F_0(\delta)=\delta^2+Q_{10}\delta+Q_{20}\ ; \tag{14a}$$

then (13) may now be written

$$F(\tau, \delta)Y=\textstyle\sum_{j=0}^{\infty}\tau^jF_j(\delta)Y=0, \tag{15}$$

and on substituting as a trial regular solution

$$Y=\tau^\varepsilon[c_0+c_1\tau+c_2\tau^2+\ldots\ldots], \tag{15a}$$

we obtain after some transformations [3, p. 62]

$$F(\tau, \delta)Y=\textstyle\sum_{m=0}^{\infty}\tau^{\varepsilon+m} [\sum_{r=0}^{m}F_{m-r}(\varepsilon+r)c_t]=0. \tag{16}$$

This vanishes identically if each coefficient is zero, or if (c_t) satisfy the relation

$$\textstyle\sum_{r=0}^{m}F_{m-r}(\varepsilon+r)c_t=0, \quad (m=0, 1, 2, \ldots). \tag{16a}$$

We may chose $c_0\neq0$, satisfying certain given initial conditions and every subsequent coefficient (c_t) is then uniquely determined. If $c_0\neq0$, ε must be a root (known as an exponent of the pole) of the indicial equation

$$F_0(\varepsilon)=\varepsilon^2+Q_{10}\varepsilon+Q_{20}=0. \tag{17}$$

For more details of the convergence see [3, p. 62]. Since $\tau=1$ is another singularity (9), the convergence is assured for $0<\tau<1$.

4. Pressure Coefficient.

From (6) one obtains $\rho=\rho_0(1-\tau)^\beta$, $\rho_\infty=\rho_0(1-\tau_\infty)^\beta$, where the subscript ∞ denotes the conditions at infinity. Since $\tau_\infty=q_\infty^2q_m^{-2}$ and $(1-\tau_\infty)=a_\infty^2a_0^{-2}=\text{const.}$, by comparison one gets

$$\rho=\rho_\infty(a_0a_\infty^{-1})^{2\beta}(1-\tau)^\beta. \tag{18}$$

From Bernoulli's equation, written in the form $qdq+\rho^{-1}dp=0$, with $qdq=\frac{1}{2}q_m^2d\tau$, and with the use of (3) and (18) one obtains after integrating

$$p=\gamma^{-1}\rho_\infty a_0^{2(\beta+1)}a_\infty^{-2\beta}(1-\tau)^{\beta+1}+\text{const.} \tag{19}$$

Since for conditions at rest we must have $p=p_0$, $\rho=\rho_0$, $\tau=0$, equations (19) and (18) give $p_0=\gamma^{-1}\rho_\infty a_0^{2(\beta+1)}a_\infty^{-2\beta}+\text{const.}=\gamma^{-1}\rho_0a_0^2+\text{const.}$, which means that the constant of integration must be equal to zero. For $p=p_\infty$, $\tau=\tau_\infty$, one has $(1-\tau_\infty)^{\beta+1}=(a_\infty a_0^{-1})^{2(\beta+1)}$ and $p_\infty=\gamma^{-1}\rho_\infty a_\infty$, which is correct. Using (19) we can represent the pressure coefficient, defined as $C_p=(p-p_\infty)(\frac{1}{2}\rho_\infty q_\infty^2)^{-1}$ in the form

$$C_p=2\gamma^{-1}M_\infty^{-2}[(a_0a_\infty^{-1})^{2\delta}(1-\tau)^\delta-1], \tag{20}$$

$$M_\infty^2=q_\infty^2a_\infty^{-2}, \quad \delta=\beta+1, \tag{20a}$$

or by means of (18)

$$C_p=2\gamma^{-1}M_\infty^{-2}[(\rho_\infty\rho^{-1})^{-\gamma}-1]. \tag{21}$$

For the conditions assumed by Chaplygin, Kármán-Tsien, and others, one has $\beta=-1/2$, $\gamma=-1$ and from (21)

$$C_p=2M_\infty^{-2}(1-\rho_\infty\rho^{-1}), \tag{22}$$

which is in full agreement with the result obtained by those investigators.

References

1) Bergman, S.: *The Hodograph Method in the Theory of Compressible Fluids.* Supplement to "Fluid Dynamics" by R. V. Mises and K. O. Friedrichs, Brown University (1941–42).

2) Mathur, P. N.: *On the Solutiou of Chaplygin's Equation by means of Kummer's Formula,* Proceedings of the Midwestern Conferences on Fluid Dynamics, I. University of Illinois (1950). Edwards Brothers, Ann Arbor, Michigan.

3) Poole, E.G.C.: *Introduction to the Theory of Linear Differential Equations.* Oxford, Clarendon Press, 1936.

4) Poritsky, H.: *Polygonal Approximation Method in the Hodograph Plane.* Appl. Mech., Trans. Am. Soc. Mech. Engr., **16** (1949), pp. 123–133.

JOURNAL OF THE PHYSICAL SOCIETY OF JAPAN Vol. 6, No. 6, NOV.—DEC., 1951

On the Plastic Deformation of Copper Single Crystals.
Part 1. Two Stages in the Progress of Deformation.

By Hiroshi KANZAKI.

Institute of Industrial Science, University of Tokyo, Chiba.

(Read November 5, 1950; Received April 16, 1951)

The stress-strain curves of copper single crystals have been obtained at room temperature. When the resolved shear strain reaches about 20 percent, the stress increases rather rapidly with increasing strain and thus the progress of deformation is found to be made of two stages. This change in the nature of work-hardening may be explained from the view of the presence of two types of strains inside work-hardened metals that has been discussed in the previous paper (J. Phys. Soc. Japan **6** (1951) 90). If this view is correct, the number of stopped dislocations is expected to show rapid increase in the second stage of deformation.

§1. Introduction.

In the previous paper,[1] the writer reported on the recovery process of cold-worked polycrystalline metals, Cu, Al and Ag, describing that the anomalous specific heat due to recovery is composed of two stages, and then concluding that the two processes observed in the experiment correspond to the recovery from two types of strains in the cold-worked metals, that is, (1) the lattice distortion, and (2) the grain fragmentation.

It was also noticed that from the standpoint of dislocation theory, the strain of the first type was the strain refered to the presence of dislocation lines themselves, and that of the second type was the local strain due to the "stopped dislocations" by Burgers.[2]

This heterogeneous property of strain-hardening seems to coincide with the experimental investigation by Suzuki.[3]

Recently, Koehler and Blewitt[4] gave attention to "change in the nature of work-hardening at small strains." From the experimental results by Heidenreich and Shockley[5] and so on, they find that for small strains the distortion is confined to the vicinity of the slip bands and for larger strains, where the rate of hardening increases, the strains become more homogeneously distributed.

According to writer's point of view, the two stages of deformation noticed by Koehler and Blewitt may be explained by the presence of two types of strains in the cold-worked metals.

For small strains (will be called as the "first stage" of deformation), dislocation lines generated at the favorable points in the surface may be able to travel on slip planes with comparative ease. In this stage, the strain due to stopped dislocations will be negligibly small.

Accompanying with the progress of deformation the interaction between dislocations (including their interaction with mosaic boundaries) will become remarkable. This "retardation effect" for passage of dislocations will proceed, as it were, "co-operatively" and, thus, for larger strains (the "second stage" of deformation) the number of stopped dislocations may show remarkable increase. In this way it is conceivable that the rate of hardening increases rapidly in this stage.

The difficulties in the passage of dislocations which grew up in the first stage will give rise to the development of new dislocations in the second stage and the deformation becomes sufficiently homogeneous that Taylor's dislocation theory can be applied.

In the present paper, the experimental results on the plastic deformation of copper single crystals are described. In order to ascertain the view described above, the relation between the stress-strain curve and the anomalous specific heat due to recovery is carefully investigated. Several discussions are given on the "two stages" of plastic deformation.

§2. Preparation of Specimens.

All specimens were prepared from the electrolytic copper of the same purity 99.98%.

The single crystals with cylindrical form were obtained by the gradual solidification from the melt and their average size was about 20 mm in diameter and about 60 mm in length. Melting was carried out in the air, but by the use of pure graphite crucibles the effect of oxidation was reduced sufficiently for our purpose. The orientation of these crystals was determined by the light figure method improved by Yamamoto.⁶⁾

In order to obtain several samples with same crystal orientation, each of these crystals was carefully cut to five or six specimens of about 10 mm high, and then compressed by the testing machine.

§ 3. Stress vs. Strain Curve.

The deformation of crystals was measured with accuracy of 2×10^{-3} mm with the usual dial gauge and this corresponds to the strain sensitivity of about 2×10^{-4}.

The resolved shear stress vs. shear curve was obtained from load vs. deformation curve according to Taylor's method.⁷⁾ The curve obtained in the compression test at room temperature (20°C) is shown in Fig. 1 (a).

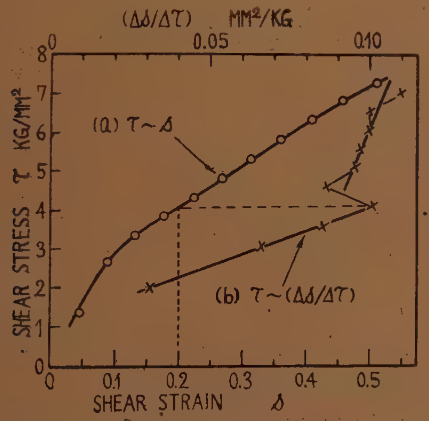

Fig. 1 (a) Resolved shear stress τ vs. shear s curve for copper single crystal deformed at room temperature.

(b) Shear stress τ vs. $(\Delta s/\Delta\tau)$ curve calculated from Fig. 1 (a).

Taylor⁸⁾ has pointed out that in aluminum crystals the stress-strain diagram can be fitted with parabolic curve corresponding to the equation

$$s=a\tau^2 \qquad (1)$$

where s is the shear strain, τ is the resolved shear stress and a is a constant.

From equation (1) we get

$$ds/d\tau=2a\tau \qquad (2)$$

and this equation can be used to judge whether $\tau-s$ curve can be fitted with parabola or not. The τ vs. $(\Delta s/\Delta\tau)$ diagram computed from Fig. 1 (a) is shown in Fig. 1 (b). This diagram shows a kink near the strain $s=0.2$. The kink should correspond to the transition from the first stage of deformation to the second stage as noted in § 1.

For the first stage, the constant a is found to be

$$a_1\doteq1.82\times10^{-18}\ (\mathrm{cm}^2/\mathrm{dyne})^2$$

and for the second stage

$$a_2=0.31\times10^{-18}\ (\mathrm{cm}^2/\mathrm{dyne})^2.$$

According to Taylor's theory of work-hardening, constant a in equation (1) is expressed as

$$a=(1/k^2G^2)(L/\lambda) \qquad (3)$$

where k is a constant, G is the rigidity modulus, and λ is the distance of slip produced by passage of one dislocation through a crystal.

The quantity L in equation (3) may be called the "mean free path" of dislocation line and from the results described above, this mean free path in the second stage must be shorter than that in the first stage of deformation.

Using the value of $k=0.2$ after Taylor,⁸⁾ the value of L is found to be

$L_1=3.84\times10^{-4}$cm for the first stage, and $L_2=0.68\times10^{-4}$ cm for the second stage.

References.

1) H. Kanzaki: J. Phys. Soc. Japan **6** (1951) 90.

2) J. M. Burgers: Proc. Phys. Soc. **52** (1940) 23.

3) T. Suzuki: Sci. Rep. RITU. **A 1** (1949) 193.

4) J. S. Koehler and T. H. Blewitt: Phys. Rev. **75** (1949) 1952.

5) R. D. Heidenreich and W. Shockley: Bristo. Conference on the Strength of Solids, Phys. Soc. London (1947) 57.

6) M. Yamamoto: Sci. Rep. Tohoku Imp. Univ. **29** (1941) 113.

7) G. I. Taylor: Proc. Roy. Soc. **116** (1927) 16, 39.

8) G. I. Taylor: Proc. Roy. Soc. **145** (1934) 388.

JOURNAL OF THE PHYSICAL SOCIETY OF JAPAN Vol. 6, No. 6, NOV.—DEC., 1951

On the Plastic Deformation of Copper Single Crystals.
Part 2. Recovery Process and Mean Length of Dislocations.

By Hiroshi KANZAKI.
Institute of Industrial Science, University of Tokyo, Chiba.

(Read November 5, 1950; Recieved April 16, 1951)

The anomalous specific heat due to recovery from strain hardening has been measured on the single crystals of copper deformed at various temperatures. The apparatus for specific heat measurement is that of Nagasaki and Takagi.

(1) The maximum value of the energy stored during deformation at room temperature is found to be 0.1 cal per gram.

(2) The energy released in the second valley of the specific heat anomaly (the energy accompanied with stopped dislocations) shows rapid increase when the resolved strain exceeds 25 percent.

(3) The recoverying temperature takes the maximum value when the resolved strain is about 25 percent.

(4) The crystals deformed at −180°C and −80°C recover sometimes below the room temperature. Results of (3) and (4) may be explained by taking account of the length of dislocation lines.

(5) The density of dislocations is calculated from the dependency of recoverying rate upon the degree of hardening. The obtained value of the separation distance of dislocations is about 200 Å and shows good agreement with the results obtained by electron microscope.

§ 1. Measurement of the Specific Heat.

The apparatus for specific heat measurement was that of Nagasaki and Takagi,[1] but the shape of specimen was slightly modified as follows.

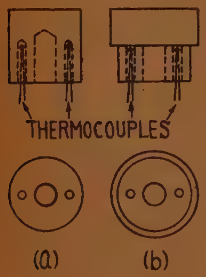

Fig. 1. Specimen used for specific heat measurement.

(a) Specimen used in the Nagasaki-Takagi method.

(b) Specimen used in our experiment.

Fig. 1 (a) shows the shape of specimen used in Nagasaki-Takagi method. Fig. 1 (b) shows the specimen used in our experiment and it is made up of two parts; the upper part is a copper single crystal subjected to cold-working and the lower part is made of thoroughly annealed silver. The lower part is necessary for the insertion of thermocouples and a heater (to give constant wattage to specimen) and this part always contributes a certain constant term to the specific heat.

In this way, working of samples (as shown in Fig. 1 (a) drilling was unavoidable in the Nagasaki-Takagi method) has been made unnecessary and we can begin the specific heat measurement immediately after samples are taken out from the testing machine; it took about twenty minutes at most for us to arrange the set for specific heat measurement.

§ 2. Energy Released during Recovery Process for Crystals deformed at Room Temperature.

Specific heat of cold-worked crystals was measured while heated at constant heating velocity of about 1°C per minute. Fig. 2 shows representative specific heat vs. temperature curves for crystals compressed at room temperature. The white circles in these curves show the results in the first heating measurements, the black circles show those in the second heating measurements, and so the difference between these two curves corresponds to the anomalous specific heat due to recovery from strain-hardening.

(1) Anomalous specific heat is composed of two stages and this result coincides with that

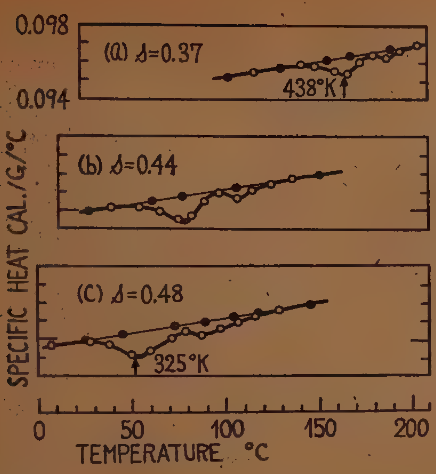

Fig. 2. Specific heat vs. temperature curves for copper single crystals deformed at room temperature.

obtained for polycrystalline copper reported in the previous paper.[2]

(2) The value of energy released in the first stage of recovery process W_1 and that released in the second stage W_2 were computed from specific heat curves and plotted against shear strain s in Fig. 3.

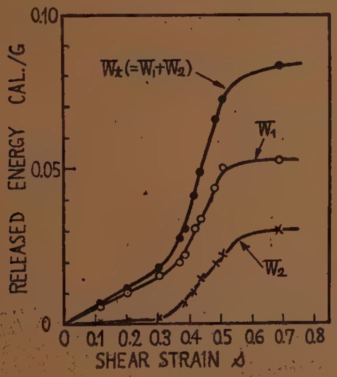

Fig. 3. Released energy vs. shear strain s.
W_1; Energy released in the first stage of recovery.
W_2; Energy released in the second stage of recovery.
W_t; Total enery released in the recovery process.

These curves show the first kink near the strain $s=0.3$ and the second kink near $s=0.5$. The first kink in Fig. 3 probably corresponds to the kink in τ vs. $(\Delta s/\Delta\tau)$ diagram (Fig. 1 (b) of Part 1). It is noticeable that the energy W_2 shows rapid increase in the second stage of hardening. This result favors with the view presented in § 1 of Part 1, because the energy W_2 may be the strain energy accompanied by the local deformation due to stopped dislocations.[2]

As can be seen in Fig. 2, the crystal deformed to $s=0.5$ recovers near room temperature. It seems natural that the origin of the second kink in Fig. 3 is the "self recovery" of deformed crystals.

(3) It is interesting to note that the maximum value of the energy stored during strain hardening is 0.1 cal. per gram at most. This value is only one fifth that of polycrystalline copper 0.5 cal. per gram.[2][3]

§ 3. Progress of Deformation and Rate of Recovery.

1. Crystals deformed at Room Temperature.

It was found that the recoverying temperature depended upon the crystal orientation as well as on the magnitude of subjected strain. The writer, however, can not yet give any conclusion upon this dependency on the crystal orientation, and only the dependency on the strain magnitude will be discussed here.

In the previous paper, the writer presented the formula to give the reaction rate of recovery process.[2] From the results obtained there, the dependency of recovering rate κ on the degree of strain-hardening is expressed by

$$\kappa = A \exp(nW/RT) \qquad (1)$$

where n is the "energy concentration factor," W is the energy released in the recovery process and A is a constant almost independent of the degree of hardening. The equation (1) expresses that the recoverying temperature becomes lower with the progress of deformation. This result has been ascertained by several authors in the case of polycrystalline metals.[2][3]

The dependency of recoverying temperature on the magnitude of strain follows equation (1) in the second stage of deformation, but does not in the first stage.

This new type of dependency in the first stage was investigated using several specimens with the same crystal orientation. These specimens were cut from the same single crystal the orientation of which was selected so as to avoid multiple slip in the first stage of deformation.

Fig. 4 shows the specific heat vs. temperature curves for these specimens subjected to different degree of deformation and Fig. 5 shows the dependency of recoverying temperature (temperature at which the first valley of the specific heat is observed) on the magnitude of the strain. In these specific heat measurements the heating velocity was kept always constant and, therefore, the appearance of the maximum recoverying temperature in Fig. 5 means the appearance of the minimum recoverying rate. This minimum of the recoverying rate also coincides with the transition from the first stage of deformation to the second.

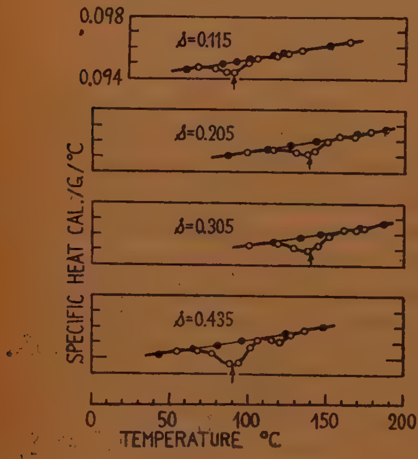

Fig. 4. Specific heat vs. temperature curves for copper single crystals with the same crystal orientation that were given different degree of deformation.

This result may be explained in a qualitative way with the following assumptions.

In the first stage of deformation, where interaction between dislocations is not yet remarkable, the dislocations will increase their lengths with their passage through crystal and the mean length of dislocations will increase as the deformation proceeds.

If dislocations are long, running through many mosaic blocks, their natural rate of diffusion will be correspondingly decreased and the raising of recoverying temperature with strain may be expected in this first stage of deformation.

At the end of the first stage the mean length of dislocations will show the tendency to saturate and, afterwards, owing to appearance of large interior stress in the domains traversed by dislocations, they may be "stopped." This corresponds to the transition from the first stage to the second stage.

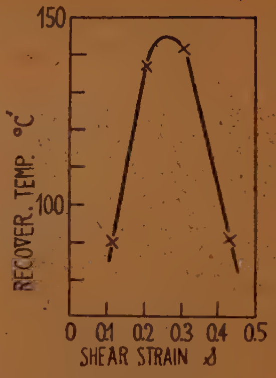

Fig. 5. Recoverying temperature vs. shear strain for crystals subjected to small strains at room temperature (for crystals shown in Fig. 4).

In the second stage of deformation the progress of hardening may be approximated by Taylor's theory, because the deformation becomes sufficiently homogeneous in this stage. This hardening process in the second stage seems to predominate in the deformation of polycrystalline metals, owing to the action of dislocations of the grain boundary and the interaction of deformations in the differently oriented grains.

The recoverying rate in the second stage will be discussed in § 4 using the formula presented in the previous paper.

2. Crystals deformed below Room Temperature.

Several crystals were compressed below room temperature; some of them at −80°C (using dry-ice and ethyl alcohol) and some of them at −180°C (using liquid oxygen). After being compressed at these temperatures, specific heat measurement of these crystals was started from room temperature.

This experimental procedure has proved a failure, because in many cases recovery had been finished below room temperature. It proved necessary to start specific heat measurement from the temperature at which crystals were deformed.

In a few cases, however, the specific heat anomaly due to recovery was observed near room temperature and such results are illustrated in Fig. 6.

It seems certain that the recoverying temperature of crystal deformed below room tem-

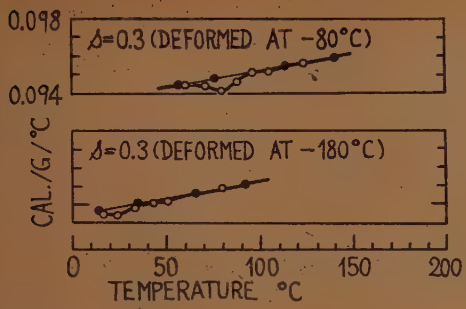

Fig. 6. Specific heat vs. temperature curves for copper single crystals deformed below room temperature.

perature is lower than that of crystal deformed at room temperature. This fact coincides with the result obtained by Paterson and Orowan.[4]

At low temperature, temperature fluctantions will not be sufficient to allow the dislocations to elongate. The low recoverying temperature of crystal deformed at low temperature may be ascribed to the short length of dislocations in it.

§4. Rate of Recovery and Dislocations in Cold Worked Copper Single Crystals.

According to the Eyring's reaction rate theory the writer gave the formula to give the recovering rate in the previous paper.[2] The value of the "energy concentration factor" n in equation (1) will be derived from the specific heat data for samples deformed to the second stage of deformation.

As we are concerned only with the first stage of recovery process,[2] the value of energy W in equation (1) is that released in the first valley of specific heat anomaly.

Two crystals with the same crystal orientation were compressed at room temperature.

One of them was deformed to the shear strain $s_1=0.37$

and the other was deformed to

$$s_2=0.48.$$

Specific heat vs. temperature curves for these crystals are shown in Fig. 2 (a) and 2 (c).

The value of energy released in the first recovery process W_1 was found to be

$$W_{11}=0.019 \text{ cal per gram},$$

and $W_{12}=0.039$ cal per gram.

The recoverying temperature T (temperature at which the first minimum of the specific heat was observed) was

$$T_1=438°\text{K}$$

and $T_2=325°\text{K}$.

The rate of recovery κ must be equal at the temperature T_1 and T_2. Thus the value of n is determined as

$$n=407.$$

Koehler[5] proposed model of the dislocation centre as a circular region of radius r_0 in the two dimensional expression. Using this model, we shall express the energy of cold-worked metal as concentrated in these circular regions. If a is the separation distance of dislocations in the dislocation lattice by Koehler, the factor n can be given by

$$n=a^2/\pi r_0^2.$$

Using Koehler's results $r_0=6.15$ Å, we have

$$a=220 \text{ Å}.$$

This value of a is in satisfactory agreement with the thickness of glide laminae about 200 Å observed in the electron microscope image by Heidenreich and Shockley,[6] and Brown.[7]

In conclusion the writer expresses his sincere thanks to Dr. Y. Tani for his valuable suggestions in the course of this work. This study was helped by the research grant given from the Ministry of Education.

References.

1) S. Nagasaki and Y. Takagi: J. of Applied Physics Japan **17** (1948) 104. (in Japanese)
2) H. Kanzaki: J. Phys. Soc. Japan **6** (1951) 90.
3) T. Suzuki. Sci. Rep. RITU. **A 1** (1949) 193.
4) M. S. Paterson and E. Orowan: Nature, vol. **162** (1948) Dec. 25.
5) J. S. Koehler: Phys. Rev. **60** (1941) 397.
6) R. D. Heidenreich and W. Shockley: Bristol Conference on the Strength of Solids, Phys. Soc. London (1947) 57.
7) A. F. Brown: Nature, **163** (1949) 1961.

JOURNAL OF THE PHYSICAL SOCIETY OF JAPAN Vol. 6, No. 6, NOV.—DEC., 1951

Application of the Theory of Supersonic Flow to the Two-dimensional Isostatical Problem in the Theory of Plasticity.

By Nobuo INOUE.

Faculty of Engineering, Doshisha University, Kyoto.

(Received April 20, 1951)

Since the fundamental equation of the two-dimensional isostatical problem in the theory of plasticity is the partial differential equation of the hyperbolic type, it may be solved by the method of characteristics, which has been effectively used in the mechanics of compressible fluid.

In this paper the author discusses the analogy between the plastic flow and the supersonic flow, by introducing the hypothetical fluid which has the special type of pressure-density relation $p/\log\rho = \text{constant}$ and all the same local Mach number $\sqrt{2}$ throughout it, and shows that the slip-lines, isostatics and boundary curves in the plastic flow correspond to respectively Mach lines, stream lines and shock waves in the supersonic flow.

By considering the stress plane similar to the hodograph plane for the supersonic fluid flow, the nonlinear problem of the plastic flow is linearized and the new plastic state of stress is obtained by superposition of particular solutions.

The case of simple waves is discussed in detail for the plastic flow as well as for the flow of hypothetical fluid here introduced.

I. Introduction.

§ 1. Recently the mechanics of compressible fluids has made a marked progress in connection with the problem of high-speed flight, especially the theory of supersonic flow having been almost completely established using the ingenious method of characteristics. Let us now pay attention to one of the other nonlinear engineering problems, i. e. the two-dimensional isostatical problem in the theory of plasticity. When we want to determine the stress distributions in purely elastic materials under certain boundary conditions, we must have equations of equilibrium of stresses and some definite relations between stress and strain such as Hooke's law. However, in the case of perfectly plastic materials, we can determine the state of stresses without any knowledge of stress-strain relations, that is, we can solve the stresses σ_x, σ_y, τ_{xy} from the two equations of equilibrium and the yield condition of perfectly plastic materials, when we restrict ourselves to two-dimensional problems assuming that the materials flow in planes parallel to the x, y plane. The partial differential equations obtained in this case are those of the hyperbolic type and are able to be treated in the similar way to the case of the supersonic flow, slip-lines corresponding to Mach lines, isostatics to stream lines and bounding curves to shock waves as will be shown in the following articles.

II. Fundamental equations and their characteristics.

§ 2. Designating by σ_x and σ_y the normal stresses in the x- and y- directions and by τ_{xy}* the shearing stress (Fig. 1.), the equations of equilibrium take the forms:

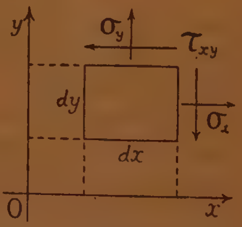

Fig. 1. Stress components in rectangular coordinates.

$$\frac{\partial \sigma_x}{\partial x} - \frac{\partial \tau_{xy}}{\partial y} = 0, \tag{1}$$

$$\frac{\partial \sigma_y}{\partial y} - \frac{\partial \tau_{xy}}{\partial x} = 0. \tag{2}$$

To these we add as the third equation, the condition of yielding:

---

* Care must be taken that the sign of τ^{xy} is taken opposite to the usual one.

$$(\sigma_x-\sigma_y)^2+4\tau_{xy}^2=4k^2, \qquad (3)$$

where k has the constant values, whenever we use the theory of constant energy of distortion or the maximum shear theory. Substituting the derivative of σ_y with respect to y obtained by differentiating Eq. (3) into Eq. (2), the fundamental equations for the stresses become:

$$\frac{\partial\sigma_x}{\partial x}-\frac{\partial\tau_{xy}}{\partial y}=0, \qquad (4)$$

$$(\sigma_x-\sigma_y)\frac{\partial\sigma_x}{\partial y}+4\tau_{xy}\frac{\partial\tau_{xy}}{\partial y}+(\sigma_y-\sigma_x)\frac{\partial\tau_{xy}}{\partial x}=0. \qquad (5)$$

On the other hand, if we consider the two-dimensional, irrotational and stationary flow of non-viscous compressible fluids, we have the fundamental equations corresponding to Eqs. (1) and (2) as follows:

$$\frac{\partial v}{\partial x}-\frac{\partial u}{\partial y}=0, \qquad (1')$$

$$(c^2-v^2)\frac{\partial v}{\partial y}-2uv\frac{\partial u}{\partial y}+(c^2-u^2)\frac{\partial u}{\partial x}=0, \qquad (2')$$

where u and v are the x- and y- components of the fluid velocity respectively, c being the local velocity of sound.

Here we make one assumption that in our fluid the adiabatic law does not hold, but the pressure-density relation is given by

$$p/\log\rho=\text{constant}.$$

The local velocity of sound and Bernoulli's equation for such a fluid take the form:

$$c=\frac{1}{\sqrt{\rho}}, \quad \frac{1}{2}(u^2+v^2)-c^2=\text{constant},$$

and so if we choose the local Mach number to be $\sqrt{2}$ at arbitrary place in this fluid, it will be maintained throughout the fluid, i.e.

$$c^2=\frac{1}{2}(u^2+v^2). \qquad (3')$$

Substituting this value of c^2 into Eq. (2′), we have:

$$\frac{\partial v}{\partial x}-\frac{\partial u}{\partial y}=0, \qquad (4')$$

$$(v^2-u^2)\frac{\partial v}{\partial y}+4uv\frac{\partial u}{\partial y}+(u^2-v^2)\frac{\partial u}{\partial x}=0. \qquad (5')$$

The theory of partial differential equations shows that the characteristic equations for the simultaneous partial differential equations (4) and (5) are given by

$$\text{C}+: \quad \frac{\partial y}{\partial\alpha}=\frac{2(k-\tau_{xy})}{\sigma_x-\sigma_y}\frac{\partial x}{\partial\alpha} \qquad (6)$$

and

$$\text{C}-: \quad \frac{\partial y}{\partial\beta}=-\frac{2(k+\tau_{xy})}{\sigma_x-\sigma_y}\frac{\partial x}{\partial\beta} \qquad (7)$$

on the physical x, y plane, while they are given by

$$\Gamma+: \quad \frac{\partial\tau_{xy}}{\partial\alpha}=\frac{\sigma_x-\sigma_y}{2(k-\tau_{xy})}\frac{\partial\sigma_x}{\partial\alpha} \qquad (8)$$

and

$$\Gamma-: \quad \frac{\partial\tau_{xy}}{\partial\beta}=-\frac{\sigma_x-\sigma_y}{2(k+\tau_{xy})}\frac{\partial\sigma_x}{\partial\beta} \qquad (9)$$

on the τ_{xy}, σ_x or stress plane, where α and β are the parameters of the characteristics. We can discuss the state of stresses by solving Eqs. (6)~(9) instead of grappling with Eqs. (1)~(3) or with Eqs. (4) and (5).

Similarly the characteristic equations for the supersonic flow governed by Eqs. (4′) and (5′) are given by

$$\text{C}+: \quad \frac{\partial y}{\partial\alpha}=\frac{u+v}{u-v}\frac{\partial x}{\partial\alpha} \qquad (6')$$

and

$$\text{C}-: \quad \frac{\partial y}{\partial\beta}=\frac{v-u}{u+v}\frac{\partial x}{\partial\beta} \qquad (7')$$

on the physical x, y plane, while they are given by

$$\Gamma+: \quad \frac{\partial u}{\partial\alpha}=\frac{u-v}{u+v}\frac{\partial v}{\partial\alpha} \qquad (8')$$

and

$$\Gamma-: \quad \frac{\partial u}{\partial\beta}=\frac{u+v}{v-u}\frac{\partial v}{\partial\beta} \qquad (9')$$

on the u, v or hodograph plane, where α and β are the parameters of the characteristics.

From Eqs. (6)~(9) we have the relations:

$$\left.\begin{aligned}
&\frac{\partial y}{\partial\alpha}\frac{\partial y}{\partial\beta}+\frac{\partial x}{\partial\alpha}\frac{\partial x}{\partial\beta}=0,\\
&\frac{\partial\sigma_x}{\partial\alpha}\frac{\partial\sigma_x}{\partial\beta}+\frac{\partial\tau_{xy}}{\partial\alpha}\frac{\partial\tau_{xy}}{\partial\beta}=0,\\
&\frac{\partial y}{\partial\alpha}\frac{\partial\sigma_x}{\partial\beta}+\frac{\partial x}{\partial\alpha}\frac{\partial\tau_{xy}}{\partial\beta}=0,\\
&\frac{\partial y}{\partial\beta}\frac{\partial\sigma_x}{\partial\alpha}+\frac{\partial x}{\partial\beta}\frac{\partial\tau_{xy}}{\partial\alpha}=0,
\end{aligned}\right\} \qquad (10)$$

and from Eqs. (6′)~(9′):

$$\left.\begin{aligned}
&\frac{\partial y}{\partial\alpha}\frac{\partial y}{\partial\beta}+\frac{\partial x}{\partial\alpha}\frac{\partial x}{\partial\beta}=0,\\
&\frac{\partial v}{\partial\alpha}\frac{\partial v}{\partial\beta}+\frac{\partial u}{\partial\alpha}\frac{\partial u}{\partial\beta}=0,\\
&\frac{\partial y}{\partial\alpha}\frac{\partial v}{\partial\beta}+\frac{\partial x}{\partial\alpha}\frac{\partial u}{\partial\beta}=0,\\
&\frac{\partial y}{\partial\beta}\frac{\partial v}{\partial\alpha}+\frac{\partial x}{\partial\beta}\frac{\partial u}{\partial\alpha}=0.
\end{aligned}\right\} \qquad (10')$$

Therefore, the curves C+ and C− and also the curves $\Gamma+$ and $\Gamma-$ intersect orthogonally, and if the stress plane and the physical plane of the plastic flow and the hodograph plane and the physical plane of the supersonic flow are superposed one upon another in the same plane the characteristics C+ and C− coincide with $\Gamma+$ and $\Gamma-$ respectively.

§ 3. At this stage we must remark that the characteristics C+ and C− in the physical plane are the network of two families of orthogonal curves called slip-lines in the plastic flow and they are known as Mach lines, in the supersonic flow, whose orthogonality is wholly due to the specific properties of our fluid.

Before proceeding further, we want to show the analogy between isostatics and stream lines. From Eqs. (6) and (7) we have:

$$\frac{\{\sqrt{2k-(\sigma_x-\sigma_y)}dx+\sqrt{2k+(\sigma_x-\sigma_y)}dy\}^2}{4k(dx^2+dy^2)}=\frac{1}{2}, \tag{11}$$

and so the angle between slip-lines and the vector, whose $x-$ and $y-$ components are $\sqrt{2k-(\sigma_x-\sigma_y)}$ and $\sqrt{2k+(\sigma_x+\sigma_y)}$ respectively, is $\pi/4$ representing the direction of isostatics (Fig. 2). Similarly we have from Eqs. (6′) and (7′):

$$\frac{(udy-vdx)^2}{(u^2+v^2)(dx^2+dy^2)}=\frac{1}{2}, \tag{11′}$$

which shows that the angle between Mach lines and stream lines is $\pi/4$ (Fig. 3).

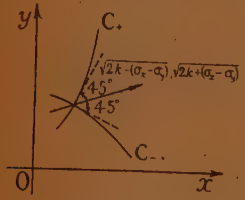

Fig. 2.
Isostatics and slip-lines.

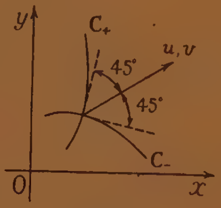

Fig. 3.
Stream lines and Mach lines.

Integration of Eqs. (8) and (9) or (8′) and (9′) readily shows that the characteristics in the stress plane are sine curves and those in the hodograph plane are logarithmic spirals as shown in Fig. 4 and Fig. 5.

III. General solution of the isostatical problem.

§ 4. The fundamental equations and the characteristics having been established so far, let us now solve these equations. First, Eqs. (8) and (9) in the preceding article may be easily integrated to give*

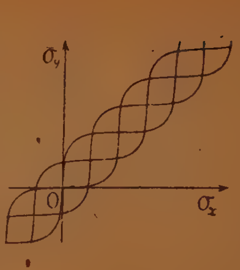

Fig. 4.
Stress curves are sine curves.

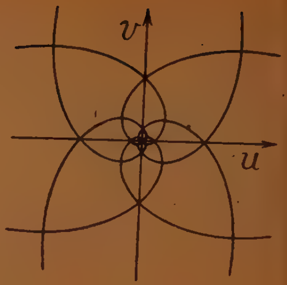

Fig. 5.
Hodograph curves are logarithmic spirals.

$$\Gamma+:\ \frac{\sigma_x+\sigma_y}{2k}+\sin^{-1}\frac{\sigma_x-\sigma_y}{2k}=4r(\beta), \tag{12}$$

$$\Gamma-:\ \frac{\sigma_x+\sigma_y}{2k}-\sin^{-1}\frac{\sigma_x-\sigma_y}{2k}=-4s(\alpha), \tag{13}$$

and so it will be seen that on the curve C+

$$\frac{dy}{dx}=\frac{2(k-\tau_{xy})}{\sigma_x-\sigma_y} \text{ and } \frac{\sigma_x+\sigma_y}{2k}+\sin^{-1}\frac{\sigma_x-\sigma_y}{2k}=\text{constant}, \tag{14}$$

and on the curve C−

$$\frac{dy}{dx}=-\frac{2(k+\tau_{xy})}{\sigma_x-\sigma_y} \text{ and } \frac{\sigma_x+\sigma_y}{2k}-\sin^{-1}\frac{\sigma_x-\sigma_y}{2k}=\text{constant}. \tag{15}$$

When there exists one-to-one correspondence between points in the physical stress planes, we have from Eqs. (12) and (13):

$$\frac{\sigma_x+\sigma_y}{2k}=2(r-s), \tag{16}$$

$$\sin^{-1}\frac{\sigma_x-\sigma_y}{2k}=2(r+s), \tag{17}$$

and from Eqs. (6) and (7):

$$\frac{\partial y}{\partial s}=\frac{2(k-\tau_{xy})}{\sigma_x-\sigma_y}\frac{\partial x}{\partial s}, \tag{18}$$

$$\frac{\partial y}{\partial r}=-\frac{2(k+\tau_{xy})}{\sigma_x-\sigma_y}\frac{\partial x}{\partial r}. \tag{19}$$

Substituting Eqs. (16) and (17) into Eqs. (18) and (19), we have:

$$\frac{\partial y}{\partial s}=\tan(r+s)\frac{\partial x}{\partial s}, \tag{20}$$

$$\frac{\partial y}{\partial r}=-\cot(r+s)\frac{\partial x}{\partial r}, \tag{21}$$

or, by eliminating y from these equations,

$$\frac{\partial^2 x}{\partial r\partial s}+\tan(r+s)\frac{\partial x}{\partial s}-\cot(r+s)\frac{\partial x}{\partial r}=0, \tag{22}$$

and from Eq. (22) we can determine x as a function of r and s. Using this solution for x

---

* Double signs before arcsines have been omitted for the sake of simplicity.

we can obtain y as a function of r and s from Eqs. (18) and (19). In this manner we can solve slip-lines C+ and C−, but practically we are interested a little in performing these operations.

§ 5. The problems which we encounter in practice is to search for slip-lines from the given stress distributions or to determine stresses which are compatible with the given slip-lines. The former one is solved immediately when we substitute the given stresses into the latter equation in Eqs. (14) or (15), and when the equations of slip-lines are known we can solve $\sigma_x-\sigma_y$ and τ_{xy} from the former equation in Eqs. (14) or (15) and the condition of yielding (3). Then, making use of the latter equation in Eqs. (14) or (15) we can solve the latter problem. Therefore, we can determine the stress distributions completely whenever an arbitrary curve is given as one of the slip-lines.

If the characteristics in the physical plane have envelopes, it is well known in the theory of supersonic flow that there exist shock waves and discontinuities occur in every physical quantities such as pressure, density and velocity etc. Corresponding to this fact the discontinuities of stresses may occur in plastic materials and the discontinuities in this case mean the bounding surface of another materials, because they will never happen in the interior of plastic materials when we are dealing with the isostatical problem in the theory of plasticity. We know from the former in Eqs. (14) or (15) that the equation of bounding curves are $\sigma_x=\sigma_y$ or, expressed in shearing stresses, $\tau_{xy}=\pm k$. Therefore, if any stress distributions at every point in plastic materials or slip-lines otherwise are given, we can determine the bounding curves, and on the contrary, if the bounding curves are given, we first seek after the families of orthogonal curves which have the given bounding curves as their envelopes, and then taking these families of orthogonal curves as slip-lines we can obtain all the possible stress distributions in the plastic materials. Lastly, in concluding this paragraph we must add one proposition, that is, the boundary curves of the region of plastic deformation with that of elastic one are represented by slip-lines as is obvious from the properties of characteristics in the theory of partial differential equations.

IV. General solution of the supersonic flow.

§ 6. Let us return now to the supersonic flow of fluid and proceed in all the same manner as already mentioned. Although the properties of supersonic flow are well known, we must study them particularly here, since our fluid has special properties as assumed in § 2.

Integration of Eqs. (8′) and (9′) gives

$$\Gamma+:\ \frac{1}{2}\log(u^2+v^2)+\tan^{-1}\frac{v}{u}+\frac{\pi}{4}=2r(\beta),\tag{12′}$$

$$\Gamma-:\ \frac{1}{2}\log(u^2+v^2)-\tan^{-1}\frac{v}{u}-\frac{\pi}{4}=-2s(\alpha),\tag{13′}$$

and so the following relations are obtained; i.e. on the curve C+:

$$\frac{dy}{dx}=\frac{u+v}{u-v}\ \text{and}\ \frac{1}{2}\log(u^2+v^2)+\tan^{-1}\frac{v}{u}=\text{constant}\tag{14′}$$

and on the curve C−:

$$\frac{dy}{dx}=\frac{u+v}{u-v}\ \text{and}\ \frac{1}{2}\log(u^2+v^2)-\tan^{-1}\frac{v}{u}=\text{constant}.\tag{15′}$$

When there exists one-to-one correspondence between points in the physical hodograph planes, we have from Eqs. (12′) and (13′):

$$\frac{1}{2}\log(u^2+v^2)=r-s,\tag{16′}$$

$$\tan^{-1}\frac{v}{u}=r+s-\frac{\pi}{4},\tag{17′}$$

and from Eqs. (6′) and (7′):

$$\frac{\partial y}{\partial s}=\frac{u+v}{u-v}\frac{\partial x}{\partial s},\tag{18′}$$

$$\frac{\partial y}{\partial r}=\frac{v-u}{u+v}\frac{\partial x}{\partial r}.\tag{19′}$$

Substituting Eqs. (16′) and (17′) into Eqs. (18′) and (19′), we have:

$$\frac{\partial y}{\partial s}=\tan(r+s)\frac{\partial x}{\partial s},\tag{20′}$$

$$\frac{\partial y}{\partial r}=-\cot(r+s)\frac{\partial x}{\partial r},\tag{21′}$$

or, by eliminating y from these equations,

$$\frac{\partial^2 x}{\partial r\partial s}+\tan(r+s)\frac{\partial x}{\partial s}-\cot(r+s)\frac{\partial x}{\partial r}=o,\tag{22′}$$

and from Eq. (22′) we can determine x as a function of r and s. Using this solution for x we can obtain y as a function of r and s from

Eqs. (18′) and (19′). In this manner we can obtain Mach lines C+ and C− in the physical plane.

V. Simple Waves.

§ 7. In order to establish the theory of slip-lines completely we want to discuss in this article the special type of slip-lines, one of the two families of which is a family of straight lines. If a certain region D in the x, y plane represents the straight line $s=$constant in the r, s plane, characteristics C+ on which the parameter r is constant are straight lines in this region D and are called simple waves as is well known.

Now we give to these straight lines the following expressions:

$$x=a(\sigma)-r\sin\omega(\sigma),\quad y=b(\sigma)+r\cos\omega(\sigma),\tag{23}$$

where σ is the parameter and r is the abscissa on these straight lines $\sigma=$constant. From Eq. (23) we have:

$$\frac{dy}{dx}=\tan\left(\frac{\pi}{2}+\omega\right),\tag{24}$$

and when the angle between the isostatics vector $(\sqrt{2k-(\sigma_x-\sigma_y)},\ \sqrt{2k+(\sigma_x-\sigma_y)})$ and the x-axis is shown by θ

$$\frac{\sqrt{2k+(\sigma_x-\sigma_y)}}{\sqrt{2k-(\sigma_x-\sigma_y)}}=\tan\theta\ \text{ and }\ \omega=\theta-\frac{\pi}{4}\tag{25}$$

by Eq. (11). Further, along the curve $\Gamma-$ in the stress plane the following relation holds (Fig. 6):

$$\frac{d\sigma_x}{d\tau_{xy}}=\tan\omega\,.\tag{26}$$

Eqs. (25) and (26) are solved to give:

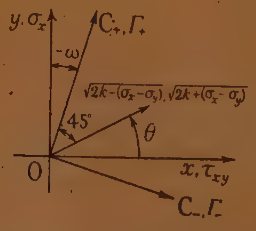

Fig. 6. Simple waves in the plastic flow.

$$\left.\begin{aligned}\sigma_x&=k\sin2\omega-2k\omega+h\,,\\ \sigma_y&=-k\sin2\omega-2k\omega+h\,,\\ \tau_{xy}&=k\cos2\omega\,,\end{aligned}\right\}\tag{27}$$

where h is a constant of integration.

Lastly, let us search for the isostatics generally when arbitrary one of them is given by the equations:

$$x=a(\sigma),\quad y=b(\sigma).\tag{28}$$

Since the slopes of the isostatics are given by $dy/dx=\tan\theta$, the following relation exists for the boundary isostatics expressed by Eq. (28):

$$\tan\theta=\frac{db}{d\sigma}\Big/\frac{da}{d\sigma}=\text{the function of }\sigma\,.\tag{29}$$

Therefore, we can solve θ as a function of σ from Eq. (29), and subtracting $\pi/4$ from this θ we obtain ω as a function of σ. Then substituting $\omega+\pi/4$ into θ of the equation:

$$\sin\theta\frac{\partial x}{\partial\sigma}-\cos\theta\frac{\partial y}{\partial\sigma}=o\,,\tag{30}$$

which stands for arbitrary isostatics, we obtain the relation:

$$(\sin\omega+\cos\omega)\frac{\partial x}{\partial\sigma}+(\sin\omega-\cos\omega)\frac{\partial y}{\partial\sigma}=o\,,\tag{31}$$

and using $\partial x/\partial\sigma$ and $\partial y/\partial\sigma$ obtained by differentiating Eq. (23) we can transform Eq. (31) into:

$$\frac{dr}{d\sigma}+r\frac{d\omega}{d\sigma}=o\,,\tag{32}$$

which is easily integrated to give:

$$r=R\exp(-\omega)\,,\tag{33}$$

where R is a constant of integration. Substituting Eq. (33) into Eq. (23) the equation of the isostatics is obtained as follows:

$$\left.\begin{aligned}x&=a(\sigma)-R[\exp(-\omega)]\sin\omega(\sigma),\\ y&=b(\sigma)+R[\exp(-\omega)]\cos\omega(\sigma).\end{aligned}\right\}\tag{34}$$

§ 8. Simple waves of the plastic flow being completely solved, we show in this paragraph those of the supersonic flow. The method of solution is all the same as before, and so it is sufficient for us here only to describe the equations corresponding to Eqs. (23)~(34) in the preceding paragraph.

Assuming the equation of the family of straight lines representing Mach lines as follows:

$$x=a(\sigma)-r\sin\omega(\sigma),\quad y=b(\sigma)+r\cos\omega(\sigma),\tag{23′}$$

slopes of Mach lines (23′) become:

$$\frac{dy}{dx}=\tan\left(\frac{\pi}{2}+\omega\right).\tag{24′}$$

On the other hand, the slopes of stream lines and the relation between ω and θ are:

$$v/u=\tan\theta\,,\quad \omega=\theta-\pi/4,\tag{25′}$$

and along the curve $\Gamma-$ in the hodograph plane the following relation holds (Fig. 7):

$$\frac{dv}{du}=\tan\omega\,.\tag{26′}$$

From Eqs. (25′) and (26′) we obtain the required solution for the velocity of fluid on

Mach lines:

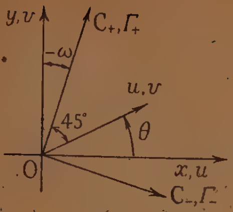

Fig. 7. Simple waves in the supersonic flow.

$$\left.\begin{aligned} u &= Ue^{-\omega}(\cos\omega - \sin\omega), \\ v &= Ue^{-\omega}(\cos\omega + \sin\omega), \end{aligned}\right\} \qquad (27')$$

where U is a constant of integration.

Secondly, when arbitrary one of the stream lines is given by the equation:

$$x = a(\sigma), \quad y = b(\sigma), \qquad (28')$$

and the slopes of the boundary stream line (28′) become:

$$\tan\theta = \frac{db}{d\sigma} \bigg/ \frac{da}{d\sigma} = \text{the function of } \sigma. \qquad (29')$$

Therefore, ω may be expressed as a function of σ.

On the other hand, the following relation holds for arbitrary stream lines:

$$\sin\theta \frac{\partial x}{\partial\sigma} - \cos\theta \frac{\partial y}{\partial\sigma} = o, \qquad (30')$$

which is transformed into:

$$(\sin\omega + \cos\omega)\frac{\partial x}{\partial\sigma} + (\sin\omega - \cos\omega)\frac{\partial y}{\partial\sigma} = o, \qquad (31')$$

and using $\partial x/\partial\sigma$ and $\partial y/\partial\sigma$ obtained by differentiating Eq. (23′) the differential equation of the abscissa on Mach lines is given by the following:

$$\frac{dr}{d\sigma} + r\frac{d\omega}{d\sigma} = o. \qquad (32')$$

Integration of this equation gives:

$$r = R\exp(-\omega), \qquad (33')$$

where R is a constant of integration, and substituting Eq. (33′) into Eq. (23′) the equation for the stream lines is obtained finally as follows:

$$\left.\begin{aligned} x &= a(\sigma) - R[\exp(-\omega)]\sin\omega(\sigma), \\ y &= b(\sigma) + R[\exp(-\omega)]\cos\omega(\sigma). \end{aligned}\right\} \qquad (34')$$

VI. Conclusions.

§ 9. The two-dimensional isostatical problem in the theory of plasticity is discussed in this paper generally, applying the method used in the theory of supersonic flow. The flow of plastic materials corresponds to that of non-viscous compressible fluid having the special type of pressure-density relation $p/\log\rho$ = constant and all the same local Mach number $\sqrt{2}$ throughout it.

Slip-lines, isostatics and boundary curves in the plastic flow correspond to Mach lines, stream lines and shock waves in the supersonic flow respectively. We have shown the method of solving these three curves from the given stress distributions and also the method of solving stress distributions when one of the three curves is given on the contrary.

Lastly, the case of simple waves being discussed, the method of solving stress distributions on them is shown together with the method of obtaining isostatics or stream lines when arbitrary one of them are given.

JOURNAL OF THE PHYSICAL SOCIETY OF JAPAN Vol. 6, No. 6, NOV.—DEC., 1951

A New Method of Measuring the Ion Current of Mass Spectrometers

By Itaru NONAKA

Department of Physics, Faculty of Science,
Kyusyu University, Fukuoka

Shinpachi HIRASAWA & Kazushige TSUTSUMI.

Matsuda Research Laboratory, Tokyo-Shibaura Electric Co.
Kawasaki

(Read March 3, 1950; Received April 30, 1951)

In most mass spectrometers the ion current received by the collector is measured by D. C. amplifiers, but it is preferable to use A. C. amplifiers, if possible, because in A. C. amplifiers there is no zero point drift and the number of stages can be easily increased.

We have intended to use an A.C. amplifier in a mass spectrometer of Nier type. The ion current was made alternating by making the potential of the first slit which pulls out the ions from the ion source to have a rectangular form of −4 volts and +1 volt relative to the ion source chamber. The ion current amplified by a three stage A.C. amplifier of 110 db was rectified and then measured by a D.C. milliammeter of 1 mA full scale. The amplifier operated very stable and the current amplification factor was about 0.7×10^{10}, the minimum ion current detectable at the collector being about 1.5×10^{-15} amperes.

§1. Introduction and the Principle of the Method.

In most mass spectrometers the ion current received by the collector is measured by D.C. amplifiers.[1][2] But it is preferable to use A.C. amplifiers, if possible, because in A.C. amplifiers there is no zero point drift and the number of stages can be easily increased.

From the above point of view, we have intended to use an A.C. amplifier in a mass spectrometer of Nier type constructed for the purpose of analysing the impurities in rare gases. To use A.C. amplifiers in mass spectrometers, the collector current must be made alternating. There will be many methods of realizing this, but it is considered to be the best method that the ion current is made alternating at the ion source, because the ion source and the collector are sufficiently separated in space and electrically, so any A.C. potential used in the ion source will induce no disturbance in the collector circuit.

The arrangements of the ion source and the collector of our mass spectrometer are shown schematically in Fig. 1. As a method of

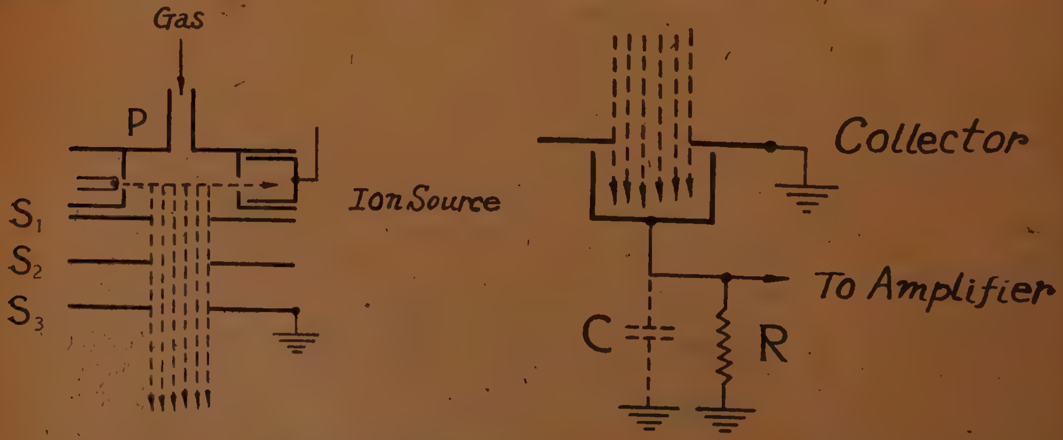

Fig. 1. Arrangements of ion source and collector.

making the ion current to be A.C., the potential of the slit S$_1$ was made to have a rectangular form of -4 volts and $+1$ volt relative to the ion chamber P. In the phase when S$_1$ is -4 volts ions are pulled out from the ion chamber, and in the phase when S$_1$ is $+1$ volt the ion current is stopped. Then the ion current reaching to the collector is considered to have a rectangular form shown in Fig. 2, (2). But the potential of the collector will have a form shown in Fig. 2, (3), because of its distributed capacity C and the high resistance R inserted in the grid circuit of the amplifier. This alternating potential of the collector can be amplified easily by an A.C. amplifier and its output can be measured by a D.C. milliammeter after being rectified. The time constant RC of the input circuit is considered to be about 10^{-2} sec, when 8×10^8 ohm is used as R, so the frequency of the rectangular potential should not be higher than about 50 cycles per second.

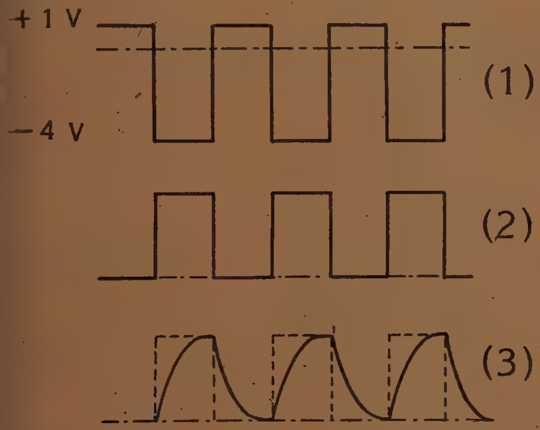

Fig. 2. (1) Potential of S$_1$ relative to ion chamber P.
(2) Collector current.
(5) Collector potential.

§2. Construction of the Mass Spectrometer.

Our mass spectrometer is all metal Nier type one[1] as shown in Fig. 3. Arrangements of the ion source and the collector are shown in Fig. 4, (A) and (B). The dimensions of the slits are as follows,

S$_1$; 1 mm×10 mm, S$_2$; 1 mm×10 mm,
S$_3$; 0.2 mm×10 mm, S$_4$; 1 mm×12 mm,
S$_5$; 3 mm×14 mm, S$_6$; 2 mm×12 mm.

The slit S$_2$ serves as a focusing electrode. S$_5$ was initially intended to be used as a suppressor[2] to reduce the low energy background ions, but as we used an A.C. amplifier any minute ripples in the potential supplied to this slit induced a large disturbance in the amplified ion current, we abondoned, therefore, this initial intention and connected it to earth potential.

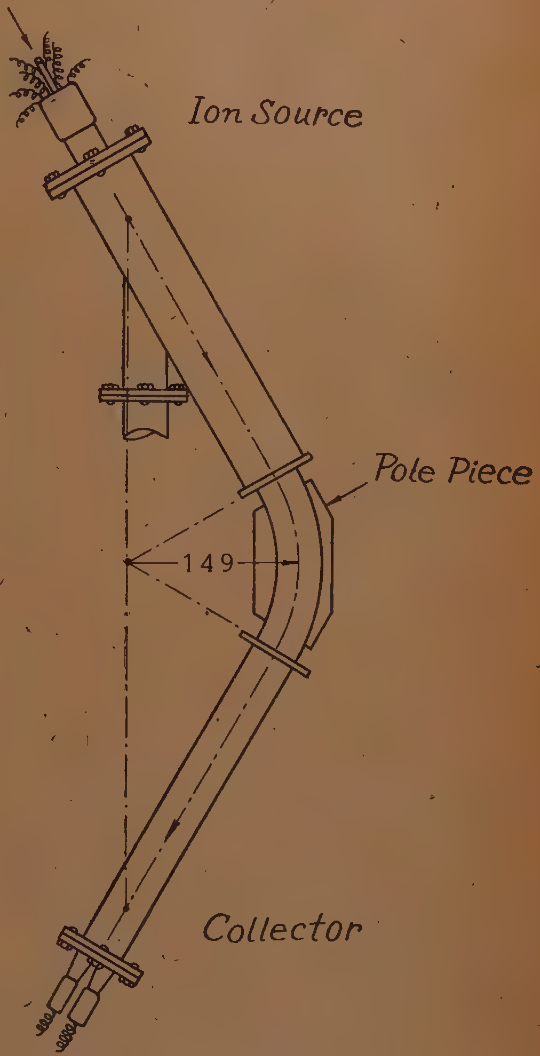

Fig. 3. Mass spectrometer body.

Evacuation was performed by a glass Hickman pump of 6 cm diameter, and the pressure was about 1×10^{-6}mm Hg when no sample gas

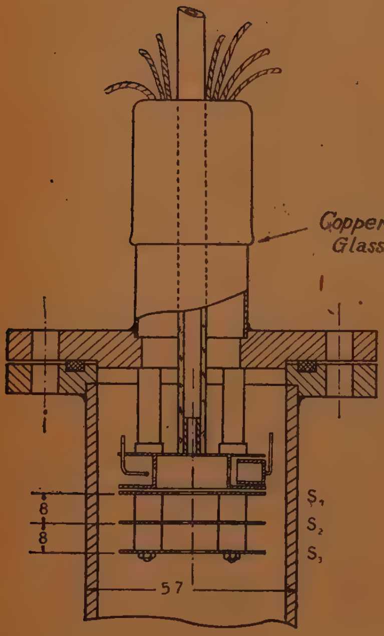

Fig. 4 (A). Ion source.

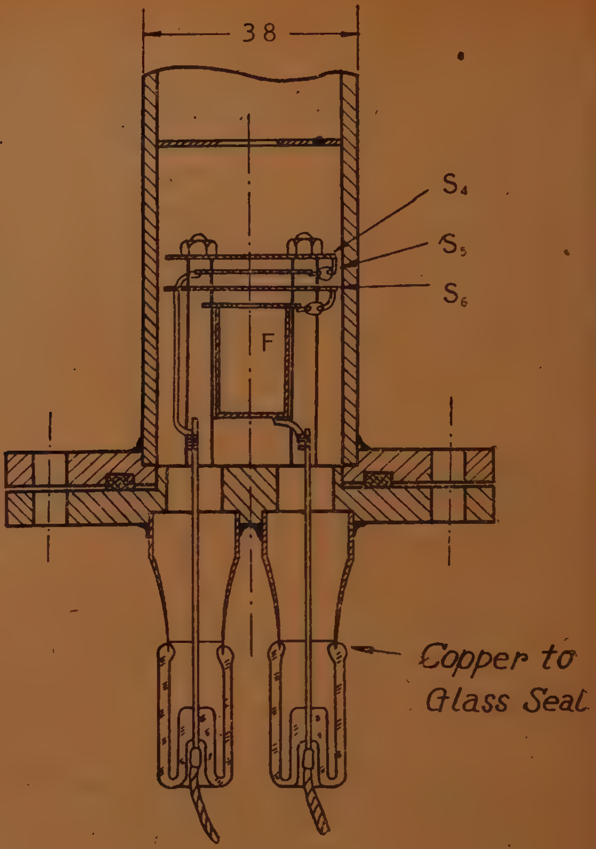

Fig. 4 (B). Collector.

flowed, and this rose to about 2×10^{-5} mm Hg when sufficient sample gas was flowing.

The pole face of the electromagnet is shaped as shown in Fig. 3, and the core has a form of rectangular cross section of 150 mm × 70 mm in dimension. The gap between the pole pieces is 15 mm, and the total winding of the two coils is 2294 turns of B.S. No. 11 wire. The current was supplied by two 6 volts batteries in series and about 3500 gauss was obtained at 2 amperes.

§ 3. Rectangular Wave Generator.

The diagram of the electric circuits for ion source is shown in Fig. 5. Most of them consist of ordinary stabilized circuits.

The rectangular wave generator circuit for pulling out ions from the ion source is shown in Fig. 6. A sinusoidal wave of 50 cycles per sec. and of about 80 volts is fed into the control grid of UZ-57, then this is converted into a rectangular wave of about 100 volts by the saturation property of the tube. This rectangular wave potential was divided adequately to give −4 volts and +1 volt on each side of zero line respectively.

§ 4. Amplifier.

(i) Amplifier circuit.

We used a three stage A.C. amplifier as shown in Fig. 7. The amplified A.C. ion current is rectified by two 6H6 rectifier tubes and is smoothed by a 8μF capacitor and a 100 kΩ resistor and then measured by a milliammeter of 1 mA full scale. The amplification factor is controled at the input of the second stage as 1/1, 1/2, 1/10 and 1/100.

To reduce the noise originated at the first tube we introduced a low pass filter of π-type between the second and the third stage. The cut off frequency of this filter was taken as 800 cycles per second. The filament current of the amplifier tubes was supplied from a 6 volts battery, and the plate voltage was supplied

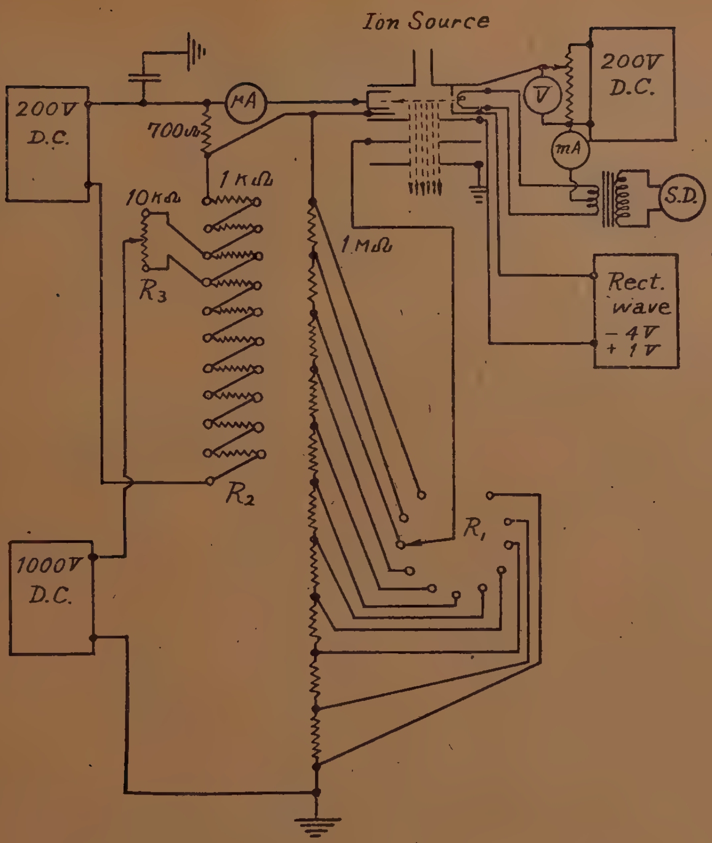

Fig. 5. Diagram of the electric circuits for ion source.

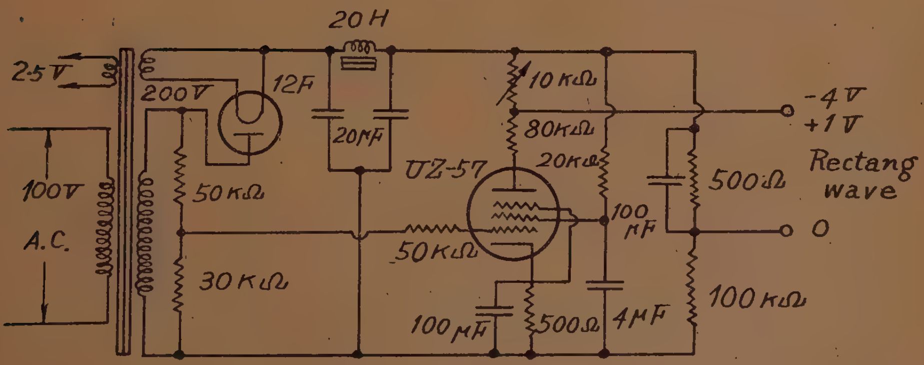

Fig. 6. Rectangular wave generator.

from a stabilized D.C. source of eliminator type.

(ii) Linearity.

The linearity of the amplifier was tested as follows; A half wave rectified A.C. potential of about 2 volts was stepped down as low as 1/10,000 of its original value by a potentiometer and supplied to the slit S_5. Through the distributed capacity between S_5 and the Faraday cage F, the above A.C. potential is induced to some extent to the input circuit of the amplifier. The output current as a function of the potentiometer tap will indicate the linearity character of the amplifier. The result

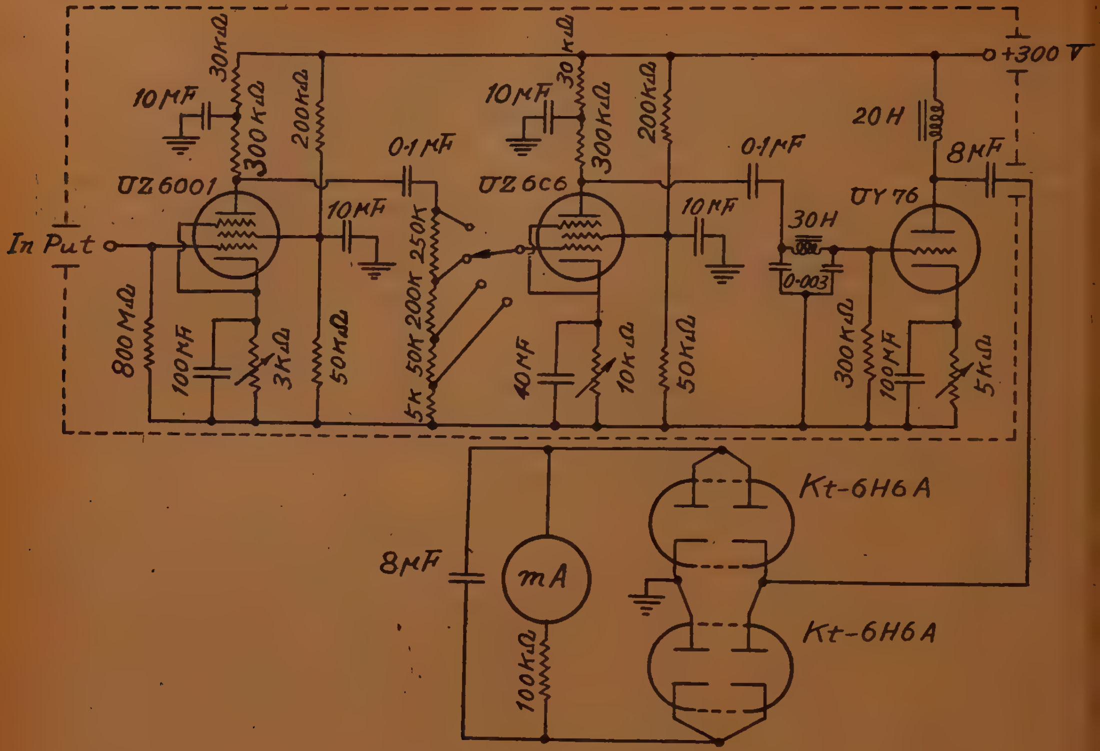

Fig. 7. Amplifier circuit.

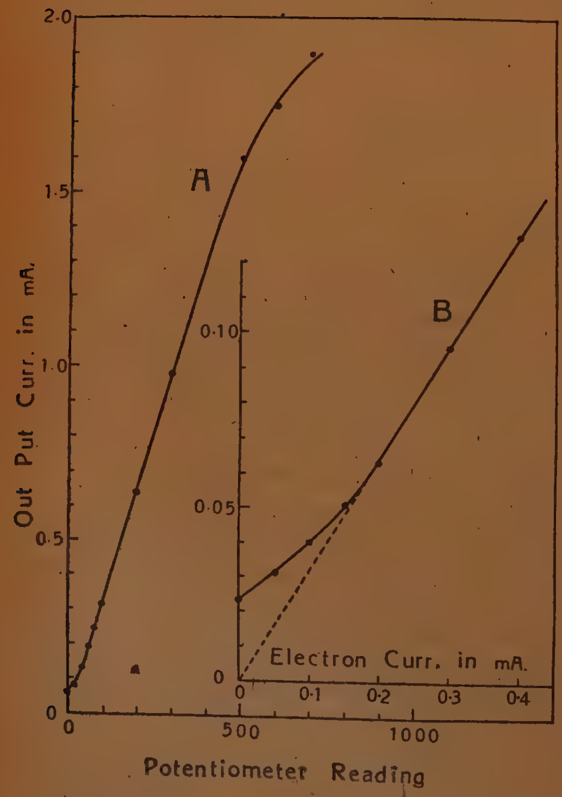

Fig. 8. Linearity of the amplifier.

of the measurement was as shown in Fig. 8, Curve (A). Except for the inital part of the curve, it is sufficiently linear as far as 1.5 mA of the output current.

The initial part of the curve was investigated in detail by another method. Namely, the spectrometer ion current was measured as a function of the electron emission current of the ion source. The result was as shown in Fig. 8, Curve (B). The noise current, when no input exists, is 0.025 mA and the output current approaches asymptotically to a straight line which passes through the zero point. The curve is practically a straight line above 0.055 mA of the output current.

The above character of the initial part of the curve can be easily understood theoretically, because the average frequency of the noise is far higher than that of the input signal (50 cycles per sec.) and the effect of the noise is considered not appear in the rectified D.C. current when the amplitude of the signal is greater than twice of that of the noise.

(iii) Amplification factor.

The voltage amplification factor of this amplifier was measured by feeding a small A.C.

signal of 0.94×10^{-4} volts into the input circuit and measuring the output voltage of the third stage to be about 40 volts, This corresponds to about 110 db of voltage amplification.

The current amplification factor including the rectifier and the measuring circuit was known to be about 0.7×10^{10}. As the minimum current detectable in the output is about 0.005 mA considering the fluctuation of the noise, the minimum ion current detectable in the collector is about 1.5×10^{-15} amperes.

§ 6. Characteristic of the Spectrometer.

(i) Effect of the Focusing Slit S_2.

When the potential of the focusing slit S_2 is varied between zero and the total accelerating potential V_0, the collector current varries as shown in Fig. 9. The maximum usually appears at $V(S_2)\approx0.8V_0$.

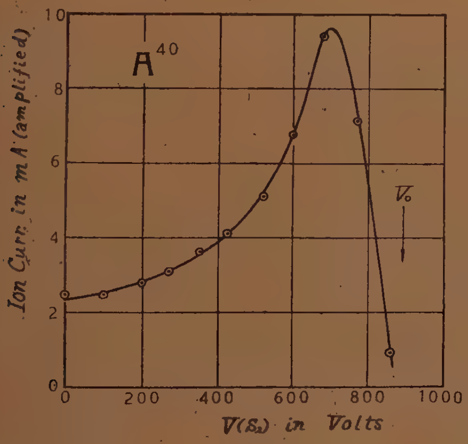

Fig. 9. Effect of the slit S_2.

(ii) Resolving Power.

Several examples of mass spectra obtained by the potential scanning method are shown in Fig. 10, 11 and 12. Fig. 10 and 11 are the spectra of mass from 17 to 71 produced by the residual gas in the spectrometer. The spectra of mass mass 17, 18, and 28 are much reduced after long evacuation, but the others are maintained almost constant, so the latters are considered to be produced by the vapour of pumping oil. Fig. 12 is the spectra of $A^+(40)$ and $Ne^+(20)$ when sufficient sample gases are let flow.

In all these cases, the breadth of the spectrum at half maximum $(\Delta V)_{1/2}$ is about 5 volts.

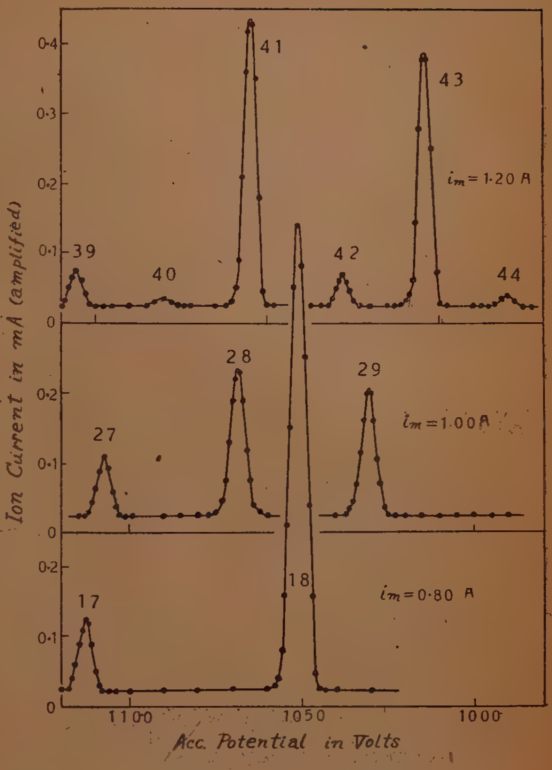

Fig. 10. Spectra of mass from 17 to 44.

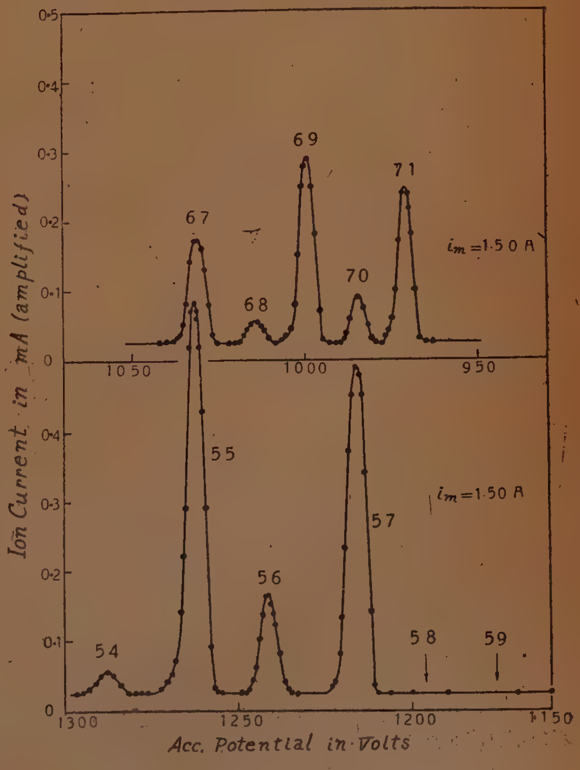

Fig. 11. Spectra of mass from 54 to 71.

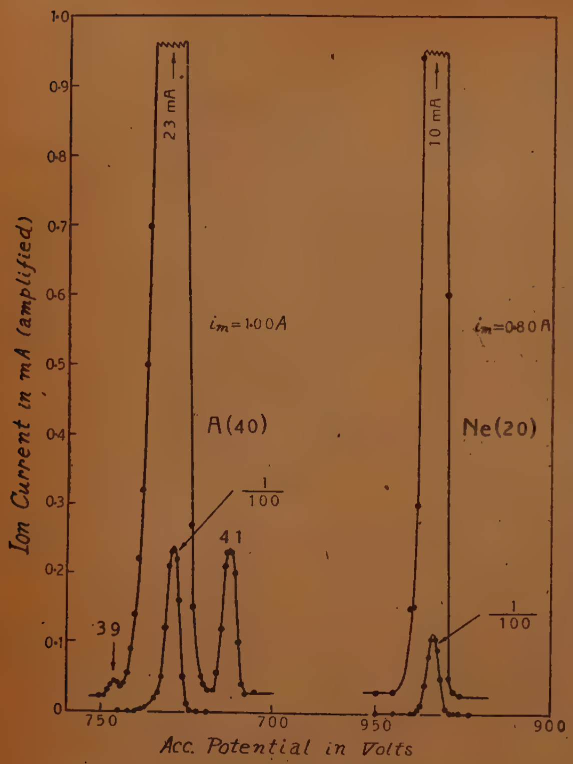

Fig. 12. A$^+$(40) and Ne$^+$(20) when sufficient sample gases are let flow.

Then the resolving power $M/\Delta M = V/(\Delta V)_{1/}$ is known to be about 200 at $V=1000$ volts. This value of the resolving power is comparatively good when we consider the dimensions of the spectrometer.

§ 7. Conclusion.

A new method of measuring the ion current of a mass spectrometer by an A.C. amplifier was attempted and a good result was obtained. A.C. amplifiers are much easier in design and in operation than D.C. amplifiers usually used for his purpose. An A.C. amplifier whose amplification band is much narrower than the one tested by us will give a more good result because of its low noise character.

This work is indebted to the Ministry of Education for the Scientific Research Expenditure.

References.

1) A.O. Nier: Rev. Sci. Inst. **18** (1947), 398.
2) A.O. Nier, C.M. Stevens, A. Hustruld and T.A. Abott: J. Appl. Phys. **18** (1947), 30.

JOURNAL OF THE PHYSICAL SOCIETY OF JAPAN, Vol. 6, No. 6, NOV.—DEC., 1951

Crystallization and Melting of Linear High Polymers as Rate Processes.

By Akiya OOKAWA.

Department of Physics and Chemistry,
Gakushuin University, Mejiro, Tokyo.

(Received May 9, 1951.)

It is characteristic with the crystalline solid of linear high polymers that the regular crystalline regions and the irregular entangled regions are mixed to form the spherulitic particles. Founded on this picture, the rate of crystallization is estimated as a function of the crystallization temperature, in line with the usual treatment on the formation of a new phase. The melting temperature in the process of heating the crystallized specimen at uniform rate is determined, on the supposition that melting is observed at temperature where the rate of melting becomes comparable with the heating rate. The theoretical results are fairly in accord with the observations on natural raw rubber. Some discussions are included relevant with the appropriateness of the model.

§ 1. Introduction.

The crystallization and melting of natural raw rubber have been investigated by Wood and Bekkedahl[1], observing the change of volume as a measure of the extent of crystallization. The main result was that the rate of crystallization had a maximum value at about −25°C and that the melting range of crystallized rubber was determined by the temperature of crystallization. The purpose of the present article is to give an explanation to these observations, without the assumption of many forms of crystalline rubber.

§ 2. Nature of the Crystal.

The dimension of a regular crystalline region in the crystalline solids of linear high polymers is much smaller than the dimension of a macromolecule. Each macro-molecule therefore belongs to many crystalline regions, which in return are expected to form the so-called fringed micelles. From the ther-modynamical viewpoint, a crystalline region amidst amorphous surroundings is in a metastable equilibrium, as one has a gain in the free energy by displacing the boundary surface into the amorphous region. However it is to be noted that, to effect the regular alignment of amorphous segments at the boundary, the statistical entanglement of the macro-molecules is progressively concentrated at the boundary. In these circumstances, the rate of growth of a crystalline region above certain limiting size may be negligibly small under normal conditions, because the rearrangement of the more entangled segments requires the larger activation energy. This is sustained by the observation[2] that in the case of rubber the limiting size of a regular crystalline region is nearly independent of the conditions of crystallization. These affairs are characteristic with the macro-molecular crystals and find no correspondency in the case of low molecular crystals, where the growth of a regular region does not effect any enhancement of irregularities at the boundary surface.

Many specimens of the crystalline solids of linear high polymers show the so-called spherulitic structure[3]. The molecular process of forming this peculier structure is not yet evident. The resemblance between the spherulitic structure of polymer solids and the polycrystalline structure of normal solids suggests, however, that each spherulitic particle originates from each centering region acting such as a crystallization nucleus does in the formation of a single-crystalline domain. The formation of each spherulitic particle as mixture of regular crystalline regions and irregular entangled regions is in accord with the formation of each crystalline region, when one suppose that, by regular alignment of a region, some next neighbouring comparatively ordered region is brought into regular alighment. In other words one can suppose that the effect of regular alignment is transferred through the region occupied by the much more entangled segments, because the entanglement of segments inhibits the random thermal motion of neighbouring segments. This patchy crystallization, so to say, proceeds with some average velocity, leaving entangled regions behind, until the spherulitic particles originating from each center come into contact with each other to cover the total volume.

The final degree of crystallization, measured by the decrease of volume, is estimated almost constant independent of the crystallization temperature[1]. It can be concluded therefrom that the ratio of the total volume of crystalline regions and that of entangled regions is nearly constant. If one suppose as above stated that the limiting size of each crystalline region is determined statistically indifferent to the crystallization condition, the average number of crystalline regions in unit volume must be constant irrespective of the crystallization temperature. In these conditions one can treat the spherulitic particles as a kind of new phase of a constant average structure, independent of the temperature. A spherulitic particle amidst amorphous surrounding is shown schematically in Fig. 1.

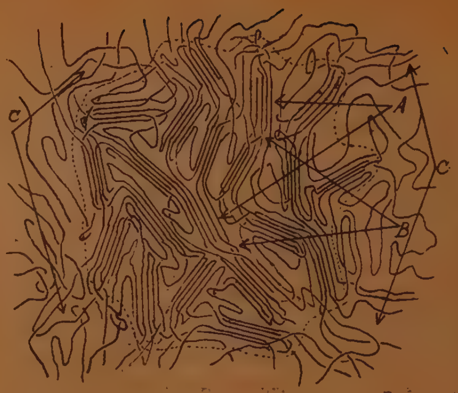

Fig. I. Schematic representation of a spherulitic particle, amidst amorphous surrounding. A: Regular crystalline region (crystallite). B: Irregular entangled region (quasi-crystalline region). C: Irregular amorphous region.

§ 3. Crystallization Curve.

A polymer system is kept at a constant temperature below its crystallization temperature. The total volume V occupied by the spherulitic particles is to be estimated in the dependence with the time.

The size distribution of the spherulitic particles is usually not uniform, the particles generated at earlier stage being greater and the ones generated at later stage smaller. On the other hand, the regions not yet occupied by the particles decrease progressively with the crystallization process. This has the effect of progressive decrease of the rates both of nucleation and of growth of the spherulitic particles.

Not to complicate the treatment, we discount for the moment the effect of the size distribution of the spherulitic particles. Then the system can be represented by the total number n and the average volume v of the particles, such as to give

$$V=nv=(4\pi/3)na^3. \tag{1}$$

We put the rate of nucleation dn/dt and the velocity of linear growth da/dt to

$$dn/dt=k_1(V_0-V)/v_1\,, \tag{2}$$

$$da/dt=k_2l_2(V_0-V)/V_0, \tag{3}$$

where V_0 is the total volume and v_1 and l_2 are an elementary volume and an elementary length, respectively for the two rate processes. k_1 and k_2 are the respective intrinsic rate constants at the initial stage, $V=0$, where the interaction of the particles is negligibly small. The decrease of the two rates with the progress of crystallization is assumed in common linearly proportional to the volume, V_0-V, left available for further crystallization.

By virtue of Eqs. (2) and (3), we have the simple relation

$$k_2l_2v_1dn/dt=k_1V_0da/dt\,,$$

or, with the initial condition

$$t=0;\quad n=0,\quad a=0, \tag{4}$$

$$a=(k_2v_1l_2/k_1V_0)n. \tag{5}$$

For the sake of simplification, we further assume the relation

$$v_1=(4\pi/3)l_2^3. \tag{6}$$

Then we have

$$2\tan^{-1}\left(\frac{n}{n_0}\right)+\log\left(\frac{n_0+n}{n_0-n}\right)=(k_1k_2{}^3)^{1/4}t\,, \tag{7}$$

where

$$n_0=(k_1/k_2)^{3/4}(V_0/v_1) \tag{8}$$

is the total number of particles at final stage. The average volume of particle increases with time according to (cf. Eq. (5)).

$$v=(n/n_0)^3v_0 \tag{9}$$

through n/n_0, where

$$v_0=(k_2/k_1)^{3/4}v_1 \qquad (10)$$

is the final average volume of a particle. The total volume V as function of time t can not be represented analytically, but it can be numerically evaluated according to

$$V=(n/n_0)^4 V_0\,, \qquad (11)$$

where n/n_0 as function of time is given by (7).

The relative number and the relative average volume of the particles depend on the ratio of the two rate constants. The larger (smaller) the rate of nucleation (the velocity of growth), the greater is the number and the smaller is the average volume, and *vice versa*. In the present approximation; however, it is remarkable that the crystallization curve, V *versus* t, is the same so long as the mean $(k_1k_2^3)^{1/4}$ is the same.

The rate of crystallization, measured by the reciprocal of the time required for one-half the total crystallization, is given by

$$\text{rate}=t^{-1}_{1/2}=C(k_1k_2^3)^{1/4}, \qquad (12)$$

where

$$C=\left\{2\tan^{-1}\left(\frac{n'}{n_0}\right)+\log\left(\frac{n_0+n'}{n_0-n'}\right)\right\}^{-1}\cong 2.14,$$

$$(n'/n_0)=(V'/V_0)^{1/4}=(1/2)^{1/4}$$

From the view point of forming the critical nucleus of the new phase, the stable particle must exceed a lower limiting critical size (see the next paragraph). This does not contradict with the initial condition (4), setting the initial average volume equal to zero. So far as the size distribution of the particles or the detailed behaviour of each particle is put out of consideration, the average volume v is to start normally from the zero value. Only the effective number n, contributing to the formation of new phase, is to be controlled by an energetic condition statistically.

§ 4. Rate of Crystallization.

The rate of crystallization is to be estimated in the dependency with the temperature of crystallization. The two rate constants are given by

$$\left.\begin{aligned} k_1&=B_1\exp(-A/kT),\\ k_2&=B_2\exp(-\bar{Q}/kT),\end{aligned}\right\} \qquad (13)$$

where B_1 and B_2 are the respective frequency factors. $\bar{Q}$ is the average activation energy determining the growth of the spherulitic particle. This is almost independent of the temperature. A is the energy required for the activation of an initial spherulitic particle of critical size. The temperature dependency of the latter quantity can be estimated quasi-thermodynamically.

We put the free energies per unit volume of the regular crystalline region and of the irregular amorphous region, respectively, to

$$f_c=e_c-Ts_c\,,\quad f_a=e_a-Ts_a\,; \qquad (14)$$

e and s are the respective internal energies and the entropies. With the irregular entangled region surrounding the crystalline region, the alignments of segments are irregular but at the same time the freedom of taking many configurations is deprived of the segments due to their mutual entanglement. It may be regitimate to approximate the free euergy of the entangled region by

$$f_g=e_a-Ts_c\,. \qquad (15)$$

The average quantities $\bar{f}$, $\bar{e}$ and $\bar{s}$ appropriate to the spherulitic particle are constant volumetric means of f_c and f_g, e_c and e_a, s_c and s_c, respectively. The difference between the amorphous phase and the spherulitic phase is given by

$$\begin{aligned} f'&=f_a-\bar{f}=(e_a-Ts_a)-(\bar{e}-T\bar{s})\\ &=(T_0-T)(s_a-s_c), \end{aligned} \qquad (16)$$

where the temperature T_0 defined by

$$e_a-\bar{e}=T_0(s_a-\bar{s}) \qquad (17)$$

is the equilibrium temperature between the two phases. In the same way we define the positive difference

$$\begin{aligned} f''&=f_g-f_a=(e_a-Ts_c)-(e_a-Ts_a)\\ &=T(s_a-s_c); \end{aligned} \qquad (18)$$

which contributes to the apparent surface energy of the spherulitic particle.

Below the equilibrium temperature, $T<T_0$, we have, in the process of forming a spherulitic particle amidst amorphous surrounding, volumic energy gain by f' and surface energy loss by f'' per unit volume (refer to Fig. 1). The net increase of the free energy by forming a spherulitic particle of radius a is given by

$$\Delta F=4\pi a^2 lf''-(4\pi/3)a^3f'\,; \qquad (19)$$

l is the depth of quasi-crystalline layer on surface of the particle. In order to form a stable new phase, we must accordingly activate the system up to the state corresponding to maximum ΔF. Putting the critical size

$$a^*=2lf''/f'=2lT/(T_0-T) \qquad (20)$$

derived from the condition

$$\partial\Delta F/\partial a=0 \qquad (21)$$

into (19), we have

$$A=\Delta F_{\max}=(16\pi/3)l^3(f''^3/f'^2). \qquad (22)$$

Introducing Eqs. (16) and (18), it follows

$$A=D\frac{T}{T_0}\frac{T^2}{(T_0-T)^2}, \qquad (23)$$

where

$$D=(16\pi/3)l^3T_0(s_a-s_c). \qquad (24)$$

This is the aimed relation between the energy A and the crystallization temperature T.

Substituting (13) into (12), we obtain rate of crystallization

$$=C(B_1B_2^3)^{1/4}\exp\left(-\frac{A+3\overline{Q}}{4kT}\right), \qquad (25)$$

which manifests the temperature dependency of the rate of crystallization. The three unknown constants $\overline{Q}$, D and T_0 can be chosen to fit the observation[1]. In order to obtain maximum rate at near −23°C and half-maxima at near −35°C and at near −13°C, we can decide as follows:

$$\left.\begin{aligned}\overline{Q}&=33{,}000\ \text{cal/mol},\\ D&=\ 1{,}100\ \text{cal/mol},\\ T&=\ 320\ ^\circ\text{K}.\end{aligned}\right\} \qquad (26)$$

The numerically evaluated rates are tabulated in Table 1 (see also Fig. 2). The full line in Fig. 2 is the theoretical curve and the observed data are reproduced by the points.

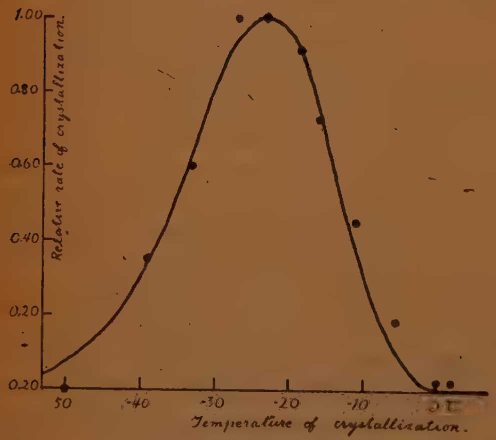

Fig. 2. Relative value of the rate of crystallization at different temperatures of crystallization. The full line is the theoretical curve estimated by (23) and (25). The experimental data are reproduced by the points.

In order to have a rate of crystallization in correct order of magnitude with the observation, Eq. (25) is compared with the absolute value at −23°C, where $t_{1/2}$ is of order of a few hours. We have accordingly

$$(B_1B_2^3)^{1/4}\cong e^{55.41}\times 60\times 60\cong 10^{27}. \qquad (27)$$

§ 5. Melting Process.

Melting range of crystallized raw rubber is estimated[1] by the observation of the volume change in process of heating the crystallized specimen at uniform rate (see Fig. 3). The melting begins at temperature several degrees above the crystallization temperature, yet far below the true equilibrium temperature, $T_0=320$°K. This is due to the melting of spherulitic particles generated at latest stage of crystallization. According to the treatment in § 4, the smallest spherulitic particle stable at temperature T has a radius a just above the critical radius a^* given by (20). These particles become unstable at temperature $T+\Delta T$, as the then stable particles must have a radius $a^*+(da^*/dT)\Delta T$, where da^*/dT is positive. On the same line, the observation on the recrystallization is easy to understand qualitatively, when one takes account of the growth of large stable particles in cost of the diminution of small unstable particles. However we must postpone further quantitative consideration on the problem, as we have started on the assumption of uniform size distribution.

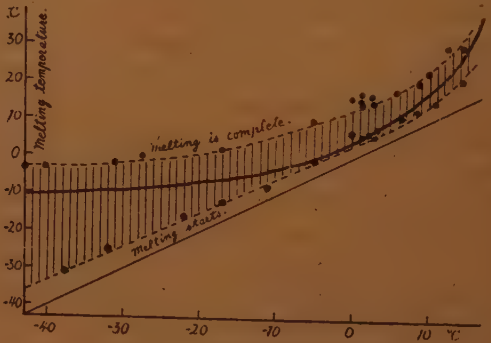

Fig. 3. Melting range of crystallized rubber as a function of the temperature of crystallization. The full line represents the temperatures estimated according to (33), where the specimen composed of uniform-sized particles melts.

On the other hand, the temperature, at which the rate of melting is great, will be relevant with the behaviour of the bulk of the spherulitic particles. In regards of the above experimental conditions, it may be regitimate to interpret the melting temperature thus estimated to be controlled by some rate processes. On the assumption that the melting temperature is that point where the rate of formation of amorphous region is comparable with the rate of heating, we can derive the dependency of the melting temperature on the crystallization temperature.

The velocity of linear growth of amorphous phase is at first controlled by the average rate constant k_2, defined in § 3. Secondly, we must take account of the detailed structure of the spherulitic particles as mixture of regular crystalline regions and the irregular entangled regions. For the melting to proceed, accordingly, it is required for the irregular regions to be disentangled. The characteristic rate constant k_3 for the disentanglement has a form

$$k_3 \doteq B_3 \exp(-Q/kT) \qquad (28)$$

with appropriate activation energy Q. The activation energy Q is, as will be shown later, expected to depend on the temperature of crystallization.

Suppose a crystallized specimen in a metastable equilibrium at a constant temperature T_m. If one increase the temperature by ΔT_m, the time t_m required for the corresponding volume change due to melting to occur will be estimated, at least in order of magnitude in analogy with (12), by

$$t_m^{-1} \simeq (k_3 k_2^3)^{1/4} \quad \text{at } T=T_m. \qquad (29)$$

In the real case, the time t_m can not be determined directly by experiment, because the melting process is likely interfered with accompanying recrystallization process. It may be not too absurd, however, to estimate t_m of order of minutes at temperatures where the melting does occur. Putting Eqs. (13) and (28) into (29), we have a relation

$$t_m^{-1} = (B_3 B_2^3)^{1/4} \exp\left(-\frac{Q+3\bar{Q}}{4kT_m}\right) \qquad (30)$$

between the melting temperature T_m and the activation energy Q.

Now, the activation energy Q, characteristic for the disentanglement in the irregular regions, depends on the crystallization temperature T_c in the following manner. Although the dimension of each regular crystalline region remains substantially constant, segments in the surrounding irregular region tend to rearrange themselves as much as possible by the respective crystallization process. It will be regitimate to assume that the rearrangement proceeds so much as the characteristic activation energy Q increases to satisfy the relation

$$k_3 \simeq t_{1/2}^{-1} \simeq (k_1 k_2^3)^{1/4} \quad \text{at } T=T_c, \qquad (31)$$

that is, so long as the rate of rearrangement decreases to a value comparable with the rate of crystallization. Putting Eqs. (13) and (28) into (31), we obtain

$$B_3 \exp\left(-\frac{Q}{kT_c}\right) = (B_1 B_2^3)^{1/4} \exp\left(-\frac{A+3\bar{Q}}{4kT_c}\right). \qquad (32)$$

This is the required relation, which gives Q as a function of T_c.

Table 1.

T°K	A kcal.	$\frac{A+3\bar{Q}}{4kT}$	$\frac{\text{rate}}{\text{max. rate}}$	T_m°K
220	3.67	58.78	0.034	262.2
230	5.17	57.01	0.202	262.6
240	7.46	55.86	0.638	263.8
245	9.00	55.51	0.905	264.6
250	10.96	55.41	1.000*	265.7
255	13.48	55.52	0.896	267.0
260	16.75	56.06	0.522	268.7
270	27.13	58.80	0.034	274.0
280	49.60	66.9	0.000	285.7
285	65.4	72.7	0.000	294.0
290	99.2	86.1	0.000	312.0

* Temperature, where the rate of crystallization is maximum.

Eliminating Q from Eqs. (30) and (32), we obtain the final relation between the melting temperature T_m and the crystallization temperature T_c

$$T_m = \frac{1}{a}\left(\frac{A+15\bar{Q}}{16k} - \frac{b}{4}T_c\right), \qquad (33)$$

where

$$\left.\begin{aligned} a &= \log\{(B_3 B_2^3)^{1/4} t_m\}, \\ b &= \log\{(B_1 B_2^3)^{1/4}/B_3\}. \end{aligned}\right\} \qquad (34)$$

The melting temperature T_m, estimated according to (33) with tentative values

$$a=60, \quad b=0, \qquad (35)$$

are tabulated in the last column of Table 1. The full line in Fig. 3 is the like theoretical curve.

§ 6. Discussions.

It can be seen that the rate of crystallization and the melting temperature of natural raw rubber crystallized at different temperatures are fairly in accord with the present theory. The following discussions may be useful relevant to the appropriateness of the introduced model.

As to the crystallization, the present theory predicts the same crystallization curve, V *versus* t, independent of the crystallization temperature, so long as the mean $(k_1k_2^3)^{1/4}$ or the rate of crystallization is the same. The crystallization curves observed at temperatures with equal rates of crystallization, one above and one below the temperature of maximum rate, however, differ from each other1). As was remarked in § 5, to treat the problem of recrystallization quantitatively, we must take account of the non-uniform size distribution of spherulitic particles. It is hoped in these regards to modify the treatment in § 3, so as to describe the growth of particles nucleated at different moments.

As to the melting, the melting range is reported1) definitely determined with the temperature of crystallization, indifferent to the extent of crystallization or the time available for crystallization. According to Eq. (31), the melting temperature T_m does depend on the time t_c required for crystallization, which replaces $t_{1/2}$ in (31). This is not a serious difficulty, however, because T_m is to depend logarithmically on t_c. On the other hand, the observation that the Stark rubber, crystallized further at 2°C, melts in two ranges is sustaining to the present theory. It is because the regions around crystallites formed at 2°C is expected to have a small activation energy Q while the regions around crystallites formed at above 25°C is expected to have a large activation energy Q. Concerning the problem, it may be interesting to observe the melting curve of a specimen crystallized to half an extent at near −25°C, where the rate of crystallization is large, and then quenched to about −50°C, where the rate is very small, to complete crystallization. From the view-point of the present rate theory, we expect the melting to occur in a single range, because the activation energies at final stage of the crystallites formed at two temperatures have almost the same value.

As the last, the activation energy $\bar{Q}$ required for the growth and diminution of the spherulitic particles was decided to have a value of 33,000 cal/mol. It seems rather too large as a quantity relevant with the interaction energy between the hydrocarbon chains. But it can be suggested that many kinetic units, the segments of the polymer molecule, are concerned in the elementary process of activation. Another knowledge concerning the elementary process of activation can be derived from the frequency factor. According to (27), (34) and (35), the frequency factors B_1, B_2 and B_3 can be determined, although with much roughness, to be of order of $10^{20}\sim10^{40}$ sec^{-1}. These are much greater than the atomic freqency ν, normally of order of $10^{10}\sim10^{13}$ sec^{-1}. Accordingly, when one expresses the frequency factor in the form

$$B=\nu \exp(\Delta S/k), \qquad (36)$$

the activation entropies ΔS are expected to have a great positive value. This circumstance suggests that the system of many kinetic units concerned with the elementary process can take enormous number of configurations in the activated state.

The present work is supported by the Science Research Expenditure of the Education Ministry.

References.

1) L. A. Wood, N. Bekkedahl; J. Appl. Phys. **17**, (1946) 362. L. A. Wood; "Advances in Colloid Science" **II**, (1946) 57.

2) S. D. Gehman; Chem. Rev. **26**, (1940) 203. J. E. Field; J. Appl. Phys. **12**, (1941) 23.

3) C. W. Bunn, T. C. Alcock; Trans. Faraday Soc. **41**, (1945) 317. W. M. D. Bryant; J. Polymer Sci. **2**, (1947) 547.

JOURNAL OF THE PHYSICAL SOCIETY OF JAPAN Vol. 6, No. 6, Nov.—DEC., 1951

Emission and Crystal Size of Oxide-Coated Cathodes.

By Jitsuo SHIMAZU.

Matsuda Research Laboratory, Tokyo Shibaura Electric Co., Kawasaki, Kanagawaken.

(Received August 8, 1950)

The thermionic emission and the crystal size of several oxide cathodes, BaO, SrO, double and triple oxide which were converted from equal molar carbonate solid solutions, were studied.

The thermionic emission of the oxides was measured by cathode ray tube and the crystal size were determined by the method of small angle x-ray scattering and the x-ray was measured by means of Geiger tube. For this purpose the oxide materials were stripped from the nickel sleeves and coated by a protective film.

The crystal size of oxides which were suitably converted from carbonates were found in the range from 200 to 300 angstroms except BaO. In the case of (BaSr)O, the emission and crystal size were measured at different stage of heat treatment. Especially such an oxide that was exposed to air after decomposition of carbonate and showed a very poor thermionic emission exhibited a decided crystal growth.

§1. Introduction.

The thermionic emission properties of oxide-coated cathodes have been investigated by many authors, but relatively few works have been reported on the physical structures of the oxides.[1)~9)] It is apparent that the emission properties or the electrical behaviours of an oxide cathode are directly related to certain chemical and physical structures, and the electrical characteristics of the oxides must ultimately be determined from their chemical nature and physical structure. X-ray and electron diffraction studies supplied some informations regarding the physical structure of the oxides. These studies have cleared the facts that when the solid solution of both barium carbonate or mechanical mixture of them are decomposed in vacuum during the formation of an oxide cathode, a simple conversion to the mixed oxides, BaO and SrO, took place;[1)~8)] further heating caused the formation of a true solid solution, (BaSr)O, for the entire proportion in composition of BaO and SrO at a rate which was temperature dependent. Further-more the composition of the activated cathode which was converted from an equal moler (BaSr)CO_3 was found to be relatively rich in SrO; especially near the surface of oxide cathodes, some several hundreds atomic layers thick of almost pure SrO layer was found as indicating preferential loss of BaO from the surface.[5)6)9)] There would be various factors that affect the thermionic properties of an oxide cathode. Benjamin and Rooksby[2)] found that the optimum d.c. emission was obtained from a bulk composition of about 65 mol percent SrO—35 mol percent BaO. Moreover, they found higher emission was obtained when the oxide was homogeneous throughout than when it consisted of two or more phases. Benjamin, Huck and Jenkins[4)] examined a lot of oxide cathodes which were converted from carbonates of various kinds of particle size, and reported that higher emission values of oxide cathodes were associated with small particle size carbonates which they believed to be converted to oxide particles of the same size. But this conclusion was denied by Eisenstein. Eisenstein[8)] studied the relationship between the crystal or particle size of the carbonates and that of the oxides, and found that the crystal size of the oxides depends primarily on the maximum temperature of treatment above 950°C and bears no relationship to the crystal size of the carbonate from which it is formed. Nothing has been reported about the exact correlation between thermionic emission of an oxide cathode and its crystal size.

The problem of oxide crystal size is however of great importance, because we have experienced poor thermionic emission from the oxide cathode whose crystal size seems to have suffered a severe crystal growth owing to the conditions during the formation of an oxide cathode. Of course, a few remarks has appeared in previous papers about the oxide crystal size. Benjamin and Rooksby[2] suggest, from the line breadth of Debye-Scherrer pattern, that the upper limit of (BaSr)O crystal size is 10^{-3} cm, while the lower limit is 10^{-5}cm. Eisenstein[8] reports, from the same method, that the average oxide crystal size of nearly pure BaO and SrO lies between 135 and 180 Å immediately afterwards the conversion from carbonate solid solution, (BaSr)CO_3, whereas, in the same stage from mechanical mixture of carbonates, $BaCO_3+SrCO_3$, the average crystal size of both BaO and SrO is in the range 240 to 325 Å. But values of emission from oxides are missing in these papers, nor the changes in crystal size at different stages of activation of an oxide cathode are reported.

In this paper the crystal size of various kinds of oxide cathodes and their thermionic emission are reported. In the (BaSr)O cathode, both emission and crystal size are studied at different stages of heat treatment; poisoning effect of air on the oxide cathode is also investigated. The crystal size determination was made by the method of small angle x-ray scattering, and the x-ray was measured by means of Geiger-counter.

§ 2. Small Angle X-ray Scattering.

Small angle x-ray scattering has has been employed since 1939 as a means for determining size parameters of finely-divided solids. Carbon blacks, colloidal particles and other substances have been studied by many investigators. Most of these works are based on such a theory that was developed by Guinier,[10] Hosemann[11] and Warren.[12] The theoretical investigations of this problem, together with the experiments have been studied thereafter and developed by many workers.[13] A simple theory of this method is described below.

We consider aggregates of identical spherical particles of radius R*, and limit our attention to small scattering angles. These spherical particles are arranged at random so as to have no definite inter-particle distances, and in any one of those particles the scattered small angle x-ray radiation is regarded as to be continuous. Then the amplitude of scattering from a single particles is expressed by expression (1) in electron unit assuming the electron density distribution ρ to be spherically symmetrical in the particle.

$$E=\int_0^R 4\pi r^2\rho\frac{\sin kr}{kr}dr=N\Phi(kR), \qquad (1)$$

where $k=2\pi\varepsilon/\lambda$, ε=scattering angle, λ=wavelength of x-ray, N=number of electrons per particle, $\Phi(kR)$=spherical shape function

and $$\Phi(x)=\frac{3}{x^2}\left\{\frac{\sin x}{x}-\cos x\right\}$$

Thus the relative intensity scattered by a single spherical particle is given by

$$I=N^2\Phi^2(kR) \qquad (2)$$

Moreover we assume that the x-rays scattered by each particle in the specimen become incoherent, as they are arranged at random and have sufficiently large inter-particle distances, so the total intensity of scattered x-ray will be a simple sum of the intensity scattered by a single particle. Therefore when M particles are present in the specimen, the total intensity is

$$I=MN^2\Phi^2(kR) \qquad (3)$$

This assumption corresponds to a simple case in which the multiple scattering, the interference among particles and the absorption of scattered x-rays are negligible**.

For practical use, the function $\Phi^2(x)$ is closely approximated by an error function having the same height and same area, $\exp.-(0.221x^2)$, then $$I=MN^2\exp.-[0.221(kR)^2],$$ or taking logarithm

$$l_nI=l_nMN^2-0.221R^2k^2{}^{***} \qquad (4)$$

Therefore the average particle size (R) is obtained from the slope of log I *vs.* k^2 curve.

By applying this method a single straight line is seldom obtained from plotting the relation log I *vs.* k^2, but usually a curved line is obtained from the observed values corresponding to the distribution of particle sizes in the specimen.

This method is applicable only for scattering angles which are small compared with the angle of the first Bragg line in the case of crystalline particles.

---

[*] ......cases of aggregates consisting of non-spherical particles was also calculated, but practically only the spherical shape function is useful.

[**] ......taking into account the inter-particle interference, a interference maximum appears in the I *vs.* (kR) curve.

[***] ......approximation $I=MN^2\exp.-[(kR)^2/5]$ is also used extensively.

§ 3. Experimental.

A schematic diagram of the apparatus used in determining x-ray scattering at small angles is shown in Fig. 1.

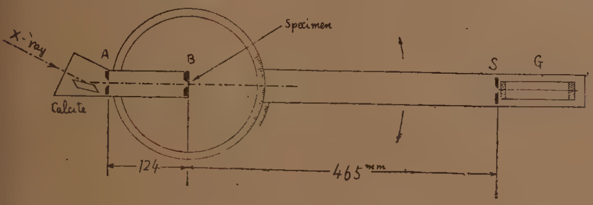

Fig. 1. Experimental alignment for small angle X-ray scattering measurement.

The Cu $K\alpha$ radiation was excited by 40 KV electrons at a current of 10mA, passed through very narrow slits, and reflected on a calcite monochromating crystal. This $K\alpha$ radiation coming from the monochro-mator was then passed through slits A and B of respective opening 0.10 by 1.5 and 0.10 by 2.5mm. These slits served both to limit the width of the primary beam and to eliminate the weaker component of the $K\alpha$ doublet. By proper alignment of the calcite crystal and the two slits, a homogeneous primary beam $K\alpha_1$ was obtained, and half width of this beam after passage through slit *B* was determined to be 1 angular minute. The scattering specimen was placed immediately behind the second slit, *B*, and the scattered radiation was observed by x-ray Geiger-counter, *G*. This Geiger detector was also found useful for alignment of the slits and selecting the irradiated position of specimen so as to be of optimum value. As it was impossible to form the oxide specimen in a homogeneous thin slab in our study and absorption of the primary x-ray beam was very strong in specimen, the optimum position for the measurement of x-ray scattering at small angles had to be chosen experimentally.

A direct reading counting rate meter was used for this purpose, then the scattered x-ray radiation was observed by means of "scale of 64" circuit. A long beaded and mica windowed Geiger-counter**** was used in this study and is shown in Fig. 2. The glass beads attached on the central string diminish the dead time of the Geiger-counter and the proportional part of counting to incident x-radiation extends (as much as 60,000 counts per minute) to the stronger irradiation of x-ray incident than that of the same dimensions and same materials but with no glass beads.[14] This Geiger-counter was mounted on a holder which was able to rotate around the center at *B*, and a slit of scanning area 0.05 by 13mm, *S*, was set immediately before the counter. The distance to scanning slit from specimen was 465 mm, and the scattered x-ray was observed at every angular minute.

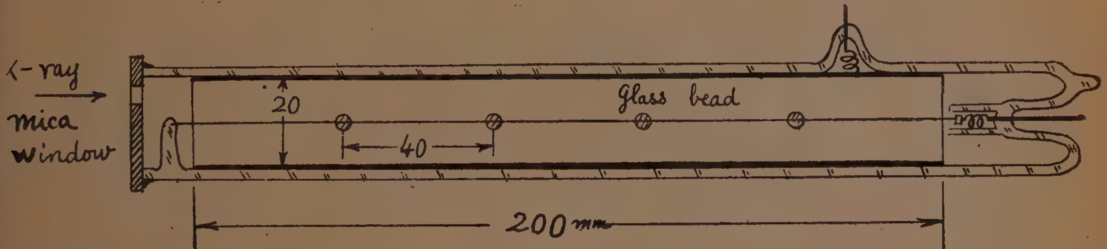

Fig. 2.

§ 4. Preparation of Oxide Samples.

We have prepared the following samples.

(a) double carbonate $(BaSr)CO_3$.

To obtain $(BaSr)CO_3$, Na_2CO_3 was added to equal molar barium nitrate and strontium nitrate aqueous solution. The temperature of precipitation was about 80°*C*. This is a carbonate solid solution which is now used extensively in commercial vacuum tubes.

(b) triple carbonate $(BaSrCa)CO_3$.

To obtain $(BaSaCa)CO_3$, Na_2CO_3 was added to equal molar $Ba(NO_3)_2$, $Sr(NO_3)_2$, and $Ca(NO_2)_2$ solution.

The temperature of precipitation was about 80°C. This triple carbonate is believed to be converted to an oxide solid solution $(BaSrCa)O$ in vacuum, as

---

**** ......filled with 152 mm Hg of Argon and 15 mm Hg of C_2H_5OH vapour.

is the case in (a). However, there is no experimental verification about this conversion.

(c) $BaCO_3$

(d) $SrCO_3$

These carbonate powders were sprayed with proper binder on nickel sleeves*****, the coated length of which was 15mm. The coated part was raised at a homogeneous temperature when the sleeve was indirectly heated in vacuum.

Each cathode was mounted in a glass bulb, a nickel cylindrical plate surrounded this cathode to measure its activity. Then each experimental diode was evacuated. Following a 60-minute baking at 300°C, cathode was heated to about 700°C and held at the temperature until the carbon residue from the coating binder was no longer visible. The heater current was then increased to maintain the sleeve temperature at about 1000°C so that the complete decomposition would take place in 10-15 minutes. Each cathode was activated to optimum condition, and the activation schedule was as follows: (1) flashed at 1370° K****** for 2 minutes, (2) then ageing at 1225° K for 20 minutes; during this ageing some 60 mA emission was drawn from the cathode.

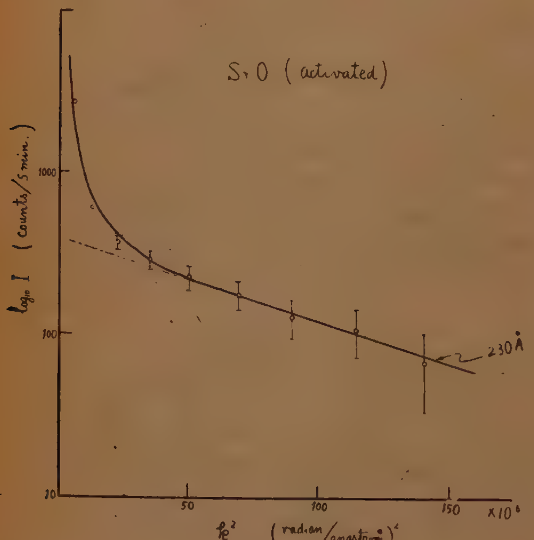

Fig. 3. (a)

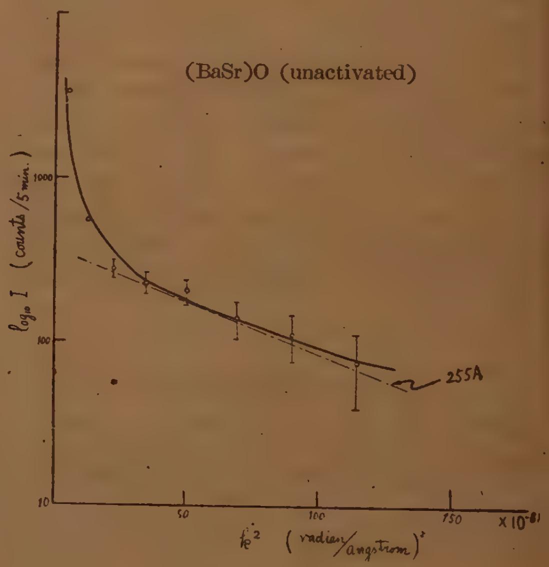

Fig. 3. (b)

The initial values of thermionic emission of the cathodes were observed by means of cathode ray tube at the testing temperature of 850°K. Finally, each cathode was prepared for x-ray examination. As is well known the alkaline earth oxides have great chemical affinities to moisture and carbon dioxide in air, so that the cathode materials must be prepared avoiding to exposure in air. A protective film technique was employed, as Eisenstein did for this purpose. The vacuum tube was opened in a air-tight glass-windowed manipulation box in which the atmosphere was maintatined chemically inert by an adequate flow of nitrogen which was carefully dried through two $CaCl_2$ drying towers and a P_2O_5 drying boat. Rubber gloves, attached to the box by the wrist bands, permitted this operation. After cracking the tube the cathode materials were stripped on a thin mica membrane and quickly coated by a protective film, polystyrene in a benzene solvent, which was thoroughly dehydrated with metallic sodium and distilled.

Poisoning effect of air to the (BaSr)O cathode was also examined from the standpoint of its crystal size. After converting the double carbonate to oxide in vacuum, the air was drawn in the bulb at the pressure of about 10^{-2} mm Hg and exposed the fresh oxide surface to this air for a few minute, then reevacuated as the usual manner. In the poisoned cathodes it seemed some permanent changes in structure should happen, for the emission of these

---

***** ......with rectangular cross section 2.4×1.2mm and 40 mm in length 99.30% Ni 0.14% Mg, 0.37% Fe etc.

****** ......these were uncorrected pyrometer temperatures.

cathodes were usually as low as $10^{-2}\sim10^{-3}$ times than that of suitably evacuated and activated oxide cathodes.

§ 5. Results and Discussion.

Some of the results are shown in Fig. 3(a) and Fig. 3(b), which are obtained for SrO and unactivated (BaSr)O respectively. In these plots the ordinates are the logarithm of counts in 5 minutes and the abscissae are k^2 in radian^2/Angstrom.[2] The observed values are shown by $\overset{\top}{\underset{\bot}{\circ}}$ in Fig. 3, and the vertical lines are the probable errors of measured points computed from the statistical fluctuations of the counting. Initially a steep decay of x-rays corresponding to the incident beam was appeared; following this the week true scattered x-rays were found to be relatively straight in log I *vs.* k^2 plots and from the slopes of the curves particle sizes were determined by the expression (4).

Because of the very strong absorption of x-ray by specimen and of the sensitivity of the detector, the weaker components of scattering that would have appeared at the larger scattering angles are missing in our observations, for which the smaller particles in the specimen would have contributed. Thus, the particle sizes determined in our study will correspond to the comparatively larger crystals in the specimen. Moreover, by this method crystal size of the order of 1000 A could not be determined. Table I shows the crystal sizes and thermionic emissions of several activated oxide cathodes.

Table I

crystal sizes and emission values of activated oxide cathodes, emissions were measured by means of cathode ray tube.

Oxides	Emission at 850°K (mA/cm^2)	Crystal Size (R) in A
(BaSr)O	98 96	325 335
(BaSrCa)O	100	230
SrO	6.4 9.3	200 230
BaO	6.9 7.3	>1000 >1000

It is seen that the crystal sizes of oxides are of the order of some hunderds angstroms except BaO. As the decomposition pressure of $SrCO_3$ is greater than that of $BaCO_3$, strontium carbonate is converted more easily than barium carbonate when heated in vacuum. Qualitatively speaking, therefore, in the single conversion processes of $BaCO_3$ and $SrCO_3$, the decomposed SrO crystals will have little chance of crystal growth compared with the BaO crystals from the standpoints of the decomposition temperature and the time duration of complete decompositions of carbonates. Of course the chemical properties of carbonate or oxide of both barium and strontium should affect and play a complicated role in conversion process.

In the case of double carbonate solid solution the conditions of conversion are more complicated. However it had been pointed out by Eisenstein that $(BaSr)CO_3$ were decomposed initially to almost pure SrO and BaO and then a true solid solution formation took place. Since the conversation of carbonate solid solution may not be regarded as a mere superposition of single carbonate decompositions of barium and strontium, it is supposed that the decomposition pressure of $(BaSr)CO_3$ lies between that of $SrCO_3$ and $BaCO_3$, and that the conversion of carbonate solid solution will take place more easily than in the case of single barium carbonate. Moreover, it is natural to think that the oxide solid solution formation will take place by mutual diffusion of Ba and Sr atoms from fine BaO and SrO crystals (which are present immediately afterwards the conversion of $(BaSr)CO_3$ through the boundary surface to the adjacent foreign oxide crystals accompanied with the simultaneous crystal growth of oxide solid solution. If it were the case, each of the BaO and SrO crystals will play mutually as if they were impurities to the foreign oxide crystals and hinder the crystal growth to each other as the thoria prevents the crystal growth of tungsten in the thoriated tungsten wire, though in our case BaO and SrO are chemically very like compounds. Similar effects will be expected in the case of triple oxide, and the oxide solid solutions will not make so remarkable crystal growth as in the case of single BaO.

Emission values of BaO in table I are small compared with that of SrO. This seems that our BaO crystals would have suffered a severe crystal growth though we have evacuated and converted the single $BaCO_3$ coating as carefully as possible. As is mentioned below the thermionic emission of a coarse-grained double oxide cathode is very smaller than that of suitably evacuated and fine-grained oxide, so the crystal size of BaO will be also of the order of hundreds angstroms like the other oxides if suitably evacuated.

Secondly the crystal size changes of (BaSr)O cathodes at different stages of heat treatment and the poisoning effect of air to oxide crystal size were studied. The results are shown in table II.

Table II.

Emission and crystal size of (BaSr)O cathodes at different stages of heat treatment and that of the poisoned.

Specimens	Treatment	Emission at 850°K	Crystal Size in A
unactivated	immediately afterwards the complete decomposition of carbonate	82 (μA/cm^2) 91 (〃) 124 (〃)	255 255 270
activated	flashed at 1370°K for 2min. activation by current drawing at 1225°K for 20 min.	98 (mA/cm^8) 96 (〃)	325 335
flashed	flashed at 1370°K for 15 min. and reactivated.	40 (mA/cm^2)	365
poisoned by air	introducting the air into bulb after decomposition and reevacuated.	0.37 (mA/cm^2) 1.2 (〃)	>1000 >1000

Eisenstein points out that the oxide crystal size depends primarily on the maximum temperature of treatment above 950°C. Then the crystal size of an unactivated cathode will correspond to the equilibrium size which depends primarily on the maximum temperature in the conversion process at which the sample is heated as oxide after decomposition. Similarly the crystal size of an activated cathode, together with the values listed in table I, will represent the equilibrium size which corresponds to flashing temperature 1370°K.

The decrease in emission appearing in case of a flashed cathode is resposible to a preferential loss of BaO from the surface. Moreover, comparing the crystal sizes of the activated and the flashed cathode we are not able to expect the time effect of heating in crystal growth. The only difference between Eisenstein's and our result is that in his study a cathode flashed for 5 minutes at 1325°K showed a rapid crystal growth in excess of 10^{-3} cm, whereas, in our observation a flashed cathode still shows the crystal size of the order of hundreds angstroms. This may be caused by the difference of measurements, line broadening and small angle scattering of x-ray.[15]

Finally a poisoned cathode by air shows a decided crystal growth and a poor thermionic emission. Such cathode does not recover its emission by any activating heat treatment. It seems that there is at present no theoretical reason for expecting such relationship between thermionic emission and crystal size of an oxide-coated cathode. On this problem Kawamura[16] suggests that in a fine oxide crystal the contribution of surface energy to the lattice energy will become appreciable and the crystal will be in the higher energy state than a large crystal so the free Ba atoms as active centers will be created more easily in a fine crystal than in a sintered stable oxide crystal.

Acknowledgment.

The author wishes to express his sincere thanks to Dr. I. Nonaka who gave many kind advices and to Dr. H. Kawamura who supposed the subject of this investigation and who gave many valuable suggestions. The author is also indebted to Dr. S. Miyake for suggestion leading to this study. Finally this work has been supported by the Scientific Research Expenditure of the Department of Eduction.

References.

1) W. G. Burgers: Zeits. f. Physik **80** (1933), 352.

2) M. Benjamin and H. P. Rooksby: Phil. Mag. **15** (1933), 810.

3) M. Benjamin and H. P. Rooksby: Phil. Mag. **16** (1933) 519.

4) M. Benjamin, R. J. Huck and R. O. Jenkins: Proc. Phys. Soc. **50** (1938) 345.

5) H. Gaertner: Phil. Mag. **19** (1935) 82.

6) J. A. Darbyshire: Proc. Phys. Soc. **50** (1938) 635 and 964.

7) H. Huber and S. Wagener: Zeits. f. tech. Physik **23** (1942) 1.

8) A. Eisenstein: J. App. Phys. **17** (1946) 434.

9) A. Eisenstein: J. App. Phys. **17** (1946) 654.

10) A. Guinier: Comptes rendus **206** (1938) 1641. Ann. de physique **12** (1939) 161.

11) R. Hosemann: Zeits. f. Physik **113** (1939) 751.

: Zeits. f. Physik **114** (1939) 133.

12) B. E. Warren: Phys. Rev. **49** (1936) 885.
J. Biscoe and B. E. Warren: J. App. Phys. **13** (1942) 364.
13) C. G. Shull and L. C. Roess: J. App. Phys. **18** (1947) 295.
L. C. Roess and C. G. Shull: J. App. Phys. **18** (1947) 308.
K. L. Yudowitch: J. App. Phys. **20** (1949) 174.
L. H. Lund and G. H. Vineyard: J. App. Phys. **20** (1949) 593.
14) I. Nonaka and J. Shimazu: J. Phys. Soc. Japan **5** (1950) 283.
15) B. Caroll and I. Fankuchen: J. Chem. Phys. **16** (1948) 153.
16) H. Kawamura: J. Phys. Soc. Japan **3** (1948) 301.

Journal of the Physical Society of Japan Vol. 6, No. 6, Nov.—Dec., 1951

On the Plastic Deformation of Zinc Bicrystal II.

By Tomoyosi KAWADA.
The Government Mechanical Laboratory, Ministry of International Trade and Industry, Suginami-ku, Tokyo.

(Received November 18, 1950)

The stress-strain curves and the change of appearance during elongation of zinc bicrystal specimens are discussed by taking account of the mutual interaction of neighbouring crystals, disregarding the mechanical properties of grain boundary. For the mutual interaction following assumptions are made: As the first step each crystal composing bicrystal specimens deforms freely, but each crystal does neither intrude into nor separate from the other at the grain boundary, nor glide on the other along the grain boundary. Thus the shape of specimen should differ from that in case of free deformation, namely, it suffers some correction so as to accord with the above-mentioned mutual interaction. For this correction of the shape some other work should be introduced in addition to the work for the free elongation of two crystals of bicrystal specimen, and from this additional work the stress-strain curves are deduced.

As described in the preceding paper, the stress-strain curves for polycrystal metals cannot be explained simply by treating the system as a set of disoriented isolated single crystals, but some assumptions should be made about the effect of grain boundary. Several workers[1] have made assumptions to discuss the stress-strain curves of polycrystal metals. In this report we intend to discuss the deforma-tion of bicrystal specimen on the basis of very simple assumptions as follows:

(1) As the first step, each crystal composing bicrystal specimen deforms freely.

(2) But, each crystal does neither intrude into nor separate from the other at the grain boundary, nor glide on the other along the grain boundary. Thus, the shape of specimen should differ from that in case of free deformation, namely, it suffers some corrections so as to accord with the above-mentioned mutual interaction. For this correction of the shape some other work should be introduced in addition to the work for the free elongation of two crystals of bicrystal specimen.

It is well known that when we elongate a single crystal with the original circular cross-section of raidus r whose direction of slip coincides with the direction of maximum slope of slip-plane, the shape of its cross-section becomes elliptic. If we denote the lengths of semi-major and semi-minor axes by a and b respectively and the elongation by ε, we obtain the following relations:

$$a=r,\quad b=r/(1+\varepsilon), \tag{1}$$

and these relations hold well for the specimen with semi-circular cross-section, too.

To discuss the stress-strain relation we use the equation:

$$\sigma = dW/dt, \qquad (2)$$

where σ is the stress and W the work necessary for the deformation. In the case of bicrystal the work W can be separated into two parts, W_0 and W', where W_0 is the work necessary for the free deformation of each of the crystals of bicrystal specimen, while W' is the work due to the mutual interaction of two crystals. We thus have

$$\sigma = d(W_0 + W')/dt \qquad (2')$$

We shall now proceed to the discussion of the result of experiments, In the case of specimen of type No. 7 the shape of its cross-section became, after elongation, elliptic as shown in Fig. 4. of the first report. If, in this case, each crystal deformed freely, the shape of its cross-section should assume the form of a half-ellipse as cut by its major-axis, and no more mutual interaction should be present than keeping the neighbouring crystals jointed at the grain boundary. This latter interaction however seems to have little influence upon the deformation and the shape of cross-section after deformation should be nearly elliptic. In Fig. 4 the radius of the specimen before test was 0.95 mm, and after elongation of 25% the lengths of the semi-major and sem-iminor axes, $a_{obs.}$ and $b_{obs.}$, became 0.94 mm and 0.75 mm respectively. Thus, $a_{obs.}$ is nearly equal to r, while $b_{obs.}$ is nearly equal to $b_{cal.} = r/(1+\varepsilon) = 0.76$ mm. As mentioned above, the effect of existence of the grain boundary is merely to join the neighbouring crystals and the work to do this is considered to be very small, i.e. W' is very small. Thus we see from (2') that the stress-strain curve rises only slightly as compared with the corresponding curve for single crystal.

Next we shall consider specimens for which α_2 takes various values from 270° to 360° (=0°) while α_1 is fixed at 90°. The deformation of one of such specimens is illustrated in Fig, 9. From this figure it will be seen that in case of free deformation of each crystal, the cross-section of the left crystal becomes half-ellipse AC_1B while that of the right crystal becomes half-ellipse $A_2C_2D_2EB_2$, namely, A displaces to A_2, B to B_2 and D to D_2 and the grain boundary of the right crystal turns to the position A_2B_2. This means that if each crystal deforms freely, both crystals overlap on the part AOA_2, while at the boundary OB one crystal separates from the other. If, as shown in Fig. 9, we denote the angle between AB and the direction perpendicular to slip direction by β and the angle between AB and A_2B_2 by γ, we get the following relation:

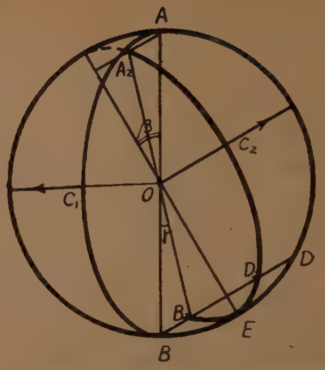

$\alpha_1 = 90°$, $\alpha_2 = 300°$, $\varepsilon = 100\%$.

Fig. 9.

$$\gamma = \beta - \tan^{-1}\{\tan\beta/(1+\varepsilon)\} \qquad (3)$$

By the assumption that each crystal does neither intrude into nor separate from the other, we can deduce roughly a general shape of the cross-section as follows: since OA_2 falls on OA and A_2 falls on A, the upper parts of the left and right crystals in the figure repel each other, and thus the upper part of the specimen swells, while OB and OB_2 adhere to each other and B_2 falls on B and thus the lower part of the specimen is depressed, and the circumferential line of the cross-section becomes smooth.

As to the work W' due to the mutual interaction, it supposingly depends upon the following factors.

(1) The work necessary for crystals to repel each other at the upper part and adhere at the lower part, which is a function of γ.

(2) The work necessary to make A_2 fall on A and B_2 on B. For example, in case when $\alpha_2 = 0$ the shape of the right crystal becomes a half-ellipse as cut by its minor axis which coincides with AB, and neither separation nor intrusion occurs. But, since the mutual distances between A and A_2, and between B and B_2 are greater some additional work must be done to make A_2 fall on A and B_2 on B.

(3) Moreover, in the case of the specimen of type No. 1, for example, the direction of slip is perpendicular to the grain boundary in the left crystal, while in the right crystal it is parallel to the grain boundary making the angle χ with the direction of specimen axis, and thus internal force may exist, making some contribu-

tion to W'.

Taking all these factors into account it is found that W' becomes greater as the value of α_2 increases from 270° to 360°, and this result coincides well with the relation between the stress-strain curve and α_2.

Next, let us draw a line from B parallel to the direction of slip as shown in Fig. 9. The part BAD deforms to $B_2A_2D_2$ and the deformation of this part will be influenced directly by the neighbouring crystals, while in the part BED the influence of neighbouring crystals upon the deformation is indirect and the effect of mutual interaction in this part will be smaller. Thus, it may be conceivable that when the stress is applied uniformly to the specimen, the part BED is apt to extend longer than the other part, Since the specimen cannot bend, there is no other way than to twist as described in the first report. i.e., the specimen twists in one direction from one end of the specimen till the middle part and then twists back to the other end. The specimens prepared in the present experiment were not thoroughly perfect in form, and so small fluctuation of the position of grain boundary may cause fluctuations in direction and magnitude of twisting.

The stress-strain curve, the change of the shape of cross-section and the twisting can be explained qualitatively by the present theory. As an example of the change of the shape of crosssection we shall consider the result of Fig. 5. If each crystal of bicrystal specimen deforms freely, the shape of the cross-section becomes as shown in Fig. 10A. The diameter of the specimen before extension was 2.25 mm, and after extension of 66% the length XY in Fig. 10B was 1.98 mm while the length of A_1B_1 was nearly 2.25 mm. This means that at A and B the specimen deforms as shown by dotted lines in Fig. 10A, which is quite alike to Fig. 10B.

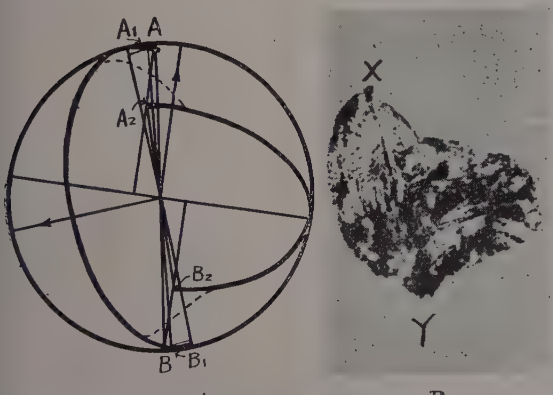

A. B.

$\alpha_1=100°$, $\alpha_2=350°$, $\varepsilon=66\%$.

Fig. 10.

Types No. 2 and No. 3 differ from types No. 8 and No. 7 only in that the angle α_2 is in opposite directions, therefore the same discussion as for types No. 8 and No. 7 can be made for the former types. The fact that the specimens of these types sometimes fractured by cleavage may be explained as follows. Since the orientations of both crystals are nearly equal in these types, the transitional lattice of the grain boundary will be nearly similar to the lattice of crystal. Thus the grain boundary will not hinder the specimen to fracture by cleavage surface.

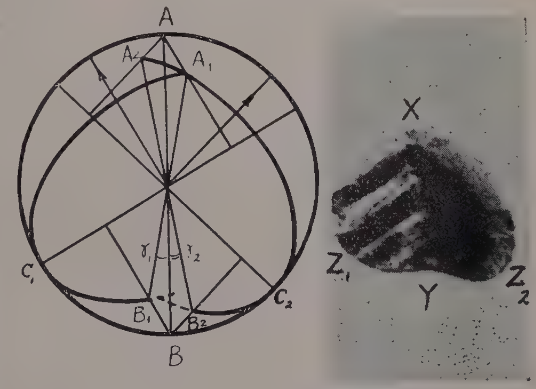

A. B.

$\alpha_1=30°$, $\alpha_2=315°$, $\varepsilon=50\%$.

Fig. 11.

Next we shall discuss the results for specimens in series B. If each crystal of specimen of type No. 16 deforms freely, each semicircle becomes $A_1C_1B_1$ and $A_2C_2B_2$ as shown in Fig. 11A. Thus it is easily conceivable that the shape of specimen becomes as shown in Fig. 11B. The radius of the specimen before tension was 0.83 mm while after elongation of 50% the dimension of the specimen changed as follows: $OZ_1=0.85$ mm, $OZ_2=0.80$ mm, $\angle YOZ_1 \doteqdot 60°$ and $\angle YOZ_2 \doteqdot 45°$, using the notation as shown in Fig. 11B. These values seem to be nearly uninfluenced by the deformation and in reality they are nearly equal to those before tension. The angle γ in this case is equal to $\gamma+\gamma_2$ as in Fig. 11A and this is twice as large as that for type No. 8, and therefore W' is greater and the stress-strain curve rises rather high.

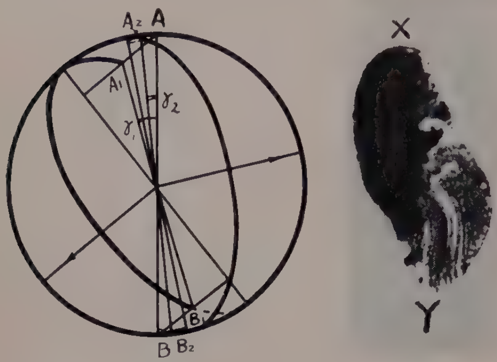

A. B.

$\alpha_1=128°$, $\alpha_2=282°$, $\varepsilon=100\%$.

Fig. 12.

When in type No. 14, each crystal deforms freely, both crystals becomes as shown in Fig. 12A. At first sight this figure seems to be a little different from that of Fig. 12B. But, if we assume that in the upper part, OA_2 falls on OA_1 and accordingly the upper part of the right crystal is depressed to compensate, while in the lower part, OB_2 falls on OB_1 and the neighbouring part swells, then this corrected figure will be quite alike to Fig. 12B. The diameter of specimen before tension was 2.23 mm and after elongation of 100% the length XY of Fig. 12B became 2.20 mm, in agreement with Fig. 12A. The angle γ in this case is equal to $\gamma_1-\gamma_2$ which is very small. Thus W' mainly due to the works as mentioned in (2) and (3) above for types No. 7 and No. 8, and these works are usually small in the present type No. 14. Thus, the stress-stratn curve rises only slightly.

Type No. 10 is almost a single crystal as a whole except for a slight deviation present between the orientation of two composing crystals, and so its stress-strain curve is nearly equal to that for single crystal.

The difference between types No. 12 and No. 16 is that the direction of slip of the right crystal is reverse and this fact does not cause any difference in the result. Thus the result of experiment for the specimen of type No. 12 is explained in exactly the same way as in the case of the specimen of type No. 16.

The remaining types in series B, i.e. types No. 9, No. 11, No. 13 and No. 15 are intermediate types and they can be explained in nearly the same way.

If, in type No. 21, each crystal deforms freely, the shape of the cross-section becomes elliptic just as in the case of single crystal. As to the mutual interaction, there is neither intrusion nor separation, but since the directions of slip of the two crystals are reverse along the grain boundary, the mutual interaction as described in (3) above for types No. 8 and No. 7 may occur. Since, however, this is small, the stress-strain curve for type No. 21 rises only slightly.

Conclusion.

By the moving-furnace method we prepared zinc bicrystal specimens, each consisting of two crystals separated by a longitudinal grain boundary. The results of tension test of these bicrystals were discussed by taking account of the mutual interaction of neighbouring crystals, disregarding, however, the mechanical properties of the grain boundary. Thus, the results of experiment could be explained fairly satisfactorily.

This experimental result, when combined with that of R. F. Miller[2], enables us to discuss the stress-strain curves for polycrystal metals by starting from those for single crystals.

In conclusion, the writer expresses his hearty thanks to Prof. S. Kaya of the University of Tokyo for his kind interest in this work. He is also much indebted to Messrs. H. Yoshida and T. Furusawa for their cooperation in preparing specimens.

References.

1) E. g., G. I. Taylor: J. Inst. Metals, **62** (1938) 303.

2) K. F. Miller: Trans. A. I. M. E. **111** (1934) 135.

JOURNAL OF THE PHYSICAL SOCIETY OF JAPAN Vol. 6, No. 6, Nov.–Dec., 1951.

On the Structure of Silicate Glasses.

By Ryosuke YOKOTA.

Matsuda Research Laboratory, Tokyo-Shibaura Electric Co.,
Kawasaki, Kanagawa-ken

(Read Nov. 4, 1950; Received April 13, 1951)

The diagram of the molecular refractien of Na_2O-SiO_2 glasses vs. composition (Na_2O mol % $=x$) is found to be linear with breaks at $x=0.231$, 0.333, 0.428 and 0.474. Analysing this fact, it is concluded that at the latter three breaks the glass has the similar local arrangement of SiO_4 tetrahedra as the silicate crystals do, which was found before by the author on X-ray and viscosity. The break at $x=0.231$ is briefly discussed. By the introduction of Na_2O or other oxides into SiO_2 glass, "solvation" takes place, and also "solvation in refractivity"—decrease of refractivity of SiO_4 tetrahedra—takes place.

These effects by the various metal ions are summarized and the characteristics of ions in gases or aqueous solutions are found to be preserved to some extent also in the silicate glasses.

§ 1. Introduction.

The X-ray investigations of Warren and his co-workers[1)] showed that in the silicate glasses the silicons and oxygens form a three dimensional random network, in which each silicon is surrounded by 4 oxygens each at the corners of a tetrahedron and some of the oxygens are bonded to 2 silicons and some to 1 silicon and there are holes in this random network in which the alkali or alkali earth atoms lie surrounded by oxygens. The author[2)] made a further refinement on the structure of the silicate glasses.

In the silicate glasses the main component is the oxygen, the electronic polarizability of which is much larger than those of other ions. Therefore we can study the structure of the silicate glasses from the investigation of the polarizability of the oxygen ion. Since many metal atoms can enter into the network of a glass, we can study the effects of these metal ions in the silicate glasses from the molecular refraction of glass containing them.

§ 2. Molecular Refraction of Na_2O-SiO_2, K_2O-SiO_2 and CaO-SiO_2 Glasses.

Molecular refraction (MR) is the sum of the ionic refraction composing the molecule. The most reliable values of the refractive indices (n_D) and the densities (ρ) of Na_2O-SiO_2, K_2O-SiO_2 and CaO-SiO_2 glases are those given by Morey and Merwin[3)]. In the first place we consider Na_2O-SiO_2 glasses whose compositions are represented by $(Na_2O)_x(SiO_2)_{1-x}$ where x is the mole fraction of Na_2O. The Lorentz-Lorenz's formula gives

$$MR=\frac{n_D^2-1}{n_D^2+2}\cdot\frac{xW_{Na_2O}+(1-x)W_{SiO_2}}{\rho}=\frac{4}{3}\pi\sum N\alpha \qquad (1)$$

where W_{Na_2O} and W_{SiO_2} are molecular weight of Na_2O and SiO_2 respectively, and α is the electronic polarizability of each atomic ion and N its number involved in 1 mol of the glass.

The mole fractions of sodium, silicon and oxygen atoms are $2x$, 1-x and 2-x respectively. There are two kinds of oxygens, one of which bonds two Si and the other bonds one Si and Na ions. We shall denote the former as O^{Si} and the latter as O^{SiNa}. And by equating the number of bonds terminating on oxygen to the number terminating on Si, we find that the mole fractions of O^{Si} and O^{SiNa} are equal to $2-3x$ and $2x$ respectively. We denote the molecular refraction of Na ion as R_{Na} and so forth. Then we have

$$\begin{aligned}MR&=(1-x)R_{Si}+2xR_{Na}+2xR_{O^{SiNa}}+(2-3x)R_{O^{Si}}\\&=(2R_{Na}+2R_{O^{SiNa}}-R_{Si}-3R_{O^{Si}})x\\&\qquad+(R_{Si}+2R_{O^{Si}}) \qquad (2)\end{aligned}$$

From the diagram of MR *vs.* x (Fig. 1) we see that MR is represented by straight lines with breaks at $x=0.231$, 0.333 and 0.428. Therefore in equation (2) the coefficient of x and $(R_{Si}+2R_{O^{Si}})$ are both constants in each range of the composition represented by the straight lines. Then

$$2R_{Na}+2R_{O^{SiNa}}-R_{Si}-3R_{O^{Si}}=\text{const.}=A \qquad (3)$$

$$R_{Si}+2R_{OSi}=\text{const.}=B \qquad (4)$$

According to Pauling[3] R_{Si} is very small (0.084 c.c./mol). Therefore R_{Si} can be assumed as constant indifferent of the state of binding. From equation (4) we can obtain R_{OSi} at each range of the composition. Then from (3) $R_{Na}+R_{OSiNa}$ is obtained at each range of the composition. R_{Na} is 0.457 c.c./mol[4] which is only about one tenth of that of oxygen ion and so may be regarded approximately as constant compared with R_O. Therefore R_{OSiNa} is obtained at each range of the composition. We have calculated A and B in equation (3) and (4) by the least square method from which R_{OSi} etc. are obtained and summarized in Table 1.

In the case of K_2O-SiO_2 glasses, we have

$$MR=(2R_K+2R_{OSiK}-R_{Si}-3R_{OSi})x+(R_{Si}+2R_{OSi})$$

The curve of MR *vs.* x is also represented by straight lines having breaks at 0.20 and 0.333.

For CaO-SiO_2 glasses we have

$$MR=(R_{Ca}+2R_{OSiCa}-R_{Si}-3R_{OSi})x+(R_{Si}+2R_{OSi})$$

The curve of MR *vs.* x is also represented by straight lines having breaks at 0.333 and 0.428.

For these glasses R_{OSi} etc. can be calculated in the same way as we have described above, which are summarized also in Table I.

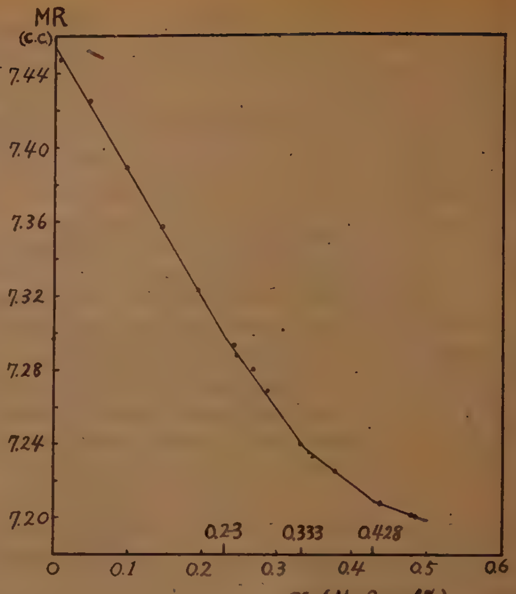

Fig. 1. Relation between MR and x.

Table II.

substance	molecular refraction	R_{OSi}
α-quartz	7.189	3.553
α-tridymite	7.411	3.663
α-cristobalite	7.435	3.676
fused silica	7.447	3.682

Table I.

	N_{Si} *	0.50∼0.435	0.435∼0.40	0.40∼0.364	0.364∼0.333
Na_2O-SiO_2 glasses	R_{OSiNa}	4.771	4.865	4.895	4.898
	R_{OSi}	3.683	3.651	3.612	3.601
CaO-SiO_2 glasses	R_{OSiCa}	—**	4.579	4.652	4.703
	R_{OSi}	—**	3.711	3.662	3.579
	N_{Si}	0.50∼0.445	0.445∼0.40	0.40∼0.364	0.364∼0.333
K_2O-SiO_2 glasses	R_{OSiK}	5.235	5.295	5.354	—
	R_{OSi}	3.676	3.639	3.602	—

§ 3. Discussions of the Results.

There are a number of ways in which silicon and oxygens can be joined together into three-dimensional structures. The structures of α-quartz, α-tridymite, α-cristobalite and fused silica are all alike in which each silicon is surrounded by four oxygens and each oxygen by two silicons with the composition formula SiO_2. The most reliable values of n_D and ρ of fused silica may be those by Sosman[5]. We may use the Lorentz-Lorenz's formula approximately using the mean refractive index for the crystal $\{(2\omega^2+\varepsilon^2)/3\}^{\frac{1}{2}}$ or $\{(\alpha^2+\beta^2+\gamma^2)/3\}^{\frac{1}{2}}$ if the birefringence of the crystal is not greater than 0.01 in refractive index.

---

* N_{Si} is silicon oxygen ratio.

** In this range the glass cannot exist in an homogeneous single phase, but it separates into two phases.

Table II showes that R_{OSi} in fused silica is the largest but rather close to that in α-cristobalite while R_{OSi} in α-quartz is the smallest. The Si–O–Si bond angles determined by the X-ray studids are 144° in α-quartz[6] and 150° in α-cristobalite[7] and about 180° in fused silica[8].

The oxygen has a tendency to have its two valence bonds make roughly the tetrahedral angle 109° like in water molecules. It seems very reasonable to assume that as this bond angle is approaching to the tetrahedral angle, that is, the covalent character of bond is the larger, the less polarizable the electron shell of the oxygen is and hence R_{OSi} decreases more and more. The tendency of R_{OSi} in Table II seems in agreement with this interpretation.

On the other hand, α-quartz is stable at room temperature, β-tridymite at high temperature (above 870° c) and β-cristobalite at higher temperature (above 1470° c) while α-tridymite and α-cristobalite are the low temperature forms of β-modifications. At higher temperatures, the covalent character of Si–O–Si bond will presumably decrease. Therefore it seems very probable that fused silica has a structure similar to that of high-temperature form of SiO_2, that is, β-cristobalite, and that β-cristobalite-like structure has been frozen before crystallization takes place.

In silicate crystals, at $N_{Si}=0.40$ $((Si_2O_5)^{--})$ the SiO_4 tetrahedra arrange themselves in sheets just like in mica.

From the length of the unit cell and Si–O distance (1.62A) the Si–O–Si bond angle is calculated to be 134°.

The fact that the values of R_{OSi} at $N_{Si}=0.40$ in Na_2O–SiO_2 and K_2O–SiO_2 glasses are smaller than those at $N_{Si}=0.50$ (SiO_2) indicates that Si–O–Si bond angle at $N_{Si}=0.40$ is smaller than 180° and is near that in mica-like sheets structures. This corresponds to the assumption that in the silicate glasses the local arrangement of SiO_4 tetrahedra is a sheet as in mica, or a chain as in amphiboles $((Si_4O_{11})^{--})$ or in pyroxenes $((SiO_3)^{--})$, or a ring as in benitoite $((Si_3O_9)^{--})$.

Further we consider the break at $N_{Si}=0.435$. For this case we may apply the treatment on the immiscibility of glass by Warren[9]. Because the number of single-bonded oxygens is the same as that of sodium atoms, it is necessary for each single-bonded oxygen to bond to more than 1 sodium, in order that each sodium shall have a reasonable number of surrounding oxygens. The distance between the two sodiums bonded to the same oxygen cannot be greater than twice the Na–O distance (2.35A). For a homogeneous glass with atoms uniformly distributed, the volume of glass containing 1 sodium atom (V_{Na}) will be of the order of magnitude of the cube of the linear separation.

$$V_{Na}=(2\times2.35)^3=104A^3$$

If the composition is represented in weight percents X of Na_2O and (100–X)% of SiO_2 and the density is denoted by ρ, the volume of 100 gm. of glass will be

$$V_{100}=(100/\rho)\times10^{24}A^3$$

The number of Na atoms in X gm. of Na_2O is given by

$$N_{Na}=(2X/W_{Na_2O})\times6.06\times10^{23}$$

The volume of glass per Na atom in A^3 is then

$$V_{Na}=V_{100}/N_{Na}$$

For the range of composition of interest, ρ has an average value of about 2.4. Therefore $X=21.7$ wt% ($N_{Si}=0.44$) is obtained and is near $X=23.5$ wt% ($N_{Si}=0.435$) at which the break occurs as mentioned above. Considering this and the fact that R_{OSi} and R_{OSiNa} are both constant in each range of composition (see Table I), we may conclude that with the introduction of Na_2O into fused silica, the cristobalite-like structure of SiO_2 changes partially to a more compact structure which involves Na ions and unsaturated oxygens, and that this change proceeds linearly with the increase of Na_2O content and comes to saturate at the composition where Na ions and unsaturated oxygens distribute uniformly, that is, at the composition $N_{Si}=0.435$. With the increase of Na_2O content beyond $N_{Si}=0.435$, Na ions and unsaturated oxygens increase so that Na ions can be surrounded by larger number of unsaturated oxygens and vice versa. In this case, it may be conceivable that the polarizablilty is larger because unsaturated oxygen is surrounded more symmetrically by the larger number of Na ions. This is the reason why there is a break at $N_{Si}=0.435$ in R_{OSi} and R_{OSiNa} and an increase in R_{OSiNa} with Na_2O content. Thus the structure of Na_2O–SiO_2 glasses the author studied before[2] is ascertained and developed.

§4. Analysis of Na_2O-CaO-SiO_2 and K_2O-CaO-SiO_2 Glasses.

Na_2O-CaO-SiO_2 glasses which are the main components of the commercial glass are represented by $(Na_2O)_x\ (CaO)_y\ (SiO_2)_{1-x-y}$ where x any y are the mole fractions of Na_2O and CaO respectively. The molecular refraction of these glasses is represented as follows.

$$\begin{aligned} MR &= (1-x-y)R_{Si}+2xR_{Na}+2xR_{OSiNa} \\ &\quad +yR_{Ca}+2yR_{OSiCa}+(2-3x-3y)R_{OSi} \\ &= (R_{Si}+2R_{OSi})+(2R_{Na}+2R_{OSiNa}-R_{Si} \\ &\quad -3R_{OSi})x+(R_{Ca}+2R_{OSiCa}-R_{Si}-3R_{OSi})y \end{aligned}$$

Calculating MR from the most reliable data of Morey and Merwin[3] and replacing Na_2O with CaO little by little keeping each SiO_2 content constant, that is, changing x little by little from 0 to $1-c$ keeping SiO_2 content $(1-x-y=c)$ constant, it is found that MR changes linearly with x and this linearity of MR holds for all values of c.

On the other hand, the molecular refraction of Na_2O-SiO_2 and CaO-SiO_2 glasses are both linear with x and y respectively having breaks at 0.231, 0.333 and 0.428. Therefore the molecular refraction of Na_2O-CaO-SiO_2 glasses is represented by the planes with the borderlines at $N_{Si}=0.435$ and 0.40. The above fact indicates that $(R_{Si}+2R_{OSi})$ and the coefficients of x and y are all constant between $N_{Si}=0.50\sim0.435$, $0.435\sim0.40$ and $0.40\sim0.364$, and that R_{OSiNa}, R_{OSiCa} and R_{OSi} at each composition range are the same as those for Na_2O-SiO_2 and CaO-SiO_2 glasses which were obtained in the preceding paragraph. In the case of K_2O-CaO-SiO_2 glasses the situation is the same.

§5. Apparent Molar Volume.

In Na_2O-SiO_2 glasses when Na_2O is introduced into fused silica, we can observe a contraction in volume, which is to be considered that of the network of SiO_4 tetrahedra. This effect is like the solvation in aqeous ionic solutions. We can introduce the apparent molar volume $(\langle MV\rangle_{AP})$ which is defined by

$$\langle MV\rangle_{AP}=\{(MV)-(1-x)(MV)_{SiO_2}\}/x \quad (5)$$

where (MV) and $(MV)_{SiO_2}$ are the molecular volumes of the glass and SiO_2 glass respectively. $\langle MV\rangle_{AP}$ in each composition range are listed in the Table III.

This table shows that introduction of Na_2O into the cristobalite-like structure of SiO_2 glass which has large void causes a very large contraction of network of SiO_4 tetrahedra, but the amount of the contraction becomes smaller with the increase of Na_2O content. On the other hand, from reliable measurements of the various silicate glasses, Huggins[10] has obtained the factors c_M (see his original paper) of each oxide assuming the volume of SiO_4 network to be that of fused silica. Using Huggins' c_M's we can predict the density of glass precisely in the silica rich regions $(N_{Si}=0.50\sim0.445)$. By simple calculations we can obtain $\langle MV\rangle_{AP}$, which are summarized in Table IV with the molecular volume of the oxide crystal $(\langle MV\rangle_c)$.

Table III.

composition range (N_{Si})	$\langle MV\rangle_{AP}$(c.c.)
0.50∼0.435	17.40
0.435∼0.40	18.59
0.40∼0.364	20.25
0.364∼0.333	22.48

The abnormal small values of $\langle MV\rangle_{AP}$ in BeO and Li_2O compared with $\langle MV\rangle_c$ indicate that the solvation effect is very large, because the ionic radii of Be and Li are very small.

Table IV.

oxide	$\langle MV\rangle_{AP}$ c.c.	$\langle MV\rangle_c$ c.c.	oxide	$\langle MV\rangle_{AP}$ c.c.	$\langle MV\rangle_c$ c.c.
Li_2O	7.8	14.8	CaO	10.3	16.5
Na_2O	17.4	27.3	ZnO	11	14.5
K_2O	31	40.6	SrO	∼15	22.1
Rb_2O	44	50.3	CdO	∼12	16.8
BeO	3	8.3	BaO	16	26.8
MgO	9.4*	11.1	PbO	19.9**	23.3***

§6. Apparent Molar Refraction.

Introduction of Na_2O to SiO_2 glass cause a decrease in the refraction of the silicon-oxygen network. In analogy with the apparent molar volume we can define here the apparent molar refraction,

$$\langle MR\rangle_{AP}=\{(MR)-(1-x)(MR)_{SiO_2}\}/x$$

where (MR) and $(MR)_{SiO_2}$ are the molecular refraction of the glass and silica glass respectively. Using the Gladstone-Dale's formula and assuming MR of the SiO_4 network to be that of fused silica, Young and Finn[11] and Huggins[12] have obtained the factors of various oxides from reliable measurements on various silicate glasses. Making use of these we can predict the refractive index of glass precisely particularly in the range of silica rich. On the other hand, we have

---

* The author calculate from the data of Larsen (Am. J. Sci. **28** (1909) 263).

** The author calculate from the data of Kordes (Z. anorg. allgem. Chem. **241** (1939) 1).

*** This value is that of litharge.

$$MR = \frac{n_D^2-1}{n_D^2+2}\cdot\frac{W}{\rho} = \frac{(n^D-1)W}{\rho}\cdot\frac{n_D+1}{n_D^2+2} \qquad (7)$$

Now we consider only the range of silica rich, that is, the range of very small value of x. Then n_D in equation (7) is nearly equal to that of silica glass (1.4585). The factor $(n_D+1)/(n_D^2+2)$ in equation (7) only varies 1.5% when n_D varies 2.5% from the value of silica glass. Therefore if we adopt 0.596 as the value of $(n_D+1)/(n_D^2+2)$ which corresponds to $n_D=1.4585$ and multiply this to $(n_D-1)W/\rho$, we can obtain the molecularr efraction by the Lorentz-Lorenz's formula within an error of about 0.5%. From the factors of Young ane Finn[11] which is represented by weight percentage and the Huggins' factors a_M (see his original paper) we can obtain $\langle MR\rangle_{AP}$ for each oxide and the 'reduced apparent molecular refraction' $\langle MR_r\rangle_{AP}$ which is defined by $(1/n)\langle MR\rangle_{AP}$ when the oxide's formula is represented by M_mO_n, considering the quantity per equal number of oxygen atom in 1 mol of the oxide. In Table V $\langle MR_r\rangle_{AP}$ is summarized.

Table V.

oxide	$\langle MR_r\rangle_{AP}$	oxide	$\langle MR_r\rangle_{AP}$
Li_2O	5.50	Pr_2O_3	9.39
Na_2O	7.18	Nd_2O_3	9.22
K_2O	11.4	Sm_2O_3	9.01
Rb_2O	14.8	Er_2O_3	9.12
Cs_2O	20.8	Gd_2O_3	8.91
BeO	3.51	TiO_2	7.45
MgO	5.09	ZrO_2	7.67
CaO	7.54	CeO_2	8.19
ZnO	7.27	ThO_2	8.90
SrO	9.83	GeO_2	5.20
CdO	9.64	SnO_2	6.74
BaO	11.8	P_2O_5	3.42
PbO	16.9	Cb_2O_5	7.28
Al_2O_3	4.24	Ta_2O_5	7.06
Ga_2O_3	5.69	Sb_2O_5	7.28
Yt_2O_3	7.72	MoO_3	5.99
In_2O_3	7.60	WO_3	6.54
La_2O_3	9.44	UO_3	6.97

The diagram of $\langle MR_r\rangle_{AP}$ *vs.* 'serial number' of the Periodic Table (Fig. 2) shows that in the higher range than serial number 4, two subgroups of each valency belong to different straight lines, that is, the subgroups which belong to the 'non-rare' gas type ion lie on straight lines which are distinguished clearly from those for the 'rare' gas type ions. This indicates that also in the silicate glasses there exists a relation between the "solvation" effect and the periodicity of atoms which is well known for the molecular refraction of aqueous ionic solutions.

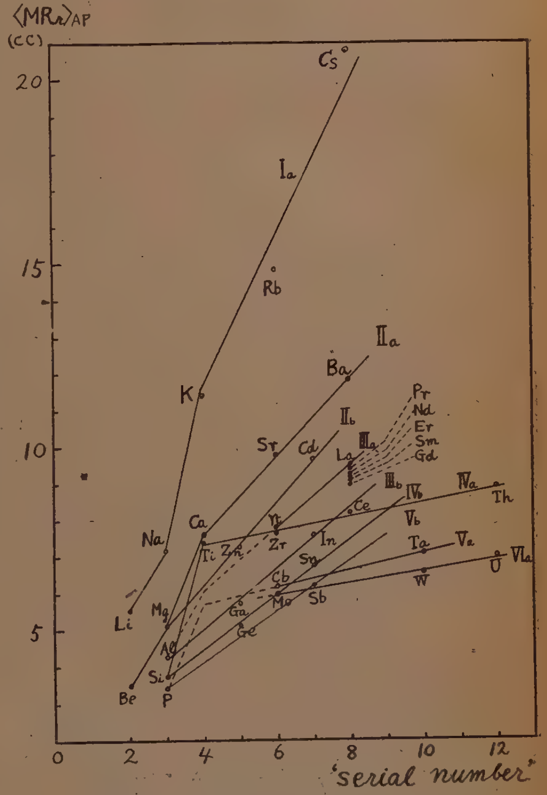

Fig. 2. Relation between $\langle MR_r\rangle_{AP}$ and 'serial number' of the Periodic Table.

References.

1) B. E. Warren and H. Krutter: J. Amer. Ceram. Soc. **19** (1936) 202; J. Biscoe and B. E. Warren: ibid **21** (1938) 259.

2) R. Yokota: J. Phys. Soc. Japan **5** (1938) 295.

3) G. W. Morey and H. E. Merwin: J. Opt. Soc. Amer. **22** (1932) 632.

4) L. Pauling: Proc. Roy. Soc. A **114** (1927) 181.

5) R. B. Sosman: The Properties of Silica.

Chemical Catalog Co. (Reinhold Publishing Corp.) New York, 1927.
6) Péi-Hsiu Wei: ZS. Krist. **92** A (1935) 355.
7) W. Niewenkamp: ZS. Krist. **92** A (1935) 82.
8) B. E. Warren: J. App. Phys. **13** (1942) 602.
9) B. E. Warren and A. G. Pincus: J. Amer. Ceram. Soc. **23** (1940) 301; B. E. Warren: J. App. Phys. **13** (1942) 602.
10) M. L. Huggins: J. Opt. Soc. Amer. **30** (1940) 420.
11) J. C. Young and A. N. Finn: J. Res. Nat. Bur. Std. **25** (1940) 759.
12) M. L. Huggins: J. Opt. Soc. Amer **30** (1940) 420; J. Amer. Ceram. Soc. **26** (1943) 4.

JOURNAL OF THE PHYSICAL SOCIETY OF JAPAN Vol. 6, No. 6, Nov.—Dec., 1951.

On the Magnetic After-Effect due to the Irreversible Displacement of the Domain Boundary (III).*

By Seijiro MAEDA.

The Research Institute for Iron, Steel and Other Metals.
Tôhoku University, Sendai

(Read, November 1950; Received April 16, 1951)

The magnetic after effect of *C*-Steel was measured in the cases of constant initial field, (saturation field) and various values of final field which correspond to various points on the descending branch of the magnetic hysteresis curve. The amount of after effect observed was larger than that of *Cr*-permalloy reported in the previous papers and the various forms of damping characteristic curves were obtained. The form of $Bn(t)$, the total change of magnetization during the period from t second after the instant of the field change, shows a slower change than $B_n(t)\propto 1/t$, for the final fields stronger than $H_f(max)$, for which the after affect takes a maximum value, and rapid change than that of $1/t$ law for the values of H_f smaller than $H_f(max)$. Furthermore the form of $B_n(t)$ was changed sensitively by the change of temperatures and tensions applied. However, it was found that these features of the characteristic curves of $B_n(t)$ were explained well quantitatively by the model based on the irreversible displacement of domain boundary. According to the theory $B_n(t)$ was given by

$$B_n(t)=kD/a\int_t^\infty \beta(H_{om})1/t^2\,dt$$

where k, D and a are constants and $\beta(H_{om})$ is an amount which depends on the form of the magnetic hysteresis loop of the specimen.

§ 1. Introduction.

Lately, the author has made an observation[1] on the magnetic after-effect of *Cr*-permalloy under different conditions and has propounded a mechanism for the magnetic after-effect assuming that irreversible displacement of the domain boundary with very small displacement velocity takes place at different regions in the medium. Subsequently the author measured the magnetic after-effect in carbon-steel and found that the behavior of the after-effect in this substance differs formally from that of *Cr*-permalloy. In this paper the experimental results obtained are described and a short discussion on the results is given based on the model mentioned above.

---

* Report from the Research Institute for Iron, Steel and Other Metals, Tôhoku University. This investigation was supported in part by the Grant-in-Aid of fundamental Scientific Researches of the Ministry of Education for 1950. Item No. D 43064, "On the Magnetic after-Effect of the Iron Alloys."

§ 2. Experimental Arrangement and Results Obtained.

Since the method and arrangement were almost the same as shown in the previous paper, the description on them was omitted here. The specimen under measurement was a wire of carbon steel with carbon content about 0.03%, the length and diameter being 60 cm and 1.2 mm respectively. After annealed at 950°C for 6 hrs in dry hydrogen atmosphere and cooled in the furnace, its magnetic hysteresis curves at different temperatures were obtained as shown in Fig. 2.

The measured quantity under question is the total change of magnetization $B_n(t)$ during the period from t seconds after the sudden change of magnetizing field from initial field H_i to final one H_f. Fig. 1 shows relation between $B_n(t)$ and t at −195°C, boiling point of liquid nitrogen. In this case the saturation field H_s was chosen as initial field H_i and the various fields which correspond to any points on the descending branch of the hysteresis loop was taken as final field H_f. For the sake of convenience, B_{no}, the value of $B_n(t)$ for $t \equiv t_0 = 1/100$ seconds was chosen as a measure of an amount of the after-effect. As can be seen from the figure, ratio of the maximum of B_{no} to B_s, the saturation value of induction, was score times larger than that in the case of Cr-permalloy and the form of $B_n(t)$ differs widely by the values of final fields H_f. There appeared B_{no} firstly at $H_f = -0.35$ Oe and increased rapidly with decreasing H_f and then showed a maximum value when H_f was about -1.4 Oe. In such a range of field the curve $\log B_n(t)$ versus $\log t$ was composed of two linear parts, the part for smaller t had an inclination smaller than minus unity and that for larger t followed approximately the law of $1/t$. The joining point of these two parts in a curve of $B_n(t)$ displaced to smaller values of t with decreasing H_f. B_{no} showed a maximum value at a field H_f (max). If H_f decreased beyond H_f (max), the joining point displaced out to the range of observation, and inclination of the curve of $\log B_n(t)$ vs $\log t$ became larger than minus unity. In this case the duration of the after-effect extensively shortened, for example, when $H_f = -3.15$ Oe its inclination was about -7 and the period of duration was about 0.015 seconds.

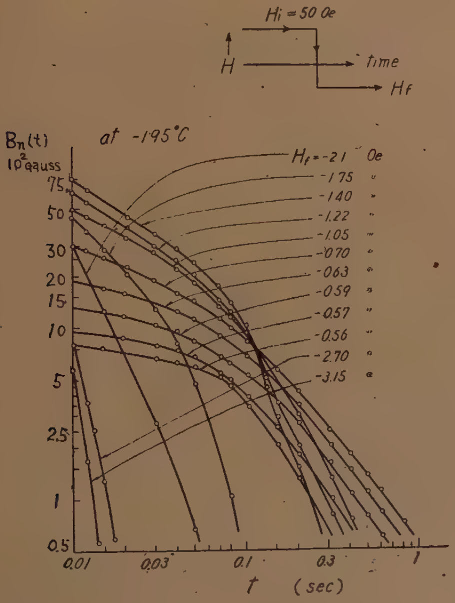

Fig. 1. Curves of $B_n(t)$ vs t for various H_f at −195°C.

In Fig. 2 the hysteresis loops and curves of B_{no} against H_f at temperatures of 950°C, 18°C and −195°C are shown. As can be seen from the hysteresis loop at −195°C, the magnetic induction B is practically regarded as a con-

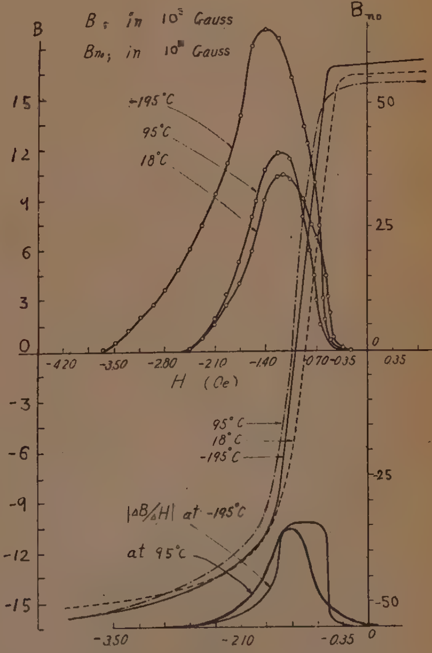

Fig. 2. $B-H$ curves and $B_{no}-H_f$ curves at different temperatures.

stant value in a range of field from H_s to -0.35 *Oe* and commences rapid increase with an almost constant value of $|\Delta B/\Delta H|$ as soon as the field decreases beyond -0.5 *Oe*. This rapid decrease of B finished when the field decreased to about -1.4 *Oe*, thereafter it approached gradually to the saturation value.

On the whole, a behavior of the change of B_{no} against field H_f was similar, to that in *Cr*-permalloy. However in the present case B_{no} was not only proportional to the value of $|\Delta B/\Delta H|$ at the final field H_f, but also depends on the other factors. For example, at -195°C the value of $|\Delta B/\Delta H|$ was almost constant in the range from $H_f = -0.6$ *Oe* to -1.4 *Oe*, while B_{no} rapidly increased with increasing H_f even in that range. It showed a maximum value at $H_f = -1.4$ *Oe*, then decreased almost proportionally to that of $|\Delta B/\Delta H|$ with the further decrease of H_f. As can be seen from the hysteresis loops, B_s decreases gradually with ascending temperature, but the coercive force at 95°C was larger than one at 18°C. Generally B_{no} decreases with ascending temperature as reported in the previous paper, but in the present case B_{no} and $|\Delta B/\Delta H|$ along the hysteresis loop showed larger value at 95°C than that at 18°C for the range of final fields less than -1.0 *Oe*. The curves of $B_n(t)$ against t at 95°C are shown in Fig. 3. At this temperature, it showed, on the whole, the similar behavior of that at -195°C, but the curves for the values of final fields which are larger than $H_f(\max)$ became so smooth that the joining point which appeared at -195°C was not observed practically, and for the smaller values of final field than $H_f(\max)$ no change was observed in the characteristic curve of $B_n(t)$ vs t at temperatures of 95°C and -195°C.

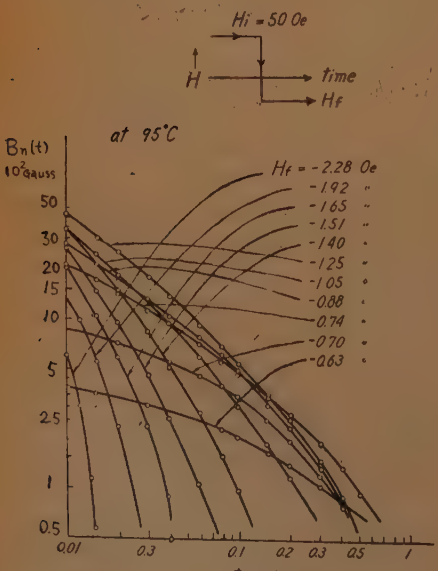

Fig. 3. Curves of $B_n(t)$ *vs* t for various H_f at 95°C.

Next, the after-effect was measured, under the condition that the field was not changed instantaneously from H_i to H_f. It was made to rest for one minute at an intermediate field H_m and then it was suddenly changed to the final value $H_f = -0.70$ *Oe*.

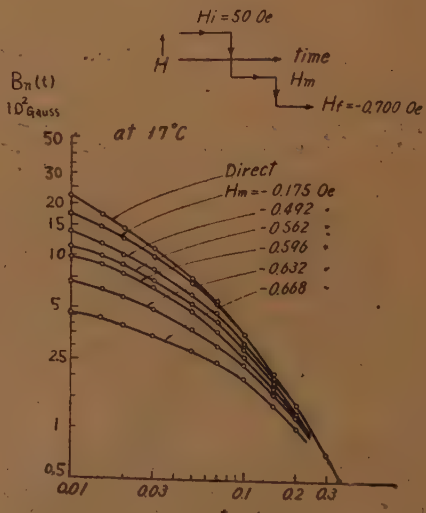

Fig. 4. Curves of $B_n(t)$ *vs* t for various H_m at 17°C.

In Fig. 4 are shown $B_n(t)$ curves for the various intermediate fields H_m. As can be seen from the figure, $B_n(t)$ was affected intensively by the intermediate field H_m in the present case. In the case of *Cr*-permalloy such an effect was not detected as described in the previous paper. The amount of the influence of H_m to the after-effect increased with decreasing $H_f - H_m$. The characteristic curves of $B_n(t)$ vs t under the influence of H_m diverged from that without the rest at intermediate field for smaller value of t, but for larger values of t both curves coincided.

In Figs. 5 and 6 are shown the curves of $B_n(t)$ vs t and $B-H$, $B_{no}-H_f$ under a ten-

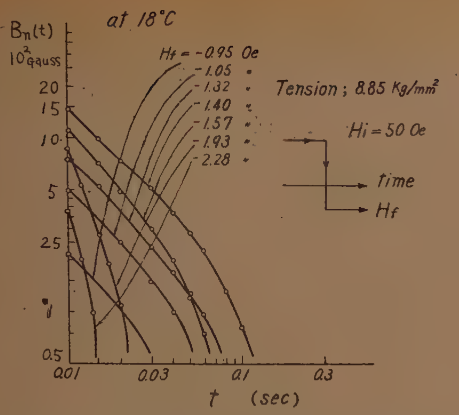

Fig. 5. Curves of $B_n(t)$ *vs* t for various H_f under a tension of 8.85 kg/mm² at 18°C.

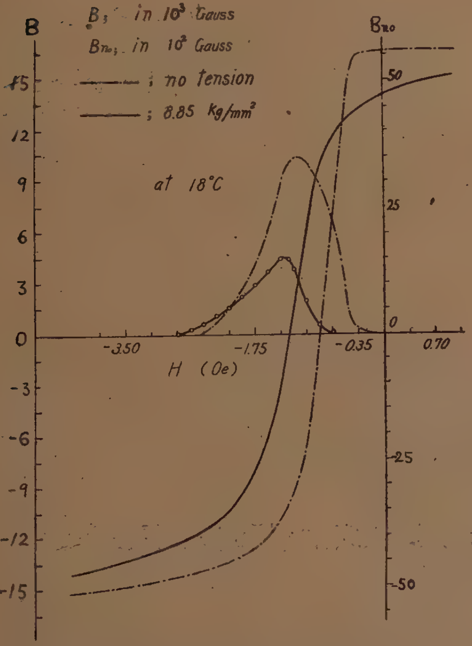

Fig. 6. $B-H$ curves and curves of B_{no} *vs* H_f under a tension of 8.85 kg/mm² and without tension.

sion of 8.85 kg/mm² respectively. As the specimen had a negative magnetostriction constant, the coercive force increased and the slope of hysteresis loop diminished by application of the tension. The kneel point of the descending branch of the hysteresis loop disappeared in this case. As can be seen in Fig. 6, the amount of after-effect became about a half value of that without tension; this is a general character in the case of a specimen with negative magnetostriction constant. The curve $B_n(t)-t$ for the various final fields larger than $H_f(\max)$ follows the law of $1/t$ approximately as shown in Fig. 5, when tension did not act.

It deviates widely from the law and for the final field smaller than $H_f(\max)$ the slope becomes greater than minus unity as in the case without tension.

§ 3. Discussion on the Experimental Results.

The experimental results mentioned in the last section is also well explained by the theory propounded previously by the author. According to this theory the displacement of the domain boundary proceeds very slowly at the special regions (length D) where the difference between the applied magnetic field H_f and peak value of critical field H_{0m} is very small. Thus the retardation of magnetization from the change of external magnetic field occurs. According to this theory the formula for induction change $B_n(t)$ is given by

$$B_n(t) = \frac{kD}{a}\int_t^\infty \beta(H_{0m})/t^2 dt\,, \qquad (1)$$

where k is constant and $\beta(H_{0m})\Delta H_f$ is the change of induction due to the irreversible displacement of domain boundaries, for which the maximum critical field are H_{0m}, by the field change ΔH_f and it is assumed, basing on the reason described in the previous paper, that $\beta(H_{0m})$ is equal to $|\Delta B/\Delta H|$ along the hysteresis loop. Parameter a is a velocity constant. The relation H_{0m} and t is given by the equation

$$t = D/[a(H_f - H_{0m})]. \qquad (2)$$

The value D/a in this equation is calculated from the relation given in the previous paper

$$t_0 = D/(a\overline{\Delta H_f}), \qquad (3)$$

and in this case the range of H_{0m} corresponding to a time interval from $t_0 = 1/100$ seconds to ∞ is $\overline{\Delta H_f}$. Now the curves of $\beta(H_{0m})$ calculated from the hysteresis loops at 95°C and −195°C are expressed in Fig. 2. Therefore $B_n(t)$ is computable by Eq. (1) using the observed $|\Delta B/\Delta H|$ and adequate value of kD/a. The value of $\overline{\Delta H_f}$ is determined from a measurement of the effect of intermediate field as given in the following pages, and as the value of $\overline{\Delta H_f}$ 0.6 *Oe* and 0.35 *Oe* is chosen for −195°C and 95°C respectively. The calculated curves of $B_n(t)$ for various values of H_f at

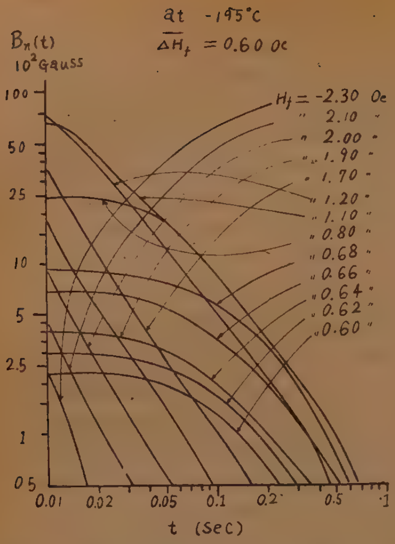

Fig. 7. Calculated curves of $B_n(t)$ *vs* t for various H_f at −195°C.

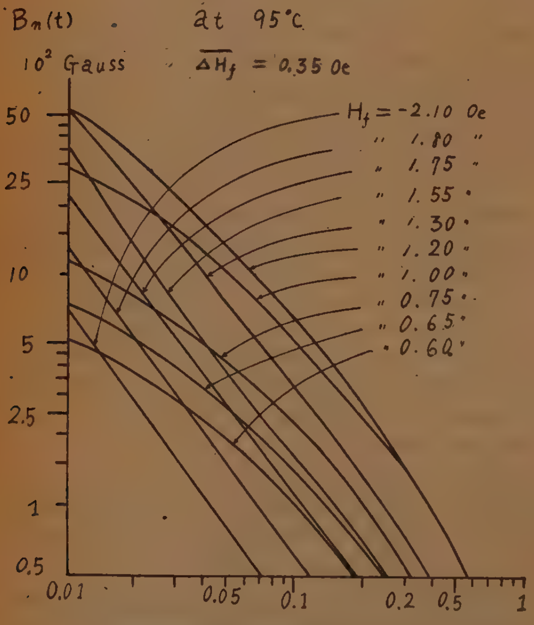

Fig. 8. Calculated curves of B_n (t) *vs* t for various H_f at 95°C.

−195°C are shown in Fig. 7. As can be seen from the figures, the theoretical curves for $B_n(t)$ coincide well qualitatively with the observed ones. However, the curves for smaller values of final field than H_f(max) show smaller inclination than that of observed one, and as shown in Fig. 9 the calculated value of B_{no} shows more rapid decrease with decreasing H_f than the observed one in same range of final field. The cause of these discrepancies are considered as follows: firstly, observed $|\Delta B/\Delta H|$ takes larger values than $\beta(H_{0m})$ in the rotation ranges of magnetization, hence a correction must be added on the value of $\beta(H_{0m})$ above obtained. Next, the value of $\overline{\Delta H_f}$ is considered here as constant for all the values of final fields, however from the observed dependence of $B_n(t)$ upon H_m, it is concluded that the value of $\overline{\Delta H_f}$ increases with decreasing H_f and this change of $\overline{\Delta H_f}$ must be taken into account in the calculation of $B_n(t)$. With these modifications on both $\beta(H_{0m})$ and $\overline{\Delta H_f}$ the theoretical curves of $B_n(t)$ will approach to the observed ones. The joining point in the theoretical $B_n(t)$ curve at low temperature is due to the rectangular form of $\beta(H_{0m})$, but with the rise of temperature the form of $\beta(H_{0m})$ becomes smooth one gradually, and hence the knick gradually disappears; compare Fig. 7 (low temperature) and Fig. 8 (high). As the amount of B_{no} is given by Eq. (1), the character of its dependence on temperature is determined by that of both $\overline{\Delta H_f}$ and $\beta(H_{0m})$. In general, B_{no} diminishes due to the strong decrease of $\overline{\Delta H_f}$ as shown in the previous paper. In the present case, the value of B_{no} at 95°C for the final field smaller than −0.90 *Oe* is larger than that at 18°C as shown in Fig. 2, and if the change of $\beta(H_{0m})$ is larger than that of $\overline{\Delta H_f}$ at both temperatures, then it is reasonable that B_{no} takes a larger value for such a range of H_f at 95°C than that at

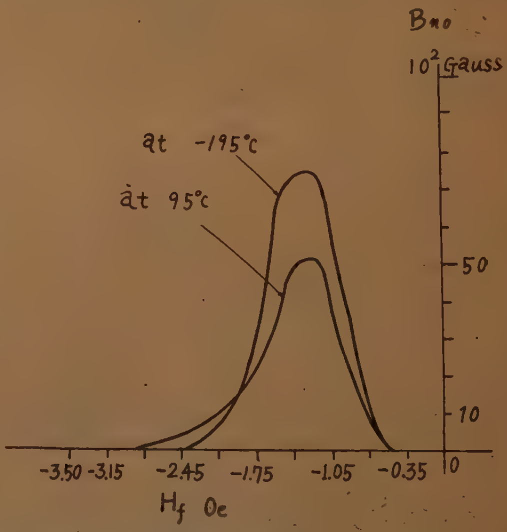

Fig. 9. Calculated curves of B_{no} *vs* H_f at −195°C and 95°C.

18°C.

Next, let us describe the effect of a rest at intermediate field H_m during the field change. When the magnetic field is maintained at H_m for sufficiently long period, all the domain boundaries for which H_{0m} takes smaller value than H_m displaces irreversibly and then the form of $B_n(t)$ shows the same characteristics as those for the final field H_m. If the external magnetic field changes subsequently to H_f, the changes of B does not occur in this case for the period from t_0 to $t_m = D/a(H_f - H_m)$ because the domain boundaries which have displaced already at the intermediate field H_m do not contribute to the after effect when the field is changed from H_m to H_f. Therefore, the values of $B_n(t)$ for value of t larger than t_m coincide that of the normal after-effect. If the difference $H_f - H_m$ and ΔH_f takes a smaller value, then the characteristics of $B_n(t)$ and the value of B_{no} approach respectively to those of the normal after-effect. The effect of H_m vanishes when the difference H_f and H_m is equal to or greater than $\overline{\Delta H_f}$, and therefore, the value of ΔH_f can be obtainable. The value of $\overline{\Delta H_f}$ is about 0.6 *Oe* for the final field $H_f = -$ 0.70 *Oe* and shows a tendency of increasing with decrease of H_f.

According to the previous paper the value of $\overline{\Delta H_f}$ is considered as almost constant in the small range of tension above mentioned, then B_{no} is strongly decreased by the tension applied due to the decrease of $\beta(H_{0m})$ as shown in Fig. 6. The curve of $B_n(t)$ vs t for the final field larger than H_f(max) becomes smooth because the form of $\beta(H_{0m})$ becomes smoother than that without tension. The form of $\beta(H_{0m})$ for the final field smaller than H_f(max) does not differ remarkably from that without tension, therefore, it is also expected that the form of $B_n(t)$ does not change by the applied tension. As stated above, the experimental results shown in Fig. 5 coincide well with theoretical results.

This investigation was carried out under the supervision of Dr. T. Hirone, Professor of Tôhoku University.

References.

1) S. Maeda: Jour. Phys. Soc. Japan. **5** (1950) 358. Jour. Phys. Soc. Japan. **6** (1951) 60.

JOURNAL OF THE PHYSICAL SOCIETY OF JAPAN Vol. 6, No. 6, Nov.—Dec., 1951

The Short Range Orders in Cu$_3$Au.

By Takehiko OGUCHI

Tokyo Institute of Technology, Oh-okayama Tokyo.

(Received April 19, 1951)

For an alloy of face centered cubic lattice consisting of A and B atoms present in the proportions 3 and 1, the short range order parameters for the sites of various distances from a given atom are calculated using the assumption of the nearest neighbour interaction at the temperatures above Curie point. The experimental results, especially the short range order parameter for *3rd* neigbour, which is inconsistent with the result obtained by Bragg-Williams' approximation, are explained qualitatively in this paper.

§ 1. Introduction.

Last year, Cowley[1] determined the short range order parameters for sites of various distance by means of the X-ray diffraction effects for an alloy Cu$_3$Au above its Curie temperature. If an Au atom is taken as origin and its site is tentatively named as β site (see Fig. 1), then *1st* and *3rd* neighbours are α sites and the probabilities that these sites are occupied by Cu atoms would be greater than that at perfect disorder. In the same way,

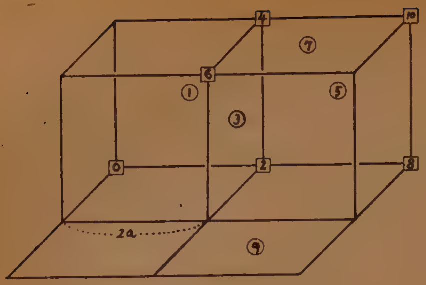

Fig. 1.

○ α site	□ β site
1 (0, a, a)	6 (2a, 2a, 2a)
2 (0, 2a, o)	7 (a, 3a, 2a)
3 (a, 2a, a)	8 (o, 4a, o)
4 (o,2a,2a)	9 (3a, 3a, o)
5 (o, 3a, a)	10 (o, 4a, 2a)

2*nd* neighbours are β sites and the probabilities that these sites are occupied by Au atom would be greater than at perfect disorder. According to Cowley's experimental results, however, the situation with respect to 3*rd* neighbours is opposite to above appreciation, though the estimations as regards 1*st* and 2*nd* neighbours turned out to be right. That is, α_1/α_1^0 and α_2/α_2^0 in Cowley's paper take positive values but α_3/α_3^0 takes negative value. Cowley explained it by his approximate theory but the author wishes to treat the same problem more rigorously by the theory of the propagation of order[2].

§2. Calculation.

Let the pair energies of Au-Au and Cu-Cu be denoted by $J/2 (J>0)$ respectively and that of Au-Cu be denoted by $-J/2$. If we introduce an external magnetic field H in place of the terms of absolute activity and consider Cu or Au atoms as scalar spins paralled or anti-parallel to the field. We can regard the system as an Ising model of ferromagnet. Let each of spins be capable of two orientations which we characterize by $\mu_i=+1$ $\mu_i=-1$. The partition function f in the face centered cubic lattice is

$$f=\sum_{\mu_i=\pm1}\exp\left(-K\sum_{<ij>}\mu_i\mu_j+C\sum_i\mu_i\right)$$
$$=(\cosh K)^{6N}(\cosh C)^N\sum_{\mu_i=\pm1}\prod_{<ij>}(1-\mu_i\mu_j\kappa)\prod_i(1+\mu_i\gamma), \qquad (1)$$

where

$$K=J/2kT, \qquad C=mH/kT,$$
$$\kappa=\tanh K, \qquad \gamma=\tanh C, \qquad (2)$$

and m is the magnetic moment of each spin and N is the total number of spins. In developing the products, we have calculated the terms up to κ^3, which are dominant for high temperatures, as following,

$$f^{\frac{1}{N}}=2(\cosh K)^6(\cosh C)(1-6\kappa\gamma^2+66\kappa^2\gamma^2-51\kappa^2\gamma^4-8\kappa^3-702\kappa^3\gamma^2+1604\kappa^3\gamma^4-914\kappa^3\gamma^6\ldots\ldots). \qquad (3)$$

The mean magnetization M/N is

$$M/Nm=\frac{\partial}{\partial C}\log f^{\frac{1}{N}}$$
$$=\gamma-12\kappa\gamma+12\kappa\gamma^3+132\kappa^2\gamma-408\kappa^2\gamma^3+276\kappa^2\gamma^5-1404\kappa^3\gamma+9404\kappa^3\gamma^3-15752\kappa^3\gamma^5+7752\kappa^3\gamma^7 \qquad (4)$$

This is taken to be 1/2 because the concentration ratio have to be 3:1. We expand γ to the positive power series of κ and from (4) we determine the coefficients of each terms as following,

$$\gamma=\frac{1}{2}+\frac{9}{2}\kappa-\frac{81}{8}\kappa^2-\frac{669}{16}\kappa^3 \qquad (5)$$

The probability that an atom on any site is an Au atom, is $f(Au)/f$, where $f(Au)$ is a partition function to be taken over the configurations allowed by the restriction by which one atom on the site is certainly an Au atom. Using (4) for γ, $f(Au)/f$ is certainly 1/4, which is of course the probability to be in proportion to the concentration ratio. Thus in this magnetic field (5), the concentration ratio is really kept as 3 : 1 at any temperature.

The correlation probabilities are calculated in the same way as in the reference (2), except that the system subjects to external magnetic field this time. The results are following,

$$C_{01}(Au,Cu)=\frac{3}{16}\left(1+\frac{3}{4}\kappa-\frac{21}{8}\kappa^2+\frac{873}{64}\kappa^3\cdot\cdot\right)$$
$$C_{02}(Au,Au)=\frac{1}{16}\left(1+\frac{27}{4}\kappa^2-\frac{297}{8}\kappa^3\cdot\cdot\right)$$
$$C_{03}(Au,Cu)=\frac{3}{16}\left(1-\frac{9}{8}\kappa^2+\frac{279}{32}\kappa^3\cdot\cdot\right)$$
$$C_{04}(Au,Au)=\frac{1}{16}\left(1+\frac{27}{16}\kappa^2-\frac{135}{8}\kappa^3\cdot\cdot\right)$$
$$C_{05}(Au,Cu)=\frac{3}{16}\left(1+\frac{243}{64}\kappa^3\cdot\cdot\right)$$
$$C_{06}(Au,Au)=\frac{1}{16}\left(1-\frac{243}{32}\kappa^3\cdot\cdot\right)$$
$$C_{07}(Au,Cu)=\frac{3}{16}\left(1+\frac{27}{32}\kappa^3\cdot\cdot\right)$$
$$C_{08}(Au,Au)=\frac{1}{16}\left(1\cdot\cdot\right)$$
$$C_{09}(Au,Cu)=\frac{3}{16}\left(1+\frac{27}{64}\kappa^3\cdot\cdot\right)$$

$$C_{0,10}(Au,Au)=\frac{1}{16}(1 \qquad \ldots). \qquad (6)$$

Notation $C_{0n}(Au, Cu)$ is the correlation probability which Au atom is on *0th* site and at the same time Cu atom is on a site of the *nth* shell of neighbours.

§ 3. Conclusion.

If the number of Cu atoms on α site etc. are denoted by $[Cu \text{ on } \alpha]$ etc., those are written by

$$[Cu \text{ on } \alpha]=\frac{N}{16}(9+3S),$$

$$[Au \text{ on } \alpha]=\frac{N}{16}(3-3S)$$

$$[Cu \text{ on } \beta]=\frac{N}{16}(3-3S),$$

$$[Au \text{ on } \beta]=\frac{N}{16}(1+3S), \qquad (7)$$

where S is the long range order parameter. If *0th* site is β site, all sites in the *3rd* shell of neighbours are β sites, but if 0th site is α site, 8 of 24 sites in the *3rd* shell are β sites but the rest 16 are α sites. Hence $C'_{03}(Au, Cu)$, where dash means the result obtained by Bragg-Williams approximation, is $\frac{1}{16}(3+S^2)$, so

$$\frac{3}{16}\leq C'_{03}(Au,Cu)\leq\frac{1}{4}. \qquad (8)$$

By the similar consideration,

$$\frac{1}{16}\leq C'_{06}(Au,Au)\leq\frac{1}{4}. \qquad (9)$$

When the temperature is high enough and power series (6) are of better convergent, the principal term except 1 is that of lowest power of κ, because κ is in proportion to inverse temperature. As easily seen from (6), in $C_{03}(Au,Cu)$ and $C_{06}(Au,Au)$, these lowest power terms are of negative signs, so $C_{03}(Au,Cu)$ and $C_{06}(Au,Au)$ are out side of the limits of (8) and (9). This theoretical result may be responsible for Cowley's experiments. The reason of this fact can be understood as follows. For example, in Fig. 2, between *0th* site and *3rd* site, there are one atom (denoted by x) connection and two atoms' (denoted by x and y) connection. If *0th* site is occupied by an Au atom, x site may be occupied by a Cu atom with higher probability than by an Au atom and this Cu atom rejects a Cu atom so strongly from *3rd* site that the effect of two atoms' connection which has a tendency to let *3rd* site be occupied by Cu atom is yet insufficient. Generally speaking, correlation probabilities are more dependent on the number of connecting atoms between them than on the mere shell number of neighbours.

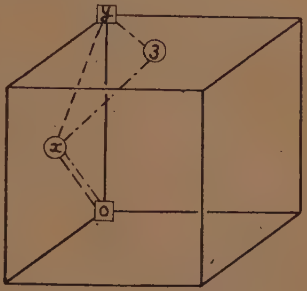

Fig. 2.

The calculation for low temperatures is also possible, but it would not correspond to the real Cu₃Au alloys. Because even for lowest temperature, Cu₃Au has a various kind of antiphases.

The author wishes to express his cordial thanks to Dr. G. H. Wannier for stimulating his interest in this problem and also to Professors Y. Takagi and R. Kubo for valuable discussions.

The expense of this research has been defrayed from the Scientific Research Expenditure of Department of Education.

References.

1) J. M. Cowley: Phys. Rev. **77** (1950) 669.
2) T. Oguchi: J. Phys. Soc. Japan **6** (1951) 31.

JOURNAL OF THE PHYSICAL SOCIETY OF JAPAN Vol. 6, No. 6, Nov.—DEC., 1951

Accurate Measurement of Lattice Constant by Means of Electron Diffraction.*
Lattice Constant of KCl Referred to Au.

By Norio KATO.**
Physical Institute, Faculty of Science, Nagoya University. Nagoya, Japan.

(Received May 10, 1951)

The experimental method adopted was the same as that of Finch and Wilman. The following effects which might cause errors in the measurement were either eliminated or proved to be of negligible order; (1) inadequate setting of specimen of photographic plate to electron beam, (2) refraction, (3) charging up of the plate, (4) temperature elevation by electron-impact.

With beaten gold foil or evaporated gold film annealed at 300° C as the standard references, the following results were obtained on the lattice constant of KCl in both cases; (1) with KCl films immediately after preparation by vacuum evaporation, it was +0.3~0.15% larger than the X-ray value, (2) by exposure of the film to air, the deviation decreased to a stationary value of +0.15% aud (3) specimen prepared by precipitation from aqueous solution showed the above stationary deviation.

§1. Introduction.

The measurement of lattice constants of crystals by X-rays is carried out using characteristic radiation whose wave-length is invariable and accurately known; while in the case of electron diffraction, the wave-length must be measured by some means for each experiment. As is well known, it can be calculated from the accelerating voltage or the velocity of electrons, provided the fundamental constants e, m, c and h are given, but this method is not usually adopted because of difficulties in obtaining a high accuracy. The usual method is a direct measurement of wave-length based on Bragg relation, $2d \sin\theta=\lambda$, assuming the X-ray value of spacing, d. (λ: the wave-length, θ : the Bragg angle.) This amounts to measure a relative value of spacing of a test specimen compared with a certain standard substance. Gold foils, smokes of metal oxides (ZnO or MgO) and evaporated alkali halides (NaCl) were proposed to be favorable for the standard substance and discussed by several authors1)2)3)4).

There is a serious difficulty, however, that the ratio of lattice constants thus determined of these substances is not in accordance with that of X-ray values. For example, Finch and Fordham5) found the lattice constants of several alkali halides to be larger as much as 0.5~0.6% than the corresponding X-ray values taking gold as the standard, though Boochs6) found no discrepancy provided the specimen was composed of fairly large crystallites. Similar discrepancies were also observed for other substances7)8)9)10). The interpretation of this discrepancy, in the case of metals and metal oxides, may be found in trivial causes such as non stoichiometric nature of surface layer. In the case of a pair of gold and alkali halides, however, it seems difficult to attribute the discrepancy to such an effect.

The author carried out measurement for a pair, gold and KCl, and found, after eliminating all conceivable errors, a disagreement with the X-ray value, though not so remarkable as that found by Finch and Fordham. He believes the result to be worthy of reporting, though the experiment was not carried out with the high resolution diffraction camera, such as constructed by Hillier and Baker11).

§2. Experimental Method and Derivation of Lattice Constant.

The method of superimposed pattern, first deviced by Finch5) was adopted in the present experiment, because it seems to be free from systematic errors compared with the other methods6)10). The specimen was prepared by

---

* The expence of this study was defrayed from the Grant in Aid for Fundamental Scientific Research of the Educational Ministry.

** Now at *Kobayasi Institute of Physical Research, Kokubunji, Tokyo, Japan.*

depositing a small amount of KCl on gold foil (see § 3). It was mounted on the specimen holder of a diffraction camera, and, using transmission method, superimposed Debye-Scherrer rings of the two substances were obtained by a single exposure. The equipment used was the one of camera-length 15cm. designed by Uyeda[12]. Though it was too small for the present purpose, the electron beam, focussed by a Wehnelt cylinder and a magnetic lens, was sharp enough to obtain good photographs on which the ring diameter was measured to 1/1000 mm.

Calculation of lattice spacing from a superimposed pattern was performed as follows: From Bragg formula

$$2d \sin \theta = \lambda , \qquad (1)$$

and geometrical relation

$$D = 2L \tan 2\theta , \qquad (2)$$

we obtain

$$2L\lambda = dD(\cos 2\theta / \cos \theta) , \qquad (3)$$

where L is the camera length and D is a ring diameter. An accurate value of $2L\lambda$ can be deduced by (3) from the measured value of D for the standard substance, because no accurate value of θ is required to calculate the term in the parenthesis. Using the mean value $2L\lambda$ deduced from the standard substance, unknown spacings of the test substance are calculated by (3) in the reverse way.

§ 3. Specimen.

In the present experiment, two sorts of gold sample, commercial beaten foil and that in a form of wire, were used. The spectroscopic analysis showed that the former contained a considerable amount of impurities, Si, Mg, Ag and Cu, while the latter only a trace of Ag.

Their lattice constant was measured by X-rays following the extrapolation method of Bradley and Jay[13]. A camera of diameter 7 cm. calibrated with quartz powder was used and copper was selected for the anti-cathode to facilitate the extrapolation. The results of measurement, corrected at 18°C, are given in Table I. The value of the wire sample coincides well with that cited by Wyckoff[17], while that of the foil deviates a little from it.

Foils were prepared from the wire sample by evaporation in vacuum and they were annealed at 300°C for 1 hour. Both sorts of foil, the beaten and the evaporated, were etched by KCN solution to have suitable thickness for diffraction specimen. In all the following descriptions, gold is assumed as the standard and the lattice constants given in Table I are used.

Two sorts of KCl sample, both extra-pure chemical reagents, were used; one produced by Merck (German) and the other by Konishi (Japanese). Their spacings were also measured by X-rays in the same method as above, using nickel anti-cathode. The measured values of both samples were in good agreement with that cited by Wyckoff[17] as shown in Table I.

Table I. X-ray value.

	KCl		Au	
Wyckoff	6.2770		4.070	
	Merck	Konishi	Wire	Foil
Present results	6.277_0 ±0.0008	6.277_3 ±0.0005	4.070_1 ±0.0002	4.071_9 ±0.0015

KCl was deposited on the gold foil by two methods: vacuum evaporation and desiccation. The former was carried out under pressures of 10^{-3}–10^{-4} mm. Hg using tungsten or molybdenum filament. The latter was attained by floating a piece of gold foil on saturated KCl solution, scooping it up by a spiral of gold wire and then desiccating rapidly above an electric furnace.

§ 4. Causes of Error.

(i) *Probable error.* An example of data is given in Table II. The probable error of the lattice constant determined from each photograph is about ±0.002 *A*.

Table II. An example of calculation.

$(hkl)_{Au}$	$L'\lambda(A\cdot mm)$	$(hkl)_{KCl}$	$a(A)$
111	17.642_4	200	6.286_4
200	17.669_9	220	6.280_7
220	17.654_6	222	6.274_9
311	17.642_7	400	6.278_7
222	17.649_5	420	6.282_6
331	17.672_5	422	6.282_6
420	17.657_4	440	6.296_9
422	17.658_3	600	6.276_1
333	17.651_8	620	6.278_7
		640	6.282_8
Average	17.655_5	Average	6.282_8
Probable error	±0.0025	Probable error	±0.0015

(ii) *Effect of unfavorable geometrical arrangement.* When the incident beam does not impinge perpendicularly on the photographic plate and the ring diameter is not measured rigorously through its center, Eq. (2) should be replaced by

$$D=2L\tan 2\theta(1+A+B+C)\,, \qquad (2)$$

where $A=2(a/D)^2$, $B=\sin\varphi\cdot\delta\cdot(a/L)$,

$$C=(1/2)\cos^2\varphi\cdot\delta^2\,.$$

The meaning of the notations is illustrated in Fig, 1.

The error due to A is easily detected because the apparent lattice constant varies systematically against the corresponding diameter when a is not small. Data with such a variation were discarded and the measurement was repeated. The cross term B is negligibly small. The error due to C can be eliminated as shown in Table III, when $L'=L(1+C)$ is taken as an effective camera length, since C is independent of D. The facility of the elimination of these errors is an advantage of this method compared with that of Boochs and of Riedmiller[10].

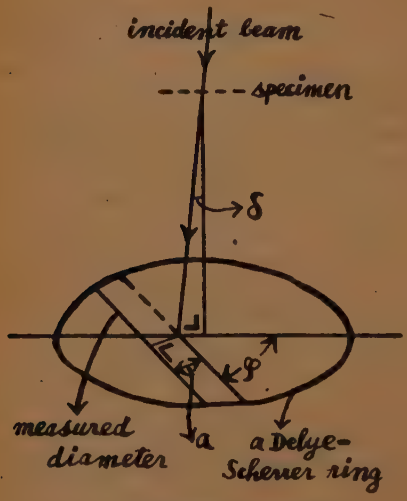

Fig. 1. Geometrical arrangement.

Table III. The result of measurements along two different diameters perpendicular to each other on one photographic plate.

Diameter	$L'\lambda(A\cdot\text{mm})$	$a(A)$
1	17.643	6.283_3
2	17.656	6.282_2
Difference	$7.3\times10^{-2}\%$	$0.8\times10^{-2}\%$

(iii) *Effect of refraction.* Since Bragg formula (1) is deduced by the kinematical theory, it is not accurate and the refraction effect in a wide sense, deduced by the dynamical theory[14], must be taken into account. Although it is not negligible in measurements as accurate as the present experiment, it should occur in a symmetrical way around a normal position of ring predicted by (1), provided that the orientation of crystallites is at random[3]. Therefore the correction is unnecessary.

(iv) *Effect of charging up on photographic plate.* In an early stage of our experiments, the value of $2L\lambda$ showed a variation as shown in Fig. 2. The form of the curve was always similar, though the magnitude of variation was not the same. The similar phenomenon was reported previously by Cosslett[15], and he interpreted it by assuming a certain contraction of lattice near the crystal surface. His interpretation, however, is not adequate for the present case, because, the same contraction for Au and KCl must be assumed to explain the result given in Fig. 2, and this is not likely to occur.

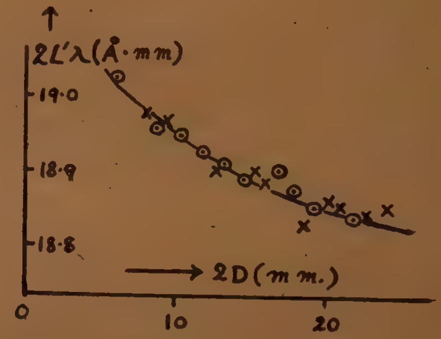

Fig. 2. The variation of $L'\lambda$.

⊙: The value calculated from KCl-ring assuming the lattice constant to be 6.282 A.

×: The value calculated from Au-ring assuming the lattice costant to be 4.070 A.

—: The curve calculated from Eq. (4) in the text.

This may be explained as an effect of charging up on the photographic plate. Since the gelatin film of the plate is a poor conductor, the incident beam produces a potential gradient in the space near the plate, and this may deflect the diffracted beams. Assuming a circular plate of diameter D_0 whose periphery is at ground potential, an approximate calculation gives the deflection, ΔD, as

$$\Delta D/D=(I_0\sigma/8\pi tE)(1/2-\log D/D_0)\,, \qquad (4)$$

where D is the diameter of a ring, I_0 the current of the incident beam and σ the specific resistance of gelatin and t the thickness of the film. The form of the curve (4) agrees qualitatively with that of Fig. 2, and a set of reasonable values: $I_0=10^{-9}$ amp., $\sigma=10^{+10}$ ohm cm, $t=0.1$ mm. and $E=4\times10^4$ volt predicts a deviation which agrees with the observed one in the order of magnitude.

This unfavorable effect was fortunately avoided by using photographic plate provided by another maker. All the following results were obtained with such plates.

(v) *Effect of retardation of electrons in specimen.* A calculation of the retardation of electrons in specimens from the Whiddington constant[18] shows that it is negligible. It may be worth while to note that the electrons which suffered inelastic scattering in a specimen are ineffective to coherent patterns such as Debye-Scherrer rings.

In the present experiment, however, a pair of photographs, in which the beam is penetrated from the side of KCl to Au and in the reversed sense, were taken in every case, but no systematic difference was observed between them.

(vi) *Effect of temperature rise due to electron beam.* The thermal expansion coefficients of KCl and *Au* are 3.8×10^{-5} deg.$^{-1}$ and 1.4×10^{-5} deg.$^{-1}$ respectively. Then, a temperature rise of about 30°C should result in a variation of 0.1% in the ratio of spacings of these substances. Therefore this effect must be studied with a great care. As the temperature of the irradiated part of the specimen is hardly measurable, the law of cooling and heating was used for the test. When the specimen is irradiated, the variaton of its temperature $\varDelta T$ may be expressed, under a certain approximation

$$\varDelta T \doteq (k/\alpha)I_0\{1-\exp(-\alpha t/c)\}\,, \quad (5)$$

where I_0 is the intensity of the electron beam, αT is the rate of heat loss and KI_0 that of heat production in the specimen, c the heat capacity of the specimen and t the time of irradiation.Using the data of stopping power of electrons and heat conductivity of gold in bulk state, the temperature rise for $t=\infty$ is estimated to be 0.3°C at most under the conditions of the present experiment. Although this value shows the effect to be negligible, an experimental proof is desirable because the estimation is very rough.

When c/α is small, $\varDelta T$ is proportional to I_0 as pointed out by Pickup[8]. Numerous experiments were carried out with various I_0 in wide range such as 1 : 100, and no effect in the lattice constant ratio was observed. If c/α is large, however, the above proof bails, because the mean value of $\varDelta T$ during the time of exposure, t, is expected to be constant provided the value of I_0t to be the same, and usually it is adjusted to have an adequate exposure, Taking this fact into consideration, numerous photographs were taken under various conditions; in some of them, exposures were made after an intense and long irradiation and in the others, they were done without any previous irradiation. No effect, however, due to the previous irradiation was found. Therefore it is believed under the conditions of present experiment the temperature rise is negligible as estimated above.

(vii) *Effects of charging up of specimen.* Charging up of the specimen must have influence on the lattice constant in some ways. One of them is the electrostatic repulsion in a crystallite which may enlarge its volume, *i.e.* the lattice constant. Another is a strong electric field between the layers of Au and KCl which may accelerate electrons. Although rigorous estimation is not possible, the crystallite would break down if such an amount of charge is accumulated in a crystallite to cause the apparent change in lattice constant of *ca.* 0.1%.

§ 5. Experimental Results.

The Debye-Scherrer rings due to evaporated KCl were found to be intense soon after the evaporation*, they became weaker and finally disappeared as the period of the exposure of specimen to air was increased. This is supposed to be caused by recrystallization, by which the area of KCl specimen effective to diffraction of electrons is decreased. This effect is enhanced by higher humidity, showing that the recrystallization occurs under the influence of water vapor in air.

The lattice constant of evaporated KCl referred to Au was found to be always larger than the X-ray value as much as 0.1-0.2%, deviations exceeding the probable error described in (i) of § 4. Tendencies were found, moreover, that the deviation varies with the mean thickness of KCl layer and the period of exposure to air, *viz.* it is smaller for thinner layer and for longer exposure. The author believes that the lattice constant of evaporated KCl is decreased by some unknown effect when the recrystallization takes place. This may also explain the smaller value for thinner layers, because the recrystallization may take place faster in thinner layers. The results obtained with a pair of beaten gold foil and Merck's KCl, corrected at 18°C, are illustrated in Fig. 3. In this figure, circles and crosses indicate the lattice constant for the case of the least period and of a few hours of exposure to air, respectively. There are observed not only the above variation (although there is one exceptional case in Fig. 3.), but also the fact that all the crosses have the same ordinate within the experimental errors. This suggests that the lattice constant takes a stationary value after the exposure described above, though the specimen exposed for a very long period can not be examined since the patterns disappear for such a specimen. The mean value of the crosses turns out to be

---

* Since the evaporation was not performed in the diffraction camera, it was inevitable to expose the sample to air for several minutes.

$$a = 6.286_5 \pm 0.0007 \text{ A} .$$

This is about 0.15% larger than the X-ray value. The similar behavior was observed for all the other samples and the mean values after a certain exposure were in good agreement with the above one as given in Table IV.

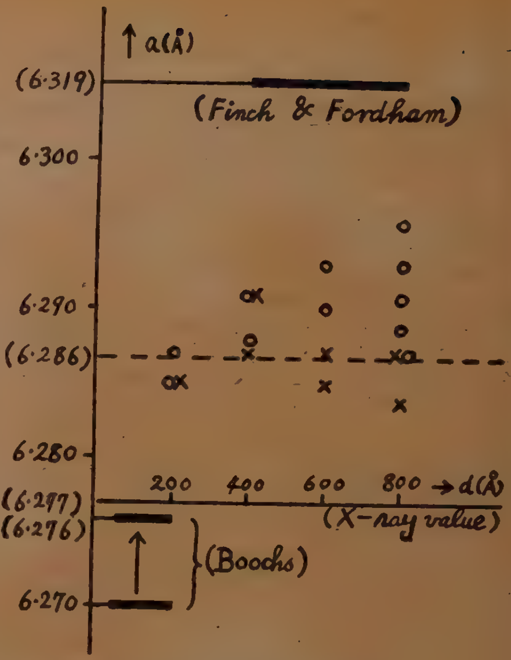

Fig. 3. Lattice constant of KCl.
a: Lattice constant of KCl.
d: Mean thickness of KCl film.
○: soon after evaporation.
×: after exposure to air.

Table IV. Experimental results.

KCl	Gold	$a(A)$	Deviation (%)
M.	E.	6.286_0	0.15
K.	E.	6.281_5	0.07
M.	B.	6.286_5	0.15
K.	B.	6.284	0.11

M. : Merck, K. : Konishi, E. : evaporated foil, B. : beaten foil.

Since the lattice constant of evaporated KCl varies with recrystallization, it is desired to obtain lattice constant of KCl specimen prepared by desiccation from the solution (§ 3). Actually the sample used for X-rays is prepared by the method of recrystallization from the solution. Although a little difficulty was encountered in obtaining good photographs with such specimens, the experiment succeeded. The mean value obtained from several specimens was found to be

$$a = 6.287 \pm 0.0007 \text{ A},$$

in good agreement with the previous value.

§ 6. Discussion.

In the preceeding section, it was described that the deviation of lattice constant of KCl referred to gold is composed of two parts: the variable and the stationary. The former may surely be correlated to the recrystallization of KCl crystallites, though it is not clear whether it is intrinsic to the substance KCl or due to some impurities introduced in the course of evaporation. On the other hand the latter may not be due to impurities, because it was observed also for desiccated specimens where the admixture of impurities seems to be impossible. It may be due to some effect other than that described in § 4.

Finch and Fordham[4)] observed a larger deviation* for KCl, NaCl *etc.*, and interpreted it as due to Lennard-Jones' effect. This interpretation, however, is not adequate for the present results because the sharpness of Debye-Scherrer rings obtained in the present experiment indicates that the deviation exists not only in a few layers near the crystal surface as in the Lennard-Jones' effect, but it extends more than $100A$ in depth below the surface. Boochs⁷⁾ found a deviation of about -0.08% immediately after evaporation. Although this seems to contradict with the present results, it is not commensurable with ours, because his specimen was composed of such small crystallites as to show diffuse rings. After exposure to air, he observed no deviation in most cases, though recognized a deviation of $+0.1\%$ only in a few exceptional cases. This seems to contradict with the present result.

---

* The author learned by Prof. Finch's communication to Prof. Uyeda, that the deviation was due to gold foil, and Dr. Garrod in his laboratory found no deviation when graphite was used as a standard.

A few speculative interpretation of the stationary part of the deviation may be possible. For example, lattice imperfection or the color centers may influence the lattice constant. Actually, the irradiated part of the specimen appears violet under a microscope. But the prevailing theory and experiment on lattice imperfection is not likely support this speculation¹⁶⁾. The variation of lattice constant of gold by etching is also not likely to be the case, though it should not be excluded *a priori*. The effect is unexplained and the author has no intention to decide whether it is to be attributable to KCl or Au.

§ 7. Acknowledgements.

It is a pleasure of the author to express his thanks to Professor R. Uyeda for his valuable advices and discussions throughout the course of the work, and to Professor G.I. Finch who gave them valuable informations in his private communication. He also expresses his indebtness to Professor K. Yamasaki in obtaining the data on spectroscopic analysis.

References.

1) L. Sturkey and L. K. Frevel, Phys. Rev. **68** (1950) 56.

2) C. S. Lu and E.W. Malmberg, Rev. Sci. Inst. **14** (1943) 271.

3) J. M. Cowley and A.L.G. Rees, Proc. Phys. Soc. London **59** (1947) 287.

4) F. W. C. Boswell, Phys. Rev. **80** (1950) 91.

5) G. I. Finch and S. Fordham, Proc. Phys. Soc. London **48** (1936) 85.

6) H. Boochs, Ann. d. Phys. Lpz. **35** (1939) 333.

7) G. I. Finch and A. Wilman, J. Chem. Soc. (1934) 751.

8) E. Pickup, Nature **137** (1936) 1072.

9) V. E. Cosslett, Proc. Phys. Soc. London **49** (1937) 121.

10) R. Riedmiller, Zeits. f. Phys. **102** (1936) 408.

11) J. Hillier and R. F. Baker, J. App. Phys. **17** (1946) 12.

12) R. Uyeda, X-rays **4** (1944) 23 (in Japanese).

13) A. J. Bradley and A. H. Jay, Proc. Phys. Soc. London **44** (1932) 563; *Ibid.* **45** (1933) 507.

14) N. Kato, Proc. Jap. Acad. **25** (1949) 41; N. Kato and R. Uyeda, Acta. Cryst. (in print).

15) V. E. Cosslett, Trans. Farad. Soc. **31**, II (1935) 1119.

16) F. Seits, Rev. Mod. Phys. **18** (1945) 384 § VII.

17) R. W. G. Wyckoff, *The Structure of Crystals, 2nd Edition, Supplement* (1935).

18) Whiddington, Proc. Roy. Soc. London A **86** (1912) 360.

JOURNAL OF THE PHYSICAL SOCIETY OF JAPAN Vol. 6, No. 6, NOV.~DEC., 1951

Mechanism of Precipitation of α from β in 60:40 Brass.

Gunji SHINODA and Yoshitsugu AMANO.
Institute for Applied Physics, Osaka University

(Read November 5,1950; Received May 26,1951)

Body-centred cubic β brass, containing ca. 40% Zn, obtained by quenching from 850°~900°C. shows reversal process of Kurdjumow and Sachs type transformation during tempering. Various intermediate structures between β and face-centred cubic α were ascertained by means of X-ray analysis using capillary and ordinary X-ray tubes. Such are body-centred and face-centred tetragonal structures having various axial ratios; therefore the transformation must take place with gradual manner, although the formation of martenstic needles are well known. The decrease of solubility of Zn in α solid solution due to lowering of the temperature, determined from X-ray data, is more significant than that of Konobejewski.

§1. The initial and final stages of the transformation.

If we quench copper-zinc alloys containing 40% of zinc, which have $\alpha+\beta$ structures in an equilibrium state, from 850°~900°C, nearly uniform β structures will be obtained. As the β phase has a body-centred cubic lattice, fairly large crystals will be obtained simply by heating at such temperatures. When such β is tempered, it decomposes into α and the mechanism was already investigated by Straumanis and Weerts[1] and a reversal process of Kurdjumow and Sachs type was confirmed. In our case, as we can start from single crystals of β the mechanism of the transformation from body-centred cubic β into face-centred cubic α will be studied much precisely. The method of the experiment* was the back reflection

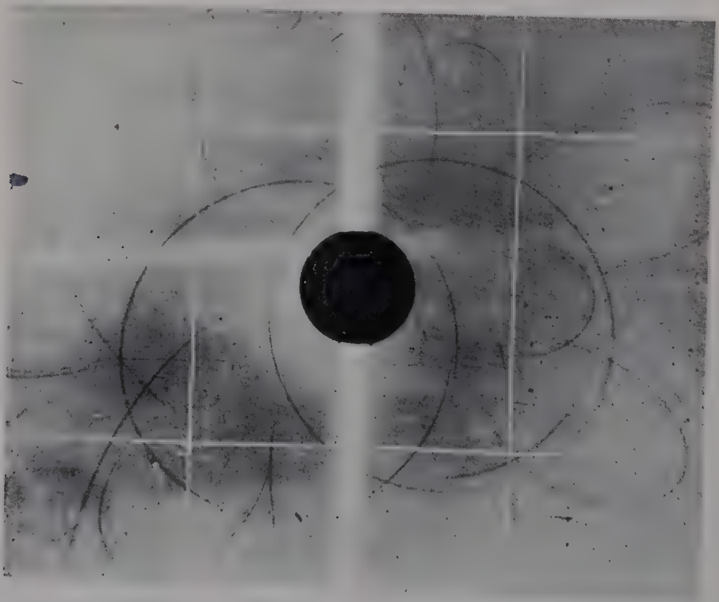

Fig. 1. β crystal by capillary X-ray tube, short flecks showing crystals. Quenched from 870°C; patterns become diffuse above 225°C; that for precipitated α (fibre) do not appeared. (original; 24 cm. × 33 cm.)

---

* Divergent X-ray was emitted from a foil placed on one side of a capillary tube of 50 cms in length. The tube was one modified that of Fujiwara.

method using capillary X-ray tube and the ordinary back reflection method, the target being copper in both cases.

One of the typical photographs obtained by capillary X-ray tube method is as shown in Fig. 1. Two complete circles intersecting with each other are due to (013) and (103) and several {321} ellipses, having well defined K_{α_1} and K_{α_2} doublet will be seen. From these ellipses we can see that the direction of the surface normal to the crystal plate coincides with [114]; the axis of the capillary tube being perpendicular to the crystal and also to the photographic film. Several short irregular lines in Fig. 1 are those due to α which exist near the boundaries, but two short arcs, one in the inner side of (013) circle and the other intersecting with (103) circle are not ones due to α. From the distance of the arc and the outer circle of (013) and the angle between the arc and the (103) circle we can see that there exists an inclusion several degrees inclined to the matrix crystal. One of the microphotographs of these inclusions is as seen in Fig. 2, the direction of (110) slip bands indicating the angle between the crystal axes of the inclusion and the matrix crystal. Of course, two arcs in Fig. 1 are due to one inclusion and as the angles are nearly equal to 3° and this nearly coincides with the angle between [013] and [103], if the latter is the rotation product of 180° about [113] axis. Therefore the inclusion and the matrix are at the twin relations, if (113) would be able to become a twinning plane. The splitting of (213) ellipse shown in Fig. 1 confirms this supposition.

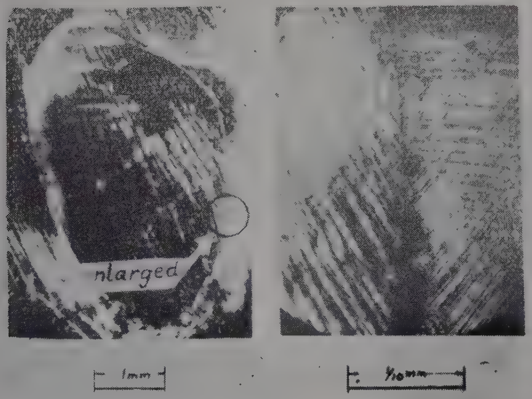

Fig. 2. Inclusion in matrix β; two sets of slip bands are intersecting with small angles.

Broadenings of circles and ellipses do not observed below 225°C, but the diameters of the inner circles gradually increase and those of outer ellipses contract at 200°C. These tendencies continued till 250°C, and, above 225°C. the circles and ellipses become diffuse and faint and finally almost disappear at about 300°C. But the positions of the inner circles do not change till the last moment of decomposition of β, therefore the skeleton of β must remain long.

The inclusion in β matrix was observed by the back reflection Laue patterns, also. As the focus of our ordinary X-ray tube was fairly sharp (0.4 mms. in diameter), we have been able to detect inclusions without using high resolving camera, such as Guinier's. The shapes of the Laue spots were as shown in Fig. 3 (A), similar to that of the slit and there would be observed dark and white bands in the spots. The dark bands corresponds to severely strained parts and white ones show the existence of inclusions. Usually another dark band exactly similar in shape to the white band will be observed in the neighbourhood of the white band. The angular separation of these dark and white bands corresponds to the angle between axes of the inclusion and the matix. Several Spot-like intensity maxima in $\{331\}_\alpha$ and $\{420\}_\alpha$ Debye-Scherrer rings are observed and some of these spot-like maxima together with some of the Laue spots split into several spots by tempering above 225°C. Moreover these spots become diffuse, but as to the spot-like maxima of {331}, only the dis-

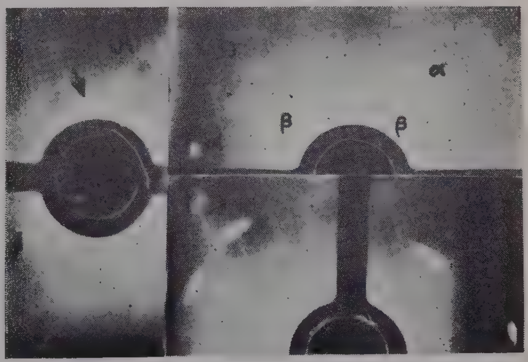

Fig. 3. Back reflection photographs.

(A) quenched from 870°C, showing an inclusion.

(B) quenched from, surface normal coincide with [114].

(C) quenched from, tempered at 400°C, the specimen same as (B).

placements of their positions to the lower lattice spacing side were observed. Fig. 4 indicates the splitting and the displacements of these patterns.

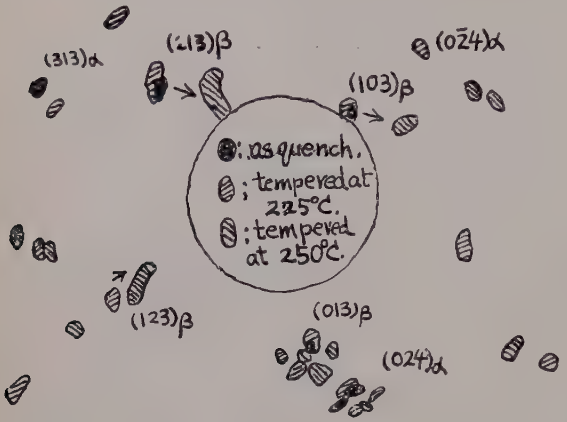

Fig. 4. Discplaements of spots by tempering after quenching; Fig. 3 (B) and (C) corresponding to the right-hand side of the figure.

At 250°C. the Laue spots become more diffuse and their positions displace as shown by the arrows in Fig. 4. At 300°C. $\{331\}_\alpha$ and $\{420\}_\alpha$ patterns displace towards the larger lattice parameter side and become remarkably strong, but the Laue spots become extremely faint and diffuse. At 350°C., these tendencies are quite the same as in 300°C. and at 400°C., sharp and strong patterns of $\{420\}_\alpha$ and $\{331\}_\alpha$ are observed as shown in Fig. 3(C).

From the symmetry of the pattern the fibrous structure cannot be explained unless we assume three axis type as shown in Fig. 5. Each fibre axis are due to either one of the rotations about [001], [010] or [100] of the β crystal and the positions of these axis and corresponding patterns are represented by △, ○ and □ respectively. Patterns due to α in Fig. 3(B) are those for precipitated ones at higher temperatures while those in (C) are due to tempering at relatively low temperature and there exists no differences in their orientations. This means the mechanism of formation of α is quite the same in both cases, whether it has been occurred under an easily diffusing state or not. Once a nucleation of α begins, its orientation prefers a certain definite direction with respect to the matrix β whether it exists in the grain boundaries or not and the further growth of the crystal must be similar to the crystallization of solid from the liquid.* And as the velocity of diffusion is large at high temperatures, precipitated α must have a stable cubic structure, while at lower temperatures there will be an intermediate structure other than cubic one. This will become clear if we consider the changes of the spacings of several atomic planes of α or β, as shown below.

§ 2. Intermediate structures between α and β.

As described above, the glancing angle for $\{313\}_\alpha$ becomes small by tempering at 225°C and then recovers at about 350°C. But the manner shown by $\{420\}_\alpha$ is somewhat different, i.e. some of them displace towards the smaller spacing side and others split into several spots as shown in Fig. 4. These changes will be originated to the following reasons.

(a) change of lattice parameter due to the change of solubility of zinc in α-solid solution.

(b) formation of an intermediate structure other than cubic one.

As was found by Konobejewski and Tarrasowa[2], the solubility of zinc in α-solid solution gradually diminishes with the fall of the temperature, so (a) must be observed. But as long as (b) do not occur, the disintegration of {420} spot cannot take place; therefore the splitting of $\{420\}_\alpha$ shows the formation of an intermediate structure.

The angles between [331] and the crystal axis are 43.5°, 43.5° and 77°, while those for [420] are 28°, 64° and 90°. Therefore, as to the spacings of {331}, if the volume of the unit cell is unaltered by the formation of a tetragonal lattice, the probability to find almost unaltered spacings will be much larger than that for altered one. But as to the {420} these changes must be occurred always and consequently the splitting will be observed. If the formation of α from β is originated to rotation about [001], the lattice parameters for [100] and [010] directions must decrease and that for [001] must increase. If rotations about these three coordinate axis occur without much differed probability, resulting microstructure will consist of martenstic α intersecting with each other at right angles. In fact, microphotographs for tempered one show martenstic structures and we can see several sets of acicular needles intersecting at right angles. Therefore, these needles must correspond to these three kinds of rotations and if these transformations are not followed by the change of atomic volume, splitting of a spot, as observed in $\{420\}_\alpha$ must take place. Thus, the spacing along [024] contracts if the contraction along the axis [001] will take place and elongates if the direction of contraction coincides with [100], provided the volume of a unit cell being unchanged. On the contrary, remarkable changes in spacings along [331] will not be observed in every case. Therefore we can calculate the value of a from the largest one of spacings for $(024)_\alpha$ spot and combining it with the values for {331} c will be obtained. Thus, as the lattice parameters of the face-centred tetragonal, following values will be obtained;

---

* Straumanis and Weerts had found 24 different orientations of α precipitated from β. But according to the present authors' experiences, certain ones of them become predominating and this is confirmed by the evidence that larger crystals of β would be obtained by repeating the heating and cooling, room temperature→870°→room temperature and so on.

$a=3.6775$ Å $c/a=0.9794$ at 225°C.
$a=3.6902$ Å $c/a=0.9891$ at 250°C.

Also, evidences of tetragonal structures will be found in Laue spots of β. The splitting of (031) spot into three, two of which appear in the outer side, shows the elongation along [001] axis and the displacements of Laue spots at 250°C., shown by arrows in Fig. 4, indicate the rotation of a surface normal caused by the dilatation along [001] axis. In consequence of this dilatation a must become small and thus a body-centred lattice with $c>a$ will be formed. As the velocity of diffusion is not so large, especially in copper[3] the lattice parameters of these intermediate crystals will not be constant and differed from place to place and circles and ellipses of the capillary X-ray photographs must become diffuse. Accordingly, the normal to the specimem tends to the lower l side as shown by an arrow in Fig. 5.

Above results were confirmed by following facts;

(c) the diameter of (103) ring becomes large with the rise of the temperature of tempering.

(d) increase of scattering in the interior of the $(321)_\beta$ ellipse.

As the angles between [009] and the normals of above surfaces are about 33° for (103), and 74.5° for (321) respectively, the spacing for the former must increase and that for the latter must decrease. Therefore, the disintegration of β into body-centred tetragonal structure is clear and one example of its lattice constants is as follows;

$a=2.945$ Å $c/a=1.0206$ for tempered at 250°C.

Both body-centred and face-centred tetragonal structures are an intermediate state between β and α, and there exist no definite boundaries between them. Therefore, this process will take place with continuous manner and no sign of an abrupt change was observed.

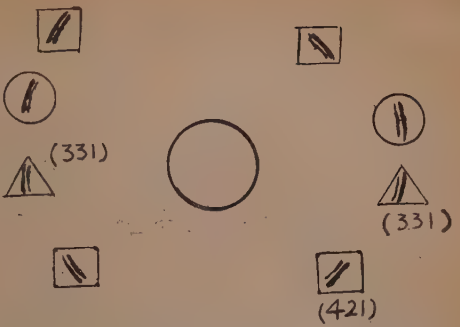

Tempered at 400°C. CuKα, back reflection.

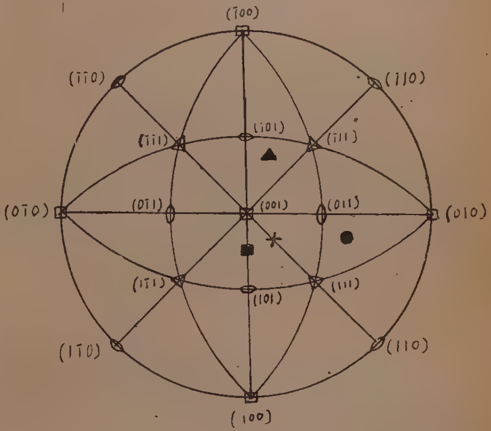

Fig. 5. Crystallographic relation between Original and precipitated α.
× : Surface normal to the original β.
■ ▲ ● : direction of fibre axes of α.

By tempering at 300°C., diffuse and faint $(\bar{2}22)$ ellipse*, belonging to a face-centred lattice, was observed in the capillary X-ray photograph; although $(301)_\beta$ circle are still remaining. Also $(204)_\alpha$ ellipse* was observed at 225°C. These confirms above conclusions**.

---

* These are not due to precipitation products, because unless a single crystal is used these patterns will not be obtained.

Phase boundary of $\alpha/\alpha+\beta$.

The solubilty limit of α will be obtained from the volume of a unit cell of α obtained by tempering at various temperatures. Above 300°C. as α become cubic and at 225° and 250°C. the spacings for {331} nearly coincide with the cube root of the volume of the unit cell, such calculation will be simple. The phase boundary calculated from the unit cell volume using Owen and Pickup's4) results is as follows;

temperature of tempering	as quench	225°	250°	00°	350°	400°
weight % Zn.	32.5	15.4	25.1	35.8	36.5	38.5

Above results lie in the side somewhat poorer in Zn than that of Konobejewski and Tarrasowa. As the values for 225° and 250°C. are calculated from the lattice parameters of the unstable and intermediate crystals, above results will not be much reliable. As to the phase boundary, the results of recent investigations on anomalies in α containing about 25% Zn, such as order-disorder transformation-like rise in specific heat, suggest another interpretations other than that of Konobejewski and Tarrasowa.

In conclution authors wish to express sincere thanks to the aid of the grant of Ministry of Education.

References.

1) M. Straumanis and J. Weerts, Z. Physik **78**, 1 (1932).

2) S. Konobejewski and W. Tarassowa: Phys. Z. Sowjetunion **10** (1936) 427.

3) F. Seitz, Phys. Rev. **74** (1948) 1513.

4) E. A. Oweri Prc. Roy. Soc. London A **140**, (1933) 179.

** Later, we have taken Kossel lines of β and confirmed above conclusions from the dilatation of (002) spacing due to tempering at 180°C and etc.

JOURNAL OF THE PHYSICAL SOCIETY OF JAPAN Vol. 6, No. 6, NOV.—DEC., 1951

The Hyperfine Structure of Sodium by a Microwave Absorption Method.

By Koichi SHIMODA and Tetsuji NISHIKAWA.

Department of Physics, Faculty of Science, University of Tokyo.

(Read in May 7, 1951, Received June 2, 1951.)

The hyperfine structure of the ground state $^2S_{1/2}$ of sodium atom, Na^{23} ($I=3/2$), has been measured by a microwave absorption method by means of a Zeeman modulation spectrograph. Among seven lines of the Zeeman components, $F=1\rightarrow F=2$, six lines have been observed. The remaining one has not been obserbed since it is not affected by weak magnetic field. The hyperfine structure separation at zero magnetic field has been obtained from the results, and it is

$$\Delta\nu=1771.70\pm0.15\ Mc/\text{sec}.$$

This is in good agreement with the known value measured by the atomic beam magnetic resonance method in the Paschen-Back region.

§1. Introduction.

The hyperfine splitting of atomic energy levels is caused chiefly by the interactions of the electrons with the nuclear magnetic dipole moment and electric quadrupole moment. Since these interactions depend on the angle between the angular momentum of nucleus, I, and that of electrons, J, the total angular momentum, F, is used to designate the each level. The ground state of sodium is $^2S_{\frac{1}{2}}$, and there is no electric multipole interactions between nucleus and electrons. For the ground state of Na^{23}, with $I=3/2$ and $J=1/2$, there are two levels for zero magnetic field, corresponding to $F=1$ and $F=2$.

The h.f.s. separation of Na^{23} was previously measured by S. Millman and P. Kusch1) by the skillful atomic beam magnetic resonance method in a strong magnetic field. We have observed the transition from the level $F=1$ to the level $F=2$, by a microwave absorption measurement in a very weak magnetic field of several Oersted. Each F level is split up into $2F+1$ magnetic levels designated by different values of the magnetic quantum number m_F, where $m_F=F, F-1, \dots, -F$.

Zeeman lines in a weak magnetic field are derived by the application of the selection rules for magnetic dipole transitions, $\Delta F=\pm1$, $\Delta m=0$, (σ-lines), and $\Delta m=\pm1$ (π-lines). For the h.f.s. lines of Na^{23}, with $I=3/2$, there will be four π-lines and three σ-lines which are given in Fig. 1.

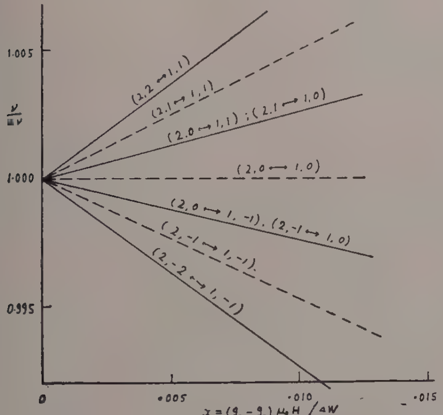

Fig. 1. h.f.s. Zeeman pattern of the ground state $^2S_{\frac{1}{2}}$ of an atom with $I=2/3$.

Since the h.f.s. transition, $F=1\rightarrow2$, is the magnetic dipole one, the probability of the induced transition is rather small.

Besides, the population of the two atomic levels differs very little, because the value of splitting, ΔW, is small compared with kT. The absorption coefficient of atomic sodium gas is, therefore, expected to be much smaller than that of the ordinary rotational absorption of polar molecules. The frequency is about 1771 Mc/sec which is considerably lower than the frequency generally used in the measurement of microwave spectroscopy, and the value $\Delta W/kT$ is only 1.7×10^{-4} at the temperature of 500°K.

We have used a Zeeman modulation method in order to attain higher sensitivity, because the absorption coefficient of the atomic sodium will be small (of the order of 10^{-9} cm^{-1}). The details of Zeeman modulation microwave spectrograph are described in the following paper.

§ 2. Experimental Apparatus.

A block diagram of the apparatus used in this experiment is given in Fig. 2. The absorption cavity in a magnetic field is excited by an unmodulated klystron oscillator through one of the waveguides coupled to the cavity, and the output is detected by a crystal detector mounted in the other waveguide.

The cavity is a cylindrical TE_{112} mode, which is degenerated for two circulary polarized modes. Two waveguides coupled to the cavity, can be rotated each other. When the polari-

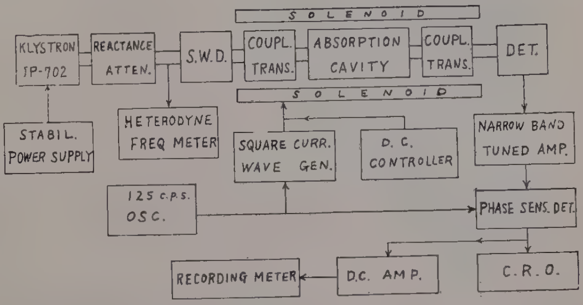

Fig. 2. Block diagram of the Zeeman modulation spectrograph used.

zations of the two waveguides are orthogonal, r. f. balancing is established and the detector is placed on zero power level. As one of the waveguides is rotated, the power level of crystal detector increases and it is possible to operate the detector at the desired power level to give the optimum noise figure.

Since the absorption frequency for h.f.s. of the ground state of Na^{23} lies in about 1770 Mc/sec, the absorption cavity has a considerably large dimension of 141 mm in diameter and 235 mm in length. In order to evacute the cavity and to raise the temperature, a particular device is needed, because the application of glass-to-copper seal or rubber packing seems impossible to such a large cavity heated up to the temperature of 500°K or more.

The absorption cavity and its accompaniment has been designed and constructed as given in Fig. 3. The inner cavity made of copper is enclosed in a vessel made of hard-glass, and it is wound by a nichrome wire so as to be heated by electric current. This is

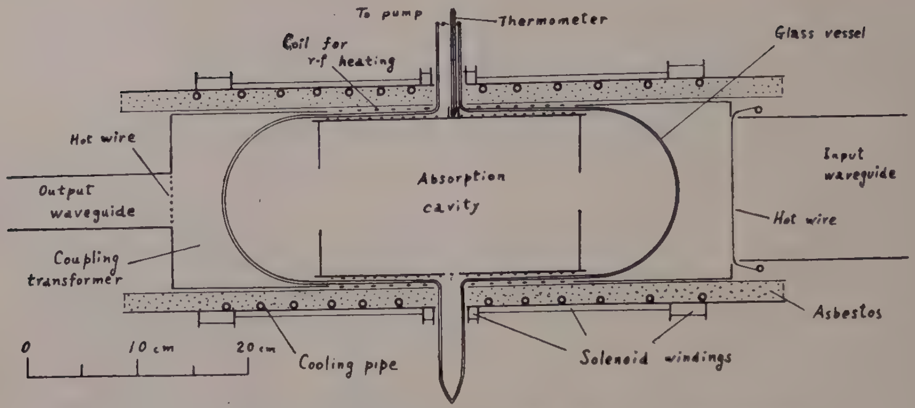

Fig. 3. Cross section of the absorption cavity and its accompaniment.

Fig. 4. Absorption cavity in a glass vessel.

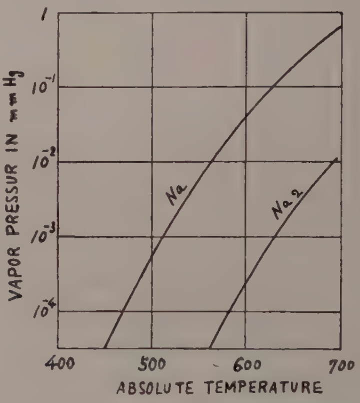

Fig. 5. Vapor pressure of sodium.

shown in a photograph in Fig. 4. Sodium has been introduced into the vessel from the left branch in Fig. 4, after it had been distilled several times in vacuum (about 10^{-2} mm Hg).

The vapor pressure data of sodium can be found elsewhere[2)], which is graphically represented in Fig. 5. The equilibrium of Na-atom and Na_2-molecule has been studied by L. C. Lewis using a molecular beam method[3)]. At the temperature of 500°K, the vapor pressure of Na_2 is less than 1 per cent of that of Na-atom. Therefore, Na_2 molecule may be neglected in studying microwave absorption at that temperature. The temperature of absorption cavity in a glass vessel is raised to about 260°C by the electric power of about 500 watts, and the pressure of Na-atom is kept at about 10^{-3} mm Hg.

The glass vessel with absorption cell is placed in a solenoid. Since the solenoid is not allowed to be heated, a narrow helical pipe is set inside it and asbestos sheets for heat insulation are packed between the solenoid and the glass vessel. We had much trouble to keep the solenoid coil insulated from water vapor that emerged not a little from asbestos, when the cavity was heated. The solenoid coil has been coated thereafter by thick bakelite-varnish and some bees-wax.

The absorption cavity is coupled to two waveguides through coupling transformer sections as shown in Fig. 3. Several hot wires are stretched parallel to the broad face of the waveguide in the openings of input and output waveguides, so that the sodium vapor may not condense on the glass wall near the coupling window.

The microwave source used is an external cavity type klystron, JP-702, manufactured by Japan Radio Company. The frequency is measured by a heterodyne wavemeter with an accuracy of $10^{-5} \sim 10^{-6}$.

The magnetic field is modulated by the frequency of 125 c.p.s. with the amplitude of 0.1~1 Oersted. When the average magnetic field is gradually changed, the modulated output of the crystal detector will appear near the absorption lines of the Zeeman pattern of the sample. The output will be visualized and recorded by a narrow-band tuned amplifier followed by a phase-sensitive detector[4)] and recording meter, or a oscilloscope. Details of these components are described in the following paper.

§3. Measurements and Results.

The preliminary measurement was made in October 1950. It was confirmed that it is possible to detect h.f.s. lines of sodium by the above mentioned method, although the obtained signal was very weak owing to the inhomogeneity of the magnetic field and by the large noise ratio of the crystal detector used.

In the later experiment, the stray magnetic field in the solenoid has been almost compensated by several permanent magnets placed arround the solenoid. It is estimated that the residual component is less than 0.1 Oersted at most. The residual field components parallel to the solenoid can be eliminated, if it exsists, by the double measurements reversing the solenoid current. In most cases, the orthogonal component effects very little on the magnetic field in the solenoid. It is less than 0.1 per cent under the axial magnetic field intensity of greater than 2 Oerated, and may be negligble in our experiment.

The solenoid coil has been designed to minimize the field inhomogeneity within a limited dimension. The large inhomogeneity of the field is, therefore, caused by the heating current in wire wound just outside the cavity wall, though it is wound bifariously. In order to avoid this effect, a method of high frequency heating has been used to heat up the cavity. The h-f oscillator is a push-pull TS-204, with input power of about 1 kilowatt, from which the effective output of 500~600 watts is obtained.

The observed results are given in Fig. 6. Since the cavity in a vacuum vessel has been tuned to the frequency of about 1766 Mc/sec., though it is tunable within ±2 Mc/sec. by adjusting coupling transformer, the measurement at the frequency outside this range is poor in its sensitivity and the results are less reliable. The measurement disturbed by some instantaneous noise such as sounds by airplanes or shocks by tramcars is also less reliable. These results are given in Fig. 6 as blank circles, and the more reliable results are shown as black spots.

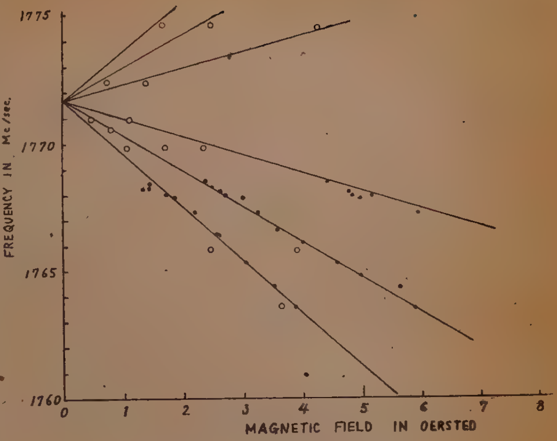

Fig. 6. Observed results.

From the results shown in Fig. 6, the hyperfine splitting of Na^{23} is obtained. It is

$$\Delta\nu = 1771.70 \pm 0.15 \text{ Mc/sec.}$$

This is in good agreement with the value obtained by S. Millman and P. Kusch in the Paschen-Back region by atomic beam method, assuming the Breit-Rabi formula[5)] of atomic energy levels with $J=1/2$. The energies of the magnetic levels are:

$$W_{I\pm\frac{1}{2}} = -\frac{\Delta W}{2(2I+1)} + g_I\mu_0 H m_F \pm \frac{\Delta W}{2} \times \left(1+\frac{4m_F x}{2I+1}+x^2\right)^{\frac{1}{2}},$$

where $\Delta W = h\Delta\nu$ is the h.f.s. separation in energy units, and μ_0 is the Bohr magneton. The parameter, x, is defined by

$$x = (g_J - g_I)\frac{\mu_0 H}{\Delta W},$$

where g_I, g_J is the gyromagnetic ratio of nucleus and electrons. The agreement of the values measured by two methods shows that the above formula is correct within the experimental accuracy.

The absorption coefficient of the atomic sodium vapor may be estimated from the output signal voltage of the crystal detector, which is about 10^{-6} volts. The loaded Q of the absorption cavity has been measured to be 850±50 with the transmission coefficient, D, of about 0.5 under the same relative orientations of waveguides as the absorption of sodium has been measured.

The absorption coefficient of the sample is known from equations (5) and (6) in the following paper. We obtain

$$\alpha=\frac{\beta}{QD}\left(\frac{\Delta P_0}{P_i}\right)^{\frac{1}{2}},\ \text{or}\ \alpha=\frac{\beta}{QD}\frac{\Delta P}{2P_i},$$

where P_i is the input power, ΔP is the power absorbed by the gas, ΔP_0 is the decrease of output power, and $\beta=2\pi/\lambda$.

If we assume the following values, $\beta=0.37$ cm^{-1}, $P_i=2\times10^{-4}$ watts, the amplitude conversion loss of the detector is 3, and the impedance of the crystal is 10^3 ohms, we have

$$\Delta P_0=9\times10^{-15}\ \text{watts}$$

and

$$\alpha=6\times10^{-9}\ \text{Np/cm}$$

On the other hand, assuming the square law detection, we obtain the value of α by the second equation. If we assume the rectified output voltage of the crystal by the input power level of P_i, is 10^{-1} volt, we have

$$\alpha=4\times10^{-9}\ \text{Np/cm},$$

where Q, D, and β are the same as above.

The absorption coefficient can be theoretically calculated. If we assume the line-breadth parameter, Δf, is 1 Mc/sec.mmHg, the absorption coefficient will be 4.3×10^{-9} Np/cm. The measured values agree too well to thisvalue.

The obserbed line breadth is 0.1~0.2 Mc/sec, which is considered to be broadened by field inhomogeneities.

In conclusion, the authors express their thanks to the Asahi Bunka-Jigyo-Dan in the Asahi Press for financial aid by the grant of subsidy in 1949 for the research on microwave spectroscopy.

References.

1) S. Millman, and P. Kusch, Phys. Rev., **58** (1940) 438.

2) R. W. Ditchburn, and J. C. Gilmour, Rev. Mod. Phys., **13** (1941) 310.

3) L. C. Lewis, Zeits. f. Phys., **69** (1931) 786.

4) R. H. Dicke, Rev. Sci. Inst., **17** (1946) 268.

5) G. Breit, and I. I. Rabi. Phys. Rev., **38** (1931) 2082. S. Millman, I. I. Rabi, and J. R. Zacharias, Phys. Rev., **53** (1938) 384.

JOURNAL OF THE PHYSICAL SOCIETY OF JAPAN Vol. 6, No. 6, Nov.—DEC., 1951

A Zeeman Modulation Microwave Spectrograph of High Sensitivity.

By Koichi SHIMODA and Tetsuji NISHIKAWA.

Department of Physics, Faculty of Science, University of Tokyo.

(Read in May 1, 1950, Received June 2, 1951)

A low frequency Zeeman modulation microwave spectrograph for observing hyperfine structure of atomic sodium has been constructed. It sexperimental details and the principle of operation are given. The sensitivity of the spectrograph may be estimated like the Stark modulation spectrograph. Since the modulation frequency cannot be chosen so high as Stark modulation, the noise figure of the crystal detector is rather large, which might be over come if the source modulation were superposed.

§1. Introduction.

In order to obtain higher sensitivity in microwave measurement, the Stark modulation method has been developed.1)-4) The Stark modulation spectrograph is effectively used for detecting absorption lines of polar molecules; but it cannot be applied to magnetic dipole absorption. For the molecules which have permanent magnetic moment, the Zeeman modulation method may be used, following the similar principle to the Stark modulation method.

The source oscillator is tuned to a fixed frequency at a certain point near the absorption frequency of the sample. As the intensity of the magnetic field is changed periodically with small amplitude, the frequency of the absorption line changes and the amount of absorption is modulated by the modulation frequency of the field, if the magnetic quantum number of the sample molecule is not zero. The output of the crystal detector is amplified by a highly selective tuned amplifier in order to be free from unwanted noises. The modulation frequency cannot be chosen so high, because the solenoid has considerable large inductance and the modulated component of the magnetic field is damped by the eddy current in the wall of the cavity. To reduce the eddy current, the frame of solenoid is slotted and the absorption cavity is also partially slotted.

§2. Details of the Zeeman Modulation Spectrograph.

Experimental details of a Zeeman modulation spectrograph for the measurement of the h.f.s. of the atomic sodium is described. Design and construction of the absorption cavity for the purpose is described in the preceeding paper, in which the block diagram is also given (Fig. 2 and Fig. 3 in the preceeding paper). The value of modulation frequency, 125 c.p.s., is chosen so that the frequency of the line alternating current, 50 c.p.s., may have little effect on the receiver and it may not be so difficult to produce nearly square current wave of the frequency in the solenoid which has the self-inductance of about 0.2 henry.

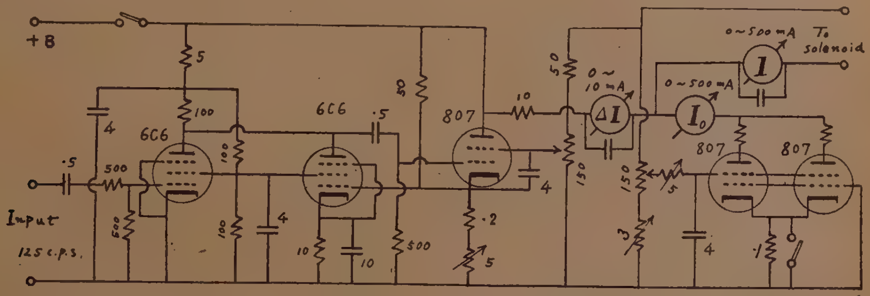

Fig. 1. Circuit diagram of the modulator.

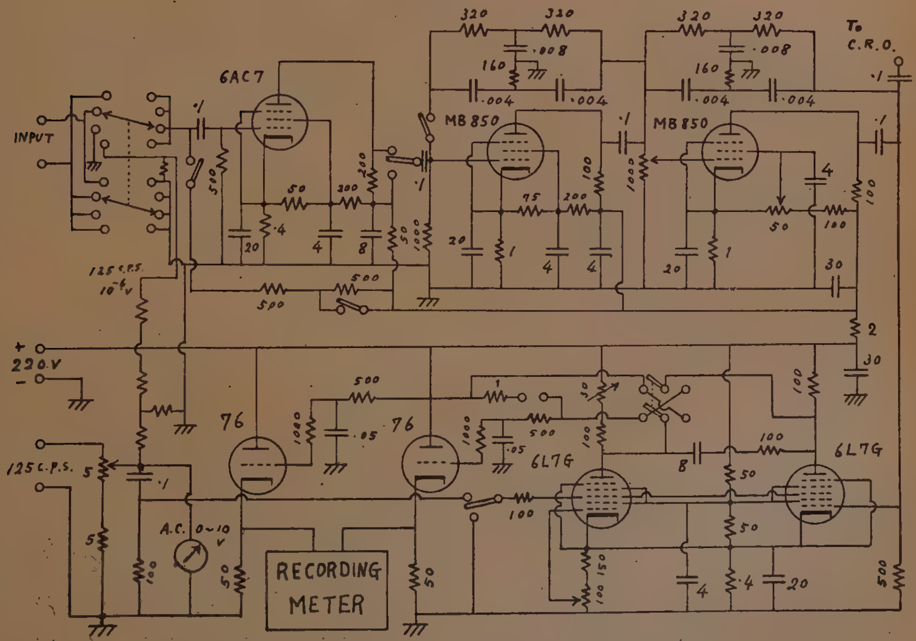

Fig. 2. Circuit diagram of the lock-in amplifier.

i) Modulator.

The circuit diagram of the modulator used is given in Fig. 1. Since the solenoid has large inductance, the voltage square wave cannot generate the square wave modulation of magnetic field. The modulator is designed to generate current square wave from the input sine wave by the intermittent operation of a sort of current stabilizer.

Since the modulator is adequately adjusted so that the pulse width and the interval may be equal, the instantaneus current is given by

$$i = I \pm \Delta I = I_0, \text{ or } I_0 + 2\Delta I.$$

ii) Detector and Lock-in Amplifier.

The crystal detector is mounted at the end of the waveguide through a ridge-to-coaxial coupler. It is tunable by two stubs on the broad face of the waveguide. The rectified output of the crystal detector is amplified by a narrow-band tuned amplifier which is given in the upper half of Fig. 2. The tuning circuit is the well known negative feedback circuit by twin. T resistance capacitance network.[5]

The half width of the frequency responce of the amplifier has been measured to be 4.5 c.p.s.. If the circuit constants, R and C, of the network are chosen so that the feedback may be slightly positive at the tuned frequency, the half width can be reduced to about 1 c.p.s., without being unstable. This is easily done by reducing the factor, K, in Fig. 3, to the value less than 0.5.[6]

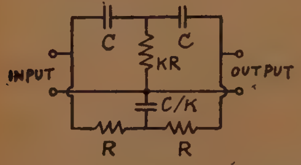

Fig. 3. Twin T resistance-capacitance feedback network.

The narrow-band amplifier is followed by a phase sensitive detector and a d.c. amplifier which are given in the lower half of Fig. 2.

The phase sensitive detector is a sort o balanced mixer, composed of a pair of mixer tubes, 6L7G, the first grids of which are driven by a reference a.c. voltage from the modulator. The input signal from the amplifier is imposed on the third grid of one of the tubes. The output voltage of this detector is amplified by a balanced d.c. amplifier through a lowpass filter. The time constant of the filter is 0.8 seconds. The d.c. amplifier is a cathode-follower type, and the output is given to a recording milliammeter.

The recorded noise level of this phase-lock-in amplifier has been measured to be about 2×10^{-9} volts, using a 6AC7 tube in the first stage. With the input voltage of 10^{-7} volts (125 c.p.s.) the maximum output current is 0.2 milli-amperes. In other words, the trans-conductance of the amplifier at its maximum gain is 2×10^{3} mhos.

The power supply for the amplifier is electronically stabilized to reduce the fluctuation sufficiently.

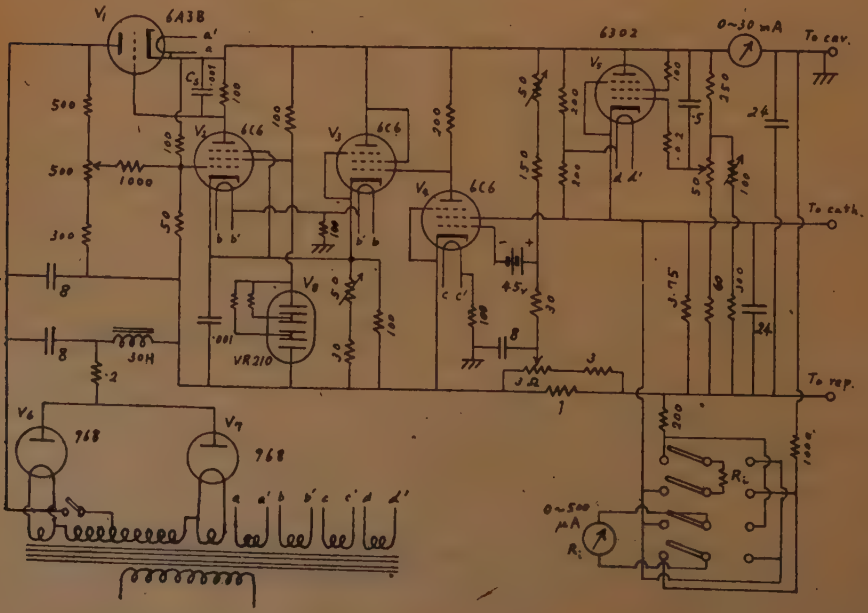

Fig. 4. Stabilized power supply for klystron tube.

iii) Microwave Source.

The source oscillator is required to generate unmodulated waves. A disc-seal klystron, JP. 702, with an external rectangular cavity is used. One side of the cavity wall is movable in order to vary the frequency and the output waveguide is coupled to the other side of the cavity. If the amplitude or the frequency of the oscillator changes with time, the output of the crystal detector fluctuates and it disturbs the measurement. Since the klystron tube generates microwaves within some limited condition of repeller and cavity voltages, the power output is easily modulated by the fluctuation of supplied voltage. A good stabilized power supply is therefore needed.

The stabilizer used for our experiment is given in Fig. 4, which is similar to that of L. C. Roess for his amplifier[7] and the best power supply for the klystron tube we have ever found elsewhere.[8,9] Three tubes V_2, V_3, and V_4 are used as a d.c. amplifier and a capacitor, C_3, has been inserted to suppress the self-oscillation. [Erratum: In Fig. 4, cathode of the tube V_4 and the negative side of the grid circuit should be inversely connected to the 3ohm resistor.]

The short time stability of the order of 10^{-4} volts or 0.01 percent has been obtained even by the use of a.c. heating of tubes. The hum voltage at the output has been reduced to less than 10^{-4} volts and the 125 c.p.s. component to about 10^{-5} volts, when the heaters of tubes are connected as shown in Fig. 4 without being floated.

iv) Wavemeter.

The output frequency of the klystron oscillator is measured by a heterodyne wavemeter within the accuracy of less than 10^{-5}. The circuit diagram of the wavemeter is given in Fig. 5.

A v.h.f. tunable oscillator beats with high harmonics of the frequency of the crystal oscillator, 5 Mc/sec., which is calibrated by standard frequency of station JJY. The microwave frequency to be measured is heterodyned by a crystal mixer with the v.h.f. tunable oscillator. Thus the microwave frequency can be determined within the accuracy of 10^{-3}; by interpolating between every 5 Mc/sec. points of the v.h.f. oscillator.

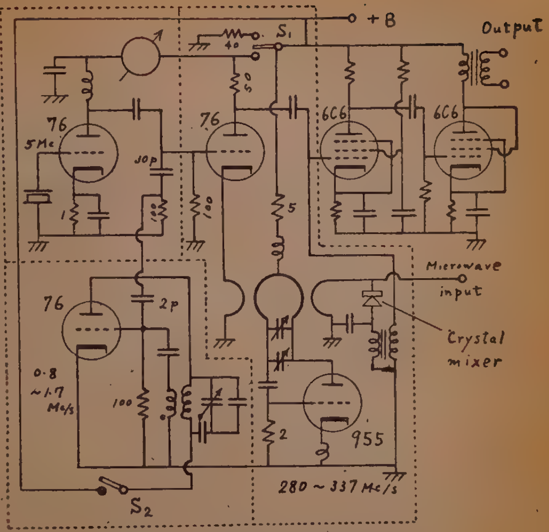

Fig. 5. Heterodyne wavemeter.

If more accurate measurements are needed, the interpolating tunable oscillator is switched on (S_2) and the frequency f_L is superposed on the triode mixer with 5 Mc/sec. output of the crystal oscillator. When the frequency of the v.h.f. oscillator, f_V, is nearly equal to

$$f_V = mf_L + 5n \text{ (Mc/sec.)}, \qquad (1)$$

beat output will apear, where m and n are integers. The frequency, f_L, is tunable by a precision variable condenser from 0.8 to 1.7 Mc/sec. Several points in the range may be heterodyned with 5 Mc/sec. crystal oscillator and the accuracy of the frequency is maintained within 7×10^{-4}. And it is adjusted that the beats are audible for $m=0\sim5$. If the v.h.f. oscillator is tuned to beat with the microwave frequency, f, to be measured,

$$Nf_V = f, \qquad (2)$$

where N is also an integer. By adjusting f_V to hold equation (2) and adjusting f_L to hold equation (1) at the same time, we can hear double beats. As the microwave frequency is very high, 10^9 or 10^{10} for example, it is not necessary to keep in perfect zero beat condition for the experimental accuracy.

Since the frequency of the crystal oscillator is easily determined within the accuracy of 10^{-6}, we fined f_V within the accuracy of less than 10^{-5} when the value of m less tnan 5 and n is about 60. Then the microwave frequency may be measured within the accuracy of 10^{-5} in the frequency range from 1000 Mc/sec. to 10000 Mc/sec. or higher.

§ 3. Minimum Detectable Absorption by the Spectrograph.

A high Q cavity resonator coupled by two waveguides is used as the absorption cell. The amplitude transmission coefficient, D, of the cavity resonator at the resonant frequency is given by

$$D^2=4Q^2/(Q_1Q_2)\,, \tag{3}$$

where Q is the loaded Q, Q_1 and Q_2 are the coupling Q-values for one and the other waveguide respectively. The loaded Q of the resonator is given by

$$\frac{1}{Q}=\frac{1}{Q_0}+\frac{1}{Q_1}+\frac{1}{Q_2}\,, \tag{4}$$

where Q_0 is the unloaded Q.

When the cavity is filled with some absorbable gas, the free space propagation constant of which is $\alpha+j\beta$, the signal output power, $\varDelta P_o$, caused by the gas absorption is given by

$$\varDelta P_o=Q^2D^2\alpha^2/\beta^2\,. \tag{5}$$

And the power absorbed by the gas, $\varDelta P$, is related to $\varDelta P_o$ by the following equation.[10)]

$$\varDelta P=(4P_t\cdot\varDelta P_o)^{\frac{1}{2}}=2QDP_t\alpha/\beta\,, \tag{6}$$

where P_t is the input power.

If we assume that the minimum detectable signal power is the same as the noise power of the receiver, we have

$$\varDelta P_{\min}=FkT\varDelta f\,, \tag{7}$$

where F is the over-all noise figure of the receiver, k is the Boltzmann constant, and $\varDelta f$ is the effective bandwidth of the receiver. To obtain the minimum absorption coefficient, $\alpha_{\min}$, we equate (7) with (5). We obtain

$$(\varDelta P_o)_{\min}=FkT\varDelta f$$

for the minimum detectable absorption. And $\alpha_{\min}$ is given by the following equation.

$$\alpha_{\min}=\frac{\beta}{QD}\left(\frac{FkT\varDelta f}{P_t}\right)^{\frac{1}{2}}\,. \tag{8}$$

In order to obtain the optimum condition of the absorption cell for the maximum sensitivity, we must maximize QD. To maximize D (or Q) within a limited value of Q (or D), we must put

$$Q_1=Q_2 \tag{9}$$

By combinig equation (3), (4) and (9), we have

$$Q=\frac{1}{2}Q_0\,, \tag{10}$$

for the optimum loaded Q of the absorption cavity under a given value of unloaded Q. In this case,

$$Q_1=Q_2=2Q_0$$

and

$$D=\frac{1}{2}\,.$$

The minimum detectable absorption coefficient for the cavity of optimum coupling is given by

$$\alpha_{\min}=\frac{2\beta}{Q}\left(\frac{FkT\varDelta f}{P_t}\right)^{\frac{1}{2}} \tag{11}$$

To obtain an estimate of the idealized limit of detection, we may assume the following values: $P_t=10^{-3}$ watts, $F=10$, $\varDelta f=1$ c.p.s., $Q=10^4$, and $\beta=0.37$ ($f=1770$ Mc/sec.). Then we have

$$\alpha_{\min}=6.1\times10^{-13}\ \text{Np/cm}.$$

In our experiment to detect the h.f.s. of atomic sodium, however, the noise figure of the crystal detector has been exceedingly large, because the frequency used for modulation and detection is very low. The values of noise figures of the crystals distribute in the range of the order of 10^5 or more, and they increase with power level. For a probable evaluation of the spectrograph used in the experiment, we put $F=10^5$, $P_t=10^{-4}$ watts, and $Q=850$, and we have

$$\alpha_{\min}=7.2\times10^{-10}\ \text{Np/cm}\,.$$

In order to be free from low frequency noise of the crystal detector and obtain higher sensitivity, we are now improving the apparatus applying also the source modulation method.

This work is indebted to the Asahi Bunka-Jigyo-Dan in Asahi press for the research subsidy and to the ministry of education for research grant.

References.

1) R. H. Hughes and E. B. Wilson: Phys. Rev., **71** (1947) 562.

2) B. P. Dailey: Phys. Rev., **72** (1947) 84.

3) K. B. McAfee, R. H. Hughes, E. B. Wilson, Rev. Sci. Inst., **20** (1949) 821.

4) A. H. Sharbauch: Rev. Sci. Inst., **21** (1950) 120.

5) H. H. Scott: I.R.E., **26** (1938) 226.

6) J. Bowers, Electronics, **20** (1947) No. 4.

7) L. C. Roess: Rev. Sci. Inst., **16** (1945) 172.

8) C. G. Montgomery, *Technique of Microwave Measurements* (McGraw-Hill Book Company, Inc., New York, 1947. Chap. 2)

9) D. R. Hamilton, J. K. Knipp, and J. B. H. Kuper: *Klystrons and Microwave Triodes* (McGraw-Hill Book Company, Inc., New York, 1948.)

10) W. Gordy: Rev. Mod. Phys., **20** (1948) 668.

Short Notes.

J. PHYS. SOC. JAPAN **6** (1951) 521.

An Electron Diffraction Study on Seleniun Rectifiers.*

By Jiro YAMAGUCHI, Saburo NAGATA and Yuichi MATSUO.

Faculty of Engineering, Osaka University.

(Received May 28, 1951).

The same specimens as investigated previously¹⁾ by X-rays, were subjected to electron diffraction study. These specimens were prepared as follows; molten selenium was set on nickel-plated steel disc and subjected to various pressures at 130°C for one hour (1st heat treatment) and treated for hours at various temperatures (2nd heat treatment). As their surfaces were rough, election diffraction patterns could not be obtained. After light polishing, they were washed in 10% caustic soda solution and cleaned carefully by alcohol and ether. This surface treatment did not cause any changes in X-ray patterns, but some influences appeared sometimes in those of electron diffraction and the rectifying characteristics of the specimens after coated with wood metal became worse. Therefore this surface treatment must be as light as possible.

The results obtained are as shown in Table I. Though we can not recognize the fibre structure** as clearly as X-rays, the higher the pressure at the first heat treatment and the lower the temperature at the second heat treatment, the clearer become the crystalline behaviours. These results almost coincide with those of X-ray study.

Table I. Electron Diffraction Patterns of Se.

Pressure at 1st heat treatment (kg/cm^2)	Without 2nd heat treatment	Temperature at 2nd heat treatment (°C)		
		170°	190°	210°
5	Diffusering	Halo	Halo	Halo
30	ring	Ring	Halo	Halo
50	Sharp ring	Sharp ring		Diffuse ring

To determine the thickness of cadmium-selenide layer of selenium rectifier, we attempted following methods. One half part of selenium rectifier plate covered with cadmium instead of wood metal was ground obliquely and electron beam was projected parallel to the grinding direction (perpendicular to the paper face) (Fig. 1.) When the position of the specimen irradiated by electron was displaced gradually by means of rotating the specimen holder, Cd at points A,B and C, CdSe*** at D,E and F and Se at G,H and I was obtained. This surface was observed by a profilometer (vertical magnification; ×1000) and $\overline{CC'}$ and $\overline{DD'}$ were calculated from $\overline{GC'}$, $\overline{FD'}$, and < AOA′.

From this result, the thickness of the CdSe layer was determined and a value lying between 0.7×10^{-4}cm. and 1.5×10^{-4} cm. was obtained. The roughness of the surface seems to be the order of $10^{-4}\sim10^{-5}$ cm. Therefore it is almost hopeless to obtain more accurate value by this profilometer method, but this result is approximately consistent with that of X-ray method.²⁾

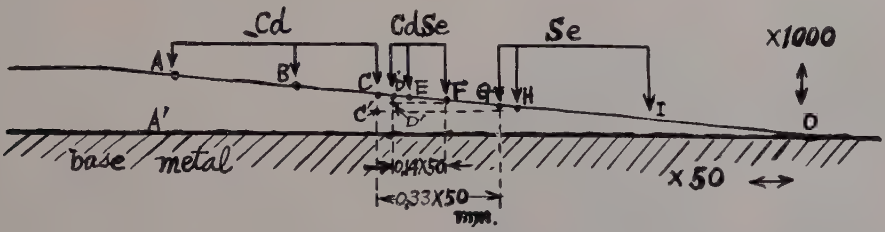

Fig. 1. Profile of Selenium rectifier plate polished obliquely.

References.

1) J. Yamaguchi & S. Katayama: J. Phys. Soc. Japan **5** (1950) 385.

2) J. Yamaguchi & S. Katayama: J. Phys. Soc. Japan **5** (1950) 386.

---

* read April, 1950.

** The direction of fibre axis was also (1120) in electron diffraction.

*** CdSe obtained in this experiment was always cubic modification.

J. PHYS. SOC. JAPAN **6** (1951) 522–523.

On the Grain Boundary Migration induced by Temperature Gradient

By Hideji SUZUKI.
The Research Institute for Iron, Steel and Other Metals, Tohoku University

(Received May 28, 1951)

In the course of the study of grain boundary migration in annealed high purity Aluminium, we have found an important phenomenon, the migration induced by temperature gradient. A typical example is shown in the photographs (×1,6). (a) represents a specimen after additional annealing for 5 hour at 659~660°C. A part of the specimen, that is, the left hand side of AB, melted owing to a temperature gradient in the electric furnance. The structure of grains in this photograph show the original one, since the etching figure preliminarily revealed before annealing is unchanged in its main aspect. The new positions of migrated boundaries are seen in this case as faint grooves, produced by "thermal etching". The grains after annealing are seen more clearly in (b), which represents the chemically etched surface of the specimen in (a). (c) is a schematic representation of the grain boundaries before (broken curves) and after (full curves) the annealing. All grain boundaries' including the island crystal E, except for the twin boundaries C and D, move towards the line of AB. Namely, the grain boundaries move in a direction opposite to the temperature gradient. In the case of the motion of the crystal E, the rate of migration of the boundary induced by the temperature gradient, though less than 0,2° C/cm, is still larger than the one resulting from the surface free energy, which takes place in the direction of the center of curvature.

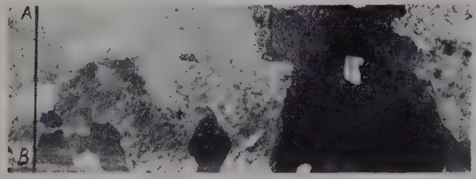

(a)

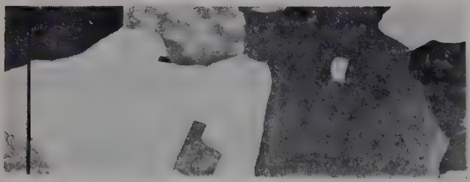

(b)

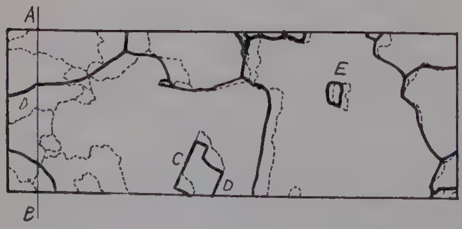

(c)

Since the parallel movement of a boundary without reduction of area does not result any change in its energy, it may be concluded that this type of migration is caused from the request of increasing the entropy of the grain boundary. The driving force of the boundary migration due to its curvature is the boundary free energy divided by the radius of curvature, while the driving force induced by temperature gradient is the product of the entropy and the temperature gradient provided the temperature dependence of the entropy is sufficiently small. The driving force of the same magnitude is sure to give the same rate of migration, so we can estimate the ratio of the boundary free energy to the boundary entropy at the melting point, by means of extrapolation of the radius of curvature to AB, which causes the same distance of migration as that due to the temperature gradient. It is remarkable that this value vanishes at the very temperature. In other words, the grain boundary free energy vanishes at the melting point.

Other experiments carried out under greater temperature gradients, such as 2°C/cm, have failed to show measurable parallel movement of the boundary in directions opposite to the temperature gradient. These experiments indicate that the grain boundary entropy increases very rapidly near the melting point. The assumption used in the estimation of the boundary free energy at the melting point, therefore, is no more correct, but the disappearance of the free energy at the temperature seems to be true, on account of the rapid increase of the entropy itself.

The explanation of the anomalous grain boundary entropy near the melting point may be given from the dislocation models of grain boundaries[1] in such a way, that the number of accessible states concerning the arrays of dislocations rapidly increases near the temperature. It is suggested that the free space concerning the thermally activated translational motion of dislocations increases rapidly near the melting point, being associated with pair creations and annihilations of dislocations, namely, the melting is nothing but the slip forced by thermal agitation.[2] The further arguments must require more precise measurement of the value of entropy. It is hoped to publish a detailed account of them in due course.

In conclusion, the author wishes to express his hearty thanks to Professors. Sakae Takeuchi and Taira Suzuki for their encouragement and valuable discussions.

References.

1) W. T, Read and W. Schockley, Phys. Rev.' **78** (1650) 275.
2) G. Leibfried, Z. Phys., **127** (1950) 344.

J. Phys. Soc. Japan **6** (1951) 523-524.

On the Crystal Structure of Cadmium Selenide of Selenium Rectifier.*

By Saburo NAGATA and Kosuke AGATA.
Faculty of Engineering, Osaka University.

(Received May 28, 1951)

Two modifications about cadmium selenide in a barrier layer of selenium rectifier,[1] have been observed by several investigators.[2] [3] [4] To ascertain these results we performed following experiments.

At first, selenium was sputtered in vacuum on steel or Nickel plates polished with 0000 emery paper and heated under atmospheric pressure. The electron-diffraction patterns for sputtered Se film have two halos. After heat-treatment, patterns show fibre structure for thin films ($<0.3\mu$, fibre axis is (1120), Fig. 1) and pollycrystalline ring for thick ones ($>1\mu$, Fig. 2). So we suppose thin Se layer closely adhering to the base metal will have preferred orientation. When the temperature of the heat treatment is raised to 50°C, its surface colour changes slightly, but its pattern does not change. The crystallization is completed with a duration as short as 30 minutes at 75°C and about 3 minutes at 100°C.

We also observed the fibre diagram and sharp ring patterns of cadmium sputtered on steel plates. (Fig. 3 and Fig. 4). The former is obtained by slow sputtering and the latter by quick one. From Fig. 3 the fibre axis of Cd is determined as $(11\bar{2}2)$.

Next we sputtered Se on nickel plate, heated at 100°C for 15 minutes and sputtered Cd on it. When Cd in the surface was dissolved in HCl, cubic CdSe was found (Table I, Fig. 5). Therefore CdSe may be produced without heat treatment. When Cd has been dissolved after heat treatment at 100°C for one hour, residual CdSe becomes hexagonal as $(10\bar{1}3)_{hex.}$ ring is observed between $(11\bar{2}0)_{hec.}$ and $(11\bar{2}2)_{hex.}$

We sputtered Se on the Cd film which was deposited on nickel plate. When surface Se was dissolved in conc. NaOH solution, $(11\bar{2}3)_{hex.}$ ring weaker than $(11\bar{2}0)_{hex.}$ was recognized, and $(400)_{cub.}$ was

Table I. CdSe (cubic)

Intensity	d obs. (A)	d calc. (A)	indices
S	3.57	3.49	(111)
S	2.14	2.14	(220)
S	1.82	1.82	(311)
W	1.36	1.39	(331)
W	1.23	1.23	(422)

Table II. CdSe (Cubic and hexagonal)

Intensity	d obs. (A)	CdSe	
		Cubic (A)	Hex. (A)
S.	3.46	(111)3.49	$(10\bar{1}1)$3.29
V.W	2.57		$(10\bar{1}2)$2.55
V.S.	2.17	(220)2.14	$(11\bar{2}0)$2.15
W	2.00		$(10\bar{1}3)$1.99
V.S.	1.84	(311)1.82	$(11\bar{2}2)$1.84
V.W	1.54	(400)1.51	
W	1.41	(331)1.39	$(12\bar{3}0)$1.42
W	1.25	(422)1.23	$(30\bar{3}1)$1.22

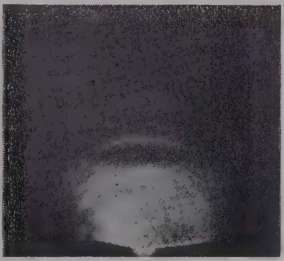

Fig. 1. Se (thin film) $L=30$ cm

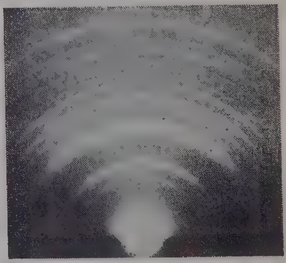

Fig. 2. Se (thick film) $L=50$ cm

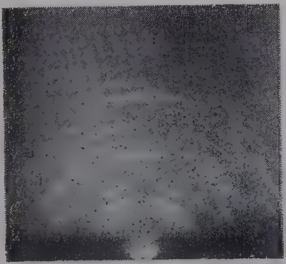

Fig. 3. Cd (slowly sputtered) $L=30$ cm

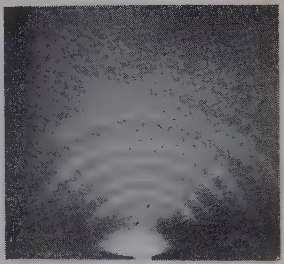

Fig. 4. Cd (quickly sputtered) $L=30$ cm

---

* read April, 1951

Fig. 5. CdSe (cubic) $L=30$ cm

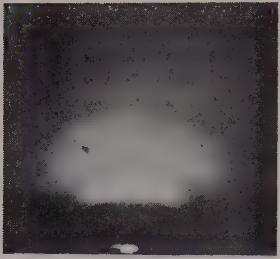
Fig. 6. CdSe (Hexagonal) $L=30$ cm

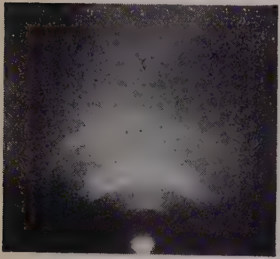
Fig. 7. CdSe (cubic and hexagonal) $L=30$ cm

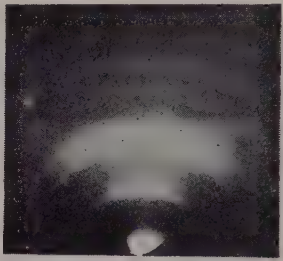
Fig. 9. CdSe (cubic and hexagonal) $L=50$ cm

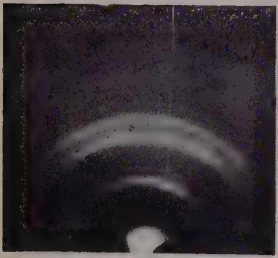
Fig. 8. CdSe (cubic) $L=50$ cm

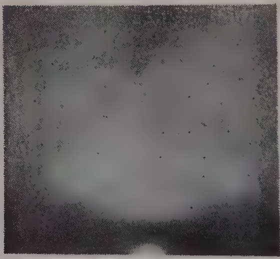
Fig. 10. CdSe (Hexagonal) $L=50$ cm

found. Therefore this photograph indicates the coexistence of hexagonal and cubic CdSe. (Table II, Fig. 7). When Se was dissolved after heat treatment at 100°C for one hour, only hexagonal pattern was obtained.

In order to make the above mentioned results conclusive, we repeated the same experiments after increasing the camera length L from 3 cm. to 50 cm. Nearly the same results were obtained, but the conclusion more certain. (Fig. 8 Fig. 9 and Fig. 10) In the case of $L=30$ cm, inner $(10\bar{1}0)$, (0002) and $(10\bar{1}1)$ rings are difficult to be resolved, but at 50 cm. well-resolved three rings were observed.

From the above experiments, it may be clear that CdSe consists of two layers, cubic one at the side of Cd and very thin hexagonal layer at the neighbourhood of Se, and by heat treatment, cubic modification transforms to hexagonal one.

The reason why cubic CdSe transforms into hexagonal by heat treatment is not known, but it may be sure that the latter is more stable than the former, because the volume per one molecule of hexagonal is smaller than cubic.

The authors wish to express their sincere thanks to Prof. S. Tanaka, Prof. G. Shinoda and Prof. J. Yamaguchi for his kind suggestions.

References.

(1) J. Yamaguchi & T. Miyauchi: J.I.E.E. Japan **71** (1951) 7.

(2) J. Yamaguchi & S. Kataya: J. Phys. Soc. Japan **5** (1950) 386.

(3) J. Yamaguchi, S. Nagata & Y. Matsuo: read at Phys. Soc. Japan, April, 1950.

(4) Y. Suge & M. Aoki: read at Soc. Applied Physics Japan,, Oct. 1950.

J. PHYS. SOC. JAPAN **6** (1951) 524–525.

Note on the Kinetic Energy of the Bloch Wall.

By Akira SUGIYAMA

Faculty of Science, Hokkaido University.

(Received April 5, 1951)

Recently, Kittel developed Becker's theory on the effective mass of the moving Bloch wall, using an approximate method valid for small velocity. In this note we shall show that more rigorous result can be obtained very easily by taking the apparent increase of the exchange energy constant into account.

In the Kittel's paper, the kinetic energy σ_k accompanying the uniform motion of the Block wall per unit area (with velocity v in the Z-direction normal to the wall) is given

$$\sigma_k=(1/8\pi\gamma^{*2})\int_{-\infty}^{\infty}(d\theta/dt)^2dz=(v^2/8\pi\gamma^{*2})\int_{-\infty}^{\infty}(d\theta/dz)^2dz$$

$$\gamma^{*2}=\gamma^2+(\lambda^2/M_s^2) \qquad (1)$$

where θ is spin direction, $\gamma=ge/2mc$ and λ is relaxation frequency. (1)

In calculating the total energy σ of the moving wall, he takes the structure $\theta°(z)$ of the resting wall itself in place of $\theta(z)$ for the moving one. That is to say, he assumes as if the structure of the wall is rigid. The structure $\theta°(z)$ of the resting wall is so determined that the structural energy σ_s (exchange energy $A(d\theta/dz)^2$+anisotropy energy $f(\theta)$) should be minimum. In this case $\int_{-\infty}^{\infty}(d\theta/dz)^2dz=\sigma_s/2A$, so σ becomes a simple sum of the structural energy σ_s^0 the resting wall and the kinetic enery

$$\sigma=\sigma_s^0+\sigma_k=\sigma_s^0(1+v^2/16\pi\gamma^{*2}A) \qquad (2)$$

However, for a large value of v, which makes

σ_k large enough compared with the structural energy, the assumption of the rigid wall will not hold any longer. Indeed the moving wall may be deformed so as to minimize the total energy σ (kinetic energy +structural energy), and the energy difference between the moving and the resting walls may be smaller than what is given in (2). As dependency of σ_k on $\theta(z)$ is of the same form as that of the exchange energy, we can treat the problem of the moving wall as resting wall in which exchange constant A increases to $A+(v^2/8\pi\gamma^{*2})$. Generally, the dependency of the energy of the resting wall on the exchange constant is $C\sqrt{A}$, where C depends only on the crystal energy constant or magnetostriction constant,

$$\sigma=C\sqrt{A+(v^2/8\pi\gamma^{*2})}=C\sqrt{A}\sqrt{1+v^2/8\pi\gamma^{*2}A}$$
$$=\sigma_s^0\sqrt{1+v^2/8\pi\gamma^{*2}A} \qquad (3)$$

Of course, our result agree with Kittel's if $v^2/8\pi\gamma^{*2}A\ll1$. But in the case when the kinetic energy is of the same order as the structural energy (for iron $v\approx 10^4$cm/sec), the difference between (2) and (3) becomes remarkable. Such an effect would be found in the magnetizing process of ferrites rather than metals. In the figure full lines are derived from (2), dotted lines from (3), and a, b, c are kinetic, structural, and total energies respectively.

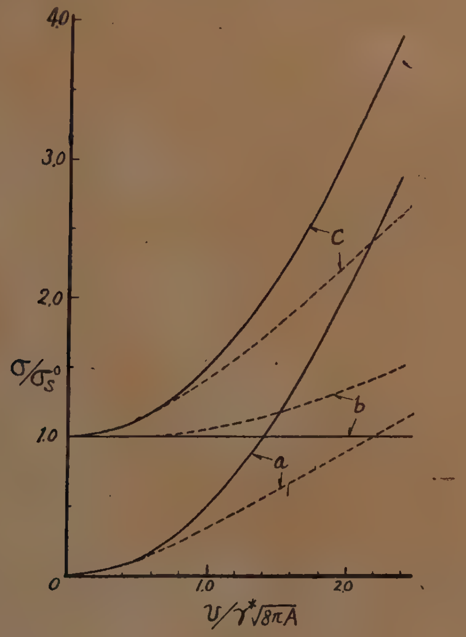

I wish to express my hearty thanks to Professor S. Miyahara for his kind discussions.

Reference.

*) C. Kittel, Phys. Rev. **80** (1950) 918.

J. Phys. Soc. Japan **6** (1951) 525–527.

Temperature Change of Intrinsic Viscosity of Polyvinyl Chloride.

By Masatami TAKEDA and Eiiti TURUTA.
Tokyo College of Science, Sinjuku, Tokyo.
(Received June 2, 1951).

Although numerous experimental studies have already been made on the flexibility and configuration of long chain polymer in solution it is still an interesting problem to study the variation of intrinsic viscosity of flexible chain polymer in solution with temperature and to analyse its experimental results with the aid of current theories of intrinsic viscosity of chain polymer. The present report deals with this problem.

The viscosity of solution of three different samples of unfractionated polyvinyl chloride (supplied by Mitui Chemical Industrial Company and purified ones by precipitation from cyclohexanone solution with methanol) in cyclohexanone, nitrobenzene and dioxane has been measured by varying the temperature from 20°C to 80°C and the intrinsic viscosity (η) has been calculated in the usual way. The experimental results are shown in Fig. 1 and 2.

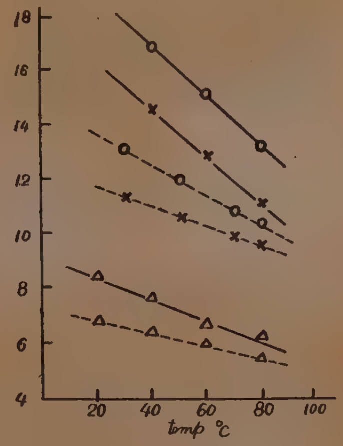

Fig. 1. The Intrinsic Viscosity of Polyvinyl Chloride in Cyclohexanone and Nitrobenzene.
○-Sample I　×-Sample II　△-Sample III
—— in Cyclohexanone
...... in Nitrobenzene
concentration g/l

As seen from Fig. 1 the values of $[\eta]$ in cyclohexanone and nitrobenzene are comparatively large and decrease linealy with rise of temperature. This fact will be explained in the following way. According to the theoretical studies of Debye[1] and Suzuki[2] the intrinsic viscosity of flexible long chain polymer is expressed by the following relation.

$$[\eta]=\frac{\pi}{6}\frac{\rho}{m}<R^2>=\frac{\pi}{6}\frac{\rho}{m}a^2n\frac{1+\cos\theta}{1-\cos\theta}\frac{1-<\cos\varphi>}{1+<\cos\varphi>} \qquad (1)$$

Where m is the mass of the structural unit of the chain, ρ the radius of the sphere which represents each unit, $<R^2>$ the average square of the distance from beginning to end of the chain, a the C-C bond distance, n the number of bond in chain, θ the angle between the two consecutive links (109°,28′), $<\cos\varphi>$ the average of rotation angle about C-C bond as seen from Fig. 3. Since the term $1-<\cos\varphi>/1+<\cos\varphi>$ in equation (1) is the sole factor dependent on temperature, we must take into consideration factors which determine rotation angle φ in chain polymer. As the most important factor we consider the potential energy of intramolecular rotation about C-C bond. The studies of Mizushima and allied[1] on the intramolecular rotation in simple molecule like 1,2 dichloro-ethane suggest that there are three potential minima about rotation angle φ in polyvinyl chloride as shown in Fig. 3. The difference of potential energy ΔE_3 between forms III and I might be much higher than ΔE_2 between form, II and I owing to intramolecular repulsive potential. Therefore only two forms II and I are considered, the term dependent on temperature in equation (1) will be expressed by following equation:

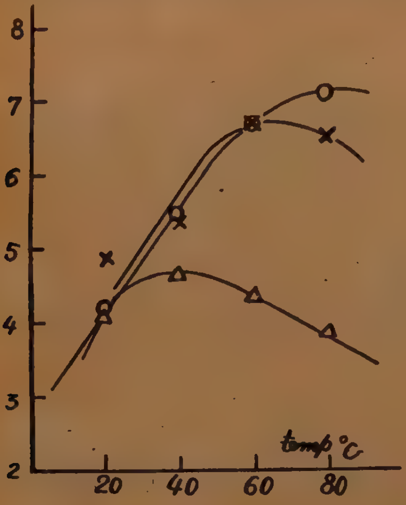

Fig. 2. The Intrinsic Viscosity of Polyvinyl Chloride in Dioxane.
○-Sample I ×-Sample II △-Sample III
Concentration g/l

$$1-<\cos\varphi>/1+<\cos\varphi>=\frac{4}{3}\exp(\Delta E_2/\mathrm{RT})+\frac{1}{3} \qquad (2)$$

From equation (1) and (2) the intrinsic viscosity can be written approximately;

$$\ln[\eta]\doteq\Delta E_2/\mathrm{RT}+\mathrm{const.} \qquad (3)$$

By applying equation (3) the difference of energy ΔE_2 is estimated from the experimental results, which is shown in Fig. 1. and tabulated in Table I. The values of ΔE_2 in Table I are independent on the average molecular weight of sample and have the same order of magnitude as the difference of potential energy (1, 2 kcal/mol) between the rotational isomers of 1, 2 dichloro-ethane. These results afford some evidence in support of our interpretation.

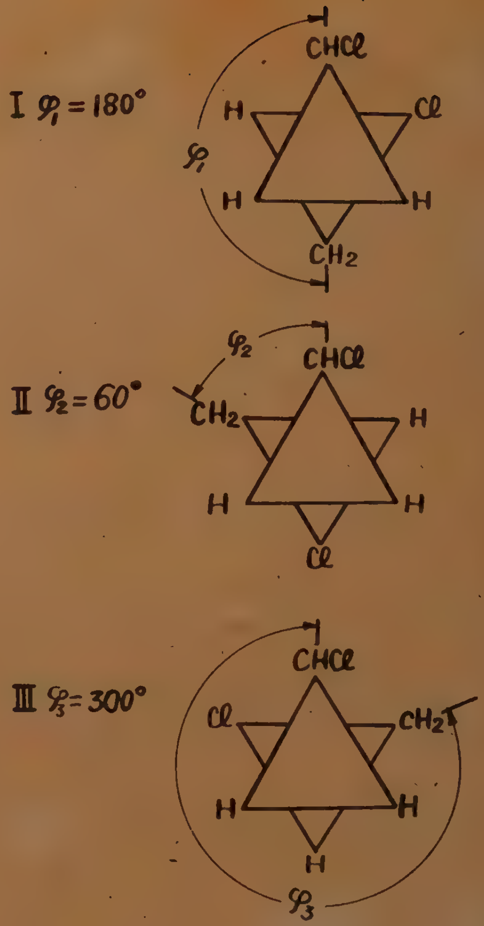

Fig. 3. Three Forms of Rotational Isomers in Polyvinyl Chloride.

Table I. ΔE_2 of Polyvinyl Chloride in Solution.

Solvent / Sample	Cyclohexanone (kcal/mol)	Nitrobenzene (kcal/mol)
I	1. 33	0, 99
II	1, 34	0, 75
III	1, 09	1, 65

The values of $[\eta]$ in dioxane shown in Fig. 2 are relatively small and increase with rise of temperature, but decrease with further rise of temperature. Thus the intrinsic viscosity of each sample has its maximum at a certain temperature. The temperature of maximum becomes higher as the average molecular weight of sample increases. Such interesting behaviour of chain polymer is not completely explained by the equation (1) and (2) and requires more advanced theories which are suggested by Flory[4] and Suzuki[5] for its interpretation. According to these theories the variation of $[\eta]$ of polyvinyl chloride in dioxane may be explained qualitatively as follows. The long range intramolecular interference of polymer in dioxane is stronger than is cyclohexanone and nitrobenzene, so that the term $<R^2>$ in equation (1) becomes smaller. With rise of temperature the micro Brownian motion of the chain increases and cancels this interference, and $<R^2>$ becomes larger. With further rise of temperature the effect of the micro Brownian motion on the intramolecu'ar potenial becomes more predominant just as in cyclohexanone and nitrobenzene. Thus $<R^2>$ becomes smaller again.

References.

1) P. Debye: J. Chem. Phys., **14** (1946) 636.
2) K. Suzuki: Bull. Chem. Soc. Japan, **20** (1947) 20.
3) S. Mizushima, Y. Morino and T. Simanouti: J. Chem. Phys., **17** (1949) 663.
4) P. J. Flory: J. Chem. Phys., **17** (1949) 223.
5) K. Suzuki: Bull. Chem. Soc. Japan, **22** (1949) 8.

J. PHYS. SOC. JAPAN **6** (1951) 527–528.

Surface Oxidation of Zincblende Cleavage Face in the Roasting Atmosphere.

By Ryoitiro SATO.
Taihei Mining and Metallurgical Laboratory.

(Received June 4, 1951).

Surface oxidation of zincblende single crystal has been investigated by several authors[1) 2) 3) 4)] by means of electron diffraction. In these experiments, where the specimen was oxidized in air at red heat, the oxidation product was always zinc oxide alone. Its orientation with respect to the substrate[5)] or the development of its crystallographic planes was discussed in detail. On the other hand, it is well confirmed that in the roasting of zincblende in its metallurgical process zinc sulphate or ferrite is also produced.

Accordingly, the following experiment was carried out, in which the heating condition might be regarded as a good idealization of the roasting oxidation; a fresh cleavage face of zincblende was buried in the zincblende powder, prepared by grinding the crystal in an agate mortar, and was then heated in an electric furnace for about 30 min. at a disired temperature. The thickness of the powder layer on the specimen was about 10mm. After cooling it to room temperature the specimen was taken out of the powder, removed for the attached particles by slight rubbing with gauze, and then inspected by electron diffraction.

The obtained results show that between 300°C, and 500°C. an orthorhombic crystal with a=8.21Å, b=5.19Å, and c=6.80Å is formed on the cleavage face (Photos.). In open air, above about 350°C. zinc oxide alone is formed, and below this temperature the oxidation does not occur. The orientation of this orthorhombic crystal is as follows: $(001)_{orthorh.}//(110)_{ZnS}$ and $[100]_{orthorh.}//[1\bar{1}0]_{ZnS}$.

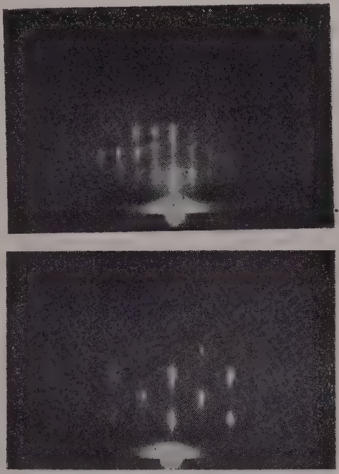

Photos. Zincblende cleavage face heated in zincblende powder at 400°C. for 30 min. Beam parallel to $[001]_{ZnS}$ (top) and $[1\bar{1}0]_{ZnS}$ (bottom).

The observed intensities of the diffraction spots show that (0kl)-reflections are missing if k+l=odd.

Since the above heating corresponds to a sulphatizing condition[6)], the product is most likely supposed to be zinc sulphate. At an early date Breithaupt[7)] found out naturally occurring anhydrous zinc sulphate and showed that it is isomorphous with lead sulphate (anglesite) and barium sulphate (barite). According to Schiff[7)] anhydrous zinc sulphate crystallizes in an orthorhombic structure, the lattice constants of which are $a=8.58$ Å, $b=6.73$ Å, and $c=4.76$ Å. However, in order to make its axial ratios agree with those given in Dana's book[9)], its b-and c-axes must be interchanged. The law of missing spectra found in the present work is not in contradiction to that given by Schiff, and this law is necessary for a crystal to belong to the space group V_h^{16}, to which anglesite and barite also belong. On these grounds the present surface product may be concluded at the present stage of study as being some form of zinc sulphate very similar to the anhydrous one.

When concentrated zincblende powder from a flotation cell is used instead of the above one, zinc ferrite ($ZnFe_2O_4$, cubic) is obtained above 600°C. It has the following two types of orientations: $(110)_{ferrite} /\!/ (110)_{ZnS}$, $[1\bar{1}0]_{ferrite} /\!/ [1\bar{1}0]_{ZnS}$ and $(113)_{ferrite} /\!/ (110)_{ZnS}$, $[1\bar{1}0]_{ferrite} /\!/ [1\bar{1}0]_{ZnS}$ or $[\bar{1}10]_{ZnS}$. This result is the same as obtained by Hagihara[10] in heating the cleavage face in vacuo (about 10^{-4} mm. Hg). This may imply that in this heating condition the supply of oxygen to the crystal suface is extremely scanty. The concentrated powder is supposed that each particle is covered with copper atoms due to the preconditioning by cupric sulphate and with collector molecules in some state. Therefore, it can be understood that its behavior in heating is different from that of the untreated powder. Iron atoms in zinc ferrite might presumably have come to the surface from the interior of the zincblende crystal, where they had been contained as impurities.

The full detail of the present work will be published in the near future.

The writer expresses his cordial thanks to Mr. H. Hagihara for his encouragement and discussions.

References.

1) T. Yamaguti, Proc. Phys-Math. Soc. Jap., **17** (1935), 443.
2) G. Aminoff and B. Broomé, Kgl. Svenska Vetenskapsekad. Handl., **16** (1938), 3.
3) R. Uyeda, S. Takagi, and H. Hagihara, Proc. Phys.-Math. Soc. Jap., **23** (1941), 1049.
4) D. M. Evans and H. Wilman, Proc. Phys. Soc., A. **63** (1950), 298.
5) H. Seifert, Z. Krist., **102** (1940), 183.
6) Y. Ogawa, J. Min. Inst. Jap., **46** (1930), 515 (in Japanese).
7) A. Breithaupt, Berg.-Hüttenm. Ztg., **11**(1852) 100.
8) K. Schiff, Z. Krist., **87** (1934) 379.
9) E. S. Dana, "*A System of Mineralogy*". (John Wiley & Sons, Inc., New York, 1915)894.
10) H. Hagihara, Read at the Annual Meeting of the Phys. Soc. Japan, April 29, 1949.

J. PHYS. SOC. JAPAN **6** (1951) 528–529.

Twin Formation of Zincblende through Oxidation-Reduction Process.

By Ryoitiro SATO.
Taihei Mining and Metallurgical Laboratory

(Received June 4, 1951).

When zincblende surfaces are heated in air at red heat, zinc oxide crystal with a complete orientation is formed thereon[1) 2) 3) 4) 5)]. The crystals of both zinc sulphide (cubic) and zinc oxide (hexagonal) are considered to be built up of the elementary tetrahedrons with each zinc ion surrounded tetrahedrally by four sulphur or oxygen ions. The mechanism for the orientation of the zinc oxide crystal with respect to the substrate is explained as follows; the sulphur ions around a zinc ion are first replaced by oxygen ions, and the oxide crystal then grows as a hexagonal lattice. As for the oxidation of the cleavage face, however, the tetrahedrons of oxide and sulphide do not remain exactly parallel to each other, i.e., the $(103)_{ZnO}$-face becomes parallel to the $(110)_{ZnS}$-face (the cleavage face), or the $[001]_{ZnO}$-axis becomes tilted from the $[11\bar{1}]_{ZnS}$-direction by about 3° nearer to the $[110]_{ZnS}$-direction (the outward normal to the cleavage face).

When the cleavage face of zincblende, oxidized beforehand in air to red heat, is again heated in pyrite (FeS_2) or chalcopyrite ($CuFeS_2$) powder above 450°C. for about 30 min., the oxide coating on the cleavage face is reduced to zinc sulphide. An electron diffraction photograph obtained from one of these speciment is reproduced in Photo.

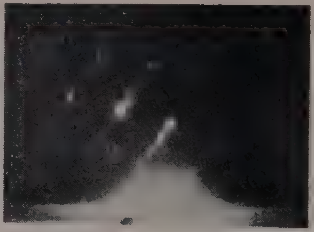

Photo. Oxide coated zincblende cleavage face heated in pyrite powder at 600°C. for 30 min. Beam parallel to $[1\bar{1}0]_{ZnS}$.

If in this reducing reaction the above-mentioned parallelism between the tetrahedrons in the original crystal and the newly produced one is considered as it was in the oxidizing reaction, the reduced sulphide should now have two orientations. This follows from the geometrical consideration of the dispositions of the elementary tetrahedrons in the crystals, i.e., the tetrahedrons building up the zinc oxide crystal (hexagonal) are of two kinds in orientation, while those of the sulphide crystal (cubic) are of only one kind. If the consideration of above parallelism happens to be true, the one of the two expected orientations of the reduced sulphide crystal must have the tilt of about 3° with respect to the original zincblende crystal, corresponding to the tilt of the $[001]_{ZnO}$-axis from the $[11\bar{1}]_{ZnS(orig.)}$-direction. The other is expected to be the twin orientation of the former along the $[11\bar{1}]_{ZnS(not\ orig.)}$-direction, which still would lie parallel to the $[001]_{ZnO}$-axis. Actually, however, the analysis of the obtained pattern shows that the two orientations of the re-

duced sulphide are as follows; the one is exactly the same as that of the original zincblende crystal, and the other is the twin of it along the [111]$_{ZnS(orig.)}$-direction. The reason for the observation of these orientations instead of the above expected ones is supposed to be that the reduced sulphide crystal prefers the orientations which is a continuation or a twin of the underlying zincblende lattice rather than orientations slightly tilted from them. It is to be added that the twin spots are predominat in intensity as compared with those due to the original orientation.

Hagihara[6] obtained a similar photograph on a naturally tarnished (110)-face of zincblende. This may suggest that such an oxidation-reduction reaction really takes place in ore deposits naturally under some circumstances.

The full detail of the present work will be published in the near future.

The writer expresses his cordial thanks to Mr. H. Hagihara for his encouragement and discussions.

References.

1) T. Yamaguchi, Proc. Phys.-Math. Soc. Jap., **17** (1935) 443.
2) G. Aminoff and B. Broomé, Kgl. Svenskapsakad. Handle., **16** (1938) 3.
3) H. Seifert, Z. Krist., **102** (1940) 183.
4) R. Uyeda, S. Takagi, and H. Hagihara, Proc. Phys.-Math. Soc. Jap., **23** (1941) 1049.
5) D.M. Evans and H. Wilman, Proc. Phys. Soc., A. **63** (1950) 298.
6) H. Hagihara, Read at the Annual Meeting of the Phys. Soc. Japan, April 29, 1949.

J. PHYS. SOC. JAPAN **6** (1951) 529–530.

Sur le Spectromètre à Orbites Spirales sans Fer

By Mitsuo SAKAI

Department of Physics, University of Tokyo.

(Received June 8, 1951)

Le spectromètre à orbites spirales sans fer a éte construit dans lintention de mesurer le spectre des rayons β d'énergie faible. Il consiste à trois couples des bobines A, B et C. (Fig. I.) Les champs magnétiques qui proviennent de chaque bobine, le champ magnétique total et son vecteur potentiel magnétique sont respectivement figurés dans la Fig. 2. On saurait facilement d'après ces figures que la bobine A sert à satisfaire la condition de convergence et B à donner le champ magnétique sur le cercle et C à la fonction auxiliaire. Cet appareil a les avantages suivants. Premièrement on peut utiliser nombreux variables. Pour conséquce on peut changer le diamètre du cercle de convergence à volonté et aussi il est très facile à établir le champ magnétique qui a un grand κ et aura un plus haut rendement Deuxièmement il n'y a point d'hystérésie.

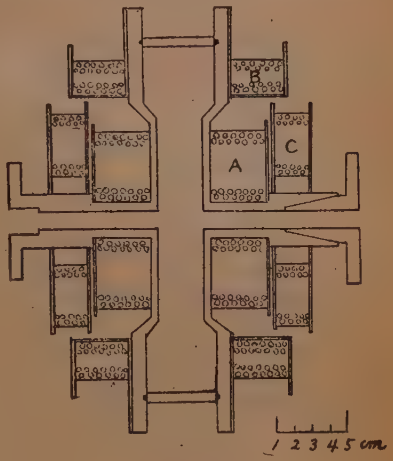

Fig. 1.

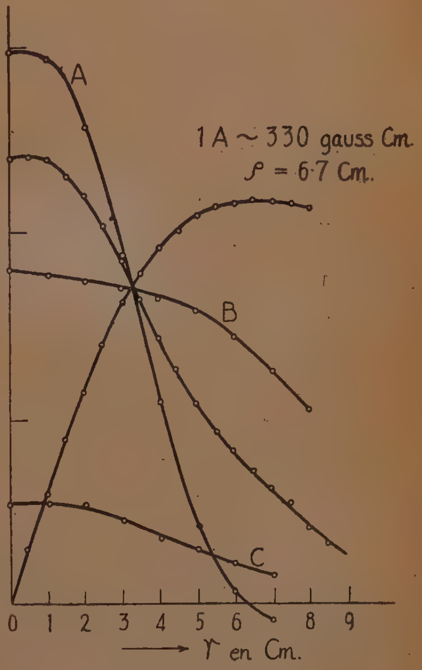

Fig. 2.

Le spectre des électrons dans le Fig. 3. est obtenu en utilisant les électrons de 6000 e.v. de l'émission de cathode froide. La Fig. 4 représente le spectre obtenu en mesurant les photoélectrons de cuivre projetés par làction des rayons Mo $K\alpha$. Dans cette mesure nous nous sommes servis du compteur avec

---

Le présent travail a été fait 1949.

la fenêtre que les électrons dont l'énergi dépasse 4000 e.v. peuvent percer. Puis une couche mince de collodion appliquée de cuivre par le procédé de *Sputtering* a servi de cible aux rayons X. En général pour mesurer les électron d'énergie faible, il faut utiliser la source très mince. Par conséquent nous nous sentons un peu difficile de l'utiliser dans l'expérience. Nous faisons conduire à la direction d'axe les rayons X étallonnés avec le systeme de fentes et le diffuseur est situé rectangulairement à ces rayons et près du plan de symetrie. Jáimerais souligner l'importance de la solution de cette difficulté.

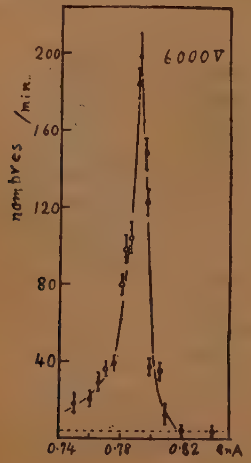

Fig. 3.

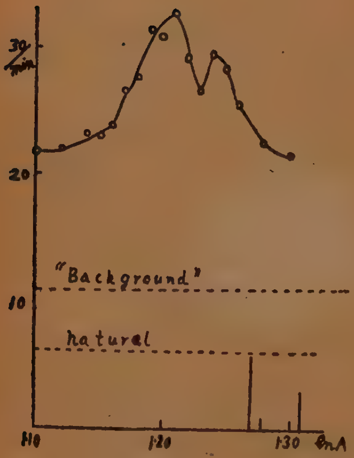

Fig. 4.

J. PHYS. SOC. JAPAN 6 (1951) 530-531.

On the Distribution of Internal Stresses of Permalloy Subjected to Field Cooling.

By Makoto OSAWA
Institute of Industrial Science, University of Tokyo.
and Ichiro SUGIURA.
Tokyo Institute of Technology.

(Received June 18, 1951.)

The magnetic properties of permalloy are well known to be very much affected by heat treatment, especially by field cooling. It is very important to study these problems from a viewpoint of the internal stress distribution. Previously, Zener[1] suggested that the mean distance between stress inhomogeneities of opposite sign may be estimated by the measurement of internal friction. We intended to investigate its variation between the state subjected and not subjected to field cooling.

Internal friction was measured by following means; a cylindrical rod of specimen of 20cm in length and 0.5cm in diameter is supported at its modes of vibration with two knife-edges and is longitudinally vibrated electromagnetically by a coil placed at one end of the of the specimen. The other end is utilized as a plate of a condenser which is connected parallel to another condenser in resonant branch of high frequency Hartley oscillator. When the specimen is vibrating, the frequency of Hartley oscillator is modulated according to the vibration, and then the frequency change is transformed into a voltage by means of Foster-Seeley circuit. Through a three stages amplifier, the out put current is measured for each driving frequency, and the internal friction is calculated from the width of resonance curve at half maximum.

The specimen was made in vacuum from electrolytic materials, its composition being 78.0% Ni, 21.5% Fe and 0.5% Mn. After being fully annealed at about 1000°C, it was subjected to various heat treatments. In very treatment, it was kept at 800°C for 30 minutes, then rapidly cooled to 490°C, and kept at 490±5°C for a certain required time, and then more rapidly cooled to room temperature. The measurement of internal friction was always made at room temperature. In the case of field cooling, magnetic field was continuously applied below the magnetic Curie temperature.

Fig. 1. shows the biasing external field *vs.* internal friction curves in the case of cooling without influence of magnetic field, Fig. 2. shows the case of field cooling. The dependency of internal friction upon the biasing field is much interesting, but detailed considerations of this problem will be made in future.

A glance of these figures shows that the internal frictions in saturated magnetization do not coincide with each other. These internal frictions are plotted against annealing times at 490±5°C in Fig. 3. In each case, a maximum appears. The internal friction in saturated magnetization is thought to be mainly due to microscopic thermal current arising from stress inhomogeneities. Now driving frequency is kept constant, so if the mean distance between stress inhomogeneities varies gradually with the time of annealing at 490±5°C, the internal friction will be maximum according to Zener's suggestion when the mean distance L fulfills the relation, $fL^2/D \doteqdot 1$, where f is the driving frequency and D is the thermal diffusion constant. For the sake of estimation of L, we take the values as follows; $D = 0.19 \text{cm}^2/\text{sec}$ and $f = 25\text{Kc}$, then we get the mean distance between stress inhomogeneities of the order of 3×10^{-3}cm for an annealing time of 5 min. in the case of field cooling and for an annealing time of 45 sec. in the other case.

A similar quantity can be calculated from Becker-Kersten's[2] theory, using measured values of initial permeability and coercive force. H. Sato[3] has already done these calculations and along these lines tried to give a qualitative explanation to the appearance of a maximum in Fig. 3 in the case of cooling without influence of magnetic field. Our observed value of L, and H. Sato's as well does not agree with the ones calculated. But, it seems difficult to explain along these lines the fact that the maximum point of internal friction in the case of field cooling shifts to longer annealing time side as compared to the one observed in the case without influence of magnetic field.

The details of the investigation will be reported elsewhere. Finally the authors express their sincere thanks to Messrs. T. Taoka and T. Nagashima for their kind cooperation in making the specimen.

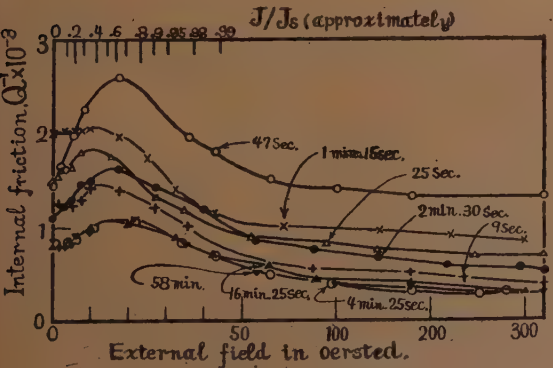

Fig. 1.

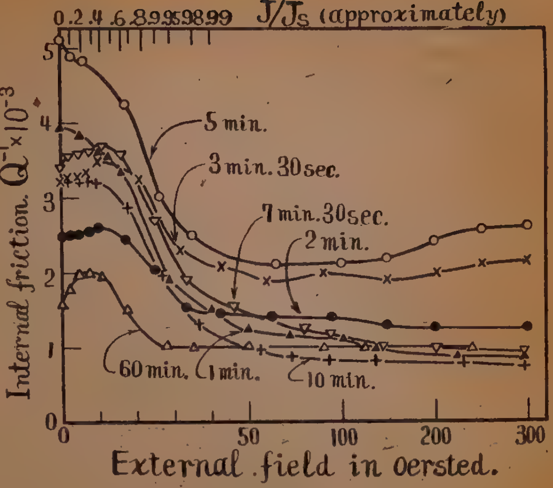

Fig. 2.

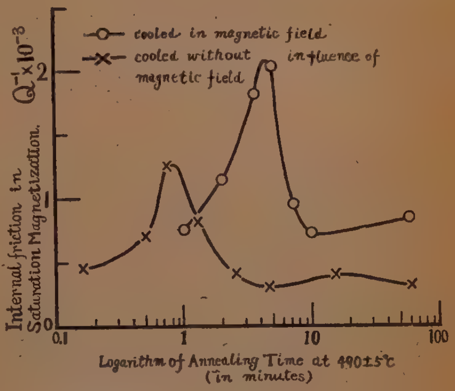

Fig. 3.

References.

1) C. Zener: Proc. Phys. Soc., **52** (1940) 152.

2) R. Becker, W. Doering; Ferromagnetismus. (1939).
Kersten, Gottschalt: Z. Tech. Phys., **21** (1940) 345.

3) H. Sato: Sci. Rep. Ritu, **A-1** (1949) 69.

J. Phys. Soc. Japan **6** (1951) 531–532.

On the Transformation of Tin at Low Temperature.

By Haruji Ishikawa.

The Government Mechanical Laboratory, Agency of Industry and Technology.

(Received June 23, 1951).

In ordinary crystalline states white tin, subjected to low temperature, scarcely transforms into grey tin, unless it is extremely pure[1], but white tin, if not extremely pure, can be transformed without much difficulties when the specimen of pure white tin is pressed into sheet form at sufficiently low temperature, for example at about −20°C, and exposed to the cold for a long period, for instance −10°∼20°C, during several ten days[2]. Some factors[2] [3] which might affect the transformability of the pure white tin specimen pressed at low temperature has just been studied and the following results obtained.

The specimen, which is pressed severely, transforms easier than that, which is deformed less severe. As the deformation proceeds the locally distorted portion of the specimen becomes more unstable, therefore can be transformed without much obstacles.

The slower is the pressing velocity, the more quickly does the specimen transform. Under the rapid pressing the generated heat pressing raises the temperature of the specimen, therefore the formation of the severe local distortion of the white tin crystal lattice may be destroyed by the vigorous heart motion of tin atoms, or the distortion momentarily produced may turn out into the local recrystallization nucleus[2].

The properties of organic solvents do not considerably affect the transformability, but the coexistence of tin ion Sn^{++} accelerates the growth of the transformation specks. As the specimen is in an extremely unstable crystalline state, the locally distorted portion of the specimen turns out spontaneously into the transformation nucleus, and the function of the organic solvents to activate the transformation has no observable influences on the transformation. But the growing velocity of the transformation nucleus can be effected considerably by them.

The temperature of the successive exposure is the most effective at about −70°C for the transformation. But this temperature seems to be not always essential to the exposure, provided the pretreatment of the specimen be adequately changed and the crystalline state become exceedingly unstable.

References.

1) E. Cohen, & C. van Eijk: Z.S. Phys. Chem., **30** (1899), 601.
E. Cohen, Z.S. Phys. Chem. **48** (1904) 243.
C. W. Mason, & W. P. Forgen: Metal and Alloys, **6** (1935) 87.
2) E. Cohen, W. A. T. Cohen-de Meester, & A.K.W.A. van Lieshout: Z.S. Phys. Chem. A, **173** (1935) 169.
3) A.E. van Arkel, & P. Poets: Z.S. Phys., **41** (1927) 701.

J. Phys. Soc. Japan **6** (1951) 532–533.

On the Effect of Electrolytic Treatment of Ni-Sleeve on Electron Emission

By Junkichi NAKAI and Shōgo NAKAMURA

Faculty of Engineering, Osaka University.

(Received June 27, 1951)

During the research of the cathode interface, we have found that the electrolytic treatment of the Ni-sleeve surface gives the good effects on the electron emission.

In order to observe the influence of the electrolytic treatment under the same degasing conditions, we have polished one half of a sleeve with 10% dilute sulphuric acid by a.c. after or before hydrogen treatment. After fully washing, the sleeve was coated with $BaCO_3$ or $(Ba\cdot Sr)CO_3$ by electrophoresis, and we have constructed a diode as Fig. 1.

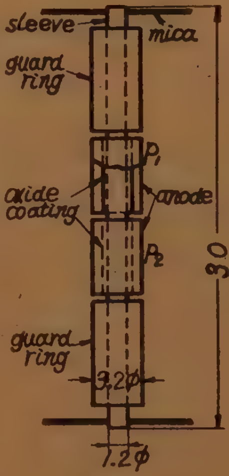

Fig. I

Fig. 1.

On the Effect
of Electrolytic Treatment
of Ni-Sleeve
on Electron Emission
By Junkichi Nakai
and Shōgo Nakamura

Fig. 2. shows an example when the carbonate was converted into oxide at about 1300°K and the cathode was activated at high temperature. However, the anode current was measured at lower tempera-

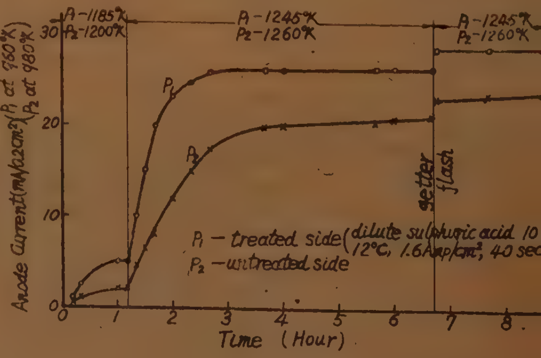

Fig. 2.

ture applying the d.c. anode voltage. In this case the cathode was activated only with the reducing action by the impurity contained in the base metal. From Fig. 2 it is evident that the emission from the electrolytically treated side p_1 is greater than the untreated side p_2.

From 32 examples it is found that the emissivity of the p_1 side is usally 1.5~2 times, in some cases 5 times, greater than of the p_2 side at the end of activation, and the work functions of the treated sides measured by the initial velocity current methode are 0.1 e. v. smaller of much smaller than that of the untreated sides.

When we examine the influences of the treatment conditions to the electron emission, we have obtained the best condition in the current density of about 1.5 amp/cm^2 at 25~30°C. By using this current density it takes about 30 sec. to take away 6μ of the Ni-sleeve surface, and it is found that there are no influences to the emission even if the polishing is carried on further.

The detailed reason of such results obtained are unknown, but we suppose as follows: on the course of manufacture of the Ni-sleeve, the reducing impurities which exist near the surface layer have been oxidized. This oxidized layer has been still remained even if it suffer the hydrogen treatment, but by the electrolytic treatment it is easily removed. Or, the contact condition between the base metal and the oxide becomes better by the electrolytic polishing.

The authors wish to express their gratitude to Prof. E. Sugata for his kind guidance and to Mr. Y. Inoguchi, Mr. K. Kozeki and Mr. Komura of N.E.C. for their valuable helps and suggestions. We also thank to Mr. T. Hirose for his cooperation in the experiments.

This work was partly supported by the Scientific Research Expenditure of the Ministry of Education.

J. PHYS. SOC, JAPAN **6** (1951) 533–534.

On the Mach Reflection of a Shock Wave.

By Ryuma KAWAMURA.

Institute of Science and Technology,
University of Tokyo.

(Received July 4, 1951)

There are two types of reflection of a shock wave at a fixed wall[1]. One is the "regular reflection" and the other the "Mach reflection". The latter occurs when the angle between the shock and the wall becomes larger than a certain limit beyond which regular reflection is theoretically impossible. In this case three shocks, named incident, reflected and Mach shocks, cross each other at one point and form Y-type configuration (Fig. 1). Although the experimental results of Mach reflection show a very beautiful coincidence with three-shock theory so far as the shock is strong, they are in disagreement with the theory when it is week[2]. The most remarkable disagreement is that Mach reflections exist where there are no non-trivial solutions for the three-shock configuration. The solutions are called trivial ones when the Mach shock is a continuation of the incident shock and the reflected shock becomes a sound wave[3]. Thus, in the region where three-shock theory cannot explain the experimental results, there arises a doubt that the trivial solution might exist at the triple point and at the same time reflected shock and Mach shock have very large curvature at that point. Therefore, it is desirable to examine the possibility of shocks having curvature at the triple point.

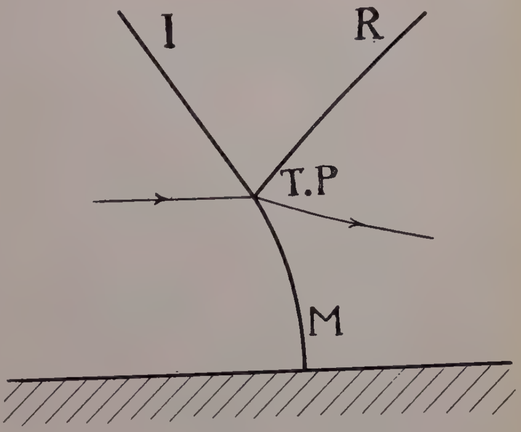

Fig. 1.

Behind a curved shock in uniform supersonic flow, the following relation is obtained (Fig. 2)[4].

$$Q(\partial\theta/\partial s)=P(\partial p/\partial s)/\rho_1 q^2\,,\quad R(\partial\theta/\partial s)=P(\partial\alpha/\partial\lambda)\,,$$

$$P=\frac{2}{\gamma+1}\sin 2\alpha\Big[1+(M_2^2-2)\sin^2(\alpha-\theta)\Big]-\frac{1}{2}\sin 2\theta\,,$$

$$Q=\sin 2\alpha\Big[\frac{2}{\gamma+1}\sin 2\alpha-\frac{\sin 2\theta}{4\cos^2(\alpha-\theta)}\Big]\,,$$

$$R=\sin 2\alpha\Big[\cos(\alpha-\theta)-\frac{1+(M_2^2-2)\sin^2(\alpha-\theta)}{2\cos(\alpha-\theta)}\Big]\,,$$

where α is the angle between the uniform flow and the shock, θ the flow direction, P the pressure, ρ_1 and q_1 the density and the velocity in front of the shock, s and λ the lengths measured along the stream line and the shock and M_2 the Mach number behind the shock. On the other hand, the following relation is obtained from the oblique shock theory[5].

$$\frac{d\theta}{d\alpha}=\cos^2\beta\Big[\frac{4}{\gamma+1}-(1+\tan\alpha\tan\beta)(1-\frac{\tan\beta}{\tan\alpha})\Big]\,,$$

$$\beta=\alpha-\theta\,.$$

It is well known that $(d\theta/d\alpha)>0$ for $M_2>1$. Therefore, for $M_2>1$,

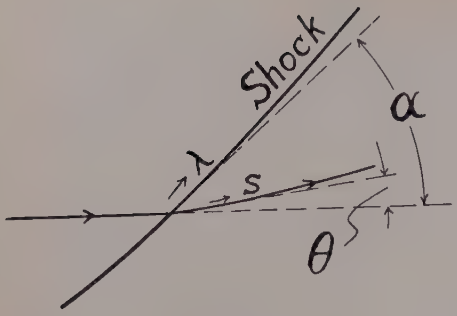

Fig. 2.

$$P=\frac{\sin^2\beta\sin 2\alpha}{2}\left[\frac{4}{\gamma+1}-(1+\tan\alpha\tan\beta)\right.$$
$$\left.\times(1-\frac{\tan\beta}{\tan\alpha})\right]+\frac{2}{\gamma+1}-(M_2^2-1)\sin\beta\sin 2\alpha>0,$$
$$Q=\frac{\sin 2\alpha}{2}\left[\frac{4}{\gamma+1}-\frac{1}{2}(1+\tan\alpha\tan\beta)\right.$$
$$\left.\times(1-\frac{\tan\beta}{\tan\alpha})\right]>0.$$

To satisfy the above requirement, $(\partial\theta/\partial s)$ and $(\partial p/\partial s)$ must have equal sign when $M_2\geqq 1$. In the trival solution of Mach reflection it is obvious that the flow is supersonic behind both of reflected and Mach shocks. There, the above relation must hold. It must be remembered in this case that the sign of θ must be different behind the Mach shock and the reflected shock because it crosses the uniform flow with greater angle than $\pi/2$. On the stream line passing through the triple point, which divides the flow field into two regions, i. e. the region behind Mach shock and that behind reflected shock, it is required that pressure and direction of flow as well as their derivatives coincide each other in both regions. Although the trivial solution satisfies the requirement so far as pressure and direction are concerned, it is impossible to satisfy generally the condition imposed on their derivatives because $(\partial\theta/\partial s)$ changes its sign across the stream line as mentioned above. Only one possible solution is $(\partial\theta/\partial s)=0$, and therefore, $(\partial p/\partial s)=0$. This means that the curvatures of reflected and Mach shock must be zero at the triple point. Thus, it is concluded that the trivial solution of Mach reflection combined with shock curvature cannot explain the existing discrepancy between theory and experiment.

References.

1) Kawamura, R.: Rep. Aeron. Res. Inst. **23** (1945).

2) Bleakney, W. and Taub, A. H.: Rev. Mod. Phys. **21** (1949).

3) Taub, A.H.: Phys. Rev. **72** (1947).

4) Lin, C.C. and Rubinov, S. I.: J. Math. Phys. **28** (1948).

5) Ferri, A.: Elem. Aerod. Supers. Flows, The Macmillan Co., New York (1949).

J. PHYS. SOC. JAPAN **6** (1951) 534–535.

A New Type of Striation Observed in an Electronmicrograph.

By Yoshinobu SEKI.

Taihei Mining & Metallurgical Laboratory,
Omiya City, Saitama Pref.

(Received July 6, 1951)

During the course of the observations of clay minerals by means of electron microscope, a new type of striation was observed. An example is represented in the Fig. 1.

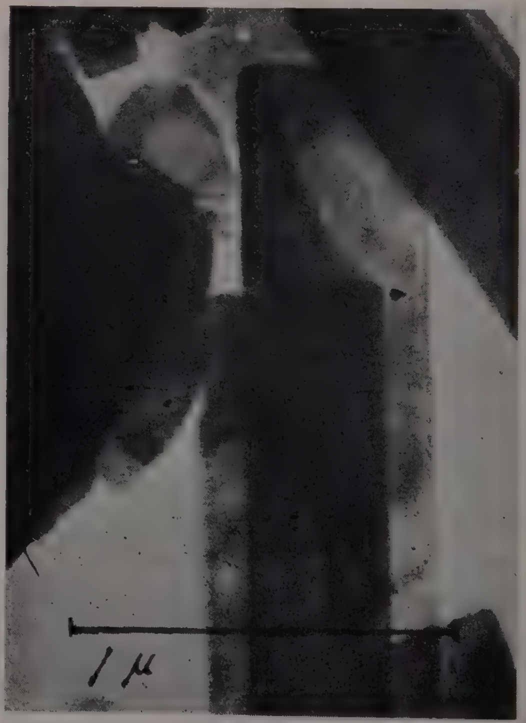

Fig. 1.

The sample was a clay mineral identified as "sericite" by comparing its *X*-ray Debye-Scherrer lines with those reported by Sudo[1] on the mineral. It is supposed that the mineral is so oriented that its *c*-axis is normal to the plane of the plate with its *a*-and *b*-axes parallel to the shorter and longer edges of the observed rectangular crystallites, respectively.

---

* *X*-ray examination was carried out by K. Suzuki of this laboratory.

The characteristic feature which distinguishes the present striation from the ones already reported by Heidenrich2)3) or by Mitsuishi, Nagasaki, and Uyeda4) is that almost parallel and equidistant black striae are observed in the region where two apparently distinct crystal flakes are overlapping to each other in almost parallel orientation. The striae end abruptly at the edge of one of the overlapping crystallites.

The separation of the striae in the figure was about 400 A, where as with the other example not reproduced here the value was about 250 A.

Another feature remarkable in the micrograph reproduced in the figure is the observation of white striae corresponding to the above black ones in some distance from the latter. They might have been caused because of their small angle diffraction and the defocussing or lens aberration.

The interpretation of the present type of striation is now being considered.

The writer expresses his thanks to the kind suggestion from Mr. H. Hagihara, Kobayashi Institute of Physical Research.

References.

1) Sudo, T.: Jour. Ceramic Associ. J.: **55** (1947) 48.

2) Heidenreich R.D. and Sturkey L.: Jour. App. Phys. **16** (1945) 97.

3) Heidenreich R.D.: Jour. App. Phys. **20** (1949) 993.

4) Mitsuishi T., Nagasaki H.. and Uyeda R.: Proc. Jap. Acad. **27** (1951) 86.

J. PHYS. SOC. JAPAN **6** (1951) 535-536.

Correlation between Ultrasonic and Infrared Absorption in Liquids.

By Yasaku WADA and Sotoshi SHIMBO.

Department of Applied Physics, Faculty of Engineering,
University of Tokyo, Tokyo, Japan.

(Received July 7, 1951)

Liquids have been classified by Pinkerton1) into four classes according to their absorption of ultrasonic waves. The first class includes carbon disulphide, benzene and most other non-associated polyatomic liquids. To the second class belong associated liquids such as water and alcohols, to the third monatomic liquids and to the fourth highly viscous liquids.

The origin of the ultrasonic absorption in the first class has been discussed by many authors and is now considered as "*volume viscosity*" of liquids. The molecular mechanism of the volume viscosity is, however, not yet conclusively explained and several types of theories have so far been proposed. According to one of them2) the volume viscosity is due to the time-lag of the variation of local order of molecular arrangement, which is solely conecerned with the intermolecular properties. An alternative theory3) assumes the volume viscosity to be caused by the time-lag of transformation of external (translational and rotational) energy of molecules into internal (vibrational) energy.

According to the latter theory the ultrasonic absorption of liquids depends also upon the intramolecular vibrations. If this be the case, the ultrasonic absorption may be expected to have some correlation to the infrared absorption. A comparison of the two quantities of various non-associated polyatomic liquids, as in Fig. 1, has brought to light the expected correlation. The absorption coefficients of ultrasonic waves divided by the square of frequency in the abscissa were adopted from the paper by Pinkerton1) who tabulated only the reliable data in several recent papers. The infrared absorption, integrated from 1000 to 2000cm^{-1} (the range was limited by the available data) was computed from the monograph by Barnes etc..4)

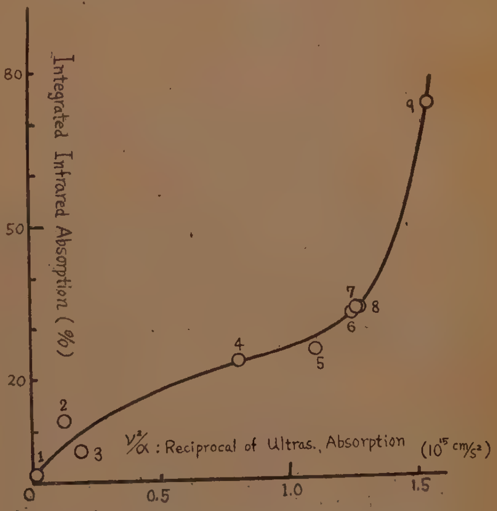

Fig. 1. Correlation between integrated infrared absorption (reduced to the equal light path) and reciprocal of ultrasonic absorption of non-associated polyatomic liquids: (1) carbon disulphide, (2) benzene, (3) carbon tetrachlorides, (4) chlorobenzene, (5) toluene, (6) n-heptane, (7) nitrobenzene, (8) m-xylene, (9) acetone.

As clearly shown in the figure, liquids of higher ultrasonic absorption are poorer infrared absorbers. The reason may be as follows. The vibrational motions of molecules of a liquids with low infrared absorption may be difficult to be excited by molecular collisions. The liquid has a long relaxational time τ in sharing the energy between vibrational motion on the one hand and translational and rotational motion on the other hand. The relaxational frequency ν_m, $\nu_m=1/2\pi\tau$, at which ultrasonic absorption becomes maximum, is thus expected to be low. Assuming the maximum absorption to be the same order with all the liquids, the lower the relaxational frequency is, the higher may be the ultrasonic absorption at the experimental frequencies, which are believed to be far below ν_m.

References.

1) J. M. M. Pinkerton: Proc. Phys. Soc., B, **62** (1949) 129.
2) J. Frenkel and J. Obrastzov: Jour. of Phys. USSR, **2** (1940) 131.
3) H. O. Kneser: Ann. Phys., **32** (1938) 277.
4) R. B. Barnes, et al., Infrared Spectroscopy. Reinhold Pub. Corp., New York, 1944.

J. Phys. Soc. Japan **6** (1951) 536–537.

The Intrinsic Permeability of Permalloy at High Frequency.

By Yoshiro Hori.

The Furukawa Physical and Chemical Research Laboratory, Shinagawaku, Tokyo,

(Received August 8, 1951)

The intrinsic permeability of ferromagnetic material at high frequency has been studied by Kreierscheimer, Wait, Dannatt etc. Iron, nickel etc. are known to have comparatively constant value up to about 100 megacycles (3m wave-lengths) and from this frequency to decrease to unity for heat waves. These experimental results gave the foundation to theoretical treatment of mechanism of magnetization at high frequecy and have been studied theoretically by Becker, Kittel etc. But in the higher permeability materials such as permalloy, the intrinsic permeability is not always constant for the variation of frequency below 100 megacycles, but decreases with increasing frequency and even for a few megacycles it is very small compared with D. C. permeability.

Recently the author measured the intrinsic permeability of many kinds of ferromagnetic materials-Armco-iron, Si-steel 78.5% Ni-permalloy at 1.0∼6.0 megacycles. Those results were read at the meeting of the Physical Society of Japan on Nov. 1950 and on April 1951. The present paper is to deal with only the results for 45% Ni-permalloy.

45% Ni-permalloy is employed effectively at high frequency because of its high resistance and relatively high permeability. The composition and D.C. magnetic character of the author's sample are shown in Table I and 2.

Table I.

Ni	Cr	Co	Mn	Si	Fe
44.20	7.51	3.25	0.80	1.92	bal.

Table II.

Initial permeability μ_0	1800
Maximum permeability μ_m	17000
Saturation B_∞ (gauss)	15000
Hysteresis Loss at saturation W_h (erg/cm^3/cycle)	240
Residual B_r (gauss)	5500
Coersive Force H_c (oersted)	0.19
Specific Resistance ρ ($\mu\Omega\cdot$cm)	104

In general, the high frequency resistance of ferromagnetic material is related to its magnetic character and A.C. by D.C. resistance ratio for straight conductors is given approximately by Zenneck's equation

$$R_\omega/R_0=0.277+0.997\pi d\sqrt{\frac{\mu r\cdot f}{4\rho}},$$

in which d is the diameter of the wire in cm, f the frequency μr the intrinsic permeability and ρ the specific resistance in e.m.u. If the high frequency

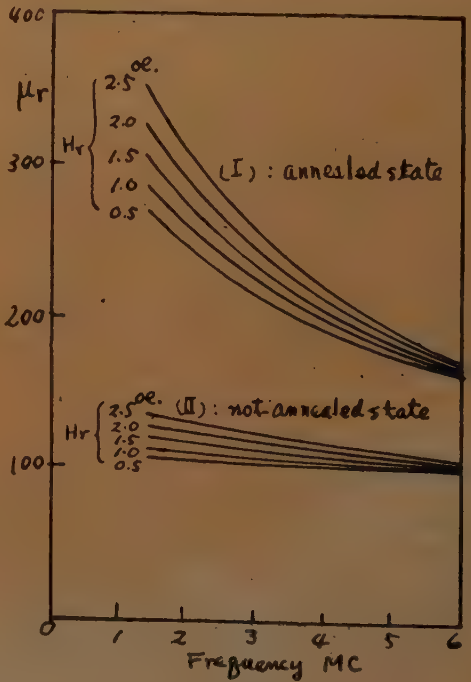

Fig. 1. Intrinsic permeability *vs* frequency curve of 45% Ni-permalloy.

resistance R_ω of ferromagnetic material is known, its intrinsic permeability μ_r can be calculated from this equation.

Substitution method was used in determining the resistance of specimen at given frequency by comparing it with the resistances of a set of standards made of 0.02 cm dia. manganin wires. The test specimen is 0.03 cm dia., 4 cm in length and was placed in a straight glass tube which was sealed in at both ends with wax.

The results are shown in Fig. 1. H_r is circular magnetic field strength given by equation $H_r=\frac{0.4i_e}{d}$ in which i_e is the effective value of electric current in ampere. In this figure, the permeability of Group II (not-annealed specimen) is comparatively constant for the variation of frequency and magnetic field, but that of Group I (annealed at 1000°C,/h_r in H_2 gas) decreases rapidly with increasing frequency and decreasing magnetic field. Dannatt's results that the permeability of material at high frequency is independent of magnetic field strength are doubtful. Initial permeability in zero field also seems somewhat to decrease with increasing frequency. Because the intrinsic permeability of permalloy varies not only in the dependence on frequency and magnetic field but also in its absolute value by heat treatment, it is predicted that it will vary with additional external strain. Fig. 2 shows these results.

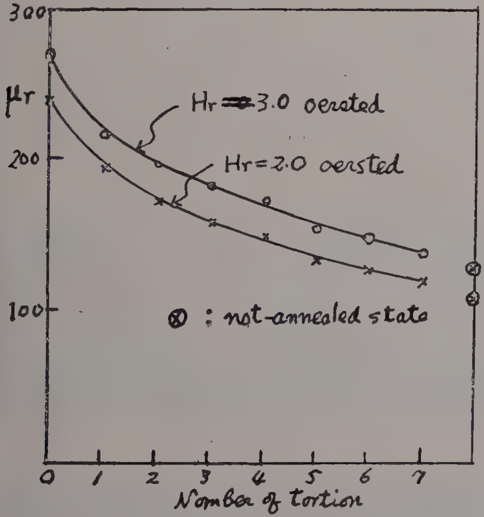

Fig. 2. Effect of strain on the intrinsic permeability of 45% Ni-permalloy at 3 MC.

When the wire specimen was strained by tortion after heat treatment at high temperature in H_2 gas, the permeability of strained specimen decreases with the increase of strain and gradually approaches that of not-annealed state.

These results show that heat treatment is effective for magnetic character of permalloy at high frequency as in the static field.

Dannatt concludes that the decrease of permeability with frequency above 10^5 cycles is due to varying demagnetization effects in the magnetic domain within the surface layer of the material. The more detailed studies of a wire of smaller diameter or a thin strip-single domain layer-will be required for fuller account of this conclusion.

References.

1) K. Kreierscheimer: Ann. d. Phys. **17** (1931) 293.
2) G.R. Wait, F. G. Brickwedde and E.L. Hall: Phys. Rev. **32** (1928) 967.
3) C. Dannatt: J.I.E.E. **79** (1936) 667.
4) R. Becker U. W. Döring: Ferromagnetismus (1938) 378.
5) C. Kittel: Phys. Rev. **70** (1946) 281.

J. Phys. Soc. Japan **6** (1951) 537-538.

Measurement of the Photoionization of Benzene and Ethylalcohol.

By Ryumyo Ito.
Institute for Optical Research, Tokyo University of Education.

(Received October, 17, 1951).

Photoionization by ultraviolet light has not yet been measured except a few alkali metal vapors on account of some experimental difficulties. In the previous paper¹⁾, the author reported that a Geiger photon counter is very useful for photometry in vacum u. v. region. In this note, it will be reported that a Geiger counter is also useful as a detector of photoionization.

The photoionization was detected, in this experiment, by a Geiger counter that could measure the intensity of the incident light by rotating it perpendicularly to its axis as shown in Fig. 1.

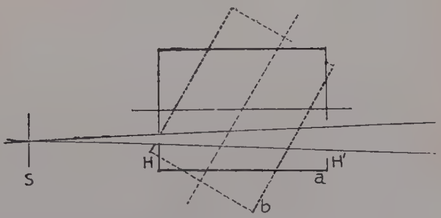

Fig. 1. Arrangement of the counter.
(a) For measurement of photoionization.
(b) For measurement of light intensity.

The photoionization is measured at the position *a* and the light intensity is measured at the position *b*. The entrance hole *H* is so small compared to the exit hole *H'* that the light that enters into the counter from *H* goes out throughly from *H'*, and there is no photoelecric emission from the inner wall of the counter. The mixture of hydrogen (about 5 mm Hg) and some organic vapor, namely benzene- or ethylalcohol-vapor (about $3-5\times10^{-2}$mm Hg) was used as the common filling for the counter, for the vacuum monochrometer and for the light source. The Werner and Lyman emission bands of hydrogen were used as the incident radiation. The intensity of the ionization and of the light were recorded on the same paper, and their ratios at various wave length are calculated. This ratios are plotted in Fig. 2. as a function of wave length of the incident radiation. For benzene, the threshold for photoionization lies at about 9.2 volt, and it agrees with the spectroscopic data for the ionization potential (9.19 volt)[2]. For ethylalcohol, however, the ionization is caused even by the light of longer wave length than that corresponding to the ionization potential (11.3 volt)[3], and it seems that some complicated processes are participating in it in this case.

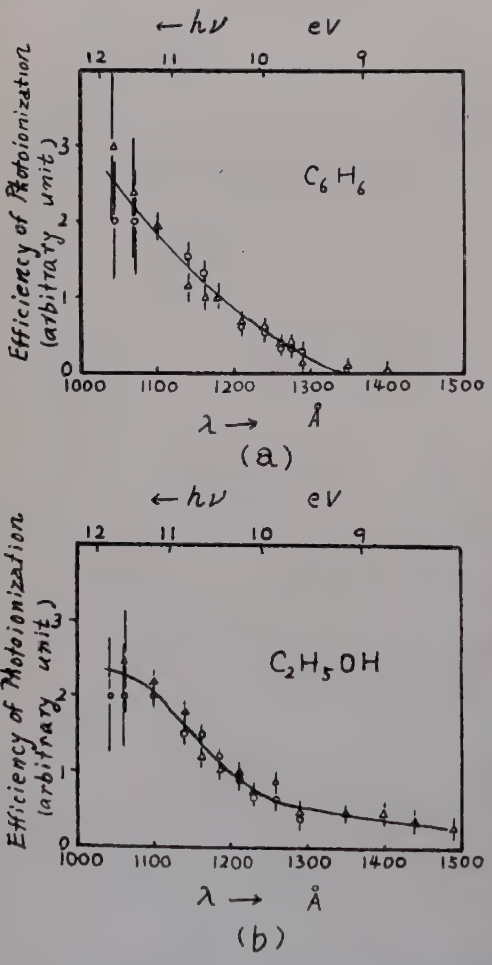

Fig. 2. Efficiency of photoionization as a function of wave length of the incident radiation. (a) benzene, (b) ethylalcohol.

The author wishes to express his sincere thanks to Prof. Y. Fujioka and Prof. Y. Tanaka for their kind suggestion and encouragements.

References.

1) Y. Fujioka and R. Ito: Hikari no Kagaku, **1** (1951) 1.
2) W. C. Price and R. W. Wood: J. Chem. Phys., **3** (1935) 439.
3) C. S. Cummings and W. Bleakney: Phys. Rev., **58** (1940) 787.

J. Phys. Soc. Japan **6** (1951) 538–539.

The Plastic Deformation of the Copper Cylinder under the Powder Pressure

By J. Nishiwaki.

Keiō University, Hiyoshi, Yokohama.

(Received October, 22, 1951).

The plastic deformation of the copper cylinder under the powder pressure prevailed in the bore of a machine gun was compared with that under the static pressure. The size of the copper cylinder used in the experiments was 8×13mm, and this was one of the common types used to measure such pressure as in the gun.

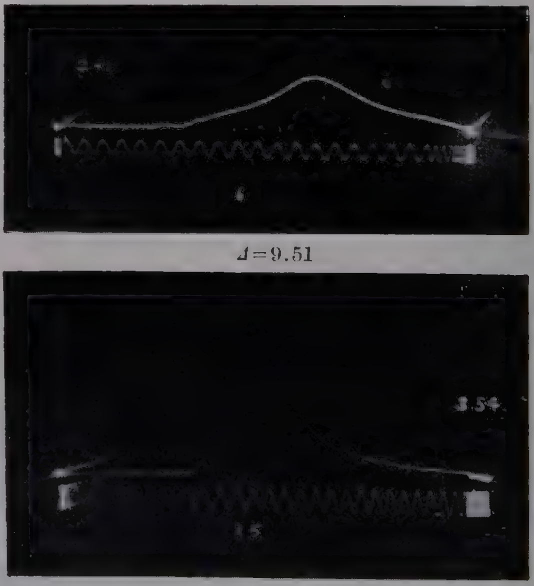

Δ=9.51

Δ=0.91

Fig. 1. (a)

The actual values of the powder pressure were evaluated from the oscillograms of it recorded by the piezo-electric indicator which consisted of a piezo-element, a direct current amplifier and a Dufour type cathode ray oscillograph. Two examples of those oscillograms are shown in Fig. 1.

The comparison was made between the both pressures, one of which was the maximum pressure P_m indicated by the piezo-indicator, and the other the value P_c given by the deformation of the cylinder from its statically calibrated curve, with regard to each density of charge Δ (ratio of the power weight to the volume of powder chamber).

The experiments were carried out in two cases A and B; in the former, the pressure acted on the rear end of the copper cylinder was recorded twice on each of eleven different values of Δ by the piezo-indicator (See Fig. 2). In the latter case, the pressure was measured five times on each of five different value of Δ, separately by either of the indicator and the cylinder.

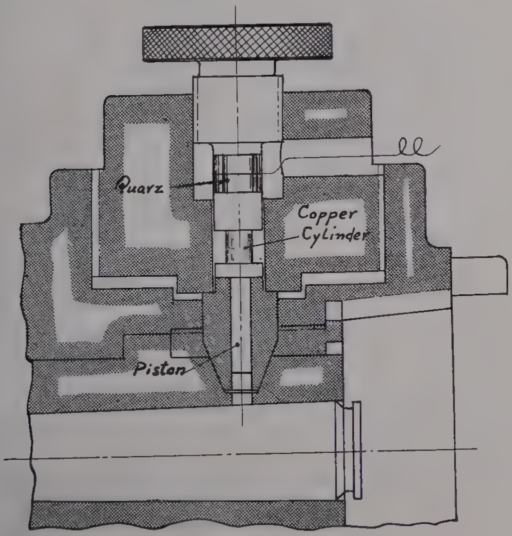

Fig. 2.

Thus, in Fig. 3, black points shows the results in the case A, blank points the results (the mean values of each five) in the case B, and the both cases indicate the same relation between P_m and P_c. As seen from this Fig., in the neighbourhood of $P_c = 30\text{kg/mm}^2$ which occurs in general in machine guns, the ratio P_m/P_c is about equal to 1.13, and this consistent with the generally adopted value 1.14 in the internal ballistics. But in the range of low values of P_c, P_m becomes smaller than P_c. Here, the copper cylinder is more compressed under the power pressure which increases rather slowly in the gun because of the small value of Δ, than under the static pressure though the maximum values of the both are equal together.

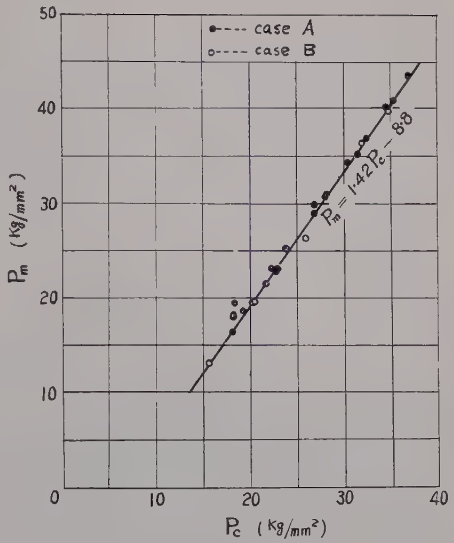

Fig. 3.

The similar phenomena has been observed by the author in the penetration test of the cylindrical bullet through the copper plate. Its deformation is most remarkable when the bullet has the critical speed just enough to be stopped by the plate itself. When the speed is more or less than this critical one, either the plate is only punched out or it repulses the bullet, and deforms little in both cases.

Hence the copper cylinder seems to have the optimum speed to deform.

The author wishes to express his thanks to Prof. M. Hirata for his advice and suggestion.

J. PHYS. SOC. JAPAN **6** (1951) 539–540.

Spark Photography employing the Mach Switch.

By J. NISHIWAKI.

Keiō University, Hiyoshi, Yokohama.

(Received October 22, 1951).

The circuit of the Mach Switch[1] was employed in an altered form as shown in Fig. 1. Instead of the spark discharges between the gaps $f_1, f_2, \ldots\ldots$, those between the gaps $F_1, F_2, \ldots\ldots$, are used as the light sources for the photographs, and F_0 connected to them in series is used for the measurement of each time intervals between the discharges of $F_1, F_2, \ldots\ldots$. Each of $F_1, F_2, \ldots\ldots$ discharges almost simultaneously with the corresponding one of $f_1, f_2, \ldots\ldots$, and F_0 discharges simultaneously with any

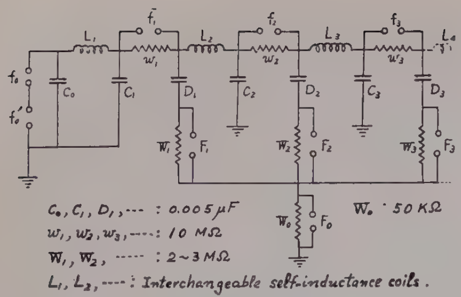

Fig. 1.

of F_1, F_2,...... Hence the gap distances of f_1, f_2, ...can be adjusted with no consideration of their own spark intensity, and the positions and distances of F_1, F_2,......may be adjusted even when the high voltage is imposed on the circuit because they are connected to the earth. The actual gaps employed as light sources are shown in Fig. 2 where the six gaps are in use, (the number of them were increased later to ten).

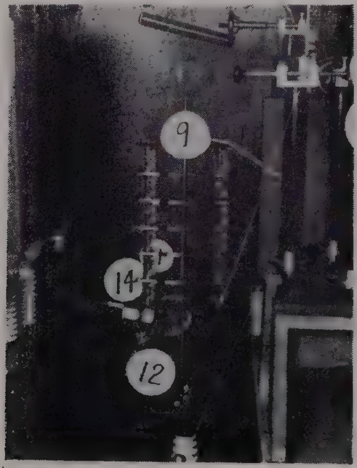

Fig. 2.

To start the circuit in connection with the phenomena, the author used the photo-electric method as shown in Fig. 3. P is the flying object to be photographed, M an induction coil and f_0 the starting spark gap which is the same as the marked one with the same letter in Fig. 1.

In order to have a large field of view the convex mirror (dia. = 58cm, focal length = 350cm) was used instead of a condenser.

To measure the time interval, a slit was illuminated from behind by F_0 and photographed by the rotating camera, the film speed of which was 38.2 m/sec. Fig. 4 shows the images of the slit and from each distance between them the time intervals can be calculated.

The results deduced from one series of the photographs which were obtained by this method with regard to the penetration of a steel rifle bullet (dia. = 6.5mm, radius of the curvature of its ogive = 6 × dia.) through a 12mm aluminium plate are shown in Fig. 5, as an example. Here, X is the depth of penetration, V the speed of the bullet and R the total resistance offered by the plate which can be seen to have the max. resistance value of about 1700 kg to this bullet.

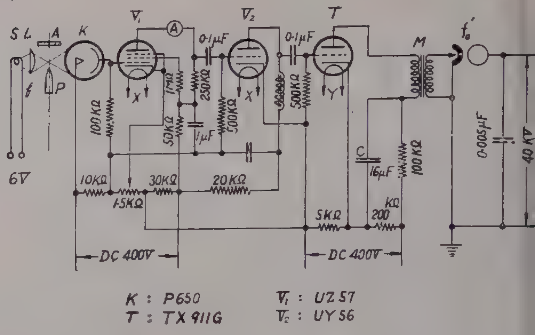

Fig. 3.

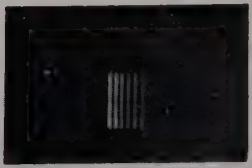

Fig. 4.

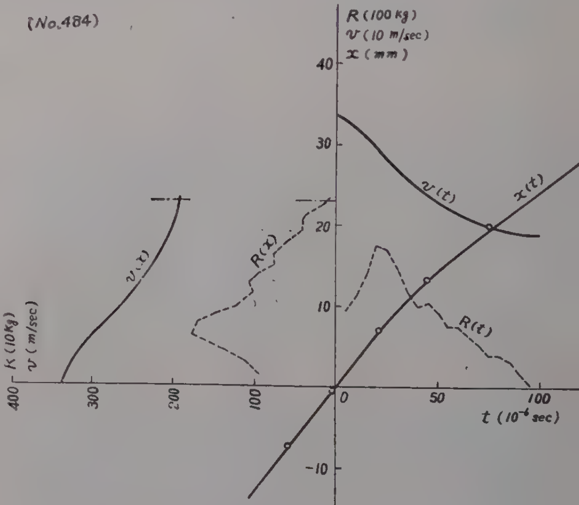

Fig. 5.

The author expresses his sincere thanks to Dr. M. Hirata for his supervision.

References.

1) C. Cranz u. H. Schardin; ZS. f. Phys. **56** (1929) 147.

J. PHYS. SOC. JAPAN **6** (1951) 541–542.

Morphological Anomaly of the Crystals of Mercury Fulminate.

By Masaji SEKIGUCHI.

Physics Department, Faculty of Engineering, Niigata University, Nagaoka.

(Received October 23, 1951)

The morphological anomaly of the crystals of mercury fulminate $Hg(CNO)_2 \frac{1}{2} H_2O$ was newly discovered as the result of the microscopic as well as *X*-ray investigations.

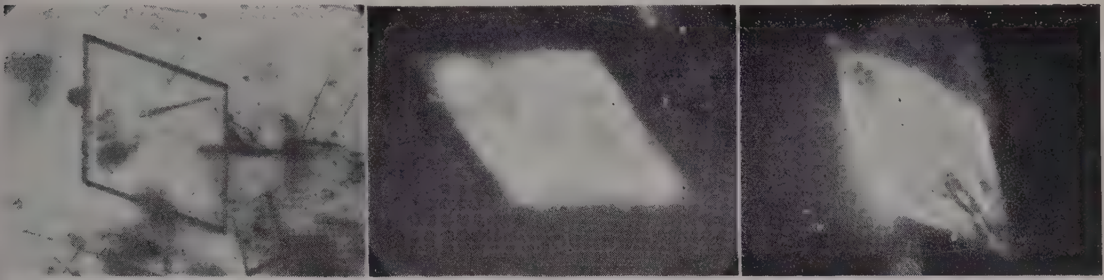

Fig. 1. (a) is the photograph of the crystal recrystallized from the solution containing ammonium hydroxide. (b) and (c) are the photographs of those grown in a usual way. All the three indicated have different angles.

The crystals were precipitated from the solution of various percentages of mercury, nitric acid and ethyl alcohol. In most cases they were thin plates, rhombic in shape (Fig. 1). The smaller interior angle θ of the rhomb was observed under the microscope, and was found to vary widely from 25° to 70°, according to the composition of the mother liquor. The correlation between angles of the rhomb and the composition of the solution is shown in Fig. 2, each circle corresponding to the θ of each crystal grown from the solution, whose compositions are

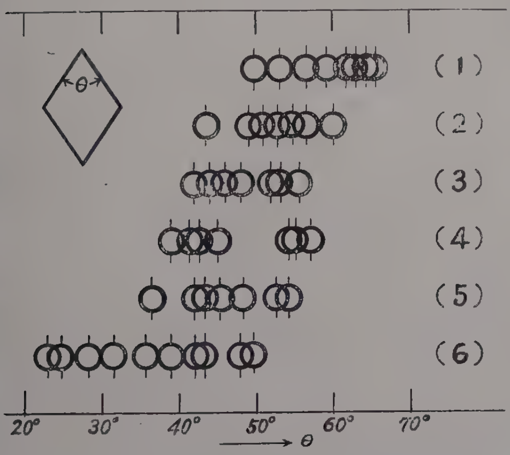

Fig. 2. The distributions of the values of the angles were shown. The right side marks (i); i=1, 2, 3, 4, 5, 6 correspond to the numbers of the solution shown in the Table I.

Table I. % of substances in the synthetic reaction. These reactions were performed at the room temperature, nearly 30°C, and the total volume of solutions was about 300cc.

Hg	HNO_3	C_2H_5OH	H_2O	Number of the solution
6.2	35.1	38.4	20.3	(1)
6.5	36.6	34.9	22.0	(2)
5.8	35.8	38.0	20.9	(3)
4.6	36.8	37.4	21.0	(4)
3.2	25.0	25.1	46.8	(5)

* The sample (6) produced a small amount of crystals which show the rhombic pyramidal forms.

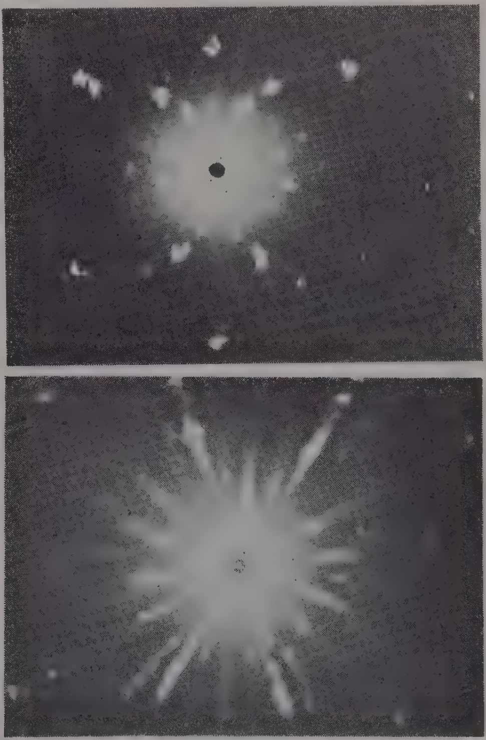

Fig. 3. The Laue patterns of the recrystallized samples from the solution containing ammonium hydroxide. The patterns show the orthorhomic symmetry.

listed in Table 1. As is easily seen from the figure, even angles of the crystals grown from the same mother liquor are not the same at all and show apparent statistical distribution.

When the crystal was again recrystallized from aqueous solution, containing small amount of NH_4OH, large and transparent crystals similar in shape as in the former case were obtained. According to the *X*-ray investigations, this recrystallized crystal belongs to the orthorhombic system and its Laue photograh was taken by means of the monochromatic copper K_α radiation. (Fig. 3) The large streaks often observed seem to suggest the variant structure of the crystal lattice, which might be closely related to the variant rhombic angles above mentioned.

Further details are now in the course of investigations.

The author expresses his gratitude to Dr. Y. Kakiuchi (Institute of Science and Technology, University of Tokyo) for his interest and discussions and also to Dr. J. Endoo (Niigata University) for his kind advices.

References.

1) M. Sekiguchi; Kagaku (Science), **20** (1650), 236.

2) 3) M. Sekiguchi; Reported at the Annual Meeting of the Phys. Soc. Japan, held at Tokyo, on 1st April 1951.

CONTENTS

(Vol. 6)

No. 1

Kōzō ISHIGURO: Numerical Tables for the Phase and Intensity Measurements of Metallic Film. I ... 1
Kōzō ISHIGURO: Numerical Tables for the Phase and Intensity Measurements of Metallic Film. II ... 5
Syû ONO: Statistical Mechanics of Adsorption from Multicomponent Systems I ... 10
Tetsuya ARIZUMI and Shin-ichiro NARITA: On the Activation of the Oxide Coated Cathode ... 15
Gen SHIRANE and Katsuo SATO: Effects of Mechanical Pressures on the Dielectric Properties of Polycrystalline Barium-Strontium Titanate ... 20
Takehiko OGUCHI: Statistics of the Three-Dimensional Ferromagnet (II) ... 27
Takehiko OGUCHI: Statistics of the Three-Dimensional Ferromagnet (III) ... 31
Shoichiro NOMURA and Shozo SAWADA: Dielectric and Thermal Properties of Barium-lead Titanates ... 36
Akira ISIHARA and Tsuyoshi HAYASHIDA: Theory of High Polymer Solutions, I. Second Virial Coefficient for Rigid Ovaloids Model ... 40
Akira ISHIHARA and Tsuyoshi HAYASHIDA: Theory of High Polymer Solutions, II. Special Forms of Second Osmotic Coefficient ... 46
Osamu TUKIZI: The Electric Susceptibility of Water Drop due to Ionic Polarization ... 51
Hisao MIYAZAWA and Jun-ichi OKADA: On the Breakdown of Alumina at Higher Temperature ... 55
Seijiro MAEDA: On the Magnetic After Effect due to the Irreversible Displacement of Domain Boundary (II) ... 60

No. 2

Kōzō ISHIGURO and Goro KUWAHARA. Determination of the Optical Constants of Ag Films from the Measurements of Intensity and Phase Change I ... 71
Kozo ISHIGURO and Goro KUWAHARA: Determination of the Optical Constants of Ag Films From the Measurements of Intensity and Phase Change II ... 76
Takeo YOKOBORI: Delayed Fracture in Creep of Copper ... 78
Takeo YOKOBORI: Fatigue Fracture of Steel ... 81
Ken-ichi KUSUKAWA: The Foundation of the Quantisation of Turbulence ... 86
Hirosi KANAZAKI: On the Recovery Process of Cold Worked Metals ... 90
Goro FUJIOKA, Isao KITA and Osamu MINAKAWA: On the Analysis of Quenching Circuit for Slow Counters ... 95
Isao KITA: On the Discharge Mechanism of Slow Counter ... 99
Goro FUJIOKA, Isao KITA and Osamu MINAKAWA: On the Temperature Effect of Geiger-Muller Counter ... 103
Yoichi UCHIDA, Masayasu UETA and Yoshio NAKAI: Studies on the K Absorption Band in the Colored Rock Salt Crystal ... 107
Tetsuya ARIZUMI and Leona ESAKI: On the Secondary Electron Emission from the Thoria Coated Cathode and the Thin Film Deposited by Evaporation from the Cathode. 113
Tetsuya ARIZUMI and Shin-ichiro NARITA: On the Schottky Effect of the Oxide Coated Cathode ... 118

No. 3

Shoichi MATSUDA: On the Superlattice Formation in Binary Alloys of Body Centred Cubic Type ... 131
Yoshiro KAINUMA: Structure of Thin Metallic Films Formed by Evaporation on Molybdenite ... 135
Atsuyoshi OKAZAKI: Faraday Effect of Strong Electrolytes in Aqueous Solution IX. The Temperature Dependence of the Molecular Rotation Constants, I ... 138
Motoharu KIMURA: On the Temperature Effects of Spurious Counts in Geiger-Muller Counters ... 141
Gunji SHINODA and Teruichi TOMURA: Improved Counting Rate Meter for X-Ray Measurement ... 148
Yukiyasu ODA, Jumpei SANADA and Shotaro YAMABE: Angular Distribution of 3.1 Mev

Neutrons Scattered by Proton........ 153

Tetsuo WAKATSUKI and Kenzo SUGIMOTO: On the Scattering of Fast-Neutrons from Li-D Reactions........ 157

Ken-ichi KUSUKAWA: On the Theory of Shock Waves Produced in the Case, that by a Rigid Wedge Moving through the Elastic Medium with Supersonic Velocities........ 163

Ken-ichi KUSUKAWA: On the Theory of Shock Wave Produced by a Rigid Cone Moves through the Elastic Medium with Super-sonic Velocities........ 166

Mitsutoshi KAWAGUCHI: Application of the M^2-expansion Method to the Compressible Flow past an Elliptic Cylinder........ 168

Hidenori HASHIMOTO: On the Subsonic Flow of a Compressible Fluid past a Rankine Ovoid........ 175

Hisashi HORIE: Excitation of Atoms by Electron Collision, I........ 179

Taro KIHARA: Determination of Intermolecular Forces from the Equation of State of Gases, II........ 184

Ryumyo ITO: Pressure Dependence of Sensibility of Photoelectron Counters........ 188

No. 4

Hisashi HORIE: Excitation of Atoms by Electron Collision. II........ 215

Takao SATO: Some Properties of the Ni-Mn Alloys of Intermediate Composition (I)........ 223

Harero IWAMURA and Nobuo SHIOTA: On Sub-boundary Structure of Aluminium........ 227

Shigeki SUWA: Anomalous Hyperfine Structure in the Spectrum of Al. II........ 231

Akio KOBAYASHI and Saburo FURUYA: Reactions of Barium Film with Oxygen, I........ 238

Takechiyo INOUYE: On the Surface Layer of Liquid Argon........ 243

Osamu SAITO: On Some Exact Solutions of the Two-Dimentional Steady Flow of Compressible Fluid........ 248

Eiichi FUKADA: On the Relation between Creep and Vibrational Loss of Polymethylmetacrylate........ 254

Zenya FUNATOGAWA: On the Magneto-Thermoelectric Power of Iron Crystal at High Temperature........ 256

Tohru KAMEI: Mechanical Barkhausen Effect........ 260

Gen SHIRANE and Sadao HOSHINO: On the Phase Transition in Lead Titanate........ 265

Akira HARASIMA: On the Lambda Point of He^4-He^3 Mixtures........ 271

Gen SHIRANE and Kazuo SUZUKI: On the Phase Transition in Barium-lead Titanate (I)........ 274

No. 5

Seizaburo KAGEYAMA: A Note on the Intensities of the Internal Conversion Lines of the Three Intense γ-rays of RaB........ 285

Taro KIHARA: The Second Virial Coefficient of Non-Spherical Molecules........ 289

Nobuhiko SAITÔ: The Effect of the Brownian Motion on the Viscosity of Solutions of Macromolecules, I. Ellipsoid of Revolution........ 297

Nobuhiko SAITÔ: The Effect of the Brownian Motion on the Viscosity of Solutions of Macromolecules, II. Rigid Chain Molecules........ 302

Nobuhiko SAITÔ and Yuichi IKEDA: The Light Scattering by Non-Spherical Particles in Solutions........ 305

Terutosi MURAKAMI, Syû ONO, Mikio TAMURA and Michio KURATA: On the Theory of Surface Tension of Regular Solution........ 309

Yoshinobu KAKIUCHI: A Statistical Theory of Molecular Rotation in Normal Solid Hydrocarbons and Alcohols........ 313

Yoshinobu KAKIUCHI, Hachiro KOMATSU and Susumu KYOYA: Proton Conduction through Solid Alcohols due to Molecular Rotation........ 321

Gen SHIRANE and Akitsu TAKEDA: On the Phase Transition in Barium-lead Titanate (II)........ 329

Etsuro SAWAGUCHI, Gen SHIRANE and Yutaka TAKAGI: Phase Transition in Lead Zirconate........ 333

Kazuo SUZUKI: On the Phase Transition in Barium-lead Titanate........ 340

Ryuji ABE: A Study of Corrosion-Process of Iron by Means of Electron Diffraction........ 345

Riitsu TAKAGI: Electron Microscope and Diffraction Studies of Chromic Oxides........ 350

Takuzo SHINDO: Space Charge Effect in the Oxide Cathode Layer........ 352

Masao TOMURA: Creep Phenomena of Selenium Rectifiers........ 357

Tomoyosi KAWADA: On the Plastic Deformation of Zinc Bicrystal, I........ 363

Noboru TOKITA and Heiji KAWAI: Young's Modulus and Internal Friction of Polyvinylalcohol 367
Akio KOBAYASHI and Hiroo HINO: Effects of Firing Temperature on the Dielectric Properties of Barium-Titanate Ceramics 371
Jien NISHIWAKI: Resistance to the Penetration of a Bullet through an Aluminium Plate. 374
Koichi SHIMODA: Mode Conversion Losses in a TE_{01} Type Cavity Resonator with Tilted End-Plate 378
Hidenori HASIMOTO: On the Asymptotic Behaviour of Three-dimensional Compressible Fluid Flow at a Great Distance from a Body, I. 383
Hiroshi SATO: Experimental Study of the Spectrum of Isotropic Turbulence, I. 387
Eiichi INOUE: Some Remarks on the Dynamical and Thermal Structure of a Heated Turbulent Fluid 392

No. 6

Ei-ichi FUKADA: The Vibrational Properties of Wood. II 417
Eiji HIRAHARA: The Physical Properties of Cuprous Sulfides-Semiconductors 422
Eiji HIRAHARA: The Electrical Conductivity and Isothermal Hall Effect in Cuprous Sulfide, Semi-Conductor 428
Kozo KOMATSU and Takeo NAGAMIYA: Theory of Specific Heat of Graphite........ 438
Seiichi SUEOKA and Masachiyo SATO: On the Stark Effect of Helium in Strong Electric Field (II)........ 444
M. Z. V. KRZYWOBLOCKI: On the Transformation of Chaplygin's Equation Into Fuchs-Frobenius Normal Form........ 452
Hiroshi KANZAKI: On the Plastic Deformation of Copper Single Crystals.
Part 1. Two Stages in the Progress of Deformation 454
Hiroshi KANZAKI: On the Plastic Deformation of Copper Single Crystals.
Part 2. Recovery Process and Mean Length of Dislocations........ 456
Nobuo INOUE: Application of the Theory of Supersonic Flow to the Two-dimentional Isostatical problem in the Theory of Plasticity........ 460
Itaru NONAKA, Shinpachi HIRASAWA and Kazushige TSUTSUMI: A New Method of Measuring the Ion Current of Mass Spectrometers 466
Akiya OOKAWA: Crystallization and Melting of Linear High Polymers as Rate Processes 473
Jitsuo SHIMAZU: Emission and Crystal Size of Oxide-Coated Cathodes........ 479
Tomoyosi KAWADA: On the Plastic Deformation of Zinc Bicrystal II........ 485
Ryosuke YOKOTA: On the Structure of Silicate Classes........ 489
Seijiro MAEDA: On the Magnetic After-Effect due to the Irreversible Displacement of Domain Boundary III........ 494
Takehiko OGUCHI: The Short Range Orders in Cu_3Au 499
Norio Kato: Accurate Measurement of Lattice Constant by Means of Electron Diffraction. Lattice Constant of KCl Referred to Au 502
Gunji SHINODA and Yoshitsugu AMANO: Mechanism of Precipitation of α from β in 60:40 Brass 508
Koichi SHIMODA and Tetsuji NISHIKAWA: The Hyperfine Structure of Sodium by a Microwave Absorption Method........ 512
Koichi SHIMODA and Tetsuji NISHIKAWA: A Zeeman Modulation Microwave Spectrograph of High Sensitivity 516

SHORT NOTES

No. 1

Hiroshi SATO and Hisao YAMAMOTO: The Behaviours of Fe-Al, Fe-Si and Fe-Al-Si Alloys Considered from the Standpoint of Ferromagnetic Superlattice........ 65
Bunsaku ARAKATSU, Masateru SONODA, Yoshiaki UEMURA, Shinjiro YASUMI and Yoshio SAJI: The Photo-disintegration of Be by the High Energy γ-rays........ 66
Hiroshi KUBOTA: OnSensitiv e Color 67
Goro MIYAMOTO: On the Spiral Orbit Spectrometer with Two Converging Circles........ 68

No. 2

Ryuzo UEDA and Takeo ICHINOKAWA: Effect of Stress on Domain Structure of Tungsten Trioxide WO_3 122
Hideo NAGASU: Statistical Features in Static Friction 123
Kin-ichi NOGA: Thermo-electromotive Force of BaO and (Ba-Sr)O 124
Takao SATO: Notes on the Thermoelectric Properties of Bismuth 125
Tasaburô YAMAGUTI and Minoru NISHINO: A New Apparatus for Electric Arc Weldings 127
Gen SHIRANE and Akitsu TAKEDA: Volume Change at Three Transitions in $BaTiO_3$ Cermamics 128
Makoto HIRABAYASHI: Existence of the Superlattice $CuAu_3$ 129

No. 3

Kikusaburo OSADA: The Ultraviolet Absorption Spectra of Glasses 191
Shozo SAWADA and Shoichiro NOMURA: On the Ferroelectric Behaviors of Sodium Vanadate 192
Jien NISHIWAKI: The Height of the Water Column Produced by the Falling Ball 193
Chiyoe YAMANAKA and Tokuo SUITA: Current Noise and Dielectric Breakdown in Alkali-halide Crystals 194
Shoten OKA and Osamu NAKADA: On the Dielectric Loss in Polydisperse Polar Polymers 195
Tihiro OHKAWA: A Proposal on the Measurement of the Recoil Spectrum using Gas Source 197
Seiichiro KUMAGAI and Ituro KIMURA: Effect of Turbulence on Flame Propagation in Gases 197
Tosio SAKURAI: On the Transformation of Long Chain Acid Amides 199
Chisato OKAZAKI and Tokuo SUITA: Electric Conduction in Ionic Crystals (Part I) 200
Nobuhiko SAITÔ: An Interpretation of the Dielectric Loss due to the Rotation of Dipoles 201
Minoru ODA and Tatuo TAKAKURA: A Study on the Solar Noise at 3300 m.c. 202
Tokuo SUITA: Dielectric Breakdown in Mixed Crystals of KCl and AgCl 202
Riitsu TAKAGI: An Electron Microscope and Diffraction Study of Metallic Smoke 204
Y. WATASE, S. MIYAKE, K. SUGA and O. KUSUMOTO: A High Pressure Cloud Chamber Observation of Cosmic Ray at 2740 m Elevation 204
Ken-ichi KUSUKAWA: Discussion of the Spectrum of Turbulence 206
Shoji KOJIMA and Kiyoe KATO: The Noise of Decaying Electrets 207
Gen SHIRANE, Etsuro SAWAGUCHI and Yutaka TAKAGI: Dielectric Properties of Lead Zirconate 208
Ryuzo UEDA: X-ray Study on Phase Transition of Lead Zirconate, $PbZrO_3$ 209
Haruhiko MORINAGA: The Construction of a Small Linear Accelerator 210
Yasuo KANAI: Current Amplification by Silicon p-n Junction 211
Hiroshi WATANABE: The Temperature Dependency of Magnetization of Ferrites on the Basic of the Theory of Ferromagnetism 212

No. 4

Yoshinobu KAKIUCHI: On the Electret 278
Ken'iti HIGASI and Yasutomo OZAWA: On High Frequency Power Loss of Dielectrics 280
Seiichi SUEOKA: On the Shape of Radio-frequency Spectrum 281
Hazimu KAWAMURA and Masami ONUKI; On the Noise of Pre-Breakdown Current 283

No. 5.

Mituso ONO: On the Deviation from the Ohm's Law at the Anode Surface of the Cuprous Oxide Rectifiers 397
Seitaro YAMAGUCHI and Masaomi TAKAHATA: On the Masses of Charged Particles of the Cosmic Radiation in Nuclear Emulsions 397
Masafumi INOKI: An Application of Proportional Counters to Mass Determination (I) ... 398
Hidenori HASIMOTO: Note on Rayleigh's Problem for a Bent Flat Plate 400
Hirobumi OURA: On the Band-System of Neutral OD 401
Yuzuru WATASE, Minoru ODA, Tadayoshi KUBOZOE and Shigeru HIGASHI: A Hodoscope Study on the Penetrating Shower 402
Yuzuru WATASE, Minoru ODA, Shigeru HIGASHI and Tadayoshi KUBOZOE: A Study on the Extensive Air Shower 403
Takeo YOKOBORI: On the Rate of the Nucleation in the Recrystallization 404

Hiroshi KUBOTA: On the Color of Chromatic Polarization........ 405
Kenzo TANAKA and Hatsujiro HASHIMOTO: On the Anomalous Structures of Zinc Oxide... 406
Hiroshi FUJITA and Akira KISHIMOTO: A Method for Determining the Concentration Dependence of Diffusion Coefficient........ 408
Mitsuo SAKAI and Yozo NOGAMI: On the Form of Pole Pieces used in New Spiral Orbit Spectrometer........ 409
Tsugihiko SATO and Syû ONO: A Note on the Hole Theory of Liquid........ 410
Nobuhiro YAMAMURO: Isotope Separation by Radiofrequency Electric Field........ 411
Chikara HAYASHI: A New Method of Trapping Oil Vapour........ 413
Chikara HAYASHI: Use of Phosphorous Pentoxide as a Dehydrating Agent in High Vacuum Technique........ 414
Kineo TSUKADA The Ion Source of Electron Oscillation Type........ 415

No. 6

Jiro YAMAGUCHI, Saburo NAGATA and Yuichi MATSUO: An Electron Diffraction Study on Selenium Rectifiers........ 521
Hideji SUZUKI: On the Grain Boundary Migration Induced by Temperature Gradient...... 522
Saburo NAGATA and Kosuke AGATA: On the Crystal Structure of Cadmium Selenide of Selenium Rectifier........ 523
Akira SUGIYAMA: Note on the Kinetic Energy of the Bloch Wall........ 524
Masatami TAKEDA and Eiiti TURUTA: Temperature Change of Intrinsic Viscosity of Polyvinyl Chloride........ 525
Ryoitiro SATO: Surface Oxidation of Zincblende Cleavage Face in the Roasting Atmosphere........ 527
Ryoitiro SATO: Twin Formation of Zincblende through Oxidation-Reduction Process...... 528
Mitsuo SAKAI: Sur le Spectrometre a Orbites Sirales Spans Fer........ 529
Makoto OSAWA and Ichiro SUGIURA: On the Distribution of Internal Stresses of Permalloy Subjected to Field Cooling........ 530
Haruji ISHIKAWA: On the Transformation of Tin at Low Temperature........ 531
Junkichi NAKAI and Shogo NAKAMURA: On the Effect of Electrolytic Treatment of Ni-Sleeve on Electron Emission........ 532
Ryuma KAWAMURA: On the Mach Reflection of a Shock Wave........ 535
Yoshinobu SEKI: A New Type of Striation Observed in an Electronmicrograph........ 534
Yasaku WADA and Sotoshi SHIMBO: Correlation between Ultrasonic and Infrared Absorption in Liquids........ 535
Yoshiro HORI: The Intrinsic Permeability of Permalloy at High Frequency........ 536
Ryumyo ITO: Measurements of the Photoionization of Benzene and Ethylalcohol........ 537
Jien NISHIWAKI: The Plastic Deformation of the Copper Cylinder under the Powder Pressure........ 538
Jien NISHIWAKI: Spark Photography Employing the Mach Switch........ 539
Masaji SEKIGUCHI: Morphological Anomaly of the Crystals of Mercury Fulminat........ 541

AUTHOR INDEX TO Vol. 6.

Page

ABE Ryuji: A Study of Corrosion-Process of Iron by Means of Electron Diffraction 435
AGATA Kosuke;
N. NAGATA and ———: On the Crystal Structure of Cadmium Selenide of Selenium Retifier...... 623
AMANO Yoshitsugu;
G. SHINODA and : Mechanism of Precipitation of α from β in 60:40 Brass... 508
ARAKATSU Bunsaku;
M. SONODA, ——— Y. UEMURA, S. YASUMI and Y. SAJI: The Photodisintegration of Be by the High Energy γ-rays...... 66
ARIZUMI Tetsuya;
S. NARITA and ———: On the Activation of the Oxide Coated Cathode 15
and L. ESAKI: On the Secondary Electron Emission from the Thoria Coated Cathode and the Thin Film Deposited by Evaporation from Cathode 113
and S. NARITA: On the Schottky Effect of the Oxide Coated Cathode 118
FUJIOKA Goro;
I. KITA, ——— and O. MINAKAWA: On the Analysis of Quenching Circuit for Slow Counters...... 95
———, I. KITA, and O. MINAKAWA: On the Temperature Effect of Geiger-Muller Counter...... 103
FUJITA Hiroshi;
A. KISHIMOTO, and : A Method for Determining the Concentration Dependence of Diffusion Coefficient...... 408
FUKADA Eiichi: On the Relation between Creep and Vibrational Loss of Polymethylmetacrylate...... 254
: The Vibrational Properties of Wood, II...... 417
FUNATOGAWA Zenya: On the Magneto-Thermoelectric Power of Iron Crystal at High Temperature 256
HIRASAWA Shinpachi;
I. NONAKA, ——— and K. TSUTSUMI: A New Method of Measuring the Ion Current of Mass Spectrometers...... 466
HARASIMA Akira: On the Lambda Point of He⁴-He³ Mixtures 271
HASIGUTI Ryukiti: Erraa; On the Theory of Recrystallization of Cold-Worked Metals... 416
HASIMOTO Hidenori: On the Subsonic Flow of a Compressible Fluid Past a Rankine Ovoid 175
———: On the Asymptotic Behaviour of Three-dimensional Compressible Fluid Flow at a Great Distance from a Body, I 383
: Note on Rayleygh's Problem for a Bent Flat Plate 400
HASHIMOTO Hatsujiro
K. TANAKA and ———: On the Anomalous Structures of Zinc Oxide...... 406
HAYASHI Chikara: A New Method of Trapping Oil Vapour 413
———: Use of Phosphorous Pentoxide as a Dehydrating Agent in High Vacuum Technique 413
HAYASHIDA Tsuyoshi;
A. ISHIHARA and ———: Theory of High Polymer Solutions, I. General Form of Second Osmotic Coefficient 414
——— and A. ISHIHARA: Theory of High Polymer Solutions, II. Special form of Second Osmotic Coefficient...... 40
HIGASI Kenichi;
Y. OZAWA and ———: On High Frequency Power Loss of Dielectrics 280
HIGASHI Shigeru;
Y. WATASE, M. ODA, T. KUBOZOE and ———: A. Hodoscope Study on the Penetrating Shower 402
Y. WATASE, M. ODA, ———, T. KUBOZOE: A Study on the Extensive Air Shower 403
HINO Hiroo;

A. KOBAYASHI and ———: Effect of Firing Temperature on the Dielectric Properties of Barium-Titanate Ceramics 371
HIRABAYASHI Makoto: Existence of the Superlattice $CuAu_3$........ 129
HIRAHARA Eiji: The Physical Properties of Cuprous Sulfides-Semiconductors 422
———: The Electrical Conductivity and Isothermal Hall Effect in Cuprous Sulfide, Semi-Conductor 428
HORI Yoshiro: The Intrinsic Permeability of Permalloy at High Frequency........ 535
HORIE Hisashi: Excitation of Atoms by Electron Collision, I........ 179
———: Excitation of Atoms by Electron Collision. II........ 215
HOSHINO Sadao;
G. SHIRANE and ———: On the Phase Transition in Lead Titanate 255
ICHINOKAWA Takeo;
— and R. UEDA: Effect of Stress on Domain Structure of Tungstein Trioxide Wo ... 122
IKEDA Yuichi;
N. SATO and ———: The Light Scattering by Non-Spherical Particles in Solutions 305
INOKI Masafumi: An Application of Proportional Counters to Mass Determination 398
INOUE Eiichi: Some Remarks on the Dynamical and Thermal Structure of a Heated Turbulent Fluid 392
INOUE Nobuo: Appllication of the Theory of Supersonic Flow to the Two-dimensional Isostatical Problem in the Theory of Plasticity 460
INOUYE Takechiyo: On the Surface Layer of Liquid Argon 243
ISHIGURO Kozo: Numerical Tables for the Phase and Intensity Measurements of Metallic Film. I........ 1
———: Numerical Tables for the Phase and Intensity Measurements of Metallic Fillm II. 5
——— and G. KUWAHARA: Determination of the Optical Constants of Ag Films from the Measurements of Intensity and Phase Change I 71
——— and G. KUWAHARA: Determination of the Optical Constants of Ag Films from the Measurements of Intensity and Phase Change II 76
——— Errata: Numerical Tables for the Phase and Intensity Measurements of Metallic Films 416
ISHIKAWA Haruji: On the Transformation of Tin at Low Temperature 531
ISHIHARA Akira;
— and T. HAYASHIDA: Theory of High Polymer Solutions, I. Second Virial Coefficient for Rigid Ovaloids Model........ 40
——— and T. HAYASHIDA: Theory of High Polymer Solutions, II, Special Forms of Second Osmotic Coefficient 46
ITO Ryumyo: Pressure Dependence of Sensibility of Photoelectron Counters 188
———: Measurements of the Photoionization of Benzene and Ethylalcohol... 537
IWAMURA Harero;
N. SHIOTA and ———: On Sub-boundary Structure of Aluminium 227
KAGEYAMA Seizaburo: A Note on the Intensities of the Internal Conversion Lines of the Three Intense γ-rays of RaB........ 285
KAKIUCHI Yoshinobu: On the Electret 278
———: A Statistical Theory of Molecular Rotation in Normal Solid Hydrocarbons and Alcohols 313
———, H. KOMATSU and S. KYOYA: Proton Conduction through Solid Alcohols due to Molecular Rotation........ 321
KAINUMA Yoshiro: Structure of Thin Metallic Films Formed by Evaporation on Molybdenite 135
KAMEI Tohru: Mechanical Barkhausen Effect 260
KANAI Yasuo: Current Amplification by Silicon p-n Junction 211
KANZAKI Hirosi: On the Recovery Process of Cold Worked Metals 90
———: On the Plastic Deformation Copper Single Crystals, Part I. Two Stages in the Progress of Deformation........ 454
———: On the Plastic Deformatin of Copper Single Crystals, Part II. Recovery Process and Mean Length of Dislocations........ 456
KATO Kiyoe;
S. KOJIMA and ———: The Noise of Decaying Electrets........ 207

KATO Norio: Accurate Measurement of Lattice Constant by Means of Electron Diffraction. Lattice Constant of KCl Referred to Au 502

KAWADA Tomoyosi: On the Plastic Deformation of Zinc Bicrystal, I 363

————: On the Plastic Deformation of Zinc Bicrystal, II 485

KAWAGUCHI Mitsutoshi: Application of the M^2-expansion Method to the Compressible Flow past an Elliptic Cylinder 168

KAWAI Heiji;

N. TOKITA and ————: Young's Modulus and Internal Friction of Polyvinyl-alcohol 367

KAWAMURA Hazimu;

M. ONUKI and ————: On the Noise of Pre-Breadknown Current 283

KAWAMURA Ryuma: On the Mach Reflection of Shock Wave 533

KIHARA Taro: Determination of Intermolecular Forces from the Equation of State of Gases, II. 184

————: The Second Virial Coefficient of Non-Spherical Molecules 289

KIMURA Ituro;

S. KUMAGAI and ————: Effect of Turbulence on Flame Propagation in Gases ... 197

KIMURA Motoharu: On the Temperature Effects of Spurious Counts in Geiger-Muller Counters 141

KISHIMOTO Akira;

H. FUJITA and ————: A Method for Determining the Concentration Dependence of Diffusion Coefficient 408

KITA Isao;

G. FUJIOKA, ———— and O. MINAKAWA: On the Analysis of Quenching Circuit for Slow Counters 95

————: On the Discharge Mechanism of Slow Counter 99

G. FUJIOKA, ———— and O. MINAKAWA: On the Temperature Effect of Geiger-Muller Counter 103

KOBAYASI Akio

———— and S. FURUYA: Reactions of Barium Film with Oxygen, I, ... 238

———— and H. HINO; Effect of Firing Temperature on the Dielectric Properties of Barium Titanate Ceramics 371

KOJIMA Shoji;

———— and K. KATO: The Noise of Decaying Electrets 207

KOMATSU Hachiro;

Y. KAKIUCHI, ———— and S. KYOYA: Proton Conduction through Solid Alcohols due to Molecular Rotation 321

KOMATSU Kozo;

———— and T. NAGAMIYA: Theory of Specific Heat of Graphite 435

KRZYWOBLOCKI. M. Z. V.: On the Transformation of Chaplygin's Equation Into Fuchs-Frobenius Normal Form 452

KUBOTA Hiroshi: On Sensitive Color 67

————: On the Color of Chromatic Polarization 405

KUBOZOE Tadayoshi;

Y. WATASE, M. ODA, ———— and S HIGASHI: A Hodoscope Study on the Penetrating Shower 402

Y. WATASE, M. ODA, S. HIGASHI, and ————: A Study on the Extensive Air Shower 403

KUMAGAI Seiichiro;

———— and I. KIMURA: Effect of Turbulence on Flame Propagation in Gases 197

KURATA Michio;

T. MURAKAMI, S. ONO, M. TAMURA and ————: On the Theory of Surface Tension of Regular Solution 309

KUSUKAWA Kenichi: The Foundation of the Quantization of Turbulence 86

————: On the Theory of Shock Waves Produced in the Case, that by a Rigid Wedge Moving through the Elastic Medium with Supersonic Velocities 163

————: On the Theory of Shock Wave Produced by a Rigid Cone Moves through the Elastic Medium with Super-sonic Velocities 166

———: Discussion of the Spectrum of Turbulence 206
Y. WATASE, S. MIYAKE, K. SUGA, O. KUSUMOTO and ———: A High Pressure Cloud Chamber Observation of Cosmic Ray at 2740 m Elevation.................... 204
KUWAHARA Goro;
K. ISHIGURO and ———: Determination of the Optical Constants of Ag Films from the Measurements of Intensity and Phase Change I 71
K. ISHIGURO and ———: Determination of the Optical Constants of Ag Films from the Measurements of Intensity and Phase Change II. 76
KYOYA Susumu;
Y. KAKIUCHI, H. KOMATSU and ———: Proton Conduction through Solid Alcohols due to Molecular Rotation 321
MAEDA Seiziro: On the Magnetic After Effect due to the Irreversible Displacement of Domain Boundary (II) 60
———: On the Magnetic After-Effect due to the Irreversivle Displacement of Domain Boundary (III) 494
MATSUDA Shoichi: On the Superlattice Formation in Binary Alloys of Body Centred Cubic Type 131
MATSUO Yuichi;
J. YAMAGUCHI, S. NAGATA and ———: An Electron Diffraction Study on Selenium Rectifiers 521
MINAKAWA Osamu;
G. FUJIOKA,I. KITA and : On the Analysis of Quenching Circuit for Slow Counters 95
G. FUJIOKA, I, KITA and———: On the Temperature Effect of Geiger-Muller Counter 103
MIYAMOTO Goro: On the Spiral Orbit Spectrometer with Two Converging Circles 68
MIYAKE S.;
Y. WATASE, ———, K. SUGA and O. KUSUMOTO: A High Pressure Cloud Chamber Observation of Cosmic Ray at 2740 m Elevation 204
MIYAZAWA Hisao;
——— and J. OKADA: On the Breakdown of Alumina at High Temperatures 55
MORINAGA Haruhiko: The Construction of a Small Linear Accelerator 210
MURAKAMI Terutosi;
——— S. ONO, M. TAMURA and M. KURATA: On the Theory of Surface Tension of Regular Solution 309
NAGAMIYA Takeo
K. KOMATSU and ———: Theory of Specific Heat of Graphite 438
NAGASU Hideo: Statistical Features in Static Friction 123
NAGATA; Saburo
J. YAMAGUCHI, ——— and Y. MATSUO: An Electron Diffraction Study on Selenium Rectifiers 521
——— and K. AGATA: On the Crystal Structure of Cadmium Selenide of Selenium Rectifier 523
NAKADA Osamu;
S. OKA and ———: On the Dielectric Loss in Polydisperse Polar Polymers 195
NAKAI Junkichi;
——— and S. NAKAMURA: On the Effect of Electrolytic Treatment of Ni-Sleeve on Electron Emission 532
NAKAI, Yoshio;
Y. UCHIDA, M. UETA and ———: Studies on the K Absorption Bank in the Colored Rock Salt Crystal 107
NAKAMURA Shogo;
——— and J. NAKAI: On the Effect of Electrolytic Treatment of Ni-Sleeve on Electron Emission 532
NARITA Shin-ichiro;
——— and T. ARIZUMI: On the Activation of the Oxide Coated Cathode 15
NISHIKAWA Tetsuji;
K. SHIMODA and ———: The Hyperfine Structure of Sodium by a Microwave Absorption Method 512

K. SHIMODA and ———: A Zeeman Modulation Microwave Spectrograph of High Sensitivity 516

NISHINO Minoru

——— and T. YAMAGUTI: A New Apparatus for Electric Arc Weldings........ 127

NISHIWAKI Jien: The Hight of the Water Column Produced by the Falling Ball........ 193

———: Resistance to the Penetration of a Bullet through an Aluminum Plate...... 374

———: Spark Photography Employing the Mach Switch........ 539

———: The Plastic Deformation of the Copper Cylinder under the Powder Pressure... 538

NOGA Ken-ichi: Thermo-electromotive Force of BaO and (Ba-Sr)O 124

NOGAMI Yozo;

M. SAKAI and ———: On the Form of Pole Pieces used in New Spiral Orbit Spectrometer 409

NOMURA Shoichiro;

——— and S. SAWADA: Dielectric and Thermal Properties of Barium-lead Titanates 36

——— and S. SAWADA: On the Ferroelectric Behaviors of Sodium Vanadate...... 192

NONAKA Itaru;

———, S. HIRASAWA and K. TSUTSUMI: A New Method of Measuring the Ion Current of Mass Spectrometers 566

ODA Minoru;

——— and T. TAKAKURA: A Study of the Solar Noise at 3300 m.c. 202

Y. WATASE, ———, S. HIGASHI and T. KUBOZOE: A Study on the Extensive Air Shower 403

Y. WATASE, ———, T. KUBOZOE and T. HIGASHI: A Hodoscope Study on the Penetrating Shower 402

ODA Yukiyasu;

———, J. SANADA and S. YAMANE: Angular Distribution of 3.1 Mev Neutrons Scattered by Proton 153

OGUCHI Takehiko: Statistics of the Three-Dimensional Ferromagnet (II) 27

———: Statistics of the Three-Dimensional Ferromagnet (III)........ 31

———: The Short Range Orders in Cu_3Au 499

OHKAWA Tihiro: A Proposal on the Measurement of the Recoil Spectrum using Gas Source 197

OKA Syoten;

——— and O. NAKADA: On the Dielectric Loss in Polydisperse Polar Polymers...... 195

OKADA Jun-ichi;

H. MIYAZAWA and ———: On the Breakdown of Alumina at High Temperatures... 55

OKAZAKI Atsuyoshi: Faraday Effect of Strong Electrolytes in Aqueous Solution IX. The Temperature Dependence of the Molecular Rotation Constants, 1 138

OKAZAKI Chisato;

———and T. SUITA: Electric Conduction in Ionic Crystals (Part I) 200

OOKAWA Akiya: Crystallization and Melting of Linear High Polymers as Rate Processes 473

ONO Mitsuo: On the Deviation from the Ohm's Law at the Anode Surface of the Cuprous Oxide Rectifiers........ 397

ONO Syû: Statistical Mechanics of Adsorption from Multicomponent System I........ 10

T. SATO and ———: A Note on the Hole Theory of Liquid 410

T. MURAKI, ———, M. TAMURA and M. KURATA: On the Theory of Surface Tension of Regular Solution 309

ONUKI Masami;

——— and H. KAWAMURA: On the Noise of Pre-Breakdown Current 283

OSADA Kikusaburo: The Ultraviolt Absorption Spectra of Glasses 191

OSAWA Makoto;

——— and I. SUGIURA: On the Distribution of Internal Stresses of Permalloy Subjected to field Cooling 530

OURA Hirobumi: On the Band-System of Neutral OD 401

OZAWA YASUTOMO;

——— and K. HIGASI: On high the Frequency Power Loss of Dielectrics........ 280

SAJI Yoshio;

B. ARAKATSU, M. SONODA, Y. UEMURA, S. YASUMI and ———: The Photo-

disintegration of Be by the High Energy γ-rays 66
SAKURAI Tosio: On the Transformation of Long Chain Acid Amides 199
SAITÔ Nobuhiko: An Interpretation of the Dielectric Loss due to the Rotation of Dipoles... 201
———: The effect of the Brownian Motion on the Viscosity of Solutions of Molecules, I. Ellipsoid of Revolution 297
———: The Effect of the Brownian Motion on the Viscosity of Solution of Macro-molecules, II. Rigid Chain Molecules 302
——— and Y. IKEDA: The Light Scattering by Non-Spherical Particles in Solutions... 530
SAKAI Mitsuo: Sur le Spectrometre a Orbites Spirales Sans Fer 529
——— and Y. NOGAMI: On the Form of Pole Pieces used in New Spiral Orbit Spectrometer 409
SANADA Jumpei:
Y. ODA, ——— and S. YAMABE: Angular Distribution of 3.1 Mev Neutrons Scattered by Proton........ 153
SATO Hiroshi;
——— and H. YAMAMOTO: The Behaviors of Fe-Al, Fe-Si and Fe-Al-Si Alloys Considered from the Standpoint of Ferromagnetic Superlattice 65
———: Experimental Study of the Spectrum of Isotropic Turbulence, I........ 387
SATŌ Katsuo
G. SHIRANE and ———: Effects of Mechanical Pressure on the Dielectric properties of Polycrystalline Barium-Strontium Titanate........ 20
SATO Masachiyo;
S. SUEOKA and ———: On the Stark Effect of Helium in Strong Electric Field (II) 444
SAITO Osamu: On Some Exact Solutions of the Two-Dimentional Steady Flow of Compressible Fluid 248
SATŌ Ryoitiro: Surface Oxidation of Zincblende Cleavage Face in the Roasting Atmosphere 527
———: Twin Formation of Zincblende through Oxidation-Reduction Process........ 528
SATŌ Takao: Notes on the Thermoelectric Properties of Bismuth........ 125
———: Some Properties of the Ni-Mn Alloys of Intermediate Composition (I) ... 223
SATO Tsugihiko;
——— and S. ONO: A Note on the Hole Theory of Liquid........ 410
SAWADA Shozo;
S. NOMURA and ———: Dielectric and Thermal Properties of Barium-Lead Titanates 36
——— and S. NOMURA: On the Ferroelectric Behaviors of Sodium Vanadate 192
SAWAGUSHI Etsuro;
———, G. SHIRABE and Y. TAKAGI: Dielectric Properties of Lead Zirconate 208
———, G, SHIRANE and Y. TAKAGI: Phase Transition in Lead Zirconate........ 333
SEKI Yoshinobu: A New type of Striation Observed in an Electronmicrograph........ 534
SEKIGUCHI Masaji: Morphological Anomaly of the Crystals of Mercury Fulminat 541
SHIMAZU Jitsuo: Emisson and Crystal Size of Oxide-Coated Cathodes 479
SHIMBO Sotoshi;
Y. WADA and ———: Correlation between Ultrasonic and Infrared Absorption in Liquids 435
SHIMODA Koichi: Mode Conversion Losses in a TE_{10} Type Cavity Resonator with Tilted End-Plate........ 378
——— and T. NISHIKAWA: The Hyperfine Structure of Sodium by a Microwave Absorption Method 512
——— and T. NISHIKAWA: A Zeeman Modulation Microwave Spectrogroph of High Sensitivity 516
SHINDO Takuzo: Space Charge Effect in the Oxide Cathode Layer........ 352
SHINODA Gunji;
——— and T. TOMURA: Improved Counting Rate Meter for X-Ray Measurement... 148
——— and Y. AMANO: Mechanism of Precipitation of α from β in 60:40 Brass... 508
SHIOTA Nobuo;
——— and H. IWAMURA: On Sub-boundary Structue of Aluminum........ 227
SHIRANE Gen;

——— and K. SATO: Effects of Mechanical Pressures on the Dielectric Properties of Polycrystaline Barium-Strontium Titanate 20
——— and A. TAKEDA: Volume Change at Three Transitions in BaTiO$_3$ Ceramics... 128
———, E. SAWAGUCHI and Y. TAKAGI: Dielectric Properties of Lead Zirconate...... 208
——— and S. HOSHINO: On the Phase Transition in Lead Titanate 265
——— and K. SUZUKI: On the Phase Transition in Barium-Lead Titanate (I)...... 274
——— and A. TAKEDA: On the Phase Transition in Barium-Lead Titanate (II)... 329
——— and E. SAWAGUCHI and Y, TAKAGI: Phase Transition in Lead Zirconate. ... 333
SONODA Masateru:
B. ARAKATSU, ———, Y. UEMURA, S. YASUMI and Y. SAJI: The Photodisintegration of Be by the High Energy γ-rays 66
SUEOKA Seiichi: On the Shape of Radio-Frequency Spectrum 281
——— and M. SATO: On the Stark Effect of Helium in Strong Electric Field (II) ... 444
SUGA K.:
S. MIYAKE, ——— Y. WATASE, and O. KUSUMOTO: A High Pressure Cloud Chamber Observation of Cosmic Ray at 2740 m Elevation 204
SUGIMOTO Kenichi;
T. WAKATSUKI and ———: On the Scattering of Fast-Neutrons from Li-D Reactions 157
T. WAKATSUKI and ———: Errata: On the Scattering of Fast-Neutrons from Li-D Reactions 284
SUGIURA Ichiro;
M. OSAWA and ———: On the Distribution of Internal Stesses of Permalloy Subjected to Field Coolling 530
SUGIYAMA Akira: Note on the Kinetic Energy of the Bloch Wall........ 524
SUITA Tokuo;
C. YAMANAKA and ———: Current Noise a Dielectric Breakdown in Alkalihalide Crystals 194
C. OKAZAKI and ———: Electric Conduction in Ionic Crystals (Part I)........ 200
———: Dielectric Breakdown in Mixed Crystals of KCl and AgCl 202
SUWA Shigeki: Anomalous Hyperfine Structure in the Spectrum of Al. II........ 231
SUZUKI Hideji: On the Grain Boundary Migration Induced by Temperature Gradient...... 522
SUZUKI Kazuo;
G. SHIRANE and ———: On the Phase Transition in Barium-Lead Titanate (I)... 274
———: On the Phase Transition in Barium-Lead Titanate........ 340
TAKEDA Akitsu;
G. SHIRANE and ———: Volume Change at Three Transitions in BaTiO Ceramics 128
TAKAGI Riitsu: An Electron Microscope and Diffraction Study of Metallic Smoke 204
———: Electron Microscope and Diffraction Studies of Chromic Oxides........ 350
TAKAGI Yutaka;
G. SHIRANE, E. SAWAGUCHI and ———: Dielectric Properties of Zirconate 208
E. SAWAGUI, G. SHIRANE and ———: Phase Transition in Lead Zirconate 333
TAKAKURA Tatsuo;
M. ODA and ———: A Study of the Solar Noise at 3300 m. c........ 202
TAKEDA Akitsu;
G. SHIRANE and ———: On the Phase Transtion in Barium-Lead Titanate (II) 329
TAKEDA Masatami;
——— and E. TURUTA: Temperature Change of Intrinsic Viscocity of Polyvinyl Chloride 525
TAKAHATA Masaomi;
——— and S. YAMAGUCHI: On the Masses of Charged Particles of the Comic Radiation in Nuclear Emulsions........ 397
TAMURA Mikio;
T. MURAKAMI, S. ONO, ——— and M. KURATA: On the Theory of Surface Tension of Regular Solution 309
TANAKA Kenzo;
——— and H. HASHIMOTO: On the Anomalous Structures of Zinc Oxide........ 406
TOKITA Noboru:
——— and H. KAWAI: Young's Modulus and Internal Friction of Polyvinylalcohol 367

TOMURA Masao: Creep Phenomena of Selenium Rectifiers 357

TOMURA Teruichi;
 G. SHINODA and ———: Improved Counting Rate Meter for X-Ray Measurement 148

TSUKADA Kineo: The Iron Source of Electron Oscillation Type.. 415

TSUTSUMI Kazushige:
 I. NONAKA, S. HIRASAWA and ———: A New Method of Measuring the Iron Current of Mass Spectrometers.. 466

TUKIZI Osamu: The Electric Susceptibility of Water Drop due to Ionic Polarization...... 51

TURUTA Eiiti;
 M. TAKEDA and ———: Temperature Change of Intrinsic Viscosity of Polyvinyl Chloride 525

UCHIDA Yoichi;
 ———, M. UETA and Y. NAKAI: Studies on the K Absorption Band in the Colored Rock Salt Crystal 107

UEDA Ryuzo
 ——— and T. ICHINOKAWA: Effect of Stress on Domain Structure of Tungsten Trioxide WO$_3$.. 122
 ———: X-Ray Study on Phase Transition of Lead Zirconate, PbZrO$_3$ 209

UEMURA Yoshiaki;
 B. ARAKATSU, M. SONODA, ———, S. YASUMI and Y. SAJI: The Photo-disintegration of Be by the High Energy γ-rays 66

UETA Masayasu;
 ———, Y. UCHIDA and Y. NAKAI: Studies on the K Absorption Band in the Colored Rock Salt Crystal 107

WADA Yasaku;
 S. SHIMBO and ———: Correlation between Ultrasonic and Infrared Aborption in Liquids 535

WAKATSUKI Tetsuo;
 ——— and K. SUGIMOTO: Errata: On the Scattering of Fast Neutrons from Li-D Reactions 284

WATANABE Hiroshi: The Temperature Dependency of Magnetization of Ferrties on the Basis of the Theory of Ferromognetism 212

WATASE Yuzuru:
 ———,S. MIYAKE, K. SUGA and O. KUSUMOTO: A High Pressure Cloud Chamber Observation of Cosmic Ray at 2740 m Elevation 204
 ———, M. ODA, S. HIGASHI and T. KUBOZOE: A Study on the Extensive Air Shower 403
 ———, M. ODA, T. KUBOZOE and S. HIGASHI: A Hydoscope Study on the Penetrating Shower 402

YAMABE Shotaro;
 Y. ODA, J. SANADA and ———: Angular Distribution of 3.1 Mev Neutrons Scattered by Proton 153

YANAGUCHI Jiro:
 ——— S. NAGATA and Y. MATSUO: An Electron Diffraction Study on Selenium Rectifiers 521

YAMAGUCHI Seitaro;
 ——— and M. TAKAHATA: On the Masses of Charged Particles of the Cosmic Radiation in Nuclear Emulsions 397

YAMAGUTI Tasaburo;
 ——— and M. NISHINO: A New Apparatus for Electric Arc Weldings 127

YAMAMOTO Hisao;
 ——— and H. SATO: The Behaviors of Fe-Al, Fe-Si and Fe-Al-Si Alloys Considered from the Standpoint of Ferromagnetic Superlattice 65

YAMAMURO Nobuhiro: Isotope Separation by Radiofrequency Electric Field 411

YAMANAKA Chiyoe;
 ——— and SUITA: Current Noise and Dielectric Breakdown in Alkalihalide Crystals 194

YASUMI Shinjiro;
 B. ARAKATSU, M. [SONODA, Y. UEMURA, ——— and Y. SAJI: The Poto-

disintegration of Be by the High Energy γ-rays 66

YOKOBORI Takeo: Delayed Fracture in Creep of Copper 78

———: Fatigue Fracture of Steel 81

———: On the Rate of the Nucleation in the Recrystallization 404

YOKOTA Ryosuke: On the Structure of Silicate Glasses 489